

Jürgen Beyerer  
Fernando Puente León  
Christian Frese

---

# Machine Vision

Automated Visual Inspection:  
Theory, Practice and Applications

 Springer

# Machine Vision

Jürgen Beyerer • Fernando Puente León  
Christian Frese

# Machine Vision

Automated Visual Inspection:  
Theory, Practice and Applications

 Springer

Jürgen Beyerer  
Fraunhofer-Institut für Optronik,  
Systemtechnik und Bildauswertung  
and Karlsruhe Institute of Technology  
Karlsruhe, Germany

Christian Frese  
Fraunhofer-Institut für Optronik,  
Systemtechnik und Bildauswertung  
Karlsruhe, Germany

Fernando Puente León  
Karlsruhe Institute of Technology  
Karlsruhe, Germany

Translator: Johannes Meyer

ISBN 978-3-662-47793-9      ISBN 978-3-662-47794-6 (eBook)  
DOI 10.1007/978-3-662-47794-6

Library of Congress Control Number: 2015947141

Springer

© Springer-Verlag Berlin Heidelberg 2016

This work is subject to copyright. All rights are reserved by the Publisher, whether the whole or part of the material is concerned, specifically the rights of translation, reprinting, reuse of illustrations, recitation, broadcasting, reproduction on microfilms or in any other physical way, and transmission or information storage and retrieval, electronic adaptation, computer software, or by similar or dissimilar methodology now known or hereafter developed.

The use of general descriptive names, registered names, trademarks, service marks, etc. in this publication does not imply, even in the absence of a specific statement, that such names are exempt from the relevant protective laws and regulations and therefore free for general use.

The publisher, the authors and the editors are safe to assume that the advice and information in this book are believed to be true and accurate at the date of publication. Neither the publisher nor the authors or the editors give a warranty, express or implied, with respect to the material contained herein or for any errors or omissions that may have been made.

Printed on acid-free paper

Springer is a brand of Springer Fachmedien Wiesbaden  
Springer Berlin Heidelberg is part of Springer Science+Business Media  
([www.springer.com](http://www.springer.com))

*Dedicated to Professor Dr.-Ing. Franz Mesch*

## Preface

Machine vision and automated visual inspection are domains of automation technology with a steadily increasing economical relevance. Although the related industry is notably expanding since the past two decades, only a part of today's visual inspection tasks have been automated. This is why there is a great potential for economization in high income countries which may lead to both reduced costs and increased quality of the produced goods.

As visual perception is the main human sensation, the automation of visual inspection is somehow fascinating—at least for the authors of this book. When talking about the automation of visual inspection one might easily think that it cannot be that hard to teach a technical visual inspection system to perceive what a human can easily see with only a glimpse. Actually, users often state: 'As humans can see that instantly, it can't be that hard to achieve the same using a machine'. The answer is not easy at all but it depends on the individual case: for humans, some things represent easy tasks which however are difficult to automate—on the contrary, many other things can be done more precisely and particularly more reliably by machines, if an automation is possible.

Automated visual inspection is a complex and multi-disciplinary topic involving optics, mechanical and electrical engineering, mathematics and computer science. Systems for automated visual inspection are usually more or less complex mechatronic systems, which can only achieve the requested performance in an economical way, if all the necessary disciplines collaborate.

Everything starts with a visual inspection task that is to be carried out using an automated approach. In this context, image acquisition plays an important role: loss of information during that step can hardly be compensated during later image processing steps. The success of a visual inspection solution depends heavily on the quality of this first step.

Fortunately, when designing an automated visual inspection system, one usually has the benefit of several degrees of freedom, in order to obtain image data with sufficient quality and significance. This is why the suitability of the image acquisition for a given problem at least partly depends on the engineer. In order to exploit those degrees of freedom at the best, this book draws particular attention to image acquisition and the acquisition constellation, consisting of the test object, the illumination and the acquisition system.

This book has the ambition to thoroughly introduce the reader into the terms of automated visual inspection. For this purpose, the Chapters 2 to 6 of the book's first part deal with the physics of image formation and the required optical principles and techniques in an adequately extensive way. Based on that foundations, image acquisition for automated visual inspection will be treated in Chapter 7. In this key chapter, a multitude of different techniques for image acquisition will be explained in a systematic way, as well as important hints and tricks will be shown which are indispensable for a good visual inspection system.

In order to enable automated analysis of images in a computer, the analog image signals have to be transformed into digital signals. The underlying theory of signal processing and the effects of local sampling and quantization will be extensively discussed, especially in terms of system theory. Among others, Chapter 8 is devoted to the basics of digital processing of analog signals and prepares the reader for the second part of the book, which focuses on image analysis. Chapters 9 to 15 cover methods, which form the individual steps leading to a final inspection result based on the acquired image data.

The depth of the explanations of all covered subjects is chosen to provide the reader with insight into the respective motivation and backgrounds. No facts are supposed 'to appear from nowhere'; the underlying concepts should be thoroughly understood. Some theorems however will not be proven in a strict mathematical way. In fact, there will be sketches of the proofs, which will present their essential idea and help to understand important concepts. For an application-oriented reader who is nevertheless interested in what happens behind the scenes, consciously omitting technically flawlessly led proofs increases the book's readability and leads to a handy amount of pages.

The book on hand is partially based on lectures held by the author J. Beyerer at the Karlsruhe Institute of Technology (KIT, formerly University of Karlsruhe) since 1994 and by the author F. Puente León, initially at Technische Universität München (TUM) since 2003 and at KIT since 2008. It addresses itself to students studying in the fields of engineering science, computer science, physics and mathematics. As all needed concepts and methods are introduced in a sufficiently exhaustive way, it should be possible for advanced bachelor students to clearly understand the presented content. Furthermore, scientists, PhD students and especially master students dealing with automated visual inspection can profit from reading the book as its topics are appropriately elaborated.

Besides theory, practice is not missed out. The authors' industrial experience, which is incorporated into many topics of the book, brings benefits even to practically oriented readers who seek for robust and economic solutions for concrete visual inspection tasks. Nonetheless, the book does not lose itself into superficial recipes but yields enough substance for a deep understanding of the presented content.

The authors want to particularly thank their following colleagues for supporting them in the creation of this book:

- Dr. Ulrich Breitmeier (Breitmeier Messtechnik GmbH, Ettlingen, Germany) for an example image of a cylindrical scanner
- Dr. Michael Fried (University of Erlangen, Germany) for an example of the Mumford-Shah-Method
- Dr. Jan Horn (Department of Measurement and Control, Karlsruhe Institute of Technology) for an image of camera based velocity measurement
- Dr. Udo Netzelmann and Dr. Günter Walle (Fraunhofer IZFP, Saarbrücken, Germany) for example images of the impulse thermography
- Arne Nowak (Fraunhofer IIS, Erlangen, Germany) for example images acquired with the POLKA camera
- Dirk Nüßler (Fraunhofer FHR, Wachtberg, Germany) for example images of inspection using terahertz radiation
- Prof. Dr. Wolfgang Osten (University of Stuttgart, Germany) for images of interferometric methods
- Prof. Dr. Jerry L. Prince (Johns Hopkins University, Baltimore, USA) for examples of active contours
- Dr. Andreas Purde (Institute for Measurement Systems and Sensor Technology, TUM, Germany) for an example for the pyramid linking method
- Dr. Anna Remelli and Dr. Claudio Sedazzari (Opto Engineering, Mantova, Italy) for examples of the hypercentric perspective
- Dr. Norman Uhlmann (Fraunhofer EZRT, Fürth, Germany) for example images of X-ray inspection

- Bernhard Schmitt M.A. (ONUK, Karlsruhe, Germany) for an aerial photograph of the Karlsruhe Palace
- Dirk vom Stein and Thomas Winkel (Inspectomation GmbH, Mannheim, Germany) for example images showing the inspection of casting cores and brake discs as well as telecentric images
- Dr. Marco Kruse (Institute of Industrial Information Technology IIIT, Karlsruhe Institute of Technology KIT) for the image of the checkerboard-shadow illusion as well as for example images concerning the restoration of uniform motion blur
- Mario Lietz (IIIT, KIT) for example images showing the division by a reference image
- Dr. Ioana Gheța (Vision and Fusion Laboratory IES, Institute for Anthropomatics, Karlsruhe Institute of Technology) for examples concerning the analysis of spectral image series
- Dr. Robin Gruna (IES, KIT) for images recorded with inverse illumination
- Dr. Matthias Michelsburg (IIIT, KIT) and Dr. Robin Gruna for hyperspectral images of food
- Thomas Stephan (IES, KIT) for images recorded with a light-field camera and for examples showing the restoration of participating media
- Dr. Matthias Hartrumpf (Fraunhofer Institute for Optronics, System Technologies and Image Exploitation IOSB, Karlsruhe, Germany) for example images showing photoelasticity and the inspection of glass preforms
- Prof. Dr. Michael Heizmann (Fraunhofer IOSB) for examples of texture analysis as well as shape from shading
- Christian Negara (Fraunhofer IOSB) for examples of the graph cut method
- Johannes Pallauf (IIIT, KIT) for the example of image restoration for uniform motion blur
- Günter Saur and Wolfgang Roller (Fraunhofer IOSB) for supplying TerraSAR-X images
- Günter Struck and Dr. Kai-Uwe Vieth (Fraunhofer IOSB) for examples of fluorescence spectroscopy
- Chen-Ko Sung (Fraunhofer IOSB) for example images of inspection based on flatbed scanners
- Dr. Stefan Werling (Fraunhofer IOSB) for deflectometric images
- Dr. Alexander Schwarz and Martina Richter (Fraunhofer IOSB) for images showing an example BRDF measurement
- Dr. Miro Taphanel (IES, KIT) for images concerning the CCT sensor
- Johannes Meyer (IES, KIT) for example images acquired with a Schlieren setup
- Dr. Yaokun Zhang (IPR, KIT) and Johannes Meyer (IES, KIT) for example OCT images

Special thanks go to Johannes Meyer (IES, KIT) for the incorporation of numerous extensions into the German version of this book ('Automatische Sichtprüfung') and for translating it into English. A big contribution to the contents presented in this book has been made especially by Dr. Stefan Werling, Dr. Christoph Lindner, Dr. Ana Pérez Grassi, Dr. Robin Gruna, Sebastian Höfer and Dr. Michael Teutsch by assisting the mentioned lectures. The authors would like to also thank all the students who were involved in creating images and diagrams. In addition, numerous students have sent in valuable suggestions for improving the book's didactic component.

Special thanks are directed to Andrey Belkin, Yvonne Fischer, Peter Frühberger, Dr. Robin Gruna, Jan Hendrik Hammer, Pilar Hernández Mesa, Christian Herrmann, Sebastian Höfer, Chettapong Janya-Anurak, Mahsa Mohammadi Kaji, Dr. Marco Kruse, Achim



Kuwertz, Ding Luo, Thomas Nürnberg, Dr. Alexey Pak, Johannes Pallauf, Julius Pfrommer, Chengchao Qu, Matthias Richter, Masoud Roschani, Lars Sommer, Thomas Stephan, Dr. Miro Taphanel, Dr. Michael Teutsch, Sebastian Vater, Markus Vogelbacher, Dr. Stefan Werling, Philipp Woock and Mathias Ziebarth for valuable comments and proofreading of the manuscript. Finally we would like to thank our publisher Springer for the excellent cooperation.

Karlsruhe, Summer 2015

*Jürgen Beyerer*  
*Fernando Puente León*  
*Christian Frese*

## Contents

<b>1 Introduction</b>	<b>1</b>
1.1 Visual inspection . . . . .	3
1.2 Optical capturing of test objects . . . . .	7
1.3 Formation and definition of an image . . . . .	9
1.4 Machine vision . . . . .	10
1.5 Practical approach for performing machine vision projects . . . . .	15
1.6 Bibliography . . . . .	16
<b>I Image Acquisition</b>	<b>19</b>
<hr/>	
<b>2 Light</b>	<b>21</b>
2.1 The phenomenon of light . . . . .	23
2.1.1 The electromagnetic spectrum . . . . .	23
2.2 Light as an electromagnetic wave . . . . .	24
2.2.1 Maxwell's equations . . . . .	24
2.2.1.1 Wave equations of the electric field . . . . .	26
2.2.2 Polarization . . . . .	31
2.2.2.1 The polarization ellipse . . . . .	31
2.2.2.2 Stokes parameters . . . . .	33
2.2.2.3 The Poincaré sphere . . . . .	35
2.2.2.4 Mueller matrices . . . . .	36
2.2.2.5 Measuring the polarization state . . . . .	41
2.2.2.6 The Jones calculus . . . . .	42
2.2.3 Huygens' principle . . . . .	44
2.2.4 Coherence . . . . .	44
2.2.5 Interference . . . . .	46
2.2.6 Diffraction . . . . .	48
2.2.6.1 Resolution of imaging systems . . . . .	58
2.2.7 Speckle . . . . .	60
2.3 Light as a quantum phenomenon . . . . .	61
2.4 The ray model of geometrical optics . . . . .	65
2.5 Summary . . . . .	66
2.6 Interaction of light and matter . . . . .	66
2.6.1 Absorption . . . . .	67
2.6.2 The law of reflection . . . . .	67
2.6.3 The law of refraction . . . . .	68
2.6.4 Scattering . . . . .	70
2.6.5 The Fresnel coefficients for reflection and transmission . . . . .	71
2.6.6 Electromagnetic waves in conductive media . . . . .	76
2.6.6.1 Complex index of refraction . . . . .	77

2.7	Light sources . . . . .	80
2.7.1	Thermal radiators . . . . .	80
2.7.1.1	Physical principles . . . . .	80
2.7.1.2	Incandescent lamps and halogen lamps . . . . .	81
2.7.2	Gas-discharge lamps . . . . .	83
2.7.3	Light-emitting diodes . . . . .	86
2.7.4	Laser . . . . .	89
2.7.5	Summary . . . . .	93
2.8	Bibliography . . . . .	93
<b>3</b>	<b>Optical Imaging</b> . . . . .	<b>97</b>
3.1	Introduction . . . . .	99
3.2	Imaging with a pinhole camera, central projection . . . . .	100
3.3	The camera model and camera calibration . . . . .	103
3.4	Optical imaging using a single lens . . . . .	106
3.4.1	The paraxial approximation and Gaussian optics . . . . .	107
3.4.2	Thin lens equation . . . . .	108
3.4.3	Bundle limitation . . . . .	114
3.4.4	Depth of field . . . . .	117
3.4.5	Telecentric imaging . . . . .	123
3.4.5.1	Defocused telecentric imaging . . . . .	124
3.4.5.2	Double-sided telecentric systems . . . . .	125
3.4.6	Perspective . . . . .	125
3.4.7	Imaging of tilted planes . . . . .	128
3.4.8	Aberrations . . . . .	133
3.4.8.1	Seidel aberrations of spherical lenses . . . . .	133
3.4.8.2	Chromatic aberration . . . . .	136
3.5	Optical instruments with several lenses . . . . .	137
3.5.1	The projector . . . . .	137
3.5.2	The microscope . . . . .	138
3.6	Bibliography . . . . .	140
<b>4</b>	<b>Radiometry</b> . . . . .	<b>143</b>
4.1	Radiometric quantities . . . . .	145
4.2	The light field of a test object . . . . .	150
4.3	The bidirectional reflectance distribution function (BRDF) . . . . .	152
4.3.1	BRDF and scattered light . . . . .	155
4.4	Formation of image values . . . . .	157
4.4.1	Application to a thin lens . . . . .	157
4.5	Bibliography . . . . .	160
<b>5</b>	<b>Color</b> . . . . .	<b>163</b>
5.1	Photometry . . . . .	165
5.2	Color perception and color spaces . . . . .	167
5.2.1	Color perception of the human eye . . . . .	167

5.2.2	Color mixing . . . . .	171
5.2.3	CIE color spaces . . . . .	173
5.2.4	Spectrophotometry for color measurement and color distance computation	185
5.2.5	Color order systems . . . . .	191
5.2.6	Other color spaces . . . . .	192
5.2.6.1	Gamma correction . . . . .	192
5.2.6.2	RGB color spaces . . . . .	193
5.2.6.3	HSI and HSV . . . . .	195
5.2.6.4	YUV and $Y C_B C_R$ . . . . .	196
5.2.6.5	Color printing and CMYK . . . . .	197
5.3	Filters . . . . .	198
5.4	Acquisition and processing of color images . . . . .	199
5.5	Bibliography . . . . .	201
<b>6</b>	<b>Sensors for Image Acquisition</b>	<b>203</b>
6.1	Point, line and area sensors . . . . .	205
6.2	Image tube cameras . . . . .	206
6.3	Photomultipliers . . . . .	206
6.3.1	Image intensifiers . . . . .	207
6.4	Photodiodes . . . . .	207
6.5	Position sensitive detectors (PSD) . . . . .	210
6.6	Charge-coupled device (CCD) . . . . .	211
6.7	Complementary metal-oxide-semiconductor (CMOS) sensors . . . . .	213
6.8	Line-scan cameras . . . . .	215
6.9	Color sensors and color cameras . . . . .	215
6.10	Infrared cameras . . . . .	216
6.10.1	Bolometer cameras . . . . .	217
6.10.2	Infrared quantum detector cameras . . . . .	217
6.11	Quality criteria for image sensors . . . . .	219
6.12	Bibliography . . . . .	220
<b>7</b>	<b>Methods of Image Acquisition</b>	<b>223</b>
7.1	Introduction . . . . .	227
7.2	Measuring optical properties . . . . .	228
7.2.1	Measurement of the complex index of refraction . . . . .	230
7.2.1.1	Reflectometry . . . . .	230
7.2.1.2	Ellipsometry . . . . .	234
7.2.2	Fluorescence . . . . .	240
7.2.3	Methods for measuring the reflectance . . . . .	242
7.2.3.1	Diffuse illumination . . . . .	242
7.2.3.2	Bright-field illumination . . . . .	243
7.2.3.3	Dark-field illumination . . . . .	244
7.2.3.4	Laser scanners . . . . .	246
7.2.3.5	Flatbed scanners . . . . .	248

7.2.4	Spectral sensors . . . . .	248
7.2.5	Light scattering methods and the inspection of surface roughness . . . . .	251
7.3	3D shape capturing . . . . .	254
7.3.1	Triangulation (point-by-point scanning) . . . . .	255
7.3.2	Light-section methods (line scanning) . . . . .	259
7.3.3	The measurement uncertainty of triangulation . . . . .	260
7.3.4	Structured illumination . . . . .	263
7.3.4.1	Stripe projection . . . . .	264
7.3.5	Deflectometry . . . . .	268
7.3.5.1	Open research questions regarding deflectometry . . . . .	276
7.3.6	The moiré method . . . . .	276
7.3.6.1	The moiré effect . . . . .	276
7.3.6.2	Mathematical model of the moiré effect . . . . .	278
7.3.6.3	Telecentric stripe projection . . . . .	279
7.3.6.4	Shadow moiré . . . . .	283
7.3.6.5	Projection moiré . . . . .	284
7.3.7	Final remark on structured illumination . . . . .	285
7.3.8	Stereo images . . . . .	285
7.3.8.1	Derivation of the fundamental matrix . . . . .	286
7.3.8.2	Stereo correspondence algorithms . . . . .	289
7.3.8.3	Stereo reconstruction . . . . .	290
7.3.8.4	Multi-camera systems . . . . .	290
7.3.8.5	Monocular stereo . . . . .	291
7.3.9	Light-field cameras . . . . .	291
7.3.10	Silhouette capturing . . . . .	296
7.3.10.1	Telecentric silhouette capturing . . . . .	298
7.3.10.2	Illumination for telecentric imaging . . . . .	298
7.3.10.3	Retroreflectors . . . . .	300
7.3.11	Shape from shading . . . . .	301
7.3.12	Autofocus sensors . . . . .	303
7.3.13	Confocal microscopy . . . . .	304
7.3.14	Confocal chromatic triangulation . . . . .	307
7.3.15	Time-of-flight sensors . . . . .	308
7.3.16	Phase-based methods . . . . .	309
7.3.16.1	Interferometry . . . . .	309
7.3.16.2	Speckle interferometry for material inspection . . . . .	314
7.3.16.3	Shearography . . . . .	315
7.3.16.4	Holography . . . . .	317
7.4	Capturing interior object structures . . . . .	320
7.4.1	Thermography . . . . .	321
7.4.2	Imaging using X-rays . . . . .	325
7.4.3	Optical coherence tomography . . . . .	330
7.4.4	Schlieren imaging and schlieren tomography . . . . .	331
7.4.5	Image acquisition using terahertz radiation . . . . .	332
7.4.6	Photoelasticity . . . . .	338

7.5	Special image acquisition methods . . . . .	344
7.5.1	Image acquisition systems with variable illumination direction . . . . .	348
7.5.2	Endoscopy . . . . .	349
7.6	Universal principles . . . . .	350
7.6.1	Suppression of extraneous light . . . . .	350
7.6.2	Inverse illumination . . . . .	351
7.7	Summary . . . . .	356
7.8	Bibliography . . . . .	358

**II Image Processing**

<b>8</b>	<b>Image Signals</b> . . . . .	<b>369</b>
8.1	Mathematical model of image signals . . . . .	373
8.2	Systems and signals . . . . .	374
8.2.1	System characteristics . . . . .	374
8.2.2	The Dirac delta function . . . . .	378
8.2.2.1	Definition of the Dirac delta function . . . . .	378
8.2.2.2	Characteristics of the Dirac delta function . . . . .	379
8.2.3	Convolution . . . . .	381
8.3	The Fourier transform . . . . .	383
8.3.1	The one-dimensional Fourier transform . . . . .	383
8.3.1.1	Definition of the Fourier transform . . . . .	383
8.3.1.2	Properties of the Fourier transform . . . . .	384
8.3.1.3	Fourier transforms of selected functions . . . . .	390
8.3.2	The one-dimensional sampling theorem . . . . .	393
8.3.3	The discrete Fourier transform (DFT) . . . . .	396
8.3.3.1	Definition of the DFT . . . . .	396
8.3.3.2	Properties of the DFT . . . . .	397
8.3.3.3	Spectral leakage . . . . .	398
8.3.3.4	The fast Fourier transform (FFT) . . . . .	400
8.3.3.5	The convolution theorem of the DFT . . . . .	401
8.3.4	The two-dimensional Fourier transform . . . . .	401
8.3.4.1	Definition of the two-dimensional Fourier transform . . . . .	401
8.3.4.2	Properties of the two-dimensional Fourier transform . . . . .	403
8.3.5	Dirac delta functions in two-dimensional space . . . . .	407
8.3.6	The two-dimensional Heaviside function . . . . .	409
8.3.7	Sampling of two-dimensional signals . . . . .	409
8.3.8	Sampling theorem for two-dimensional signals . . . . .	413
8.3.9	The two-dimensional DFT . . . . .	414
8.3.9.1	Calculation of the 2-D DFT in practice . . . . .	416
8.3.9.2	The convolution theorem of the 2-D DFT . . . . .	417
8.3.9.3	The meaning of magnitude and phase . . . . .	417
8.3.9.4	Examples of the two-dimensional DFT . . . . .	418
8.4	Examples of use concerning system theory and the Fourier transform . . . . .	425

8.5	Image signals as stochastic processes . . . . .	432
8.5.1	Moments of stochastic processes . . . . .	433
8.5.2	Stationarity and ergodicity . . . . .	436
8.5.3	Passing a stochastic process through an LSI system . . . . .	440
8.6	Quantization . . . . .	445
8.6.1	Optimal quantization . . . . .	446
8.6.2	The quantization theorem . . . . .	448
8.6.3	Modeling of the quantization . . . . .	453
8.7	The Karhunen–Loève transform . . . . .	455
8.7.1	Definition of the Karhunen–Loève transform . . . . .	456
8.7.2	Properties of the Karhunen–Loève transform . . . . .	457
8.7.3	Examples of application of the Karhunen–Loève transform . . . . .	460
8.8	Bibliography . . . . .	464
<b>9</b>	<b>Preprocessing and Image Enhancement</b> . . . . .	<b>465</b>
9.1	Simple image enhancement methods . . . . .	467
9.1.1	Contrast adjustment by histogram stretching . . . . .	467
9.1.2	Histogram manipulation . . . . .	469
9.1.3	Pseudo-color and false-color images . . . . .	472
9.1.3.1	Pseudo-color images . . . . .	472
9.1.3.2	False-color images . . . . .	473
9.1.4	Image sharpening . . . . .	474
9.2	Reduction of systematic errors . . . . .	476
9.2.1	Geometric rectification . . . . .	476
9.2.1.1	Bilinear interpolation . . . . .	478
9.2.1.2	Interpolation in the context of system theory . . . . .	479
9.2.2	Suppression of inhomogeneities . . . . .	480
9.2.2.1	Signal model . . . . .	480
9.2.2.2	Homogeneity . . . . .	481
9.2.2.3	Homomorphic filtering . . . . .	483
9.2.2.4	Homogenization . . . . .	485
9.3	Attenuation of random disturbances . . . . .	491
9.3.1	Linear filters . . . . .	491
9.3.1.1	Low-pass filters for noise reduction . . . . .	496
9.3.1.2	Moving average filter . . . . .	497
9.3.1.3	Cone low-pass filter . . . . .	500
9.3.1.4	Gaussian low-pass filter . . . . .	500
9.3.1.5	Ideal low-pass filters . . . . .	505
9.3.1.6	Constructing high-pass filters, band-stop filters, and band-pass filters from a given low-pass filter . . . . .	506
9.3.1.7	Excursus: The Z-transform . . . . .	506
9.3.2	Noise reduction using nonlinear filters . . . . .	509
9.3.2.1	The median filter . . . . .	509
9.3.2.2	Filters based on order statistics . . . . .	513
9.3.2.3	Bilateral filters . . . . .	514

9.4	Image registration . . . . .	515
9.5	Bibliography . . . . .	518
<b>10</b>	<b>Image Restoration</b>	<b>521</b>
10.1	Signal model . . . . .	523
10.2	Inverse filter . . . . .	527
10.3	The Wiener filter . . . . .	533
10.4	The geometric mean filter . . . . .	538
10.5	Optimal constraint filter . . . . .	540
10.6	Restoration problems in matrix notation . . . . .	543
10.7	Restoration for participating media . . . . .	546
10.8	Spatially-varying image restoration . . . . .	548
10.9	Bibliography . . . . .	549
<b>11</b>	<b>Segmentation</b>	<b>553</b>
11.1	Region-based segmentation . . . . .	556
11.1.1	Segmentation by feature-based classification . . . . .	556
11.1.2	Region growing methods . . . . .	562
11.2	Edge-oriented methods . . . . .	562
11.2.1	Gradient filters . . . . .	564
11.2.1.1	Construction of symmetric linear gradient filters . . . . .	566
11.2.1.2	Differentiation using the DFT . . . . .	568
11.2.1.3	Gradient-of-Gaussian filter . . . . .	570
11.2.1.4	Simple edge operators . . . . .	572
11.2.2	Edge detection using the second derivative . . . . .	572
11.2.3	The watershed transformation . . . . .	576
11.3	Diffusion filters . . . . .	578
11.3.1	Linear, homogeneous, isotropic image diffusion . . . . .	579
11.3.2	Linear, inhomogeneous, isotropic image diffusion . . . . .	580
11.3.3	Nonlinear, inhomogeneous, isotropic image diffusion . . . . .	581
11.3.4	Nonlinear, inhomogeneous, anisotropic image diffusion . . . . .	581
11.4	Active contours . . . . .	586
11.4.1	Gradient vector flow . . . . .	591
11.4.2	Vector field convolution . . . . .	593
11.5	Segmentation according to Mumford and Shah . . . . .	594
11.6	Segmentation using graph cut methods . . . . .	596
11.7	Bibliography . . . . .	604
<b>12</b>	<b>Morphological Image Processing</b>	<b>607</b>
12.1	Binary morphology . . . . .	609
12.1.1	Point sets and structuring elements . . . . .	609
12.1.2	Erosion and dilation . . . . .	611
12.1.2.1	Duality of erosion and dilation . . . . .	618



12.1.3	Opening and closing . . . . .	620
12.1.4	Border extraction . . . . .	623
12.1.5	Region filling . . . . .	624
12.1.6	Component labeling and connected component analysis . . . . .	624
12.1.7	The hit-or-miss operator . . . . .	626
	12.1.7.1 Thinning . . . . .	627
	12.1.7.2 Thickening . . . . .	629
12.1.8	Skeletonization . . . . .	630
12.1.9	Pruning . . . . .	632
12.2	Gray-scale morphology . . . . .	634
	12.2.1 The point set of a gray-scale image . . . . .	634
	12.2.2 Erosion and dilation . . . . .	636
	12.2.3 Opening and closing . . . . .	641
	12.2.4 Edge detection . . . . .	643
12.3	Bibliography . . . . .	645
<b>13</b>	<b>Texture Analysis</b> . . . . .	<b>649</b>
13.1	Types of textures . . . . .	652
	13.1.1 Structural texture type . . . . .	653
	13.1.2 Structural-statistical texture type . . . . .	653
	13.1.3 Statistical texture type . . . . .	654
13.2	Visual inspection tasks regarding textures . . . . .	655
13.3	Model-based texture analysis . . . . .	656
	13.3.1 Analysis of structural textures . . . . .	656
	13.3.2 Analysis of structural-statistical textures . . . . .	660
	13.3.3 Autoregressive models for analyzing statistical textures . . . . .	663
	13.3.4 Separation of line textures . . . . .	666
13.4	Feature-based texture analysis . . . . .	671
	13.4.1 Basic statistical texture features . . . . .	672
	13.4.2 Co-occurrence matrix . . . . .	673
	13.4.3 Histogram of oriented gradients . . . . .	676
	13.4.4 Run-length analysis . . . . .	677
	13.4.5 Laws' texture energy measures . . . . .	678
	13.4.6 Local binary patterns . . . . .	680
13.5	Bibliography . . . . .	681
<b>14</b>	<b>Detection</b> . . . . .	<b>685</b>
14.1	Detection of known objects by linear filters . . . . .	688
	14.1.1 Unknown background . . . . .	688
	14.1.2 White noise as background . . . . .	690
	14.1.3 Correlated, weakly stationary noise as background . . . . .	692
	14.1.4 Discrete formulation of the matched filter . . . . .	693
14.2	Detection of unknown objects (defects) . . . . .	697

- 14.3 Detection of straight lines . . . . . 699
  - 14.3.1 The Radon transform . . . . . 699
    - 14.3.1.1 Definition . . . . . 699
    - 14.3.1.2 The Fourier slice theorem . . . . . 702
    - 14.3.1.3 Efficient computation of the Radon transform . . . . . 703
  - 14.3.2 Detection of line-shaped structures . . . . . 706
    - 14.3.2.1 Signal-to-noise ratio (SNR) . . . . . 706
    - 14.3.2.2 Detection using correlation filters . . . . . 707
    - 14.3.2.3 Examples of applications . . . . . 707
  - 14.3.3 The Hough transform for the detection of lines . . . . . 710
  - 14.3.4 The Hough transform for the detection of curves . . . . . 711
  - 14.3.5 The generalized Hough transform . . . . . 714
  - 14.3.6 Implicit shape models . . . . . 715
- 14.4 Corner detection . . . . . 715
- 14.5 Bibliography . . . . . 717
- 15 Image Pyramids, the Wavelet Transform and Multiresolution Analysis** . . . . . 721
  - 15.1 Image pyramids . . . . . 723
    - 15.1.1 Gaussian pyramid . . . . . 725
    - 15.1.2 Laplacian pyramid . . . . . 726
    - 15.1.3 Pyramid linking . . . . . 727
  - 15.2 Wavelets . . . . . 728
    - 15.2.1 Continuous wavelet transform . . . . . 728
    - 15.2.2 Discretization of the wavelet transform . . . . . 731
  - 15.3 Multiresolution analysis . . . . . 733
  - 15.4 The fast wavelet transform . . . . . 738
  - 15.5 The two-dimensional wavelet transform . . . . . 742
  - 15.6 Scale-invariant features . . . . . 744
  - 15.7 Bibliography . . . . . 749

**III Appendix** **751**

- A Mathematical Foundations** . . . . . 753
  - A.1 The intercept theorem . . . . . 755
  - A.2 Inverse problems . . . . . 756
  - A.3 Bibliography . . . . . 757
- B The Fourier Transform** . . . . . 759
  - B.1 The one-dimensional Fourier transform . . . . . 761
    - B.1.1 Definition . . . . . 761
    - B.1.2 Properties and characteristics . . . . . 762
    - B.1.3 Correspondences . . . . . 763

B.2	The $n$ -dimensional Fourier transform . . . . .	765
B.2.1	Definition . . . . .	765
B.2.2	Correspondences of the two-dimensional Fourier transform . . . . .	765
B.3	The discrete Fourier transform . . . . .	766
	<b>List of Symbols</b>	769
	<b>List of Abbreviations</b>	785
	<b>Index</b>	789

Chapter 1  
**Introduction**

**1**

# 1

## 1 Introduction

1.1	Visual inspection . . . . .	3
1.2	Optical capturing of test objects . . . . .	7
1.3	Formation and definition of an image . . . . .	9
1.4	Machine vision . . . . .	10
1.5	Practical approach for performing machine vision projects . . . . .	15
1.6	Bibliography . . . . .	16

# 1 Introduction

Machine vision and automated visual inspection are rapidly finding their way into industrial measurement and quality control in the technical and engineering sectors. This development especially benefits from increasingly powerful computers and reasonably priced camera components.

This book provides insight into the fascinating and very up-to-date topic of automated visual inspection and image processing. An extensive content is presented in an easily comprehensible way and is explained using various examples. No particular previous knowledge is required.

## 1.1 Visual inspection

Nearly all industrially produced goods are more or less intensively visually inspected. Formerly, this task was either carried out by special personnel, appropriately trained for this, or by normal employees in addition to their usual duty. But ever since the 1970s, automated visual inspection systems have continued to spread in industry and related sectors, with double-digit percentage annual growth for decades.

Visual inspection means inspecting by looking. On the one hand, visual inspection is supposed to ensure specific quality characteristics of intermediate or final goods, and on the other hand, it can be used to detect and analyze variations of a manufacturing process.

The individual tasks of visual inspection can be divided into the following inspection categories:

- Completeness: Recognition of known objects, patterns
  - e.g., at an assembly site: are all components assembled?
  - e.g., charging: is the package filled completely?
  - e.g., assembly of circuit boards: have all components been placed?
- Correctness of position and orientation
  - e.g., at an assembly site: are all components at the right place and oriented correctly?
- Persistence of dimensions, shape and angles of components and tools
  - determination of measurements
  - are all necessary specifications and tolerance agreements fulfilled?
- Surface condition, texture
  - is the surface condition as intended?
  - is the surface homogeneous and does it meet the specific tolerance limits?
- Optical properties
  - color
  - reflection behavior
- Identification of materials
  - e.g., automated sorting of different synthetic materials
  - e.g., detecting and removing impurities from bulk goods streams (food, synthetic granulates, etc.)
- Defects: Both aesthetic and technical defects:
  - e.g., detection of varnish runs on varnished surface (aesthetic defect)
  - e.g., detection of scratches on optical components (technical defect)

Although the human visual system, consisting of eyes and brain, has numerous astonishing capabilities which nowadays cannot be provided by a machine with a competitive performance, visual inspection carried out by humans comes with some severe disadvantages. Among others, manual visual inspection is:

- monotonous,
- laborious,
- fatiguing,
- subjective,
- lacking in good reproducibility,
- costly to document in detail,
- too slow in many cases,
- expensive.

The automation of visual inspection promises relief. An adequate automated system works without fatigue, yields impartial and reproducible results, and allows a complete and detailed documentation.

It is not always reasonable to aim for a fully automated solution. Many successfully implemented visual inspection systems have technically solved the part of the task that can well be automated. Everything else, particularly what can be done especially well by a human, will be done manually and thus, a human–computer system is established, combining the strengths of technology with those of a human in a symbiotic way.

Possible examples are automated visual inspection systems detecting defects which are configured to be relatively sensitive, in order to ensure a high detection rate (i.e., the count of detected defects in relation to the actual amount of occurring defects), so that as few defects as possible remain undetected. Such a high detection sensitivity will inevitably lead to a high rate of false alarms (i.e., the detection of defects which actually are not present), which would lead to many discarded test objects. If those test objects that were potentially affected by a defect later undergo manual visual inspection by a human, a hybrid visual inspection system with different advantages has been created. On the one hand, the number of test objects which have to be inspected by a human are significantly reduced by employing the automated pretest, which will save labor costs. On the other hand, such a two-step procedure and the complementary strengths of technology and humans usually leads to a significantly increased quality of inspection.

Table 1.1 compares humans and technical visual inspection systems with respect to their sensor systems and data processing [11].

In contrast to technical visual inspection systems, the human visual system can easily be fooled when viewing optical illusions, which shows directly that the two systems work quite differently. The following example, which goes back to Adelson, shows the difficulties of humans in absolutely capturing two colors, here, two shades of gray [1].

For a human observer, it is hard to believe that the zones 'A' and 'B' of the checkerboard in Fig. 1.1 have the same gray value. But it can be verified quickly by covering the figure with a consistently colored piece of paper having holes at exactly the positions of the respective zones.

The checkerboard's digital image is represented by a matrix of gray values. A technical visual system would just compare the values corresponding to the two zones, notice their equality, and would not be fooled.

Table 1.1. Comparison of humans and machines with respect to their special abilities concerning visual inspection.

	Human visual system (eyes and brain)	Technical visual inspection system (image device and computer)
<b>Sensors:</b>	<ul style="list-style-type: none"> <li>- Low optical resolution;</li> <li>- Intensity values and dimensions cannot be captured absolutely as there is no geometric or radiometric standard;</li> <li>- Limited to visible light;</li> <li>- Spectral perception with three channels.</li> </ul>	<ul style="list-style-type: none"> <li>- High optical resolution;</li> <li>- Absolute intensity values and dimensions can be captured;</li> <li>- Light outside of the visible part of the spectrum can be used;</li> <li>- Multichannel spectral resolution is possible.</li> </ul>
<b>Image processing and analysis:</b>	<ul style="list-style-type: none"> <li>- Huge amount of parallel, highly interconnected, and slow neurons;</li> <li>- 'Programmed' by learning from examples.</li> </ul>	<ul style="list-style-type: none"> <li>- One or more powerful processors;</li> <li>- Algorithms usually need to be explicitly designed.</li> </ul>
<b>Special abilities:</b>	<ul style="list-style-type: none"> <li>- Experience and background knowledge;</li> <li>- Adaptability and learning aptitude;</li> <li>- Active vision by immediately varying the inspection setup (visual control loop);</li> <li>- Enormous cognitive capabilities;</li> <li>- Intuition.</li> </ul>	<ul style="list-style-type: none"> <li>- Precise calculations;</li> <li>- High processing speed;</li> <li>- Lossless saving of large amounts of data ('photographic memory').</li> </ul>

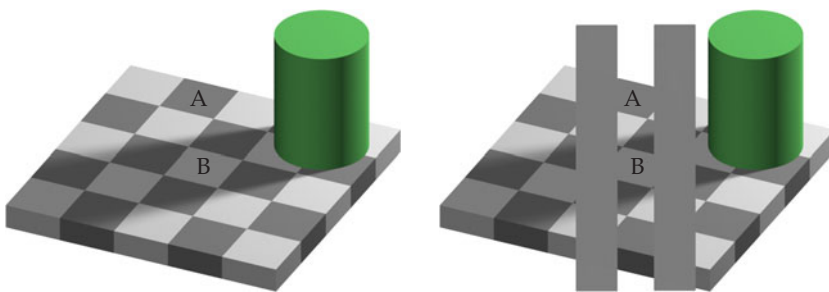


Figure 1.1. Checkered shadow illusion, adapted from Adelson [1]. The right image proves that zones 'A' and 'B' have the same gray value.



Furthermore, humans do not have a ‘photographic memory’ for hues and color intensities. For example, if one wants to do a mending job and thus needs to buy the same color in which the object to be repaired is painted, one will certainly fail and buy the wrong color if one only uses one’s memory of the desired color.

With a technical system, hues and color intensities can be quantitatively compared without any difficulty if the corresponding images have been acquired under the same conditions.

Not only can the human visual system be fooled in radiometric terms, but also in geometric terms, as it is illustrated in Fig. 1.2. Further optical illusions can be found, e.g., in [1–3].

Finally, Figs. 1.3 and 1.4 show the enormous cognitive capabilities of the human visual system [10].

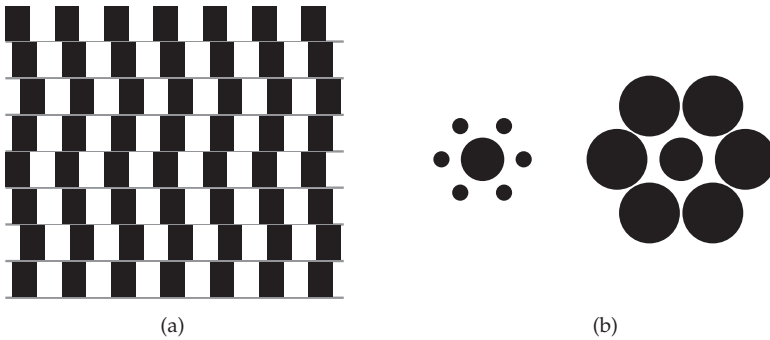


**Figure 1.2.** Optical illusions: (a) It is hard to believe that the horizontal lines are parallel and straight. (b) The circles in the middle of the two rosettes are equally sized [14]. In a digital image, this can easily be calculated by a computer, which cannot be fooled.

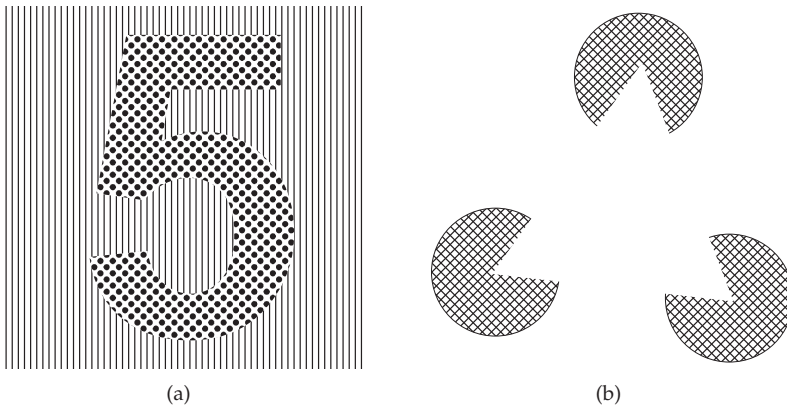


**Figure 1.3.** Nontrivial visual interpretation tasks which can be easily done by humans: (a) Without any hesitation, a human can recognize the character ‘5’. A computer would have to first discriminate between the two textures, recognize connected areas, and then classify the dotted area as a ‘5’ by comparing it with known patterns. (b) Humans, thanks to their cognitive capabilities and intuition, come to recognize a triangle partially covering all three circles.

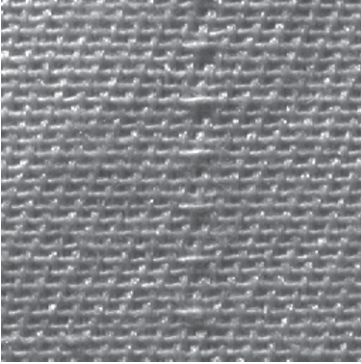


**Figure 1.4.** A human can spontaneously recognize the flaw in the textile patch. For an automated recognition, the anomaly has to be adequately described in order to formulate a computational detection method (source: Brodatz [7]).

Those examples clearly show that a human solves certain visual tasks quickly and without any problems. However, a human does not know how it is actually being done. Humans are not conscious of the underlying process: they are not aware of their algorithms.

For the development of technical visual inspection systems, usually a concrete coding is necessary. A common misconception in the practical field of automated visual inspection is the idea that if a problem is easy to solve for a human, it has to be particularly easy to create equivalent automated programs.

Recent approaches try to avoid the explicit formulation of algorithms by employing machine learning methods [9, 11, 15].

A human inspects actively. If one believes that one is not able to see well enough what one is being looking for while examining a test object, a human will more or less specifically vary their 'image acquisition' by changing the perspective and/or the illumination in order to optimize their view of the current task, or will use other optical means (mirrors, magnifiers, etc.). The technical emulation of this process is called 'active vision' or 'active visual inspection' in terms of this book. Important examples include robot-based visual inspection systems that make use of a robot in order to systematically change the image acquisition configuration of the test object, the illumination, and the camera [4, 8, 12, 16].

## 1.2 Optical capturing of test objects

Of course, when using automated visual inspection, only those object properties can be inspected that can be optically acquired. Such properties can be divided into different classes. In addition, light has various parameters, which are altered by the test object in a characteristic way, so that they can be used to draw a conclusion about the object's properties. This section will sketch which of a test object's properties can be acquired using which optical method. This topic will be thoroughly covered in later chapters, as soon as the required terms and formalisms have been introduced.

Light, emitted by a light source, illuminates the test object. Because of the interaction with the test object, the irradiated light will be partly absorbed, partly altered, partly reflected, and partly dispersed. By receiving a part of the light sent off by the test object with an optical observing instrument (e.g., a camera), data can be acquired that contains informa-

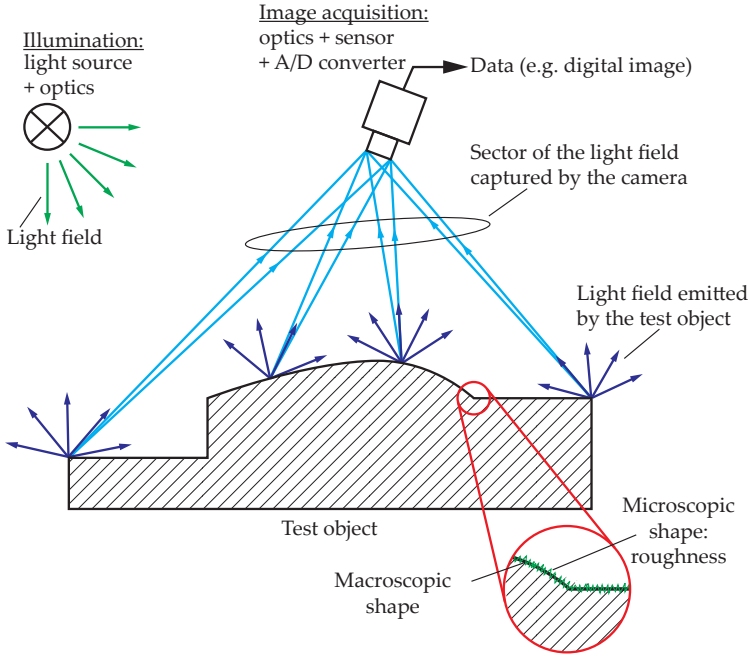


Figure 1.5. Optically acquiring information about a test object.

tion about the test object (Fig. 1.5). The following image processing methods try to regain that information.

In terms of information technology, the light emitted by a light source can be seen as a carrier signal that gets modulated by placing the test object in its path. Thus, the modulated light contains information about the test object. This modulation of the information can be based on various physical phenomena. This is why the light may encode the information about the test object in different ways. In a manner of speaking, those physical phenomena create diverse optical information channels:

- Distribution of the light intensity with respect to position and orientation;
- Spectrum (distribution of the intensity with respect to the wavelength);
- Polarization (the distribution of the directions of the electric field vectors perpendicular to the direction of propagation of the light);
- Coherence (the light wave's temporal and spatial relations);
- Phase (the current state of the oscillation in the direction of propagation);
- Time dependence (the dependence of the value of the intensity and other parameters on time).

These physical parameters of the light will be covered in detail in Chap. 2.

The irradiated light is influenced by the spatial shape and effective optical material properties of the test object. This is why one can only expect to get information about the test object's shape and optical properties by evaluating the observed light.

When testing transparent or partially transparent objects, which are permeable to light, the interaction not only takes place on the surface of the object but also inside the object.

However, opaque objects, which are not transparent and where the interaction with the light mainly takes place on the object's surface, play an important role in automated visual inspection.

The interaction of the test object and the irradiated light can pragmatically be described by a suitable reflection function, which can cover more or less the physical properties with respect to the relevant phenomena. Basically, the irradiated light is multiplicatively related to the reflection function. The result is a description of the emission of the modified light into the surrounding space. Depending on the definition of such a reflection function, only optical material properties or additional shape-based effects, like a dispersion of the light caused by the surface's roughness, are captured.

Chapter 4 will cover models for reflectance functions. Image acquisition methods for acquiring an object's properties will be discussed in Chap. 7.

### 1.3 Formation and definition of an image

The task of imaging each of the test object's points of interest to just a single point on the sensor is, for the purpose of automated visual inspection, solved by the imaging optics (e.g., the camera lenses). This means that every divergent beam of light (bundle of rays) coming from a test object point  $G$  should be converted into a convergent beam focused at a single point  $B$  on the sensor by the imaging optics (Fig. 1.6). If imaging optics yield such a point-to-point correspondence  $B' = \mathcal{A}\{G\}$ , the imaging is called sharp (see Chap. 3). In the image plane, the convergent beams form an image of the observed object space, which can be viewed using a screen, for example.

A digital camera uses a two-dimensional sensor placed in the image plane. The transformation of the irradiated light on the sensor into a digital signal is performed on the sensor and by the downstream electronic components (Chap. 6). This two-dimensional signal represents the **image** of the observed objects.

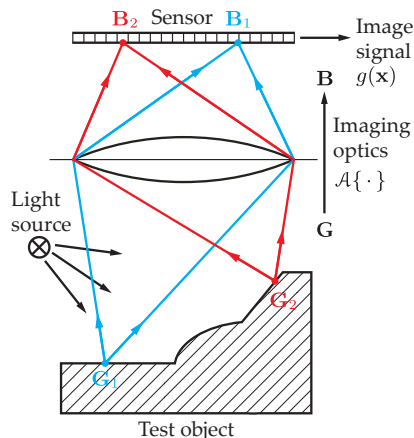


Figure 1.6. The imaging optics establish a correspondence between the points of the object and the image points located on the sensor.

1.1

**Definition 1.1: Image**

Mathematically speaking, an image can be modeled as a function

$$\mathbf{g} : \Omega_{\mathbf{g}} \rightarrow \mathbb{R}^Q, \quad \Omega_{\mathbf{g}} \subseteq \mathbb{R}^2 \quad (1.1)$$

assigning an **image value**  $\mathbf{g}$  to every position  $\mathbf{x}$  within the image:

$$\mathbf{g}(\mathbf{x}) = \begin{pmatrix} g_1(\mathbf{x}) \\ g_2(\mathbf{x}) \\ \vdots \\ g_Q(\mathbf{x}) \end{pmatrix} \quad \text{with} \quad \mathbf{x} = \begin{pmatrix} x \\ y \end{pmatrix}. \quad (1.2)$$

In general, the function  $\mathbf{g}$  is vectorial. Usually, its domain is rectangular and can thus be written as a Cartesian product of two intervals,  $\Omega_{\mathbf{g}} = [0, M) \times [0, N)$ . The dimension  $Q$  of the space of the image values can be interpreted as the number of image channels.  $\diamond$

**Example 1.1 (Gray-scale image):** A **gray-scale image** has only one channel ( $Q = 1$ ) and  $g(\mathbf{x}) = g(x, y)$  represents the gray value at position  $\mathbf{x}$ .

Distance and topographical data can also be considered as an image, with a one-dimensional domain, and are usually called **range images**. In this case,  $g(x)$  represents the distance or the height of the relief at point  $x$ .  $\blacksquare$

**Example 1.2 (Color image):** The usual **color image** has three channels ( $Q = 3$ ). For example,  $g_1(\mathbf{x})$  represents the red component,  $g_2(\mathbf{x})$  the green component, and  $g_3(\mathbf{x})$  the blue component at the point  $\mathbf{x}$ . Color images will be discussed in detail in Chap. 5.

But even higher dimensions can be used to represent the spectrum of visible and invisible light, leading to a higher spectral resolution. In this case, each of the  $Q > 3$  channels corresponds to a certain band of the spectrum. Such an image is called a **multispectral image**. For large  $Q$  (usually in three digits) and the resulting fine spectral resolution, the image is a so-called **hyperspectral image**.  $\blacksquare$

For the computational processing of an image, what is used is not the continuous image signal  $\mathbf{g}(\mathbf{x})$  but a digital signal  $\mathbf{g}_{mn}$  that is the result of spatially sampling  $\mathbf{g}(\mathbf{x})$ . Furthermore, the image values are quantized into  $K$  steps, resulting in a digital signal  $\mathbf{g}_{mn}$  with

$$\begin{aligned} (m, n) &\in \{0, 1, 2, \dots, M-1\} \times \{0, 1, 2, \dots, N-1\} \subset \mathbb{Z}^2, \\ \mathbf{g}_{mn} &\in \{0, 1, 2, \dots, K-1\}^Q \subseteq \mathbb{Z}^Q. \end{aligned} \quad (1.3)$$

These  $M \times N$  discrete image points are called **pixels** (picture elements). The mathematical description of continuous and discrete image signals will be covered in detail in Chap. 8.

1.4

**1.4 Machine vision**

Typical machine vision systems consist of the structure shown in Fig. 1.7, which is to be read bottom-up. This figure is deliberately shaped like a pyramid based on the process of image

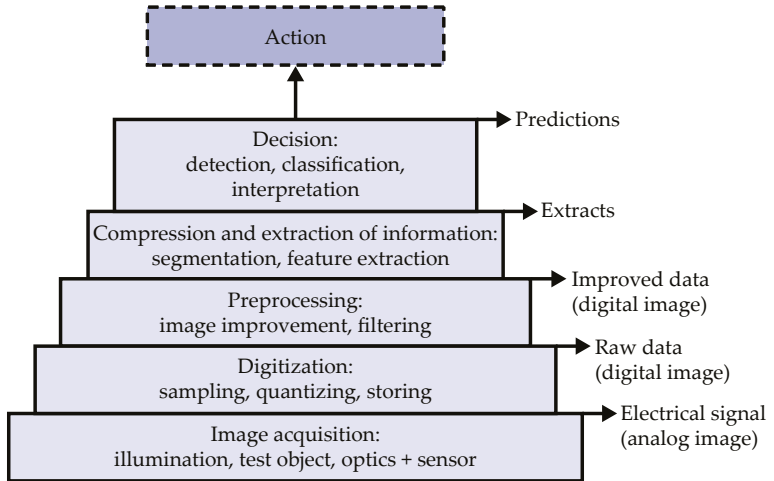


Figure 1.7. The processing chain of machine vision systems.

acquisition. The suitability and quality of this level is crucial for the whole chain of visual inspection tasks.

The amount and quality of information that is contained in the acquired image data depends entirely on the step of image acquisition. Information that is not acquired during this step can be recovered only with difficulty, or even not at all, by subsequent image processing steps, regardless of how much effort is spent on them. Many visual inspection systems failing in practice did not adhere to this simple rule.

The light that is emitted by the light source interacts with the test object, passes through the imaging optics, and finally reaches the sensor, where it is transformed into an electrical signal. This analog signal, which is usually an electrical voltage, is discretized and limited with respect to space and amplitude. In such a representation, it can be saved as a digital image and processed by a computer. But besides the information relevant for visual inspection, this raw data usually contains disturbing and irrelevant components, such as noise, inhomogeneities, and so on. The subsequent image restoration process tries to retain the relevant information and compensate for the irrelevant signal components. As a result, improved image data is obtained, which is separated into meaningful regions (segmentation, see Chap. 11) and/or is processed so as to extract the parameters relevant for the task (features). Finally, decisions can be made on the basis of this condensed information: such decisions can be detection (e.g., of a defect), classification (e.g., of different objects) or interpretation (e.g., inference of production parameters), depending on the visual inspection task.

A subsequent action can then be taken, depending on and adapted to that decision, such as discarding or keeping the test object, or selectively altering production parameters, for example.

It cannot be stressed sufficiently often that a well-considered image acquisition system can have an enormous impact on the capabilities of an automated visual inspection system. The huge amount of optical and geometrical degrees of freedom of the image acquisition setup (light source, test object, optics, and sensors) offers a huge design space whose oppor-

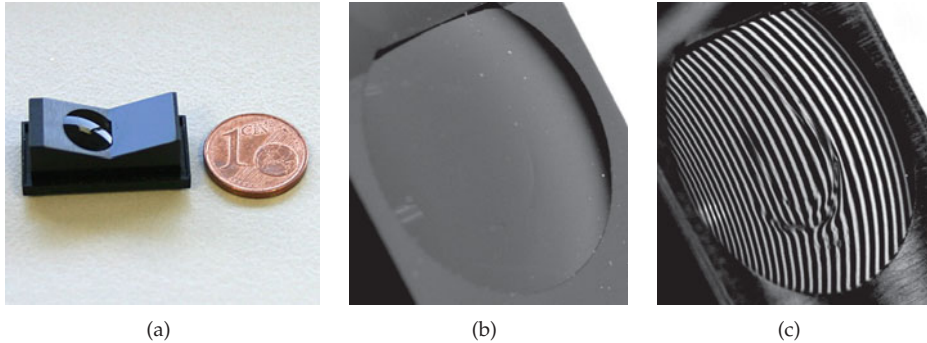


**Figure 1.8.** Inspection of the plastic lens of a rain sensor used for controlling windshield wipers: (a) Comparison of the rain sensor's size with the size of a one-cent coin. (b) Macro-image of the lens with homogeneous illumination. (c) A deformed stripe pattern reflected by the lens.

tunities, however, can only be systematically exploited with the necessary knowledge and a concept adequately adjusted to the problem at hand. Effort spent at this stage usually turns out to be a good investment in the final capabilities of the visual inspection system. For some tasks, it is even possible to obtain images during the image acquisition phase that are so expressive and easily interpretable, that the subsequent image processing steps are nearly trivial. The following three examples will illustrate this.

---

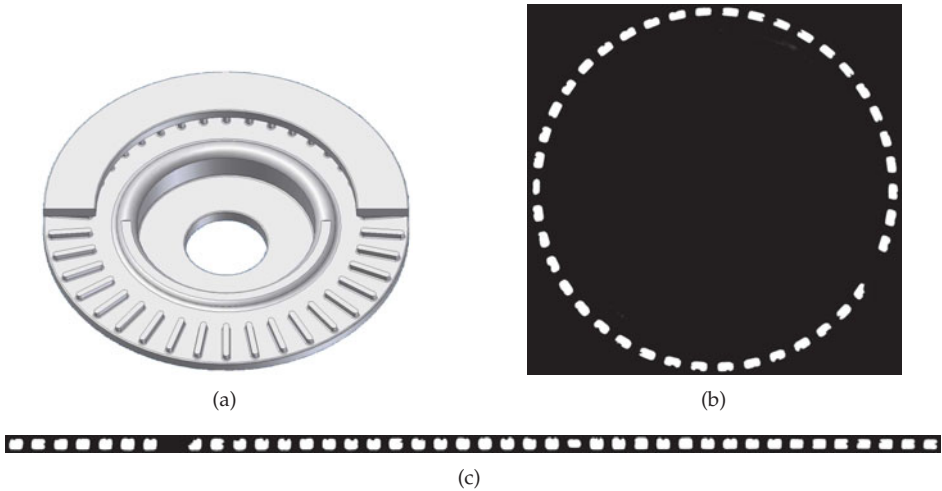
**Example 1.3 (Plastic lens):** Figure 1.8(a) shows the plastic optics of an infrared rain sensor used for controlling windshield wipers in automobiles. There is a transfer-molded lens mounted on top, which has a little depression caused by cooling; a defect which has to be detected.

Figure 1.8(b) shows a macro-image of the lens region with spatially homogeneous illumination. With some effort, one might spot the defect on the right side. As the dust particles are visible as prominently as the defect, this image would not be suitable for a reliably working automated visual inspection.

With the so-called deflectometric image acquisition (see Sec. 7.3.5) where the image of a stripe pattern mirrored by the lens is observed, the defect is clearly visible (Fig. 1.8(c)). The depression results in an increased contrast, caused by a distinct local deformation of the stripe pattern, which constitutes the foundation for a very reliable automated defect detection. ■

---

**Example 1.4 (Brake disks):** Nowadays, the brake disks of most automobiles are internally ventilated for cooling reasons, see Fig. 1.9(a). Brake disks are usually made out of gray iron. The cavities are formed by sand cores whose fixation is destroyed after the metal's solidification, so that the sand can be removed from the cavities. These sand cores are more or less breakable. Broken sand cores result in partially or completely closed ventilation channels, rendering a brake disk unusable. Quite often, the castings are manually or visually inspected by humans. Because of the radially placed channels, the worker has to rotate the brake disk in order to check whether all channels are free. Considering



**Figure 1.9.** Automated visual inspection of the ventilation channels of a brake disk: (a) Sketch of an internally ventilated brake disk with radially arranged ventilation channels; (b) Result of the image acquisition; (c) The section of the acquired image that is relevant for the inspection transformed into polar coordinates (source: inspectomation GmbH).

that such castings may have a weight of between 15 and 50 kg and are produced in one-second cycles, it becomes clear that this duty puts a heavy burden on a human worker.

This inspection task can be automated very well. In this example, a method is employed that yields an extremely high-contrast image that can be used to simultaneously check whether all ventilation channels are free. This is achieved by transforming the conic bunch of the camera's rays of sight into a radial bunch of beams using a cone-shaped mirror, which offers a view through all channels; for details see Sec. 7.3.10. The image acquisition results in a binary image (black and white image), which makes the further analysis nearly trivial and thus extremely reliable; see Fig. 1.9(b).

As this image only contains useful information along a narrow circular ring, that structure can be cut out and transformed into a polar coordinate system, where it will have a stripe-like shape and can hence be visualized on a display in a space-efficient way; see Fig. 1.9(c). ■

---

**Example 1.5 (Puncture needle):** For the drop-wise blood collection from a fingertip for rapid medical tests, puncture needles with a facettedly sharpened tip are used; see Fig. 1.10. In the context of quality control, the needle's facets (planar, smoothed surfaces) should be inspected. If that task is to be automated, the borders between the different facets in the image have to be found computationally. When using an image like Fig. 1.10, this will only be achievable if one accepts certain errors, as the left and upper facet appear to be almost identical.

The images of Fig. 1.11 show that this can be done considerably better [13]. By using nearly parallel (collimated) light coming from certain directions, the single facets and the needle's contour are accentuated, which makes the successive image analysis quite easy



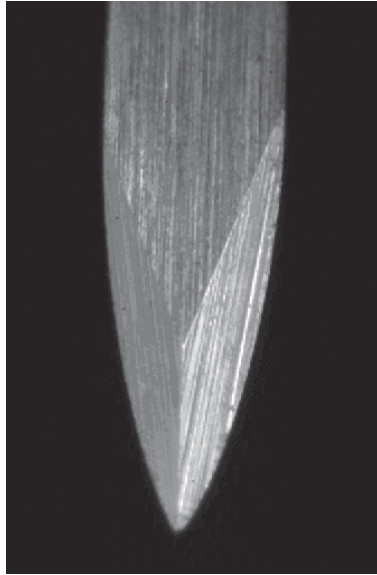


**Figure 1.10.** Puncture needle for blood collection with a faceted tip. The needle's diameter is approximately 0.8 mm.

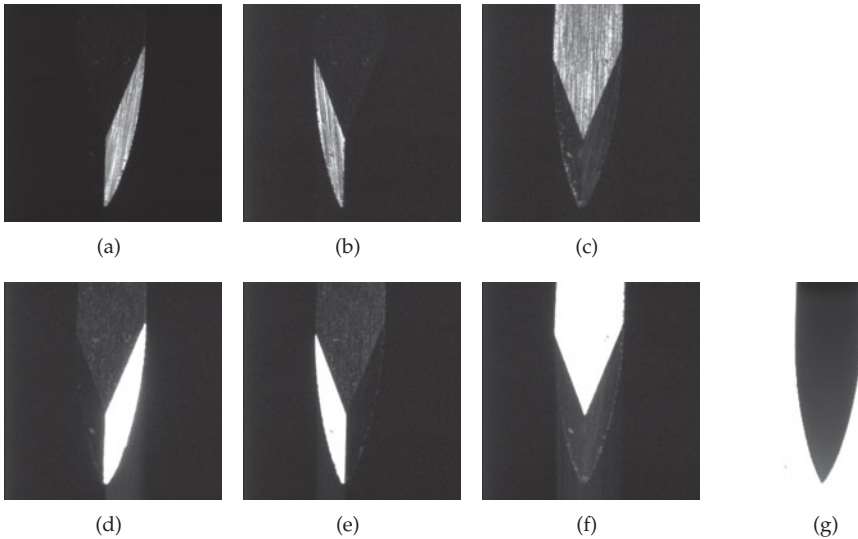


**Figure 1.11.** Tip of a puncture needle illuminated with parallel light coming from different directions with different intensities: (a)–(c) Images on which the illumination direction was chosen in such a way that the light was mainly directly reflected into the camera by one of the facets. Only the corresponding facet appears bright. (d)–(f) Additionally, the camera can be overdriven by increasing the intensity, yielding nearly binary images of the facets, which are well-suited for measuring the facets' geometry. (g) Under back-light conditions, the needle is visible as a high-contrast silhouette.

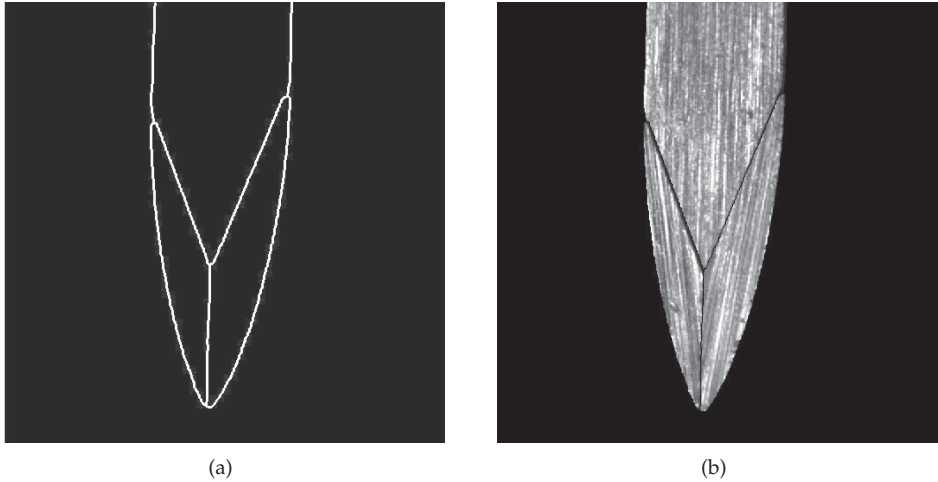


**Figure 1.12.** Analysis of the images from Fig. 1.11: (a) Contours of the facets derived from the images; (b) Synthesized image out of the original image series. The texture of every facet shows high-contrast.

and promises reliable results. It is clear that given such an image series, one can easily synthesize expressive intermediate results, as shown in Fig. 1.12, or one can perform the measurements of the extracted contours of the test object. ■

These three examples show quite clearly the potential of an elaborated image acquisition that is adapted to the concrete problem. In contrast to the other sectors, one has a huge influence on the image acquisition process in the domain of automated visual inspection. When composing automated visual inspection systems, one usually has many degrees of freedom in designing the setup of the illumination, the test object, the optics, and the sensors. In order to be able to use these in a creative way, a solid understanding of the relevant physical background is needed, of course.

It is not always possible to acquire all the necessary aspects for solving a visual inspection task in a single image. If enough inspection time is available, multiple images can be acquired while selectively varying the image acquisition setup. In an extreme case, one could use an optimal image recording setup for each single aspect of interest and combine the analysis of the single images into an overall test result. But in most cases, the benefits of such brute force methods are at odds with the economic, temporal, and spatial restrictions on the visual inspection system, so that usually the images have to be captured, which simultaneously cover multiple aspects of the visual inspection task in equal quality.

## 1.5 Practical approach for performing machine vision projects

Concerning a practical machine vision project, there are numerous questions which are important for a reliably functioning system, as well as for a successful project execution between the user (customer) and the system supplier, which cannot be covered within the scope of this book.

How is the machine vision task specified? A specification sheet usually answers questions like ‘what’ and ‘why.’ On that foundation, the so-called functional specifications are derived, describing ‘how’ and ‘by what means’ the task is to be solved. Both documents can be written collaboratively, however, usually the specification sheet is the concern of the user and the functional specifications belong to the domain of the system supplier.

There are important questions concerning the selection of the examples (the training set and the test sets) based on which the system is to be developed and tested later on and, of course, the required performance of the system for being acceptable to the customer. A good overview of everything that should be kept in mind when developing an automated visual inspection system can be found in [5,6,17,18].

## 1.6 Bibliography

- [1] Edward Adelson. Lightness Perception and Lightness Illusions. In Michael S. Gazzaniga, editor, *The New Cognitive Neurosciences*, pages 339–351. MIT Press, Cambridge, MA, 2nd edition, 2000.
- [2] Edward H. Adelson. Lightness Perception and Lightness Illusions. <http://persci.mit.edu/gallery>, <http://web.mit.edu/persci/gaz/gaz-teaching/index.html>, 2011.
- [3] Ivan Artamonov. *Optische Täuschungen*. Deutsch, 5th edition, 2006.
- [4] Jonathan Balzer and Stefan Werling. Principles of Shape from Specular Reflection. *Measurement*, 43(10):1305–1317, 2010.
- [5] Bruce Batchelor and Paul Whelan. *Intelligent vision systems for industry*. Springer, 1997.
- [6] Norbert Bauer, editor. *Guideline for industrial image processing*. Fraunhofer-Allianz Vision, 2003.
- [7] Phil Brodatz. *Textures: A photographic album for artists and designers*. Dover, 1966.
- [8] Marco Huber. Probabilistic Active Vision: An Overview. Technical Report IES-2010-01. In Jürgen Beyerer and Marco Huber, editors, *Proceedings of the 2010 Joint Workshop of Fraunhofer IOSB and Institute for Anthropomatics, Vision and Fusion Laboratory*, volume 7 of *Karlsruher Schriften zur Anthropomatik*, pages 1–16. KIT Scientific Publishing, 2011.
- [9] Marco Huber, Tobias Dencker, Masoud Roschani, and Jürgen Beyerer. Bayesian Active Object Recognition via Gaussian Process Regression. In *Proceedings of the 15th International Conference on Information Fusion*, 2012.
- [10] Axel Korn. *Bildverarbeitung durch das visuelle System*. Springer, 1982.
- [11] Axel Korn. *Verarbeitung und Auswertung von Signalen bildgebender Sensoren*. VDI-Verlag, 1995.
- [12] Lucas Paletta and Axel Pinz. Active object recognition by view integration and reinforcement learning. *Robotics and Autonomous Systems*, 31:71–86, 2000.
- [13] Fernando Puente León and Jürgen Beyerer. Active vision and sensor fusion for inspection of metallic surfaces. In David P. Casasent, editor, *Intelligent Robots and Computer Vision XVI: Algorithms, Techniques, Active Vision, and Materials Handling*, volume 3208 of *Proc. SPIE*, pages 394–405, 1997.
- [14] Brian Roberts, Mike Harris, and Tim Yates. The roles of inducer size and distance in the Ebbinghaus illusion (Titchener circles). *Perception*, 34(7):847–856, 2005.
- [15] Michael Sabourin and Amar Mitiche. Optical character recognition by a neural network. *Neural Networks*, 5(5):843–852, 1992.
- [16] Konstantinos Tarabanis, Peter Allen, and Roger Tsai. A survey of sensor planning in computer vision. *IEEE Transactions on Robotics and Automation*, 11(1):86–104, February 1995.
- [17] Verein Deutscher Ingenieure und Verband der Elektrotechnik, Elektronik und Informationstechnik. *Industrielle Bildverarbeitung – Grundlagen und Begriffe*. Beuth Verlag, Berlin, 2010.

- [18] Verein Deutscher Ingenieure and Verband der Elektrotechnik, Elektronik und Informationstechnik. *Industrielle Bildverarbeitung – Leitfaden für die Erstellung eines Lastenhefts für Bildverarbeitungssysteme*. Beuth Verlag, Berlin, 2011.



Part I  
**Image Acquisition**





Chapter 2

**Light**

**2**

---

## 2 Light

2.1	The phenomenon of light . . . . .	23
2.1.1	The electromagnetic spectrum . . . . .	23
2.2	Light as an electromagnetic wave . . . . .	24
2.2.1	Maxwell's equations . . . . .	24
2.2.1.1	Wave equations of the electric field . . . . .	26
2.2.2	Polarization . . . . .	31
2.2.2.1	The polarization ellipse . . . . .	31
2.2.2.2	Stokes parameters . . . . .	33
2.2.2.3	The Poincaré sphere . . . . .	35
2.2.2.4	Mueller matrices . . . . .	36
2.2.2.5	Measuring the polarization state . . . . .	41
2.2.2.6	The Jones calculus . . . . .	42
2.2.3	Huygens' principle . . . . .	44
2.2.4	Coherence . . . . .	44
2.2.5	Interference . . . . .	46
2.2.6	Diffraction . . . . .	48
2.2.6.1	Resolution of imaging systems . . . . .	58
2.2.7	Speckle . . . . .	60
2.3	Light as a quantum phenomenon . . . . .	61
2.4	The ray model of geometrical optics . . . . .	65
2.5	Summary . . . . .	66
2.6	Interaction of light and matter . . . . .	66
2.6.1	Absorption . . . . .	67
2.6.2	The law of reflection . . . . .	67
2.6.3	The law of refraction . . . . .	68
2.6.4	Scattering . . . . .	70
2.6.5	The Fresnel coefficients for reflection and transmission . . . . .	71
2.6.6	Electromagnetic waves in conductive media . . . . .	76
2.6.6.1	Complex index of refraction . . . . .	77
2.7	Light sources . . . . .	80
2.7.1	Thermal radiators . . . . .	80
2.7.1.1	Physical principles . . . . .	80
2.7.1.2	Incandescent lamps and halogen lamps . . . . .	81
2.7.2	Gas-discharge lamps . . . . .	83
2.7.3	Light-emitting diodes . . . . .	86
2.7.4	Laser . . . . .	89
2.7.5	Summary . . . . .	93
2.8	Bibliography . . . . .	93

## 2 Light

### 2.1 The phenomenon of light

Optical image acquisition and measurement methods rely on the properties of light. Light can be described physically in two very different ways: as a wave or as a particle. Depending on the concrete physical scenario in question, the one or the other perspective is more useful for describing an observed effect. Both of them are legitimate, but neither explains all observed phenomena. This is often referred to as the **wave–particle duality**.<sup>1</sup>

In the particle model, light consists of **photons** (light quanta). In a vacuum, these massless light particles move in straight lines with a constant velocity of  $c \approx 300,000$  km/s. Matter can absorb photons and absorb their energy; conversely, energy can be emitted in the form of light. An effect which can only be explained by the particle model is **quantization**: for a fixed wavelength, there exists a minimum amount of energy below which light of a certain wavelength cannot fall. That amount corresponds to the energy of a single photon. The quantizing of light and its consequences are covered in Sec. 2.3. The model of electromagnetic waves describes visible, as well as invisible light, as a wave spreading in space. The wave is characterized by its wavelength  $\lambda$  or, alternatively, by its frequency  $\nu$ , with

$$\nu = \frac{c}{\lambda}. \quad (2.1)$$

The wavelength of light visible to humans is in the range of 380 nm up to 780 nm. In the particle model, different frequencies correspond to different energies:

$$E = h\nu \quad (2.2)$$

with **Planck's constant**  $h \approx 6.626 \cdot 10^{-34}$  Js, which is a fundamental physical constant. Wave-optical effects usually occur when the size of the present objects is close to the wavelength of the light, as can be the case for suitably narrow slits, for example. Interference and diffraction are two prominent examples of phenomena that can only be explained by the wave model. They will be covered in Sec. 2.2. Section 7.3.16 describes optical measurement methods which rely on the wave characteristics of light.

At many points of this book, the conditions of geometric optics are assumed to be satisfied, so that the following simplification can be applied: light is described by rays and bundles of rays which propagate in a straight line. When hitting objects, they get dispersed, refracted, or reflected. Wave-optical effects can be neglected in this case. However, this assumption only holds as long as all relevant geometrical structures, such as the objects and object distances, are significantly larger than the light's wavelength. The consequences of wave-optical effects on the imaging systems covered here will be analyzed in Sec. 2.2.6.1.

#### 2.1.1 The electromagnetic spectrum

Visible light accounts for only a small part of the whole electromagnetic spectrum (see Fig. 2.1). It covers the wavelength range of about 380 nm to 780 nm [39]. Although auto-

---

<sup>1</sup>A unified treatment is possible within the theory of quantum electrodynamics, which is beyond the scope of this book.



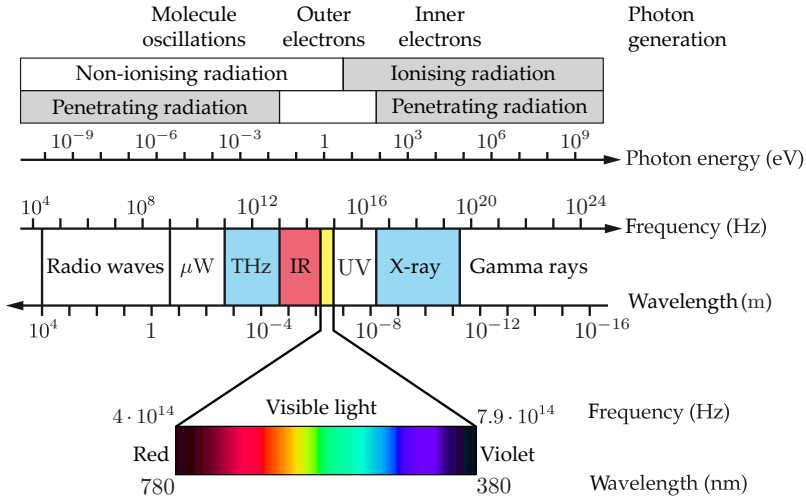


**Figure 2.1.** The electromagnetic spectrum ( $\mu\text{W}$  = microwaves, THz = Terahertz-radiation, IR = infrared, UV = ultra-violet).

mated visual inspection and image processing are not limited to the visible spectrum, it is crucial that suitable light sources and sensors are available (see Sec. 2.7, and Chap. 6 and Chap. 7).

Depending on the excitation energies of the possible vibrations of the molecule and transfers of inner and outer electrons, photons can be emitted or absorbed in the corresponding spectral range (Fig. 2.1). A photon’s energy is specified in eV. One electron volt,  $1 \text{ eV} \approx 1.602 \cdot 10^{-19} \text{ J}$ , is the kinetic energy received by an electron passing through an electric field with a potential difference of 1 V.

## 2.2 Light as an electromagnetic wave

### 2.2.1 Maxwell’s equations

Maxwell’s equations are a set of linear partial differential equations describing light and all other electromagnetic phenomena in a macroscopic way with respect to SI units [32]:

$$\text{rot } \mathbf{H} = \mathbf{J} + \frac{\partial \mathbf{D}}{\partial t}, \tag{2.3}$$

$$\text{rot } \mathbf{E} = -\frac{\partial \mathbf{B}}{\partial t}, \tag{2.4}$$

$$\text{div } \mathbf{B} = 0, \tag{2.5}$$

$$\text{div } \mathbf{D} = \rho. \tag{2.6}$$

All electromagnetic phenomena are solutions of those equations under certain initial and boundary conditions.<sup>2</sup>

Maxwell's equations cover the magnetic field strength  $\mathbf{H}$  in units of  $\text{Am}^{-1}$ , the electric field strength  $\mathbf{E}$  in units of  $\text{Vm}^{-1}$ , the magnetic flux density  $\mathbf{B}$  in units of  $\text{T} = \text{Vsm}^{-2}$ , and the electric flux density  $\mathbf{D}$  in units of  $\text{Asm}^{-2}$ . The vector  $\mathbf{J}$  denotes the electric current density specified in  $\text{Am}^{-2}$ , and  $\rho$  is the electric charge density specified in  $\text{Asm}^{-3}$ . The field strengths and flux densities are vectors in a three-dimensional space:  $\mathbf{H} = (H_x, H_y, H_z)^T$ ; similarly, this also applies for the other quantities.

The first of Maxwell's equations, (2.3), shows that both an electric current and a so-called displacement current caused by a change of the electric flux density can induce a magnetic field  $\mathbf{H}$ . Conversely, an electric field  $\mathbf{E}$  is induced by a time-varying magnetic flux density  $\mathbf{B}$ , cf. (2.4). The third equation, (2.5), states that magnetic field lines do not come from so-called monopoles, but form closed curves. Hence, there are no magnetic charges. Finally, Equation (2.6) says that electric charges  $\rho$  are the sources of an electric field  $\mathbf{E}$  [35]. The field strengths, flux densities, and current densities are related as follows:

$$\mathbf{D} = \varepsilon \mathbf{E}, \quad (2.9)$$

$$\mathbf{B} = \mu \mathbf{H}, \quad (2.10)$$

$$\mathbf{J} = \sigma \mathbf{E}. \quad (2.11)$$

The permittivity  $\varepsilon$ , the magnetic permeability  $\mu$ , and the specific electrical conductance  $\sigma$  are properties of the medium containing the field.<sup>3</sup> The specific conductance is the reciprocal of the specific resistance. Materials with  $\sigma \approx 0$  do not conduct any current. They are called isolators or dielectrics. A material's permittivity or dielectric constant  $\varepsilon$  can be expressed as the product of the vacuum permittivity  $\varepsilon_0$  and the material's relative permittivity  $\varepsilon_r$ :

$$\varepsilon = \varepsilon_0 \varepsilon_r. \quad (2.12)$$

---

<sup>2</sup>This formulation uses the vectorial differential operators, curl and divergence, which are defined as follows for a vector-valued function  $\mathbf{F} : \mathbb{R}^3 \rightarrow \mathbb{R}^3$ :

$$\text{rot } \mathbf{F} := \begin{pmatrix} \frac{\partial F_z}{\partial y} - \frac{\partial F_y}{\partial z} \\ \frac{\partial F_x}{\partial z} - \frac{\partial F_z}{\partial x} \\ \frac{\partial F_y}{\partial x} - \frac{\partial F_x}{\partial y} \end{pmatrix}, \quad (2.7)$$

$$\text{div } \mathbf{F} := \frac{\partial F_x}{\partial x} + \frac{\partial F_y}{\partial y} + \frac{\partial F_z}{\partial z}. \quad (2.8)$$

<sup>3</sup>In anisotropic media, tensors have to be used instead of the scalar coefficients  $\varepsilon$ ,  $\mu$  and  $\sigma$  [17]. For high field strengths, the linear equations (2.9) and (2.10) are no longer valid. In terms of describing light transport, such high electric field strengths are relevant for focused laser light, for example [20]. In some materials, also lower field strengths might cause saturation effects, leading to nonlinear behavior which can be technically exploited for frequency multiplication of light, for example. Nd:YAG lasers use this principle to transform infrared light of the wavelength  $\lambda = 1064 \text{ nm}$  into visible green light with  $\lambda = 532 \text{ nm}$  (see Sec. 2.7.4).

The permittivity of the vacuum<sup>4</sup> is

$$\varepsilon_0 \approx 8.854 \cdot 10^{-12} \frac{\text{As}}{\text{Vm}}. \quad (2.13)$$

Similarly, the magnetic permeability  $\mu$  can be expressed as a product of the vacuum permeability  $\mu_0$  and the relative permeability  $\mu_r$  of the material:

$$\mu = \mu_0 \mu_r. \quad (2.14)$$

For a vacuum,  $\mu_r = 1$  and  $\varepsilon_r = 1$ . The vacuum permeability<sup>5</sup> is given by

$$\mu_0 = 4\pi \cdot 10^{-7} \frac{\text{Vs}}{\text{Am}}. \quad (2.15)$$

The relative permeability depends on whether the material is magnetic or not. For non-magnetic materials,  $\mu_r \approx 1$ ; for magnetic substances it is possible that  $\mu_r \gg 1$ .

### ⊗ 2.2.1.1 Wave equations of the electric field

Electromagnetic waves in a non-conducting, infinitely wide, and homogeneous medium will now be considered. Here,  $\sigma = 0$  (dielectric),  $\varepsilon$  and  $\mu$  are constant with respect to the position  $\mathbf{x}$ . There are no free charge carriers, implying  $\rho = 0$ . The elimination of  $\mathbf{H}$ ,  $\mathbf{B}$  and  $\mathbf{D}$  from Maxwell's equations (2.3) to (2.6) yields the wave equation:

## 2.1

### Theorem 2.1: Wave equation

The wave equation of the electric field in a dielectric, infinitely spread, homogeneous medium is given by<sup>6</sup>

$$\Delta \mathbf{E} = \varepsilon \mu \frac{\partial^2 \mathbf{E}}{\partial t^2}. \quad (2.17)$$

Its simplest solution is

$$\mathbf{E}(\mathbf{x}, t) = E \mathbf{e}_1 w \left( t - \frac{\mathbf{e}_3^T \mathbf{x}}{v} \right) \quad (2.18)$$

with<sup>7</sup>

$$v^2 = \frac{1}{\varepsilon \mu}. \quad (2.19)$$

<sup>4</sup>The constant  $\varepsilon_0$  is also referred to as the electric field constant.

<sup>5</sup>The constant  $\mu_0$  is also referred to as the magnetic field constant.

<sup>6</sup>With the vectorial Laplace operator  $\Delta$ :

$$\Delta \mathbf{F} := \begin{pmatrix} \frac{\partial^2 F_x}{\partial x^2} + \frac{\partial^2 F_x}{\partial y^2} + \frac{\partial^2 F_x}{\partial z^2} \\ \frac{\partial^2 F_y}{\partial x^2} + \frac{\partial^2 F_y}{\partial y^2} + \frac{\partial^2 F_y}{\partial z^2} \\ \frac{\partial^2 F_z}{\partial x^2} + \frac{\partial^2 F_z}{\partial y^2} + \frac{\partial^2 F_z}{\partial z^2} \end{pmatrix}. \quad (2.16)$$

<sup>7</sup>In many books the argument of  $w$  in (2.18) is expressed as  $t \pm \frac{\mathbf{e}_3^T \mathbf{x}}{v}$ . However, the sign can be included in the direction vector  $\mathbf{e}_3$ , which can be arbitrarily chosen.

Here,  $w(\cdot)$  is an arbitrary, twice differentiable function,  $E$  is the amplitude<sup>8</sup> and  $\mathbf{e}_i \in \mathbb{R}^3$ ,  $i \in \{1, 2, 3\}$  are unit vectors defining a rectangular coordinate system:

$$\|\mathbf{e}_i\| = 1, \quad \mathbf{e}_i^T \mathbf{e}_k = \delta_i^k, \quad \mathbf{e}_1 \times \mathbf{e}_2 = \mathbf{e}_3. \quad (2.20)$$

Inserting this electric field into Maxwell's equations yields the following magnetic field strength:

$$\mathbf{H}(\mathbf{x}, t) = \sqrt{\frac{\varepsilon}{\mu}} E \mathbf{e}_2 w\left(t - \frac{\mathbf{e}_3^T \mathbf{x}}{v}\right). \quad (2.21)$$

The factor  $Z := \sqrt{\frac{\mu}{\varepsilon}}$  is called the wave impedance of the medium. In vacuum,  $Z_0 = \sqrt{\frac{\mu_0}{\varepsilon_0}} = 376.73 \Omega$ .  $\diamond$

The solution given by (2.18) and (2.21) describes a plane transverse electromagnetic wave. The meaning of this statement is as follows.

The only variable factor occurring in the wave function is the function  $w(\cdot)$ . Its argument  $t - \frac{\mathbf{e}_3^T \mathbf{x}}{v}$  is called the phase or propagator of the electromagnetic wave. The function  $w(\cdot)$  has a certain value  $w_0$ , whenever the propagator is constant:

$$t - \frac{\mathbf{e}_3^T \mathbf{x}}{v} = \text{const.} \quad \Rightarrow \quad w_0 = w\left(t - \frac{\mathbf{e}_3^T \mathbf{x}}{v}\right) = \text{const.} \quad (2.22)$$

As  $t - \frac{\mathbf{e}_3^T \mathbf{x}}{v} = \text{const.}$  is the equation of a plane, a plane wave is at hand. Differentiating (2.22) with respect to the time  $t$  yields

$$v = \mathbf{e}_3^T \dot{\mathbf{x}} \quad \Leftrightarrow \quad \dot{\mathbf{x}} = v \mathbf{e}_3, \quad (2.23)$$

where  $\dot{\mathbf{x}} := \frac{d}{dt} \mathbf{x}$  denotes the derivative of the vector  $\mathbf{x}$  with respect to time. According to the last equation, the wave's propagation velocity is  $v \mathbf{e}_3$ ; this is also called the phase velocity.<sup>9</sup> According to (2.19) the velocity is  $v = \frac{1}{\sqrt{\varepsilon \mu}}$  and the propagation direction of the wave is given by the unit vector  $\mathbf{e}_3$ .

The velocity of light waves propagating through a medium can be expressed as follows, using (2.12) and (2.14):

$$v = \frac{1}{\sqrt{\varepsilon \mu}} = \frac{1}{\sqrt{\varepsilon_0 \varepsilon_r \mu_0 \mu_r}} = \frac{1}{\sqrt{\varepsilon_0 \mu_0}} \frac{1}{\sqrt{\varepsilon_r \mu_r}} = \frac{c}{n}, \quad (2.24)$$

with

$$c = \frac{1}{\sqrt{\varepsilon_0 \mu_0}} = 299,792,458 \text{ m/s} \quad (2.25)$$

<sup>8</sup>The amplitude is the maximum deflection of a wave function with respect to the arithmetic mean.

<sup>9</sup>The phase velocity describes the velocity of the propagation of the phase front (the sets of positions with the same phase). However, the transport of energy and information through a wave is described by another kind of velocity, the so-called group velocity, which is identical to the phase velocity in special cases.

In example 8.28 in Sec. 8.4, the Fourier transform is used to define and explain the group velocity.

denoting the speed of light in vacuum [20], and  $n$  denoting the index of refraction of the medium,

$$n := \sqrt{\varepsilon_r \mu_r} \quad (2.26)$$

The index of refraction indicates to what extent the light propagates more slowly in the medium than in vacuum. The light's wavelength in the medium is  $\frac{\lambda_0}{n}$ , where  $\lambda_0$  is its wavelength in vacuum.

With (2.18), (2.21) and (2.20), the following holds for electromagnetic waves:

$$\mathbf{E} \parallel \mathbf{e}_1 \perp \mathbf{e}_3, \quad (2.27)$$

$$\mathbf{H} \parallel \mathbf{e}_2 \perp \mathbf{e}_3. \quad (2.28)$$

Hence both the electric and the magnetic field strength are perpendicular to the propagation direction  $\mathbf{e}_3$ . This property of electromagnetic waves is called **transversality**. If an electromagnetic wave is spatially strictly constricted, as in a single-mode fiber<sup>10</sup> for example, the exclusive transversality is no longer guaranteed and the solutions to the wave equation will also contain longitudinal field components.

In this book, what will be used for explaining optical phenomena is mainly geometric optics, in terms of 'light rays' (see Sec. 2.4 and Chap. 3). Light rays are an idealized and demonstrative concept for describing the spatial propagation of electromagnetic waves. They propagate perpendicularly to the surfaces of constant phase of the electromagnetic wave.

---

**Example 2.1 (Plane wave):** A plane wave  $w(t - \frac{\mathbf{e}_3^T \mathbf{x}}{v})$  propagates rectilinearly in space. The light rays propagate parallel to the propagation direction  $\mathbf{e}_3$ . The wave fronts, which form the surfaces of constant phase, are perpendicular to the direction of propagation, see Fig. 2.2(a). ■

---

**Example 2.2 (Spherical waves):** Spherical waves are also solutions of the wave equation (2.17). Then,  $w(\cdot)$  in Equation (2.18) turns into

$$\frac{1}{r} w \left( t - \frac{\mathbf{x}^T \mathbf{e}_r}{v} \right) = \frac{1}{r} w \left( t - \frac{r}{v} \right), \quad (2.29)$$

with  $r = \|\mathbf{x}\| = \sqrt{x^2 + y^2 + z^2}$ . In contrast to a plane wave, the propagation direction

$$\mathbf{e}_r = \frac{\mathbf{x}}{\|\mathbf{x}\|} \quad (2.30)$$

depends on the position. Originating from a common point of origin, the light rays spread in all spatial directions. The surfaces of constant phase are concentric spheres around that point, Fig. 2.2(b). The field strength decreases proportionally to  $\frac{1}{r}$ , so that

---

<sup>10</sup>In a single-mode fiber, only the fundamental mode, that is, the mode with the lowest frequency, is propagable. A mode is a field corresponding to an eigenfunction of the boundary value problem of Maxwell's equations. The diameter of the core of a single-mode fiber, which carries the wave, is only a few multiples of the light's wavelength. For higher diameters, multiple wave modes can propagate simultaneously. As different modes propagate with different velocities, single-mode fibers yield the lowest signal distortions for optical information transfer [25].

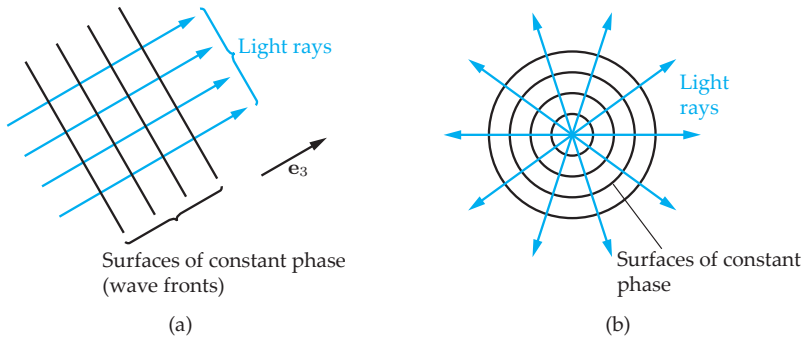


Figure 2.2. Relation between the wave model and the particle model of light: (a) A plane wave, (b) A spherical wave.

the energy remains constant for the phase surfaces increasing with  $r^2$ . The light rays are perpendicular to the wave fronts and thus form a concentric bundle of rays. ■

Diffraction is caused by the wave properties of light, and cannot be explained using the geometric ray model (see Sec. 2.2.6). However, it is possible to use light rays as a model for electromagnetic waves as long as diffraction effects are neglected.

In the following, only harmonic waves will be considered, i.e., for which the function  $w(\cdot)$  of (2.18) takes the special form

$$w\left(t - \frac{\mathbf{e}_3^T \mathbf{x}}{v}\right) = e^{j(\omega t - \mathbf{k}^T \mathbf{x} + \varphi)}, \quad (2.31)$$

with the imaginary unit  $j := \sqrt{-1}$ , the angular frequency  $\omega = 2\pi\nu$ , the electromagnetic wave's frequency  $\nu$  in  $\text{Hz} = \text{s}^{-1}$ , the wave vector  $\mathbf{k} = \frac{2\pi}{\lambda} \mathbf{e}_3 = \frac{2\pi\nu}{c} \mathbf{e}_3$ , the angular wave number<sup>11</sup>  $k = \|\mathbf{k}\| = \frac{2\pi}{\lambda}$ , the wavelength  $\lambda$  in m, and the constant  $\varphi$  describing the initial phase. Thus, the electric and magnetic field strengths have to be expressed as complex-valued functions:<sup>12</sup>

$$\underline{\mathbf{E}}(\mathbf{x}, t) = E \mathbf{e}_1 e^{j(\omega t - \mathbf{k}^T \mathbf{x} + \varphi)}, \quad (2.32)$$

$$\underline{\mathbf{H}}(\mathbf{x}, t) = \sqrt{\frac{\varepsilon}{\mu}} E \mathbf{e}_2 e^{j(\omega t - \mathbf{k}^T \mathbf{x} + \varphi)}. \quad (2.33)$$

The 'real' fields—in the physical sense—are obtained by taking the real part using Euler's formula  $e^{j\varphi} = \cos \varphi + j \sin \varphi$ :

$$\mathbf{E}(\mathbf{x}, t) = \Re\{\underline{\mathbf{E}}(\mathbf{x}, t)\} = E \mathbf{e}_1 \cos(\omega t - \mathbf{k}^T \mathbf{x} + \varphi), \quad (2.34)$$

$$\mathbf{H}(\mathbf{x}, t) = \Re\{\underline{\mathbf{H}}(\mathbf{x}, t)\} = \sqrt{\frac{\varepsilon}{\mu}} E \mathbf{e}_2 \cos(\omega t - \mathbf{k}^T \mathbf{x} + \varphi). \quad (2.35)$$

Chapter 8 will show that any wave can be derived from harmonic waves by means of Fourier synthesis. This is why considering the special case of harmonic waves is a sensible option.

<sup>11</sup>Henceforth called the wave number.

<sup>12</sup>The complex-valued formulation allows an elegant mathematical description of harmonic waves, but without a concrete physical correspondence. Henceforth, complex-valued field strengths are denoted by underscored  $\underline{\mathbf{E}}, \underline{\mathbf{H}}$ .

As Maxwell's differential equations are linear, a linear superposition of harmonic solutions will also yield a solution of the system of differential equations. Also, harmonic waves constitute a basis for the function space of arbitrary wave functions  $w(\cdot)$ .

For illustrative purposes, the following coordinate system is usually used:

$$\mathbf{e}_1 := \mathbf{e}_x = \begin{pmatrix} 1 \\ 0 \\ 0 \end{pmatrix}, \quad \mathbf{e}_2 := \mathbf{e}_y = \begin{pmatrix} 0 \\ 1 \\ 0 \end{pmatrix} \quad \Rightarrow \quad \mathbf{e}_3 = \mathbf{e}_z = \begin{pmatrix} 0 \\ 0 \\ 1 \end{pmatrix}. \quad (2.36)$$

Additionally,  $\varphi := 0$  is assumed, resulting in the propagator of  $\omega t - \mathbf{k}^T \mathbf{x}$ . Figure 2.3 shows such an electromagnetic wave. The wave propagates in the direction of the coordinate system's  $z$ -axis, the electric field oscillates in the  $x,z$ -plane, perpendicular to the magnetic field oscillating in the  $y,z$ -plane (transversality).

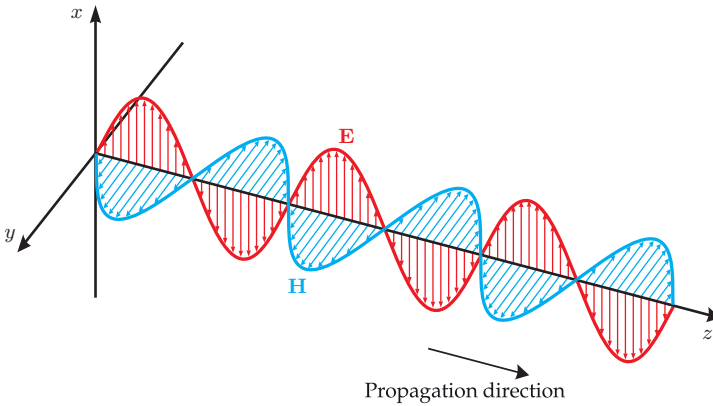


Figure 2.3. Illustration of an electromagnetic wave.

The electromagnetic wave's **energy flux** is described by the Poynting vector [20,32]:

$$\mathbf{P} := \mathbf{E} \times \mathbf{H}. \quad (2.37)$$

The surface power density or intensity of the electromagnetic radiation can be expressed as a function of time

$$\|\mathbf{P}\| = \sqrt{\frac{\varepsilon}{\mu}} E^2 \cos^2(\omega t - \mathbf{k}^T \mathbf{x} + \varphi), \quad (2.38)$$

and is in  $\text{W}/\text{m}^2$  units. The Poynting vector  $\mathbf{P}$  is oriented in the direction of the energy transport, which is the propagation direction of the wave. Image sensors and the human eye usually capture the light's intensity by observing it for a period of time which is significantly longer than the duration of one oscillation of the visible electromagnetic waves. Thus, the measured value is an average of the intensity over time, and is proportional to the square of the amplitude of the electric field strength  $E$  [20]:

$$I = \overline{\|\mathbf{P}\|} = \frac{1}{2} \sqrt{\frac{\varepsilon}{\mu}} E^2 = \frac{1}{2Z} E^2. \quad (2.39)$$

The electric field's periodic change, the direction of the field vectors and the wave's phase cannot be directly captured by image sensors.

To simplify matters, only the electric field  $\mathbf{E}$  will be considered from now on. This is not a restriction as the magnetic field  $\mathbf{H}$  of the electromagnetic wave clearly results from  $\mathbf{E}$  by means of Maxwell's equations.

➤ **2.2.2 Polarization**

Until now, the vector of the electric field strength  $\mathbf{E}$  has been part of a plane like the  $x, z$ -plane in Fig. 2.3. In this case, the light is said to be linearly polarized.

As the wave equation is linear, the sum of two solutions

$$\mathbf{E}(\mathbf{x}, t) = E_1 \mathbf{e}_1 \cos(\omega t - \mathbf{k}^T \mathbf{x} + \varphi_1) + E_2 \mathbf{e}_2 \cos(\omega t - \mathbf{k}^T \mathbf{x} + \varphi_2) \tag{2.40}$$

is also a solution. The electric field strengths in the directions of  $\mathbf{e}_1$  and  $\mathbf{e}_2$  are shifted in phase if  $\varphi_1 \neq \varphi_2$ .

W.l.o.g.  $\mathbf{e}_1 = \mathbf{e}_x$ ,  $\mathbf{e}_2 = \mathbf{e}_y$  and  $\mathbf{k} = \frac{2\pi}{\lambda} \mathbf{e}_z$  are assumed. Then, (2.40) takes the following form:

$$\mathbf{E}(\mathbf{x}, t) = \begin{pmatrix} E_x(\mathbf{x}, t) \\ E_y(\mathbf{x}, t) \\ E_z(\mathbf{x}, t) \end{pmatrix} = \begin{pmatrix} E_{0x} \cos(\omega t - k z + \varphi_x) \\ E_{0y} \cos(\omega t - k z + \varphi_y) \\ 0 \end{pmatrix}. \tag{2.41}$$

Now, the vector  $\mathbf{E}$  of the electric field strength does not only oscillate within a plane, it also rotates around the  $z$ -axis (Fig. 2.4). The rotation is characterized by the wave's angular frequency  $\omega$ . Hence, one rotation is completed after the period  $t = \frac{2\pi}{\omega} = \frac{1}{\nu}$ .

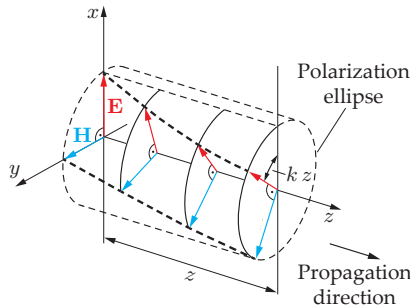


Figure 2.4. Spatial position of the field vectors of a right-handed elliptically polarized light wave for a fixed point of time  $t = \text{const.}$  [20].

➤ **2.2.2.1 The polarization ellipse**

In order to get a geometric view of the electromagnetic wave's polarization, the electric field vector (2.41) is projected onto a plane perpendicular to the propagation direction and thus parallel to the  $x, y$ -plane. W.l.o.g.  $z = \frac{\varphi_x}{k}$  is assumed to represent this plane.

$$E_x(\mathbf{x}, t)|_{z=\frac{\varphi_x}{k}} =: E_x = E_{0x} \cos(\omega t), \tag{2.42}$$

$$E_y(\mathbf{x}, t)|_{z=\frac{\varphi_x}{k}} =: E_y = E_{0y} \cos(\omega t - \varphi_x + \varphi_y) = E_{0y} \cos(\omega t + \delta), \tag{2.43}$$



with  $\delta := \varphi_y - \varphi_x$ . Using  $\cos(\omega t + \delta) = \cos \omega t \cos \delta - \sin \omega t \sin \delta$ ,  $\frac{E_x}{E_{0x}} = \cos \omega t$  and  $\sin \omega t = \sqrt{1 - \cos^2 \omega t} = \sqrt{1 - \left(\frac{E_x}{E_{0x}}\right)^2}$ , the time parameter  $t$  can be eliminated, yielding an implicit description of the curve in terms of  $E_x$  and  $E_y$ :

$$E_y = E_{0y} \frac{E_x}{E_{0x}} \cos \delta - E_{0y} \sqrt{1 - \frac{E_x^2}{E_{0x}^2}} \sin \delta \quad (2.44)$$

$$\Leftrightarrow \frac{E_y}{E_{0y}} - \frac{E_x}{E_{0x}} \cos \delta = -\sqrt{1 - \frac{E_x^2}{E_{0x}^2}} \sin \delta. \quad (2.45)$$

Squaring this equation results in the so-called **polarization ellipse** [5]:

$$\frac{E_x^2}{E_{0x}^2} + \frac{E_y^2}{E_{0y}^2} - \frac{2 E_x E_y}{E_{0x} E_{0y}} \cos \delta = \sin^2 \delta. \quad (2.46)$$

During the wave's propagation,  $\mathbf{E}$  rotates around the  $z$ -axis. If it is projected onto the plane perpendicular to the propagation direction, the end of the electric field strength's vector rotates on the polarization ellipse (Fig. 2.5).

The following holds with respect to the direction angle  $\psi$  and the ellipticity angle  $\chi$ :

$$\tan 2\psi = \frac{2 E_{0x} E_{0y}}{E_{0x}^2 - E_{0y}^2} \cos \delta, \quad 0 \leq \psi \leq \pi, \quad (2.47)$$

$$\sin 2\chi = \frac{2 E_{0x} E_{0y}}{E_{0x}^2 + E_{0y}^2} \sin \delta, \quad -\frac{\pi}{4} \leq \chi \leq \frac{\pi}{4}. \quad (2.48)$$

The direction angle  $\psi$  denotes the angular displacement of the polarization ellipse, and the ellipticity angle  $\chi$  quantifies its ellipticity (Fig. 2.5). The ellipticity angle  $\chi$  and the ellipse's semi-axes  $a$  and  $b$  are related as follows:

$$\tan \chi = \mp \frac{b}{a}. \quad (2.49)$$

The parameters  $\psi$  and  $\chi$  indeed provide a descriptive characterization of the polarization ellipse, but are hard to measure in practice. This is why other parameters are more commonly used to describe the polarization of electromagnetic waves.

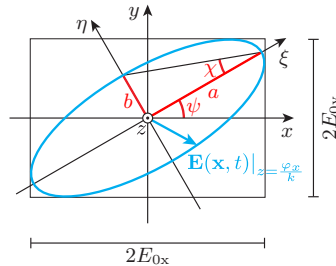


**Figure 2.5.** Illustration of the polarization ellipse with the semi-axes  $a$  and  $b$ , the direction angle  $\psi$  and the ellipticity angle  $\chi$ . The  $z$ -axis protrudes from the plane of the paper.

⊙ 2.2.2.2 Stokes parameters

The Stokes parameters<sup>13</sup> provide a complete description of the polarization state of light by means of measurable quantities [6, 30]. As explained in Sec. 2.2.1.1, only time-averaged values of the field strengths can be measured. These are expressed by the following notation:

$$\overline{E(t)} := \lim_{T \rightarrow \infty} \frac{1}{T} \int_0^T E(t) dt. \tag{2.50}$$

The Stokes parameters, which constitute a four-dimensional vector  $\mathbf{S} \in \mathbb{R}^4$ , are defined as follows with respect to  $E_x(\mathbf{x}, t)$  and  $E_y(\mathbf{x}, t)$  from (2.41) [19, 20]:

$$\mathbf{S} = \begin{pmatrix} S_0 \\ S_1 \\ S_2 \\ S_3 \end{pmatrix} := 2 \begin{pmatrix} \overline{E_x^2(\mathbf{x}, t)} + \overline{E_y^2(\mathbf{x}, t)} \\ \overline{E_x^2(\mathbf{x}, t)} - \overline{E_y^2(\mathbf{x}, t)} \\ \frac{2 \overline{E_x(\mathbf{x}, t) E_y(\mathbf{x}, t)} \cos \delta}{2 \overline{E_x(\mathbf{x}, t) E_y(\mathbf{x}, t)} \sin \delta} \end{pmatrix} = \begin{pmatrix} E_{0x}^2 + E_{0y}^2 \\ E_{0x}^2 - E_{0y}^2 \\ 2 E_{0x} E_{0y} \cos \delta \\ 2 E_{0x} E_{0y} \sin \delta \end{pmatrix} \tag{2.51}$$

$$= (E_{0x}^2 + E_{0y}^2) \begin{pmatrix} 1 \\ \cos 2\chi \cos 2\psi \\ \cos 2\chi \sin 2\psi \\ \sin 2\chi \end{pmatrix}. \tag{2.52}$$

The last transformation is obtained using (2.47), (2.48), and trigonometric identities. The components  $S_i$ ,  $i \in \{0, 1, 2, 3\}$  of the Stokes vector are physically observable properties of polarized light:

- $S_0$  is proportional to the light’s intensity according to (2.39) [30].
- $S_1$  denotes the domination of the horizontal component over the vertical component, i.e., of the linear horizontal polarization (LHP) over the linear vertical polarization (LVP).
- $S_2$  denotes the domination of the component oriented at  $45^\circ$  over the component oriented at  $-45^\circ$  (L+45P over L-45P).
- $S_3$  denotes the domination of the circular components rotating clockwise over the components rotating counterclockwise (right circularly polarized RCP over left circularly polarized LCP).

The following three degenerate polarization states for light of intensity  $I_0$  are typical special cases [6]:

- LHP: linearly, horizontally polarized

$$\mathbf{S}_{\text{LHP}} = 2Z I_0 \begin{pmatrix} 1 \\ 1 \\ 0 \\ 0 \end{pmatrix} \longleftrightarrow E_{0y} = 0, \psi = 0, \chi = 0, \tag{2.53}$$

where  $Z = \sqrt{\frac{\mu}{\epsilon}}$  denotes the medium’s wave impedance, cf. (2.21), (2.39).

---

<sup>13</sup>Named after George Gabriel Stokes (1819–1903).

- LVP: linearly, vertically polarized

$$\mathbf{S}_{\text{LVP}} = 2Z I_0 \begin{pmatrix} 1 \\ -1 \\ 0 \\ 0 \end{pmatrix} \quad \updownarrow \quad E_{0x} = 0, \psi = \frac{\pi}{2}, \chi = 0 \quad (2.54)$$

- L+45P: linearly polarized with an angle of  $45^\circ$  between the polarization plane and the coordinate system

$$\mathbf{S}_{\text{L+45P}} = 2Z I_0 \begin{pmatrix} 1 \\ 0 \\ 1 \\ 0 \end{pmatrix} \quad \nearrow \quad E_{0x} = E_{0y} = E_0, \quad \delta = 0, \psi = \frac{\pi}{4}, \chi = 0 \quad (2.55)$$

- L-45P: linearly polarized with an angle of  $-45^\circ$  between the polarization plane and the coordinate system

$$\mathbf{S}_{\text{L-45P}} = 2Z I_0 \begin{pmatrix} 1 \\ 0 \\ -1 \\ 0 \end{pmatrix} \quad \searrow \quad E_{0x} = E_{0y} = E_0, \quad \delta = \pi, \psi = \frac{3}{4}\pi, \chi = 0 \quad (2.56)$$

- RCP: right circularly polarized (clockwise rotation)

$$\mathbf{S}_{\text{RCP}} = 2Z I_0 \begin{pmatrix} 1 \\ 0 \\ 0 \\ 1 \end{pmatrix} \quad \circlearrowright \quad E_{0x} = E_{0y} = E_0, \quad \delta = \frac{\pi}{2}, \psi = 0, \chi = \frac{\pi}{4} \quad (2.57)$$

- LCP: left circularly polarized (counter-clockwise rotation)

$$\mathbf{S}_{\text{LCP}} = 2Z I_0 \begin{pmatrix} 1 \\ 0 \\ 0 \\ -1 \end{pmatrix} \quad \circlearrowleft \quad E_{0x} = E_{0y} = E_0, \quad \delta = -\frac{\pi}{2}, \psi = 0, \chi = -\frac{\pi}{4} \quad (2.58)$$

In the case of a circularly polarized light wave, the field strength vectors have the shape of a screw for a fixed point of time  $t = \text{const.}$  (cf. Fig. 2.4). When time proceeds, this screw is moved along the direction of propagation (positive  $z$ -direction). This is why the field strength vector rotates around the  $z$ -axis in a plane perpendicular to the direction of propagation. The direction of rotation<sup>14</sup> of the circularly polarized light is related to the time-dependent states of the electric field strength vector in a plane  $z = \text{const.}$  for a view in the reverse direction of propagation, i.e., in the direction of the negative  $z$ -axis [20, 34].

For the general case of elliptically polarized light, the light is neither linearly nor circularly polarized. In (2.40), the two components of the electric field strength in the directions of  $\mathbf{e}_1$  and  $\mathbf{e}_2$  have fixed relations with respect to their phase and amplitude. Both subfields

<sup>14</sup>The terms right-handed and left-handed are not uniquely defined in the literature [22, 32].

are said to be **coherent**.<sup>15</sup> The resulting polarized light (usually polarized elliptically) is then called completely polarized.

For unpolarized light, there is no consistent relation between the phase and the amplitude of the two field strengths: they are incoherent. This is why the two terms  $S_2$  and  $S_3$  of the Stokes vector (2.52), which contain combinations of both fields, vanish when temporally averaged. If in addition the electric field does not have a predominant direction,  $S_1$  will be zero as well. Therefore, unpolarized light is described by the following Stokes vector:

$$\mathbf{S}_{\text{unp}} = \begin{pmatrix} S_0 \\ 0 \\ 0 \\ 0 \end{pmatrix} = 2Z I_0 \begin{pmatrix} 1 \\ 0 \\ 0 \\ 0 \end{pmatrix}. \quad (2.59)$$

In unpolarized light, all polarization states occur with equal probability.

Partly polarized light is a mixture of completely polarized and unpolarized light:

$$\mathbf{S}_{\text{teilp}} = \begin{pmatrix} S_0 \\ S_1 \\ S_2 \\ S_3 \end{pmatrix} = (1-p) \begin{pmatrix} S_0 \\ 0 \\ 0 \\ 0 \end{pmatrix} + p \begin{pmatrix} S_0 \\ S_1 \\ S_2 \\ S_3 \end{pmatrix}. \quad (2.60)$$

The factor  $p \in [0, 1]$  is called the degree of polarization and is defined as the amount of intensity of completely polarized light  $I_{\text{pol}}$  with respect to the total intensity  $I_{\text{total}}$ :

$$p := \frac{I_{\text{pol}}}{I_{\text{total}}} = \frac{\sqrt{S_1^2 + S_2^2 + S_3^2}}{S_0}. \quad (2.61)$$

The following holds:

$$S_0^2 \geq S_1^2 + S_2^2 + S_3^2. \quad (2.62)$$

The two terms are equal for completely polarized light.

An incoherent superposition of polarized light waves can be described by the sum of the respective Stokes vectors [20].

### ④ 2.2.2.3 The Poincaré sphere

Except for the total intensity, the angles  $\psi$  and  $\chi$  in Sec. 2.2.2 completely characterize polarized light. Depicting  $2\psi$  and  $2\chi$  on the surface of a sphere provides a clear representation of the whole state  $\mathbf{P}$  of completely polarized light. This representation is called the **Poincaré sphere** (Fig. 2.6). The azimuth or geographic longitude of a polarization state is  $2\psi$ . Meridians on the sphere represent polarization ellipses with equal orientations  $\psi$  and different ellipticities  $\chi$ . The elevation or latitude is  $2\chi$ . Latitudes represent polarization ellipses with the same shape but different orientations  $\psi$ . The sphere's radius  $S_0$  is the intensity of the electromagnetic wave. The components  $S_1$ ,  $S_2$ ,  $S_3$  of the Stokes vector are the Cartesian coordinates of the polarization state  $\mathbf{P}$ .

The two intersections of a straight line passing through the center of the sphere with its surface correspond to orthogonal polarization states:

<sup>15</sup>Inside a subfield, temporal coherence (see Sec. 2.2.4) is not strictly necessary; as for example, white light can be linearly polarized.

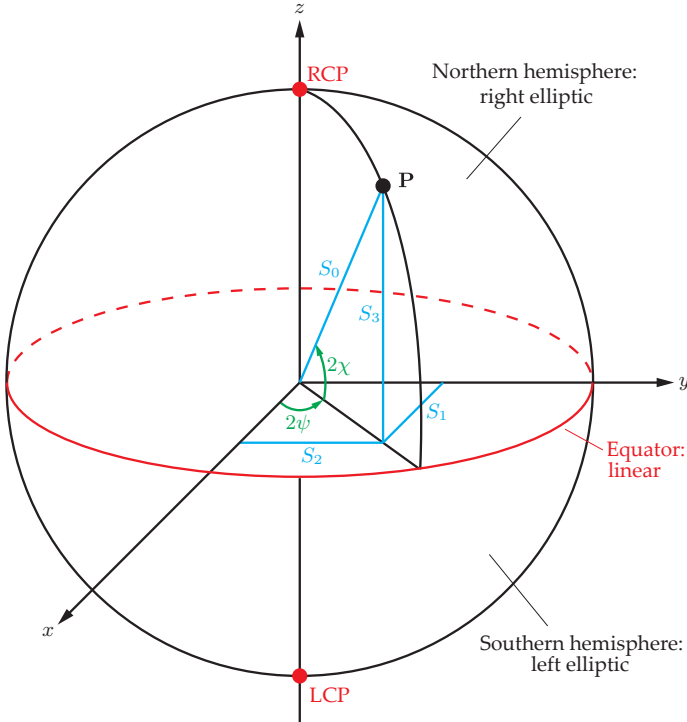


Figure 2.6. Illustration of the polarization state on the Poincaré sphere.

- at the equator: orthogonal linear polarization with a difference in the direction angle of  $\Delta\psi = \frac{\pi}{2}$ ;
- at the poles: left and right circular polarization;
- elsewhere: elliptic polarization states with  $\Delta\psi = \frac{\pi}{2}$  and equal absolute ellipticity angles  $\chi$  with inverse direction of rotation.

#### ⊗ 2.2.2.4 Mueller matrices

The influence of optical elements on the polarization state can be described using the so-called **Mueller matrices**.

A transformation between two polarization states represented by the Stokes vectors  $\mathbf{S}_{\text{in}}$  and  $\mathbf{S}_{\text{out}}$  can be expressed as a multiplication by a Mueller matrix  $\mathbf{M}$ :

$$\mathbf{S}_{\text{out}} = \mathbf{M} \mathbf{S}_{\text{in}}. \quad (2.63)$$

The Mueller matrices of some optical elements are presented in [6, 12]. A linear polarizer is a component which lets only light with a certain polarization direction pass. By means of a linear polarizer, polarized light can be obtained from unpolarized light. Linear polarizers can be constructed out of wire grids or films absorbing electric fields parallel to the grid structure and allowing the orthogonally polarized components to pass through [31].

- Ideal linear polarizer with forward direction  $x$  (horizontal):

$$\mathbf{M}_H = \frac{1}{2} \begin{pmatrix} 1 & 1 & 0 & 0 \\ 1 & 1 & 0 & 0 \\ 0 & 0 & 0 & 0 \\ 0 & 0 & 0 & 0 \end{pmatrix}. \quad (2.64)$$

- Ideal linear polarizer with forward direction  $y$  (vertical):

$$\mathbf{M}_V = \frac{1}{2} \begin{pmatrix} 1 & -1 & 0 & 0 \\ -1 & 1 & 0 & 0 \\ 0 & 0 & 0 & 0 \\ 0 & 0 & 0 & 0 \end{pmatrix}. \quad (2.65)$$

The effect of multiple optical elements located in sequence along the light path can be calculated by multiplying the corresponding Mueller matrices. The matrix belonging to the optical element next to the light source is on the right hand side of the multiplication. As a first example, the concatenation of a horizontal and a vertical linear polarizer is considered:

$$\mathbf{M} = \mathbf{M}_V \mathbf{M}_H = \mathbf{0}. \quad (2.66)$$

Such ‘crossed’ linear polarizers do not let any light pass through.

- Rotator by the angle  $\gamma$ :

$$\mathbf{M}_{\text{Rot}}(\gamma) = \begin{pmatrix} 1 & 0 & 0 & 0 \\ 0 & \cos 2\gamma & -\sin 2\gamma & 0 \\ 0 & \sin 2\gamma & \cos 2\gamma & 0 \\ 0 & 0 & 0 & 1 \end{pmatrix}. \quad (2.67)$$

By a rotator, the polarization ellipse is rotated by the angle  $\gamma$  without its ellipticity  $\chi$  being modified [6]:

$$\psi \mapsto \psi + \gamma, \quad (2.68)$$

$$\chi \mapsto \chi. \quad (2.69)$$

Besides the rotation, a rotator does not induced further changes in the polarization state. Some materials, such as quartz crystals with a certain orientation, as well as certain solutions, lead to a rotation of the polarization state. There are both left and right rotating materials. The rotation angle increases in proportion to the layer thickness and additionally in proportion to the concentration of the solution. Materials rotating the polarization state are called **optically active**. This property can be used to optically measure the concentration of the corresponding solutions, e.g., of certain sugars.

When an optical element with the Mueller matrix  $\mathbf{M}_0$  is rotated around the  $z$ -axis by the angle  $\gamma$  relative to the  $x$ -axis, its Mueller matrix  $\mathbf{M}(\gamma)$  can be calculated as follows [12]:

$$\mathbf{M}(\gamma) = \mathbf{M}_{\text{Rot}}(\gamma) \mathbf{M}_0 \mathbf{M}_{\text{Rot}}(-\gamma). \quad (2.70)$$

- For a linear polarizer  $\mathbf{M}_H$  rotated by  $\gamma = \frac{\pi}{4}$  ( $45^\circ$ ), this expression yields

$$\mathbf{M}_{L+45P} = \frac{1}{2} \begin{pmatrix} 1 & 0 & 1 & 0 \\ 0 & 0 & 0 & 0 \\ 1 & 0 & 1 & 0 \\ 0 & 0 & 0 & 0 \end{pmatrix}. \quad (2.71)$$

- Equivalently, a linear polarizer  $\mathbf{M}_H$  rotated by  $\gamma = -\frac{\pi}{4}$  ( $-45^\circ$ ) around the  $z$ -axis is given by

$$\mathbf{M}_{L-45P} = \frac{1}{2} \begin{pmatrix} 1 & 0 & -1 & 0 \\ 0 & 0 & 0 & 0 \\ -1 & 0 & 1 & 0 \\ 0 & 0 & 0 & 0 \end{pmatrix}. \quad (2.72)$$

- The Mueller matrix of a linear polarizer  $\mathbf{M}_H$  rotated by  $\gamma$  can be expressed generally as

$$\mathbf{M}_{\text{Lin}}(\gamma) = \frac{1}{2} \begin{pmatrix} 1 & \cos 2\gamma & \sin 2\gamma & 0 \\ \cos 2\gamma & \cos^2 2\gamma & \sin 2\gamma \cos 2\gamma & 0 \\ \sin 2\gamma & \sin 2\gamma \cos 2\gamma & \sin^2 2\gamma & 0 \\ 0 & 0 & 0 & 0 \end{pmatrix}. \quad (2.73)$$

Surprisingly, the following equation is no contradiction to (2.66),

$$\mathbf{M}_V \mathbf{M}_{L+45P} \mathbf{M}_H = \frac{1}{8} \begin{pmatrix} 1 & 1 & 0 & 0 \\ -1 & -1 & 0 & 0 \\ 0 & 0 & 0 & 0 \\ 0 & 0 & 0 & 0 \end{pmatrix} \neq \mathbf{0}. \quad (2.74)$$

Thus, the insertion of an additional linear polarizer rotated by  $45^\circ$  allows light to pass through the optical system of two crossed linear polarizers, which before had been completely absorbing [41].

Another optical element changing the polarization state is the so-called **retardation plate**, which is also called retarder or waveplate. Certain optically anisotropic materials, e.g., crystals, have the property of being **birefringent** or **birefractive**. If such a material is aligned in the right way with respect to the incoming light, birefringence causes linearly polarized light of a certain orientation  $\psi$  to pass the material at a higher speed than linearly polarized light with the orthogonal orientation  $\psi + \frac{\pi}{2}$ . The first orientation is therefore called the ‘fast axis’ and the latter one, the ‘slow axis’. The respective refraction indices of the medium are denoted by  $n_f$  and  $n_s$ . Arbitrarily polarized light can be decomposed into a linearly polarized component parallel to the fast axis and a linearly polarized component parallel to the slow axis. The different speeds of the two components while passing the medium result in a shift of phase,

$$\Delta\varphi = 2\pi \frac{d(n_s - n_f)}{\lambda}, \quad (2.75)$$

where  $d$  denotes the medium’s layer thickness and  $\lambda$  the light’s wavelength in vacuum. In this case, the thickness is measured along the direction of propagation of the light, i.e., it corresponds to the optical path the light propagated inside the medium. The propagation

velocities of the two components are  $v_f = \frac{c}{n_f}$  and  $v_s = \frac{c}{n_s}$ . As defined, it is  $v_f > v_s$ , implying  $n_f < n_s$ . Thus, the optical path difference is  $d(n_s - n_f) > 0$ .

**Example 2.3 (Quarter-wave plate):** According to (2.75), a retardation plate with  $\Delta\varphi = \frac{\pi}{2}$  causes a path difference of a quarter wavelength:  $d(n_s - n_f) = \frac{\lambda}{4}$ . This is why such a plate is called  $\frac{\lambda}{4}$ -plate or quarter-wave plate (QWP). Now assume that linearly vertically polarized light hits a quarter-wave plate. The propagation direction of the light is assumed to be perpendicular to the drawing plane in Fig. 2.7.

- 1st case: the polarization direction matches with the plate's fast axis, see Fig. 2.7(a). The LVP-light passes through the plate with a speed of  $v_f$ . Because of the alignment, the polarization component in the direction of the slow axis is zero. This is why the light stays linearly vertically polarized after passing the plate.
- 2nd case: the polarization plate is assumed to be rotated by an angle of  $\alpha = \frac{\pi}{4}$  in relation to the polarization plane; see Fig. 2.7(b). The linearly vertically polarized light can now be expressed as a sum of the components  $\mathbf{E}_f$  and  $\mathbf{E}_s$  parallel to the fast or the slow axis, respectively. For  $\alpha = \frac{\pi}{4}$ , both components have the same absolute value:  $\|\mathbf{E}_s\| = \|\mathbf{E}_f\|$ . When passing the retardation plate,  $\mathbf{E}_s$  will receive a phase delay of one-quarter of a wavelength  $\Delta\varphi = \frac{\pi}{2}$ . Because  $\|\mathbf{E}_f\| = \|\mathbf{E}_s\|$ , one must have  $\chi = \frac{\pi}{4}$  in (2.48). Hence, according to (2.57), a QWP transforms LVP-light into circularly polarized light.
- 3rd case: for angles of  $\alpha \neq 0, \alpha \neq (2k+1)\frac{\pi}{4}, k \in \mathbb{Z}$ , between the retardation plate's fast axis and the polarization plane of the incoming light, LVP-light will be transformed into elliptically polarized light. ■

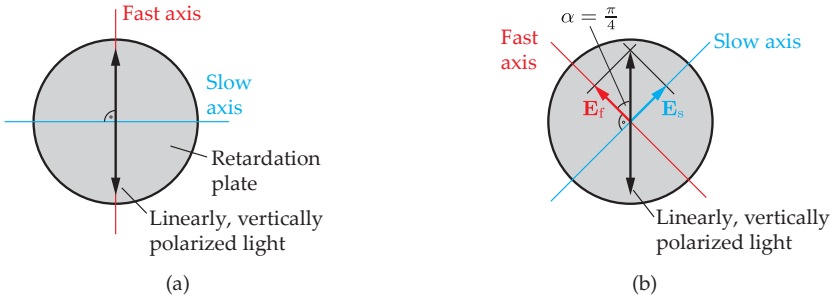


**Figure 2.7.**  $\frac{\lambda}{4}$ -retardation plate: (a) if the polarization direction of the linearly polarized light is equal to the fast axis of the retardation plate, the polarization state remains unchanged. (b) If the polarization direction does not equal the axes of the retardation plate, the electric field strength can be expressed as the sum of the components  $\mathbf{E}_s$  and  $\mathbf{E}_f$ . For  $\alpha = \frac{\pi}{4}$ , the linearly polarized light is transformed into circularly polarized light.

The Mueller matrix of a retardation plate is

$$M_{WP}(\Delta\varphi) = \begin{pmatrix} 1 & 0 & 0 & 0 \\ 0 & 1 & 0 & 0 \\ 0 & 0 & \cos \Delta\varphi & \sin \Delta\varphi \\ 0 & 0 & -\sin \Delta\varphi & \cos \Delta\varphi \end{pmatrix}. \tag{2.76}$$



The following convention is used for the alignment of the plate: the fast axis is along the  $x$ -axis of the coordinate system and the slow axis is along the  $y$ -axis [12]. The Mueller matrix of a retardation plate which has been rotated by an arbitrary angle  $\gamma$  can be calculated according to (2.70), by multiplying the Mueller matrices of the rotator. Of particular technical relevance is the quarter-wave plate. Its Mueller matrix can be obtained by inserting  $\Delta\varphi = \frac{\pi}{2}$  into (2.76):

$$\mathbf{M}_{\text{QWP}} = \begin{pmatrix} 1 & 0 & 0 & 0 \\ 0 & 1 & 0 & 0 \\ 0 & 0 & 0 & 1 \\ 0 & 0 & -1 & 0 \end{pmatrix}. \quad (2.77)$$

The QWP transforms linearly polarized light with a polarization plane tilted by  $45^\circ$  with respect to the fast axis into circularly polarized light, and vice versa.

The following generally holds: by using a QWP and a linear polarizer in the correct alignment, it is possible to obtain completely polarized light with an arbitrary polarization state  $(\psi, \chi)$  from unpolarized light (Fig. 2.8). A linear polarizer rotated by an angle  $\gamma$  around the optical axis in combination with a QWP rotated by  $\alpha$  results in:

$$\mathbf{S} = \mathbf{M}_{\text{Rot}}(\alpha) \mathbf{M}_{\text{QWP}} \mathbf{M}_{\text{Rot}}(-\alpha) \mathbf{M}_{\text{Lin}}(\gamma) \mathbf{S}_{\text{unp}} \quad (2.78)$$

$$= \frac{1}{2} \begin{pmatrix} 1 \\ \cos^2 2\alpha \cos 2\gamma + \cos 2\alpha \sin 2\alpha \sin 2\gamma \\ \sin 2\alpha \cos 2\alpha \cos 2\gamma + \sin^2 2\alpha \sin 2\gamma \\ \sin 2\alpha \cos 2\gamma - \cos 2\alpha \sin 2\gamma \end{pmatrix} \quad (2.79)$$

$$= \frac{1}{2} \begin{pmatrix} 1 \\ \cos 2\alpha \cos(2\alpha - 2\gamma) \\ \sin 2\alpha \cos(2\alpha - 2\gamma) \\ \sin(2\alpha - 2\gamma) \end{pmatrix}. \quad (2.80)$$

The last equation is obtained using the trigonometric addition theorems. It can be used to calculate the rotation angles  $\alpha$  and  $\gamma$  which have to be set in order to obtain polarized light with the Stokes vector  $\mathbf{S}$ . Because  $S_1^2 + S_2^2 + S_3^2 = S_0^2$  and (2.62), completely polarized light is created.

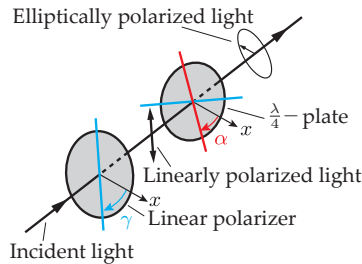


Figure 2.8. Transformation of unpolarized light into elliptically polarized light using a linear polarizer and a  $\frac{\lambda}{4}$ -plate.

A  $\frac{\lambda}{2}$ -plate or a half-wave plate (HWP) with  $\Delta\varphi = \pi$  has the Mueller matrix

$$M_{\text{HWP}} = \begin{pmatrix} 1 & 0 & 0 & 0 \\ 0 & 1 & 0 & 0 \\ 0 & 0 & -1 & 0 \\ 0 & 0 & 0 & -1 \end{pmatrix}. \tag{2.81}$$

The HWP inverts the angles of the orientation and the ellipticity of the polarization ellipse [6]:

$$\psi \mapsto \frac{\pi}{2} - \psi, \tag{2.82}$$

$$\chi \mapsto \chi - \frac{\pi}{2}. \tag{2.83}$$

According to (2.59), unpolarized light  $S_{\text{unp}}$  stays unpolarized after passing a retardation plate:

$$M_{\text{WP}}(\Delta\varphi) S_{\text{unp}} = S_{\text{unp}}. \tag{2.84}$$

If polarized light is reflected by inhomogeneous layers (such as milk glass, for example) or by diffusely scattering surfaces (especially if there happen to be multiple reflections), many small single reflections with effectively stochastic phasing are superposed to form the reflected light, which is therefore partially depolarized (see Fig. 2.9) [30]. The change of the polarization state after a reflection is caused by the rotation of the coordinate system of the transversal wave with respect to the direction of propagation (Fig. 2.9) and by the different intensities of the reflection of light that is polarized parallel and perpendicular to the incidence plane (cf. Sec. 2.6.5).

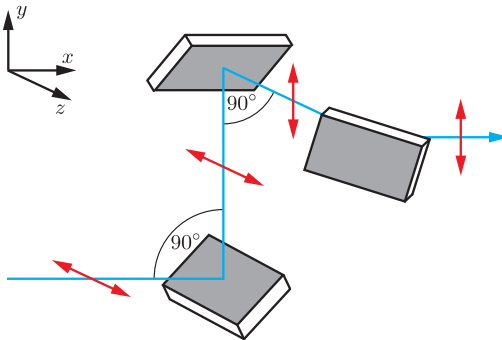


**Figure 2.9.** Change of polarization direction caused by multiple reflections. Linearly polarized light with a direction of incidence parallel to the  $x$ -axis is firstly reflected in  $y$ -direction, then in  $z$ -direction and finally in  $x$ -direction again.

⊙ **2.2.2.5 Measuring the polarization state**

By means of a combination of retardation plates and polarizers, the Stokes vector, and thus the polarization state, of the irradiated light can be measured. At first, the light of interest passes a  $\Delta\varphi$  retardation plate having its fast axis aligned along the  $x$ -axis of the coordinate system. Then, it passes a linear polarizer whose forward direction is tilted by the angle  $\gamma$  with respect to the  $x$ -axis. The remaining light intensity  $I(\gamma, \Delta\varphi)$  is measured by a detector (Fig. 2.10).

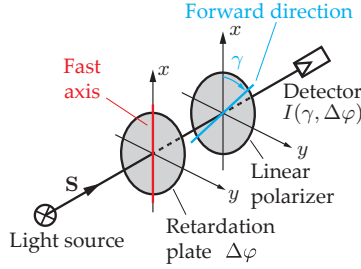


Figure 2.10. Measuring the Stokes vector  $\mathbf{S}$ .

In the mathematical model, the intensity is obtained as the Stokes vector's first coordinate after multiplying the incoming light  $\mathbf{S}$  with the Mueller matrices of the retardation plate and the polarizer:

$$I(\gamma, \Delta\varphi) = \frac{1}{2Z} \begin{pmatrix} 1 & 0 & 0 & 0 \end{pmatrix} \mathbf{M}_{\text{Lin}}(\gamma) \mathbf{M}_{\text{WP}}(\Delta\varphi) \mathbf{S} \quad (2.85)$$

$$= \frac{1}{2Z} \begin{pmatrix} 1 & 0 & 0 & 0 \end{pmatrix} \quad (2.86)$$

$$\frac{1}{2} \begin{pmatrix} 1 & \cos 2\gamma & \sin 2\gamma \cos \Delta\varphi & \sin 2\gamma \sin \Delta\varphi \\ \cos 2\gamma & \cos^2 2\gamma & \sin 2\gamma \cos 2\gamma \cos \Delta\varphi & \sin 2\gamma \cos 2\gamma \sin \Delta\varphi \\ \sin 2\gamma & \sin 2\gamma \cos 2\gamma & \sin^2 2\gamma \cos \Delta\varphi & \sin^2 2\gamma \sin \Delta\varphi \\ 0 & 0 & 0 & 0 \end{pmatrix} \begin{pmatrix} S_0 \\ S_1 \\ S_2 \\ S_3 \end{pmatrix} \\ = \frac{1}{4Z} (S_0 + S_1 \cos 2\gamma + S_2 \sin 2\gamma \cos \Delta\varphi + S_3 \sin 2\gamma \sin \Delta\varphi). \quad (2.87)$$

By varying  $\gamma$  and  $\Delta\varphi$  in the right way, a system of linear equations can be obtained whose solution determines the components of the Stokes vector of the light of interest. A possible choice is  $\gamma \in \{0, \frac{\pi}{4}, \frac{\pi}{2}\}$  and  $\Delta\varphi \in \{0, \frac{\pi}{2}\}$  which yields [6]:

$$S_0 = 2Z (I(0, 0) + I(\frac{\pi}{2}, 0)), \quad (2.88)$$

$$S_1 = 2Z (I(0, 0) - I(\frac{\pi}{2}, 0)), \quad (2.89)$$

$$S_2 = 4Z I(\frac{\pi}{4}, 0) - S_0, \quad (2.90)$$

$$S_3 = 4Z I(\frac{\pi}{4}, \frac{\pi}{2}) - S_0. \quad (2.91)$$

### ⊗ 2.2.2.6 The Jones calculus

Besides the Stokes vectors and Mueller matrices, the Jones calculus is an alternative representation of the polarization state [6, 12, 20]. Jones vectors are compact: they are two-dimensional but complex-valued. Jones vectors can only be used to describe the polarization state of completely polarized light. In contrast, Stokes vectors can also represent unpolarized or partly-polarized light.

If a polarized light wave is described as in (2.41),

$$E_x(\mathbf{x}, t) = E_{0x} \cos(\omega t - k z + \varphi_x), \quad (2.92)$$

$$E_y(\mathbf{x}, t) = E_{0y} \cos(\omega t - k z + \varphi_y), \quad (2.93)$$

the corresponding Jones vector (sometimes called Maxwell vector or Maxwell column) is given by

$$\mathbf{E} := \begin{pmatrix} E_{0x} e^{j\varphi_x} \\ E_{0y} e^{j\varphi_y} \end{pmatrix} \in \mathbb{C}^2. \quad (2.94)$$

In contrast to the Stokes vector, which contains intensity values, the Jones vector uses amplitude and phase values to describe the light wave. The light intensity can be obtained from the norm of the Jones vector:

$$I = \frac{1}{2Z} \|\mathbf{E}\|^2 = \frac{1}{2Z} (\mathbf{E}^*)^T \mathbf{E} = \frac{1}{2Z} (E_{0x}^2 + E_{0y}^2), \quad (2.95)$$

with  $\mathbf{E}^*$  denoting the complex conjugate of  $\mathbf{E}$ .

The considerations of Sec. 2.2.2.2 directly result in the Jones vectors for degenerate polarization states:

$$\mathbf{E}_{\text{LHP}} = \begin{pmatrix} 1 \\ 0 \end{pmatrix}, \quad \mathbf{E}_{\text{LVP}} = \begin{pmatrix} 0 \\ 1 \end{pmatrix}, \quad (2.96)$$

$$\mathbf{E}_{\text{L+45P}} = \frac{1}{\sqrt{2}} \begin{pmatrix} 1 \\ 1 \end{pmatrix}, \quad \mathbf{E}_{\text{L-45P}} = \frac{1}{\sqrt{2}} \begin{pmatrix} 1 \\ -1 \end{pmatrix}, \quad (2.97)$$

$$\mathbf{E}_{\text{RCP}} = \frac{1}{\sqrt{2}} \begin{pmatrix} 1 \\ j \end{pmatrix}, \quad \mathbf{E}_{\text{LCP}} = \frac{1}{\sqrt{2}} \begin{pmatrix} 1 \\ -j \end{pmatrix}. \quad (2.98)$$

The superposition of two light waves corresponds to the sum of their Jones vectors, as the complex-valued amplitudes are added during the superposition. This is true for coherent as well as for incoherent superposition. Conversely, the sum of two Jones vectors always yields another Jones vector representing a valid polarization state. So in contrast to the Stokes vectors, the set of Jones vectors is closed under addition. The Jones calculus can be used to describe interference phenomena as the Jones vectors contain the phase information of the superposed waves.

A polarizing optical element is modeled with a Jones matrix  $\mathbf{J} \in \mathbb{C}^{2 \times 2}$ . The polarization state  $\mathbf{E}_{\text{out}}$  of an incoming light wave  $\mathbf{E}_{\text{in}}$  that passes the optical element can be obtained similarly to (2.63):

$$\mathbf{E}_{\text{out}} = \mathbf{J} \mathbf{E}_{\text{in}}. \quad (2.99)$$

The Jones matrices for linear polarizers, rotators and retardation plates are

$$\mathbf{J}_{\text{H}} = \begin{pmatrix} 1 & 0 \\ 0 & 0 \end{pmatrix}, \quad \mathbf{J}_{\text{Rot}}(\gamma) = \begin{pmatrix} \cos \gamma & -\sin \gamma \\ \sin \gamma & \cos \gamma \end{pmatrix}, \quad (2.100)$$

$$\mathbf{J}_{\text{V}} = \begin{pmatrix} 0 & 0 \\ 0 & 1 \end{pmatrix}, \quad \mathbf{J}_{\text{Lin}}(\gamma) = \begin{pmatrix} \cos^2 \gamma & \sin \gamma \cos \gamma \\ \sin \gamma \cos \gamma & \sin^2 \gamma \end{pmatrix}, \quad (2.101)$$

$$\mathbf{J}_{\text{QWP}} = \begin{pmatrix} 1 & 0 \\ 0 & -j \end{pmatrix}, \quad \mathbf{J}_{\text{WP}}(\Delta\varphi) = \begin{pmatrix} 1 & 0 \\ 0 & e^{-j\Delta\varphi} \end{pmatrix}. \quad (2.102)$$

Multiple optical elements aligned in a row can be expressed by multiplying their Jones matrices.

### 2.2.3 Huygens' principle

The propagation of waves can be explained descriptively and nevertheless exactly by means of Huygens' principle.

The spatial propagation of a wave in an interval  $[t, t + \Delta t]$  can be interpreted as follows: at time  $t$ , every point of the wave front emits a spherical wave with radius  $v \Delta t$  at time  $t + \Delta t$ . At time  $t + \Delta t$ , the envelope of all these spherical waves is the wave front, which has by now propagated over the duration of time  $\Delta t$  (Fig. 2.11). Hence, Huygens' principle represents a connection between the Examples 2.1 and 2.2: a plane wave can be expressed as a composition of an infinite number of spherical waves.

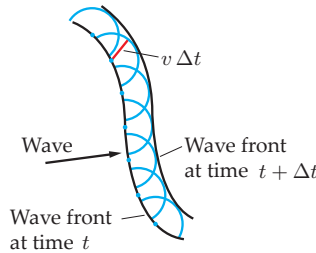


Figure 2.11. Propagation of a wave according to Huygens' principle.

### 2.2.4 Coherence

Coherence describes the property of light having fixed phase and amplitude relations in different locations and points of time. A characteristic value for the temporal coherence is the coherence length

$$d_K = \frac{c}{\Delta\nu}. \quad (2.103)$$

The frequency bandwidth  $\Delta\nu$  is the difference between the highest and the lowest occurring light frequencies. The speed of light in vacuum is denoted by  $c$ . In contrast to monochromatic or laser light, white (broadband) light has a small coherence length (see Table 2.1).

In order to clarify the term coherence length, consider a plane wave propagating in the direction of the  $z$ -axis. Light with a spectral bandwidth  $\Delta\nu$  is assumed, so that  $\nu \in [\nu_0 - \frac{1}{2}\Delta\nu, \nu_0 + \frac{1}{2}\Delta\nu]$ . The differences in phase of the components with the highest and lowest frequencies are obtained by insertion into the propagator  $\omega t - k z = 2\pi \nu t - \frac{2\pi}{\lambda} z$  of (2.31):

$$\Delta\varphi(z, t) = 2\pi (\nu_0 - \frac{1}{2}\Delta\nu) t - \frac{2\pi}{\lambda_1} z - \left( 2\pi (\nu_0 + \frac{1}{2}\Delta\nu) t - \frac{2\pi}{\lambda_2} z \right) \quad (2.104)$$

$$\text{with } \lambda_1 = \frac{c}{\nu_0 - \frac{1}{2}\Delta\nu} \quad \text{and} \quad \lambda_2 = \frac{c}{\nu_0 + \frac{1}{2}\Delta\nu}. \quad (2.105)$$

Table 2.1. Bandwidth and coherence length of white and monochromatic light [30].

	$\Delta\nu$	$d_K$	$\frac{d_K}{\lambda}$
White light	$2 \cdot 10^{14}$ Hz	1.5 $\mu\text{m}$	3
Frequency stabilized helium-neon laser, $\lambda = 633$ nm	$5 \cdot 10^6$ Hz	60 m	$10^8$

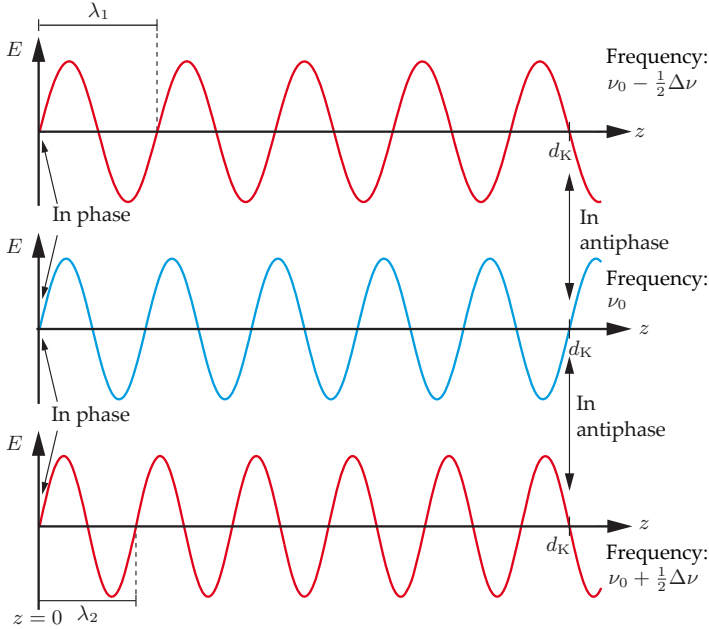


Figure 2.12. Illustration of the connection between the coherence length  $d_K$  and the frequency bandwidth  $\Delta\nu$ .

The coherence length  $d_K$  is the length over which high-frequency waves have to propagate in order to be exactly one period ahead of the low-frequency waves and to oscillate in antiphase to the center frequency  $\nu$  (Fig. 2.12). Assuming  $t = 0$  in Equation (2.104) leads to the following definition:

$$\frac{2\pi}{\lambda_2} d_K - \frac{2\pi}{\lambda_1} d_K = 2\pi \tag{2.106}$$

$$\Leftrightarrow \left( \frac{1}{\lambda_2} - \frac{1}{\lambda_1} \right) d_K = 1 \tag{2.107}$$

$$\Leftrightarrow \frac{\Delta\nu}{c} d_K = 1 \tag{2.108}$$

$$\Leftrightarrow d_K = \frac{c}{\Delta\nu} . \tag{2.109}$$

This relation can be shown more elegantly using the Fourier transform as shown in Sec. 8.4.

Coherence can only occur if the considered light is emitted by the same light source, as the stochastic processes of different physical sources are not related to each other [30]. For light of one single source, temporal coherence means that the phases of light waves emitted at different points of time share a fixed relation: given the phase at a certain point of time, the phase corresponding to a future point of time can be predicted. The coherence length is the period of time or the distance for which that relation remains valid. The fraction  $\frac{d_K}{\lambda}$  represents the number of successive coherent wavelengths. In contrast, spatial coherence regards fixed phase correlations along a wave front, and hence perpendicular to the direction of propagation.

Some wave-optical phenomena can only occur if coherent light is present. In the domain of automated visual inspection, such effects can either be exploited and used as measurement techniques or they can be disturbing, as is the case for the speckle noise affecting triangulation. Whether coherent or incoherent illumination is more suitable depends on the particular inspection task. The following sections will further discuss the mentioned wave-optical effects.

### 2.2.5 Interference

Interference occurs if two or more electromagnetic waves superpose each other. The intensity of the resulting wave does not necessarily have to be the sum of the intensities of the superposed waves. In fact, constructive interference might yield a higher intensity, and destructive interference can result in a reduced intensity or even in a complete extinction of the waves.

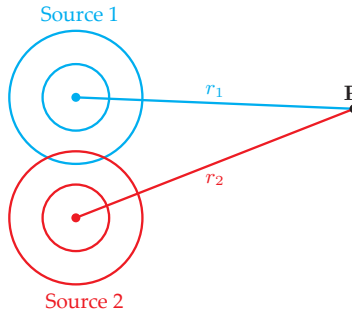


Figure 2.13. Coherent superposition of two light waves at the point P.

As an example of the mathematical description of interference, consider a scalar field of two coherent light sources (Fig. 2.13). The electric field strengths  $E_1(r_1, t)$  and  $E_2(r_2, t)$  of the two idealized light waves with identical wavelengths  $\lambda$  will be assumed to be given by

$$E_1(r_1, t) = E_{01} \cos 2\pi \left( \frac{t}{T} - \frac{r_1}{\lambda} - \delta_1 \right), \quad (2.110)$$

$$E_2(r_2, t) = E_{02} \cos 2\pi \left( \frac{t}{T} - \frac{r_2}{\lambda} - \delta_2 \right), \quad (2.111)$$

with the wave amplitudes  $E_{01}$  and  $E_{02}$ , respectively.

The superposition of the two waves at a point **P** yields the electric field strength

$$E = E_1(r_1, t) + E_2(r_2, t). \quad (2.112)$$

The light's intensity  $I$  is equal to the time average  $\overline{E^2}$  of the squared field strength,

$$I = \frac{1}{Z} \overline{E^2}, \quad (2.113)$$

$$\overline{E^2} := \frac{1}{t_2 - t_1} \int_{t_1}^{t_2} E^2 dt, \quad (2.114)$$

with  $Z$  denoting the wave impedance of the medium (see Sec. 2.2.1.1). The intensities  $I_1$  and  $I_2$  of the irradiated wave are

$$I_i = \frac{1}{2Z} E_{0i}^2, \quad i = 1, 2. \quad (2.115)$$

The intensity of the waves interfering at point  $\mathbf{P}$  is

$$I = \frac{1}{Z} \overline{(E_1(r_1, t) + E_2(r_2, t))^2} \quad (2.116)$$

$$\begin{aligned} &= \frac{1}{Z} \left( \overline{E_{01}^2 \left( \cos 2\pi \left( \frac{t}{T} - \frac{r_1}{\lambda} - \delta_1 \right) \right)^2} + \overline{E_{02}^2 \left( \cos 2\pi \left( \frac{t}{T} - \frac{r_2}{\lambda} - \delta_2 \right) \right)^2} \right. \\ &\quad \left. + 2E_{01}E_{02} \overline{\cos 2\pi \left( \frac{t}{T} - \frac{r_1}{\lambda} - \delta_1 \right) \cos 2\pi \left( \frac{t}{T} - \frac{r_2}{\lambda} - \delta_2 \right)} \right) \end{aligned} \quad (2.117)$$

$$\begin{aligned} &= \frac{1}{2Z} \left( \overline{E_{01}^2 + E_{01}^2 \cos 4\pi \left( \frac{t}{T} - \frac{r_1}{\lambda} - \delta_1 \right)} + \overline{E_{02}^2 + E_{02}^2 \cos 4\pi \left( \frac{t}{T} - \frac{r_2}{\lambda} - \delta_2 \right)} \right. \\ &\quad \left. + 2E_{01}E_{02} \overline{\cos 2\pi \left( \frac{r_2 - r_1}{\lambda} + \delta_2 - \delta_1 \right)} \right. \\ &\quad \left. + 2E_{01}E_{02} \overline{\cos 2\pi \left( \frac{2t}{T} - \frac{r_2 + r_1}{\lambda} - \delta_2 - \delta_1 \right)} \right). \end{aligned} \quad (2.118)$$

The last equation is obtained using the trigonometric addition theorems. Assuming  $\frac{t_2 - t_1}{T} \rightarrow \infty$  results in

$$I = \frac{1}{2Z} \left( E_{01}^2 + E_{02}^2 + 2E_{01}E_{02} \cos 2\pi \left( \frac{r_2 - r_1}{\lambda} + \delta_2 - \delta_1 \right) \right) \quad (2.119)$$

$$I = I_1 + I_2 + 2\sqrt{I_1 I_2} \cos 2\pi \left( \frac{r_2 - r_1}{\lambda} + \delta_2 - \delta_1 \right). \quad (2.120)$$

Hence, the total intensity is given by the sum of the single intensities,  $I_1$  and  $I_2$ , and the interference term.

In the case of coherent light, the interference term is maximal if  $\delta_1 = \delta_2 = 0$  for

$$\cos 2\pi \left( \frac{r_2 - r_1}{\lambda} \right) = 1 \quad \Rightarrow \quad 2\pi \frac{r_2 - r_1}{\lambda} = 2\pi n, \quad (2.121)$$

This occurs if the difference  $\Delta d := r_2 - r_1$  between the lengths of the two paths from each light source to the point  $\mathbf{P}$  is an integer multiple of the wavelength  $\lambda$ :

$$2\pi \frac{\Delta d}{\lambda} = 2\pi n \quad \Leftrightarrow \quad \Delta d = n\lambda, \quad n \in \mathbb{Z}. \quad (2.122)$$

In this case, both waves have exactly the same phase and superpose with each other constructively.

A minimum is obtained if

$$\cos 2\pi \left( \frac{r_2 - r_1}{\lambda} \right) = -1 \quad \Rightarrow \quad 2\pi \frac{r_2 - r_1}{\lambda} = \pi + 2\pi n \quad (2.123)$$

$$2\pi \frac{\Delta d}{\lambda} = (2n + 1)\pi \quad \Leftrightarrow \quad \Delta d = \frac{2n + 1}{2}\lambda, \quad n \in \mathbb{Z}. \quad (2.124)$$



The two waves hit each other with a displacement of one-half of the wavelength, which is why their electric fields neutralize each other. If the intensities  $I_1$  and  $I_2$  are equal, the intensities of the resulting minima will be  $I = 0$ .

The contrast<sup>16</sup> of an interference pattern is defined as

$$V := \frac{I_{\max} - I_{\min}}{I_{\max} + I_{\min}}, \quad (2.125)$$

with the intensity  $I_{\max}$  of its maximum and  $I_{\min}$  of its minimum. If the path difference between the two interfering light waves equals the coherence length,  $\Delta d = d_K$ , a contrast of  $V = \frac{1}{e}$  results [27]. If incoherent light is present, no interference effects can be observed, as the relations between the phases of the wave are completely random, and therefore constructive and destructive coherence neutralize themselves because of the temporal averaging. This is why the interference term in (2.120) vanishes and one has, instead,

$$I = I_1 + I_2. \quad (2.126)$$

Such an addition of intensities is only valid for incoherent light. For coherent light, the electric field strengths have to be added.

## ➤ 2.2.6 Diffraction

Diffraction of electromagnetic waves is another effect that can only be explained by means of the wave properties of light. Light does not travel in a straight line through a slit or an aperture without changing direction. Rather, it creates a diffraction pattern. The object causing the diffraction is usually called ‘the obstacle’  $H$ . Diffracted light can also reach areas lying in the shadow of the obstacle that would not be reachable according to geometric optics. For a physical description of diffraction, two cases have to be considered:

- Fresnel diffraction, also called near-field diffraction: the distance between the obstacle and the light source and/or the observation point is finite. In this case, spherical waves have to be used as a model.
- Fraunhofer diffraction or far-field diffraction: The distance between the obstacle, the light source and the observation point is very large—ideally, infinite. Then, plane waves can be used as a model. Fraunhofer diffraction is a special case of Fresnel diffraction, since plane waves can be considered as spherical waves with an infinite radius [20].

In general, diffraction can be quantitatively described using Kirchhoff’s diffraction formula [5]. But in the following, only Fraunhofer diffraction will be considered, as the distances involved in many optical systems used for automated visual inspection are large enough to justify this approximation. There are, in fact, some particular optical systems achieving higher resolutions by measuring the near-field, such as special micro- or spectrometers, for example [4]; but for automated visual inspection, they are only used in exceptional cases.

Assume now that there is an aperture that is illuminated by plane waves from an infinitely far light source. The term aperture denotes the opening of a diaphragm limiting the expansion of the observed light bundle (see also Sec. 3.4.3). The resulting electric field is observed on the opposite side of the aperture, at a great distance (called ‘the far distance’).

According to Huygens’ principle, each of the aperture’s points  $(x, y)$  emits an ‘elementary wave’ in the shape of a spherical wave. The electric field at the aperture can be described by

<sup>16</sup>In this context, the contrast is also called the visibility.

the aperture function  $\underline{P}(x, y)$  as a complex amplitude:

$$\underline{P}(x, y) = |\underline{P}(x, y)| e^{j\varphi(x, y)}. \quad (2.127)$$

One area element  $dA$  of the aperture corresponds to the following part  $d\underline{E}$  of the electric field at position  $\mathbf{B}$  in the observation space:

$$d\underline{E}(X, Y, Z) = \underline{P}(x, y) dA \frac{1}{r} e^{j(2\pi f r - \omega t)}. \quad (2.128)$$

The first factor is the aperture function, the last one represents the wave function of the spherical wave emitted at the point  $(x, y)$ . The aperture's coordinates are denoted by the lower case letters  $(x, y)$  and the coordinates of space by the capital letters  $(X, Y, Z)$ . The  $z$ -axis of the coordinate system is located in the optical axis perpendicular to the aperture. The distance  $r$  between the aperture and the point  $\mathbf{B}$  is

$$r = \sqrt{(X - x)^2 + (Y - y)^2 + Z^2}. \quad (2.129)$$

The spatial frequency of the light is  $f = \frac{1}{\lambda} = \frac{1}{2\pi} \|\mathbf{k}\|$  in units of  $\text{m}^{-1}$ , where  $\mathbf{k} \in \mathbb{R}^3$  is the wave vector. The angular frequency is  $\omega = 2\pi\nu$ . The frequency is  $\nu = \frac{1}{T} = \frac{c}{\lambda}$ , in units of  $\text{Hz} = \text{s}^{-1}$ .

The distance to the center of the aperture is denoted by  $R = \sqrt{X^2 + Y^2 + Z^2}$ . In the Fraunhofer case,  $R \gg X, Y \gg x, y$  and  $R \approx Z$ , so that

$$r \approx \sqrt{X^2 - 2xX + Y^2 - 2yY + Z^2} \quad (2.130)$$

$$\approx \sqrt{R^2 - 2(xX + yY)} \quad (2.131)$$

$$= R \sqrt{1 - 2 \frac{xX + yY}{R^2}}. \quad (2.132)$$

Now, the function  $R \sqrt{1 - 2 \frac{xX + yY}{R^2}}$  can be expanded in a Taylor series around  $\chi = 0$  and cut off after the first term:

$$r \approx R \left( 1 - \frac{xX + yY}{R^2} \right). \quad (2.133)$$

This expression can now be inserted into (2.128):<sup>17</sup>

$$d\underline{E}(X, Y, Z)|_{Z \approx R} \approx \underline{P}(x, y) dA \frac{1}{r} e^{j(2\pi f R(1 - \frac{xX + yY}{R^2}) - \omega t)}. \quad (2.134)$$

The whole electric field at the point  $(X, Y, Z)$  can be obtained by integrating this equation over the aperture:

$$\underline{E}(X, Y, Z)|_{Z \approx R} \approx \frac{1}{R} e^{j(2\pi f R - \omega t)} \iint \underline{P}(x, y) e^{-j2\pi f \frac{xX + yY}{R}} dx dy. \quad (2.135)$$

<sup>17</sup>Since the far field is considered,  $R \rightarrow \infty$  and hence  $r \approx R$  can be employed in the denominator because of (2.133). In contrast, the phase of the electromagnetic wave is calculated in the exponent, so that distances in the order of one wavelength are relevant, which is why the more precise approximation (2.133) has to be used in the exponent.

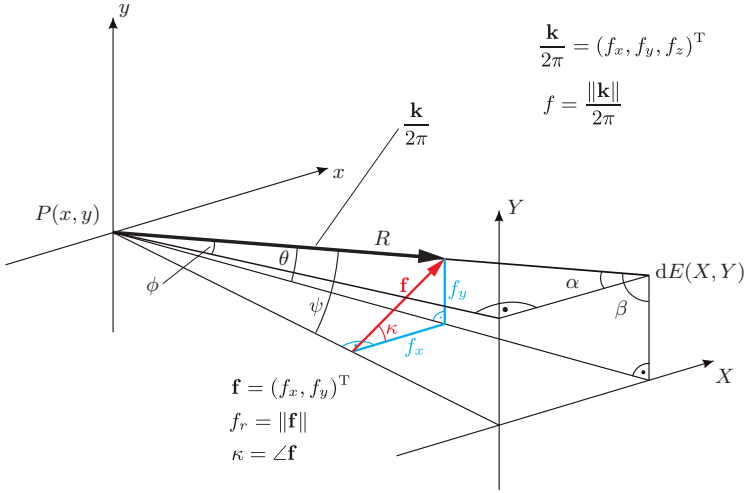


Figure 2.14. Geometric configuration used to derive the diffraction pattern.

Figure 2.14 uses the following trigonometric equations:

$$\frac{X}{R} = \sin \phi = \cos \alpha, \quad (2.136)$$

$$\frac{Y}{R} = \sin \theta = \cos \beta. \quad (2.137)$$

Hence, the spatial frequencies  $f_x, f_y$  in the image plane can be expressed as

$$f_x = f \cos \alpha = f \sin \phi = f \frac{X}{R}, \quad (2.138)$$

$$f_y = f \cos \beta = f \sin \theta = f \frac{Y}{R}. \quad (2.139)$$

The exponent of the integrand from (2.135) can now be rewritten as

$$-j2\pi f \frac{xX + yY}{R} = -j2\pi (f_x x + f_y y) \quad (2.140)$$

and the electric field strength can be expressed as a function of the spatial frequency:

$$\underline{E}(f_x, f_y, R) = \frac{1}{R} e^{j(2\pi f R - \omega t)} \iint \underline{P}(x, y) e^{-j2\pi(f_x x + f_y y)} dx dy \quad (2.141)$$

$$= \frac{1}{R} e^{j(2\pi f R - \omega t)} \underline{E}(f_x, f_y) \quad (2.142)$$

with

$$\underline{E}(f_x, f_y) := \iint \underline{P}(x, y) e^{-j2\pi(f_x x + f_y y)} dx dy \quad (2.143)$$

$$= \mathcal{F}\{\underline{P}(x, y)\}. \quad (2.144)$$

This double integral is equivalent to the operator  $\mathcal{F}\{\cdot\}$  of the two-dimensional Fourier transform (cf. Chap. 8). Thus, the electric field of the diffraction is the Fourier transform of the aperture function:

---

**Theorem 2.2: Fraunhofer diffraction**

The field distribution  $\underline{E}(f_x, f_y)$  in the image plane in a distance of  $R$  to the aperture plane is the spatial Fourier transform of the aperture function  $\underline{P}(x, y)$ . Conversely, the aperture function can be calculated as the inverse Fourier transform of the electric field in the image plane:

$$\underline{E}(f_x, f_y) = \mathcal{F}\{\underline{P}(x, y)\} = \iint \underline{P}(x, y) e^{-j2\pi(f_x x + f_y y)} dx dy, \quad (2.145)$$

$$\underline{P}(x, y) = \mathcal{F}^{-1}\{\underline{E}(f_x, f_y)\} = \iint \underline{E}(f_x, f_y) e^{j2\pi(f_x x + f_y y)} df_x df_y. \quad (2.146)$$

◇

Similar to the reciprocity of the Fourier transform, the following quantitative relation holds for the size of the aperture and the diffraction pattern:

- A small aperture, e.g., a pinhole diaphragm or a narrow slit, results in a wide Fourier transform. The electric field in the image plane extends to large values of  $X$  and  $Y$ , i.e., large angles  $\phi, \theta$ . For small apertures, the diffraction effects are significantly stronger.
- A big aperture, e.g., a lens or a wide slit, results in a spatially narrow diffraction pattern. The influence of diffraction is reduced for larger apertures, and can finally be neglected.

In order to be able to observe Fraunhofer diffraction from a limited distance to the aperture, a special optical setup is needed since the necessary infinite distance cannot be directly realized. Figure 2.15 shows such a setup. A point source of light is located in the focus of a collecting lens L1, illuminating the aperture plane with parallel waves. A second lens, L2, images the Fraunhofer diffraction pattern from infinity to the screen. This screen is positioned at a distance equal to the focal length of the lens (cf. Chap. 3). The electric field in the focal plane is the Fourier transform of the aperture function.

The diffraction patterns of some apertures will now be treated.

---

**Example 2.4 (Single-slit diffraction):** The simplest aperture is a single slit. The slit is assumed to be parallel to the  $y$ -axis, to be infinitely spread in the  $y$ -direction, and to have a width of  $d$  in the  $x$ -direction (Fig. 2.16). Then, the aperture function is given by<sup>18</sup>

$$P(x, y) = P_0 \operatorname{rect}\left(\frac{x}{d}\right) 1(y). \quad (2.147)$$

---

<sup>18</sup>For this and the following examples, both the aperture function  $P(x, y)$  and the electric field  $E(x, y)$  are assumed to be real-valued and are thus written without underscores.

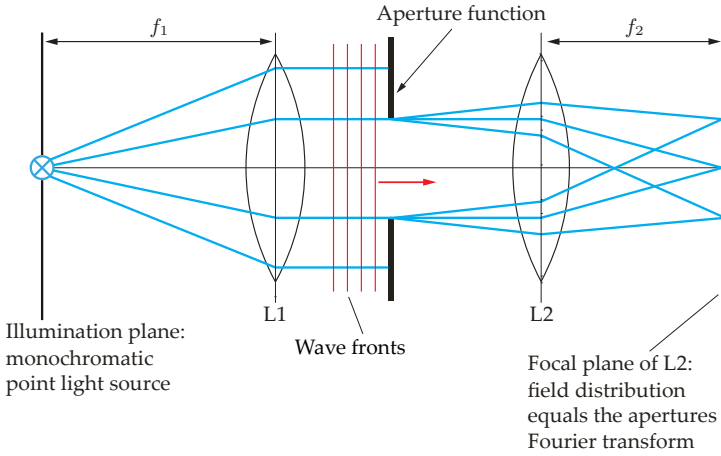


Figure 2.15. Optical realization of the Fourier transform using the principle of diffraction.

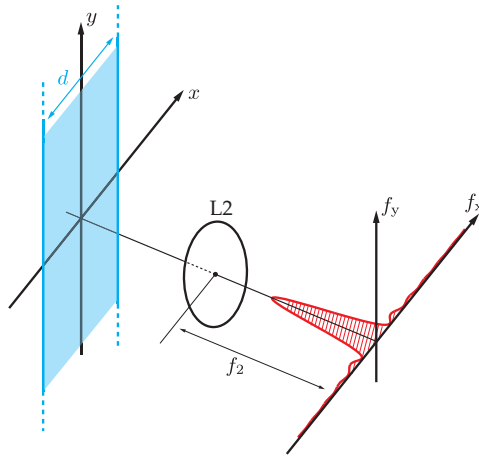


Figure 2.16. Single-slit diffraction. The diffraction pattern is visualized on a screen at a finite distance by the lens L2.

The electric field after the diffraction caused by the single slit is obtained by calculating the Fourier transform of the aperture function:

$$E(f_x, f_y) = \mathcal{F}\{P(x, y)\} = \underbrace{P_0 d \operatorname{sinc}(d f_x)}_{E(f_x)} \delta(f_y), \tag{2.148}$$

$$E(f_x) = P_0 d \frac{\sin(\pi d f_x)}{\pi d f_x}. \tag{2.149}$$

Supposing

$$\gamma := \pi d f_x = \pi d f \sin \phi, \tag{2.150}$$

the previous equation can be rewritten as

$$E(\gamma) = P_0 d \frac{\sin \gamma}{\gamma}. \quad (2.151)$$

The intensity is proportional to the square of the electric field strength

$$I(\gamma) = I_0 \left( \frac{\sin \gamma}{\gamma} \right)^2. \quad (2.152)$$

Minima of intensity are observed for

$$\sin \gamma = 0 \wedge \gamma \neq 0 \quad \Rightarrow \quad \gamma = n\pi, \quad n = \pm 1, \pm 2, \pm 3, \dots, \quad (2.153)$$

so, because of (2.150) and  $f = \frac{1}{\lambda}$ , for

$$\sin \phi = n \frac{\lambda}{d}. \quad (2.154)$$

The maxima are not directly obvious. Therefore, the derivative of  $I(\gamma)$  is calculated using the quotient rule, and its zeros are found:

$$0 = \frac{dI(\gamma)}{d\gamma} = I_0 \frac{2 \sin \gamma (\gamma \cos \gamma - \sin \gamma)}{\gamma^3}. \quad (2.155)$$

A maximum is obtained for  $\gamma = 0$ . As shown, the remaining solutions of  $\sin \gamma = 0$  are minima of the intensity. Further maxima are given by

$$\gamma \cos \gamma - \sin \gamma = 0 \quad \Leftrightarrow \quad \tan \gamma = \gamma, \quad (2.156)$$

which can only be solved numerically. A good approximation for higher order diffractions  $n$  is given by

$$\gamma \approx \left(n + \frac{1}{2}\right) \pi, \quad n = \pm 1, \pm 2, \pm 3, \dots \quad (2.157)$$

$$\sin \phi \approx \left(n + \frac{1}{2}\right) \frac{\lambda}{d}. \quad (2.158)$$

Figure 2.17 shows the curve of intensities calculated according to (2.152). The intensities are maximal for  $\gamma = 0; \pm 1.43\pi; \pm 2.46\pi; \pm 3.47\pi; \dots$ , and the zeros are located at  $\gamma = \pm\pi; \pm 2\pi; \pm 3\pi; \dots$

Equations (2.154) and (2.158) show that the angles  $\phi$  of the diffraction maxima tend towards zero for  $d \gg \lambda$ , and that the extent of the diffraction becomes negligible. Hence, for a slit that is wide compared to the wavelength, diffraction effects only occur very close to the image point, so the imaging methods of geometric optics are a good approximation. For slits with a width of  $d$  on the order of the wavelength  $\lambda$ , diffraction effects occur even under very large angles  $\phi$ , which is why wave-optical effects can no longer be neglected.

The Dirac delta function  $\delta(f_y)$  in (2.148) shows that when using the setup from Fig. 2.15, there can only be a diffraction pattern for  $f_y \rightarrow 0$  (see Sec. 8.2.2 for a further description of Dirac delta functions). The Fraunhofer diffraction pattern is emitted under an angle of  $\theta = 0$ , is thus parallel to the optical axis, and is focused on the  $f_x$ -axis by the lens (see Fig. 2.16).

The single slit also yields a descriptive explanation of the diffraction effect. Light hav-

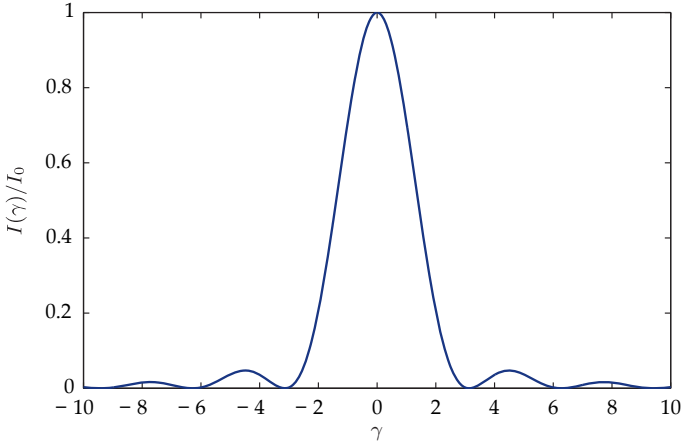


Figure 2.17. Distribution of intensities resulting from single-slit diffraction.

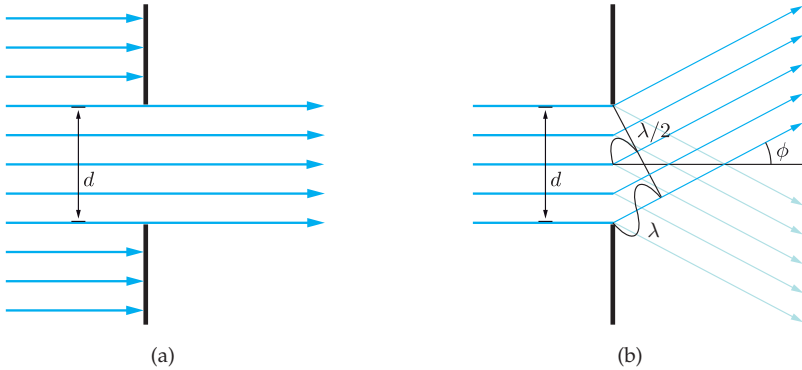


Figure 2.18. Single-slit diffraction: (a) Central maximum of intensities, all rays are in phase; (b) Minima of intensities: Rays that are  $\frac{d}{2}$  apart from each other in the aperture plane are in antiphase [20].

ing a propagation direction parallel to the irradiated light wave is in phase and forms the central maximum (Fig. 2.18). The first zero of the intensities occurs for  $\sin \phi = \frac{\lambda}{d}$ . If Huygens’ principle is applied and light leaves the single slit in this direction, with an angle of  $\phi$ , the phases of the marginal ray and of the central ray (cf. Chap. 3) are shifted by  $\frac{\lambda}{2}$ , which results in destructive interference. Equivalently, for any other ray of the bundle, there exists another ray passing through the slit at a distance of  $\frac{d}{2}$  from it and having a relative phase shift of  $\frac{\lambda}{2}$ . In total, all pairs of rays extinguish each other, which is why there is an intensity minimum in the direction of  $\phi$ . ■

**Example 2.5 (Diffraction caused by a rectangular aperture):** A rectangular aperture of size  $c \times d$  can be interpreted as a two-dimensional generalization of the single slit. The aperture

function is

$$P(x, y) = P_0 \operatorname{rect}\left(\frac{x}{c}\right) \operatorname{rect}\left(\frac{y}{d}\right). \quad (2.159)$$

The Fourier transform yields the electric field in the image plane

$$E(f_x, f_y) = \mathcal{F}\{P(x, y)\} = P_0 c d \operatorname{sinc}(c f_x) \operatorname{sinc}(d f_y). \quad (2.160)$$

The intensities of the diffraction pattern are given by

$$I(\gamma, \eta) = I_0 \left(\frac{\sin \gamma}{\gamma}\right)^2 \left(\frac{\sin \eta}{\eta}\right)^2 \quad (2.161)$$

with

$$\gamma = \pi c f_x = \pi c f \sin \phi, \quad (2.162)$$

$$\eta = \pi d f_y = \pi d f \sin \theta. \quad (2.163)$$

Figure 2.19 shows the resulting diffraction pattern. ■

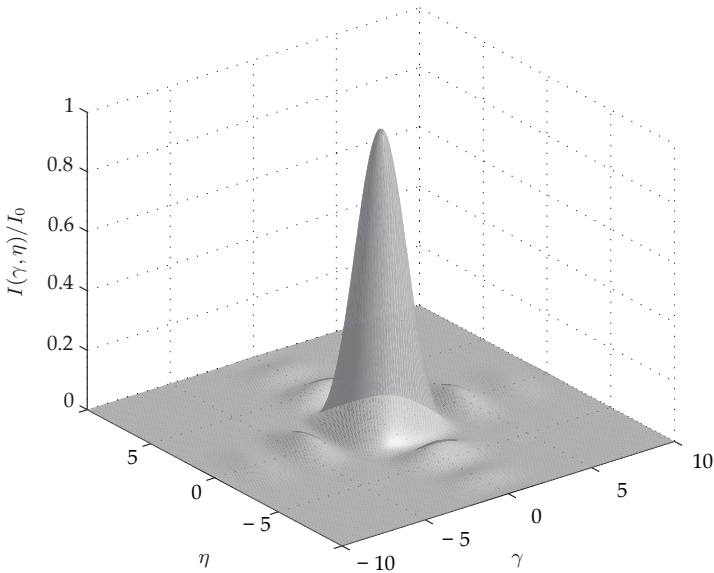


Figure 2.19. Distribution of intensities for diffraction caused by a rectangular aperture.

---

**Example 2.6 (Pinhole diffraction):** As most imaging systems in practice use circular lenses and apertures, diffraction caused by a circular aperture is quite important. The aperture function of a pinhole aperture with diameter  $D$  is given by

$$P(x, y) = P_0 \operatorname{rect}\left(\frac{\|\mathbf{x}\|}{D}\right) = \begin{cases} P_0 & \text{if } \sqrt{x^2 + y^2} \leq \frac{1}{2}D \\ 0 & \text{otherwise} \end{cases}. \quad (2.164)$$



In order to be able to calculate the diffraction pattern, at first a coordinate transformation into polar coordinates is performed both for the position and for the spatial frequency (cf. Fig. 2.14):

$$x = r \cos \varphi, \quad y = r \sin \varphi, \quad (2.165)$$

$$f_x = f_r \cos \kappa, \quad f_y = f_r \sin \kappa. \quad (2.166)$$

This yields

$$P(r, \varphi) = P_0 \operatorname{rect}\left(\frac{r}{D}\right) = \begin{cases} P_0 & \text{if } r \leq \frac{1}{2}D \\ 0 & \text{otherwise} \end{cases}. \quad (2.167)$$

The Fourier transform of this aperture function is given by

$$E(f_r, \kappa) = \mathcal{F}\{P(r, \varphi)\} = \int_0^{\frac{1}{2}D} \int_0^{2\pi} P_0 e^{-j2\pi f_r r \cos(\varphi - \kappa)} d\varphi r dr, \quad (2.168)$$

The argument of the exponential function is obtained from (2.165) and (2.166) by means of the trigonometric addition theorems.

The function  $P(r, \varphi)$  is rotationally symmetric, as it does not depend on  $\varphi$ . Hence,  $E(f_r, \kappa)$  is also rotationally symmetric, i.e., constant with respect to  $\kappa$ . This is why it is sufficient to evaluate the integral for a single  $\kappa$ . Here,  $\kappa = 0$  is chosen.

The integral is given by the Bessel functions of the first kind, which are defined by

$$J_n(z) = \frac{j^{-n}}{2\pi} \int_0^{2\pi} e^{j(z \cos \xi + n\xi)} d\xi \quad (2.169)$$

and satisfy

$$J_n(-z) = (-1)^n J_n(z) \quad (2.170)$$

as well as

$$\int_0^x \xi J_0(\xi) d\xi = x J_1(x). \quad (2.171)$$

For the electric field strength in the case of pinhole diffraction, this implies

$$E(f_r) = P_0 \int_0^{\frac{1}{2}D} \int_0^{2\pi} P_0 e^{-j2\pi f_r r \cos \varphi} d\varphi r dr \quad (2.172)$$

$$= P_0 \int_0^{\frac{1}{2}D} 2\pi J_0(2\pi f_r r) r dr, \quad (2.173)$$

where the sign of the exponent can be omitted because of (2.170). Using (2.171) results in

$$E(f_r) = 2\pi P_0 \frac{D}{2} \frac{J_1(\pi f_r D)}{2\pi f_r}. \quad (2.174)$$

Setting

$$\gamma := \pi f_r D = \frac{\pi}{\lambda} D \sin \psi \quad (2.175)$$

with the angle  $\psi$  between the wave vector  $\mathbf{k}$  and the optical axis, as shown in Fig. 2.14, results in

$$E(\gamma) = \frac{\pi}{2} P_0 D^2 \frac{J_1(\gamma)}{\gamma}. \quad (2.176)$$

Squaring that expression yields the intensity of the pinhole diffraction pattern [20]:

$$I(\gamma) = 4 I_0 \frac{J_1^2(\gamma)}{\gamma^2}. \quad (2.177)$$

The main maximum of the intensity is reached for  $\gamma = 0$ . A numerical approximation for the first minimum is  $\gamma \approx 3.83$  and

$$\psi \approx \sin \psi \approx 3.83 \frac{\lambda}{\pi D} \approx 1.22 \frac{\lambda}{D}. \quad (2.178)$$

Figure 2.20 shows the diffraction pattern of a circular aperture. The circular intensity structures are called Airy disks. ■

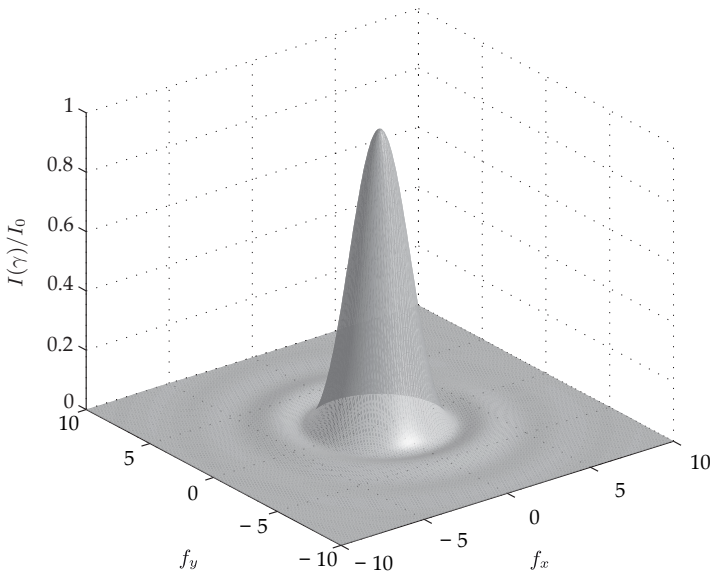


Figure 2.20. Distribution of intensities for pinhole diffraction.

Babinet's principle states that complementary apertures lead to the same diffraction pattern [5,20]. Two apertures are called complementary if the first aperture is opaque exactly where the second aperture is transparent and vice versa. If both apertures are aligned behind each other in a row, no light can pass them [5]. W.l.o.g. the two apertures  $P_1(\mathbf{x})$  and  $P_2(\mathbf{x})$  are

assumed to be given by

$$P_1(\mathbf{x}) : \mathbb{R}^2 \rightarrow \{0, 1\}, \quad (2.179)$$

$$P_2(\mathbf{x}) = 1 - P_1(\mathbf{x}). \quad (2.180)$$

Their Fraunhofer diffraction patterns can be obtained by means of the Fourier transform:

$$\mathcal{F}\{P_2\} = \mathcal{F}\{1\} - \mathcal{F}\{P_1\} \quad (2.181)$$

$$\Leftrightarrow E_2(\mathbf{f}) = \delta(\mathbf{f}) - E_1(\mathbf{f}), \quad \text{with } \mathbf{f} = (f_x, f_y)^T. \quad (2.182)$$

Except for the origin  $\mathbf{f} = \mathbf{0}$ , it holds

$$E_2(\mathbf{f}) = -E_1(\mathbf{f}). \quad (2.183)$$

As the intensity is proportional to the square of the electric field strength, the diffraction patterns of an aperture and its complement match each other except for the difference in the origin, which is the direct component [41].

An application of diffraction is the spectral decomposition of light. The positions of the diffraction maxima depend on the wavelength, as given by (2.158). This is why gratings can be used to redirect the light to different directions depending on the respective wavelengths [30, 35]. Then, the spatial distribution of the intensities can be used to infer the spectral distribution of the intensities (see Sec. 7.2.4).

### ⊙ 2.2.6.1 Resolution of imaging systems

The resolution of an optical system is its ability to create different images out of different objects. The minimum observation angle under which two objects can still be discriminated in the image, is a measure for the resolution. Usually, a small observation angle implies that two objects are close to each other, as in microscopic images for example. However, this does not necessarily have to be true, as when capturing distant objects with a telescope.

The physically possible resolution of an optical system, as well as its sharpness, are limited by diffraction.

When an image is formed, the diffraction patterns of all the object points are additively superposed on each other on the image plane. In the following, two point light sources are considered (Fig. 2.21). Additionally, a circular aperture with a diameter  $D$  is assumed, as is common for practical imaging systems. According to Ex. 2.6, both objects cause rotationally symmetric diffraction patterns, the so-called Airy disks. When using white light, the Airy disks of the different wavelengths are superposed on each other. As the extent of the diffraction patterns depends on the wavelength, no sharp minima or maxima will be visible. In fact, the point-shaped object appears as a blurred disk.

Usually, diffraction patterns have an infinite extent but their intensities decay quickly after the first order diffraction. This is why, for large observation angles of the two objects, the diffraction patterns are practically completely separated in the image plane. The two images can be resolved without any problems.

Decreasing the angle  $\Delta\varphi$  between the two objects will eventually lead to a significant overlap of the two diffraction patterns. Nevertheless, they might still be resolvable if the distance between the two main maxima is large enough; see Fig. 2.22(a). There are different criteria concerning this limit [20]. One possibility is the so-called **Rayleigh criterion**: two

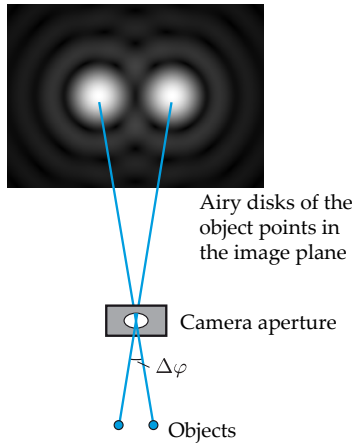


Figure 2.21. Superposition, in the image plane, of the diffraction patterns of two object points.

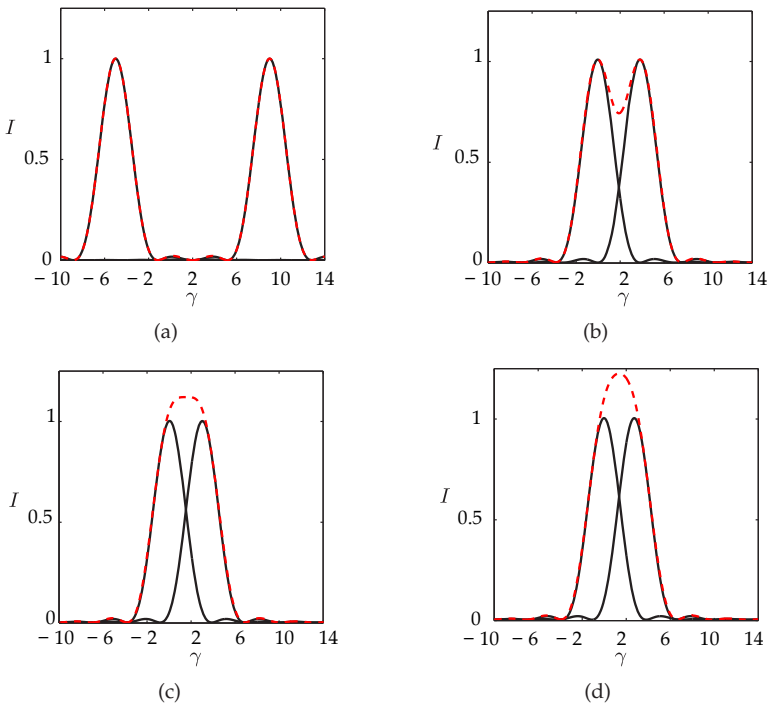


Figure 2.22. Resolution of imaging systems for two superposed Airy diffraction patterns: (a) Clearly resolvable diffraction patterns; (b) Rayleigh criterion; (c) Sparrow's resolution limit; (d) Diffraction patterns which can no longer be resolved.

images are said to be barely resolvable, if the center of the first Airy disk is located at the position of the second diffraction pattern's first minimum, see Fig. 2.22(b). In this case, the following holds for an observation angle  $\Delta\varphi$ :

$$\Delta\varphi = \psi_{\min}, \quad (2.184)$$

with  $\psi_{\min}$  denoting the angle of the first diffraction minimum according to (2.178). This implies

$$\Delta\varphi \approx 1.22 \frac{\lambda}{D}. \quad (2.185)$$

The resolving power is then quantified by the reciprocal of the latter expression:

$$\frac{1}{\Delta\varphi} \propto \frac{D}{\lambda}. \quad (2.186)$$

Hence, there are two possible ways to increase the resolving power: increasing the aperture diameter  $D$ , and using light of a shorter wavelength  $\lambda$ . However, both alternatives are technically limited and involve other disadvantages, e.g., a reduced depth of field (see Sec. 3.4.4).

Diffraction is an insuperable physical limitation to the maximum possible resolving power of an imaging system. An optical system is called diffraction limited if all geometrical aberrations can be neglected in comparison to diffraction, so that the system's resolution and sharpness is mainly limited by diffraction effects.

**Sparrow's resolution limit** describes the absolute limit of resolving two diffraction patterns when seen by a human observer. Two Airy disks cannot be distinguished if the intensity between the two main maxima does not decrease, see Fig. 2.22(c). Mathematically formulated, Sparrow's criterion is satisfied if the second derivative of the intensity is equal to zero in the center between the two image points [20]. For two object points of the same brightness, this is the case for

$$\Delta\varphi \approx 0.95 \frac{\lambda}{D}. \quad (2.187)$$

Further improvements of the resolution limitation caused by diffraction can be achieved by means of image restoration methods: by applying suitable image filters, diffraction effects can be mitigated to a certain extent (see Chap. 10). The success of such an image restoration depends, among other things, on the noise contained in the image signal and on the precision of the employed diffraction and imaging models.

### ➤ 2.2.7 Speckle

If coherent light is scattered by randomly positioned surface points, a spatially irregular and temporally stable interference pattern appears, which is called **Speckle**. For example, speckle can be observed if coherent light is reflected by a rough surface (Fig. 2.23).

According to Huygens' principle, each surface point emits a spherical wave with the phase of the irradiated light. If the surface's structure is irregular, then the interference pattern will also have an irregular, grainy structure.

The **roughness**  $R$  is defined by the fluctuations of the surface relief. There are different characteristic values used for quantifying roughness. A simple choice is the difference  $R_t$  between the maximum and the minimum of the surface relief (cf. Fig. 2.23).

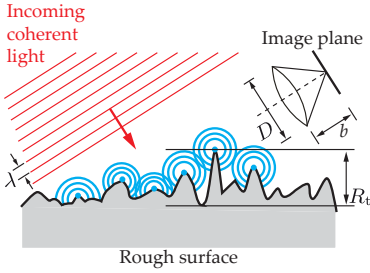


Figure 2.23. Formation of speckle caused by the reflection of a coherent light wave by a rough surface.

If  $R \gg \lambda$ , then the light’s phases are approximately uniformly distributed on  $[0, 2\pi]$  because of the light’s periodicity in  $\lambda$ .

If the reflections are observed using a camera, each object point will lead to a diffraction pattern of the imaging optic on the image plane around the geometric image of the object. If the optics are diffraction limited and if the aperture is circular, the diffraction pattern will be an Airy disk. The diffraction patterns interfere with each other and the image sensor captures an intensity image showing the speckle (Fig. 2.24). The mean diameter  $\mu_d$  of the speckle grains is equal to the diameter of the central maximum of the Airy disk [24],

$$\mu_d = 2 \psi_{\min} b \approx 2.44 \frac{\lambda}{D} b, \tag{2.188}$$

where  $\lambda$  is the wavelength,  $D$  is the imaging optic’s diameter limiting the light, and  $b$  is the so-called image distance (cf. Fig. 2.23 and Chap. 3). ‘Stopping down,’ i.e., reducing  $D$  or increasing the  $f$ -number  $O := \frac{f}{D}$ , increases the diameter of the observed speckle grains because of the increasing diffraction.

The probability of the speckle’s intensity  $I$  being inside the interval  $[I_0, I_0 + dI]$  can be calculated by means of the assumed uniform distribution of the phase shifts between the coherent elementary waves [14], yielding an exponential distribution:

$$\Pr\{I \in [I_0, I_0 + dI]\} = f_I(I_0) dI = \frac{1}{E\{I\}} e^{-\frac{I_0}{E\{I\}}}, \quad I_0 \geq 0, \tag{2.189}$$

with  $E\{I\}$  denoting the expected value of the intensity. Thus, the standard deviation is given by

$$\sqrt{\text{Var}\{I\}} = E\{I\}. \tag{2.190}$$

Therefore, the intensity fluctuations of the speckle are of the same order of magnitude as the mean value. In addition, the probability density  $f_I$  reaches its maximum for  $I = 0$  and decreases exponentially for higher intensities. Hence, the intensity ‘black’ is most likely. In all, speckle is a very high contrast pattern. Because of the intensity’s positivity and (2.190), the fluctuations of speckle can be modeled in a signal theoretical sense as multiplicative noise with a correlation length of about  $\mu_d$  (for a mathematical description of noise, see Sec. 8.5.3).

### 2.3 Light as a quantum phenomenon

By means of the model of an electromagnetic wave, light’s propagation phenomena, especially diffraction and interference effects, can be correctly described and calculated. But the

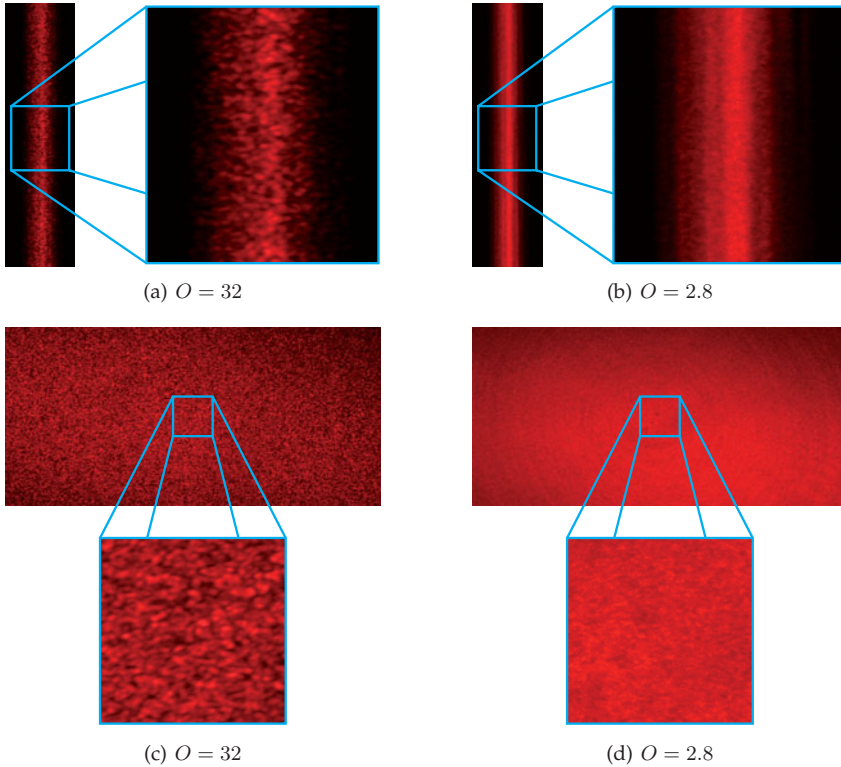


**Figure 2.24.** Speckle seen when observing the scattered light of a laser with the wavelength  $\lambda = 660 \text{ nm}$  on a dull white surface: (a) Laser line of width 1 mm, imaged with a small aperture; (b) Laser line for a large aperture; (c), (d) Laser ray widened to an area of about  $5 \text{ cm} \times 5 \text{ cm}$ . The focal distance of the camera lens is  $f = 100 \text{ mm}$ . The object distance is approximately  $g \approx 500 \text{ mm}$ .

electrodynamic model of Maxwell's equations cannot explain how light is measured using a detector. If a metal surface is irradiated with light, electrons might be freed, which is the so-called photo-electric effect. For a long period of time it was not clear why the photo-electric effect only takes place for light of a certain wavelength and does not depend only on the intensity of the light. On the basis of Max Planck's quantum hypothesis of 1900, it was possible for Albert Einstein to logically explain the photo-electric effect in 1905. For this discovery he was awarded the Nobel Prize in 1921.

In order to be able to satisfactorily explain all phenomena of light, it has to be considered to have wave characteristics and particle characteristics simultaneously (wave-particle duality). The 'light particles' are the quanta of light, and are called **photons**. For questions concerning light propagation, the wave model is suitable, but in order to be able to understand the detection of light, the particle model has to be used. Both perspectives are joined in the field of quantum electrodynamics, which is beyond the scope of this book [40].

As the electric field of light oscillates at a very high frequency, it cannot be directly measured. Instead, only the energetic impact of the light caused by the incoming photons and their energy can be measured. The product of the photon energy and the number of absorbed

photons per time and per detector area is equivalent to the intensity (power per area), which is proportional to the square of the electric field strength in the electromagnetic perspective.

In terms of quantum physics, the electric field strength can be interpreted as a probability amplitude for photons [41]. The resulting intensity (the squared absolute value) can be interpreted as a probability density for finding photons in the electromagnetic wave. In the domain of quantum physics, the wave model and the particle model are related in a stochastic way. This is why the measurement of light intensity, as it is done by every light detector, is a process that has to be described statistically.

Photons have no rest mass. Their energy depends on the frequency  $\nu$  of the light:

$$E_{\text{photon}} = h\nu = \frac{hc}{\lambda}. \quad (2.191)$$

The constant of proportionality  $h \approx 6.626 \cdot 10^{-34}$  Js is called **Planck's constant** [20]. As before, the speed of light in vacuum is denoted by  $c$  and the corresponding wavelength is denoted by  $\lambda$ .

Equation (2.191) implies that a light wave of a certain energy has to consist of a finite number of photons. As a light wave has to consist of at least one single photon, it cannot fall below the frequency-dependent energy of a single photon. In the perspective of the particle model, the distribution of light cannot be exactly described by continuous functions and without considering quantization. Continuous functions like the electric field distribution of a diffraction pattern (2.149) have to be replaced by probability density functions of the position of the photons.

In the following, the influence of quantization on the image acquisition process is described. To this end, monochromatic light with a wavelength  $\lambda$  is assumed. If a sensor with a linear characteristic is used, the intensity which is measured by the image sensor and which results in the image value  $g$  of an image point is proportional to the product of a camera pixel's area  $A$ , the irradiance  $E$  (see Chap. 4), and the exposure time  $T$ :

$$g \propto EAT. \quad (2.192)$$

Equivalently, a difference in the irradiance of  $\Delta E$  causes an image value difference  $\Delta g$ :

$$\Delta g \propto \Delta EAT. \quad (2.193)$$

Dividing the right hand side by the energy  $E_{\text{photon}}$  of a single photon results in the number of photons. However, an image sensor does not detect every single photon. The image sensor's quantum efficiency  $\alpha \in [0, 1]$  describes what fraction of the incoming photons is really registered. Thus, the average number of effective photons  $\mu_n$  contributing to an image value difference  $\Delta g$  is given by:

$$\mu_n = \frac{\Delta EAT}{E_{\text{photon}}} \alpha = \frac{\Delta EAT\lambda}{hc} \alpha. \quad (2.194)$$

As it is the aim of an image sensor to transform light energy into electric energy, the mean number of effective photons  $\mu_n$  is equivalent to the number of generated electrons.

The photon count  $n$  is a random variable with the expected value  $\mu_n$ :

$$E\{n\} = \mu_n. \quad (2.195)$$



If the radiation field is unlimited to a certain extent—which is usually the case in the practice of automated visual inspection—the random variable  $n$  is approximately Poisson distributed with the expected value  $\mu_n$  [23,28]:

$$n \sim P_{\text{Poisson}}(\mu_n) = e^{-\mu_n} \frac{(\mu_n)^n}{n!}, \quad (2.196)$$

$$\text{Var}\{n\} = E\{(n - \mu_n)^2\} = \mu_n. \quad (2.197)$$

The parameter  $\mu_n$  of the Poisson distribution is equivalent to both the distribution's expected value and to its variance. In terms of the image acquisition process, the stochastic distribution of the photon count results in the measured image values being superposed with a noise signal. A surface of equal brightness is not always mapped to the same image value but is affected by variations. These quantum effects can affect two neighboring pixels of a homogeneous area as well as the values of a pixel corresponding to pictures of an image series taken of a constant scene which might show significant differences in their image values.

A measure of the impact of these random effects on the image signal is given by the signal-to-noise ratio:

$$SNR = \frac{E\{n\}^2}{\text{Var}\{n\}} = \mu_n. \quad (2.198)$$

Thus, a higher mean number of effective photons  $\mu_n$  results in a better quality of the image signal. According to (2.194), this can be achieved by

- providing a high irradiance  $E$ , e.g., by means of a bright illumination and a big aperture diameter  $D$ ;
- using an image sensor with large pixel areas  $A$ ;
- using an image sensor with a high quantum efficiency  $\alpha$ ;
- setting a long exposure time  $T$ ;
- or by means of long-wave light with low-energy photons.

---

**Example 2.7 (Quantum effects on the image sensor):** The effects of quantum statistics on the image acquisition process will be explained by means of the example of the CCD sensor DALSA FT18 (cf. Chap. 6). A wavelength  $\lambda = 550 \text{ nm}$  and an exposure time  $T = 40 \text{ ms}$  are assumed. The sensor has pixels with size  $7 \mu\text{m} \times 7 \mu\text{m}$  and a quantum efficiency of  $\alpha = 0.22$ . The saturation charge of a pixel is  $4.5 \cdot 10^4$  electrons. When using a quantization of 256 image values, the image value of 255 is equivalent to the maximum brightness of the image:  $\mu_n = 45,000$  electrons. The associated number of incoming photons is 204,545 and is obtained by dividing by  $\alpha$ . An image value difference of  $\Delta g = 1$  is, on average, equivalent to 176 electrons or 802 photons.

According to (2.191), a single photon has an energy of  $E_{\text{photon}} = 3.61 \cdot 10^{-19} \text{ J}$ . The saturation irradiance equivalent to a maximum image value  $g = 255$  is given by

$$E_{\text{Saturation}} = \frac{\mu_n E_{\text{photon}}}{AT\alpha} \approx 0.038 \text{ W/m}^2, \quad (2.199)$$

using (2.194). Compared to the irradiance of the sun, which is about  $1,000 \text{ W/m}^2$  over the whole electromagnetic spectrum, this value is rather small [37]. ■

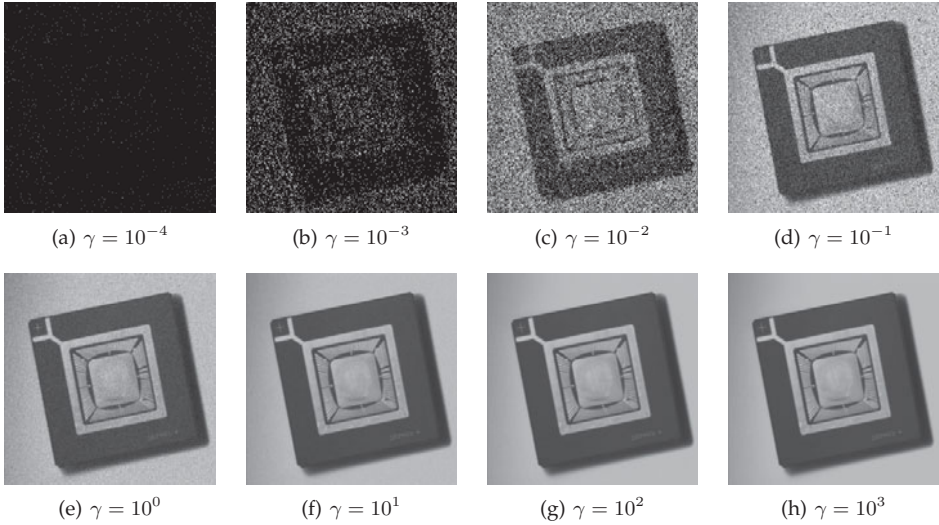


Figure 2.25. Simulation of the Poisson distributed photon count during image acquisition.

**Example 2.8 (Poisson process):** The effects of light quantization on image acquisition can be simulated by a Poisson process. Therefore, a known gray-scale image  $g(\mathbf{x})$  is used. For every image pixel  $\mathbf{x}$ , a Poisson process  $P_{\text{Poisson}}(\gamma g(\mathbf{x}))$  is simulated. The resulting gray values are scaled by the factor  $\frac{1}{\gamma}$  and again form an image  $g_\gamma(\mathbf{x})$ . The parameter  $\gamma$  is equivalent to the mean number of photons resulting in a gray value difference of  $\Delta g = 1$ . For different values of  $\gamma = 10^i$ , different images are obtained, in accordance with

$$g_\gamma(\mathbf{x}) := \frac{n(\mathbf{x})}{\gamma}, \quad n(\mathbf{x}) \sim P_{\text{Poisson}}(\gamma g(\mathbf{x})). \quad (2.200)$$

Figure 2.25 shows a series of images for which the Poisson distributions of the photon count with different parameters have been simulated. It is obvious that the standard deviation of the gray values decreases for increasing  $\gamma$ . According to (2.198), the signal-to-noise ratio is  $SNR = \gamma g(\mathbf{x})$  and increases linearly with  $\gamma$ . For  $\gamma = 1$ , the expected value of the Poisson process is equal to  $g(\mathbf{x})$ . In this case, a single photon causes a gray value difference of  $\Delta g = 1$ . For  $\gamma = 10^3$ , 1,000 photons are necessary to reach the next quantization interval. 255,000 photons cause a saturation at the maximum gray value of 255. The latter case approximately corresponds to the image sensor of the previous example. ■

## 2.4 The ray model of geometrical optics

Compared to wave optics, the ray model of light is quite simplified. It is a usable approximation if all relevant dimensions are significantly greater than the light's wavelength. The ray model can be used to describe optical imaging systems consisting of lenses and mirrors, using only elementary geometric equations (see Chap. 3).

Table 2.2. Suitability of the different models of light.

Dimensions	Number of photons	Geometric optics	Wave optics	Photon statistics
$l \gg \lambda$	$\frac{\Delta E A T \lambda \alpha}{h c} \gg 1$	×		
$l \gg \lambda$		×		×
	$\frac{\Delta E A T \lambda \alpha}{h c} \gg 1$		×	
			×	×

As described in Sec. 2.2.1.1, a light ray is parallel to the direction of propagation of the electromagnetic wave, and therefore perpendicular to the wave fronts. Light rays travel in straight lines inside a homogeneous medium.

Geometric optics neglects the wave properties of light, and assumes a straight-line propagation of the light rays. This is why the imaging process can be described using no more than elementary geometry. Therefore, the **intercept theorem** is the most important tool. It is explained in Appendix A.1.

## 2.5

## 2.5 Summary

This chapter has introduced the reader to different models explaining light. Each model describes the reality only partially and approximately. The suitability of the approximation depends on the specific application. In this context, the following two criteria are especially relevant:

- Is the smallest relevant dimension  $l$  of the optical system greater than the light's wavelength  $\lambda$ ? If yes, geometric optics can be used as a suitable model. Otherwise, wave-optical effects should be taken into consideration.
- What is the number of photons, according to (2.194)? If the number of photons is too small, photon statistics have to be taken into account. Otherwise, they can be neglected.

Table 2.2 summarizes the criteria regarding the applicability of the different perspectives on optical phenomena.

## 2.6

## 2.6 Interaction of light and matter

When light hits matter, different interactions might take place, yielding a variety of optical phenomena. Light can be absorbed and transformed into heat; it can be reflected, or diffusely scattered. Transparent and partially transparent materials let a part of the light pass through (this is called transmission), however, it usually does not propagate in a straight line across the interface between the materials (refraction).

### 2.6.1 Absorption

Matter can absorb light and transform it into heat or, rarely, into other forms of energy [16]. Absorption can be based on different processes. For example, electrons can be elevated to higher energy levels by the energy of the photon, or the molecules and the lattice can be set into oscillations, which are also energetically quantized. Furthermore, liquids and gases possess material-dependent and quantized rotation states, which can also be activated by absorbing photons. After absorption, the photons either get emitted again with a lower energy and thus a longer wavelength, or their energies are completely transformed into heat without emitting any radiation, because of further interactions, e.g., collisions. The transformation into heat is called dissipation. In the case of conductive materials, an electric current caused by the electric field of the irradiated light can arise, which will also lead to a loss of radiation energy.

As according to (2.191), the photon energy depends on the frequency, the absorption often varies with the light's frequency. The spectral components which are absorbed and the amount of absorbed energy depends on the physical and chemical properties of the atoms, molecules, or solid state bodies.

Selective absorption of certain spectral components and a simultaneous reflection of the remaining light causes an object to appear colored. If an object absorbs the whole of visible light, it appears black. As is known, such objects are heated most intensely under irradiation.

### 2.6.2 The law of reflection

If light is reflected at an interface, part of the irradiated light is emitted back in the medium with a fixed angle of reflection, without crossing the boundary. The direction of the reflection only depends on the relation between the direction of incidence and the normal to the surface. The reflected light ray is located in the plane spanned by the incident light ray and the surface normal.

The law of reflection can be derived using Huygens' principle. For that purpose, the ideal case of an infinitely spread plane wave is considered. As the reflected wave moves in the same medium as the incident wave, both waves propagate with the same speed. If the incident wave front which runs through point **A** in Fig. 2.26, reaches point **B** after propagating for the distance  $l_1$ , the wave coming from point **A** has also propagated for a distance of  $l_r = l_1$ , which results in

$$l_r = l_1 \quad \Rightarrow \quad \theta_r = \theta_1. \quad (2.201)$$

Hence in the case of reflection, the angle of incidence is equal to the angle of reflection. The angle of incidence is the angle between the surface normal  $\mathbf{n}$  and the direction of incidence of the incident light rays. Similarly, the angle of reflection is between the surface normal and the direction of propagation of the outgoing light ray. The following holds for the wave vector  $\mathbf{k}_r$  of the reflected wave:

$$\mathbf{k}_r = (\mathbf{I} - 2\mathbf{n}\mathbf{n}^T)\mathbf{k}_1, \quad (2.202)$$

with  $\mathbf{k}_1$  denoting the wave vector of the incident light wave,  $\mathbf{n}$  denoting the normal vector of the interface and  $\mathbf{I}$  denoting the identity matrix [1, 29]. On the one hand, this vectorial formulation of the law of reflection states that the angle of incidence is equal to the angle of reflection, and on the other hand it implies that the wave vectors of the incident wave and of

the reflected wave are coplanar to the normal vector of the interface, so that all three vectors are located in the plane of incidence.

### ► 2.6.3 The law of refraction

Inside matter, light propagates with a speed  $v$ , which is slower than the speed of light in vacuum  $c$ . From (2.24) and (2.26) it follows that

$$v = \frac{c}{n}. \quad (2.203)$$

The index of refraction  $n$  depends on the material and on the wavelength. If two materials, referred to as 1 and 2, have respective refraction indices  $n_1 > n_2$ , material 1 is called the optically denser medium and material 2 is called the less optically dense medium.

In general, light does not go through two media of different refraction indices in a straight line, but is refracted at the interface. This phenomenon can be explained by means of Huygens' principle (see Sec. 2.2.3). A wave front of an incoming electromagnetic wave tilted at some angle to the interface reaches point **A** on the interface in Fig. 2.26 at time  $t$ . Then, point **A** emits a spherical wave into medium 2, which propagates with reduced speed, and at time  $t + \Delta t$  reaches a distance of  $l_2$ . At this time, the incoming wave front reaches point **B**, which emits another spherical wave. The superposition of all spherical waves in medium 2 emitted by the points of the interface forms a plane wave front of the transmitted electromagnetic wave. Because of the different propagation velocities, this wave does not propagate in the same direction as the incident wave.

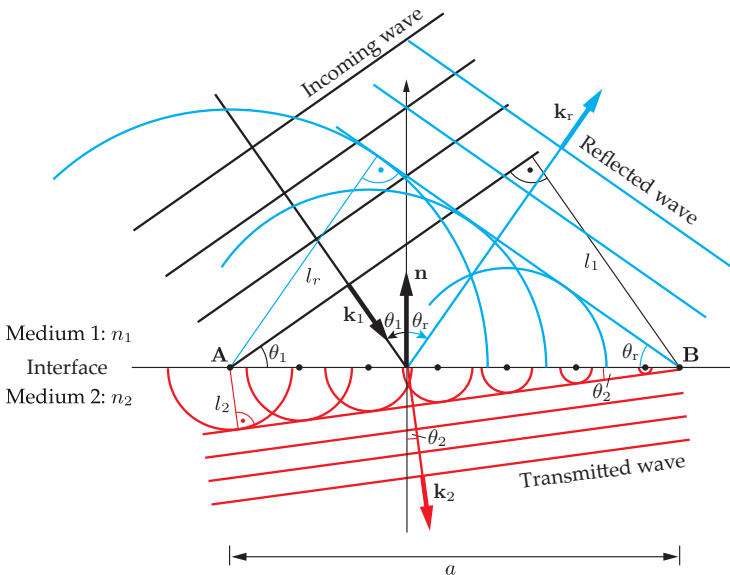


Figure 2.26. Deriving the laws of reflection and refraction by applying Huygens' principle in the plane of incidence.

Figure 2.26 yields the following quantitative relation:

$$\Delta t = \frac{l_1}{v_1} = \frac{l_2}{v_2}. \quad (2.204)$$

Equation (2.203) implies

$$l_1 n_1 = l_2 n_2. \quad (2.205)$$

The angle  $\theta_1$  between the normal vector of the interface and the direction of propagation of the incident wave is called the angle of incidence. The corresponding angle  $\theta_2$  of the transmitted wave is called the angle of refraction [3]. The following relations can be derived from the geometry of Fig. 2.26:

$$\sin \theta_1 = \frac{l_1}{a}, \quad (2.206)$$

$$\sin \theta_2 = \frac{l_2}{a}. \quad (2.207)$$

**Snell's law of refraction** is the result of replacing  $l_1$  and  $l_2$  in (2.205) by inserting these relations.

---

### Theorem 2.3: Snell's law of refraction

2.3

For the transition of light from a medium with the index of refraction  $n_1$  into a medium with the index of refraction  $n_2$ , the following holds for the angle of incidence  $\theta_1$  and the angle of refraction  $\theta_2$ :

$$n_1 \sin \theta_1 = n_2 \sin \theta_2. \quad (2.208)$$

The refracted light ray is located in the plane of incidence spanned by the incident light ray and the surface normal. When moving to a optically denser medium, the light is refracted towards the normal to the surface. In the case of a less optically dense medium, it is refracted away from the normal to the surface. Incoming light in the direction of the surface normal is not refracted at all:  $\theta_1 = 0 \Rightarrow \theta_2 = 0$ .  $\diamond$

The law of refraction can also be expressed using vectors. The unit vectors  $\mathbf{s}_1$  and  $\mathbf{s}_2$  in the directions of the wave vectors  $\mathbf{k}_1$  and  $\mathbf{k}_2$  of the incoming or of the refracted wave, can be derived from Fig. 2.26 [13]:

$$\mathbf{s}_2 = \frac{n_1}{n_2} \left( \mathbf{s}_1 - \mathbf{n} \left( \mathbf{s}_1^T \mathbf{n} + \sqrt{\left( \frac{n_2}{n_1} \right)^2 - 1 + (\mathbf{s}_1^T \mathbf{n})^2} \right) \right) \quad (2.209)$$

with

$$\mathbf{k}_1 = \frac{2\pi}{\lambda_1} \mathbf{s}_1, \quad \|\mathbf{s}_1\| = 1, \quad \mathbf{k}_2 = \frac{2\pi}{\lambda_2} \mathbf{s}_2, \quad \|\mathbf{s}_2\| = 1. \quad (2.210)$$

Because of

$$n_1 \lambda_1 = n_2 \lambda_2 \quad (2.211)$$

the wave vector  $\mathbf{k}_2$  of the refracted wave is given by

$$\mathbf{k}_2 = \frac{n_2}{n_1} \frac{2\pi}{\lambda_1} \mathbf{s}_2 \quad (2.212)$$

$$= \frac{2\pi}{\lambda_1} \left( \mathbf{s}_1 - \mathbf{n} \left( \mathbf{s}_1^T \mathbf{n} + \sqrt{\left( \frac{n_2}{n_1} \right)^2 - 1 + (\mathbf{s}_1^T \mathbf{n})^2} \right) \right) \Big|_{\mathbf{s}_1 = \frac{\lambda_1}{2\pi} \mathbf{k}_1} \quad (2.213)$$

$$= \mathbf{k}_1 - \mathbf{n} \left( \mathbf{k}_1^T \mathbf{n} + \sqrt{\left( \frac{2\pi}{\lambda_1} \right)^2 \left( \frac{n_2^2}{n_1^2} - 1 \right) + (\mathbf{k}_1^T \mathbf{n})^2} \right). \quad (2.214)$$

The law of refraction is the foundation for the construction of optical imaging systems (see Chap. 3), such as lenses [29].

As the index of refraction varies with the wavelength of the light, it has to be interpreted as a function of the wavelength if a high precision is desired:  $n = n(\lambda)$ . The effect of wavelength-dependent refraction is called **dispersion** [41]. The magnitude of this effect depends on the specific material. It can be used in order to investigate the spectrum of the observed light (Sec. 7.2.4). For example, a prism can decompose light into different color components. However, dispersion is often an undesired effect of optical systems, as it might cause imaging errors, the so-called aberrations (Sec. 3.4.8.2).

### 2.6.4 Scattering

Besides reflection, transmission and absorption, real surfaces redirect a varying amount of the incident light to other directions. This light is called scattered light.

#### Definition 2.1: Scattered light

Scattered light is the light that is emitted by an illuminated surface and whose direction is not equal to the direction of reflection or transmission obtained via the law of reflection (2.201) or the law of refraction (2.208).  $\diamond$

Different phenomena can cause light scattering [23,36]. On rough surfaces with microscopic irregularities with sizes on the order of the wavelength of the light, the local surface orientation differs from the macroscopic shape. Therefore, the incident light might be reflected in other directions than that predicted by the law of reflection. It is also possible that the light is repeatedly reflected by surface elements with randomly distributed orientations. The extreme case of perfectly diffuse reflection is the Lambertian radiator, for which the emitted radiance is equal in all spatial directions. It appears to be equally bright when seen from every spatial direction (see Chap. 4). Often, mixtures of scattering and reflection can be observed, e.g., the weak specular reflection, which occurs for emission directions slightly different from the direction of the law of refraction (Fig. 2.27). Another phenomenon is the so-called subsurface scattering in partially transparent materials: light crosses the interface with a certain probability and is then reflected into a stochastically distributed direction.

Scattering might also be caused by particles located in gases, such as in the air [16]. As such phenomena are of no particular importance for automated visual inspection, they are not covered any further in this book. The occurrence of scattering can depend on the wavelength.

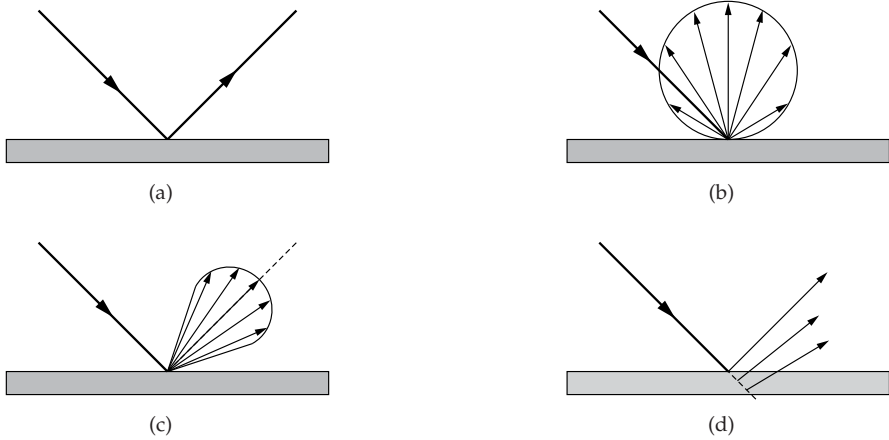


Figure 2.27. Different kinds of scattering caused by surfaces: (a) Perfectly specular reflection; (b) Lambertian reflection; (c) Weakly specular reflection; (d) Volume scattering.

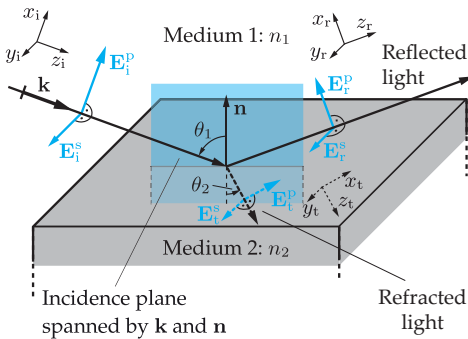


Figure 2.28. Plane of incidence for reflection and refraction at an interface. The illustration shows the components polarized parallel and perpendicular to the plane of incidence, respectively, for the incident wave  $E_i^p, E_i^s$ , the reflected wave  $E_r^p, E_r^s$  and the transmitted wave  $E_t^p, E_t^s$ . Additionally, the corresponding coordinate systems are depicted.

2.6.5 The Fresnel coefficients for reflection and transmission

The Fresnel coefficients give a quantitative measure for the amount of light reflected or transmitted after hitting an interface.

For the quantitative description of the reflection of an electromagnetic wave by the interface between two media, two different polarizations have to be distinguished (Fig. 2.28):

1. The electric field strength  $E^s$  is directed perpendicular to the plane of incidence.
2. The electric field strength  $E^p$  is directed parallel to the plane of incidence.

The following assumptions are made:

- There is no surface current density on the interface, so no current flows.
- There are no charges deposited on the interface, so its surface charge density is zero.
- The infinite half-space behind the interface, as observed by the light source, is completely filled by the second medium.

The incident wave, the reflected wave, and the transmitted wave are assumed to be plane waves. The following constraints, which can be used to calculate the laws of reflection and



refraction and the coefficients for reflection and refraction, can be derived from Maxwell's equations:

- The tangential components of  $\mathbf{E}$  and  $\mathbf{H}$  are continuous at the interface.
- The normal components of  $\mathbf{D}$  and  $\mathbf{B}$  are continuous at the interface [32].

## 2.4

**Theorem 2.4: Fresnel coefficients of reflection and transmission**

The Fresnel coefficients of reflection and transmission  $r_{12}^s$ ,  $r_{12}^p$ ,  $t_{12}^s$  and  $t_{12}^p$  are defined as the quotients of the reflected amplitude (respectively, of the transmitted amplitude) by the incident amplitude of the electric field strengths denoted by  $E_r$ ,  $E_t$  and  $E_i$ . This implies the following for the components that are polarized perpendicularly to the plane of incidence [5,35]:

$$r_{12}^s = \frac{E_r^s}{E_i^s} = \frac{n_1 \cos \theta_1 - n_2 \cos \theta_2}{n_1 \cos \theta_1 + n_2 \cos \theta_2}, \quad (2.215)$$

$$t_{12}^s = \frac{E_t^s}{E_i^s} = \frac{2n_1 \cos \theta_1}{n_1 \cos \theta_1 + n_2 \cos \theta_2}. \quad (2.216)$$

If the electric field of the incoming light is polarized parallel to the plane of incidence, the coefficients are

$$r_{12}^p = \frac{E_r^p}{E_i^p} = \frac{n_2 \cos \theta_1 - n_1 \cos \theta_2}{n_2 \cos \theta_1 + n_1 \cos \theta_2}, \quad (2.217)$$

$$t_{12}^p = \frac{E_t^p}{E_i^p} = \frac{2n_1 \cos \theta_1}{n_2 \cos \theta_1 + n_1 \cos \theta_2}. \quad (2.218)$$

In any case, the law of refraction holds for the incidence angle  $\theta_1$  and the refraction angle  $\theta_2$ : that is,  $n_1 \sin \theta_1 = n_2 \sin \theta_2$ . If the coefficient of reflection is negative, the phase of the reflected wave is shifted by  $\pi$  with respect to the incoming wave.  $\diamond$

In order to describe the reflection and transmission of arbitrarily polarized light, the electric field strength  $\mathbf{E}$  is represented in the plane perpendicular to the propagation direction. In a coordinate system with a basis vector  $\mathbf{e}_p$  parallel to the plane of incidence and a basis vector  $\mathbf{e}_s$  perpendicular to the plane of incidence, one has  $\mathbf{E} = E_i^p \mathbf{e}_p + E_i^s \mathbf{e}_s$  and the polarization components  $E_i^p$ ,  $E_i^s$  can be multiplied by the Fresnel coefficients of reflection and transmission in order to obtain the reflected and transmitted components.

Using (2.39) and (2.26), the intensities of the incoming wave, the reflected wave, and the transmitted wave at the interface<sup>19</sup> are given by

$$I_i = \frac{1}{2} c \varepsilon_0 n_1 E_i^2, \quad (2.219)$$

$$I_r = \frac{1}{2} c \varepsilon_0 n_1 E_r^2, \quad (2.220)$$

$$I_t = \frac{1}{2} c \varepsilon_0 n_2 E_t^2. \quad (2.221)$$

The energy flux of the electromagnetic wave, described by the Poynting vector (2.37), is directed in the direction of propagation. The intensity given by the surface power density has to be measured perpendicularly to the direction of propagation of the light (Fig. 2.29).

<sup>19</sup>To simplify matters, only the relevant case of non-magnetic materials is considered ( $\mu_r = 1$ ). The general formulations for  $\mu_r \neq 1$  can be found in [5,20] for example.

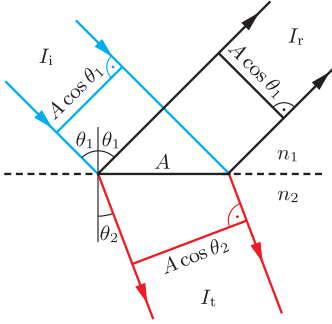


**Figure 2.29.** Determining the intensities of the incident, reflected, and refracted electromagnetic wave as surface power densities perpendicular to the respective propagation direction.

The reflectance  $R$  (respectively, the transmittance  $T$ ) describes the quotient of the reflected (respectively, the transmitted) intensity by that of the incoming radiation. As the intensity is proportional to the squared absolute value of the electric field strength, the Fresnel coefficients have a quadratic influence on the reflectance and the transmittance:

$$R_{12} = \frac{I_r \cos \theta_1}{I_i \cos \theta_1} = \frac{I_r}{I_i} = \left| \frac{E_r^2}{E_i^2} \right| = |r_{12}|^2, \quad (2.222)$$

$$T_{12} = \frac{I_t \cos \theta_2}{I_i \cos \theta_1} = \left| \frac{E_t^2}{E_i^2} \right| \frac{n_2 \cos \theta_2}{n_1 \cos \theta_1} = \frac{n_2 \cos \theta_2}{n_1 \cos \theta_1} |t_{12}|^2. \quad (2.223)$$

These equations can now be applied to the components of the light that are parallelly or perpendicularly polarized with respect to the plane of incidence [20]:

$$R_{12}^s = |r_{12}^s|^2, \quad R_{12}^p = |r_{12}^p|^2, \quad (2.224)$$

$$T_{12}^s = \frac{n_2 \cos \theta_2}{n_1 \cos \theta_1} |t_{12}^s|^2, \quad T_{12}^p = \frac{n_2 \cos \theta_2}{n_1 \cos \theta_1} |t_{12}^p|^2. \quad (2.225)$$

One always has  $T_{12}^s \leq T_{12}^p$  and  $R_{12}^s \geq R_{12}^p$ .

The intensity of the light polarized perpendicularly to the plane of incidence is given by

$$I_r^s \cos \theta_1 + I_t^s \cos \theta_2 = \frac{1}{2} c \varepsilon_0 n_1 (E_r^s)^2 \cos \theta_1 + \frac{1}{2} c \varepsilon_0 n_2 (E_t^s)^2 \cos \theta_2 \quad (2.226)$$

$$= \frac{1}{2} c \varepsilon_0 n_1 R_{12}^s (E_i^s)^2 \cos \theta_1 + \frac{1}{2} c \varepsilon_0 n_1 T_{12}^s (E_i^s)^2 \cos \theta_1 \quad (2.227)$$

$$= \frac{1}{2} c \varepsilon_0 n_1 (E_i^s)^2 \cos \theta_1 = I_i^s \cos \theta_1. \quad (2.228)$$

As regards reflectance and transmittance, this implies

$$R_{12}^s + T_{12}^s = 1. \quad (2.229)$$

Similarly, for light polarized in parallel to the plane of incidence,

$$R_{12}^p + T_{12}^p = 1. \quad (2.230)$$

The energy of the incoming light is distributed without loss over the reflected and the transmitted light of the same polarization. As no energy is exchanged between the two polarization components, they can be examined independently [5]. For  $n_1 \rightarrow n_2$ , it is  $R \rightarrow 0$  and  $T \rightarrow 1$ , which means that a homogeneous medium transmits light without reflection.

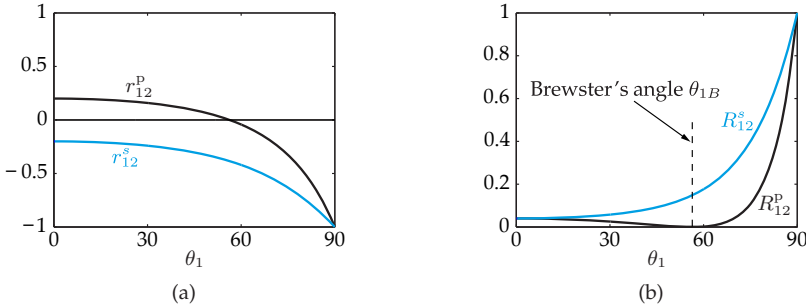


**Figure 2.30.** Reflection at the interface of air  $n_1 = 1$  and glass  $n_2 = 1.5$ . (a) Fresnel coefficients of reflection; (b) Reflectances.

Reversing the path of the light causes the coefficients of reflection and transmission to change in the following way [35]:

$$r_{21}^s = -r_{12}^s, \quad t_{21}^s = \frac{n_2 \cos \theta_2}{n_1 \cos \theta_1} t_{12}^s = \frac{1 - (r_{12}^s)^2}{t_{12}^s}, \quad (2.231)$$

$$r_{21}^p = -r_{12}^p, \quad t_{21}^p = \frac{n_2 \cos \theta_2}{n_1 \cos \theta_1} t_{12}^p = \frac{1 - (r_{12}^p)^2}{t_{12}^p}. \quad (2.232)$$

The phenomena which might occur when light is reflected or refracted at an interface differ according to whether there is a transition from a more to a less optically dense medium or from a less to a more optically dense medium.

First, the case  $n_1 < n_2$  will be considered. Figure 2.30 shows the Fresnel coefficients for reflection and the reflectance for an interface between air and glass with  $n_1 = 1$ ,  $n_2 = 1.5$  with respect to the angle of incidence  $\theta_1$ .

For dielectric media (non-conductors) 1 and 2,  $r_{12}^p$  and also  $R_{12}^p$  have a zero at the so-called Brewster's angle  $\theta_1 = \theta_{1B}$ . For this angle, the directions of the reflected wave and the transmitted wave are perpendicular:  $\theta_{2B} = \frac{\pi}{2} - \theta_{1B}$ . Therefore,

$$\cos \theta_{2B} = \sin \theta_{1B}. \quad (2.233)$$

By means of the trigonometric addition theorems and the law of refraction, it can be verified that  $r_{12}^p = 0$  for  $\theta_{1B}$ . Now, (2.217) results in an equation, which allows the determination of Brewster's angle:

$$\tan \theta_{1B} = \frac{n_2}{n_1}. \quad (2.234)$$

Light reflected through Brewster's angle is completely linearly polarized, perpendicular to the plane of incidence, as all of the parallel polarized light is transmitted. This effect can be used in order to obtain linearly polarized light. Another application is the suppression of reflections: if an image is acquired at an angle equal to Brewster's angle, only the perpendicularly polarized component of the reflected light is observed. If the perpendicularly polarized light is suppressed by a polarizing filter, the reflected light is completely blocked. The image will only contain light that has been diffusely scattered by the surface or which has been transmitted through the medium from the other side [16, 35].

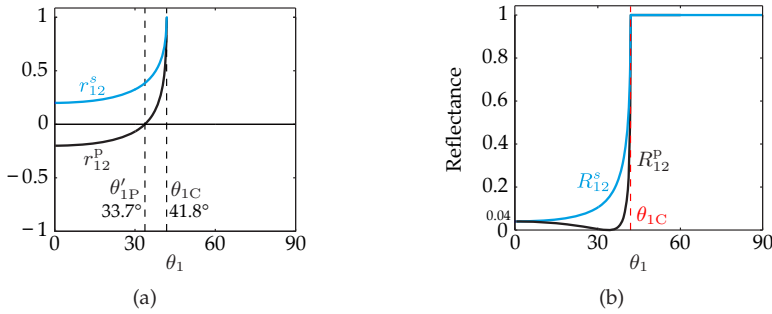


Figure 2.31. Reflection at the interface of glass,  $n_1 = 1.5$ , and air,  $n_2 = 1$ . (a) Fresnel coefficients of reflection; (b) Reflectances.

If light propagates from a more to a less optically dense medium, other phenomena can be observed [20, 25]: for  $n_1 > n_2$ , one has  $\theta_1 < \theta_2$  according to the law of refraction (2.208). Therefore, the angle of incidence can be so large that  $\sin \theta_2$  would have to be larger than 1. Such an angle of refraction is physically impossible. The maximum possible angle of refraction is  $\theta_2 = 90^\circ$ . If the corresponding angle of incidence is exceeded, no light is transmitted into the second medium. Instead, all the light is reflected. This phenomenon is called **total internal reflection**. Total internal reflection occurs whenever the angle of incidence  $\theta_1$  exceeds the **critical angle**  $\theta_{1C}$ :

$$\theta_2 = \frac{\pi}{2} \quad \Rightarrow \quad n_1 \sin \theta_{1C} = n_2 \quad \Leftrightarrow \quad \theta_{1C} = \arcsin \frac{n_2}{n_1}. \quad (2.235)$$

For  $\theta_1 \geq \theta_{1C}$ , the Fresnel reflectances are equal to 1. The phases of the components polarized parallel and perpendicular to the plane of incidence are shifted. The actual phase shift can be calculated from the Fresnel coefficients of reflection by using the complex trigonometric functions [18]. Figure 2.31 gives an example for the case of the interface between glass (with  $n_1 = 1.5$ ) and air (with  $n_2 = 1$ ).

Total internal reflection is used for constructing optical fibers and fingerprint scanners for instance. For the latter, total internal reflection is disturbed at the spots where the finger is in contact with the device, so that they are clearly visible in the observed camera image. This principle is called frustrated total internal reflection.

For the case  $n_1 > n_2$ , there also exists a polarization angle  $\theta'_{1P}$  for which  $r_{12}^p$  has a zero. This polarization angle is the equivalent of Brewster's angle  $\theta_{1B}$  (which was for the case  $n_1 < n_2$ ). One has  $\theta'_{1P} + \theta_{2P} = \frac{\pi}{2}$ , with  $\theta_{2P}$  denoting Brewster's angle for an incident wave originating from medium 2.

The reflection at the interface between two materials is described by the following Mueller matrix [6]:

$$\begin{aligned} \mathbf{M}_{\text{Reff}} &= \frac{1}{2} \left( \frac{\tan(\theta_1 - \theta_2)}{\sin(\theta_1 + \theta_2)} \right)^2 \cdot \begin{pmatrix} c_p^2 + c_m^2 & c_p^2 - c_m^2 & 0 & 0 \\ c_p^2 - c_m^2 & c_p^2 + c_m^2 & 0 & 0 \\ 0 & 0 & -2c_p c_m & 0 \\ 0 & 0 & 0 & -2c_p c_m \end{pmatrix} \\ &= \frac{1}{2} \begin{pmatrix} R_{12}^p + R_{12}^s & R_{12}^p - R_{12}^s & 0 & 0 \\ R_{12}^p - R_{12}^s & R_{12}^p + R_{12}^s & 0 & 0 \\ 0 & 0 & 2\sqrt{R_{12}^p R_{12}^s} & 0 \\ 0 & 0 & 0 & 2\sqrt{R_{12}^p R_{12}^s} \end{pmatrix} \end{aligned} \quad (2.236)$$

with

$$c_p := \cos(\theta_1 + \theta_2), \quad (2.237)$$

$$c_m := \cos(\theta_1 - \theta_2). \quad (2.238)$$

The matrix can be expressed as a function of either the angles of incidence and refraction  $\theta_1$  and  $\theta_2$ , or of the reflectances  $R_{12}^p$  and  $R_{12}^s$ . The refraction indices are indirectly included by the law of refraction  $n_1 \sin \theta_1 = n_2 \sin \theta_2$  or by the calculation of the coefficients of reflection. In the employed convention for naming coordinates, the  $x$ -axis corresponds to a polarization parallel to the plane of incidence and the  $y$ -axis corresponds to a polarization perpendicular to the plane of incidence (cf. Fig. 2.28). For example, the Stokes vector  $\mathbf{S}_{\text{LHP}}$  from (2.53) for linearly horizontally polarized light describes light that is polarized parallel to the plane of incidence [11, 34].

## ► 2.6.6 Electromagnetic waves in conductive media

Until now, only non-conductive materials, i.e., materials satisfying  $\sigma = 0$ , have been considered. Now, a homogeneous, conductive medium with  $\sigma = \text{const.} > 0$  is considered. Hence, the conductivity is constant with respect to space and time.

In this case, the wave equation (2.17) is given by

$$\Delta \mathbf{E} = \varepsilon \mu \frac{\partial^2 \mathbf{E}}{\partial t^2} + \sigma \mu \frac{\partial \mathbf{E}}{\partial t}. \quad (2.239)$$

A complex harmonic ansatz results in the following equation of a plane monochromatic wave for the angular frequency  $\omega$ :

$$\underline{\mathbf{E}}(\mathbf{x}, t) = \mathbf{E} e^{-\eta \mathbf{e}_3^T \mathbf{x}} e^{j(\omega t - k \mathbf{e}_3^T \mathbf{x})}, \quad \|\mathbf{e}_3\| = 1. \quad (2.240)$$

This equation describes an electromagnetic transverse wave propagating in the direction  $\mathbf{e}_3$ . The field's amplitude  $\mathbf{E}$  is perpendicular to the direction of propagation  $\mathbf{e}_3$ .<sup>20</sup> In conductive media, the so-called attenuation describes the increasing decay of the wave in the direction of its propagation, which is governed by the additional factor  $e^{-\eta \mathbf{e}_3^T \mathbf{x}}$  (see [32]). The wavelength

<sup>20</sup>Actually, in the case of conductive materials,  $\mathbf{E} \perp \mathbf{e}_3$  is only an approximation, as there is a small longitudinal component [20, p. 110].

is denoted by  $\lambda = \frac{2\pi}{k}$ , the phase velocity by  $v = \frac{\omega}{k}$ , the attenuation factor by

$$\eta = \omega \sqrt{\frac{\mu \varepsilon}{2} \left( \sqrt{1 + \frac{\sigma^2}{\omega^2 \varepsilon^2}} - 1 \right)} \quad (2.241)$$

and the wavenumber by

$$k = \omega \sqrt{\frac{\mu \varepsilon}{2} \left( \sqrt{1 + \frac{\sigma^2}{\omega^2 \varepsilon^2}} + 1 \right)}. \quad (2.242)$$

### ⊙ 2.6.6.1 Complex index of refraction

Formally, a complex-valued index of refraction  $\underline{n} \in \mathbb{C}$  can be introduced in order to describe the optical properties of conductive media [20,25]:

$$\underline{n} = n - jd, \quad (2.243)$$

$$n = \frac{\lambda_0}{2\pi} k = \frac{c}{\omega} k = \frac{c}{v}, \quad (2.244)$$

$$d = \frac{\lambda_0}{2\pi} \eta = \frac{c}{\omega} \eta. \quad (2.245)$$

The speed of light in vacuum is denoted by  $c$ , the vacuum wavelength by  $\lambda_0$ . The real part of the index of refraction represents the decrease of the phase velocity of a wave in the medium compared to the vacuum velocity. The imaginary part describes the medium's attenuation characteristics<sup>21</sup>.

W.l.o.g. the vector  $\mathbf{e}_3 = (0, 0, 1)^T$  is chosen such that  $\mathbf{e}_3^T \mathbf{x} = z$  and the amplitude  $\mathbf{E}$  is parallel to the  $x, y$ -plane. Then, (2.240) yields

$$\underline{\mathbf{E}}(\mathbf{x}, t) = \mathbf{E} e^{j(\omega t - k_0 \underline{n} z)} \quad (2.246)$$

with  $k_0 = \frac{2\pi}{\lambda_0}$ .

The intensity (power per area)  $I(\mathbf{x})$  of the wave is proportional to the time-averaged square of the real part  $\|\Re\{\underline{\mathbf{E}}(\mathbf{x}, t)\}\|^2$  of the field strength:

$$I(\mathbf{x}) = I_0 e^{-a z} = I_0 e^{-2\eta z} \quad \text{with} \quad I_0 = \left. \frac{\|\Re\{\underline{\mathbf{E}}(\mathbf{x}, t)\}\|^2}{Z} \right|_{x=0} = \frac{\|\mathbf{E}\|}{2Z}. \quad (2.247)$$

The intensity of the wave decreases exponentially in the direction of propagation. The absorption coefficient  $a$  is given by

$$a = 2\eta = \frac{4\pi}{\lambda_0} d. \quad (2.248)$$

The absorption coefficient and the complex index of refraction only describe the absorption caused by the conductivity but not the dissipative absorption, which was covered in Sec. 2.6.1.

---

<sup>21</sup>The real part and the imaginary part of the complex index of refraction depend on the frequency of the light. However, if considered as functions of the frequency, the two components are not independent from each other. In fact, they are related via an integral transform by the so-called Kramers-Kronig relations, and can be calculated from each other [41].

**Table 2.3.** Complex refractive indices  $\underline{n}_2 = n - jd$ , penetration depths  $\delta$ , and reflectances  $R$  for the medium air ( $n_1 = 1$ ) and light with a wavelength of  $\lambda = 589 \text{ nm}$  coming in perpendicularly ( $\theta_1 = \theta_2 = 0$ ) for selected materials [20,25].

Material	$n$	$d$	$\delta$	$R$
Vacuum	1	0	$\rightarrow \infty$	0
Air	$\approx 1$	0	$\rightarrow \infty$	0
Glass	1.5	0	$\rightarrow \infty$	0.04
Aluminum	1.44	5.23	8.96 nm	0.83
Silver	0.18	3.64	12.90 nm	0.95
Iron	2.27	3.37	13.90 nm	0.59
Copper	0.62	2.63	17.80 nm	0.74
Tin	1.5	5.30	8.84 nm	0.83

The distance  $\delta$  in the medium after which the energy of the wave is reduced to  $I_0 e^{-1}$ , i.e., by  $\approx 63\%$ , is called the **penetration depth**. Hence, by (2.247), it is  $a\delta = 1$ :

$$\delta := \frac{1}{a} = \frac{1}{2\eta} = \frac{\lambda_0}{4\pi d}. \quad (2.249)$$

After reaching a depth of about 4 to 5 times the penetration depth, the intensity is reduced to 1.8% or 0.67%, respectively. Therefore, only surface layers down to a depth of 4 to 5 times the penetration depth can be examined optically by means of automated visual inspection. Deeper areas remain optically hidden. Table 2.3 shows the complex refractive indices and penetration depths for some materials.

Snell's law of refraction and the formulas of the Fresnel coefficients are also valid for conductive materials with complex refractive indices. In general, this results in complex angles and angle functions, which are indeed hard to imagine but can still be mathematically handled.

---

**Example 2.9 (Complex refraction index):** At the interface between air, having a real-valued index of refraction  $n_1 = 1$ , and a conductive medium 2, having a complex-valued index of refraction  $\underline{n}_2 \in \mathbb{C}$ , the law of refraction is as follows:

$$\sin \theta_1 = \underline{n}_2 \sin \theta_2. \quad (2.250)$$

Because  $\sin \theta_1 \in \mathbb{R}$  and  $\underline{n}_2 \in \mathbb{C} \setminus \mathbb{R}$ , the term  $\sin \theta_2$  has to be complex as well. ■

The following holds for complex-valued trigonometric functions as well as for their real-valued pendants:

$$\sin^2 \varphi + \cos^2 \varphi = 1. \quad (2.251)$$

Hence, the following expression for  $\cos \theta_2$  is inserted into the Fresnel coefficients for the important case of  $n_1$  being real and  $\underline{n}_2$  being complex:

$$\cos \theta_2 = \sqrt{1 - \sin^2 \theta_2} = \sqrt{1 - \left( \frac{n_1 \sin \theta_1}{n_2 - jd_2} \right)^2}. \quad (2.252)$$

**Example 2.10 (Perpendicular reflection):** For perpendicularly incident light,  $\theta_1 = 0 = \theta_2$  by the law of refraction. Here,  $n_1 = 1$  is assumed for air or a vacuum and  $\underline{n}_2 = n_2 - jd_2$  is assumed to be complex. This results in the following reflectance [3],

$$R_{12} := R_{12}^p = R_{12}^s = \left| \frac{1 - n_2 + jd_2}{1 + n_2 - jd_2} \right|^2 = \frac{(1 - n_2)^2 + d_2^2}{(1 + n_2)^2 + d_2^2}. \quad (2.253)$$

It is not necessary to distinguish between light which is polarized parallel or perpendicularly with respect to the plane of incidence if it is coming in perpendicularly to the interface.<sup>22</sup> Intensively absorbing materials, e.g., metals, have a high values of  $d_2^2$ , which results in high reflectance values (see Table 2.3). ■

For  $d \neq 0$ , the Fresnel coefficients are complex, but their squared absolute values, which are the reflectances, remain real. The reflectance  $R^p$  of conductive materials can never have a zero, since the real part and the imaginary part of the numerator cannot be zero simultaneously. Nevertheless,  $r^p$  typically has a minimum at the so-called principal angle  $\theta_1^*$ . This difference in the reflection behavior can be used to classify materials into metals and dielectric materials [38].

**Example 2.11 (Reflectance of tantalum):** Figure 2.32 shows the Fresnel reflectances of an example of the interface between air (with  $n_1 = 1$ ) and the metal tantalum (with  $\underline{n}_2 = 1.72 - j2.09$ ) at a wavelength of  $\lambda = 632.8$  nm. ■

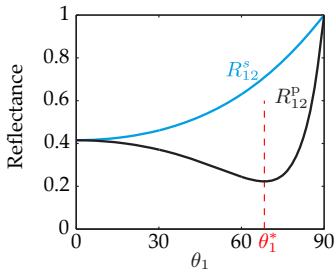


**Figure 2.32.** The Fresnel reflectances for the transition from air to tantalum with respect to the angle of incidence  $\theta_1$  [35, P. 18].

The real part of the index of refraction only weakly depends on  $\nu$  for non-conductive materials (dielectrics,  $\sigma = 0$ ) as it depends on  $\epsilon_r$  and  $\mu_r$  and hence only indirectly on the frequency  $\nu$ . This dependency is notably increased for conductive materials, as the angular frequency  $\omega = 2\pi\nu$  explicitly influences  $n$  and  $d$ . This effect can be exploited to classify unknown materials by acquiring images at different wavelengths (see Sec. 7.2.1).

Although metals are highly absorbing, the energy of an electromagnetic wave is only slightly reduced by a reflection. Silver, for example, absorbs only approximately 5% of a

<sup>22</sup>Generally  $r_{12}^s = -r_{12}^p$  for perpendicular reflections (cf. (2.215), (2.217), Fig. 2.30(a)). The different sign of the coefficients of reflection is caused just by a rotation of the coordinate system, whose  $z$ -axis is always directed along the propagation direction of the transversal wave. This is why the  $x$ -axis (parallel polarization) is rotated by  $180^\circ$  for a perpendicular reflection and the direction of the  $y$ -axis (perpendicular polarization) remains unaffected (so-called Verdet convention [22], cf. Fig. 2.28). In contrast, with respect to a stationary coordinate system located on the reflecting surface, the parallel and perpendicular polarized components are subject to the same changes of phase.



wave's energy at a wavelength  $\lambda = 589 \text{ nm}$ , leaving the remaining energy to the reflected wave. Because of the low penetration depth, which is much smaller than the wavelength, the wave only touches very few electrons, whose motions (electric currents) cause the absorption [20].

Transparent material layers are thin compared to the penetration depth  $\delta$ .

The reflection at metal surfaces notably depends on the surface's quality, which is affected by roughness, contaminations, oxide layers, etc.

## 2.7 Light sources

The illumination of the test object plays an important role in the field of automated visual inspection. A suitable illumination can highlight the object's properties of interest, and thus facilitate image processing. Illumination and image acquisition methods will be covered in Chap. 7. This section will briefly discuss the physical and technical foundations of artificial light sources [9, 15].

One can distinguish between thermal and luminescent radiators, based on the physical principles used to create the light. Inside a **thermal radiator**, a local thermal equilibrium is present. The radiation power and its spectrum depend only on the radiating body and its temperature. The energy necessary for emitting light is supplied in the form of heat. The thermal radiator's state of matter can be either solid or gaseous. This principle is used by incandescent and halogen lamps, where the heat is generated from an electric current. Sunlight is also a form of thermal radiation [16].

A **luminescent radiator** directly transforms the supplied energy into radiation. The energy is not available in the form of heat but as potential energy, and there is no thermal equilibrium. Gas-discharge lamps, light-emitting diodes, and lasers are examples of luminescent radiators.

### 2.7.1 Thermal radiators

#### 2.7.1.1 Physical principles

Matter spontaneously emits electromagnetic radiation. The energy of that radiation comes from the movements of the molecules, atoms, and electrons. It is these very movements on which the concept of temperature is based. This is why more radiation is emitted when the temperature rises. The ideal thermal radiator is the so-called blackbody radiator [30].

### 2.5 Theorem 2.5: Planck's law

The spectral radiance of a blackbody is described by Planck's law [9]:

$$L_{\lambda}(\lambda) = \frac{2hc^2}{\lambda^5} \frac{1}{\exp\left(\frac{hc}{k\lambda T}\right) - 1}. \quad (2.254)$$

The temperature in Kelvin of a blackbody radiator is denoted by  $T$ , while  $\lambda$  is the wavelength of the emitted light,  $c$  denotes the speed of light in vacuum,  $h$  is Planck's constant (see Sec. 2.3), and  $k \approx 1.38 \cdot 10^{-23} \text{ J/K}$  is Boltzmann's constant.  $\diamond$

A so-called gray-body radiator only reaches a lower radiance, which however is proportional to (2.254). A light source's correlated color temperature is the temperature a blackbody radiator must have in order to emit light of an apparent color equivalent to that of the light source [39]. The term color temperature can be used for the color characterization of light even if it is not emitted by a thermal radiator. In this case, the color temperature does not depend on the physical temperature of the light source.

The total radiation power of a half-space (factor  $\pi$ ) and for all wavelengths is given by the surface power density described by the Stefan–Boltzmann law:

$$\int_0^{\infty} \pi L_{\lambda}(\lambda) d\lambda = \frac{2\pi k^4}{15 h^3 c^2} T^4 \approx 5.67 \cdot 10^{-8} \text{ W m}^{-2} \text{ K}^{-4} T^4. \quad (2.255)$$

Hence, the radiation power, which is the product of the surface power density and the area  $A$ , increases with the fourth power of the temperature. Simultaneously, for increasing temperature, the maximum of the spectral radiance is shifted towards shorter wavelengths (Fig. 2.33). The wavelength of maximum emission is given by Wien's displacement law:

$$\lambda_{\max} \approx \frac{2.898 \cdot 10^{-3} \text{ K m}}{T}. \quad (2.256)$$

The apparent color of a blackbody radiator shifts from red to yellow to white for increasing temperatures (see also Sec. 5.2.4).

Thermal radiators emit a continuous spectrum over a wide range of wavelengths. For technically feasible temperatures, the largest part of the radiation power is emitted as infrared light (Fig. 2.33). The amount of radiation power in the visible part of the spectrum is relatively small. This is why light sources based on the principle of thermal radiation only have a small light yield<sup>23</sup> but a high heat dissipation.

Only for higher temperatures does the maximum intensity of a blackbody radiator shift into the visible part of the spectrum. As the total intensity increases with the temperature's fourth power, by (2.255), the spectra of different temperatures can only be visualized using a double logarithmic scale as in Fig. 2.34.

### ⊗ 2.7.1.2 Incandescent lamps and halogen lamps

Incandescent lamps and halogen lamps are thermal radiators which can be physically modeled as gray-body radiators. A current-carrying wire heated due to its electric resistance serves as a radiator. This filament consists of tungsten (also known as wolfram), which is the metal with the highest melting point: 3,683 K [2]. Nevertheless, the melting point is the limiting factor for the maximum temperature and thus also for the performance of incandescent lamps. The slow vaporization of the tungsten limits the lifetime of the lamp. In order to increase the stability of the tungsten filament, the bulb is filled with an noble gas, like nitrogen for example. The operating temperature of incandescent lamps filled with gas is between 2,600 K and 3,000 K (see [30]).

**Halogen lamps** allow higher temperatures from 3,000 K up to 3,400 K, so that more of the emitted radiation belongs to the visible part of the spectrum, and so the lamp's light yield

<sup>23</sup>Light yield is the relation between the amount of the emitted luminous flux  $\Phi_1$  and the absorbed electrical power  $P$ . Luminous flux is a measure of the energy of the visible part of electromagnetic radiation; see Chap. 4.

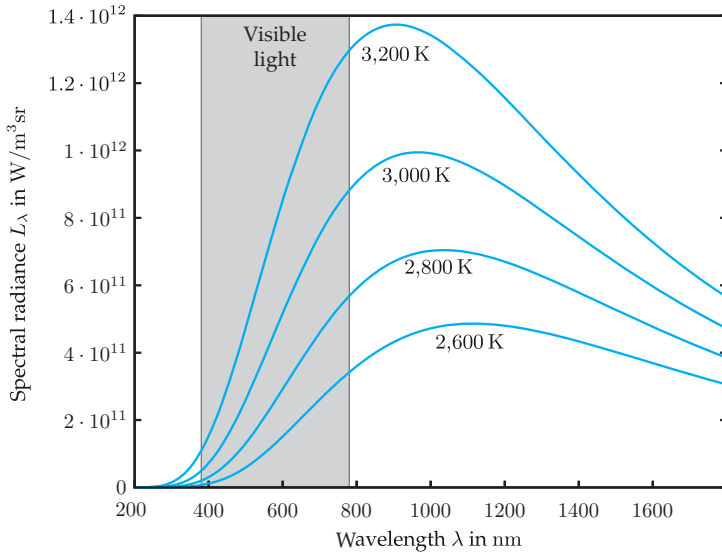


Figure 2.33. Spectrum of blackbody radiators according to Planck's law.

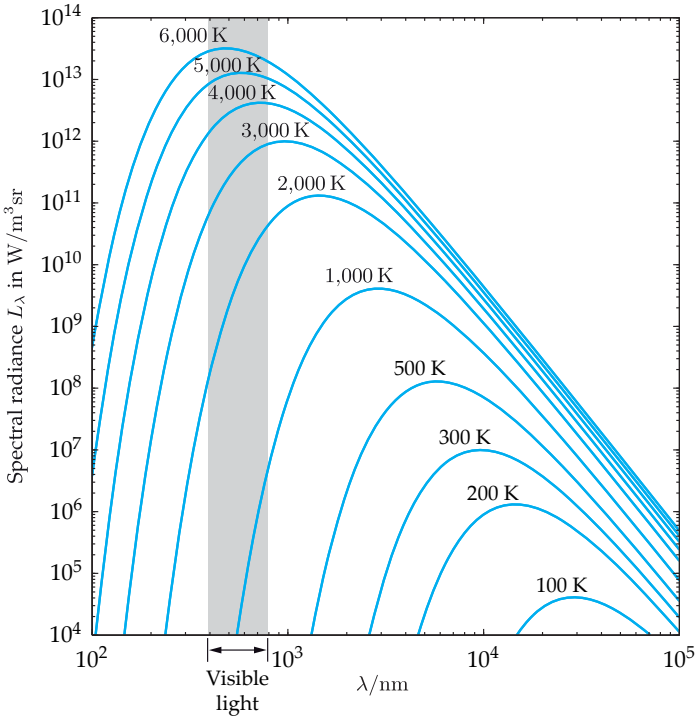


Figure 2.34. Spectrum of blackbody radiators according to Planck's law visualized in a double logarithmic plot.

is increased (cf. Fig. 2.33). This is achieved by using halogen compounds inside the gas, which react with the vaporized tungsten and transport it back to the filament. This process is called the halogen cycle. The regeneration of the filament results in a longer lifetime of the lamp. Halogen lamps are much more compact than incandescent lamps, in order to ensure the required temperature to prevent the tungsten halogenide from condensing on the bulb. Usually iodine is used as a halogen.

The operating data of incandescent and halogen lamps mainly depend on the temperature. As the filament's temperature is caused by an electric current, it can be manipulated by altering the operating voltage. The operating data can usually be approximated by power laws depending on the relation of the operating voltage  $U$  to the nominal voltage  $U_N$  of the lamp [30]. Figure 2.35 and Table 2.4 show these operating laws for a light flux of  $\Phi_l$ , an electric power consumption of  $P$ , current  $I$ , light yield  $\eta$ , and lifetime  $Z$ , for the example of a halogen lamp. Overvoltage severely reduces the lamp's lifetime. Conversely, the lifetime can be significantly increased by lowering the operating voltage, which will cause only a slightly decreased light yield. Incandescent and halogen lamps can be operated with either direct or alternating current.

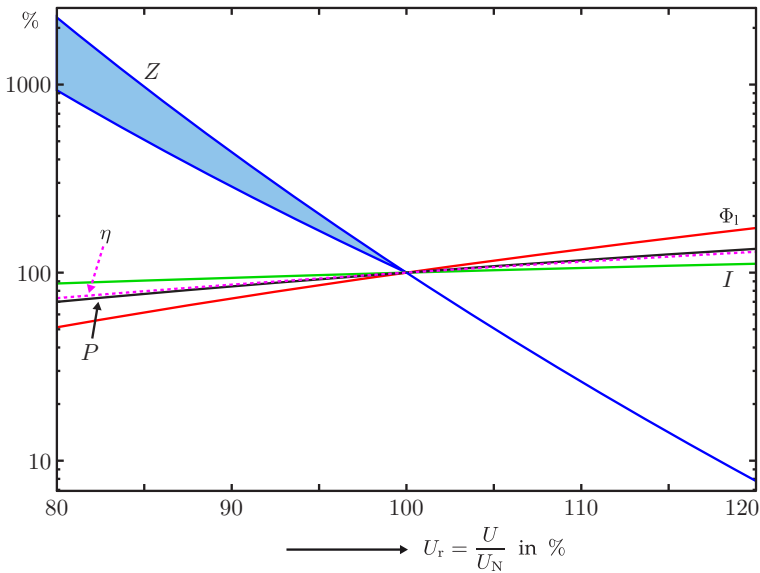


Figure 2.35. Operating laws for halogen lamps plotted using a logarithmic scale [30].

### 2.7.2 Gas-discharge lamps

Gas-discharge lamps use the principle of electroluminescence: atoms are excited or ionized in a strong electric field when they are hit by accelerated particles (electrons or ions). The absorbed energy is released in the form of light.

In **high pressure discharge lamps**, the energy is supplied by arc discharges. Ions enable an electric current to flow between both electrodes. Other atoms get hit by the ions, are excited, and also emit light. Such lamps can be filled with gases, especially noble gases, and

**Table 2.4.** Operating laws for incandescent and halogen lamps as functions of the relation between the operating and the nominal voltage  $U_r = \frac{U}{U_N}$  [30].

	Incandescent lamp	Halogen lamp
Current	$I \propto U_r^{0.5}$	$I \propto U_r^{0.6}$
Electric power	$P \propto U_r^{1.5}$	$P \propto U_r^{1.6}$
Light flux	$\Phi_1 \propto U_r^{3.8}$	$\Phi_1 \propto U_r^{3.0}$
Light yield	$\eta \propto U_r^{2.3}$	$\eta \propto U_r^{1.4}$
Temperature	$T \propto U_r^{0.4}$	$T \propto U_r^{0.34}$
Lifetime	$Z \propto U_r^{-14}$	$Z \propto U_r^{-14}$ if $U > U_N$ $Z \propto U_r^{-14}$ up to $U_r^{-10}$ if $U < U_N$

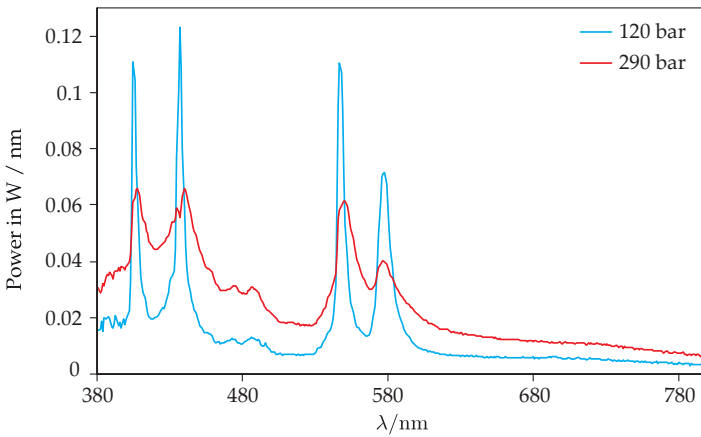


**Figure 2.36.** Spectra of mercury-vapor high pressure lamps [8].

metallic vapors. Metals only start to vaporize when the temperature rises after the gas fill has been ignited.

Typically, the spectrum of a gas-discharge lamp is wider and smoother for higher operating pressures (Fig. 2.36). Different physical mechanisms contribute to this effect, which widens the lines in the spectrum that are usually rather thin because of the discrete excited states of the molecules: Doppler broadening, bremsstrahlung and radiative recombination [9]. Doppler broadening is based on the collisions between the gas molecules moving with a continuously distributed velocity. Their kinetic energy is increased for higher temperatures and pressures. Bremsstrahlung occurs whenever charged particles hit matter and are strongly decelerated. The wavelengths of the emitted light depend on the velocity of the particles, which is continuously distributed. If positive ions and electrons combine to form electrically neutral atoms, also a continuous spectrum is emitted as the recombination partners have randomly distributed kinetic energies.

Furthermore, increasing the operating pressure leads to an increased luminance, which means that the geometric extent of the light emission can be spatially narrowed. High pressure discharge lamps are usually very compact and are a nearly perfect point light source.

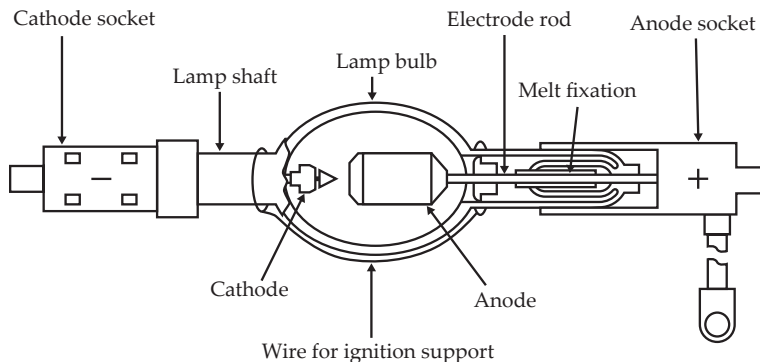


Figure 2.37. Schematic of a xenon short-arc lamp (based on a drawing of Osram AG).

These properties are even more marked for super high pressure lamps, e.g., the xenon short-arc lamps (Fig. 2.37). In the visible domain, the spectrum of these lamps is very similar to the spectrum of daylight. But much of the energy is emitted in the near infrared region of the spectrum, so that the light yield of the xenon short-arc lamp is not as high as it is for other gas-discharge lamps. Another disadvantage is the necessary safety precautions, because of the explosion hazard caused by the high pressure.

For electroluminescent lamps, usually mercury is used. Metal halide compounds<sup>24</sup> can be added to mercury-vapor high pressure lamps in order to influence the emitted spectrum. Depending on the mixture, the result might be a higher light yield or a smoother spectrum. A broadband spectrum, which is similar to the spectrum of daylight, is especially useful for color rendering. The electric power  $P$  of mercury-vapor high pressure lamps ranges between 35 and 3,500 W, and the light yield  $\eta$  ranges from 65 to 120 lm/W. The lamp's mean lifetime is about 6,000 operating hours.

**Low pressure discharge lamps** emit line spectra corresponding to the atoms' discrete excited states. A broad spectrum can only be achieved using luminescent material. The walls of fluorescent lamps are coated with such fluorescent materials (see Sec. 7.2.2 for fluorescence). They absorb the light of short wavelengths, like the ultraviolet radiation of the gas discharge for example, and emit light of longer wavelengths. However, a considerable amount of energy is lost during this process, in the form of heat. Figure 2.38 shows the setup of a fluorescent lamp. The so-called energy-saving lamps are compactly constructed mercury-vapor fluorescent lamps.

The pressure inside of low pressure discharge lamps is between 1 and  $10^3$  Pa, which is much less than the pressure of the surrounding air. These lamps are usually operated with mercury-vapor or sodium-vapor. The line spectra of the gas-discharge processes depend on the structure of the energy levels of these elements. Among others, the spectral lines of the mercury-vapor lamp are at 184.9; 253.6; 296.7; 365.0; 435.8; 546.1 and 577 nm, which partly correspond to the ultraviolet part of the spectrum [21]. Thus, the efficient generation of light is only possible if luminescent materials are used. The discharge of low pressure sodium-vapor produces a narrow-band spectrum around 590 nm. This light is visible and appears to

<sup>24</sup>This is why such lamps are also called 'metal-halide lamps' — however, they rely on a different principle than the halogen lamps introduced in Sec. 2.7.1.2.

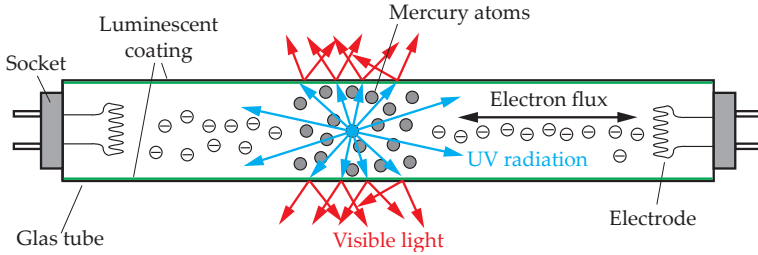


Figure 2.38. Schematic of a mercury-vapor fluorescent lamp.

be colored in the range from yellow to orange. Therefore, sodium-vapor lamps can be used without luminescent materials and reach a high light yield. They are often used if a higher light yield is more important than complete color rendering, as is the case for street-lights, for example. Both low pressure and high pressure discharge lamps can be operated with sodium-vapor.

Mercury and sodium are suitable for discharge lamps as they offer low ionization energies, suitable excitation energies for optical radiation, and high vapor pressures. Besides, the cross section<sup>25</sup> for electron excitation is about three to four times higher than for noble gases.

Gas-discharge lamps are typically operated with alternating current. As the electric resistance decreases for an increasing discharge current, operating a gas-discharge lamp with constant voltage would lead to severe instabilities and finally to the lamp's destruction. Therefore, all gas-discharge lamps have to be operated with an electrical ballast. Current sources<sup>26</sup> limit the current while operating the lamp, so that the lamp's nominal power cannot be exceeded. Additionally, they control the ignition of the gas-discharge by preheating the electrodes and stabilizing the electric arc. As the temperature and pressure have to be established first, gas-discharge lamps need some minutes to reach their specified spectrum and their full luminosity. They cannot be operated in a pulsed way. The number of power cycles negatively affects the lifetime of the lamp. Operating gas-discharge lamps with a common 50 Hz alternating current might result in stroboscopic effects of about 100 Hz, which can lead to significant differences in the brightness of acquired images if a short exposure time is chosen. Modern lamps usually avoid this effect by using high frequency ballasts. Especially xenon lamps can also be used as flashlights.

### ➤ 2.7.3 Light-emitting diodes

**Light-emitting diodes** or **LEDs** are semiconductors which also use the principle of electroluminescence to emit light. LEDs have been available since the 1960s. At first, their efficiency was very low, so that they were mainly used as signal or warning lamps. Nowadays, the development of LEDs has come so far that they can be used for illumination purposes.

<sup>25</sup>The cross section of an atom is a measure of the probability of electron excitation. It can be interpreted as the atom's virtual cross-sectional area.

<sup>26</sup>In the domain of electrical engineering, the terms voltage and current source have to be distinguished. A voltage source supplies an approximately constant voltage and has a low internal resistance. Current sources, on the other hand, provide an approximately constant current and have a high internal resistance.

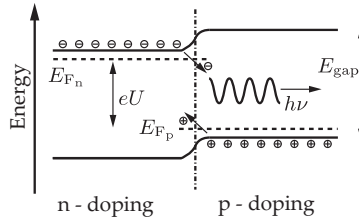


Figure 2.39. Band model of a light-emitting diode [9].

Table 2.5. Bandgaps  $E_{gap}$  and emitted wavelengths  $\lambda$  of III-V-compound semiconductors for light-emitting diodes [9].

Compound	$E_{gap}$ in eV	$\lambda$ in nm
AlN (aluminum nitride)	6.02	206
GaN (gallium nitride)	3.34	371
GaAs (gallium arsenide)	1.35	918
InN (indium nitride)	2.0	620
InP (indium phosphide)	1.27	976
InAs (indium arsenide)	0.36	3,400
InSb (indium antimonide)	0.163	7,610

LEDs are diodes operated in forward current. The electric voltage supplies the electrons with energy, so that they can move from the valence band to the conduction band. By moving back from the semiconductor's n-doped conduction band to the energetically lower p-doped material, energy is freed, which is released in the form of photons. The number of photons emitted per unit of time is approximately proportional to the number of charge carriers running through the LED per unit of time, and thus to the electric current. The photon energy  $h\nu$  nearly equals the bandgap:  $E_{gap} \approx h\nu$  (Fig. 2.39). The spectrum of LEDs is narrow-band. The wavelength is in the visible, the ultraviolet or in the near infrared part of the spectrum, depending on the semiconductor material and the doping.

A common choice for LEDs is the so-called III-V-compound semiconductors. These materials are compounds of elements of the periodic system's third main group, like aluminum, gallium or indium for example, and of the fifth main group, like nitrogen, phosphor, arsenic or antimony for example. Table 2.5 shows some III-V-semiconductors with their corresponding bandgaps and wavelengths. By using mixed crystals, the complete spectrum can nowadays be covered (see Fig. 2.40(a)). White LEDs can be constructed on the basis of blue LEDs. In order to achieve a broadband spectrum, a luminescent material is used, which fluoresces in the spectrum's yellow part (see Fig. 2.40(b)). Mixing the blue and yellow light leads to a white color impression.

Alternative materials for LEDs are organic semiconductors (OLEDs) and II-VI-semiconductor compounds. Some of these materials are still under development or being researched.

As the static electric resistance of a diode decreases with increasing current, LEDs may only be operated using a current source delivering a constant current. An LED must not be



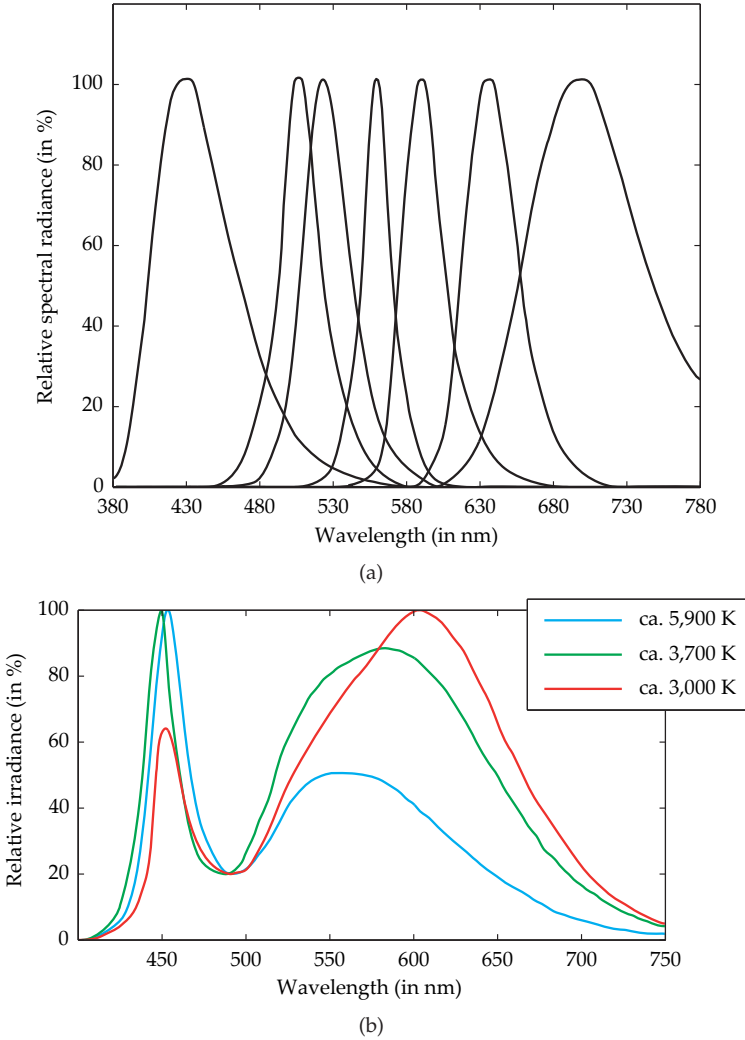


**Figure 2.40.** Spectra of light-emitting diodes: (a) Narrow-band spectra of different light-emitting diodes (adapted from [9]); (b) Spectra of white light-emitting diodes with different color temperatures (adapted from [7]).

directly connected to a voltage source because then the current would increase uncontrollably, leading to the destruction of the LED. Voltage sources delivering a constant voltage  $U_0$  can be approximately transformed into current sources by connecting them in series with an ohmic resistor  $R$  (Fig. 2.41). Let  $U_F$  be the voltage drop across the diode and  $I_0$  the desired current. Then, for  $U_0 \gg U_F$ , the required resistor  $R$  is calculated by

$$R = \frac{U_0 - U_F}{I_0}. \quad (2.257)$$

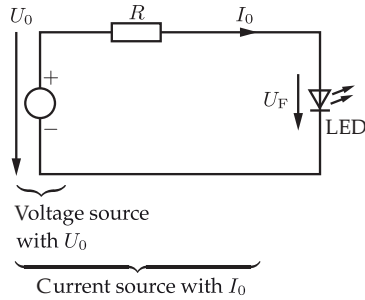


Figure 2.41. Circuit for operating a light-emitting diode.

Because  $U_0 \gg U_F$ , a change of  $U_F$  only leads to a small change of  $I$ :

$$\Delta I \approx -\frac{1}{R} \Delta U_F = -\frac{I_0}{U_0 - U_F} \Delta U_F. \quad (2.258)$$

Because of much power being dissipated across the resistor, this circuit is not suitable for illumination purposes. Some LEDs come with already integrated constant current sources.

Compared to other light sources, LEDs offer a very high durability. Common LEDs operate for about 100,000 hours and even high performance diodes can reach a durability of 30,000–50,000 hours. The light's intensity slowly decreases with increasing age of the diode. The sudden failure of an LED is unusual. As mentioned earlier, LEDs show a narrow-band emission, so that no energy is emitted in the infrared and ultraviolet part of the spectrum, which leads to a high light yield. LEDs can be pulsed with high frequencies and modulated by a time dependent current. Besides, LEDs are unable to implode, mechanically robust, and immune to shocks and vibrations, a characteristic which is highly desirable in the domain of automation technology. As the light-emitting crystal can be chosen to be very small, an LED approximately represents a point light source.

A major disadvantage of LEDs is that a huge number of LEDs is needed to reach the light intensity of a single conventional light source. This results in additional effort for designing appropriate circuit boards carrying LED arrays, which then are no longer a point light source. LEDs have to be operated at a low voltage using a current source, and cannot be directly connected to the mains voltage. Their efficiency and spectrum depend on the operating temperature.

### ► 2.7.4 Laser

Besides the spontaneous emission of photons of energy  $h\nu_{21} = E_2 - E_1$ , a **stimulated emission** can be observed when excited atoms change from an energy level  $E_2$  to a lower energy level  $E_1 < E_2$ .<sup>27</sup> During stimulated emission, a photon with the frequency  $\nu_{21}$  triggers an atom at the energy level  $E_2$  to emit a photon of equal frequency, phase, direction, and polarization [26]. Hence, the emitted photon is coherent with the triggering photon. **Lasers** rely

<sup>27</sup>This effect can only be explained using quantum mechanics. It was first described by Albert Einstein [10].

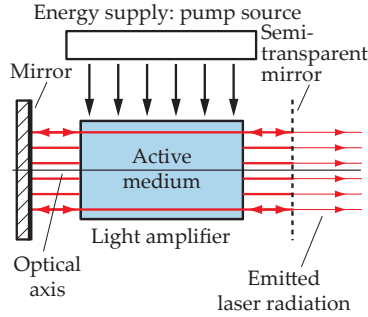


Figure 2.42. Principle of a laser.

on this process.<sup>28</sup> ‘Laser’ is an abbreviation for ‘Light Amplification by Stimulated Emission of Radiation.’

If light with a frequency of  $\nu_{21}$  is sent into a material offering enough atoms at the energy level  $E_2 > E_1$ , so that stimulated emissions can occur with a sufficiently high probability, the light can be coherently amplified. Such a material is an optical amplifier of light.

If an amplifier is fed back with the output signal and if the amplification exceeds the losses, the system starts to oscillate. This principle is well known in terms of the acoustic feedback generated by the system microphone–amplifier–speaker.

The feedback for a laser is achieved by using mirrors that reflect the amplified light back into the excited material (Fig. 2.42). Thus, a laser is a light oscillator.

**The amplifier:** In thermal equilibrium, the occupation numbers  $N_i$  of the energy levels  $E_i$ ,  $i = 1, 2$  comply with the Boltzmann distribution

$$N_2 = N_1 e^{-\frac{E_2 - E_1}{kT}} = N_1 e^{-\frac{h\nu_{21}}{kT}}, \quad (2.259)$$

with  $T$  the absolute temperature in Kelvin,  $k$  Boltzmann’s constant, and  $h$  Planck’s constant [26]. For room temperature,  $T = 300$  K, the occupation numbers for an optical photon of  $E_2 - E_1 \approx 2.5$  eV comply with  $\frac{N_2}{N_1} \approx 4 \cdot 10^{-44}$ , which means that the higher energy level  $E_2$  is weakly populated compared to  $E_1$ . That difference decreases for increasing temperature, but nevertheless  $N_2 < N_1$ .

A usable amplification by stimulated emission can only be achieved if a so-called population inversion  $N_2 > N_1$  is present, which is not possible in thermal equilibrium.

To establish the disequilibrium necessary for a population inversion, energy has to be supplied. This process is called pumping, and can be achieved by optical, chemical, or electrical means.

Together, the light-amplifying medium and the pump source form the amplifier. Depending on the kind of laser, gases, liquids or solids can be used as active media. A light-amplifying medium which is activated by a pump is called an active medium.

<sup>28</sup>The first laser was built by T. Maiman in 1960. Earlier, in the 1950s, C. Townes, A. Prokhorov and N. Basov developed the so-called Maser (microwave-laser) for which they were awarded the Nobel prize (Physics) in 1964.

The amplification of light of the frequency  $\nu_{21}$  which propagates through the active medium caused by stimulated emission increases exponentially with increasing propagation.

**Feedback:** Light propagating in parallel to the optical axis (Fig. 2.42) is amplified by a factor  $> 1$  each time it passes through the active medium, so that the light intensity increases exponentially with the number of iterations. Because some of the light is extracted through the semitransparent mirror, but mainly because of the limited supply of pumping energy, the amplification and thus also the laser's intensity become saturated. Only light travelling parallel to the optical axis is amplified. Light in other directions will quickly leave the optical resonator, which consists of the two mirrors. There are also types of resonators with curved mirrors.

Traveling along the different paths through the medium between the mirrors produces a path-dependent phase shift, which depends on the frequency and the length of the path. Due to this phase shift, those frequencies are preferred, that reenter the medium with equal phase, leading to the production of a standing wave. The two mirrors act as an extreme narrow-band bandpass filter, like a so-called Fabry-Pérot interferometer [20, 41]. Actually, not only photons of the exact frequency  $\nu_{21}$  are amplified, but also frequencies in a certain range  $\Delta\nu$  around  $\nu_{21}$ , caused by line spreading effects. The resonator then selects the frequencies, resulting in a standing wave.

Hence, the mirror system of the optical resonator causes a feedback and also a narrow-band selection of frequencies and directions.

**Starting the oscillation:** The optical resonator begins to oscillate because of the transition from the pumped energy level to the lower one, which results in a spontaneous emission of photons, which have a frequency  $\nu_{21}$  and propagate parallel to the optical axis. Other spontaneously emitted photons, which do not comply with these conditions, will not be sufficiently amplified or fed back. Only the photons with a frequency of about  $\nu_{21}$  and a propagation direction approximately parallel to the optical axis will be massively amplified, and will dominate all other light in the resonator.

**Practical realization:** Usable lasers make use of further energy levels. Practically relevant lasers usually work with four energy levels  $E_3 > E_2 > E_1 > E_0$ . Starting from  $E_0$ , level  $E_3$  is excited by pumping. Because of a so-called relaxation, some atoms change to level  $E_2$  while emitting the energy difference in the form of heat. Now there is a population inversion for  $E_2$  with respect to  $E_1$ , which is used for the stimulated emission of photons with the frequency  $\nu_{21}$ . Also by relaxation, the excitation state  $E_1$  is reduced to the level  $E_0$  (Fig. 2.43).

Level  $E_3$  is necessary to optically pump the laser. If  $E_1$  is weakly populated compared to  $E_0$  in the case of a thermal equilibrium, significantly less pumping effort is necessary to establish a population inversion between  $E_2$  and  $E_1$ , as would be necessary for the system of  $E_2$  and  $E_0$  [26, 41].

The most important lasers for the field of automated visual inspection that are commercially available are:

- Semiconductor lasers (laser diodes), which are pumped by an electric current.
- Nd:YAG-lasers are solid-state lasers where neodymium ions are embedded in an yttrium aluminum garnet crystal. Nd:YAG-Lasers are optically pumped. Initially, they yield light

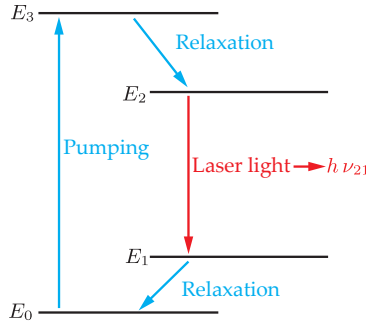


Figure 2.43. Energy system consisting of four levels of atoms in an active medium of a laser.

Table 2.6. Maximum values of laser parameters that can currently be reached [41].

Shortest wavelength	3.6 nm
Maximum power (commercial, continuous wave, non-pulsed operation)	30,000 W
Maximum intensity (pulsed and focused)	$10^{26}$ W/m <sup>2</sup>
Highest pulse energy (with a duration of ca. 3 ns and a wavelength $\lambda = 1.06 \mu\text{m}$ )	120,000 J
Minimum frequency bandwidth, relative frequency bandwidth and maximum coherence length	
– Dye laser (dyes used as active media, wavelength is adjustable)	$\Delta\nu = 0.5$ Hz, $\frac{\Delta\nu}{\nu} \approx 10^{-15}$
– Helium-neon and solid-state lasers	$\Delta\nu = 10^{-3}$ Hz
Shortest impulse duration and length	$t_P = 4.5$ fs = $4.5 \cdot 10^{-15}$ s, $l_P = c t_P = 1.3 \mu\text{m}$

with the wavelength  $\lambda = 1064$  nm. Nonlinear optical effects can double the frequency, leading to green light with the wavelength  $\lambda = 532$  nm.

Laser light is sharply bundled, nearly monochromatic, has long coherence lengths, and can yield very high intensities. Table 2.6 shows the maximum performance characteristics that can nowadays be achieved by lasers. But not all of these characteristics can be realized simultaneously in a single laser.

The use of lasers in automated visual inspection will be discussed in Chap. 7. As laser light can be harmful for the human eye because of the high radiation intensity, safety precautions are necessary, depending on the actual power and the spectral range (see also Sec. 7.2.3.4).

**Remark:** If lasers and other light sources are compared to electric signal sources, the laser is the equivalent to a sine wave oscillator and the other light sources represent noise generators.

### 2.7.5 Summary

Table 2.7 summarizes the important properties of some light sources, such as the lifetime, the possibility of being operated in a pulsed way, and the spectrum. For good color rendering, a broad spectrum similar to the spectrum of daylight is necessary, as is emitted by a blackbody radiator, for example. In contrast to all other light sources, lasers can emit linearly polarized light with a long coherent length. So for some applications, e.g., interferometry, laser light is needed (see Sec. 7.3.16.1). A disadvantage of coherent light is the occurrence of speckle.

The luminances of some natural light sources are shown in Table 2.8. Apart from lasers, the highest luminances can be achieved using xenon short-arc lamps, whereas the luminances of fluorescent lamps is rather low. Having a high luminance is important if an illumination method needs a well-defined control of the light rays, which is only possible with a point light source.

The extent to which image acquisition is influenced by the spectrum of the illumination depends on the light source as well as on the spectral sensitivity of the sensors used (see Chap. 6). The product of the two wavelength dependent functions and the sensor-specific integration over the wavelength ranges determines the measured intensity (also compare to Chap. 5).

## 2.8 Bibliography

- [1] Jonathan Balzer. *Regularisierung des Deflektometrieproblems – Grundlagen und Anwendung*. PhD thesis, Universität Karlsruhe (TH), 2008.
- [2] Walter Benenson, John Harris, Horst Stöcker, and Holger Lutz, editors. *Handbook of physics*. Springer, 3rd edition, 2006.
- [3] Ludwig Bergmann, Clemens Schaefer, Heinz Niedrig, and Hans-Joachim Eichler, editors. *Lehrbuch der Experimentalphysik*, volume 3: Optik: Wellen- und Teilchenoptik. De Gruyter, 10th edition, 2004.
- [4] Eric Betzig and Jay Trautman. Near-field optics: microscopy, spectroscopy, and surface modification beyond the diffraction limit. *Science*, 257(5067):189–195, July 1992.
- [5] Max Born and Emil Wolf. *Principles of optics: electromagnetic theory of propagation, interference and diffraction of light*. Cambridge University Press, 7th edition, 2006.
- [6] Edward Collett. *Field guide to polarization*. SPIE Press, 2005.
- [7] Cree, Inc. Cree<sup>®</sup> XLamp<sup>®</sup> MC-E LED Product family data sheet. [www.cree.com/products/pdf/XLampMC-E.pdf](http://www.cree.com/products/pdf/XLampMC-E.pdf), 2012.
- [8] Guenther Derra, Holger Moench, Ernst Fischer, Hermann Giese, Ulrich Hechtfisher, Gero Heusler, Achim Koerber, Ulrich Niemann, Folke-Charlotte Noertemann, Pavel Pekarski, Jens Pollmann-Retsch, Arnd Ritz, and Ulrich Weichmann. UHP lamp systems for projection applications. *Journal of Physics D: Applied Physics*, 38:2995–3010, 2005.
- [9] Rainer Dohlus. *Photonik: Physikalisch-technische Grundlagen der Lichtquellen, der Optik und des Lasers*. Oldenbourg, 2010.
- [10] Albert Einstein. Zur Quantentheorie der Strahlung. *Physikalische Zeitschrift*, 18:121–128, 1917.
- [11] Hiroyuki Fujiwara. *Spectroscopic Ellipsometry: Principles and Applications*. Wiley, 2007.
- [12] Anthony Gerrard and James Burch. *Introduction to matrix methods in optics*. Wiley, 1975.
- [13] Andrew Glassner. Surface Physics for Ray Tracing. In Andrew Glassner, editor, *An Introduction to Ray Tracing*, pages 121–160. Academic Press, 1989.

Table 2.7: Comparison of the properties of artificial light sources.

	Durability	Suitability pulsed operation	for Spectrum	Polarization	Coherence	Speckle
Halogen lamp	3,000 h	good	'gray' radiator	no	low	no
Fluorescent lamp	4,000 h up to 25,000 h	no	continuous, depending on the luminescent materials	no	low	no
Metal vapor lamps	6,000 h	no	continuous, with superposed lines	no	low	no
Xenon short-arc lamp	1,000 h	no	in the visible part: similar to the blackbody radia- tion	no	low	no
Light-emitting diode	100,000 h <sup>a</sup>	very good	monochrome: 30–40 nm line width	no	low	no
Laser	high for diode- lasers	very good, pulsed operation possible	line spectrum, monochromatic	yes	high	yes

<sup>a</sup>for high performance LEDs 30,000–50,000 h

Table 2.8. Luminance of different light sources [33].

Type	Light source	Luminance $L_1$ in $\text{cd}/\text{cm}^2$
Natural	Noon sun	100,000 – 150,000
	Full moon	0.25 – 0.35
	Clear sky	0.3 – 0.7
	Cloudy sky	0.01 – 0.2
Artificial	Xenon short-arc lamp	20,000 – 500,000
	Arc lamp	20,000 – 180,000
	Mercury-vapor high pressure lamp	20,000 – 40,000
	Incandescent lamp, clear	200 – 5,000
	Sodium-vapor high pressure lamp, clear	300 – 550
	Fluorescent lamp	0.3 – 3
	Light-emitting diode	0.01 – 5,000

- [14] Joseph Goodman. Statistical Properties of Laser Speckle Patterns. In John Dainty, editor, *Laser Speckle and Related Phenomena*, volume 9 of *Topics in Applied Physics*, pages 9–75. Springer, 1975.
- [15] Roland Grisar. Sources for Optical Sensing. In E. Wagner, R. Dändliker, and K. Spenner, editors, *Optical Sensors*, volume 6 of *Sensors*, pages 117–142. VCH, 1992.
- [16] Tobias Haist. *Optische Phänomene in Natur und Alltag*. <http://www.optipina.de>, 2010.
- [17] Oliver Heavens. *Thin film physics*. Methuen, 1970.
- [18] Oliver Heavens and Robert Ditchburn. *Insight into optics*. Wiley, 1991.
- [19] Eugene Hecht. Note on an Operational Definition of the Stokes Parameters. *American Journal of Physics*, 38(9):1156–1158, September 1970.
- [20] Eugene Hecht. *Optics*. Addison-Wesley, San Francisco, 4th edition, 2002.
- [21] Hans-Jürgen Hentschel, editor. *Licht und Beleuchtung: Grundlagen und Anwendungen der Lichttechnik*. Hüthig, 5th edition, 2002.
- [22] R. Holm. Convention Confusions. In Edward Palik, editor, *Handbook of Optical Constants of Solids*, volume 2nd, pages 21–55. Academic Press, 1991.
- [23] Bernd Jähne. *Practical handbook on image processing for scientific and technical applications*. CRC Press, 2nd edition, 2004.
- [24] Robert Jones and Catherine Wykes. *Holographic and speckle interferometry*. Cambridge University Press, 2nd edition, 1989.
- [25] Dietrich Kühlke. *Optik: Grundlagen und Anwendungen*. Deutsch, Frankfurt am Main, 2nd edition, 2007.
- [26] Hans-Jörg Kull. *Laserphysik: Physikalische Grundlagen des Laserlichts und seine Wechselwirkung mit Materie*. Oldenbourg, 2010.
- [27] Ulrich Neuschaefer-Rube. *Optische Oberflächenmesstechnik für Topografie und Material*. Habilitationsschrift, Universität Gesamthochschule Kassel, 2002.
- [28] Bahaa Saleh and Malvin Teich. *Fundamentals of photonics*. Wiley, 2nd edition, 2007.
- [29] Eugen Schäfer. *Technische Optik*. Vieweg, 1997.
- [30] Gottfried Schröder and Hanskarl Treiber. *Technische Optik*. Vogel, Würzburg, 9th edition, 2002.



- [31] William Shurcliff. *Polarized light: production and use*. Harvard University Press, 1962.
- [32] Károly Simonyi. *Foundations of electrical engineering*, volume 3: Fields–Networks–Waves. Pergamon Press, 1963.
- [33] Alma Taylor. *Illumination Fundamentals*. Rensselaer Lighting Research Center, 2000.
- [34] Harland Tompkins and Eugene Irene, editors. *Handbook of ellipsometry*. Andrew, 2005.
- [35] Harland Tompkins and William McGahan. *Spectroscopic ellipsometry and reflectometry: a user's guide*. Wiley, 1999.
- [36] Hans Völz. *Industrial color testing*. VCH, 1995.
- [37] Volker Wittwer. Solarenergie. In Hans-Jörg Bullinger, editor, *Technologieführer: Grundlagen, Anwendungen, Trends*, pages 350–355. Springer, 2007.
- [38] Lawrence Wolff. Polarization-Based Material Classification from Specular Reflection. *IEEE Transactions on Pattern Analysis and Machine Intelligence*, 12(11):1059–1071, November 1990.
- [39] Günter Wyszecki and Walter Stiles. *Color Science*. Wiley, 2nd edition, 2000.
- [40] Amnon Yariv. *Quantum electronics*. Wiley, 3rd edition, 1989.
- [41] Wolfgang Zinth and Ursula Zinth. *Optik: Lichtstrahlen – Wellen – Photonen*. Oldenbourg, München, 4th edition, 2013.



Chapter 3  
**Optical Imaging**

# 3

## 3 Optical Imaging

3.1	Introduction . . . . .	99
3.2	Imaging with a pinhole camera, central projection . . . . .	100
3.3	The camera model and camera calibration . . . . .	103
3.4	Optical imaging using a single lens . . . . .	106
3.4.1	The paraxial approximation and Gaussian optics . . . . .	107
3.4.2	Thin lens equation . . . . .	108
3.4.3	Bundle limitation . . . . .	114
3.4.4	Depth of field . . . . .	117
3.4.5	Telecentric imaging . . . . .	123
3.4.5.1	Defocused telecentric imaging . . . . .	124
3.4.5.2	Double-sided telecentric systems . . . . .	125
3.4.6	Perspective . . . . .	125
3.4.7	Imaging of tilted planes . . . . .	128
3.4.8	Aberrations . . . . .	133
3.4.8.1	Seidel aberrations of spherical lenses . . . . .	133
3.4.8.2	Chromatic aberration . . . . .	136
3.5	Optical instruments with several lenses . . . . .	137
3.5.1	The projector . . . . .	137
3.5.2	The microscope . . . . .	138
3.6	Bibliography . . . . .	140

## 3 Optical Imaging

### 3.1 Introduction

Ideally, the imaging optics of an automated visual inspection system images every relevant point of the test object to exactly one point on the sensor. In other words, the diverging light bundle coming from a point  $G$  of the test object is transformed into a light bundle converging at some point  $B$  on the sensor. Such a correspondence of two points  $B = \mathcal{A}\{G\}$  yields a sharp optical imaging.

An ideal imaging optic  $\mathcal{A}\{\cdot\}$  transforms every homocentric beam<sup>1</sup> into another beam whose rays intersect in the sensor plane (Fig. 3.1). Such optics can sharply image every visible point to the sensor. Physically feasible optics can only approximate an ideal imaging optic.

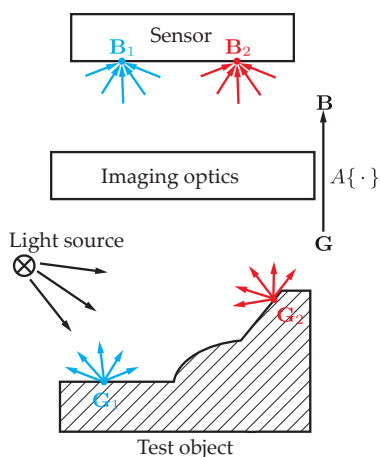


Figure 3.1. The role of the imaging optics in capturing a test object.

Propagation, diffraction, and interference of light are thoroughly described by Maxwell's equations and their solutions. Maxwell's equations are a set of partial differential equations. In order to use them to solve a given optical task, the task's physical conditions have to be formulated as boundary values (see Chap. 2). In combination with Maxwell's equations, these boundary values constitute a boundary value problem which has to be solved. For simple conditions, such as planar, infinitely spread surfaces, or homogeneous materials, the boundary values can be easily formulated and the corresponding equations can be solved analytically.

Unfortunately, that is not possible for realistic visual inspection tasks. Let a test object have the dimensions length  $\times$  width  $\times$  height = 10 cm  $\times$  10 cm  $\times$  1 cm and suppose that the shortest wavelength is  $\lambda = 500$  nm. Then, it would be necessary to provide boundary values, such as the electric field strength, polarization, and relevant material properties, for

<sup>1</sup>A bundle of light rays intersecting in a single point.

each point on a grid spaced more finely than the wavelength. The values in the case of this example would require  $8 \cdot 10^{14}$  points. For an opaque object, it would indeed be sufficient to consider only a thin layer of the surface, but this would still result in a tremendous number of boundary values: about  $10^{11}$ . It is apparent that this approach is unsuitable for practical visual inspection tasks. So, an extensive simplification is needed that would still allow deriving valid results and performing sufficiently accurate calculations.

A substantial but practically still very useful and descriptive simplification is the use of geometric optics, where the light is described by rays. Formally, the transition from Maxwell's equations to geometric optics can be achieved by letting the wavelength approach zero [22]. In a practical sense this means that all relevant dimensions of the optical system have to be significantly larger than the wavelength of the light used if the task is to be adequately handled with geometric optics.

The light rays correspond to the Poynting vector (2.37) of an electromagnetic wave. However, a single light ray in the sense of an isolated light transport along a straight line or a curve is a contradiction in terms. An infinitesimally small light ray would violate just those suppositions of geometric optics, that all dimensions have to be larger than the wavelength. Therefore, light rays are always light bundles with a finite extent, which has to be wide compared to the wavelength.

For geometric optics, the laws of reflection and refraction are important, as well as the straight propagation of light in homogeneous media. Aside from Maxwell's equations (see Sec. 2.6), these laws can also be derived using geometric optics and Fermat's principle. According to this famous principle, which can be deduced from Maxwell's equations, propagating light always takes the path of the least optical distance (the optical distance is the product of the refraction index and the geometric distance) [22]. The propagation of light rays in inhomogeneous media can also be described using this principle.

In this chapter, models for optical imaging using lenses and lens systems will be described on the basis of geometric optics. The following topics will be covered:

- The easiest optical imaging system: the pinhole camera,
- imaging with a lens,
- telecentric imaging,
- the lens systems which are used in cameras, microscopes or projectors.

On the one hand, these models will serve for the qualitative comprehension of the different imaging systems and the selection of the optical system suitable for the actual task. On the other hand, they provide a quantitative description of the image acquisition process. For the latter, the model parameters have to be known with sufficient precision. The determination of these parameters can be conducted using calibration methods, which are also covered in this chapter.

### 3.2 Imaging with a pinhole camera, central projection

The simplest model of a camera is the pinhole camera. An ideal pinhole camera consists of a diaphragm, with an infinitesimally small hole, that is parallel to an image plane (see Fig. 3.2). It accepts exactly one light ray of a light bundle coming from an object point. The distance between the aperture and the image plane is called the **image distance** and is denoted by  $b$ . In the case of a pinhole camera, the optical mapping of an object point  $\mathbf{x}_c$  to an image point

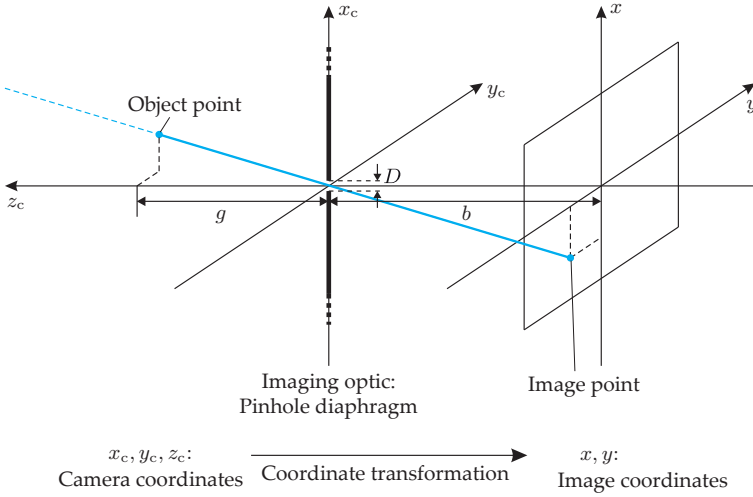


Figure 3.2. Pinhole camera.

$x$  can be mathematically described using a central projection:

$$\mathbb{R}^3 \rightarrow \mathbb{R}^2, \tag{3.1}$$

$$\begin{pmatrix} x_c \\ y_c \\ z_c \end{pmatrix} \mapsto \begin{pmatrix} x \\ y \end{pmatrix} = -\frac{b}{z_c} \begin{pmatrix} x_c \\ y_c \end{pmatrix}. \tag{3.2}$$

The intercept theorem A.1 (see Fig. 3.2) directly leads to these equations. As the mapping comes with a point reflection in the projection center, an inverted image is created in the  $x_c, y_c$ -plane. The ratio of the image size to the object size is  $V = -\frac{b}{z_c}$ , with the negative sign denoting the inversion of the image.

The origin of the coordinate system  $(x_c, y_c, z_c)^T$  is located in the center of the aperture, which coincides with the  $x_c, y_c$ -plane. The  $z_c$ -axis, which is the optical axis of the pinhole camera, is perpendicular to the aperture, runs through the center of the pinhole, and is directed away from the camera. Hence, the coordinate system is set by the spatial position of the camera and is therefore called the **camera coordinate system**. The coordinates with respect to the image plane are called the **image coordinates** and are denoted by  $(x, y)^T$ .<sup>2</sup>

Now, it is beneficial to introduce an alternative mathematical description of the central projection, which allows an elegant representation in the form of a linear mapping. This is

<sup>2</sup>In this book, image coordinates are always related to right-handed coordinate systems. However, for digitally representing images, often left-handed coordinate systems are used, having the origin in the upper left corner with the  $y$ -axis pointing downwards. The transformation between these coordinate systems and the image coordinates used for this book is given by:

$$[0, M - 1] \times [0, N - 1] \rightarrow [0, M - 1] \times [0, N - 1], \quad \begin{pmatrix} x \\ y \end{pmatrix} \mapsto \begin{pmatrix} x \\ N - 1 - y \end{pmatrix}. \tag{3.3}$$

This coordinate transformation might have to be taken into account when implementing image processing algorithms.

why points are expressed by their **homogeneous coordinates**. The transformation from the Cartesian coordinates of a point  $x_1, \dots, x_N$  to homogeneous coordinates  $x'_1, \dots, x'_N$  is done by appending an additional coordinate  $w$ :

$$(x_1, \dots, x_N)^T \mapsto (x_1 w, \dots, x_N w, w)^T =: (x'_1, \dots, x'_N, w)^T. \quad (3.4)$$

The reverse transformation is done by dividing by  $w$ :

$$(x'_1, \dots, x'_N, w)^T \mapsto \left( \frac{x'_1}{w}, \dots, \frac{x'_N}{w} \right)^T = (x_1, \dots, x_N)^T. \quad (3.5)$$

Therefore, one must always have  $w \neq 0$  for homogeneous coordinates.

Using homogeneous coordinates, the central projection can now be expressed as [4]

$$\begin{pmatrix} x' \\ y' \\ w \end{pmatrix} = \begin{pmatrix} -b & 0 & 0 & 0 \\ 0 & -b & 0 & 0 \\ 0 & 0 & 1 & 0 \end{pmatrix} \begin{pmatrix} x'_c \\ y'_c \\ z'_c \\ w_c \end{pmatrix}. \quad (3.6)$$

In homogeneous coordinates, the central projection is a linear mapping, whereas in Cartesian coordinates a division is required.

The central projection (3.2) is not injective and thus is not invertible. Every object point positioned on a line of sight running through the optical center is mapped to the same image point (see Fig. 3.3). Hence, the reconstruction of a transparent or a partly transparent object from a single picture is impossible. However, even opaque objects, which are not transparent, suffer a loss of information: indeed, each image point is the result of exactly one object point but the size of the object and its distance to the camera cannot be extracted from the image signal. The **magnification**  $V = -\frac{b}{z_c}$  of the central projection depends on the distance and thus the mapping does not preserve lengths. For each image point, only the line of sight, on which the corresponding object has to lie, is known. The line of sight is a straight line emerging from the image point and running through the projection center of the camera. Sectors of the scene lying behind an opaque object are hidden in the perspective of the camera and therefore are not visible in the image.

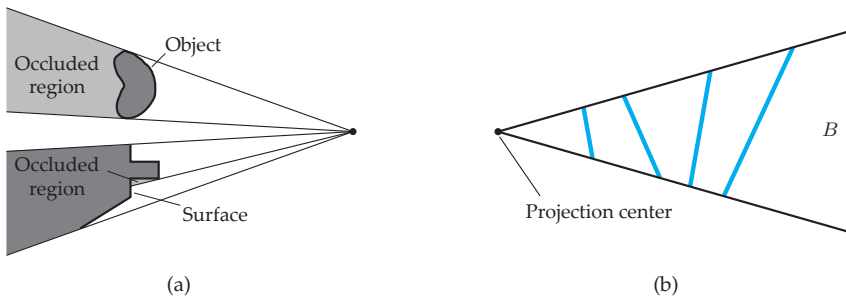


**Figure 3.3.** Visualization of the loss of information caused by the central projection: (a) Occlusion of remote object points; (b) All shown objects (blue) lead to the same image (red).

Theoretically, the pinhole camera has an unlimited depth of field<sup>3</sup>. This is possible, since for an ideal pinhole camera, only one of the light bundles coming from an object point is accepted. For sharp imaging, the aperture diameter  $D$  would need to be chosen to be very small. But in that case, only a little light would reach the sensor and so long exposure times would be necessary. Therefore, the optical imaging of a pinhole camera is called faint. For a practical realization of a pinhole camera, of course an aperture diameter of  $D > 0$  has to be chosen, which allow light bundles with a certain extent pass the aperture. Hence, the optical imaging cannot be ideally sharp. In order to ensure that the simplification of using the model of light rays is valid, it is even necessary to choose an aperture diameter of  $D > \lambda$  (see Sec. 2.2.6).

### 3.3 The camera model and camera calibration

Although it is only an approximation, the pinhole camera is often used to model real cameras. Then the task of estimating the model parameters for a given camera has to be carried out. This task is called **camera calibration**. The whole set of camera parameters consists of the intrinsic and the extrinsic camera parameters. The intrinsic parameters describe the properties of the imaging optics and the image sensor inside the camera. The extrinsic parameters represent the camera's position and orientation in space.

Before the actual camera calibration will be explained, the model (3.2) has to be appropriately extended. Besides the image and camera coordinate systems, the world coordinate system is introduced and will be denoted by  $(x_w, y_w, z_w)^T$ . The spatial position and orientation of the world coordinate system are arbitrary but fixed. The transformation from world coordinates to camera coordinates can be expressed by a rotation and a subsequent translation:

$$\begin{pmatrix} x_c \\ y_c \\ z_c \end{pmatrix} = \mathbf{R} \begin{pmatrix} x_w \\ y_w \\ z_w \end{pmatrix} + \mathbf{t}, \quad (3.7)$$

where  $\mathbf{t} \in \mathbb{R}^3$  is the translation vector and  $\mathbf{R} \in \mathbb{R}^{3 \times 3}$  an orthogonal rotation matrix. Together,  $\mathbf{R}$  and  $\mathbf{t}$  encode the extrinsic camera parameters with 6 degrees of freedom. A matrix  $\mathbf{R}$  is called orthogonal if  $\mathbf{R}^T \mathbf{R} = \mathbf{I}$ .

In homogeneous coordinates (3.4), the rotation and translation can be combined into a single linear mapping:

$$\begin{pmatrix} x'_c \\ y'_c \\ z'_c \\ w_c \end{pmatrix} = \begin{pmatrix} \mathbf{R} & \mathbf{t} \\ 0 & 0 & 0 & 1 \end{pmatrix} \begin{pmatrix} x'_w \\ y'_w \\ z'_w \\ w_w \end{pmatrix}. \quad (3.8)$$

Up to this point, the pinhole camera has been described only in terms of the image distance  $b$ . Now, the image sensor is also modeled (see Chap. 6). The pixel sizes in the  $x$ - and  $y$ -directions are denoted by  $(s_x, s_y)^T$ . Besides, the origin of the image coordinate system can be displaced by an offset  $(o_x, o_y)^T$  with respect to the intersection of the optical axis and the

<sup>3</sup>The depth of field is the part of the object space that can be mapped sharply onto the image plane (see Sec. 3.4.4).



image plane. So, the mapping between camera and image coordinates is given by

$$\begin{pmatrix} x \\ y \end{pmatrix} = -\frac{b}{z_c} \begin{pmatrix} \frac{x_c}{s_x} \\ \frac{y_c}{s_y} \end{pmatrix} + \begin{pmatrix} o_x \\ o_y \end{pmatrix} \quad (3.9)$$

and, expressed in homogeneous coordinates,

$$\begin{pmatrix} x' \\ y' \\ w \end{pmatrix} = \begin{pmatrix} -\frac{b}{s_x} & s_s & o_x & 0 \\ 0 & -\frac{b}{s_y} & o_y & 0 \\ 0 & 0 & 1 & 0 \end{pmatrix} \begin{pmatrix} x'_c \\ y'_c \\ z'_c \\ w_c \end{pmatrix}. \quad (3.10)$$

For the sake of completeness, the parameter  $s_s$  is included, which allows modeling a system of skew coordinates. For the sensors of today's cameras,  $s_s = 0$  can be assumed.

Inserting (3.8) in (3.10) yields

$$\begin{pmatrix} x' \\ y' \\ w \end{pmatrix} = \underbrace{\begin{pmatrix} -\frac{b}{s_x} & s_s & o_x & 0 \\ 0 & -\frac{b}{s_y} & o_y & 0 \\ 0 & 0 & 1 & 0 \end{pmatrix} \begin{pmatrix} \mathbf{R} & \mathbf{t} \\ 0 & 0 & 0 & 1 \end{pmatrix}}_{=: \mathbf{P}} \begin{pmatrix} x'_w \\ y'_w \\ z'_w \\ w_w \end{pmatrix}. \quad (3.11)$$

The matrix  $\mathbf{P} \in \mathbb{R}^{3 \times 4}$  is called the **projection matrix** or **camera matrix** of the camera. It completely describes the imaging process of a pinhole camera. Its 12 degrees of freedom can be interpreted as the 6 extrinsic parameters, the 5 intrinsic parameters  $\frac{b}{s_x}$ ,  $\frac{b}{s_y}$ ,  $s_s$ ,  $o_x$ , and  $o_y$ , and the free scaling parameter belonging to the transformation into homogeneous coordinates.

Finally, the transformation from world coordinates to image coordinates is given by ( $s_s = 0$ )

$$x = -\frac{b}{s_x} \frac{r_{11}x_w + r_{12}y_w + r_{13}z_w + t_1}{r_{31}x_w + r_{32}y_w + r_{33}z_w + t_3} + o_x, \quad (3.12)$$

$$y = -\frac{b}{s_y} \frac{r_{21}x_w + r_{22}y_w + r_{23}z_w + t_2}{r_{31}x_w + r_{32}y_w + r_{33}z_w + t_3} + o_y. \quad (3.13)$$

The process of acquiring these parameters or the matrix  $\mathbf{P}$  is called camera calibration. The common calibration methods can be divided into two steps:

1. Determination of a set of corresponding world and image points i.e., of pairs  $((x_{wi}, y_{wi}, z_{wi})^T, (x_i, y_i)^T)$ ,  $i = 1, \dots, m$ ;
2. Calculating the camera parameters using these corresponding points.

The first step is done by capturing multiple configurations of a calibration object. The world coordinates of some distinguished points have to be known—either from the construction of the calibration object, or by exact measurements. Then, these points have to be identified and localized in the captured images, preferably in an automatic fashion. Hence, regular and clearly visible structures, such as a checkerboard, are very suitable. The corners and edges of the board's squares are detected using image processing methods (see Sections 14.4 and 11.2).

It is not sufficient to use the corresponding points of a single plane of the object space, since the resulting system of equations would be underdetermined. Therefore, a three-

dimensional calibration object is used or multiple spatially different configurations of a flat calibration pattern are captured [21]. A calibration object should consist of multiple planar surfaces with different distances from the camera, like a dice. The captured calibration images must contain enough corresponding points, so that the resulting system of equations has a unique solution and is numerically well-conditioned.

In the second step, suitable mathematical and numerical methods are used to solve the system of equations:

$$(x'_i, y'_i, w_i)^T \propto \mathbf{P} (x'_{wi}, y'_{wi}, z'_{wi}, w_{wi})^T \quad i = 1, \dots, m. \quad (3.14)$$

As the transformation into homogeneous coordinates is not completely unique because of the scaling factor, only the proportionalities of the vectors on both sides of the equation can be demanded. As a possible interpretation, the vectors  $(x_i, y_i, w_i)^T$  and  $\mathbf{P} \mathbf{x}_{wi}$  are parallel and the cross product of parallel vectors has to be equal to the zero vector:  $(x_i, y_i, w_i)^T \times \mathbf{P} \mathbf{x}_{wi} = \mathbf{0}$ . With the vector  $\mathbf{p}_j^T$  representing row  $j$  of the matrix  $\mathbf{P}$ , one has [8]:

$$\begin{pmatrix} \mathbf{p}_2^T w_i - \mathbf{p}_3^T y_i \\ \mathbf{p}_3^T x_i - \mathbf{p}_1^T w_i \\ \mathbf{p}_1^T y_i - \mathbf{p}_2^T x_i \end{pmatrix} \mathbf{x}_{wi} = \mathbf{0} \quad (3.15)$$

$$\Leftrightarrow \underbrace{\begin{pmatrix} \mathbf{0}^T & w_i \mathbf{x}_{wi}^T & -y_i \mathbf{x}_{wi}^T \\ -w_i \mathbf{x}_{wi}^T & \mathbf{0}^T & x_i \mathbf{x}_{wi}^T \\ y_i \mathbf{x}_{wi}^T & -x_i \mathbf{x}_{wi}^T & \mathbf{0}^T \end{pmatrix}}_{\in \mathbb{R}^{3 \times 12}} \underbrace{\begin{pmatrix} \mathbf{p}_1 \\ \mathbf{p}_2 \\ \mathbf{p}_3 \end{pmatrix}}_{=: \mathbf{p} \in \mathbb{R}^{12}} = \mathbf{0}. \quad (3.16)$$

This equation is linear with respect to the unknown entries of the matrix  $\mathbf{P}$ , in contrast to the non-linear dependencies in (3.12), (3.13). However, the equations are linearly dependent, so that one of them can be omitted. Thus each pair of points yields two equations. In order to determine the 11 degrees of freedom, at least 6 corresponding points are necessary. A set of  $m$  corresponding points, leads to the system of equations  $\mathbf{A} \mathbf{p} = \mathbf{0}$  with  $\mathbf{A} \in \mathbb{R}^{2m \times 12}$ . This overdetermined system of linear equations can be used to estimate the entries of  $\mathbf{p}$  by using the method of least squares, which minimizes the algebraic error

$$\varepsilon = \|\mathbf{A} \mathbf{p} - \mathbf{0}\| = \|\mathbf{A} \mathbf{p}\|. \quad (3.17)$$

A numerical solution of this estimation problem can be achieved using the singular value decomposition of the system of equations. Then, the singular vector corresponding to the smallest singular value represents the solution sought.

In order to increase the numerical stability of this method, the image points should be scaled appropriately [8].

Usually, more than the necessary 6 pairs of points are used in order to allow for possibly inaccurate measurements of the world and image coordinates. In addition, wrongly matched pairs of points can lead to critical outliers in the set of corresponding world and image points. If enough correct pairs of points are available, the influence of any outliers can be reduced by using stable estimation methods such as RANSAC or 'least median of squares' [8].

The projection matrix can be used to calculate that line of sight of an image point  $\mathbf{x}$  on which the captured object point is located [8]. A point  $\mathbf{x}_w$  lying on the line of sight can be

obtained by inverting the projection  $\mathbf{x} = \mathbf{P} \mathbf{x}_w$  using the pseudoinverse matrix

$$\mathbf{x}_w = \mathbf{P}^T (\mathbf{P} \mathbf{P}^T)^{-1} \mathbf{x}. \quad (3.18)$$

The second known point on the line of sight is the projection center  $\mathbf{c}$ , which is the eigenvector of the eigenvalue 0 of the projection matrix:

$$\mathbf{P} \mathbf{c} = \mathbf{0}. \quad (3.19)$$

So, the points lying on the line of sight are given by the line

$$(1 - \lambda) \mathbf{x}_w + \lambda \mathbf{c} \quad (3.20)$$

with the free parameter  $\lambda$ .

For special lens systems and for the sake of very high precision, it might be necessary to abandon the model of the pinhole camera. Then, the lines of sight do not intersect each other in a single point but are characterized by their intersections with two parallel planes. Related calibration methods can be found in [7] for example.

## 3.4

### 3.4 Optical imaging using a single lens

As mentioned earlier, the practical use of pinhole cameras is very limited because of their low light yield. In order to obtain a well lit image, it is necessary to sharply capture a bigger segment of the light bundle coming from an object point on the image plane. This can be achieved by using imaging optics like those used in cameras. Usually, the imaging optics have several lenses. A **lens** is an optical component made out of glass or plastic. Precise refraction of the incoming light is achieved by its bent shape (Fig. 3.5(a)). Incoming light rays parallel to the optical axis are refracted in such a way that they intersect at the focal point of the lens (Fig. 3.4). The focal length  $f$  (the distance between the lens and the focal point) and the radius of curvature  $R$  of the two surfaces of the lens are related as follows:

$$R = 2f \frac{n_2 - n_1}{n_1}, \quad (3.21)$$

with  $n_2$  denoting the the refraction index of the lens material and  $n_1$  that of the surrounding medium [9, 22].

At first, optical imaging with a single lens will be described. Most of the important effects can be described using this setup.

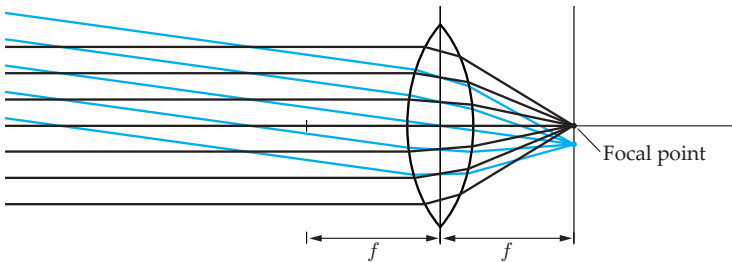


Figure 3.4. Incoming light, parallel to the axis, is focused on the focal plane of the lens.

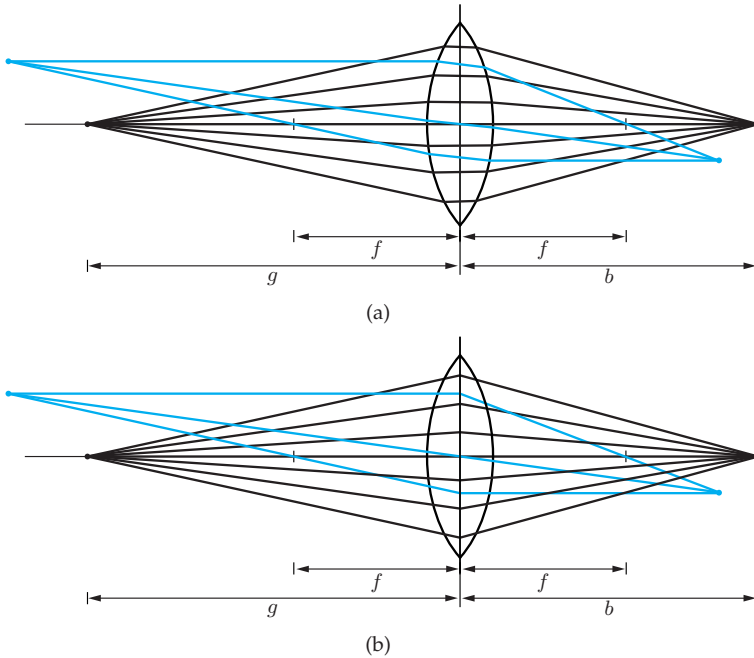


Figure 3.5. Optical imaging with a thin converging lens: (a) Refraction of the light on the curved interfaces of the lens; (b) Idealized refraction of spherical lenses in the sense of Gaussian optics.

Alternatively, the imaging optics can be constructed by using curved mirrors [15]. Whether mirrors or lenses are more suitable often depends on construction limitations: big lens systems, for telescopes used in astronomy for example, would be too heavy and might be deformed by their own weight.

### 3.4.1 The paraxial approximation and Gaussian optics

Most lenses and lens systems have rotational symmetry. The axis of symmetry is called the **optical axis**. Imaging systems where the light coming from the observed objects is approximately parallel to the optical axis are of great importance: as the angles  $\alpha$  between the incoming light ray and the optical axis are small in this case, the approximation  $\sin \alpha \approx \alpha$  can be employed. The result is a linear formulation of the law of refraction (2.208) from Sec. 2.6.3:

$$n_1 \sin \theta_1 = n_2 \sin \theta_2 \quad \rightsquigarrow \quad n_1 \theta_1 \approx n_2 \theta_2. \quad (3.22)$$

This linearization is called the paraxial approximation. Here, spherical interfaces transform homocentric bundles into bundles that are also homocentric (Fig. 3.5(b)). A bundle is called homocentric if all of its light rays intersect in one common point.

By applying the paraxial approximation, one can elegantly calculate, using matrix operations, the imaging properties of systems with many lenses that are centered around the same optical axis [5, 9]. Refracting surfaces as well as the propagation paths of the light are described by  $2 \times 2$  matrices. The light rays are modeled as two-dimensional column vec-

tors, which essentially represent their direction and their distance from the optical axis. The propagation of rays through the system is calculated by successive multiplications of their vectors by the matrices of the optical elements.

The paraxial model is only an approximation: real lenses produce aberration. If spherical lenses<sup>4</sup> were ideal imaging systems, one lens would be sufficient for image acquisition. High-quality lens systems are constructed out of several lenses in order to correct the aberrations of the single lenses. Thus, the construction of complicated optical systems offers many degrees of freedom, such as the radii of curvature, the positions, and the materials (i.e., refraction indices), which can be precisely adjusted in order to minimize aberration. The simplified equations obtained by the paraxial approximation still hold for such corrected lens systems. This practice, which is called Gaussian Optics, is the main one to be used throughout this book. The aberration of real lenses and lens systems are covered in Sec. 3.4.8.

### ▶ 3.4.2 Thin lens equation

A sufficiently large amount of the light reaching the camera from an object point has to be collected and focused on preferably one single point on the light sensitive sensor. This is achieved, for example, by a thin converging lens, which will now be used to describe the basic principles of imaging optics. In this context, ‘thin’ means that the focal length  $f$  of the lens is significantly greater than its thickness. In this case, the optical imaging can be well-approximated by refraction on a plane. This plane is called the principal plane of the lens. The model of a thin lens allows approximating the real refraction on the interface between the lens and the surrounding medium by the refraction on the principal plane (Fig. 3.5). As this approximation is sufficient for most applications in the field of automated visual inspection, the model of the thin lens is the one chiefly used in this book.

Figure 3.6 shows a thin, circularly shaped lens, focusing the light rays which originate from an object point and then pass through the lens to hit the image plane that contains the sensor at a single point.

The incoming light parallel to the optical axis is focused on the focal point by a converging lens. The focal point is located on the optical axis. Its distance from the optical center of the lens is called the **focal length** and denoted by  $f$ . The optical path can be constructed based on the following consideration: a light ray which comes in perpendicularly to the lens plane is refracted and then passes through the focal point (ray 2 in Fig. 3.6). Due to the intercept theorem, one has

$$\frac{G}{f} = -\frac{B}{b-f}. \quad (3.23)$$

The image size  $B$  and the object size  $G$  describe the distance of an image or object point from the optical axis. As they are signed, the inverted image produced by the central projection leads to either  $G \geq 0, B \leq 0$  or  $G \leq 0, B \geq 0$ , so the negative sign of (3.23) is necessary. The object distance  $g$  and the image distance  $b$  are also signed: a positive image distance has a positive value of  $z_c$  and is therefore placed on the left side of the lens by convention—however, a positive image distance has a negative value of  $z_c$  and hence is located on the right side of the lens. Therefore,  $g > 0, b > 0$  for the most frequent setups of real imaging

---

<sup>4</sup>Parts of the interfaces of spherical lenses are parts of spherical surfaces. They are much more easy to produce than aspherical lenses, and are thus significantly cheaper.

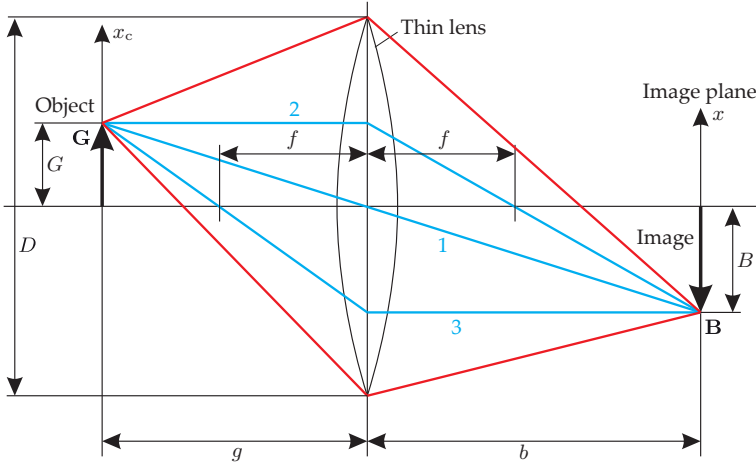


Figure 3.6. Optical imaging with a lens. The extent of the pictured bundle is colored in red. The rays, which are used to graphically construct the imaging system, are drawn in blue (1: principal ray, 2, 3: parallel rays).

systems with a converging lens. The conventions for the signs of the variables are summarized in Table 3.1.

Rays passing through the center of the lens are not refracted (ray 1 in Fig. 3.6). As with the pinhole camera (3.2), this leads to

$$\frac{G}{g} = -\frac{B}{b}. \tag{3.24}$$

If all light rays passing from  $G$  through the lens intersect in the image plane  $b$ , the object point  $G$  is displayed as a single sharp image point  $B$ . That condition has to hold especially for the parallel and principal ray, i.e., Equations (3.23) and (3.24) have to hold simultaneously. Manipulations of this system of equations result in the **thin lens equation**:

**Theorem 3.1: Thin lens equation**

For a focused optical imaging with object distance of  $g$ , an image distance of  $b$  and a thin lens with focal length  $f$ , it holds

$$\frac{1}{f} = \frac{1}{g} + \frac{1}{b}. \tag{3.25}$$

◇

Hence, a lens with focal length  $f$  can only achieve a sharp imaging on the image plane  $b$  of the plane at the distance  $g = \frac{bf}{b-f}$ . In contrast to the pinhole camera, the depth of field is limited (cf. Sec. 3.4.4), but the light yield is significantly better.

In order to sharply image an object plane that is perpendicular to the optical axis and is at a distance  $g$  from the lens plane, the image distance has to be chosen as follows:

$$b = \frac{gf}{g-f} = \frac{f}{1 - \frac{f}{g}}. \tag{3.26}$$

**Table 3.1.** Conventions for the signs of the quantities of an optical imaging with a single lens [22].

Variable	positive value	negative value
Focal length $f$	image-side focal point on the right side of the lens	image-side focal point on the left side of the lens
Object distance $g$	object point <b>G</b> on the left side of the lens	object point <b>G</b> on the right side of the lens
Image distance $b$	image point <b>B</b> on the right side of the lens	image point <b>B</b> on the left side of the lens
Object size $G$	object point <b>G</b> above the optical axis	object point <b>G</b> beneath the optical axis
Image size $B$	image point <b>B</b> above the optical axis	image point <b>B</b> beneath the optical axis

Adjusting a camera's image distance with respect to the object distance is called focusing. For increasing object distances, the image distance decreases. The extreme case  $g \rightarrow \infty$  leads to  $b \rightarrow f$ . As with the pinhole camera, the magnification depends on the distance:

$$V = \frac{B}{G} = -\frac{b}{g} \quad (3.27)$$

$$= -\frac{f}{g-f} = -\frac{1}{\frac{g}{f}-1}. \quad (3.28)$$

For a constant object distance  $g$ , the magnification increases with increasing focal length  $f$ . For capturing remote objects, telephoto lenses with long focal lengths can be used. Wide-angle lenses with shorter focal lengths have a low magnification but are able to capture a wider angular range of the object space. However, images captured with a wide-angle lens are more intensely affected by distortions of perspective. Zoom lenses allow adjusting the focal length by shifting the relative positions of the different lenses in the system.

Before the lens camera can be further investigated, two important terms have to be introduced.

### 3.1 Definition 3.1: Aperture stop

The aperture stop is the diaphragm with the maximum limiting influence on the ray bundle of the optical system (see also Sec. 3.4.3).  $\diamond$

### 3.2 Definition 3.2: Principal ray

The principal ray is that ray which connects an object point with the corresponding image point and intersects the optical axis in the plane of the aperture stop. The principal ray determines the magnification factor, particularly in the case of defocused imaging.  $\diamond$

In Fig. 3.6, the lens itself limits the ray bundle of the optical system. So, the aperture stop is circularly shaped with diameter  $D$  and is aligned in the lens plane.

The following remarks summarize the considerations concerning optical imaging systems using a single lens.

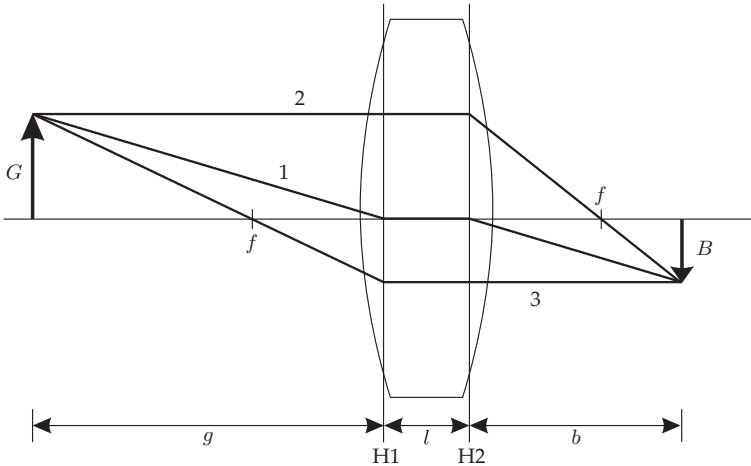


Figure 3.7. Construction of the optical path for a thick lens 1: principal ray, 2, 3: parallel rays, H1, H2: principal planes).

- ⊖ The magnification factor  $|V| = -\frac{B}{G} = \frac{b}{g}$  depends on the object distance  $g$ . If the magnification factor is unknown or if the object distance is variable, no quantitative information can be acquired about the lateral dimensions of the imaged object. The imaging does not preserve lengths.
- ⊖ In contrast to a pinhole camera, when a lens is used for optical imaging, the depth of field is limited.
- ⊕ The amount of light received by the sensor increases for larger aperture stops and can thus be adjusted within a certain range. Especially for large  $D$ , optical imaging systems using a lens have a significantly higher light yield than a pinhole camera.
- ⊖ Spherical lenses are affected by aberration and have unfavorable properties in several aspects. Among others, they suffer from geometric distortions and focus errors. However, some of these drawbacks can be minimized by stopping down, i.e., reducing the aperture diameter  $D$  (see Sec. 3.4.8).

In order to reduce aberration, high-quality lens systems have several lenses. When constructing such lens systems, the optical effects of one of the installed lenses are exploited to (at least partially) neutralize the aberration due to the remaining lenses, and vice versa.

Up to this point, only the  $x, z$ -plane has been considered. However, this simplification is not too severe because of the rotational symmetry around the  $z$ -axis. An arbitrary object point could be moved into the  $x, z$ -plane by a suitable rotation of the coordinate system around the  $z$ -axis (cf. Fig. 3.2). Thus, the listed equations also hold for the three-dimensional case.

In the thin lens model, the refraction is considered to take place at a plane and not at the two interfaces of the surrounding media. This model is refined by the thick lens model, describing the refraction by using two principal planes H1, H2 and the focus length  $f$  [2, 17].



As before, when constructing the optical path, parallel rays run through the focal point<sup>5</sup> on the other side of the lens (see Fig. 3.7). When entering the space between the principal planes, the principal ray is located on the optical axis; when leaving, its angle to the optical axis equals its angle of incidence [17, 19]. Between the principal planes, all rays are parallel to the optical axis.

Actually, in the context of the paraxial approximation, the thick lens model can be used to exactly describe complicated imaging systems consisting of several axially centered lenses. Therefore, compound lens systems, as are often used in commercially available cameras, can also be handled with the thin lens equation (3.25). The only important difference is that ‘object distance’ and ‘image distances’ now refer to the corresponding principal plane (see Fig. 3.7). The distance  $l$  between the principal planes does not have to be taken into account in the thin lens equation.

Depending on the object distance and the imaging optic, the resulting image can be of two kinds:

---

### 3.3 Definition 3.3: Real image

A real image results if the light rays reflected by an object point indeed intersect in one image point. If a screen is placed at that position, the image will become visible.  $\diamond$

Usually, a real image can be directly observed, i.e., without the need of an additional optical system. All the optical imaging methods covered up to this point, which employ a converging lens and for which  $g > f$ , produce a real image.

---

### 3.4 Definition 3.4: Virtual image

In the case of a virtual image, no physically real light rays intersect at the image point. The light rays rather diverge or are parallel. Only from the perspective of an observer do the light rays seem to intersect in a common point. A virtual image cannot be visualized using a screen.  $\diamond$

If a virtual image is produced, the imaging optic is usually located between the image and the observer [22]. An everyday example is an image of an object in a plane mirror.

A converging lens produces a virtual image if the captured object is closer to the lens than its focal point:  $g < f$ . The light rays coming from the object diverge instead of intersecting in a real image point. However, for an observer, a virtual image, which seems to be located behind the object, is visible, because the diverging light rays are focused on an image plane by the lens of the human eye. In order to geometrically construct the image point, the ray passing through the focal point on the image side is extended back into the object space until it intersects with the principal ray (Fig. 3.8). This principle is used by magnifiers.

In contrast to the convex lenses covered up to this point (which have been converging lenses, i.e., positive lenses) **concave lenses** (negative lenses) can only produce virtual images. The virtual image is closer to the lens than the object and is therefore reduced in size. A parallel ray is refracted in such a way that it seems to be coming from the focal point located

---

<sup>5</sup>Assuming that the media on either side of the lens have the same refraction index, something which is often true, as for a lens surrounded by air. Otherwise, the focal lengths of the two sides of the lens would differ, which would have to be taken into account when constructing the optical path [17].

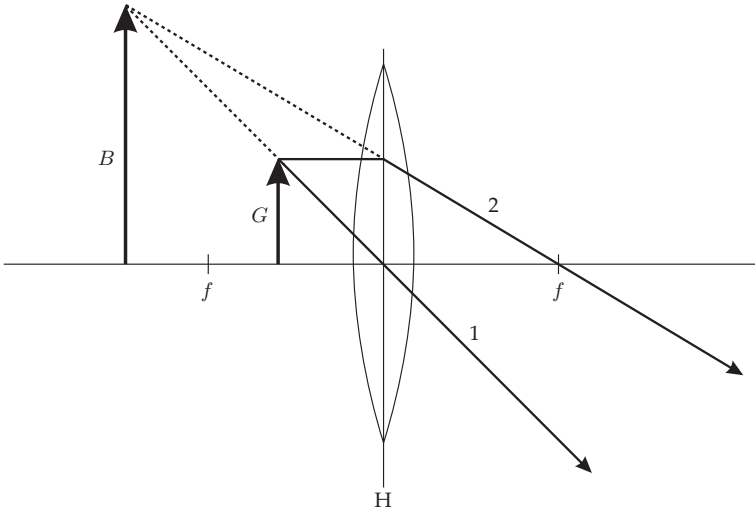


Figure 3.8. Constructing a virtual image for a convex lens (1: principal ray, 2: parallel ray, H: principal plane).

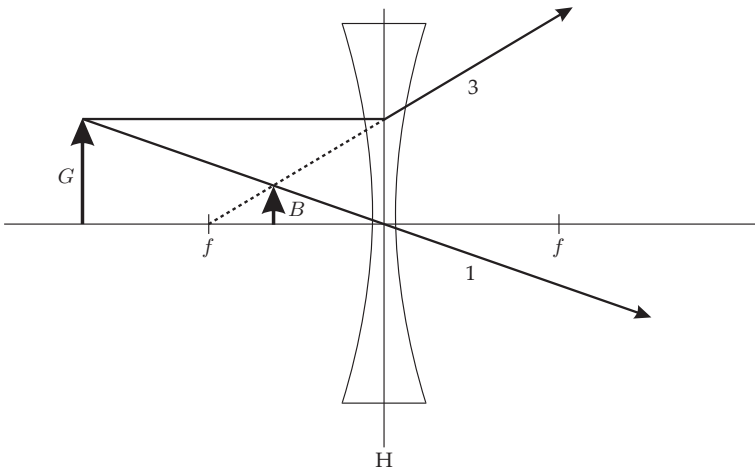


Figure 3.9. Imaging with a concave lens (1: principal ray, 3: parallel ray, H: principal plane).

Table 3.2. Imaging using a lens.

Case no. in Fig. 3.10	Lens type	Object position $g$	Image			
			type	position $b$	orientation	relative size
1	convex	$2f < g < \infty$	real	$f < b < 2f$	upside down	demagnified
2	convex	$g = 2f$	real	$b = 2f$	upside down	equally sized
3	convex	$f < g < 2f$	real	$2f < b < \infty$	upside down	magnified
	convex	$g = f$		$b \rightarrow \infty$	image in infinite distance	
4	convex	$0 < g < f$	virtual	$b < -g$	upright	magnified
	concave	$0 < g < \infty$	virtual	$ b  < g,$ $ b  <  f $	upright	demagnified

on the object side of the lens (Fig. 3.9). Formally, this corresponds to a negative focal length  $f$ . A common use for concave lenses are eyeglasses for people suffering from near-sightedness.

Table 3.2 summarizes the different cases of real and virtual images. Figure 3.10 shows the relation between image distance and object distance for convex lenses: the image distance is drawn as a function of the object distance. Both quantities are expressed as multiples of the focal length.

➤ **3.4.3 Bundle limitation**

In terms of geometric optics, construction rays and light bundles are distinguished. Construction rays were used in the previous section in order to geometrically determine the image point corresponding to an object point. **Light bundles** describe the radiant power passing through the optical system and can be used to give information about the brightness, aberration, resolution, and depth of focus of the image.

Basically, two physical stops limit the transport of the light through an optical system (see Fig. 3.11):

1. The **aperture stop** limits the size of the ray bundles.
2. The **field stop** limits the field of view.

The aperture stop (see Def. 3.1) limits the angle of aperture  $2\alpha$  of the ray bundle coming from the axial object point [12]. Therefore, the aperture stop is critical for the light yield of the optical system.

---

**3.5 Definition 3.5: Field stop**

The field stop limits the field of view. It determines which part of the object space is captured.



Based on these principles, further terms can be defined [6]:

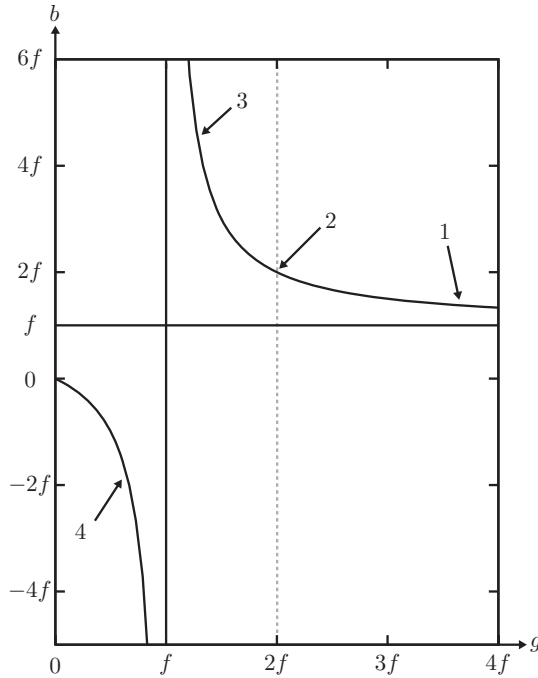


Figure 3.10. Relation between object and image distance for an optical imaging using a convex lens [6]. The part of the hyperbola for  $g > f$  corresponds to an imaging process producing a real image, the part  $g < f$  represents an imaging process resulting in a virtual image. The numbers identify the different cases in Table 3.2.

---

#### Definition 3.6: Entrance pupil

3.6

The **entrance pupil** is the image of the aperture stop on the object side. ◇

In order to determine the entrance pupil<sup>6</sup>, the image of the aperture, which is the result of the optical elements aligned between the aperture stop and the captured object, is identified. This image might also be a virtual image on the image side of the aperture stop, as shown in Fig. 3.13. If there are no lenses on the object side of the aperture stop, the entrance pupil is equal to the aperture stop.

---

#### Definition 3.7: Exit pupil

3.7

The **exit pupil** is the image of the aperture stop on the image side. ◇

---

#### Definition 3.8: Entrance window and exit window

3.8

The **entrance window** is the image of the field stop in the object space. The **exit window** is the image of the field stop in the image space. ◇

---

<sup>6</sup>The term ‘pupil’ originates from the fact that the visible pupil of the human eye is the object-side image of the aperture of the iris and acts as the eye’s aperture, limiting the amount of light received.

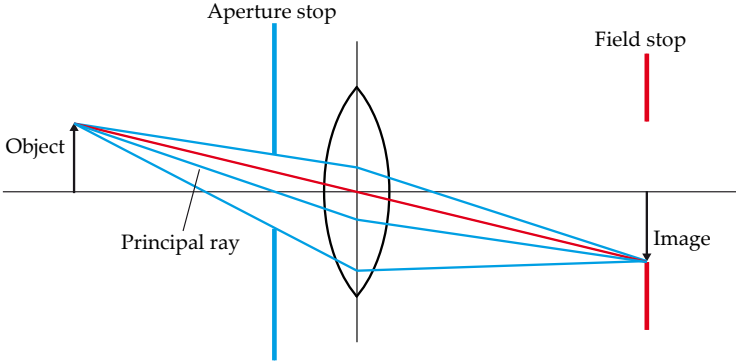


Figure 3.11. Aperture stop and field stop.

The exit pupil is the image of the entrance pupil when the optical system as a whole is considered. Similarly, the exit window is the image of the entrance window. The pupils of an optical system are never equal to the windows of the system [17].

The **principal ray** (see Def. 3.2) of a light bundle runs through the center of the aperture stop. So it passes through the center of the entrance pupil on the object side and the center of the exit pupil on the image side (cf. Figures 3.12 and 3.13).

### 3.9

#### Definition 3.9: Marginal ray

The **marginal ray** runs from the axial object point to the border of the aperture and finally to the corresponding axial image point. One-half of the angle of aperture  $\alpha$  of the marginal ray is an indicator for the light yield of the optical system.  $\diamond$

In order to determine which physical element represents the aperture stop for a given optical system, the images, on the object side, of all stops and lens mounts have to be constructed [5]. Now, the light bundle is further investigated, that comes from the point on the optical axis belonging to the plane in the object space that should be sharply captured. The image of a stop that limits this light bundle most of all, i.e., is visible under the smallest angle from the perspective of the origin of the light bundle, is the entrance pupil. The corresponding stop or lens mount is the optical system's aperture stop [12, 17]. Its image on the image side is the exit pupil. An equivalent approach can be used to determine the field stop of a given optical system: at first, the images on the object side of all limiting optical elements, such as the stops, lens mounts, and the image sensor, are constructed. Then, one considers the principal rays that originate from the intersection of the optical axis and the plane of the entrance pupil and are directed into the object space. The image on the object side that most limits those principal rays is the entrance window (Fig. 3.12). The corresponding optical element is the field stop. The exit window is the image on the image side of the field stop. In the case of a camera, the image sensor is usually both the field stop and the exit window.

Figures 3.12 and 3.13 show different configurations of the aperture and field stops. In either case, the aperture stop is closer to the lens than the focal point, leading to pupils represented by virtual images. Figure 3.14 shows an example of a system having several lenses.

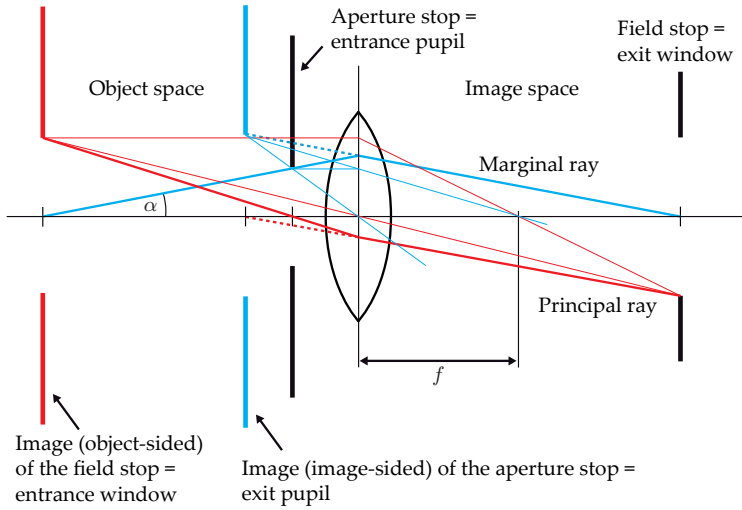


Figure 3.12. Aperture stop between object and lens.

Light bundles can be used to explain the effect of **vignetting**: The light bundle of non-axial object points might be further limited in composite lens systems, for example by lens mounts (see Fig. 3.15). This limitation of the effective aperture for non-axial object points is called vignetting. The maximum diameter of non-axial light bundles is smaller than for axial light bundles. This results in the image's getting darker towards the periphery. Vignetting can be minimized by reducing the aperture, so that all light bundles are limited to the same diameter.

### 3.4.4 Depth of field

According to the thin lens equation (3.25), exactly one object plane perpendicular to the optical axis is captured sharply on the image plane. All objects which are not located exactly at that distance from the camera will appear blurred. As the dimensions of the light sensitive elements on a semiconductor sensor are finite, a certain blur corresponding to a specific range of object distances can be tolerated.<sup>7</sup>

In this section, a relation between the tolerable blur and the depth of field is derived in terms of the parameters of the camera.

#### Definition 3.10: Depth of field

The depth of field of an optical system is the length of the interval with respect to  $z_c$  containing objects which are captured with tolerable sharpness.  $\diamond$

Let  $D$  be the diameter of the circularly shaped **entrance pupil** and  $O := \frac{f}{D}$  the so-called **focal ratio** or  **$f$ -number**. The diameter of the entrance pupil determines the extent of the light bundle on the object side that reaches the image plane after passing the aperture.

<sup>7</sup>Besides the dimensions of the light sensitive elements of a sensor, the acceptable defocus blur also depends on the size of the blur caused by aberration (see Sec. 3.4.8), which will not be discussed here.



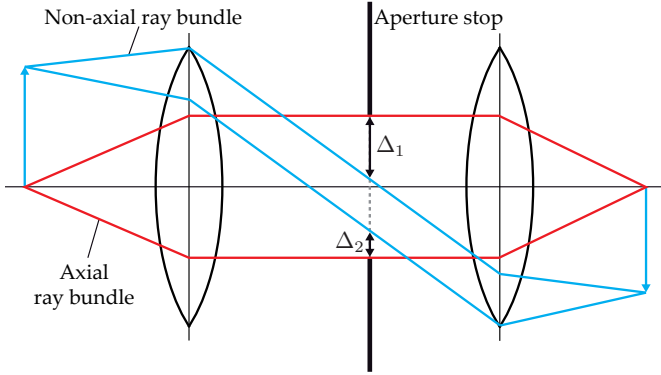


Figure 3.15. Vignetting caused by lens mounts. The maximum diameter of the non-axial ray bundle is reduced by  $\Delta_1 + \Delta_2$  with respect to the diameter of the axial ray bundle.

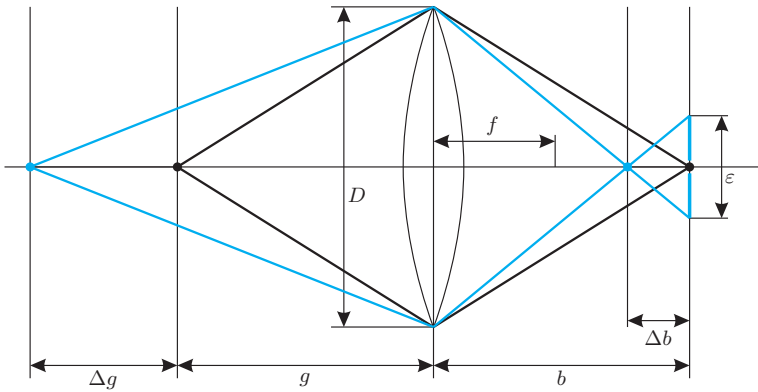


Figure 3.16. Defocused optical imaging with a thin converging lens. In this case, the lens mount is the aperture stop and also the entrance and exit pupil.

From a geometric point of view, a blurred object point is captured on the image plane as a disk having the shape of the aperture (see Fig. 3.16). From now on, the diameter of this blur disk will be denoted by  $\epsilon$ .

The maximum tolerable diameter  $\epsilon_{\max}$  can be chosen depending on the application in view. Usually,  $\epsilon_{\max}$  is comparable to the distances between the pixels of the image sensor. Only for bigger blur disks, one object point has a significant influence on more than one sensor element.

Next, an object point at a distance of  $\Delta g$  from the sharply captured plane  $z_c = g$  will be considered. According to the thin lens equation (3.25), it will be sharply captured on a plane with distance  $\Delta b$  from the image plane:

$$\frac{1}{f} = \frac{1}{g + \Delta g} + \frac{1}{b - \Delta b}. \tag{3.29}$$



In addition, applying the intercept theorem to Fig. 3.16 yields

$$\frac{\varepsilon}{D} = \frac{\Delta b}{b - \Delta b}. \quad (3.30)$$

In order to obtain an expression for the depth of field  $\Delta g$  in terms of the blur disk's diameter  $\varepsilon$ , at first, Equations (3.25) and (3.29) are solved for  $b$  and  $b - \Delta b$ :

$$b = \frac{fg}{g - f}, \quad (3.31)$$

$$b - \Delta b = \frac{f(g + \Delta g)}{g + \Delta g - f}. \quad (3.32)$$

Subtracting the second equation from the first leads to a formula for  $\Delta b$ :

$$\Delta b = \frac{fg}{g - f} - \frac{f(g + \Delta g)}{g + \Delta g - f}. \quad (3.33)$$

Inserting (3.32) and (3.33) into (3.30) and solving the resulting equation for  $\Delta g$  yields

$$\frac{\varepsilon}{D} = \left( \frac{fg}{g - f} - \frac{f(g + \Delta g)}{g + \Delta g - f} \right) \frac{g + \Delta g - f}{f(g + \Delta g)} \quad (3.34)$$

$$\Leftrightarrow \frac{\varepsilon}{D} = \frac{g(g + \Delta g - f)}{(g - f)(g + \Delta g)} - 1 \quad (3.35)$$

$$\Leftrightarrow \varepsilon(g - f)(g + \Delta g) = D(g(g + \Delta g - f) - (g - f)(g + \Delta g)) \quad (3.36)$$

$$\Leftrightarrow (\varepsilon(g - f) - Df)\Delta g = D(g(g - f) - (g - f)g) - \varepsilon(g - f)g \quad (3.37)$$

$$\Leftrightarrow \Delta g = \frac{\varepsilon g(g - f)}{Df - \varepsilon(g - f)}. \quad (3.38)$$

Canceling the last denominator by  $(g - f)$  finally results in the desired formula for the depth of field:

$$\Delta g = \Delta g(\varepsilon) = \frac{\varepsilon g}{\frac{Df}{g - f} - \varepsilon}. \quad (3.39)$$

Now, let the tolerable blur disk have a diameter of  $\varepsilon_{\max} > 0$ . Inserting  $\varepsilon = \varepsilon_{\max}$  into (3.39) yields the tolerable difference of the focal plane in the direction away from the camera:  $\Delta g_{\text{far}} = \Delta g(\varepsilon_{\max}) > 0$ . The plane of focused imaging has a distance of  $z_c = -b$  from the lens and is located in the image space as shown in Fig. 3.16. The expression  $\varepsilon = -\varepsilon_{\max}$  leads to the tolerable difference  $\Delta g_{\text{near}} = \Delta g(-\varepsilon_{\max}) < 0$  of the focal plane with respect to the direction of the camera's line of sight. The negative sign indicates that the focal plane is located behind the image plane  $z_c = -b$ . Thus, the depth of field surrounding the plane  $z_c = g$  is given by  $[g + \Delta g_{\text{near}}, g + \Delta g_{\text{far}}]$ . Object points located inside that interval are considered to be captured with sufficient sharpness.

In the case of  $\varepsilon_{\max} \ll \frac{Df}{g - f}$ , the following approximation can be used:

$$\Delta g_{\text{far, near}} \approx \pm \varepsilon_{\max} \frac{g(g - f)}{Df} = \pm \varepsilon_{\max} O \frac{g(g - f)}{f^2}. \quad (3.40)$$

In practice, the aperture is the main free parameter. Stopping down, i.e., increasing the  $f$ -number  $O$  or reducing the aperture diameter  $D$ , increases the depth of field but simultaneously reduces the light yield. The extreme case  $D \rightarrow 0$  results in the pinhole camera.

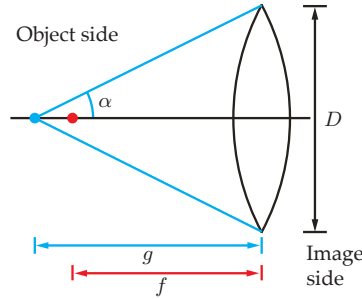


Figure 3.17. Illustration of the definition of the numerical aperture  $NA$  and the  $f$ -number  $O$  for a thin lens. Here, the lens mount is both the aperture stop and entrance pupil.

Common lens systems usually allow selecting an  $f$ -number from among the following powers of  $\sqrt{2}$ : 1, 1.4, 2, 2.8, 4, 5.6, 8, 11, 16, 22, 32, and 45. Each step halves the area of the aperture.

As the  $f$ -number  $O$  is most suitable for describing the limitation of light bundles for objects far away from the lens,  $g \gg f$ , another quantity is used for objects located near the lens: the **numerical aperture**  $NA$ . It is defined as the product of the sine of one-half of the aperture angle  $\alpha$  of a light bundle coming from an axial object point, and the refraction index  $n$  of the medium between object and the lens (Fig. 3.17):

$$NA := n \sin \alpha \tag{3.41}$$

$$= n \frac{\frac{D}{2}}{\sqrt{\left(\frac{D}{2}\right)^2 + g^2}}. \tag{3.42}$$

Therefore, the numerical aperture depends on the object distance. For microscope lens systems, which are preferably used if  $g \approx f$  and  $b \gg f$ , the numerical aperture  $NA$ , instead of the  $f$ -number  $O$ , is used to describe the bundle limitation. In this case, the two quantities are related as follows:

$$b \gg f \quad \rightsquigarrow \quad g = \frac{bf}{b-f} = \frac{f}{1-\frac{f}{b}} \approx f, \tag{3.43}$$

$$g \approx f \quad \rightsquigarrow \quad NA \approx n \frac{\frac{D}{2}}{\sqrt{\left(\frac{D}{2}\right)^2 + f^2}}, \tag{3.44}$$

$$O = \frac{f}{D} \quad \Rightarrow \quad NA \approx \frac{n}{\sqrt{1+4O^2}}, \tag{3.45}$$

$$O \approx \frac{1}{2} \sqrt{\left(\frac{n}{NA}\right)^2 - 1}. \tag{3.46}$$

Three examples will show to what extent the depth of field can vary for different imaging situations.

**Example 3.1 (Longshot):** First, a **longshot** will be considered. In this case one has  $g \gg f$ , so that the approximation (3.40) is no longer valid and the exact equation (3.39) has to be used to calculate the depth of field.

Let the light sensitive elements of a CCD sensor (see Chap. 6) have dimensions of  $10\ \mu\text{m}$ . Therefore,  $\varepsilon_{\text{max}} = 10\ \mu\text{m}$  is chosen. In addition, the following parameters are given: the  $f$ -number is  $O = 11$ , the object distance is  $g = 2\ \text{m}$ , and the focal length is  $f = 15\ \text{mm}$ . Inserting those values into the equation for the depth of field yields

$$\varepsilon = +10\ \mu\text{m} \quad \Rightarrow \quad \Delta g_{\text{far}} \approx +66\ \text{m}, \quad (3.47)$$

$$\varepsilon = -10\ \mu\text{m} \quad \Rightarrow \quad \Delta g_{\text{near}} \approx -1\ \text{m}, \quad (3.48)$$

and in all,

$$g \in [1\ \text{m}, 68\ \text{m}] \quad \Rightarrow \quad |\varepsilon| \leq 10\ \mu\text{m}. \quad (3.49)$$

The depth of field is very asymmetric and is large compared to the object distance of 2 meters. ■

**Example 3.2 (Macro shot):** On the other hand, for a **macro shot** with  $g \approx b \approx 2f$  and a magnification of  $V \approx 1$ , the depth of field is dramatically reduced. In this case, the approximation (3.40) can be used and simplifies to the following expression because of the special relation between the object distance, the image distance, and the focal length:

$$\Delta g_{\text{far,near}} \approx \pm 2\varepsilon O. \quad (3.50)$$

Because  $\varepsilon_{\text{max}} = 10\ \mu\text{m}$  and  $O = 11$ , the resulting depth of field  $\Delta g_{\text{far,near}} \approx \pm 0,2\ \text{mm}$  is symmetric. ■

**Example 3.3 (Microscope image):** Finally, a **microscope image** is considered. Because of the enormous magnification<sup>8</sup>  $|V| = \frac{b}{g} \gg 1$ , but  $g \approx f$ , so the thin lens equation becomes the following:

$$b = \frac{f^2}{g - f}. \quad (3.52)$$

The depth of field is obtained from (3.40):

$$\Delta g_{\text{fern,nah}} \approx \pm \varepsilon_{\text{max}} O \frac{g}{b} = \pm \frac{\varepsilon_{\text{max}} O}{|V|}. \quad (3.53)$$

The depth of field is extremely small for microscope images, as can be exemplified by supposing the lens system has a magnification of  $|V| = 20$  and a numerical aperture  $NA = 0.4$ , which are common values for such systems. In the case of air ( $n \approx 1$ ), one has  $O \approx 1.15$  according to (3.46). For  $\varepsilon_{\text{max}} = 10\ \mu\text{m}$ , the depth of field is  $\Delta g_{\text{far,near}} \approx \pm 0.57\ \mu\text{m}$ . ■

<sup>8</sup>Microscope lens systems are usually labeled by their magnification  $|V|$  and their numerical aperture  $NA$  (see also Sec. 3.5.2). The relations with the usual quantities of a camera lens systems (focal length  $f$  and  $f$ -number  $O$ ) are given by (3.45), (3.46) and (3.43), leading to

$$|V| = \frac{b - f}{f} \quad \Leftrightarrow \quad f = \frac{b}{V + 1}. \quad (3.51)$$

### 3.4.5 Telecentric imaging

For a usual lens system, the magnification depends on the distance:  $|V| = \frac{b}{g}$ . This circumstance often complicates the analysis of the captured images. Especially for measurement applications, one would like to have a constant magnification that does not depend on the object distance.

This goal is achieved by the principle of **telecentric imaging**. Inside a telecentric system with diameter  $D$ , a stop with diameter  $D' \ll D$  is placed, perpendicular to the optical axis, in the plane of the image-side focal point. This stop is called a **telecentric stop**. As it limits the optical ray bundle of the system the most, it also constitutes the aperture stop. The telecentric stop requires all principal rays to pass through the focal point on the image side. Because of the geometry of the optical path, the only rays to reach the image plane are those that are approximately parallel to the optical axis on the object side (see Fig. 3.18). These rays lead to a practically parallel projection of the object space, which is why the magnification no longer depends on the object distance. According to the intercept theorem, the magnification for this optical imaging system is

$$V = \frac{B}{G} = -\frac{b-f}{f}. \quad (3.54)$$

For a constant image distance  $b$ , the magnification is independent of the object distance  $g$ . Therefore, telecentric imaging preserves lengths and can be used to measure object dimensions.

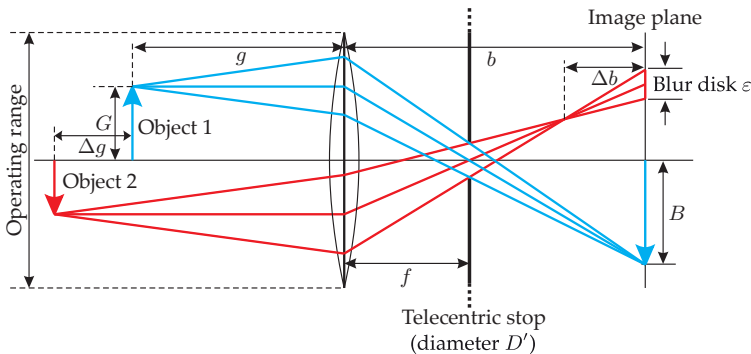
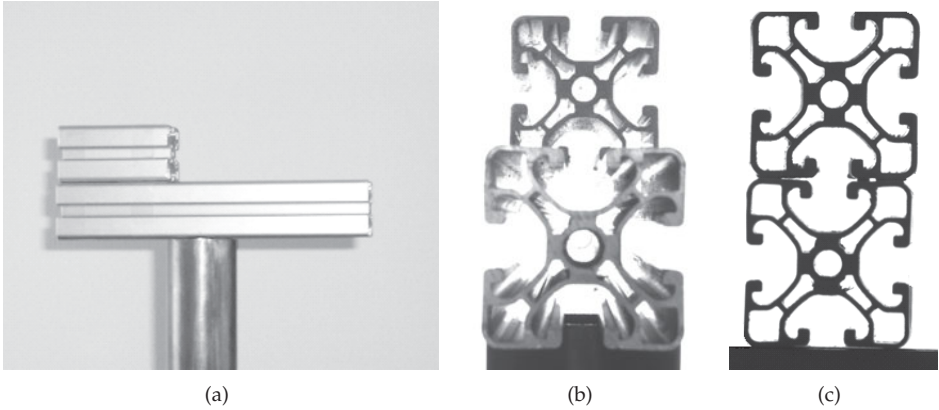


Figure 3.18. Principle of telecentric imaging.

**Example 3.4 (Telecentric image acquisition):** The constant magnification of a telecentric system can be demonstrated by Fig. 3.19. The observed scene consists of two aluminum profiles with equal cross sections but different lengths, and therefore different distances from the camera (Fig. 3.19(a)). Therefore, when one of the usual lens systems is used, the aluminum profile at the bottom appears to be larger (Fig. 3.19(b)). In contrast, the magnification of a telecentric system is independent of the object distance, leading to two equally sized silhouettes (Fig. 3.19(c)). ■

However, telecentric systems also have some disadvantages: as only light that enters in parallel can reach the image plane, only objects placed directly in front of the lens are visible.



**Figure 3.19.** Images captured with a telecentric system: (a) Two aluminum profiles captured from the right side by a camera, (b) Images captured by a usual (entocentric) system, (c) Images captured by a telecentric system.

Thus, the lateral operating range of a telecentric system is smaller than the diameter  $D$  of the lens. In particular, no objects larger than  $D$  can be captured. Therefore, telecentric systems with large entrance lenses are necessary for many applications. Nowadays, such lenses with diameters up to 30 cm are available (cf. Fig. 7.76(a) on p. 299).

The narrow telecentric stop leads to a considerable loss of captured light. At the same time, the small aperture diameter yields an increased depth of field.

High quality telecentric systems consist of several lenses in order to reduce aberration. An entrance lens with a large diameter is combined with a standard lens system whose entrance pupil represents the telecentric stop [13]. The typical parameters of such a system are the operating distance  $g$ , the lateral object-side operating range, and the size of the sensor onto which the complete operating range is to be mapped. Both the size of the sensor and the operating range define the magnification. An important parameter influencing the system's quality is the telecentric range. If an object point is moved parallel to the optical axis inside the telecentric range, the corresponding image point will be laterally moved by no more than some tolerable limit (typically  $1\ \mu\text{m}$ ).

#### ⊙ 3.4.5.1 Defocused telecentric imaging

With telecentric systems, as is the case with all optical imaging systems using a lens, only one plane of the object space can be captured exactly in focus. Object points which are not part of that particular plane are captured with the same magnification but appear in the form of a symmetric blur disk instead of a single sharp point. The position of the center of the blur disk is exactly where the point would be located if the corresponding object point was moved, in parallel to the optical axis, to the focused plane. This characteristic of telecentric systems, which is very beneficial for measurement applications, is demonstrated by Fig. 3.18: the center of the blur disk is defined by the intersection of the image plane and the principal ray of the light bundle [12]. As the principal ray is parallel to the optical axis on the object side, its path is independent of the object distance. Therefore, also the center of the blur disk is invariant to changing object distances. However, it is important to note that

adjusting the focus configuration changes the magnification (see (3.54)). The magnification is only constant when the parameters  $f$  and  $b$  are held constant.

Now, an equation for the depth of field  $\Delta g(\varepsilon)$  of a telecentric system is derived, similarly to the approach in Sec. 3.4.4. As before, Equations (3.25), (3.29), and their transformations (3.32) and (3.33), hold.

Applying the intercept theorem in Fig. 3.18 leads to

$$\frac{\varepsilon}{D'} = \frac{\Delta b}{b - f - \Delta b}. \quad (3.55)$$

According to (3.33) and (3.32), respectively,  $\Delta b$  and  $b - \Delta b$  are inserted:

$$\frac{\varepsilon}{D'} = \frac{\frac{fg}{g-f} - \frac{f(g+\Delta g)}{g+\Delta g-f}}{\frac{f(g+\Delta g)}{g+\Delta g-f} - f} = \frac{\frac{g}{g-f} - \frac{g+\Delta g}{g+\Delta g-f}}{\frac{-g+\Delta g}{g+\Delta g-f} - 1} \quad (3.56)$$

$$= \frac{\frac{g(g+\Delta g-f) - (g+\Delta g)}{g-f}}{f} \quad (3.57)$$

$$= \frac{g^2 + g\Delta g - fg - g^2 - g\Delta g + fg + f\Delta g}{(g-f)f} = \frac{\Delta g}{g-f}. \quad (3.58)$$

This finally yields the following expression for the depth of field of a telecentric imaging system:

$$\Delta g = \Delta g(\varepsilon) = \frac{\varepsilon}{D'} (g - f). \quad (3.59)$$

### 3.4.5.2 Double-sided telecentric systems

Up to this point, object-side telecentric systems have been considered, where the light rays on the object side are parallel to the optical axis. However, for image-side telecentric systems, the optical path between the lens and the image plane is parallel to the optical axis. This is achieved by placing a telecentric stop at the focal point on the object side of the lens [17, 18]. This setup has the advantage that the magnification is independent of the image distance:

$$|V| = \left| \frac{B}{G} \right| = \frac{f}{g-f}.$$

Both principles can be combined, to make a double-telecentric system, if two lenses are arranged in such a way that the telecentric stop is simultaneously located at the image-side focal point of the first lens and at the object-side focal point of the second lens (Fig. 3.20). Then, the principal rays are parallel to the optical axis on both sides of the system. This configuration is used inside telescopes in order to magnify objects that are infinitely far-away, and image them onto an infinitely far-away image plane. However, there is only a limited range of distances within which a real image is obtained: for equal focal lengths  $f_1 = f_2$  it can be up to twice the focal length  $g \in (0, 2f_1)$ . Figure 3.20 shows the special case when the object is closer to the object-side lens than its focal point, leading to a virtual intermediate image  $B'$ . An advantage of image-side telecentric systems is the independence of the magnification from the image distance: according to the intercept theorem,  $V = \frac{B}{G} = -\frac{f_2}{f_1}$  in Fig. 3.20. Therefore, focusing is possible without changing the magnification [12, 20].

### 3.4.6 Perspective

This section describes, in a more general context, the difference between ordinary lens systems and telecentric systems. Three **perspectives** are distinguished for optical imaging:

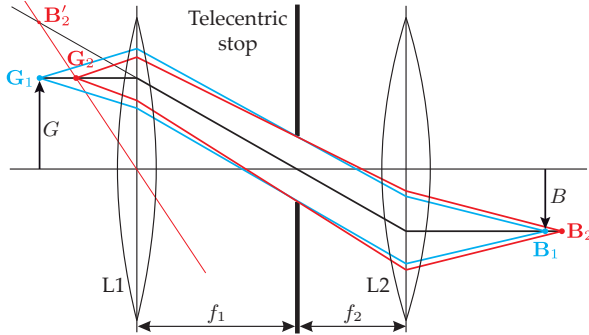


**Figure 3.20.** Double-telecentric imaging [12, 20]. The lens L1 produces the virtual image  $B'_2$  of the object  $G_2$ . This virtual image is mapped to the real image  $B_2$  by the lens L2. The magnification  $V = \frac{B}{G}$  of double-telecentric imaging is independent of the image distance and the object distance, as can be seen by comparison with the point pair  $G_1$  and  $B_1$ .

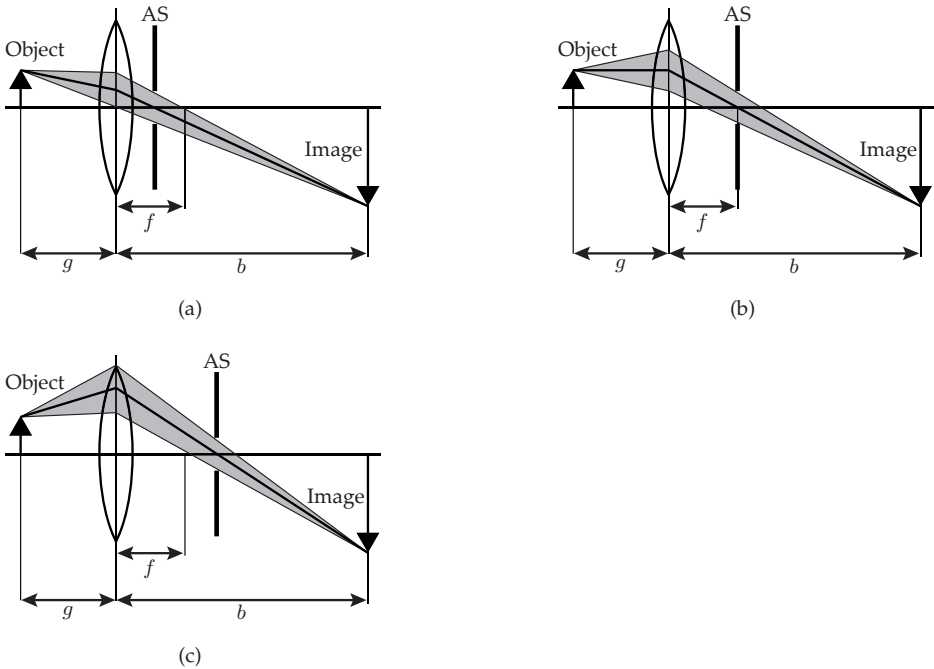


**Figure 3.21.** Optical paths for different perspectives: (a) Entocentric; (b) Telecentric; (c) Hypercentric (AS = aperture stop).

- **Entocentric perspective:** The aperture stop is located in front of the image-side focal point (see Fig. 3.21(a)). This applies to the ordinary lens systems. The perspective center is located between the object and the observer. Therefore, more remote objects appear smaller than less remote ones (see Fig. 3.22).

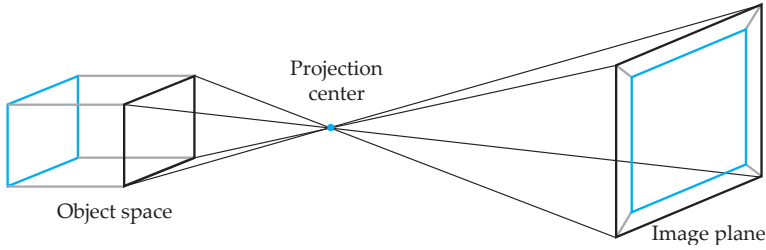


Figure 3.22. Projection for an entocentric perspective.

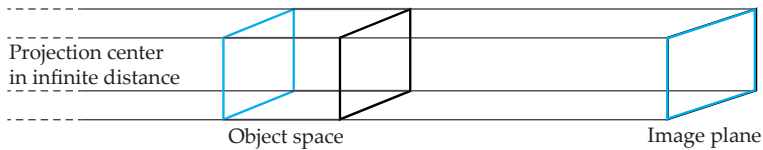


Figure 3.23. Projection for a telecentric perspective (visualization without considering the image inversion because of the central projection, compare Sec. 3.2).

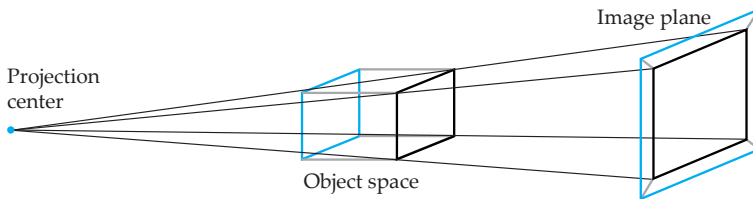


Figure 3.24. Projection for a hypercentric perspective (visualization without considering the image inversion).

- **Telecentric perspective:** The aperture stop is placed at the image-side focal point. As described in Sec. 3.4.5, the magnification is then independent of the object distance. As the perspective center is located at an infinite distance, its optical imaging is that of a parallel projection (Fig. 3.23).
- **Hypercentric perspective:** The aperture stop is located between the image-side focal point and the image plane. For this kind of imaging and from the perspective of the camera, the perspective center is located in the object space behind the object (see Fig. 3.24). Therefore, remote objects appear larger than near objects. Thus, surfaces which are arranged in parallel to the optical axis and are oriented away from it can be captured—such as the outer sides of a die or a cylinder (see Fig. 3.26). This unusual characteristic of hypercentric systems can be useful for some applications in the field of automated visual inspection. However, as can be seen in Fig. 3.21(c), the lenses of a hypercentric lens systems have to be larger than the objects to be captured. The hypercentric perspective is typical for X-ray images (see Sec. 7.4.2).

Depending on the perspective of the optical imaging, different parts of an object's surface are visible or occluded (Fig. 3.25).

The arrangement of the aperture stop has no influence on the position of the focused plane, the corresponding image plane, or the magnification. The thin lens equation (3.25)



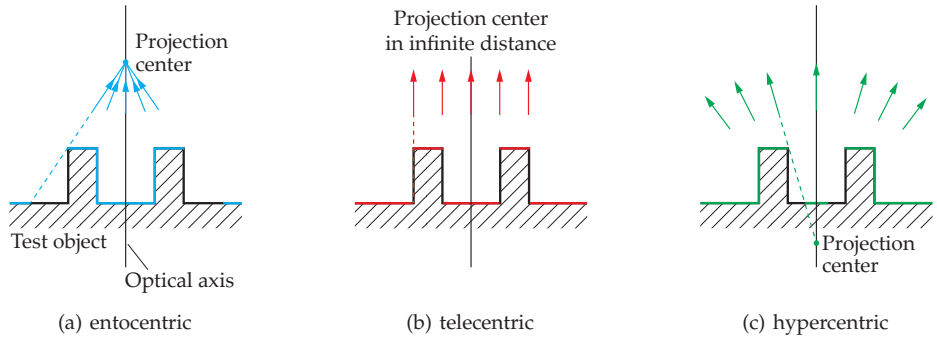


Figure 3.25. Visibility and occlusion of parts of the object space for different perspectives. The surfaces visible in the camera image are highlighted in different colors.



Figure 3.26. Hypercentric lens: (a) Imaging configuration; (b) Camera image. Both the cap and the outer surface of the cylindrically shaped test object are captured in the image, making it possible to measure, e.g., the object’s diameter and height (source: Opto Engineering srl).

holds, independent of the position of the aperture stop. The stop partly blocks the light bundle coming from an object point. For a sharp image produced by an ideal lens system, this has no influence on the position of the image, as all the rays of the light bundle intersect at the same image point. Therefore, the methods of Sec. 3.4.2 for geometrically determining the image point remain valid, even if the principal and parallel rays are not able to pass the stop [12]. However, for a blurred image, the light bundle produces a blur disk in the image plane. If now the aperture stop blocks a notable amount of the light bundle, the position of the center of the blur disk might vary considerably. Its position depends on the principal ray of the remaining light bundle, whose optical path is clearly different in the three perspectives (Fig. 3.21).

➤ 3.4.7 Imaging of tilted planes

Up to now, the lens plane was assumed to be parallel to the image plane and therefore the focused plane was also parallel to those two planes. Now, the general case is considered,

where the image plane and the focused plane might be tilted with respect to the lens plane. The conditions which are now necessary for the formation of a sharp optical imaging will be developed.

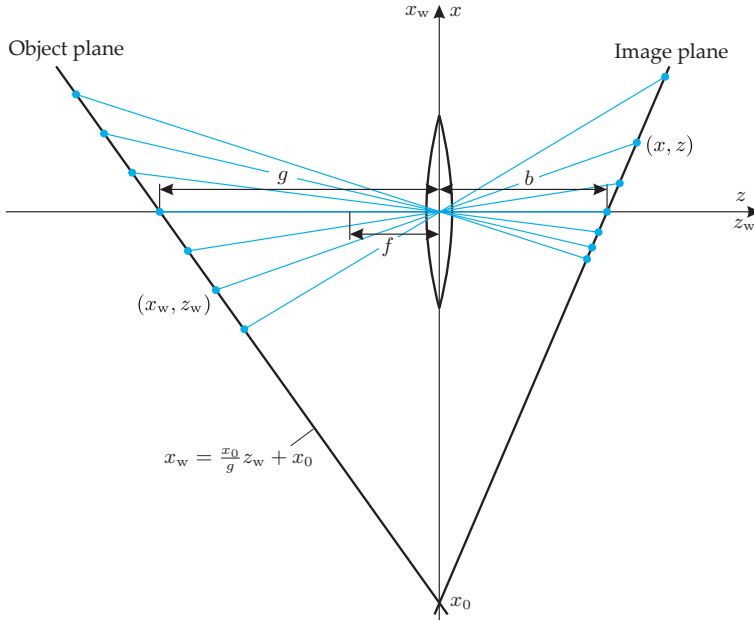


Figure 3.27. Imaging with tilted object planes.

At first, the problem is examined in the  $x, z$ -plane of the camera coordinate system. The object points  $(x_w, z_w)$ , which are located on the line

$$x_w = \frac{x_0}{g} z_w + x_0 \tag{3.60}$$

are to be sharply captured (see Fig. 3.27). So, the geometrical position of their sharp images  $(x, z)$  are of interest. By using this variable, the thin lens equation (3.25) becomes

$$\frac{1}{f} = \frac{1}{-z_w} + \frac{1}{z} \Leftrightarrow z_w = \frac{z f}{f - z} . \tag{3.61}$$

Applying the intercept theorem to Fig. 3.27 yields

$$\frac{x_w}{x} = \frac{z_w}{z} \Leftrightarrow x_w = \frac{z_w}{z} x . \tag{3.62}$$

Inserting  $z_w$  and  $x_w$  into (3.60) results in

$$x = x_0 \left( \frac{1}{g} - \frac{1}{f} \right) z + x_0 . \tag{3.63}$$

Hence, the image points are also part of a line going through the point  $(x_0, 0)$ . This leads to the following consideration for the three-dimensional case: in order to map two planes

sharply to each other, their line of intersection has to be part of the lens plane. This necessary condition is called the **Scheimpflug condition** [16].

### 3.2 Theorem 3.2: Imaging of tilted planes

If the line of intersection of two planes is located in the lens plane (the Scheimpflug condition) and if the thin lens equation (3.25) holds for a point on the object plane and the corresponding point on the image plane, the entire two planes are sharply imaged to each other.<sup>9</sup>  $\diamond$

**Proof 3.1 (Imaging of tilted planes):** As usual, the  $z$ -axis is assumed to be equal to the optical axis and the origin is assumed to be located in the center of the lens. So, the principal plane of the lens is given by

$$E_0 = \{\mathbf{x} = (x, y, z)^T \mid z = 0\}. \quad (3.64)$$

Suppose the object-side plane  $E_1$  and the image-side plane  $E_2$  are given in general form by

$$E_1 = \{\mathbf{x} = (x, y, z)^T \mid a_1x + b_1y + c_1z + d_1 = 0\}, \quad (3.65)$$

$$E_2 = \{\mathbf{x} = (x, y, z)^T \mid a_2x + b_2y + c_2z + d_2 = 0\}. \quad (3.66)$$

Suppose the intersection of those two planes is a line in the lens plane  $E_0$ . This implies

$$E_1 \cap E_0 = E_1 \cap E_2 = E_0 \cap E_2. \quad (3.67)$$

The line of intersection  $E_1 \cap E_0$  is described by the system of equations

$$z = 0 \quad (3.68)$$

$$a_1x + b_1y + d_1 = 0. \quad (3.69)$$

Similarly, the line of intersection  $E_0 \cap E_2$  is characterized by

$$z = 0 \quad (3.70)$$

$$a_2x + b_2y + d_2 = 0. \quad (3.71)$$

Because of (3.67), the coefficients of both representations are equal, except for a scaling factor:

$$d_2 := d_1, \quad b_2 = b_1, \quad a_2 = a_1. \quad (3.72)$$

Suppose the lens has a focal length  $f > 0$ . Let  $\mathbf{x}_1 \in E_1$  and  $\mathbf{x}_2 \in E_2$  be the assumed pair of points complying with the thin lens equation. Hence, the two construction rays (the principal ray and the parallel ray) for  $\mathbf{x}_1$  intersect at  $\mathbf{x}_2$ . Because of the choice of origin,  $\mathbf{x}_2 = \lambda \mathbf{x}_1$  for a suitable  $\lambda \in \mathbb{R}$ . Inserting that expression into the thin lens equation results

<sup>9</sup>In the strict sense, only the part of the plane on the object side that is located in the half space  $z < -f$  is mapped to a real image.

in

$$\frac{1}{f} = \frac{1}{-z_1} + \frac{1}{z_2} = -\frac{1}{z_1} + \frac{1}{\lambda z_1}. \quad (3.73)$$

Solving that equation for  $\lambda$  yields

$$\lambda = \frac{f}{z_1 + f}, \quad \text{if } z_1 \neq -f. \quad (3.74)$$

With (3.72), the assumption  $\mathbf{x}_2 \in E_2$  can be expressed as

$$a_1 \lambda x_1 + b_1 \lambda y_1 + c_2 \lambda z_1 + d_1 = 0 \quad (3.75)$$

$$\Leftrightarrow a_1 x_1 + b_1 y_1 + c_2 z_1 + d_1 \frac{z_1 + f}{f} = 0 \quad (3.76)$$

$$\Leftrightarrow a_1 x_1 + b_1 y_1 + \left( c_2 + \frac{d_1}{f} \right) z_1 + d_1 = 0 \quad (3.77)$$

$\mathbf{x}_1 \in E_1$  leads to

$$a_1 x_1 + b_1 y_1 + c_1 z_1 + d_1 = 0. \quad (3.78)$$

Subtracting that equation from (3.77) yields

$$\left( c_2 + \frac{d_1}{f} - c_1 \right) z_1 = 0. \quad (3.79)$$

Assuming  $z_1 \neq 0$  (necessary for optical imaging) leads to

$$c_2 + \frac{d_1}{f} - c_1 = 0. \quad (3.80)$$

This results in the following representation of the plane on the image side:

$$E_2 = \left\{ \mathbf{x} = (x, y, z)^T \mid a_1 x + b_1 y + \left( c_1 - \frac{d_1}{f} \right) z + d_1 = 0 \right\} \quad (3.81)$$

Now, let  $\mathbf{x}_1 \in E_1$  be an arbitrary point on the object-side plane. For its sharp image  $\mathbf{x}_2$ , one has

$$\frac{1}{f} = \frac{1}{-z_1} + \frac{1}{z_2} \quad (3.82)$$

$$\Rightarrow z_2 = \frac{f}{z_1 + f} z_1. \quad (3.83)$$

As  $\mathbf{x}_2$  is located on a line of sight passing through the origin of the coordinate system and  $\mathbf{x}_1$ ,

$$\mathbf{x}_2 = \frac{f}{z_1 + f} \mathbf{x}_1. \quad (3.84)$$

It now remains to prove that  $\mathbf{x}_2 \in E_2$ . Inserting (3.84) into the plane of Equation (3.81) and multiplying by  $\frac{z_1+f}{f}$  yields

$$a_1x_1 + b_1y_1 + \left(c_1 - \frac{d_1}{f}\right)z_1 + d_1\frac{z_1+f}{f} = 0 \tag{3.85}$$

$$\Leftrightarrow a_1x_1 + b_1y_1 + c_1z_1 + d_1 = 0. \tag{3.86}$$

The last equation holds since  $\mathbf{x}_1 \in E_1$ . As  $\mathbf{x}_1$  was chosen arbitrarily, every point of  $E_1$  is sharply mapped to a point of  $E_2$ . ■

Equation (3.81) describes how to choose the tilted image plane for a given object plane.

For tilted planes, (3.61) shows that the magnification depends on the position:

$$V = \frac{x}{x_w} = \frac{z}{z_w} = 1 - \frac{z}{f} = \frac{f}{f+z_w}. \tag{3.87}$$

Because the object plane is tilted,  $z_w$  is spatially variable. The depth of field is also spatially variable, as it depends on the distance  $z_w$  between the lens plane and the object point. The depth of field also depends on the position, as it is connected to the distance between the lens plane and the object point via (3.39).

Ordinary cameras can be considered as a limiting case of Theorem 3.2: In this case, the image and object planes are parallel and thus intersect each other at infinity. As soon as the thin lens equation (3.25) holds for one pair of points, the entire planes are sharply mapped to each other.

An application for imaging of tilted planes according to the Scheimpflug condition is laser triangulation, see Sec. 7.3.1 and 7.3.2.

**Example 3.5 (Focused imaging of tilted planes):** Some special lenses, like a so-called **tilt-shift lens** (Fig. 3.28(a)), allow tilting the optical axis of the lens with respect to the image plane. By means of theorem 3.2 it is therefore possible to tilt the focused plane in the object space with respect to the image plane, so that the focused plane can be adjusted for the imaged object. As an example, Fig. 3.28(b) shows an image of a printed circuit board

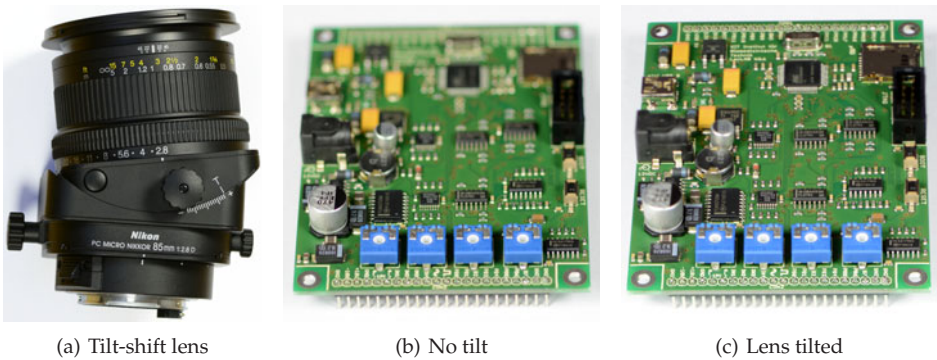


**Figure 3.28.** Focused imaging of tilted planes by means of a tilt-shift lens: (a) Tilted lens; (b) Image of a PCB without tilting the lens; (c) Image of a PCB with a tilted lens. Both images were acquired with an open stop.

(PCB) without tilting the lens; here, a focused imaging is only achieved for the parts of the object that are near to the camera. By tilting the focused plane in the object space it was possible to obtain a focused imaging of nearly the whole PCB, as it can be seen in Fig. 3.28(c). ■

### 3.4.8 Aberrations

Ideal optical imaging can only be approximated by real optical systems, which suffer from so-called aberration [1, 9, 20]. This can partly be alleviated in appropriately designed lens systems, if several lenses with different curvatures and material characteristics are employed in combination. In addition, the effects of most kinds of aberration can be diminished by decreasing the diameter of the aperture.

There is monochromatic aberration, caused by undesired variations of the optical path depending on the angle with the optical axis, and there is chromatic aberration, caused by dispersion. Some kinds of aberration lead to a blurred image (focus errors), others to a systematic variation of the positions of the image points with respect to the ideal model (position errors). Position errors are particularly important for measurement applications. They either have to be avoided by using high-quality optical components or have to be compensated for by a suitable calibration.

#### 3.4.8.1 Seidel aberrations of spherical lenses

In Gaussian Optics, a linear approximation of the law of refraction is used (see Sec. 3.4.1). In this case, the approximation error of the sine function is dominated by a third order term. The aberration caused by neglecting the cubic term of the sine function in the law of refraction is called the Seidel aberrations (third-order image errors). This leads to different undesirable effects affecting optical imaging with spherical lenses, and are described in what follows.

**Spherical aberration:** Because of spherical aberration, an incident homocentric light bundle is not exactly focused on a single point. The intersections of the light rays are located at different distances from the lens, making it impossible to achieve an exact focusing. Light rays passing through the margin of a lens are refracted more intensely than in Gaussian Optics, so that their intersections are closer to the principal plane than the intersections of rays which are closer to the optical axis (Fig. 3.29(a)).

Aspherical lenses, whose surfaces are not parts of a spherical surface, can avoid spherical aberration. However, they are much more costly to make.

**Coma:** An increasing absolute value of the angle of incidence leads to a change of the shape of the blurred image [11]. The image of a point-shaped object might look like a comet with a tail (Fig. 3.29(b)). Therefore, this effect is called coma.

**Astigmatism:** Astigmatism is also related to the angle of incidence of a light bundle. The focus lengths of light rays in the tangential and the sagittal plane differ from each other. The tangential plane of a light ray is spanned by the principal ray of the light bundle and the optical axis. The sagittal plane contains the principal ray and is perpendicular to the tangential plane. Light rays in the tangential plane are more intensely refracted by spherical lenses, as the lens appears to be perspectively reduced in the tangential direction and thus

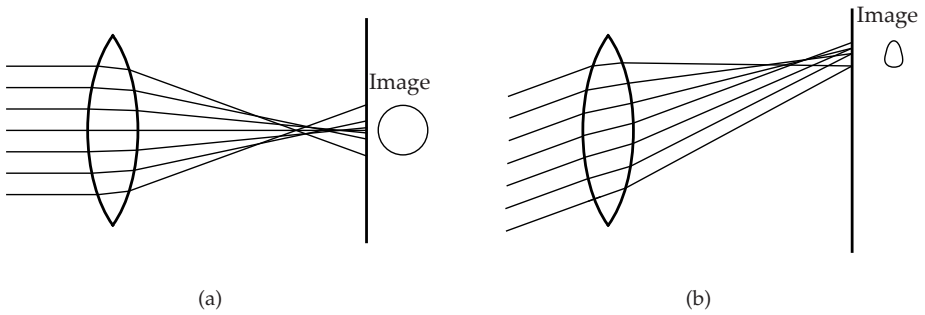


Figure 3.29. Seidel aberrations: (a) Spherical aberration; (b) Coma.

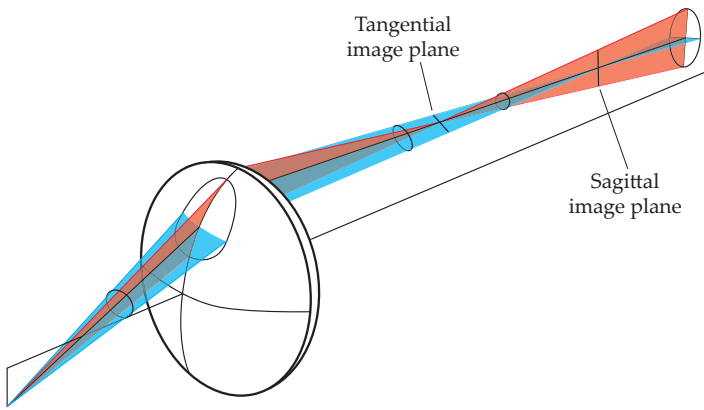


Figure 3.30. Astigmatism: The tangential light bundle is refracted to a larger extent than the sagittal light bundle.

appears to be more curved than in the sagittal direction. Therefore, the tangential focal length of the lens is shorter than its sagittal focal length. In the tangential component of the image distance, a point-shaped object is imaged as a line on the sagittal plane and in the sagittal component of the image distance, it is imaged as a line on the tangential plane. In between, a point-shaped object forms an image of a blurred ellipse (Fig. 3.30).

**Curvature of field:** In Gaussian Optics, a plane perpendicular to the optical axis in object space is focused to a plane in image space. In the case of image field curvature, the imaged points are not located on a planar surface but on a curved surface (Fig. 3.31). There is then no way of adjusting the image plane to sharply capture the whole object plane.

An additional astigmatism leads to different surfaces of sharp images for rays of the tangential and the sagittal planes.

**Radial distortion:** Distortion is caused by optics with spatially varying magnification. They can cause straight lines in the object space to be mapped to curves in the image space. If the degree of the distortion only depends on the distance between the object point and the optical axis, the distortion is called radial. Then, lines intersecting the optical axis are mapped to lines. Straight lines lying aside the optical axis are mapped to curved lines.

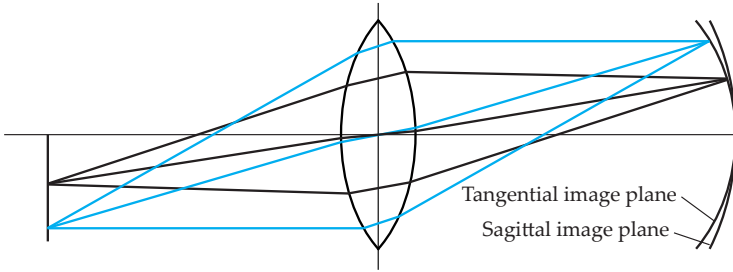


Figure 3.31. The sharp image of an object plane is geometrically formed as a curved surface. Astigmatism leads to different surfaces for the rays of the tangential and the sagittal planes.

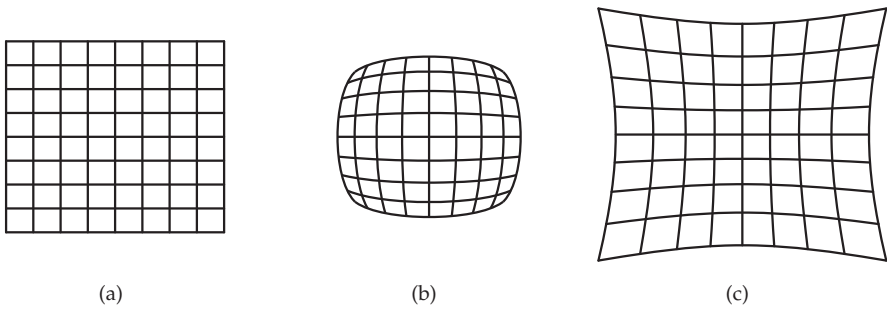


Figure 3.32. Image deformations caused by radial lens distortion: (a) Ideal, free of distortion,  $a = 0$ ; (b) Barrel-shaped distortion,  $a < 0$ ; (c) Pincushion distortion,  $a > 0$  in (3.88).

If the magnification is reduced towards the image border, a barrel-shaped distortion is caused (Fig. 3.32(b)). Many wide-angle lenses suffer from this aberration. On the other hand, the distortion caused by an increase of magnification towards the image border is called pincushion distortion (Fig. 3.32(c)). The kind and extent of the distortion are influenced by the position of the aperture stop [14].

A radial distortion can be represented by the following model:

$$\begin{pmatrix} x_v \\ y_v \end{pmatrix} = \begin{pmatrix} x \\ y \end{pmatrix} + a \underbrace{((x - o_x)^2 + (y - o_y)^2)}_{= r^2} \begin{pmatrix} x - o_x \\ y - o_y \end{pmatrix}. \tag{3.88}$$

The coordinates of a distorted image point,  $(x_v, y_v)^T$ , are obtained by the sum of the idealized image coordinates  $(x, y)$  of (3.12), (3.13), and an error term depending only on the radial distance  $r$  from the image point to the intersection  $(o_x, o_y)$  of the optical axis with the image plane. More detailed models also take higher powers of  $r$  into account. The distortion parameter  $a$  can be estimated using calibration methods [10, 21]. The case  $a > 0$  leads to pincushion distortion and  $a < 0$  to barrel-shaped distortion. When  $a = 0$ , one has ideal distortion-free imaging.



### 3.4.8.2 Chromatic aberration

As the refractive index of a material might depend on the wavelength of the light, light of different wavelengths is refracted by different amounts by a lens (see Sec. 2.6.3). In the visible part of the spectrum, the refraction index decreases with increasing wavelength. Therefore, light of a shorter wavelength is more sharply refracted, so that the focal point is nearer to the principal plane of the lens. Because of this chromatic aberration, light of different wavelengths cannot be sharply imaged simultaneously (Fig. 3.33(a)). This blur has to be taken into account even if gray-scale sensors are used. For color sensors, there are additional color distortions around the edges (the so-called color fringes) caused by the differently focused color channels. If an optical system is not symmetric with respect to a principal plane perpendicular to the optical axis, the magnification can also depend on the wavelength [1]. This is already the case for a simple system consisting of a single lens and a stop. Because of the wavelength dependence of the focal length, the direction of the principal ray varies and thus the magnification depends on the wavelength (Fig. 3.33(b)).

Chromatic aberration can be reduced by composing lens systems out of materials with different dispersion. A system of two lenses with exactly equal focal points for two wavelengths is called an achromat. A system that corrects for chromatic aberration for three wavelengths is called an apochromat. An apochromat usually consists of three lenses [17].

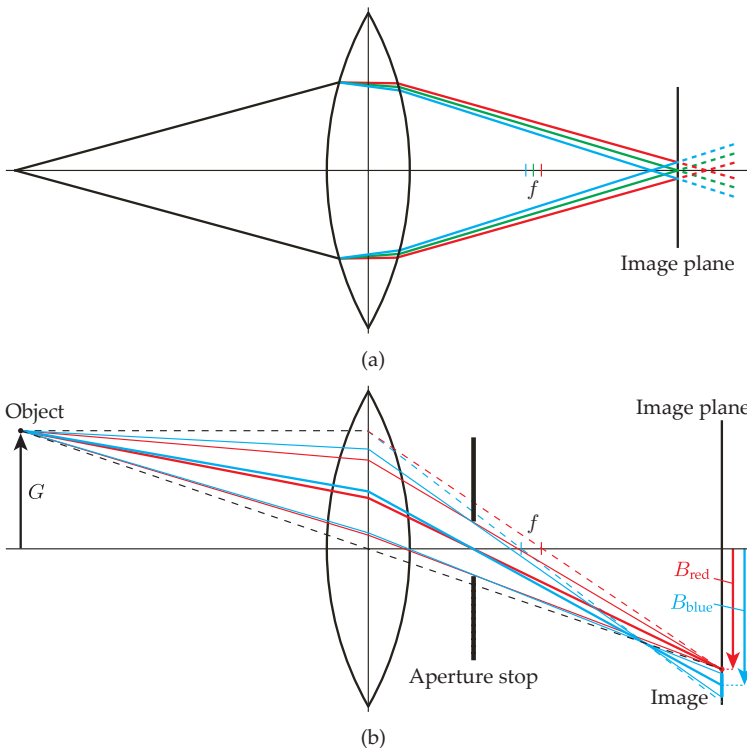


**Figure 3.33.** Chromatic aberrations: (a) Axial / longitudinal aberration: Chromatic aberration causes the focal length  $f$  of the lens and the image distance to vary with the wavelength of the light; (b) Transverse / lateral aberration: The magnification of a system with several optical elements might depend on the wavelength.

Chromatic aberration can be completely avoided by using mirror optics, as the direction of reflection is independent of the wavelength. However, in some imaging optics, wavelength-dependent focusing can be useful (see Sec. 7.3.13).

Finally, it has to be taken into account that all types of aberration can arise simultaneously. For example, Seidel aberrations occur to different extents for different wavelengths.

Diffraction limited lens systems are extremely high quality lens systems for which all types of aberration are corrected up to the point that the influence of aberration is less than the limitations caused by the wave nature of light.

## 3.5 Optical instruments with several lenses

This section introduces two particularly important optical instruments for automated visual inspection, which contain several lenses: the projector and the microscope.

### 3.5.1 The projector

At first, an illumination system with two lenses, L1 and L2, will be considered (Fig. 3.34). The light source is sharply mapped to the lens plane of L2. Then, L2 maps the plane of its entrance window to the projection plane, so that structures positioned in its entrance window are magnified and can be displayed on a screen. The structures of the light source, which are visible in the plane of L2, vanish. The illuminance of the receiver depends only on the aperture stop, and the size of the captured plane depends only on the field stop. Thus, this lens system allows a homogeneous illumination (without visible structures of the light source) with independent and variable adjustment of the illuminance and field size.

Besides the suppression of the spatial structure of the light source and the homogenization of the illuminance in the projection plane, lens L1 has another important function: by mapping the light source to L2, the whole light captured by L1 is used to illuminate the projection plane. For a good light yield, the diameter of L1 should be large compared to the distance between L1 and the light source.

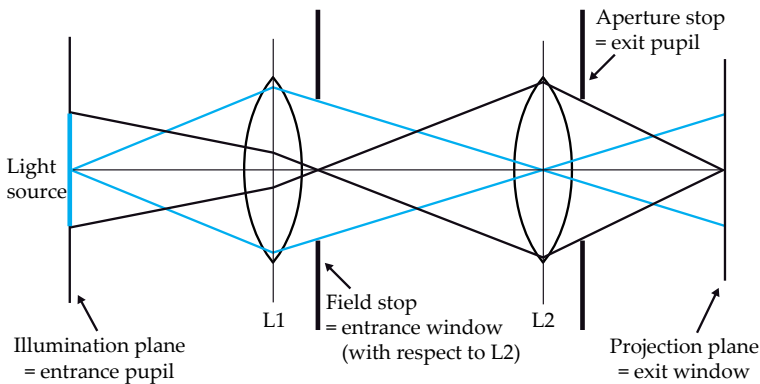


Figure 3.34. Optical path of the imaging rays (black) and of the illumination (blue) for a projector.

A famous application of this type of lens system is the **slide projector**. In this case, L1 is the condenser, L2 is another lens system, and the exit window is given by the screen. The slide is located in the entrance window of L2.

The same principle is used by many **video projectors**. Here, transparent liquid crystal displays controlled by a computer are placed in the entrance window [3].

The projector is particularly important for automated visual inspection, as it can project light patterns used for surface measurements with triangulation (Sec. 7.3.4) and as it is necessary for inverse illumination (Sec. 7.6.2).

### ► 3.5.2 The microscope

The microscope is an optical instrument for magnifying very small objects [17]. With visible light, useful magnifications of up to approximately  $|V| = 2\,000$  are realizable. The maximum magnification is limited by the wave nature of light.

A microscope for direct use by a human observer consists of two lenses (or two lens systems): the objective lens and the ocular. The capturing lens leads to a real, inverted, and magnified image of the object in the plane of the field stop. The field stop is placed in the focal plane of the ocular on the object side. Therefore, the ocular produces a virtual image at an infinite distance, allowing comfortable focusing for the human eye. The exit pupil of the ocular is equal to the entrance pupil of the eye. The ocular uses the principle of a magnifying glass. The aperture stop regulates the illuminance and the field stop adjusts the size of the visible area. A measuring grid can be placed in the field stop.

Important parameters for a microscope lens are its magnification and numerical aperture. The numerical aperture is defined as  $NA = n \sin \alpha$ , with  $\alpha$  denoting one-half of the angle of the aperture, and  $n$  denoting the refraction index of the material in between the object and the lens (see Fig. 3.35). As microscopes are preferably used with  $g \approx f$ , the numerical aperture corresponds to the width of the light bundle and is used instead of the  $f$ -number  $O$  (cf. (3.45)). In automated visual inspection, usually air is the medium between the lens and the test object, so that the refraction index is  $n \approx 1$ . As shown in Sec. 2.2.6.1, the diffraction-limited resolution is improved for increasing  $D$ , and so according to (3.45) for an increasing numerical aperture.

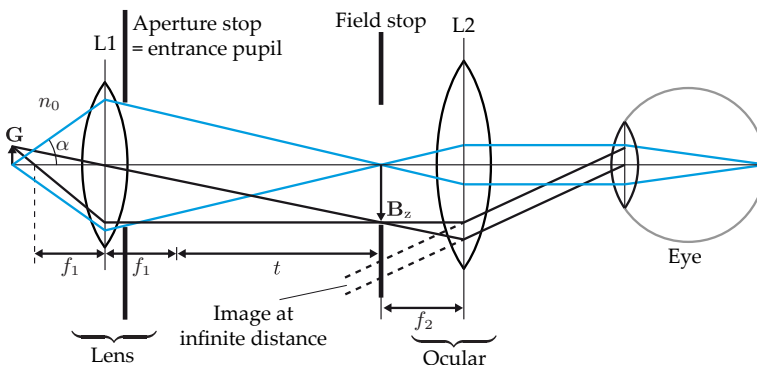


Figure 3.35. Optical path of the imaging rays (black) and the light bundle (blue) for a microscope.

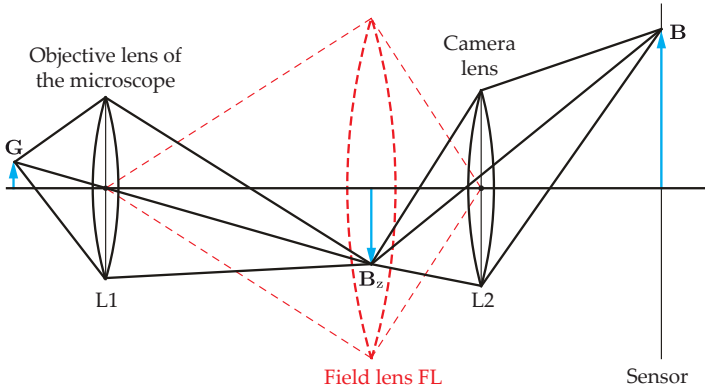


Figure 3.36. Combination of microscope and camera.

The magnification of the microscope is given by the product of the magnifications of the two subsequent optical imaging processes:

$$V_{\text{Microscope}} = V_{\text{Objective}} V_{\text{Ocular}} . \tag{3.89}$$

An important parameter of a microscope is the so-called tube length  $t$ , which is defined as the difference between the image distance  $b_1$  of the capturing lens and the focal length  $f_1$ :

$$t := b_1 - f_1 . \tag{3.90}$$

Most microscopes use the standard tube length,  $t = 160$  mm.

Of particular importance for automated visual inspection is the combination of a microscope and an electronic camera (Fig. 3.36). The camera's lens, which replaces the ocular, receives the intermediate image  $B_z$  produced by the microscope lenses as a sharp image on the sensor. Again, the overall magnification is the product of the magnifications of the single optical elements.

For a better light yield and a more homogeneous image brightness, a field lens (dashed lines in Fig. 3.36) can be placed in the plane of the intermediate image, which maps the exit pupil of the microscope lens L1 to the entrance pupil of the camera lens L2.

For another important variant, the image plane of the microscope lens has infinite distance:  $g_1 = f_1, b_1 \rightarrow \infty$ . Here, the light originating from an object plane is transformed into a parallel bundle of rays with a defined direction. The focused plane of the camera lens is then placed at infinity:  $g_2 \rightarrow \infty, b_2 = f_2$ . The resulting total magnification is obtained from Fig. 3.37:

$$\tan \gamma = \frac{G}{f_1}, \quad \tan \gamma = -\frac{B}{f_2}, \tag{3.91}$$

$$\Rightarrow V = \frac{B}{G} = -\frac{f_2}{f_1} . \tag{3.92}$$

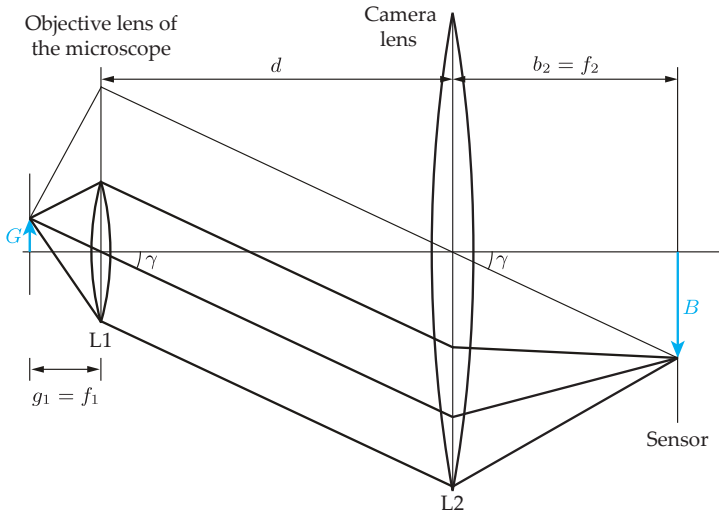


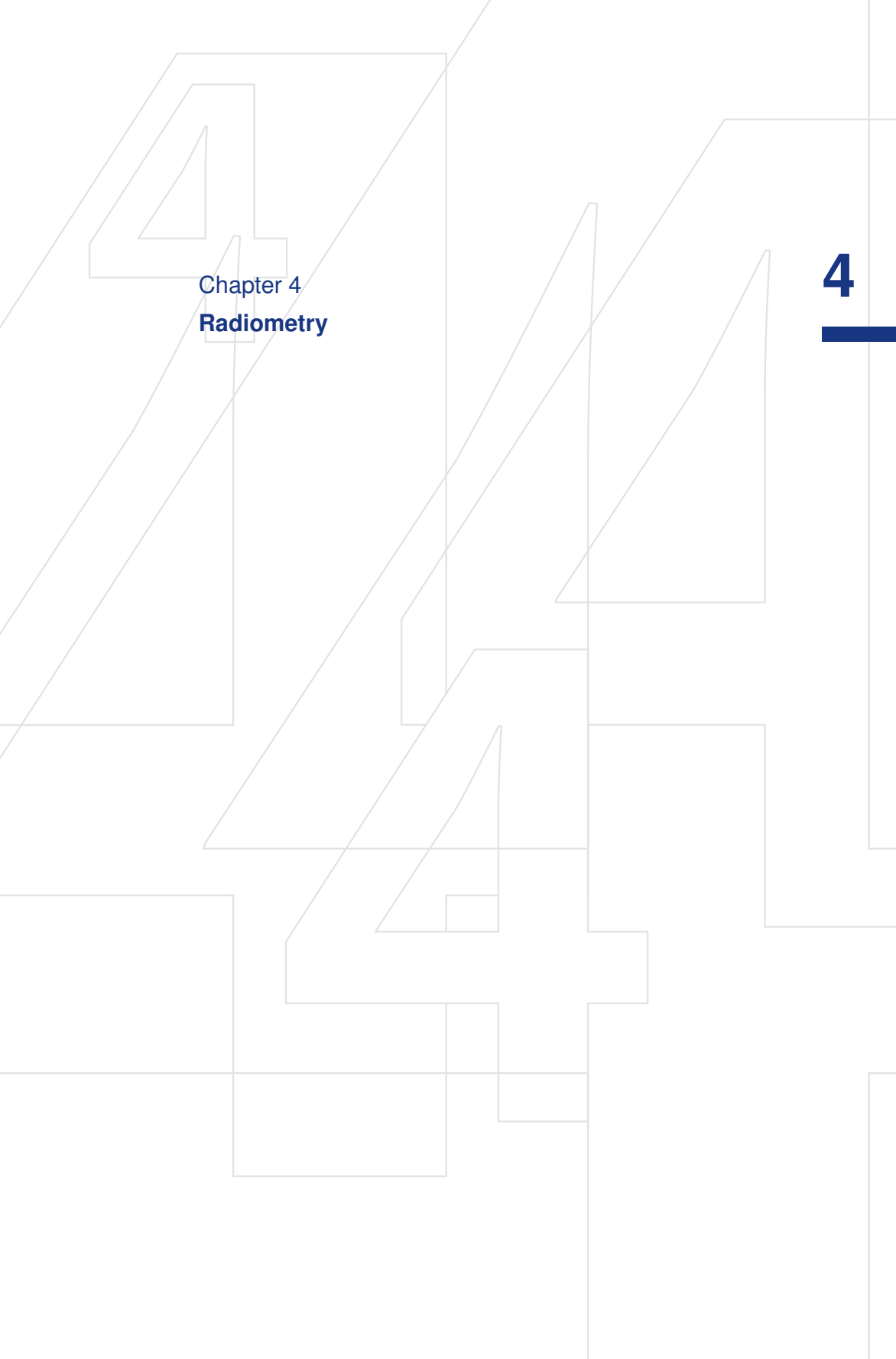
Figure 3.37. The image plane of the objective lens of the microscope is at infinite distance, resulting in a parallel light bundle that reaches the camera.

## 3.6

### 3.6 Bibliography

- [1] Ludwig Bergmann, Clemens Schaefer, Heinz Niedrig, and Hans-Joachim Eichler, editors. *Lehrbuch der Experimentalphysik*, volume 3: Optik: Wellen- und Teilchenoptik. De Gruyter, 10th edition, 2004.
- [2] Max Born and Emil Wolf. *Principles of optics: electromagnetic theory of propagation, interference and diffraction of light*. Cambridge University Press, 7th edition, 2006.
- [3] Rainer Dohlus. *Photonik: Physikalisch-technische Grundlagen der Lichtquellen, der Optik und des Lasers*. Oldenbourg, 2010.
- [4] Olivier Faugeras. *Three-Dimensional Computer Vision*. MIT Press, 1993.
- [5] Anthony Gerrard and James Burch. *Introduction to matrix methods in optics*. Wiley, 1975.
- [6] John Greivenkamp. *Field guide to geometrical optics*. SPIE Press, 2004.
- [7] Tobias Hanning. *High Precision Camera Calibration*. Habilitationsschrift, Universität Passau, 2011.
- [8] Richard Hartley and Andrew Zisserman. *Multiple View Geometry in Computer Vision*. Cambridge University Press, 2nd edition, 2003.
- [9] Eugene Hecht. *Optics*. Addison-Wesley, San Francisco, 4th edition, 2002.
- [10] Ramesh Jain, Rangachar Kasturi, and Brian Schunck. *Machine vision*. McGraw-Hill, 1995.
- [11] Dietrich Kühlke. *Optik: Grundlagen und Anwendungen*. Deutsch, Frankfurt am Main, 2nd edition, 2007.
- [12] Karl Lenhardt. Optical Systems in Machine Vision. In Alexander Hornberg, editor, *Handbook of Machine Vision*, pages 205–331. Wiley-VCH, 2006.
- [13] Ulrich Lübbert and Frank Muth. Beleuchtung und Optik für die genaue Vermessung von Werkstücken mit bildgebenden Sensoren. *IITB-Mitteilungen*, pages 9–14, 1993.
- [14] Frank L. Pedrotti, Leno S. Pedrotti, and Leno M. Pedrotti. *Introduction to optics*. Pearson Prentice Hall, 3rd edition, 2007.
- [15] José-Philippe Pérez. *Optik*. Spektrum, 1996.

- [16] Theodor Scheimpflug. Der Photoperspektograph und seine Anwendung. *Photographische Korrespondenz*, 43:516–531, 1906.
- [17] Gottfried Schröder and Hanskarl Treiber. *Technische Optik*. Vogel, Würzburg, 9th edition, 2002.
- [18] Rainer Schuhmann and Thomas Thöniß. Telezentrische Systeme für die optische Meß- und Prüftechnik. *Technisches Messen*, 65(4):131–136, 1998.
- [19] Warren Smith. *Modern optical engineering: the design of optical systems*. McGraw-Hill, New York, 1966.
- [20] Carsten Steger, Markus Ulrich, and Christian Wiedemann. *Machine vision algorithms and applications*. Wiley-VCH, 2008.
- [21] Zhengyou Zhang. Flexible camera calibration by viewing a plane from unknown orientations. In *Proceedings of the Seventh IEEE International Conference on Computer Vision*, volume 1, pages 666–673, 1999.
- [22] Wolfgang Zinth and Ursula Zinth. *Optik: Lichtstrahlen – Wellen – Photonen*. Oldenbourg, München, 4th edition, 2013.



Chapter 4  
**Radiometry**

# 4

## 4 Radiometry

4.1 Radiometric quantities . . . . .	145
4.2 The light field of a test object . . . . .	150
4.3 The bidirectional reflectance distribution function (BRDF) . . . . .	152
4.3.1 BRDF and scattered light . . . . .	155
4.4 Formation of image values . . . . .	157
4.4.1 Application to a thin lens . . . . .	157
4.5 Bibliography . . . . .	160



## 4 Radiometry

### 4.1 Radiometric quantities

The field of **photometry** is concerned with measuring the intensity and power of visible light with respect to the sensitivity of the human eye (see Chap. 5). Visible light is only a part of the whole electromagnetic spectrum (see Sec. 2.1.1). The respective wavelengths range from about 380 nm to 780 nm. Of course, physical measurements of intensity, power, etc., can be obtained for the whole electromagnetic spectrum without respect to the human eye, as is done in the domain of **radiometry** or **radiation physics**.

The **radiant flux**  $\Phi$  is the total amount of radiant power passing through some two-dimensional surface  $A$ . If, for example,  $A$  is surrounding an isolated light source in the absence of other sources, the radiant flux is the total power of the electromagnetic radiation emitted by the source; see Fig. 4.2(a) on p. 147.

The electromagnetic field of the light and  $\Phi$  are related via the Poynting vector  $\mathbf{P} = \mathbf{E} \times \mathbf{H}$  (2.37):

$$\Phi = \int_A \mathbf{P}^T \mathbf{n} dA = \frac{\Delta n}{\Delta t} h \nu, \quad [\Phi] = 1 \text{ W}, \quad (4.1)$$

with  $\mathbf{n}$  denoting the normal vector perpendicular to the infinitesimal surface element of area  $dA$ . The right hand side of (4.1) represents the photon model for monochromatic light with photons of energy  $h \nu$  (cf. Sec. 2.3). For a photon flux of  $\frac{\Delta n}{\Delta t}$ ,  $\Delta n$  photons pass through the area  $A$  in one direction during the period  $\Delta t$ .

The **luminous flux**  $\Phi_1$  is the photometric quantity corresponding to the radiant flux, and represents the measure of the radiant power which is perceived by the sensitivity of the human visual perception of brightness. It is measured in lumens (lm); cf. Table 4.1 on p. 150. A luminous flux of 683 lm corresponds to a radiant power of 1 W for a wavelength of 555 nm. The relation between radiometric quantities and photometric quantities is further described in Sec. 5.1.

In order to define further radiometric quantities, the concept of solid angle has to be introduced.

#### Definition 4.1: Solid angle

The solid angle  $\Omega_A$  of some surface  $A$  with respect to a point  $\mathbf{P}$  is defined as the surface area  $A_K$  of the projection of  $A$  onto the unit sphere surrounding  $\mathbf{P}$  (Fig. 4.1). In the same way one defines the solid angle  $d\Omega_A$  of an infinitesimal surface element  $dA$ . If  $\theta$  denotes the angle between the surface normal and the normal of the unit sphere at the intersection with the line of sight towards  $\mathbf{P}$ , and if  $r$  is the length of the line of sight from  $dA$  to  $\mathbf{P}$ , then

$$d\Omega_A = \frac{dA \cos \theta}{r^2}. \quad (4.2)$$

The unit of a solid angle is called a steradian (sr). ◇

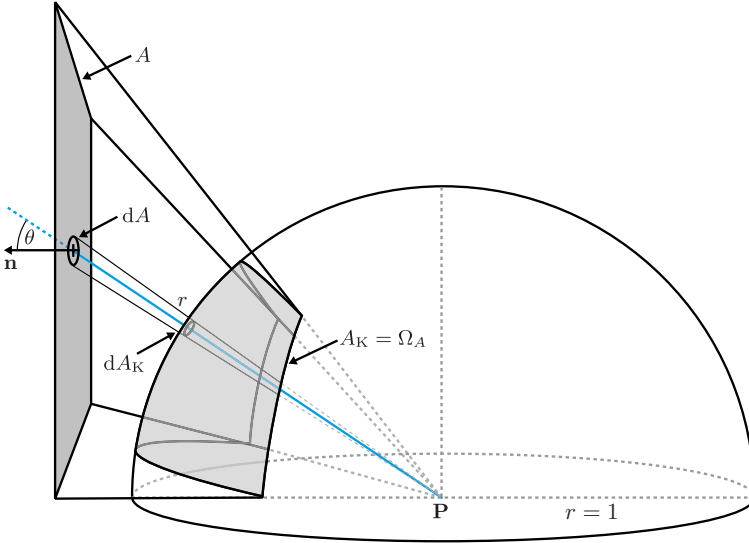


Figure 4.1. Solid angle.

If a surface element in spherical coordinates is denoted by the polar angle  $[\theta_1, \theta_2]$  and the azimuth  $[\varphi_1, \varphi_2]$ , it covers the following solid angle when observed from  $\mathbf{P}$ :

$$\Omega = \int_{\varphi_1}^{\varphi_2} \int_{\theta_1}^{\theta_2} \sin \theta \, d\theta \, d\varphi. \tag{4.3}$$

A half-space has a solid angle of  $2\pi$ :

$$\Omega_{\text{Halfspace}} = \int_0^{2\pi} \underbrace{\int_0^{\pi/2} \sin \theta \, d\theta}_{= 1} \, d\varphi = 2\pi. \tag{4.4}$$

The solid angle can be interpreted as a three-dimensional generalization of the planar angle from plane geometry [7]. In a plane, an angle is defined by two rays originating from a point  $\mathbf{P}$ . The angle is characterized by the length of the arc cut out of the unit circle around  $\mathbf{P}$  by the two lines. Equivalently, the solid angle is given by a homocentric bundle of rays intersecting in  $\mathbf{P}$ . A measure of the solid angle is the area of the surface cut out of the unit sphere around  $\mathbf{P}$  by the bundle of rays [9].

The **radiant intensity**  $I$  denotes the density of the power emitted in the direction  $\mathbf{r}$  from a point  $\mathbf{x}$  (Fig. 4.2(b)):

$$I(\mathbf{r}, \mathbf{x}) = \frac{d\Phi}{d\Omega}(\mathbf{r}, \mathbf{x}). \tag{4.5}$$

Similarly, the **luminous intensity**  $I_l$  is the density of the luminous flux emitted from  $\mathbf{x}$  in the direction  $\mathbf{r}$  and is measured in units of candelas:  $1 \text{ cd} = 1 \text{ lm/sr}$ .

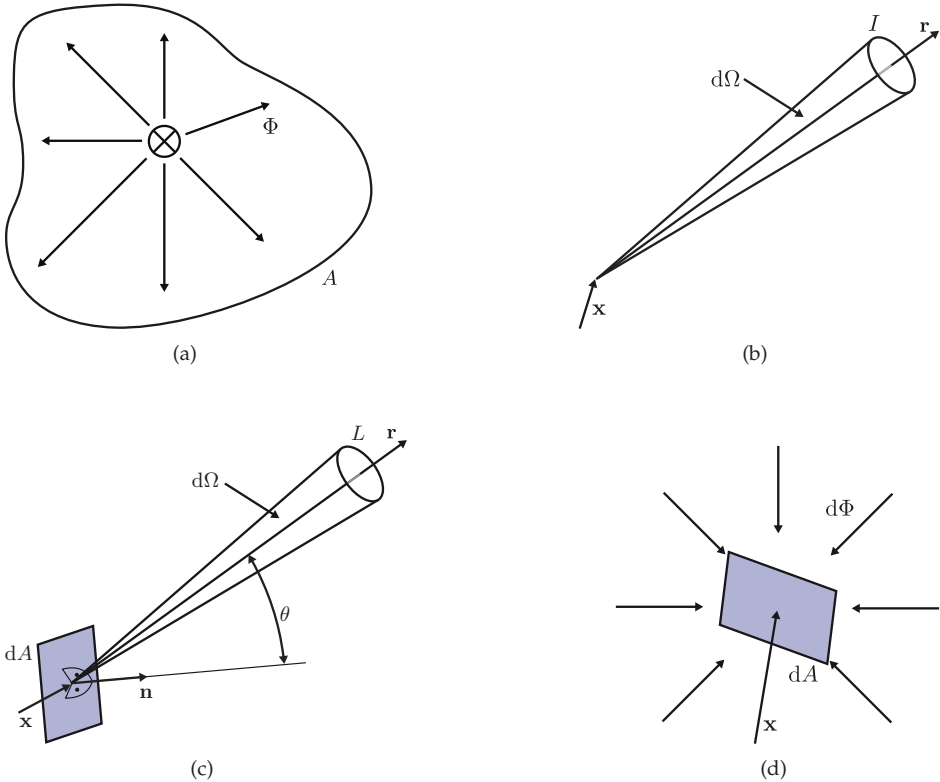


Figure 4.2. Visualization of radiometric quantities: (a) Radiant flux  $\Phi$ ; (b) Radiant intensity  $I$ ; (c) Radiance  $L$ ; (d) Irradiance  $E$ .

The **radiance**  $L$  is the surface density of the radiant intensity emitted by the surface element  $dA$ , projected in the propagation direction  $\mathbf{r}$  (cf. Fig. 4.2(c)):

$$L(\mathbf{r}, \mathbf{x}) = \frac{dI}{dA \cos \theta}, \tag{4.6}$$

with  $\mathbf{x}$  denoting the position of the surface element  $dA$  and  $\theta$  denoting the angle between the surface normal of  $dA$  and the direction of the radiation  $\mathbf{r}$ . Inserting (4.5) results in

$$L(\mathbf{r}, \mathbf{x}) = \frac{d^2\Phi}{d\Omega dA \cos \theta}. \tag{4.7}$$

The corresponding photometric quantity is called the **luminance**  $L_1$ . Conversely, the radiant flux can be obtained by integrating over the radiance [9]:

$$\Phi = \int_A \int_{\Omega} L(\mathbf{r}, \mathbf{x}) \cos \theta d\Omega dA. \tag{4.8}$$

Radiance describes the radiation intensity flowing through the surface element  $dA$  in the direction  $\mathbf{r}$ . It can be defined for surface elements of a light source as well as for any arbitrary surface element in space [9].

## 4.1

**Theorem 4.1: Fundamental law of radiometry**

Suppose that two surface elements  $dA_1$  and  $dA_2$ , at a distance of  $r$  from each other, radiate with a radiance of  $L_1$  and  $L_2$ , respectively (Fig. 4.3). In order to calculate the radiant flux between the two surface elements, to begin with, let  $dA_1$  be the sender and  $dA_2$  the receiver. The differential radiant flux originating from  $dA_1$  and ending at  $dA_2$  is

$$d^2\Phi_{1\rightarrow 2} = L_1 dA_1 \cos \theta_1 d\Omega_1 = L_1 \frac{dA_1 \cos \theta_1 dA_2 \cos \theta_2}{r^2}. \quad (4.9)$$

According to (4.2), the following holds for the solid angle  $d\Omega_1$  under which  $dA_2$  is visible from  $dA_1$ :

$$d\Omega_1 = \frac{dA_2 \cos \theta_2}{r^2}. \quad (4.10)$$

Similarly, swapping the roles of sender and receiver results in the differential radiant flux from  $dA_2$  to  $dA_1$ :

$$d^2\Phi_{2\rightarrow 1} = L_2 dA_2 \cos \theta_2 d\Omega_2 = L_2 \frac{dA_1 \cos \theta_1 dA_2 \cos \theta_2}{r^2}. \quad (4.11)$$

Hence, the differential flux exchanged between the two surface elements is given by

$$d^2\Phi_{1\leftrightarrow 2} = (L_1 - L_2) \frac{dA_1 \cos \theta_1 dA_2 \cos \theta_2}{r^2}. \quad (4.12)$$

This equation describes the radiant flux between two surface elements and is called the **fundamental law of radiometry** [2, 9]. The corresponding relation between the photometric quantities of luminous flux and luminance is called the **fundamental law of photometry**.  $\diamond$

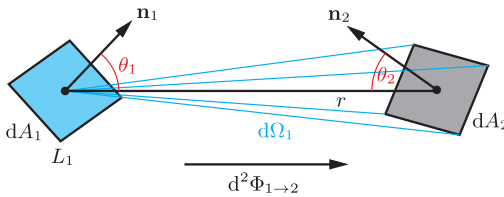


**Figure 4.3.** Visualization of the fundamental law of radiometry: Differential radiant flux  $d^2\Phi_{1\rightarrow 2}$  from  $dA_1$  to  $dA_2$ , with  $\theta_i$  denoting the angle between the normal to the surface and the ray of sight (adapted from [2]).

The **irradiance**  $E$  is the surface density of the radiant flux arriving at point  $\mathbf{x}$  on a surface (Fig. 4.2(d)):

$$E(\mathbf{x}) = \frac{d\Phi}{dA}(\mathbf{x}). \quad (4.13)$$

The irradiance  $E_1$  on the surface element  $dA_1$  that is caused by the radiance  $L_2$  of the surface element  $dA_2$ , can be calculated by integrating (4.11) over all spatial directions  $\mathbf{r}$  by means of (4.10):

$$E_1(\mathbf{x}) = \frac{d\Phi_{2\rightarrow 1}(\mathbf{x})}{dA_1} = \int_{\mathbf{r}} L_2(\mathbf{r}, \mathbf{x}) \cos \theta_1(\mathbf{r}, \mathbf{x}) d\Omega_1(\mathbf{r}, \mathbf{x}). \quad (4.14)$$

In photometry, the **illuminance**  $E_l$  is the surface density of the luminous flux incident at point  $\mathbf{x}$ . Its unit is lux:  $1 \text{ lx} = 1 \text{ lm/m}^2$ .

Integrating the radiant flux over time results in the the **radiant energy** that has passed through the respective surface:

$$Q = \int_{t_1}^{t_2} \Phi(t) dt. \quad (4.15)$$

The corresponding photometric quantity is called the **luminous energy**. It is calculated by integrating the luminous flux  $\Phi_1$ .

Temporal integration of the irradiance results in the **radiant exposure**  $H$ :

$$H = \int_{t_1}^{t_2} E(t) dt. \quad (4.16)$$

It represents the radiant energy's surface density:

$$H = \int_{t_1}^{t_2} \frac{d\Phi}{dA}(t) dt = \frac{dQ}{dA}. \quad (4.17)$$

The corresponding photometric quantity is called the **luminous exposure**  $H_1$ .

The radiant exposure is the quantity which is measured by an image sensor and which is encoded in the image values (intensity values) of the resulting image. Equivalently, the human eye is sensitive to the quantity of luminous exposure. Assuming a fixed observation time and an irradiance that is approximately constant for the period of the observation, the image values can also be interpreted as a representation of the irradiance.<sup>1</sup>

Table 4.1 summarizes the radiometric and photometric quantities and their units.

The spectral density  $X_\lambda$  of each radiometric quantity  $X$  can be written as a function of the wavelength  $\lambda$  [9]:

$$X_\lambda(\lambda) = \frac{dX}{d\lambda}. \quad (4.18)$$

The spectral density  $X_\lambda(\lambda)$  represents the component of the radiometric quantity  $X$  that is caused by wavelengths within the interval  $[\lambda, \lambda + d\lambda]$ . For example, the spectral radiant flux  $\Phi_\lambda$  describes the distribution of the radiant power over the wavelengths of the spectrum. Thus, it characterizes the contributions of the different parts of the electromagnetic spectrum to the total radiant flux  $\Phi$ . The original radiometric quantity  $X$  can be obtained by integrating the spectral density  $X_\lambda$  over the wavelength:

$$X = \int_0^\infty X_\lambda(\beta) d\beta. \quad (4.19)$$

---

<sup>1</sup>In the strict sense, one must distinguish between sensors measuring the real energy, e.g., a bolometer (see Sec. 6.10.1), and sensors counting photons. If a large interval of wavelengths is captured, the photon count is not equivalent to the energy, and therefore not to the irradiance, as the photon energy depends on the wavelength.

Table 4.1. Correspondences of radiometric and photometric quantities [2,3,9,10].

	Radiometric quantity	Symbol Unit	Formula	Symbol Unit	Photometric quantity
Concerning radiation field	Radiant flux	$\Phi$ W		$\Phi_1$ lm	Luminous flux
	Radiant energy	$Q$ J	$\int \Phi dt$	$Q_1$ lm s	Luminous energy
Concerning sender	Radiant intensity	$I$ W/sr	$\frac{d\Phi}{d\Omega}$	$I_1$ cd	Luminous intensity
	Radiance	$L$ $\frac{W}{m^2 sr}$	$\frac{dI}{dA \cos \theta}$	$L_1$ cd/m <sup>2</sup>	Luminance
Concerning receiver	Irradiance	$E$ W/m <sup>2</sup>	$\frac{d\Phi}{dA}$	$E_1$ lx	Illuminance
	Radiant exposure	$H$ J/m <sup>2</sup>	$\int E dt$	$H_1$ lx s	Luminous exposure
Physical				Physiological	

## 4.2

## 4.2 The light field of a test object

As mentioned in Chap. 1, a test object introduces a characteristic modulation to the irradiated light, so that one can obtain information about the test object from the emitted light. By means of the radiometric quantities introduced in the previous section, this modulation can now be mathematically modeled.

The radiation from a surface element in a spatial direction is quantified by the radiance  $L$  in  $\frac{W}{m^2 sr}$ . The radiance of the light source LS is denoted by  $L_{LS}$ , the radiance of the test object's surface SF is denoted by  $L_{SF}$ , and the irradiance  $E$  on the surface is denoted by  $E_{SF}$  in  $W/m^2$ . Points located on the light source and on the surface are denoted by world coordinates:  $\xi_w$  and  $\mathbf{x}_w \in \mathbb{R}^3$ , respectively. The direction of the light rays is described by pairs of angles  $\alpha = (\alpha_1, \alpha_2)$ ,  $\beta = (\beta_1, \beta_2)$ ,  $\gamma = (\gamma_1, \gamma_2)$  with respect to the world coordinate system. The notation of image coordinates is  $(x, y)^T$ , as usual.

The radiance emitted by a point on the surface of some object is additively composed of two components: the active self-radiation of the surface element and the (passively) reflected light:<sup>2</sup>

$$L = L_{\text{active}} + L_{\text{passive}}. \quad (4.20)$$

For light sources, the component  $L_{LS, \text{passive}}$  corresponds to the light that is first reflected back to the light source by the test object and the surroundings and then reflected again. Compared to the self-radiation of the light source, this component can mostly be neglected.

Conversely, for illuminated test objects, the component  $L_{SF, \text{active}}$  can mostly be neglected. Exceptions are self-radiating test objects, such as hot and glowing objects producing thermal radiation in the visible part of the spectrum (see Sec. 2.7.1.1). When imaging in the

<sup>2</sup>Additivity of radiance holds only for non-coherent light.

thermal infrared spectrum, one observes even a significant self-radiation from objects that are commonly considered 'cold'.

Each point of an object surface (whether of the test object, the light source, or another surrounding object) is illuminated from and illuminates all object points which are visible from its perspective. Because of the high speed of light, and since the radiance decreases exponentially for an increasing number of reflections, a stationary state of the mutual illumination of all objects is reached practically instantaneously<sup>3</sup> after turning on a light source.

Depending on the application, the model used for describing the radiance can have different levels of detail. With

$$L_{LS}^i(\xi_w, \alpha, \lambda), \quad i = 0, 1, 2, 3, \quad (4.21)$$

the radiance of a light source at point  $\xi_w \in LS$  in the direction  $\alpha$  for the wavelength  $\lambda$  can be described with respect to the  $i$ th component of the Stokes polarization vector (see Sec. 2.2.2.2).

The illumination of the test object by the light source produces a local irradiance  $E_{SF}$  on the test object's surface, which depends on the direction of the illumination and on the surface gradient, cf. (4.14). Some of the irradiated light is emitted back into space by the surface. This passive illumination by the surface can be modeled as follows:

$$L_{SF,passive}^j(x_w, \beta, \lambda', \{R^{ij}(x_w, \gamma, \beta, \lambda, \lambda')\}, \{L_{LS}^i(\xi_w, \alpha, \lambda)\}), i, j \in \{0, 1, 2, 3\}. \quad (4.22)$$

This formula is quite complicated. For example, fluorescent objects irradiated with light of a certain wavelength  $\lambda$  may emit light at a longer wavelength  $\lambda' > \lambda$  (see Sec. 7.2.2). The light emitted in direction  $\beta$  from the surface point  $x_w$  generally depends on the whole light of the light source reaching the respective point. This dependency is expressed by means of the curly braces  $\{ \cdot \}$ . Hence,  $L_{SF}^j$  is a functional of the functions  $L_{LS}^i$  and  $R^{ij}$ .

The reflection function  $R^{ij}(\cdot)$  describes how the irradiance from the direction  $\gamma$  at point  $x_w$  is turned into an emission in direction  $\beta$ . The indices  $i$  and  $j$  denote the influence of the  $i$ th component of the Stokes vector of the irradiated light on the  $j$ th component corresponding to the emitted light. As, due to multiple reflections, the surface might illuminate itself, e.g., in the case of illuminated cavities, the emitted radiance at  $x_w$  depends on the reflectance of the whole surface. This is why the reflection function  $R^{ij}$  influences the functional  $L_{SF}^j$  as a whole, as is denoted by the curly braces.

The light emitted by the test object can be measured by a sensor. Here, the sensor is modeled as a camera consisting of a lens system and a sensor chip. If the surface point  $x_w$  is imaged by the lenses onto the image sensor, the light emitted by the test object is integrated and results in the image value  $g(x, y)$ .

Figure 4.4 illustrates the formulations mentioned. The effect of the test object's reflecting light back to the light source can mostly be neglected. In many of the practical applications of automated visual inspection, also neglected are multiple reflections at the object surface. Light reaching the surface from a certain direction  $\gamma$  is then emitted in the directions  $\beta$  according to a multiplication with the reflectance  $R(\dots, \gamma, \beta, \dots)$ . This simplification results in the bidirectional reflectance distribution function (BRDF), which will be introduced in the following section. Due to this assumption, the dependence on the function  $\{R(\cdot)\}$  as a whole vanishes, and only the values of the function at  $(x_w, \gamma)$  have to be considered.

<sup>3</sup>Temperature changes of the objects due to the absorption of radiation are neglected.

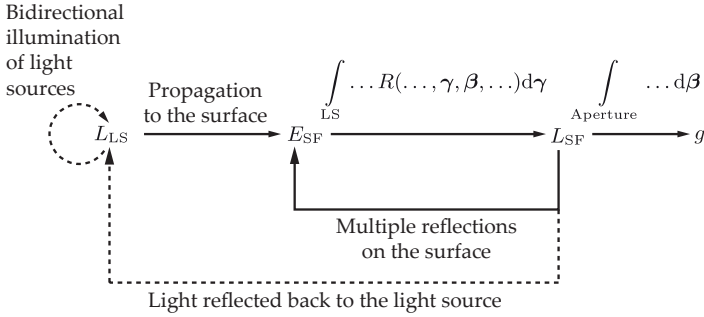


Figure 4.4. Model of the formation of the light field by the reflection of the light emitted by the light source on the object surface. The dotted transitions can mostly be neglected.

For a given scene of a test object and an illumination, the radiance  $L_{SF}^j(\cdot)$  is called the light field or the plenoptic function [1]. The light field describes the set of all light rays emitted by the test object and contains all information about the test object which can be optically obtained, with respect to the chosen level of detail and the given illumination. The light field determines the set of all possible images that could be acquired of the scene under the given combination of illumination and test object.

In practice, a complete acquisition of the light field is not possible. Nevertheless, the light field is a helpful concept and represents the basis for a new kind of camera: the so-called light field cameras (see Sec. 7.3.9).

### 4.3 The bidirectional reflectance distribution function (BRDF)

The **bidirectional reflectance distribution function (BRDF)** [8] completely describes the reflection properties of a surface element  $dA$ . To simplify matters, any dependencies on the wavelengths and polarization and any fluorescent effects are at first neglected in the following considerations.

#### 4.2 Definition 4.2: Bidirectional reflectance distribution function (BRDF)

The BRDF is defined using the differential reflection factor

$$\rho(\theta_i, \varphi_i, \theta_e, \varphi_e) = \frac{d\Phi_e}{d\Phi_i} = \frac{dE_e}{dE_i} = \frac{dL_e d\Omega_e \cos \theta_e}{dL_i d\Omega_i \cos \theta_i}, \tag{4.23}$$

with the polar angle  $\theta_i$ , the azimuthal angle  $\varphi_i$ , the solid angle  $\Omega_i$ , the radiant flux  $\Phi_i$ , the irradiance  $E_i$ , and the radiance  $L_i$  of the incident light. The corresponding quantities of the light emitted by  $dA$  are denoted by  $\theta_e, \varphi_e, \Omega_e, \Phi_e, E_e,$  and  $L_e$  (cf. Fig. 4.5). The conversion is carried out according to (4.7). The angles refer to the normal of the surface element.

The BRDF is given by

$$BRDF(\theta_i, \varphi_i, \theta_e, \varphi_e) := \frac{\rho(\theta_i, \varphi_i, \theta_e, \varphi_e)}{d\Omega_e \cos \theta_e} = \frac{dL_e(\theta_e, \varphi_e)}{dE_i(\theta_i, \varphi_i)}. \tag{4.24}$$

Hence, the BRDF describes the reflectance of the surface with respect to the directions of the incident and emitted light. ◇



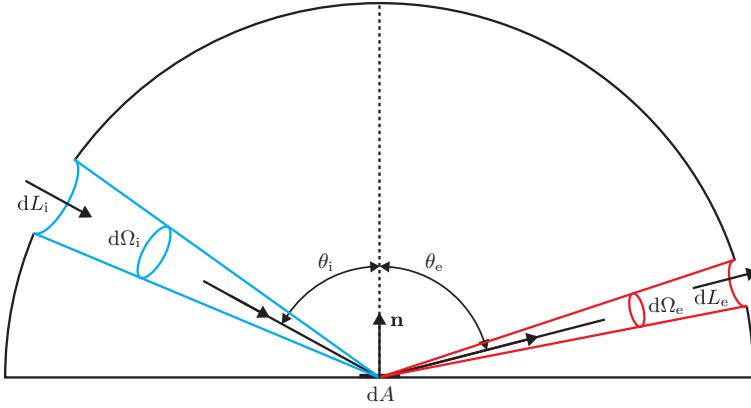


Figure 4.5. Illustration of the definition of the bidirectional reflectance distribution function (BRDF).

The intensity on the image plane of an optical imaging system is proportional to  $L_e$  (see Sec. 4.4.1). If the BRDF of the captured object, the angle of view, and the illumination parameters are known, the captured intensity can be calculated using

$$dL_e(\theta_e, \varphi_e) = BRDF(\theta_i, \varphi_i, \theta_e, \varphi_e) dE_i(\theta_i, \varphi_i), \tag{4.25}$$

by integrating over all directions  $(\theta_i, \varphi_i)$  of the incident light and all directions  $(\theta_e, \varphi_e)$  of the emitted light which reach the image sensor. If the BRDF of a surface is considered as a function of positions  $(x, y)$  and of the wavelength  $\lambda$  of the light (Fig. 4.6), it can be combined with the surface relief  $z(x, y)$ , which will yield an extensive description of the surface of an opaque object  $o$ , which will be sufficient for many automated visual inspection tasks:

$$o := \begin{pmatrix} BRDF(x_w, y_w, \theta_i, \varphi_i, \theta_e, \varphi_e, \lambda) \\ z(x_w, y_w) \end{pmatrix} \tag{4.26}$$

$$dL_e(x_w, y_w, \theta_e, \varphi_e, \lambda) = BRDF(x_w, y_w, \theta_i, \varphi_i, \theta_e, \varphi_e, \lambda) dE_i(x_w, y_w, \theta_i, \varphi_i, \lambda) \tag{4.27}$$

By the **Helmholtz reciprocity principle**, the BRDF is symmetric, so that the directions of incidence and reflection can be interchanged:

$$BRDF(\theta_i, \varphi_i, \theta_e, \varphi_e) = BRDF(\theta_e, \varphi_e, \theta_i, \varphi_i). \tag{4.28}$$

Hence, the propagation direction can be inverted, as is always the case for electromagnetic waves.

Usually, completely measuring or modeling the four-dimensional BRDF is not practicable. However, for many applications, simple special cases and their linear combinations are sufficient. Two special cases will now be presented [5].

The **Lambertian reflectance model** describes a perfectly scattering surface: the incident light is uniformly emitted into all directions of a half-space, independent of the direction of incidence. The resulting BRDF is of the following form:

$$BRDF(\theta_i, \varphi_i, \theta_e, \varphi_e) = \frac{R}{\pi}, \quad R \in [0, 1]. \tag{4.29}$$

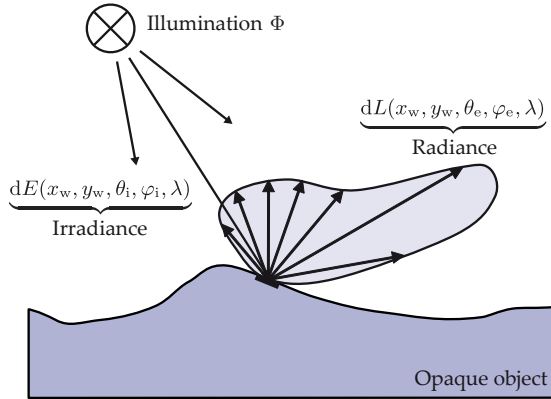


Figure 4.6. The radiance emitted by an opaque surface of an object can be calculated with the BRDF according to (4.27), if the irradiance is known.

The material constant  $R$  is called the **albedo** and describes the ratio between the scattered and incident radiation. The fraction equal to  $1 - R$  of the incident luminous flux is absorbed. The case  $R = 1$  represents total scattering and  $R = 0$  total absorption. Perfectly **specular reflectance** results in the following BRDF:

$$BRDF(\theta_i, \varphi_i, \theta_e, \varphi_e) = \delta\left(\mathbf{n} - \frac{\mathbf{e} - \mathbf{i}}{\|\mathbf{e} - \mathbf{i}\|}\right), \quad \|\mathbf{n}\| = \|\mathbf{e}\| = \|\mathbf{i}\| = 1, \quad (4.30)$$

with  $\mathbf{n}$  denoting the unit vector of the surface normal,  $\mathbf{e}$  denoting the direction of the emitted light, and  $\mathbf{i}$  denoting the direction of the incident light. Incident light is reflected into exactly one direction, which is the reflection of the direction of incidence at the surface normal within the plane of incidence (see Fig. 4.7). This can be validated by inserting Equation (4.30) into the vectorial formulation of the law of reflection (2.202).

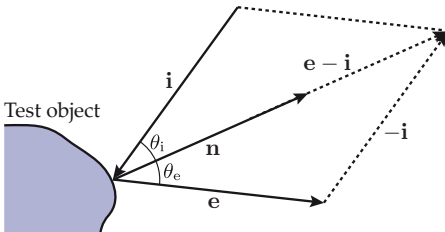


Figure 4.7. Relation between the surface normal  $\mathbf{n}$ , the direction of incidence  $\mathbf{i}$ , and the direction of the emitted radiation  $\mathbf{e}$ , for perfectly specular reflection.

Now, the concept of the BRDF will be used to review the considerations of Sec. 4.2 once more. At the position  $\mathbf{x}_w$ , Equation (4.20) can be formulated as

$$L(\mathbf{x}_w, \theta_e, \varphi_e) = L_{\text{active}}(\mathbf{x}_w, \theta_e, \varphi_e) + \int_{\Omega^+(\mathbf{x}_w)} BRDF(\mathbf{x}_w, \theta_i, \varphi_i, \theta_e, \varphi_e) L(\mathbf{x}_w, \theta_i, \varphi_i) \cos \theta_i \, d\Omega_i \quad (4.31)$$

with  $\Omega^+(\mathbf{x}_w)$  denoting the upper hemisphere at the position  $\mathbf{x}_w$ , oriented in the direction of the normal vector at that position. In this case, the consideration of the upper hemisphere implies an opaque object.

Equation (4.31) again points out the recursive characteristics of the propagation of light caused by multiple reflections at object surfaces. The awkward formulation of Equation (4.31) can be improved by introducing an integral light transport operator  $\mathcal{T}$  [6]:

$$\mathcal{T}L = \mathcal{T}\{L\}(\mathbf{x}_w, \theta_e, \varphi_e) := \int_{\Omega^+(\mathbf{x}_w)} BRDF(\mathbf{x}_w, \theta_i, \varphi_i, \theta_e, \varphi_e) L(\mathbf{x}_w, \theta_i, \varphi_i) \cos \theta_i d\Omega_i. \quad (4.32)$$

By this means, Equation (4.31) can be expressed as

$$L = L_{\text{active}} + \mathcal{T}L. \quad (4.33)$$

Recursively replacing the  $L$  of the right-hand side of this equation by the equation itself leads to the infinite series [6]:

$$L = \sum_{k=0}^{\infty} \mathcal{T}^k L_{\text{active}}. \quad (4.34)$$

This clearly implies that the irradiance  $L$  at the position  $\mathbf{x}_w$  is caused by light that might be actively emitted at that position ( $k = 0$ ), together with light from the active light sources that is reflected at that position for the first time ( $k = 1$ ), by light that is reflected at that position for the second time ( $k = 2$ ), and so on.

#### 4.3.1 BRDF and scattered light

By (4.27), the relation between the incident irradiance  $E_i(\mathbf{x}_w, \theta_i, \varphi_i, \lambda)$  and the emitted radiance  $L_e(\mathbf{x}_w, \theta_e, \varphi_e, \lambda)$  is given by the bidirectional reflectance distribution function  $BRDF(\mathbf{x}_w, \theta_i, \varphi_i, \theta_e, \varphi_e, \lambda)$ . The BRDF depends on the different physical properties of the object:

1. Material properties described by the complex refractive index  $\underline{n}(\mathbf{x}_w, \lambda)$ , resulting in a wavelength-dependent reflection (cf. Sec. 2.6.6.1).
2. **Scattering** of the light caused by inner microscopic structures of the material which are smaller than the resolution of the sensor, e.g., turbidities or pigments.
3. **Roughness** of the surface, i.e., unresolved microstructure of the surface relief.

The BRDF depends on both the material and the relief. Eventually, the impact of the microstructure of the surface on the BRDF depends on the spatial resolution of the illumination compared to the roughness of the surface. Similarly, the roughness influences the intensity measured by the sensor of an optical imaging system capturing a surface, as the BRDF phenomenologically relates the irradiated irradiance  $E_i$  to the reflected radiance  $L_e$ .

For technically measuring the BRDF of the surface, the size of the illuminating bundle of rays coming from the direction  $(\theta_i, \varphi_i)$  plays an important role. The observed reflection and scattering phenomenon is spatially averaged over the illuminated spot. Therefore, the precision of an empirically measured BRDF always depends on the resolution of the measurement system used.

Now assume that the surface is uniformly illuminated from the direction  $(\theta_i, \varphi_i)$  and the resulting scattered light is imaged in the direction  $(\theta_e, \varphi_e)$  on a sensor of finite size. This time, spatial averaging takes place for the image on the sensor plane. Both cases show that the spatial and angular resolution always have to be considered if the BRDF is to be used in a practical application.

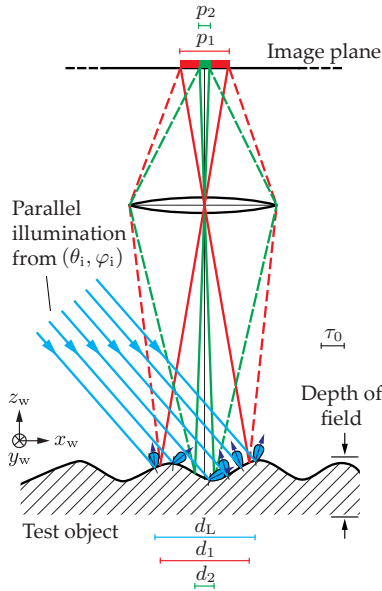


Figure 4.8. Relation between roughness and the scattering properties of a surface.

These considerations are now illustrated by means of Fig. 4.8. The diameter of the illuminated spot on the surface is denoted by  $d_L$ . A possible characterization of the surface's roughness is the length  $\tau_0$  for which the surface can be linearly approximated, so that the mean difference from a plane does not exceed a certain threshold. The diameter of a sensor element in the image plane is denoted by  $p_1$  and  $p_2$  respectively, with  $p_1 < p_2$ . Now,  $d_1$  and  $d_2$  are assumed to denote the diameters of the images of these sensor elements on the surface produced by an optical imaging. In order to allow the application of geometric optics,  $d_1, d_2, d_L, \tau_0 \gg \lambda$  is assumed.

Under these circumstances, the process of observation can be qualitatively described as follows:

1. Scattering of the irradiated light on the object's surface:

For the case  $d_L > \tau_0$ , parallel irradiated light is scattered because of the material's properties (pale blue cones in Fig. 4.8) as well as because of microscopic variations in the directions of the surface normals (blue arrows) inside the illuminated spot. Both effects contribute to the scattering of the light and thus to the BRDF.

## 2. Image acquisition with a camera:

The following proportionality holds for the intensity  $g$  measured by a camera pixel:

$$g \propto \int_{A_{\text{Pixel}}} \int_{\Omega_{\text{Lens}}} L(\mathbf{x}_w, \theta_e, \varphi_e) d\Omega(\mathbf{x}_w, \theta_e, \varphi_e) \cos \alpha(\mathbf{x}_w) dA(\mathbf{x}_w). \quad (4.35)$$

Here, the area  $A_{\text{Pixel}}$  of the light sensitive element and the lens' solid angle  $\Omega_{\text{Lens}}$  are the integration domains and  $\alpha(\mathbf{x}_w)$  denotes the angle between the normal of the surface element  $dA$  and the observation direction.

- a) The roughness is averaged by the sensor element's image on the surface:  $d_1 > \tau_0$  (red optical path in Fig. 4.8)

In this case, the contribution of the microstructure of the surface relief to the captured intensity value is averaged over the object-sided image of the sensor. The surface's microstructure remains unresolved.

- b) The object-sided image of the sensor elements are of sizes less than or equal to the size of the spatial structures of the surface relief:  $d_2 \lesssim \tau_0$  (green optical path)

The surface's microstructure is resolved.

These considerations, which take geometric and optical laws into account, show that the BRDF is based neither solely on the material's properties nor on the surface relief, and is therefore a border case of the object's optical properties and spatial shape. Hence, measuring the scattered light provides information on both the test object's optical properties and its roughness (see Sec. 7.2.5).

---

**Example 4.1 (Automated system for measuring the BRDF):** Since even in its simplest form, the BRDF has four arguments, obtaining a high-resolution measurement of the BRDF is very time-consuming. Additionally, the BRDF has a high dynamic range especially for specular or partly specular surfaces, requiring sensitive sensors and surroundings that absorb as much light as possible. Figure 4.9 shows a system realizing an automated measurement of the BRDF and Fig. 4.10 shows the measurements obtained using that system. ■

## 4.4 Formation of image values

### 4.4.1 Application to a thin lens

In this section, the formation of an image value in a camera in the case of a focused optical imaging will be modeled as a function of radiometric quantities [4, 11].

An image sensor is assumed, which measures the energy transported by incoming photons. Radiometrically speaking, the sensor integrates the illuminance over the exposure time. The derived equations are valid for both gray and color values.

Let  $d\Omega$  denote a solid angle element (equivalent to a surface element) of the ray bundle with respect to the center of the lens. By (4.2), the surface elements  $dA_G$  of the captured

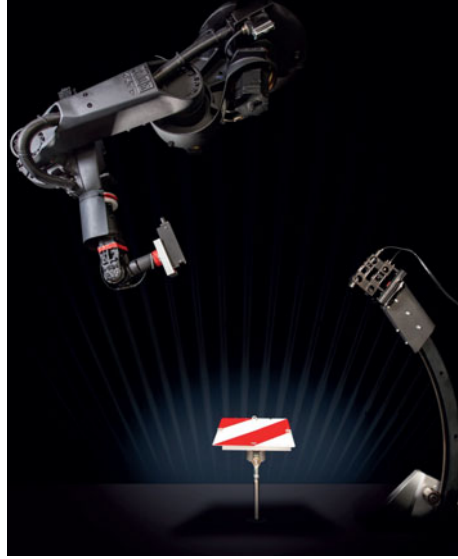


**Figure 4.9.** Automated system for obtaining BRDF measurements, at Fraunhofer-IOSB. In order to realize such a system, a light source (right) is arranged so that the direction of incidence of the emitted light is  $(\theta_i, \varphi_i)$ . The test object is placed on a rotary table in the middle of the setup, so that the azimuth  $\varphi_i$  can be varied. The robot shown on the left allows arbitrary positions of the sensor with respect to the direction of observation  $(\theta_e, \varphi_e)$ .

object and of the image plane  $dA_B$  are related as follows:

$$d\Omega = \frac{dA_G \cos \beta}{\left(\frac{g}{\cos \alpha}\right)^2} = \frac{dA_B \cos \alpha}{\left(\frac{b}{\cos \alpha}\right)^2} \quad (4.36)$$

with

$$\cos \alpha = \frac{b}{r_B} = \frac{g}{r_G}. \quad (4.37)$$

The angle between the principal ray and the optical axis is denoted by  $\alpha$ , the angle between the object-sided surface element and the principal ray is denoted by  $\beta$ , the lengths of the image-sided and object-sided lines of sight to the center of the lens are  $r_B$  and  $r_G$ ; as usual, the image distance is denoted by  $b$ , and  $g$  denotes the object distance (see Fig. 4.11). Reformulating that equation and crossing out  $\cos^2 \alpha$  results in

$$\frac{dA_G}{dA_B} = \frac{\cos \alpha}{\cos \beta} \left(\frac{g}{b}\right)^2. \quad (4.38)$$

When seen from the perspective of the object point  $G$ , a circularly shaped lens with an area of  $A_{\text{Lens}}$  and a diameter  $D$  has the solid angle

$$\Omega_{\text{Lens}} = \frac{A_{\text{Lens}} \cos \alpha}{r_G^2} = \frac{D^2 \pi}{4} \frac{\cos \alpha}{\left(\frac{g}{\cos \alpha}\right)^2} = \frac{\pi}{4} \left(\frac{D}{g}\right)^2 \cos^3 \alpha, \quad (4.39)$$

as long as  $r \gg D$  holds. Let  $L_G$  denote the radiance of the object's surface, which is assumed to be constant with respect to the directions of the light emitted to the lens. Then (4.7) yields

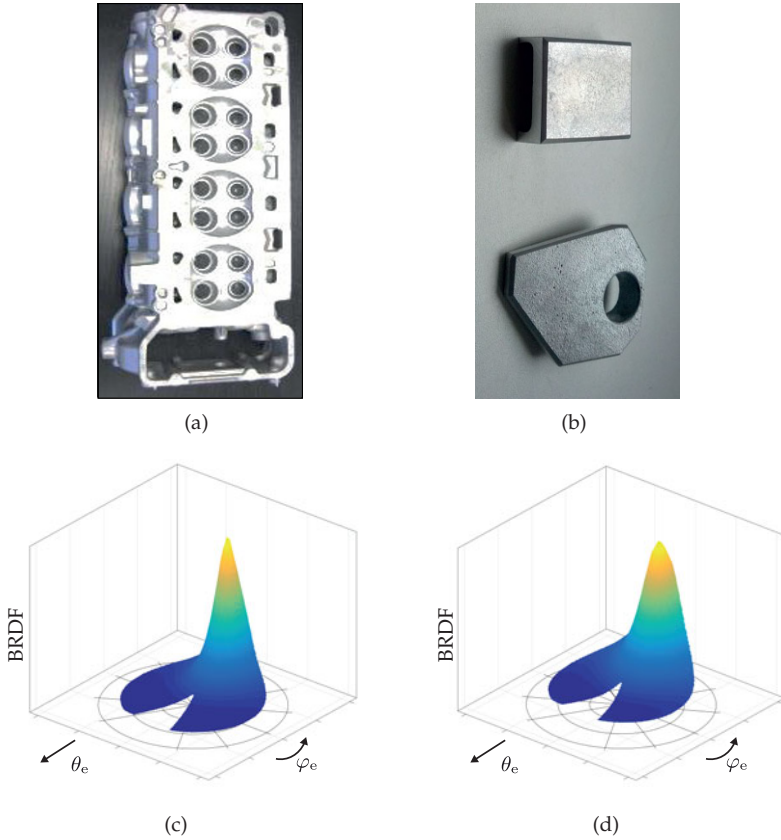


**Figure 4.10.** Measuring the BRDF of a cylinder head. (a) A cast aluminum cylinder head. Some parts of its surface were molded by a steel coquille and the other parts were molded by sand cores. (b) Two parts of its surface, which have been carved out for obtaining BRDF measurements; top: the part molded by the coquille; bottom: the part molded by the sand cores. (c) Section of the BRDF of the surface molded by the coquille as a function of  $(\theta_e, \varphi_e)$  for  $\theta_i = 50^\circ, \varphi_i = 0^\circ$ . (d) Section of the BRDF of the surface formed by the sand cores as a function of  $(\theta_e, \varphi_e)$  for  $\theta_i = 50^\circ, \varphi_i = 0^\circ$ . The cone of the scattering is wider, compared to (c).

the radiant flux  $d\Phi$  of the surface element  $dA_G$  through the lens:

$$d\Phi = L_G \Omega_{\text{Lens}} dA_G \cos \beta = \frac{\pi}{4} \left( \frac{D}{g} \right)^2 \cos^3 \alpha \cos \beta L_G dA_G . \tag{4.40}$$

The irradiance at the surface element  $dA_B$  on the image plane is

$$E_B = \frac{d\Phi}{dA_B} = \frac{\pi}{4} \left( \frac{D}{g} \right)^2 \cos^3 \alpha \cos \beta L_G \frac{dA_G}{dA_B} . \tag{4.41}$$

Inserting (4.38) yields the equation sought:

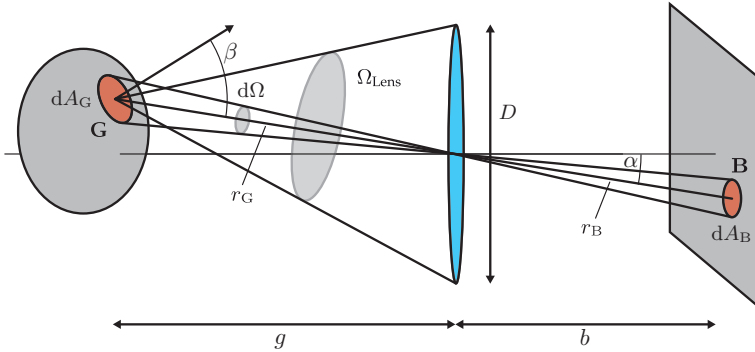


Figure 4.11. Calculation of the irradiance in the image plane of a thin lens.

#### 4.2

#### Theorem 4.2: $\cos^4$ law

For an optical imaging with a thin lens of diameter  $D$ , an image distance  $b$  and an angle  $\alpha$  between the principal ray and the optical axis,

$$E_B = \frac{\pi}{4} \left( \frac{D}{b} \right)^2 \cos^4 \alpha L_G. \quad (4.42)$$

Hence, the irradiance  $E_B$  on the image sensor is proportional to the radiance  $L_G$  on the object's surface. This equation is known as the  $\cos^4$  law.  $\diamond$

The  $\cos^4$  law (4.42) can be interpreted as follows:

- The image value is proportional to the radiance  $L_G$  of the object's surface.
- For a focused optical imaging, the image value is independent of the object distance  $g$ .
- The image value increases with the squared diameter  $D$  of the lens and is therefore proportional to the lens's area (or to the aperture in general).
- The image value decreases in the direction of the image boundary ( $E_B$  decreases for increasing  $\alpha$ ).
- For optical systems consisting of multiple lenses, this effect is usually dominated by vignetting (Sec. 3.4.3).

For longshots,  $b \approx f$ , and therefore

$$E_B \approx \frac{\pi}{4} \cos^4 \alpha \frac{L_G}{O^2}, \quad (4.43)$$

with  $O := \frac{f}{D}$  denoting the f-number, which was introduced in Sec. 3.4.4. As expected, the image value, and with it the brightness of the image, are inversely proportional to the squared f-number. For a constant aperture size of  $D$ , the image's brightness decreases reciprocally with the squared focal length  $f$ .

#### 4.5

### 4.5 Bibliography

- [1] Edward H. Adelson and John Y. A. Wang. Single Lens Stereo with a Plenoptic Camera. *IEEE Transactions on Pattern Analysis and Machine Intelligence*, 14(2):99–106, 1992.



- [2] Helmut Budzier and Gerald Gerlach. *Thermal infrared sensors: theory, optimization, and practice*. Wiley, 2010.
- [3] Rainer Dohlus. *Photonik: Physikalisch-technische Grundlagen der Lichtquellen, der Optik und des Lasers*. Oldenbourg, 2010.
- [4] Marc Ebner. *Color constancy*. Wiley, 2007.
- [5] Ramesh Jain, Rangachar Kasturi, and Brian Schunck. *Machine vision*. McGraw-Hill, 1995.
- [6] James T. Kajiya. The rendering equation. In *Siggraph Computer Graphics*, volume 20, pages 143–150. ACM, 1986.
- [7] Herman Keitz. *Light calculation and measurements: An introduction to the system of quantities and units in light-technology and to photometry*. Macmillan, 2nd edition, 1971.
- [8] F. Nicodemus, J. Richmond, J. Hsia, I. Ginsberg, and T. Limperis. *Geometrical Considerations and Nomenclature for Reflectance*. U.S. Department of Commerce, 1977.
- [9] Otto Reeb. *Grundlagen der Photometrie*. Braun, Karlsruhe, 1962.
- [10] Michael Reisch. *Halbleiter-Bauelemente*. Springer, 2005.
- [11] Emanuele Trucco and Alessandro Verri. *Introductory Techniques for 3-D Computer Vision*. Prentice Hall, 1998.

The background features a complex arrangement of thin, light gray lines that form various geometric shapes, including rectangles, trapezoids, and large, sweeping curves. These lines overlap and intersect, creating a sense of depth and movement. The overall aesthetic is clean and modern.

Chapter 5  
**Color**

# 5

## 5 Color

5.1	Photometry . . . . .	165
5.2	Color perception and color spaces . . . . .	167
5.2.1	Color perception of the human eye . . . . .	167
5.2.2	Color mixing . . . . .	171
5.2.3	CIE color spaces . . . . .	173
5.2.4	Spectrophotometry for color measurement and color distance computation	185
5.2.5	Color order systems . . . . .	191
5.2.6	Other color spaces . . . . .	192
5.2.6.1	Gamma correction . . . . .	192
5.2.6.2	RGB color spaces . . . . .	193
5.2.6.3	HSI and HSV . . . . .	195
5.2.6.4	YUV and $YC_B C_R$ . . . . .	196
5.2.6.5	Color printing and CMYK . . . . .	197
5.3	Filters . . . . .	198
5.4	Acquisition and processing of color images . . . . .	199
5.5	Bibliography . . . . .	201

## 5 Color

### 5.1 Photometry

In photometry, all quantities are with reference to the perception of brightness by the human eye. The sensitivity of the human eye can be described by a function  $V(\lambda)$  of the wavelength. This so-called **luminosity function** varies for different ambient conditions, such as photopic vision or scotopic vision, for example (Fig. 5.1), which refer to human perception at daylight or in darkness. The luminosity function of the light-adapted eye is used for defining the photometric base system. It is scaled to have a maximum value of 1. The luminosity function can be empirically measured using a psychophysical method similar to the method described in Sec. 5.2.3. However, the perception of brightness of the human eye is not a metric quantity: differences and ratios cannot be quantified by human perception. The corresponding conclusions for photometric quantities do not represent the human perception of brightness [36].

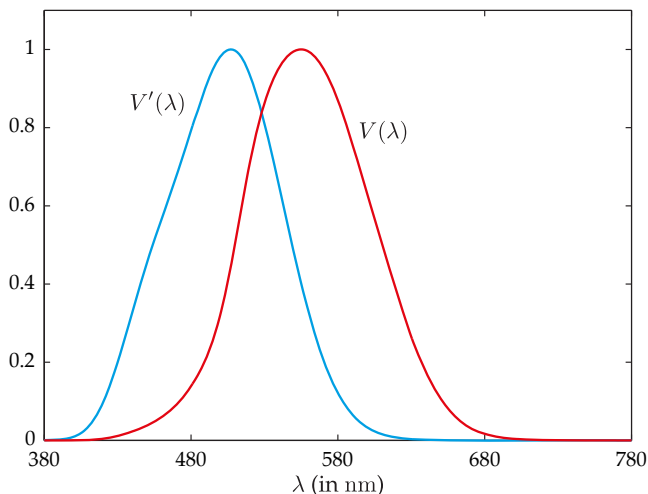


**Figure 5.1.** Sensitivity of the human eye to brightness (adopted from [43]).  $V(\lambda)$ : Range of photopic vision (light-adapted eye),  $V'(\lambda)$ : Range of scotopic vision (dark-adapted eye).

Now the general connection between radiometric and photometric quantities will be described. Let  $X$  be a radiometric quantity and  $X_\lambda(\lambda)$  its spectral density, so that integrating over the whole range of wavelengths yields the quantity  $X$  (cf. Sec. 4.1):

$$X = \int_0^\infty X_\lambda(\beta) d\beta, \quad \forall \lambda \quad X_\lambda(\lambda) \geq 0. \quad (5.1)$$

Then the corresponding photometric quantity  $X_1$  is defined by

$$X_1 = K_m \int_{\lambda_1}^{\lambda_2} X_\lambda(\beta) V(\beta) d\beta, \quad (5.2)$$

with the constant  $K_m$  linking the radiometric and photometric quantities and systems of units. For the photometric base system, it is  $K_m = 683 \frac{\text{lm}}{\text{W}}$ ,  $\lambda_1 = 380 \text{ nm}$  and  $\lambda_2 = 780 \text{ nm}$ .

The sensitivity to brightness of the human eye rapidly decreases at the margins of the visible part of the spectrum, so that the borders of the visible part cannot be exactly defined. A sensitivity to brightness is verifiable for the range of 360 nm up to 830 nm [43]. Outside of the interval from 410 nm to 720 nm, the sensitivity of the human eye is very low [24].

**Example 5.1 (Luminous flux of a blackbody radiator):** Let the blackbody radiator of Sec. 2.7.1.1 have a temperature of  $T = 2,500 \text{ K}$  and an area of  $A = 1 \text{ mm}^2$ . Using (4.8) and (4.3) in combination with Planck’s law (2.254) leads to the spectral radiant flux  $\Phi_\lambda(\lambda)$  of the blackbody radiator:

$$\Phi_\lambda(\lambda) = \int_A \int_{\Omega_{\text{Halfspace}}} L_\lambda(\lambda) \cos \theta \, d\Omega \, dA \tag{5.3}$$

$$= A \int_0^{2\pi} \int_0^{\frac{\pi}{2}} L_\lambda(\lambda) \cos \theta \sin \theta \, d\theta \, d\varphi \tag{5.4}$$

$$= A \pi L_\lambda(\lambda). \tag{5.5}$$

Now, by (5.2), the luminous flux can be calculated by integration of the product  $\Phi_\lambda(\lambda) V(\lambda)$ :

$$\Phi_1 = 683 \text{ lm/W} \int_{380 \text{ nm}}^{780 \text{ nm}} \Phi_\lambda(\lambda) V(\lambda) \, d\lambda \approx 17.7 \text{ lm}. \tag{5.6}$$

Figure 5.2 illustrates this calculation. ■

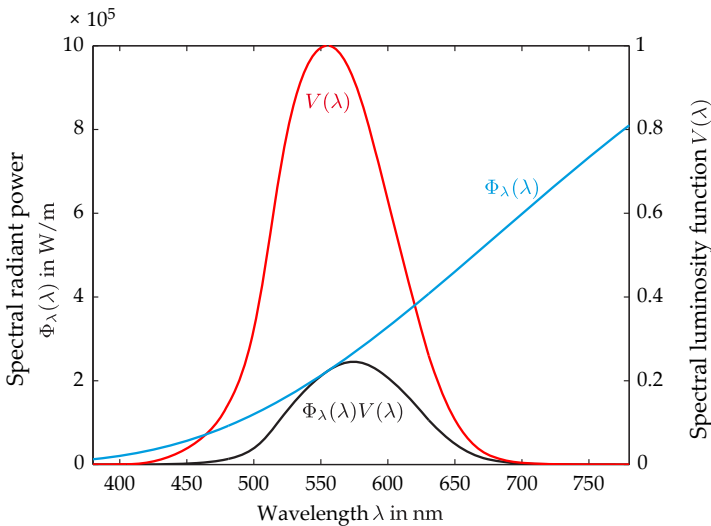


Figure 5.2. The luminous flux of a blackbody radiator [28].

## 5.2 Color perception and color spaces

Color is a sensation arising in the human brain caused by the electromagnetic radiation perceived by the eye [42]. The perceived color depends on the spectrum of the observed light and thus on the distribution of the intensity with respect to the wavelength. In addition, other ambient conditions, such as previous color impressions or nearby color impressions, affect the perception of color (cf. Chap. 1).

Color is neither a property nor a state of an object or a material, as one and the same object might lead to varying color perceptions under different ambient conditions. The most important parameter is the spectrum of the illumination. Color perception is mainly caused by the interaction of

- the spectrum and the direction of the illumination,
- the spectral reflection, scattering, absorption and transmission properties of the observed object (cf. Sec. 2.6)
- and the biological properties of the observer.

Because of the central role played by the human observer in defining and measuring color, the following section will cover the perception of color of the human<sup>1</sup> eye. Then, the foundations of the mixture of color will be covered. In addition, color spaces will be described, which allow quantifying colors and color differences. Why color spaces are chosen to be three-dimensional, and thus contain less information than a continuous electromagnetic spectrum, will be motivated. Therefore, different spectra might lead to the same color impression.

### 5.2.1 Color perception of the human eye

The human eye is constructed according to the principle of the pinhole camera (see Chap. 3): Together, the cornea and the lens collect the incident light that reaches the retina after passing the vitreous humor (the part of the eyeball between the lens and the retina, see Fig. 5.3). The light is refracted mainly at the interface between the air and the cornea. The shape of the lens can be adapted by muscular strength, which is why the eye can focus on different distances. Five different kinds of light sensitive receptors are contained in the retina:

- Rods for scotopic vision,
- three kinds of cones for photopic vision,
- photosensitive retinal ganglion cells for the circadian clock [6].

Rod cells (rods) are spread over the whole retina [15]. They are very sensitive to light and allow sight under very low illumination, for example at dawn. Rods cannot induce a color impression.

There are three kinds of cone cells (cones) which differ in their spectral sensitivity. They enable the perception of color. The fovea, the central point of sharp vision that is located near the optical axis, is mainly surrounded by cone cells. The rest of the retina, which is used for peripheral vision, is dominated by rod cells (Fig. 5.4). The sensitivity to brightness of the cone cells is very low, so that a color impression is not possible for a low illumination.

---

<sup>1</sup>For other creatures, the perception of color differs essentially from that of the human. Some animals cannot perform a spectral resolution of light but can only perceive brightness; others possess more than three types of color receptors and thus can tell two colors apart that cannot be distinguished by humans because of their spectral composition. Besides, not the same part of the spectrum is visible for all creatures. Some animals can even perceive ultraviolet radiation.

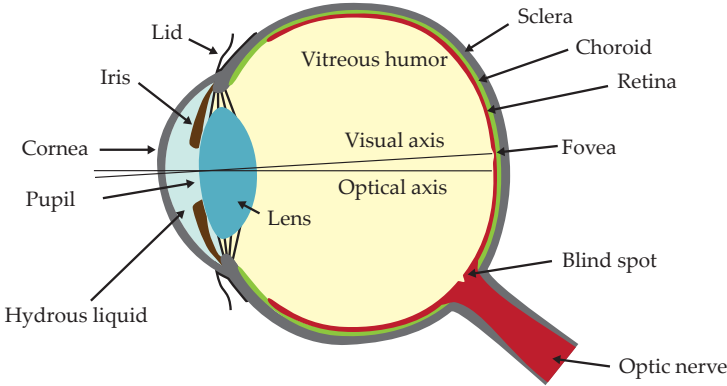


Figure 5.3. Sketch of the human eye [29].

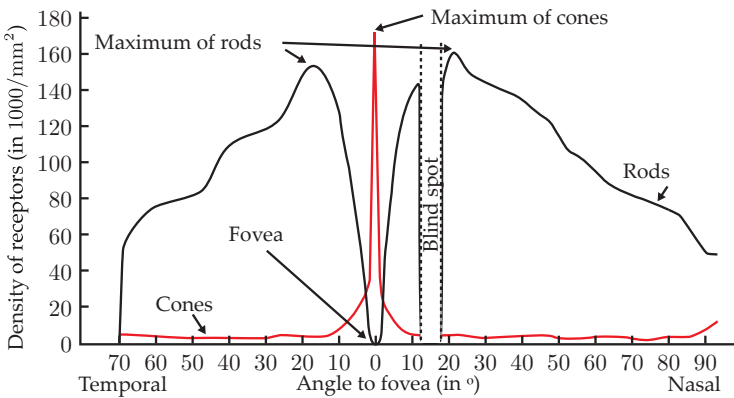


Figure 5.4. Spatial distribution of rod and cone cells on the retina [17,29,34].

Between scotopic and photopic vision, the spectral sensitivity  $V(\lambda)$  varies considerably. It is shifted to shorter wavelengths for scotopic vision, as can be seen in Fig. 5.1.

Figure 5.5 shows the spectral sensitivity of the three types of cones, scaled to a maximum of one. Depending on their part of the spectrum, the cones are called S-, M- and L-cones (short, medium, long wavelengths). S-cones are sensitive to short-wave light in the violet and blue part of the spectrum, M-cones to medium wavelengths corresponding to the green part of the spectrum, and L-cones to long-wave green, yellow and red light. Therefore, the three types of cones are sometimes referred to as blue, green, and red receptors, or as  $\beta$ ,  $\gamma$  and  $\rho$  cones. However, it is important to note that the receptors are not only sensitive to the spectral range represented by their names. L-cones, for example, are even more sensitive to yellow than to red light. The spectral ranges of  $\gamma$  and  $\rho$  lie quite close to each other. That is why the human eye is able to resolve colors in the green and yellow part of the spectrum in great detail [20].

The number of the three types of cones differ. Approximately 7% to 10% of the cones located in the fovea are  $\beta$  receptors [12,37]. The amounts of the two remaining types vary

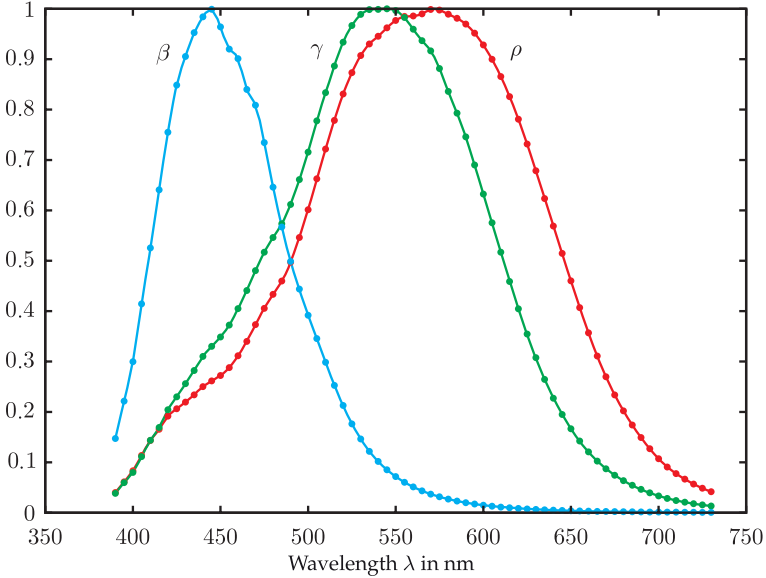


Figure 5.5. Spectral sensitivity of cone cells, scaled to a maximum of one [37].

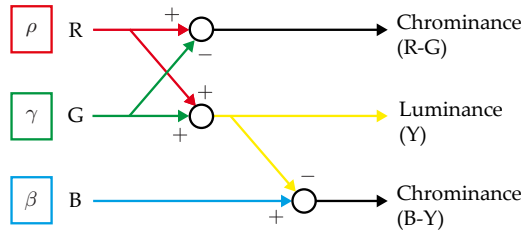


Figure 5.6. Physiological processing of the sensory stimuli of the cones [37].

greatly, depending on the actual individual. On average there are about 31%  $\gamma$  and 61%  $\rho$  receptors [30].

Three combined neural signals are formed from the sensory stimuli of the three kinds of cones (Fig. 5.6). The perceived intensity of the  $\gamma$  and  $\rho$  receptors are summed up and yield the luminance channel  $Y$ , responsible for the perceived brightness.<sup>2</sup> The less frequent  $\beta$  receptors play an unimportant role in the perception of brightness. In addition, two chrominance channels are formed, which are responsible for color perception: The red-green-chrominance is the difference  $R - G$  of the signals coming from the  $\rho$  and  $\gamma$  cones, and the blue-yellow-chrominance is the difference between  $B - Y$  of the  $\beta$  signals and the luminance channel [7, 17, 38]. Because of this kind of processing, a color cannot be simultaneously perceived as

<sup>2</sup>In the strict sense, the human perception of brightness and the photometric measurement of luminance have to be kept separate, as the perceived brightness is not a metric quantity, for example [14, 35]. However, for the purposes of this book, the terms brightness and luminance correspond to the photometric luminosity function of Sec. 5.1.



blueish and yellowish or reddish and greenish, whereas smooth transitions between other colors like yellow and green or blue and red are quite possible.

The number of different kinds of cones or the number of color channels of the human visual system show that a physiological color impression can be definitely characterized by three quantities. Such a three-dimensional vector is called a **tristimulus**. During visual perception, a **color stimulus**, defined by the spectrum of the incident light, is converted into a tristimulus. Mathematically speaking, the spectrum can be described as a function  $I(\lambda)$ : the light's intensity as a function of the wavelength  $\lambda$ . Therefore the space of possible spectra is infinite-dimensional. Thus, the spectrum cannot be uniquely reconstructed from the three-dimensional tristimulus. In fact, different spectra can lead to the same color impression and so to the same tristimulus. Two different color stimuli or spectra  $I_1(\lambda)$  and  $I_2(\lambda)$  with one and the same tristimulus are called **metameric**. Thus, a tristimulus can be defined as set of all metameric color impressions  $I(\lambda)$  leading to that tristimulus. This results in an equivalence relation, inducing a partition of the set of all color impressions.

**Example 5.2 (Metameric color impressions):** Figure 5.7 shows two spectra which are metameric for the CIE standard observer (see Sec. 5.2.3). Only for two narrow lines are the two spectra not equal to zero. Those lines do not overlap, but still, the colors of the two spectra perceived by the human eye equal each other: they are perceived as blue. So, generally, the tristimulus does not contain any information about the distribution of intensities in a spectral range. ■

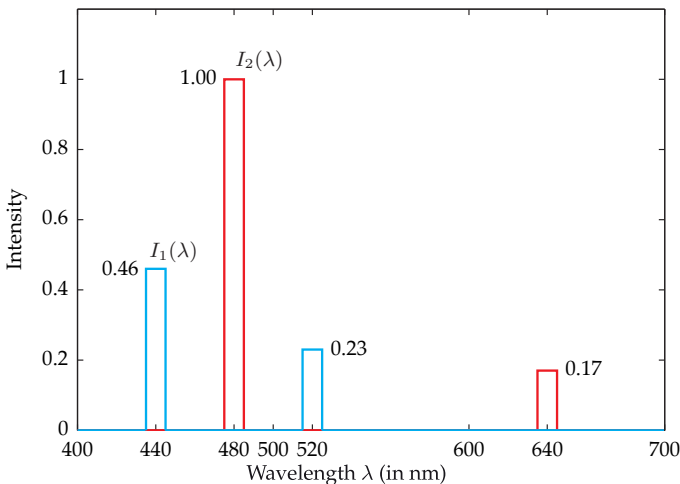


Figure 5.7. Two metameric narrow-band spectra  $I_1(\lambda)$  (blue) and  $I_2(\lambda)$  (red) with disjoint supports [43].

If the colors of two objects are compared, it is important to note that the observed tristimulus also depends on the spectrum of the illumination. Therefore, the tristimulus varies depending on the light source. A very impressive example of this effect is the mineral alexandrite. In daylight, it leads to a greenish and, in the case of an incandescent lamp, to a reddish color impression.

For a certain illumination, two metameric objects might look the same and for another illumination they might look different. Only if the spectral reflectances of the two objects are equal, do they produce the same color impression for every arbitrary illumination. Those color impressions are said to be isometric. However, there are also metameric pairs that look the same for many different light sources. The same is true for the case of different observers: as the physiological perception of color can have individual differences, metameric color impressions can be equal for one observer and differ for another observer. Isometric color impressions with equal spectra are perceived as equal by all observers [5].

Human perception can partially compensate for the influences of illumination [17,38]—especially for broadband spectra of illumination like the sunlight for different times of the day or direct and indirect (shadow) daylight, for example (cf. Fig. 1.1 on p. 5). The different adaptation of the color perception to the ambient light can, to a first order approximation, be modeled as a linear transformation (vector space homomorphism) of the space of tristimuli [8,43]. In the field of photography too, methods are used to make color rendering independent of the spectrum of the illumination [13,26]. Such methods are related to the term white balance or color balance.

### 5.2.2 Color mixing

The two fundamentally different principles of color mixing are additive and subtractive color mixing. The incoherent superposition of light of different colors is called additive color mixing. Physically, the spectra of the intensities of the two light waves  $I_1(\lambda)$  and  $I_2(\lambda)$  are added according to (2.126):

$$I(\lambda) = I_1(\lambda) + I_2(\lambda). \quad (5.7)$$

The resulting spectrum  $I(\lambda)$  represents a color impression, leading to a perceived tristimulus. **Grassmann's laws** represent a connection between the tristimuli of the summands and the resulting tristimulus:

1. Three primary colors and an additional color impression are considered. Then the intensities of the three primary colors can be chosen in such a way that two identical color impressions are created by inner or outer color mixing. For inner color mixing, the three primary colors are mixed with each other with varying intensities and result in the fourth color. For outer color mixing, one or two of the three primary colors are mixed with the fourth color, resulting in the mixture of the remaining colors.
2. In additive color mixing, each color can be replaced by a metameric color, without changing the color impression.
3. All color mixings are continuous.

These empirical laws were formulated in 1853 [4, 19]. The three primary colors correspond to the three dimensions of the space of the tristimuli and to the number of different kinds of color receptors of the human eye. However, it is not always possible to reproduce an arbitrary color by mixing the three primary colors. In fact, there are cases where only the additive mixture of one or two of the primary colors with the fourth color can lead to a match with the mixture of the remaining primary colors. This issue will be further discussed in the following section.

The continuity of the color mixture corresponds to the linear superposition of the spectra of the intensities. Continuously changing a primary color leads to a continuous change of

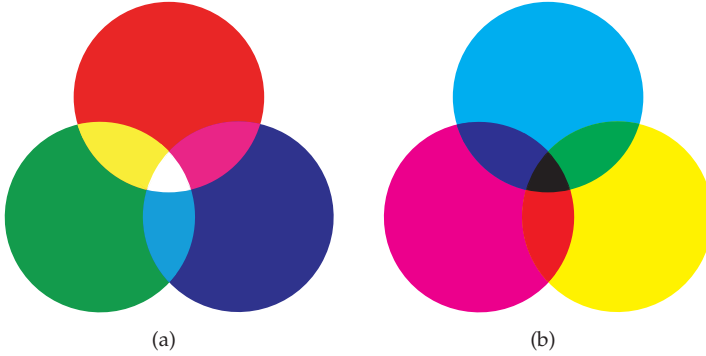


Figure 5.8. Color mixing with three primary colors: (a) Additive, (b) Subtractive.

the mixed color. Uniformly mixing the primary colors leads to a white color impression (Fig. 5.8 (a)). If no visible light is emitted by an object, it appears black.

There are arbitrarily many bases of mixture components, which can be used to mix a given color. Therefore a base system has to be defined. The chosen primary colors have to meet the condition that none of them can result from the mixture of the remaining primary colors [43]. For additive color mixing, usually red, green and blue are chosen as the primary colors. Additive color mixing is used in displays and projectors, for example (see Sec. 5.2.6.2).

Subtractive color mixing occurs if colorants are mixed. A colorant is a coloring material like a pigment or soluble dye, for example. The effect of colorants is based on a wavelength dependent absorption: in some parts of the spectrum, a certain amount of the incident light is absorbed, in other parts it is reflected or transmitted. The color impression is caused by the spectrum that remains after the absorption. If two colorants are mixed with each other, the spectral parts of absorption are combined and so less light is reflected. Thus, a certain part of the observed spectrum is removed, which is why this kind of color mixing is called subtractive. The resulting color impression also depends on the illumination. White corresponds to a complete reflection without any absorption and thus cannot be achieved by subtractive color mixing of two or more colorants. If a colorant is added, the absorption is always increased.

For subtractive color mixing, cyan, magenta and yellow are usually chosen as the primary colors. Mixing these three colorants results in gray or black (Fig. 5.8 (b)). For economic reasons, black is usually not produced by mixing colors but is provided as an additional colorant. The resulting color system is called CMYK (cyan, magenta, yellow, key) and is a common color system in the field of color printing (see Sec. 5.2.6.5). The combination of different color filters is also a form of subtractive color mixing (Sec. 5.3).

The subtractive mixing of absorbing colorants can be approximately described by using the Lambert–Beer law of absorption [5]. The absorption  $A_{\text{Col}}(\lambda)$  of a colorant as a function of the wavelength is the product of the material dependent absorption constant  $a_{\text{Col}}(\lambda)$ , the thickness of the coating  $d_{\text{Col}}$ , and the chemical concentration  $c_{\text{Col}}$  of the colorant:

$$A_{\text{Col}}(\lambda) = a_{\text{Col}}(\lambda) d_{\text{Col}} c_{\text{Col}}. \quad (5.8)$$

If two colorants with known concentrations  $c_{\text{Col1}}$  and  $c_{\text{Col2}}$  are mixed in a common, homogeneous layer of thickness  $d_{\text{Col}}$ , the absorptions are added:

$$A_{\text{Col}}(\lambda) = A_{\text{Col1}}(\lambda) + A_{\text{Col2}}(\lambda) \quad (5.9)$$

$$= a_{\text{Col1}}(\lambda) d_{\text{Col}} c_{\text{Col1}} + a_{\text{Col2}}(\lambda) d_{\text{Col}} c_{\text{Col2}}. \quad (5.10)$$

If the illumination's spectrum is  $I_{\text{Light}}(\lambda)$ , the transmitted spectrum of the colorant is exponentially dependent on the absorption:

$$I_{\text{Col}}(\lambda) = I_{\text{Light}}(\lambda) e^{-A_{\text{Col}}(\lambda)} = I_{\text{Light}}(\lambda) e^{-(A_{\text{Col1}}(\lambda) + A_{\text{Col2}}(\lambda))}. \quad (5.11)$$

Besides absorption, scattering is also important for most colorants. Often, the scattering is caused by a white colorant or a base material (color printing or textiles for example), whereas the remaining colorants of the mixture do not exhibit notable scattering [5]. A model for subtractive color mixing that pays attention to scattering is the so-called Kubelka–Munk theory [41]. If two colorants with concentrations  $c_{\text{Col1}}$  and  $c_{\text{Col2}}$  are mixed, the quotient of the absorption  $a_{\text{Col}}(\lambda)$  and the scattering  $s_{\text{Col}}(\lambda)$  is given by:

$$\frac{a_{\text{Col}}(\lambda)}{s_{\text{Col}}(\lambda)} = \frac{c_{\text{Col1}} a_{\text{Col1}}(\lambda) + c_{\text{Col2}} a_{\text{Col2}}(\lambda)}{c_{\text{Col1}} s_{\text{Col1}}(\lambda) + c_{\text{Col2}} s_{\text{Col2}}(\lambda)}. \quad (5.12)$$

The spectral reflectance  $R_{\text{Col}}(\lambda)$  of a colorant is connected to its absorption and scattering as follows:

$$\frac{a_{\text{Col}}(\lambda)}{s_{\text{Col}}(\lambda)} = \frac{(1 - R_{\text{Col}}(\lambda))^2}{2R_{\text{Col}}(\lambda)}, \quad (5.13)$$

$$R_{\text{Col}}(\lambda) = 1 + \frac{a_{\text{Col}}(\lambda)}{s_{\text{Col}}(\lambda)} - \sqrt{\left(\frac{a_{\text{Col}}(\lambda)}{s_{\text{Col}}(\lambda)}\right)^2 + 2 \frac{a_{\text{Col}}(\lambda)}{s_{\text{Col}}(\lambda)}}. \quad (5.14)$$

The resulting spectrum of intensities is given by

$$I_{\text{Col}}(\lambda) = I_{\text{Light}}(\lambda) R_{\text{Col}}(\lambda). \quad (5.15)$$

In order to reduce the influence of specular reflections, an additional correction of the spectral reflectance can be performed [5]. In general however, the resulting equations only approximately model subtractive color mixing [41].

### 5.2.3 CIE color spaces

The already mentioned tristimulus is the fundamental term for colorimetry. If two color impressions  $I(\lambda)$  cannot be distinguished when compared two each other or other colors, they have exactly the same tristimuli. A tristimulus can be measured by comparing it to a mixture of three primary colors, which are distinctively defined by their spectra. So the tristimulus is defined by a psychophysical measurement method, that allows a quantitative measurement. A tristimulus is an objective quantity inasmuch as it is independent of the color impression caused by the corresponding color stimulus.

The process for measuring the tristimulus of a light source was standardized in 1931 by the CIE<sup>3</sup> [11]. The observer simultaneously views the light of the sample light source and the incoherent superposition of three light sources of three primary colors (Fig. 5.9). The

<sup>3</sup>Commission Internationale de l'Éclairage – International Commission on Illumination

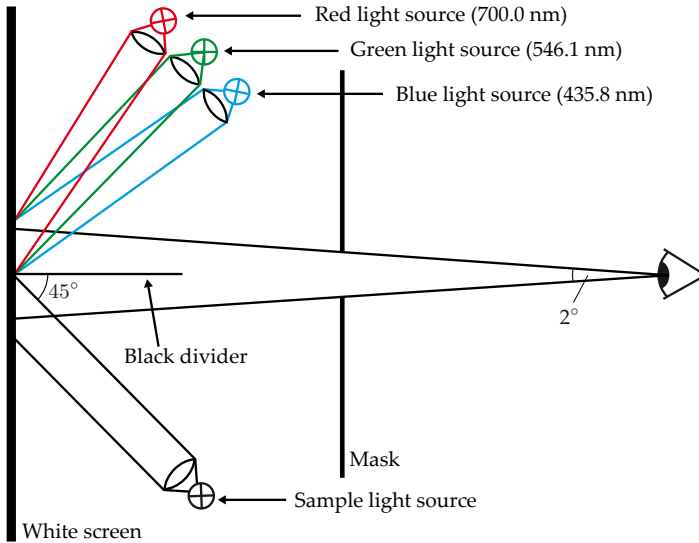


Figure 5.9. Experiment for empirically determining the color of a light source in terms of the CIE primary colors [5].

intensities of the light sources emitting the primary colors are adjusted, so that their additive superposition cannot be distinguished from the sample light source. The color coordinates of the tristimulus of the sample light source are now given by the chosen ratios of the three light sources.

In order to make the experiment as objective as possible, the test conditions were exactly defined. The observer simultaneously views the sample light source and the mixture of the three primary colors on an untextured surface. The surface is illuminated under an angle of approximately  $45^\circ$  and is observed under an angle of about  $0^\circ$  with allowed differences of  $5^\circ$  or  $10^\circ$  respectively [14].<sup>4</sup> The bundle of rays of illumination and observation are supposed to be parallel, with a maximum difference of  $5^\circ$  in the direction of the principal ray [43]. The field of view has an extent of  $2^\circ$ , so that the illuminated surface is imaged on the fovea of the eye.<sup>5</sup> The measurement is done by an observer with a relaxed, normal eye (neither shortsighted nor farsighted), that is light adapted. Only one eye is used for the observation.

Nearly monochromatic light sources with wavelengths of 700 nm (red), 546.1 nm (green) and 435.8 nm (blue) are used for the comparison.<sup>6</sup> The measured ratios of these three CIE primary light sources are called the color values.

Figure 5.10 shows the empirically determined color values of the spectral colors. A spectral color or a monochromatic color is a spectrum having only a narrow maximum for a certain wavelength  $\lambda_0$  and having values equal to zero otherwise. Color values as a function

<sup>4</sup>For alternative configurations of illumination and observation, see [43].

<sup>5</sup>As the distribution of receptors differs for the fovea and the remaining retina, the color impression depends on whether the image is imaged on the fovea or on the periphery. Therefore an additional standard with a field of view of  $10^\circ$  was defined later on [5, 43].

<sup>6</sup>The latter two wavelengths correspond to the spectral lines of a mercury-vapor lamp and can thus be generated at low cost [14].

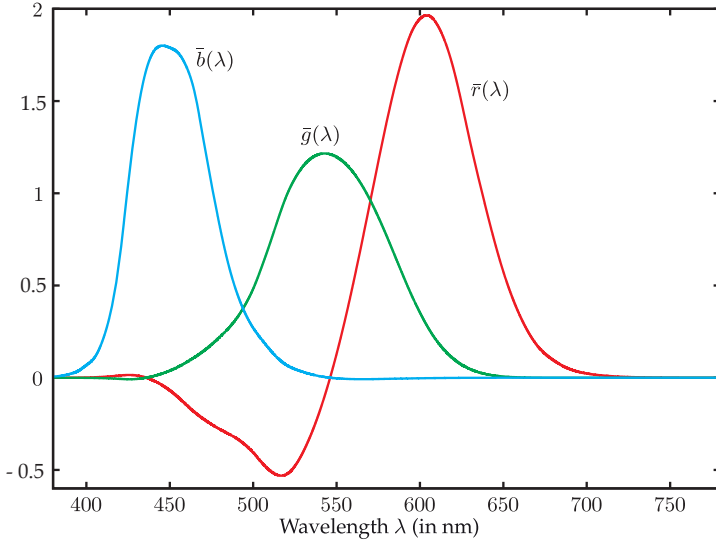


Figure 5.10. Color values of the monochromatic spectral colors with respect to the CIE primary colors (adopted from [43]).

of the wavelength  $\lambda$  of the monochromatic light are denoted by  $\bar{r}(\lambda)$ ,  $\bar{g}(\lambda)$  and  $\bar{b}(\lambda)$ . The color values of an arbitrary spectrum  $I(\lambda)$  can be calculated by multiplying the spectrum by these functions and then integrating:

$$\begin{aligned}
 R_{\text{CIE}} &= \int_{380 \text{ nm}}^{780 \text{ nm}} I(\lambda) \bar{r}(\lambda) d\lambda, \\
 G_{\text{CIE}} &= \int_{380 \text{ nm}}^{780 \text{ nm}} I(\lambda) \bar{g}(\lambda) d\lambda, \\
 B_{\text{CIE}} &= \int_{380 \text{ nm}}^{780 \text{ nm}} I(\lambda) \bar{b}(\lambda) d\lambda.
 \end{aligned}
 \tag{5.16}$$

These functions were scaled so that a white color stimulus leads to three identical color values  $R_{\text{CIE}} = G_{\text{CIE}} = B_{\text{CIE}}$  [43]. A white color stimulus is a spectrum having a constant intensity for all wavelengths belonging to the visible part of the spectrum:

$$I_{\text{E}}(\lambda) = \begin{cases} 1 & \text{if } 360 \text{ nm} \leq \lambda \leq 830 \text{ nm} \\ 0 & \text{otherwise} \end{cases}.
 \tag{5.17}$$

Now, the condition  $R_{\text{CIE}} = G_{\text{CIE}} = B_{\text{CIE}}$  becomes

$$\int_{380 \text{ nm}}^{780 \text{ nm}} \bar{r}(\lambda) d\lambda = \int_{380 \text{ nm}}^{780 \text{ nm}} \bar{g}(\lambda) d\lambda = \int_{380 \text{ nm}}^{780 \text{ nm}} \bar{b}(\lambda) d\lambda.
 \tag{5.18}$$

This condition sets the relative scaling of the three spectral functions. This absolute scaling ensures that the area under the curves is equal to the area under the luminosity function

$V(\lambda)$  of Fig. 5.1 [14]:

$$\int_{380 \text{ nm}}^{780 \text{ nm}} \bar{r}(\lambda) d\lambda = \int_{380 \text{ nm}}^{780 \text{ nm}} \bar{g}(\lambda) d\lambda = \int_{380 \text{ nm}}^{780 \text{ nm}} \bar{b}(\lambda) d\lambda = \int_{380 \text{ nm}}^{780 \text{ nm}} V(\lambda) d\lambda. \quad (5.19)$$

Because of this scaling, the weights  $\bar{r}$ ,  $\bar{g}$ ,  $\bar{b}$  do not correspond to the radiation intensity of the three primary light sources. In fact, the weight  $\bar{g} = 1$  corresponds to an intensity of the green primary light source that is 1.3791 times higher than the intensity of a blue primary light source with a weight of  $\bar{b} = 1$ . For a red primary light source, the weight  $\bar{r} = 1$  corresponds even to 72.0962 times the intensity of  $\bar{b} = 1$ , as the sensitivity of the human eye to brightness decreases extensively for  $\lambda = 700 \text{ nm}$  (cf. Fig. 5.1).

However, not all colors can be mixed from the three CIE primary light sources under the described test conditions. Sometimes it is necessary to mix the sample light source with one of the primary light sources, in order to achieve equal colors. In this case, a negative component is assigned to the respective primary light source. Figure 5.10 shows that this is the case for the red CIE primary light source and a spectral color of wavelength 500 nm. In fact,  $\bar{g}(\lambda)$  is negative until 440 nm and  $\bar{b}(\lambda)$  is negative starting from 550 nm.

Therefore, a transformed color space was defined, where no negative weights are possible. As computers were not that powerful in former times, the transformation should also reduce the costs for calculating the integrals (5.16) [14, 43]. In addition, one of the resulting standard color values was supposed to be equal to the luminosity function, making the additional calculation of the brightness of a color stimulus.

The transformed color space is called the CIE XYZ color space. Its coordinates are the tristimulus values  $X, Y, Z$ . The transformed color value functions of the monochromatic spectral colors are called the color matching functions  $\bar{x}(\lambda), \bar{y}(\lambda), \bar{z}(\lambda)$ . The transformation of the color space  $(R_{\text{CIE}}, G_{\text{CIE}}, B_{\text{CIE}})^T$  of the CIE primary light sources to the CIE XYZ color space  $(X, Y, Z)^T$  of the virtual primary colors is a vector space homomorphism:

$$\begin{pmatrix} X \\ Y \\ Z \end{pmatrix} = \mathbf{A} \begin{pmatrix} R_{\text{CIE}} \\ G_{\text{CIE}} \\ B_{\text{CIE}} \end{pmatrix} \quad \mathbf{A} \in \mathbb{R}^{3 \times 3}. \quad (5.20)$$

This equation also transforms the color value functions:

$$\begin{pmatrix} \bar{x}(\lambda) \\ \bar{y}(\lambda) \\ \bar{z}(\lambda) \end{pmatrix} = \mathbf{A} \begin{pmatrix} \bar{r}(\lambda) \\ \bar{g}(\lambda) \\ \bar{b}(\lambda) \end{pmatrix}. \quad (5.21)$$

The degrees of freedom in the choice of the matrix  $\mathbf{A}$  were used according to the following criteria [5, 14]:

- The tristimulus values  $X, Y, Z$  of all real color stimuli are nonnegative:

$$X \geq 0, \quad Y \geq 0, \quad Z \geq 0. \quad (5.22)$$

- The real color stimuli preferably occupy an extensive area in the plane  $X + Y + Z = 1$  of the nonnegative tristimulus values.
- The tristimulus value  $Y$  corresponds to the photopic brightness  $V$  of a color stimulus. Therefore, the color matching function  $\bar{y}(\lambda)$  has to be equal to the photopic luminosity

function  $V(\lambda)$ . Thus, the following has to hold for suitable weights  $L_R, L_G, L_B$ :

$$\forall \lambda : \quad V(\lambda) = \bar{y}(\lambda) = L_R \bar{r}(\lambda) + L_G \bar{g}(\lambda) + L_B \bar{b}(\lambda). \quad (5.23)$$

Thus, two color stimuli having identical tristimuli in the CIE XYZ color space also have the same brightness. This is an advantage for image processing, as the  $Y$ -channel of transformed color image equals the corresponding gray-scale image [27].

- Still, the white color stimulus (5.17) is given by three equal XYZ values  $X = Y = Z$ . Therefore, in analogy to (5.18), the following has to hold for the color matching functions  $\bar{x}(\lambda)$ ,  $\bar{y}(\lambda)$  and  $\bar{z}(\lambda)$ :

$$\int_{380 \text{ nm}}^{780 \text{ nm}} \bar{x}(\lambda) d\lambda = \int_{380 \text{ nm}}^{780 \text{ nm}} \bar{y}(\lambda) d\lambda = \int_{380 \text{ nm}}^{780 \text{ nm}} \bar{z}(\lambda) d\lambda. \quad (5.24)$$

- The white point  $(R_{\text{CIE}}, G_{\text{CIE}}, B_{\text{CIE}})^T = (1, 1, 1)^T$  is mapped to  $(X, Y, Z)^T = (1, 1, 1)^T$  [14].
- The color matching function  $\bar{z}(\lambda)$  is equal to zero, starting from a preferably low maximum wavelength  $\lambda_{\bar{z} \text{ max}}$ :

$$\forall \lambda \geq \lambda_{\bar{z} \text{ max}} : \quad \bar{z}(\lambda) = 0. \quad (5.25)$$

- The transformation is invertible.

The following transformation matrix  $\mathbf{A}$  was chosen to meet these conditions to a large extent [14]:

$$\mathbf{A} = \begin{pmatrix} 0.49 & 0.31 & 0.20 \\ 0.17697 & 0.81240 & 0.01063 \\ 0.00 & 0.01 & 0.99 \end{pmatrix}. \quad (5.26)$$

The factors  $L_R = 0.17697$ ,  $L_G = 0.81240$ ,  $L_B = 0.01063$  for the construction of the luminosity function of (5.23) are located in the second row of the matrix. The contribution of the short-wave  $B$ -channel to the luminosity function is very low. Figure 5.11 shows the CIE color matching functions for monochromatic light that result from the transformation of the color matching functions of the CIE primary light sources of Fig. 5.10.

The inverse transformation is given by

$$\begin{pmatrix} R_{\text{CIE}} \\ G_{\text{CIE}} \\ B_{\text{CIE}} \end{pmatrix} = \mathbf{A}^{-1} \begin{pmatrix} X \\ Y \\ Z \end{pmatrix} \quad (5.27)$$

with

$$\mathbf{A}^{-1} \approx \begin{pmatrix} 2.365 & -0.8965 & -0.4681 \\ -0.5152 & 1.426 & 0.08876 \\ 0.005204 & -0.01441 & 1.009 \end{pmatrix}. \quad (5.28)$$

The basis vectors of the CIE XYZ color space are called **virtual primary colors**. Their coordinates with respect to the CIE primary light sources are given by the columns of the inverse



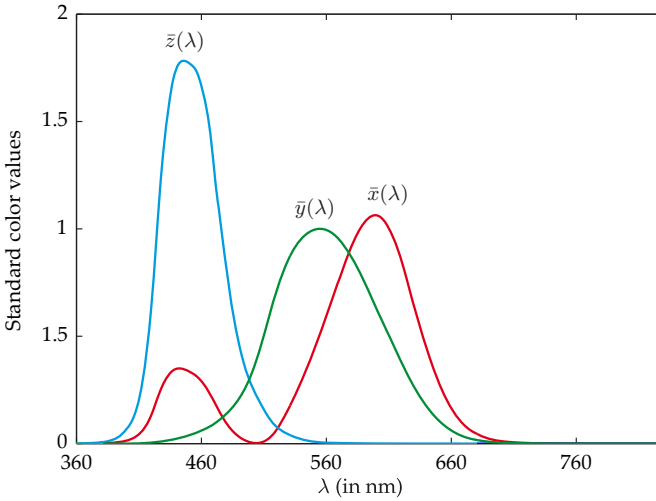


Figure 5.11. CIE color matching functions for monochromatic light of wavelength  $\lambda$  (adopted from [43]).

transformation matrix  $\mathbf{A}^{-1}$ :

$$\mathbf{X}_{\text{prim}} = \begin{pmatrix} 2.365 \\ -0.5152 \\ 0.005204 \end{pmatrix}, \quad \mathbf{Y}_{\text{prim}} = \begin{pmatrix} -0.8965 \\ 1.426 \\ -0.01441 \end{pmatrix}, \quad \mathbf{Z}_{\text{prim}} = \begin{pmatrix} -0.4681 \\ 0.08876 \\ 1.009 \end{pmatrix}. \quad (5.29)$$

The vector space homomorphism corresponds to a change of basis from the primary light sources to the virtual primary colors. The basis vectors of the virtual primary colors are more spread than those of the primary light sources, so that all real colors can be described with positive tristimulus values (Fig. 5.12). Whereas the basis vector  $\mathbf{Y}_{\text{prim}}$  corresponds to the brightness of a color stimulus, the brightness of the virtual primary colors  $\mathbf{X}_{\text{prim}}$  and  $\mathbf{Z}_{\text{prim}}$  is zero.

The color matching functions can be used to calculate the tristimulus values  $X, Y, Z$  for a given color stimulus  $I(\lambda)$ :

$$X = k \int_{360 \text{ nm}}^{830 \text{ nm}} I(\lambda) \bar{x}(\lambda) d\lambda, \quad (5.30)$$

$$Y = k \int_{360 \text{ nm}}^{830 \text{ nm}} I(\lambda) \bar{y}(\lambda) d\lambda, \quad (5.31)$$

$$Z = k \int_{360 \text{ nm}}^{830 \text{ nm}} I(\lambda) \bar{z}(\lambda) d\lambda, \quad (5.32)$$

$$k = \frac{100}{\int_{360 \text{ nm}}^{830 \text{ nm}} I_{\text{achromatic}}(\lambda) \bar{y}(\lambda) d\lambda}. \quad (5.33)$$

The color matching functions are defined on the interval from [360 nm, 830 nm] [43]. However, on the boundary of their domain, they take on very small values, as the human eye is not sensitive to wavelengths there. Therefore, it has nearly no effect on the tristimulus

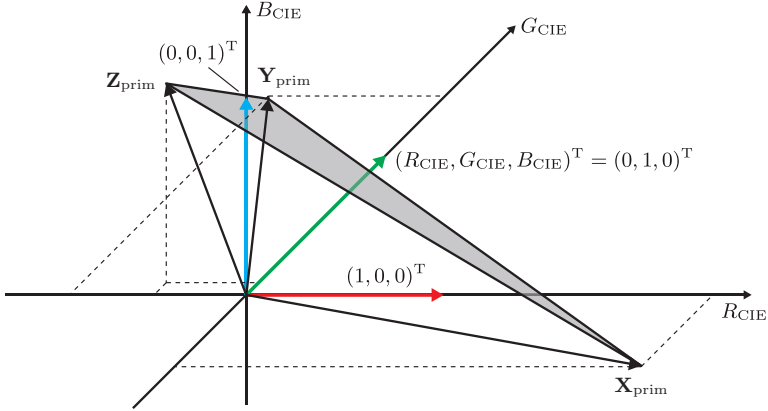


Figure 5.12. Position of the virtual primary colors in the color space of the CIE primary light sources. The colored vectors are the basis vectors of the CIE primary light sources.

values, if in (5.30)–(5.33) a smaller integration interval, like [380 nm, 780 nm], is chosen. The function  $I_{\text{achromatic}}(\lambda)$  describes a reference spectrum of a white color impression, like the standard illuminant D65. Because of the scaling factor  $k$ , the chosen white color stimulus is assigned the brightness  $Y = 100$ . If the XYZ tristimulus values of two light sources with the spectra  $I_1(\lambda), I_2(\lambda)$  are equal to each other, i.e.,  $X_1 = X_2, Y_1 = Y_2, Z_1 = Z_2$ , then they appear to have equal colors and brightnesses to a healthy human eye.

In order to characterize a color without paying attention to brightness, a two-dimensional space is sufficient. For this purpose, the normalized color values  $x, y$  and  $z$  can be calculated from the tristimulus values  $X, Y$  and  $Z$ :

$$\begin{aligned}
 x &= \frac{X}{X + Y + Z}, \\
 y &= \frac{Y}{X + Y + Z}, \\
 z &= \frac{Z}{X + Y + Z}.
 \end{aligned}
 \tag{5.34}$$

This transformation corresponds to a central projection of the point  $(X, Y, Z)^T$  onto the plane  $X + Y + Z = 1$ , with the projection center being located at the origin of the coordinate system. Because  $x + y + z = 1$ , one of the three normalized color values is redundant, so that  $z$  can be omitted. This corresponds to an additional parallel projection of the plane  $X + Y + Z = 1$  to the plane  $Z = 0$  [8, 14].

The normalized color values  $x$  and  $y$  characterize a color independently of its brightness, and are therefore often referred to as chromaticity coordinates. Together with the brightness or luminance channel  $Y$ , they describe a unique tristimulus. The inverse transformation of

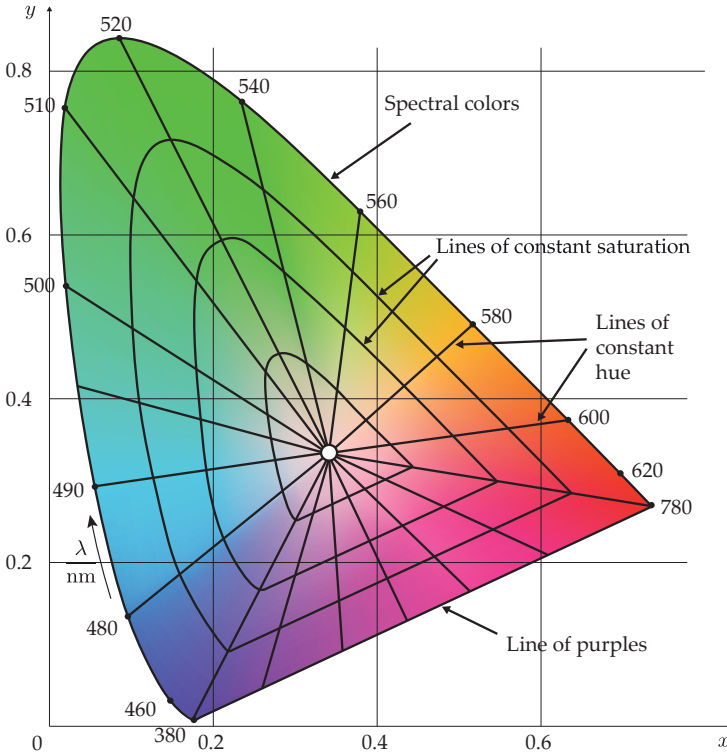


Figure 5.13. CIE chromaticity diagram.

the triplet  $(x, y, Y)$  to the CIE XYZ color space given by

$$\begin{aligned}
 X &= \frac{x}{y} Y, \\
 Y &\mapsto Y, \\
 Z &= \frac{z}{y} Y = \frac{1 - x - y}{y} Y.
 \end{aligned}
 \tag{5.35}$$

A linear transformation of the color values corresponds to a non-linear projective transformation of the normalized color values. For example the normalized color values  $r_{\text{CIE}} = \frac{R_{\text{CIE}}}{R_{\text{CIE}} + G_{\text{CIE}} + B_{\text{CIE}}}$ ,  $g_{\text{CIE}} = \frac{G_{\text{CIE}}}{R_{\text{CIE}} + G_{\text{CIE}} + B_{\text{CIE}}}$ ,  $b_{\text{CIE}} = \frac{B_{\text{CIE}}}{R_{\text{CIE}} + G_{\text{CIE}} + B_{\text{CIE}}}$ , which are calculated from the color values  $R_{\text{CIE}}, G_{\text{CIE}}, B_{\text{CIE}}$  according to (5.16) and the analog of (5.34), are connected to the normalized color values  $x, y, z$  as follows [43]:

$$\begin{pmatrix} x \\ y \\ z \end{pmatrix} = \frac{1}{0.66697 r_{\text{CIE}} + 1.1324 g_{\text{CIE}} + 1.20063 b_{\text{CIE}}} \mathbf{A} \begin{pmatrix} r_{\text{CIE}} \\ g_{\text{CIE}} \\ b_{\text{CIE}} \end{pmatrix}.
 \tag{5.36}$$

The coefficients of the denominator are given by the column sums of the matrix  $\mathbf{A}$  from (5.26).

With the components  $x$  and  $y$ , a color is described independent of its brightness. The drawing of the colors in the  $x, y$ -plane is called the **CIE chromaticity diagram** (Fig. 5.13). All possible coordinates are located inside the triangle  $x \geq 0, y \geq 0, x + y \leq 1$ . However, not all points inside this triangle correspond to a real color impression. The spectral colors lie on a closed curve that partly represents the border of perceivable colors. A part of that region's border cannot be described by pure spectral colors and is called the line of purples. Because of (5.24), the white point is located at  $x = y = \frac{1}{3}$ . The saturation decreases along a line from the border of the chromaticity diagram to its center, the achromatic component of the color increases, and the color fades. However, the hue remains unchanged. It is characterized by the intersection of the line and the curves of the spectral colors. The wavelength corresponding to that intersection is called the dominant wavelength of the hue if the intersection and the color are on the same side of the white point. There is no dominant wavelength for colors between the white point and the line of purples. Instead, the complementary wavelength can be specified, which lies on the opposite side of the white point and is given by the intersection of the line with the curve of the spectral color on the opposite side of the white point.

These lines of constant hues are crossed by curves of constant saturation, on which only the hue is variable. The colors of maximum saturation are located on the border of the chromaticity diagram. There are no metameric color stimuli for these fully saturated colors, i.e., the spectrum is fully described by the tristimulus. The tristimuli on the curve of spectral colors are caused by monochromatic line spectra. For all colors inside the chromaticity diagram, there are infinitely many metameric spectra. The probability that a spectrum that is randomly chosen from a uniform distribution is metameric to a given color increases for decreasing saturation and has its maximum for the white point [43].

The chromaticity diagram directly shows which colors can be composed from given base colors by additive color mixing:

---

#### Theorem 5.1: Additive color mixing

Let  $(x_i, y_i)$ ,  $i = 1, \dots, N$  be the  $(x, y)$  chromaticity coordinates of  $N$  colors inside the chromaticity diagram. Additive color mixing of these colors with arbitrary weighting factors  $\alpha_i$  results in all colors that lie inside the convex hull of the points  $(x_i, y_i)$  in the chromaticity diagram. In particular:

- $N = 2$ : Out of two colors, all colors that lie on their connecting line can be composed by using additive color mixing.
- $N = 3$ : Out of three colors, all colors that lie inside a triangle in the chromaticity diagram, whose corners consist of the original three colors, can be composed by using additive color mixing of those three colors.  $\diamond$

---

**Proof 5.1 (Additive color mixing):** First consider the case  $N = 2$ . Let the two base colors have the chromaticity coordinates  $(x_1, y_1)^T, (x_2, y_2)^T$  in the chromaticity diagram. Let  $(X_1, Y_1, Z_1)^T, (X_2, Y_2, Z_2)^T$  be the XYZ tristimuli of the corresponding light sources. By (5.7), the additive mixture of the two light sources in combination with the weighting factors  $\alpha_1$  and  $\alpha_2$  corresponds to the weighted sum of their spectra of intensities in accor-

dance with (5.7):

$$I(\lambda) = \alpha_1 I_1(\lambda) + \alpha_2 I_2(\lambda). \quad (5.37)$$

Because of the linearity of the integral in (5.30)–(5.32), the tristimuli are added with the same weighting factors:

$$X = \alpha_1 X_1 + \alpha_2 X_2, \quad Y = \alpha_1 Y_1 + \alpha_2 Y_2, \quad Z = \alpha_1 Z_1 + \alpha_2 Z_2.$$

This leads to the chromaticity values

$$x = \frac{\alpha_1 X_1 + \alpha_2 X_2}{\alpha_1(X_1 + Y_1 + Z_1) + \alpha_2(X_2 + Y_2 + Z_2)} \quad (5.38)$$

$$= \frac{X_1 + \frac{\alpha_2}{\alpha_1} X_2}{X_1 + Y_1 + Z_1 + \frac{\alpha_2}{\alpha_1}(X_2 + Y_2 + Z_2)}, \quad (5.39)$$

$$y = \frac{\alpha_1 Y_1 + \alpha_2 Y_2}{\alpha_1(X_1 + Y_1 + Z_1) + \alpha_2(X_2 + Y_2 + Z_2)} \quad (5.40)$$

$$= \frac{Y_1 + \frac{\alpha_2}{\alpha_1} Y_2}{X_1 + Y_1 + Z_1 + \frac{\alpha_2}{\alpha_1}(X_2 + Y_2 + Z_2)}. \quad (5.41)$$

These color values lie on a line through  $(x_1, y_1)^T$  and  $(x_2, y_2)^T$ :

$$\frac{y - y_1}{x - x_1} = \frac{y_2 - y_1}{x_2 - x_1}. \quad (5.42)$$

For a fixed  $\alpha_2$  and  $\alpha_1 \rightarrow 0$ , it follows that  $(x, y)^T \rightarrow (x_2, y_2)^T$ , and for  $\alpha_1 \rightarrow \infty$ , it follows that  $(x, y)^T \rightarrow (x_1, y_1)^T$ .

Conversely, suppose that a mixed color  $(\beta x_1 + (1 - \beta)x_2, \beta y_1 + (1 - \beta)y_2)^T$  lies on the connecting line, with  $0 \leq \beta \leq 1$ . This mixed color is obtained by combining the two corresponding light sources with weighting factors  $\alpha_1 = \beta(X_2 + Y_2 + Z_2)$  and  $\alpha_2 = (1 - \beta)(X_1 + Y_1 + Z_1)$ . Colors not lying on that line cannot be mixed from the two light sources.

The last statement can be generalized to explain the case for  $N = 3$ : it is clear that two colors can be combined to mix a color on their connecting line. Now, this mixed color can be added to the third base color. With this procedure, an arbitrary point inside the triangle can be constructed.

An analogous induction step results in the proof for general  $N$ . ■

For two or three base colors, their mix ratios are set by the sought-for mixed color. For more than three colors, the mix ratios are no longer unique, but for suitable base colors, a larger area of the chromaticity diagram can be covered.

As the chromaticity diagram is convex, for each mixed color there is always a corresponding real color stimulus. Two colors are called complementary colors if their connecting line goes through the white point [19]. The color white can be produced by an additive mixture of two complementary colors. If two complementary colors are maximally saturated, at least one of them has to be a pure spectral color.

Color spaces that are produced by a projective transformation of the chromaticity diagram, like (5.36) for example, also have these properties of additive color mixing, as a projective transformation always maps lines to lines [43]. An example for such a color space is

the CIELUV color space with the coordinates  $L^*$ ,  $u^*$  and  $v^*$ , which will not be covered in this book.

The coordinates of the virtual primary colors  $\mathbf{X}_{\text{prim}}$ ,  $\mathbf{Y}_{\text{prim}}$ ,  $\mathbf{Z}_{\text{prim}}$  in the  $x, y$  chromaticity diagram are  $(1, 0)^T$ ,  $(0, 1)^T$  and  $(0, 0)^T$ . Although they do not correspond to real color stimuli, all real colors can be mixed from these virtual base colors, as they are part of the corresponding triangle. This also shows that it is not possible in general to obtain all colors by mixing three real base colors. This is because all mixable colors lie inside a triangle and the special shape of the chromaticity diagram can never be contained in a triangle having real colors as corners. This consideration explains why it is not possible to obtain all real colors by mixing the CIE primary light sources. In the chromaticity diagram, the CIE primary light sources are located on the border of the real colors at  $(x, y)^T = (0.73; 0.27)^T$ ,  $(0.27; 0.72)^T$  and  $(0.17; 0.0089)^T$ , which can be calculated using (5.26) and (5.34) (Fig. 5.15). Certain shades of green and blue cannot be mixed from these light sources. For monochromatic colors, this is the case if there are negative color values in Fig. 5.10.

In contrast to the additive case, subtractive color mixing cannot be explained so easily using the chromaticity diagram. This is because the chromaticity diagram is defined over the additive color mixing used in the empirical experiment Fig. 5.9 for measuring colors. In order to calculate the subtractive mixture of two colorants, the Lambert–Beer law or the Kubelka–Munk equations of Sec. 5.2.2 have to be applied to their absorption and scatter. Then, the spectrum of the mixed color can be used to calculate its tristimulus value. A direct calculation based on the tristimulus values of the base colors is not possible. For subtractive color mixing, the mixed color is generally not part of the line connecting the base colors in the chromaticity diagram. The set of possible mix colors is usually not given by the induced triangle<sup>7</sup> but by an area bordered by nonlinear curves. It is often possible that colors outside the triangle can be obtained by subtractive color mixing [5]. However, it is not possible to obtain all perceivable colors by combining only a few colors with subtractive color mixing. This is why the print of this book is limited to a reduced set of colors, so that all printed chromaticity diagrams and visualizations of color spaces have to be considered as rough approximations of the actual colors.

The visualization of colors in the chromaticity diagram is limited by the following constraints<sup>8</sup>:

- The tristimulus values  $x, y$  do not correspond to intuitive coordinate axes, like hue and saturation for example.
- The distance between two colors is not characterized by the distance between the corresponding points in the chromaticity diagram. For example, green colors are resolved in much more detail than blue colors. The distance between two colors that can barely be distinguished by the human eye is described by the MacAdam ellipses in the chromaticity diagram or the  $(x, y, Y)$  space. They are considerably larger for shades of green than for shades of red, violet and especially blue. Besides, the ellipses are very eccentric, which means that a distance in the  $x$ -direction in the chromaticity diagram corresponds to a distinctively smaller visually perceived difference between colors than the same distance in the  $y$ -direction, or vice versa.

<sup>7</sup>Or a polygon, if more than three base colors are used.

<sup>8</sup>Besides, it is very unpleasant that the position of perfect black  $X = Y = Z = 0$  in the chromaticity diagram is not well-defined according to (5.34) [5].

Because of these limitations, other color spaces are more suitable for some applications than is the chromaticity diagram. A possibility for constructing a color space with clear coordinate axes and consistent color distances is given by the opponent-process theory. Here, colors are circularly arranged around the white point, so that opposed colors always exclude each other. This process conforms to the physiological theory of color perception sketched in Sec. 5.2.1 (cf. Fig. 5.6).

The **CIELAB color space** with coordinates  $L^*$ ,  $a^*$  and  $b^*$  is based on the opponent-process theory. The brightness is denoted by  $L^*$  and is obtained from the cube root of the tristimulus value  $Y$ . This transformation ensures that equal differences in  $L^*$  approximately correspond to equal differences in the perceived brightness [5]. The definition of the CIELAB coordinates  $a^*$  and  $b^*$  is based on empirical observations, resulting in an approximately equidistant color space. The  $a^*$ -axis describes the difference between the red and green components of the color, so that negative values correspond to green and positive values to red colors. Similarly, negative values on the  $b^*$ -axis describe blue and positive values yellow colors (Fig. 5.14). The white point is located at  $L^* = 100$ ,  $a^* = b^* = 0$ . All points on the line  $a^* = b^* = 0$  correspond to achromatic colors, and perfect black is located at  $L^* = 0$ .

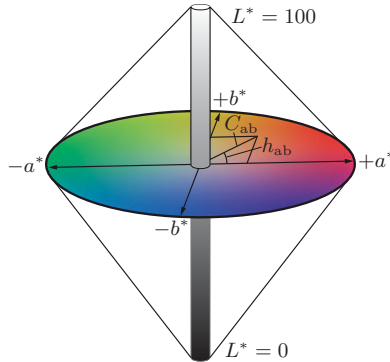


Figure 5.14. The CIELAB color space with the coordinates  $L^*$ ,  $a^*$ ,  $b^*$  as well as the polar coordinates  $C_{ab}$ ,  $h_{ab}$ .

The coordinate transformation is defined with respect to the white point  $(X_N, Y_N, Z_N)^T$  in the XYZ color space. The triplet  $(X_N, Y_N, Z_N)^T$  represents the tristimulus value of the white light source or its reflection on an ideally matte white material. This point of the XYZ color space is mapped to the white point of the CIELAB space. Because of (5.33),  $Y_N = 100$ . Furthermore,  $X_N \approx 95.0$  and  $Z_N \approx 108.8$  for the standard illuminant D65.

Transformations between the XYZ and the CIELAB color space are made by using the following equations [5, 8, 43]:

$$L^* = 116 f\left(\frac{Y}{Y_N}\right) - 16 \quad (5.43)$$

$$a^* = 500 \left( f\left(\frac{X}{X_N}\right) - f\left(\frac{Y}{Y_N}\right) \right) \quad (5.44)$$

$$b^* = 200 \left( f\left(\frac{Y}{Y_N}\right) - f\left(\frac{Z}{Z_N}\right) \right) \quad (5.45)$$

$$f(\chi) = \begin{cases} \sqrt[3]{\chi} & \text{if } \chi > 0.008856 \\ 7.787\chi + \frac{16}{116} & \text{if } \chi \leq 0.008856 \end{cases} \quad (5.46)$$

$$Y = Y_N f^{-1}\left(\frac{L^* + 16}{116}\right) \quad (5.47)$$

$$X = X_N f^{-1}\left(\frac{a^*}{500} + f\left(\frac{Y}{Y_N}\right)\right) \quad (5.48)$$

$$Z = Z_N f^{-1}\left(-\frac{b^*}{200} + f\left(\frac{Y}{Y_N}\right)\right) \quad (5.49)$$

$$f^{-1}(\alpha) = \begin{cases} \alpha^3 & \text{if } \alpha > 0.207 \\ \frac{\alpha - \frac{16}{116}}{7.787} & \text{if } \alpha \leq 0.207 \end{cases} \quad (5.50)$$

As this is a nonlinear, non-projective transformation, lines in the XYZ color space are not, in general, mapped to lines in the CIELAB space [43].

Another color space is obtained by using polar coordinates for the CIELAB coordinates  $a^*$  and  $b^*$ . In this case, the angle is called the hue angle  $h_{ab}$ . The radius is called the chroma  $C_{ab}$  and is a measure of the distance to the achromatic point, like the saturation [5].

$$h_{ab} = \arctan \frac{b^*}{a^*} \in [0, 2\pi), \quad (5.51)$$

$$C_{ab} = \sqrt{a^{*2} + b^{*2}}. \quad (5.52)$$

The coordinates  $L^*$ ,  $C_{ab}$  and  $h_{ab}$  yield a clearly interpretable color space.

#### ► 5.2.4 Spectrophotometry for color measurement and color distance computation

The definition of the XYZ color space is based on the results of empirical experiments for measuring a color by determining the corresponding mix ratios of three base colors (Fig. 5.9). For automated inspection of colors in terms of quality inspection, usually another measurement method is used: the spectrum of intensity is spectrometrically measured and then the tristimulus is calculated. This method is called spectrophotometry. For most applications, it is sufficient to discretely sample the spectrum, with distances of about 10 nm, for example. In this case, the integrals needed for the calculation of the tristimulus values are approximated by sums [5].

The spectrum of the intensity is measured by splitting the light into its wavelength components based on dispersion or diffraction (see Chap. 2). Depending on the wavelength, the light is deflected in different directions. Then, spatially arranged detectors allow a spectrally resolved measurement (see also Sec. 7.2.4). The result is a spectrum of intensities  $I(\lambda)$  of the incident light, which can be inserted into (5.30)–(5.32) for the calculation of the tristimulus values. The tristimulus values (or corresponding coordinates of other color spaces) characterize the color of the observed light source.

However, often the color of a test object is of interest, instead of the color of a light source. In this case, the object is illuminated with broadband light and the diffusely reflected light is measured using a spectrometer. As the spectrum of the illumination can be measured separately, a compensation can be used to obtain the spectral reflectance  $R(\lambda)$  of the test object, which will be independent of the illumination [33].

An alternative to broadband illumination is a series of illuminations with monochromatic light of different wavelengths. Monochromatic light can be generated by dispersion



or diffraction followed by the use of a stop that lets only a small part of the spectrum pass through it. Then, a usual broadband detector can be used for capturing the reflected light. By using a camera, the reflectance can be measured in a spatially resolved way, for which a scanning process would be necessary in the case of the spectrometrical method.

Monochromatic illumination has the advantage of avoiding fluorescent excitation, so that for fluorescent materials the reflectance not caused by fluorescence can be measured. However, if the fluorescent color is of interest, a broadband illumination, with a spectrum in the range of the required fluorescent excitation, has to be used.

For the reflectance of a non-fluorescent object, one always has<sup>9</sup>

$$\forall \lambda : 0 \leq R(\lambda) \leq 1. \quad (5.53)$$

The perceived color of an object not only depends on its reflectance, but also on the illumination. The intensity  $I(\lambda)$  of the light emitted by the object is the product of the illumination's intensity  $I_{\text{light}}(\lambda)$  and the object's reflectance  $R(\lambda)$ :

$$I(\lambda) = I_{\text{light}}(\lambda) R(\lambda). \quad (5.54)$$

Now, this intensity  $I(\lambda)$  can be inserted into (5.30)–(5.32), in order to obtain the object's color with respect to the illumination  $I_{\text{light}}(\lambda)$  and the CIE normal observer. The set of realizable object colors is called the Roesch color solid. For a given illumination, not all perceivable colors can be emitted, as an object color might achieve only limited brightness even for ideal reflection, as the spectrum of the illumination is multiplied by parts of the spectrum of low intensity [43].

The intensity  $I_{\text{light}}(\lambda)$  of the illumination used for the calculation does not have to be equal to the real light source used for measuring the spectrum of the reflectance. In fact, different virtual and idealized illuminations can be used for the same spectrophotometric measurement of the reflectance, which meet the requirements of the inspection task. If, for example, the visual impression of the test object is to be tested, usually a spectrum similar to daylight is suitable for the illumination. For such applications, the standard illuminant D65 was standardized by the CIE. It represents the spectrum of daylight with a correlated color temperature of approximately 6,500 K which corresponds to the spectrum of a blackbody radiator of a temperature of 6,500 K. Differences from Planck's law are caused by absorption and scattering effects of the Earth's atmosphere. However it is important to note that the spectral composition of daylight might vary considerably because of clouds or the position of the sun. The standard illuminant D65 corresponds to daylight for a cloudy sky. It cannot be directly emitted by an artificial light source but is mainly used for calculations. Figure 5.16 shows the D65 spectrum together with the spectrum of the CIE standard illuminant A, which corresponds to an incandescent lamp and is therefore similar to Planck's radiation curve (2.254), as well as spectrum E of (5.17), that is constant with respect to the wavelength. As the standard illuminant A has a color temperature of 2,856 K, it has a considerably higher level of red components and lower blue components than the daylight spectrum (Fig. 5.15). The spectra are standardized except for a constant scaling factor. The intensities of the invisible ultraviolet part of the spectrum are also defined, as they are important for fluorescent

---

<sup>9</sup>In contrast, fluorescent materials might emit more light for certain wavelengths than is irradiated (see Sec. 7.2.2).

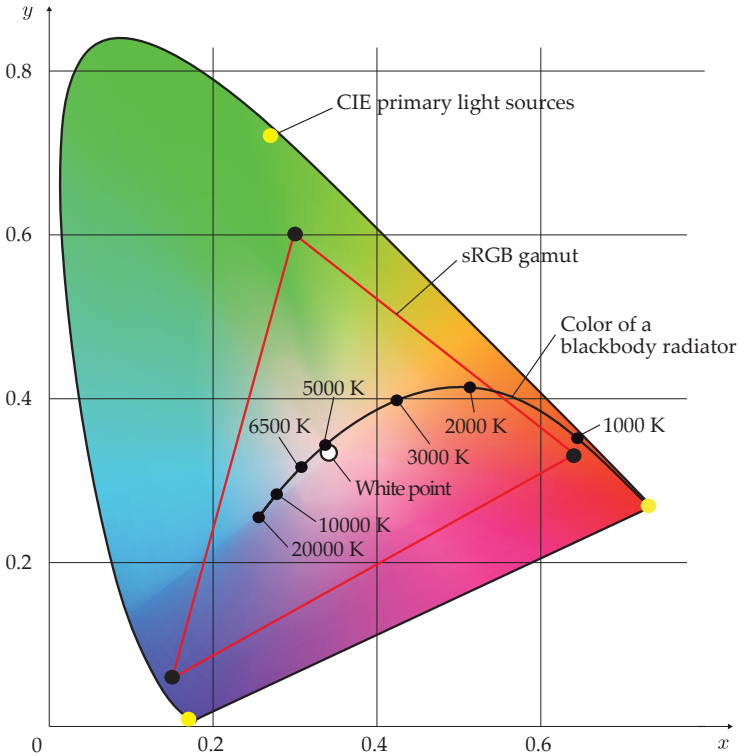


Figure 5.15. The color of a blackbody radiator with respect to its temperature as well as the position of the CIE primary light sources and the sRGB gamut in the chromaticity diagram.

excitation (see Sec. 7.2.2). The suitability of a light source for the measurement of colors can be judged by its color rendering index [43].

**Example 5.3 (Spectrophotometric color measurement and metamerism):** Figure 5.17 shows three hypothetical spectral reflectance distributions  $R_i(\lambda)$ ,  $i = 1, 2, 3$  [43]. The corresponding tristimulus values and normalized color values for an illumination with the standard illuminant D65 are to be calculated. Therefore, the spectra of intensity  $I_i(\lambda) = I_{D65}(\lambda) R_i(\lambda)$  are calculated using (5.54) and are inserted into (5.30)–(5.33). The limits for all integrals in this example are set to the interval from [380 nm, 760 nm], for which reflectance data are available. This leads to the following results for the three objects::

$$k_{D65} \approx \frac{1}{105.68 \text{ nm}}, \tag{5.55}$$

$$X \approx 29.6, \quad Y \approx 30.2, \quad Z \approx 35.7. \tag{5.56}$$

All three objects have the same tristimulus values. For a human observer, they are metameric under D65 illumination, although their reflectance spectra  $R_i(\lambda)$  differ considerably from each other.

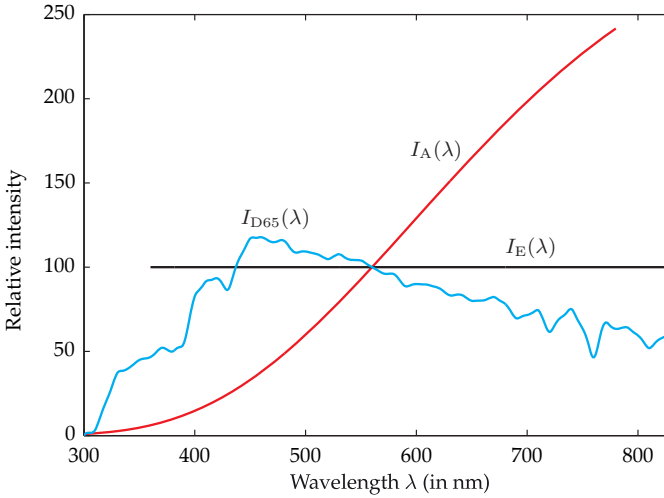


Figure 5.16. Relative spectra of intensities of the CIE standard illuminants D65, A and E [10,43].

Using (5.34), the calculation of the normalized color values leads to

$$x \approx 0.31, \quad y \approx 0.32. \quad (5.57)$$

These values correspond to a pale blueish gray. ■

A spectrum that is metameric to a given color impression can be constructed using the calculus of variations [40]. Usually, the spectral reflectance curves of two metameric objects have at least three intersections, with two of them located near the maxima of absorption of the three types of cones of the human eye. Metameric colors can also be designed in such a way that they are metameric for more than one type of light [43].

Besides the spectrum of the illumination, also its direction and the direction of the observation might influence the resulting color impression. This effect can be modeled by the wavelength dependent BRDF from Sec. 4.3. In everyday life, directional color impressions can be observed for so-called fickle textiles.

The phenomenon of metamerism can not only arise for different light sources but also for different observers. Although two colors might be metameric for one observer, another observer might be able to distinguish them even under the same conditions of illumination and observation. The CIE standard observers are the result of an average of a comparatively small number of test subjects. The individual perception of colors can differ from this average, even if no color blindness is present. An especially important physiological difference is given by the yellow staining of the lens of an aged eye [5].

An important application of color measurement in automated visual inspection is the verification of the colors of products. For example, the difference of the color of a test object from the color of a reference object should be within a tolerable interval [41]. In order to quantitatively specify this inspection task, a distance function for colors is needed. The color difference is defined in a color space where equal distances of coordinates approximately correspond to color differences that are visually perceived as equal. Then, the color differ-

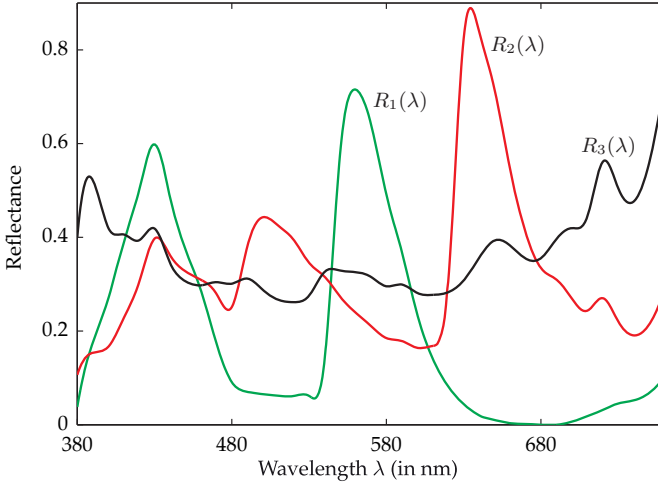


Figure 5.17. Spectral reflectance of three metameric objects, appearing equal to each other when illuminated with the standard illuminant D65 [43].

ence  $\Delta E$  can be defined as the Euclidean distance between two points in this color space. For the CIELAB color space, this leads to

$$\Delta E = \sqrt{(\Delta L^*)^2 + (\Delta a^*)^2 + (\Delta b^*)^2} \tag{5.58}$$

$$= \sqrt{(L_1^* - L_2^*)^2 + (a_1^* - a_2^*)^2 + (b_1^* - b_2^*)^2}, \tag{5.59}$$

with the CIELAB coordinates  $(L_1^*, a_1^*, b_1^*)^T$  and  $(L_2^*, a_2^*, b_2^*)^T$  of the two colors of interest [43]. Color differences on the order of  $\Delta E \approx 1$  are visually perceivable. However, the CIELAB color space is only approximately equidistant, so that the comparability of color differences in remote regions of the color space is limited, especially for notably different hues [5]. Therefore the Euclidean color difference can be modified by different correction factors [31].

Besides, it is preferable that the color difference can be decomposed into brightness, saturation and hue, as in many cases there are different tolerances for these different quantities. The brightness difference  $\Delta L^*$  and the chroma difference<sup>10</sup>  $\Delta C$  can be calculated as follows:

$$\Delta L^* = L_1^* - L_2^*, \tag{5.60}$$

$$\Delta C = C_1 - C_2. \tag{5.61}$$

The remaining part of  $\Delta E$  is the hue difference  $\Delta H$  [41]:

$$\Delta H = \text{sgn}(a_2^*b_1^* - a_1^*b_2^*) \sqrt{(\Delta E)^2 - (\Delta L^*)^2 - (\Delta C)^2}. \tag{5.62}$$

The connection between differences in the hue angle  $h$  and in  $\Delta H$  is as follows:

$$\Delta H = 2\sqrt{C_1 C_2} \sin\left(\frac{\Delta h}{2}\right) \approx \sqrt{C_1 C_2} \Delta h, \quad \Delta h = h_1 - h_2. \tag{5.63}$$

<sup>10</sup>At this point, the subscripts of  $C_{ab}$  and  $h_{ab}$  are omitted, as only the CIELAB color space is considered.

This approximation is valid for small hue differences.

The color difference  $\Delta E$  of two metameric spectra can be interpreted as the degree of metamerism with respect to the chosen light source. If, for a given light source, the reflectance spectra  $R_1(\lambda)$  and  $R_2(\lambda)$  have identical tristimuli and thus a color difference  $\Delta E = 0$ , their color difference  $\Delta E'$  for a second light source is called their **metamerism index** with respect to a change of the light source. The metamerism indices for different typical light sources can be used to judge the degree of metamerism of two metameric objects [43].

**Example 5.4 (Color difference and the metamerism index):** The three metameric reflectance spectra  $R_i(\lambda)$  from Ex. 5.3 will now be examined for the CIE standard illuminant A. (5.54) and (5.30)–(5.33) lead to

$$k_A \approx \frac{1}{107.90 \text{ nm}} \tag{5.64}$$

$$X_1 \approx 28.6 \qquad Y_1 \approx 31.0 \qquad Z_1 \approx 10.4 \tag{5.65}$$

$$X_2 \approx 37.1 \qquad Y_2 \approx 30.3 \qquad Z_2 \approx 11.7 \tag{5.66}$$

$$X_3 \approx 34.0 \qquad Y_3 \approx 30.5 \qquad Z_3 \approx 11.4 \tag{5.67}$$

If illuminated with the standard illuminant A, the colors of three objects differ, whereas they were metameric when illuminated with D65.

By employing (5.34), the normalized color values are

$$x_1 \approx 0.41 \qquad y_1 \approx 0.44 \tag{5.68}$$

$$x_2 \approx 0.47 \qquad y_2 \approx 0.38 \tag{5.69}$$

$$x_3 \approx 0.45 \qquad y_3 \approx 0.40 \tag{5.70}$$

These values also represent shades of gray, this time, however, with nuances of yellow and orange. This is because the standard illuminant A has a higher intensity of the long-wave, yellow to red part of visible light than does D65, and a lower intensity for the short-wave blue light.

In order to measure the color difference between the three metameric objects, their tristimulus values are transformed in the CIELAB color space using (5.43)–(5.46):

$$Y_N = 100 \qquad X_N \approx 109.83 \qquad Z_N \approx 35.55 \tag{5.71}$$

$$L_1^* \approx 62.5 \qquad a_1^* \approx -19.1 \qquad b_1^* \approx 2.7 \tag{5.72}$$

$$L_2^* \approx 61.9 \qquad a_2^* \approx 12.4 \qquad b_2^* \approx -3.8 \tag{5.73}$$

$$L_3^* \approx 62.1 \qquad a_3^* \approx 1.8 \qquad b_3^* \approx -2.4 \tag{5.74}$$

Figure 5.17 can be used to qualitatively verify that, for example,  $R_1(\lambda)$  in fact has a higher green component (negative  $a_1^*$ ) and  $R_2(\lambda)$  has a higher red component (positive  $a_2^*$ ).

Now, the CIELAB coordinates will be used in combination with (5.58) and (5.60) to calculate the color differences  $\Delta E_{ij}$  of the reflectance spectra  $R_i(\lambda)$  and  $R_j(\lambda)$  for the

standard illuminant A as well as the corresponding brightness differences  $\Delta L_{ij}^*$ :

$$\Delta E_{12} \approx 32.2 \qquad \Delta L_{12}^* \approx 0.59 \qquad (5.75)$$

$$\Delta E_{13} \approx 21.6 \qquad \Delta L_{13}^* \approx 0.45 \qquad (5.76)$$

$$\Delta E_{23} \approx 10.7 \qquad \Delta L_{23}^* \approx -0.13 \qquad (5.77)$$

These color differences are considerably higher than the perception threshold. As expected, the color difference of the spectra  $R_1(\lambda)$  from the  $R_2(\lambda)$ , which has extensive maxima for different wavelengths, is higher than that from the uniformly distributed spectrum  $R_3(\lambda)$ . At the same time, the color differences  $\Delta E_{ij}$  are the metamerism indices corresponding to the change from the standard illuminant D65 to standard illuminant A.

In order to calculate the other components of the color difference, first the opponent-process components will be transformed into the polar coordinates' chroma (5.52) and hue angle (5.51):

$$C_1 \approx 19.3 \qquad h_1 \approx 3.00 \qquad (5.78)$$

$$C_2 \approx 13.0 \qquad h_2 \approx 5.98 \qquad (5.79)$$

$$C_3 \approx 3.1 \qquad h_3 \approx 5.36 \qquad (5.80)$$

The approximately uniformly distributed spectrum  $R_3(\lambda)$  has a considerably lower chroma  $C$  than the two other spectra with extensive maxima.

Next, the chroma differences and the hue differences can be calculated using (5.61) and (5.62) respectively:

$$\Delta C_{12} \approx 6.3 \qquad \Delta H_{12} \approx -31.6 \qquad \Delta h_{12} \approx -2.98 \qquad (5.81)$$

$$\Delta C_{13} \approx 16.3 \qquad \Delta H_{13} \approx -14.2 \qquad \Delta h_{13} \approx -2.36 \qquad (5.82)$$

$$\Delta C_{23} \approx 9.9 \qquad \Delta H_{23} \approx 3.9 \qquad \Delta h_{23} \approx 0.62 \qquad (5.83)$$

Using the approximation of (5.63) for determining the hue difference  $\Delta h_{ij}$  is only sensible for the last pair ( $R_2(\lambda), R_3(\lambda)$ ), as the other hue differences are so large that the approximation is no longer sufficiently precise. ■

### 5.2.5 Color order systems

In a color order system, the colors are systematically ordered according to specified criteria [5,41]. An example of such criteria are the axes hue, saturation, and brightness (Fig. 5.18). The criteria do not necessarily have to be numerically quantified. The colors can be chosen in such a way that two neighboring colors will always have the same visually perceived difference. Often, color order systems contain physically real colored material samples and are specially designed for certain materials and product lines. Color order systems can be used to specify the tolerance for a product. For this purpose, the maximum differences from the preferred product color are marked for each direction of the color order system. If an automated quality assessment is to be used, the limits obtained by the color order system can be used to derive thresholds for the color difference  $\Delta E$  from the reference color.

A common color order system is the Munsell color system with the criteria of value, chroma, and hue [4,5,32].

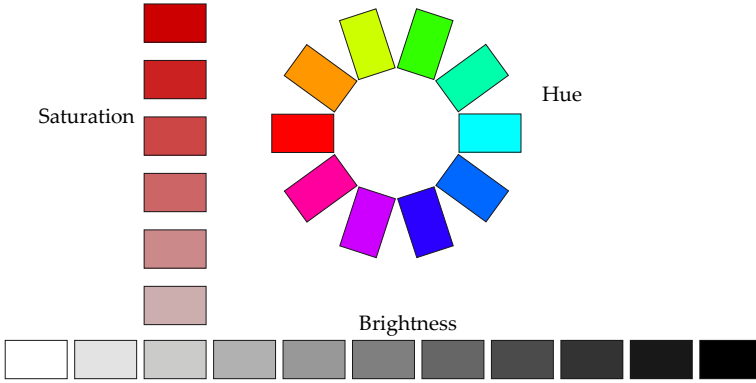


Figure 5.18. Brightness, saturation, and hue in the sense of a color order system.

➤ **5.2.6 Other color spaces**

The CIE color spaces of Sec. 5.2.3 are used for describing and measuring colors and their distances. There are many other color spaces which have been defined for special applications, such as the rendering of colors on computer and television screens by the additive color mixing of certain base colors, as well as color rendering by subtractive mixing of colorants for printing methods, for example.

Figure 5.19 shows a classification of these color spaces based on the criteria of the application and from the physiological and technical viewpoints [37].

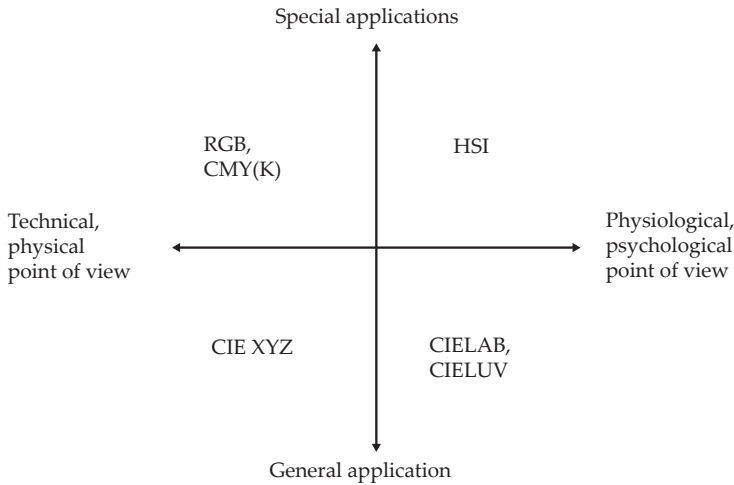


Figure 5.19. Criteria for classifying the different color spaces.

➤ **5.2.6.1 Gamma correction**

For displaying images, on displays for example, usually image values are used which are not proportional to the observed intensities. This approach compensates for the nonlinear human perception of intensities, as well as the nonlinear characteristics of displays, cameras,

etc. Gamma correction is therefore used for different color spaces which are especially used for rendering colors on displays.

The adaption to the human perception of brightness is done by transforming the physical intensity  $I$  to the image value  $g$  as follows:

$$g = f_\gamma(I) = I^\gamma, \quad I \in [0, 1]. \quad (5.84)$$

Initially, the intensity values are scaled to the interval  $[0, 1]$ . The gamma corrected image values are also located within the interval  $[0, 1]$ , with  $f_\gamma(0) = 0$  and  $f_\gamma(1) = 1$ . The transformation is monotonic and invertible. The inverse transformation is

$$I = f_\gamma^{-1}(g) = g^{\frac{1}{\gamma}}. \quad (5.85)$$

In practice, the inverse transformation is affected by a quantization error, as the image values are usually quantized. Gamma correction allows a much better exploitation of the available quantization intervals in accordance with the human perception of brightness. Gamma correction can be applied to a gray-scale image as well as to each of the channels of a color image.

For low intensities  $I \leq I_0$ , the modified gamma correction changes the transformation characteristic curve to form a line, in order to avoid a too steep or too flat curve [9]. It is defined as follows:

$$f_{\gamma, I_0}(I) := \begin{cases} (1+d)I^\gamma - d & \text{if } I_0 < I \leq 1 \\ sI & \text{if } 0 \leq I \leq I_0 \end{cases} \quad (5.86)$$

with

$$d := \frac{1}{I_0^\gamma (\gamma - 1) + 1} - 1, \quad (5.87)$$

$$s := \frac{\gamma}{I_0(\gamma - 1) + I_0^{1-\gamma}}. \quad (5.88)$$

The inverse transformation is given by

$$f_{\gamma, I_0}^{-1}(g) = \begin{cases} \left(\frac{g+d}{1+d}\right)^{\frac{1}{\gamma}} & \text{if } sI_0 < g \leq 1 \\ \frac{g}{s} & \text{if } 0 \leq g \leq sI_0. \end{cases} \quad (5.89)$$

### ⊙ 5.2.6.2 RGB color spaces

Technical color spaces describe the colors that can be rendered by a certain device. Usually, not all perceivable colors can be expressed in these color spaces. The set of colors that can be rendered is called the gamut of the device [8]. For additive color mixing, the gamut corresponds to a triangle in the chromaticity diagram (Sec. 5.2.3). The base colors of common displays, projectors, and cameras are red, green and blue. In RGB color spaces, the ratios of these three base colors are described by a vector  $(R, G, B)^T \in [0, 1]^3$  (Fig. 5.20). Generally, the RGB color spaces and gamuts of different devices do not match each other, as different base colors are used.



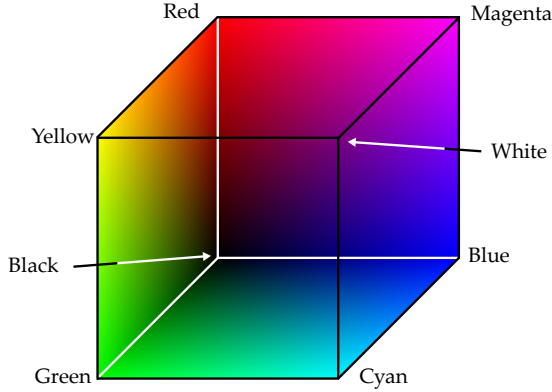


Figure 5.20. The RGB color space, as a cube.

The sRGB color space is a device-independent RGB standard [8, 39]. It is based on three reference light sources with the following normalized color values (Fig. 5.15):

$$\begin{array}{lll}
 x_R = 0.64 & x_G = 0.30 & x_B = 0.15 \\
 y_R = 0.33 & y_G = 0.60 & y_B = 0.06
 \end{array} \tag{5.90}$$

The linear sRGB color values  $R_s, G_s, B_s$  are the result of a linear transformation of the normalized color values  $X, Y, Z$ :

$$\begin{pmatrix} R_s \\ G_s \\ B_s \end{pmatrix} = \mathbf{A}_{\text{sRGB}} \begin{pmatrix} X \\ Y \\ Z \end{pmatrix} \tag{5.91}$$

with

$$\mathbf{A}_{\text{sRGB}} = \begin{pmatrix} 3.2410 & -1.5374 & -0.4986 \\ -0.9692 & 1.8760 & 0.0416 \\ 0.0556 & -0.2040 & 1.0570 \end{pmatrix}. \tag{5.92}$$

The sRGB color values  $R_s, G_s,$  and  $B_s$  are within the range  $[0, 1]$ . If negative values arise in (5.91), they are set to 0; values greater than 1 are set to 1. The corresponding colors cannot be displayed in the sRGB color space. For such colors, the transformation cannot be inverted.

Subsequent to the linear transformation, a nonlinear gamma correction is performed in order to correct the color rendering on typical displays (see Sec. 5.2.6.1). For  $\gamma = \frac{1}{2.4}$  and  $I_0 = 0.00304$ , Equation (5.86) leads to the following formula for the nonlinearly gamma corrected sRGB color values  $R'_s, G'_s, B'_s$ :

$$\begin{pmatrix} R'_s \\ G'_s \\ B'_s \end{pmatrix} = \begin{pmatrix} f_{\gamma, I_0}(R_s) \\ f_{\gamma, I_0}(G_s) \\ f_{\gamma, I_0}(B_s) \end{pmatrix}, \tag{5.93}$$

$$f_{\gamma, I_0}(x) = \begin{cases} 1.055 x^{\frac{1}{2.4}} - 0.055 & \text{if } x > 0.00304 \\ 12.92 x & \text{if } x \leq 0.00304. \end{cases} \tag{5.94}$$

The nonlinearly gamma corrected sRGB color values are also within the range  $[0, 1]$ . Usually these color values are used for saving images, as in the JPEG standard, for example. So the color values of a color image do not correspond to the radiometric intensities and should thus be inversely transformed before performing any further processing that assumes a linear relation between the color values and the intensities.

Usually, an additional scaling and quantization is performed in order to save images to files. For the typical 8-bit resolution per color channel, the sRGB values are multiplied by  $2^8 - 1 = 255$  and quantized to integer values.

For the inverse transformation to CIE normalized color values, first the scaling has to be undone, leading to the nonlinearly gamma corrected sRGB color values  $R'_s, G'_s, B'_s$  within the interval  $[0, 1]$ . Then, the gamma correction is reversed:

$$\begin{pmatrix} R_s \\ G_s \\ B_s \end{pmatrix} = \begin{pmatrix} f_{\gamma, I_0}^{-1}(R'_s) \\ f_{\gamma, I_0}^{-1}(G'_s) \\ f_{\gamma, I_0}^{-1}(B'_s) \end{pmatrix}, \quad (5.95)$$

$$f_{\gamma, I_0}^{-1}(x) = \begin{cases} \left(\frac{x+0.055}{1.055}\right)^{2.4} & \text{if } x > 0.03928 \\ \frac{x}{12.92} & \text{if } x \leq 0.03928. \end{cases} \quad (5.96)$$

Now, the tristimulus values  $X, Y, Z$  can be calculated from the linear sRGB color values  $R_s, G_s$  and  $B_s$ :

$$\begin{pmatrix} X \\ Y \\ Z \end{pmatrix} = \mathbf{A}_{\text{sRGB}}^{-1} \begin{pmatrix} R_s \\ G_s \\ B_s \end{pmatrix} \quad (5.97)$$

with the inverse transformation matrix

$$\mathbf{A}_{\text{sRGB}}^{-1} = \begin{pmatrix} 0.4124 & 0.3576 & 0.1805 \\ 0.2126 & 0.7152 & 0.0722 \\ 0.0193 & 0.1192 & 0.9505 \end{pmatrix}. \quad (5.98)$$

The columns of the matrix  $\mathbf{A}_{\text{sRGB}}^{-1}$  represent the tristimulus values  $X, Y, Z$  of the sRGB base colors of (5.90). Further, the white point  $(R_s, G_s, B_s)^T = (1, 1, 1)^T$  is identical to the CIE standard illuminant D65.

### ⊗ 5.2.6.3 HSI and HSV

The RGB color values can be transformed into further color spaces with clearly interpretable coordinates, such as brightness, hue, and saturation. Among these color spaces there are HSV, HSL (HLS), and HSI, which pursue similar goals but are not identical [9]. In the following, the transformation into the **HSI color space** will be discussed [18]. The coordinates of this color space correspond to the hue  $H_{\text{HSI}}$ , the saturation  $S_{\text{HSI}}$ , and the intensity  $I_{\text{HSI}}$ . Similar to the polar coordinates of the CIELAB color space, the hues are represented by an angle, but are located within a triangle instead of a circle.

HSI color spaces can be defined on the basis of device dependent or of standardized RGB colors with or without gamma correction. The following equations give the transformation

from gamma corrected sRGB coordinates to HSI coordinates:

$$H_{\text{HSI}} = \arctan \frac{\sqrt{3}(G'_s - B'_s)}{2R'_s - G'_s - B'_s} \quad (5.99)$$

$$I_{\text{HSI}} = \frac{1}{3}(R'_s + G'_s + B'_s) \quad (5.100)$$

$$S_{\text{HSI}} = 1 - \frac{\min\{R'_s, G'_s, B'_s\}}{I_{\text{HSI}}} \quad (5.101)$$

As the intensity coordinate  $I_{\text{HSI}}$  uses equal weights for all three color channels, it does not correspond to the human perception of brightness. For the inverse transformation from the HSI space to the sRGB space, different cases have to be considered, depending on the sector of the color triangle in which the hue  $H$  is located:

$$h := H_{\text{HSI}} - \frac{2}{3}\pi \left\lfloor \frac{3H_{\text{HSI}}}{2\pi} \right\rfloor \quad (5.102)$$

$$p := I_{\text{HSI}}(1 - S_{\text{HSI}}) \quad (5.103)$$

$$q := I_{\text{HSI}} \left( 1 + \frac{S_{\text{HSI}} \cos h}{\cos(\frac{\pi}{3} - h)} \right) \quad (5.104)$$

$$t := 3I_{\text{HSI}} - p - q \quad (5.105)$$

$$(R'_s, G'_s, B'_s)^{\text{T}} = \begin{cases} (q, t, p)^{\text{T}} & \text{if } 0 \leq H_{\text{HSI}} < \frac{2}{3}\pi \\ (p, q, t)^{\text{T}} & \text{if } \frac{2}{3}\pi \leq H_{\text{HSI}} < \frac{4}{3}\pi \\ (t, p, q)^{\text{T}} & \text{if } \frac{4}{3}\pi \leq H_{\text{HSI}} < 2\pi \end{cases} \quad (5.106)$$

The coordinates of the **HSV color space** are the hue value  $H_{\text{HSV}}$ , the saturation value  $S_{\text{HSV}}$ , and the brightness value  $V_{\text{HSV}}$ . They are calculated from the RGB values, which are within the range  $[0, 1]$ , as follows [9]:

$$m := \min\{R'_s, G'_s, B'_s\}, \quad (5.107)$$

$$V_{\text{HSV}} := \max\{R'_s, G'_s, B'_s\}, \quad (5.108)$$

$$S_{\text{HSV}} := \begin{cases} \frac{V_{\text{HSV}} - m}{V_{\text{HSV}}} & \text{if } V_{\text{HSV}} \neq 0 \\ 0 & \text{if } V_{\text{HSV}} = 0, \end{cases} \quad (5.109)$$

$$H_{\text{HSV}} := \begin{cases} \frac{\pi}{3} \left( \frac{G'_s - B'_s}{V_{\text{HSV}} - m} \right) & \text{if } V_{\text{HSV}} = R'_s \\ \frac{\pi}{3} \left( \frac{B'_s - R'_s}{V_{\text{HSV}} - m} + 2 \right) & \text{if } V_{\text{HSV}} = G'_s \\ \frac{\pi}{3} \left( \frac{R'_s - G'_s}{V_{\text{HSV}} - m} + 4 \right) & \text{if } V_{\text{HSV}} = B'_s. \end{cases} \quad (5.110)$$

The hue  $H_{\text{HSV}}$  is undefined for achromatic colors with  $V_{\text{HSV}} = R'_s = G'_s = B'_s = m$ .

#### ⊗ 5.2.6.4 YUV and YC<sub>B</sub>C<sub>R</sub>

Distinct color spaces have been defined for encoding television signals. The RGB coordinates are transformed into a brightness coordinate and two chroma coordinates. The gamma corrected brightness coordinate  $Y'$  was chosen to correspond to the signal of black-and-white television, so that color television would be backwards compatible when it was introduced. The chroma coordinates can be compressed more densely, as the resolution of the human

eye is higher for brightness than it is for chroma. The transformation formulas are applied to the sRGB space as well as to device dependent RGB color spaces.

The European PAL television color encoding system uses the YUV color space. The brightness coordinate  $Y'$  is given by the weighted sum of the gamma corrected RGB color values [35]:

$$Y' = 0.299 R'_s + 0.587 G'_s + 0.114 B'_s. \quad (5.111)$$

The chroma coordinates  $U$  and  $V$  are defined as follows:

$$U = 0.492 (B'_s - Y'), \quad (5.112)$$

$$V = 0.877 (R'_s - Y'). \quad (5.113)$$

As this is a linear transformation, it can be expressed by matrix multiplication as in (5.91) and (5.92). The inverse transformation is performed by multiplication by the inverse transformation matrix. The YIQ color space is a variant of the YUV color space [9].

The  $YC_B C_R$  color space is used for encoding digital image and video data—as in the JPEG standard, for example. The chroma coordinates  $C_B$  and  $C_R$  are defined as follows:

$$C_B = 0.564 (B'_s - Y'), \quad (5.114)$$

$$C_R = 0.713 (R'_s - Y'). \quad (5.115)$$

Again, this transformation is linear and can thus be expressed by matrix multiplication [9]. Furthermore, the standard ITU BT.601 contains suggestions for how to apply that transformation to quantized signals [23].

### ⊗ 5.2.6.5 Color printing and CMYK

The CMYK color space is used for color printing. For subtractive color mixing, the base colors cyan, magenta and yellow are used, which are complementary to the additive base colors red, green and blue: Cyan pigments absorb red light, magenta absorbs green, and yellow absorbs blue. Therefore, the RGB and CMY color values are, ideally, connected as follows:

$$\begin{pmatrix} C \\ M \\ Y \end{pmatrix} = \begin{pmatrix} 1 \\ 1 \\ 1 \end{pmatrix} - \begin{pmatrix} R \\ G \\ B \end{pmatrix}. \quad (5.116)$$

In general, however, the additive as well as the subtractive base colors are device dependent, so that these equations are only an approximation. Additionally, the spectra of absorption of the subtractive base colors often overlap each other, so that in the strict sense, the three components  $C$ ,  $M$  and  $Y$  cannot be considered to be independent of each other. In fact, the nonlinear laws of subtractive color mixing of Sec. 5.2.2 have to be applied. Generally, the gamut of printers does not match that of computer screens.

As, in practice, the mixture of the three subtractive base colors does not yield a perfect black, color printers use a black pigment as an additional base color. This is also sensible for reasons of economy. The black coordinate in the color space is denoted by  $K$  (for Key). It can be chosen as the minimum of the other three color values:

$$K = \min\{C, M, Y\}. \quad (5.117)$$

In this case, the components  $C$ ,  $M$  and  $Y$  can be reduced, which can be done using different formulas [9]. The resulting process is called the four color process. Additional base colors can be added in order to extend the gamut of the printer.

The transformation between different device dependent color spaces can be done by using color profiles [8,22]. They either specify transformation matrices like (5.92) for the base colors of the device, or extensive tables for color conversion which might also contain non-linear relations. In particular, such tables contain information on how colors that are outside of the gamut can best be approximated by the device.

### 5.3 Filters

Color filters, also called spectral filters, are optical elements which let only a certain range of wavelengths pass through them. Mounting such filters in front of a single channel, broad-band, gray-scale camera, yields a sensor which is sensitive to a certain spectral range [25]. If particular object's properties of interest are present in this spectral range, then, for example, two materials might be better discriminable in a single image of the filtered light than in an image acquired without a spectral filter, where the influences of other spectral ranges could be disturbing. Common RGB cameras also use filters in order to capture the three color channels (see Sec. 6.9). By using more cameras with their respective filters, the spectrum can be sampled more finely. Filters can also be used to suppress extraneous light by illuminating and observing the test object under a certain spectral range. For illumination with a particular spectral range, spectral filters can be mounted in front of a light source. However, for reasons of efficiency, light sources that emit the desired spectrum by themselves should be preferred, such as light emitting diodes of the respective color, for example (see Sec. 2.7).

Selective transmission is either based on absorption or on interference. **Absorption filters** contain colorants absorbing certain ranges of wavelengths. For absorption filters, the laws of subtractive color mixing apply (Sec. 5.2.2). According to the Lambert–Beer law (5.10), (5.11), absorption increases exponentially with the thickness of the filter [43]. The variety of absorption filters is limited by the available colorants. The absorption leads to a heating of the filter, which can be a problem if the filter is placed directly in front of a light source.

**Interference filters** consist of a series of thin layers which are separated by defined distances of a few wavelengths [21, 45]. At these layers, multiple reflections occur. The distances between the layers are chosen in such a way that there is constructive interference for light of the wavelength of interest and destructive interference for all other wavelengths (cf. Sec. 2.2.5). In contrast to absorption filters, interference filters appear in the complementary color of the transmitted spectrum if they are viewed under daylight, as the reflected components of the light are dominant.

Multiple degrees of freedom for the design of these filters are given by the thickness, the optical material's characteristics, and the refraction indices of the layers used. The different parts of the waves that are reflected or transmitted at the interfaces interfere with each other and result in the spectral transmission characteristics. There are variants with dielectric layers and with thin metal coatings.

Interference filters can be constructed for nearly every arbitrary transmission characteristic, and allow steep edges in the transmitted spectrum. As the filtered light is not absorbed

but reflected, heating is low even under intensive illumination. Therefore, their durability is high even for high radiant fluxes.

However, there is a major disadvantage: depending on the angle of incidence to the optical axis, the path that the light takes between the reflecting layers varies, changing the maximum of the constructive interference. Therefore, interference filters are only suitable for approximately perpendicularly incoming light. In contrast, the wavelength corresponding to the spectral maximum of transmission of absorption filters is independent of the angle of incidence. Only the absolute value of the absorption increases, according to the Lambert–Beer law, because of the increased optical path for diagonally incident light.

A fundamental disadvantage of spectral filters is the loss of light caused by unwanted reflections.

---

**Example 5.5 (Spectral filters):** Figure 5.21 shows an series of images of a scene, captured by a gray-scale camera and different spectral filters. The nine interference filters have a transmission bandwidth of approximately 50 nm and nearly completely cover the visible spectrum up to the near infrared. The scene consists of multiple orange colored objects, whose colors are barely distinguishable in a single RGB image. However, the colors of the different objects are metameric, so that the intensities captured in the image series vary markedly. The wooden block, for example, has a lower reflectance at 400 nm than the plastic model of the industrial robot, whereas it is the other way round for 500 nm. The spectral image series can accordingly be used to segment and classify the colorants or the objects. Methods for the further processing and analysis of the image series are described in Sec. 8.7.

This image series was sequentially captured with a camera by exchanging the filters in front of the camera between the single recordings (cf. Sec. 7.2.4). For some applications it might be necessary to simultaneously capture the images, as the available time might be limited or moving objects have to be captured. Then, multiple gray-scale cameras with different spectral filters can be organized in an array. However, the imaging geometry will then be different for the single images because of the stereo effect, which can severely complicate the analysis of the image series. On the other hand, additional information about the 3D shape of the observed objects is gained [16]. ■

## 5.4 Acquisition and processing of color images

For many applications of automated visual inspection, recording and analyzing gray-scale images is sufficient. However, in some cases, the consideration of multiple color or spectral channels can bring considerable advantages. Examples are the detection, segmentation, and classification of objects which mainly differ because of their color or their spectral reflectance (see Sec. 7.2.2, 7.6.2) as well as color encoding of patterns for 3D shape capturing (Sec. 7.3.4.1). The color of a test object can be important for different reasons: for food, it provides information on condition and quality; for some technical products, it has to be inspected for aesthetic reasons, and in other applications printed color codings are used to identify electrical components or pharmaceuticals, for example [1–3,27].

As RGB image sensors (see Sec. 6.9) are cheap and common components, the use of such sensors is suitable as long as their attainable spectral resolution is sufficient for the particular

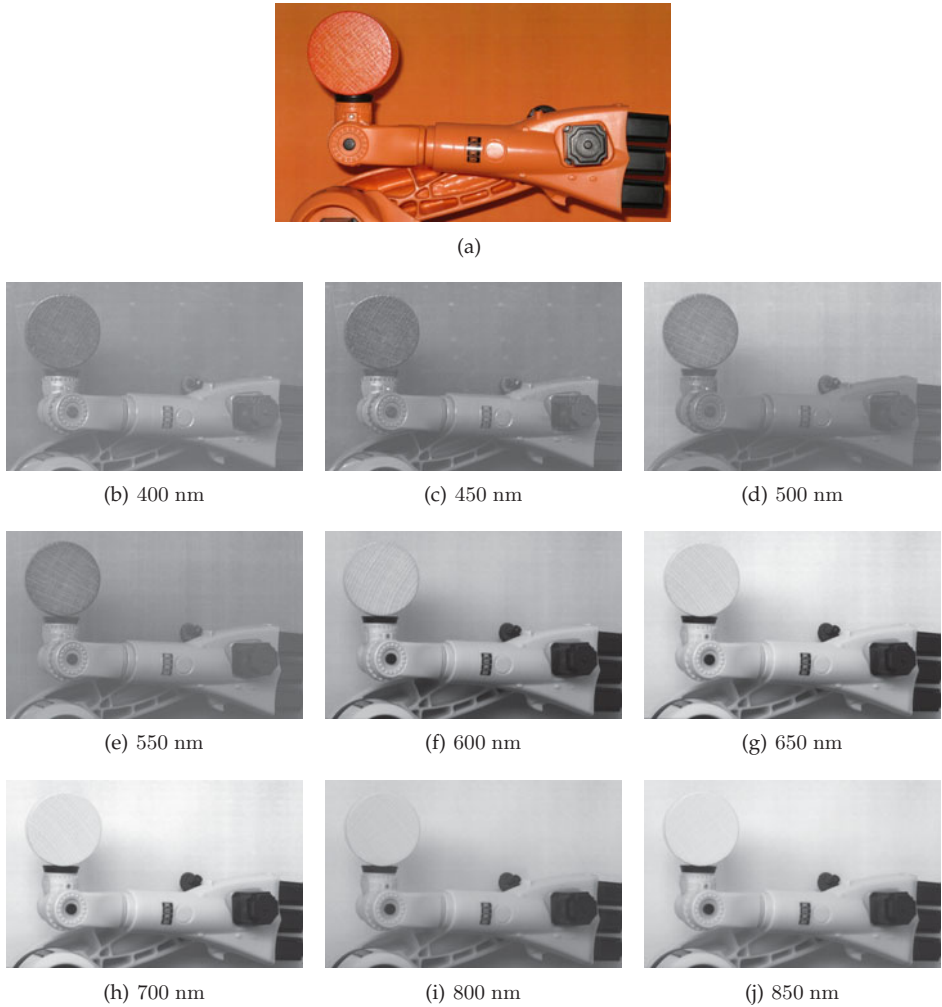


**Figure 5.21.** Examples of image acquisition with spectral filters. (a) RGB camera image of a scene with model robot, a wooden cube and an orange background; (b)–(j) Images of the same scene with a gray-scale camera and different spectral filters with a transmission bandwidth of approximately 50 nm and the specified transmission wavelength.

application. Such cameras produce images with three channels. The three color values of a pixel represent the coordinates in a device dependent RGB color space or ideally in the sRGB color space. By using the transformations described in this chapter, the RGB images can be transformed into other color spaces, like the HSI color space if a color classification independent of brightness is needed. The RGB image can be converted into a gray-scale image by using (5.111) if that is sufficient for some steps of the processing chain [8].

For other inspection tasks, a finer resolution of the spectrum might be necessary, for example if metameric colors have to be distinguished or if spectral channels outside the visible part of the spectrum are needed. In this case, gray-scale cameras with the corresponding fil-

ters (Sec. 5.3) or spectrophotometers (Sec. 7.2.4) can be used to capture the spectral channels. A fine sampling of the spectrum can be used to obtain color and color difference measures for monitoring production processes, as described in Sec. 5.2.4 [14].

Many algorithms originally used for processing gray-scale images can be directly used for color images by applying them separately to the single channels of the color image. Examples are linear filters for smoothing (see Chap. 9), where the separate processing of each channel is equivalent to a vectorial processing [18]. Other operations, such as the computation of gradients or the median filter, cannot be applied to color images that way [30, 44]. For many segmentation and classification methods, the vector of a pixel's color values can be used as a multidimensional feature vector (cf. Chap. 11).

## 5.5 Bibliography

- [1] Bruce Batchelor, editor. *Machine Vision Handbook*. Springer, 2012.
- [2] Bruce Batchelor and Paul Whelan. *Intelligent vision systems for industry*. Springer, 1997.
- [3] Sarah Bee and Mark Honeywood. Colour Sorting in the Food Industry. In Mark Graves and Bruce Batchelor, editors, *Machine vision for the inspection of natural products*. Springer, 2003.
- [4] Ludwig Bergmann, Clemens Schaefer, Heinz Niedrig, and Hans-Joachim Eichler, editors. *Lehrbuch der Experimentalphysik*, volume 3: Optik: Wellen- und Teilchenoptik. De Gruyter, 10th edition, 2004.
- [5] Roy Berns, Fred Billmeyer, and Max Saltzman. *Billmeyer and Saltzman's principles of color technology*. Wiley, 3rd edition, 2000.
- [6] David Berson, Felice Dunn, and Motoharu Takao. Phototransduction by retinal ganglion cells that set the circadian clock. *Science*, 295(5557):1070–1073, 2002.
- [7] Josef Bigun. *Vision with direction*. Springer, 2006.
- [8] Wilhelm Burger and Mark Burge. *Principles of digital image processing*, volume 2: Core algorithms. Springer, 2009.
- [9] Wilhelm Burger and Mark Burge. *Principles of digital image processing*, volume 1: Fundamental techniques. Springer, 2009.
- [10] CIE – International Commission on Illumination. <http://www.cie.co.at/>, 2011.
- [11] Commission Internationale de l'Éclairage, editor. *CIE Colorimetry*. Joint ISO/CIE Standard ISO 11664 / CIE S 014-1, 2007.
- [12] Michael D'Zmura. Psychology of Color Perception. In Lynn Nadel, editor, *Encyclopedia of Cognitive Science*, volume 1, pages 560–568. Nature, 2003.
- [13] Marc Ebner. *Color constancy*. Wiley, 2007.
- [14] Hugh Fairman, Michael Brill, and Henry Hemmendinger. How the CIE 1931 Color-Matching Functions Were Derived from Wright-Guild Data. *Color Research and Application*, 22(1):11–23, 1997.
- [15] David Falk, Dieter Brill, and David Stork. *Ein Blick ins Licht: Einblicke in die Natur des Lichts und des Sehens, in Farbe und Fotografie*. Birkhäuser, 1990.
- [16] Ioana Gheța, Michael Heizmann, and Jürgen Beyerer. 3D fusion of stereo and spectral series acquired with camera arrays. In Yufeng Zheng, editor, *Image Fusion and Its Applications*, pages 73–92. InTech, 2011.
- [17] Eugen Bruce Goldstein. *Sensation and perception*. Wadsworth Cengage, 9th edition, 2014.
- [18] Rafael Gonzalez and Richard Woods. *Digital image processing*. Pearson Prentice Hall, 3rd edition, 2008.



- [19] Hermann Graßmann. Zur Theorie der Farbenmischung. *Annalen der Physik*, 165(5):69–84, 1853.
- [20] Tobias Haist. *Optische Phänomene in Natur und Alltag*. <http://www.optipina.de>, 2010.
- [21] Oliver Heavens. *Thin film physics*. Methuen, 1970.
- [22] International Color Consortium, editor. *Specification ICC.1:2010 (Profile version 4.3.0.0) Image technology colour management – Architecture, profile format, and data structure*. ISO 15076-1, 2010.
- [23] International Telecommunication Union, editor. *Studio encoding parameters of digital television for standard 4:3 and wide-screen 16:9 aspect ratios*. Recommendation ITU-R BT.601-7, 2011.
- [24] Bernd Jähne. *Practical handbook on image processing for scientific and technical applications*. CRC Press, 2nd edition, 2004.
- [25] Ingmar Jahr. Lighting in Machine Vision. In Alexander Hornberg, editor, *Handbook of Machine Vision*, pages 73–203. Wiley-VCH, 2006.
- [26] Ramesh Jain, Rangachar Kasturi, and Brian Schunck. *Machine vision*. McGraw-Hill, 1995.
- [27] Erik Klaas. Farbbildverarbeitung. In Bernd Breuckmann, editor, *Bildverarbeitung und optische Messtechnik in der industriellen Praxis*, pages 54–65. Franzis, 1993.
- [28] Siegfried Kokoschka. *Script zur Vorlesung Grundlagen der Lichttechnik*. Lichttechnisches Institut der Universität Karlsruhe (TH), 2003.
- [29] Helga Kolb, Ralph Nelson, Eduardo Fernandez, and Bryan Jones. Webvision – The Organization of the Retina and Visual System. <http://webvision.med.utah.edu/book/>, 2012.
- [30] Hsien-Che Lee. *Introduction to color imaging science*. Cambridge University Press, 2005.
- [31] M. Luo, G. Cui, and B. Rigg. The Development of the CIE 2000 Colour-Difference Formula: CIEDE2000. *Color Research and Application*, 26(5):340–350, October 2001.
- [32] *The Munsell book of color*. Munsell Color, 2009.
- [33] Burkhard Neumann. *Bildverarbeitung für Einsteiger*. Springer, 2005.
- [34] Gustav Østerberg. Topography of the layer of rods and cones in the human retina. *Acta ophthalmologica, Supplementum*, (6), 1935.
- [35] Charles Poynton. *Digital video and HDTV: algorithms and interfaces*. Morgan Kaufmann, 2003.
- [36] Otto Reeb. *Grundlagen der Photometrie*. Braun, Karlsruhe, 1962.
- [37] Georgios Sakas, Stefan Thiemert, and Christoph Jung. Vorlesung Bildverarbeitung. <http://www.gris.informatik.tu-darmstadt.de/teaching/courses/ss11/bv/index.de.htm>, 2011.
- [38] Frank Schaeffel. Processing of Information in the Human Visual System. In Alexander Hornberg, editor, *Handbook of Machine Vision*, pages 1–33. Wiley-VCH, 2006.
- [39] Michael Stokes, Matthew Anderson, Srinivasan Chandrasekar, and Ricardo Motta. A Standard Default Color Space for the Internet – sRGB. <http://www.w3.org/Graphics/Color/sRGB>, 1996.
- [40] Kotaro Takahama and Yoshinobu Nayatani. New Method for Generating Metameric Stimuli of Object Colors. *Journal of the Optical Society of America*, 62(12):1516–1520, 1972.
- [41] Hans Völz. *Industrial color testing*. VCH, 1995.
- [42] Edward Wilson. *The social conquest of earth*. Liveright, 2013.
- [43] Günter Wyszecki and Walter Stiles. *Color Science*. Wiley, 2nd edition, 2000.
- [44] Silvano Di Zeno. A Note on the Gradient of a Multi-Image. *Computer Vision, Graphics, and Image Processing*, 33:116–125, 1986.
- [45] Wolfgang Zinth and Ursula Zinth. *Optik: Lichtstrahlen – Wellen – Photonen*. Oldenbourg, München, 4th edition, 2013.

A large, light gray, stylized number '6' is positioned in the upper left quadrant of the page. It is composed of several overlapping, curved lines that form a modern, geometric shape.

Chapter 6

**Sensors for Image Acquisition**

**6**

---

**6 Sensors for Image Acquisition**

6.1	Point, line and area sensors . . . . .	205
6.2	Image tube cameras . . . . .	206
6.3	Photomultipliers . . . . .	206
6.3.1	Image intensifiers . . . . .	207
6.4	Photodiodes . . . . .	207
6.5	Position sensitive detectors (PSD) . . . . .	210
6.6	Charge-coupled device (CCD) . . . . .	211
6.7	Complementary metal-oxide-semiconductor (CMOS) sensors . . . . .	213
6.8	Line-scan cameras . . . . .	215
6.9	Color sensors and color cameras . . . . .	215
6.10	Infrared cameras . . . . .	216
6.10.1	Bolometer cameras . . . . .	217
6.10.2	Infrared quantum detector cameras . . . . .	217
6.11	Quality criteria for image sensors . . . . .	219
6.12	Bibliography . . . . .	220

## 6 Sensors for Image Acquisition

The image of a scene that has to be inspected is imaged to the image plane by imaging optics. For further processing of the resulting image, the spatial distribution of the irradiance is first converted into an analog electrical signal, which is then spatially and temporally sampled, quantized, and finally stored.

A system for digitizing images has to be able to spatially divide the captured image into separate elements (pixels), to address these elements individually, to integrate the irradiance over a defined period of time, and then to measure, quantize, and save the image value of each pixel. Therefore, it has to provide the following five components:

1. A sampling aperture, which can address a single pixel and ignore the rest of the image. This aperture determines the size of the pixels.
2. A scanning mechanism, which moves the sampling aperture over the image, in order to provide access to the different pixels. The scanning mechanism determines the distances between the pixels.<sup>1</sup>
3. A light sensor using the sampling aperture to determine the irradiance for each pixel, and subsequently producing an electrical output signal. For this purpose there can be used, e.g., light sensitive resistors, photodiodes, phototransistors, CCD sensors, and CMOS sensors.
4. A quantizer—also called an analog to digital converter—which samples the image values (gray or color values).
5. A storage unit, which stores the single image values for further processing.

Usually, components 1 to 3 are realized inside the camera and components 4 and 5 are provided by an additional device, called the frame grabber, inside a computer.

However, nowadays, there are several cameras available which already contain all these components and can directly provide a computer with digital images.

### 6.1 Point, line and area sensors

There are many ways of capturing the whole area of an image:

- An **area sensor** yields an image pixel for each sensor element. The image size is set by the physical number of the sensor's rows and columns. Usually, all pixels are simultaneously exposed for a certain period of time. CCD and CMOS chips as well as the formerly used image tube cameras are examples of area sensors.
- A **line-scan sensor** is composed of a single line of pixels. Therefore, for each recording cycle, only a single line of the image can be captured. A two-dimensional image is created by moving the test object with respect to the sensor and subsequently assembling the captured lines to form the whole image.
- A **point sensor** can only capture a single intensity value in one recording cycle. In order to obtain a two-dimensional image, a laminar scan in column and row directions has to be performed.

---

<sup>1</sup>Hence, the pixel distances  $\Delta x$  and  $\Delta y$  do not have to be equal to the pixel size. For example, for the CCD sensor that is presented later on in this chapter, the pixel size is usually smaller than the distance between pixels.

## 6.2 Image tube cameras

Historically, **image tube cameras** have been the first electronic cameras. They were developed for the domain of television, but are not used anymore. An electromagnetically steered electron ray is used to capture line by line the image formed on a special semiconductor photo layer by the charge carriers which are generated by the incoming photons. The sampling aperture is given by the diameter of the electron ray,  $\Delta x$  corresponds to the sampling rate of a connected analog-to-digital converter, and  $\Delta y$  is the minimum possible distance between the scanning lines. Drawbacks of this kind of cameras are their sensitivity to electromagnetic fields as well as their large size and power consumption.

## 6.3 Photomultipliers

Similar to image tube cameras, a **photomultiplier** consists of a vacuum tube with a photocathode. Typically, alkali metals are used for the photocathode, as its work function, i.e., the energy needed to strike out an electron, is notably low. Cesium alloys are especially suitable, and can detect light with a maximum wavelength of approximately 900 nm [21]. The electrons of the photocathode, which are emitted because of the photoelectric effect, are attracted by a positively charged metal tile which is called the dynode (Fig. 6.1). The impact on the dynode produces further electrons, which are accelerated in the direction of the next dynode [5,7,11]. A cascade of multiple dynodes with increasing positive voltage results in an exponential amplification of the electron count. The electrons that finally reach the anode discharge over a resistor and produce a voltage which is proportional to the rate of photons. The rate of photons  $\frac{\Delta n}{\Delta t}$  denotes the number of photons  $\Delta n$  arriving at the photocathode during the period of time  $\Delta t$ .

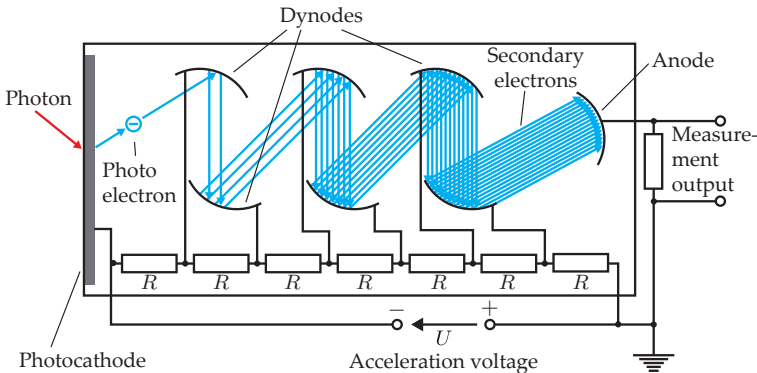
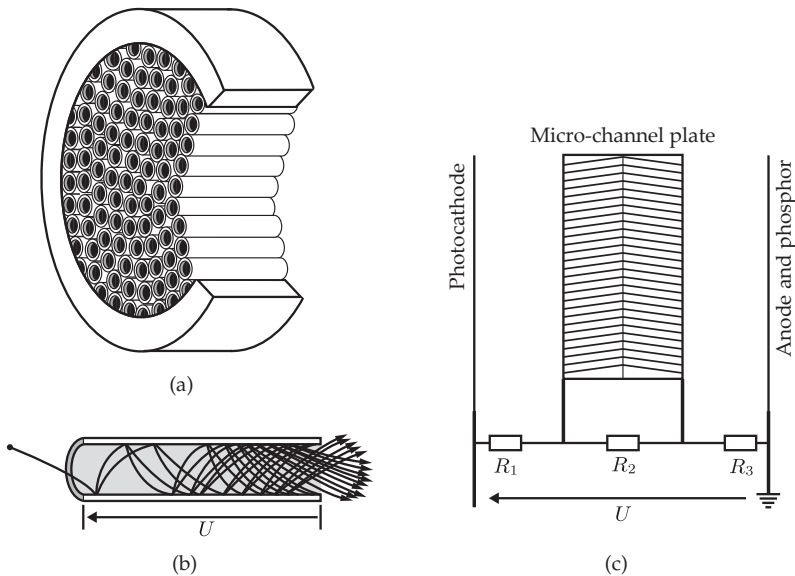


Figure 6.1. Schematic of a photomultiplier.

Photomultipliers are very sensitive. They can be used to detect single photons. They are primarily used in physical measuring instruments [9] as well as for visual inspection tasks, where only little light is available, like for fluorescence effects, for example (see Sec. 7.2.2).

### 6.3.1 Image intensifiers

The principle of a photomultiplier can also be used for area sensors in the form of the so-called **image intensifiers**. They can capture scenes even for very small rates of photons, and are used in X-ray inspection systems or night vision devices, for example. In an image intensifier, the photocathode is succeeded by a so-called **micro-channel plate**, which is a semiconductor plate with periodically arranged, cylindrical holes called channels; see Fig. 6.2(a). The channels are slightly tilted with respect to the direction of incidence of the electrons, so that the electrons hit the walls of the channels many times and strike out further electrons; see Fig. 6.2(b). These electrons are accelerated by a voltage drop along the channels and finally hit a special semiconductor detector or a screen, where again photons are created which can be viewed with a common image sensor. The resistors  $R_1$ ,  $R_2$  and  $R_3$  in Fig. 6.2(c) represent a voltage divider, which determines the voltage over the three regions of the space between the photocathode and the micro-channel plate, inside the micro-channel plate, and between the micro-channel plate and the anode.



**Figure 6.2.** A micro-channel plate used for image intensification: (a) Schematic; (b) Principle of electron multiplication; (c) Wiring. [21]

## 6.4 Photodiodes

A **photodiode** is a semiconductor element that can transform light energy into electrical energy [1, 16]. A single photodiode can be considered as a point sensor. Its principle is similar to that of the pixels of line and area sensors (see Sections 6.6 and 6.7).

In semiconductors such as silicon, gallium, and compound semiconductors, for example, only a few electron–hole pairs are present, so that the conductivity is very low. An applied voltage leads to the flow of only a very low current.

In order to produce electron–hole pairs, at least the energy  $E_{\text{gap}}$  of the bandgap between the valence band and the conduction band has to be provided. The difference between the energies of the valence and the energetically higher conduction band is referred to as the bandgap. If an electron is lifted to the conduction band, a so-called hole remains in the valence band. Electrons or holes, which are located in the conduction or the valence band, are movable and can thus contribute to a current flow.

With a certain probability, irradiated photons can produce electron–hole pairs inside the semiconductor, which leads to an increased conductance of the material. This probability is the quantum efficiency of the semiconductor. In order to lift an electron from the valence to the conduction band, the energy  $h\nu$  of the irradiated photon has to be greater than the bandgap  $E_{\text{gap}}$  (cf. Sec. 2.3).

This is called the inner photoelectric effect, as the generated charge carriers do not leave the material, in contrast to the normal photoelectric effect. In addition, no work function is needed and thus the necessary photon energy  $h\nu$  can be lower, or the cutoff wavelength  $\lambda_{\text{max}}$  can be longer.

By **doping** the semiconductor, i.e., by contaminating the pure semiconductor with atoms of other elements in a defined way, selective holes (p-type doping) can be made in the valence band or electrons (n-type doping) can be inserted into the conduction band. A pn junction acts like a diode, and so a significant current can flow only in one direction. Arranging such a pn junction in the reverse direction, i.e., attaching the negative pole to the p-type doped part and the positive pole to the n-doped part, results in a very small reverse current, which—in the case of a photodiode—is also called dark current. Irradiated photons can produce electron–hole pairs which are attracted by the electric field and produce an electrical current which is proportional to the rate of photons.

If this current runs through a resistor, the voltage drop can be measured (Fig. 6.3). For many applications of automated visual inspection, the dark current  $I_{\text{dark}}$  is much smaller than the photocurrent  $I_{\text{photo}}$ .

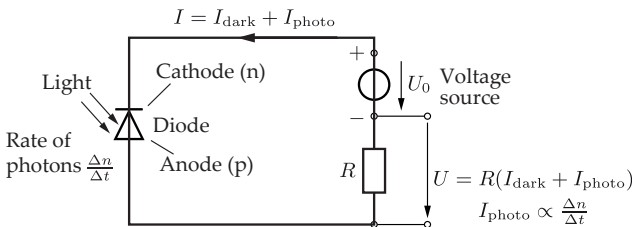


Figure 6.3. Wiring of a photodiode for operation in reverse direction.

In order to increase the quantum efficiency, photodiodes are usually realized as p–i–n diodes (Fig. 6.4). The wide and undoped intrinsic region, which is located between the p-type doped and the n-type doped region, is less conductive and leads to a reduced dark current. The larger width increases the probability of an incoming photon’s producing an electron–hole pair before leaving the material.

Besides the pairs of charge carriers which are generated by exploiting the bandgap, the energy gap between the doping levels and the conduction band can be also be used for the photon-triggered generation of pairs of charge carriers. With special dopings, very small

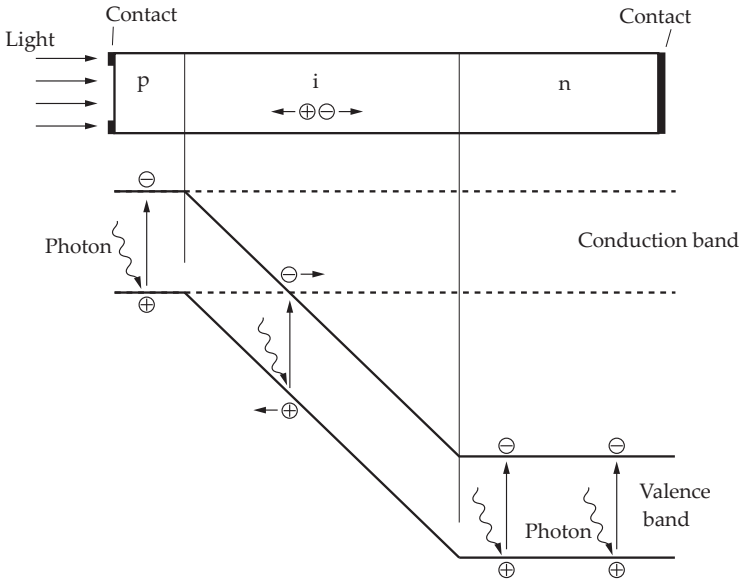


Figure 6.4. Photodiode: Structure of the semiconductor with p-type and n-type doping as well as intrinsic regions and the corresponding band model [16].

differences of energy levels can be achieved, allowing the detection of infrared light, which has longer wavelengths than visible light. According to the Boltzmann statistics [17], small differences in the energy levels  $E_{Diff}$ , which are proportional to  $e^{-\frac{E_{Diff}}{kT}}$ , result in a thermally filled conduction band, even for room temperature. Therefore, semiconductors to be used for the detection of long-wave light have to be cooled.

The bandgaps and the corresponding cutoff wavelengths of different semiconductor materials are listed in Table 6.1.

Table 6.1. Bandgap  $E_{gap}$  and cutoff wavelength  $\lambda_{max}$  of different semiconductors [21].

Compound	$E_{gap}$ in eV	$\lambda_{max}$ in nm
CdS (Cadmium sulfide)	2.42	510
CdSe (Cadmium selenide)	1.70	730
CdTe (Cadmium telluride)	1.56	790
GaAs (Gallium arsenide)	1.42	880
Si (Silicon)	1.12	1,100
Ge (Germanium)	0.66	1,880
PbS (Lead sulfide)	0.41	3,020
InSb (Indium antimonide)	0.17	7290



## 6.5 Position sensitive detectors (PSD)

A **position sensitive detector** is a sensor that can measure the location of an incident bundle of light rays [11]. For some applications, it is therefore an alternative to a line-scan camera, which consists of multiple linearly arranged light sensitive elements.

The detector has a p-i-n surface composition and is operated in the inverse direction, like a photodiode. It is elongated perpendicular to the p-i-n junction (Fig. 6.5). On both ends, the p-type doped layer is equipped with electrodes, A and B respectively. The n-type doped layer on the backside is thoroughly metallized and connected by the electrode C.

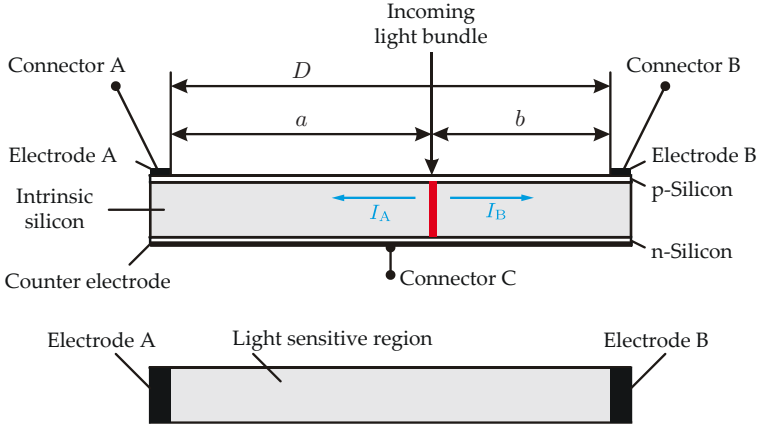


**Figure 6.5.** A position sensitive detector for one-dimensional position measurements. The ends of the light sensitive region  $D$  are linked to connectors A and B. The whole n-type doped silicon layer on the backside is connected to the electrode C and serves as the counter electrode for applying the bias voltage.

An incoming ray of light produces pairs of charge carriers mainly in the undoped intrinsic layer, which are siphoned off by the field of the bias voltage and produce a current flow to the connectors A and B. As the same voltage falls on both sides,  $U_{AC} = U_{BC}$ , the total current flowing through C is divided by the reciprocals of the resistors  $R_A$  and  $R_B$ . On the other hand, the resistors are proportional to the distances  $a$  and  $b$ ; see Fig. 6.6.

Then, Ohm's law  $U = RI$  results in

$$U_{AC} = U_{BC} \Leftrightarrow R_A I_A = R_B I_B \quad (6.1)$$

$$\Leftrightarrow \frac{I_A}{I_B} = \frac{R_B}{R_A} = \frac{b}{a} = \frac{D-a}{a} = \frac{D}{a} - 1 \quad (6.2)$$

$$\Rightarrow a = D \frac{I_B}{I_A + I_B}. \quad (6.3)$$

This simple calculation of the one-dimensional position  $a$  of the incoming light from the measured currents  $I_A$  and  $I_B$  can be realized by a simple analog circuit. There are also two-dimensional PSD sensors, which can measure the  $x$  and  $y$  position of the incoming ray of light [15]; see Fig. 6.7.

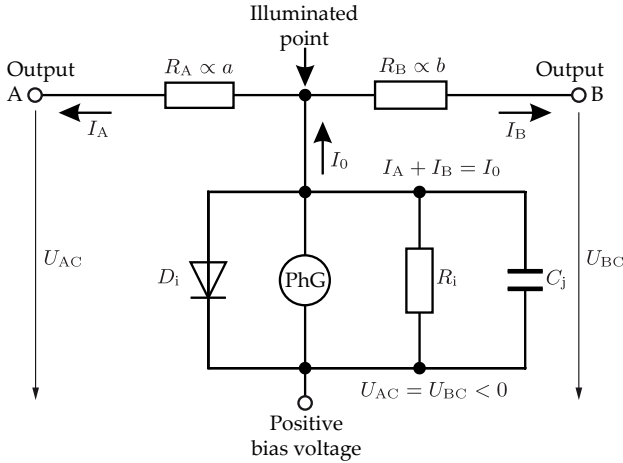


Figure 6.6. Equivalent circuit diagram for the position sensitive detector of Fig. 6.5. The illuminated point on the light sensitive layer serves as a photodiode and thus as a photocurrent generator PhG with a parallel circuit of an ideal diode  $D_i$ , an internal resistance  $R_i$ , and the junction capacitance  $C_j$ , which do not have any influence on the ratio  $\frac{I_A}{I_B}$ . The two regions  $a$  and  $b$ , which are not illuminated, act like two resistors  $R_A$  and  $R_B$  dividing the total current  $I_0$  into two signal currents  $I_A$  and  $I_B$ .

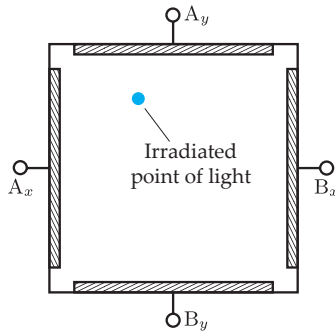


Figure 6.7. Sketch of a two-dimensional PSD sensor seen from above.

## 6.6 Charge-coupled device (CCD)

Nowadays, it is mostly **CCD cameras** that are used for image acquisition. A charge-coupled device (CCD) sensor consists of a geometrically very exact grid of light sensitive cells, as in Fig. 6.8. The photons striking the semiconductor material produce electron–hole pairs. The electrons are accumulated in a space-charge region. The single pixels do not directly touch each other, but are separated by bars (bold lines in Fig. 6.8(b)) and potential barriers in order to prevent the charge carriers from reaching adjacent cells.

The dark-gray elements represent horizontal and vertical shift registers, which allow a charge transport on the chip. Therefore, at least one of the three single elements, which are denoted by the thin lines in Fig. 6.8(b), forms a potential barrier (three-phase shift register). By appropriately driving the device, the potential barriers can be moved and the single charges can be read out in the form of an analog shift register (bucket-brigade circuit); see

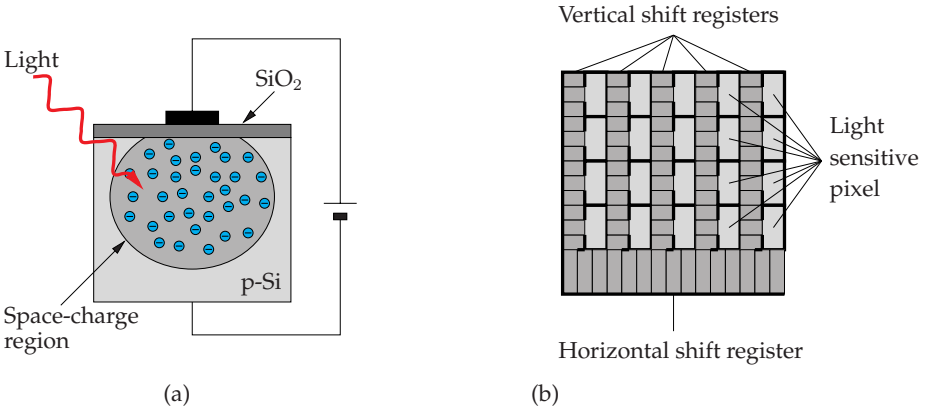


Figure 6.8. Schematic of an interline-transfer sensor: (a) A single pixel viewed from the side; (b) The complete sensor, viewed from above.

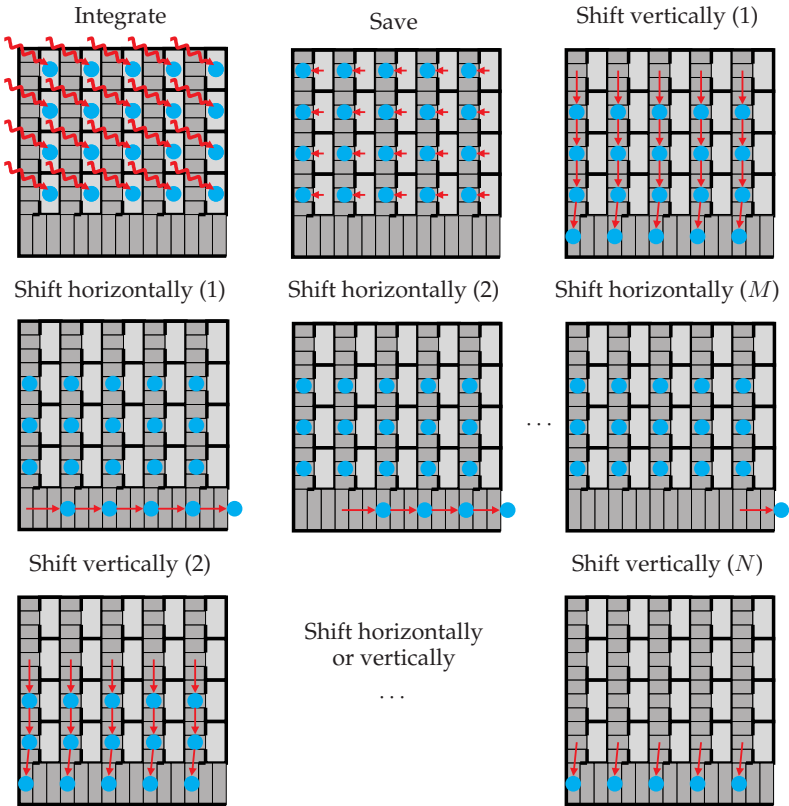


Figure 6.9. Operation of an interline-transfer sensor.

Table 6.2. Common characteristics of commercially available cameras for machine vision.

Number of pixels	640 × 480 – 4800 × 3200
Size of pixel	ca. 2 × 2 μm <sup>2</sup> – 10 × 10 μm <sup>2</sup>
Electronic shutter speed (exposure time)	ca. 10 μs – several seconds (long-exposure)
Frame rate (decreases for increasing image size)	ca. 3 Hz – 200 Hz
SNR	50 dB – 60 dB

Fig. 6.9: after the sensor has been exposed for a specified period of time and the produced charge carriers have been integrated, the collected charge of all the pixels is transferred to the adjacent, shaded vertical readout registers. Afterwards, the charges are moved into the shaded horizontal shift register line by line, which is then read out step by step [9]. After each complete flushing of the horizontal readout register, it is filled again by vertical shifting the next row until the sensor is completely read out.

The described chip is an **interline-transfer sensor** [12]. It is afflicted with the disadvantage that about one-half of the area is covered by the non light-sensitive shift registers. In contrast, for **full-frame sensors**, nearly the whole area of the chip serves as a photo detector. For the readout process, the charges are shifted through the light sensitive elements. Therefore, an exposure during the readout process distorts the captured image. Thus, the control of the exposure time is not realized electronically on the chip (electronic shutter), but by a mechanical stop. The proportion of the whole area of the chip occupied by the light sensitive regions is called the **fill factor**.

The advantages of CCD sensors are their small size, low weight and price, the very accurate geometry of the pixels, and their robustness to shocks and electromagnetic fields.

Table 6.2 shows the usual characteristics for commercially available CCD cameras that are used in machine vision. Besides these, there are special CCD chips with very extreme properties: up to about 100 megapixels, even shorter exposure times, higher SNR due to active cooling, and so on.

In contrast to other integrated circuits (ICs), a further miniaturization of camera chips is counterproductive: the size of the pixels and their distance have to be significantly larger than the wavelength. Smaller pixels will yield no additional information. Besides, the light sensitivity is proportional to the pixel area, so that miniaturization would lead to a reduced sensitivity and increased quantum noise (cf. Sec. 2.3).

## 6.7 Complementary metal-oxide-semiconductor (CMOS) sensors

The relevance of CMOS cameras is steadily increasing for automated visual inspection as well as for optical measurement. CMOS is an abbreviation for ‘complementary metal oxide semiconductor,’ a common design principle for semiconductor circuits. By using the same cost-efficient manufacturing process, the controlling and processing electronics can be integrated in the CMOS camera chip, whereas separate control units are necessary for CCD sensors.

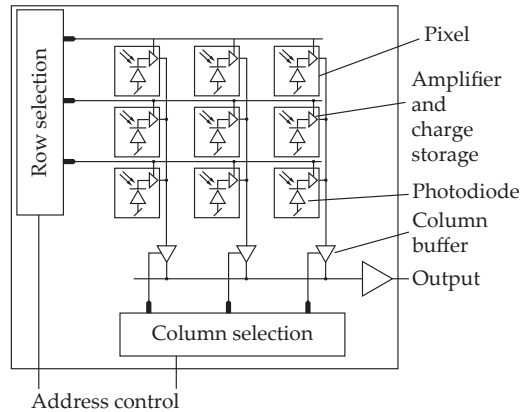


Figure 6.10. Schematic of a CMOS sensor chip with address lines and a separate amplification step per pixel [3].

The detection of photons is based on the same principle as in CCD sensors. However, the readout methods are different: the charge storages of the single pixels can be directly controlled by transistors and address lines (Fig. 6.10). This allows the readout of an arbitrary image region with a higher frequency. There is no need for shift registers. Often, there is already an amplification circuit inside the pixel as a first processing step. However, this might also be a drawback, as the amplification factors of the single pixels can be different because of manufacturing tolerances.

The main advantages of CMOS image sensors over CCD image sensors are the free and random access to the pixels, the large temperature range, the low power consumption, the low production costs, the need for only one operating voltage, the absence of blooming, smear, or time lag, and the possibility of integrating electronic circuits on-chip.

The technical characteristics of common CMOS camera sensors are quite equal to those of CCD cameras (Table 6.2).

### ➤ High-dynamic range CMOS sensors

With help of the CMOS technology, sensors with a significantly larger dynamic range can be realized. Such high dynamic range CMOS (HDRC) sensors are especially suitable for outdoor applications, where the light's intensity might vary notably between direct sunlight and shadows. But there are also tasks in automated visual inspection that need a high dynamic range (i.e., a large range of values), as for the online control of welding processes, for example. For HDRC sensors, the relation between the number of absorbed photons and the output signal of the sensor is no longer linear, but has a logarithmic characteristic. This is achieved by letting the photo current induced by the light drain off over a pn junction in the forward direction. As with diodes, the current increases exponentially with the voltage on the one hand and the voltage is logarithmically related to the photo current on the other hand. A dynamic range of about 120 dB can be typically achieved with HDRC sensors.

## 6.8 Line-scan cameras

Line-scan cameras only use a single line of photosensitive elements, where the sampling aperture is given by the size of the light sensitive area and  $\Delta x$  by the distance between the single elements. Scanning in the  $y$  direction (column direction) is carried out by moving the object relative to the sensor, e.g., for the observation of conveyor belts in assembly lines with a fixed line-scan camera or for the scanning of photographic material with a moving line in a flatbed scanner. The row distance  $\Delta y$  is given by the relative speed of the object and the sensor, as well as by the rate at which the lines are read out.

**Example 6.1 (Image acquired by a line-scan camera):** Figure 6.11 shows an image of a cylinder wall of a combustion engine, which has been acquired with a ‘cylinder scanner’ performing an rotational azimuthal movement of the line-scan camera at a constant distance from the cylinder wall. ■



**Figure 6.11.** Image of a cylinder wall of a combustion engine, captured with a line-scan camera (source: Breitmeier Messtechnik GmbH).

With a line-scan camera, high resolutions of typically up to 16,384 pixels can be achieved, as they usually have a higher number of pixels than a single line of an area sensor. Besides, it is easier to provide a targeted and homogeneous illumination [20]. Hence, the use of line-scan cameras is especially suitable for the automated visual inspection of continuous products on conveyor belts. The camera can be clocked by an incremental encoder, which measures the speed of the conveyor belt. By this means, a single image line always corresponds to the same spatial movement independently of the belt's speed. If an area camera is used for such an application, the captured images have to be registered after the recording.

Multiline-scan cameras are also commercially available: they contain several lines located near each other. The lines are equipped with different optical filters, in order to gain multichannel information such as multispectral or hyperspectral images. There are also hyperspectral line-scan cameras, with several hundred lines.

Similar to area sensors (see Sections 6.6 and 6.7), line-scan cameras can be realized with either CCD or CMOS technology.

## 6.9 Color sensors and color cameras

Common **color cameras** provide the three color channels red, green and blue for every image pixel. For such cameras, usually a color filter is placed in front of the camera chip, letting only one of the three base colors pass for each pixel. The colors are arranged so that they are located close to each other on the CCD or CMOS chip. The commonly used Bayer filter

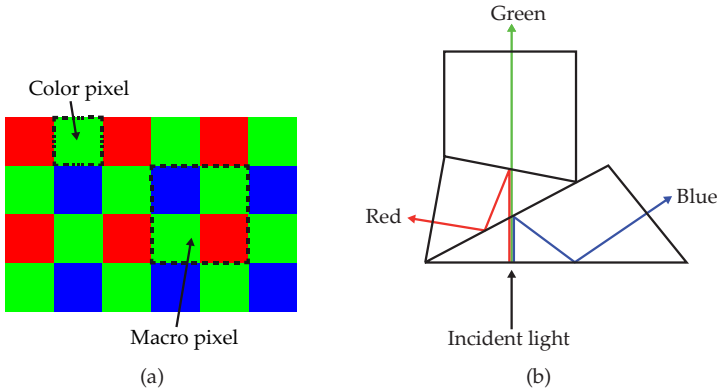


**Figure 6.12.** Color cameras. (a) Arrangement of colors for a Bayer filter; (b) 3-Chip color camera with dichroic beam splitters.

uses a  $2 \times 2$  section of the pixel matrix to form a macro pixel; see Fig. 6.12(a). A macro pixel contains two green pixels, one red pixel, and one blue pixel, since the human eye is more sensitive to green light. So actually, only one color channel per pixel is captured. The other two channels have to be interpolated from neighboring pixels, which is called demosaicing [14]. For line-scan cameras, it is sensible to use a separate line per color channel.

The disadvantages of macro pixel color cameras are their lower lateral resolution and the loss of light caused by the color filters. Thus, premium cameras sometimes use another principle for recording colors. The incident light is split into the three color components by using dichroic beam splitters [2, 10]. Some wavelengths are reflected by these beam splitters, and others are transmitted. The dichroic effect is based on the interference on multiple thin dielectric layers. By using suitable prisms, each color component is directed to its corresponding detector; see Fig. 6.12(b). There is no need for an interpolation. The camera's optics and mechanics have to be manufactured and adjusted in a very precise way, so that the positions of the pixels of the three components match exactly.

## 6.10

### 6.10 Infrared cameras

Cameras for the infrared part of the spectrum can mainly be realized by means of the following two principles: as an array of thermometers (bolometer cameras), or as quantum detectors analogous to the camera sensors for visible light (photonic cameras).

The infrared spectrum can be further divided into several bands; see Table 6.3. The near infrared is directly adjacent to the visible light and can still be detected with silicon image sensors. For longer wavelengths, other materials have to be used for quantum detectors. Finally, the far infrared is followed by the THz-part of the spectrum.

An important application of infrared images is measuring the temperature distribution of an object with so-called thermographic cameras in the medium-wavelength infrared (MWIR) and the long-wavelength infrared (LWIR) (see Table 6.3). Any object emits infrared radiation, with increasing intensity for higher temperatures (see Sec. 2.7.1.1). Thus, an infrared image can be used to calculate the spatial temperature distribution of the observed

Table 6.3. Different wavelength regions of the infrared spectrum.

Description	Abbreviation	$\lambda$ in $\mu\text{m}$
Near infrared	NIR	0.75 – 1.4
Short-wavelength infrared	SWIR	1.4 – 3.0
Medium-wavelength infrared	MWIR	3.0 – 8.0
Long-wavelength infrared	LWIR	8.0 – 15.0
Far infrared	FIR	15.0 – 1000

Table 6.4. Typical operating characteristics of uncooled bolometer cameras [8].

<b>Number of pixels</b>	640 × 480
<b>Size of pixel</b>	20 × 20 $\mu\text{m}^2$ – 50 × 50 $\mu\text{m}^2$
<b>NETD</b>	ca. 70 mK – 100 mK
<b>Material</b>	VO <sub>x</sub> (Vanadium oxide), Si (Silicon), Ti (Titanium)

object, if its material properties are known. Some manufacturing errors can be detected by the use of this temperature distribution [19].

### 6.10.1 Bolometer cameras

The measuring principle of bolometers is based on the temperature dependency of the electric resistance. The black detector area is heated by the absorption of electromagnetic radiation (cf. Sec. 2.6.1). The measured quantity is the electric resistance of a metal or a semiconductor inside the detector [5]. The measurement gives information on the intensity of the incident radiation. Hence, in contrast to quantum detectors, bolometers are based on an indirect principle of operation (Fig. 6.13). Point sensors as well as area sensors can be constructed that employ the principle of the bolometer. The sensor's temperature is regulated to the desired value, which can be on the order of room temperature. Each of the thermal resistors is supplied with a constant current, so that the temperature dependent change of its resistance leads to a proportional change of the voltage. Because of their principle of operation, bolometers suffer from a certain lag, and neighboring pixels might influence each other (crosstalk) because of heat conductance.

Bolometers are broadband sensors, which do not have a cutoff wavelength and can capture the spectrum from the near infrared up to THz radiation. They can be operated without active cooling, so that they can be used to produce cheap infrared cameras. Instead of the SNR, the so-called NETD (noise equivalent temperature difference) is commonly used to judge the signal quality of infrared cameras [8]. Table 6.4 shows the typical operating characteristics of an uncooled bolometer camera.

### 6.10.2 Infrared quantum detector cameras

An alternative to bolometers in the near and medium-wavelength infrared is given by semiconductor sensors that—among other principles—use the inner photoelectric effect to detect electromagnetic radiation. Special semiconductor materials with special dopings allow even infrared photons with low energies to produce electron–hole pairs [8, 19]. The principle of



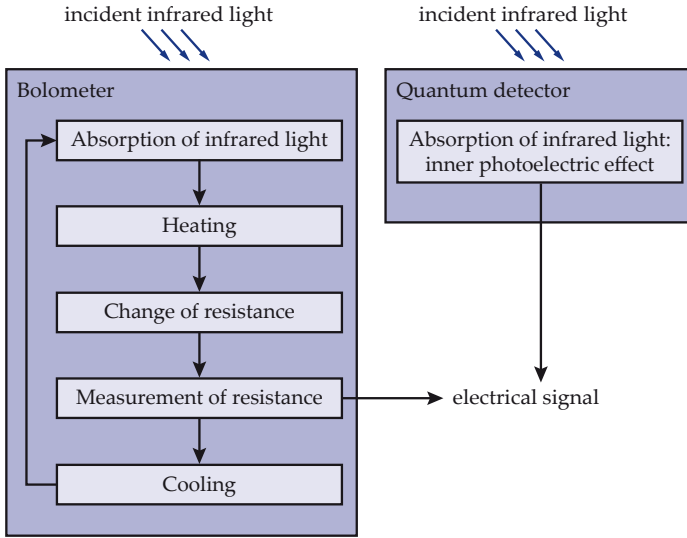


**Figure 6.13.** Indirect principle of operation of a bolometer sensor compared to the direct principle of operation of a quantum detector [8].

operation is the same as that of photodiodes: absorbed IR photons lead to an electric current proportional to the number of photons, because of the inner photoelectric effect.

Since at room temperature there are many charge carriers which are generated thermally, the sensors have to be intensively cooled. For the detection of medium-wavelength infrared (MWIR), temperatures of about 140 K are necessary and even 80 K for long-wavelength infrared (LWIR). The cooling is performed with liquid nitrogen or electrically driven Stirling engines, which are cheaper and operationally safer.

Depending on the application, semiconductor materials with different cutoff wavelengths are available (Table 6.5). Some materials can be combined to form a dual band sensor, so that two different spectral ranges can be measured simultaneously, resulting in a two-channel image [6]. As an example, the combination of gallium arsenide and aluminum gallium arsenide can be used to detect medium- and long-wavelength infrared. For

**Table 6.5.** Properties of infrared quantum detector cameras: Cutoff wavelength  $\lambda_{max}$ , NETD for an object temperature of 300 K, distance of pixel in  $\mu\text{m}$ , available array size (according to [8]).

Material	$\lambda_{max}$	NETD/mK	Pixel distance	Number of pixels
HgCdTe (Mercury cadmium telluride)	12.0 $\mu\text{m}$	10	15–40	1280 $\times$ 1024
InSb (Indium antimonide)	5.0 $\mu\text{m}$	20	15–50	1024 $\times$ 1024
GaAs/AlGaAs (Gallium arsenide)	9.5 $\mu\text{m}$	10 / 30	25–50	640 $\times$ 512
PtSi (Platinum silicide)	5.4 $\mu\text{m}$	60	20–25	800 $\times$ 512

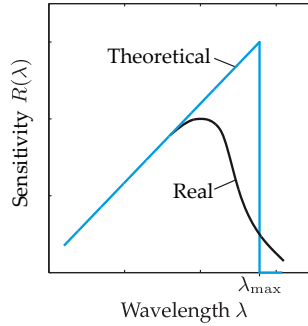


Figure 6.14. Theoretical and real sensitivity of quantum detectors with respect to the wavelength [4].

a constant quantum efficiency, the sensitivity of quantum detectors increases with the wavelength, because then a constant intensity results in more flowing photons (Fig. 6.14).

## 6.11 Quality criteria for image sensors

There are numerous criteria that can be used to judge the performance of image sensors, and especially semiconductor sensors [9, 18]. Some of these criteria are presented here:

- Quantum efficiency: the quantum efficiency is the relation of produced electrons to the number of striking photons.
- Full well capacity: the full well capacity denotes the maximum number of electrons that can be collected by a single pixel (cf. Sec. 2.3).
- Fill factor: ratio of the area of the light sensitive regions to the area of the entire chip (cf. Sec. 6.6).
- Noise ratio: there are different sources of electrical noise in image sensors. Noise can be produced during the transport of charges or inside the readout amplifier. The noise can be quantified as the relation of the output signal to its standard deviation.
- Dark current: the dark current is the signal of the image sensor without any illumination. An ideal sensor would produce a dark current that is equal to zero, which is not the case for real sensors, especially because of thermal noise. The dark current can be significantly reduced by actively cooling the sensor [9].
- Dynamic range: a sensor's dynamic range is the relation of the maximum output signal to the standard deviation of the dark current.
- Homogeneity: ideally, all pixels of a sensor behave identically. However, manufacturing tolerances result in different amplifications and noise performances (fixed pattern noise).
- Artifacts: depending on the construction principle of the image sensor, disturbing artifacts can arise in the image under certain circumstances.
- Blooming is an effect where the charges of overexposed pixel flow to neighboring pixels, which will then produce an output signal which is too high.
- Smear consists of stripes in the image which are caused by the shift registers of the CCD chips.

- Addressing: some sensors allow a high frequency readout of selected image regions. Other sensors allow aggregating neighboring pixel on the level of charges, resulting in an undersampled image.
- Power consumption.

It is not easy to compare CMOS and CCD sensors in terms of these criteria, as the original disadvantages of these technologies have more and more been overcome because of further development [13]. CMOS sensors have the advantage in terms of power consumption, addressing, and dynamic range (especially HDR sensors), and are less prone to artifacts, blooming, and smear, due to their construction. CCD chips stand out for a higher homogeneity and a lower dark current.

## 6.12 Bibliography

- [1] Jörg Angerstein. UV-Visible and Near IR Semiconductor Sensors. In E. Wagner, R. Dändliker, and K. Spenner, editors, *Optical Sensors*, volume 6 of *Sensors*, pages 173–199. VCH, 1992.
- [2] Bruce Batchelor and Paul Whelan. *Intelligent vision systems for industry*. Springer, 1997.
- [3] Nicolas Blanc. CCD versus CMOS – has CCD imaging come to an end? In Dieter Fritsch and Rudolf Spiller, editors, *Photogrammetric Week*. Wichmann, 2001.
- [4] Helmut Budzier and Gerald Gerlach. *Thermal infrared sensors: theory, optimization, and practice*. Wiley, 2010.
- [5] Axel Donges and Reinhard Noll. *Lasermesstechnik: Grundlagen und Anwendungen*. Hüthig, 1993.
- [6] Arnold Goldberg, Theodore Fischer, Stephen Kennerly, Samuel Wang, Mani Sundaram, Parvez Uppal, Michael Winn, Gregory Milne, and Mark Stevens. Dual Band QWIP MWIR/LWIR Focal Plane Array Test Results. In Eustace Dereniak and Robert Sampson, editors, *Infrared Detectors and Focal Plane Arrays VI*, volume 4028, pages 276–287. Proc. SPIE, 2000.
- [7] Jörg Haus. *Optical sensors: basics and applications*. Wiley-VCH, 2010.
- [8] Thomas Hierl. Hochauflösende Infrarot-Detektormatrizen. In Norbert Bauer, editor, *Handbuch zur Industriellen Bildverarbeitung*, pages 41–47. Fraunhofer IRB Verlag, Stuttgart, 1st edition, 2007.
- [9] Bernd Jähne. *Practical handbook on image processing for scientific and technical applications*. CRC Press, 2nd edition, 2004.
- [10] Erik Klaas. Farbbildverarbeitung. In Bernd Breuckmann, editor, *Bildverarbeitung und optische Messtechnik in der industriellen Praxis*, pages 54–65. Franzis, 1993.
- [11] Alexander Koch, Michael Ruprecht, Olaf Toedter, Gerd Häusler, Stefan Blosssey, Harald Schoenfeld, and Veit Windbichler. *Optische Messtechnik an technischen Oberflächen*. expert Verlag, 1998.
- [12] Reimar Lenz. Grundlagen der Videometrie, angewandt auf eine ultra-hochauflösende CCD-Farbkamera. *Technisches Messen*, 57(10):366–380, 1990.
- [13] Dave Litwiller. CMOS vs. CCD: Maturing Technologies, Maturing Markets. *Photonics Spectra*, 39(8):54–61, 2005.
- [14] Horst Mattfeldt. Camera Systems in Machine Vision. In Alexander Hornberg, editor, *Handbook of Machine Vision*, pages 361–426. Wiley-VCH, 2006.
- [15] Tilo Pfeifer and Robert Schmitt. *Fertigungsmesstechnik*. Oldenbourg, 3rd edition, 2010.
- [16] Michael Reisch. *Halbleiter-Bauelemente*. Springer, 2005.
- [17] Bahaa Saleh and Malvin Teich. *Fundamentals of photonics*. Wiley, 2nd edition, 2007.
- [18] Peter Schwider. CCD- und CMOS-Bildsensoren. In Norbert Bauer, editor, *Handbuch zur Industriellen Bildverarbeitung*, pages 36–40. Fraunhofer IRB Verlag, 1st edition, 2007.

- [19] Bernd Schönbach. Wärmebildkameras und IR-Bildverarbeitung. In Bernd Breuckmann, editor, *Bildverarbeitung und optische Messtechnik in der industriellen Praxis*, pages 21–53. Franzis, 1993.
- [20] Kai Taeubner. Zeilenkameras. In Norbert Bauer, editor, *Handbuch zur Industriellen Bildverarbeitung*, pages 32–34. Fraunhofer IRB Verlag, 1st edition, 2007.
- [21] Wolfgang Zinth and Ursula Zinth. *Optik: Lichtstrahlen – Wellen – Photonen*. Oldenbourg, München, 4th edition, 2013.

Chapter 7

**Methods of Image Acquisition**

**7**

## 7 Methods of Image Acquisition

7.1	Introduction . . . . .	227
7.2	Measuring optical properties . . . . .	228
7.2.1	Measurement of the complex index of refraction . . . . .	230
7.2.1.1	Reflectometry . . . . .	230
7.2.1.2	Ellipsometry . . . . .	234
7.2.2	Fluorescence . . . . .	240
7.2.3	Methods for measuring the reflectance . . . . .	242
7.2.3.1	Diffuse illumination . . . . .	242
7.2.3.2	Bright-field illumination . . . . .	243
7.2.3.3	Dark-field illumination . . . . .	244
7.2.3.4	Laser scanners . . . . .	246
7.2.3.5	Flatbed scanners . . . . .	248
7.2.4	Spectral sensors . . . . .	248
7.2.5	Light scattering methods and the inspection of surface roughness . . . . .	251
7.3	3D shape capturing . . . . .	254
7.3.1	Triangulation (point-by-point scanning) . . . . .	255
7.3.2	Light-section methods (line scanning) . . . . .	259
7.3.3	The measurement uncertainty of triangulation . . . . .	260
7.3.4	Structured illumination . . . . .	263
7.3.4.1	Stripe projection . . . . .	264
7.3.5	Deflectometry . . . . .	268
7.3.5.1	Open research questions regarding deflectometry . . . . .	276
7.3.6	The moiré method . . . . .	276
7.3.6.1	The moiré effect . . . . .	276
7.3.6.2	Mathematical model of the moiré effect . . . . .	278
7.3.6.3	Telecentric stripe projection . . . . .	279
7.3.6.4	Shadow moiré . . . . .	283
7.3.6.5	Projection moiré . . . . .	284
7.3.7	Final remark on structured illumination . . . . .	285
7.3.8	Stereo images . . . . .	285
7.3.8.1	Derivation of the fundamental matrix . . . . .	286
7.3.8.2	Stereo correspondence algorithms . . . . .	289
7.3.8.3	Stereo reconstruction . . . . .	290
7.3.8.4	Multi-camera systems . . . . .	290
7.3.8.5	Monocular stereo . . . . .	291
7.3.9	Light-field cameras . . . . .	291
7.3.10	Silhouette capturing . . . . .	296
7.3.10.1	Telecentric silhouette capturing . . . . .	298
7.3.10.2	Illumination for telecentric imaging . . . . .	298
7.3.10.3	Retroreflectors . . . . .	300
7.3.11	Shape from shading . . . . .	301
7.3.12	Autofocus sensors . . . . .	303
7.3.13	Confocal microscopy . . . . .	304

7.3.14	Confocal chromatic triangulation . . . . .	307
7.3.15	Time-of-flight sensors . . . . .	308
7.3.16	Phase-based methods . . . . .	309
7.3.16.1	Interferometry . . . . .	309
7.3.16.2	Speckle interferometry for material inspection . . . . .	314
7.3.16.3	Shearography . . . . .	315
7.3.16.4	Holography . . . . .	317
7.4	Capturing interior object structures . . . . .	320
7.4.1	Thermography . . . . .	321
7.4.2	Imaging using X-rays . . . . .	325
7.4.3	Optical coherence tomography . . . . .	330
7.4.4	Schlieren imaging and schlieren tomography . . . . .	331
7.4.5	Image acquisition using terahertz radiation . . . . .	332
7.4.6	Photoelasticity . . . . .	338
7.5	Special image acquisition methods . . . . .	344
7.5.1	Image acquisition systems with variable illumination direction . . . . .	348
7.5.2	Endoscopy . . . . .	349
7.6	Universal principles . . . . .	350
7.6.1	Suppression of extraneous light . . . . .	350
7.6.2	Inverse illumination . . . . .	351
7.7	Summary . . . . .	356
7.8	Bibliography . . . . .	358





## 7 Methods of Image Acquisition

### 7.1 Introduction

This chapter covers different methods for image acquisition in automated visual inspection. Selecting the appropriate acquisition method depends on the properties of interest of the investigated object (Fig. 7.1):

- optical properties like reflectance, color, texture, and index of refraction as a function of position, or
- geometrical properties like the three-dimensional shape of the object.

Methods for measuring the reflectance, such as homogeneous illumination methods as well as laser and flatbed scanners, will be covered in Sec. 7.2. In addition, the measurement of the complex index of refraction will be discussed, which can be used for material classification (Fig. 7.2).

There are numerous methods for capturing the 3D shape of an object; they rely on three different measurement principles (Fig. 7.3):

- Triangulation,
- intensity, or
- length of the optical path (i.e., time of flight).

Section 7.3 covers the capturing of 3D shapes, and is structured according to the above listing. The triangulation methods are further divided into passive (especially stereo) and active methods. The latter use targeted and sometimes patterned illumination in order to capture the object's shape.

Intensity based methods detect changes in the intensity of the scattered and transmitted light in order to reconstruct the object's shape. Examples include silhouette capturing, capturing the shape from shading, focus sensors, and confocal microscopy.

Time of flight methods measure the period of time it takes for the light to reach the object and return to the detector. The elapsed time is used to calculate the distance to the object.

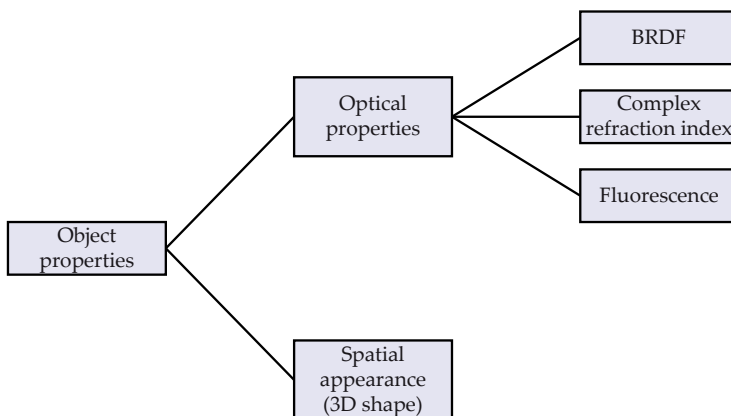


Figure 7.1. Object properties that can be optically measured.

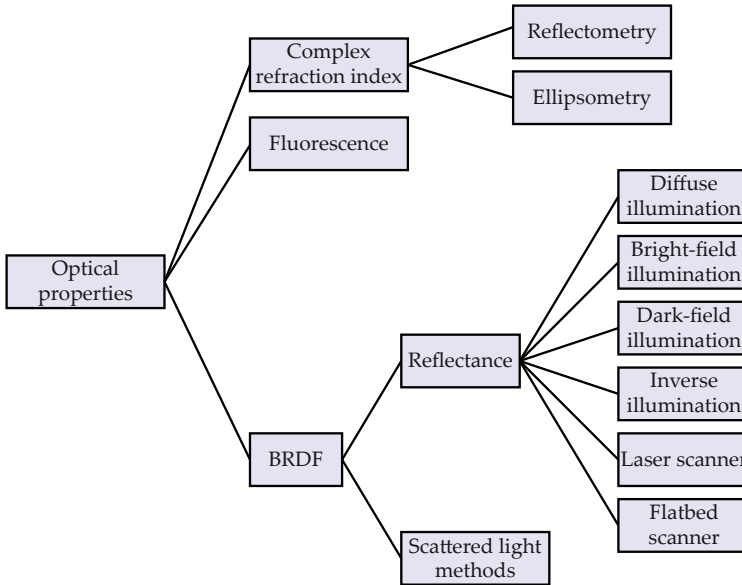


Figure 7.2. Taxonomy of methods for capturing optical properties.

Instead of directly measuring the time of flight, the resulting shift of phase can be measured. This can be done, e.g., by exploiting interference effects, which have been covered in Sec. 2.2.

Besides an object's macroscopic 3D shape, sometimes also its inner structures are of interest. Methods like thermal imaging, terahertz and X-ray imaging, as well as photoelasticity, allow the detection of defects in the interior of an object (Sec. 7.4). Later on, some special image acquisition and illumination methods will be covered in Sec. 7.5.

Finally, Sec. 7.6 will present some common principles which can be used for reflectance measurements as well as for 3D shape capturing. These include inverse illumination methods and approaches compensating for the background illumination.

## 7.2 Measuring optical properties

The optical properties of an object are determined by its interaction with light in accordance with the phenomena described in Sec. 2.6. To begin with, the measurement of the complex index of refraction will be covered; this relies on the physical basics from Chap. 2. By means of the complex index of refraction, the investigated material can be classified and layer thicknesses can be determined. Afterwards, fluorescence will be briefly discussed, which can also be used for material classification.

Section 7.2.3 presents methods for measuring the reflectance that can be used for defect detection, for example. Readers who are mainly interested in that topic may at first skip Sections 7.2.1 and 7.2.2, as they are not necessary for understanding the subsequent content. Finally, Sec. 7.2.5 covers methods based on scattered light that give information about an object's reflectance as well as about its microscopic structure, and thus about its 3D shape.

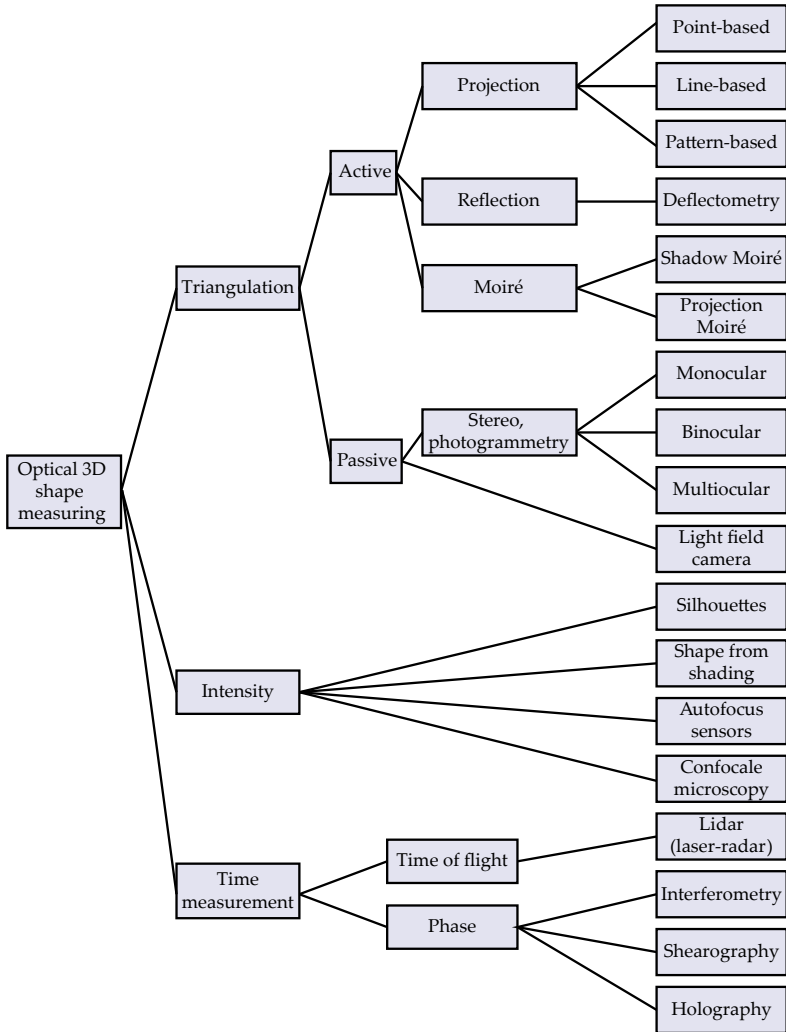


Figure 7.3. Taxonomy of methods for capturing 3D shape.

## 7.2.1 Measurement of the complex index of refraction

As described in Sec. 2.6.6.1, the index of refraction of electrically conducting materials can be considered as a complex number. The complex index of refraction  $\underline{n}$  is a characteristic material property. Thus, by measuring the complex index of refraction, especially metals can be classified and sorted.

### 7.2.1.1 Reflectometry

Reflectometry is a method for measuring layer thicknesses and indices of refraction. For spectroscopic reflectometry, the Fresnel reflectances, which describe the relation between the reflected and the incident intensities, are obtained for different wavelengths. As a generalization of the definition in Sec. 2.6.5, the absolute reflectance can be measured, describing the relation between the reflected and incident intensities of light for an object with several (boundary) layers. The wavelengths used can range from ultraviolet light up to infrared light:  $\lambda \in [200 \text{ nm}, 2000 \text{ nm}]$ . The parameter estimation is done by using a layer model containing the thicknesses and the indices of refraction of the layers as parameters. By adjusting the method to conform with the measured data, the quantities sought can be estimated by a regression analysis.

Typical reflectometers illuminate and observe the surface of interest perpendicularly. Therefore, the distinction between s and p waves is omitted, as the Fresnel reflectances of perpendicular and parallel polarization are equal for an angle of incidence of  $\theta = 0^\circ$ :  $R_{12}^s = R_{12}^p$  (see Ex. 2.10). Therefore, the mathematical relations are simplified because of the perpendicular orientation with respect to the surface.

**Example 7.1 (Layer model):** A layer model might be defined as follows (Fig. 7.4): the air between the measurement instrument and the object's surface is the first layer. Its index of refraction is  $\underline{n}_1 = n_1 \approx 1$ . The thickness of the adjacent layer consisting of medium 2 is denoted by  $h$  and its complex index of refraction by  $\underline{n}_2$ . The next material is medium 3, with a complex index of refraction  $\underline{n}_3$ . The observation direction is perpendicular to the surface, so that the angles of incidence are  $\theta_1 = \theta_2 = \theta_3 = 0$ . ■

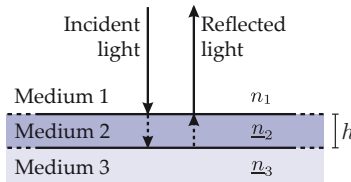


Figure 7.4. Layer model for reflectometry.

If cameras are used as the detectors, a spatially resolved reflectometry is possible. Figure 7.5 shows a setup for reflectometry with two cameras. The scene is illuminated by a monochromatic light source providing parallel light of intensity  $I(\mathbf{x}, \lambda)$ , whose wavelength  $\lambda$  can be adjusted. A beam splitter causes half of this light to be transmitted and the other half to be reflected. The reflected part of the light illuminates the test object with intensity  $\frac{1}{2}I(\mathbf{x}, \lambda)$ . The light that is reflected by the object is captured by a camera with a telecentric lens system. The measured intensity is denoted by  $I_1(\mathbf{x}, \lambda)$ . The part that is transmitted by the beam

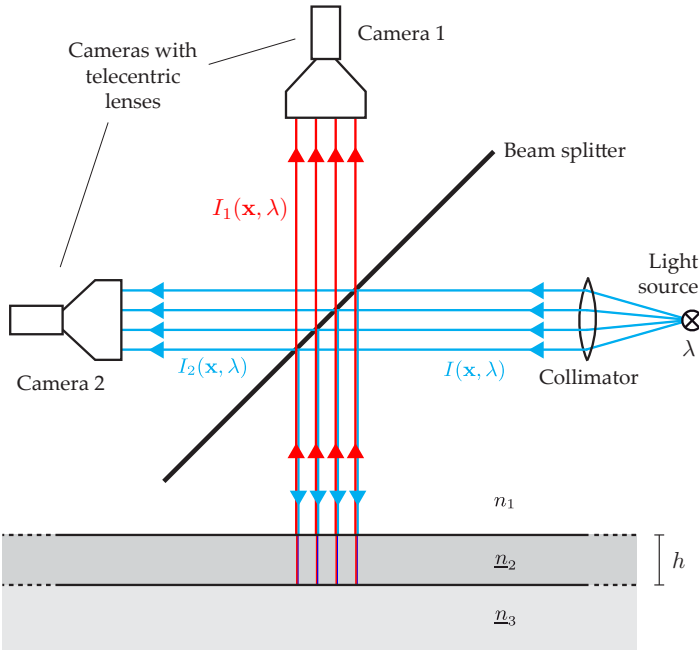


Figure 7.5. Measurement setup for spatially resolved reflectometry.

splitter directly reaches a second camera with a telecentric lens system, which measures the intensity  $I_2(\mathbf{x}, \lambda) = \frac{1}{2}I(\mathbf{x}, \lambda)$ . Radiometrically calibrating those two cameras, so that the measured gray values can be interpreted as intensity values, results in the following formula for the absolute reflectance:

$$R(\mathbf{x}, \lambda) = 2 \frac{I_1(\mathbf{x}, \lambda)}{I_2(\mathbf{x}, \lambda)}. \quad (7.1)$$

There are two alternatives to the described setup:

- The second camera is omitted. The intensity  $I_1$  of the test object is compared to the intensity  $I_{1,\text{Ref}}$  measured for a reference sample. Then, the relative reflectance can be calculated:

$$R_{\text{rel}}(\mathbf{x}, \lambda) = \frac{I_1(\mathbf{x}, \lambda)}{I_{1,\text{Ref}}(\mathbf{x}, \lambda)}. \quad (7.2)$$

- Instead of monochromatic light, broadband light can be used in combination with a spectrally resolving camera (hyperspectral camera), see Sec. 7.2.4. However, only one line of the object's surface can then be investigated per image. For a complete investigation, the surface has to be scanned in a direction perpendicular to this scan line.

The reflection caused by the described layer model can be quantitatively modeled. Between the two interfaces, the light can be reflected multiple times and its phase shifted by  $\beta$  when passing layer 2. This results in a total phase shift of  $2\beta$ , as the layer is traversed twice. The superposition of the phase shifted, reflected light waves can be calculated by means of a

geometric series [166]. For light coming in perpendicularly, this results in

$$R = \left| \frac{r_{12} + r_{23} e^{-j2\beta}}{1 + r_{12} r_{23} e^{-j2\beta}} \right|^2, \quad (7.3)$$

$$\beta := 2\pi \frac{h}{\lambda} n_2, \quad (7.4)$$

where the  $r_{ij}$  denote the Fresnel coefficients of reflection in accordance with Eqs. (2.215) and (2.217) in Chap. 2.

The absolute reflectance  $R = R(\mathbf{x}, \lambda, h, \underline{n}_2, \underline{n}_3)$  is a function of the model parameters  $h$ ,  $\underline{n}_2$  and  $\underline{n}_3$ . These parameters are estimated by means of a regression analysis:

$$(\hat{h}, \hat{\underline{n}}_2, \hat{\underline{n}}_3) = \arg \min_{h, \underline{n}_2, \underline{n}_3} \sum_{\lambda=\lambda_{\min}}^{\lambda_{\max}} (R_{\text{measured}}(\mathbf{x}, \lambda) - R_{\text{model}}(\mathbf{x}, \lambda, h, \underline{n}_2, \underline{n}_3))^2. \quad (7.5)$$

The spectral sampling is done for discrete wavelengths  $\lambda \in [\lambda_{\min}, \lambda_{\max}]$ . If  $\underline{n}_2$  or  $\underline{n}_3$  is known, the regression analysis can be simplified accordingly. The special case of a single dielectric layer  $n_2$  surrounded by air with  $n_1 \approx 1$  yields

$$R = \left( \frac{n_2 - 1}{n_2 + 1} \right)^2 \quad (7.6)$$

with the closed-form solution [84]

$$n_2 = \frac{1 + \sqrt{R}}{1 - \sqrt{R}}. \quad (7.7)$$

**Example 7.2 (Reflectance):** We now introduce a model for a silicon dioxide layer ( $\text{SiO}_2$ ) with a thickness of  $h = 2 \mu\text{m}$  on a silicon crystal (Si) [166, S. 59].

Medium 1	Air	$n_1 = 1$	
Medium 2	$\text{SiO}_2$	$\underline{n}_2 = n_2 = 1.46$	
Medium 3	Si	$\underline{n}_3 = 3.88 - j0.02$	(for $\lambda = 633 \text{ nm}$ )

Figure 7.6 shows the reflectance  $R$  in accordance with (7.3) for this model with respect to the wavelength  $\lambda$ . ■

The measured reflectance varies periodically with respect to the wavelength (Fig. 7.6). The maxima (minima) of the intensity are caused by constructive (destructive) interference of the waves reflected by the two interfaces. In the case of real-valued indices of refraction  $\underline{n}_1 = n_1$ ,  $\underline{n}_2 = n_2$  and  $\underline{n}_3 = n_3$  and in accordance with (2.121), there are maxima for

$$\cos 2\beta = 1, \quad \beta = k\pi, \quad k \in \mathbb{Z}, \quad (7.8)$$

and minima for  $\cos 2\beta = -1, \beta = k\pi + \frac{\pi}{2}$ . These maxima (minima) are located on the upper (lower) envelope  $R_u(\lambda)$  ( $R_l(\lambda)$ ) of the reflectance:

$$R_u(\lambda) = \left| \frac{n_3 - n_1}{n_3 + n_1} \right|^2, \quad (7.9)$$

$$R_l(\lambda) = \left| \frac{n_1 n_3 - n_2^2}{n_1 n_3 + n_2^2} \right|^2. \quad (7.10)$$

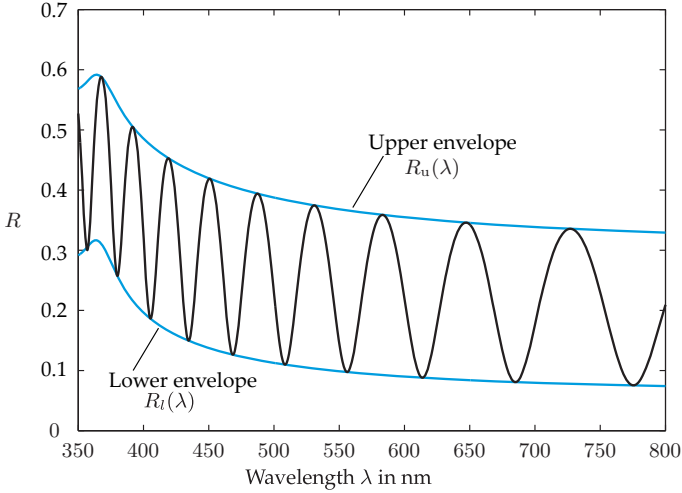


Figure 7.6. Reflectance for the model of Ex. 7.2 as well as the upper and lower envelope with respect to the wavelength  $\lambda$ .

These formulas hold for the practically relevant case of  $n_1 < n_2 < n_3$ . For the case of  $n_1 < n_3 < n_2$ , the locations of the minima and maxima as well as the upper and lower envelope are interchanged [72].

If medium 1 is air, with  $n_1 \approx 1$ , the following simplification results:

$$R_u(\lambda) = \left| \frac{n_3 - 1}{n_3 + 1} \right|^2, \tag{7.11}$$

$$R_l(\lambda) = \left| \frac{n_3 - n_2^2}{n_3 + n_2^2} \right|^2. \tag{7.12}$$

The upper envelope corresponds to the reflection on medium 3 in the absence of layer 2.

The indices of refraction  $n_2$  and  $n_3$  depend on the wavelength  $\lambda$ . For common materials, the indices of refraction are well known functions of the wavelength [106,129].

For a dielectric medium 2 with  $n_2 = n_2$ , Eq. (7.8) yields the following simple formula for two consecutive maxima (minima) of the reflectance with wavelengths  $\lambda_i$  and  $\lambda_{i+1}$ ,

$$2 \frac{h}{\lambda_{i+1}} n_2 = k, \tag{7.13}$$

$$2 \frac{h}{\lambda_i} n_2 = k + 1, \tag{7.14}$$

resulting in the following approximation for the thickness  $h$  of the layer:

$$h \approx \frac{\lambda_i \lambda_{i+1}}{2n_2 (\lambda_{i+1} - \lambda_i)} \tag{7.15}$$

The formula would be exact if  $n_2$  and  $n_3$  did not depend on  $\lambda$  [166].

### ⊙ 7.2.1.2 Ellipsometry

Ellipsometric methods can be used to determine the complex index of refraction  $\underline{n}$  of a material [140, 165, 166]. In addition, the thickness  $h$  of thin layers can be measured together with their complex indices of refraction. The layers are required to be thinner than about 4 times the penetration depth (see Sec. 2.6.6.1):  $h < 4\delta$ .

The investigated material is illuminated with light of known polarization. Afterwards, the polarization state of the reflected light<sup>1</sup> is measured. The change of the polarization state can be used to calculate the material's complex index of refraction.

Ellipsometry measures the complex quotient

$$\rho := \frac{r_{12}^p}{r_{12}^s} \quad (7.16)$$

of the Fresnel reflection coefficients  $r_{12}^p$  and  $r_{12}^s$  for light polarized parallel or perpendicularly with respect to the plane of incidence (see Sec. 2.6.5). The complex number  $\rho$  can be expressed in polar coordinates:

$$\rho = \tan \Psi e^{j\Delta} \quad (7.17)$$

with

$$\Psi := \arctan \frac{|r_{12}^p|}{|r_{12}^s|} \quad \Psi \in [0, \frac{\pi}{2}) \quad (7.18)$$

$$\Delta := \Delta\varphi_i - \Delta\varphi_r \quad \Delta \in [0, 2\pi), \quad (7.19)$$

where  $\Delta\varphi_i$  denotes the difference of phase of the p and s waves of the incident light and  $\Delta\varphi_r$  is the corresponding phase difference of the reflected wave [166]. The quantities  $\Psi$  and  $\Delta$  describe the change of the polarization ellipse caused by the reflection. In the field of ellipsometry, they are usually determined by numerically solving a system of nonlinear equations.

For the identification of materials, an angle of incidence of  $\theta_i > 0$  is necessary, as for perpendicularly incident light one has  $r_{12}^p = r_{12}^s$  and therefore in (7.16),  $\rho = 1$  independently of the material's index of refraction. The ellipsometer has to be carefully adjusted so that the angle of incidence is equal to the observation angle,  $\theta_i = \theta_r$ . Furthermore, the angle of incidence has to be known, in order to make possible the determination of the properties of the material and the thicknesses of the layers. This is why the surface normal corresponding to the point of observation has to be known. Hence, the usual ellipsometers can only investigate planar surfaces. Completely capturing arbitrarily shaped objects requires the simultaneous measurement of the surface relief [117].

For material classification under uncontrolled geometric conditions, as in sorting bulk goods, the reflectometric or ellipsometric analysis of single bright reflections can be sufficient. For complex surfaces, such reflections arise whenever the local surface normal, the direction of incidence, and the direction of observation fulfill the law of reflection. Then, the geometric constellation is known for the corresponding points and an ellipsometric analysis is possible. This partial information might be beneficial for the identification of materials, even if no completely controlled ellipsometry or reflectometry can be performed.

---

<sup>1</sup>Related methods observe the light that is transmitted by thin layers.



Different measurement setups and methods are common for ellipsometry. Now, two possibilities will be presented:

**The null ellipsometer:** The null ellipsometer uses a monochromatic, unpolarized light source. The incident light goes through a linear polarizer with an adjustable angle of rotation  $\gamma_1$  and a retardation plate, typically a  $\frac{\lambda}{4}$  plate. After being reflected by the test object, the light goes through another linear polarizer with an angle of rotation of  $\gamma_2$  to reach a detector (Fig. 7.7). This second polarizer is called the analyzer.

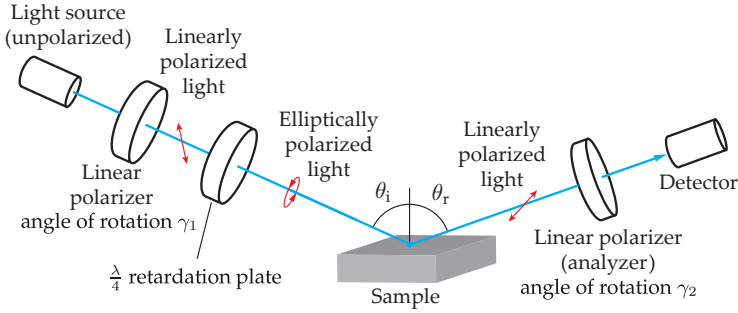


Figure 7.7. Setup of a null ellipsometer (adapted from [166]).

For the ellipsometric measurement, the angles of rotation  $\gamma_1$  and  $\gamma_2$  are adjusted, so that no more light reaches the detector. As the resulting intensity measured by the detector is null, this method is called ‘null’ ellipsometer.

The combination of a linear polarizer and a  $\frac{\lambda}{4}$  plate can be used to produce light with an arbitrary polarization state  $(\psi, \chi)$  (Sec. 2.2.2.4). In general, the null ellipsometer uses light which is elliptically polarized in such a way that it becomes linearly polarized by the reflection at the object’s surface. The polarization direction can then be determined with the analyzer.

The calculus of Mueller matrices of Sec. 2.2.2.4 leads to the following description of the null ellipsometer:

$$\mathbf{M}_{\text{Lin}}(\gamma_2) \mathbf{M}_{\text{Obj}}(\Psi, \Delta) \mathbf{M}_{\text{QWP}}(\alpha) \mathbf{M}_{\text{Lin}}(\gamma_1) \mathbf{S}_{\text{unp}} = \mathbf{0}. \tag{7.20}$$

Here, the Mueller matrices  $\mathbf{M}_{\text{Lin}}(\gamma)$  of the linear polarizers are given by (2.73), the Mueller matrix  $\mathbf{M}_{\text{QWP}}(\alpha)$  of the rotated retardation plates by (2.77) and (2.70), and the Stokes vector  $\mathbf{S}_{\text{unp}}$  of the unpolarized light source by (2.59). The reflection at the test object is modeled by the Mueller matrix  $\mathbf{M}_{\text{Obj}}(\Psi, \Delta)$ . This matrix is obtained as the product of the matrix  $\mathbf{M}_{\text{WP}}(\Delta)$  from (2.76), describing the retardation effect of the conducting material, with the matrix  $\mathbf{M}_{\text{Reff}}(R_{12}^s, R_{12}^p)$  from (2.236), describing the reflection of the light intensity at the object’s surface [35,165]:

$$\begin{aligned} \mathbf{M}_{\text{Obj}}(\Psi, \Delta) &= \mathbf{M}_{\text{WP}}(\Delta) \mathbf{M}_{\text{Reff}}(R_{12}^s, R_{12}^p) = \mathbf{M}_{\text{Reff}}(R_{12}^s, R_{12}^p) \mathbf{M}_{\text{WP}}(\Delta) \\ &= \frac{1}{2} \begin{pmatrix} R_{12}^s + R_{12}^p & R_{12}^p - R_{12}^s & 0 & 0 \\ R_{12}^p - R_{12}^s & R_{12}^s + R_{12}^p & 0 & 0 \\ 0 & 0 & 2\sqrt{R_{12}^s R_{12}^p} & 0 \\ 0 & 0 & 0 & 2\sqrt{R_{12}^s R_{12}^p} \end{pmatrix} \mathbf{M}_{\text{WP}}(\Delta) \end{aligned}$$

$$= \frac{R_{12}^s}{2} \begin{pmatrix} 1+\tan^2 \Psi & -1+\tan^2 \Psi & 0 & 0 \\ -1+\tan^2 \Psi & 1+\tan^2 \Psi & 0 & 0 \\ 0 & 0 & 2 \tan \Psi & 0 \\ 0 & 0 & 0 & 2 \tan \Psi \end{pmatrix} \mathbf{M}_{\text{WP}}(\Delta) \quad (7.21)$$

$$= \frac{R_{12}^s}{2} \begin{pmatrix} 1+\tan^2 \Psi & -1+\tan^2 \Psi & 0 & 0 \\ -1+\tan^2 \Psi & 1+\tan^2 \Psi & 0 & 0 \\ 0 & 0 & 2 \tan \Psi \cos \Delta & 2 \tan \Psi \sin \Delta \\ 0 & 0 & -2 \tan \Psi \sin \Delta & 2 \tan \Psi \cos \Delta \end{pmatrix} \quad (7.22)$$

These equations are obtained by means of the definition of  $\Psi$  from (7.18). The parameters  $\Psi$  and  $\Delta$  are the only unknowns in (7.20), as the common pre-factor  $R_{12}^s$  can be eliminated. Therefore, the system of equations (7.20) leads to a formula for calculating the sought for parameters  $\Psi$  and  $\Delta$ . If the retardation plate is rotated by an angle of  $\alpha = -45^\circ$  with respect to the optical axis, the following simple formulas apply for the angles of rotation  $\gamma_1$  and  $\gamma_2$  of the linear polarizer [117, 165, 171]:

$$\Psi = |\gamma_2|, \quad (7.23)$$

$$\Delta = 2\gamma_1 + \frac{\pi}{2}. \quad (7.24)$$

These equations can be verified by insertion into (7.20).

**An ellipsometer with a rotating analyzer:** For an ellipsometer with a rotating analyzer, a series of measurements of intensities is recorded for discrete angles of rotation  $\gamma_i$  of the analyzer. The setup consists of a monochromatic light source yielding unpolarized light and a fixed linear polarizer, so that the investigated material sample is illuminated with linearly polarized light of a fixed polarization plane (Fig. 7.8). The reflected light reaches the detector by passing through the rotating analyzer. The intensities  $I(\gamma_i)$  measured at the points of time  $t_i$ ,  $i = 1, \dots, N$  correspond to the different angles  $\gamma_i = \gamma(t_i)$  of the analyzer.

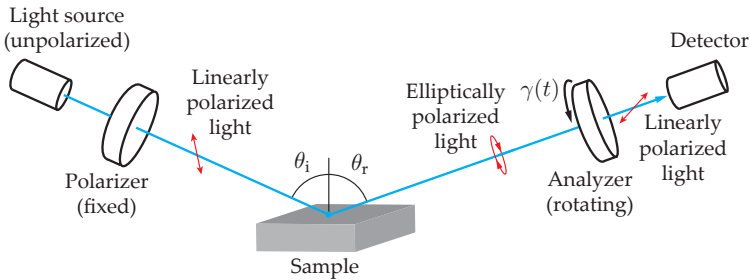


Figure 7.8. Setup of an ellipsometer with rotating analyzer (adapted from [166]).

The Mueller matrices lead to the following system of equations

$$(1, 0, 0, 0) \mathbf{M}_{\text{Lin}}(\gamma_i) \mathbf{M}_{\text{Obj}}(\Psi, \Delta) \mathbf{S}_{\text{Lin}} = I(\gamma_i) \quad i = 1, \dots, N, \quad N \geq 2.$$

As with the null ellipsometer, the Mueller matrices of the analyzer  $\mathbf{M}_{\text{Lin}}(\gamma_i)$  and of the reflection  $\mathbf{M}_{\text{Obj}}(\Psi, \Delta)$  are given by (2.73) and (7.22), respectively. The Stokes vector  $\mathbf{S}_{\text{Lin}}$  describes the linearly polarized light leaving the polarizer (cf. Sec. 2.2.2.2). The multiplication by the row vector  $(1, 0, 0, 0)$  models the measurement of the intensities, which are encoded in the

first component  $S_0$  of the resulting Stokes vector  $\mathbf{S}$ . For the null ellipsometer, again only the intensity  $S_0$  is measured, but because of (2.62),  $S_0 = 0$  already implies  $\mathbf{S} = \mathbf{0}$ .

For  $N \geq 2$  measurements, the resulting system of nonlinear equations is overdetermined, so that the parameters  $\Psi$  and  $\Delta$  can be numerically calculated. A disadvantage of the ellipsometer with rotating analyzer is the reduced measurement sensitivity for  $\Delta \approx k\pi$ ,  $k \in \mathbb{Z}$ , as the quantities of interest are related via  $\cos \Delta$  to the measurements and the minimum gradient of the cosine function is located at those positions. Unfortunately, exactly those regions are of particular interest for the identification of materials (Fig. 7.9). The null ellipsometer avoids that problem by using the retardation plate [117, 166].

For both variants of ellipsometers shown, a camera can also be used as a detector, so that  $\Psi$  and  $\Delta$  can be obtained as a function of position. In this case, the result is a two-channel image with a  $\Psi$  and a  $\Delta$  channel. This method is called **imaging ellipsometry** [171]. The imaging lens is placed between the test object and the analyzer.

**Application to material classification:** The measured quantities  $\Psi$  and  $\Delta$  are connected with the Fresnel coefficients of reflection  $r_{12}^s, r_{12}^p$  as follows:

$$\tan \Psi = \frac{|r_{12}^p|}{|r_{12}^s|}, \quad (7.25)$$

$$\tan \Delta = \frac{\Im \left\{ \frac{r_{12}^p}{r_{12}^s} \right\}}{\Re \left\{ \frac{r_{12}^p}{r_{12}^s} \right\}}. \quad (7.26)$$

The coefficients of reflection are related with the complex indices of refraction  $\underline{n}_1, \underline{n}_2$  as described in Sec. 2.6.5. Therefore, the two parameters  $n, d$  of a complex index of refraction can be obtained by numerically solving a system of nonlinear equations involving the two measured quantities  $\Psi$  and  $\Delta$ . A known  $\underline{n}_1$  (in many applications it is  $\underline{n}_1 = n_1 \approx 1$  for air) results in the following conditional equation for  $\underline{n}_2$  [166]:

$$\underline{n}_2 = \underline{n}_1 \tan \theta_1 \sqrt{1 - \frac{4\rho \sin^2 \theta_1}{(\rho + 1)^2}}. \quad (7.27)$$

Here,  $\theta_1$  is the angle of incidence and  $\rho = \tan \Psi e^{j\Delta}$  is defined in by (7.17).

As the complex index of refraction is a characteristic material property, ellipsometry can be of great use for material identification, especially for different metals. Possible applications might be related to the semiconductor industry as well as to sorting recyclable materials. Figure 7.9 and Table 7.1 show the material constants of different materials and compounds.

For the reflection at non-conductive materials with real-valued indices of refraction, the phase state of the light remains unchanged: for real-valued  $n$ , the Fresnel coefficients of reflection are also real-valued, leading to  $\Delta = 0$  in (7.26).

**Determination of layer thicknesses:** Ellipsometry allows the simultaneous determination of the thicknesses of the layers and of their complex indices of refraction.

Here, the simplest case of a single layer with a thickness of  $h$  and a complex index of refraction  $\underline{n}_2$  on a substrate with complex index of refraction  $\underline{n}_3$  is considered (Fig. 7.10). A medium is called a substrate if no reflections of its lower interface reach the measurement

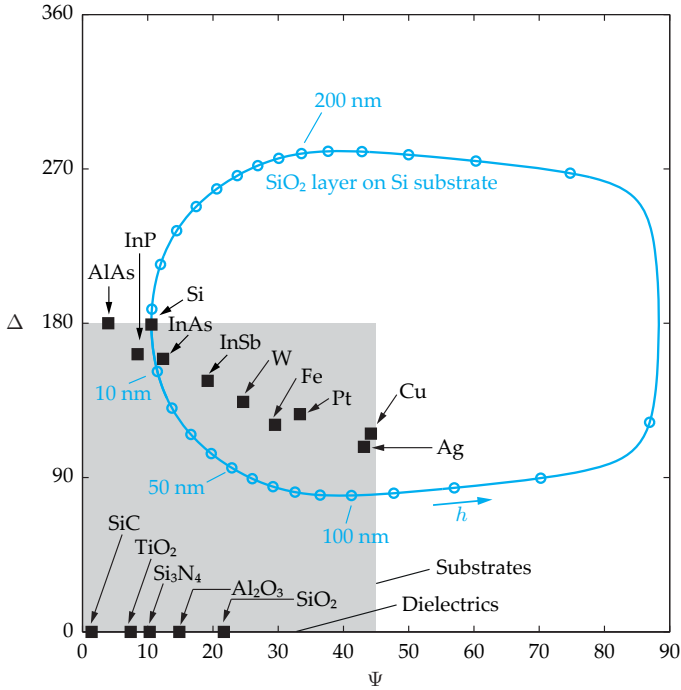


**Figure 7.9.** Characteristic ellipsometric quantities  $\Psi$ ,  $\Delta$  (in degrees) of different materials, under the conditions mentioned in Table 7.1. The characteristic quantities of substrates without covering layers lie in the highlighted quadrant, and for non-conductive materials, they are located on the axis  $\Delta = 0$ . The trajectory of a  $\text{SiO}_2$  layer on silicon is drawn with respect to the layer thickness. The periodic trajectory starts for a layer thickness of  $h \rightarrow 0$  at the characteristic quantities of silicon and reaches this point again for  $h \approx 283$  nm. Multiples of 10 nm are marked on this trajectory [166].

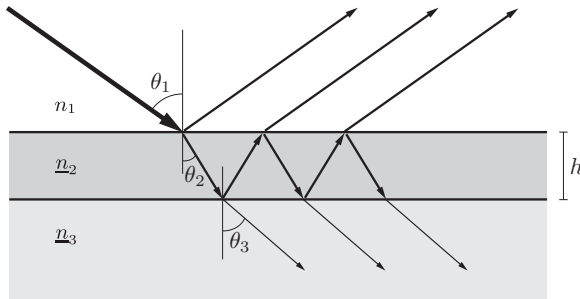


**Figure 7.10.** Multiple reflections at the boundaries of thin layers [166].

**Table 7.1.** Complex index of refraction  $\underline{n} = n - jd$  and characteristic ellipsometric quantities  $\Psi$ ,  $\Delta$  in degrees for different metals, compounds and semiconductors (chemical elemental formula and name) for a wavelength of  $\lambda = 633$  nm. The provided values of  $\Psi$  and  $\Delta$  are valid for an angle of incidence of  $\theta_1 = 70^\circ$  in air,  $\underline{n}_1 = n_1 \approx 1$  [166].

Material	$n$	$d$	$\Psi$	$\Delta$
W (Tungsten)	3.64	2.91	24.62	134.13
Fe (Iron)	2.43	3.30	29.51	120.77
Pt (Platinum)	2.33	4.15	33.33	126.99
Cu (Copper)	0.25	3.41	43.14	107.90
Ag (Silver)	0.13	3.99	44.20	115.63
SiC (Silicon carbide)	2.63	0.00	1.40	0.00
TiO <sub>2</sub> (Titanium oxide)	2.20	0.00	7.39	0.00
Si <sub>3</sub> N <sub>4</sub> (Silicon nitride)	2.02	0.00	10.30	0.00
Al <sub>2</sub> O <sub>3</sub> (Aluminum oxide)	1.77	0.00	14.84	0.00
SiO <sub>2</sub> (Silicon dioxide)	1.46	0.00	21.67	0.00
AlAs (Aluminum arsenide)	3.11	0.00	3.95	180.00
InP (Indium phosphide)	3.54	0.31	8.45	161.95
Si (Silicon)	3.88	0.02	10.57	179.23
InAs (Indium arsenide)	3.96	0.61	12.35	159.24
InSb (Indium antimonide)	4.28	1.80	19.19	146.40

instrument. This is the case for an absorbing material, for example, as soon as the layer thickness exceeds one multiple of the penetration depth.

Multiple reflections arise inside layer 2. Their sum can be calculated by a complex geometric series [166]. Irradiation originating from the medium with the complex index of refraction  $\underline{n}_1$  results in the following total coefficients of reflection:

$$r_{123}^p = \frac{r_{12}^p + r_{23}^p e^{-j2\beta}}{1 + r_{12}^p r_{23}^p e^{-j2\beta}}, \quad (7.28)$$

$$r_{123}^s = \frac{r_{12}^s + r_{23}^s e^{-j2\beta}}{1 + r_{12}^s r_{23}^s e^{-j2\beta}}, \quad (7.29)$$

$$\beta := \frac{2\pi h}{\lambda} \underline{n}_2 \cos \theta_2, \quad (7.30)$$

$$\underline{n}_1 \sin \theta_1 = \underline{n}_2 \sin \theta_2. \quad (7.31)$$

For a real  $n_2$ , the coefficients of reflection and thus the characteristic ellipsometric quantities are periodic with respect to the layer thickness  $h$  (Fig. 7.9). The period length is obtained for  $\beta = \pi$ . In order to estimate the sought for quantities, several ellipsometric measurements with light of different wavelengths are necessary. This method is called **spectroscopic ellipsometry**. The ellipsometric measurements  $\Psi(\lambda)$  and  $\Delta(\lambda)$  for different vacuum wavelengths  $\lambda$  provide sufficiently many equations so that  $\underline{n}_2$ ,  $\underline{n}_3$  and  $h$  can be numerically determined. For a deeper discussion of spectroscopic ellipsometry, see [165,166].

Reflectometry as well as ellipsometry can be used to measure layer thicknesses and complex indices of refraction [9]. Reflectometry stands out for its low time demand and high spatial resolution because of the perpendicular observation. Ellipsometry allows the measurement of thin layers and is robust to rough surfaces, which can cause errors for the reflectometric measurement of the coefficients of reflection, as the light that is scattered by rough surfaces cannot be captured. Spectroscopic ellipsometry is superior for complicated tasks with several layers of unknown materials [166].

### 7.2.2 Fluorescence

Another effect used for material classification is **fluorescence**: after being suitably excited, some materials emit light with a characteristic spectrum.

In fluorescence, photons with a wavelength of  $\lambda$  are absorbed by the material and excite bound electrons in such a way that they reach a higher energy level because of energy from the absorbed light. The excited electrons do not immediately go back to their original energy level, but take on an intermediate energy level at first. Therefore, photons are emitted that are of a lower energy and thus of a longer wavelength  $\lambda_F$ . In this case, there occurs the Stokes shift:

$$\lambda_F > \lambda. \quad (7.32)$$

However, the excited electron states are also partially dissipated into thermal energy. Thus, fewer photons are emitted than absorbed. This can be quantitatively expressed using the quantum efficiency:

$$\frac{n(\lambda_F)}{n(\lambda)} < 1. \quad (7.33)$$

Here,  $n(\lambda)$  denotes the number of absorbed photons of wavelength  $\lambda$  and  $n(\lambda_F)$ , the number of emitted photons of wavelength  $\lambda_F$ .

The emission is distributed omnidirectionally and uniformly, i.e., on average, the same number of photons are emitted in every direction (Fig. 7.11).

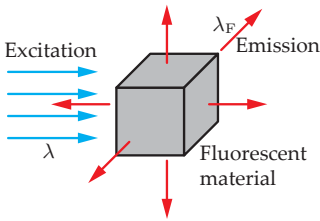


**Figure 7.11.** After an excitation with the wavelength  $\lambda$ , some materials omnidirectionally emit a characteristic fluorescence spectrum of wavelengths  $\lambda_F > \lambda$ .

In fact, the transition does not take place between only two energy levels but between energy bands, especially for liquids and solids. Even for monochromatic excitation, this results in fluorescence spectra that can be temporally and spectrally investigated in order to identify materials. This method is called **fluorescence spectroscopy**. The intensity spectrum can be expressed as a sum of the spectra of the non-fluorescent reflection and the fluorescent emission [178]. Thus, by using a monochromatic illumination, exclusively the fluorescence spectrum is measured outside the wavelength of the illumination.

After turning off the exciting light source, the fluorescent light does not instantly vanish, but typically fades exponentially with time constants between  $10^{-7}$  s and  $10^{-8}$  s. For longer time constants, the effect is called phosphorescence. There are materials with time constants of minutes or even hours, which can be used to produce phosphorescent paint [73]. These coatings save the absorbed light energy for a longer period of time and fluoresce in the absence of illumination. Even under daylight, luminous paints can appear as very bright if they emit more light in a certain spectral range than they absorb in the respective section of the spectrum. This is possible, as incident short-wave light is converted into another spectral range via fluorescence [66].

The fluorescent light has a notably lower intensity than the exciting light, because of the omnidirectional emission on the one hand and the quantum efficiency on the other hand.

As the spectrum of the emitted fluorescent light depends on the material, it can be used for material classification. An application is the sorting of minerals. Fig. 7.12 shows the fluorescence colors of different minerals in the CIE XYZ color space (see Sec. 5.2.3). The example from Fig. 7.13 shows that usually fluorescent light is not monochromatic, so that a spectrally resolved measurement can further improve the classification results [118].

For material classification, short-wave light, e.g., blue, violet or ultraviolet (UV) light or X-rays, are used for excitation because of (7.32). Figure 7.14 shows the fluorescence of leaded glass under UV illumination. Depending on the amount of lead oxide, the observed fluorescence effect is present with different intensities.

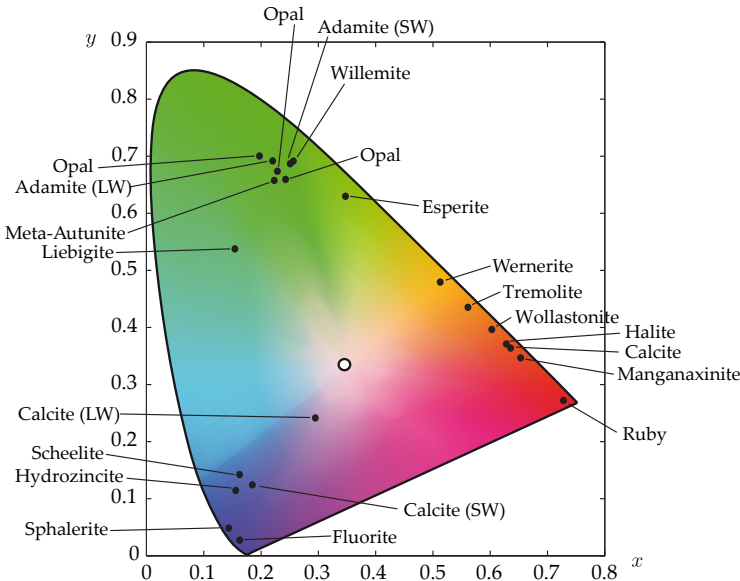


**Figure 7.12.** Fluorescent colors of minerals [118]. In some cases, different samples of the same mineral from different locations show notably different fluorescent colors. Besides, a material's fluorescence can vary with the spectrum of the exciting light. This figure shows measurements of short-wave UV light (SW, maximum of intensity for  $\lambda = 254$  nm) and long-wave UV light (LW,  $\lambda = 365$  nm), that corresponds to the spectral lines of a mercury vapor lamp.

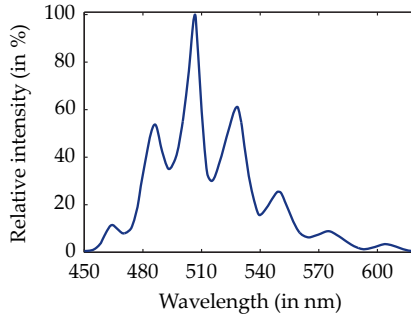


Figure 7.13. Fluorescence spectrum of the mineral liebigite [118].

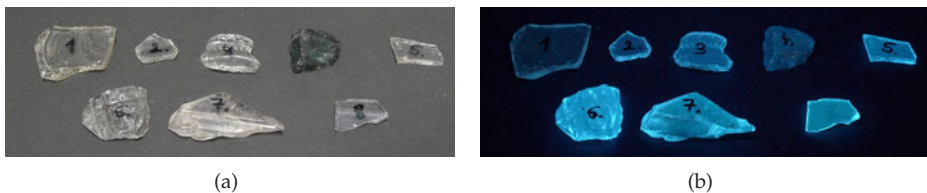


Figure 7.14. Shards of lead glass with varying amounts of lead oxide. (a) Image under white light illumination. (b) Fluorescence under UV illumination, here UV-C illumination of wavelength  $\lambda = 254$  nm (mercury line) and an irradiance of  $3 \frac{\text{mW}}{\text{cm}^2}$ .

### 7.2.3 Methods for measuring the reflectance

The reflectance properties of an object can be described by the bidirectional reflectance distribution function (BRDF) with respect to all directions of incidence of light and all directions of observation (see Sec. 4.3). However, for most applications, a subset of the information contained in the BRDF is sufficient: in extreme cases, even a single reflection factor which completely connects the irradiated light and the light captured by the sensor can be sufficient. In general, the reflectance at different points of the object can differ, and even vary with the wavelength of the light, so that it has to be considered as a function of position and wavelength.

This section covers image acquisition and illumination methods that can be used to capture images which are mainly influenced by the position-dependent reflectance of a test object's surface.

For capturing the reflectance, methods allowing a homogeneous illumination of the whole test object are needed in order to achieve a constant influence of the illumination on the observed image. These include diffuse illumination, bright field illumination, and dark field illumination, which will be covered in the following sections [14, 88].

Besides camera systems, laser scanners and flatbed scanners can also be used for capturing the reflectance.

#### 7.2.3.1 Diffuse illumination

Diffuse light has no distinct preferred direction and illuminates the scene homogeneously from all directions.



For example, diffuse illumination can be realized by an areal light source or the light scattered by an illuminated homogeneous plane. For automated visual inspection, a diffusely scattering screen in the shape of a hemisphere, which is illuminated by circularly arranged light sources and reflectors, can be used, for example (see Fig. 7.15).

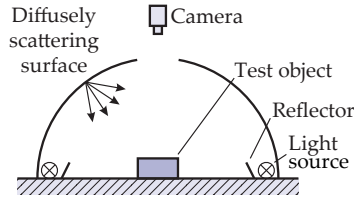


Figure 7.15. Diffuse illumination using a screen in the shape of a hemisphere (adapted from [14]).

In contrast to direct illumination, diffuse illumination causes no shadows. Even for intensely reflecting surfaces, there are nearly none of the highlights that can be caused by the direct reflection of the light source into the camera. However, there are still highlights at positions where the surface normal, the illumination direction, and the sensor position obey the law of reflection, but only with a significantly reduced contrast. Also, structures caused by the surface relief only yield a low contrast, as the intensity of the illumination and thus the luminance of the object only depend on the range of the solid angle through which a point on the object's surface can see the light source. Figure 7.17 compares directional and diffuse illumination for an application to forensic science.

### 7.2.3.2 Bright-field illumination

For bright-field illumination, the luminous flux (cf. Chap. 4) of the light source is directly aimed at the camera. A high light yield can be achieved by reflections of the illumination at the test object's surface, for example, see Fig. 7.16(a).

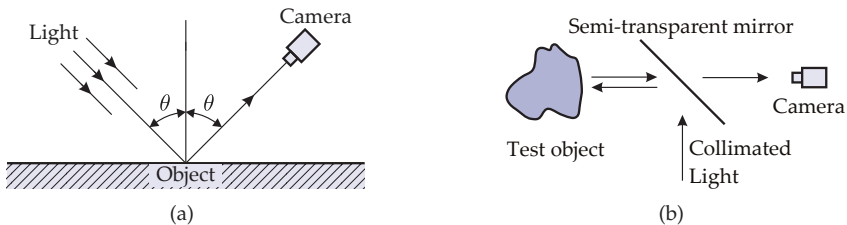
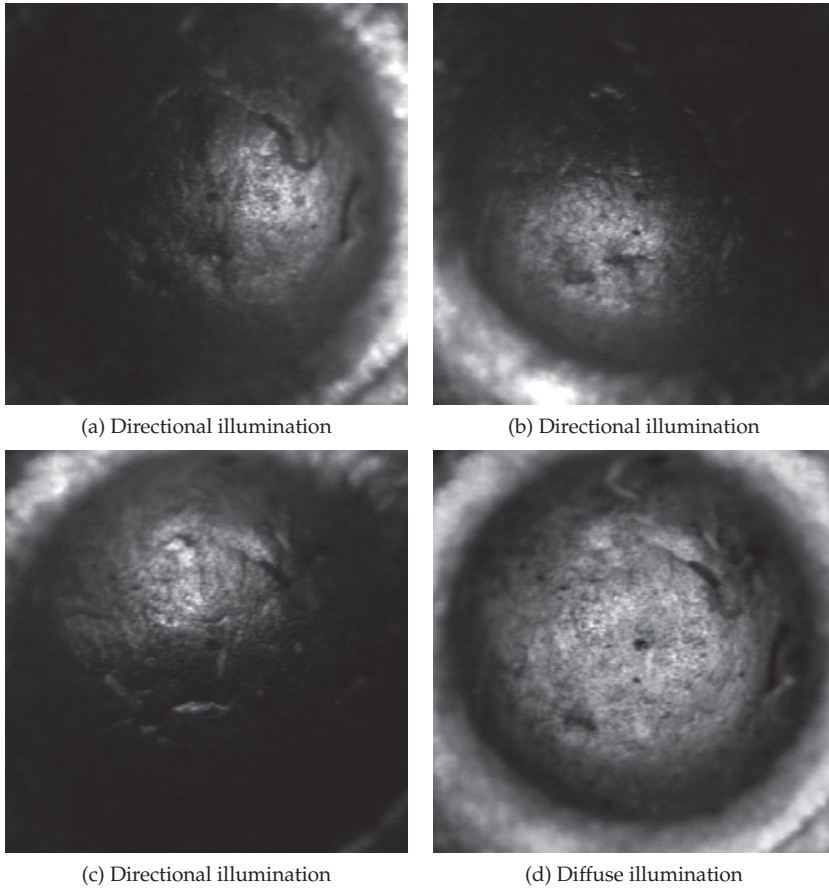


Figure 7.16. Capturing reflectance in bright-field: (a) Principle of bright-field illumination; (b) Coaxial bright-field illumination using a semi-transparent mirror [14].

A semi-transparent mirror can be used to realize a coaxial bright-field illumination. The light is mirrored into the observation light path, allowing an unshadowed view into cavities, see Fig. 7.16(b). Such semi- or partially transparent mirrors, as well as beam splitters, are often needed for setting up image acquisition systems. They reflect half of the incoming light (or some other fixed ratio) and transmit the remaining part.

Alternatively to mirroring the optical path, the camera can be aimed directly at the light source. The test object is located between the light source and the camera, so that shad-



**Figure 7.17.** Images of the mark left by a firing pin on the back of a bullet casing, taken for automatically identifying firearms: (a)–(c) Directional illumination; (d) Diffuse illumination.

ows are captured. This setup can be used to detect defects in the object's silhouette (see Sec. 7.3.10).

### ⊗ 7.2.3.3 Dark-field illumination

For dark-field illumination, the luminous flux coming from the light source is not targeted on the camera. Only scattered light reaches the camera (Fig. 7.18).

Light with an angle of incidence of nearly  $90^\circ$  yields high-contrast images of fine surface structures.

Fig. 7.19 shows dark-field illuminated images of mirrors. The illumination reaches the camera neither directly nor by reflections at the mirror. Only the light scattered by scratches on the mirror reaches the camera, so that defects are made clearly visible as bright regions in the image.

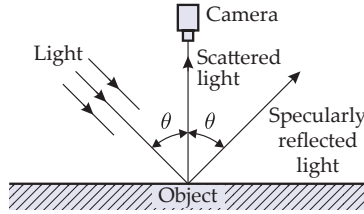


Figure 7.18. Dark-field illumination.

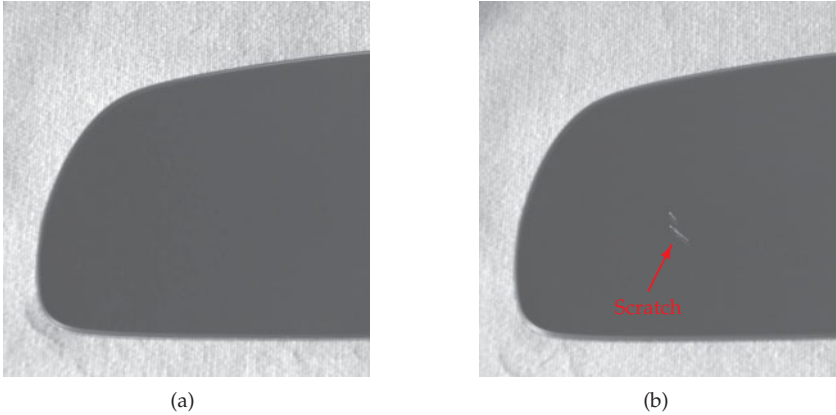


Figure 7.19. Dark field illuminated images of wing mirrors for the detection of scratches: (a) Reference object; (b) Test object with scratches.

**Example 7.3 (Multi-channel inspection of transparent objects):** A further example of an application is the inspection of transparent objects like glass blanks (Fig. 7.20(b)). Typical defects of such objects are:

- Differences in transparency,
- scratches and bubbles as well as
- scattering particles on the surface (dust, imprinting or pressure).

In order to detect such defects, the illumination conditions have to be optimized in dependence on the actual defect class. Since in this case, color information is of no special importance, multiple narrow-band light sources can be used to simultaneously realize different illumination setups that can be separately captured by a multispectral camera (e.g., an RGB camera).

Figure 7.20(a) shows such a setup, where a transmission image is obtained in the red channel of the camera by means of a coaxial bright-field illumination (red LEDs) and a retroreflective foil [68]. The green channel is used to capture scattering particles on the surface of the test object, which are illuminated by a low-angle dark-field illumination. By means of the blue illumination, which is also arranged in a dark-field setup, fluffs, scratches and bubbles appear in high contrast.

Figure 7.20(c) shows an example image of a glass blank with two enclosed bubbles appearing in blue. The red channel is used to realize a further inspection in transmis-

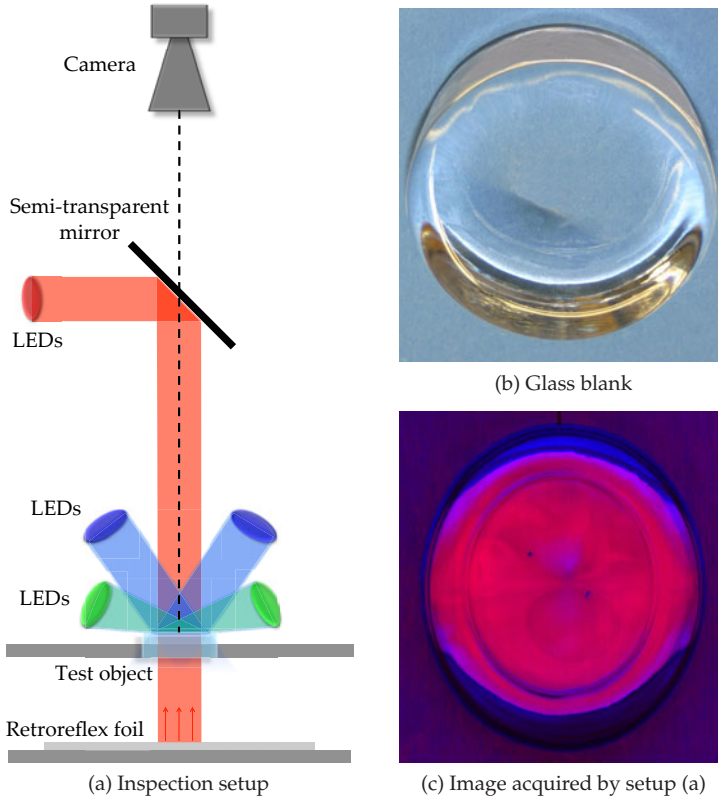


Figure 7.20. Simultaneous inspection of glass in bright field and dark field by means of color multiplex.

sion. The low intensity values of the green channel indicate that there are no scattering particles on the object's surface. ■

#### ④ 7.2.3.4 Laser scanners

Scanning systems provide an alternative for area image acquisition with a single camera. This is possible for the acquisition of the reflectance considered here, as well as for the measurement of the 3D structure, based on, for example, the principle of triangulation. It is sufficient to use the combination of a directional laser illumination and a single point sensor, like a photodiode, for example, or a photomultiplier, for capturing the brightness (see Chap. 6). An area sensor is not necessary.

**Laser scanners** use a deflected laser beam to sequentially illuminate all points along a line on the object. The laser beam can be controlled by a galvanometer-driven rotating mirror or a rotating polygonal wheel. As usual in the field of automated visual inspection, first surface mirrors are used, i.e., mirrors having only a single reflecting layer. In contrast, the usual second surface mirrors have a glass plate mounted in front of the mirroring layer, which already reflects part of the light. This additional reflection is superposed with the intended reflection, causing a perturbed image.

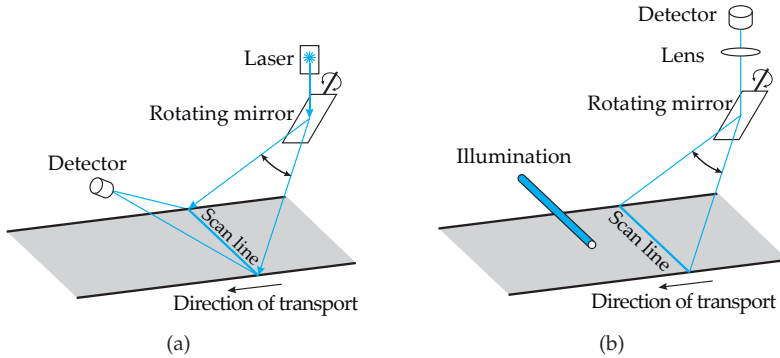


Figure 7.21. Visual inspection of continuous products with a scanning image acquisition: (a) Flying-spot scanner; (b) Flying-image scanner (adapted from [49]).

In combination with a suitable detector, the reflectance of the test object can be detected, as the high irradiance of the laser allows a suppression of extraneous light. Line-by-line scanning is especially suitable for continuous products on a conveyor belt. Such sensors are often (see Fig. 7.21(a)), but not exclusively (see Fig. 7.21(b)), operated using laser light. Telecentric scanners are also possible (Fig. 7.22). Here, the laser beam originates from the same direction for all object positions and all surface points are observed from the same direction. This results in a spatially homogeneous sensitivity of the sensor, as the incident angle and the reflection angle remain unchanged:  $\theta_i$  and  $\theta_e$  in Fig. 7.22 are constant with respect to the position. Only the solid angle through which the sensor appears, from the perspective of the illuminated spot, is still position-dependent. To realize the optical paths of illumination and observation for telecentric laser scanners, parabolic reflectors as well as cylindrical lenses can be used [49].

In the ideal case, the sensitivity with respect to the reflectance should be independent of the position of the scanned point. However, this cannot be attained by any real setup. The remaining position dependence can be further reduced by a calibration, i.e., by measuring and computationally compensating for the dependencies.

The laser scanners presented here use a bright field illumination. Alternatively, laser scanners can also be operated with dark field illumination or triangulation (Sec. 7.3.1, 7.3.2). In addition, lasers are used for time of flight measurements operated in scanning mode (Sec. 7.3.15).

The monochromatic, directional laser light allows a rather easy realization of diffraction limited imaging optics (i.e., optics for which the size of the light spot is only limited by diffraction, not by geometrical aberration, see Sec. 2.2.6.1). Because of the high luminance, a small aperture diameter can be used, resulting in a high depth of field. At the same time, stopping down reduces aberration (cf. Sec. 3.4.8). Due to the monochromaticity of laser light, no chromatic aberration can arise in the optical path of either the illumination or the observation (see Sec. 3.4.8.2). This allows the use of inexpensive optics, as, for example, a single lens is often sufficient. Besides, an effective suppression of extraneous light is possible by placing narrow-band filters in front of the detector. The small movable elements of the scanning optics allow high sampling rates.

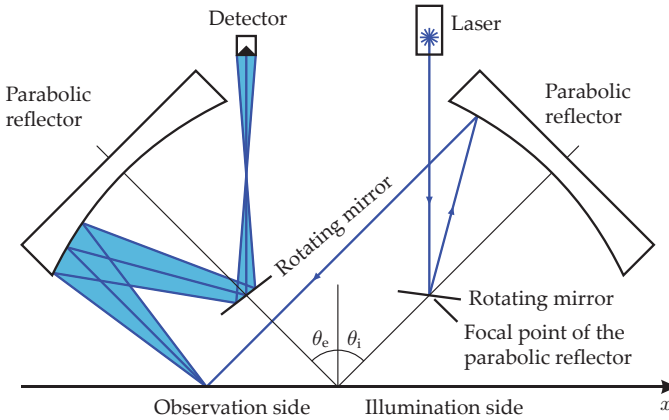


Figure 7.22. Setup of a telecentric laser scanner with two parabolic reflectors (adapted from [49]).

Its disadvantages are the interference effects (speckle patterns) of the coherent laser light (see Sec. 2.2.7). In addition, the monochromatic illumination does not allow the acquisition of color features. As the use of laser light can be hazardous to the human eye, appropriate preventive safety measures are required [43–45, 158].

### 7.2.3.5 Flatbed scanners

A **flatbed scanner** consists of a line-scan camera which is moved by a linear actuator perpendicularly to the direction of the sensor line. The object that has to be scanned, which often is a printed paper (or a slide), is placed on a glass plate covering the scanning unit. The linear motion of the line camera produces a two-dimensional image of the object.

For automated visual inspection, flatbed scanners can be used to obtain images of objects with planar surfaces (Fig. 7.23). This image acquisition method allows the measurement of the respective side of the object, as the planar surface is imaged without any geometrical distortions. Another application is checking the completeness of construction kits (Fig. 7.24). The line sensor of a flatbed scanner can achieve very high resolutions.

### 7.2.4 Spectral sensors

Some applications require a finer resolution of the spectrum than can be achieved using color cameras. The principle of construction of color cameras (see Sec. 6.9) cannot be directly applied to the problem of spectral measurements. Spectral sensors need to sample a three-dimensional space consisting of two spatial and one spectral dimension. As a color camera only has a two-dimensional image sensor, further spectral channels placed on that sensor would inevitably reduce the spatial resolution and yield only a low spectral resolution. Two possible principles for spectral sensors will be presented:

- Multiple images are taken sequentially with a gray-scale camera, where a certain filter is placed in front of the lens for each image. The filters can be mounted on a wheel, which is automatically rotated into the corresponding position before acquiring the image. This principle can only be used to capture static scenes.

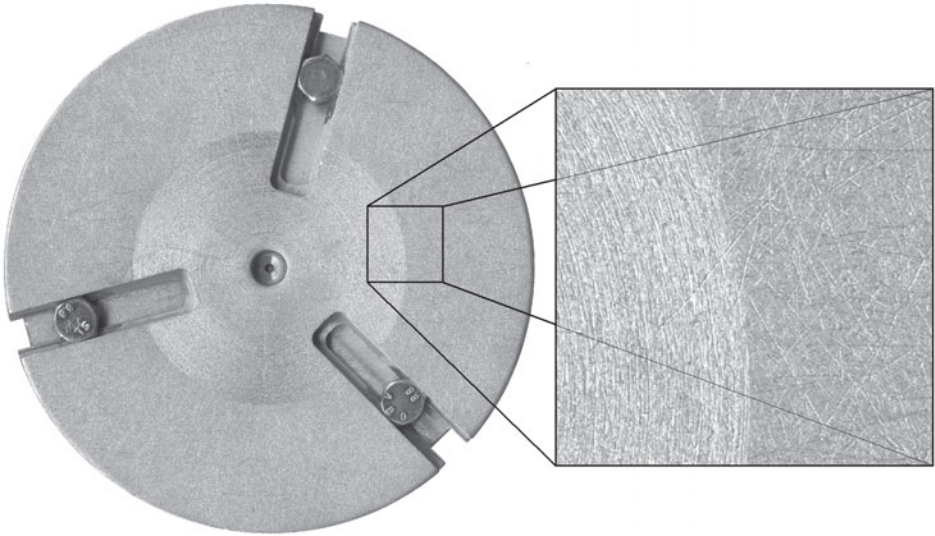
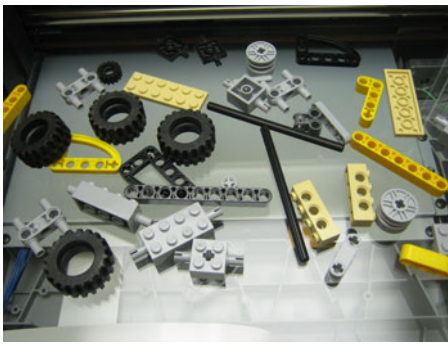
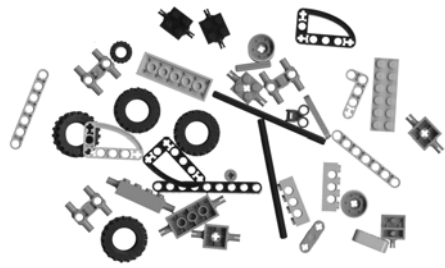


Figure 7.23. Image of a metal flange with a diameter of about 15 cm, acquired with a flatbed scanner. The magnification on the right shows that the image has a high resolution and fine details, e.g., scratches are clearly visible.



(a)



(b)

Figure 7.24. Checking the completeness of a toy construction kit: (a) Camera image; the analysis is complicated by perspective distortions and reflections; (b) This image of the same scene taken by a flatbed scanner is homogeneously illuminated and free of distortions.

- A spectrally resolving camera provides the spectrum of an image line (Fig. 7.25). A diffraction optic achieves a wavelength-dependent deflection of the light, so that each line of the image sensor corresponds to a certain narrow spectral band. Because of a slit shaped stop, only a single plane of the object space is imaged. One coordinate axis of the resulting image corresponds to the wavelength of the measured intensity values and the other axis represents the spatial position of the inspected image point, as usual. Two-dimensional surfaces can be investigated by performing a scan perpendicular to the imaged plane. This so-called push broom technique is especially suitable for continuous products on a conveyor belt.

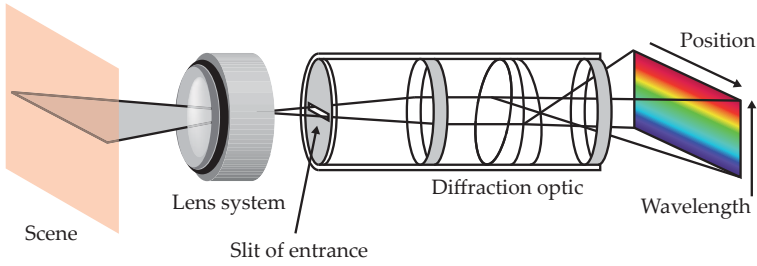


Figure 7.25. Spectrally resolving line camera.

Possible applications for spectral measurement are the observation of coloring processes and especially the classification of materials: different materials are characterized by different spectra of absorption, so that their spectra of reflectance differ from each other. Such materials can be distinguished by spectral measurements. Hence, the described imaging techniques can be used for sorting plastics, minerals, or glasses, as well as to detect contaminants in food (see Sec. 7.6.2) and for recycling processes [7].

This measurement principle can also be used outside the visible spectrum, of course. The energy levels of molecular oscillations are mainly in the infrared region of the spectrum. As chemical compounds have characteristic levels of molecular oscillations, molecular materials can be well classified by using the spectrally resolved absorption in the infrared spectrum [25]. The measured intensity values of different parts of the spectrum can be combined to form a feature vector which serves as input for a classifier. An example is the sorting of plastics by using the measured spectrum in the range of the near infrared [117]. As an example, Fig. 7.26 shows mean point spectra of different plastics. The infrared spectrum is not suitable for classifying atomic materials, as their excitation states can only be reached with higher energies and with shorter wavelengths.

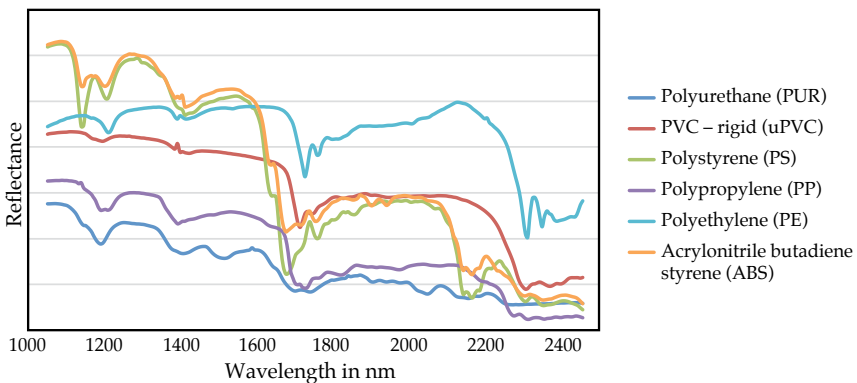
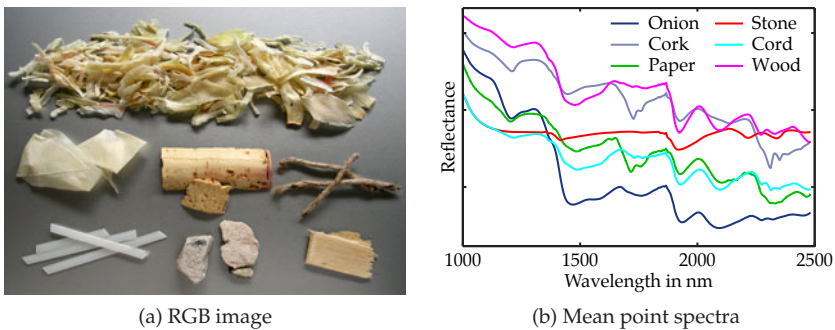


Figure 7.26. Mean point spectra of different plastics.



**Example 7.4 (Hyperspectral sorting of food):** As an example of hyperspectral material classification, the separation of dried onions from contaminants like stones or packaging materials (wood, paper, etc.) is considered [113]. Figure 7.27(a) shows an RGB image of the mentioned materials; Fig. 7.27(b) shows the corresponding mean spectra in the near infrared (1000 nm–2500 nm). For certain regions of wavelengths, the differences between the NIR spectra of onions and contaminants are especially large, which is why these regions can be used for classification.

Figure 7.28(a) shows an RGB image of a sample consisting of onions and contaminants that have to be separated. To the naked eye, everything seems to be identical. A hyperspectral camera has been used to acquire 237 images of the same sample with wavelengths in the region of 1000 nm up to 2500 nm. Figures 7.28(b)–(g) show six channels of the hyperspectral image. By combining three of these images into a false color image (cf. Sec. 9.1.3), the contaminants can be visually detected in the resulting image (Fig. 7.28(h)) without any problems. ■



**Figure 7.27.** Dried onions mixed with different contaminants (paper, cork, cords, plastics, stones, wood): (a) RGB image; (b) mean point spectra of the materials.

### 7.2.5 Light scattering methods and the inspection of surface roughness

In automated visual inspection, light scattering methods allow a characterization of the microstructure of the surface, based on the distribution of the angles of the scattered light [29, 74]. Microscopic surface properties, like roughness, are important quality criteria for certain products. Different parameters exist for characterizing the surface roughness, which are obtained by mechanically touching the surface [117]. However, the microscopic surface structure can also be investigated with optical methods, like the measurement of the scattering characteristics of the surface, for example (cf. Sec. 2.6.4).

For light scattering methods, the surface is usually illuminated with a monochromatic light beam—for example, a laser light beam—on an area  $A$  through the angles of incidence  $\theta_i, \varphi_i$  (Fig. 7.29). Depending on the surface's structure, the light is scattered through angles which have a certain distribution (see Sec. 2.6.4). The intensities of the scattered light are measured on a planar sensor with respect to the angle of incidence. The measurement is resolved for the polar angle  $\theta_s$  and the azimuth angle  $\varphi_s$  with respect to the plane of incidence. The polar angle at which the scattered light is observed with respect to the test object's normal, is called the scattering angle  $\theta_s$  [60]. By the law of reflection, the following applies for

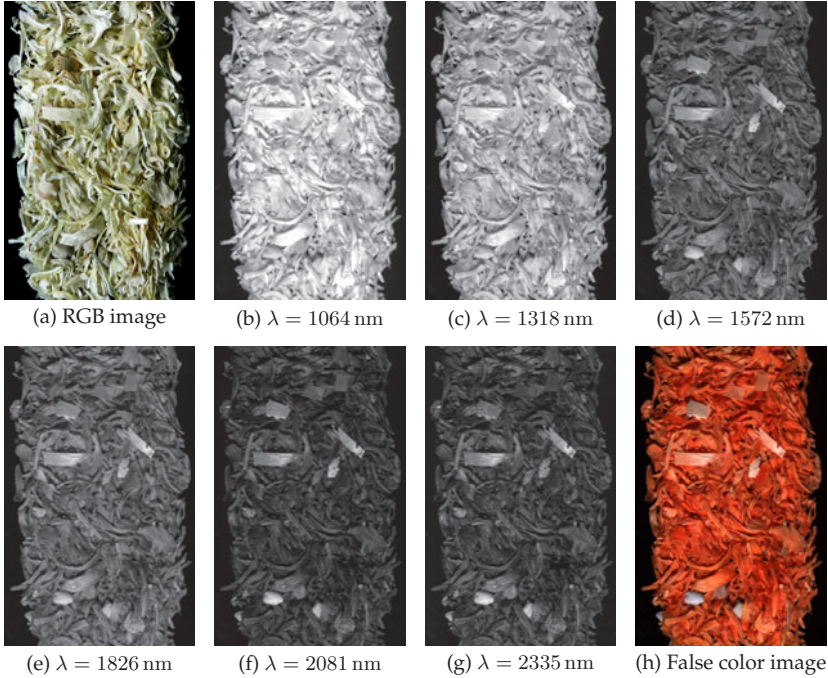


**Figure 7.28.** Example of a hyperspectral image of dried onions mixed with contaminants: (a) RGB image; (b)–(g) channels of the hyperspectral image corresponding to different wavelengths; (h) false color image whose red channel corresponds to 1064 nm, whose green channel corresponds to 1572 nm and whose blue channel corresponds to 2081 nm.

Fig. 7.29:

$$\theta_r = \theta_i, \quad (7.34)$$

$$\varphi_r = \varphi_i + \pi. \quad (7.35)$$

If the reflective properties of the surface are described by the bidirectional reflectance distribution function  $BRDF(\theta_i, \varphi_i, \theta_e, \varphi_e, \lambda)$  (see Sec. 4.3), then

$$\theta_e = \theta_s, \quad (7.36)$$

$$\varphi_e = \varphi_i + \pi + \varphi_s. \quad (7.37)$$

With respect to the area element  $\Delta\Omega$  of a solid angle, the following applies to the intensity  $I(x, y)$  of the scattered light on the screen:

$$I(x, y) \propto BRDF(\theta_i, \varphi_i, \theta_s, \varphi_i + \pi + \varphi_s, \lambda) \Delta\Omega, \quad (7.38)$$

$$x = x(\rho, \theta_s, \varphi_s), \quad (7.39)$$

$$y = y(\rho, \theta_s, \varphi_s), \quad (7.40)$$

with  $\rho$  denoting the distance between the test object and the screen (see Fig. 7.29). Hence, a two-dimensional section of the BRDF is measured by the scattering light method. The

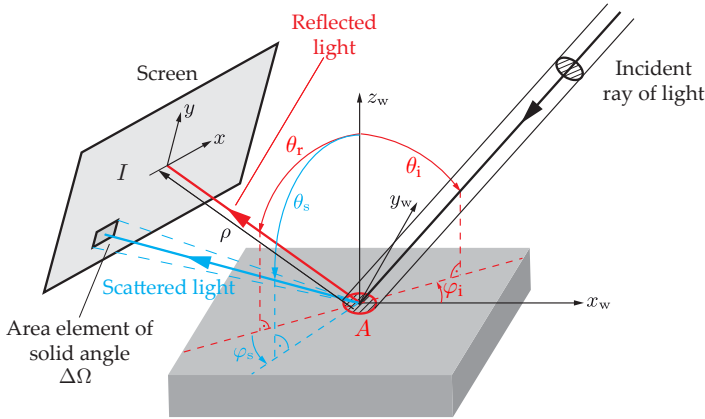


Figure 7.29. Setup for measuring scattered light.

measurement result provides information about the microscopic structure of the surface. As optical properties of the material, such as the complex index of refraction as well as the microscopic shape of the object, influence the BRDF, it is not possible to clearly separate the measurement of the optical properties from the capturing of the test object's shape.

Preferably, the screen should be a Lambertian radiator, so that the irradiated light is omnidirectionally scattered. Then, the distribution of intensities on the screen could be imaged by a camera and quantitatively analyzed in terms of the geometric constellation of the test object and the image plane.

- The properties of the object are observed only locally inside the region  $A$ . This is sensible for representatively inspecting homogeneous 3D textured surfaces. The area  $A$  should be considerably larger than the coarsest structure of the surface.
- The distribution of the scattered light can be used to produce texture features based on a local and/or weighted integral of  $I(x, y)$ . Under certain conditions, parameters describing the 3D roughness of the 3D microstructure can also be estimated from  $I(x, y)$  [60, 155].
- Light scattering methods are described by the norm ISO 13696 [42].

Surface structures produce characteristic scattered light images, which can be exploited for automated visual inspection. Even without performing a quantitative analysis of scattered light images, they can be used to check for the constancy of a surface forming process. If the comparison of the scattered light image with a reference image shows significant differences, the surface structure produced might have changed.

**Example 7.5 (A light scattering method):** Figure 7.30 shows a possible setup for acquiring light scattering images. The surface is illuminated at an angle of  $\theta_i = 45^\circ$  using a laser beam with a diameter of 1 mm, a wavelength of 405 nm, and a power of 5 mW. The scattered light is observed on a planar screen of size  $200 \times 300 \text{ mm}^2$ , which is located  $\rho = 100 \text{ mm}$  behind the sample. The normal of the screen is contained in the plane spanned by the optical axis of the camera and the laser beam. Figure 7.31 shows light scattering images of different materials, acquired with the described setup. ■

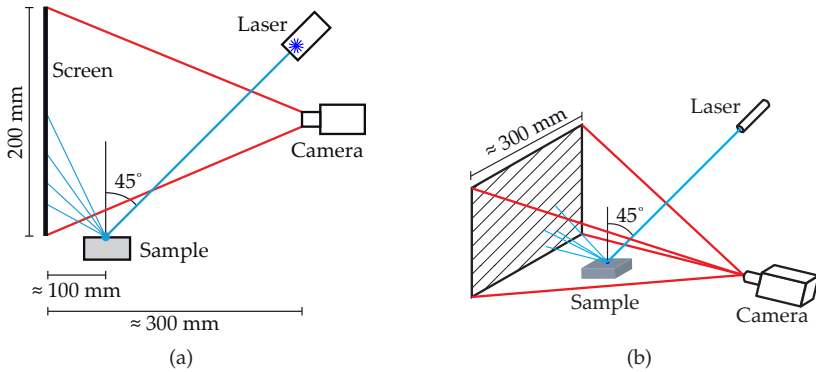


Figure 7.30. Example of a setup for capturing scattered light images.

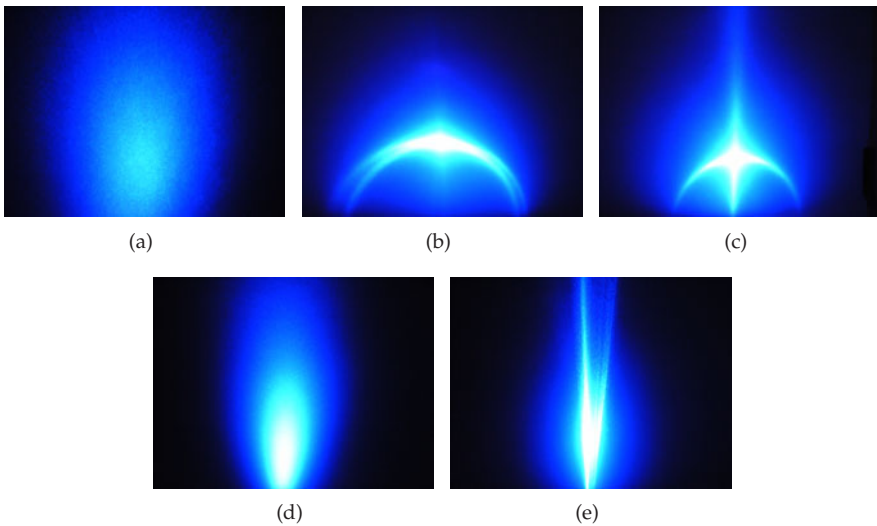


Figure 7.31. Light scattering images of different surfaces: (a) Sandblasted steel; (b) Smoothed steel surface with a set of grooves; (c) Ground steel with two series of rills intersecting under an angle of  $90^\circ$ ; (d) Aluminum foil, rough side (e) Aluminum foil, smooth side.

The described scattering light method captures a section of the BRDF of the illuminated surface point for a selected direction of illumination  $(\theta_i, \varphi_i)$ . By varying the direction of illumination, as well as the position of the screen and the camera, additional function values of the BRDF can be sampled, so that it can finally be approximated by a suitable function class [82].

### 7.3

## 7.3 3D shape capturing

In terms of automated visual inspection, image acquisition can provide at least two kinds of information about the test object: its optical properties and its shape. While the previous

sections covered the determination of its optical properties, methods for capturing its three-dimensional shape will now be discussed.

### 7.3.1 Triangulation (point-by-point scanning)

Triangulation is a method for measuring distances. It is based on the geometry of planar triangles. Such a triangle is explicitly defined by two angles and the length of one side. For triangulation, the length of one of the sides of the triangle is determined—the so-called base—as well as the two adjacent angles (Fig. 7.32). The remaining quantities can now be calculated, especially the distance between the measured point and the sensor. In the case of laser triangulation, one angle and one side's length are known because of the construction of the setup; then the second angle is measured. In contrast, for stereo reconstruction, the two angles are measured and the length of the base is known.

For the triangulation method considered here, the test object is illuminated with a laser beam. The laser beam, scattered on the object's surface, is observed with a detector. Therefore, it is necessary that the surface be neither an ideal mirror nor an ideal absorber, but scatter some of the light in the direction of the detector (Fig. 7.33(b)). For triangulation, opaque materials are best suited—transparent or partially transparent materials widen the beam spot on the surface because some of the light is scattered by the inner structures, which results in an increased measurement uncertainty (Fig. 7.33(a)). In order to completely capture the object's shape using triangulation, the gradient of the surface has to be limited in order to avoid shadowing effects (Fig. 7.33(c)).

For the setup illustrated in Fig. 7.34, the Scheimpflug condition (see Sec. 3.4.7) is satisfied, so that the illuminated point is focused on the detector regardless of the object distance if the lens system is focused for a single point located on the laser beam. Because of the known position of the detector and the laser, the position of the object can be calculated: there is a bijective mapping between the depth  $z$  of the object point and the displacement  $x$  of the scattered laser light on the detector. A line camera or a position sensitive detector can be used as a detector (cf. Sec. 6.8 and 6.5).

If a line-scan camera is used in combination with a suitable model and a suitable interpolation, the imaged laser point can be localized with sub-pixel accuracy [127]. In addition, the quality of the image  $\mathbf{B}$  of a point  $\mathbf{G}$  can be judged. If necessary, the measurement error can be reduced by suitable methods of signal processing. For example, if the light spot is

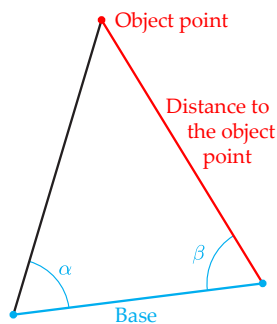
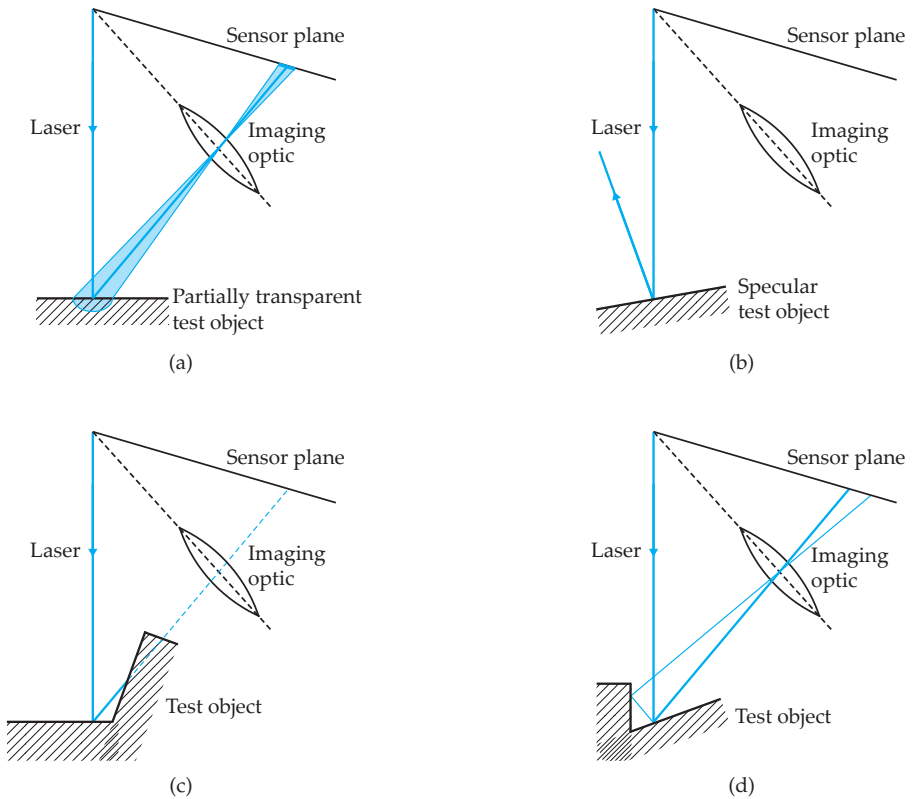


Figure 7.32. Principle of range measurement by triangulation: The sought distance to the object can be calculated from the measured base length and the measured angles  $\alpha$  and  $\beta$ .



**Figure 7.33.** Problems that might arise for the triangulation of an object point: (a) Widening of the light spot because of a partially transparent object; (b) No (or too little) light reaches the detector because of a perfectly specular (partially specular) surface; (c) The surface relief causes shadowing effects obstructing the optical path of observation; (d) Multiple reflections on the object lead to additional image points.

widened on a partially transparent surface, the center of the intensities measured on the line camera can be estimated. Multiple reflections caused by an extensively specular surface can be detected and discarded during the 3D reconstruction (Fig. 7.33(d)). A position sensitive detector allows a greater frequency of measurement and the suppression of extraneous light by modulation [45, 117].

**Example 7.6 (Triangulation setup):** The mapping  $x \mapsto z$  for the geometry of Fig. 7.35 will now be explicitly determined, cf. [45, 117, 121]. The base length  $l$ , the angle  $\beta$ , and the focal length  $f$  of the lens are assumed to be known because of the construction or calibration of the sensor. The image coordinate  $x$  is measured. The origin of the  $x$ -axis and the  $z$ -axis (laser beam) is considered to be located at their intersection  $\mathbf{O}$  with the lens plane.

The triangle  $\mathbf{ORB}$  results in the following formula for calculating the image distance

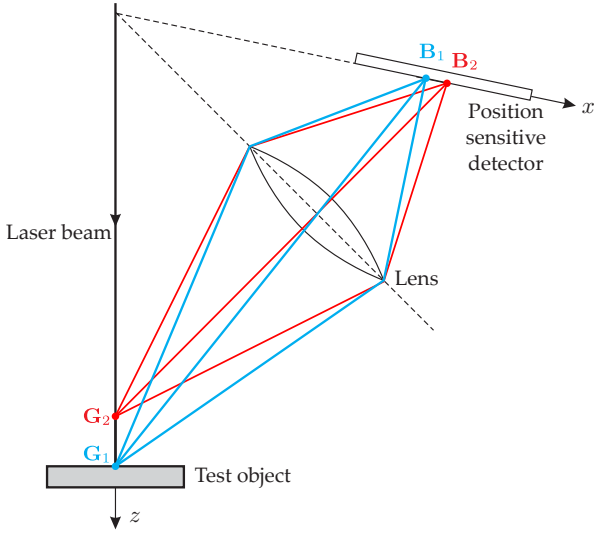


Figure 7.34. Pointwise laser triangulation (adapted from [45]).

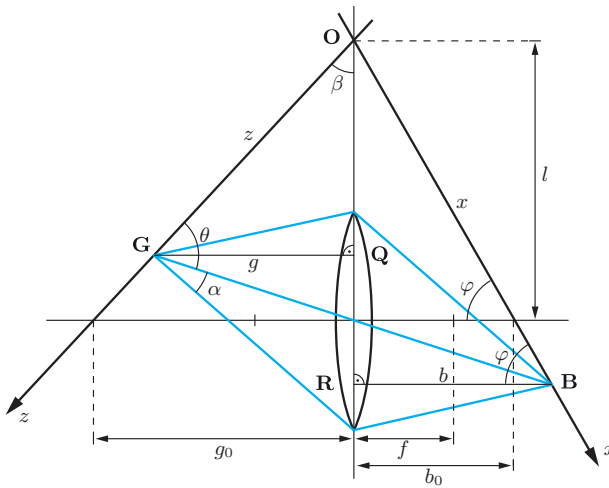


Figure 7.35. Geometry of a triangulation setup.

$b$  from the measurement  $x$ :

$$b = x \cos \varphi. \tag{7.41}$$

As usual, the object distance  $g$  of the sharp imaging is calculated by using (3.25):

$$g = \frac{bf}{b-f} = \frac{xf \cos \varphi}{x \cos \varphi - f}. \tag{7.42}$$

Now, the triangle  $OGQ$  yields the object distance  $z$ :

$$z = \frac{g}{\sin \beta} = \frac{x f \cos \varphi}{(x \cos \varphi - f) \sin \beta}. \quad (7.43)$$

As the Scheimpflug condition is fulfilled by this setup, the angle  $\varphi$  is uniquely determined by the dimensions of the setup (see Sec. 3.4.7). For Fig. 7.35, the object distance  $g_0$  and the image distance  $b_0$  of the sharp imaging on the optical axis result in

$$\tan \beta = \frac{g_0}{l}, \quad (7.44)$$

$$\tan \varphi = \frac{l}{b_0}. \quad (7.45)$$

The thin lens equation (3.25) yields

$$\frac{1}{b_0} = \frac{1}{f} - \frac{1}{g_0}. \quad (7.46)$$

Hence,

$$\tan \varphi = l \left( \frac{1}{f} - \frac{1}{g_0} \right) = \frac{l}{f} - \frac{1}{\tan \beta}, \quad (7.47)$$

$$\cos \varphi = \frac{1}{\sqrt{1 + \left( \frac{l}{f} - \frac{1}{\tan \beta} \right)^2}}, \quad (7.48)$$

and finally

$$z = \frac{x f}{\left( x - f \sqrt{1 + \left( \frac{l}{f} - \frac{1}{\tan \beta} \right)^2} \right) \sin \beta}. \quad (7.49)$$

So the relation between  $x$  and  $z$  is nonlinear. This is caused by the tilt of the planes which are subject to the imaging process [45]. Among other things, this nonlinear relation results in a variable sensitivity of the triangulation if a detector with homogeneous resolution along the  $x$ -axis is used. ■

The sensitivity of this measurement principle is improved for increasing triangulation angles  $\theta$ , as the same difference of height  $\Delta z$  results in an increasing difference of the position  $\Delta x$  on the sensor (Fig. 7.36). However, there must not be any occlusions, neither in the optical path of the illumination nor in the optical path of the observation. For a large  $\theta$ , this condition limits the allowed surface gradient and therefore the class of possible test objects. Thus,

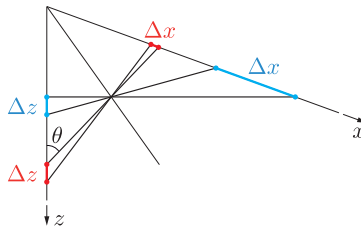


Figure 7.36. The sensitivity  $-\frac{dx}{dz}$  increases monotonically with the triangulation angle  $\theta$ .



a tradeoff between the objectives of sensitivity and of occlusion avoidance has to be made during the design process of the setup.

Triangulation methods can attain a measurement uncertainty on the order of  $1\ \mu\text{m}$ . However, for non-ideally opaque test objects, the resolution is correspondingly lower.

A triangulation measurement yields only a single point of the surface relief. If the whole surface is to be captured, a time consuming scanning has to be performed.

### 7.3.2 Light-section methods (line scanning)

Light-section methods also use the principle of triangulation, but capture a one-dimensional section of the object with each measurement. Light is projected in the shape of a fan on the surface, mostly by using a laser. The light scattered by the object is captured by an area camera (a 2D sensor). Cylindrical lenses placed in front of the laser are a simple way of producing the light fan. Better results are achieved by using special optics that can offer a nearly constant intensity along the projected line.

In the ideal case, the light fan, the imaging optics, and the sensor satisfy the Scheimpflug condition, so that all the points on the light fan can be sharply imaged, see Fig. 7.39(b). However, for standard cameras and lens systems, the planes of the sensor and the imaging optic are parallel, so that the geometry required by the Scheimpflug condition cannot be realized. Therefore, the lens system would need to be tilted with respect to the sensor, for example, with a bellows. In practice, this is sometimes omitted (for reasons of cost, among others)—as in the following example.

The setup of Fig. 7.37 results in a depth value for each image column, describing a one-dimensional relief of the surface in total. By performing a scan perpendicular to the direction

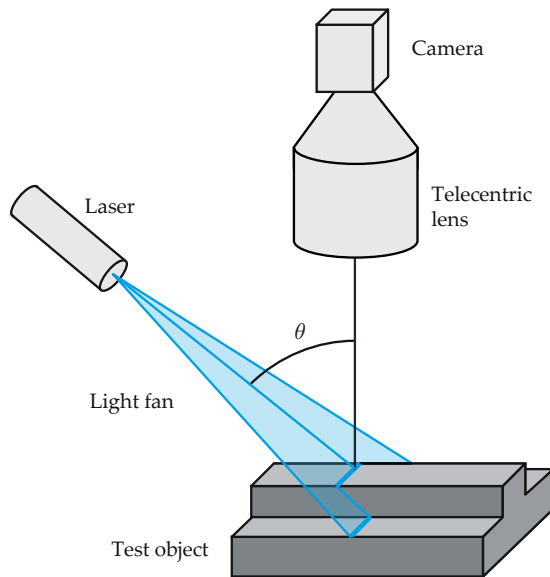


Figure 7.37. Light-section sensor with telecentric observation, used for depth measurement based on the principle of triangulation.

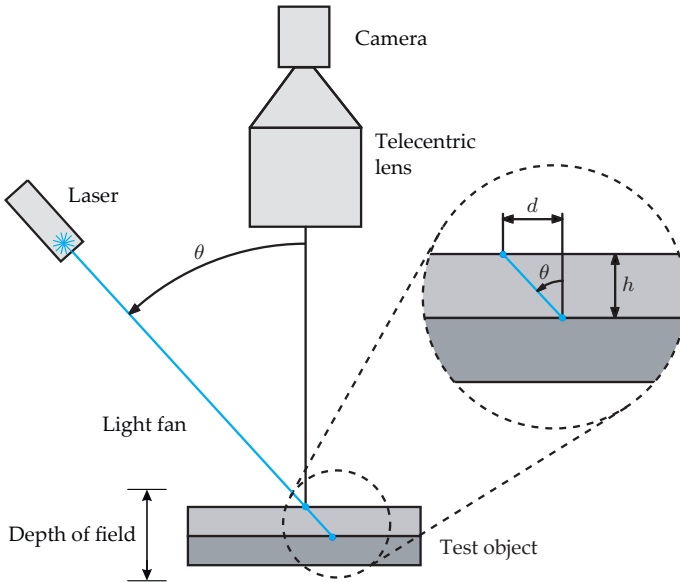


Figure 7.38. Calculation of the height difference for the light-section method.

of observation, a two-dimensional surface can be reconstructed. Therefore, a conveyor belt can be used to move the test objects past the light-section sensor, similar to the acquisition of intensities with line cameras (cf. Sec. 6.8).

For the setup of Fig. 7.38, the height difference  $h$  of the test object can be calculated as follows using the lateral displacement  $d$  of the detected light fan and the triangulation angle  $\theta$ :

$$h = \frac{d}{\tan \theta}. \quad (7.50)$$

**Example 7.7 (Capturing the 3D shape of a cylinder head):** Figure 7.40 shows the 3D capture of a cylinder head by employing an illumination with a fan-shaped laser and an evaluation based on triangulation (light-section method). ■

### 7.3.3 The measurement uncertainty of triangulation

The lower limit of the measurement uncertainty of triangulation methods is limited by several factors:

1. Imaging quality of the pattern projection;
2. Imaging quality of the optics used for imaging the distorted pattern onto the sensor;
3. Resolution of the sensor;
4. Speckle caused by the light's coherency (see Sec. 2.2.7). Speckle can be modeled as multiplicative noise.

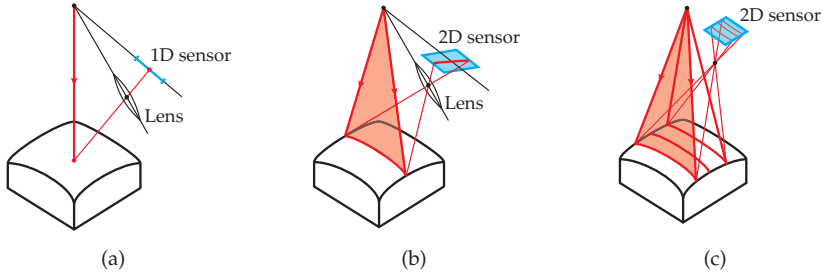


**Figure 7.39.** Extension of the pointwise triangulation method to line sampling and area sampling (adapted from [121]). (a) For point-by-point triangulation, the laser beam, imaging optics and 1D sensor satisfy the Scheimpflug condition, so that the triangulated object point can be sharply imaged, regardless of its distance. (b) For line scanning triangulation (light-section method), the light fan, imaging optics, and 2D sensor satisfy the Scheimpflug condition, so that all object points on the light fan can be sharply imaged, regardless of their distance. (c) For the quasi simultaneous capturing of the object's surface by using a stripe projection method, only an intermediate plane of the surface can fulfill the Scheimpflug condition together with the 2D sensor. Only the regions surrounding that plane are located in the depth of field.

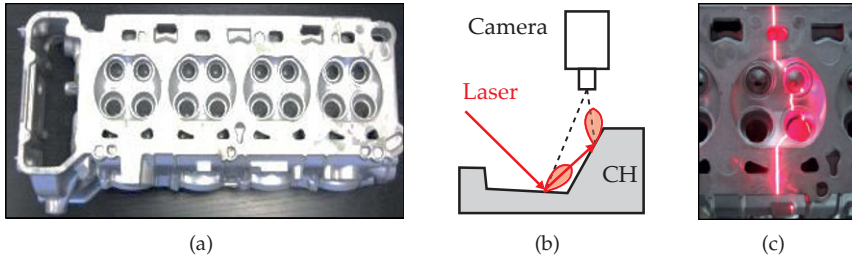


**Figure 7.40.** Capturing the 3D shape of a cylinder head (CH) by means of the light-section principle: (a) Cast aluminum cylinder head. Its surface is bare, rough, and intensely reflecting. The exact shape of the combustion chambers and the location of the inlet port and the outlet port are of particular importance. (b) The laser fan, which illuminates the surfaces, is skew with respect to the surface. The camera observes the scene from above. The intense reflectance might cause multiple reflections (denoted by the cones of scattered light in the image), which have to be suppressed during image processing. (c) In the perspective of the camera, the laser line seems to be deformed by the shape of the surface. By means of the lateral displacement of the laser line, the height of the relief can be determined for every point of the line.

This applies to all methods using active illumination: point, line and stripe projection and general pattern projection.

The measurement uncertainty is typically specified as the standard deviation of the measured value [85]. Concerning triangulation, one distinguishes between the lateral measurement uncertainty  $\sigma_1$  parallel to the test object's surface and the vertical measurement uncertainty  $\sigma_v$  perpendicular to the surface.

Manufacturers of triangulation sensors often specify only the sensor's resolution, which must not be mixed up with the measurement uncertainty. Generally, the measurement uncertainty is markedly higher than the sensor's resolution, which is specified as the relation of the vertical size of the measurement range and the sampling intervals of the sensor.

The best case of uncertainty factors (1) and (2) is achieved by diffraction limited imaging optics. For such optics, all aberrations (see Sec. 3.4.8) are corrected, so that they can be neglected. Then, the smallest points of the projected pattern are imaged in the shape of

diffraction patterns, which depend on the aperture of the optics used and on the wavelength (see Sec. 2.2.6.1). Diffraction results in a systematic error of the measurement. In principle, image restoration methods can be used to compensate for diffraction effects in the image (see Chap. 10). However, noise often limits the possible improvement.

Besides the imaging optics, also the characteristics of the light source are important, which often differ significantly from the often assumed ideal case, e.g., of a point light source.

The resolution of the sensor (3) can at least be nominally as fine as desired if continuous sensors like PSDs (Sec. 6.5) are used.

Speckle (4) leads to a stochastic distortion and mainly depends on the coherence properties of the light used.

The roughness of many common surfaces has an amplitude  $R$  which is significantly larger than the wavelength  $\lambda$  of the used light. The term ‘roughness’ refers to the microstructure of the surface relief that is superposed on the nominally desired or expected surface during manufacturing [41].

Roughness leads to scattered light, which is necessary for triangulation methods. The lateral measurement uncertainty is mainly determined by the spatial resolution  $w$  of the projected light pattern:  $\sigma_1 \sim w$ . It is not sensible to ask for a vertical measurement uncertainty much smaller than  $R$ .

According to Huygen’s principle, every surface point inside the illuminated region acts like a point source of a spherical waves with the phase of the light incident at that point (see Sec. 2.2.3). The microstructure of a rough surface is irregular, so that the emitted spherical waves have quasi-stochastic differences of phase and are superposed on each other to produce a spatially irregular, temporally constant interference pattern. For coherent light, e.g., that from a laser, this interference pattern shows extensive contrasts between spatially adjacent points with constructive and destructive interference if the coherence length is greater than the surface’s roughness  $R$ . This phenomenon is called speckle.

If the light pattern is imaged onto a sensor, speckle causes a multiplicative spatial noise on the sensor plane.

As all triangulation methods rely on the measurement of the projected pattern’s image, which is affected by speckle, speckle increases the measurement uncertainty of all triangulation methods.

For several optical measurement methods, the theoretical lower bounds for the minimum possible measurement uncertainty have been derived in the form of standard deviations [46, 71]. For projection based triangulation methods with coherent light, this lower bound for the vertical measurement uncertainty is given by

$$\sigma_v = \frac{\lambda}{2\pi \sin \alpha \sin \theta} \quad (7.51)$$

with the wavelength  $\lambda$ , the triangulation angle  $\theta$ , and the angle bisector  $\alpha$  of the object-sided aperture (see Fig. 7.35). For  $\lambda = 660 \text{ nm}$ ,  $\theta \in [45^\circ, 60^\circ]$  and  $2\alpha \in [6^\circ, 18^\circ]$ ,  $\sigma_v$  is approximately in the range of  $0.8 \text{ }\mu\text{m} < \sigma_v < 2.8 \text{ }\mu\text{m}$ . Increasing  $\theta$  as well as increasing  $\alpha$  decreases the lower bound of the measurement uncertainty  $\sigma_v$ .

The use of white light, i.e., incoherent light or light with a coherence length that is significantly smaller than  $R$ , avoids or reduces the speckle effect and lowers the theoretical lower bound by a factor of up to 10.

Technically achievable measurement uncertainties are about 5 times higher than the theoretical lower bound [127].

### 7.3.4 Structured illumination

Pointwise triangulation results in the 3D coordinates of a single point for each measurement; with a light-section sensor, a line on the test object along the intersection with the two-dimensional light fan can be simultaneously measured. In order to measure a three-dimensional surface relief without moving the sensor or the test object, the principle of the light-section can be generalized by projecting several light fans on the test object at once. However, the identification of the single stripes in the observed image might be problematic, especially on object edges. In order to achieve a unique assignment between the projected stripes and the stripes observed in the image, specially designed heterogeneous light patterns can be used instead of a simple stripe pattern. The selected pattern has to ensure that there are no ambiguities between the projected and the observed stripes, so that the triangles needed for the distance measurement are well-defined. The patterns can either be generated by a laser with the appropriate optics, or by a video projector controlled by a computer. In contrast to pointwise triangulation and to the light-section method, the Scheimpflug condition cannot be fulfilled for the whole surface, but only for a single plane, which is most reasonably chosen to be at the medium object distance (Fig. 7.39(c)). Thus, the measurement range and the resolution are limited by the depth of field of the observation.

Methods of this kind are summarized by the term **structured illumination**. An inhomogeneous light pattern  $b(\mathbf{x})$  is projected on the object's surface in order to acquire a surface relief  $z(\mathbf{x})$ . If the scene is observed with a camera, the pattern appears to be distorted if the camera and the projection do not share the same perspective. The distortion is caused by the locally varying displacements of the pattern due to the object's geometry. The relief can be quantitatively reconstructed from the observed signal  $b_{\text{dist}}(\mathbf{x})$  (Fig. 7.41). Alternatively, a qualitative analysis without explicit reconstruction can also be performed, for example to detect defects, which are highlighted by a local difference of the observed pattern from a reference pattern. Often, stripe patterns are used, which will be covered in detail in the following section.

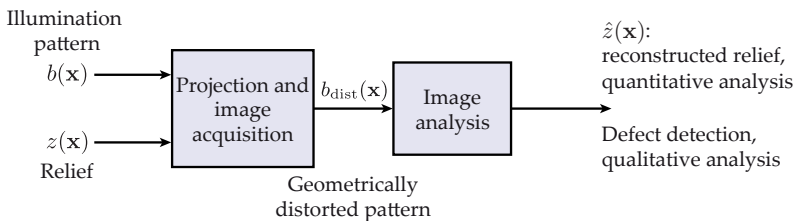


Figure 7.41. Signal model of pattern projection.

As only the pattern's geometric displacement and distortion is measured, and not its intensity, the measurement is largely independent of the surface's optical properties (color, reflectance, scatter). The only requirement is that a part of the light is scattered to the sensor. Therefore, the surface must be neither an ideal mirror nor an ideal absorber (see Sec. 7.3.1 and Fig. 7.33(b)). For specular surfaces, deflectometric methods can be used, which will be covered later on in Sec. 7.3.5.

### 7.3.4.1 Stripe projection

For the areal application of the principle of triangulation to complex objects, the problem of ambiguous correspondences between the observed image points and the points of the illumination pattern arises. A unique identification of a point can be achieved by using encoded illumination sequences where every illumination beam is assigned an unambiguous code word (Fig. 7.42). For example, the  $x$  coordinate of a light spot of the projector or the screen can be represented in the Gray code, as illustrated in Fig. 7.43. The  $m$ th image corresponds to the  $m$ th bit of the encoded image coordinates. A projector pixel is displayed as white if the  $m$ th bit of its coordinate is equal to 1 and black if it is 0.

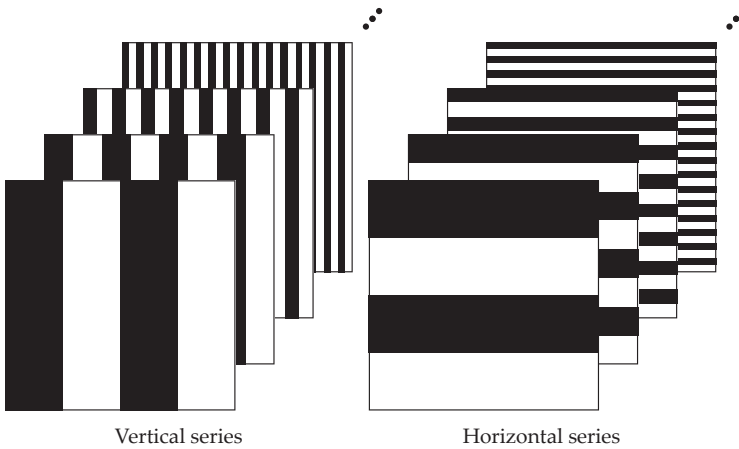


Figure 7.42. Image series used for binary coding the pixel position in the projected pattern.

This bitwise representation can be composed to form an encoded image series. The number of images corresponds to the number of bits of the discretization of the coordinate values. Another image series can be used to encode the  $y$  position, so that a unique two-dimensional correspondence is established. In general, the number  $Q$  of projector patterns needed for the  $M \cdot N$  binary represented projector beams (projector pixels) is

$$Q = \lceil \lg(M \cdot N) \rceil = \lceil \lg M + \lg N \rceil. \quad (7.52)$$

In contrast to binary numbers, the adjacent code words of the Gray code only differ from each other in exactly one bit. The code word corresponding to a binary number  $x$  can be calculated using a binary XOR operation:

$$x \mapsto x \text{ XOR } \left\lfloor \frac{x}{2} \right\rfloor. \quad (7.53)$$

The Gray code is more robust than using binary numbers: a faulty decoding inside the transition from a black to a white stripe leads to the neighboring code word of the Gray code, so that the actual influence of the decoding error in this quite frequently arising situation is limited. As the code words of spatially adjacent pattern points differ only in one bit per coordinate, there is only one image in the whole image series with a white–black transition between the adjacent pattern points. Another advantage of the Gray code is the minimum stripe width of two pixels, in contrast to binary numbers, where stripes with a width of one

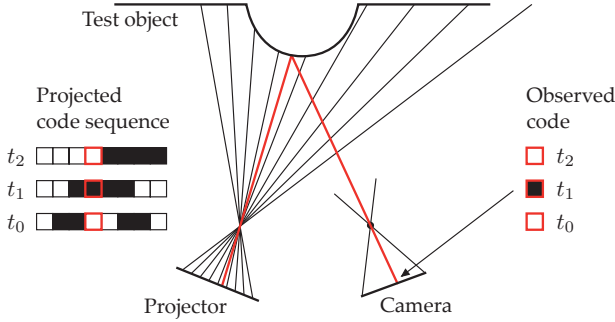


Figure 7.43. Decoding a pixel coordinate from successive Gray code images.

pixel can arise for the coding of the least significant bit [64]. For a robust decoding, the additional projection of a complete black and a complete white image allows the determination of an individual binarization threshold for each image pixel [122]. This leads to a decoding that is robust to variations in the surface's reflectance.

Besides binary coding, also  $n$ -adic codes can be used, which offer  $n$  different values and not only black and white [139]. In the actual pattern, those values can be represented either by  $n$  different gray values or  $n$  different colors. An important advantage of  $n$ -adic codes is the reduced number  $Q_n < Q$  of necessary patterns that have to be projected: the binary logarithm  $\text{ld}$  in (7.52) can be replaced by the logarithm to the base  $n$ :

$$Q_n = \lceil \log_n M + \log_n N \rceil. \tag{7.54}$$

Unfortunately, it is harder to reliably distinguish the  $n$  values in the camera image. Depending on the test object's reflectance and geometry, some projected colors or gray values might appear very similar in the image. Colored objects can even change the spectral composition of the reflected light, which can complicate or hinder the decoding of color patterns. For example, a white surface illuminated by a red light source might look exactly the same as a red surface illuminated by a white light source. For test objects which are largely homogeneous and of which the reflectance properties are known a priori, the used patterns can be appropriately adjusted, in order to avoid such ambiguities. This problem is quite serious if the characteristics of the test object are unknown or inhomogeneous. In such a case, the system usually has to undergo a calibration of colors [139].

Phase-shifting methods are an alternative to Gray code sequences. They use periodic patterns and multiple images to reconstruct the phase of the observed pattern. Typically, sine waves of the form  $g_{x,\varphi_x}(\mathbf{x}) = \frac{1}{2}(1 + \sin(f_x x + \varphi_x))$  and  $g_{y,\varphi_y}(\mathbf{x}) = \frac{1}{2}(1 + \sin(f_y y + \varphi_y))$  are used. A single image is not sufficient for uniquely determining the phase. At least three different images with differently moved patterns are necessary. Additional images increase the method's robustness. The different patterns can be generated by varying the offset of the phase  $\varphi_x$  or  $\varphi_y$ . Often, phase-shifting methods with four images are used. In such a case, the values of  $k\frac{\pi}{4}$ ,  $k = 0, 1, 2, 3$  can be used for the offset (see also Sec. 7.3.16.1). As only the relations of intensities are used for the analysis, phase-shifting methods are also independent of the absolute properties of reflectance of the investigated surface.

Phase-shifting methods allow a decoding at the sub-pixel level and can also be used for blurred images: as a sine pattern has no higher harmonics, its form remains unchanged even for the defocused imaging which corresponds to a low pass filter in the sense of system theory (see Chap. 8). Only the amplitude and thus the contrast is reduced. On the other hand, the phase information allows no unambiguous correspondence between the image coordinates and the pattern coordinates, as equal phase values arise several times in the pattern. For continuous surfaces, a phase unwrapping can be used to estimate a globally unambiguous correspondence [59, 157]. Alternatively, many pattern sequences with different frequencies  $f_x, f_y$  can be used to calculate a unique assignment. Combining this method with a Gray code sequence is also possible [95].

Besides a temporally sequential coding in an image series, a spatial coding could be considered [139]. Therefore, the position's codeword is distributed over a neighborhood of the pattern points. As a matter of principle, the correspondence can only be established for a region of the pattern and not for single points of the pattern, leading to a reduced spatial resolution compared to the temporally sequential coding. Furthermore, a spatially distributed codeword is mapped to different image regions if it is projected on an edge of the object. In this case, a correct decoding is hardly possible, leading to incomplete correspondences and therefore to an incomplete 3D reconstruction. An advantage of the spatial coding is the reduced number of patterns that have to be projected, leading to a reduction of the time consumed by the inspection process. In the extreme case, a single pattern is sufficient for capturing the 3D surface, so that even moving objects can be measured. The coding of the spatial patterns is usually based on sequences of pseudorandom numbers. Hence, patterns can be constructed where each region of a fixed size is globally identified and thus encodes the position in the pattern without any ambiguity. Again, the pattern can be represented by binary values, by multiple gray values or by different colors (Fig. 7.44).

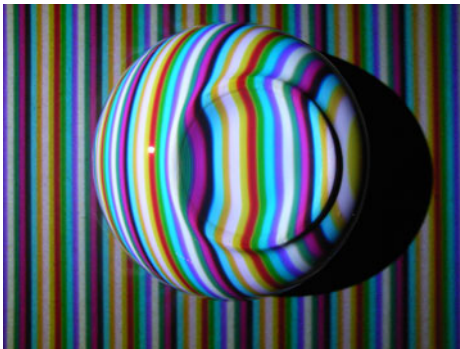


**Figure 7.44.** Projection of a periodic pattern of colored stripes on a sample scene consisting of a cup placed upside down on a sheet of paper. Some colors like white, yellow and blue occur multiple times in one period, but can be unambiguously identified because of the neighboring stripes.

As another alternative, the coordinates can be directly encoded by an intensity value or by a certain wavelength. The resulting projected image shows a gradient of gray values or of monochromatic colors. However, the variant based on intensities is very prone to noise and thus cannot achieve the same robustness and resolution as does the temporally sequential pattern projection [139]. The disadvantages of direct encoding are especially severe for test objects with inhomogeneous reflectance or color.



An additional constraint which can be used for 3D reconstruction based on projected pattern sequences results from the epipolar geometry between the projector and the camera (cf. Sec. 7.3.8).

As soon as the correspondence between image points and projector points is established, the surface relief sought can be calculated similarly to the methods of triangulation and light section (Sec. 7.3.1).

**Example 7.8 (Inspection of cylinder heads):** Figure 7.45 shows the application of the stripe projection method to reconstructing the 3D relief of a diesel engine. The holes for the

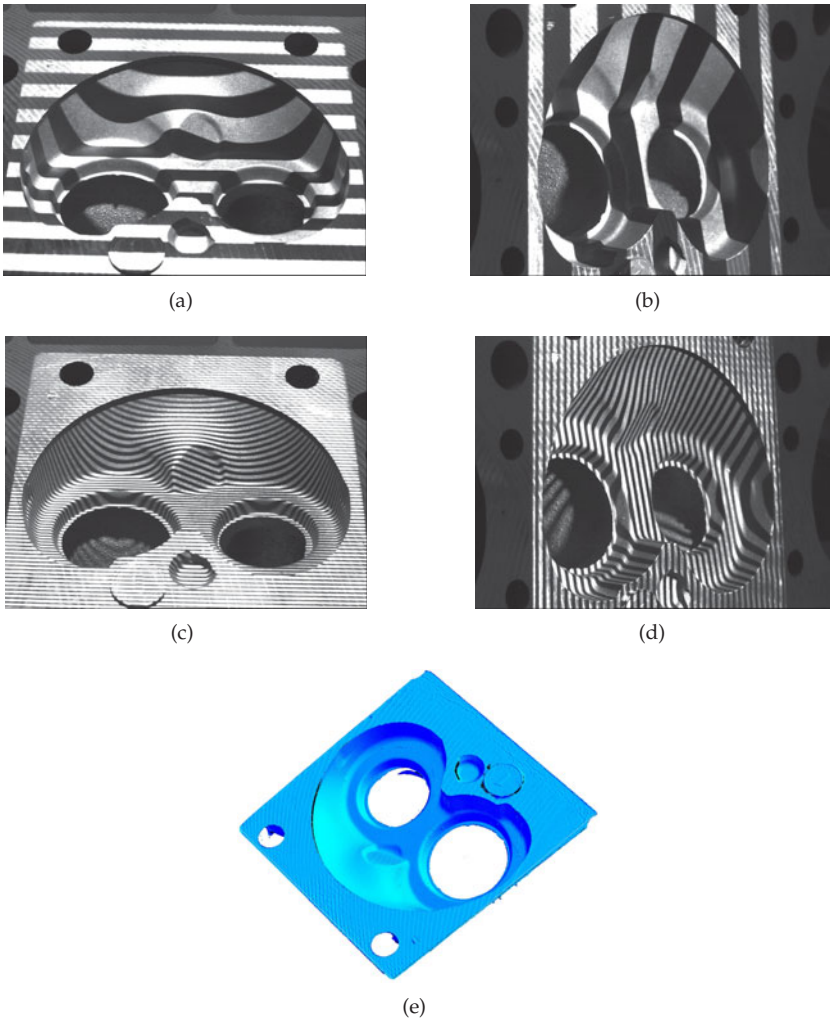


**Figure 7.45.** Inspection of the combustion chamber of a cylinder head: (a)–(d) Single images of the projected sequence of stripe patterns; (e) 3D reconstruction (source: inspectomation GmbH).

two valves are clearly visible. The horizontal and vertical positions are both encoded by a sequence of stripe images. In order to reduce occlusions, images taken from two different perspectives are necessary. ■

### 7.3.5 Deflectometry

The projection methods considered until now are mostly independent of the *optical* properties of the objects, e.g., color, reflectance and scattering characteristics, as they rely on the deformation of the projected pattern by the surface *relief*. However, they require the surface to scatter at least some of the light back to the sensor. Hence, the surface must neither absorb all the light, nor be an ideal mirror.

In fact, for specular surfaces, the related method **deflectometry** can be applied. This method is based on the human approach of inspecting specular surfaces: one observes the mirror image of the surrounding environment in the surface and searches for local distortions in order to detect defects.

For deflectometry, a camera observes the image of a pattern which is mirrored in the object surface (see Fig. 7.46). Here, the pattern is generated on a screen or on a display (Fig. 7.47). In the following, the term pattern generator will be used to denote the screen or the display of the deflectometric setup. In contrast to stripe projection, the pattern is not projected (i.e., imaged) onto the surface.

Unlike stripe projection, where the camera is focused on the image of a projection onto the object surface, the camera directly observes the pattern generator. This is the reason for the main difference between the two methods regarding their sensitivity with respect to the surface gradient: stripe projection is locally insensitive to a varying surface gradient, as it relies on scattered light. In contrast, deflectometry is very sensitive to local differences in the surface gradient, as a change of the surface normal implies a change of the optical path of the reflection (Fig. 7.48). Therefore, deflectometry is suitable for detecting surface defects affecting the surface gradient.

For defect detection, often a single image with a suitable pattern is sufficient. This is illustrated by Fig. 7.49 by means of an example of a plastic lens for infrared light, which is

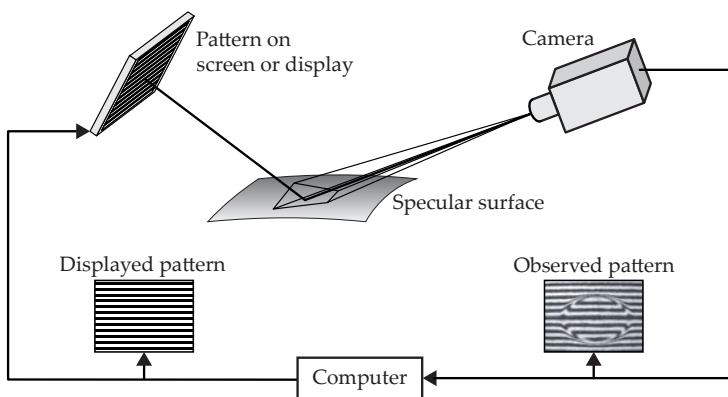


Figure 7.46. Setup of pattern generator and camera for deflectometry.

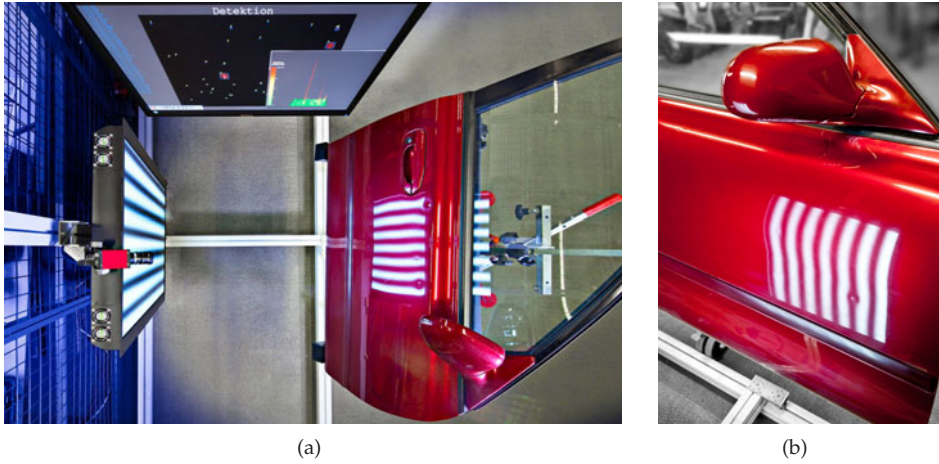


Figure 7.47. Deflectometric setup for the inspection of a coated car door: (a) Setup of pattern generator, test object and camera; (b) When observing the reflected stripe pattern, a defect is clearly visible.

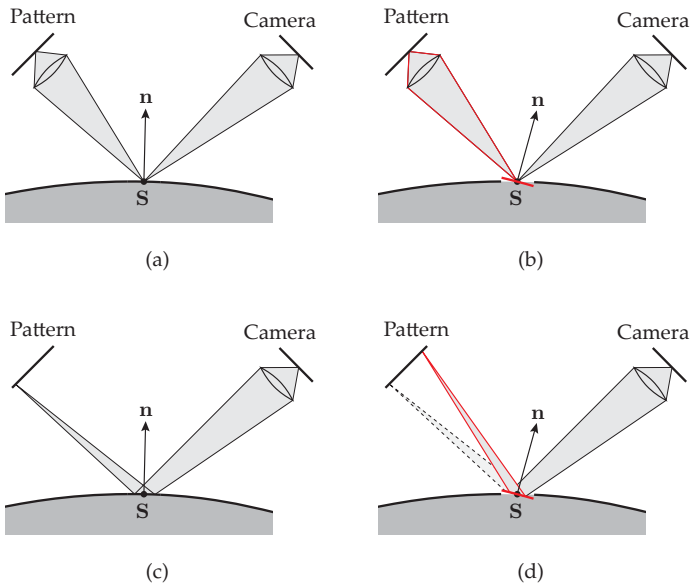
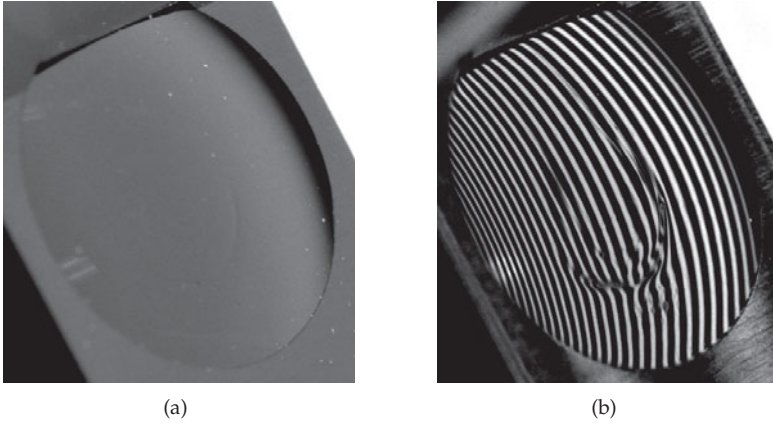
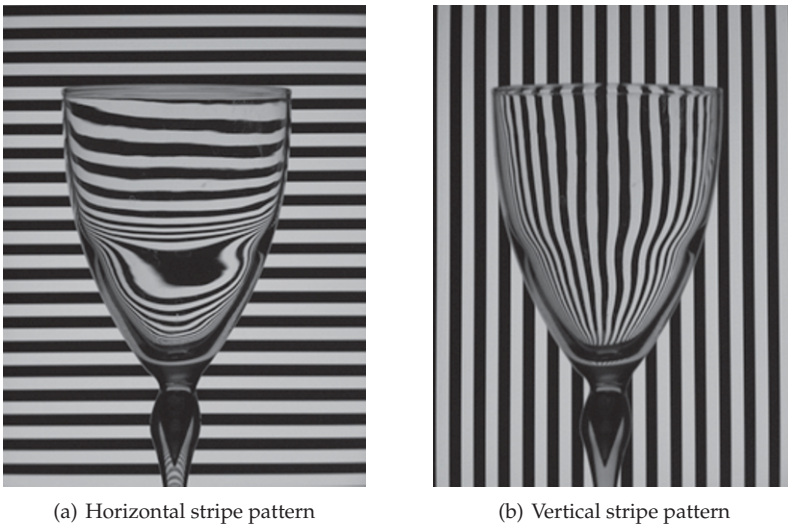


Figure 7.48. Comparison of the optical paths of stripe projection and deflectometry [20]: (a), (b) As the pattern is imaged onto the surface and the camera is focused on the surface, the stripe projection method is locally insensitive to the surface gradient; (c), (d) As the camera is focused on the pattern generator, deflectometry is locally sensitive to the surface gradient.

opaque for the illumination used for image acquisition. The local irregularity of the observed stripe pattern clearly represents the defect, whereas dust particles dominate the defect under



**Figure 7.49.** Inspection of a plastic lens with a diameter of about 1 cm: (a) Image acquired under diffuse illumination; (b) Image acquired with deflectometry.



**Figure 7.50.** Image of a transparent object acquired using deflectometry and transmitted light.

diffuse illumination. An inverse pattern which has been specifically adapted to the reference object could be a possible choice, see Sec. 7.6.2.

For the inspection of transparent objects, deflectometry can also be performed in transmission: the refraction at the surface of the transparent object causes the pattern to be distorted depending on the object geometry [13]. Figure 7.50 shows an example.

In order to achieve a further inspection and reconstruction of the surface geometry, an assignment between the image points of the camera and of the pattern generator is required. In order to obtain this assignment, the pattern sequences described in Sec. 7.3.4.1 can be used (Fig. 7.51). For the Gray code method, the camera must be focused on the pattern

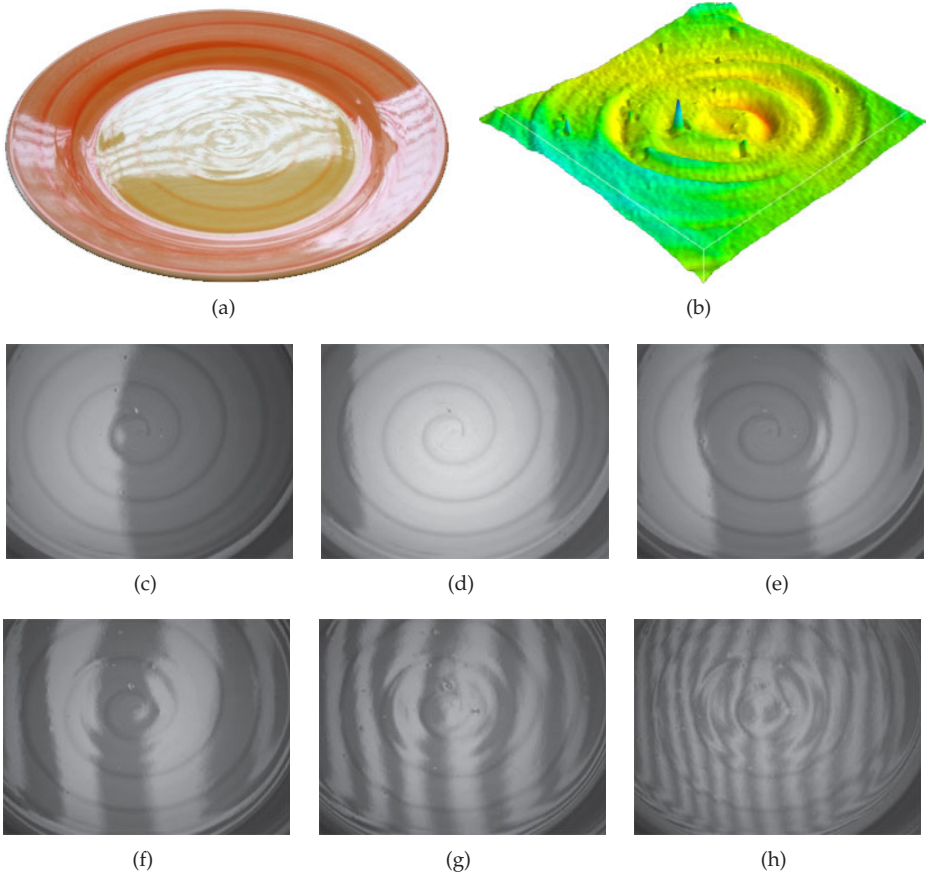


**Figure 7.51.** Deflectometric inspection of a glazed plate: (a) Image of the test object; (b) Deflectometric reconstruction of the local surface gradient; (c)–(h) Observed reflection of some stripe patterns of the horizontal Gray code sequence.

generator in order to allow a reliable decoding. However, this reduces the lateral resolution on the object surface (Fig. 7.52): the observed intensity value is an average of a region on the test object surface. As phase-shifting methods are not susceptible to blur, the camera can be focused on the object surface [173]. Thus, a better detection of spatially limited defects can be achieved. Now, the observed intensity value is an average of a region on the pattern generator, which is why the resolution of the surface gradient is higher if the camera is focused on the pattern generator. The sensitivity to the surface gradient is further improved by a greater distance between the pattern generator and the surface. However, an increased distance reduces the captured measurement field and the range of measurable gradients.

In the following, a mathematical description of the deflectometry problem will be derived. The notation employed is introduced by means of Fig. 7.53. Let  $\mathbf{O}$  denote the origin of the camera coordinate system, let  $\mathbf{S}$  denote the observed surface point, and let  $\mathbf{L}$  denote the point on the pattern generator that is reflected in  $\mathbf{S}$ . The vectors  $\sigma\mathbf{s}$  and  $\mathbf{l}$  denote the posi-

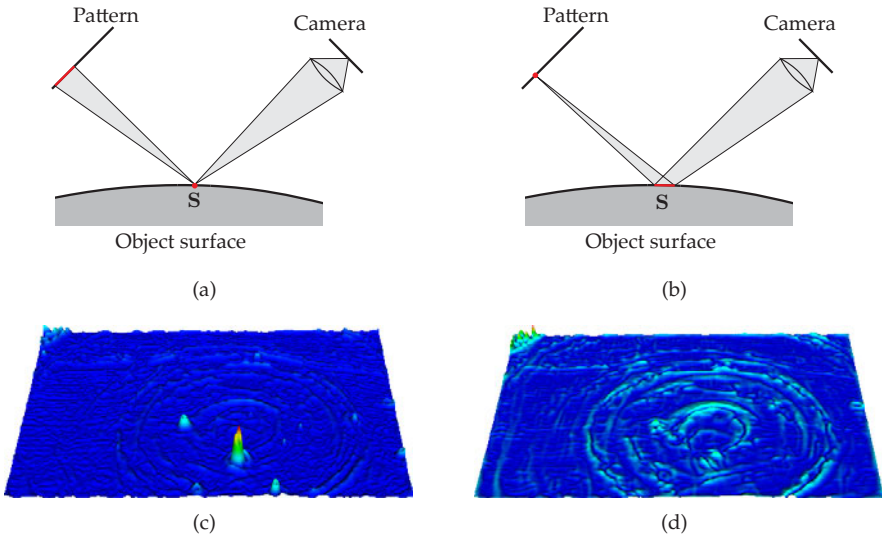


**Figure 7.52.** Different focus adjustments of a camera in deflectometry: (a) Focusing the surface of the test object; (b) Focusing the pattern generator; (c) Reconstruction of the plate of Fig. 7.51(a) when focusing the surface; (d) Reconstruction of the plate when focusing the pattern generator.

tion vectors corresponding to  $S$  and  $L$  with respect to  $O$ . The unit vector  $s$  in the observation direction is known by means of the calibration of the camera. Similarly,  $l$  can be determined via a calibration of the system and from the assignment of the camera point to a pattern generator point obtained by decoding the image sequence. The distance  $\sigma$  of the point  $S$  from the origin  $O$ , the reflection vector  $\rho r$ , and the surface normal  $n$  of the point  $S$  are unknown. The vector  $\rho r$  consisting of the unit vector  $r$  and length  $\rho$  describes the reflected ray running from  $L$  to  $S$ .

With regard to this notation, the vectorial law of reflection (2.202) is given by

$$r = s - 2n n^T s, \quad \|n\| = 1, \quad \|r\| = 1, \quad \|s\| = 1. \tag{7.55}$$

Furthermore, in Fig. 7.53, we have

$$l = \sigma s + \rho r. \tag{7.56}$$

This results in

$$l - \rho(s - 2n n^T s) - \sigma s = 0. \tag{7.57}$$

This system of equations is under-determined. Hence, the deflectometric reconstruction problem has no unique solution when considering single points.

Considering all rays yields the following system of equations:

$$l_{ij} - \rho_{ij}(s_{ij} - 2n_{ij} n_{ij}^T s_{ij}) - \sigma_{ij} s_{ij} = 0, \quad i \in \{0, \dots, I - 1\}, \quad j \in \{0, \dots, J - 1\}. \tag{7.58}$$

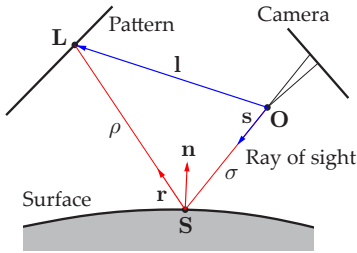


Figure 7.53. Notation for the principle of deflectometric measurement [11,20].

Here,  $i$  and  $j$  enumerate the camera pixels or the corresponding rays of sight  $s_{ij}$ . This system of equations is under-determined too.

An alternative approach to solving the deflectometric reconstruction problem is possible using the concept of normal fields. By means of a deflectometric measurement, which for every ray of sight  $s_{ij}$  determines the corresponding vector  $l_{ij}$  by obtaining the decoded assignment, it is possible to calculate, for every point in the three-dimensional measurement range, the respective normal that would correspond to a specular surface if this surface contained this very point (Fig. 7.54). For every point in the field of view, a normal vector is obtained that obeys the law of reflection together with the rays of sight corresponding to the pair  $(s_{ij}, l_{ij})$  of the deflectometric measurement.

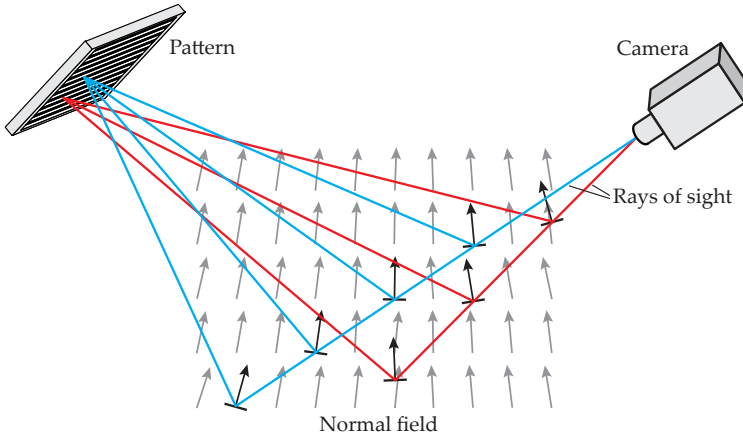


Figure 7.54. Normal field of a deflectometric measurement.

The calculation of the normals is based on an alternative formulation of the law of reflection [11]. The considered 3D point is unambiguously characterized by its sight vector  $\sigma s$ . The tangent plane to a specular surface at this point is spanned by two orthogonal vectors  $a(\sigma s)$  and  $b(\sigma s)$ . The vector  $a(\sigma s)$  is located in the reflection plane which contains the rays of sight  $s$  and  $r$  (Fig. 7.55). It is defined as

$$a(\sigma s) := s + r(\sigma s) = s + \frac{l(\sigma s) - \sigma s}{\|l(\sigma s) - \sigma s\|}. \tag{7.59}$$

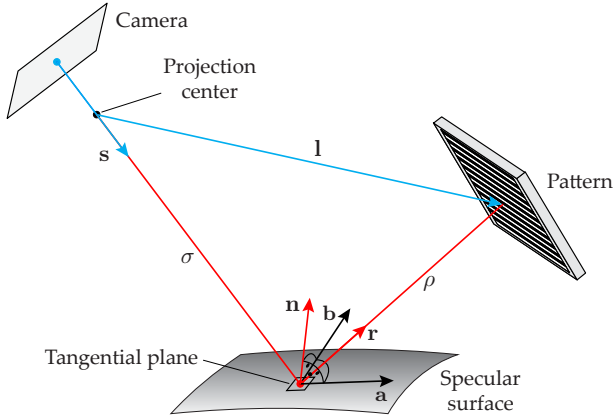


Figure 7.55. The vectors  $\mathbf{a}$  and  $\mathbf{b}$  span the tangential plane to the surface.

These equations are obtained using (7.56). This vector is perpendicular to the corresponding surface normal:

$$\mathbf{a}(\sigma\mathbf{s})^T \mathbf{n}(\sigma\mathbf{s}) = (\mathbf{s} + \mathbf{r}(\sigma\mathbf{s}))^T \frac{1}{\|\mathbf{n}(\sigma\mathbf{s})\|} (\mathbf{r}(\sigma\mathbf{s}) - \mathbf{s}) \quad (7.60)$$

$$= \frac{1}{\|\mathbf{n}(\sigma\mathbf{s})\|} (\mathbf{s} + \mathbf{r}(\sigma\mathbf{s}))^T (\mathbf{r}(\sigma\mathbf{s}) - \mathbf{s}) \quad (7.61)$$

$$= \frac{1}{\|\mathbf{n}(\sigma\mathbf{s})\|} (\mathbf{s}^T \mathbf{r}(\sigma\mathbf{s}) - 1 + 1 - (\mathbf{r}(\sigma\mathbf{s}))^T \mathbf{s}) = 0. \quad (7.62)$$

The second basis vector is chosen to be perpendicular to the reflection plane:

$$\mathbf{b}(\sigma\mathbf{s}) := \mathbf{l}(\sigma\mathbf{s}) \times \sigma\mathbf{s}. \quad (7.63)$$

Thus, this vector is also orthogonal to  $\mathbf{a}(\sigma\mathbf{s})$  and to  $\mathbf{n}(\sigma\mathbf{s})$ :

$$(\mathbf{a}(\sigma\mathbf{s}))^T \mathbf{b}(\sigma\mathbf{s}) = 0, \quad (7.64)$$

$$(\mathbf{b}(\sigma\mathbf{s}))^T \mathbf{n}(\sigma\mathbf{s}) = 0. \quad (7.65)$$

This implies that the tangential plane sought is in fact spanned by  $\mathbf{a}(\sigma\mathbf{s})$  and  $\mathbf{b}(\sigma\mathbf{s})$ . Now, the corresponding normal vector can be calculated, as it is the unit vector perpendicular to the basis vectors:

$$\mathbf{n}(\sigma\mathbf{s}) = \frac{\mathbf{a}(\sigma\mathbf{s}) \times \mathbf{b}(\sigma\mathbf{s})}{\|\mathbf{a}(\sigma\mathbf{s}) \times \mathbf{b}(\sigma\mathbf{s})\|}. \quad (7.66)$$

Together with (7.59) and (7.63), this equation describes the normal field of the deflectometric measurement. For each ray of sight  $\mathbf{s}$  and for each assumed distance  $\sigma$  to the specular surface, i.e., for each position vector  $\sigma\mathbf{s}$ , the deflectometric measurement can be evaluated using the assignment  $\mathbf{l}(\sigma\mathbf{s})$  encoded by the illumination series. Hence, for every length  $\sigma$  of the observation vector  $\sigma\mathbf{s}$ , a corresponding surface normal can be found. Therefore, the formulation of deflectometric measurement using the normal field again shows that no unique solution exists (Fig. 7.56). If a continuous and differentiable surface is assumed, the solution set of this system of equations is a one-dimensional manifold [11]. For every ray of sight  $\mathbf{s}$ ,



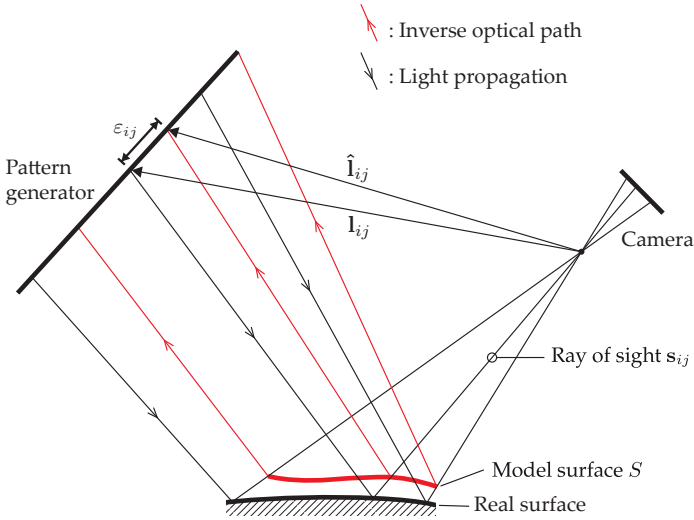


Figure 7.56. Fitting a surface model to the measured normal field for the reconstruction of specular surfaces.

there exists a one-dimensional space of infinitely many pairs of distances  $\sigma$  and surface normals  $\mathbf{n}$  which reflect the ray of sight to the same pattern point and therefore result in the same observation by the camera. In order to obtain a unique solution for the constructed surface, additional information is required.

The following provides a formal specification of the reconstruction problem: a surface  $S$  is to be obtained, whose normals  $\mathbf{n}_S$  are as close to the normal field  $\mathbf{n}$  of the deflectometric measurement as possible:

$$J(S) = \int_S \|\mathbf{n}_S - \mathbf{n}\|^2 ds, \tag{7.67}$$

$$S_{\text{opt}} = \arg \min_S J(S). \tag{7.68}$$

As mentioned above, this is an ill-posed problem (cf. Appendix A.2), as there does not exist a unique solution. The space of possible solutions is one-dimensional. This is why the determination of a single parameter is sufficient to regularize the problem and to reconstruct the surface. In general, this parameter has to be obtained by an additional measurement [12]. For this purpose, an additional deflectometric image can be acquired by varying the position of the camera or of the pattern generator (stereo deflectometry). For partially specular surfaces, other methods for 3D shape capturing, e.g., the laser triangulation of a single surface point or shading methods, can also yield the required additional information (see Sec. 7.3.1 and 7.3.11).

By means of this additional information, the surface can be reconstructed by integrating the normal field. A possible approach is a regular surface  $(x, y, f(x, y))$  with surface relief  $z = f(x, y)$ , so that the normal can be written as [12]:

$$\mathbf{n} = \left( -\frac{\partial f}{\partial x}, -\frac{\partial f}{\partial y}, 1 \right)^T. \tag{7.69}$$

The orthogonality (7.62), (7.65) of the basis vectors  $\mathbf{a}(\mathbf{x}) = (a_x, a_y, a_z)^T$ ,  $\mathbf{b}(\mathbf{x}) = (b_x, b_y, b_z)^T$  of the tangent plane yields the following quasilinear partial differential system of equations:

$$a_x(x, y, f) \frac{\partial f}{\partial x} + a_y(x, y, f) \frac{\partial f}{\partial y} = a_z(x, y, f), \quad (7.70)$$

$$b_x(x, y, f) \frac{\partial f}{\partial x} + b_y(x, y, f) \frac{\partial f}{\partial y} = b_z(x, y, f). \quad (7.71)$$

This system can be solved by means of the method of characteristics expansion [11]. A single known 3D point of the surface obtained by a regularization method can be used as the initial condition. The result of the integration is a surface  $S = \{(x, y, f(x, y))^T\}$  which corresponds to the measured normal field.

In general, a deflectometric measurement covers only a small section of the specular surface, as depending on the curvature of the surface, the observed pattern is visible only in a small region of the camera image. This region is enlarged for larger pattern generators. For some applications, a spherically shaped pattern generator might be beneficial [95]. However, for automated visual inspection of larger objects, usually multiple deflectometric measurements have to be combined. For a possible realization, the pattern generator and the camera can be combined into a single sensor head, which can be arbitrarily positioned and aligned by an industrial robot [173].

### ⊗ 7.3.5.1 Open research questions regarding deflectometry

By means of differential geometric methods, recent research [108] has shown that nearly all surfaces can be unambiguously reconstructed by a deflectometric measurement (7.58), without the need for regularization or additional data. However, additional regularizing information can significantly increase the precision of the reconstruction [128].

Current research is especially focused on the question, for which subset of all surfaces does the reconstruction problem remain ambiguous, and for which subset is it unique. Apparently it would be sufficient if a surface could be locally unambiguously reconstructed from the deflectometric measurement. Starting from this local reconstruction, the normal field could be integrated, so that the uniqueness could be propagated to the whole surface [128].

## ⊗ 7.3.6 The moiré method

### ⊗ 7.3.6.1 The moiré effect

The moiré effect can be caused by two superposed regular structures. Patterns can be observed, that have significantly lower spatial frequencies than the original structures. An example of the moiré effect is that caused by two regular stripe structures with slightly different periods, shown in Fig. 7.57(a). Microscopic differences in the grid structure can lead to macroscopic effects. In everyday life, such effects are often caused by the superposition of two identical fences at different distances. In this case, the apparent differences of the periods are caused by the distance-dependent magnification of the optical imaging. Other grid structures can also generate moiré effects, see Fig. 7.58. Besides varying stripe spaces and different magnifications, also the relative rotation of the two grids can cause a moiré effect, see Fig. 7.57(b). In this case, the moiré stripes are parallel to the angle bisector of the rotation [47, 145].

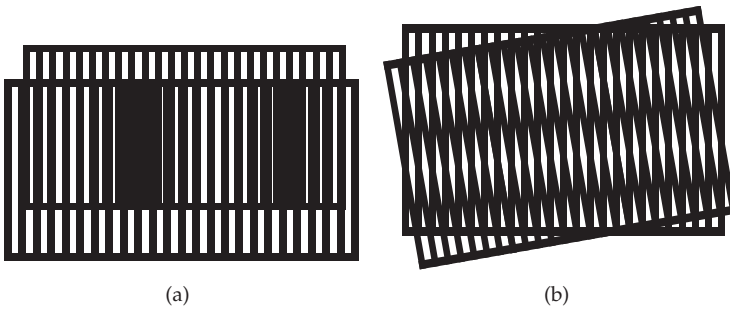


Figure 7.57. Moiré effect caused by the superposition of two stripe structures: (a) Different stripe distances; (b) Rotated stripe pattern.

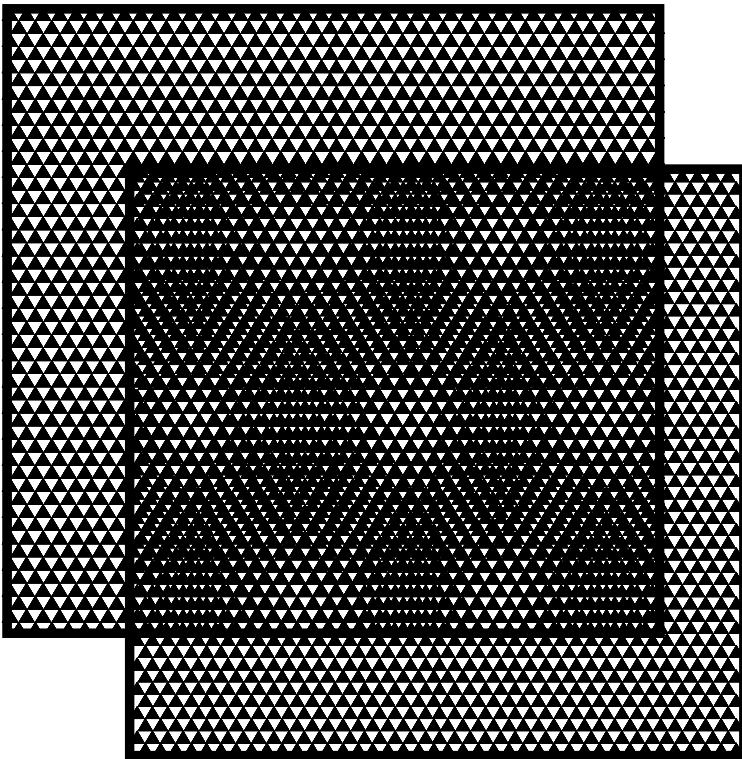


Figure 7.58. Moiré effect caused by the superposition of two triangle patterns with slightly different scales.

For application to automated visual inspection, a grid on the test object's surface is observed together with a reference structure. The resulting moiré image contains information about the surface relief and about possible defects. Generally, methods using the multiplicative superposition of projected light structures and reference structures are called moiré methods. Moiré methods can also be used to measure the mechanical stress inside strained components (cf. Sec. 7.4.6).

For other situations of image acquisition, the moiré effect can be an undesired phenomenon. Together with the grid structures contained in the observed scene, the image sensor's grid structure (see Chap. 6) might lead to moiré patterns. This can often be seen on photos or TV recordings of striped or checkered clothes.

### ⊙ 7.3.6.2 Mathematical model of the moiré effect

The transparency of a structure can be described by a transparency function  $p(\mathbf{x})$  of the position  $\mathbf{x}$ , with  $0 \leq p(\mathbf{x}) \leq 1$ . For completely transparent regions,  $p(\mathbf{x}) = 1$ ; for lightproof regions,  $p(\mathbf{x}) = 0$ . The observed irradiance  $E_e$  is given by the product of the incident light  $E_i$  and the transparency function  $p$ :

$$E_e(\mathbf{x}) = p(\mathbf{x}) E_i. \quad (7.72)$$

Here, the illuminance  $E_i$  is assumed to be constant with respect to the position. If two grids are superposed, their transparency functions  $p_1(\mathbf{x})$  and  $p_2(\mathbf{x})$  are multiplied [80]:

$$E_e(\mathbf{x}) = p_2(\mathbf{x}) p_1(\mathbf{x}) E_i. \quad (7.73)$$

Periodic stripe patterns can be characterized by their density of stripes  $f_k$ , which is defined as the quotient of the number of stripes  $N_k$  by the pattern's length  $l_k$  in the direction of the periodicity:

$$f_k = \frac{N_k}{l_k}, \quad k = 1, 2. \quad (7.74)$$

A moiré effect, as in Fig. 7.57(a), is created by patterns with different densities of stripes:  $f_1 \neq f_2$ .

Moiré stripes of maximum brightness can arise at positions where the transparent regions of the two grids overlap:  $p_1(\mathbf{x}) = 1 = p_2(\mathbf{x})$ . Between two bright moiré stripes, one of the two structures has exactly one additional stripe [10, 47]. For  $f_1 > f_2$ , this results in

$$N_1 = N_2 + 1. \quad (7.75)$$

Let  $l_M$  denote the distance between two adjacent moiré stripes with maximum brightness. In combination with Eq. (7.74), this results in

$$l_M f_1 = l_M f_2 + 1. \quad (7.76)$$

Therefore, the following holds for the density of stripes  $f_M$  of the moiré pattern:

$$f_M = \frac{1}{l_M} = f_1 - f_2. \quad (7.77)$$

Hence, the density of stripes  $f_M$  of the moiré pattern is the difference between the densities of the stripes of the two real patterns [66]. This also applies if the transparency functions are given by trigonometric oscillations. Assuming a sine pattern in the  $x$ -direction,  $p_k(\mathbf{x}) =$

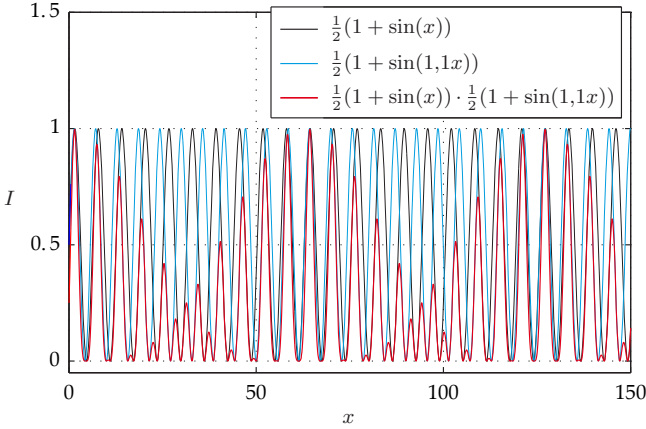


**Figure 7.59.** Moiré effect caused by the multiplicative superposition of two sine waves. The base frequency of the moiré oscillation corresponds to the difference between the two original frequencies, in accordance with (7.77) and (7.78).

$\frac{1}{2}(1 + \sin(2\pi f_i x)) 1(y)$ ,  $k = 1, 2$ , (7.73) yields:<sup>2</sup>

$$\begin{aligned}
 E_e(\mathbf{x}) &= \frac{1}{4}(1 + \sin(2\pi f_2 x) + \sin(2\pi f_1 x) + \sin(2\pi f_2 x) \sin(2\pi f_1 x)) 1(y) E_i \\
 &= \frac{1}{4}(1 + \sin(2\pi f_2 x) + \sin(2\pi f_1 x) \\
 &\quad + \frac{1}{2}(\cos(2\pi(f_1 - f_2)x) - \cos(2\pi(f_1 + f_2)x))) 1(y) E_i.
 \end{aligned}
 \tag{7.78}$$

This expression is obtained using the trigonometric addition formulas [31]. The moiré pattern is described by the sum of several trigonometric wave functions. The frequency of the low-frequency component is given by the difference between the two original frequencies:  $f_M = f_1 - f_2$ . This oscillation is additively superposed on components with higher frequencies (Fig. 7.59).

⊗ **7.3.6.3 Telecentric stripe projection**

As an example of the moiré method used for automated visual inspection, the analysis of the special case of parallel projected periodic structures (Fig. 7.60) will now be performed. The periodic structure is projected onto the investigated surface by a telecentric illumination. For image acquisition, a telecentric system of optics is also used, so that the magnification of the pattern’s distortion is independent of the distance of the object.

Let  $\alpha$  denote the angle between the optical path of the illumination and the  $z$ -axis. It is assumed that no occlusions can occur:  $\frac{\partial z(\mathbf{x})}{\partial x} > -\cot \alpha$ . In the plane  $z = 0$ , the illuminance of the desired illumination pattern is

$$b(\mathbf{x}) = E p(2\pi f_0 x) 1(y), \tag{7.79}$$

---

<sup>2</sup>Two waves with slightly different frequencies are multiplied. The multiplicative superposition does not correspond to the additive superposition, which leads to the so-called beats. The moiré patterns are also based on a multiplicative superposition and not on an additive superposition like the interference patterns described in Sec. 2.2.5

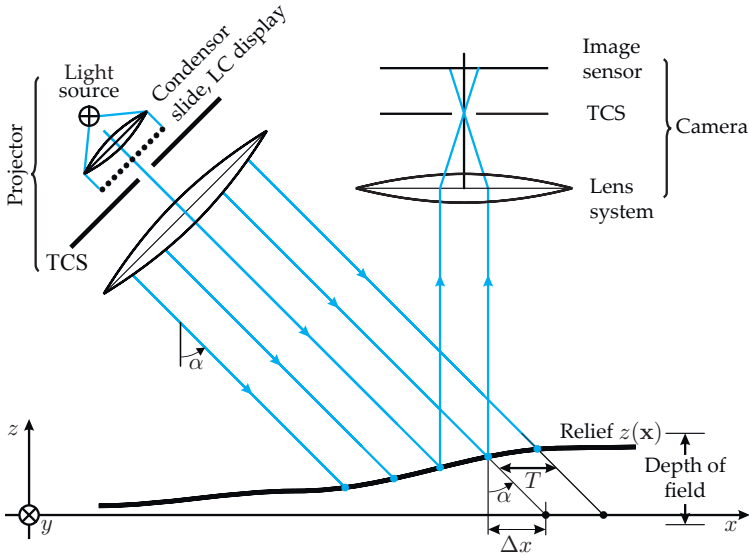


Figure 7.60. Parallel projection of periodic line or stripe structure (TCS = telecentric stop).

where  $p$  has period  $T$ :

$$\forall x : p(2\pi f_0 x) = p(2\pi f_0(x + T)) . \tag{7.80}$$

Here,  $f_0 = \frac{1}{T}$  is the spatial repetition rate and has the unit  $\frac{1}{\text{m}}$ . The constant amplitude of the irradiance  $E$  is in units of  $\frac{\text{W}}{\text{m}^2}$ . Because of the relief  $z(x)$ , the pattern appears to be distorted:

$$b_{\text{dist}}(x, y) = b(x + \Delta x, y) \tag{7.81}$$

$$= E p(2\pi f_0 x + 2\pi f_0 z(\mathbf{x}) \tan \alpha) , \tag{7.82}$$

with  $\Delta x = z(\mathbf{x}) \tan \alpha$ . Now, let  $p(2\pi f_0 x) := 1 + \cos(2\pi f_0 x + \varphi_0)$ , i.e., the constant component of the first harmonic of the stripe pattern is considered. This results in

$$b_{\text{dist}}(\mathbf{x}) = E (1 + \underbrace{\cos(2\pi f_0 x + 2\pi f_0 z(\mathbf{x}) \tan \alpha + \varphi_0)}_{=: \varphi(\mathbf{x})}) . \tag{7.83}$$

Hence, the relief  $z(\mathbf{x})$  linearly modulates the phase  $\varphi(\mathbf{x})$  of the distorted pattern.

**Parenthesis 7.1 (Spatial frequency):** A temporal harmonic oscillation is described by an equation of the form

$$h(t) = \cos(2\pi f t + \varphi_0) . \tag{7.84}$$

Here,  $\varphi_0$  is a constant,  $f$  the oscillation's frequency, and  $T = 1/f$  its period. The frequency is in units of  $\text{s}^{-1}$ .

If  $f = f(t)$  is a function of the time that changes slowly with respect to the period  $1/f$ ,

it is called the **instantaneous frequency** at the time  $t$ . It arises from the partial derivative of the phase term with respect to the time:

$$f(t) = \frac{1}{2\pi} \frac{\partial(2\pi f(t)t + \varphi_0)}{\partial t} \tag{7.85}$$

Similarly, a spatial harmonic oscillation dependent of the position  $\mathbf{x} = (x, y)^T$  can be expressed by the following equation:

$$h(\mathbf{x}) = \cos(2\pi \mathbf{f}^T \mathbf{x} + \varphi_0) = \cos(2\pi(f_x x + f_y y) + \varphi_0). \tag{7.86}$$

Here,  $\mathbf{f} = (f_x, f_y)^T$  denotes the vector of the spatial frequency. The units of  $f_x, f_y$  are  $m^{-1}$ . Then,

$$\|\mathbf{f}\| = \sqrt{f_x^2 + f_y^2}, \quad T = \frac{1}{\|\mathbf{f}\|}, \quad \gamma = \arctan \frac{f_y}{f_x}, \tag{7.87}$$

$$T_x = \frac{T}{\cos \gamma}, \quad T_y = \frac{T}{\sin \gamma}, \quad T_x = \frac{1}{f_x}, \quad T_y = \frac{1}{f_y}, \tag{7.88}$$

see Fig. 7.61. The special case  $\gamma = 0$  yields

$$h(\mathbf{x}) = \cos \left( 2\pi \begin{pmatrix} f_0 \\ 0 \end{pmatrix}^T \begin{pmatrix} x \\ y \end{pmatrix} \right) = \cos(2\pi f_0 x) 1(y), \tag{7.89}$$

i.e., the oscillation is constant with respect to  $y$ .

The **local spatial frequency** is defined in the same fashion:

$$\mathbf{f}(\mathbf{x}) = \begin{pmatrix} f_x(\mathbf{x}) \\ f_y(\mathbf{x}) \end{pmatrix} := \frac{1}{2\pi} \text{grad } \varphi(\mathbf{x}) = \frac{1}{2\pi} \begin{pmatrix} \frac{\partial \varphi(\mathbf{x})}{\partial x} \\ \frac{\partial \varphi(\mathbf{x})}{\partial y} \end{pmatrix}. \tag{7.90}$$

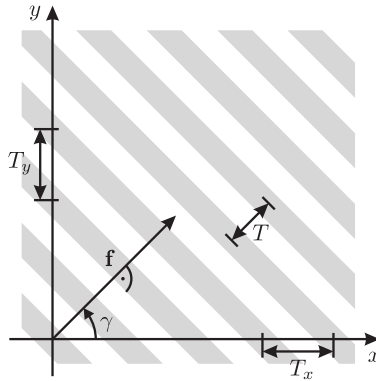


Figure 7.61. Definition of the spatial frequency.

In accordance with (7.90), the local spatial frequency for  $b_{\text{dist}}(\mathbf{x})$  can be calculated using (7.83):

$$\mathbf{f}(\mathbf{x}) = \begin{pmatrix} f_0 + f_0 \tan \alpha \frac{\partial z}{\partial x} \\ f_0 \tan \alpha \frac{\partial z}{\partial y} \end{pmatrix} = \begin{pmatrix} f_0 \\ 0 \end{pmatrix} + f_0 \tan \alpha \text{grad } z(\mathbf{x}). \quad (7.91)$$

So the ‘local density of stripes’ is a linear function of the relief’s gradient. It would now be beneficial to suppress the additive carrier frequency  $(f_0, 0)^T$ . Therefore, the principle of ‘coherent demodulation’ is applied: after a multiplication with the carrier wave  $\cos(2\pi f_0 x)$ , a moving averaging is performed:

$$\tilde{b}(\mathbf{x}) := \frac{1}{T} \int_x^{x+T} b_{\text{dist}}(\xi, y) \cos(2\pi f_0 \xi) \, d\xi \quad (7.92)$$

$$= \frac{E}{T} \underbrace{\int_x^{x+T} \cos(2\pi f_0 \xi) \, d\xi}_{= 0} \quad (7.93)$$

$$+ \frac{E}{T} \int_x^{x+T} \cos(2\pi f_0 \xi + 2\pi f_0 \tan \alpha z(\xi, y) + \varphi_0) \cos(2\pi f_0 \xi) \, d\xi$$

$$= \frac{E}{2T} \int_x^{x+T} \underbrace{\cos(2\pi f_0 \tan \alpha z(\xi, y) + \varphi_0)}_{\approx \text{const. for } \xi \in [x, x+T]} \, d\xi \quad (7.94)$$

$$+ \frac{E}{2T} \underbrace{\int_x^{x+T} \cos(4\pi f_0 \xi + 2\pi f_0 \tan \alpha z(\xi, y) + \varphi_0) \, d\xi}_{\approx 0}.$$

The last equation is obtained using the trigonometric equation

$$\cos v \cos w = \frac{1}{2} (\cos(v - w) + \cos(v + w)) \quad (7.95)$$

which is a result of the addition formulas [31]. Assuming that  $z(\mathbf{x})$  changes slowly with respect to  $x$  compared to  $\cos(2\pi f_0 x)$ , the second integral can be omitted and the first integrand is nearly constant for  $\xi \in [x, x+T]$ . This leads to the following approximation:

$$\tilde{b}(\mathbf{x}) \approx \frac{E}{2} \cos(\underbrace{2\pi f_0 \tan \alpha z(\mathbf{x}) + \varphi_0}_{=: \psi(\mathbf{x})}). \quad (7.96)$$

Inserting the phase  $\psi(\mathbf{x})$  of the latter expression into the definition of the local spatial frequency results in

$$\mathbf{f}(\mathbf{x}) = \frac{1}{2\pi} \text{grad } \psi(\mathbf{x}) = \underbrace{f_0 \tan \alpha}_{= \text{const.}} \text{grad } z(\mathbf{x}). \quad (7.97)$$

So the ‘local density of stripes’ is proportional to the gradient of the relief and the stripes correspond to contour lines. However, the gradient’s *direction* in the contour map is ambiguous. This problem is solved by moving the test object in  $z$ -direction and acquiring and analyzing multiple images.



For this example, there are basically two methods than can be used for the coherent demodulation and thus for the transformation of the projected stripe image into a contour map:

- computationally processing the stripe image  $b_{\text{dist}}(\mathbf{x})$ ,
- optical interference with a reference stripe pattern (moiré effect). The reference stripe pattern represents the carrier oscillation, with which the observed stripe pattern has to be multiplied. The defocused optical imaging and the limited spatial resolution of the sensor represent kind of a low-pass filter, which carries out the local spatial averaging. The demodulation is done optically and thus without any loss of time.

The camera images can be immediately visually interpreted, as the visible stripes correspond to contour lines of the object. Most of the other methods for 3D shape capturing do not have a similar characteristic. The coherent demodulation of the stripe image allows to infer information about the test object's microscopic shape properties from the macroscopic stripe structure.

#### ⊙ 7.3.6.4 Shadow moiré

For **shadow moiré**, a grid is placed immediately above the surface of the investigated object. The setup is illuminated by a point light source with an incidence angle of  $\alpha$  (Fig. 7.62). A camera observes the resulting moiré pattern. The camera's direction of observation is chosen to be as perpendicular as possible to the surface, in order to minimize perspective distortions [102]. Parallel light is not used for this method as it would require large lenses or mirrors. Instead, a point light source is placed at a distance (preferably a large distance) from the surface. This increases the lateral range of the investigated surface, as the incident light can be assumed to be approximately parallel, resulting in an acquisition of the surface with an acceptable measurement uncertainty. However, a real light source always has a finite dimension, resulting in blurred shadows: regions of attenuated shades arise on the surface, from where the light source is only partially occluded (Fig. 7.63). Only inside the umbra is the light source completely hidden. The irradiated light intensity  $I$  decreases gradually from the brightly illuminated regions towards the umbra [51, 66].

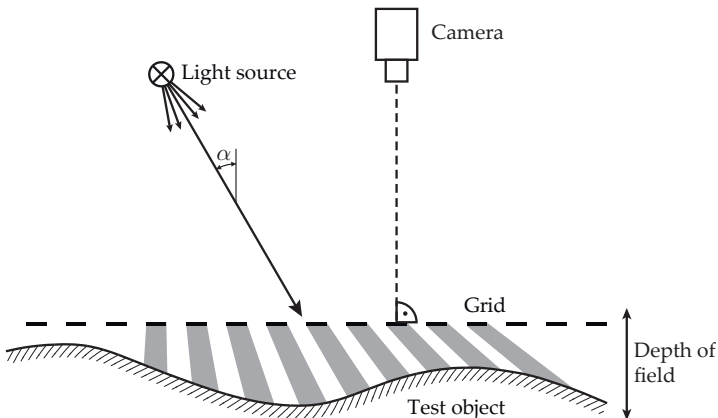


Figure 7.62. Shadow moiré system [102].

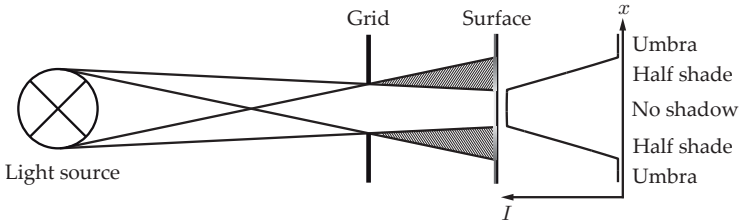


Figure 7.63. Blurred shadows in the case of a real light source.

The model of the multiplicative transparency function from (7.73) can only be approximately realized: the distance of the grid to the surface can only be reduced up to a certain extent, which leads to blurred shadows and a limited depth. Besides, the projection of the stripe pattern and the entocentric observation are affected by perspective distortions. Therefore, the moiré stripes can only be interpreted as ‘qualitative contour lines.’

### ⊙ 7.3.6.5 Projection moiré

For **projection moiré**, a grid structure is projected onto the surface (cf. Sec. 3.5.1). A reference grid is placed in front of the camera [80]. By this means, test objects can be investigated at greater distances. The optical setup has to be adjusted so that the optical imaging between the two grids and the surface is focused (Fig. 7.64). The reference grid can also be placed directly on the camera chip [79], see Fig. 7.65.

The entocentric projection of the grid onto the surface causes perspective distortions. Therefore, the moiré stripes do not correspond to the surface’s contour lines if periodic grids are used. This effect can be compensated for, by using special irregular grids or by performing a post processing with respect to calibration images [102].

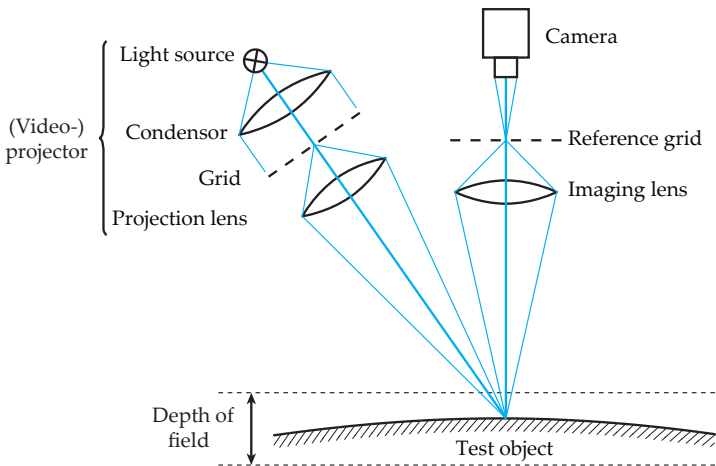


Figure 7.64. System for projection moiré [102].

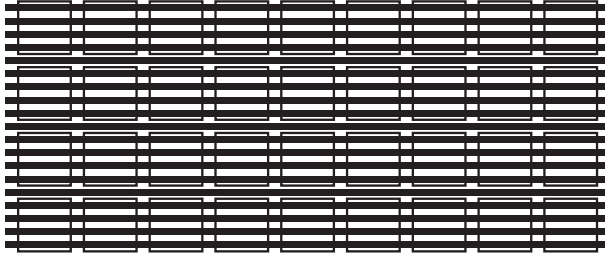


Figure 7.65. Image sensor with reference grid [102].

In general, the surface relief cannot be uniquely reconstructed from the contour map. However, this can be achieved using projections of multiple phase shifted grid structures [102, 132] (cf. Sec. 7.3.4.1 and 7.3.16.1).

### 7.3.7 Final remark on structured illumination

Whether structured or homogeneous illumination is indicated mainly depends on the properties of interest of the object: while structured illumination is useful for acquiring its surface relief, homogeneous illumination can be used to obtain optical properties such as color, texture, or reflectance.

### 7.3.8 Stereo images

If an object point is viewed from two different viewpoints, its object distance, i.e., its distance to the camera, can be calculated using the principle of stereo imaging.

This will now be shown for the simplest case of two cameras with coplanar image planes (Fig. 7.66). Let  $g$  denote the object distance sought,  $G$  the object size (with respect to the marked coordinate axis),  $b$  the image distance of the two cameras,  $B_1$  and  $B_2$  the image sizes (with respect to the optical axes of the respective camera), and  $a$  the distance between the optical centers of the cameras. The parallax (or disparity)  $p$  is defined as  $p := B_1 - B_2$ . The intercept theorem implies

$$\frac{B_1}{b} = \frac{\frac{a}{2} - G}{g}, \quad (7.98)$$

$$\frac{-B_2}{b} = \frac{\frac{a}{2} + G}{g}. \quad (7.99)$$

Adding these two equations followed by some simple arithmetic yields

$$g = \frac{ab}{p}. \quad (7.100)$$

Hence, the distance is inversely proportional to the parallax.

If the two cameras are not parallel, the necessary information about their relative position has to be acquired by a calibration process. In this case, the so-called reconstruction problem, i.e., the determination of the three-dimensional coordinates of an object point with known image coordinates, leads to a system of linear equations depending on the camera parameters (cf. Sec. 3.3).

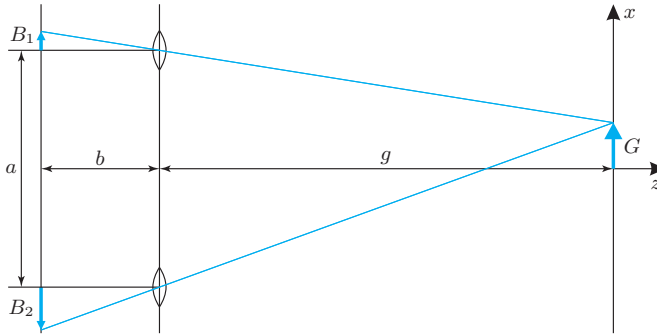


Figure 7.66. Principle of stereo images with cameras arranged in parallel.

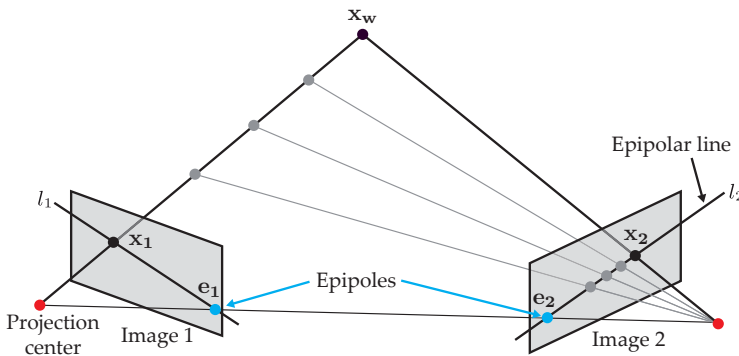


Figure 7.67. Epipolar geometry: The possible corresponding points  $x_2$  in the right image are located on a line  $l_2$  running through the intersection of the epipolar plane and the image plane [51]. The image planes are mirrored by the optical centers marked in red. This way of representation is common in projective geometry.

The second important aspect of stereo image analysis is the so-called **correspondence problem**: which image point of the second camera corresponds to a given image point of the first camera? The geometry of the central projection implies that an object point  $x_w$ , together with its two image points  $x_1, x_2$ , has to be part of a common plane. Except for some degenerate cases, this plane is unambiguously defined by the image point of the first camera and the two optical centers of the projection. It is called the **epipolar plane**, and it intersects the image plane of the second camera in a line called the **epipolar line** (see Fig. 7.67). The corresponding image point has to be located on this epipolar line. In the simple case of coplanar image planes, the epipolar lines are always axis-parallel. Otherwise, they can be calculated by a simple matrix multiplication if the image point of one camera is given. The required matrix is called the **fundamental matrix** of the stereo setup, and it can be estimated using the already mentioned calibration method.

### 7.3.8.1 Derivation of the fundamental matrix

Epipolar geometry is the intrinsic geometry of the central projection with respect to two camera perspectives. It does not depend on the scene, but only on the cameras and their

spatial arrangement. This intrinsic geometry is algebraically embodied by the fundamental matrix  $\mathbf{F}$  [67, Chap. 9].

---

**Theorem 7.1: The fundamental matrix**

For a given stereo setup of two cameras, there exists a fundamental matrix  $\mathbf{F} \in \mathbb{R}^3$  such that the following equation applies for every point correspondence  $\mathbf{x}'_1 \leftrightarrow \mathbf{x}'_2$ , expressed in homogeneous image coordinates:

$$\mathbf{x}'_2{}^T \mathbf{F} \mathbf{x}'_1 = 0. \quad (7.101)$$

The vector of coefficients  $\mathbf{l}_2$  of the epipolar line  $l_2$  of image 2 containing the corresponding point  $\mathbf{x}_2$  for a given image point  $\mathbf{x}_1$  of image 1 is defined by

$$\mathbf{l}_2 \propto \mathbf{F} \mathbf{x}'_1. \quad (7.102)$$

Thus, the epipolar line is defined by the equation  $\mathbf{x}'_2{}^T \mathbf{l}_2 = 0$ . Conversely, the normal form of the epipolar line  $l_1$  in image 1 for a given image point  $\mathbf{x}_2$  of image 2 is obtained by

$$\mathbf{l}_1 \propto \mathbf{x}'_2{}^T \mathbf{F}. \quad (7.103)$$

All epipolar lines of an image  $i$  intersect in a single point, the so-called epipole  $\mathbf{e}_i$ . The epipoles  $\mathbf{e}_1$  of image 1 and  $\mathbf{e}_2$  of image 2 are the solution of the system of linear equations

$$\mathbf{F} \mathbf{e}'_1 = \mathbf{0}, \quad \mathbf{e}'_2{}^T \mathbf{F} = \mathbf{0}. \quad (7.104)$$

◇

---

**Proof 7.1 (The fundamental matrix):** Suppose two cameras with the projection matrices  $\mathbf{P}_1, \mathbf{P}_2$  (see Sec. 3.3) and assume a point correspondence  $\mathbf{x}'_1 \leftrightarrow \mathbf{x}'_2$  given in homogeneous image coordinates. Within the scope of this proof, in contrast to the usual notation, the components of the homogeneous vector will be marked by numeral indices:

$$\mathbf{x}'_i = (x'_i, y'_i, w_i)^T =: (x'_{i1}, x'_{i2}, x'_{i3})^T, \quad i = 1, 2. \quad (7.105)$$

Both points are images of the same spatial point with the homogeneous world coordinates  $\mathbf{x}'_w = (x'_w, y'_w, z'_w, w_w)^T$ . Denoting the rows of the projection matrices by  $\mathbf{p}_{1i}^T, \mathbf{p}_{2i}^T$ , we obtain the following system of equations [67, Sec. 17.1]:

$$\begin{cases} \mathbf{x}'_1 \propto \mathbf{P}_1 \mathbf{x}'_w \\ \mathbf{x}'_2 \propto \mathbf{P}_2 \mathbf{x}'_w \end{cases} \quad (7.106)$$

$$\Leftrightarrow \begin{cases} -\alpha_1 \begin{pmatrix} x'_{11} \\ x'_{12} \\ x'_{13} \end{pmatrix} + \begin{pmatrix} \mathbf{P}_{11}^T \\ \mathbf{P}_{12}^T \\ \mathbf{P}_{13}^T \end{pmatrix} \begin{pmatrix} x'_w \\ y'_w \\ z'_w \\ w_w \end{pmatrix} = \mathbf{0} \\ -\alpha_2 \begin{pmatrix} x'_{21} \\ x'_{22} \\ x'_{23} \end{pmatrix} + \begin{pmatrix} \mathbf{P}_{21}^T \\ \mathbf{P}_{22}^T \\ \mathbf{P}_{23}^T \end{pmatrix} \begin{pmatrix} x'_w \\ y'_w \\ z'_w \\ w_w \end{pmatrix} = \mathbf{0} \end{cases} \quad (7.107)$$

$$\Leftrightarrow \underbrace{\begin{pmatrix} \mathbf{P}_{11}^T & x'_{11} & 0 \\ \mathbf{P}_{12}^T & x'_{12} & 0 \\ \mathbf{P}_{13}^T & x'_{13} & 0 \\ \mathbf{P}_{21}^T & 0 & x'_{21} \\ \mathbf{P}_{22}^T & 0 & x'_{22} \\ \mathbf{P}_{23}^T & 0 & x'_{23} \end{pmatrix}}_{=: \mathbf{A}} \underbrace{\begin{pmatrix} x'_w \\ y'_w \\ z'_w \\ w_w \\ -\alpha_1 \\ -\alpha_2 \end{pmatrix}}_{=: \mathbf{v}} = \mathbf{0}. \quad (7.108)$$

Here,  $\alpha_i \neq 0$  are suitable scaling factors for the representation in homogeneous coordinates. The  $6 \times 6$  matrix  $\mathbf{A}$  is singular and thus  $\det \mathbf{A} = 0$ , as it maps the vector  $\mathbf{v} \neq \mathbf{0}$  to  $\mathbf{0}$  in (7.108). The Laplace expansion [30,37] of this determinant along the last two columns results in a sum where each term is the product of exactly one component of  $x'_i$ , one component of  $x'_2$ , and a  $4 \times 4$  determinant that is independent of  $x'_i$ :

$$\sum_{k=1}^3 \sum_{l=1}^3 \phi_{kl} x'_{1l} x'_{2k} = 0. \quad (7.109)$$

The coefficients  $\phi_{kl}$  result from the  $4 \times 4$  minors of the first four columns of  $\mathbf{A}$  with suitable signs, and only depend on the projection matrices [48,67]. The matrix  $\mathbf{F} = (\phi_{kl}) \in \mathbb{R}^{3 \times 3}$  is the fundamental matrix of the cameras  $\mathbf{P}_1$  and  $\mathbf{P}_2$ . Equation (7.109) can now be expressed as a matrix equation:

$$\mathbf{x}'_2{}^T \mathbf{F} \mathbf{x}'_1 = 0. \quad (7.110)$$

The epipolar line  $l_2$  in image 2 corresponding to the point  $\mathbf{x}_1$  in image 1 can be expressed in normal form by  $\mathbf{x}'_2{}^T \mathbf{l}_2 = 0$ . A comparison of this equation with (7.101) leads to  $\mathbf{l}_2 \propto \mathbf{F} \mathbf{x}'_1$ . Equivalently, the epipolar line  $l_1$  in image 1 corresponding to the point  $\mathbf{x}_2$  can be obtained in accordance with the formula  $\mathbf{l}_1 \propto \mathbf{F}^T \mathbf{x}'_2$ .

The epipole  $\mathbf{e}_2$  is the intersection of all epipolar lines  $l_2$  in image 2, i.e., mathematically speaking,  $0 = \mathbf{e}'_2{}^T \mathbf{l}_2 = \mathbf{e}'_2{}^T \mathbf{F} \mathbf{x}'_1$ . As this equation applies for all  $\mathbf{x}'_1$ , we have  $\mathbf{e}'_2{}^T \mathbf{F} = \mathbf{0}$ . Equivalently, the epipole  $\mathbf{e}_1$  corresponds to the right eigenvector of  $\mathbf{F}$  with eigenvalue 0:  $\mathbf{F} \mathbf{e}'_1 = \mathbf{0}$ . ■

As the epipoles are the eigenvectors of the fundamental matrix with eigenvalue 0, the fundamental matrix has to be singular:  $\det \mathbf{F} = 0$ . Together with the arbitrary scaling factor of the homogeneous coordinates, this constraint implies that a fundamental matrix has seven degrees of freedom [48,67].

Accordingly, at least seven point correspondences  $\mathbf{x}_{1,k} \leftrightarrow \mathbf{x}_{2,k}$ ,  $k = 1, \dots, 7$  are necessary to estimate the fundamental matrix. These point correspondences lead to equations of the

form

$$\mathbf{x}'_{1,k}{}^T \mathbf{F} \mathbf{x}'_{2,k} = 0, \quad (7.111)$$

which, as in (7.109), are linear with respect to the entries of the fundamental matrix. Numerical methods for solving the resulting system of equations are known as the seven-point algorithms or the eight-point algorithms if exactly seven or eight or more point correspondences are used. The numerical stability can be improved using suitable normalization methods [48, 67].

Epipolar geometry not only applies to the two cameras of a stereo setup, but also to the projector and the camera of a pattern projection system (see Sec. 7.3.4.1). A given projector point has to be mapped to its corresponding epipolar line in the camera image, regardless of the observed test object. This can be used to verify the assignment resulting of the decoded pattern sequence, given a suitable calibration of the projector-camera setup [40, 86].

### ⊗ 7.3.8.2 Stereo correspondence algorithms

Although the correspondence problem is reduced to a one-dimensional search by the epipolar conditions, its solution is still challenging. First of all, finding the correct correspondence is complicated by the fact that the same object usually appears differently in the two images. On the one hand, the observed shape and size of the object differ, depending on the camera position, because of the perspective imaging. Further, certain parts of the scene might be occluded in the perspective of one of the two cameras. On the other hand, the measured intensities are only equal if Lambertian reflection is used. Especially surfaces with specular reflections can lead to completely different images, so that a correct correspondence can hardly be found. In order to achieve identical intensities, differences between the imaging optics and the image sensors of the cameras have to be avoided or compensated for by calibration.

Besides, ambiguities can prevent a successful search for correspondences. Thus, the achievable quality mainly depends on the observed scene: if there are only periodic, faint, or even no structures along the epipolar line, a correct local assignment is hardly possible. Therefore, many methods try to regularize the problem by implicitly assuming a spatially smooth surface [77]. However, this is disadvantageous for the lateral resolution.

There are numerous algorithms for the stereo correspondence problem, which differ significantly concerning quality and computational complexity. Examples are correlation methods, dynamic programming, minimization of energy functions, and diffusion methods based on differential equations. A comparison of these methods can be found in [141], and, for multi-view stereo systems, in [148].

An alternative for the determination of a dense relief are feature-based stereo correspondence methods, which only find the correspondences for some image features, which can be well identified and localized. For example, edges or corners can be used as features (cf. Sec. 14.4). Besides the reduced computation time, these methods stand out because the features used can be localized with sub-pixel accuracy, which results in a better accuracy of the depth reconstruction. It is also possible to combine feature-based and dense correspondence algorithms [57].

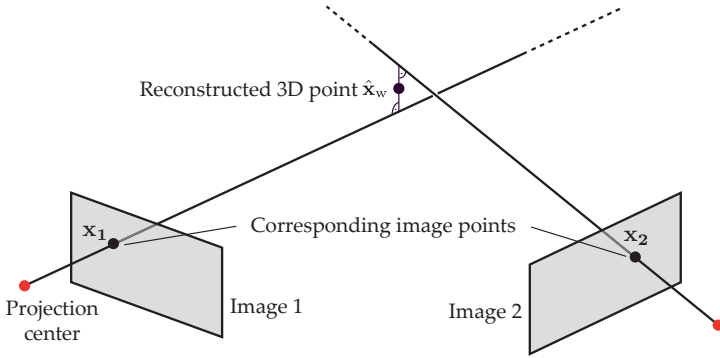


**Figure 7.68.** Stereo reconstruction: Generally, the lines of sight of two corresponding image points  $x_1 \leftrightarrow x_2$  do not exactly intersect [51].

### 7.3.8.3 Stereo reconstruction

If a camera is intrinsically calibrated, the line of sight for every image point is quantitatively known in terms of the camera coordinate system (cf. Sec. 3.3). If a pair of corresponding points are found in a pair of two intrinsically and extrinsically calibrated cameras, the intersection of the corresponding lines of sight yields the object point sought. Thus, the 3D coordinates of an object point corresponding to two image points can be calculated.

Generally, the two lines of sight do not exactly intersect because of noise and a limited resolution [51]. Therefore, the point  $\hat{x}_w$  in the three-dimensional space is used as an estimate for the object point  $x_w$  that is closest to the two lines of sight (Fig. 7.68). The homogeneous coordinates of this point are obtained by applying the least squares method to the system of equations

$$x'_1 \times P_1 \hat{x}'_w = 0, \quad (7.112)$$

$$x'_2 \times P_2 \hat{x}'_w = 0, \quad (7.113)$$

with  $x'_1 \leftrightarrow x'_2$  denoting the pair of corresponding image points in homogeneous coordinates and  $P_1, P_2$  denoting the projection matrices of the cameras.

A detailed mathematical formulation of reconstruction and calibration methods can be found in the textbooks [48, 67].

### 7.3.8.4 Multi-camera systems

By using more than two cameras, the search for correspondences as well as the reconstruction can be improved. Using several images reduces the ambiguities in the sought for assignments of the correspondence problem. Also the problems of occlusion are less severe than for only two cameras.

The idea of the fundamental matrix can be generalized to three cameras and, with certain limitations, also for systems with four and more cameras [48, 67]. This leads to the so-called trifocal tensor of size  $3 \times 3 \times 3$  for three cameras.

The precision of the reconstruction can be improved using **bundle adjustment** [110, Sec. 4.3]. Let  $M$  object points  $x_{w,j}, j = 1, \dots, M$  be observed by  $N$  cameras with projection matrices  $P_i, i = 1, \dots, N$ . Each point yields  $2N$  equations of the form (3.12), (3.13),



resulting in a total of  $2NM$  equations. As the coordinates of the object points represent  $3M$  unknowns, the system of equations is already overdetermined for  $N \geq 2$  cameras. The least squares method can be used to find a solution with minimum error [67, Sec. 18.1].

If the extrinsic camera parameters are unknown but enough point correspondences are available, they can be considered to be additional unknowns and can be estimated simultaneously. As each calibration method is affected by different errors and as the camera parameters can vary with time, it might be useful to also estimate the intrinsic parameters at the same time. In this case, a total of  $11N$  unknown camera parameters have to be estimated.

For bundle adjustment, a huge system of nonlinear equations has to be solved. For this case, special numerical methods are suitable, which exploit the system's sparse structure [110].

#### 7.3.8.5 Monocular stereo

For a static scene, it makes no difference if it is viewed by  $N$  cameras simultaneously or if a single camera is subsequently moved to the  $N$  positions. However, in the case of a moved camera, it is often necessary to estimate the extrinsic camera parameters at the same time, as the movement cannot be reproduced with a sufficient accuracy. This can be done similarly to what was described in the previous section [39]. For some applications, the movement of the camera is a side effect, for example, if it is mounted on a mobile robot. The stereo reconstruction based on such image sequences is also referred to by the term 'structure from motion'.

#### 7.3.9 Light-field cameras

A light-field camera or plenoptic camera is a special camera which is able to capture a section of the light field. The light field  $L(\mathbf{x}_w, \beta)$  introduced in Sec. 4.2 describes the radiance of all light rays coming from a point  $\mathbf{x}_w$  of the test object in the direction  $\beta$  under conditions of constant illumination [3,4]. To simplify matters, the light field's dependencies on the wavelength and the polarization state of the light are omitted in this introduction to the light-field camera. Furthermore, the test object is assumed to be opaque, and the medium surrounding the object is assumed to be optically transparent, so that there are no interactions, such as scatter, between the light field and the medium.

The light field  $L(\mathbf{x}_w, \beta)$  is a five-dimensional function of the position  $\mathbf{x}_w = (x_w, y_w, z_w)^T \in \mathbb{R}^3$  and the direction  $\beta = (\beta_1, \beta_2)$ . If  $L(\mathbf{x}_w, \beta)$  is known for all of the surface's points  $\mathbf{x}_w \in \text{SF}$ , then the light field  $L(\mathbf{u}, \beta)$ ,  $\mathbf{u} \in \mathbb{R}^3$  induced by the test object is uniquely defined for the surrounding space. The light field  $L(\mathbf{u}, \beta)$  describes the radiance of all light rays running through the point  $\mathbf{u}$  in the direction  $\beta$ , and thus denotes the distribution of directions of the radiance in every spatial point (Fig. 7.69).

Although the light field's argument  $(\mathbf{u}, \beta)$  is five-dimensional, a four-dimensional representation is sufficient. As long as no occlusions arise, the light field is intrinsically four-dimensional, as the radiance along a line is constant in that case and thus independent of the object distance (cf. Sec. 4.4.1). A line in space is unambiguously determined by four parameters, for example by its intersection  $(x_w, y_w)^T$  with the plane  $z_w = 0$ , together with the azimuthal and polar angles [104].

Hence, to a certain extent, the light field  $L(\mathbf{u}, \beta)$  contains all possible images of the test object that can be captured under the given constellation of test object and light source. A camera acquires a part of the light field in the form of a two-dimensional image. The image

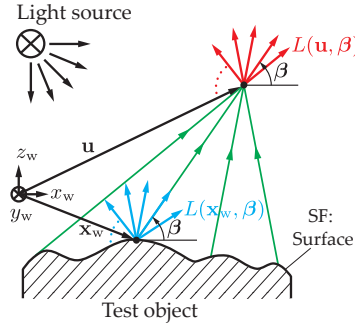


Figure 7.69. Light field of a test object.

of a camera with arbitrary extrinsic and intrinsic parameters is uniquely determined by the light field. Thus, the light field is also called the plenoptic function.<sup>3</sup>

As it is hardly practical to capture the whole light field, it is mainly used in a conceptual sense. If it was completely available, the images for all possible camera perspectives and camera parameters could be calculated. For hypothetically measuring the whole light field, pinhole cameras could be placed at every point in space, recording images from two opposed directions. In fact, because of the four-dimensional argument of the function  $L(u, \beta)$  and because of the assumptions made above, it would be sufficient to capture the light field on an infinitely large plane.

With a light field camera or a plenoptic camera it is possible to measure a section of the light field on a plane. It can be constructed from a main lens, a microlens array, and an image sensor, see Fig. 7.70(a). The main lens's focal length is assumed to be  $f$  and the aperture diameter to be  $D$ . The main lens achieves a sharp imaging of a plane of the object space onto the microlens array [120]. Each microlens sharply images the main lens plane to the image sensor. The microlens array consists of  $N' \times N'$  lenses arranged in an equidistant rectangular grid. To simplify matters, the number of microlenses is assumed to be quadratic, which is not necessary in general. The focal length of each microlens is assumed to be  $f'$  and the aperture diameter to be  $D'$ . The sensor chip is assumed to be a square as well and to have  $N \times N$  pixels.

At first, the optical imaging performed by the main lens is assumed to yield a sharp image of the object on the plane of the microlens array. In the case of a conventional camera, the camera chip would replace the microlens array and integrate the light rays coming from the object, and thus the information about the rays' directions would be lost. However, in a light-field camera, the light rays reach the image sensor behind the microlens array, which has a higher spatial resolution than the microlens array:  $N > N'$ .

The intensity of the light coming from the object is measured with respect to the direction. The pixel positions beneath a microlens correspond to the direction of the incident light. Therefore, a section of the light field can be captured.

<sup>3</sup>*Plenus* is the Latin word for 'complete.' The concept of the plenoptic function was already mentioned by Leonardo da Vinci [103]. He said that every illuminated body fills the surrounding space with a continuum of latent images. He used the term 'pyramid' for the bundle of rays coming from an object and running through a certain point in space.

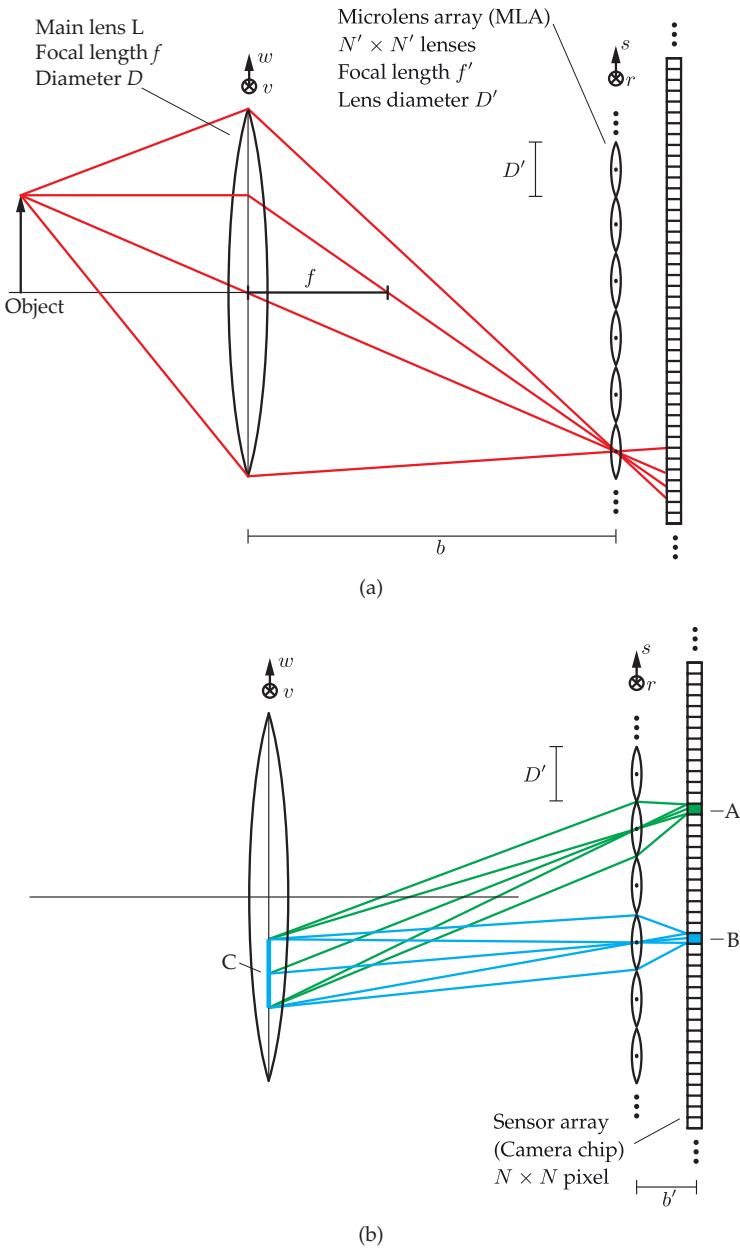
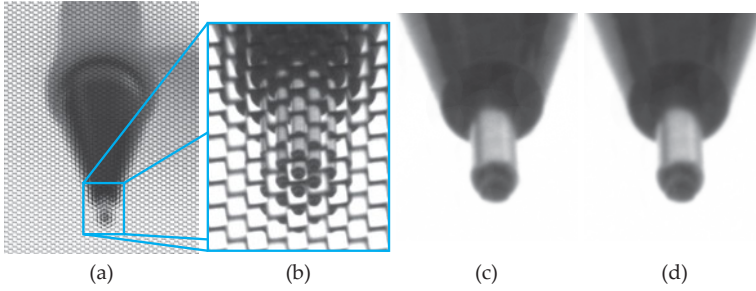


Figure 7.70. Setup of a light-field camera: (a) Optical imaging by the main lens; (b) Optical imaging by the microlens array.



**Figure 7.71.** Image of the top of a drop action pencil recorded with a light-field camera: (a) Raw data of the image sensor; (b) Section of the pencil's top, the regions of the single microlenses are clearly visible; (c), (d) Images synthesized from the raw data with horizontally displaced perspectives.

For an optimal setup, the images generated by the microlenses on the sensor chip must neither overlap nor have too big gaps between each other, which would give away some of the directional resolution [120]. This is fulfilled if

$$\frac{D}{b} = \frac{D'}{b'} . \tag{7.114}$$

In this case, an image that is imaged from the main lens to the sensor chip by a microlens covers approximately  $\eta := \left(\frac{N}{N'}\right)^2$  pixels. Thus, the direction of the incident light is captured (sampled) at  $\eta$  discrete values.

The  $N^2$  pixels of the image sensor can be divided into  $(N')^2$  fields, cf. Fig. 7.71(a). Each field corresponds to a microlens and captures the locally incident light intensity with respect to the direction, cf. Fig. 7.71(b).

For acquiring the direction, a reduction of the spatial resolution has to be accepted. A discrete image with  $(N')^2$  pixels is recorded, in which the light's direction is captured at each pixel in  $\eta$  steps.

In order to describe the light-field camera, an alternative set of parameters is used for the light field. Each ray of light is unambiguously described by its intersections  $(v, w)$  and  $(r, s)$  with two parallel planes. The principal plane of the main lens is chosen to be the  $(v, w)$ -plane and the  $(r, s)$ -plane is assumed to be the plane of the microlens array. So, the light field can be expressed as  $L(v, w, r, s)$  inside the section captured by the camera.

The pixel A on the image sensor in Fig. 7.70(b) is mapped to the main plane by the microlens in front of it. Only light going through the main lens's region denoted by C reaches pixel A. Hence, the pixel A is assigned a partial aperture C on the main lens. For rectangular pixels and rectangular microlenses, this describes a four-dimensional cuboid in the  $(v, w, r, s)$ -space which is integrated by the pixel A. In the system theoretical sense, this corresponds to a moving average over a four-dimensional interval with the size of this cuboid, and a subsequent sampling.

The other microlenses also image the partial aperture on a certain pixel of the sensor chip, for example on pixel B. All these pixels capture light coming from the object space through the partial aperture C. The result is an image of  $(N')^2$  pixels, imaged by the partial aperture C.

On the other hand, each of the  $\eta$  pixels illuminated by the same microlens as  $A$ , corresponds to another partial aperture of the main lens. Thus, the main lens is divided into  $\eta$  partial apertures which, in the ideal case, do not overlap.

Hence, the light-field camera simultaneously captures  $\eta$  images from different perspectives with  $(N')^2$  pixels per image. As the perspectives correspond to the partial apertures, they are located on the main lens. The resulting images can be analyzed using multiocular stereo methods, in order to reconstruct the 3D shape of the test object. Therefore, a light-field camera is also a 3D camera [4]. The maximum available stereo base is given by the diameter  $D$  of the main lens. Thus, the 3D reconstruction is well-conditioned, especially for closeup and macro images, which are typical for many visual inspection tasks.

Inside the captured section of the light field, not only can the perspective be changed, but also virtual cameras with arbitrary synthetic perspectives and aperture can be positioned and the images that they would capture can be calculated, cf. Fig. 7.71(c), (d).

Based on the captured section of the light field, the depth of field and the focused plane of synthesized images can be changed afterwards within a certain range, by calculating the images of virtual cameras. The subsequent focusing can be calculated by the addition of displaced partial apertures [119, 120].

The possibility of capturing images with increased depth of field is of particular importance for automated visual inspection. The relevant aperture for the images on the sensor chip is the diameter  $D'$  of a microlens, which is significantly smaller than the diameter of the main lens. As stopping down increases the depth of field, the captured light field has the potential of producing images with increased depth of field (cf. Sec. 3.4.4). In fact, it can be shown that the depth of field of a suitably synthesized image of a light-field camera is about  $\frac{N}{N'}$  times larger than for a conventional camera with an aperture stop of the same diameter  $D$  [120].

The captured section of the light field is limited by the main lens's aperture in the  $v,w$ -plane, and by the dimension of the microlens array in the  $r,s$ -plane. So a higher depth of field can be achieved using a light-field camera without stopping down and without losing light. This also leads to a significantly higher signal-to-noise ratio than conventional cameras have [120].

Meanwhile, the first light-field cameras are commercially available. They have the following technical data and operating characteristics:

- Prototype of Stanford University [120]:
  - Sensor chip with  $N \approx 4,000$  (16 megapixels), pixel distance  $\Delta x = 9 \mu\text{m}$ ,
  - microlens array with  $N' = 296$ ,  $D' = 125 \mu\text{m}$ , focal length  $f' = 500 \mu\text{m}$ , f-number  $O' = \frac{f'}{D'} = 4$ ,
  - effective resolution:  $292 \times 292$  in the  $r,s$ -plane (spatial resolution),  $\eta^2 \approx 14 \times 14$  in the  $v,w$ -plane (directional resolution),
- microlens array with  $N' = 1080$  [50],
- few microlenses, thus a high directional resolution,
- lens array with neighboring microlenses of different focal lengths,
- focusing of the microlenses on the sharply imaged plane of the main lens, so that each microlens generates a sharp miniature image on the image sensor [58].

### 7.3.10 Silhouette capturing

The bright field and dark field illumination setups covered in Sec. 7.2.3 can be used not only for capturing the reflectance but also for inspecting the silhouette of a test object. An object's silhouette is the projection of its 3D structure onto a plane. Inspecting the silhouette can detect differences in shape which influence the captured silhouette. Often, the inspection of the silhouette from only a few directions is sufficient for detecting the relevant defects of the component. A complete 3D reconstruction is not necessary for this kind of application.

Figure 7.72 shows the principle of silhouette capturing using a bright field setup. The camera is aimed straight at a planar light source. The test object is placed between the light source and the camera, generating shadows. In the camera image, the edges between the shadows and the light source's image correspond to the object's silhouette.

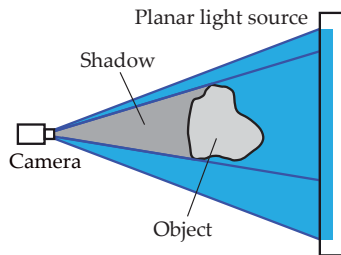


Figure 7.72. Silhouette capturing with bright field illumination.

**Example 7.9 (Brake disk inspection):** A complicated example of an application of bright field silhouette capturing is shown in Fig. 7.73: the automated visual inspection of ventilated brake disks [23]. The ventilation channels of the brake disk are arranged radially, see Fig. 7.73(b). All ventilation channels have to be checked for contaminants which might hinder the airflow. A cone-shaped mirror is used to radially illuminate the test object. A cylindrical retroreflector is placed inside the brake disk (see Sec. 7.3.10.3). The reflected light reaches the camera by traversing the same optical path and an additional semi-transparent mirror. In the resulting image, faultless ventilation channels form circularly arranged bright regions, see Fig. 7.73(c). For partially or completely blocked channels, the corresponding regions remain dark. The image produced can be considered as a binary image, and thus is easy to analyze. ■

Laser scanners (see Sec. 7.2.3.4) can also be operated in bright field mode to produce shadows for silhouette capturing (Fig. 7.74). A rotating mirror or polygonal wheel is used to direct the laser onto different positions on the test object in order to achieve a sequential sampling. The period of time during which the detector receives no signal is used to calculate the test object's diameter.

Dark-field methods can also be used for silhouette capturing. An exemplary application is the visual inspection of transparent objects like glass or plastic bottles [14]. The planar illumination is occluded with a mask which is slightly larger than the camera's field of view (Fig. 7.75). Because of the scattered light, the edges of the transparent object appear especially bright in the camera image while the background remains dark. This setup can also be used to highlight differences in reflectance and scratches.

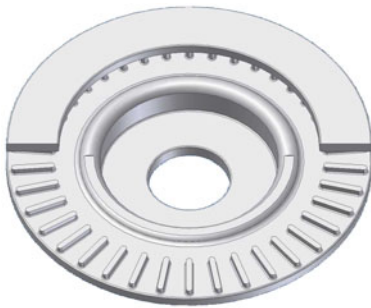
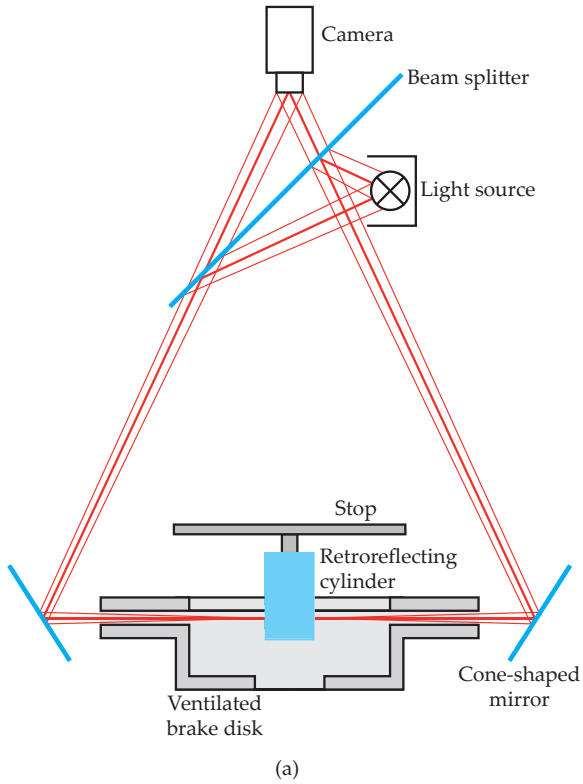


Figure 7.73. Automated visual inspection of a brake disk's ventilation channels: (a) Setup of the inspection system; (b) Sketch of a ventilated brake disk; (c) Resulting image (source: inspection GmbH).

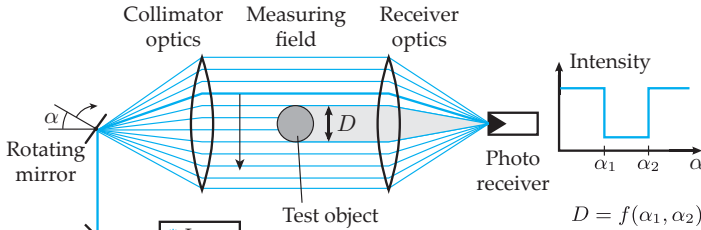


Figure 7.74. Using a telecentric laser scanner for silhouette capturing in accordance with the principle of shadow casting [163]).

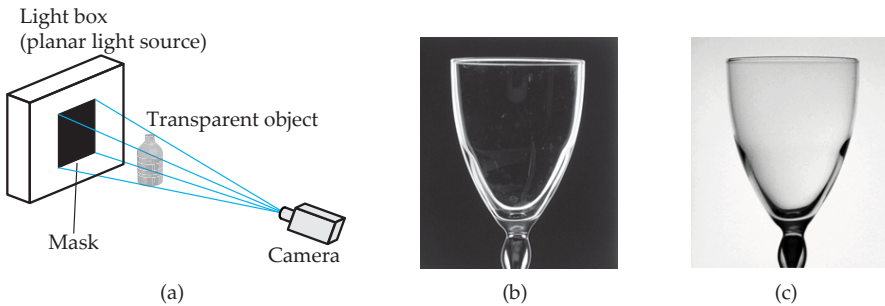


Figure 7.75. Dark-field illumination used for capturing the silhouette of transparent objects: (a) Principle [14]; (b) Dark-field image; (c) Bright-field image of the same object.

### ⊗ 7.3.10.1 Telecentric silhouette capturing

Figure 7.76(a) shows an image acquisition system with a telecentric lens used for silhouette capturing. A light box (left) realizes a planar bright-field illumination. For small objects, a telecentric illumination would also be possible.

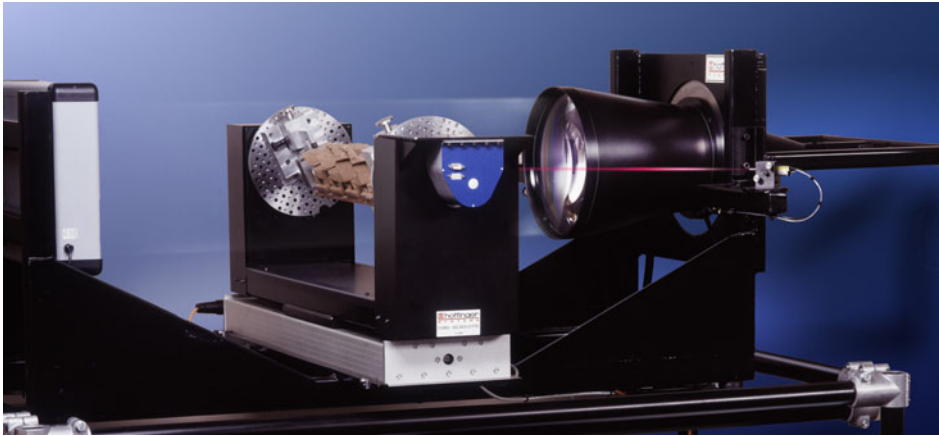
### ⊗ 7.3.10.2 Illumination for telecentric imaging

For optical measurement, the use of diffuse illumination in combination with telecentric lenses can lead to faulty measurement results: for example, a non-parallel illumination (marked red in Fig. 7.77) might lead to an object's diameter being systematically measured too small.

A possible solution to this problem is a telecentric illumination [109]. As can be seen in Fig. 7.78, the light source is positioned at the focal point of a second lens. Therefore, the optical path of illumination is also parallel to the optical axis of the telecentric lens and the object's diameter will be correctly measured. However, it is quite costly to precisely set up the two optical elements to have exactly parallel optical paths.

Another way to achieve parallel illumination is given by the setup shown in Fig. 7.79, where a semi-transparent mirror is used in combination with a **retroreflector**. Together with the lens, the light source and the semi-transparent mirror lead to a coaxial illumination that is parallel to the optical axis, as long as the length along the optical path from the light source to the lens exactly equals the focal length. As the light is reflected by the retroreflector, it reaches the lens parallel to the optical axis. The use of a retroreflector instead of a mirror is advantageous, as there is no need for an arrangement exactly parallel to the optical axis.

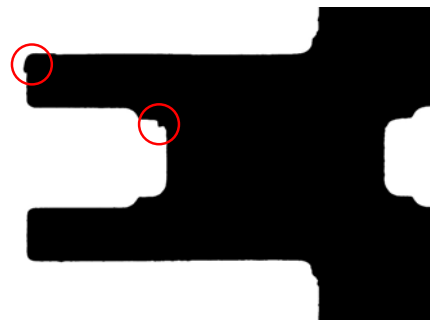




(a)



(b)



(c)

Figure 7.76. Silhouette inspection using bright-field illumination: (a) Image acquisition system with bright field illumination and telecentric lens; (b) Silhouette of a reference object (crank shaft); (c) Test object with defects (marked red) (source: inspectomat GmbH).

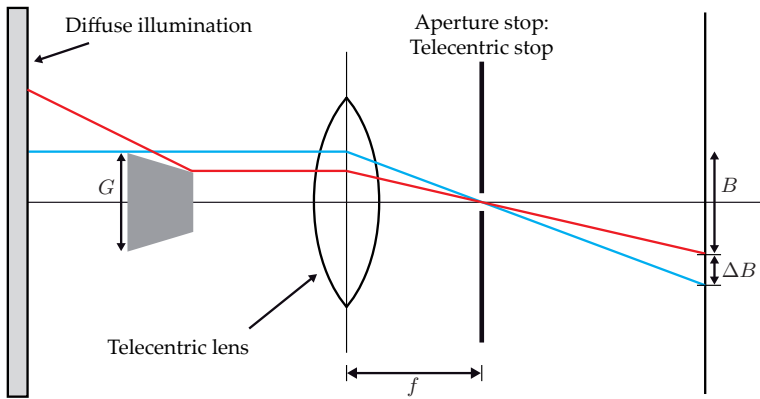


Figure 7.77. Telecentric imaging using diffuse illumination.

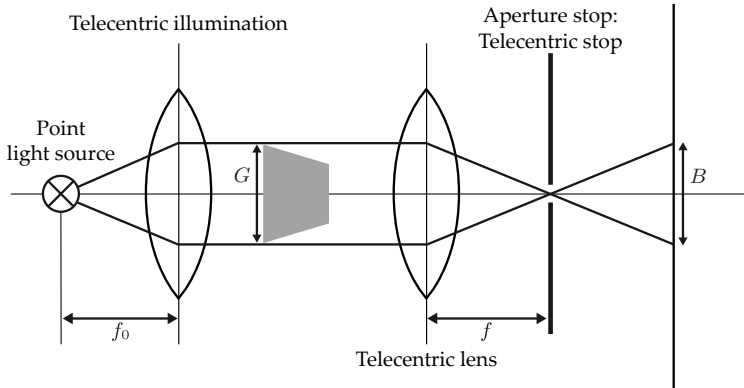


Figure 7.78. Telecentric illumination.

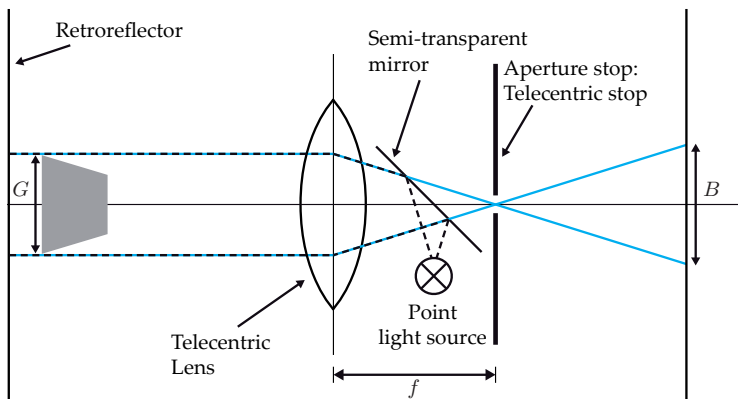


Figure 7.79. Telecentric illumination using a retroreflector.

### 7.3.10.3 Retroreflectors

A retroreflector mirrors an incoming ray of light so that it takes the optical path where it came from but in reverse direction [137]. In contrast to a plane mirror, a rotation of the retroreflector does not change the direction of reflection. For some applications of automated visual inspection, this insensitivity is advantageous, as an exact adjustment of the reflector becomes unnecessary. Retroreflectors are mainly known for their use in transportation, where they are used in vehicles, bicycles, reflector posts, and clothes. If a retroreflector is illuminated in darkness by a headlamp of a car, for example, the light is reflected back to the car and is highly visible to the driver.

Here, two possibilities for constructing retroreflectors are presented (Fig. 7.80). Small glass spheres embedded in a carrier material reflect the incident light on their backsides. A second possibility is given by rectangular tetrahedra with three specular sides and one open side. In both cases, there is a small displacement  $\Delta$  between the incoming and the reflected ray of light, which depends on the size of the individual retroreflecting elements.

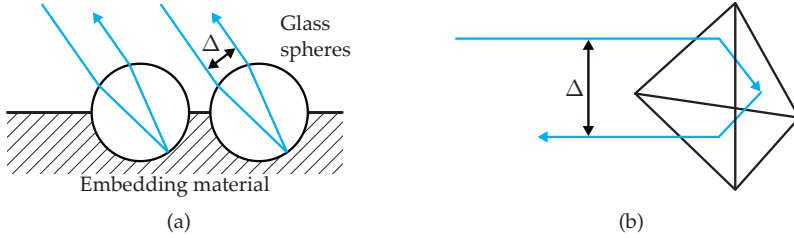


Figure 7.80. Structure of retroreflectors: (a) Glass spheres; (b) Triple mirrors: the three mirrors are arranged to be pairwise perpendicular.

7.3.11 Shape from shading

The radiance  $L$  emitted by the surface partly depends on the surface normal and the direction of illumination (cf. Sec. 4.3). The method **shape from shading** tries to exploit this dependency in order to calculate the surface normal for known illumination parameters and to reconstruct the object’s 3D shape by integration.

Often, the Lambertian model of reflectance (4.29) is assumed for the test object. Then, the radiance  $L_e$  observed by a camera is given by

$$L_e(\theta_e, \varphi_e) = BRDF(\mathbf{x}, \theta_i, \varphi_i, \theta_e, \varphi_e) E_i(\theta_i, \varphi_i) \tag{7.115}$$

$$= \frac{R(\mathbf{x})}{\pi} \frac{d\Phi_i}{dA}(\theta_i, \varphi_i) \tag{7.116}$$

$$= \max \left\{ 0, \frac{R(\mathbf{x})}{\pi} \Phi_i \mathbf{i}^T \mathbf{n}(\mathbf{x}) \right\}. \tag{7.117}$$

The collimated radiant flux emitted by the light source is denoted by  $\Phi_i$ ,  $\mathbf{i}$  represents the illumination direction, and  $\mathbf{n}(\mathbf{x})$  denotes the surface normal for position  $\mathbf{x}$ , with  $\mathbf{i}$  and  $\mathbf{n}(\mathbf{x})$  being unit vectors. The inner product in Eq. (7.117) describes the projection of the parallel light coming from direction  $\mathbf{i}$  onto the surface. The maximization takes into account that the light source might be located behind the surface: in this case, the surface is not illuminated and there is a shadowing effect. If the illumination conditions are assumed to be known, two mathematical problems have to be solved in order to reconstruct the surface relief:

1. Determination of the normal vector by solving (7.117) for an unknown reflectance  $c(\mathbf{x})$ .
2. Reconstruction of the surface relief from the normal field  $\mathbf{n}(\mathbf{x})$ .

The normal field can be integrated as with deflectometry (see Sec. 7.3.5). As it is an ill-posed problem, a stable numerical solution is rather hard to obtain. Therefore, methods related to the calculus of variations can be used, for example [81, 169].

Another way to regularize the shading problem is to use several images with varying illuminations (Fig. 7.81). This method is known by the term **photometric stereo**. The use of specifically selected illumination directions allows a closed form mathematical solution [87]. For general directions of illumination, it is rather easy to solve Eq. (7.117) for the normal field [76]. Each image yields an equation

$$g_k(\mathbf{x}) = \frac{R(\mathbf{x})}{\pi} \Phi_i \mathbf{i}_k^T \mathbf{n}(\mathbf{x}) \quad k = 1, \dots, n, \tag{7.118}$$

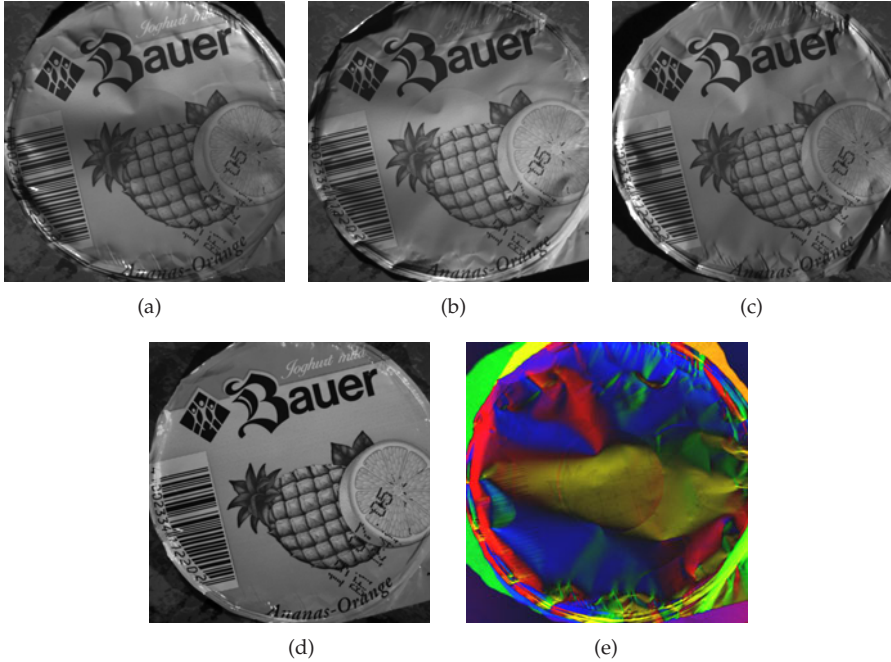


**Figure 7.81.** Example images of shape from shading: (a)–(c) Images of a packaging foil with different illumination directions; (d) Calculated reflectance  $R(\mathbf{x})$ ; (e) Normal field  $\mathbf{n}(\mathbf{x})$  in pseudo colors (cf. Sec. 9.1.3).

with  $\mathbf{i}_k$  denoting the illumination direction of the  $k$ th image. Here, the assignment between the radiance  $L_e$  and the measured image values  $g_k(\mathbf{x})$ , to which  $L_e$  is proportional, is determined (cf. Sec. 4.4.1), and a shadow-free illumination is assumed. The scalar equations can be arranged in a system of linear equations

$$\mathbf{g}(\mathbf{x}) = \frac{R(\mathbf{x})}{\pi} \Phi_i \mathbf{B}^T \mathbf{n}(\mathbf{x}) \quad (7.119)$$

with  $\mathbf{g} := (g_1, \dots, g_n)^T$  and  $\mathbf{B} := (\mathbf{i}_1, \dots, \mathbf{i}_n)$ . For  $n = 3$ ,  $\mathbf{B}$  is invertible if and only if the illumination directions  $\mathbf{i}_k$  are not coplanar. In this case, a unique solution exists. For  $n > 3$ , the pseudoinverse can be used to obtain a least squares solution of the system:

$$\mathbf{v}(\mathbf{x}) := \mathbf{n}(\mathbf{x}) R(\mathbf{x}) = \pi \Phi_i^{-1} (\mathbf{B}\mathbf{B}^T)^{-1} \mathbf{B} \mathbf{g}(\mathbf{x}) \quad (7.120)$$

By means of this equation, the reflectance of the surface and the surface normal at point  $\mathbf{x}$  can be calculated:

$$R(\mathbf{x}) = \|\mathbf{v}(\mathbf{x})\|, \quad (7.121)$$

$$\mathbf{n}(\mathbf{x}) = \frac{\mathbf{v}(\mathbf{x})}{R(\mathbf{x})}. \quad (7.122)$$

A color coded illumination sequence [87,107] can be used to detect the reflectance in different spectral ranges. In the case of a known, wavelength-independent reflectance, the surface can be simultaneously illuminated from different directions in different spectral ranges, so that

a single image acquired with a color camera is sufficient for the reconstruction, and even moving objects can be captured.

### 7.3.12 Autofocus sensors

In an **autofocus sensor**, the light of a laser diode is shed onto the investigated object by a collimator and another, movable, lens [99, 131]. The reflected light reaches the detector by going through a beam splitter (see Fig. 7.82). The lens is now moved to a position that minimizes the blur disk on the sensor. For a cylindrical lens, the required direction in which to move can be obtained by means of the blur disk's shape. Depending on the sign of the difference of intensities,  $(a + c) - (b + d)$ , on the 4-quadrant detector in Fig. 7.83, the lens is moved towards a focused imaging. The distance to the test object can be calculated from the position of the correctly focused lens.

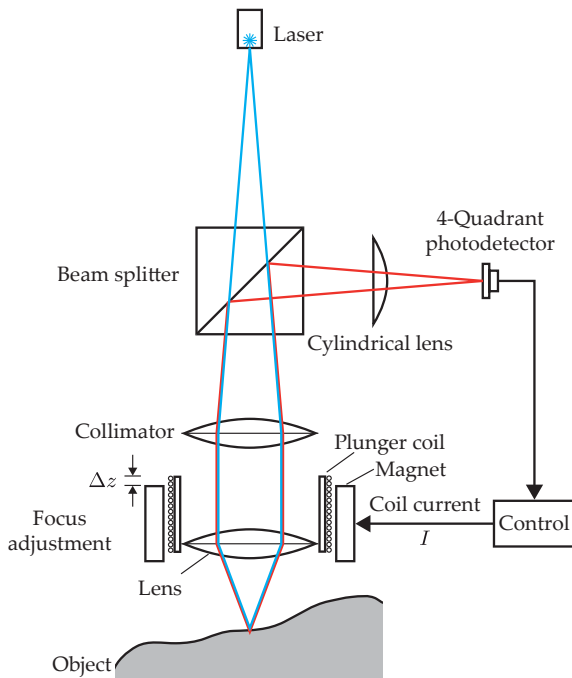
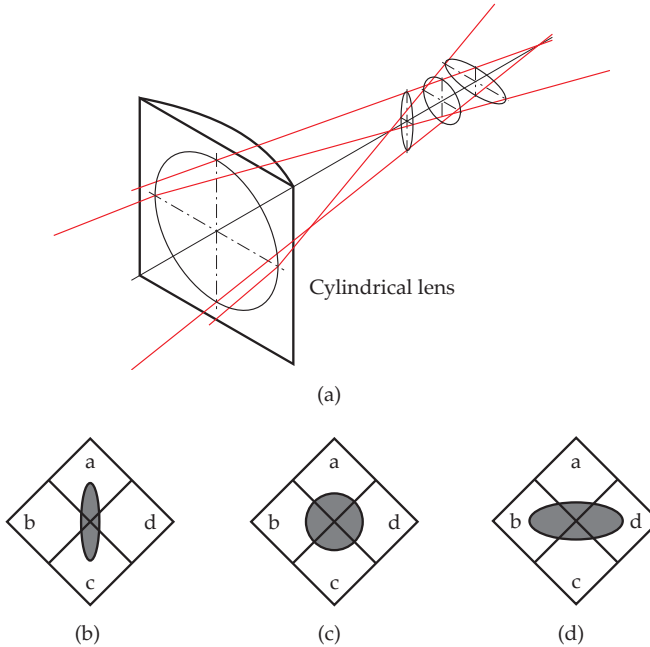


Figure 7.82. Autofocus sensor: Optical path and electromechanic focus correction.

A plunger coil system can be used to vertically shift the lens, like moving the membrane of a speaker. The lens is attached to a linear spring with a force  $F$  which is proportional to the elongation in  $z$ -direction,  $F \propto \Delta z$ . For a magnetic field that is homogeneous in the  $z$ -direction, the current inside the coil is proportional to the elongation:  $I \propto F \propto \Delta z$ . Hence, this current  $I$  is a signal which can be used to calculate the position of the lens and therefore also of the object.

Due to its wide use in CD and DVD players, autofocus sensors represent a fully developed and inexpensive technique. However, a well-reflecting, non-scattering, and opaque



**Figure 7.83.** Principle of astigmatic focus detection using a cylindrical lens and a 4-quadrant photo detector. (a) Distortion of the ray bundle in the case of a cylindrical lens; (b) Image on a 4-quadrant detector caused by an object distance which is too low; (c) Focused imaging; (d) Distance too large.

surface is necessary. As autofocus sensors are point sensors, an areal inspection is relatively time consuming.

The depth of field that can be achieved is about 10 to 25 nm. The measurement range is approximately 1 mm. The lateral resolution depends on the size of the light spot on the test object's surface, and is about 1 to 10  $\mu\text{m}$  [28, 99]. The measurement frequency is limited by the dynamic properties of the electromechanic drive system as well as by the characteristics of the investigated surface relief. It can reach up to 10 kHz [99].

### ► 7.3.13 Confocal microscopy

Example 3.3 showed that the depth of field of microscopes is very small. This effect can be used for 3D reconstruction: only those structures are visible in the image that are very close to the focused object plane. Other structures are nearly invisible, as they appear intensely blurred. The distance between the test object and the lens is systematically varied, and an image series with different object positions is acquired [142]. In this **focus series**, a maximum of a suitable local image feature is determined for each pixel position. For this feature, contrast measures can be used, which can be realized by a high-pass filter [133]. As the imaging conditions of the single images are known, the 3D shape of the object can be reconstructed.

In addition to focused observation, focused illumination is used for **confocal microscopy** [114]. A light source is imaged to the test object via a beam splitter. On the reverse optical path, the scattered light reaches the sensor (see Fig. 7.84). A pinhole allows only focused light

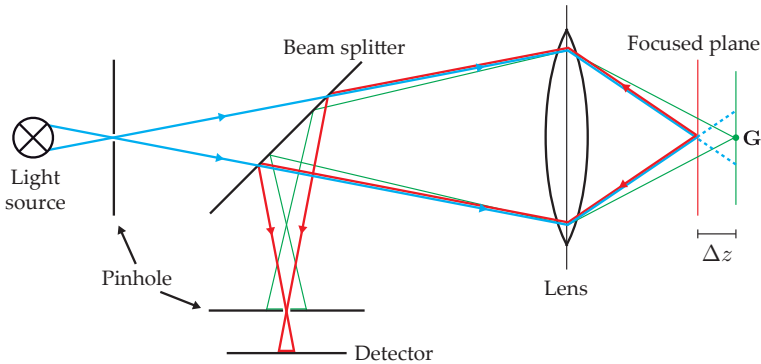


Figure 7.84. Optical path in the case of confocal microscopy. The illumination rays are colored in blue, the optical path of the optical imaging is drawn in red and green. The defocused light bundle, which is colored in green, can hardly pass the diaphragm of the detector.

to reach the detector. In the case of refraction limited optics, the pinhole is manufactured to have the size of an Airy disk (cf. Sec. 2.2.6).

Since the illumination and the image acquisition optics both are focused on a plane, an even higher depth resolution in the nanometer range is possible [170]. The irradiance on the object decreases proportionally to the square of the difference in depths,  $\Delta z$ , from the focused plane, as the illuminated area grows quadratically. Similarly, the irradiance emitted by the object decreases quadratically with respect to  $\Delta z$ . Due to the pinhole, only the intensity corresponding to a constant area of the diaphragm finally hits the detector. In all, the intensity emitted by an object point  $G$  and which is measured by the detector is approximately proportional to  $(\Delta z)^{-4}$ .

Often, a laser is used as a light source and a photodiode or a photomultiplier serves as a sensor [87]. The maximum intensity is observed if the object is located in the plane that is focused in the object space. This maximum is found by moving the object along the optical axis of the microscope. In contrast to the focus series method mentioned above, in this case only a single object point can be measured with a series of images acquired in the  $z$ -direction. In order to obtain the whole 3D structure, an additional two-dimensional scan in the lateral direction has to be performed. For example, the confocal laser scanning microscopy uses movable mirrors to sequentially scan the object [136].

Alternatively, suitable optical elements can be used for simultaneously measuring several points. Both methods allow an areal depth measurement by recording an image series, and the amount of time consumed is on the order of seconds.

A fast two-dimensional lateral scanning in the  $x,y$ -plane can be achieved by means of a multi-pinhole diaphragm and a two-dimensional sensor array, see Fig. 7.85(a). This multi-pinhole diaphragm can be realized as a so-called Nipkow disk, for example. For a Nipkow disk, the pinholes are arranged spirally. The disk rotates at a fast speed and half of it is placed in the optical path, see Fig. 7.85(b). Due to the simultaneous use of multiple pinholes and the fast switching between the pinhole arrangements caused by the rotation, a fast lateral scan can be attained.

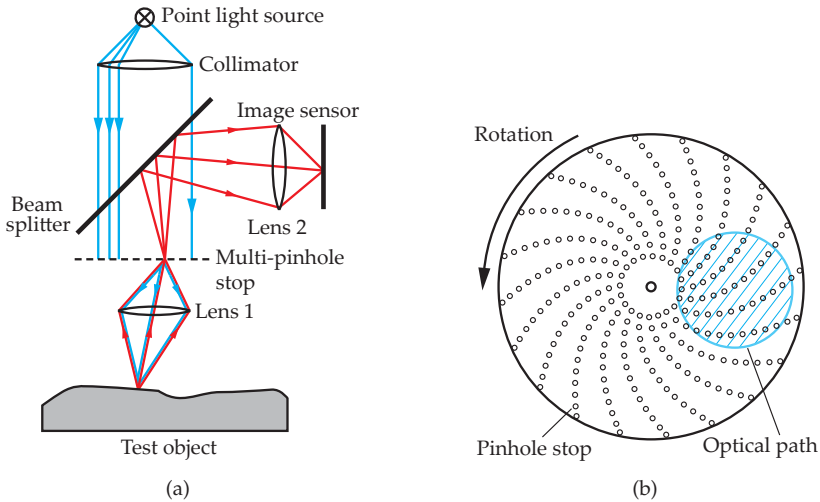


Figure 7.85. Confocal microscope with multi-pinhole diaphragm: (a) Optical path inside the microscope; (b) Nipkow disk.

An alternative for the multi-pinhole diaphragm is a rotating microlens array [164]. The microlenses replace the lenses one and two in the optical path. Compared to the multi-pinhole stop, the microlens array offers a much better light yield. There are different possibilities for vertical scanning:

- Vertically moving the lens;
- Vertically moving the test object;
- Vertical oscillation of the object-sided focal point by oscillating optical elements in the optical path [143];
- Chromatic parallelization.

This last possibility will now be briefly described. The height  $z$  is mapped to the light's wavelength, so that the mechanical vertical scan can be replaced by a spectral analysis. Thus, a fast simultaneous capturing of an interval in the  $z$ -direction is possible. A lens with extensive chromatic aberration is used, so that the illumination is focused in different depths depending on the wavelength (see Sec. 3.4.8.2). A diffraction grating is placed in front of the image sensor, resulting in a spectral decomposition of the incident light (Fig. 7.86). Now, the spatial maximum of intensities on the sensor corresponds to the wavelength of optimal focus and thus to the object's distance  $z$ .

Independent of its actual realization, the vertical scan yields a so-called confocal curve for each point. The location of the maximum intensity corresponds to the  $z$ -position of the surface point. The half width of the confocal curve mainly depends on the lens' numerical aperture. The maximum gets narrower for increasing numerical aperture. The minimum width which can be reached is on the order of the wavelength of the light used. By matching the curve for the discrete measurements using a regression analysis, the height  $z$  can be determined with a resolution in the nm-range [170].

The main application of confocal microscopy is capturing the profile of technical surfaces and the 3D microscopy of partially transparent objects, e.g., in biology or medicine.



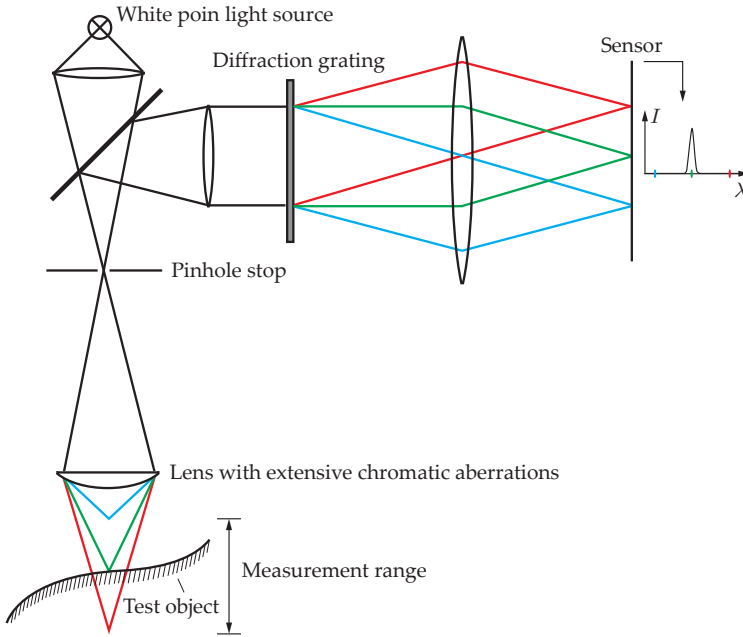


Figure 7.86. Chromatic parallelization of the vertical scan of a confocal microscope.

Besides the 3D structure, reflectance information can also be retrieved from the image series. By means of **image fusion**, an image can be calculated showing all object parts in focus [133]. In many cases, such an image cannot be realized by means of a single-shot image.

#### 7.3.14 Confocal chromatic triangulation

A confocal chromatic triangulation (CCT) sensor [159, 160] combines the principle of a confocal chromatic microscope with the principle of triangulation. With respect to the measurement plane, the optical path of the illumination and the optical path of the observation are tilted by an angle of  $\theta$ . Such optics are also called a confocal  $\theta$ -microscope [153] or dual-axes confocal microscopy [172].

The CCT sensor is a line-scan sensor that captures the height  $z(x, y)$  of an object's surface in a one-dimensional scanning process. In order to enable directly adjacent measurements, the confocal approach employs a slit in the  $y$ -direction as its aperture. The tilt of the optical path of the illumination and of the optical path of the observation improves the vertical resolving power and is especially beneficial for small numerical apertures [149]. Figure 7.87 shows the principle of the setup of a CCT sensor.

In confocal chromatic microscopy, the height  $z$  is encoded in the wavelength  $\lambda$ , which is spectroscopically measured so that  $z$  can be estimated. In order to speed up the method, a CCT sensor uses line cameras with  $Q$  channels instead of a spectroscopic estimation of the wavelength. Each of the channels is equipped with specially optimized interference filters

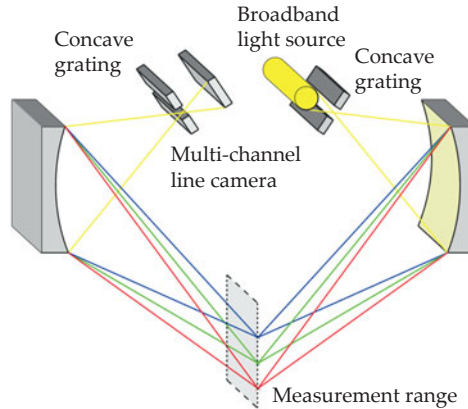


Figure 7.87. Setup principle of a CCT sensor.

[161], so that the  $Q$  observed intensity values allow a fast and sufficiently accurate estimation of the wavelength.

In principle, this method allows the construction of very fast sensors. By employing a line camera with  $Q$  channels, only a small amount of data has to be acquired, allowing a high line rate and thus a high scanning speed.

### ► 7.3.15 Time-of-flight sensors

A further principle of 3D measurement is based on the light's time of flight. If it takes time  $t$  for the light to reach the object and to get back to sensor, the object distance  $d$  is given by

$$d = \frac{1}{2} c t \quad (7.123)$$

with  $c$  denoting the velocity of light. Due to the high velocity of light, a highly resolved time measurement is needed in order to achieve the desired precision. A point sensor using the time of flight principle usually uses a pulsed laser as a light source. The time measurement has to be synchronized with the clock of the laser. Alternatively, code sequences can be modulated onto the light source, so that the time of flight can be obtained by searching for the maximum of the cross correlation of the sent and the received signal [111].

A 2D section of the object space can be measured using a single scan. Such a sensor is called a **lidar sensor**. This term refers to 'light detection and ranging', and has been chosen analogously to 'radar' (radiowave detection and ranging). Usually, the scan is performed with a rotating mirror. The result of a measurement is the distance of the object points from the sensor, given as a function of the angle in the scanning plane. Typical operating characteristics show a field of view of  $90^\circ$  with an angular resolution of  $0.5^\circ$ , a maximum range of 80 m, and a depth resolution of 1 cm [151]. Dynamic scenes can cause a distortion of the measured object geometry, as the object points are not measured simultaneously. Lidar sensors are often used in robotics.

In order to obtain information about the whole three-dimensional space, either an additional scan or a rotational movement can be performed, or several laser scanners can be aligned above each other, resulting in multiple rows in the depth image.

In automated visual inspection, time of flight sensors can only be used for macroscopic inspection scenarios with structures having sizes of centimeters or larger, because of the sensor's low resolution.

### ➤ 7.3.16 Phase-based methods

As an alternative to time of flight measurements, the light's phase shift can be analyzed. An important kind of measurement based on this principle is called interferometry.

#### ➤ 7.3.16.1 Interferometry

The goal of interferometry is the exact measurement of the surface relief of a specular or diffusely reflecting, smooth surface with a measurement uncertainty in the submicrometer range. It is only sensible to demand such an accuracy if the surface's roughness is of lower or equal dimensions.

The measurement principle is based on the optical interference (see Sec. 2.2.5) of the optical path of observation with a reference ray. Coherent, monochromatic light is split into a 'reference wave' and a 'measurement wave.' The reference wave travels over a reference path of known length, and the measurement wave travels along a path which includes the test object. The optical difference between the two paths is called the optical path difference, and produces a phase shift between the two waves.

If now both waves are superposed, an interference pattern arises and its intensity is measured. The interference pattern depends on the optical path difference and therefore on the lengths of the two paths.

From the observation of one or more interference patterns, information about the test object, e.g., about its surface relief, can be computationally extracted.

As the coherent light waves are periodic, the interference effects are also periodic with respect to the optical path difference. Thus, the reconstruction of the surface based on the interference pattern is an ill-posed inverse problem, which can generally only be uniquely solved by using regularizations (see Appendix A.2). A possible regularization approach can be given, e.g., by the previous knowledge that the variations of the surface relief are limited. Another regularization method is based on additional measurements with varying wavelengths. Both approaches will now be described.

Smooth surfaces with a roughness which is small compared to the wavelength  $\lambda$  result in macroscopic interference patterns, which are characterized by interference stripes. This effect is used for classic interferometry.

However, if the wavelength is small compared to the variations of the surface profile of the test object, the observed interference patterns will be dominated by speckle. In this case, speckle interferometry can be used, which is briefly described in Sec. 7.3.16.2.

A laser with wavelength  $\lambda$  can be used as a monochromatic light source for an interferometer. The laser's coherence length should be larger than the dimensions of interest [135]. The laser light is split by a beam splitter (Fig. 7.88). The reference beam is mirrored by a planar first surface mirror in order to reach the intensity detector. The measurement beam is reflected by the test object, causing the length of the optical path to vary according to the geometry of the object. The length of the measurement path between the beam splitter and the test object is denoted by  $z$ , the length of the reference path between the beam splitter and

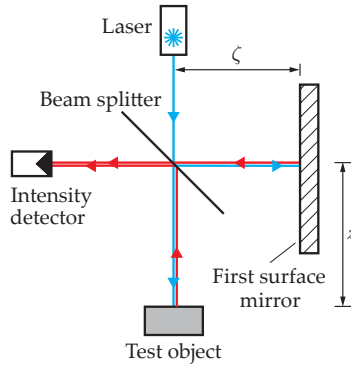


Figure 7.88. Principle of interferometry.

the first surface mirror is denoted by  $\zeta$ . As these paths are traveled by the incident and by the reflected light, their optical lengths are twice as long:  $2z, 2\zeta$ .

The detector measures the interference between the light from the measurement path and that which has travelled the reference path, cf. Fig. 7.98 on page 320. The reference mirror and the test object need to have similar reflectances in order to yield clearly distinctive interference stripes. In accordance with (2.122), the measured intensity  $I(z, \zeta)$  is maximal if the optical path difference is  $2z - 2\zeta = k\lambda$  for  $k \in \mathbb{Z}$ . This is the case for constructive interference. The intensity is minimal for destructive interference, i.e., if the optical path difference is  $(k + \frac{1}{2})\lambda$ . The intensity is periodic in  $\frac{\lambda}{2}$  with respect to  $z$  and  $\zeta$ :

$$I(z, \zeta) = I(z + k\frac{\lambda}{2}, \zeta) = I(z, \zeta + l\frac{\lambda}{2}), \quad k, l \in \mathbb{Z}. \tag{7.124}$$

So only in the range  $z \in [z_0, z_0 + \frac{\lambda}{4}]$ , can the object distance  $z$ , which is sought, be obtained without any ambiguities (Fig. 7.89).

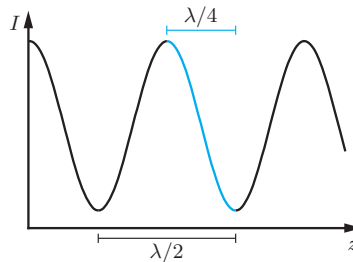


Figure 7.89. Unambiguous range for distance measurement based on interferometry.

The range of distances which can be measured without ambiguities can be increased by means of a long-wave light source. However, this approach is technically and economically limited, so that only wavelengths up to the infrared range with wavelengths  $\lambda > 10 \mu\text{m}$  are possible.

The use of several different wavelengths  $\lambda_1, \lambda_2, \dots$  allows performing interferometry with synthetic wavelengths  $\Lambda_i$ , which can be significantly longer than the physical wave-

lengths  $\lambda_1, \lambda_2, \dots$  [168]. Two wavelengths  $\lambda_1 > \lambda_2$  lead to a synthetic wavelength

$$\Lambda = \frac{\lambda_1 \lambda_2}{\lambda_1 - \lambda_2}. \quad (7.125)$$

The resulting wavelength is longer than either of the two original wavelengths if

$$0 < \lambda_2 < \lambda_1 < 2\lambda_2 \quad \Leftrightarrow \quad \Lambda > \max\{\lambda_1, \lambda_2\} = \lambda_1. \quad (7.126)$$

For  $\lambda_1 \in (\lambda_2, 2\lambda_2]$  it holds  $\Lambda \in [\lambda_1, \infty)$ .

The synthetic wavelength  $\Lambda$  increases the range of unambiguous distance measurement to  $\frac{\Lambda}{4}$ . So in principle, this range can be arbitrarily extended. Interferometry with multiple wavelengths can be performed using time division multiplexing, by sequentially using  $\lambda_1$  and  $\lambda_2$  and computationally analyzing the two interference images. Alternatively, an optically parallelized measurement is also possible, as some of the computations can be done optically and others electronically [168].

For capturing 3D images using interferometry, the surface's roughness has to be small compared to the wavelength: the variations in distance inside the measurement spot that corresponds to the image of a camera pixel on the test object's surface have to be small compared to the wavelength. This applies to the physical wavelength  $\lambda$  for single wavelength interferometry, as well as to the synthetic wavelength  $\Lambda$  for interferometry using several wavelengths. So in the case of interferometry, the measurement uncertainty is in principle limited only by the surface's roughness [168].

For simultaneously capturing a surface relief  $z(\mathbf{x})$  using interferometry, the Twyman-Green interferometer can be used, for example [24, 135]. Here, the test object's surface relief is simultaneously compared to a reference plane  $\zeta(\mathbf{x})$  for each line of sight of the camera. For the simplest case, a planar mirror arranged perpendicularly to the optical axis is used as the reference plane, so that  $\zeta(\mathbf{x}) = \zeta = \text{const.}$  (Fig. 7.90). The reference and measurement beams interfere in the image plane, producing an interference image  $I(z(\mathbf{x}), \zeta, \mathbf{x})$ .

In Fig. 7.90, a pinhole diaphragm is placed in the focal plane of the lens L1. The Fourier transform of the incident laser beam appears in this plane (cf. Sec. 2.2.6). In the focal plane of L1, the pinhole diaphragm acts like a low-pass filter: low spatial frequencies are allowed to pass, whereas high spatial frequencies are blocked. Thus, the laser beam is homogenized with respect to its cross section.

Typical interference images showing characteristic interference stripes for different surface defects are represented in Fig. 7.99 on page 320. As the distances of the interference stripes caused by the extrema of  $I(z(\mathbf{x}), \zeta, \mathbf{x})$  correspond to an optical path difference of only half of a wavelength, interferometric methods are very sensitive.

For the reconstruction of a relief  $z(\mathbf{x})$  with a height difference of  $|\max_{\mathbf{x}}\{z(\mathbf{x})\} - \min_{\mathbf{x}}\{z(\mathbf{x})\}| > \frac{\lambda}{4}$ , methods for phase unwrapping are necessary (cf. Sec. 7.3.4.1). By assuming a certain smoothness of  $z(\mathbf{x})$ , a continuous relief  $\hat{z}(\mathbf{x})$  can be reconstructed.

Moving the reference surface in parallel results in an image series  $I(z(\mathbf{x}), \zeta_t, \mathbf{x})$ , which can be used to estimate the phase.

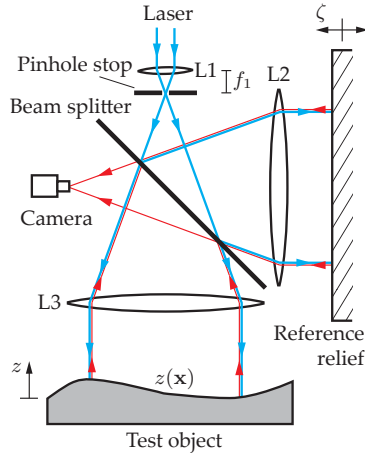


Figure 7.90. Setup of a Twyman–Green interferometer.

In accordance with (2.120), and putting  $r_1 = 2\zeta$ ,  $r_2 = 2z$  and  $\delta_1 = \delta_2 = 0$ , we obtain

$$I = I_1 + I_2 + 2\sqrt{I_1 I_2} \cos \varphi, \quad (7.127)$$

$$\varphi = \frac{4\pi}{\lambda} (z - \zeta), \quad \varphi = \varphi(\mathbf{x}) = \varphi(z(\mathbf{x}) - \zeta(\mathbf{x})). \quad (7.128)$$

As  $\varphi$  is a function of  $z$  and  $\zeta$ , it is indirectly a function of the position  $\mathbf{x}$ . As, in general,  $I_1$  and  $I_2$  are also functions of the position  $\mathbf{x}$ ,

$$I(z(\mathbf{x}), \zeta(\mathbf{x}), \mathbf{x}) = a(\mathbf{x}) + b(\mathbf{x}) \cos \varphi(\mathbf{x}). \quad (7.129)$$

To simplify matters, this will now be written as

$$I = a + b \cos \varphi. \quad (7.130)$$

By deliberately varying the reference path's length, specific phase shifts  $\psi_q$  can be realized:

$$I_q = a + b \cos(\varphi + \psi_q), \quad \psi_q := q \frac{2\pi}{Q}, \quad Q \in \mathbb{N}, \quad q = 0, \dots, Q-1. \quad (7.131)$$

For  $Q \geq 3$ , this yields a system of nonlinear equations with a unique solution, of which the phase  $\varphi$  and also the quantity sought,  $z$ , can be calculated [36, 95, 101, 124, 156]. The function  $I_q$  is periodic with respect to  $q$  and contains only harmonic oscillations, except for the direct component. If the discrete Fourier transform is calculated for  $I_q$  (see Chap. 8), the argument of that complex number results in the solution

$$\varphi_w = -\arctan \frac{\sum_{q=0}^{Q-1} I_q \sin \psi_q}{\sum_{q=0}^{Q-1} I_q \cos \psi_q}, \quad Q \geq 3. \quad (7.132)$$

As the tangent function has multiple branches, this equation is only valid for the main branch and takes values in the interval  $(-\frac{\pi}{2}, \frac{\pi}{2})$ . By considering the cases of positive and negative signs of the numerator and denominator of the argument of the arctangent function, the two branches adjacent to the main branch can be used in order to extend the unam-

biguous range to  $(-\pi, \pi)$ . With respect to  $z$ , this corresponds to an unambiguous range of length  $\frac{\lambda}{2}$ .

**Example 7.10 (Phase-shifting methods):** Choosing  $Q = 4$  leads to the simple formula

$$\varphi_w = -\arctan \frac{I_1 - I_3}{I_0 - I_2}. \quad (7.133)$$

Because of its high robustness compared to the case of the minimal  $Q = 3$ , this method is frequently used. ■

Due to the ambiguities of the arctangent function, the calculated phase  $\varphi_w$  differs from the actual phase  $\varphi$ , as all phase values are mapped to the interval  $(-\pi, \pi)$ : they are said to be ‘wrapped’ by this interval, which is why the subscript ‘w’ has been chosen. Equality holds only modulo  $2\pi$ :

$$\varphi_w(\mathbf{x}) = \frac{4\pi}{\lambda} (z(\mathbf{x}) - \zeta(\mathbf{x})) \pmod{2\pi}. \quad (7.134)$$

This can be rewritten as

$$\varphi_w(\mathbf{x}) = \varphi(\mathbf{x}) + 2\pi n(\mathbf{x}) \quad \text{with } n(\mathbf{x}) \in \mathbb{Z}. \quad (7.135)$$

For interference stripes,  $n(\mathbf{x})$  is also called the order of interference [124]. For  $z(\mathbf{x})$ , the unambiguous range is  $(\zeta(\mathbf{x}) - \frac{\lambda}{4}, \zeta(\mathbf{x}) + \frac{\lambda}{4})$ .

By assuming  $z(\mathbf{x})$  and hence also  $\varphi(\mathbf{x})$  to be continuous and smooth,  $n(\mathbf{x})$  can be obtained so that the reconstructed phase  $\hat{\varphi}(\mathbf{x})$  no longer shows  $2\pi$ -discontinuities. This approach is called **phase unwrapping** [59]. Then, estimations of the depth values  $z(\mathbf{x})$  can be calculated from the reconstructed phase:

$$\hat{\varphi}(\mathbf{x}) = \varphi_w(\mathbf{x}) - 2\pi \hat{n}(\mathbf{x}), \quad (7.136)$$

$$\hat{z}(\mathbf{x}) = \frac{\lambda}{4\pi} \hat{\varphi}(\mathbf{x}) + \zeta(\mathbf{x}). \quad (7.137)$$

**White light interferometry** uses broadband light with a short coherence length in contrast to the previously mentioned methods [15]. The constructive interference shows an absolute maximum for  $z = \zeta$ . The higher-order maxima are much smaller for short coherent white light, as for some spectral parts of the white light there is constructive interference and simultaneously there is destructive interference for other spectral parts. The result is a spatially varying spectral composition of the observed interference image, depending on the difference  $z - \zeta$ , i.e., the acquired image represents a color encoding of the relief [1].

In a white light interferometer, the reference plane can be moved in order to calculate the interference maximum for each pixel in the resulting image series (Fig. 7.91). Then, there is a unique solution for the reconstruction of the surface relief.

In the white light interferometer shown in Fig. 7.92, the reference mirror is integrated into the lens system, so that the same focusing optic can be used for both optical paths. To obtain the image series, the test object is moved in the  $z$ -direction relative to the interferometer.

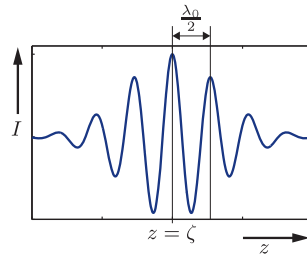


Figure 7.91. Intensity  $I$  measured by a white light interferometer with respect to the object displacement  $z$  and the mean wavelength  $\lambda_0$  of the white light.

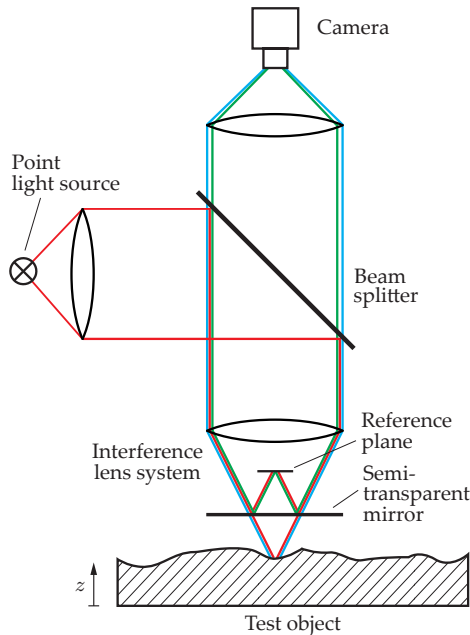


Figure 7.92. Setup of a white light interferometer.

### 7.3.16.2 Speckle interferometry for material inspection

Capturing a rough surface using an interferometer results in an interference pattern which is dominated by speckle. This interference pattern is very sensitive to deformations of the test object's surface [45,97,176].

For speckle interferometry, intensity images of the unstressed and the mechanically stressed test object are acquired by an interferometer and are denoted by  $g_1(\mathbf{x})$  and  $g_2(\mathbf{x})$ . The differences in the interference patterns visible in  $g_1(\mathbf{x})$  and  $g_2(\mathbf{x})$  can be used to computationally infer the surface's deformation. Thus, deformations in the sub-wavelength range can be detected.

Whereas there are no macroscopic interference stripes visible in the images  $g_1(\mathbf{x})$  and  $g_2(\mathbf{x})$  of a rough surface, the difference  $g_2(\mathbf{x}) - g_1(\mathbf{x})$  yields an image with a pattern of interference stripes representing the shape differences of the object in the unstressed and the



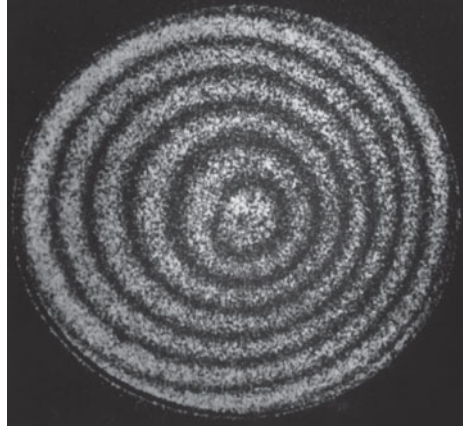


Figure 7.93. Speckle interferogram of a disk that is mechanically stressed at its center (source: Prof. Dr. W. Osten [125]).

stressed states [70]. Figure 7.93 shows such a speckle interferogram  $g_2(\mathbf{x}) - g_1(\mathbf{x})$  of a disk-shaped object, with  $g_1(\mathbf{x})$  acquired in an unstressed state and  $g_2(\mathbf{x})$  in a state of applied mechanical stress.

Shearography is a special variant of speckle interferometry that is successfully used in practice.

### ⊗ 7.3.16.3 Shearography

Shearography is a coherent optical method using a special variant of speckle interferometry [83] with the goal of visualizing the inner defects of a test object leading to a local deformation of the surface if mechanical force is applied. Deformations in the sub-wavelength range can be detected and measured. Shearography can be used for partially specular as well as for rough surfaces, which are present in many manufacturing processes. Surfaces with a size up to  $1 \text{ m}^2$  can be inspected with a single image [94].

The test object is illuminated with coherent light, typically emitted by a laser. A shear element is used to image two object points  $\mathbf{G}$  and  $\mathbf{G}'$  to the same sensor point  $\mathbf{B}$  (Fig. 7.94). The amount of shear corresponds to the distance  $\Delta x$  between the two points  $\mathbf{G}$  and  $\mathbf{G}'$  in the  $x$ -direction. The light waves emitted by  $\mathbf{G}$  and  $\mathbf{G}'$  interfere at the point  $\mathbf{B}$ . Two displaced coherent subimages are produced on the image sensor, which interfere with each other [45].

Successively, two images  $g_1(\mathbf{x})$  and  $g_2(\mathbf{x})$  of the unstressed and the stressed object are captured. The stress can be produced mechanically or thermally.

The result of the image acquisition is the difference of the two intensity images  $g_1(\mathbf{x})$  and  $g_2(\mathbf{x})$ :

$$\Delta g(\mathbf{x}) = g_1(\mathbf{x}) - g_2(\mathbf{x}). \quad (7.138)$$

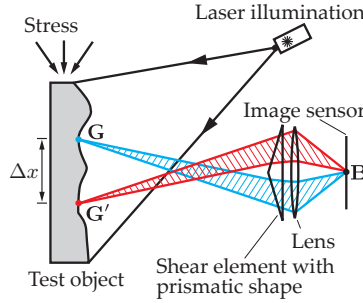


Figure 7.94. Principle of shearography.

This difference image is the basis for the following image analysis. The following approximation applies for small  $\Delta x$  [94]:

$$\Delta g(\mathbf{x}) \approx a(\mathbf{x}) + b(\mathbf{x}) \sin \left( \underbrace{\mathbf{v}^T(\mathbf{x}) \frac{\partial \mathbf{d}(\mathbf{x})}{\partial x} \frac{\pi \Delta x}{\lambda}}_{=: \varphi(\mathbf{x})} \right). \quad (7.139)$$

Here, the additive distortion term is denoted by  $a(\mathbf{x})$ , the multiplicative distortion term by  $b(\mathbf{x})$ , the shear by  $\Delta x$ , the wavelength of the coherent light by  $\lambda$ , and the stress-caused, relative displacement in 3D between the two object points that are imaged to the point  $\mathbf{x}$  is  $\mathbf{d}(\mathbf{x})$ . The vector field of the magnification  $\mathbf{v}(\mathbf{x})$  depends on the constellation of the setup. If a fixed  $\mathbf{x}$  and a small  $\Delta x$  is assumed, so that the sine function can be linearly approximated, the difference image  $\Delta g(\mathbf{x})$  represents the partial derivative of the displacement field  $\mathbf{d}(\mathbf{x})$ , except for an additive constant and a multiplicative constant.

Shearography is a self-referencing image acquisition method because of the following two characteristics: on the one hand, two coherent subimages are produced on the image sensor; on the other hand, the images corresponding to the stressed and the unstressed state are subtracted. Thus, the method is very insensitive to displacements of the test object, which might happen due to an inaccurate positioning of the object. This insensitivity is represented by (7.139) as follows: in the case of a translation, the displacement field remains constant with respect to the position,

$$\mathbf{d}_{\text{Rigid}}(\mathbf{x}) = \text{const.} \quad \Rightarrow \quad \frac{\partial \mathbf{d}_{\text{Rigid}}(\mathbf{x})}{\partial x} = 0. \quad (7.140)$$

As only a partial derivative of  $\mathbf{d}(\mathbf{x})$  influences (7.139), a rigid translation of the whole test object has no influence on the result.

Local depressions or bulges in the object's surface caused by the stress are represented in  $\Delta g(\mathbf{x})$  as characteristic stripe patterns, which are shaped slightly like a butterfly (Fig. 7.95) [94, 125].

By rotating the shear element by  $90^\circ$  around the optical axis, information about the partial derivative  $\frac{\partial \mathbf{d}(\mathbf{x})}{\partial y}$  in  $y$ -direction can be obtained equivalently.

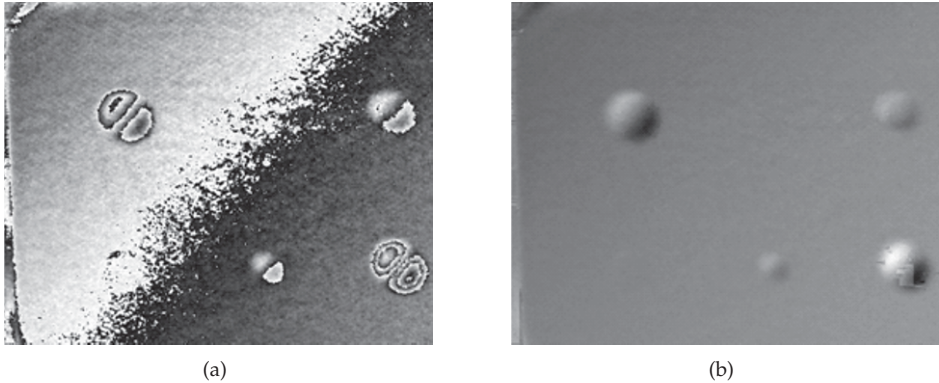


**Figure 7.95.** Shearographic inspection of a stressed aircraft component: (a) The shearogram  $\Delta g(x)$  shows local deformations in the characteristic shape of a butterfly pattern, which are caused by cavities inside the object; here, the stress has been thermally applied by heating the surface with a flash of light; (b) Demodulated phase image  $\varphi(x)$ , cf. (7.139) (source: Prof. Dr. W. Osten [125]).

#### ⊙ 7.3.16.4 Holography

Holography<sup>4</sup> captures and stores the interference pattern of a reference wave and an object wave. This recording is called a hologram. For a later readout, the hologram is illuminated with the reference wave, resulting in the reconstruction of the object wave.

The light of the reference wave and of the object wave comes from a coherent light source (e.g., laser light). The object wave is diffusely reflected by the investigated object. Together, both waves produce an interference pattern which is saved inside the recording medium, see Fig. 7.96(a). In accordance with (2.120), the interference pattern contains the phase information of the object wave. The recording of the phase information is a peculiarity of holography, as usual camera setups can only capture the light's intensity. This is indirectly achieved by recording the intensity of the interference pattern [45]. Wet-chemical photographic plates can be used as recording media, which can be photographically processed to a hologram after the exposure. However, there are also phase holograms where the information is encoded in the thickness of a transparent layer.

If the processed hologram is illuminated only with the reference wave, the holographically reconstructed object wave is produced on side (2), see Fig. 7.96(b). This effect can be explained as follows: if in Fig. 7.96(a) the object wave was subtracted in the whole space while conserving the interference pattern, it would disappear on side (1), whereas it would reappear on side (2) with a negative sign. As the wave's sign is irrelevant for the intensity captured by the camera, the holographic reconstruction would look exactly like the originally captured object.

Holographic interferometry can be used to compare arbitrarily shaped test objects having a rough surface structure with a reference object [38, 145, 176]. The reference object and test object can be physically different objects, whose difference has to be quantitatively determined, or one and the same object in a stressed and an unstressed state.

<sup>4</sup>Holography—originating from ‘holos’ and ‘graphe,’ Greek for ‘whole’ and ‘drawing’—was invented by Dennis Gábor in 1948, who was awarded the Nobel Prize in Physics in 1971 [55, 73].

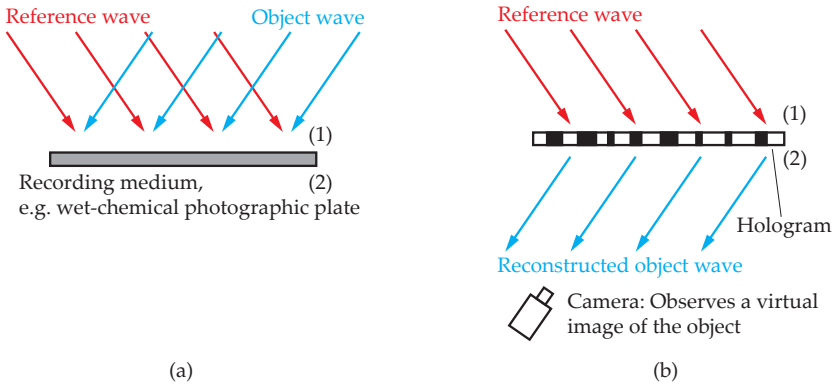


Figure 7.96. Principle of holography: (a) Recording the hologram; (b) Holographic reconstruction.

Arbitrarily shaped macroscopic test objects with a spatial structure longer than multiple wavelengths  $\lambda$  would lead to very large variations in the optical path difference between the reference and the object wave, which would produce an extremely dense pattern of interference stripes when using conventional interferometry: this would not be resolvable with a camera. In this case, a holographic comparison can be successful. Holographic methods allow the inspection of diffusely scattering surfaces of arbitrarily shaped objects [45].

The object wave of the reference object is saved inside a hologram on the basis of a primary reference wave. During the inspection process, the primary reference wave is used to reconstruct the object wave of the reference object, which is now used as the secondary reference wave. This wave contains the phase shift information in accordance with the relief of the reference object.

During inspection, the primary reference wave is used to produce an object wave of the test object by reflection. Additionally, the primary reference is used to read out the reference object's hologram producing the secondary reference wave.

The superposition of the object wave of the test object and the secondary reference wave yields an interference pattern corresponding to the optical path difference in the size of the relief differences between the test and reference object (desired relief).

Figure 7.97 shows a concrete setup for holographic interferometry. For hologram acquisition, the reference object is illuminated with coherent light. Additionally, a beam splitter is used to reflect the illuminating reference wave onto the recording medium, where it interferes with the object wave, which is diffusely reflected by the reference object, see Fig. 7.97(a). A wet-chemical photographic plate or a sensor array can be used as recording medium.

For automated visual inspection, the test object is placed at the same position that the reference object was at before, see Fig. 7.97(b). The object wave of the test object and the secondary reference wave, i.e., the holographically reconstructed object wave of the reference object, produce an interference pattern on the camera's image sensor. The interference pattern depends only on the difference between the reference and the test object. The corresponding phase differences and thus the optical path differences can be quantitatively calculated from the interference pattern, so that a quantitative measurement of the differences between both objects is possible in the sub-wavelength range. However, holographic

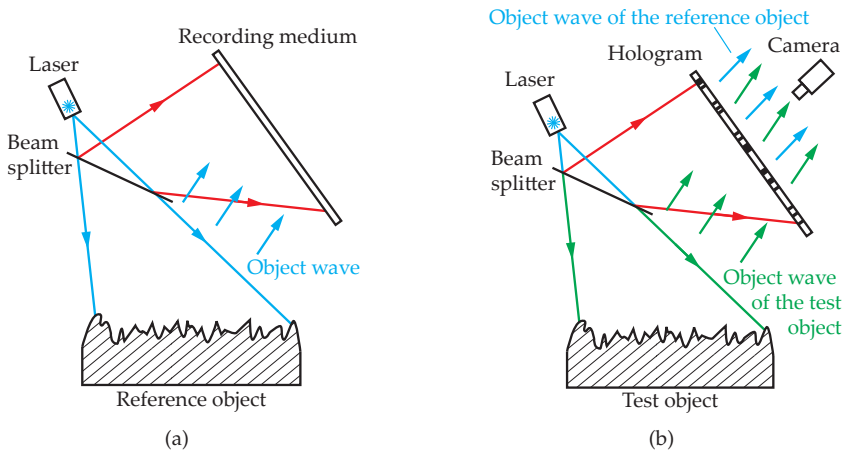


**Figure 7.97.** Automated visual inspection using holographic interferometry: (a) Recording a hologram of the reference object; (b) Interference of the secondary reference wave (object waves of the reference object) with the object wave of the test object (sketch of the principle).

systems are usually quite space consuming, as the different optical paths of reference and measurement have to be physically realized [70].

An example of the result of a holographic image acquisition is illustrated in Fig. 7.98. The secondary reference wave used for generating the interference stripes is generated with a hologram of the reference object, in this case of a cylinder having the desired geometry. Thus, the interferogram only shows stripes resulting from the optical path differences and therefore of the shape differences between the reference and the current test object. Such differences can be measured in the sub-wavelength range. Defects of the test object cause characteristic patterns of the interference stripes in the hologram (Fig. 7.99).

Instead of a wet-chemical film, also a sensor array, i.e., a camera chip without imaging optics, can be used for recording a hologram. If that sensor array is replaced by a light modulator, i.e., a transparent display during inspection, which displays the recorded hologram, an electro-optical realization of the holographic interferometry is realized.

An even more sophisticated alternative is given by digital holography [91]: the holograms of the reference object and the test object are captured by the sensor array and are then computationally evaluated. There is no physical interference between the two object waves. In fact, the phases are reconstructed point-wise in accordance with Huygens' principle and are then subtracted from each other. The result can be used to quantitatively calculate the difference between the reference and the test object.

For rough surfaces, the interference patterns show no stripe structure, as they are dominated by speckle. However, interferometry can still be used if there is the possibility of deliberately shifting the phase of the reference and the measurement path. A series of at least three recordings with different phase shifts is sufficient for a point-wise reconstruction of the phase [45].

If a spatial light modulator is used instead of the hologram, synthetically produced holograms of reference objects can be displayed. This is referred to as 'computer generated holograms' (CGH).

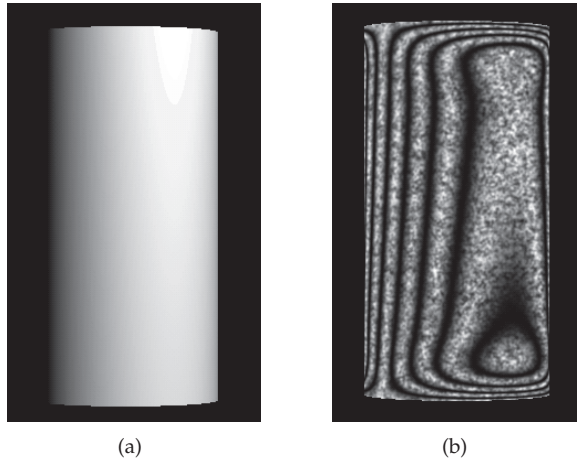


**Figure 7.98.** Simulation of the recording of a cylinder using holographic interferometry: (a) Cylinder; (b) Holographic interferogram (source: Prof. Dr. W. Osten [125]).

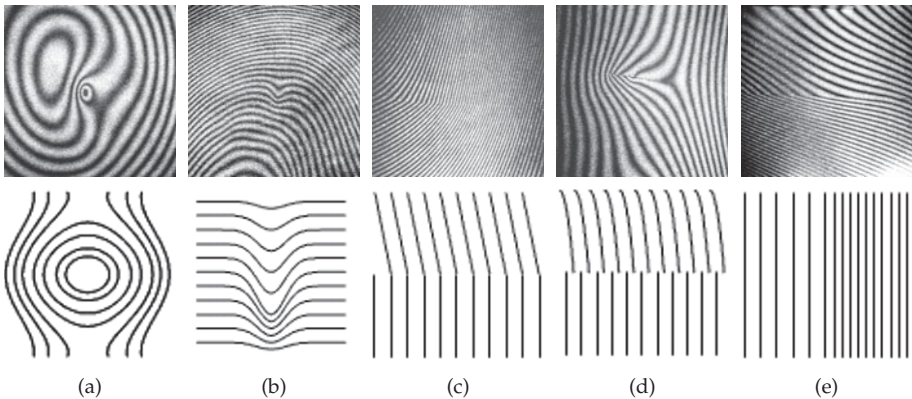


**Figure 7.99.** Patterns in the hologram corresponding to different types of defects: (a) Bull's eye; (b) Groove; (c) Bend; (d) Displacement; (e) Compression; Upper row: Holographic interference patterns; Lower row: Schematic illustration of the characteristic stripes (source: Prof. Dr. W. Osten [125]).

An extensive description of automated visual inspection methods based on shearography, interferometry and holography is given in [125].

## 7.4 Capturing interior object structures

Special inspection methods using electromagnetic waves can capture not only the surface of opaque objects but also the structures within test objects. On the one hand, the radiation in those parts of the spectrum can be used, for which the investigated objects are transparent, e.g., X-rays or terahertz radiation (Sec. 7.4.2, 7.4.5). On the other hand, effects on the object's surface can be observed that are caused by inner structures. This is the case for thermography, for example, which is covered in the following section.

A typical inspection task is the detection of inner defects like cavities, delaminations, inclusions of impurities, glue failures, etc.

### 7.4.1 Thermography

Thermography observes the heat radiation of a test object using a thermal imaging camera, in order to detect defects on or beneath the surface. The heat radiation of objects at room temperature ( $T \approx 300$  K) shows wavelengths in the infrared region above approximately  $4 \mu\text{m}$ . In accordance with Planck's law (2.254), each body with a temperature above absolute zero emits electromagnetic radiation and is therefore luminous. In accordance with Wien's displacement law (2.256), the maximum emission is given at  $\lambda_{\text{max}} \approx 9.66 \mu\text{m}$  for a temperature of  $T = 300$  K.

The emitted radiation of an object at room temperature can be captured by a thermal imaging camera. For homogeneous materials, typically temperature differences of a few  $10 \text{ mK}$  can be resolved.

Most real objects emit less radiation than the ideal black body. This effect can be taken into account by introducing a multiplicative factor  $\varepsilon$ ,

$$I_{\text{real}}(\lambda, T, \theta, \varphi) = \varepsilon(\lambda, T, \theta, \varphi) I_{\text{Planck,black}}(\lambda, T), \quad \varepsilon \in [0, 1], \quad (7.141)$$

where  $\varepsilon$  usually depends on the wavelength  $\lambda$ , the absolute temperature  $T$ , and the direction of the radiation  $(\theta, \varphi)$ . If this dependency can be neglected, i.e., if  $\varepsilon \approx \text{const.}$ , the object is called a gray radiator.

The factor  $\varepsilon$  is called the emissivity, and depends on characteristics of the object's surface, especially on its roughness. For a known spectral emissivity, the measured intensity values can be used to calculate the object point's temperature using the formulas described in Sec. 2.7.1.1.

In accordance with Kirchhoff's law, the emissivity of an opaque object equals its absorptivity. Absorptivity and reflectance  $R$  sum to 1, i.e., opaque objects absorb a certain ratio of the incident light and reflect the remaining part. Together, this implies

$$\varepsilon = 1 - R. \quad (7.142)$$

In particular, extensively reflecting surfaces emit only a little thermal radiation.<sup>5</sup> For example, the mean emissivity of polished aluminum is only  $\varepsilon \approx 0.05$  for a temperature of  $100 \text{ }^\circ\text{C}$ , whereas the reflectance is very high  $R \approx 0.95$ . In contrast, for the same temperature, anodized aluminum has a mean emissivity of  $\varepsilon \approx 0.55$  and a corresponding reflectance of  $R \approx 0.45$ . The emissivities of other materials are tabulated in [5].

Care must be taken during the thermal inspection of intensely reflecting surfaces, as the ambient radiation reflected by the test object might be higher than its self-radiation and can thus represent an immense perturbation.

Figure 7.100 shows a taxonomy of thermographic methods. Static thermography captures and analyzes the emitted radiation of a test object in a state of a temporally constant, i.e., stationary temperature distribution. Passive static thermography records the self-radiation of the surface. Illuminating the surface with thermal infrared and observing the reflected radiation is called active static thermography. If the surface has spatially

<sup>5</sup>Hence, perfect black objects, which do not reflect any light, have the maximum achievable emissivity  $\varepsilon = 1$ . Thus, they are ideal thermal radiators (cf. Sec. 2.7.1.1).

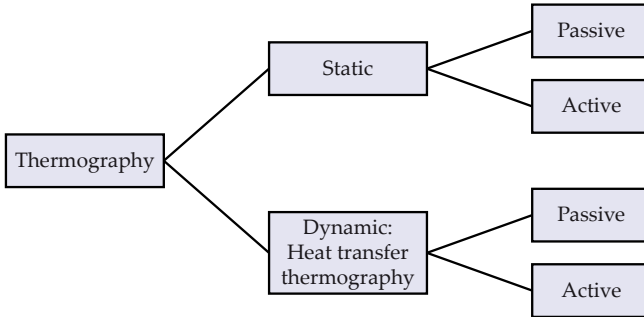


**Figure 7.100.** Taxonomy of thermographical methods. The active methods selectively illuminate or heat the test object. Passive methods use no illumination or energy emission for the inspection task, but observe the object's self-radiation.

constant temperature for example, passive thermography can be used to detect and quantify emissivity-dependent local variations or defects of the surface. In accordance with (7.142), the variations depending on emissivity are equivalent to reflectance-dependent variations.

Heat transfer thermography is of particular importance for automated visual inspection and nondestructive material inspection. It can be used to test components for inner defects, which are not directly visible on the surface.

This method captures the transient heat conduction on the test object by using a temporally resolved thermal imaging camera. Therefore, heat transfer thermography is also referred to as dynamic thermography. Visual inspection exploits the effect of local defects temporarily resulting in local contrasts in the thermal image of the transient heat conduction.

The method's name is motivated by the effect of heat spreading to colder regions of the object during transient heat conduction. If the transient heat conduction is not caused by the inspection procedure but by a manufacturing-dependent heating for example, the method is called passive heat transfer thermography.

Active heat transfer thermography is particularly important. Here, a heat distribution is deliberately induced in the test object and the subsequent transient heat conduction is observed by continuously measuring the emitted heat radiation. For example, the object can be heated using a radiant heater, a flashbulb, ultrasound, microwave radiation, heated media (air, water) or induction.

Transient heat conduction processes are described by the diffusion equation [6]. It is a linear partial differential equation:

$$\operatorname{div}(D \operatorname{grad}(T)) = \rho c \frac{\partial T}{\partial t} \quad (7.143)$$

with the temperature  $T = T(x, y, z, t)$  in K, the thermal conductivity  $D = D(x, y, z)$  (representing the diffusion coefficient in this case) in  $\text{W K}^{-1} \text{m}^{-1}$ , the heat capacity  $c = c(x, y, z)$  in  $\text{Ws kg}^{-1} \text{K}^{-1}$  and the volumetric mass density  $\rho = \rho(x, y, z)$  in  $\text{kg m}^{-3}$ . For media with anisotropic thermal conductivity,  $D$  is a tensor of order two, which can be represented by a  $3 \times 3$ -matrix; also see Sec. 11.3.

In combination with boundary and initial conditions, the temperature field  $T(x, y, z, t)$  can be calculated of the diffusion equation as a function of position and time.



Defects resulting in spatial inhomogeneities of  $D$ ,  $\rho$  or  $c$ , induce local temporary temperature differences during heating or cooling processes. If these temperature differences are captured by a thermal imaging camera with sufficient contrast, the defects can be detected on basis of the measurement. Typical defects which can be identified with heat transfer thermography include air inclusions, glue failures, delaminations and entrapped moisture.

Figure 7.101(a) shows an example setup for defect detection using heat transfer thermography. At first, the test object is heated by a radiation source, for example a flashbulb. Then, the infrared radiation emitted by the object is captured using a thermal imaging camera. Immediately after the heating, a spatially homogeneous temperature gradient can be observed, Fig. 7.101(c). Afterwards, the heat is transferred into the object's interior. Defects inside the object lead to irregularities during this process. For example, a cavity usually shows a lower thermal conductivity than the material of the test object. Hence, the heat of the material above the cavity is transferred more slowly, so that a locally raised temperature is visible on the corresponding spot on the object's surface during the cooling process, Fig. 7.101(d).

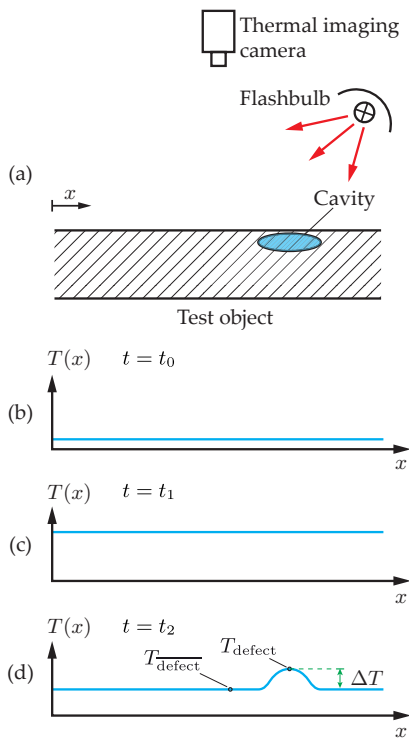


**Figure 7.101.** Detection of defects using heat transfer thermography: (a) Principle sketch of the setup, (b) Temperature distribution for the time  $t_0$ , before the heating, (c) Temperature distribution for the time  $t_1$ , immediately after the heating, (d) Temperature distribution for the time  $t_2$ , during image acquisition for defect detection. For this illustration and to simplify matters, a spatially constant temperature rise caused by the flashbulb is considered; this is not the case in practice. Instead, at time  $t = t_2$ , there would be a temperature gradient typical for the test object and the constellation of illumination, which can be eliminated during image pre-processing, so that only the difference image with respect to the reference object is further analyzed.

Depending on the material and on the position and size of the defect, there is an optimal time  $t_{\text{opt}}$  when the defect is visible with maximum thermal contrast in the temperature profile  $T(x)$ . The image should be taken exactly at this time. If typical defects arise at a known depth in a component, for example, in the case of the lamination or adhesion of layers with a known thickness, the optimal imaging time  $t_{\text{opt}}$  for observing the maximal thermal contrast  $A(t)$  can be calculated by numerically solving the differential equation (7.143). Alternatively,

this time can be empirically determined by observing the temporal gradient of the thermal contrast of objects with typical defects.

The thermal contrast  $A(t)$  is defined as

$$A(t) := \frac{|\Delta T(t)|}{T_{\text{defect}}(t)} = \frac{|T_{\text{defect}}(t) - T_{\text{defect}}^{\text{mean}}(t)|}{T_{\text{defect}}(t)}, \quad (7.144)$$

with the spatially extremal temperature  $T_{\text{defect}}$  in the region of the defect at time  $t$  and the mean temperature  $T_{\text{defect}}^{\text{mean}}(t)$  around the defect at time  $t$ . Generally, the thermal contrast is reduced for smaller and deeper defects.

For unknown and variable defect depths and sizes, an image series can be recorded during the transient heat conduction and can be subsequently analyzed. Defects near (far from) the surface show a maximum local thermal contrast in early (later) recordings of the image series.

The most important variants of active heat transfer thermography are pulse thermography and lock-in thermography. **Pulse thermography** heats the surface with a short pulse of a high-performance heat source, for example by a flashbulb or a radiant heater. Then, the cooling process is observed with a thermal imaging camera.

Figure 7.102 shows a thermal images of a steel ring with an inner nickel coating of a thickness of 100  $\mu\text{m}$ , which has to be inspected for adhesion errors between the steel and the nickel [116]. Because of the high thermal diffusivity of nickel, the thermal diffusion time is on the order of some milliseconds, so that a fast thermal imaging camera is needed. In the pseudocolor image, blue colors correspond to room temperature, red colors to temperatures which are some 10 K above room temperature. Approximately 30 up to 50 ms after the heating by the flashbulb, temperature contrasts of badly adherent regions are visible, where

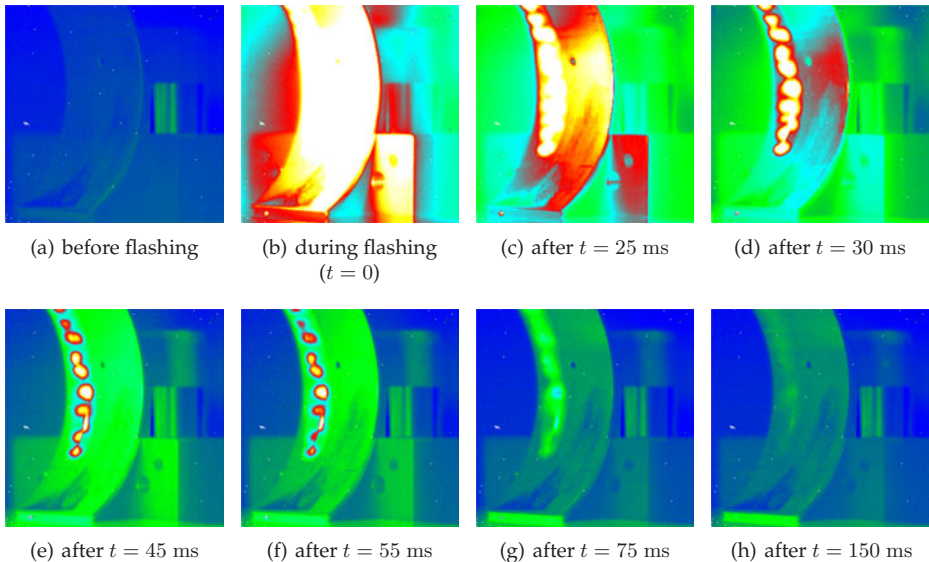


**Figure 7.102.** Inspection of the adhesion of nickel coated steel component by pulse thermography (source: U. Netzmann, G. Walle, Fraunhofer IZFP [116]).

the heat is only slowly being transferred. After about 150 ms, the temperature distribution reaches the original state as it was before the heating.

**Lock-in thermography** periodically heats the test object's surface, ideally with sinusoidally modulated heating power,

$$P(t) = \frac{1}{2} P_{\max} (1 + \sin 2\pi f_0 t). \quad (7.145)$$

The frequency  $f_0$  has to be adjusted in accordance with the specific time constants of the test object's heat transfer. A thermal imaging camera is used to capture an image series  $\{g(\mathbf{x}, n\Delta t)\}$ ,  $n = 0, \dots, N - 1$ , and the hypothesis of the sampling theorem,  $\Delta t < \frac{1}{2f_0}$  has to be satisfied, i.e., two or more samples are required per period  $f_0^{-1}$  (see Sec. 8.3.2).

During the transient state of some periods  $f_0^{-1}$ , the image series is coherently demodulated with the carrier signals  $\sin(2\pi f_0 t)$ ,  $\cos(2\pi f_0 t)$  and thus the amplitude and phase are measured for each surface point (cf. Sec. 7.3.6.3). The low susceptibility of the lock-in principle leads to a higher sensitivity than with pulse thermography; however, a longer measurement time of about 10 periods is necessary:  $10f_0^{-1}$ .

The inspection of solar cells [100] or of composite materials [98] are examples of applications of lock-in thermography.

### 7.4.2 Imaging using X-rays

X-rays<sup>6</sup> refers to electromagnetic radiation with wavelengths from about 10 nm down to 1 pm =  $10^{-12}$  m. This corresponds to frequencies from approximately  $2 \cdot 10^{16}$  up to  $5 \cdot 10^{19}$  Hz and photon energies from about 100 eV up to some MeV. So the X-rays are adjacent to the shorter wavelengths of the UV region.

Because of their high photon energy  $E = \frac{hc}{\lambda}$  (2.191), X-rays are ionizing, and are thus harmful to humans. Therefore, X-ray devices used in automated visual inspection have to be adequately shielded. There are legal safety provisions for using X-rays [32].

X-rays have a high penetration of matter because of their high energy. This is reduced with increasing mass density. The goal of using X-rays in automated visual inspection is the visualization of structures and defects within components.

**Generating X-rays:** Inside a vacuum tube, an electron beam is accelerated by a high voltage  $U$  and focused on a metal plate (typically consisting of tungsten, copper, or molybdenum) [131]. The electrons are sharply decelerated inside the metal. As accelerated or decelerated charges emit electromagnetic radiation, broadband X-rays are produced, which is called bremsstrahlung<sup>7</sup> [73]. The maximum photon energy is determined by the kinetic energy of a single electron. During acceleration by the voltage  $U$ , an electron receives the kinetic energy  $E = eU$ , with  $e \approx 1.602 \cdot 10^{-19}$  C denoting the elementary charge of an electron. In accordance with (2.191), this results in X-rays with a minimum wavelength of

$$\lambda_{\min} = \frac{hc}{eU}. \quad (7.146)$$

Hence, the voltage  $U$  can be used to adjust the maximum photon energy and thus the minimum wavelength of the X-rays. Typically, the photon energy is denoted in eV for X-rays

<sup>6</sup>X-rays were discovered in 1895 by Wilhelm Conrad Röntgen.

<sup>7</sup>*bremsen* is the German word for 'to decelerate'

and corresponds to the acceleration voltage. One electron-volt  $1 \text{ eV} \approx 1.602 \cdot 10^{-19} \text{ J}$  is the kinetic energy an electron receives by an acceleration voltage of  $1 \text{ V}$ . Typical acceleration voltages are in the range of some  $10 \text{ kV}$  up to some  $100 \text{ kV}$ .

The continuous spectrum of the bremsstrahlung is superposed with a line spectrum which depends on the material of the anode and is caused by high-energy electron transitions of the atoms' electron hull (characteristic X-rays).

A higher acceleration voltage and thus a higher energy of the photons results in a higher penetration depth of the generated X-rays. The X-rays are said to be 'harder' for higher voltage.

**Imaging geometry for X-rays:** Basically, electromagnetic rays can be influenced by refraction, reflection, or diffraction, using lenses, mirrors, or gratings (cf. Chap. 2).

For soft X-rays, which are defined as X-rays of a wavelength larger than the inter-atomic distances in solids, matter acts like a homogeneous continuum. For hard X-rays, which have wavelengths smaller than the inter-atomic distance, the matter's discrete structure is of importance. As the index of refraction of solids is nearly 1 for X-rays, no really effective X-ray lenses or X-ray mirrors for steeply incoming rays can be produced. The surface of such mirrors would need to have a roughness smaller than the wavelength, which is technically infeasible. In the best case, mirrors for grazing X-rays can be achieved, as the ratio of the reflected light increases up to total reflection<sup>8</sup> (see Sec. 2.6.5). Existing X-ray lens systems and telescopes use hyperbolic or parabolic reflectors, arranged in a grazing manner with respect to the incoming radiation [73].

Resulting from the mentioned problems for directing the X-rays, usually simple projecting X-ray paths are used for automated visual inspection. Therefore, the most important optical elements used in combination with X-rays are absorbing diaphragms made of dense materials, like lead, for example.

Because of the very short wavelengths of X-rays compared to the typically relevant structures inside test objects, X-rays are well suited for the use of geometric optics. Diffraction effects can usually be neglected.

Practical imaging systems with X-rays consist of a point source of the X-rays and a screen which spatially measures the incident radiation which traversed the test object. Because of the rays' geometry, this corresponds to a central projection with the X-ray's point source being the center of the projection (cf. Sec. 3.2). In accordance with the intercept theorem that has been applied to Fig. 7.103, the magnification is given by

$$V := \frac{B}{G} = \frac{a+b}{a} = 1 + \frac{b}{a}, \quad V > 1, \quad (7.147)$$

with  $a$  denoting the distance between the source and the object,  $b$  denoting the distance between the object and the image plane, and  $B$  and  $G$  denoting the image size and the object size in the usual notation. The measurement uncertainty for measuring structures inside

---

<sup>8</sup>In accordance with Sec. 2.6.5, total reflection can only arise for the transition from a more to a less optically dense medium. Some materials have an index of refraction  $n < 1$  for X-rays, so that total reflection can occur for the transition from vacuum or air into such a material. This phenomenon can be used for constructing X-ray lenses [73].

By the way, the exceeding of the speed of light  $c$  in vacuum by the phase velocity in a medium with  $n < 1$  is no contradiction with the special theory of relativity, as the group velocity (see example 8.28), which is the one relevant for the transport of energy and information, is always less than or equal to  $c$ .

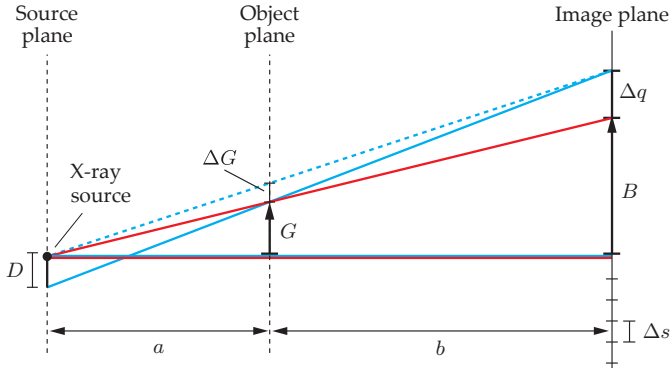


Figure 7.103. Image formation by X-ray projection and consequences of the source's finite diameter  $D$ .

test objects depends on the diameter  $D$  of the X-ray source. A smaller focal spot of the electrons on the X-ray tube's tungsten plate allows imaging smaller structures (Fig. 7.103). In accordance with the intercept theorem, the resulting geometric blur  $\Delta q$  is given by

$$\Delta q = \frac{b}{a} D = (V - 1) D. \quad (7.148)$$

Microfocus X-ray tubes can achieve a minimal diameter of the focal spot of  $D = 1 \mu\text{m}$  [52].

Besides the diameter  $D$  of the X-ray source, the discretization  $\Delta s$  of the imaging sensor also has an effect on the measurement uncertainty. In this case, the measurement uncertainty is defined as the maximum deviation  $\Delta G$  when determining  $G$ . It can be derived using the maximum deviation  $\Delta B$  in the image plane:

$$G + \Delta G = \frac{B + \Delta B}{V}, \quad (7.149)$$

$$\Delta B = \Delta q + \Delta s, \quad (7.150)$$

$$\Rightarrow \Delta G = \frac{\Delta q + \Delta s}{V} = \frac{V - 1}{V} D + \frac{\Delta s}{V}. \quad (7.151)$$

A high magnification  $V \rightarrow \infty$  implies  $\Delta G \rightarrow D$  and an insignificant influence of the discretization by the sensor. If the image plane is located close to the object, i.e.,  $b \rightarrow 0$  and  $V \rightarrow 1$ , then  $\Delta G \rightarrow \Delta s$  and the impact of the finite diameter of the source can be neglected.

The practically achievable resolution limit for test objects in the range of millimeters is about  $2.5 \mu\text{m}$  [52].

**Radiometry:** X-rays are attenuated when passing through matter. Measuring the remaining X-rays gives information about the thickness and structure of the test object. The influence of the test object on the X-rays is described by the absorption coefficient  $\mu(\mathbf{x})$ , which is a function of the position  $\mathbf{x}$ :

$$\mu(\mathbf{x}) : \mathbb{R}^3 \rightarrow [0, \infty). \quad (7.152)$$

Now, a point X-ray source is assumed to be located in the coordinate system's origin  $\mathbf{O}$ , so that the distance  $r$  to the source is given by  $r = \|\mathbf{x}\| = \sqrt{x^2 + y^2 + z^2}$  (Fig. 7.104). The

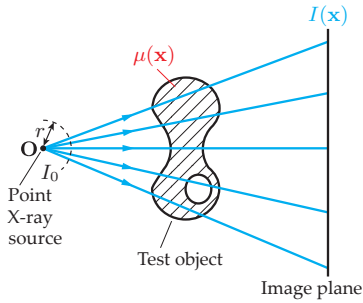


Figure 7.104. Absorption of X-rays inside the test object.

X-rays's intensity (power per area)  $I$  changes by  $dI$  if  $r$  is increased by  $dr$ :

$$dI = -I \frac{2}{r} dr - I \mu dr. \quad (7.153)$$

The first term results from the conservation of energy for spherical waves, the second describes the absorption inside the medium. Integration of this differential equation from  $r_0$  to  $r$  yields

$$I(\mathbf{x}) = I_0 \frac{r_0^2}{r^2} \exp\left(-\int_{r_0}^r \mu\left(\frac{\mathbf{x}}{\|\mathbf{x}\|} \rho\right) d\rho\right), \quad (7.154)$$

with  $r_0 > 0$  representing the radius of the X-ray source. The term  $r^{-2}$  explains the reduced intensity due to the properties of a spherical wave and conservation of energy, as the sphere's surface grows quadratically with respect to the propagation radius. The exponential function corresponds to the Lambert–Beer law of absorption. Inside a homogeneous medium,  $\mu = \text{const.}$ , the X-rays' intensity decreases exponentially with  $r$ , as homogeneous layers of equal density absorb the same proportion of radiation. If, for example, one-half of the radiation is absorbed after travelling  $r_1$ , the next half is absorbed in the adjacent layer of the same thickness  $r_1$ , so that one-quarter of the original intensity remains. A journey of  $3r_1$  reduces the intensity to one-eighth, resulting in an exponential decrease [19]. The absorption coefficient  $\mu$  is approximately proportional to  $\lambda^3 Z^3$ , with the X-rays' wavelength  $\lambda$  and the atomic number  $Z$  of the medium's atoms [131].

### Challenges of imaging using X-rays:

- In practice, optical manipulation of the X-rays is extremely difficult. Unlike in the visible spectrum, an optical point-to-point imaging can hardly be achieved.
- The exponential damping of the X-rays, as in the Lambert–Beer law, leads to a very high dynamic range of intensities, especially for test objects with large differences of densities. This leads to high demands on the dynamic range of the sensor.
- The X-rays are partly scattered on the outer electrons of the test object's atoms. This so-called Compton scattering changes the photons' propagation direction and increases their wavelength, as they lose some of their energy. This generates diffusely scattered X-rays, which reduce the contrast of the resulting image.
- The intensity measured in the image plane is the result of a line integral over the distance covered by the light inside the test object. Structures along this line are superposed in the intensity signal. Reconstructing the properties of the object  $\mu(\mathbf{x})$  from the measured

intensity  $I(x)$  is an inverse problem, which can only be satisfyingly solved by combining the X-ray images acquired from different directions. This approach is used in tomography [92].

**Tomography:** For simple visual inspection tasks, the analysis of a single X-ray image can be sufficient. For more exact investigations of the test object's geometry and inner structures, several images with different rotations have to be captured. Therefore, the object is incrementally rotated around a fixed axis. The 3D reconstruction of the test object from the intensity images corresponds to the inverse Radon transform, which is covered in Chap. 14. It yields the absorption coefficient  $\mu(x)$  as a three-dimensional function of the measured volume. Then, arbitrary sectional images through the object's interior can be calculated, which is why the method is called tomography<sup>9</sup>. As the reconstruction is very complicated, and has only become feasible because of efficient computers and algorithms, it is also-called 'computed tomography' [92, 93, 131].

**Detection of X-rays:** Area sensors for industrial applications mainly rely on the scintillation principle [17, 131]. X-rays strike a scintillation layer, where they are converted into visible light by fluorescence (cf. Sec. 7.2.2). This visible light is captured by an adjacent image sensor or by a camera. So-called image intensifiers perform an electronic preamplification employing the principle of photomultipliers (cf. Sec. 6.3) before the conversion into an image.

**Example 7.11 (Nondestructive material inspection using X-rays):** X-ray images can reveal the inner defects of components. For example, Fig. 7.105 shows the aluminum cast part of a chassis component. The projected X-ray image in Fig. 7.105(b) was captured with an acceleration voltage of  $U = 140$  kV, a tube current of 5 mA, and an exposure time of 500 ms. In the image, defects are visible as slightly brighter spots compared to the surrounding, because the thickness of the material is reduced in the locations of these defects, and so the X-rays are less attenuated. However, it is still hard for a human to see these defects in the

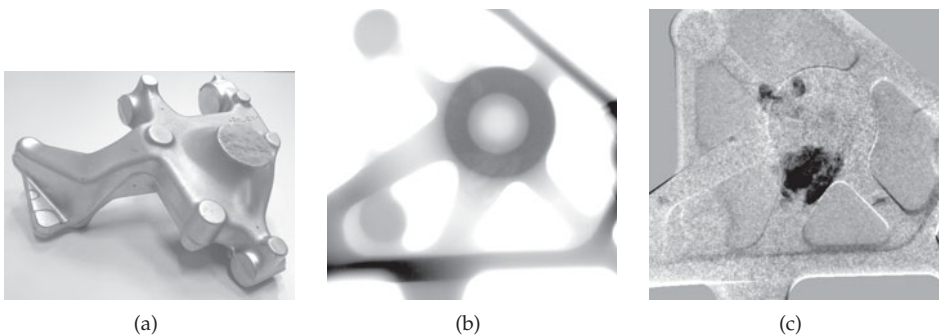


**Figure 7.105.** Inspection of a chassis component for inner defects: (a) Image of the aluminum cast part; (b) X-ray image of the test object; (c) Difference image with respect to the image of a reference object (source: Dr. N. Uhlmann, Fraunhofer EZRT).

<sup>9</sup>*tomos* is Greek for 'section'

X-ray absorption image. Thus, the difference image, i.e., the difference from a reference image, is calculated for defect detection, see Fig. 7.105(c). ■

### 7.4.3 Optical coherence tomography

Optical coherence tomography (OCT) is a method for the detection of the inner structure of an object, and is based on interference. Similar to white light interferometry (Sec. 7.3.16.1), it uses a light source with a short coherence length. The light coming from a reference path interferes with the light reflected by the object's inner structure [54]. The known length of the reference path, for which there is an interference maximum, can be used to infer the depth of the observed object point. The intensity of that maximum gives information about the optical properties of the material inside the object. Distortions because of multiple reflections and scattered light are reduced, as there is no constructive interference because of the different path lengths. Figure 7.106 illustrates this principle.

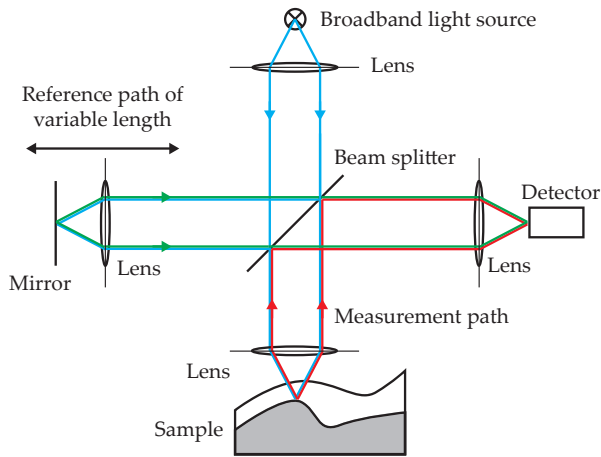


**Figure 7.106.** Principle of optical coherence tomography. The light source emits broadband light with a short coherence length, which is split by a beam splitter. The first half of the light traverses the so-called reference path, which consists of an axially movable mirror. It subsequently reaches the beam splitter a second time, and is then focused on the detector. The other half is focused onto the investigated sample, is eventually reflected by the inner structures, is subsequently deflected by the beam splitter to be finally focused on the detector, where it interferes with the reference light bundle (adapted from [54]).

In order to capture a whole volume, a lateral scanning can be performed or area image sensors can be used. Different variants of the setup are possible [8, 144, 154]. Of particular importance is the use of a spectral sensor to capture the interference pattern. The Fourier transform can be used to calculate the interference curve from the spectrum, replacing the time consuming mechanical movement of the reference mirror.

The achievable resolution in the longitudinal direction along the optical axis depends on the coherence length of the illumination used, and is on the order of a few micrometers. The lateral resolution is mainly determined by the imaging optics.



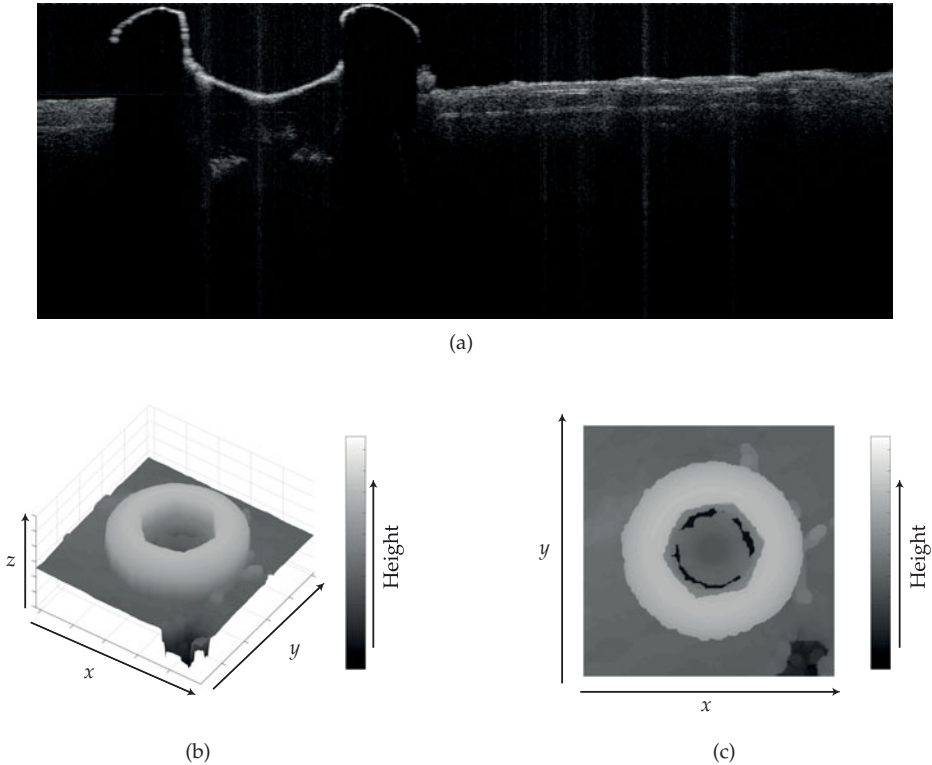


**Figure 7.107.** OCT used for supporting a cochlea implantation: (a) Image of a two-dimensional OCT scan in the  $x, z$ -plane showing the section of a titanium screw; (b) By combining several scans of different positions  $y$ , the surface of the titanium screw and of the skull has been reconstructed; (c) Top view: the hexagonal socket of the titanium screw (source: IPR Karlsruhe Germany).

Medical imaging is the most important application for optical coherence tomography. By using an illumination in the near-infrared, penetration depths of some millimeters can be achieved for tissues. The resolution is significantly higher than for alternative measurement methods like ultrasonography [8].

Figure 7.107 shows images of an application in which OCT has been used to detect the 3D position and orientation of titanium screws placed in the skull of a patient to allow a precise localization during a cochlea implantation.

In automated visual inspection, optical coherence tomography is used for the detection of defects beneath the surface, for example, of ceramic components or silicon semiconductors [65,154].

#### 7.4.4 Schlieren imaging and schlieren tomography

In media with an inhomogeneous index of refraction, i.e., one which is spatially varying, light rays do not follow a straight line but are deflected depending on the gradient of the index of refraction. The measurement of this effect can provide information about the distribution of the index of refraction and thus about the corresponding properties of the

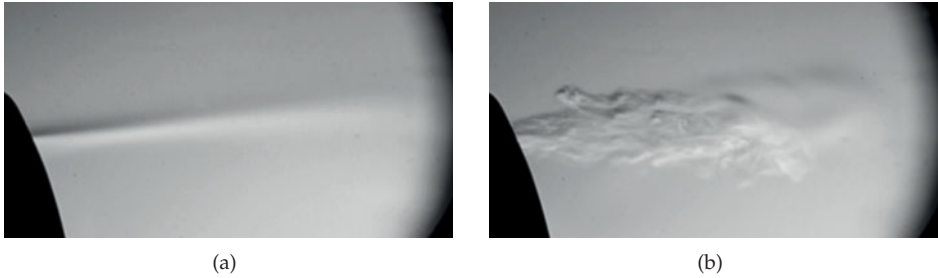


Figure 7.108. Schlieren images of a stream of butane gas. The nozzle, from which the gas is escaping, is located in the center of the left image margin. (a) Laminar flow; (b) Turbulent flow.

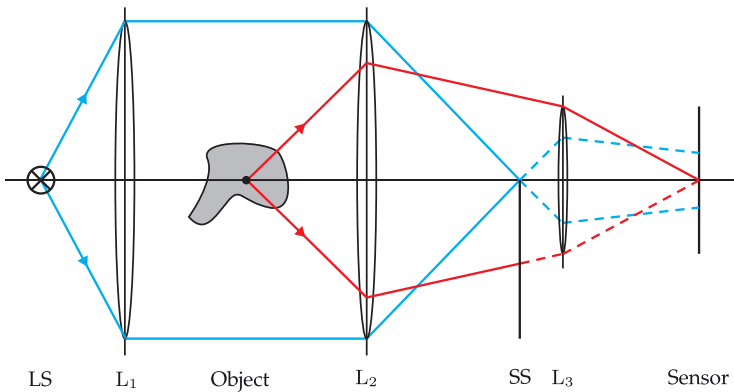


Figure 7.109. Principle of schlieren imaging. The light of the light source LS, collimated by  $L_1$ , illuminates a transparent object. The lens  $L_2$  focuses the collimated light. A schlieren stop (SS) is placed at the focal point of  $L_2$ , which ideally halves the luminance if no object is present. Light rays that are deflected upwards (downwards) because of the object pass the schlieren stop (are blocked) and result in a brightening (a darkening) on the sensor. The resulting intensity structures are called ‘schlieren.’ Together, the lenses  $L_2$  and  $L_3$  realize a focused imaging of the object on the sensor.

medium [147]. For transforming the deflection of the ray in an intensity image, a so-called schlieren stop can be used, which is placed asymmetrically in the optical path. Therefore, the changed direction of the deflected light rays result in structures of varying intensity—so-called ‘schlieren’—on the image sensor. If the investigated medium is captured from different projection directions, tomographic methods can be used to reconstruct the distribution of the index of refraction inside the medium.

Schlieren imaging and schlieren tomography can be used to investigate flames, flows (see Fig. 7.108), and transparent objects, for example.

Figure 7.109 shows the principle of the setup used for schlieren imaging.

#### ► 7.4.5 Image acquisition using terahertz radiation

Electromagnetic radiation in the frequency range from 100 GHz up to 10 THz is called terahertz radiation or THz radiation<sup>10</sup> [138]. The definition of the frequency range is not stan-

<sup>10</sup>1 THz =  $10^{12}$  Hz

standardized: some sources give the interval from 300 GHz to 3 THz [126]. This corresponds to wavelengths in the range from 1 mm down to 0.1 mm, which is called the submillimeter band.

THz radiation is located between the infrared and microwaves. This domain had remained technically unused for a long time, as no industrially usable technologies for efficiently generating and detecting THz radiation were available. The frequencies were too high for high-frequency electronics while the quantum energies were too low for optical sensors. This circumstance is referred to as the ‘terahertz gap.’

Modern laser technologies led to a breakthrough. THz imaging is a current area of research, and the first commercial systems are now available for quality testing. There is still a high development potential for this technology for automated quality testing.

Because of the low photon energy, THz radiation is not ionizing and is therefore considered to be harmless for humans.

THz radiation can penetrate nonconductive materials well, such as plastics, dry paper, and dry wood. In contrast, THz radiation is absorbed by conductive materials, and especially by water. The moisture in the air already leads to a notable attenuation.

The photon energy of THz radiation is on the order of the excitation energies of the molecular and lattice oscillations, so that substances can be identified by absorption spectroscopy using THz radiation. For example, a popular application is the detection of explosives, which usually contain or consist of organic compounds with excitation energies in the THz range.

In the field of automated visual inspection<sup>11</sup>, THz radiation can especially visualize inner structures and defects that are not visible in other spectral ranges when viewed from the outside. Here are some concrete sample applications:

- Detection of contaminants in food, for example in chocolate [90].
- Inspecting objects through paper and plastic packages, which are opaque for visible light.
- Detection of cavities in ceramic and plastics [134].
- Visualization of hidden items under clothes for security checks, e.g., in airports.
- Detection of native metals<sup>12</sup> in rocks in the field of automated sorting of bulk goods.

In accordance with Planck’s law (2.254), each object emits THz radiation depending on its temperature. Due to Wien’s displacement law (2.256), the maximum intensity of the emitted radiation for objects of low temperature is in the THz range (Table 7.2). Although the maximum intensity is shifted into the infrared range for indoor temperatures, the intensity of the emitted THz radiation increases further, as the self-radiation increases intensely in accordance with the Stefan–Boltzmann law (2.255) (cf. Fig. 2.34 on page 82). The radiation of this thermal emission is incoherent and thus the emitter represents a noise generator in the THz range. By the way, at room temperature, thermal self-radiation in the THz range can be used to detect items covered by clothes.

As an alternative to the passive measurement of self-radiation, it is also possible to actively illuminate the test object with THz radiation. Mainly the transmitted radiation is observed. As both variants are currently being researched, it is not yet known which method

---

<sup>11</sup>Or, rather, in the field of quality testing or nondestructive material inspection, since THz radiation lies outside the visible part of the spectrum, there is no *visual* inspection in the strict sense.

<sup>12</sup>Chemical elements that are found in their pure form in nature are called native.

**Table 7.2.** Wavelength and frequency of the intensity maxima of the thermal self-radiation of a black body radiator in accordance with (2.256), (2.1).

Temperature $T$	Wavelength $\lambda$	Frequency $\nu$
$\approx 1$ K	3 mm	100 GHz
$\approx 10$ K	0.3 mm	1 THz
$\approx 100$ K	30 $\mu\text{m}$	10 THz

will be used for which application in the future. In the following, active THz methods will be described.

Among others, technically relevant methods for **generating** THz radiation are [126, 150]:

- Electronic frequency multipliers using the nonlinearity of GaAs Schottky diodes. This method generates coherent, narrow-band THz radiation in form of a continuous wave (CW).
- Difference-frequency generation of two lasers with frequencies that differ by the amount of the sought for THz frequency, inside a nonlinear<sup>13</sup> optical material. This principle can be realized using a two-color diode laser [78]. Again, coherent narrow-band CW THz radiation is generated.
- An ultra-short laser pulse with a duration of from about 20 up to about 100 fs is sent through a nonlinear optical material.<sup>14</sup> Due to its short duration, such a pulse is broadband and has a high electric field strength.<sup>15</sup> Because of the spectral ratios of the laser with frequency differences in the THz range, a broadband THz pulse is generated in nonlinear optical materials. These methods are called optical rectification. The broadband THz pulse is coherent with the generating laser pulse.
- An ultra-short laser pulse strikes a semiconductor material (typically GaAs) connected to a voltage source by two electrodes. There, the laser pulse creates short lived charge carriers, which lead to an extremely short current pulse with a duration of some picoseconds<sup>16</sup>. Then, this current pulse generates a radiation pulse in the THz range. Such a component is called a **photoconductive antenna** (PCA) [96]. The THz radiation generated is broadband and coherent with the generating laser pulse.

THz radiation can be imaged using metallic reflectors and special lenses made from THz-transparent materials such as silicon (Si), for example.

The following possibilities, among others, exist for the **detection** of THz radiation [126]:

- A photoconductive antenna can also be used as a detector. As a receiver, it is operated as a source of a photocurrent. An ultra-short laser pulse generates short lived charge

<sup>13</sup>Inside a nonlinear optical medium, the propagation of light can no longer be described by using linear differential equations, as certain material properties depend on the light's intensity. The principle of superposition does not apply [130].

<sup>14</sup>1 fs =  $10^{-15}$  s (femtosecond)

<sup>15</sup>Because of the reciprocity of the Fourier transform (see Chap. 8), a short pulse has a broadband spectrum. As the energy is concentrated in a short period of time, the laser pulse has a high instantaneous power and thus a high electric field strength.

<sup>16</sup>1 ps =  $10^{-12}$  s

carriers, which are accelerated by the electric field of the simultaneously present THz radiation and are extracted in the form of a current on the electrodes.

- **Freespace electrooptic sampling:** A linearly polarized ultra-short laser pulse is sent collinearly to the THz radiation through a certain material, which is birefringent in the presence of THz radiation [34].

If no THz radiation is present, a  $\frac{\lambda}{4}$ -plate is used to generate circularly polarized light from the laser. Then, a Wollaston prism decomposes the polarized laser light into two equally intense light rays, which are polarized perpendicularly towards each other and finally reach two photodetectors. The resulting electrical signals are subtracted, so that a signal value of zero results in the absence of THz radiation. Such detectors are therefore called **balanced detectors**. If THz radiation is present, the polarization direction of the laser is rotated and the  $\frac{\lambda}{4}$ -plate generates elliptically polarized light. In this case, the balance of the two detectors is disturbed and the resulting electrical signal is proportional to the electric field strength of the THz radiation.

- **Bolometers** (cf. Sec. 6.10.1): Matter is heated by THz radiation and therefore its electrical resistance changes. Bolometers can be combined with area sensors, however they are quite insensitive and are not suitable for a coherent detection unlike the triggered methods mentioned above are.

**Systems for THz imaging:** Besides bolometer-based detection, which is quite insensitive, THz detectors are inapplicable for practically usable arrays because of their cost. Thus, two-dimensional scans have to be used to capture test objects, which is still very time consuming [138].

The methods for generating and detecting THz radiation, which use ultra-short laser pulses and for which there is a fixed temporal relation between the laser pulse and the THz pulse, allow the realization of coherent THz imaging systems with extremely high signal-to-noise ratios: up to  $10^6$  [138]. In this way, the synchronization between the laser and the THz pulses as well as the possibility of optically clocking the detectors with the laser light can be used. The ultra-short laser pulses have a typical duration between 20 and 100 fs for a repetition rate of 10 to 100 MHz.

Figure 7.110 shows an example of the setup of a THz imaging system. The laser light is split into two halves by a beam splitter. The first half generates the coherent THz radiation, the second half is sent to the PCA acting as the receiver over a variable delay line, which allows varying of the optical path length and thus the time of flight. Hence, the detector and the THz pulses are synchronously activated for very short periods of time. As the laser pulse is much shorter than the THz pulse, and as the laser pulse on the detector can be shifted relative to the THz pulse by the variable delay line, the THz pulse can be temporally sampled, so that the amplitude, the time of flight, and the spectrum of the THz pulse can be measured.

Depending on the wavelength and the bandwidth of the THz radiation, the attainable spatial **resolution** ranges from centimeters down to submillimeters [138, 162]. Figure 7.111 shows an example of an application where contaminants in chocolate are detected [123].

**THz imaging using the compressed sensing approach:** An alternative to the time-sequential scanning with a mechanical movement of the test object and to a costly sensor array is the **compressed sensing** approach [33, 175]. Figure 7.112 illustrates this principle.

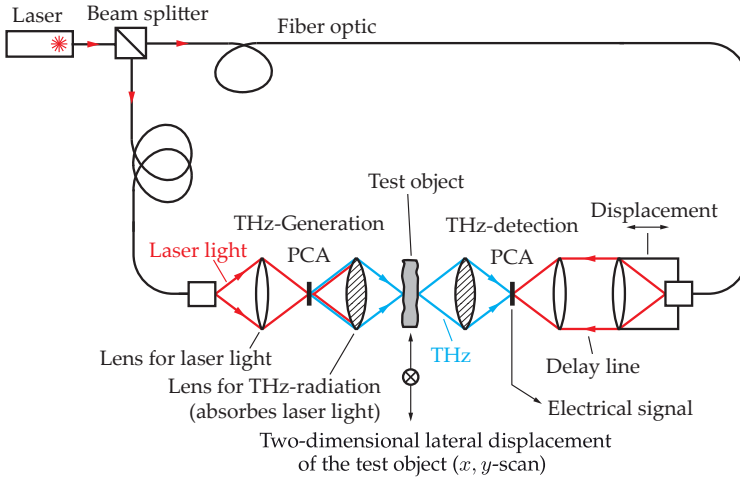


Figure 7.110. Setup of a THz imaging system using PCAs.

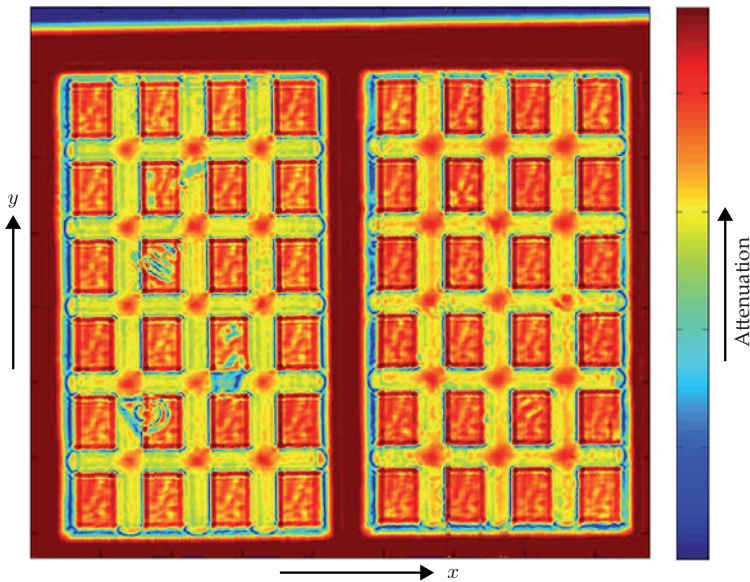


Figure 7.111. THz image of chocolate bars. Left: Multiple contaminants of metal, glass, and plastics. Right: A reference object without contaminants [123]. The pseudo colors show the spatial distribution of the absorption coefficients, measured in transmission (source: D. Nüßler, Fraunhofer FHR [123]).

The test object is illuminated with THz radiation through a THz-transparent lens L1. Another lens L2 focuses the intensity  $i(x)$ , which has passed through the test object, onto a mask. This mask contains variable elements that can be set either to be transparent or absorbing. The radiation which is able to pass the mask through the transparent elements is focused by the lens L3 onto a THz detector in the form of a point sensor. The scalar measurement  $I$  corresponds to an integral over the intensities reaching L3 through the transparent

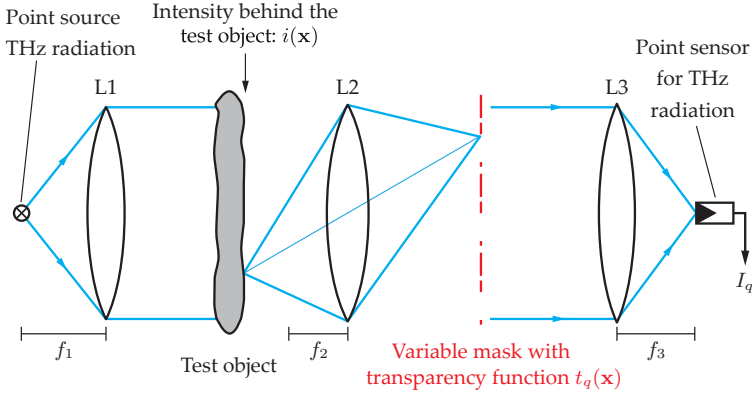


Figure 7.112. Principle of THz imaging using compressed sensing approach.

elements of the mask. Compressed sensing uses many measurements with different configurations  $q = 1, \dots, Q$  of the mask. The resulting  $I_q$ -tuple of measurements gives information about the properties of the test object.

As an alternative to the setup with lenses, reflectors can also be used to construct an imaging system. The mask could as well be realized in the form of an array of addressable micro-mirrors in combination with appropriately arranged reflectors.

Mathematically speaking, the process of the measurement can be described as follows:  $\mathbf{i} := \text{col}\{i(\mathbf{x})\} \in \mathbb{R}^{N^2}$  is assumed to be the column vector of the intensity which has passed through the test object, and  $\mathbf{t}_q := \text{col}\{t_q(\mathbf{x})\} \in [0, 1]^{N^2}$  the transparency vector of the variable mask in configuration  $q$ , in which an  $N \times N$  alignment of the image points is employed. All configurations of the mask are represented by the transparency matrix  $\mathbf{T} := (\mathbf{t}_1, \mathbf{t}_2, \dots, \mathbf{t}_Q)^T \in [0, 1]^{Q \times N^2}$ . The measured intensities are denoted by  $\mathbf{I} = (I_1, \dots, I_Q)^T \in \mathbb{R}^Q$ . A measurement using the mask's configuration  $q$  can now be expressed as follows:

$$I_q \propto \sum_{\mathbf{x}} t_q(\mathbf{x}) i(\mathbf{x}) = \mathbf{t}_q^T \mathbf{i}. \tag{7.155}$$

The intensity vector  $\mathbf{I}$  is given by

$$\mathbf{I} = \mathbf{T} \mathbf{i}. \tag{7.156}$$

If the transparency vectors  $\{\mathbf{t}_q | q = 1, \dots, Q\}$  are linearly independent, they span a  $Q$ -dimensional vector space. The formation of the intensity vector  $\mathbf{I}$  corresponds to a projection of the signal  $\mathbf{i}(\mathbf{x})$  onto this vector space. Compressed sensing now chooses a  $Q \ll N^2$  and achieves a sufficient reconstruction of the signal  $\mathbf{i}(\mathbf{x})$  by choosing an adequate  $\{\mathbf{t}_q\}$ . The reconstruction  $\hat{\mathbf{i}}$  can be calculated using the pseudoinverse  $\mathbf{T}^T(\mathbf{T}\mathbf{T}^T)^{-1}$  from (7.156):

$$\hat{\mathbf{i}} = \mathbf{T}^T(\mathbf{T}\mathbf{T}^T)^{-1}\mathbf{I}. \tag{7.157}$$

The use of the pseudoinverse is required, as (7.156) is, when  $Q < N^2$ , an underdetermined system of equations for  $\mathbf{i}$ .

It is necessary to choose a basis of functions  $\{t_q(\mathbf{x}) \mid q = 1, \dots, Q\}$  that is appropriate for the expected test objects, so that  $Q \ll N^2$  allows a suitable reconstruction. Instead of  $N^2$  scan iterations, only  $Q$  recordings are needed, without any mechanical movement. Only the configuration of the transparent mask has to be varied.

Such a system is also called a single-pixel camera [33]. Of course, the principle of compressed sensing can be applied to any other frequency band of the electromagnetic spectrum.

#### 7.4.6 Photoelasticity

Methods based on photoelasticity are used for optically visualizing and measuring the mechanical states of stress in transparent materials. These methods have been known for quite some time.<sup>17</sup> Originally, transparent models of real structural components were qualitatively inspected under stress and their stress distributions were then quantitatively measured. However, for quantitatively measuring the stress, the state of stress has to be biaxial.<sup>18</sup> The classical model-based visualization of tension has meanwhile been replaced by FEM calculations.<sup>19</sup> These computed simulations have a significantly lower cost and are not limited to biaxial states of stress.

Nowadays, photoelasticity methods are used in automated visual inspection for the fast inspection of transparent components for internal stresses and tension distributions under stress. Instead of designing models, the actual elements are inspected. In general, they have neither biaxial states of stress nor prismatic geometries, so that things are much more complicated.

Photoelasticity allows both a fast, qualitative inspection and a quantitative 3D reconstruction of the stress state. During a qualitative inspection, high stress gradients (high tensions) can be identified from the high density of stripes (i.e., a large number of stripes) in a photoelasticity image, cf. Fig. 7.115 on page 342. The quantitative 3D reconstruction of a triaxial state of stress can be achieved by using the methods of tensor tomography [146,167]. As these methods are very complicated, only the qualitative detection is covered in this book.

The principle of photoelasticity relies on the fact that certain transparent materials become birefringent under mechanical stress, whereas they show homogeneous and isotropic refraction in their unstressed state (see also Sec. 2.2.2.4 for birefringence). This effect is called stress induced birefringence. For example, birefringence arises for glass, Plexiglas<sup>20</sup> and synthetic resin.

Instead of the scalar, spatially independent index of refraction  $n$  for the unstressed state, a symmetric tensor  $\mathbf{N}$  has to be used for the index of refraction in the stressed state:

$$\mathbf{N} = \begin{pmatrix} n_x & n_{xy} & n_{xz} \\ n_{xy} & n_y & n_{yz} \\ n_{xz} & n_{yz} & n_z \end{pmatrix}. \quad (7.158)$$

For isotropic refraction, the scalar index of refraction  $n$  corresponds to a refraction tensor  $\mathbf{N} = n \mathbf{I}$  with  $\mathbf{I}$  denoting the identity matrix.

<sup>17</sup>They were first described by the Scottish physicist David Brewster [26,27].

<sup>18</sup>The total applied stress consists of two superposed tensions in perpendicular directions.

<sup>19</sup>The finite element method

<sup>20</sup>In Europe, Plexiglas<sup>®</sup> is a registered trademark of Evonik Industries AG.



The stress state in a three-dimensional body is described by the stress tensor  $\mathbf{S}$ , which can also be represented by a symmetric  $3 \times 3$  matrix [18]:

$$\mathbf{S} = \begin{pmatrix} \sigma_x & \tau_{xy} & \tau_{xz} \\ \tau_{xy} & \sigma_y & \tau_{yz} \\ \tau_{xz} & \tau_{yz} & \sigma_z \end{pmatrix}. \tag{7.159}$$

The diagonal elements  $\sigma_i$  are called the normal stresses, and describe the stress state perpendicular to an intersecting plane with the normal vector  $\mathbf{e}_i$ ,  $i \in \{x, y, z\}$ . The normal stresses result from tensile tensions, pressure, or bending (Fig. 7.113). The shear stresses  $\tau_{ij}$  are directed in the direction  $\mathbf{e}_j$ , tangential to the intersecting plane perpendicular to  $\mathbf{e}_i$ ,  $i, j \in \{x, y, z\}$ . They result from shear or torsion. The stresses describe the force affecting a spatial element of the object per area, and are measured in units of  $\text{N}/\text{m}^2$ . In the case of a biaxial stress state, all stresses perpendicular to a plane vanish, resulting in  $\sigma_z = \tau_{xz} = \tau_{yz} = 0$  [177].

In general, the tensor  $\mathbf{S}$  describes a triaxial stress state. By means of the principal axis transformation (principal component analysis, see Sec. 8.7),  $\mathbf{S}$  can be represented as a diagonal matrix. The tensor is transformed into the coordinate system of its eigenvectors. In this coordinate system, all shear stresses disappear:

$$\tilde{\mathbf{S}} = \begin{pmatrix} \sigma_1 & 0 & 0 \\ 0 & \sigma_2 & 0 \\ 0 & 0 & \sigma_3 \end{pmatrix}. \tag{7.160}$$

The eigenvalues  $\sigma_1 \geq \sigma_2 \geq \sigma_3$  are called the principal stresses. The corresponding eigenvectors  $\boldsymbol{\epsilon}_1$ ,  $\boldsymbol{\epsilon}_2$  and  $\boldsymbol{\epsilon}_3$  are directed along the principal axes. The normal stress reaches its maximum  $\sigma_1$  (its minimum  $\sigma_3$ ) for the intersection plane with the normal vector  $\boldsymbol{\epsilon}_1$  (respectively  $\boldsymbol{\epsilon}_3$ ).

The stress tensor  $\mathbf{S}$  and the index of refraction tensor  $\mathbf{N}$  have the same principal axes. The two tensors are related as follows [2, 146, 167]:

$$\mathbf{N} = n \mathbf{I} + A \text{trace}(\mathbf{S}) \mathbf{I} + B \mathbf{S}. \tag{7.161}$$

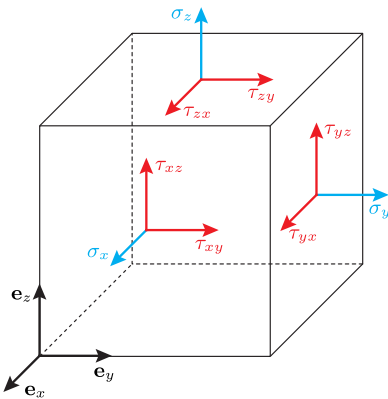


**Figure 7.113.** Stress state of a volume element. The equilibrium conditions of the torque around the coordinate axis result in  $\tau_{xy} = \tau_{yx}$ ,  $\tau_{xz} = \tau_{zx}$ ,  $\tau_{yz} = \tau_{zy}$ .

Here,  $n$  is the scalar index of refraction of the unstressed material and  $A$  and  $B$  are photoelasticity material constants. Usually, the stress tensor  $\mathbf{S} = \mathbf{S}(x, y, z)$  as well as the index of refraction tensor  $\mathbf{N} = \mathbf{N}(x, y, z)$  are functions of the position  $\mathbf{x} = (x, y, z)^T$ . Such spatially variant tensors are called tensor fields. In accordance with (7.161), the stress tensor field can be calculated from the index of refraction tensor field measured with photoelasticity methods [146].

For an illumination with a plane light wave propagating in the  $z$ -direction, only those components of the index of refraction tensor are effective that are perpendicular to  $\mathbf{e}_z$ . In this case, the refraction can be characterized by a reduced index of refraction tensor  $\mathbf{N}_z$ , which can be written as a  $2 \times 2$  matrix:

$$\mathbf{N}_z = (\mathbf{e}_x, \mathbf{e}_y)^T \mathbf{N} (\mathbf{e}_x, \mathbf{e}_y) \quad \text{with} \quad \mathbf{e}_i^T \mathbf{e}_j = \delta_{ij}, \quad i, j \in \{x, y, z\}. \quad (7.162)$$

The principal axis transformation of  $\mathbf{N}_z$  yields the slow and fast axes of the birefringence in the  $\mathbf{e}_x, \mathbf{e}_y$ -plane (cf. Sec. 2.2.2.4). The eigenvalues are the corresponding indices of refraction  $n_s$  and  $n_f$  with  $n_s > n_f$  [2, 146, 167].

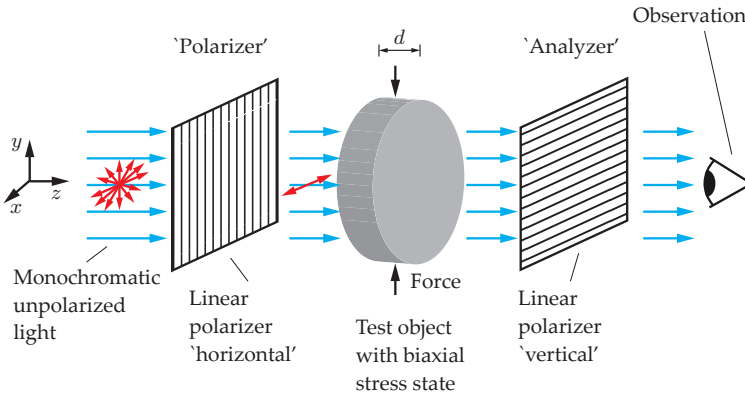


Figure 7.114. Polariscope with crossed linear polarizers.

Classic photoelasticity requires a biaxial ('planar') stress state. These stresses only affect the directions parallel to the  $x, y$ -plane and are independent of  $z$ . The inspection is carried out in the  $z$ -direction. The simplest variant of a 'polariscope' as shown in Fig. 7.114 uses dark-field illumination. The monochromatic illumination passes through the polarizer, the transparent test object, the analyzer, and finally reaches the observer. In an unstressed state, the test object does not change the linear polarization state of the incident light, so that it is blocked by the analyzer which is rotated by  $90^\circ$  with respect to the polarizer. The result is a homogeneous, dark image. Mechanically stressing the test object induces birefringence, which usually transforms the linearly polarized light into elliptically polarized light. A part of this light can now pass the analyzer, so that bright structures can be observed.

For a transmittance  $T$  with respect to the light intensity, the following holds for the polariscope from Fig. 7.114 [56, 145]:

$$T \propto \sin^2(2\gamma) \sin^2 \left( \frac{C d \pi}{\lambda} (\sigma_1 - \sigma_2) \right). \quad (7.163)$$

Here,  $C$  is another photoelasticity material constant,  $d$  the thickness of the object in the  $z$ -direction,  $\lambda$  the wavelength of the monochromatic light, and  $\gamma$  is the angle between the polarizer's polarization direction and one of the two principal stress directions  $\epsilon_1$  or  $\epsilon_2$  [115, 145]. Because of  $\sin^2(2\gamma) = \sin^2(2(\frac{\pi}{2} - \gamma))$  it is of no importance which of the two orthogonal principal stress directions is chosen.

In the image, dark lines arise at positions where the transmittance  $T$  reaches zero, which represent the zeros of one of the two  $\sin^2$  terms:

— **Isoclines** arise for

$$\sin^2(2\gamma) = 0 \quad \Leftrightarrow \quad 2\gamma = k\pi \quad \Leftrightarrow \quad \gamma = k\frac{\pi}{2}, \quad k \in \mathbb{Z}. \quad (7.164)$$

Isoclines<sup>21</sup> connect the points  $(x, y)$  where the principal stress direction  $\epsilon_1(x, y)$  equals the direction of the polarizer and the principal stress direction  $\epsilon_2(x, y)$  equals the direction of the analyzer, or vice versa. If the polarizer and the analyzer are in a crossed state, and are simultaneously rotated, the isoclines move. Systematically moving the polarizer and the analyzer while maintaining their crossed state allows capturing an image series that can be used to reconstruct the field of directions of the principal stresses and thus the lines of the principal stresses: for each point of an isocline, the principal stress direction is given by the angle  $\gamma$  of the polarized light—and the second one is orthogonal [177].

— **Isochromates** are given for

$$\sin^2\left(\frac{C d \pi}{\lambda} (\sigma_1 - \sigma_2)\right) = 0 \quad (7.165)$$

$$\Leftrightarrow \frac{C d \pi}{\lambda} (\sigma_1 - \sigma_2) = k\pi \quad (7.166)$$

$$\Leftrightarrow \sigma_1(x, y) - \sigma_2(x, y) = k \frac{\lambda}{C d}, \quad k \in \mathbb{Z}. \quad (7.167)$$

With an increasing gradient of the principal stress differences, the isochromates are spatially denser. The isochromates represent the 'contours' of the 'stress mountains' [145]. By quantitatively evaluating the stripe pattern of the isochromates, the difference between the principal stresses  $\sigma_1 - \sigma_2$  can be quantitatively determined. Therefore, the isochromates are counted, starting from the 'zero isochromate,' which corresponds to the unstressed state with  $k = 0$ . The principal stress difference is equal to the maximum shear stress  $\tau_{\max}$  (principal shear stress), which plays an important role in tests for stability [177].

The isochromates remain unchanged if the polarizer and analyzer are simultaneously rotated. Using white instead of monochromatic light leads to different stripe patterns for each wavelength because of the wavelength dependence of (7.163). These stripe patterns are superposed to a colored stripe image. This effect is the origin of the term isochromate. Only the isochromate for  $k = 0$  is independent of the wavelength and is thus visible as a dark line also for white light.

If additional  $\frac{\lambda}{4}$  retardation plates are placed behind the polarizer and in front of the analyzer of the polariscope of Fig. 7.114, which are rotated by the angle  $\alpha = \frac{\pi}{4}$  around the

<sup>21</sup>Generally, isoclines and isochromates are defined as the lines of constant angle  $\gamma$  (constant difference between the principal stresses  $\sigma_1 - \sigma_2$ ). But as the zeros of the two  $\sin^2$  terms result in clearly visible line structures, here isoclines and isochromates are defined as the zero lines of the two  $\sin^2$  terms.

polarizer's polarization direction, circularly polarized light illuminates the test object. Therefore, the factor  $\sin^2(2\gamma)$  in (7.163) is averaged to a nonzero constant, so that there are no more isoclines and the isochromates remain isolated.

There are numerous other variants of polariscopes, which use linearly or circularly polarized light, operate with transmitted or reflected light, and with dark field or bright field illumination [177]. For example, the polariscope from Fig. 7.114 can be used with bright field illumination if the analyzer is rotated by  $90^\circ$ , so that the forward directions of the polarizer and the analyzer are equal.

In automated visual inspection, the analysis of stresses in transparent models of real components is hardly interesting. Rather, the stresses caused by tensions or by internal stress in transparent test objects consisting of birefringent material are to be visualized and evaluated. Examples include components made out of glass or transparent plastics. However, in general, these are triaxial stress states which are much harder to measure. The photoelasticity effect in the direction of observation is integrated. Additional difficulties arise if the test object does not possess a prismatic geometry. Then its interfaces cannot be arranged to be perpendicular to the light rays, which means that the light is refracted. Thus, it will not be parallel to the polariscope's optical axis inside as well as outside the object. If the stress states are supposed to be reconstructed for each point, tensor tomography has to be used [2, 146, 167]. Here, the object has to be placed in an immersion bath with an index of refraction adequate to avoid refraction, and an image series of different rotations of the object has to be recorded (cf. Sec. 7.4.2 and 7.5). Thus, a 3D reconstruction of the stress state is very costly.

For a qualitative photoelasticity analysis, the stripe image of the test object can be compared to stripe images of reference objects. Another possibility for defect detection is searching for regions with a high local stripe density. To evaluate the stripe images of isoclines and isochromates, methods similar to moiré methods can be used [10, 47].

---

**Example 7.12 (Photoelasticity inspection of a lens):** The lens blank of Fig. 7.115(a) is to be inspected using photoelasticity. The image acquisition uses a scanning system that can

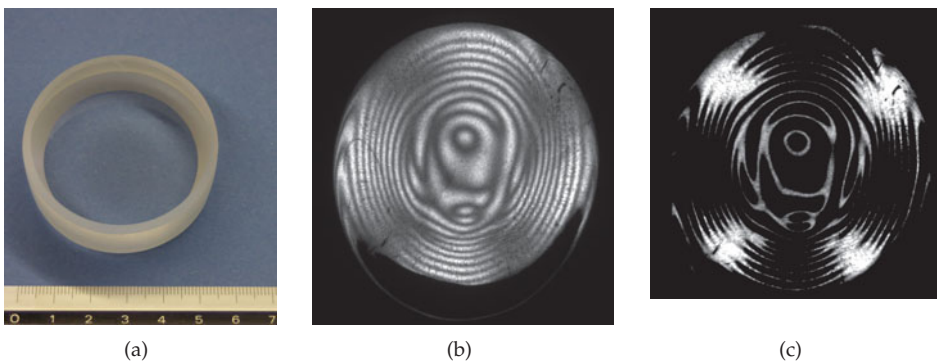


**Figure 7.115.** Inspection of a lens blank using photoelasticity: (a) Photograph of the test object together with a cm scale in order to visualize the dimensions; (b) Total intensity of a photoelasticity image; (c) Photoelasticity images for crossed polarizers.

simultaneously capture the light for parallel and crossed polarizers. Monochromatic laser light is used as illumination, which is linearly polarized by the polarizer. The image 7.115(b) is the result of the summed intensities for the parallel and crossed polarizers, whereas Fig. 7.115(c) only shows the component of the crossed polarizer and analyzer, as in the setup of Fig. 7.114. The asymmetric lines might be a sign of an inhomogeneous stress distribution. In addition to the test for stress, defects like entrained bubbles or inclusions can be detected in the intensity image. ■

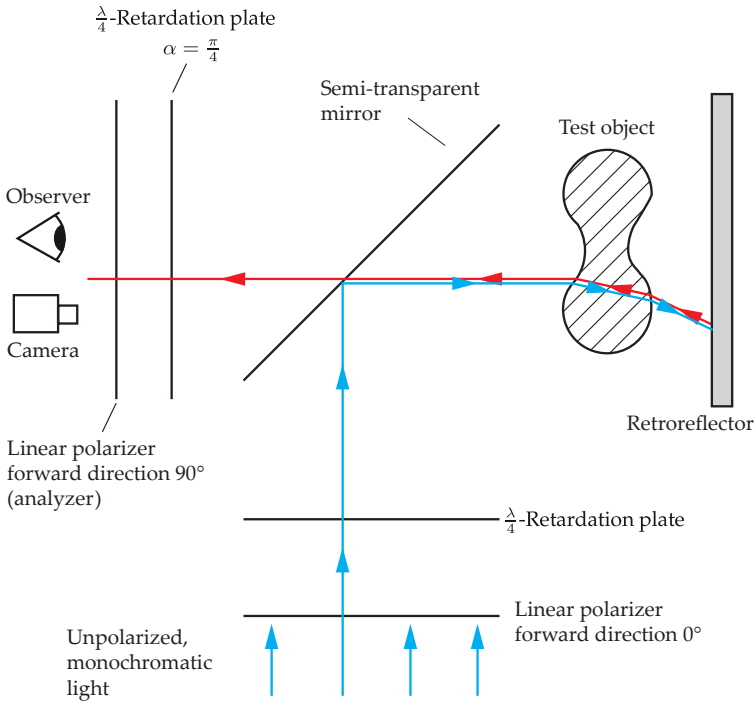
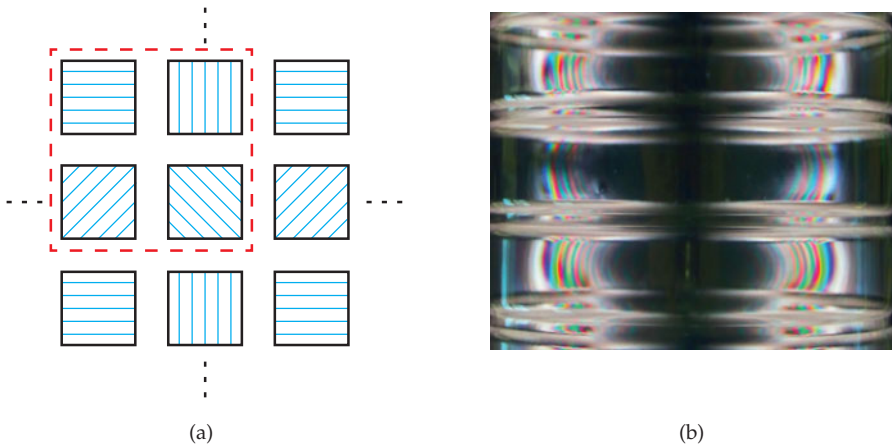


Figure 7.116. Polariscope for automated visual inspection.

Figure 7.116 shows a setup for a polariscope used in automated visual inspection for qualitative defect detection. The polariscope uses circularly polarized light, so that no isoclines are visible and the dark lines correspond only to isochromates. In this case, reflections are observed. Because of the retroreflector, which conserves the polarization (see Sec. 7.3.10.3), the direction of the light on the observation side is parallel to the optical axis even for test objects without a prismatic shape, as the light propagates back along the same optical path. In this way, the refraction at the object's borders is compensated for (cf. Sec. 7.5).

**Example 7.13 (Camera with individual polarization filters per pixel):** The so-called POLKA of the Fraunhofer IIS is a CMOS camera having a linear polarization filter in front of every single pixel. The polarization filters are oriented at  $0^\circ$ ,  $45^\circ$ ,  $90^\circ$  or  $135^\circ$ ; see Fig. 7.117.

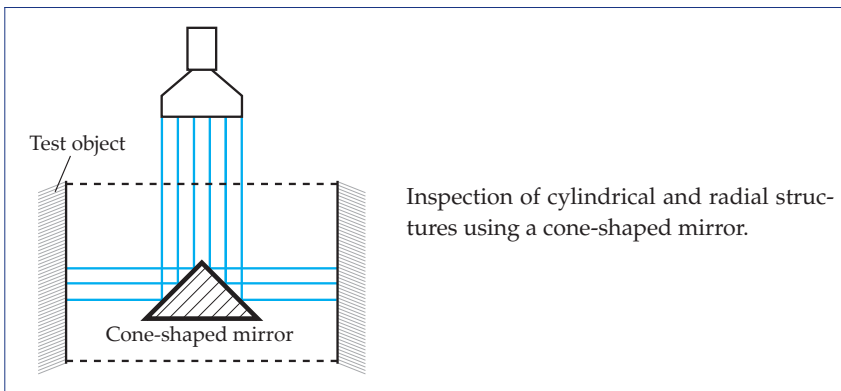
In order to obtain the full resolution of  $640 \times 480$  pixels for each of the four polarization channels, a spatial interpolation is applied to compensate for the spatial displacements

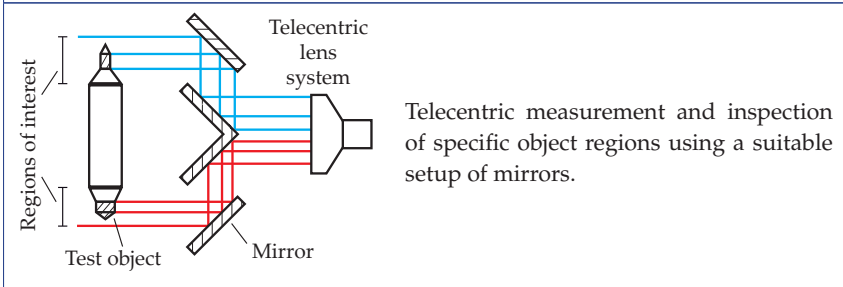
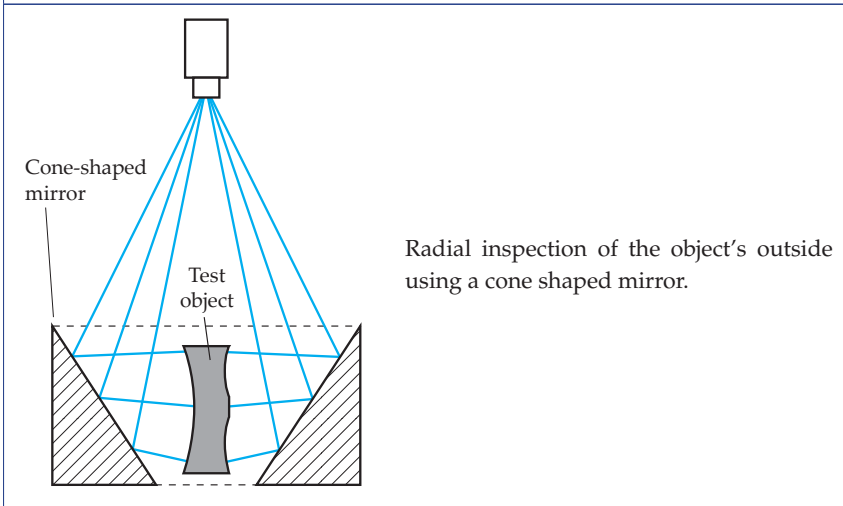
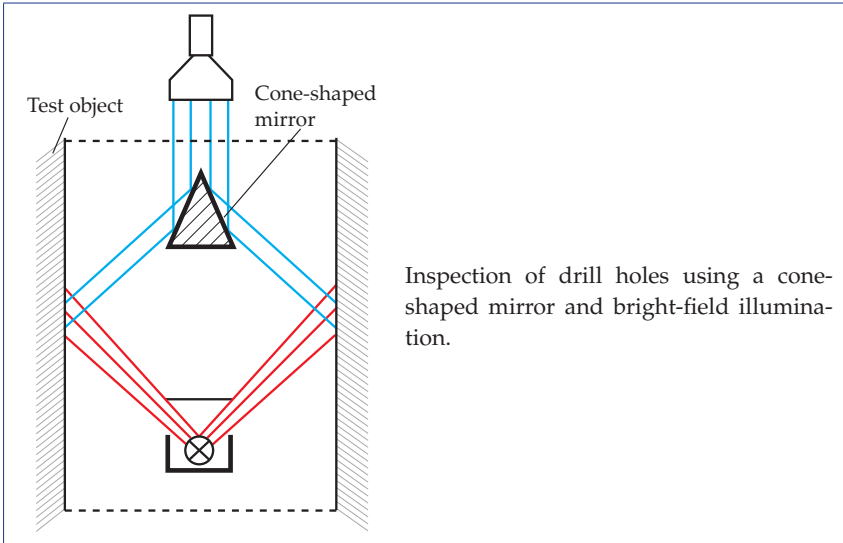


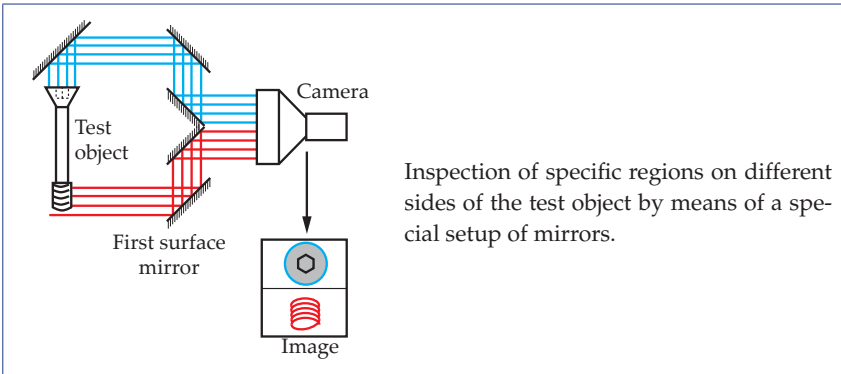
**Figure 7.117.** (a) Principle of the camera chip of the polarization camera POLKA. Groups of four adjacent camera pixels are equipped with individual linear polarization filters having the orientations of  $0^\circ$ ,  $45^\circ$ ,  $90^\circ$  and  $135^\circ$ ; (b) Transmission image of a plastic bottle (PET bottle) for linearly polarized illumination. The four channels are visualized as a false color image using CMYK color encoding. The polarization changes caused by mechanical stress are clearly visible (source: A. Nowak, Fraunhofer IIS Erlangen, Germany).

of the pixels and for their disjoint arrangement. This camera is capable of acquiring 100 images per second, allowing to partially determine the polarization state of the captured light; see Sec. 2.2.2.5. ■

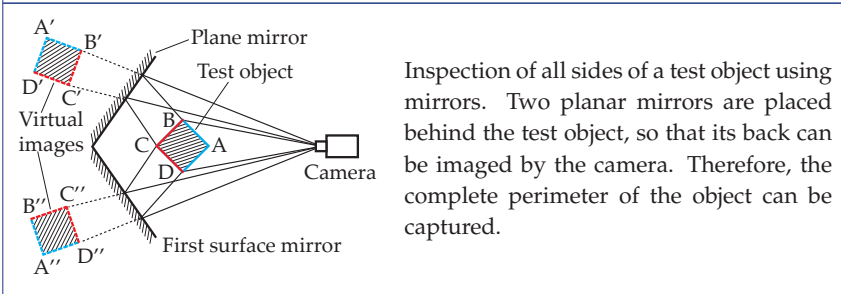
## 7.5 Special image acquisition methods



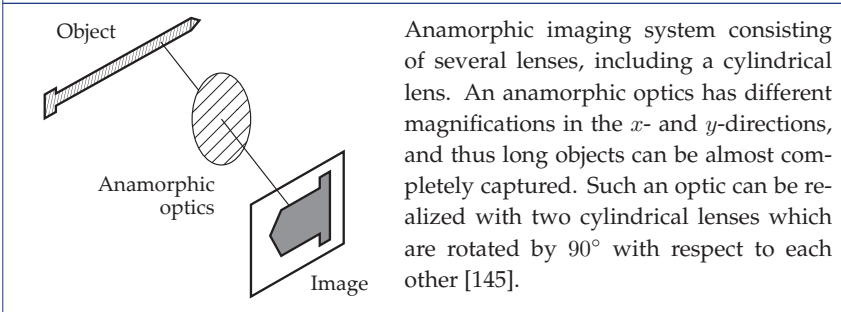




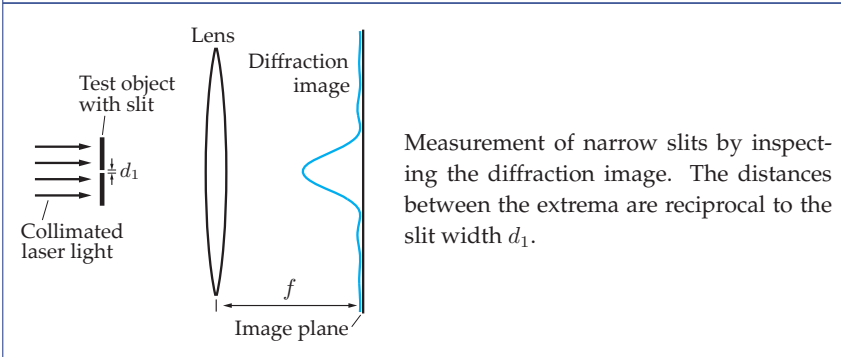
Inspection of specific regions on different sides of the test object by means of a special setup of mirrors.



Inspection of all sides of a test object using mirrors. Two planar mirrors are placed behind the test object, so that its back can be imaged by the camera. Therefore, the complete perimeter of the object can be captured.

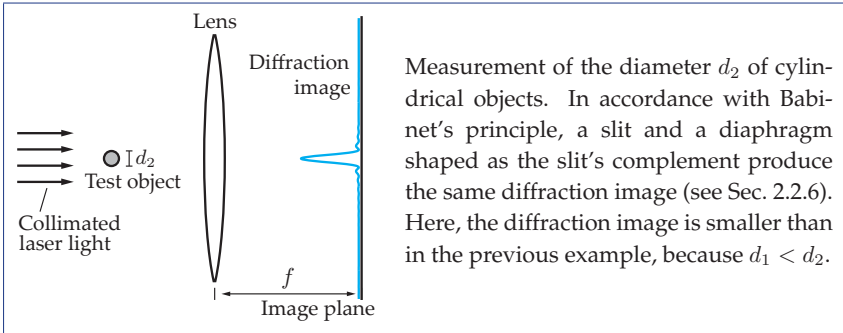


Anamorphic imaging system consisting of several lenses, including a cylindrical lens. An anamorphic optics has different magnifications in the  $x$ - and  $y$ -directions, and thus long objects can be almost completely captured. Such an optic can be realized with two cylindrical lenses which are rotated by  $90^\circ$  with respect to each other [145].

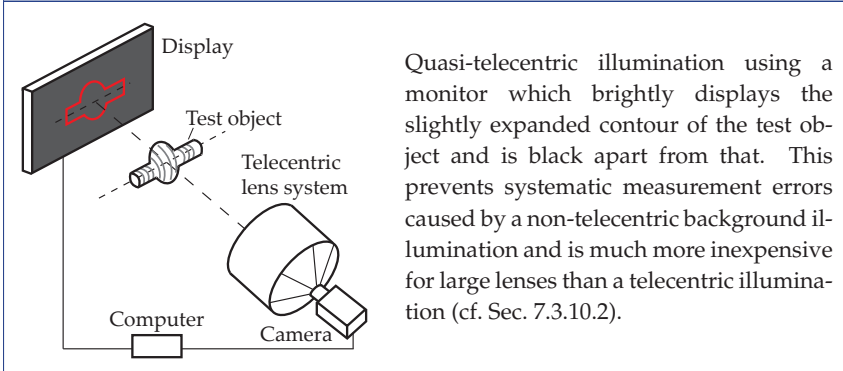


Measurement of narrow slits by inspecting the diffraction image. The distances between the extrema are reciprocal to the slit width  $d_1$ .

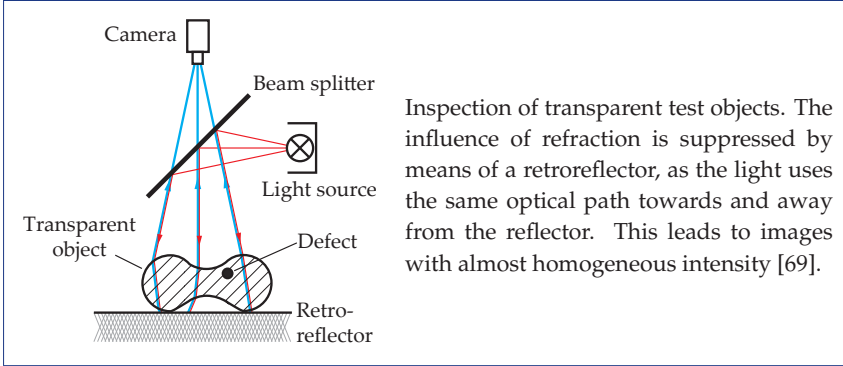




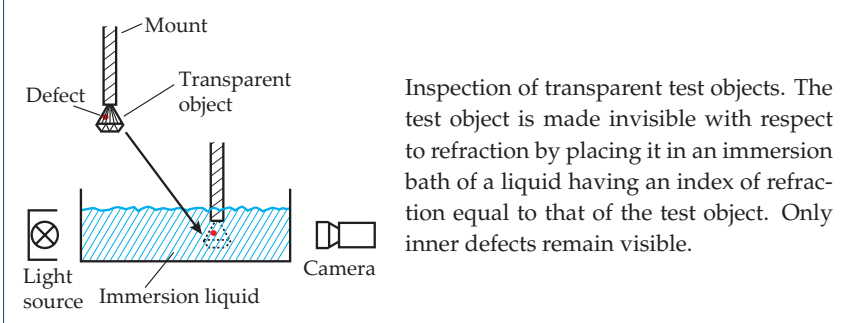
Measurement of the diameter  $d_2$  of cylindrical objects. In accordance with Babinet's principle, a slit and a diaphragm shaped as the slit's complement produce the same diffraction image (see Sec. 2.2.6). Here, the diffraction image is smaller than in the previous example, because  $d_1 < d_2$ .



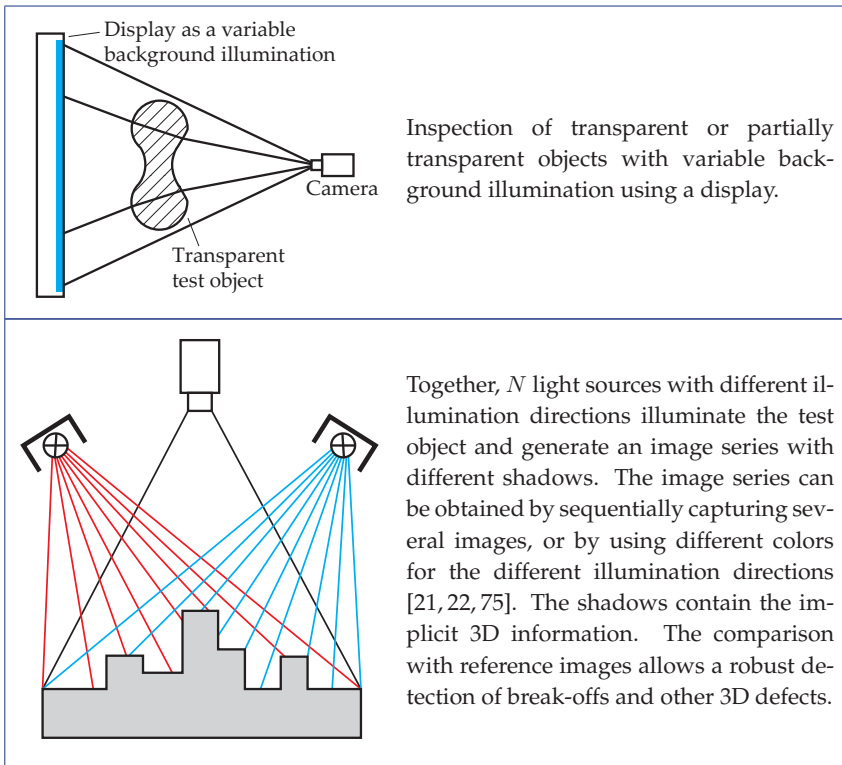
Quasi-telecentric illumination using a monitor which brightly displays the slightly expanded contour of the test object and is black apart from that. This prevents systematic measurement errors caused by a non-telecentric background illumination and is much more inexpensive for large lenses than a telecentric illumination (cf. Sec. 7.3.10.2).



Inspection of transparent test objects. The influence of refraction is suppressed by means of a retroreflector, as the light uses the same optical path towards and away from the reflector. This leads to images with almost homogeneous intensity [69].



Inspection of transparent test objects. The test object is made invisible with respect to refraction by placing it in an immersion bath of a liquid having an index of refraction equal to that of the test object. Only inner defects remain visible.



### ► 7.5.1 Image acquisition systems with variable illumination direction

For some inspection tasks, it is beneficial to vary the illumination direction. Figure 7.118 shows a possible system setup [62, 89]. The illumination is carried out by a video projector which is controlled by a computer. The divergent projection rays are parallelized by a collecting lens which is specifically arranged so that the projection center of the projector's lens system is located at the lens' focal point. Because of the size required, the use of a Fresnel lens as collecting lens is adequate. Such lenses are known from overhead projectors, which were common before the introduction of computer controlled projectors.

After the collecting lens, the illumination reaches a reflector which has the shape of an elliptic paraboloid. This reflector focuses the parallelized light to its focal point, where the test object is located. The reflector does not have to be a perfect mirror, as it is only used to redirect the light and not for the actual optical imaging. The illumination direction can now be varied by selectively turning on the corresponding projector pixels and by setting the remaining pixels to dark. In addition, an arbitrary light pattern can be projected, which is transformed into the corresponding field of illumination directions. The azimuthal as well as the elevation angle of the illumination direction are variable.

The camera is placed opposite to the projector and observes the object through a slit in the reflector. Depending on the task, the use of a telecentric lens might be beneficial. With this setup, image series with varying illumination directions can be captured with the

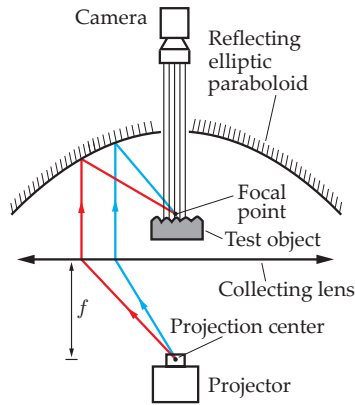


Figure 7.118. Image acquisition system with variable illumination direction.

image frequency of the camera. An example of such an image series has already been shown in Fig. 7.17. However, only objects that are small, compared to the projector's size, can be inspected in this way, as the intensity of the illumination drops rapidly outside the reflector's focal point.

Alternatively, variable illumination directions can be realized by means of arrays of light emitting diodes or a bright computer display [75, 112, 133].

### 7.5.2 Endoscopy

An endoscope is a slim optical system which can be inserted into a test object in order to capture images. Image acquisition is performed using a miniature camera inside the endoscope or by a camera which is placed outside and which receives the light through special imaging optics. For example, endoscopes with a panoramic view can be used to inspect drill holes [152]. Besides acquiring the image, often the endoscope has to also carry out the illumination of the object's interior. This can be achieved by including a light source within the endoscope or by using a separate instrument (Fig. 7.119).

The following operating principles of an endoscope are possible:

- 'Rigid' endoscopes: the image is transferred by a lens system to a camera placed outside the test object.
- 'Flexible' endoscopes: a bundle of optical fibers transfers the image through the endoscope to a camera placed outside the test object. The flexibility of the endoscope allows the inspection of interior spaces with complicated shapes.
- Endoscopes with a miniaturized camera: the camera is located directly on the top of the endoscope. The image is transferred electronically. Therefore, such an endoscope is also flexible. Because of the advancements in the miniaturization of cameras, such endoscopes are currently gaining popularity.
- Stereo endoscopes for capturing the 3D structures of interior spaces. However, stereo reconstruction is complicated by the very short stereoscopic base length, which is limited by the restrictions on the geometry of the endoscope (cf. Sec. 7.3.8). Another alternative

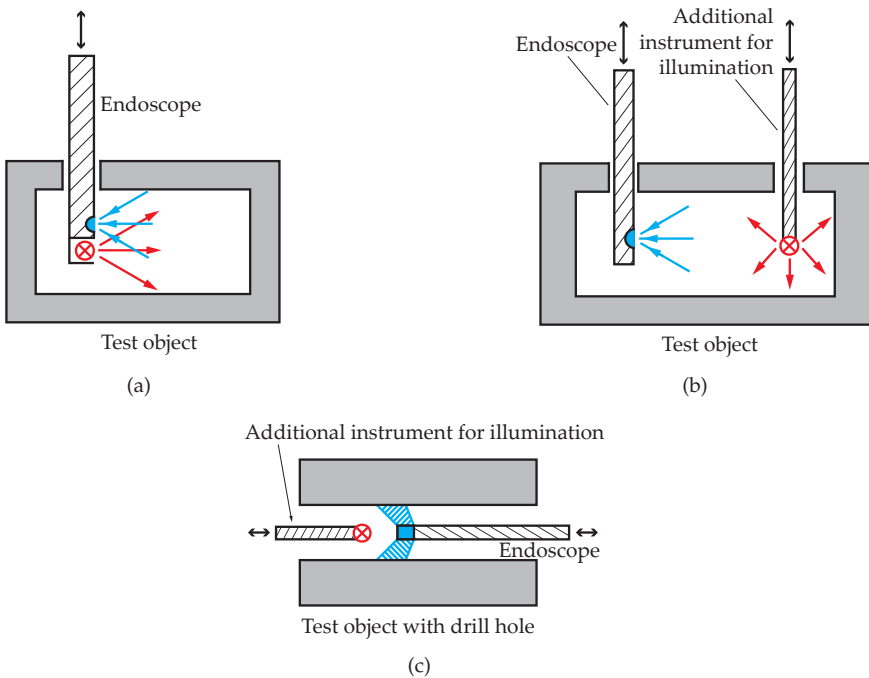


**Figure 7.119.** Examples of endoscopes: (a) Endoscope with integrated illumination; (b) Additional instrument for illumination; (c) Endoscope with panoramic view for the inspection of drill holes.

for 3D capturing is a stereo reconstruction from several images of a conventional endoscope undergoing specified displacements.

The necessary miniaturization of the optical elements and the tight spaces inside the inspected objects result in images with reduced quality. Especially endoscopes that are based on optical fibers have low resolution.

Because of the constellation of the image acquisition, it is often useful to enhance the image quality by a subsequent geometric correction (see Sec. 9.2.1). For example, a transformation into polar coordinates can be used in order to undistort panoramic images [152].

## 7.6 Universal principles

### 7.6.1 Suppression of extraneous light

Extraneous light constitutes a serious problem for the reproducibility and image quality of image acquisition in automated visual inspection. For example, sunlight shining through the windows of a workshop might cause overexposure and lead to unusable images, whereas objects lying in the shadow can show poor contrast.

Consequently, it is always beneficial for automated visual inspection to provide a controlled illumination that is adequate for the subsequent image processing steps. Therefore,

uncontrolled extraneous light usually constitutes a source of noise and its influence should be minimized.

Thus, the suppression of extraneous light is an important foundation for a robust visual inspection system. The following methods can be used for the suppression of extraneous light:

- **Isolation:** by isolating the visual inspection system from sunlight or the ambient illumination, a specific and reproducible illumination can be achieved.
- **Modulation** of the illumination and the corresponding demodulation at the sensor. Example: by a temporal sinusoidal modulation of the laser light source of a triangulation setup with the frequency  $f_0$  and by using an appropriate narrow-band electronic band-pass filter subsequent to the sensor, light not fluctuating with the frequency  $f_0$  is blocked.
- **High signal-to-noise ratio** by means of a high-leveled wanted signal. This is achieved by bright field illumination, for example. Another possibility is illumination with a flash and the use of a synchronized shutter.
- **Narrow-band illumination** (ideally, monochromatic) and narrow-band optical filters placed in front of the camera (cf. Sec. 5.3). By concentrating the illumination energy on a small wavelength band, a high signal-to-noise ratio can be achieved in that band. Optical filters that let only the desired band pass can be used in front of the camera. However, it is necessary that the test object have suitable reflectance properties in the chosen wavelength range.
- **Reference image** of the perturbations and consideration in the successive computational processing. The influence of extraneous light has to be constant for the time between the recording of the reference image and the actual image acquisition of the test object. If necessary, a reference image has to be captured immediately before each image acquisition, in order to capture the current extraneous light.

In the case of targeted illumination with a light source that can be turned on and off, a simple additional image can be captured with no artificial illumination in order to capture exclusively the extraneous light. Then the influence of the extraneous light on the actual images can be compensated for computationally.

Another approach is the estimation of the changed illumination conditions on the basis of the image data, without capturing special reference images.

An effective suppression of extraneous light usually facilitates further image processing steps and improves the quality of the results.

### ► 7.6.2 Inverse illumination

A carefully designed illumination setup can considerably simplify the processing of the captured images. The principle of inverse illumination is a way to acquire images that are easy to evaluate. Especially the differences between a test and a reference object can then be detected very quickly.

Since both, illumination and image acquisition are well adapted for a reference object, the resulting image  $g_{\text{ref}}(\mathbf{x})$  is easy to evaluate. This image can be characterized by a homogeneous intensity or a regular pattern, for example. Certain properties of the reference object are neutralized to a certain extent by the illumination. Differences between the investigated properties of the object result in significant variations in the observed image  $g_{\text{test}}(\mathbf{x})$ , which

can be robustly detected with simple image processing methods. In large part, feature extraction is done during image acquisition, so that the computational complexity of the image processing steps is reduced.

For certain objects, the dark field illumination of Sec. 7.2.3.3 can be considered as inverse illumination. An example are the mirrors shown in Fig. 7.19: an intact mirror ideally results in a homogeneous black image, whereas a scratch generates scattered light and is therefore highlighted.

Another application of inverse illumination is the **sorting of bulk goods**. Contaminants in bulk goods are to be detected and sorted out. The bulk good falls off a conveyor belt and is observed during the flight phase by a line camera or a color sensor. Pneumatic-driven nozzles are used for removing the contaminants. The nozzles are arranged in a line. If a contaminant is detected, it is blown into a separate bin by the appropriate nozzle. The nozzles have to be controlled in real time, while the material is falling. Thus, very efficient image processing methods are needed.

Possible sorting criteria are mainly the shape, the size and the spectral reflectance (or 'color') of the particles. High contrast images of reflectance differences can be recorded using inverse illumination: a line camera observes the bright field of a spectrally adjustable light source, see Fig. 7.120(a). A simple way to realize such a light source is with a computer display. The light source is configured to generate the same spectrum as the bulk goods with the desired properties. Additionally, the falling bulk goods are illuminated by white light from the observation direction. Ideally, the spectrum of the white light reflected by the bulk goods equals the light of the background light source, resulting in a homogeneous image. Contaminants with different reflectance are then clearly visible and can be much more easily detected than without inverse illumination (Fig. 7.120). Example applications are the sorting of food, plastic granulates, and minerals [16, 63].

For sorting bulk goods, a spatially homogeneous inverse illumination is used in order to neutralize the spectral reflectance of the reference particles and therefore also their presence in the camera image. Besides, a spatially variant inverse illumination is possible, which

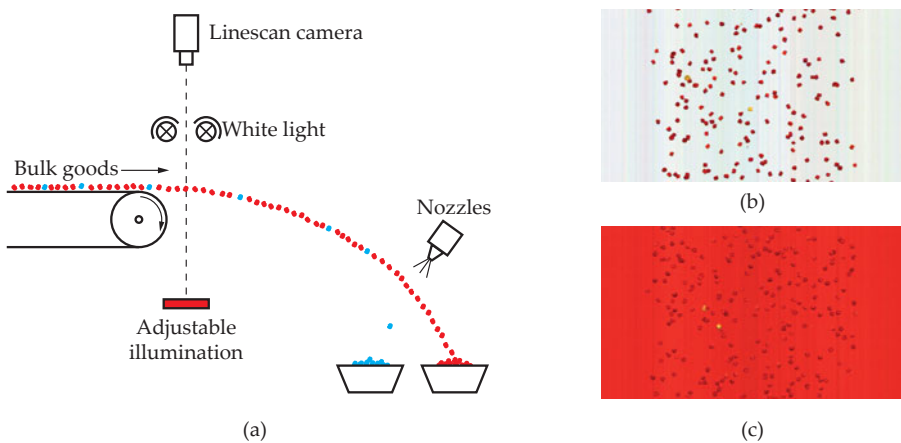


**Figure 7.120.** Inverse illumination for sorting bulk goods: (a) Sorting site with inverse illumination; (b) White light image of plastic granulates without adjusted background; (c) Image with inverse background illumination.

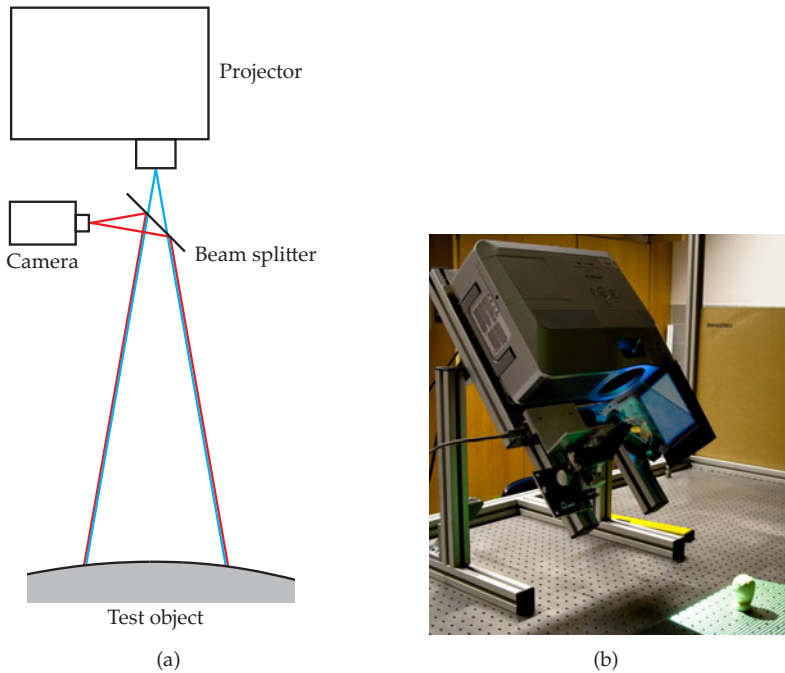
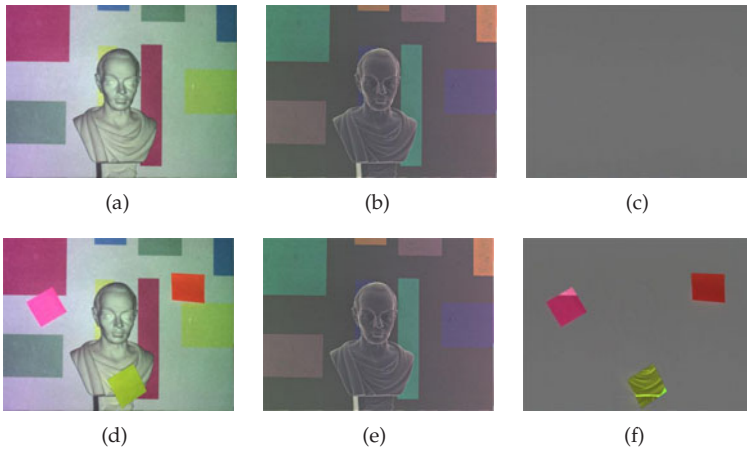


Figure 7.121. Setup for variable, coaxial inverse illumination.

could neutralize the inhomogeneous reflectance of a reference object, resulting in a homogeneous camera image. This can be realized by means of a video projector that illuminates the object through a semi-transparent mirror arranged coaxially to the camera (Fig. 7.121). The projected illumination is iteratively adjusted to the reference object by minimizing the observed difference from the desired homogeneous camera image [53, 61, 174]. Because of this adapted inverse illumination, the reference object is observed as an area of homogeneous intensity. Differences in the object's reflectance are visible with a high signal-to-noise ratio on this homogeneous area (Fig. 7.122).

Another degree of freedom of the illumination and image acquisition is the polarization. The polarization state of the light being reflected by an object mainly depends on its material properties (also see Sec. 7.2.1.2). The reflection of linearly polarized light on a metal surface results in light with a defined polarization state. If such a metal surface is illuminated with linearly polarized light, the reflected light remains linearly polarized. So the metal surface appears dark if a polarizer is placed in front of the camera whose polarization direction is perpendicular ('crossed') to the polarization direction of the reflected light, see Fig. 7.123(a). In accordance with the principle of inverse illumination, the result is a homogeneous dark image which can easily be tested for local anomalies. Especially non-metallic materials partially depolarize the light because of multiple inner reflections. This light is then only partially absorbed by the polarizer in front of the camera, so that non-metals appear bright in the camera image, see Fig. 7.123(b).



**Figure 7.122.** Examples of variable inverse illumination using the setup of Fig. 7.121: (a) Scene; (b) Projected inverse illumination; (c) Camera image; (d) Modified scene; (e) Projected inverse illumination (identical to (b)); (f) Corresponding camera image.

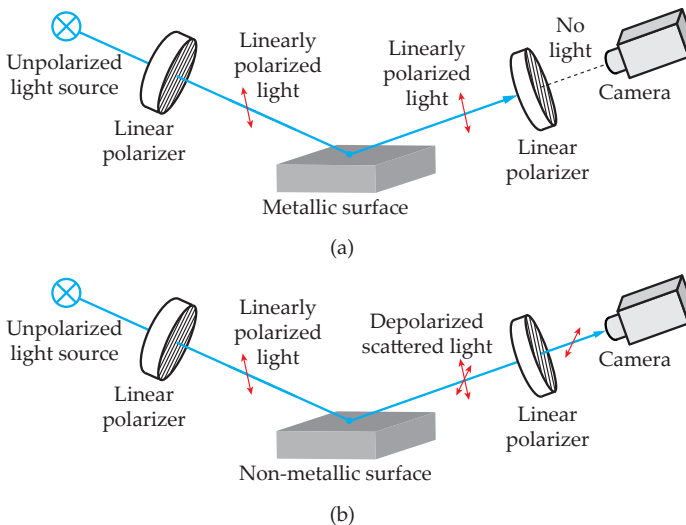


**Figure 7.123.** Discrimination of metals from non-metals by using polarization effects: (a) Linearly polarized light remains linearly polarized after being reflected by the surface of a metal and is therefore blocked by a crossed polarizer; (b) Non-metals partially depolarize the reflected light, so that it can partly pass the crossed polarizer.



**Example 7.14 (Inspection of sand cores):** An application of polarized inverse illumination is shown in Fig. 7.124. For the inspection of sand cores used for casting the cylinder heads of a four-valve engine, the metallic ring sockets of the valves have to be tested for contamination with sand. The sockets, made of tempered steel, are placed on the sand core before it is used to cast the cylinder head from aluminum. Thus, sand contaminants might lead to an incomplete bonding between the steel and the cast aluminum.

Under unpolarized illumination, sand and metal can barely be distinguished, as reflections of the sand cores are visible in the metal surface. By using inverse illumination, the metal surfaces appear dark and can be clearly separated from the sand. Sand fins on the metal can easily be detected. ■

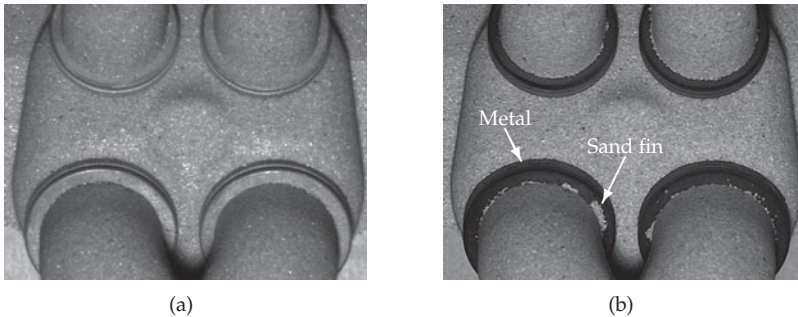


**Figure 7.124.** Polarized illumination for the detection of sand fins in the sand cores of combustion chambers: (a) Images acquired using unpolarized light; (b) Images acquired with linearly polarized illumination, observed through a polarizer crossed to the reflected light.

The principle of inverse illumination can also be applied to the 3D capturing that uses the principle of triangulation. In this case, inverse patterns adjusted for the specific object are used instead of the object-independent encoding sequences of the method of structured illumination (see Sec. 7.3.4.1). An inverse pattern can be projected for an areal triangulation, which appears as a regular stripe pattern in the perspective of the camera [105]. A similar approach can also be used for deflectometry: the inverse pattern reflected by the reference object appears as a regular stripe pattern. Defects result in a change in the regular structure, which is easy to detect. The inverse pattern can be calculated from the correspondence between the camera points and the screen points of the reference object [173]. Fig. 7.125 shows an example. The reflection of the inverse pattern (Fig. 7.125(d)) by an intact object with the desired geometry shows a regular stripe pattern (Fig. 7.125(b))—but the reflection by a defective, deformed object has distorted stripes (Fig. 7.125(c)). By computationally projecting the observed image column-by-column, an easy evaluation and defect detection is possible (Fig. 7.125(e), (f)). The vertical projection corresponds to the Radon transform for the angle  $\varphi = 0$ , see Chap. 14.

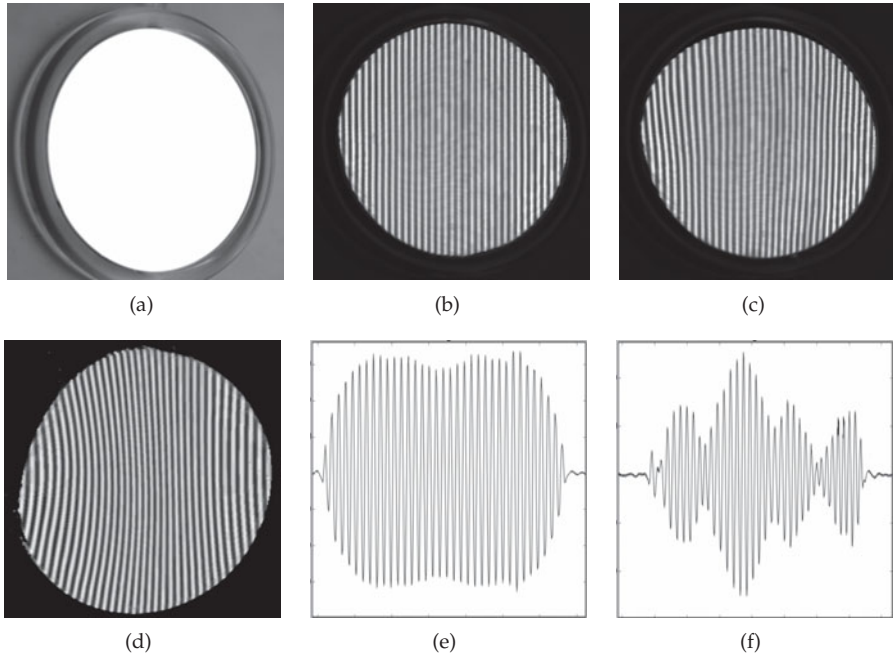


**Figure 7.125.** Inverse pattern for the deflectometric inspection of a magnifying mirror: (a) Reference object; (b) Deflectometric image of the intact reference object; (c) Deflectometric image of a deformed object, here, an arched mirror; (d) Inverse pattern displayed by the pattern generator; (e) Evaluation for the reference object, vertical projection of (b); (f) Evaluation for the deformed object, vertical projection of (c).

## 7.7 Summary

This chapter presented image acquisition methods for automated visual inspection. In order to select the most appropriate method, the first question to answer is which of the object's properties are relevant for the inspection task: the optical properties like reflectance and the complex index of refraction, or the object's geometry?

Figure 7.126 shows the taxonomy of the optical methods for capturing 3D shapes. The methods based on the principle of time of flight or focus have the advantage of allowing a coaxial scanning, i.e., regions can be measured which can only be reached through a small entrance, like a drill hole. This is not possible for triangulation or shading methods, as the different perspectives of illumination and observation that are necessary require a sufficiently large angle.

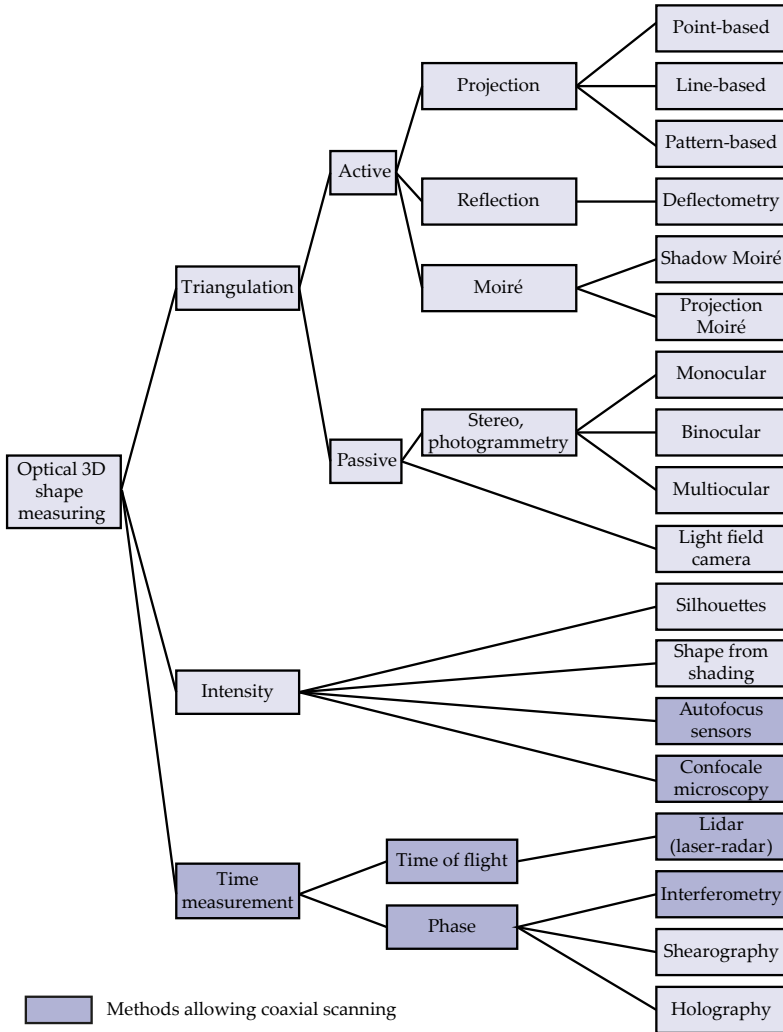


Figure 7.126. Taxonomy of the methods for optically capturing 3D shapes.

## 7.8 Bibliography

- [1] Bernd Aatz, Dieter Müller, and Heimo Weber. Interferometrisches Messen mechanischer Bauteile. In Bernd Breuckmann, editor, *Bildverarbeitung und optische Messtechnik in der industriellen Praxis*, pages 231–255. Franzis, 1993.
- [2] Hillar Aben. *Integrated photoelasticity*. McGraw-Hill, 1979.
- [3] Edward Adelson and James Bergen. The Plenoptic Function and the Elements of Early Vision. In Michael Landy and J. Anthony Movshon, editors, *Computational Models of Visual Processing*, pages 3–20. MIT Press, 1991.
- [4] Edward H. Adelson and John Y. A. Wang. Single Lens Stereo with a Plenoptic Camera. *IEEE Transactions on Pattern Analysis and Machine Intelligence*, 14(2):99–106, 1992.
- [5] Jochen Aderhold and Peter Meinlschmidt. Grundlagen der Infrarot-Thermographie. In Norbert Bauer, editor, *Handbuch zur Industriellen Bildverarbeitung*, pages 360–363. Fraunhofer IRB Verlag, Stuttgart, 1st edition, 2007.
- [6] Jochen Aderhold and Peter Meinlschmidt. Online-Thermographie als Werkzeug zur Qualitätskontrolle. In Norbert Bauer, editor, *Handbuch zur Industriellen Bildverarbeitung*, pages 364–368. Fraunhofer IRB Verlag, 1st edition, 2007.
- [7] Jochen Aderhold and Peter Meinlschmidt. Spektroskopische Charakterisierung von Oberflächen. In Norbert Bauer, editor, *Handbuch zur Industriellen Bildverarbeitung*, pages 145–151. Fraunhofer IRB Verlag, 1st edition, 2007.
- [8] Stephen Anderson. Optical Coherence Tomography. *SPIE Professional*, pages 16–19, 2014.
- [9] David Aspnes. The Accurate Determination of Optical Properties by Ellipsometry. In Edward Palik, editor, *Handbook of Optical Constants of Solids*, pages 89–112. Academic Press, 1985.
- [10] Anand Asundi. Photoelasticity and Moiré. In Pramod Rastogi, editor, *Optical Measurement Techniques and Applications*, pages 183–215. Artech House, 1997.
- [11] Jonathan Balzer. *Regularisierung des Deflektometrieproblems – Grundlagen und Anwendung*. PhD thesis, Universität Karlsruhe (TH), 2008.
- [12] Jonathan Balzer and Stefan Werling. Principles of Shape from Specular Reflection. *Measurement*, 43(10):1305–1317, 2010.
- [13] Bruce Batchelor, editor. *Machine Vision Handbook*. Springer, 2012.
- [14] Bruce Batchelor, Denys Hill, and David Hodgson, editors. *Automated visual inspection*. IFS, 1985.
- [15] Wilfried Bauer. Weißlichtinterferometrie. In Norbert Bauer, editor, *Handbuch zur Industriellen Bildverarbeitung*, pages 297–301. Fraunhofer IRB Verlag, 1st edition, 2007.
- [16] Sarah Bee and Mark Honeywood. Colour Sorting in the Food Industry. In Mark Graves and Bruce Batchelor, editors, *Machine vision for the inspection of natural products*. Springer, 2003.
- [17] Rolf Behrendt, Peter Schmitt, and Norman Uhlmann. Bildgebende Röntgensensoren. In Norbert Bauer, editor, *Handbuch zur Industriellen Bildverarbeitung*, pages 72–74. Fraunhofer IRB Verlag, 1st edition, 2007.
- [18] Wolfgang Beitz and Karl-Heinz Küttner, editors. *Dubbel Handbook of Mechanical Engineering*. Springer, 1994.
- [19] Roy Berns, Fred Billmeyer, and Max Saltzman. *Billmeyer and Saltzman's principles of color technology*. Wiley, 3rd edition, 2000.
- [20] Jürgen Beyerer and Denis Pérard. Automatische Inspektion spiegelnder Freiformflächen anhand von Rasterreflexionen. *Technisches Messen*, 64(10):394–400, 1997.
- [21] Jürgen Beyerer and Mohammed Seiraffi. Qualitätssicherung in Kernmachereien und Gießereien durch den Einsatz automatischer Sichtprüfungssysteme. *Gießerei-Praxis*, (6):245–254, 2000.
- [22] Jürgen Beyerer and Mohammed Seiraffi. Verfahren und Vorrichtung zur Objekterkennung. Patent PCT/DE1999/004070, 2000.

- [23] Jürgen Beyerer, Dirk vom Stein, and Thomas Klawitter. Automatische Sichtprüfung belüfteter Bremsscheiben. *Giesserei-Erfahrungsaustausch*, 47(7):283–286, 2003.
- [24] Stephan Bichmann. 3-D-Formprüfinterferometrie. In Norbert Bauer, editor, *Handbuch zur Industriellen Bildverarbeitung*, page 62. Fraunhofer IRB Verlag, 1st edition, 2007.
- [25] Gerra Bosco. James L. Waters Symposium 2009 on near-infrared spectroscopy: meeting report. *Trends in Analytical Chemistry*, 29(3):197–208, 2010.
- [26] David Brewster. Experiments on the depolarisation of light as exhibited by various mineral, animal, and vegetable bodies, with a reference of the phenomena to the general principles of polarisation. *Philosophical Transactions of the Royal Society of London*, 105:29–53, 1815.
- [27] David Brewster. On the communication of the structure of doubly refracting crystals to glass, muriate of soda, fluor spar, and other substances, by mechanical compression and dilatation. *Philosophical Transactions of the Royal Society of London*, 106:156–178, 1816.
- [28] Rainer Brodmann. Autofokussensor. In Tilo Pfeifer, editor, *Optoelektronische Verfahren zur Messung geometrischer Größen in der Fertigung*, pages 123–139. expert Verlag, 1993.
- [29] Rainer Brodmann and Walter Kimmelman. Streulichtsensor. In Tilo Pfeifer, editor, *Optoelektronische Verfahren zur Messung geometrischer Größen in der Fertigung*, pages 96–122. expert Verlag, 1993.
- [30] Joel G. Broida and S. Gill Williamson. *A comprehensive introduction to linear algebra*. Addison-Wesley, 1989.
- [31] Ilja Bronshtein, Konstantin Semendyayev, Gerhard Musiol, and Heiner Mühlig. *Handbook of Mathematics*. Springer, 6th edition, 2015.
- [32] Bundesamt für Strahlenschutz (Hrsg.). Verordnung über den Schutz vor Schäden durch Röntgenstrahlung (Röntgenverordnung – RöV). [http://www.bfs.de/de/bfs/recht/rsh/volltext/1A\\_Atomrecht/1A\\_14\\_RoeV\\_1011.pdf](http://www.bfs.de/de/bfs/recht/rsh/volltext/1A_Atomrecht/1A_14_RoeV_1011.pdf), 2011.
- [33] Wai Chan, Kriti Charan, Dharmpal Takhar, Kevin Kelly, Richard Baraniuk, and Daniel Mittleman. A single-pixel terahertz imaging system based on compressed sensing. *Applied Physics Letters*, 93(12):121105, 2008.
- [34] CMDITR Photonics Wiki. Terahertz Radiation. <http://www.photonicswiki.org>, 2010.
- [35] Edward Collett. *Field guide to polarization*. SPIE Press, 2005.
- [36] Katherine Creath. Phase-Measurement Interferometry Techniques. In Emil Wolf, editor, *Progress in Optics*, volume 26, pages 349–393, 1988.
- [37] Charles Curtis. *Linear algebra: an introductory approach*. Springer, 1993.
- [38] René Dändliker and Pierre Jacquot. Holographic Interferometry and Speckle Methods. In E. Wagner, R. Dändliker, and K. Spenner, editors, *Optical Sensors*, volume 6 of *Sensors*, pages 589–628. VCH, 1992.
- [39] Thao Dang. *Kontinuierliche Selbstkalibrierung von Stereokameras*. PhD thesis, Universität Karlsruhe (TH), 2007.
- [40] Colin Davies and Mark Nixon. A Hough Transform for Detecting the Location and Orientation of three-Dimensional Surfaces Via Color Encoded Spots. *IEEE Transactions on Systems, Man, and Cybernetics Part B*, 28(1):90–95, 1998.
- [41] Deutsches Institut für Normung, editor. *Gestaltabweichungen*. DIN 4760, Beuth, 1982.
- [42] *Optik und optische Instrumente - Bestimmung von Streustrahlung, hervorgerufen durch optische Komponenten*. DIN EN ISO 13696:2002-12, Beuth, 2002.
- [43] Deutsches Institut für Normung, editor. *Sicherheit von Lasereinrichtungen - Teil 1: Klassifizierung von Anlagen und Anforderungen*. DIN EN 60825-1; VDE 0837-1, Beuth, 2008.
- [44] Rainer Dohlus. *Photonik: Physikalisch-technische Grundlagen der Lichtquellen, der Optik und des Lasers*. Oldenbourg, 2010.
- [45] Axel Donges and Reinhard Noll. *Lasermesstechnik: Grundlagen und Anwendungen*. Hüthig, 1993.

- [46] Rainer Dorsch, Gerd Häusler, and Jürgen Herrmann. Laser triangulation: fundamental uncertainty in distance measurement. *Applied Optics*, 33(5):1306–1314, 1994.
- [47] Augusto Durelli and Vincent Parks. *Moiré analysis of strain*. Prentice Hall, Englewood Cliffs, NJ, 1970.
- [48] Olivier Faugeras and Quang-Tuan Luong. *The Geometry of Multiple Images*. MIT Press, 2001.
- [49] Thomas Finke. *Laserscanner in der automatischen Sichtprüfung*. PhD thesis, Universität Karlsruhe (TH), 1996.
- [50] Udo Flohr and Birte Schlund. Erst schießen, dann schärfen. *Technology Review*, (3):8–9, 2012.
- [51] David Forsyth and Jean Ponce. *Computer Vision – A Modern Approach*. Prentice Hall, Upper Saddle River, NJ, 2003.
- [52] Theobald Fuchs, Randolf Hanke, and Michael Maisl. Röntgenbasierte Methoden für die zerstörungsfreie Prüfung. In Norbert Bauer, editor, *Handbuch zur Industriellen Bildverarbeitung*, pages 316–321. Fraunhofer IRB Verlag, 1st edition, 2007.
- [53] Kensaku Fujii, Michael Grossberg, and Shree Nayar. A projector-camera system with real-time photometric adaptation for dynamic environments. In *Proc. IEEE Conference on Computer Vision and Pattern Recognition*, volume 1, pages 814–821, 2005.
- [54] James Fujimoto, Mark Brezinski, Guillermo Tearney, Stephen Boppart, Brett Bouma, Michael Hee, James Southern, and Eric Swanson. Optical biopsy and imaging using optical coherence tomography. *Nature Medicine*, 1(9):970–972, 1995.
- [55] Dennis Gabor. A New Microscopic Principle. *Nature*, 161(4098):777–778, 1948.
- [56] Martin-Mathias Gaupp. *Die digitale Bildverarbeitung als Hilfsmittel in der Spannungsoptik – Verfahren und Möglichkeiten*. PhD thesis, Universität Stuttgart, 1989.
- [57] Andreas Geiger, Martin Roser, and Raquel Urtasun. Efficient Large-Scale Stereo Matching. In *Asian Conference on Computer Vision*, 2010.
- [58] Todor Georgiev and Andrew Lumsdaine. Focused plenoptic camera and rendering. *Journal of Electronic Imaging*, 19(2):021106–021106, 2010.
- [59] Dennis Ghiglia and Mark Pritt. *Two-dimensional phase unwrapping: theory, algorithms, and software*. Wiley, 1998.
- [60] Stefan Glied. *Entwicklung und Anwendung eines Messsystems zur Bestimmung des totalen Streulichts von optischen und technisch rauhen Oberflächen und Schichten*. PhD thesis, Technische Universität Ilmenau, 2003.
- [61] Robin Gruna and Jürgen Beyerer. On Scene-Adapted Illumination Techniques for Industrial Inspection. In *Proc. IEEE Instrumentation and Measurement Technology Conference*, pages 498–503, May 2010.
- [62] Robin Gruna and Jürgen Beyerer. Acquisition and Evaluation of Illumination Series for Unsupervised Defect Detection. In *Proc. IEEE Instrumentation and Measurement Technology Conference*, pages 192–197, May 2011.
- [63] Robin Gruna, Kai-Uwe Vieth, Matthias Michelsburg, and Fernando Puenta León. Hyperspectral Imaging – From Laboratory to In-line Food Sorting. In László Baranyai, editor, *Second International Workshop on Image Analysis in Agriculture*, pages 79–90, 2010.
- [64] Jens Gühring. *3D-Erfassung und Objektrekonstruktion mittels Streifenprojektion*. PhD thesis, Universität Stuttgart, 2002.
- [65] Gabe Guss, Isaac Bass, Richard Hackel, Christian Mailhot, and Stavros Demos. High-resolution 3D imaging of surface damage sites in fused silica with optical coherence tomography. In *Laser-Induced Damage in Optical Materials, Proc. SPIE*, volume 6720, pages 67201F–67201F, 2007.
- [66] Tobias Haist. *Optische Phänomene in Natur und Alltag*. <http://www.optipina.de>, 2010.
- [67] Richard Hartley and Andrew Zisserman. *Multiple View Geometry in Computer Vision*. Cambridge University Press, 2nd edition, 2003.

- [68] Matthias Hartrumpf and Rüdiger Heintz. Device and method for the classification of transparent components in a material flow. Patent WO 2009/049594 A1, 2009.
- [69] Matthias Hartrumpf, Kai-Uwe Vieth, Thomas Längle, and Günter Struck. Neues Verfahren zur Sichtprüfung transparenter Materialien. In *Sensorgestützte Sortierung*, pages 57–58, 2008.
- [70] Jörg Haus. *Optical sensors: basics and applications*. Wiley-VCH, 2010.
- [71] Gerd Häusler, Peter Ettl, M. Schenk, Gunther Bohn, and Ildiko Laszlo. Limits of Optical Range Sensors and How to Exploit Them. In Toshimitsu Asakura, editor, *International Trends in Optics and Photonics*, pages 328–342. Springer, 1999.
- [72] Oliver Heavens. *Thin film physics*. Methuen, 1970.
- [73] Eugene Hecht. *Optics*. Addison-Wesley, San Francisco, 4th edition, 2002.
- [74] Karl Hehl, Albrecht Hertzsch, Knut Kröger, and Horst Truckenbrodt. Topographiemessungen technischer Oberflächen mit einer Streulichtanordnung. *Technisches Messen*, 70(1):4–9, 2003.
- [75] Michael Heizmann. *Auswertung von forensischen Riefenspuren mittels automatischer Sichtprüfung*. PhD thesis, Universität Karlsruhe (TH), 2004.
- [76] Michael Heizmann and Ioana Gheța. Methoden der 3-D-Vermessung von Oberflächen. In Norbert Bauer, editor, *Handbuch zur Industriellen Bildverarbeitung*, pages 159–168. Fraunhofer IRB Verlag, 1st edition, 2007.
- [77] Heiko Hirschmüller. Stereo Processing by Semiglobal Matching and Mutual Information. *IEEE Transactions on Pattern Analysis and Machine Intelligence*, 30(2):328–341, February 2008.
- [78] Stefan Hoffmann and Martin Hofmann. Terahertz-Strahlung entgeht nichts. *Rubin*, (1):42–48, 2005.
- [79] Heinrich Höfler and Michael Seib. Überblick über die verschiedenen Moiré-Techniken. *Vision and Voice Magazine*, 4(2):145–151, 1990.
- [80] Heinrich Höfler and Michael Seib. Optical Surface and Morphology Inspection Techniques. In E. Wagner, R. Dändliker, and K. Spenner, editors, *Optical Sensors*, volume 6 of *Sensors*, pages 551–587. VCH, 1992.
- [81] Berthold Horn and Michael Brooks, editors. *Shape from Shading*. MIT Press, 1989.
- [82] D. Hünerhoff, U. Grusemann, and A. Höpe. New robot-based gonireflectometer for measuring spectral diffuse reflection. *Metrologia*, 43(2):11–16, 2006.
- [83] Y. Hung and Y. Liang. Image-shearing camera for direct measurements of surface strains. *Applied Optics*, 18(7):1046–1051, 1979.
- [84] W. Hunter. Measurement of Optical Constants in the Vacuum Ultraviolet Spectral Region. In Edward Palik, editor, *Handbook of Optical Constants of Solids*, pages 69–88. Academic Press, 1985.
- [85] International Organization for Standardization, editor. *Guide to the expression of uncertainty in measurement*. 1995.
- [86] Minoru Ito and Akira Ishii. A three-level checkerboard pattern (TCP) projection method for curved surface measurement. *Pattern Recognition*, 28(1):27–40, 1995.
- [87] Bernd Jähne. *Practical handbook on image processing for scientific and technical applications*. CRC Press, 2nd edition, 2004.
- [88] Ingmar Jahr. Lighting in Machine Vision. In Alexander Hornberg, editor, *Handbook of Machine Vision*, pages 73–203. Wiley-VCH, 2006.
- [89] Markus Jehle, Christoph Sommer, and Bernd Jähne. Learning of Optimal Illumination for Material Classification. In *Pattern Recognition – 32nd DAGM Symposium*, pages 563–572, 2010.
- [90] Christian Jördens and Martin Koch. Detection of foreign bodies in chocolate with pulsed terahertz spectroscopy. *Optical Engineering*, 47(3):037003–037003, 2008.
- [91] Werner Jüptner. Holografische Interferometrie. In *Optische Messung technischer Oberflächen in der Praxis*, pages 287–296. VDI-Verlag, 2007.

- [92] Avinash Kak and Malcolm Slaney. *Principles of computerized tomographic imaging*. Society for Industrial and Applied Mathematics, 2001.
- [93] Willi Kalender. *Computed tomography: fundamentals, system technology, image quality, applications*. Publicis, 3rd edition, 2011.
- [94] Michael Kalms, Wolfgang Osten, and Werner Jüptner. Scherografie – die Umsetzung des Prinzips in ein mobiles Prüfsystem. *Technisches Messen*, 69(5):217–226, 2002.
- [95] Sören Kammel. *Deflektometrische Untersuchung spiegelnd reflektierender Freiformflächen*. PhD thesis, Universität Karlsruhe (TH), 2005.
- [96] K. Kawase, T. Shibuya, K. Suizu, and S. Hayashi. THz wave generation and imaging for industrial applications. In Mehdi Anwar, Nibir Dhar, and Thomas Crowe, editors, *Proc. SPIE Terahertz Physics, Devices, and Systems IV: Advanced Applications in Industry and Defense*, volume 7671, 2010.
- [97] Alexander Koch, Michael Ruprecht, Olaf Toedter, Gerd Häusler, Stefan Blosssey, Harald Schoenfeld, and Veit Windbichler. *Optische Messtechnik an technischen Oberflächen*. expert Verlag, 1998.
- [98] Antje Kochan. *Untersuchungen zur zerstörungsfreien Prüfung von CFK-Bauteilen für die fertigungsbegleitende Qualitätssicherung im Automobilbau*. PhD thesis, Technische Universität Dresden, 2011.
- [99] Friedel Koerfer and Robert Schmitt. In-Prozess Mikrostrukturprüfung. In Norbert Bauer, editor, *Handbuch zur Industriellen Bildverarbeitung*, pages 182–187. Fraunhofer IRB Verlag, 1st edition, 2007.
- [100] Matthias Krauß, Guido Mahler, David Pfengler, and Birgit Vollheim. Solarzellenprüfung mittels lichtmodulierter Lock-In-Thermographie. In Norbert Bauer, editor, *Handbuch zur Industriellen Bildverarbeitung*, pages 411–416. Fraunhofer IRB Verlag, 1st edition, 2007.
- [101] Thomas Kreis, Jürgen Geldmacher, and Werner Jüptner. Phasenschiebe-Verfahren in der interferometrischen Meßtechnik: Ein Vergleich. In Wilhelm Waidelich, editor, *Kongress Laser in der Technik*, pages 119–126, 1993.
- [102] Robert Lalla. *Verfahren zur Auswertung von Moiréaufnahmen technischer Oberflächen*. PhD thesis, Universität Karlsruhe (TH), 1993.
- [103] Leonardo da Vinci. *The notebooks of Leonardo da Vinci*. Edited by Jean Paul Richter, Dover, 1970.
- [104] Marc Levoy and Pat Hanrahan. Light field rendering. In *Proc. ACM SIGGRAPH*, pages 31–42, 1996.
- [105] Wansong Li, Thorsten Bothe, Wolfgang Osten, and Michael Kalms. Object adapted pattern projection—Part I: generation of inverse patterns. *Optics and Lasers in Engineering*, 41:31–50, 2004.
- [106] David Lide, editor. *Handbook of chemistry and physics*. CRC Press, 89th edition, 2008.
- [107] Michael Liepert. 3-D-Oberflächeninspektionssystem mit fotometrischem Stereo. In Norbert Bauer, editor, *Handbuch zur Industriellen Bildverarbeitung*, pages 169–172. Fraunhofer IRB Verlag, 1st edition, 2007.
- [108] Miaomiao Liu, Richard Hartley, and Mathieu Salzmann. Mirror surface reconstruction from a single image. In *Proceedings of 2013 IEEE Conference on Computer Vision and Pattern Recognition (CVPR)*, pages 129–136, 2013.
- [109] Ulrich Lübbert and Frank Muth. Beleuchtung und Optik für die genaue Vermessung von Werkstücken mit bildgebenden Sensoren. *IITB-Mitteilungen*, pages 9–14, 1993.
- [110] Thomas Luhmann, Stuart Robson, Stephen Kyle, and Jan Boehm. *Close-range photogrammetry and 3D imaging*. De Gruyter, 2nd edition, 2014.
- [111] Hans Dieter Lüke. *Korrelationssignale: Korrelationsfolgen und Korrelationsarrays in Nachrichten- und Informationstechnik, Messtechnik und Optik*. Springer, 1992.
- [112] Reinhard Malz. *Codierte Lichtstrukturen für 3-D-Meßtechnik und Inspektion*. PhD thesis, Universität Stuttgart, 1992.



- [113] Matthias Michelsburg, Robin Gruna, Kai-Uwe Vieth, and Fernando Puente León. Spektrale Bandselektion für das Filterdesign optischer Inspektionssysteme. *Technisches Messen*, 78(9):384–390, 2011.
- [114] Marvin Minsky. Microscopy apparatus. Patent US 3013467, 1957.
- [115] Robert Müller. *Handbuch der Modellstatik*. Springer, 1971.
- [116] Udo Netzelmann. Impuls- und Lock-In-Thermographie. In Norbert Bauer, editor, *Handbuch zur Industriellen Bildverarbeitung*, pages 373–377. Fraunhofer IRB Verlag, 1st edition, 2007.
- [117] Ulrich Neuschaefer-Rube. Optische Oberflächenmesstechnik für Topografie und Material. Habilitationsschrift, Universität Gesamthochschule Kassel, 2002.
- [118] Don Newsome and Peter Modreski. The colors and spectral distributions of fluorescent minerals. *Journal of the Fluorescent Mineral Society*, 10:7–57, 1981.
- [119] Ren Ng. Fourier slice photography. In *Proc. ACM SIGGRAPH*, pages 735–744, 2005.
- [120] Ren Ng, Marc Levoy, Mathieu Brédif, Gene Duval, Mark Horowitz, and Pat Hanrahan. Light Field Photography with a Hand-held Plenoptic Camera. Technical Report CTSR 2005-02, Stanford University, 2005.
- [121] Reinhard Noll. Lasertriangulation. In Norbert Bauer, editor, *Handbuch zur Industriellen Bildverarbeitung*, pages 56–60. Fraunhofer IRB Verlag, 1st edition, 2007.
- [122] Gunther Notni. Verfahren zur optischen 3-D-Messtechnik. In Norbert Bauer, editor, *Handbuch zur Industriellen Bildverarbeitung*, pages 214–231. Fraunhofer IRB Verlag, 1st edition, 2007.
- [123] Dirk Nüßler, Christian Krebs, Stefan Schneider, and Eva Schlauch. Material Analysis for the Millimeter Wave Frequencies. In *Proc. International Radar Symposium (IRS)*, 2007.
- [124] Wolfgang Osten. *Digitale Verarbeitung und Auswertung von Interferenzbildern*. Akademie-Verlag, 1991.
- [125] Wolfgang Osten. Digital Image Processing for Optical Metrology. In William Sharpe, editor, *Springer handbook of experimental solid mechanics*, pages 481–564. Springer, 2008.
- [126] Creidhe O’Sullivan and J. Anthony Murphy. *Field guide to terahertz sources, detectors, and optics*. SPIE Press, 2012.
- [127] Peter Ott and Gao Jun. Optische Grenzen von Triangulationsmethoden auf technischen Oberflächen. In Norbert Bauer, editor, *Handbuch zur Industriellen Bildverarbeitung*, pages 281–287. Fraunhofer IRB Verlag, 1st edition, 2007.
- [128] Alexey Pak. Stability of absolute depth reconstruction from deflectometric measurement data. In *Proceedings of SPIE Optical Engineering and Applications*, pages 92030E–92030E-7, 2014.
- [129] Edward Palik, editor. *Handbook of Optical Constants of Solids*. Academic Press, 1998.
- [130] Frank L. Pedrotti, Leno S. Pedrotti, and Leno M. Pedrotti. *Introduction to optics*. Pearson Prentice Hall, 3rd edition, 2007.
- [131] Tilo Pfeifer and Robert Schmitt. *Fertigungsmesstechnik*. Oldenbourg, 3rd edition, 2010.
- [132] Daniel Post, Bongtae Han, and Peter Ifju. Moiré Methods for Engineering and Science – Moiré Interferometry and Shadow Moiré. In Pramod Rastogi, editor, *Photomechanics*, pages 151–196. Springer, 2000.
- [133] Fernando Puente León and Jürgen Beyerer. Datenfusion zur Gewinnung hochwertiger Bilder in der automatischen Sichtprüfung. *Automatisierungstechnik*, 45(10):480–489, 1997.
- [134] Ehsan Rahani, Tribikram Kundu, Ziran Wu, and Hao Xin. Mechanical Damage Detection in Polymer Tiles by THz Radiation. *IEEE Sensors Journal*, 11(8):1720–1725, 2011.
- [135] Harald Rein and Pirmin Gerspacher. Interferometrische Meßtechnik und Streifenanalyse. In Bernd Breuckmann, editor, *Bildverarbeitung und optische Messtechnik in der industriellen Praxis*, pages 66–100. Franzis, 1993.

- [136] Franz Reischer and Bernhard Zimmermann. Laser Scanning Mikroskopie – Schnell und berührungslos Oberflächen dreidimensional analysieren. In *Optische Messung technischer Oberflächen in der Praxis*, pages 131–139. VDI-Verlag, 2007.
- [137] Justin Rennilson. Retroreflection. In Casimer DeCusatis, editor, *Handbook of applied photometry*, pages 289–325. Springer, 1998.
- [138] Stefan Riehemann, Boris Pradarutti, and Gunther Notni. Bildgebende Terahertz-Systeme zur Qualitätssicherung. In Norbert Bauer, editor, *Handbuch zur Industriellen Bildverarbeitung*, pages 420–425. Fraunhofer IRB Verlag, 1st edition, 2007.
- [139] Joaquim Salvi, Jordi Pagès, and Joan Batlle. Pattern codification strategies in structured light systems. *Pattern Recognition*, 37:827–849, 2004.
- [140] Indu Saxena. Ellipsometry. In Pramod Rastogi, editor, *Optical Measurement Techniques and Applications*, pages 406–409. Artech House, 1997.
- [141] Daniel Scharstein and Richard Szeliski. A Taxonomy and Evaluation of Dense Two-Frame Stereo Correspondence Algorithms. *International Journal of Computer Vision*, 47(1-3):7–42, 2002.
- [142] Torsten Scheuermann. *Berührungslose Gestaltvermessung von Mikrostrukturen durch Fokussuche*. PhD thesis, Universität Stuttgart, 1997.
- [143] Anton Schick. Konfokale 3-D-Bildaufnahme zur Oberflächenanalyse. In Norbert Bauer, editor, *Handbuch zur Industriellen Bildverarbeitung*, pages 188–192. Fraunhofer IRB Verlag, 1st edition, 2007.
- [144] Joseph Schmitt. Optical Coherence Tomography (OCT): A Review. *IEEE Journal of Selected Topics in Quantum Electronics*, 5(4):1205–1215, 1999.
- [145] Gottfried Schröder and Hanskarl Treiber. *Technische Optik*. Vogel, Würzburg, 9th edition, 2002.
- [146] Dietrich Schupp. *Optische Tensortomographie zur Untersuchung räumlicher Spannungsverteilungen*. PhD thesis, Universität Karlsruhe (TH), 2000.
- [147] Alexander Schwarz. *Multitomographische Temperaturmessung in Flammen mit einem Schlierenmeßaufbau*. PhD thesis, Universität Karlsruhe (TH), 1995.
- [148] Steven Seitz, Brian Curless, James Diebel, Daniel Scharstein, and Richard Szeliski. A Comparison and Evaluation of Multi-View Stereo Reconstruction Algorithms. In *Proc. IEEE Conference on Computer Vision and Pattern Recognition (CVPR)*, pages 519–528, 2006.
- [149] C. Sheppard. Fundamental reduction of the observation volume in far-field light microscopy by detection orthogonal to the illumination axis: confocal theta microscopy. *Optics communications*, 119(5):693–695, 1995.
- [150] Pavel Shumyatsky and Robert Alfano. Terahertz sources. *Journal of Biomedical Optics*, 16(3), 2011.
- [151] Sick AG. LMS Fast Laser Measurement Systems. Product Information, 2007.
- [152] Klaus Spinnler. Inspektion von Bohrungen und Rohren mit Panorama-Endoskopie. In Norbert Bauer, editor, *Handbuch zur Industriellen Bildverarbeitung*, pages 124–131. Fraunhofer IRB Verlag, 1st edition, 2007.
- [153] Ernst Stelzer and Steffen Lindek. Fundamental reduction of the observation volume in far-field light microscopy by detection orthogonal to the illumination axis: confocal theta microscopy. *Optics Communications*, 111(5):536–547, 1994.
- [154] David Stifter. Beyond biomedicine: a review of alternative applications and developments for optical coherence tomography. *Applied Physics B*, 88(3):337–357, 2007.
- [155] John Stover. *Optical scattering: measurement and analysis*. SPIE Optical Engineering Press, 2nd edition, 1995.
- [156] Yves Surrel. Design of algorithms for phase measurements by the use of phase stepping. *Applied Optics*, 35(1):51–60, 1996.
- [157] Yves Surrel. Fringe Analysis. In Pramod Rastogi, editor, *Photomechanics*, pages 55–102. Springer, 2000.

- [158] Ernst Sutter. *Schutz vor optischer Strahlung: Laserstrahlung, inkohärente Strahlung, Sonnenstrahlung; Normenreihe DIN EN 60825 (VDE 0837)*, volume 104 of *VDE-Schriftenreihe Normen verständlich*. VDE-Verlag, 3rd edition, 2008.
- [159] Miro Taphanel. Device for Optically Determining the Surface Geometry of a Three-dimensional Sample. Patent WO 2013/064395 A1, 2013.
- [160] Miro Taphanel and Jürgen Beyerer. Fast 3D in-line sensor for specular and diffuse surfaces combining the chromatic confocal and triangulation principle. In *Proc. IEEE International Instrumentation and Measurement Technology Conference (I2MTC 2012)*, pages 1072–1077, 2012.
- [161] Miro Taphanel, Bastiaan Hovestreydt, and Jürgen Beyerer. Speed-up Chromatic Sensors by Optimized Optical Filters. In *Proc. SPIE Optical Measurement Systems for Industrial Inspection VIII*, volume 8788, pages 87880S–87880S–10, 2013.
- [162] Michael Theuer, Garik Torosyan, Frank Ellrich, Joachim Jonuscheit, and René Beigang. Terahertz-Bildgebung in industriellen Anwendungen. *Technisches Messen*, 75(1):64–70, 2008.
- [163] Jürgen Thiel and Bernhard Brand. Laserscanner. In Tilo Pfeifer, editor, *Optoelektronische Verfahren zur Messung geometrischer Größen in der Fertigung*, pages 85–95. expert Verlag, 1993.
- [164] Hans Tiziani, Michael Wegner, and Daniela Steudle. Confocal principle for macro- and microscopic surface and defect analysis. *Optical Engineering*, 39(1):32–39, 2000.
- [165] Harland Tompkins and Eugene Irene, editors. *Handbook of ellipsometry*. Andrew, 2005.
- [166] Harland Tompkins and William McGahan. *Spectroscopic ellipsometry and reflectometry: a user's guide*. Wiley, 1999.
- [167] Ansgar Trächtler. *Tomographische Methoden in der Meßtechnik*, volume 897 of *Fortschritt-Berichte VDI*, 8. VDI-Verlag, 2001.
- [168] Johannes Trautner, Karl Walcher, Gerd Leuchs, Bernd Bodermann, and Harald Telle. Mehrwellenlängen-Interferometrie zur absoluten Abstandsmessung und 3D-Bildgebung. *Technisches Messen*, 67(10):406–409, 2000.
- [169] Emanuele Trucco and Alessandro Verri. *Introductory Techniques for 3-D Computer Vision*. Prentice Hall, 1998.
- [170] Jürgen Valentin and Mark Weber. Konfokale Mikroskopie zur Rauheits- und Schichtdickenmessung. In *Optische Messung technischer Oberflächen in der Praxis*, pages 113–122. VDI-Verlag, 2007.
- [171] Matthias Vaupel. Abbildende Ellipsometrie und ihre Anwendungen. In *Optische Messung technischer Oberflächen in der Praxis*, pages 141–150. VDI-Verlag, 2007.
- [172] D. Wang, Y. Chen, Y. Wang, and J. Liu. Comparison of line-scanned and point-scanned dual-axis confocal microscope performance. *Optics letters*, 38(24):5280–5283, 2013.
- [173] Stefan Werling. *Deflektometrie zur automatischen Sichtprüfung und Rekonstruktion spiegelnder Oberflächen*. PhD thesis, Karlsruhe Institute of Technology, 2011.
- [174] Gordon Wetzstein and Oliver Bimber. Radiometric compensation through inverse light transport. In *Proc. 15th Pacific Conference on Computer Graphics and Applications*, pages 391–399, 2007.
- [175] Rebecca Willett, Roummel Marcia, and Jonathan Nichols. Compressed sensing for practical optical imaging systems: a tutorial. *Optical Engineering*, 50(7):072601–072601, 2011.
- [176] Horst Winterberg. Holografie und Speckle-Meßtechnik. In Bernd Breuckmann, editor, *Bildverarbeitung und optische Messtechnik in der industriellen Praxis*, pages 101–123. Franzis, 1993.
- [177] Helmut Wolf. *Spannungsoptik*. Springer, 2nd edition, 1976.
- [178] Günter Wyszecki and Walter Stiles. *Color Science*. Wiley, 2nd edition, 2000.



Part II  
**Image Processing**





Chapter 8  
**Image Signals**

## 8 Image Signals

8.1	Mathematical model of image signals . . . . .	373
8.2	Systems and signals . . . . .	374
8.2.1	System characteristics . . . . .	374
8.2.2	The Dirac delta function . . . . .	378
8.2.2.1	Definition of the Dirac delta function . . . . .	378
8.2.2.2	Characteristics of the Dirac delta function . . . . .	379
8.2.3	Convolution . . . . .	381
8.3	The Fourier transform . . . . .	383
8.3.1	The one-dimensional Fourier transform . . . . .	383
8.3.1.1	Definition of the Fourier transform . . . . .	383
8.3.1.2	Properties of the Fourier transform . . . . .	384
8.3.1.3	Fourier transforms of selected functions . . . . .	390
8.3.2	The one-dimensional sampling theorem . . . . .	393
8.3.3	The discrete Fourier transform (DFT) . . . . .	396
8.3.3.1	Definition of the DFT . . . . .	396
8.3.3.2	Properties of the DFT . . . . .	397
8.3.3.3	Spectral leakage . . . . .	398
8.3.3.4	The fast Fourier transform (FFT) . . . . .	400
8.3.3.5	The convolution theorem of the DFT . . . . .	401
8.3.4	The two-dimensional Fourier transform . . . . .	401
8.3.4.1	Definition of the two-dimensional Fourier transform . . . . .	401
8.3.4.2	Properties of the two-dimensional Fourier transform . . . . .	403
8.3.5	Dirac delta functions in two-dimensional space . . . . .	407
8.3.6	The two-dimensional Heaviside function . . . . .	409
8.3.7	Sampling of two-dimensional signals . . . . .	409
8.3.8	Sampling theorem for two-dimensional signals . . . . .	413
8.3.9	The two-dimensional DFT . . . . .	414
8.3.9.1	Calculation of the 2-D DFT in practice . . . . .	416
8.3.9.2	The convolution theorem of the 2-D DFT . . . . .	417
8.3.9.3	The meaning of magnitude and phase . . . . .	417
8.3.9.4	Examples of the two-dimensional DFT . . . . .	418
8.4	Examples of use concerning system theory and the Fourier transform . . . . .	425
8.5	Image signals as stochastic processes . . . . .	432
8.5.1	Moments of stochastic processes . . . . .	433
8.5.2	Stationarity and ergodicity . . . . .	436
8.5.3	Passing a stochastic process through an LSI system . . . . .	440
8.6	Quantization . . . . .	445
8.6.1	Optimal quantization . . . . .	446
8.6.2	The quantization theorem . . . . .	448
8.6.3	Modeling of the quantization . . . . .	453
8.7	The Karhunen–Loève transform . . . . .	455
8.7.1	Definition of the Karhunen–Loève transform . . . . .	456

8.7.2	Properties of the Karhunen–Loève transform . . . . .	457
8.7.3	Examples of application of the Karhunen–Loève transform . . . . .	460
8.8	Bibliography . . . . .	464





## 8 Image Signals

### 8.1 Mathematical model of image signals

An image signal  $g(\mathbf{x})$  acquired by the methods described in Chap. 7 is a function  $g: \mathbb{R}^2 \rightarrow \mathbb{R}^Q$ , which—in the general case—maps the whole image plane to vectorial values, where  $Q$  denotes the number of channels (cf. Sec. 1.3). At first, both the domain and the range of the image signal are considered to be continuous. In this case,  $g(\mathbf{x})$  is called a *continuous image signal* or an *analog image signal*.

In order to store and process such signals using a computer, they have to be transformed into an adequate representation. This transformation is called **digitization** and has to carry out a discretization of the values of the function  $g$  and the positions  $x$ , as well as limit the spatial domain to a finite section and the values of the function to a finite range. The resulting digital signal is denoted by  $g_{mn}$ . Figure 8.1 shows the effect of digitization on the example of a one-dimensional, scalar image signal  $g(x): \mathbb{R} \rightarrow \mathbb{R}$ .

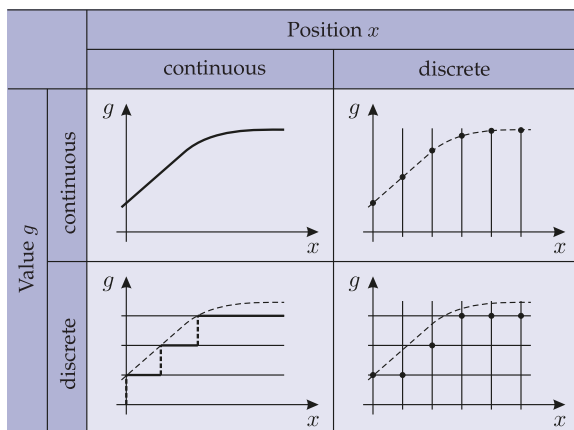


Figure 8.1. Discretization of position and function values.

In general, digitization involves an enormous loss of information, as infinitely many different vector-valued functions  $g(\mathbf{x})$  are mapped to one and the same matrix  $g_{mn}$ ; obviously this mapping is not invertible. On the one hand, a coarse discretization of the position and the function values is beneficial, as it reduces the needed storage and computing time. On the other hand, a fine discretization results in less loss of information and in images of higher quality, see Fig. 8.2. Thus, in practice it is a common problem to find an adequate trade-off between coarse and fine discretization, so that the information necessary for the actual application is preserved in the digital signal.

At first, the following qualitative and subjective approach can be used to solve this problem: in order to achieve a satisfying visual impression, detailed images require a fine spatial discretization. On the other hand, for images with less details, a fine discretization of the function values is necessary to avoid phantom edges. Figures 8.3 and 8.4 show a scalar

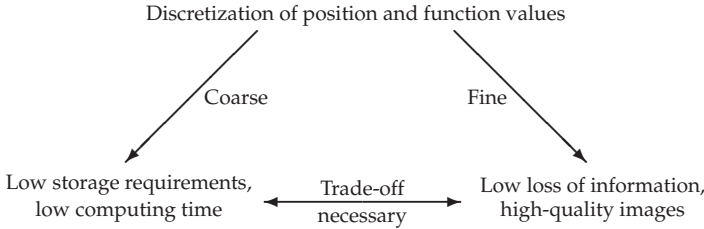


Figure 8.2. Consequences of the discretization of position and function values.

test image with different resolutions of position and function values and confirm this first approach.

As a rule of thumb, the discretization of the image should result in at least  $256 \times 256$  pixels and  $64 = 2^6$  values per channel, especially if a satisfying visual impression is required. The typical cameras used for visual inspection to capture two-dimensional images have approximately  $512^2$ – $4096^2$  image points and  $2^8$ – $2^{16}$  values per channel. However, to obtain a quantitative description of the effects of discretization, mathematical tools are needed, which will be described in the following sections.

## 8.2

### 8.2 Systems and signals

In general, a set of interacting components executing a certain task is called a **system**. In information technology, this is usually the transformation of certain input variables to a set of output variables. Thus, a system will now be considered as a rule for transforming an input signal  $g(\mathbf{x})$  to an output signal  $k(\mathbf{x})$ . Mathematically, this rule is described by the operator  $\mathcal{S}\{\cdot\}$ :

$$k(\mathbf{x}) = \mathcal{S}\{g(\mathbf{x})\}. \quad (8.1)$$

Such a system can be represented according to Fig. 8.5. The arrows show that the signals are carried in a certain direction, i.e., that the output values do not influence the input values. The system is therefore non-reactive.

Before covering some important mathematical tools for representing and analyzing systems, some criteria for classifying systems will be presented in the following subsection. To simplify matters, scalar image signals are considered.

#### 8.2.1 System characteristics

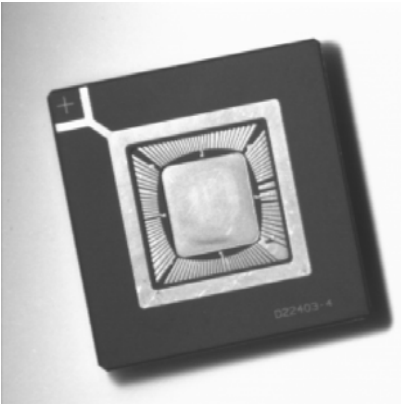
In this book, systems are generally considered to be *deterministic*, i.e., an input signal corresponds to a unique output signal.

## 8.1

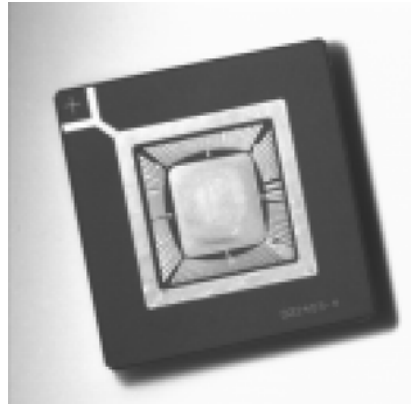
### Definition 8.1: Linearity

A system  $\mathcal{S}$  is called linear if the following equation holds for arbitrary signals  $g(\mathbf{x})$  and  $h(\mathbf{x})$  and arbitrary constants  $a$  and  $b$ :

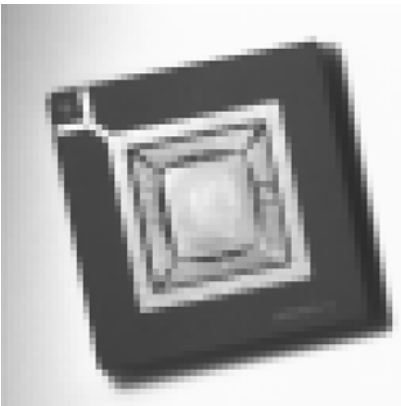
$$\mathcal{S}\{a g(\mathbf{x}) + b h(\mathbf{x})\} = a \mathcal{S}\{g(\mathbf{x})\} + b \mathcal{S}\{h(\mathbf{x})\}. \quad (8.2)$$



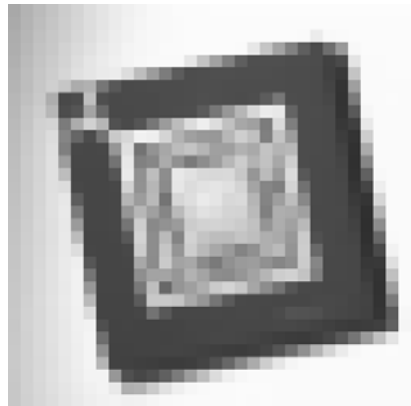
(a)  $256 \times 256$



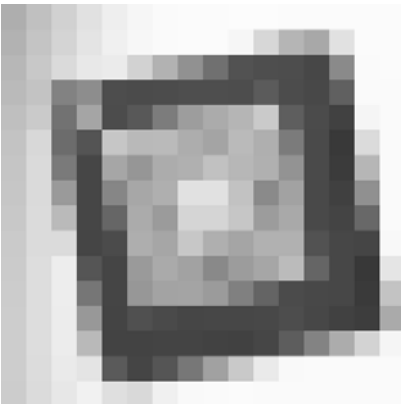
(b)  $128 \times 128$



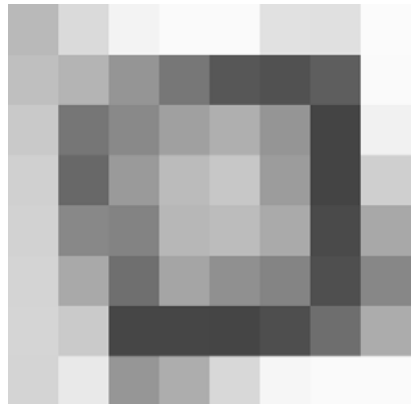
(c)  $64 \times 64$



(d)  $32 \times 32$

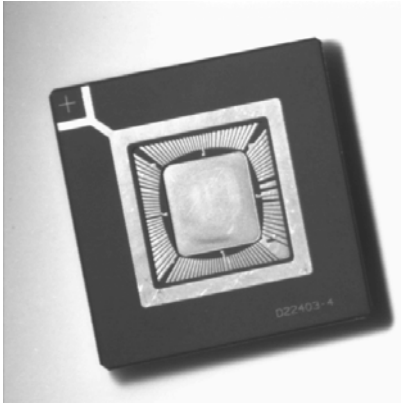


(e)  $16 \times 16$

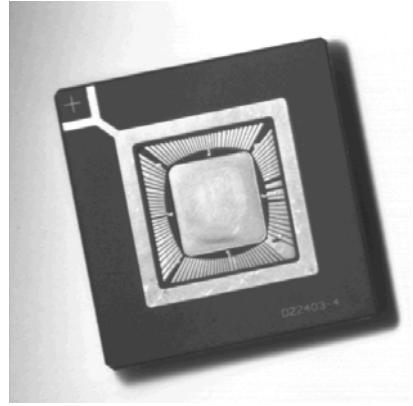


(f)  $8 \times 8$

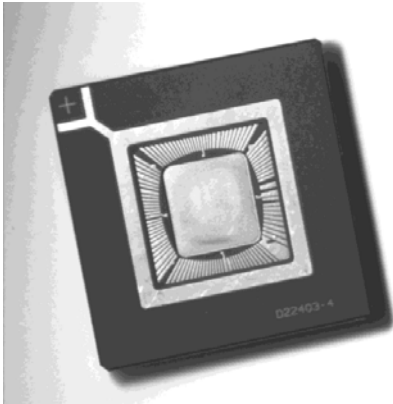
Figure 8.3. Spatial discretization: Test image with different spatial resolutions.



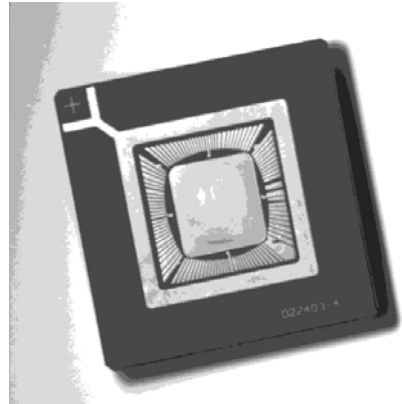
(a) 64 Gray values



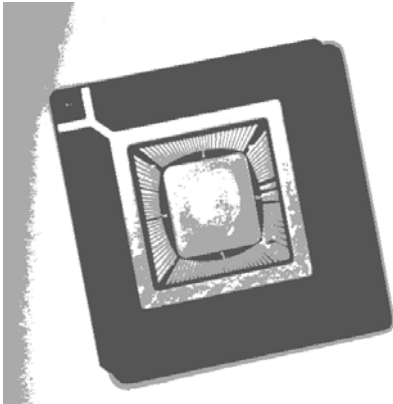
(b) 32 Gray values



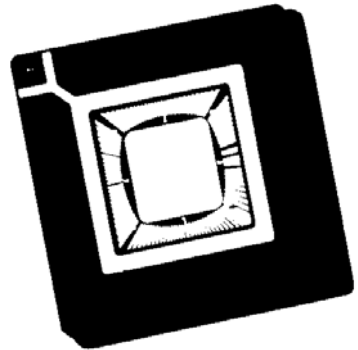
(c) 16 Gray values



(d) 8 Gray values



(e) 4 Gray values



(f) 2 Gray values

Figure 8.4. Discretization of function values: Test image with different resolutions of gray values.

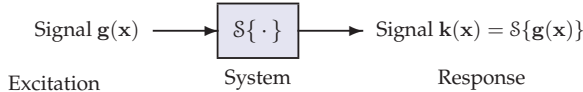


Figure 8.5. Passing a signal through a system.

Accordingly, if an input signal is composed of the superposition of several signals, a linear system produces an output signal which is the weighted sum of their corresponding output signals (the superposition principle).  $\diamond$

**Definition 8.2: Shift invariance**

A system  $S$  is called shift invariant if

$$S\{g(\mathbf{x} - \mathbf{x}_0)\} = k(\mathbf{x} - \mathbf{x}_0) \quad \text{with} \quad k(\mathbf{x}) = S\{g(\mathbf{x})\}. \quad (8.3)$$

So, the output signal corresponding to an input signal shifted by the vector  $\mathbf{x}_0$  will be identical to the output signal of the original input signal except for the displacement  $\mathbf{x}_0$ . Hence, the system is independent of the position  $\mathbf{x}$ .  $\diamond$

Linear, shift invariant methods allow a simple mathematical treatment of numerous important systems; for this reason, they have great practical relevance.

**Definition 8.3: Memoryless**

A system  $S$  is called memoryless if

$$S\{g(\mathbf{x})\} = \nu(g(\mathbf{x})) \quad \text{with} \quad \nu : \mathbb{R} \rightarrow \mathbb{R}, \quad (8.4)$$

i.e., if the output signal  $S\{g(\mathbf{x})\}$  depends only on the value of the input signal  $g(\mathbf{x})$  at the position  $\mathbf{x}$ .  $\diamond$

**Example 8.1 (Moving average):** As a first example system, consider the moving average:

$$S\{g(\mathbf{x})\} := \frac{1}{T^2} \int_{x-\frac{T}{2}}^{x+\frac{T}{2}} \int_{y-\frac{T}{2}}^{y+\frac{T}{2}} g(\boldsymbol{\alpha}) \, d\boldsymbol{\alpha} = k(\mathbf{x}). \quad (8.5)$$

This system is linear, shift invariant, and not memoryless.  $\blacksquare$

**Example 8.2 (Exponentiation):** Next, consider exponentiation:

$$S\{g(\mathbf{x})\} := g^p(\mathbf{x}) = k(\mathbf{x}). \quad (8.6)$$

This system is non-linear, shift invariant, and memoryless.  $\blacksquare$

**Example 8.3 (Ideal modulator):** Finally, consider the ideal modulator:

$$\mathcal{S}\{g(\mathbf{x})\} := m(\mathbf{x}) \cdot g(\mathbf{x}). \quad (8.7)$$

This system is linear and memoryless. As

$$\mathcal{S}\{g(\mathbf{x} - \mathbf{x}_0)\} = m(\mathbf{x}) \cdot g(\mathbf{x} - \mathbf{x}_0) \quad (8.8)$$

$$\neq m(\mathbf{x} - \mathbf{x}_0) \cdot g(\mathbf{x} - \mathbf{x}_0) = k(\mathbf{x} - \mathbf{x}_0), \quad (8.9)$$

the system is shift variant. ■

## 8.2.2 The Dirac delta function

### 8.2.2.1 Definition of the Dirac delta function

In contrast to functions, distributions are not defined by their values at the different positions  $\mathbf{x}$  or times  $t$ , but by their characteristics [6,24]. Especially because of its ability to extract the value of a given function  $g(x)$ , the so-called **Dirac Delta Function**  $\delta(x)$  (also called the  $\delta$ -distribution or ‘ $\delta$ -function’) is of special importance in the field of signal analysis.

#### 8.4 Definition 8.4: The Dirac delta function

The Dirac delta function is defined by

$$g(x_0) = \int_{-\infty}^{\infty} \delta(x - x_0) g(x) dx \quad \text{with } g(x) \text{ continuous at } x_0. \quad (8.10)$$

Together with the integral, this results in the extraction of the value of  $g(x)$  at the position  $x_0$ . ◇

Apparently, the ‘ $\delta$ -function’ is not a function in the usual sense but rather a distribution, as  $\delta(x)$  is defined by its effect on functions  $g(x)$  after multiplication and integration and not by its function values.

As  $g(x)$  might have arbitrary values for  $x \neq x_0$ , one must have  $\delta(x) = 0$  for these  $x$ . In addition, setting  $g(x) \equiv 1$  in (8.10) immediately implies

$$\int_{-\infty}^{\infty} \delta(x) dx = 1. \quad (8.11)$$

Thus, the Dirac delta function can be seen as a very narrow, impulse-shaped function with an integral of one, which can be approximated by an appropriate function. Choosing a rectangular impulse results in the following approximation:

$$\delta_\varepsilon(x) := \frac{1}{\varepsilon} \text{rect}\left(\frac{x}{\varepsilon}\right) \quad (8.12)$$

with the **rectangular function**

$$\text{rect}\left(\frac{x}{\varepsilon}\right) := \begin{cases} 1 & \text{if } |x| < \frac{\varepsilon}{2} \\ 0 & \text{otherwise} \end{cases}, \quad (8.13)$$

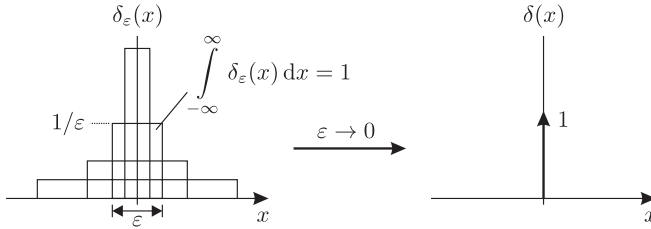


Figure 8.6. Approximation of the Dirac delta function by the rectangular function. The Dirac delta function is represented by an arrow and its weight (integral) by the length of the arrow.

where the width of the impulse is denoted by  $\varepsilon$ , see Fig. 8.6. For  $\varepsilon \rightarrow 0$ , the approximation  $\delta_\varepsilon(x)$  has the same characteristics as the Dirac delta function:

$$\lim_{\varepsilon \rightarrow 0} \int_{-\infty}^{\infty} \delta_\varepsilon(x - x_0) g(x) dx = g(x_0), \quad g(x) \text{ continuous in } x_0, \quad (8.14)$$

as the approximation  $g(x) \approx g(x_0)$  holds for a sufficiently small neighborhood of  $\varepsilon$  around  $x_0$  because of the continuity of  $g(x)$ , see Fig. 8.7. Therefore, the approximation  $\delta_\varepsilon(x)$  results in the  $\delta$ -distribution:

$$\delta_\varepsilon(x) \xrightarrow{\varepsilon \rightarrow 0} \delta(x). \quad (8.15)$$

⊗ 8.2.2.2 Characteristics of the Dirac delta function

The Dirac delta function has the following characteristics:

- **Even:** The Dirac delta function acts like an even function, i.e.,  $\delta(x)$  is axially symmetric to the line  $x = 0$ :

$$\delta(x) = \delta(-x). \quad (8.16)$$

- **Descriptive characterization:** By (8.15), the Dirac delta function can be interpreted as an infinitely narrow rectangular function of infinite height:

$$\delta(x) \text{ '}' \begin{cases} 0 & \text{for } x \neq 0 \\ \infty & \text{for } x = 0 \end{cases}. \quad (8.17)$$

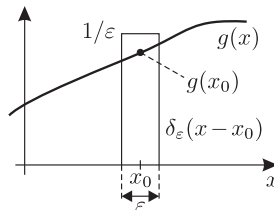


Figure 8.7. Transition  $\delta_\varepsilon(x) \rightarrow \delta(x)$ .

Table 8.1. Formulas for Dirac delta functions.

Definition	$\int_{-\infty}^{\infty} \delta(x - x_0) u(x) dx = u(x_0) \quad \text{with } u(x) \text{ continuous at } x = x_0$
Orthogonality	$\int_{-\infty}^{\infty} \delta(x - x_1) \delta(x - x_2) dx = \delta(x_1 - x_2)$
Gating characteristic	$\delta(x - x_0) u(x) = \delta(x - x_0) u(x_0)$
Coordinate transformation	$\delta(a(x)) = \sum_{i=1}^N  a'(x_i) ^{-1} \delta(x - x_i) \quad \text{with simple zeros at } a(x_i) = 0$
Similarity transformation	$\delta(kx) =  k ^{-1} \delta(x) \quad \text{with } k \text{ real-valued } \neq 0$
Convolution	$u(x) * \delta(x - x_0) = u(x - x_0)$
$n$ -dimensional Dirac delta function	$\delta(\mathbf{x}) = \delta(x_1, x_2, \dots, x_n) = \delta(x_1) \delta(x_2) \dots \delta(x_n), \quad \mathbf{x} \in \mathbb{R}^n$

- **The unit step function as an integral:** The integration of the Dirac delta function results in the **unit step function** (also called the **Heaviside function**):

$$H(x) = \int_{-\infty}^x \delta(\xi) d\xi, \quad (8.18)$$

which is defined as

$$H(x) := \begin{cases} 0 & \text{if } x < 0 \\ \frac{1}{2} & \text{if } x = 0 \\ 1 & \text{if } x > 0 \end{cases}. \quad (8.19)$$

Hence, the Dirac delta function  $\delta(x)$  is the derivative of the unit step function  $H(x)$  in the sense of distribution theory.

Table 8.1 summarizes the most important formulas concerning Dirac delta functions. In order to demonstrate how to calculate using the Dirac delta function, the proof of the similarity transformation will now be given as an example.

**Proof 8.1 (The similarity transformation):** In order to prove the formula for the similarity transformation of Table 8.1,  $x_0 = 0$  is inserted into (8.10),

$$\int_{-\infty}^{\infty} g(x) \delta(x) dx = g(0), \quad (8.20)$$



and the approximation (8.15) is used:

$$\int_{-\infty}^{\infty} g(x) \delta(kx) dx \stackrel{\text{Evenness}}{\downarrow} = \int_{-\infty}^{\infty} g(x) \delta(|k|x) dx \quad (8.21)$$

$$= \lim_{\varepsilon \rightarrow 0} \int_{-\infty}^{\infty} g(x) \frac{1}{\varepsilon} \text{rect}\left(\frac{|k|x}{\varepsilon}\right) dx \quad (8.22)$$

$$= \frac{1}{|k|} \lim_{\gamma \rightarrow 0} \int_{-\infty}^{\infty} g(x) \underbrace{\frac{1}{\gamma} \text{rect}\left(\frac{x}{\gamma}\right)}_{\delta_{\gamma}(x)} dx \quad \text{with} \quad \gamma := \frac{\varepsilon}{|k|} \quad (8.23)$$

$$= \frac{1}{|k|} g(0), \quad (8.24)$$

which leads immediately to the similarity transformation

$$\delta(kx) = |k|^{-1} \delta(x). \quad (8.25)$$

■

See [6,24] for a deeper insight into the theory of distributions.

### ► 8.2.3 Convolution

#### Definition 8.5: Convolution

The **convolution** of two functions is defined by the following integral:

$$g(x) * h(x) := \int_{-\infty}^{\infty} g(\alpha) h(x - \alpha) d\alpha = \int_{-\infty}^{\infty} g(x - \alpha) h(\alpha) d\alpha. \quad (8.26)$$

Figure 8.8 illustrates this operation. ◇

The convolution of an arbitrary function  $g(x)$  with the Dirac delta function shifted from  $x_0$  by  $\delta(x - x_0)$  corresponds to a displacement of  $g(x)$  by  $x_0$ :

$$g(x) * \delta(x - x_0) = \int_{-\infty}^{\infty} g(\alpha) \delta(\underbrace{x - x_0 - \alpha}_{= 0 \Leftrightarrow \alpha = x - x_0}) d\alpha = g(x - x_0). \quad (8.27)$$

In particular, for  $x_0 = 0$ , (8.27) implies

$$g(x) * \delta(x) = g(x). \quad (8.28)$$

Hence, the Dirac delta function  $\delta(x)$  is the identity for the operation of convolution.

Next, a common linear and shift invariant system (**LSI system**)  $\mathcal{S}\{\cdot\}$  will be considered. Such a system operates on signals which depend on  $x$ . By (8.28), the response of the LSI

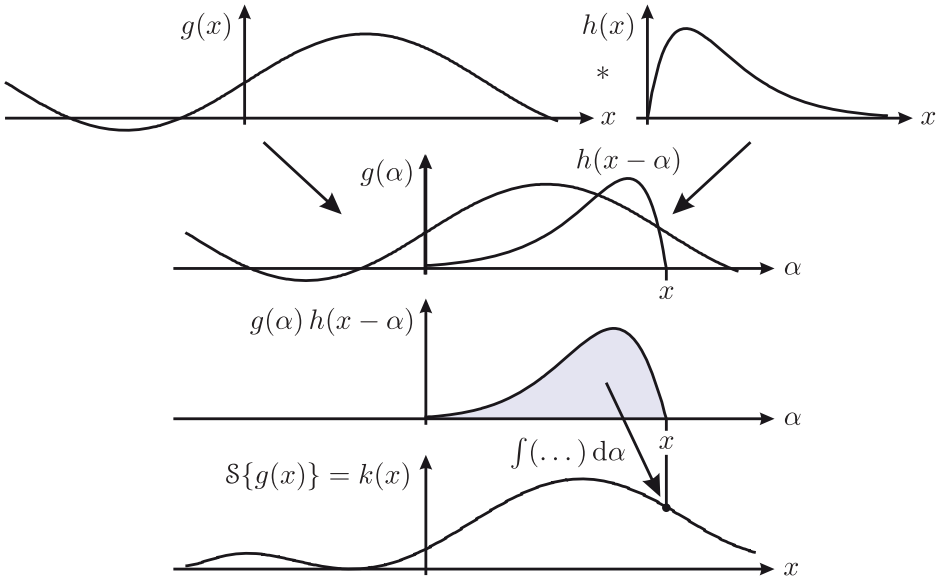


Figure 8.8. Convolution.

system  $\mathcal{S}\{\cdot\}$  to the input signal  $g(x)$  can be expressed using a convolution integral:

$$\mathcal{S}\{g(x)\} = \mathcal{S}\{g(x) * \delta(x)\} = \mathcal{S}\left\{\int_{-\infty}^{\infty} g(\alpha) \delta(x - \alpha) d\alpha\right\} \quad (8.29)$$

Linearity (8.2)

$$\downarrow \\ = \int_{-\infty}^{\infty} g(\alpha) \underbrace{\mathcal{S}\{\delta(x - \alpha)\}}_{h(x - \alpha)} d\alpha = g(x) * h(x). \quad (8.30)$$

The response  $h(x) = \mathcal{S}\{\delta(x)\}$  of the LSI system  $\mathcal{S}\{\cdot\}$  to the Dirac delta function is called the **impulse response** of the system  $\mathcal{S}\{\cdot\}$ . Hence, the response of a linear, shift invariant system to an input signal  $g(x)$  is given by the convolution of  $g(x)$  with the impulse response  $h(x)$  of the system. A system is completely characterized by its corresponding impulse response  $h(x)$  [18].

## 8.3 The Fourier transform

### 8.3.1 The one-dimensional Fourier transform

#### 8.3.1.1 Definition of the Fourier transform

The Fourier transform<sup>1</sup> transforms a one-dimensional, usually real-valued function  $g(x)$  into a complex-valued function  $G(f)$  of the frequency  $f$ .

#### Definition 8.6: The Fourier transform

The Fourier transform maps the function  $g(x)$  to a complex-valued function  $G(f) : \mathbb{R} \rightarrow \mathbb{C}$  according to the following integral transform:

$$G(f) := \int_{-\infty}^{\infty} g(x) e^{-j2\pi fx} dx =: \mathcal{F}\{g(x)\}. \quad (8.31)$$

The formula for the inverse transformation<sup>2</sup> of the complex-valued Fourier transform  $G(f)$  to the original function  $g(x)$  is given by [18]:

$$g(x) = \int_{-\infty}^{\infty} G(f) e^{j2\pi fx} df = \mathcal{F}^{-1}\{G(f)\}. \quad (8.32)$$

The Fourier transform  $G(f)$  is called the **spectrum** of the signal  $g(x)$ .  $\diamond$

As (8.31) and (8.32) represent a bijection,  $G(f)$  is just another representation of  $g(x)$ . In order to be able to better distinguish between these two domains, lower-case letters are used for the spatial signals and capital letters for the transformed complex functions in the Fourier domain. The variable  $f \in \mathbb{R}$  is the frequency corresponding to  $x$ ; its unit is:  $[f] = [x]^{-1}$ . In order to distinguish it from a frequency of time, this frequency is called the “spatial frequency.” In other definitions of the Fourier transform, often the angular frequency  $\omega = 2\pi f$  is used instead of the usual frequency  $f$ .

The use of the symbol of correspondence  $\circ\bullet$  is quite common. The expression

$$g(x) \circ\bullet G(f) \quad (8.33)$$

states that the functions  $g(x)$  and  $G(f)$  are a pair of corresponding functions.

Because of Euler’s formula

$$e^{j2\pi fx} = \cos(2\pi fx) + j \sin(2\pi fx) \quad (8.34)$$

<sup>1</sup>Named after Jean-Baptiste Joseph Fourier, 1768–1830, French mathematician and physicist.

The reader might wonder why the Fourier transform is discussed instead of the Laplace transform. This is because the Laplace transform of a two-dimensional image would result in a four-dimensional parameter space [18], which would lead to unreasonably high costs for analyzing a two-dimensional signal. Additionally, in a manner of speaking, the Fourier transform exists in nature and can be used to explain some of the basic effects of physical systems (cf. Sec. 8.4).

<sup>2</sup>Strictly speaking, the set of functions  $g(x)$  would need to be restricted to ensure the validity of (8.31) and (8.32), as jump discontinuities in  $g(x)$  for example would be transformed into the average of the left- and right-hand limits after being transformed and inversely transformed. However, as such functions have nearly no practical relevance, they are ignored for the rest of this book [11].

the Fourier spectrum of a signal is, in general, complex-valued. Therefore, for each frequency  $f$ , the spectrum can be expressed as a magnitude and a phase, or as a real part and an imaginary part:

$$G(f) = |G(f)| \cdot e^{j\varphi(f)} = \Re\{G(f)\} + j\Im\{G(f)\}. \quad (8.35)$$

The **magnitude spectrum**  $|G(f)|$  can be calculated from  $G(f)$  using the Pythagorean theorem:

$$|G(f)| = \sqrt{\Re\{G(f)\}^2 + \Im\{G(f)\}^2}. \quad (8.36)$$

This shows which frequencies contribute to  $g(x)$  and to what extent.

The **phase spectrum**  $\varphi(f)$  corresponds to the angle or the argument of the complex number  $G(f)$ :

$$\varphi(f) = \angle G(f) = \begin{cases} \arctan\left(\frac{\Im\{G(f)\}}{\Re\{G(f)\}}\right) & \text{for } \Re\{G(f)\} \geq 0 \\ \arctan\left(\frac{\Im\{G(f)\}}{\Re\{G(f)\}}\right) - \pi & \text{for } \Re\{G(f)\} < 0 \end{cases}. \quad (8.37)$$

The inverse Fourier transform (8.32) allows a descriptive interpretation of the complex Fourier spectrum: the signal  $g(x)$  is additively synthesized from uncountably many complex harmonic oscillations, which are weighted by  $G(f)$ . On the other hand, the Fourier transform provides a related analysis: it decomposes a function  $g(x)$  into a continuum of harmonic functions with different spatial frequencies. The fine details of  $g(x)$  correspond to the high-frequency parts of the spectrum  $G(f)$ . The coarse features, i.e., the parts of  $g(x)$  that change slowly with respect to  $x$ , are represented by the low-frequency parts of  $G(f)$ .

The Fourier transform is a global transform: for each frequency  $f$ ,  $G(f)$  depends on the whole function  $g(x)$ .

**The existence of the Fourier integral:** As the Fourier integral (8.31) is an improper integral, it does not necessarily exist for arbitrary functions  $g(x)$  [11]. Because

$$\left| \int_{-\infty}^{\infty} g(x) e^{-j2\pi ft} dx \right| \leq \int_{-\infty}^{\infty} |g(x)| dx, \quad (8.38)$$

the Fourier integral (8.31) converges if the the function  $g(x)$  is absolutely integrable<sup>3</sup>:

$$\int_{-\infty}^{\infty} |g(x)| dx < \infty. \quad (8.39)$$

This is always the case for real, spatially limited functions.

### ⊗ 8.3.1.2 Properties of the Fourier transform

In signal processing, the Fourier transform is an important analysis and design tool, which can be used to concisely describe and treat many different issues and problems. However in

---

<sup>3</sup>However, this condition is only sufficient: it is not necessary. In fact, the Fourier transform will also be calculated for some functions that do not comply with (8.39), e.g., for the complex harmonic function  $g(x) = e^{j2\pi f_0 x}$ , which has a constant magnitude:  $|e^{j2\pi f_0 x}| \equiv 1$ , see (8.88). Then, the existence of the Fourier transform  $G(f)$  has to be taken in the sense of the theory of distributions.

practice, using the improper integrals (8.31) and (8.32) is unhandy. Instead, tables are used, which provide common formulas and Fourier correspondences (cf. Appendix B). The most important properties and formulas will now be derived.

**Theorem 8.1: Linearity**

8.1

The Fourier transform (8.31) is a linear signal transformation. By (8.2),

$$\mathcal{F}\{a g(x) + b h(x)\} = a G(f) + b H(f) \tag{8.40}$$

for arbitrary constants  $a$  and  $b$ .

The same holds for the inverse Fourier transform (8.32). ◇

**Theorem 8.2: Scaling property**

8.2

Multiplying the variable  $x$  by a constant  $k \in \mathbb{R} \setminus \{0\}$  results in a **spatial scaling** of the signal  $g(x)$  [14]. The Fourier transform of the scaled signal  $g(kx)$  is given by

$$\mathcal{F}\{g(kx)\} = \int_{-\infty}^{\infty} g(kx) e^{-j2\pi f x} dx \quad \left| \begin{array}{l} \tau = kx \\ d\tau = k dx \end{array} \right. \tag{8.41}$$

$$= \begin{cases} \frac{1}{|k|} \int_{-\infty}^{\infty} g(\tau) e^{-j2\pi \frac{f}{k} \tau} d\tau & \text{for } k < 0 \\ \frac{1}{|k|} \int_{-\infty}^{\infty} g(\tau) e^{-j2\pi \frac{f}{k} \tau} d\tau & \text{for } k > 0 \end{cases} \tag{8.42}$$

Fourier transform of  $g(x)$  at  $\frac{f}{k}$

$$= \frac{1}{|k|} G\left(\frac{f}{k}\right) \quad \text{with} \quad g(x) \circ \bullet G(f). \tag{8.43}$$

So, the two representations of the signal are reciprocal with respect to the coordinates  $x$  and  $f$  in the spatial or in the spatial frequency domain respectively. Stretching  $g(x)$  by the factor  $k$  results in shrinking the corresponding spectrum by the factor  $k$  in the direction of the abscissa and scaling by  $|k|^{-1}$  in the direction of the ordinate. ◇

To demonstrate the convolution property of the Fourier transform, the convolution of the signals  $g(x)$  and  $h(x)$  will be transformed into the spatial frequency domain:

$$\mathcal{F}\{g(x) * h(x)\} = \int_{-\infty}^{\infty} \int_{-\infty}^{\infty} g(\alpha) h(x - \alpha) d\alpha e^{-j2\pi f x} dx \tag{8.44}$$

$$= \int_{-\infty}^{\infty} g(\alpha) \int_{-\infty}^{\infty} h(x - \alpha) e^{-j2\pi f x} dx d\alpha. \tag{8.45}$$

The substitution  $\beta := x - \alpha$  results in

$$\mathcal{F}\{g(x) * h(x)\} = \int_{-\infty}^{\infty} g(\alpha) \int_{-\infty}^{\infty} h(\beta) e^{-j2\pi f(\alpha+\beta)} d\beta d\alpha \quad (8.46)$$

$$= \underbrace{\int_{-\infty}^{\infty} g(\alpha) e^{-j2\pi f\alpha} d\alpha}_{G(f)} \cdot \underbrace{\int_{-\infty}^{\infty} h(\beta) e^{-j2\pi f\beta} d\beta}_{H(f)}. \quad (8.47)$$

### 8.3 Theorem 8.3: Convolution theorem

The convolution of two functions is transformed by the Fourier transform into the multiplication of their spectra:

$$g(x) * h(x) \quad \circ \bullet \quad G(f) \cdot H(f). \quad (8.48)$$

In addition,

$$g(x) \cdot h(x) \quad \circ \bullet \quad G(f) * H(f), \quad (8.49)$$

holds [18]. So, multiplying two signals corresponds to convolving their Fourier spectra.  $\diamond$

Hence, the Fourier transform is a homomorphism, which can be used to transform the comparatively complicated operation of convolution into a much simpler one: multiplication. So, convolution in the spatial domain can be realized by means of

$$g(x) * h(x) = \mathcal{F}^{-1}\{\mathcal{F}\{g(x)\} \cdot \mathcal{F}\{h(x)\}\}. \quad (8.50)$$

### 8.4 Theorem 8.4: Differentiation theorem

The differentiation of a signal  $g(x)$  can be expressed using the inverse Fourier transform (8.32):

$$\frac{d}{dx} g(x) = \frac{d}{dx} \int_{-\infty}^{\infty} G(f) e^{j2\pi fx} df \quad (8.51)$$

$$= \int_{-\infty}^{\infty} j2\pi f G(f) e^{j2\pi fx} df \quad (8.52)$$

$$= \mathcal{F}^{-1}\{j2\pi f G(f)\}. \quad (8.53)$$

So, differentiating results in multiplying the Fourier spectrum  $G(f)$  by the factor  $j2\pi f$ . By (8.53), multiple differentiation implies the following correspondence:

$$\frac{d^n g(x)}{dx^n} \quad \circ \bullet \quad (j2\pi f)^n G(f), \quad n \in \mathbb{N}. \quad (8.54)$$

$\diamond$

Qualitatively, the derivative property states that the low-frequency parts are attenuated and the high-frequency parts are amplified by differentiation. As is known, the derivative of an additive constant is equal to zero. Such a constant can be considered as the so-called direct (DC) component of the signal  $g(x)$ , which is located at  $f = 0$  in the spatial frequency domain and is multiplied by  $j2\pi 0 = 0$  for a differentiation in the spatial domain.

**Theorem 8.5: The shift property (spatial displacement)**

8.5

To demonstrate the shift property of the Fourier transform, the spatially shifted signal  $g(x - x_0)$  is transformed into the frequency domain:

$$\mathcal{F}\{g(x - x_0)\} = \int_{-\infty}^{\infty} g(x - x_0) e^{-j2\pi f x} dx \quad \left| \begin{array}{l} \alpha = x - x_0 \\ d\alpha = dx \end{array} \right. \quad (8.55)$$

$$= \int_{-\infty}^{\infty} g(\alpha) e^{-j2\pi f(\alpha + x_0)} d\alpha \quad (8.56)$$

$$= e^{-j2\pi f x_0} G(f). \quad (8.57)$$

◇

Because  $|e^{-j2\pi f x_0}| = 1$ , the magnitude spectrum remains unchanged by a spatial displacement: only the phase is affected. Later on, this will be interpreted as follows: the spatial information of a signal is encoded in the phase of the corresponding Fourier transform, see Sec. 8.3.9.3.

**Theorem 8.6: The modulation property (frequency displacement)**

8.6

Analogously, shifting the spectrum by the frequency  $f_0$  results in

$$\mathcal{F}^{-1}\{G(f - f_0)\} = \int_{-\infty}^{\infty} G(f - f_0) e^{j2\pi f x} df \quad \left| \begin{array}{l} \alpha = f - f_0 \\ d\alpha = df \end{array} \right. \quad (8.58)$$

$$= \int_{-\infty}^{\infty} G(\alpha) e^{j2\pi(\alpha + f_0)x} d\alpha \quad (8.59)$$

$$= e^{j2\pi f_0 x} g(x). \quad (8.60)$$

An ideal modulation by the function  $e^{j2\pi f_0 x}$  shifts the Fourier spectrum by  $f_0$ . ◇

**Theorem 8.7: The central ordinate theorem**

8.7

Using the inverse Fourier transform (8.32), the value of  $g(x)$  for  $x = 0$  is

$$g(0) = \int_{-\infty}^{\infty} G(f) e^{j2\pi f x} df \Big|_{x=0} = \int_{-\infty}^{\infty} G(f) df. \quad (8.61)$$

Equivalently, according to (8.31), the Fourier spectrum at  $f = 0$  is

$$G(0) = \int_{-\infty}^{\infty} g(x) e^{-j2\pi f x} dx \Big|_{f=0} = \int_{-\infty}^{\infty} g(x) dx. \quad (8.62)$$

Here,  $G(0)$  denotes the DC component of the signal  $g(x)$ .  $\diamond$

## 8.8

**Theorem 8.8: Reflection**

By (8.32), a reflection of the signal  $g(x) = g^*(x) \in \mathbb{R}$  in the origin results in

$$g(-x) = \int_{-\infty}^{\infty} G(f) e^{-j2\pi f x} df. \quad (8.63)$$

Complex conjugation results in the following formula:

$$g^*(-x) = g(-x) = \int_{-\infty}^{\infty} G^*(f) e^{j2\pi f x} df = \mathcal{F}^{-1}\{G^*(f)\}. \quad (8.64)$$

In particular, the magnitude  $|G(f)|$  of the Fourier spectrum remains unchanged after a reflection.  $\diamond$

## 8.9

**Theorem 8.9: The Fourier transform of real-valued signals**

By complex conjugation, one obtains the following result for the Fourier transform of the real-valued signal  $g(x) = g^*(x) \in \mathbb{R}$ :

$$G^*(f) = \left( \int_{-\infty}^{\infty} g(x) e^{-j2\pi f x} dx \right)^* = \int_{-\infty}^{\infty} g^*(x) e^{j2\pi f x} dx \quad (8.65)$$

$$= \int_{-\infty}^{\infty} g(x) e^{-j2\pi(-f)x} dx = G(-f). \quad (8.66)$$

This results in the symmetry of the magnitude (i.e., the magnitude spectrum is an even function):

$$|G(f)| = |G(-f)| \quad (8.67)$$

and the skew-symmetry of the phase (i.e., the phase spectrum is an odd function):

$$\angle G(f) = -\angle G(-f). \quad (8.68)$$

So the Fourier transform of a real-valued signal has a Hermitian symmetry.  $\diamond$



To derive the Plancherel theorem, the Fourier transform of the complex conjugation of the signal,  $g^*(x)$ , is needed. By (8.31), it is

$$\mathcal{F}\{g^*(x)\} = \int_{-\infty}^{\infty} g^*(x) e^{-j2\pi fx} dx = \left( \int_{-\infty}^{\infty} g(x) e^{j2\pi fx} dx \right)^* \quad (8.69)$$

$$= G^*(-f). \quad (8.70)$$

---

### Theorem 8.10: The Plancherel theorem

8.10

The Plancherel theorem (often referred to as Parseval's theorem) is of great practical importance. According to this theorem, certain operations—especially the inner product of signals [18] and the calculation of the signal energy—can be performed equally well in the spatial and the spatial frequency domain. To derive this theorem, the Fourier transform of the product of the functions  $g(x)$  and  $h^*(x)$  will be calculated. By (8.49) and (8.70), it is

$$\mathcal{F}\{g(x)h^*(x)\} = G(f) * H^*(-f). \quad (8.71)$$

Expressing the Fourier transform and the convolution as integrals,

$$\int_{-\infty}^{\infty} g(x)h^*(x) e^{-j2\pi fx} dx = \int_{-\infty}^{\infty} G(\alpha) H^*(\alpha - f) d\alpha, \quad (8.72)$$

and finally inserting  $f = 0$  results in the general formulation of the Plancherel theorem:

$$\int_{-\infty}^{\infty} g(x)h^*(x) dx = \int_{-\infty}^{\infty} G(f)H^*(f) df. \quad (8.73)$$

This equation establishes an identity between the inner product<sup>4</sup> of the signals  $g(x)$  and  $h(x)$  in the spatial and spatial frequency domains [18].

An important special case of the Plancherel theorem arises for  $g(x) = h(x)$ :

$$\int_{-\infty}^{\infty} |g(x)|^2 dx = \int_{-\infty}^{\infty} |G(f)|^2 df =: E_g. \quad (8.74)$$

According to this formula, the energy  $E_g$  of a signal  $g(x)$  can be obtained by calculating the energy density via integration in the time domain  $|g(x)|^2$ , as well as in the spatial frequency domain  $|G(f)|^2$ . As the signal  $g(x)$  and the spectrum  $G(f)$  contain the same amount of energy, the law of conservation of energy applies for the Fourier transform.  $\diamond$

---

<sup>4</sup>Equation (8.73) is an inner product of so-called energy signals [18]. These signals are square-integrable. As, in practice, image signals are always spatially restricted and have a limited amplitude, they are square-integrable and can be handled with the Plancherel theorem.

### 8.3.1.3 Fourier transforms of selected functions

**Example 8.4 (Fourier transform of the rectangular function):** The Fourier transform of a rectangular function, scaled to have an area of one,

$$g(x) = \frac{1}{L} \operatorname{rect}\left(\frac{x}{L}\right) \quad (8.75)$$

is given by

$$G(f) = \frac{1}{L} \int_{-\frac{L}{2}}^{\frac{L}{2}} e^{-j2\pi fx} dx = \frac{j}{2\pi fL} \underbrace{(e^{-j\pi fL} - e^{j\pi fL})}_{-2j \sin(\pi fL)} \quad (8.76)$$

$$= \frac{\sin(\pi fL)}{\pi fL} = \operatorname{sinc}(fL). \quad (8.77)$$

Here,

$$\operatorname{sinc}(w) := \frac{\sin(\pi w)}{\pi w} \quad (8.78)$$

is the so-called **cardinal sine function** or **sinc function**, and is illustrated in Fig. 8.9. ■

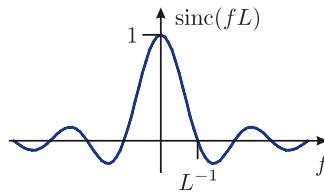


Figure 8.9. Sinc function.

**Example 8.5 (Fourier transform of the Dirac delta function):** For  $L \rightarrow 0$ , (8.15), (8.75) and (8.77) result in the following correspondence:

$$\delta(x) \quad \circ \rightarrow \bullet \quad 1 = \operatorname{sinc}(0). \quad (8.79)$$

Similarly,  $L \rightarrow \infty$  implies

$$1 \quad \circ \rightarrow \bullet \quad \delta(f). \quad (8.80)$$

Equations (8.79) and (8.80) illustrate the reciprocity of the spatial and the frequency domain. ■

**Example 8.6 (Fourier transform of the sign function):** The sign function  $\operatorname{sgn}(x)$  is defined as

$$\operatorname{sgn}(x) := \begin{cases} +1 & \text{if } x > 0 \\ 0 & \text{if } x = 0 \\ -1 & \text{if } x < 0 \end{cases}. \quad (8.81)$$

In order to calculate the corresponding Fourier transform, the sign function is expressed using the Heaviside function  $H(x)$  from (8.18):

$$\operatorname{sgn}(x) = 2H(x) - 1. \tag{8.82}$$

Differentiating that expression results in

$$\frac{d}{dx}\operatorname{sgn}(x) = 2\delta(x), \tag{8.83}$$

as the Dirac delta function is the derivative of the Heaviside function (see Sec. 8.2.2.2). According to (8.54), the Fourier transform sought can be calculated:

$$j2\pi f \cdot \mathcal{F}\{\operatorname{sgn}(x)\} = 2 \tag{8.84}$$

and so

$$\operatorname{sgn}(x) \quad \circ\bullet \quad \frac{1}{j\pi f}. \tag{8.85}$$



**Example 8.7 (Fourier transform of the Heaviside function):** The Heaviside function  $H(x)$  of (8.19) can be expressed by the sign function of (8.81):

$$H(x) = \frac{1}{2} + \frac{1}{2} \cdot \operatorname{sgn}(x). \tag{8.86}$$

With (8.80) and (8.85) this immediately implies

$$H(x) \quad \circ\bullet \quad \frac{1}{2}\delta(f) + \frac{1}{j2\pi f} \tag{8.87}$$



**Example 8.8 (Fourier transform of a complex harmonic):** The Fourier transform of a complex harmonic oscillation follows directly from the modulation property (8.60) and from (8.80):

$$g(x) = e^{j2\pi f_0 x} = 1 \cdot e^{j2\pi f_0 x} \quad \circ\bullet \quad \delta(f - f_0). \tag{8.88}$$

This is a Dirac delta function in the frequency domain at the position  $f_0$ .



**Example 8.9 (Fourier transform of the cosine function):** Using Euler's formula (8.34), the cosine function can be expressed as

$$g(x) = \cos(2\pi f_0 x) = \frac{1}{2} (e^{-j2\pi f_0 x} + e^{j2\pi f_0 x}). \tag{8.89}$$

Together with (8.88), this immediately results in the following correspondence:

$$\cos(2\pi f_0 x) \quad \circ\bullet \quad \frac{1}{2} (\delta(f + f_0) + \delta(f - f_0)). \tag{8.90}$$

Compared to the spectrum of a complex harmonic oscillation, the Fourier transform of the cosine function is composed of an additional Dirac delta function at the position  $-f_0$ . This confirms the symmetry property of the Fourier spectrum of real-valued signals discussed in Theorem 8.9. ■

**Example 8.10 (Fourier transform of the impulse train):** The **impulse train** and its Fourier transform are of great importance for describing sampling processes. The impulse train  $g(x)$  can be expanded in a Fourier series because of its periodicity [3, 4, 11, 18]:

$$g(x) = \sum_{m=-\infty}^{\infty} \delta(x - m \Delta x) \stackrel{!}{=} \sum_{k=-\infty}^{\infty} a_k e^{j2\pi \frac{k}{\Delta x} x}. \quad (8.91)$$

The coefficients  $a_k$  of the Fourier series are calculated as follows [3]:

$$a_k = \frac{1}{\Delta x} \int_{-\frac{\Delta x}{2}}^{\frac{\Delta x}{2}} \underbrace{g(x)}_{\delta(x)} e^{-j2\pi \frac{k}{\Delta x} x} dx = \frac{1}{\Delta x}. \quad (8.92)$$

The following correspondence of the impulse train (8.91) results from (8.92) and (8.88):

$$g(x) = \frac{1}{\Delta x} \sum_{k=-\infty}^{\infty} e^{j2\pi \frac{k}{\Delta x} x} \quad \circ \bullet \quad \frac{1}{\Delta x} \sum_{k=-\infty}^{\infty} \delta\left(f - \frac{k}{\Delta x}\right). \quad (8.93)$$

So the Fourier transform of the impulse train is again an impulse train in the spatial frequency domain:

$$\sum_{m=-\infty}^{\infty} \delta(x - m \Delta x) \quad \circ \bullet \quad f_0 \sum_{k=-\infty}^{\infty} \delta(f - k f_0), \quad f_0 = \frac{1}{\Delta x}. \quad (8.94)$$

The distances between the peaks of the Dirac delta functions in the spatial domain and those in the spatial frequency domain are linked reciprocally. ■

**Example 8.11 (Fourier transform of the Gaussian function):** The **Gaussian function**

$$h(x) = \frac{1}{\sqrt{2\pi}\sigma} e^{-\frac{x^2}{2\sigma^2}} \quad (8.95)$$

is, for example, used as an impulse response for low-pass filtering, which is why its Fourier transform is often useful (cf. Sec. 9.3.1.4). Applying the Fourier transform to (8.95) results in

$$H(f) = \int_{-\infty}^{\infty} h(x) e^{-j2\pi f x} dx = \frac{1}{\sqrt{2\pi}\sigma} \int_{-\infty}^{\infty} e^{-\frac{x^2}{2\sigma^2}} e^{-j2\pi f x} dx \quad (8.96)$$

$$= \frac{1}{\sqrt{2\pi}\sigma} \int_{-\infty}^{\infty} e^{-\left(\frac{x^2}{2\sigma^2} + j2\pi f x\right)} dx. \quad (8.97)$$

By completing the square, the exponent of (8.97) can be expressed as

$$\frac{x^2}{2\sigma^2} + j2\pi fx = \left(\frac{x}{\sqrt{2\sigma}}\right)^2 + 2\frac{x}{\sqrt{2\sigma}}j\pi\sqrt{2\sigma}f + (j\pi\sqrt{2\sigma}f)^2 - (j\pi\sqrt{2\sigma}f)^2 \quad (8.98)$$

$$= \left(\frac{x}{\sqrt{2\sigma}} + j\pi\sqrt{2\sigma}f\right)^2 - (j\pi\sqrt{2\sigma}f)^2 \quad (8.99)$$

$$= \frac{(x + j\pi 2\sigma^2 f)^2}{2\sigma^2} + (\pi\sqrt{2\sigma}f)^2. \quad (8.100)$$

Using this expression in (8.97) results in

$$H(f) = \frac{1}{\sqrt{2\pi}\sigma} e^{-(\pi\sqrt{2\sigma}f)^2} \int_{-\infty}^{\infty} e^{-\frac{(x+j2\pi\sigma^2 f)^2}{2\sigma^2}} dx. \quad (8.101)$$

And, finally, by substituting  $u = x + j2\pi\sigma^2 f$  and  $du = dx$ , it follows

$$H(f) = \frac{1}{\sqrt{2\pi}\sigma} e^{-(\pi\sqrt{2\sigma}f)^2} \int_{-\infty}^{\infty} e^{-\frac{u^2}{2\sigma^2}} du = e^{-(\pi\sqrt{2\sigma}f)^2}. \quad (8.102)$$

Here, the integral of the Gaussian function can be found in [5] for example. So the Fourier transform of the Gaussian function is again a Gaussian function in the spatial frequency domain. The widths of the functions  $h(x)$  and  $H(f)$  have a reciprocal relation. ■

### 8.3.2 The one-dimensional sampling theorem

Section 8.1 qualitatively discussed, by at least how many values a function should be sampled, i.e., spatially discretized, so that not too much information of the signal is lost during the digitization. The **sampling theorem** gives a quantitative answer to this problem and formulates a concrete condition that ensures an error-free reconstruction of the function from its samples.

---

#### Theorem 8.11: The Nyquist-Shannon sampling theorem for one-dimensional signals

8.11

For a signal with limited bandwidth

$$g(x) \quad \circ \bullet \quad G(f) \quad \text{with} \quad G(f) = 0 \quad \text{if} \quad |f| \geq \frac{F}{2} \quad (8.103)$$

an error-free reconstruction can be obtained from its samples  $g(m \Delta x)$ ,  $m \in \mathbb{Z}$  by applying a suitable low-pass filter if the sampling frequency  $f_A = \frac{1}{\Delta x}$  is chosen such that

$$f_A \geq F. \quad (8.104)$$

◇

If  $f_A$  is fixedly specified, a low-pass filter (a so-called **anti-aliasing filter** for suppressing the high-frequency components of the signal) has to be applied to  $g(x)$  before the sampling, in order to restrict the frequency band to  $(-\frac{f_A}{2}, \frac{f_A}{2})$ .

Figure 8.10 illustrates the sampling theorem. The band-limited signal  $g(x)$  is sampled via multiplication by an impulse train, which results in the sampled signal  $g_*(x)$ . According to the convolution theorem (8.49) of the Fourier transform, the multiplication of  $g(x)$  by

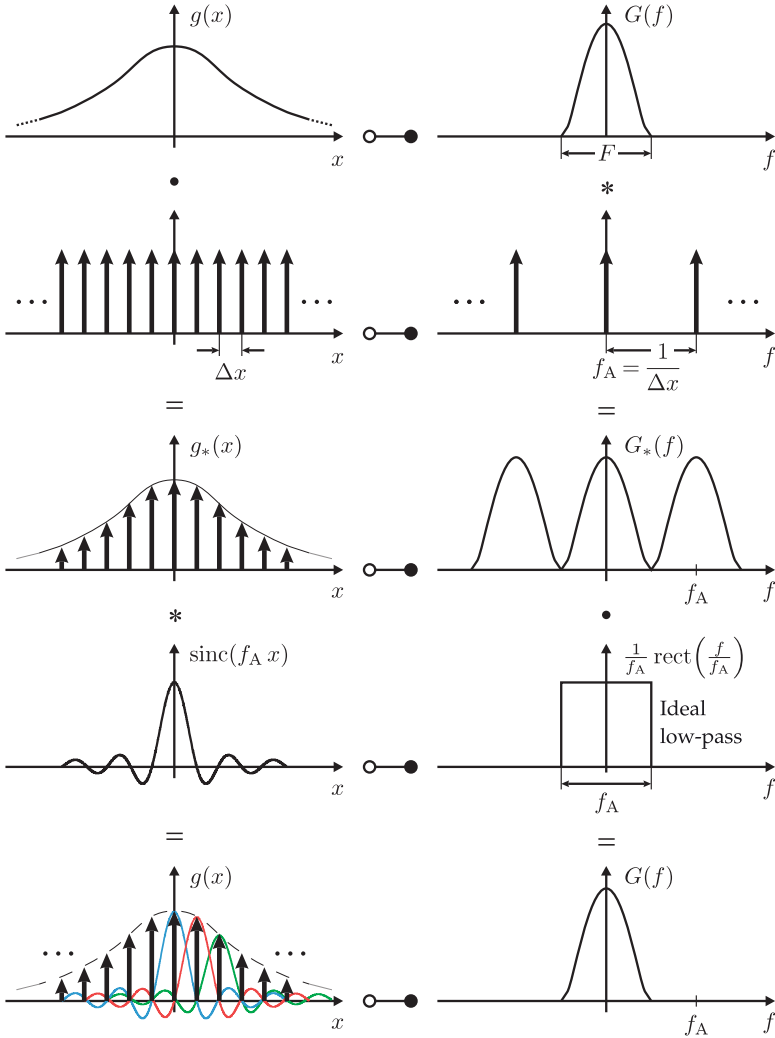


Figure 8.10. The sampling theorem.

the impulse train corresponds to the convolution of the spectrum  $G(f)$  with the Fourier transform of the impulse train—which, by (8.94), is again an impulse train—in the spatial frequency domain, resulting in a periodic repetition of the spectrum by (8.27):

$$g(x) \cdot \sum_{m=-\infty}^{\infty} \delta(x - m \Delta x) \quad \circ \bullet \quad G(f) * f_A \sum_{k=-\infty}^{\infty} \delta(f - k f_A), \quad (8.105)$$

$$g_*(x) \quad \circ \bullet \quad G_*(f) = f_A \sum_{k=-\infty}^{\infty} G(f - k f_A) \quad (8.106)$$

with

$$g_*(x) = \sum_{m=-\infty}^{\infty} g(m \Delta x) \delta(x - m \Delta x). \tag{8.107}$$

The reconstruction is based on the suppression of the periodic repetition of the spectrum via a multiplication by an ideal low-pass; in the spatial domain, this filtering corresponds to a convolution with the sinc function:

$$g_*(x) * \text{sinc}(f_A x) \quad \circ\bullet \quad G_*(f) \cdot \frac{1}{f_A} \text{rect}\left(\frac{f}{f_A}\right). \tag{8.108}$$

If the condition  $f_A \geq F$  of the sampling theorem is met, this filtering yields the error-free reconstruction of the signal

$$g(x) = \sum_{m=-\infty}^{\infty} g(m \Delta x) \text{sinc}(f_A(x - m \Delta x)) \quad \circ\bullet \quad G(f). \tag{8.109}$$

As

$$\text{sinc}(f_A(n \Delta x - m \Delta x)) = \delta_{mn} = \begin{cases} 1 & \text{if } m = n \\ 0 & \text{if } m \neq n \end{cases} \tag{8.110}$$

for the sampling positions  $x = n \Delta x, n \in \mathbb{Z}$ , the resulting values at these positions directly correspond to the samples and the values between these positions are interpolated without errors.

However, if that condition is not met because the choice of sampling frequency  $f_A$  was too low, the spectra in  $G_*(f)$  will overlap each other. Then, no error-free reconstruction of the original signal can be obtained.

**Remarks:**

- The sampling theorem not only applies to the sampling of spatial signals  $g(x)$ , but also to the sampling of the Fourier transforms  $G(f)$  of spatially limited signals  $g(x)$  with  $g(x) = 0$  if  $|x| \geq \frac{L}{2}$ . The corresponding condition is

$$(\Delta f)^{-1} \geq L. \tag{8.111}$$

- A signal can be either spatially limited or band-limited, but not both at the same time. In order to clarify this property, the windowing (i.e., multiplication) of an arbitrary signal  $g(x)$  by the rectangular window function

$$w(x) = \text{rect}\left(\frac{x}{L}\right) \quad \circ\bullet \quad W(f) = L \text{sinc}(fL) \tag{8.112}$$

will be considered. This windowing results in the spatial limitation of the signal  $g(x)$  to the interval of  $[-\frac{L}{2}, \frac{L}{2}]$  and corresponds to the convolution with a sinc function in the frequency domain:

$$g_w(x) = g(x) \text{rect}\left(\frac{x}{L}\right) \quad \circ\bullet \quad G_w(f) = G(f) * L \text{sinc}(fL). \tag{8.113}$$

As the sinc function is infinitely spread, the convolution  $G(f) * L \text{sinc}(fL)$  results in an infinitely spread spectrum  $G_w(f)$ , i.e., the windowed signal  $g_w(x)$  is not band-limited.

### ► 8.3.3 The discrete Fourier transform (DFT)

#### ⊗ 8.3.3.1 Definition of the DFT

As the digital representation of an unlimited continuous signal would consume infinitely much storage, the Fourier transform (8.31) cannot be used in a computer. Thus, the discrete Fourier transform (DFT), which is suitable for computers, is used as an approximation of the Fourier transform and will now be explained. Based on the Fourier transform

$$G(f) = \int_{-\infty}^{\infty} g(x) e^{-j2\pi f x} dx \quad (8.114)$$

the following approximation can be obtained by sampling the signal  $g(x)$ ,  $x = n \Delta x$  together with a rectangular integration:

$$G(f) \approx \sum_{n=-\infty}^{\infty} g(n \Delta x) e^{-j2\pi f n \Delta x} \Delta x. \quad (8.115)$$

Limiting the summation to a limited region of the signal results in

$$G(f) \approx \sum_{n=0}^{N-1} g(n \Delta x) e^{-j2\pi f n \Delta x} \Delta x. \quad (8.116)$$

Finally, with  $f = l \Delta f$ ,  $l \in \mathbb{Z}$  and a discretization of the spatial frequency that corresponds to a sampling in the spatial frequency domain with a frequency step size of  $\Delta f = f_A/N = 1/(N \Delta x)$ , we obtain

$$G(l \Delta f) \approx \underbrace{\sum_{n=0}^{N-1} g(n \Delta x) e^{-j2\pi \frac{nl}{N}} \Delta x}_{=: G_l} \quad (8.117)$$

#### 8.7 Definition 8.7: The discrete Fourier transform (DFT)

The discrete Fourier transform (DFT) of a discrete signal  $g_n$  is given by

$$G_l = \sum_{n=0}^{N-1} g_n e^{-j2\pi \frac{ln}{N}} \quad \text{with} \quad g_n := g(n \Delta x). \quad (8.118)$$

The spectrum  $G_l$ , with discrete frequencies, can be used to reconstruct the discrete signal by performing the inverse DFT:

$$g_n = \frac{1}{N} \sum_{l=0}^{N-1} G_l e^{j2\pi \frac{ln}{N}}. \quad (8.119)$$

The factor  $\frac{1}{N}$  can be arbitrarily distributed between the forward transformation and the inverse transformation. Here, different definitions are common.  $\diamond$

Table 8.2 summarizes the relation between the position  $x$  together with the spatial frequency  $f$  and their corresponding discrete quantities. In particular, the resolution of the frequency

$$\Delta f = \frac{f_A}{N} = \frac{1}{N \Delta x} \quad (8.120)$$



Table 8.2. Relations between continuous and discrete quantities.

	Continuous		Discrete	
Position	$x$	=	$n \Delta x$	
Spatial frequency	$f$	=	$l \Delta f$	with $\Delta f = f_A/N$ $f_A = (\Delta x)^{-1}$

corresponds to the reciprocal of the signal length  $N \Delta x$  and is therefore completely determined by the size of the sampling steps  $\Delta x$  and the number  $N$  of samples.

Figure 8.11 illustrates the DFT schematically, based on a one-dimensional spatial signal  $g(x)$  (a). The sampling corresponds to a multiplication of the signal  $g(x)$  by an impulse train (b) and results in a periodic repetition of the spectrum  $G_*(f)$  (c) which, in this case, is affected by an **aliasing error**, as the hypotheses of the sampling theorem were violated. The multiplication by the rectangular window function (d) limits the number of samples of the spatially discrete signal  $g_n$  to  $N$  (e). In the Fourier domain, this windowing corresponds to a convolution with a sinc function, resulting in a defocused spectrum (**spectral leakage**, see Sec. 8.3.3.3). Finally, during the discretization of the frequency, the spectrum is sampled via multiplication by an impulse train (f), causing a periodic repetition of the signal  $g_n$  in the spatial domain. The information contained in the resulting spectrum  $G_l$  is concentrated in discrete frequencies, which is why this loss of information is also called the **picket-fence effect**.

⊗ 8.3.3.2 Properties of the DFT

In this subsection, the main differences between the continuous Fourier transform (8.31) and the DFT (8.118) will be discussed. Because of the simultaneous discretization of the spatial frequency and the position, the DFT periodically repeats the signals  $g_n$  and  $G_l$  implicitly:

$$g_n = g_n + k N, \tag{8.121}$$

$$G_l = G_l + k N. \tag{8.122}$$

Therefore, the DFT spectrum  $G_l$  describes the signal  $g_n$  only inside the so-called Nyquist band  $[-f_A/2, f_A/2]$ .

Although the spatially discrete signal  $g_n$  is the result of the sampling of the continuous signal  $g(x)$ ,

$$g_n = g(x)|_{x=n\Delta x}, \tag{8.123}$$

in general, the DFT spectrum  $G_l$  is only an approximation to the samples  $G(f)|_{f=l\Delta f}$  of the continuous Fourier spectrum  $G(f)$ :

$$G_l \stackrel{\text{generally}}{\neq} G(f)|_{f=l\Delta f}. \tag{8.124}$$

Besides the loss of information caused by the discretization of the frequency, the differences between  $G(f)$  and  $G_l$  can be explained by overlapping bands (**aliasing**) and by the effect of spectral leakage. The aliasing error resulting from the violation of the hypotheses of the sampling theorem is practically inevitable, as image signals are generally spatially limited

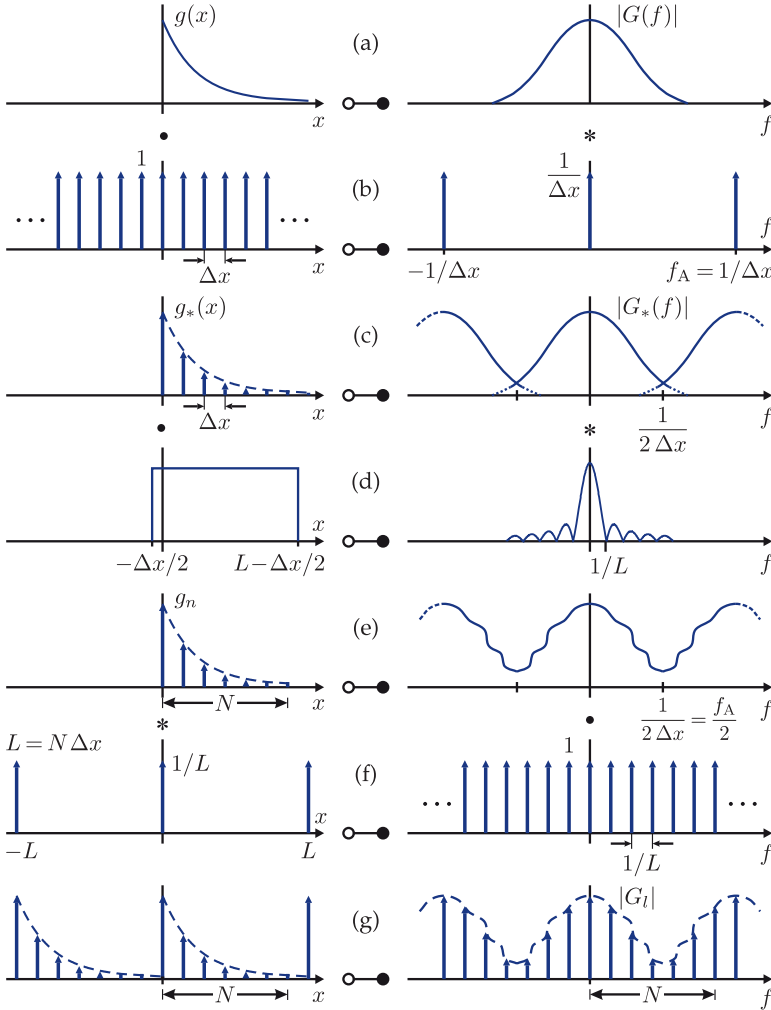


Figure 8.11. Discrete Fourier transform [4]. As  $G(f)$ ,  $G_*(f)$  and  $G_t$  are complex-valued, only their absolute values are shown.

and hence cannot be simultaneously band-limited. The following section covers the effects of spectral leakage and shows the possibilities which can be used to mitigate these effects.

⊗ **8.3.3.3 Spectral leakage**

Spectral leakage describes the impact of the spatial limitation of a signal on its Fourier transform. Figures 8.11(c)–(e) already showed that multiplication of the spatial signal  $g_*(x)$  by a rectangular windowing function  $w(x) = \text{rect}(\frac{x-x_0}{L})$  results in the convolution of the spectrum  $G_*(f)$  with the Fourier transform  $W(f)$  of the spatial window and, thus to a blurring of  $G_*(f)$ . Now, two further interpretations of spectral leakage will be discussed.

- The periodic repetition (8.121) of the spatial signal  $g_n$  usually results in discontinuities or ‘bends’ between the single repetitions. The description of such artefacts requires parts of a broadband spectrum, which are represented by the spectral leakage.
- The inverse DFT (8.119) corresponds to an approximation of the signal  $g(x)$  by a linear combination of  $N$  periodic basis functions  $e^{j2\pi l \Delta f x}$ ,  $l = 0, \dots, N - 1$ , which span an  $N$ -dimensional space of functions  $\mathcal{U}$ . For  $g(x) \in \mathcal{U}$ ,  $g(x)$  can be approximated without errors, i.e., it can be transformed without spectral leakage. For  $g(x) \notin \mathcal{U}$ , the DFT represents an orthogonal projection of  $g(x)$  onto  $\mathcal{U}$ : the difference between the original and the projection corresponds to the spectral leakage. In this case, usually all basis functions are needed for the approximation.

As mentioned above, there are certain cases which are not affected by spectral leakage even though the signal is windowed. In order to demonstrate this, the DFT of a harmonic oscillation will be considered in the following example.

---

**Example 8.12 (DFT of a harmonic oscillation):** The DFT of a harmonic function

$$g(x) = \cos(2\pi f_0 x) \quad (8.125)$$

of frequency  $f_0$  is considered, which has been sampled with  $N = 32$  samples and a sampling step distance of  $\Delta x = 1$  (see Fig. 8.12). Employing (8.120), the frequency resolution is given by

$$\Delta f = \frac{1}{N \Delta x} = \frac{1}{32}. \quad (8.126)$$

If the ratio of the spatial frequency  $f_0$  and the frequency resolution  $\Delta f$  is an integer, there is no spectral leakage [4, 18]. Figure 8.12 (top) shows an oscillation with the frequency  $f_0 = 1/8$ , which results in an integer ratio of  $f_0/\Delta f = 4$ . Hence, the sampled signal consists of exactly four periods of the oscillation, for which reason a periodic repetition does not result in any change of the signal. Only the two Dirac delta functions, which correspond to the cosine oscillation, are visible in the DFT spectrum, cf. (8.90).

However, this is not the case for the oscillation with the spatial frequency  $f_0 = 1/9.143$ , shown in Fig. 8.12 (center). Here, the sampling signal covers  $f_0/\Delta f = 3.5$  periods of the oscillation, so that periodic repetitions show distinct discontinuities. The DFT spectrum clearly shows the effect of spectral leakage.

In order to reduce spectral leakage, the sampling signal  $g_n$  can be multiplied by a window function  $w_n$ , which can smooth the discontinuities between the single repetitions. However, it has to be accepted that the border regions of  $g(x)$  will not be represented in the spectrum to their full extent [16]. Signals which are compact in the spatial frequency domain are especially suitable window functions [14]. In Fig. 8.12 (bottom), a Hann window was used:

$$w_n := \frac{1}{2} \left( 1 - \cos\left(\frac{2\pi n}{N}\right) \right), \quad x \in [0, N]. \quad (8.127)$$

The DFT spectrum of the windowed signal shows a notably reduced spectral leakage in contrast to the DFT spectrum of the original signal. ■

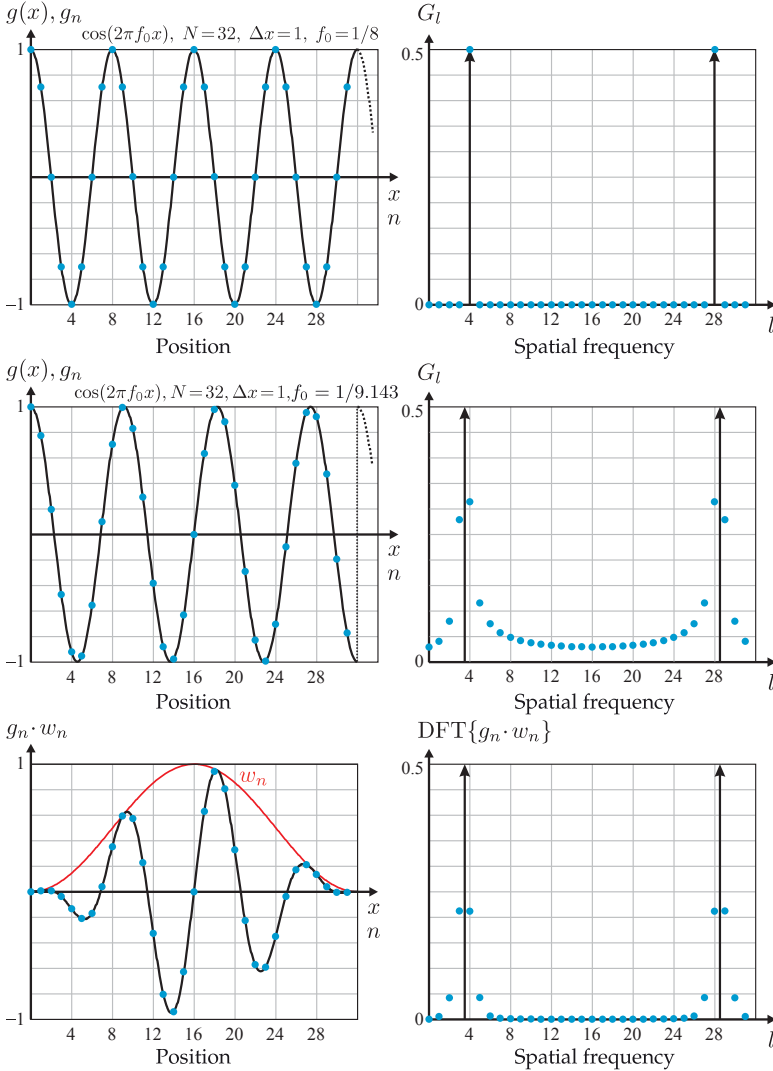


Figure 8.12. Spectral leakage: (top) DFT of an oscillation without spectral leakage; (center) DFT of an oscillation with spectral leakage; (bottom) Reduction of spectral leakage by windowing [4].

8.3.3.4 The fast Fourier transform (FFT)

The DFT  $G_l$  has very high computational costs, as all signal values  $g_n, n \in \{0, \dots, N - 1\}$  have to be taken into account for the calculation of each frequency index  $l$ . The **fast Fourier transform** represents a fast algorithm for the calculation of the DFT, which yields the same result as the DFT but needs fewer operations [4, 8, 13]. Approximately

- $N^2$  complex additions and multiplications are needed by the DFT and
- $N \lg N$  complex additions and multiplications are needed by the FFT.

For the FFT,  $N$  is assumed to be a power of two, because this allows the most efficient implementation of the FFT algorithm.

However, the speedup of the FFT with respect to the DFT first becomes noticeable for signal lengths greater than  $N = 16$ . As an example, a signal of length  $N = 1024$  will be considered. In this case, the DFT would require  $N^2 \approx 10^6$  complex additions and multiplications; in contrast, the FFT would be finished after only  $N \log N \approx 10^4$  operations.

A detailed description of the FFT is given in the book [4].

### 8.3.3.5 The convolution theorem of the DFT

The convolution theorem (8.48) says that the convolution of two signals corresponds to the multiplication of their Fourier transforms. If for performing a filtering operation, the convolution of a signal  $g_n$  and a long impulse response  $h_n$  has to be calculated, it might be beneficial, in terms of computational complexity, to perform this operation in the spatial frequency domain. Therefore, at first the signal  $g_n$  and the impulse response  $h_n$  are transformed using the FFT algorithm. Then, the resulting DFT spectra  $G_l$  and  $H_l$  are multiplied together, and the result is transformed back into the spatial domain using the FFT algorithm again:

$$\text{DFT}^{-1}\{G_l \cdot H_l\} = \sum_{\nu=0}^{N-1} g_{\nu} h_{(n-\nu) \bmod N} = g_n * h_n = k_n. \quad (8.128)$$

cyclic  
↓

Here, it has to be taken into account that the DFT results in an  $N$ -periodic repetition of both the signals  $g_n$ ,  $h_n$  and the result of the convolution  $k_n$ ; so filtering in the DFT spectrum results in a cyclic convolution. Hence, the index  $n - \nu$  inside the convolution sum of (8.128) has to be interpreted as modulo  $N$ .

To illustrate cyclic convolution, assume the original signal  $g_n$  has length  $Q$ , and the impulse response  $h_n$  has length  $P$ . A convolution in the spatial domain without repetitions would result in a signal of length  $P + Q - 1$ . Thus, the result of the cyclic convolution only equals the convolution in the spatial domain if the following condition is met (see Fig. 8.13):

$$N \geq P + Q - 1. \quad (8.129)$$

In order to ensure compliance with this condition, the length  $N$  of the signals  $g_n$  and  $h_n$  can be increased by appending zeros (the so-called *zero padding*) before the actual transformation. The error caused by disregarding this rule is the so-called **end effect**.

## 8.3.4 The two-dimensional Fourier transform

### 8.3.4.1 Definition of the two-dimensional Fourier transform

In order to use the Fourier transform for two-dimensional signals, the integral kernel  $e^{-j2\pi f x}$  in (8.31) has to be defined as a function of four variables,  $e^{-j2\pi(f_x x + f_y y)}$  [1].

---

#### Definition 8.8: The two-dimensional Fourier transform

The two-dimensional Fourier transform maps a two-dimensional function  $g(\mathbf{x}) : \mathbb{R}^2 \rightarrow \mathbb{C}$  of position  $\mathbf{x} = (x, y)^T$  to a two-dimensional function  $G(\mathbf{f}) : \mathbb{R}^2 \rightarrow \mathbb{C}$  of spatial frequency

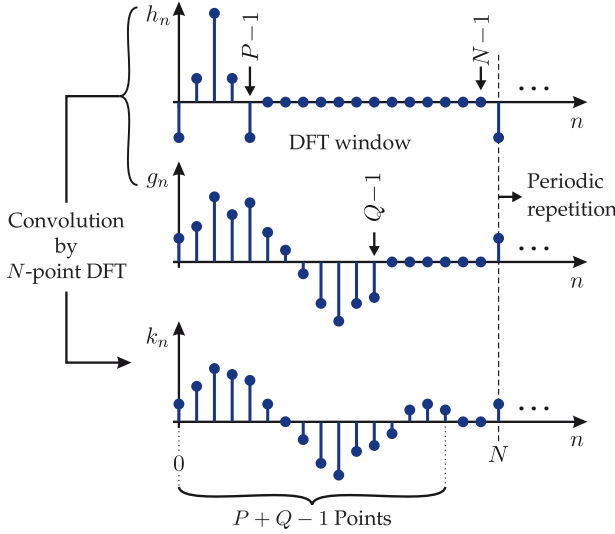


Figure 8.13. Cyclic convolution resulting from the DFT.

$\mathbf{f} = (f_x, f_y)^T$ , according to the following integral transform:

$$G(\mathbf{f}) = \mathcal{F}\{g(\mathbf{x})\} := \int_{-\infty}^{\infty} \int_{-\infty}^{\infty} g(\mathbf{x}) e^{-j2\pi\mathbf{f}^T\mathbf{x}} d\mathbf{x} \tag{8.130}$$

$$= \int_{-\infty}^{\infty} \underbrace{\left( \int_{-\infty}^{\infty} g(\mathbf{x}) e^{-j2\pi f_x x} dx \right)}_{\text{separability}} e^{-j2\pi f_y y} dy \tag{8.131}$$

with  $\mathbf{f}^T\mathbf{x} = f_x x + f_y y$ . Because

$$e^{-j2\pi\mathbf{f}^T\mathbf{x}} = e^{-j2\pi f_x x} \cdot e^{-j2\pi f_y y}, \tag{8.132}$$

the integral kernel of the Fourier transform can be factored, resulting in the separability (8.131) of the Fourier transform: a two-dimensional Fourier transform can be achieved by two one-dimensional Fourier transform. The vectorial formulation (8.130) can also be used for the  $n$ -dimensional case  $\mathbf{x} \in \mathbb{R}^n, \mathbf{f} \in \mathbb{R}^n$  if the integration is done  $n$  times.

The inverse transformation of the Fourier transform  $G(\mathbf{f})$  to the original function  $g(\mathbf{x})$  is performed according to the following formula:

$$g(\mathbf{x}) = \mathcal{F}^{-1}\{G(\mathbf{f})\} = \int_{-\infty}^{\infty} \int_{-\infty}^{\infty} G(\mathbf{f}) e^{j2\pi\mathbf{f}^T\mathbf{x}} d\mathbf{f}. \tag{8.133}$$

The Fourier transform  $G(\mathbf{f})$  is called the spectrum of the signal  $g(\mathbf{x})$ . ◇

From now on, the symbol  $\circ\bullet$  will be used to denote two-dimensional Fourier correspondences.

Although the Fourier transform is defined for complex-valued signals  $g(\mathbf{x}) : \mathbb{R}^2 \rightarrow \mathbb{C}$ , in image processing, it is mostly applied to real-valued signals, i.e.,  $g(\mathbf{x}) : \mathbb{R}^2 \rightarrow \mathbb{R}$ .

⊗ 8.3.4.2 Properties of the two-dimensional Fourier transform

In addition to Sec. 8.3.1, this subsection will present some further properties of the Fourier transform, which are of great practical relevance, especially for the two-dimensional case.

**Theorem 8.12: The separation theorem**

If the variables  $x$  and  $y$  of the function  $g(\mathbf{x})$  are separable, the function can be factored. Because of the separability of the Fourier transform, the factors can be transformed independently:

$$g(\mathbf{x}) = g_1(x) g_2(y) \quad \circ\bullet \quad G(\mathbf{f}) = G_1(f_x) G_2(f_y) \tag{8.134}$$

with

$$g_1(x) \quad \circ\bullet \quad G_1(f_x) \quad \text{and} \quad g_2(y) \quad \circ\bullet \quad G_2(f_y). \tag{8.135}$$

So each factor is subject to a separate, one-dimensional transform. ◇

**Example 8.13 (2D Fourier transform of a separable function):** Consider the function given by

$$g(\mathbf{x}) = \delta(x) \cos(2\pi f_{y_0} y). \tag{8.136}$$

According to the separation theorem (8.134), the Fourier transform is given by

$$G(\mathbf{f}) = 1(f_x) \frac{1}{2} (\delta(f_y + f_{y_0}) + \delta(f_y - f_{y_0})). \tag{8.137}$$

Here, the expression  $1(f_x)$  indicates that  $G(\mathbf{f})$  is independent<sup>5</sup> of  $f_x$ . Figure 8.14 illustrates the function  $g(\mathbf{x})$  and its spectrum  $G(\mathbf{f})$ . ■

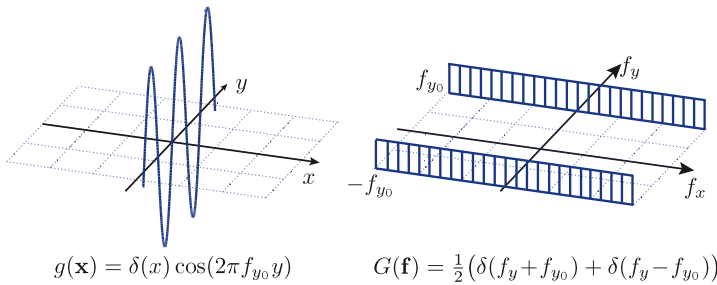


**Figure 8.14.** Example of applying the separation theorem. The interpretation of this figure is not straightforward, as the two graphs represent the weights of Dirac delta functions. Details of these so-called slice functions will be given in Sec. 8.3.5.

<sup>5</sup>The function  $1(u) : \mathbb{R} \rightarrow \{1\}$  or  $1(u) \equiv 1$  is constant with respect to its argument  $u$  and thus represents a redundant factor. However, it is used as a mental note in signals with multidimensional arguments, in order to allow especially a correct multidimensional Fourier transform.

**Example 8.14 (Fourier transform of the two-dimensional Gaussian function):** The two-dimensional Gaussian function  $h(\mathbf{x})$  can be expressed as a product of two one-dimensional Gaussians as in (8.95):

$$h(\mathbf{x}) = \frac{1}{2\pi\sigma^2} e^{-\frac{\|\mathbf{x}\|^2}{2\sigma^2}} = \underbrace{\frac{1}{\sqrt{2\pi}\sigma}}_{h(x)} e^{-\frac{x^2}{2\sigma^2}} \cdot \underbrace{\frac{1}{\sqrt{2\pi}\sigma}}_{h(y)} e^{-\frac{y^2}{2\sigma^2}}. \quad (8.138)$$

The separation theorem (8.134) and equation (8.102) yield the Fourier transform  $H(\mathbf{f})$ :

$$H(\mathbf{f}) = H(f_x) H(f_y) = e^{-(\pi\sqrt{2}\sigma f_x)^2} e^{-(\pi\sqrt{2}\sigma f_y)^2} = e^{-2\pi^2\sigma^2\|\mathbf{f}\|^2}. \quad (8.139)$$

$H(\mathbf{f})$  is also a Gaussian function. ■

### 8.13 Theorem 8.13: Linear coordinate transformations

A linear coordinate transformation is the multi-dimensional analogon to one-dimensional spatial scaling. Here, a linear transformation of the position vector  $\mathbf{x} = (x, y)^T$  by the invertible  $2 \times 2$  matrix  $\mathbf{A}$  is considered:

$$\boldsymbol{\xi} = \mathbf{A}\mathbf{x}, \quad \det \mathbf{A} \neq 0. \quad (8.140)$$

The spectrum of the transformed signal  $g(\boldsymbol{\xi}) = g(\mathbf{A}\mathbf{x})$  is given by

$$\mathcal{F}\{g(\mathbf{A}\mathbf{x})\} = \int_{-\infty}^{\infty} \int_{-\infty}^{\infty} g(\mathbf{A}\mathbf{x}) e^{-j2\pi\mathbf{f}^T\mathbf{x}} d\mathbf{x} \quad \text{with} \quad d\boldsymbol{\xi} = |\det \mathbf{A}| d\mathbf{x} \quad (8.141)$$

$$= |\det \mathbf{A}|^{-1} \int_{-\infty}^{\infty} \int_{-\infty}^{\infty} g(\boldsymbol{\xi}) e^{-j2\pi((\mathbf{A}^{-1})^T\mathbf{f})^T\boldsymbol{\xi}} d\boldsymbol{\xi} \quad (8.142)$$

$$= |\det \mathbf{A}|^{-1} G((\mathbf{A}^{-1})^T\mathbf{f}). \quad (8.143)$$

As an example, Fig. 8.15 shows a rectangular signal that has been rotated, shrunk/stretched, and sheared. The rotation is represented by the corresponding transformation matrix

$$\mathbf{A} = \begin{pmatrix} \cos \alpha & \sin \alpha \\ -\sin \alpha & \cos \alpha \end{pmatrix}, \quad (8.144)$$

the shrinking and stretching is represented by

$$\mathbf{A} = \begin{pmatrix} k_1 & 0 \\ 0 & k_2 \end{pmatrix} \quad (8.145)$$

and the shear by

$$\mathbf{A} = \begin{pmatrix} 1 & -a \\ 0 & 1 \end{pmatrix}. \quad (8.146)$$

Figure 8.15(b) shows, in particular, that rotationally symmetric signals have rotationally symmetric spectra. ◇



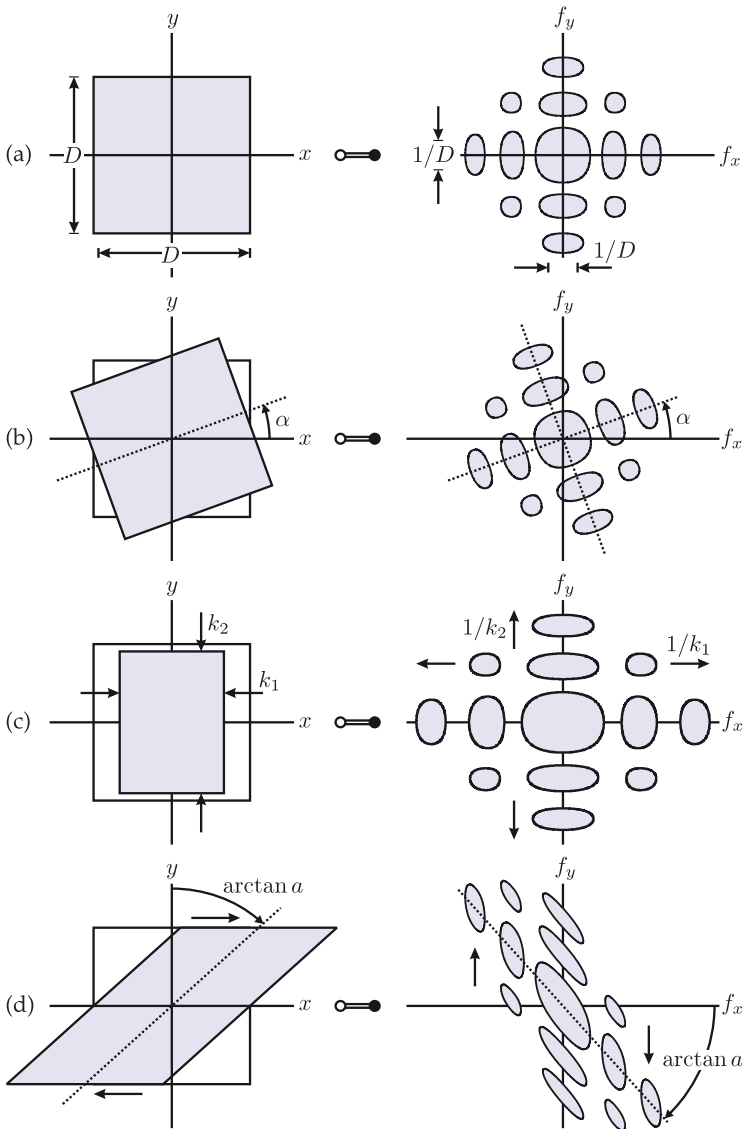


Figure 8.15. Examples of linear coordinate transformations: (a) Original; (b) Rotation; (c) Shrinking/Stretching; (d) Shear [1].

8.14

**Theorem 8.14: The convolution theorem**

As was the case for one dimension, the convolution of two multi-dimensional functions  $g(\mathbf{x})$  and  $h(\mathbf{x})$  is also transformed into the product of their spectra by the Fourier transform:

$$k(\mathbf{x}) = g(\mathbf{x}) ** h(\mathbf{x}) = \int_{-\infty}^{\infty} \int_{-\infty}^{\infty} g(\alpha, \beta) h(x - \alpha, y - \beta) d\alpha d\beta \tag{8.147}$$



$$K(\mathbf{f}) = G(\mathbf{f}) \cdot H(\mathbf{f}). \tag{8.148}$$

Here, the operator  $**$  denotes a two-dimensional convolution. ◇

**Example 8.15 (System-theoretical description of optical imaging):** Optical imaging with a single lens can be approximated by a linear, shift invariant system. The impulse response  $h(\mathbf{x})$  represents the response of the system to a Dirac delta function  $\delta(\mathbf{x})$ , which can be imagined as an input image of a bright point in front of a dark background (see Fig. 8.16). Therefore, the impulse response  $h(\mathbf{x})$  is also called the **point spread function (PSF)**.

The Fourier transform of the impulse response is called the **optical transfer function (OTF)**  $H(\mathbf{f})$  of the imaging system.

In particular, this description also covers the case of a defocused optical imaging (cf. Sec. 3.4.4):

$$h(\mathbf{x}) = k \operatorname{rect} \left( \frac{\|\mathbf{x}\|}{\varepsilon} \right) \iff H(\mathbf{f}) = k \frac{\varepsilon}{2} \cdot \frac{J_1(\pi\varepsilon\|\mathbf{f}\|)}{\|\mathbf{f}\|}. \tag{8.149}$$

Here,  $J_n$  represents the  $n$ th order Bessel function of the first kind; cf. (2.169) [5]. Figure 8.17 shows the optical transfer function  $H(\mathbf{f})$  of the defocused optical imaging, which has low-pass characteristics. The first zeros of  $H(\mathbf{f})$  are located on the circle  $\|\mathbf{f}\| = 1.22\varepsilon^{-1}$ . For the transition  $\varepsilon \rightarrow 0$  to sharp optical imaging, these zeros move towards infinity, resulting in  $H(\mathbf{f}) \equiv 1$ , which represents an ideal optical transfer function in the spatial frequency domain and a Dirac delta function in the spatial domain. ■

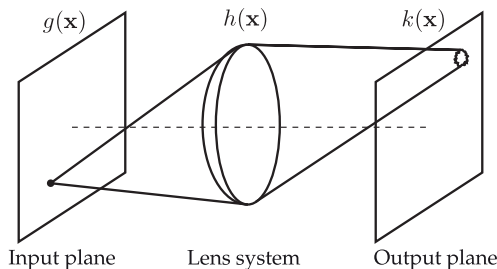


Figure 8.16. System-theoretic view of optical imaging as a linear, shift invariant system.

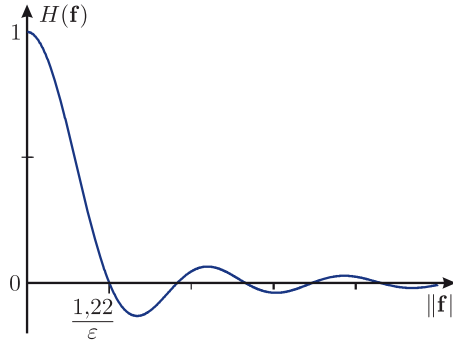


Figure 8.17. Optical transfer function of defocused optical imaging. Because of the rotational symmetry, the visualization of a radial section of  $H(\mathbf{f})$  is sufficient. Qualitatively, this function resembles the sinc function.

► 8.3.5 Dirac delta functions in two-dimensional space

In the two-dimensional space, two important cases have to be considered regarding Dirac delta functions. For a scalar argument  $x$ , the two-dimensional  $\delta(x)$  is implicitly constant with respect to the second spatial variable  $y$ . So, the Dirac delta function can be imagined to be stretched in the  $y$ -direction to form an infinitely spread **slice function** (cf. Fig. 8.14 right side). The following formula provides an explicit expression of these considerations:

$$\delta(x) = \delta(\mathbf{x}^T \mathbf{e}_x) = \delta(x) 1(y) \quad \circ\bullet \quad 1(f_x) \delta(f_y) = \delta(f_y) = \delta(\mathbf{f}^T \mathbf{e}_y). \tag{8.150}$$

This slice function can be informally characterized as follows:

$$\delta(x) \text{ '}' = \begin{cases} \infty & \text{if } x = 0, \text{ i.e., on the } y\text{-axis} \\ 0 & \text{otherwise} \end{cases}. \tag{8.151}$$

By introducing basis vectors  $\mathbf{e}_\varphi$  and  $\mathbf{e}_{\varphi\perp}$  that are rotated by an angle  $\varphi$ ,

$$\mathbf{e}_\varphi = (\cos \varphi, \sin \varphi)^T, \quad \mathbf{e}_{\varphi\perp} = (-\sin \varphi, \cos \varphi)^T, \tag{8.152}$$

and the distance  $d \in \mathbb{R}$  to the origin, an arbitrarily positioned slice function can be described:

$$\delta(\mathbf{x}^T \mathbf{e}_\varphi - d). \tag{8.153}$$

The distance  $d$  can also be expressed via the vector

$$\mathbf{d} := \mathbf{e}_\varphi d, \tag{8.154}$$

so that (8.153) leads to:

$$\delta(\mathbf{x}^T \mathbf{e}_\varphi - d) = \delta(\mathbf{x}^T \mathbf{e}_\varphi - \mathbf{d}^T \mathbf{e}_\varphi) = \delta((\mathbf{x} - \mathbf{d})^T \mathbf{e}_\varphi). \tag{8.155}$$

With (8.150), (8.154) and by means of the shift property (8.57), the following holds for an arbitrarily positioned slice function:

$$\delta((\mathbf{x} - \mathbf{d})^T \mathbf{e}_\varphi) \quad \circ\bullet \quad \delta(\mathbf{f}^T \mathbf{e}_{\varphi\perp}) e^{-j2\pi \mathbf{f}^T \mathbf{d}} = \delta(\mathbf{f}^T \mathbf{e}_{\varphi\perp}) e^{-j2\pi \mathbf{f}^T \mathbf{e}_\varphi d}. \tag{8.156}$$

The slice function  $\delta(\mathbf{f}^T \mathbf{e}_{\varphi\perp})$  runs through the origin of the spatial frequency domain and is perpendicular to the slice function  $\delta(\mathbf{x}^T \mathbf{e}_\varphi - d)$  in the spatial domain.

In the second important case, the Dirac delta function has a vectorial argument. Here, the original definition (8.10) is extended to two dimensions.

**8.9 Definition 8.9: The two-dimensional Dirac delta function**

The two-dimensional Dirac delta function is defined as

$$\int_{-\infty}^{\infty} \int_{-\infty}^{\infty} \delta(\mathbf{x} - \mathbf{x}_0) g(\mathbf{x}) \, d\mathbf{x} = g(\mathbf{x}_0) \quad \text{with } g(\mathbf{x}) \text{ continuous at } \mathbf{x}_0. \tag{8.157}$$

As in the one-dimensional case, the two-dimensional Dirac delta function, if used as an integral kernel, results in an extraction of the value of the function  $g(\mathbf{x})$  at the position  $\mathbf{x}_0$ .  $\diamond$

The two-dimensional Dirac delta function can be approximated as follows:

$$\delta_\epsilon(\mathbf{x} - \mathbf{x}_0) = \frac{1}{\epsilon^2} \operatorname{rect}\left(\frac{x - x_0}{\epsilon}\right) \operatorname{rect}\left(\frac{y - y_0}{\epsilon}\right) \xrightarrow{\epsilon \rightarrow 0} \delta(\mathbf{x} - \mathbf{x}_0). \tag{8.158}$$

According to (8.12), this corresponds to the product of the approximations  $\delta_\epsilon(x)$  and  $\delta_\epsilon(y)$  of two one-dimensional Dirac delta functions, see Fig. 8.18.

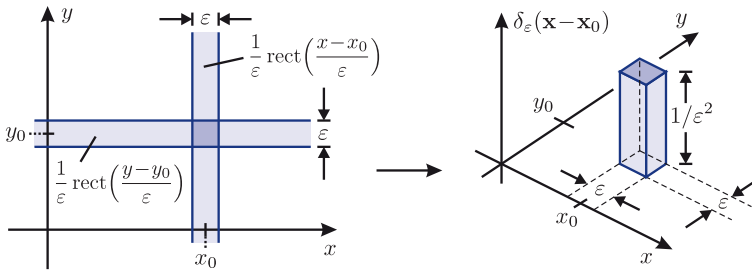


Figure 8.18. Approximation of the two-dimensional Dirac delta function.

The following formula holds for the two-dimensional Dirac delta function:

$$\delta(\mathbf{x}) = \delta(x) \delta(y), \tag{8.159}$$

i.e., the two-dimensional Dirac delta function can be expressed by two orthogonally aligned slice functions (a dyadic product). Furthermore,

$$\int_{-\infty}^{\infty} \int_{-\infty}^{\infty} \delta(\mathbf{x}) \, d\mathbf{x} = 1, \tag{8.160}$$

$$g(\mathbf{x}) ** \delta(\mathbf{x} - \mathbf{x}_0) = g(\mathbf{x} - \mathbf{x}_0). \tag{8.161}$$

According to (8.158), the two-dimensional Dirac delta function can be imagined as an infinitely narrow function of infinite height:

$$\delta(\mathbf{x}) \text{ 'is' } \begin{cases} \infty & \text{if } \mathbf{x} = \mathbf{0} \\ 0 & \text{otherwise} \end{cases}. \tag{8.162}$$

### 8.3.6 The two-dimensional Heaviside function

The two-dimensional Heaviside function allows the signal-theoretical modeling of so-called step edges (see Sec. 11.2) in images.

A Heaviside function, which changes from zero to one at the transition from the left to the right half-space of  $\mathbb{R}^2$ , can be expressed by

$$H(x) = H(x) 1(y) = H(\mathbf{x}^T \mathbf{e}_x) 1(\mathbf{x}^T \mathbf{e}_y). \quad (8.163)$$

Together, the separation theorem (8.134) and the correspondence for the one-dimensional Heaviside function (8.87) allow the calculation of the Fourier transform of the two-dimensional Heaviside function:

$$\mathcal{F}\{H(\mathbf{x}^T \mathbf{e}_x) 1(\mathbf{x}^T \mathbf{e}_y)\} = \mathcal{F}\{H(\mathbf{f}^T \mathbf{e}_x)\} \delta(\mathbf{f}^T \mathbf{e}_y) \quad (8.164)$$

$$= \left( \frac{1}{j2\pi f_x} + \frac{1}{2} \delta(f_x) \right) \delta(f_y) \quad (8.165)$$

$$= \frac{\delta(f_y)}{j2\pi f_x} + \frac{1}{2} \delta(\mathbf{f}) \quad (8.166)$$

$$= \frac{\delta(\mathbf{f}^T \mathbf{e}_y)}{j2\pi \mathbf{f}^T \mathbf{e}_x} + \frac{1}{2} \delta(\mathbf{f}). \quad (8.167)$$

Now, the orientation of the step edge will be generalized by a rotation. Therefore, the coordinate system is rotated by an angle  $\varphi$ , resulting in the corresponding basis vectors  $\mathbf{e}_\varphi = (\cos \varphi, \sin \varphi)^T$  and  $\mathbf{e}_{\varphi\perp} = (-\sin \varphi, \cos \varphi)^T$ . Replacing the previous basis vectors in (8.167) by these rotated basis vectors yields<sup>6</sup> the Fourier transform of the step edge that runs through the origin of the coordinate system and has been rotated by the angle  $\varphi$ :

$$\mathcal{F}\{H(\mathbf{x}^T \mathbf{e}_\varphi)\} = \frac{\delta(\mathbf{f}^T \mathbf{e}_{\varphi\perp})}{j2\pi \mathbf{f}^T \mathbf{e}_\varphi} + \frac{1}{2} \delta(\mathbf{f}). \quad (8.168)$$

A last generalization considers a distance of  $d$  to the origin:

$$H(\mathbf{x}^T \mathbf{e}_\varphi - d). \quad (8.169)$$

So, the shift property (8.57) implies

$$H(\mathbf{x}^T \mathbf{e}_\varphi - d) \rightsquigarrow \mathcal{F}\{H(\mathbf{x}^T \mathbf{e}_\varphi)\} e^{-j2\pi \mathbf{f}^T \mathbf{e}_\varphi d} \quad (8.170)$$

$$= \left( \frac{\delta(\mathbf{f}^T \mathbf{e}_{\varphi\perp})}{j2\pi \mathbf{f}^T \mathbf{e}_\varphi} + \frac{1}{2} \delta(\mathbf{f}) \right) e^{-j2\pi \mathbf{f}^T \mathbf{e}_\varphi d}. \quad (8.171)$$

See Fig. 8.19 for an additional illustration.

### 8.3.7 Sampling of two-dimensional signals

Similar to Sec. 8.3.2, the sampling of two-dimensional signals can mathematically be described by a multiplication of the continuous signal  $g(\mathbf{x})$  by a two-dimensional impulse train

<sup>6</sup>It holds  $g(\mathbf{x}^T \mathbf{e}_\varphi) = g(\mathbf{x}^T \mathbf{e}_\varphi) 1(\mathbf{x}^T \mathbf{e}_{\varphi\perp})$ .

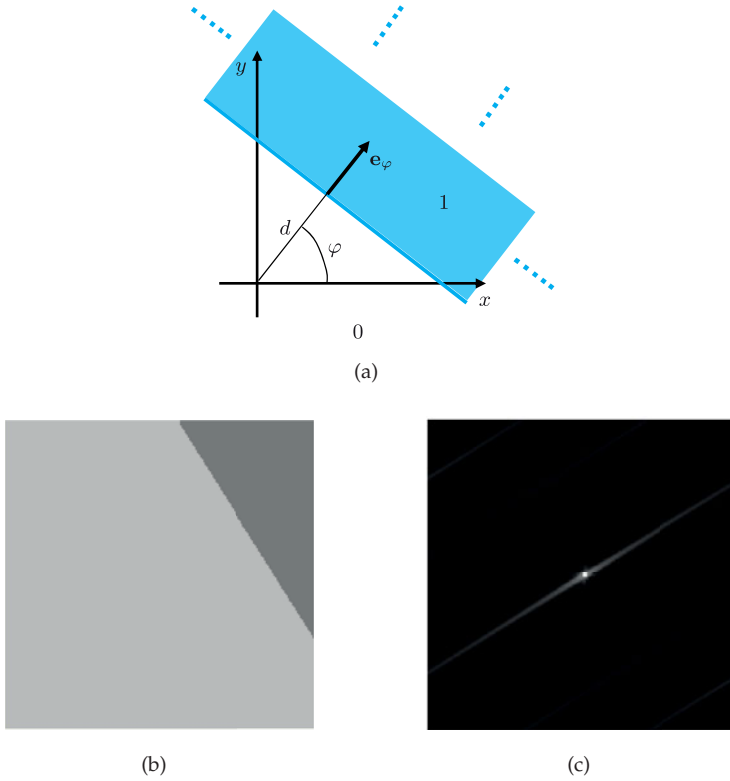


**Figure 8.19.** The Heaviside function: (a) Signal model for a step edge in an image: The blue half-plane of  $\mathbb{R}^2$  is assumed to have the image value 1 and the remaining half-plane has the value of 0; (b) Gray-scale image  $g(\mathbf{x})$  with a step edge; (c) Two-dimensional Fourier transform of  $g(\mathbf{x})$ , visualized as  $\log(1 + |\text{DFT}\{g(\mathbf{x})\}|)$ . For the two-dimensional DFT, see Sec. 8.3.9. The spectrum is concentrated on a line, which runs through the origin and is perpendicular to the step edge.

$r(\mathbf{x})$ , which acts as a sampling grid (cf. Fig. 8.20):

$$r(\mathbf{x}) = \sum_{m=-\infty}^{\infty} \sum_{n=-\infty}^{\infty} \delta(\mathbf{x} - m \Delta x \mathbf{e}_x - n \Delta y \mathbf{e}_y) \tag{8.172}$$

$$= \left( \sum_{m=-\infty}^{\infty} \delta(x - m \Delta x) \right) \left( \sum_{n=-\infty}^{\infty} \delta(y - n \Delta y) \right) \tag{8.173}$$

⊥

$$R(\mathbf{f}) = \left( \frac{1}{\Delta x} \sum_{k=-\infty}^{\infty} \delta\left(f_x - \frac{k}{\Delta x}\right) \right) \left( \frac{1}{\Delta y} \sum_{l=-\infty}^{\infty} \delta\left(f_y - \frac{l}{\Delta y}\right) \right) \tag{8.174}$$

$$= \frac{1}{\Delta x \Delta y} \sum_{k=-\infty}^{\infty} \sum_{l=-\infty}^{\infty} \delta\left(\mathbf{f} - \frac{k}{\Delta x} \mathbf{e}_x - \frac{l}{\Delta y} \mathbf{e}_y\right). \tag{8.175}$$

Here, the two-dimensional series of 2D Dirac delta functions (8.172) can be described by a multiplication of two orthogonal series of slice functions (8.173). For the transition into the frequency space, the separation theorem of the Fourier transform is used, so that the one-dimensional transform of each of the two factors can be calculated. Hence, the Fourier transform  $R(f)$  of the sampling grid  $r(x)$  is a two-dimensional impulse train too (cf. Fig. 8.20).

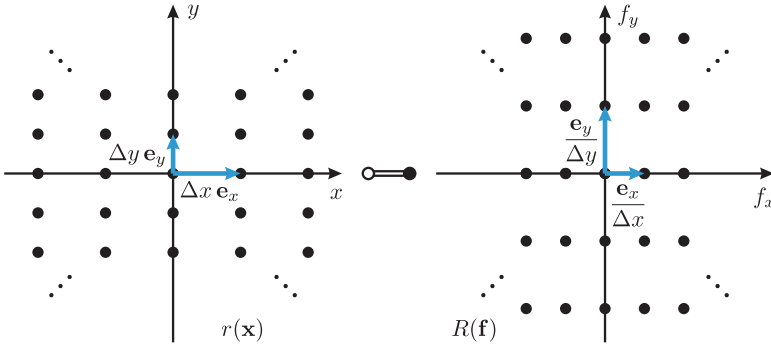


Figure 8.20. Two-dimensional sampling grid  $r(x)$  and Fourier transform  $R(f)$ .

The sampling grid  $r(x)$  and  $R(f)$  are uniquely determined by the ‘grid vectors’  $\Delta x e_x$  and  $\Delta y e_y$  (or by  $\frac{e_x}{\Delta x}$  and  $\frac{e_y}{\Delta y}$ ). Except for a translation, each regular sampling grid can be obtained by a linear coordinate transformation of the axis-parallel grid (8.172). According to (8.140), the position vector  $x$  is multiplied by the invertible transformation matrix  $A$ :

$$\tilde{r}(x) = \sum_m \sum_n \delta(Ax - m \Delta x e_x - n \Delta y e_y), \quad \det A \neq 0 \tag{8.176}$$

$$= \sum_m \sum_n \delta(A(x - m \underbrace{\frac{\Delta x}{A} A^{-1} e_x}_{=: b_1} - n \underbrace{\frac{\Delta y}{A} A^{-1} e_y}_{=: b_2})) \tag{8.177}$$

$$\propto \sum_m \sum_n \delta(x - m b_1 - n b_2). \tag{8.178}$$

The locations of the Dirac delta functions are determined via the zeros of their arguments. Because of the invertibility of  $A$ ,

$$A\xi = 0 \quad \Leftrightarrow \quad \xi = 0, \tag{8.179}$$

which explains the transition from (8.177) to (8.178). The coefficient in (8.178) is omitted, as only the location of the Dirac delta functions is of interest. The Fourier transform of (8.176) results in:

$$\tilde{R}(f) \propto \sum_k \sum_l \delta((A^{-1})^T f - k \frac{e_x}{\Delta x} - l \frac{e_y}{\Delta y}) \tag{8.180}$$

$$= \sum_k \sum_l \delta((A^{-1})^T (f - k \underbrace{A^T \frac{e_x}{\Delta x}}_{=: w_1} - l \underbrace{A^T \frac{e_y}{\Delta y}}_{=: w_2})) \tag{8.181}$$

$$\propto \sum_k \sum_l \delta(f - k w_1 - l w_2). \tag{8.182}$$

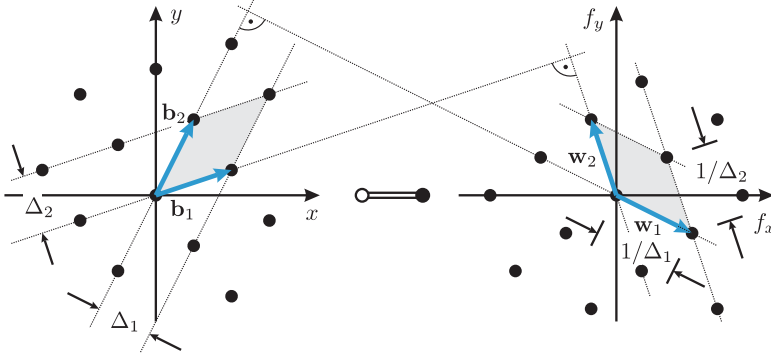


Figure 8.21. Basis vectors for describing a skew sampling grid  $\tilde{r}(x)$  and its spectrum  $\tilde{R}(f)$  [1].

Because of the coordinate transformation, the axis-parallel grid  $r(x)$  is generally turned into a skew sampling grid  $\tilde{r}(x)$ , which is determined by the grid vectors  $\mathbf{b}_1, \mathbf{b}_2$  in the spatial domain and by the grid vectors  $\mathbf{w}_1$  and  $\mathbf{w}_2$  in the frequency domain (cf. Fig. 8.21). The inner products of the grid vectors result in

$$\mathbf{b}_1^T \mathbf{w}_1 = \Delta x \mathbf{e}_x^T \underbrace{(\mathbf{A}^{-1})^T \mathbf{A}^T}_{\mathbf{I}} \frac{\mathbf{e}_x}{\Delta x} = 1, \tag{8.183}$$

$$\mathbf{b}_1^T \mathbf{w}_2 = \Delta x \mathbf{e}_x^T \underbrace{(\mathbf{A}^{-1})^T \mathbf{A}^T}_{\mathbf{I}} \frac{\mathbf{e}_y}{\Delta y} = 0, \tag{8.184}$$

$$\mathbf{b}_2^T \mathbf{w}_2 = 1, \tag{8.185}$$

$$\mathbf{b}_2^T \mathbf{w}_1 = 0. \tag{8.186}$$

Here,  $\mathbf{I}$  denotes the identity matrix. This implies the following formula expressed in matrix notation:

$$\begin{pmatrix} \mathbf{b}_1^T \mathbf{w}_1 & \mathbf{b}_1^T \mathbf{w}_2 \\ \mathbf{b}_2^T \mathbf{w}_1 & \mathbf{b}_2^T \mathbf{w}_2 \end{pmatrix} = (\mathbf{b}_1, \mathbf{b}_2)^T (\mathbf{w}_1, \mathbf{w}_2) = (\mathbf{w}_1, \mathbf{w}_2)^T (\mathbf{b}_1, \mathbf{b}_2) = \mathbf{I} \tag{8.187}$$

and thus

$$(\mathbf{w}_1, \mathbf{w}_2) = \begin{pmatrix} \mathbf{b}_1^T \\ \mathbf{b}_2^T \end{pmatrix}^{-1}, \quad (\mathbf{b}_1, \mathbf{b}_2) = \begin{pmatrix} \mathbf{w}_1^T \\ \mathbf{w}_2^T \end{pmatrix}^{-1}. \tag{8.188}$$

By using these equations, the sampling grid in the spatial frequency domain corresponding to a sampling grid in the spatial domain can be calculated and vice versa. The sampling grids of the two domains are related via the following reciprocity [1]:

$$\det(\mathbf{b}_1, \mathbf{b}_2) = \frac{1}{\det(\mathbf{w}_1, \mathbf{w}_2)}. \tag{8.189}$$

So, the area of the parallelogram spanned by  $\mathbf{b}_1$  and  $\mathbf{b}_2$  is reciprocal to the area of the parallelogram spanned by  $\mathbf{w}_1$  and  $\mathbf{w}_2$ .



Finally, the sampling of a continuous signal can be described as follows, using the sampling grid  $\tilde{r}(\mathbf{x})$ :

$$g_*(\mathbf{x}) = g(\mathbf{x}) \cdot \tilde{r}(\mathbf{x}) \iff G_*(\mathbf{f}) = G(\mathbf{f}) ** \tilde{R}(\mathbf{f}) \tag{8.190}$$

or

$$\sum_{m,n} g(m\mathbf{b}_1 + n\mathbf{b}_2) \delta(\mathbf{x} - m\mathbf{b}_1 - n\mathbf{b}_2) \iff \propto \sum_{k,l} G(\mathbf{f} - k\mathbf{w}_1 - l\mathbf{w}_2), \tag{8.191}$$

respectively. Now, the values of the sampling positions  $\mathbf{x} = m\mathbf{b}_1 + n\mathbf{b}_2$  yield the two-dimensional, spatially discrete signal

$$g_{mn} := g(m\mathbf{b}_1 + n\mathbf{b}_2), \quad m, n \in \mathbb{Z}. \tag{8.192}$$

Because of the sampling, the spectrum  $G(\mathbf{f})$  is periodically repeated according to the sampling grid  $\tilde{R}(\mathbf{f})$ . The convolution (8.190) causes each Dirac delta function  $\tilde{R}(\mathbf{f})$  to reproduce the original spectrum  $G(\mathbf{f})$  at its position.

8.3.8 Sampling theorem for two-dimensional signals

The sampling condition (8.103) can be generalized to two-dimensional signals, so that a complete and error-free reconstruction of the continuous signal  $g(\mathbf{x})$  can be calculated from the discrete samples  $g_{mn}$ .

**Theorem 8.15: Sampling theorem for two-dimensional signals**

8.15

Let  $g(\mathbf{x})$  be band-limited, i.e., there is a finite region  $\Omega_G \in \mathbb{R}^2$  such that

$$G(\mathbf{f}) = 0 \quad \text{if} \quad \mathbf{f} \notin \Omega_G. \tag{8.193}$$

The signal  $g(\mathbf{x})$  can be reconstructed without errors from its samples  $g_{mn}$ , which were obtained using a regular sampling grid, if no overlaps occur for the periodic repetition of the spectrum  $G(\mathbf{f})$ .  $\diamond$

For the reconstruction of the continuous signal  $g(\mathbf{x})$ , an interpolation filter with the impulse response  $i_{\Omega_G}(\mathbf{x})$  can be used:

$$i_{\Omega_G}(\mathbf{x}) = \mathcal{F}^{-1}\{I_{\Omega_G}(\mathbf{f})\} \quad \text{with} \quad I_{\Omega_G}(\mathbf{f}) := \begin{cases} 1 & \text{if } \mathbf{f} \in \Omega_G \\ 0 & \text{otherwise} \end{cases}. \tag{8.194}$$

The two-dimensional convolution of the discrete signal  $g_{mn}$  with  $i_{\Omega_G}(\mathbf{x})$  corresponds to the multiplication of the spectrum  $G_*(\mathbf{f})$  by the transfer function  $I_{\Omega_G}(\mathbf{f})$  in the spatial frequency domain, and yields the following reconstruction:

$$g(\mathbf{x}) = \sum_m \sum_n g_{mn} i_{\Omega_G}(\mathbf{x} - m\mathbf{b}_1 - n\mathbf{b}_2) \iff G(\mathbf{f}). \tag{8.195}$$

In order to achieve the optimal sampling—i.e., as coarse as possible—of a signal  $g(\mathbf{x})$ , the periodically repeated spectra  $G(\mathbf{f} - k\mathbf{w}_1 - l\mathbf{w}_2)$  in the frequency domain have to be located as close as possible without overlapping each other. This is illustrated by the following example.

**Example 8.16 (Optimal sampling):** A band-limited image signal  $g(\mathbf{x})$  with the spectrum  $G(\mathbf{f})$  is considered, according to Fig. 8.22 (top left). Now a sampling grid  $r(\mathbf{x})$  is required that samples the image most sparsely. The closest arrangement of the spectra (Fig. 8.22 top right) is used, to obtain the grid vectors  $\mathbf{w}_1, \mathbf{w}_2$  of the optimal sampling grid  $R(\mathbf{f})$  in the spatial frequency domain (Fig. 8.22 bottom right). Finally, the grid vectors  $\mathbf{b}_1, \mathbf{b}_2$  of the sampling grid  $r(\mathbf{x})$  can be calculated in the spatial domain using (8.188) (Fig. 8.22 bottom left).

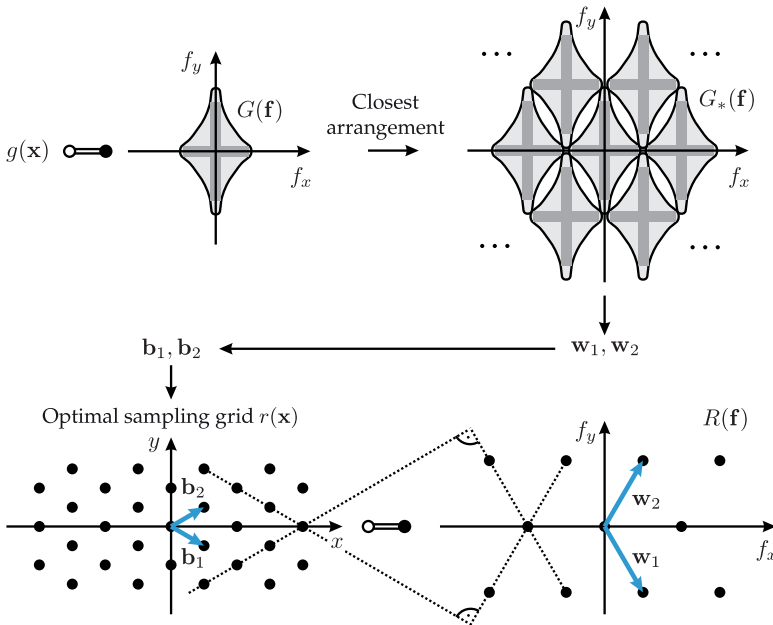
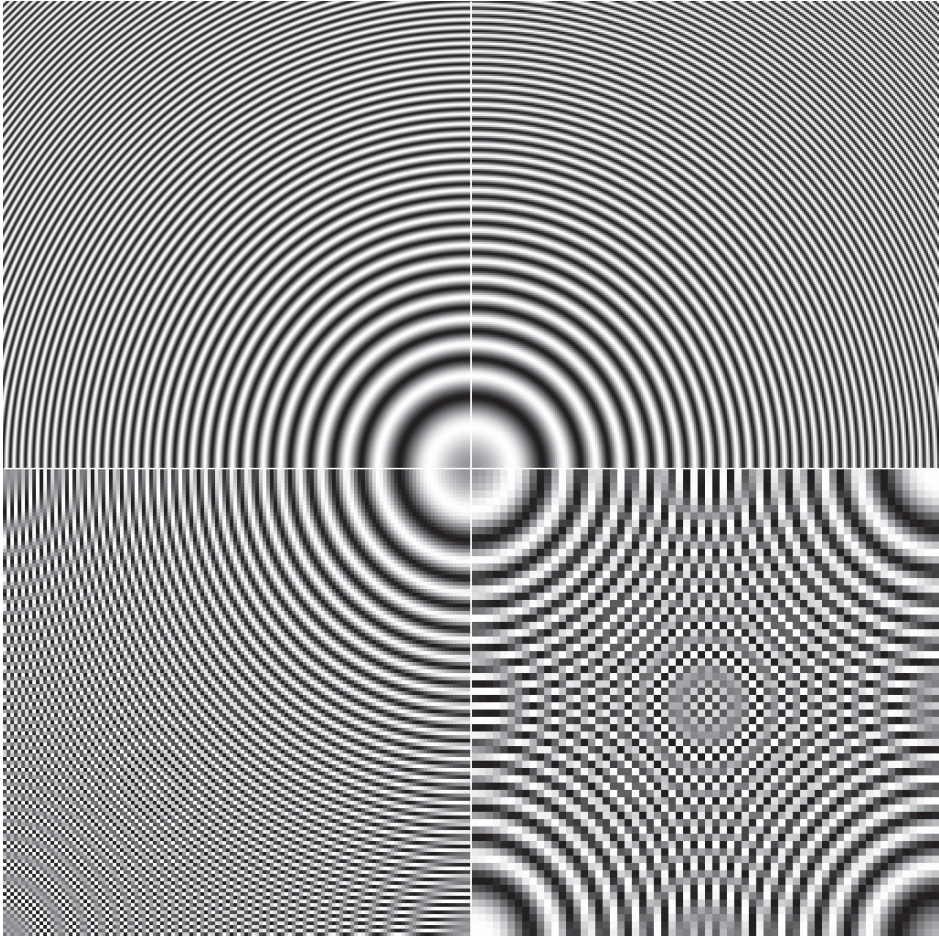


Figure 8.22. Construction of an optimal sampling grid  $r(\mathbf{x})$ .

**Example 8.17 (Image signals affected by aliasing):** If the conditions of the sampling theorem are violated by a two-dimensional signal, in general not only the magnitude of the image's frequency components is changed, but also the direction of the corresponding harmonic functions (cf. Fig. 8.23). For band-limited signals (8.193), aliasing can be avoided by choosing a sampling rate sufficiently high such that the sampling condition is met. Alternatively, a low-pass filtering of the input image can be performed prior to the discretization, which can, for example, be realized by a defocused optical imaging, as in (8.149).

### 8.3.9 The two-dimensional DFT

Obviously, the DFT (8.118) can be extended to two dimensions because of the separability of the Fourier transform.



**Figure 8.23.** Test image with concentric circles affected by aliasing: the upper left quadrant was sampled with  $512 \times 512$  pixels, the upper right quadrant with  $256 \times 256$  pixels, the lower left quadrant with  $128 \times 128$  pixels, and the lower right quadrant with  $64 \times 64$  pixels. Test image (top left) on the basis of [12].

---

#### Definition 8.10: The two-dimensional DFT

The two-dimensional discrete Fourier transform (2D-DFT) of a signal  $g_{mn}$  is given by

$$G_{kl} := \sum_{m=0}^{M-1} \left( \sum_{n=0}^{N-1} g_{mn} e^{-j2\pi \frac{nl}{N}} \right) e^{-j2\pi \frac{mk}{M}} \quad (8.196)$$

$$= \sum_{m=0}^{M-1} \sum_{n=0}^{N-1} g_{mn} e^{-j2\pi \left( \frac{mk}{M} + \frac{nl}{N} \right)}. \quad (8.197)$$

The discrete spectrum  $G_{kl}$  can be used to reconstruct the discrete signal by using the inverse 2D-DFT:

$$g_{mn} = \frac{1}{MN} \sum_{k=0}^{M-1} \sum_{l=0}^{N-1} G_{kl} e^{j2\pi(\frac{mk}{M} + \frac{nl}{N})}. \tag{8.198}$$

Similarly to the DFT,  $g_{mn}$  and  $G_{kl}$  are implicitly *periodically* repeated by the 2D-DFT in the directions of each coordinate (cf. Fig. 8.24). ◇

The position vector  $\mathbf{x}$  (the spatial frequency vector  $\mathbf{f}$ ) and the corresponding indices  $m, n$  ( $k, l$ ) are related according to the following formulas:

$$\mathbf{x} = (m \Delta x, n \Delta y)^T, \tag{8.199}$$

$$\mathbf{f} = \left( \frac{k}{M \Delta x}, \frac{l}{N \Delta y} \right)^T. \tag{8.200}$$

⊗ **8.3.9.1 Calculation of the 2-D DFT in practice**

Because of the separability of the Fourier transform, the 2D-DFT (8.196) can be calculated by a row-wise 1D-DFT and a subsequent column-wise 1D-DFT, or vice versa. The computational complexity is

- $N^2 M^2$  complex multiplications and additions for a direct calculation,
- $MN(\text{ld } M + \text{ld } N)$  complex multiplications and additions by using the 1D-FFT.

The frequencies of the section of the DFT spectrum resulting from the frequency limitation are arranged in an unfamiliar way (hatched window in Fig. 8.24). The origin of the coordinate system is located in the bottom left corner  $(k, l) = (0, 0)$  of the window; the center of the window corresponds to the highest spatial frequencies of the image. By swapping the four quadrants of the DFT window, the familiar arrangement of the DFT spectrum, where the origin of the coordinate system is located at the position  $(M/2, N/2)$ , can be obtained. This consideration also applies to the spatial domain.

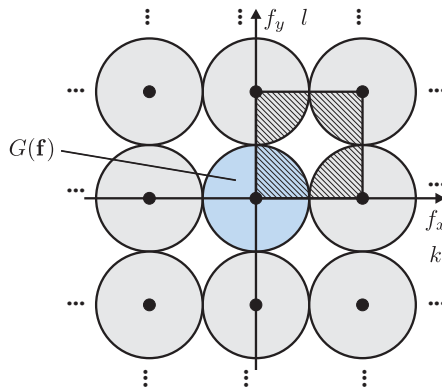


Figure 8.24. Periodic repetition of the spectrum  $G(\mathbf{f})$ , as well as the section resulting from the DFT.

⊗ 8.3.9.2 The convolution theorem of the 2-D DFT

Also the two-dimensional convolution of two signals can often be realized more efficiently using the spatial frequency domain and the FFT algorithm:

$$\text{DFT}^{-1}\{G_{kl} \cdot H_{kl}\} = g_{mn} \underbrace{**}_{\text{cyclic convolution}} h_{mn} = \sum_{\mu=0}^{M-1} \sum_{\nu=0}^{N-1} g_{\mu,\nu} h_{(m-\mu) \bmod M, (n-\nu) \bmod N} \cdot \quad (8.201)$$

As described in Sec. 8.3.3.5, this is a cyclic convolution. In order to avoid the end effect, the image has to be enlarged in both dimensions by appending enough zeros (**zero padding**) (cf. Fig. 8.25).

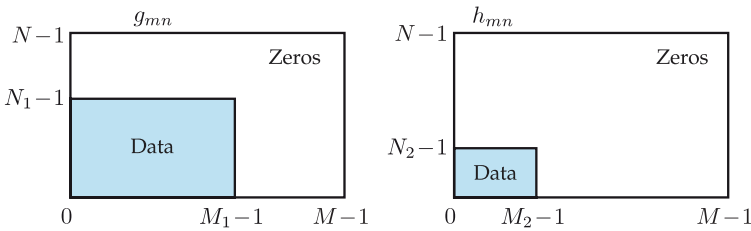


Figure 8.25. Avoiding the end effect by zero padding.

⊗ 8.3.9.3 The meaning of magnitude and phase

As it is a complex-valued quantity, the DFT spectrum (8.196) can be separated into magnitude and phase. Mostly, only the magnitude spectrum is presented: it describes which spatial frequencies contribute to the image and to what extent. Hence, it describes whether the image structures are long-wave ('smooth') or high-frequency ('rough').

However, according to the shift property (8.57), the phase spectrum contains the important information about the position of this structures. So, a displacement of an image signal  $g(x)$  by the vector  $x_0$  results in the following correspondence:

$$g(x - x_0) \iff G(f) e^{-j2\pi f^T x_0} \quad (8.202)$$

Because  $|e^{-j2\pi f^T x_0}| = 1$ , *only* the phase of the spectrum but not its magnitude is changed by a displacement of  $x_0$ . The importance of the phase of the spectrum will be illustrated by the following example.

---

**Example 8.18 (Importance of the phase spectrum):** The discrete Fourier transforms of the images  $g_1(x)$  and  $g_2(x)$  from Fig. 8.26(a) and (b) are calculated. Next, the phases  $\varphi_1(f)$  and  $\varphi_2(f)$  of the two Fourier transforms are swapped. Then, the inverse DFT is applied to both images, cf. Fig. 8.26(c) and (d). The results clearly show that the structures of the original images were mainly contained in the phase spectrum. Therefore, a signal cannot be reconstructed without the phase information. ■

(a)  $g_1(\mathbf{x})$ (b)  $g_2(\mathbf{x})$ (c)  $\mathcal{F}^{-1}\{|G_1(\mathbf{f})| e^{j\varphi_2(\mathbf{f})}\}$ (d)  $\mathcal{F}^{-1}\{|G_2(\mathbf{f})| e^{j\varphi_1(\mathbf{f})}\}$ 

**Figure 8.26.** Example illustrating the meaning of magnitude and phase. The information about the position of image structures is contained in the phase spectrum in the spatial frequency domain.

### ⊗ 8.3.9.4 Examples of the two-dimensional DFT

In the examples of this section, the two-dimensional DFT will be applied to test signals and to real images. For the definition of some important test signals, the spatially discrete Dirac delta function has to be introduced first.

#### 8.11 Definition 8.11: The spatially discrete Dirac delta function

The one-dimensional spatially discrete Dirac delta function is defined as follows:

$$\delta_n := \begin{cases} 1 & \text{if } n = 0 \\ 0 & \text{otherwise} \end{cases} . \quad (8.203)$$

The two-dimensional spatially discrete Dirac delta function is defined by

$$\delta_{mn} := \delta_m \cdot \delta_n = \begin{cases} 1 & \text{if } m = 0 \text{ and } n = 0 \\ 0 & \text{otherwise} \end{cases} . \tag{8.204}$$

◇

**Example 8.19 (DFT of a horizontal line):** An image with a horizontal line can be mathematically modeled by using a spatially discrete ‘slice function’

$$g_{mn} = \delta_{n-n_0} \tag{8.205}$$

as in Fig. 8.27(a). The two-dimensional DFT yields

$$G_{kl} = \sum_{n=0}^{N-1} \left( \sum_{m=0}^{M-1} g_{mn} e^{-j2\pi \frac{mk}{M}} \right) e^{-j2\pi \frac{nl}{N}} \tag{8.206}$$

$$= \sum_{n=0}^{N-1} \delta_{n-n_0} \underbrace{\sum_{m=0}^{M-1} e^{-j2\pi \frac{mk}{M}}}_{= M \delta_k} e^{-j2\pi \frac{nl}{N}} \tag{8.207}$$

$$= M \delta_k e^{-j2\pi \frac{n_0 l}{N}} . \tag{8.208}$$

The magnitude of the DFT spectrum

$$|G_{kl}| = M \delta_k \tag{8.209}$$

is independent of  $l$  and the vertical displacement  $n_0$  and corresponds to a line of Dirac delta functions through the origin of the coordinate system that is perpendicular to the original line, see Fig. 8.27(a, bottom). As the periodic repetition of the image  $g_{mn}$  causes no corruption of the signal, the DFT spectrum is not affected by spectral leakage despite the spatial restriction. ■

**Example 8.20 (DFT of a diagonal line):** The image of the diagonal line in Fig. 8.27(b, top) can be described for  $M = N$  by the function

$$g_{mn} = \delta_{m+n-M+1} . \tag{8.210}$$

A two-dimensional DFT yields

$$G_{kl} = \sum_{n=0}^{M-1} \left( \sum_{m=0}^{M-1} \delta_{m+n-M+1} e^{-j2\pi \frac{mk}{M}} \right) e^{-j2\pi \frac{nl}{M}} \tag{8.211}$$

$$= \sum_{n=0}^{M-1} e^{-j2\pi \frac{(M-1-n)k}{M}} e^{-j2\pi \frac{nl}{M}} \tag{8.212}$$

$$= e^{j2\pi \frac{k}{M}} \sum_{n=0}^{M-1} e^{j2\pi \frac{n}{M} (k-l)} \tag{8.213}$$

$$= M \delta_{k-l} e^{j2\pi \frac{k}{M}} . \tag{8.214}$$

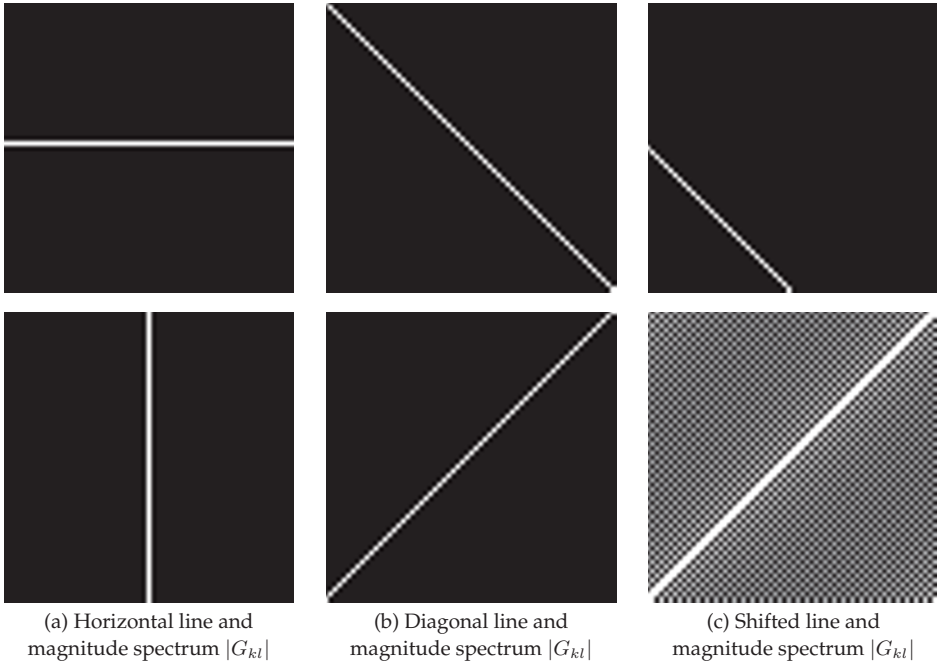


**Figure 8.27.** Examples of the two-dimensional DFT of line images: (top) Line images  $g_{mn}$ ; (bottom) Magnitude spectra  $|G_{kl}|$ . For a better visualization of spectral leakage, the magnitude spectra in (c) have been transformed by  $\log(1 + |G_{kl}|)$ .

### The DFT magnitude spectrum

$$|G_{kl}| = M \delta_{k-l} \quad (8.215)$$

corresponds to a line of Dirac delta functions which is perpendicular to the original line in  $g_{mn}$ . Together with Example 8.19, this is a confirmation of Theorem 8.13 and thus, a rotation of the image results in a rotation of the Fourier spectrum by the same angle (cf. Fig. 8.15). Also in this case, there is no spectral leakage, as the periodic repetition of the image is free from discontinuities on its boundaries, see Fig. 8.27(b).

Although the DFT magnitude spectrum still represents a line after a displacement, as in Fig. 8.27(c), the windowing results in a considerable spectral leakage (cf. Sec. 8.3.3.3). For a better visualization of the spectral leakage, the logarithms of the magnitude spectra are presented in Fig. 8.27(c). ■

---

**Example 8.21 (DFT of a periodic groove texture):** If a texture consists of straight, parallel grooves, then, according to the Examples 8.19, 8.20 and because of the linearity of the Fourier transform, the corresponding spectral components are concentrated along a line that runs through the origin of the coordinate system and is perpendicular to the grooves. If also the grooves are periodic, as shown in Fig. 8.28(a), the spectral components form a weighted comb of Dirac delta functions ('line spectrum'), see Fig. 8.28(b). A logarithm



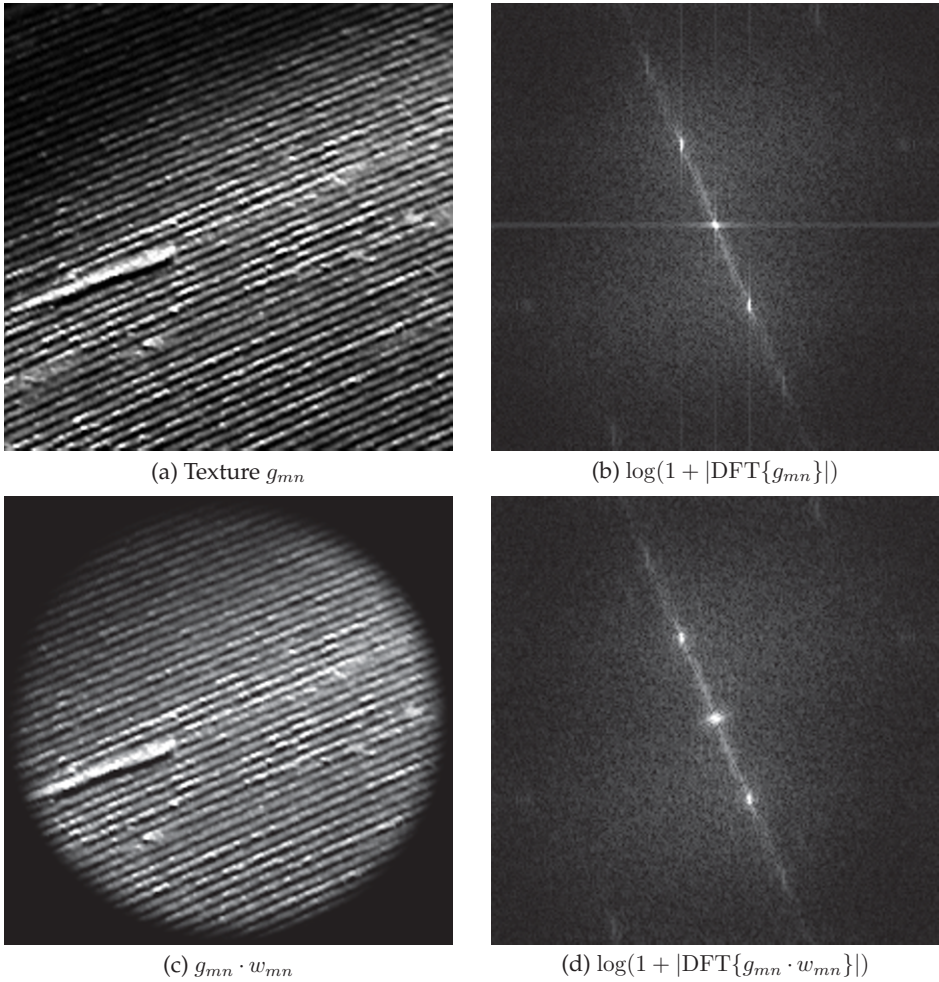


Figure 8.28. The DFT of a periodic groove texture, affected by spectral leakage.

has been applied to the DFT magnitude spectrum, in order to reduce the dynamics, for visualization reasons.

As the original image  $g_{mn}$  is darkened towards the upper and left image borders, the implicit periodic repetition of the image by the DFT causes brightness discontinuities, which result in spectral leakage as explained in Sec. 8.3.3.3. Spectral leakage is clearly visible in the form of the horizontal and vertical smear of the Dirac delta functions in Fig. 8.28(b).

In order to reduce the spectral leakage, the original image is multiplied by a smooth, rotationally symmetric window function  $w_{mn}$ , see Fig. 8.28(c). In the corresponding DFT magnitude spectrum Fig. 8.28(d), indeed, the horizontal and vertical lines are gone; however, the Dirac delta functions are slightly more blurred. ■

**Example 8.22 (DFT of a rectangle):** Figure 8.29(a) shows an image  $g_{mn}$  of a rectangle. In the continuous case, such a signal can be represented by a product of two shifted, one-dimensional rectangular functions (8.13):

$$g(\mathbf{x}) = \frac{1}{L_x L_y} \operatorname{rect}\left(\frac{x - x_0}{L_x}\right) \operatorname{rect}\left(\frac{y - y_0}{L_y}\right). \quad (8.216)$$

By the shift property (8.57) and the separation property (8.134) of the Fourier transform, the magnitude spectrum consists of the product of two sinc functions (cf. Fig. 8.9):

$$|G(\mathbf{f})| = |\operatorname{sinc}(f_x L_x)| \cdot |\operatorname{sinc}(f_y L_y)|. \quad (8.217)$$

Figure 8.29(b) shows the DFT magnitude spectrum  $|\operatorname{DFT}\{g_{mn}\}|$ , which has been calculated from the discrete signal  $g_{mn}$ . The effects of shrinking or stretching a signal are clearly visible. A wide rectangle yields narrow structures in the Fourier domain and a narrow rectangle results in wide structures. This circumstance again confirms the reciprocity of the Fourier transform. The more compact a function is in the spatial domain, the wider its Fourier transform will be in the spatial frequency domain. In image processing, this reciprocity is called the **uncertainty principle** of position and spatial frequency. ■

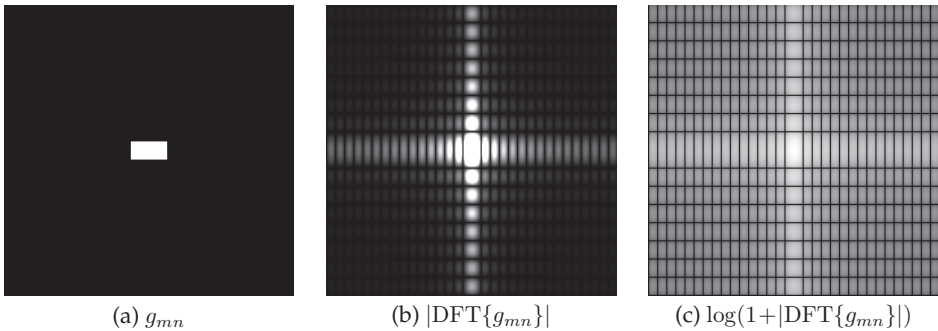


Figure 8.29. The two-dimensional DFT of a rectangle.

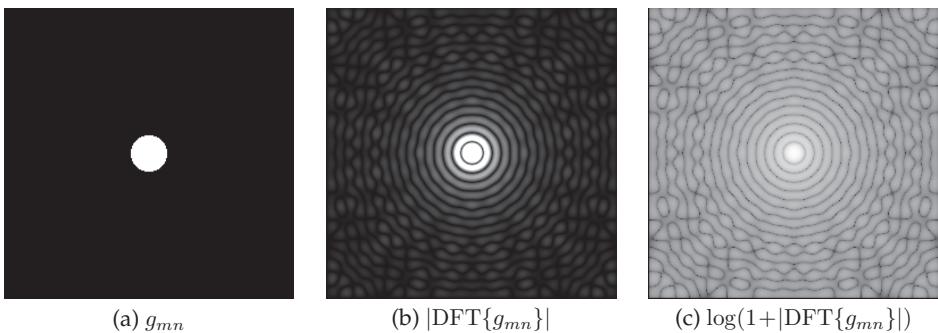


Figure 8.30. The two-dimensional DFT of a circular disk.

**Example 8.23 (DFT of a circular disk):** Figure 8.30 shows an image  $g_{mn}$ , which is the result of the spatial discretization of the function of a circular disk

$$g(\mathbf{x}) = \text{rect}\left(\frac{\|\mathbf{x}\|}{D}\right) \quad (8.218)$$

of diameter  $D$ . By (8.149), the Fourier transform

$$G(\mathbf{f}) = \frac{D}{2} \cdot \frac{J_1(\pi D \|\mathbf{f}\|)}{\|\mathbf{f}\|}, \quad (8.219)$$

shows circular structures, which are aligned around the origin of the coordinate system. The square of the magnitude formally corresponds to the Airy disk in Fig. 2.20. These circular structures are clearly visible in the DFT magnitude spectrum shown in Fig. 8.30(b). The application of the logarithm (Fig. 8.30(c)) reveals that the zeros do not form perfect concentric circles anymore, because of the spatial discretization. ■

**Example 8.24 (DFT of two circular disks):** Figure 8.31 shows an image  $g_{mn}$  of two spatially discretized circular disks. By extending (8.218), this signal can be described as follows in the continuous space:

$$g(\mathbf{x}) = \text{rect}\left(\frac{\|\mathbf{x}\|}{D}\right) ** (\delta(\mathbf{x} - \mathbf{x}_0) + \delta(\mathbf{x} + \mathbf{x}_0)) \quad (8.220)$$

$$= \text{rect}\left(\frac{\|\mathbf{x} - \mathbf{x}_0\|}{D}\right) + \text{rect}\left(\frac{\|\mathbf{x} + \mathbf{x}_0\|}{D}\right). \quad (8.221)$$

The convolution property of the Fourier transform yields the spectrum

$$G(\mathbf{f}) = \mathcal{F}\left\{\text{rect}\left(\frac{\|\mathbf{x}\|}{D}\right)\right\} \cdot 2 \cos(2\pi \mathbf{f}^T \mathbf{x}_0) \quad (8.222)$$

$$= D \frac{J_1(\pi D \|\mathbf{f}\|)}{\|\mathbf{f}\|} \cos(2\pi \mathbf{f}^T \mathbf{x}_0). \quad (8.223)$$

In contrast to the Fourier spectrum (8.219) of the circular disc, in this case the Fourier spectrum is modulated by a cosine oscillation, as illustrated by the dark lines in the DFT

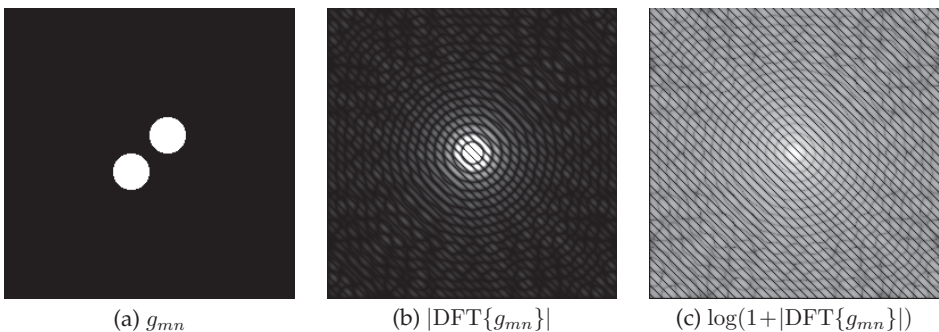
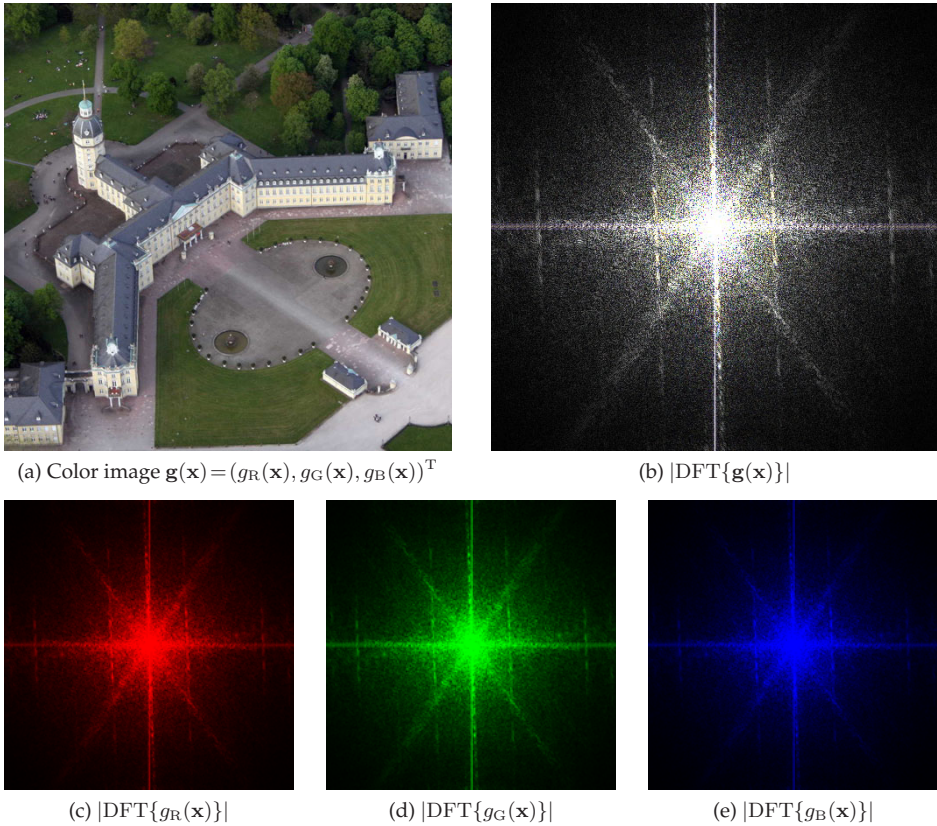


Figure 8.31. The two-dimensional DFT of two circular disks.



**Figure 8.32.** The DFT of an aerial image of the Karlsruhe Palace (source: ONUK). The magnitude spectra have been clipped to 1% of the maximum value.

magnitude spectrum shown in Fig. 8.31(b) and (c), which are perpendicular to the position vector  $\mathbf{x}_0$ . ■

**Example 8.25 (DFT of a color aerial image):** Figure 8.32(a) shows an RGB color image  $\mathbf{g}(\mathbf{x})$  of the Karlsruhe Palace. To calculate the DFT magnitude spectrum shown in Fig. 8.32(b), the DFT was applied to each of the three color channels separately. The (colored) results are shown in Figs. 8.32(c)–(e). Because the three color channels are very similar, the spectra shown in Figs. 8.32(c)–(e) only differ slightly. The line shaped structures of the original image (mainly the wings of the building and the paths) produce orthogonal structures in the magnitude spectrum, which run through the origin of the coordinate system (cf. Examples 8.19 and 8.20). Because of the periodic repetition of the image, the DFT spectrum is affected by spectral leakage, which is especially visible due to the vertical line running through the center of the coordinate system.

In addition, four weaker vertical structures can be seen on both sides of the center, which describe the regular horizontal arrangement of the building's windows, that can

be approximated by a rectangular oscillation in the spatial domain. The lines located closer to the origin correspond to the fundamental oscillation; the outer lines describe the first odd-numbered harmonic with three times the spatial frequency. ■

## 8.4 Examples of use concerning system theory and the Fourier transform

System theory provides methods that allow a consistent description of the behavior of various physical systems. In particular, these include the representation of systems in the frequency domain by means of the Fourier transform. This section discusses exemplary applications of automated visual inspection from the perspective of system theory.

**Example 8.26 (Moiré methods):** The creation of moiré images, as shown in Sec. 7.3.6.4, can graphically be described in the Fourier domain. If a parallel, spatially constant illumination is considered in Fig. 7.62, then the spatial frequency spectrum of the illumination signal is proportional to a Dirac delta function, see Fig. 8.33(a). To simplify matters, a cosine grid is assumed, so that the multiplication of the transparency function of the grid and the constant illumination results in a cosine shaped modulation as in Fig. 8.33(b). A phase modulation caused by the surface relief results in a widening of the spectral lines, hence, the bandwidth of the resulting shadow image is widened (see Fig. 8.33(c)). The observation by the camera results in another multiplication of the moiré pattern with the cosine transparency function of the grid, resulting in a demodulation of the shadow image as in Fig. 8.33(d). Finally, the limited spatial resolution of the captured image, which might for example be caused by a defocused optical imaging, represents a low-pass filter (LP), which suppresses the high-frequency structures. The resulting low-pass signal (Fig. 8.33(e)) corresponds to the captured moiré image [15]. ■

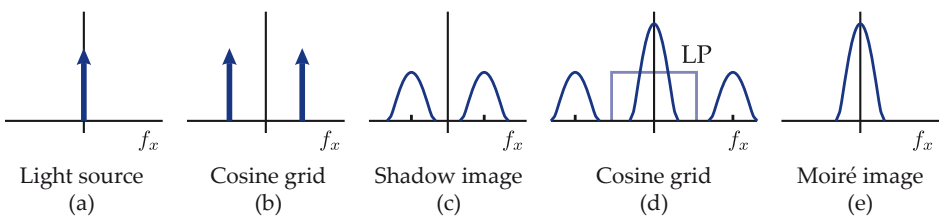


**Figure 8.33.** System-theoretical description of shadow moiré: (a) Spatially coherent light; (b) Cosine-shaped modulation, multiplication of the transparency function of the grid with the constant illumination; (c) Surface relief causes a phase modulation  $\rightarrow$  widening of the spectral lines; (d) Second grid results in a demodulation by another multiplication by the transparency function of the grid; (e) Limited spatial resolution of the camera results in a low-pass filtering, i.e., suppression of high-frequency structures.

**Example 8.27 (Defocused optical imaging):** As in Example 8.15, a defocused optical imaging (Fig. 8.34) can be approximated by an LSI system. For this purpose, incoherent light is assumed, so that the image  $g(x)$  in the input plane as well as its imaging  $k(x)$  describe intensities (i.e., power per area). By (2.126), the superposition of these images is free from

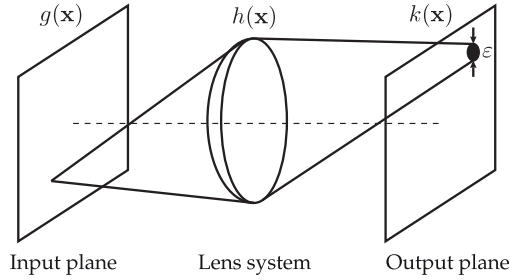


Figure 8.34. Defocused optical imaging.

interference.

If, as in Fig. 3.16, all object points have a distance of  $\Delta g$  from the focused plane, they are imaged to the image plane in the shape of blur disks with diameter  $\varepsilon(\Delta g)$ . The output image

$$k(\mathbf{x}) = g(\mathbf{x}) ** h(\mathbf{x}) \quad \Leftrightarrow \quad K(\mathbf{f}) = G(\mathbf{f}) H(\mathbf{f}) \quad (8.224)$$

is the result of a two-dimensional convolution of the input image  $g(\mathbf{x})$  with the impulse response

$$h(\mathbf{x}) \approx \frac{4}{\pi\varepsilon^2} \operatorname{rect}\left(\frac{\|\mathbf{x}\|}{\varepsilon}\right). \quad (8.225)$$

Because

$$\int_{-\infty}^{\infty} \int_{-\infty}^{\infty} h(\mathbf{x}) \, d\mathbf{x} = 1, \quad (8.226)$$

the optical imaging is lossless. Similar to (8.149), the Fourier transform of the point spread function (8.225) yields the optical transfer function of the defocused imaging:

$$H(\mathbf{f}) = \frac{2}{\pi\varepsilon} \cdot \frac{J_1(\pi\varepsilon\|\mathbf{f}\|)}{\|\mathbf{f}\|}. \quad (8.227)$$

Defocused optical imaging has the characteristics of a low-pass filter (cf. Fig. 8.17), and can therefore be used as an anti-aliasing filter for example.

In order to illustrate the effects of negative values of the transfer function of defocused optical imaging (Fig. 8.17), a so-called **Siemens star** (Fig. 8.35(a)) is used. Figure 8.35(b) shows the result of the convolution of the Siemens star with a point spread function (8.225) in the shape of a circular disk. Towards the borders of the image, the white and black sectors of the Siemens star appear to be defocused because of the limited resolution of the simulated optical imaging. Towards the center, i.e., for increasing absolute spatial frequencies, the sectors change their polarity several times, according to the alternating positive and negative values of the transfer function. In the center of the image, a homogeneous gray region is visible, corresponding to the cutoff region of the filter. ■

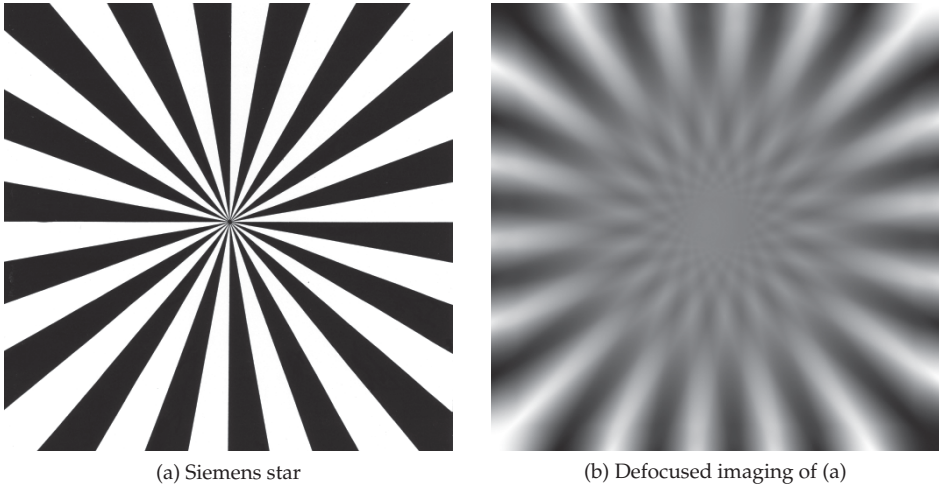


**Figure 8.35.** Simulation of the impact of negative values of the transfer function  $H(\mathbf{f})$  of defocused optical imaging. The contrast inversion caused by the defocused imaging can be directly seen in (a) if the image is viewed from a very close distance, so that the eyes are not able to establish a focused optical imaging anymore.

---

**Example 8.28 (Group velocity):** Consider a wave packet with electric field

$$\mathbf{E}(\mathbf{x}, t) = E_y(x, t) \mathbf{e}_y, \quad (8.228)$$

where

$$E_y(x, t) = \int_{-\infty}^{\infty} E_y(\nu) e^{j(2\pi\nu t - k(\nu)x)} d\nu. \quad (8.229)$$

So,  $E_y(x, t)$  is the result of the Fourier synthesis of infinitesimal harmonic waves  $e^{j(2\pi\nu t - k(\nu)x)} d\nu$ , weighted by  $E_y(\nu)$ .

The spectrum  $E_y(\nu)$  is assumed to be narrow-band, in the sense that

$$\int_{\mathcal{B}} |E_y(\nu)|^2 d\nu \gg \int_{-\infty}^{\infty} |E_y(\nu)|^2 d\nu - \int_{\mathcal{B}} |E_y(\nu)|^2 d\nu \quad (8.230)$$

with  $\mathcal{B} := [\nu_0 - \frac{\Delta\nu}{2}, \nu_0 + \frac{\Delta\nu}{2}]$  and  $\Delta\nu \ll \nu_0$ .

The wave number  $k(\nu)$  is given by  $k(\nu) = \frac{2\pi n\nu}{c}$  and  $n = n(\nu)$  may depend on the frequency  $\nu$  of the light. Calculating the derivative with respect to  $\nu$  results in

$$k'(\nu) = \frac{dk}{d\nu} = \frac{2\pi}{c} \left( \frac{dn}{d\nu} \nu + n \right). \quad (8.231)$$

As the spectrum is assumed to be narrow-band,  $k(\nu)$  can be linearly approximated with sufficient precision. The substitution  $\nu := \nu_0 + \delta$  yields  $k(\nu) \approx k(\nu_0) + k'(\nu_0) \delta$ .

Then,  $E_y(x, t)$  can be approximated as follows.

$$E_y(x, t) \approx \int_{-\infty}^{\infty} E_y(\nu_0 + \delta) e^{j(2\pi(\nu_0 + \delta)t - (k(\nu_0) + k'(\nu_0)\delta)x)} d\delta \quad (8.232)$$

$$\approx e^{j(2\pi\nu_0 t - k(\nu_0)x)} \cdot \int_{-\infty}^{\infty} \underbrace{E_y(\nu_0 + \delta)}_{=: W(\delta)} e^{j2\pi\left(t - \frac{k'(\nu_0)}{2\pi}x\right)\delta} d\delta \quad (8.233)$$

$$\approx e^{j(2\pi\nu_0 t - k(\nu_0)x)} \cdot w\left(t - \frac{k'(\nu_0)}{2\pi}x\right). \quad (8.234)$$

Here,  $w(\cdot) \circlearrowleft W(\cdot)$ .

As  $W(\delta)$  is assumed to be narrow-band with respect to  $\nu_0$ ,  $w(\xi) = \mathcal{F}^{-1}\{W(\delta)\}$  with  $\xi := \left(t - \frac{k'(\nu_0)}{2\pi}x\right)$  is spatially broad because of the reciprocity of the Fourier transform. I.e., the spatial extent of  $w(\xi)$  is much larger than the wavelength  $\lambda_0 = \frac{2\pi}{k(\nu_0)}$ .

So, the result can be interpreted as follows:

$$E_y(x, t) = \underbrace{e^{j(2\pi\nu_0 t - k(\nu_0)x)}}_{\substack{\text{High-frequency} \\ \text{harmonic wave} \\ \text{with frequency } \nu_0}} \cdot \underbrace{w\left(t - \frac{k'(\nu_0)}{2\pi}x\right)}_{\substack{\text{Low-frequency} \\ \text{wave compared to} \\ \text{the frequency } \nu_0}}. \quad (8.235)$$

Both waves are linked via a multiplication. In order to obtain the propagation velocity of the waves, the respective phase term is set to a constant and the derivative with respect to the time is calculated:

$$2\pi\nu_0 t - k(\nu_0)x = \text{const.} \quad \frac{d}{dt} \rightarrow \dot{x} = \frac{2\pi\nu_0}{k(\nu_0)} = v_{\text{Phase}}, \quad (8.236)$$

$$t - \frac{k'(\nu_0)}{2\pi}x = \text{const.} \quad \frac{d}{dt} \rightarrow \dot{x} = \frac{2\pi}{k'(\nu_0)} = v_{\text{Group}}. \quad (8.237)$$

The first term is the phase velocity, which is already known from Sec. 2.2. The wave described by the second term propagates with the group velocity

$$v_{\text{Group}} = \frac{2\pi}{k'(\nu_0)} = \frac{c}{n(\nu_0) + n'(\nu_0)\nu_0} \quad (8.238)$$

with  $n' = \frac{dn}{d\nu}$ .

As can be seen, the group and phase velocities  $v_{\text{Phase}} = \frac{c}{n(\nu_0)}$  equal each other in media with a refractive index  $n'(\nu) \equiv 0$  that is constant with respect to the frequency  $\nu$ .

For  $n' > 0$  one has  $v_{\text{Group}} < v_{\text{Phase}}$ , and for  $n' < 0$ , one has  $v_{\text{Group}} > v_{\text{Phase}}$ .

Figure 8.36 illustrates these considerations for the case  $n' > 0$ , i.e., for  $v_{\text{Group}} < v_{\text{Phase}}$ .

Media with  $n' \equiv 0$  are called dispersion-free. Media with frequency-dependent refractive indices are called dispersive media.

---

**Example 8.29 (Coherent optical image filtering):** As shown in Sec. 2.2.6, the Fraunhofer diffraction image of an object illuminated by a plane wave corresponds to the Fourier transform of the object. This effect can be exploited to realize a linear optical filtering of an image  $g(x)$  in real-time. The use of coherent illumination, e.g., a laser, is necessary.



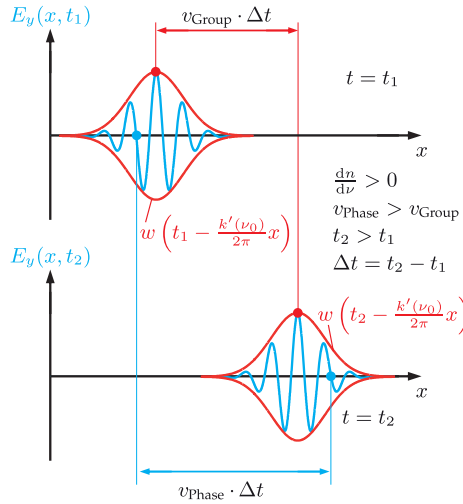


Figure 8.36. A wave packet  $E_y(x, t)$  at two different times  $t_1$  and  $t_2$  for the case of  $v_{Group} < v_{Phase}$ . While the high-frequency wave propagates faster, the whole wave group moves with the speed of the envelope  $w\left(t - \frac{k'(\nu_0)}{2\pi}x\right)$  drawn in red.

Figure 8.37 shows the setup used for coherent optical image filtering. The collimating lens produces a plane wave from the monochromatic light of the laser, which illuminates the input image  $g(x)$ . This can be a stop, a grating, or a transparency function, for example. As the system uses coherent light, all signals can be considered as electric fields.

Because of the lens  $L_1$ , the far-field diffraction of  $g(x)$ , which represents the Fourier plane, is imaged to its focal plane, where it can be manipulated via a multiplication by an optical filter  $H(f)$ . Another lens  $L_2$  performs a second Fourier transform of the filtered Fourier spectrum and images it to the output field  $k(x)$ .

In order to understand how a lens performs a Fourier transform, consider a point of

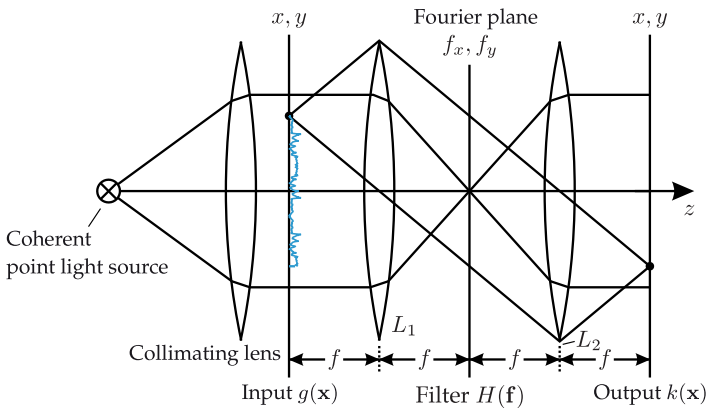


Figure 8.37. Coherent optical image filtering.

light placed in the input plane  $g(\mathbf{x}) = \delta(\mathbf{x})$ . This point of light is focused by  $L_1$  and ensures a constant illumination  $G(\mathbf{f}) = 1$  in the Fourier plane. On the other hand, for a constant illumination  $g(\mathbf{x}) = c$  placed in the input plane, all parallel illumination rays are focused by the lens  $L_1$ , resulting in a Dirac delta function in the Fourier plane  $G(\mathbf{f}) = c \delta(\mathbf{f})$ . ■

**Example 8.30 (Coherence length):** Consider a plane electromagnetic wave which propagates in  $x$ -direction and has the shape of a Gaussian envelope, so that its duration is approximately limited:

$$\mathbf{E}(\mathbf{x}, t) = \mathbf{e}_y E_0 \exp\left(-\frac{1}{2} \left(\frac{t - \frac{x}{c}}{\sigma_t}\right)^2\right) \cos\left(2\pi f_0 \left(t - \frac{x}{c}\right)\right). \tag{8.239}$$

Here,  $2\sigma_t$  is a measure of its duration, and thus, for the length  $2\sigma_x = 2\sigma_t c$  of the wave packet, see Fig. 8.38(a).

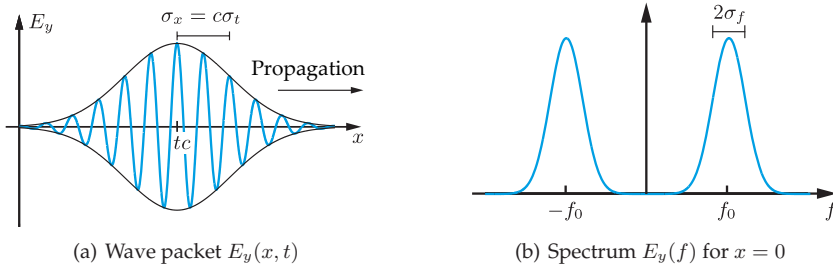


**Figure 8.38.** Relation between coherence length and bandwidth: (a) Wave packet  $E_y(x, t)$ ; (b) Spectrum  $E_y(f)$  for  $x = 0$ .

As position and time are linearly linked in the propagator  $2\pi f_0(t - \frac{x}{c})$ , the spectral components of the wave can be obtained by calculating its Fourier transform *with respect to time* for a constant  $x$ . Let  $x := 0$  and furthermore, w.l.o.g., the coefficients are omitted:

$$E_y(t) = \exp\left(-\frac{1}{2} \left(\frac{t}{\sigma_t}\right)^2\right) \cos(2\pi f_0 t) \tag{8.240}$$

↕

$$E_y(f) = \mathcal{F}\left\{\exp\left(-\frac{1}{2} \left(\frac{t}{\sigma_t}\right)^2\right)\right\} * \frac{1}{2}(\delta(f + f_0) + \delta(f - f_0)). \tag{8.241}$$

Using

$$e^{-\pi t^2} \quad \circ \bullet \quad e^{-\pi f^2}, \tag{8.242}$$

the similarity transform

$$g(at) \quad \circ \bullet \quad |a|^{-1} G\left(\frac{f}{a}\right) \tag{8.243}$$

and

$$a := \frac{1}{\sqrt{2\pi}\sigma_t}, \quad (8.244)$$

results in

$$\exp\left(-\frac{1}{2} \frac{t^2}{\sigma_t^2}\right) \quad (8.245)$$

↓

$$\sqrt{2\pi}\sigma_t \exp\left(-\frac{1}{2}(2\pi\sigma_t f)^2\right) = \sqrt{2\pi} \exp\left(-\frac{1}{2} \frac{f^2}{\sigma_f^2}\right) \quad (8.246)$$

with

$$\sigma_f := \frac{1}{2\pi\sigma_t}. \quad (8.247)$$

Finally,

$$E_y(f) = \sqrt{\frac{\pi}{2}}\sigma_t \left( \exp\left(-\frac{1}{2} \left(\frac{f+f_0}{\sigma_f}\right)^2\right) + \exp\left(-\frac{1}{2} \left(\frac{f-f_0}{\sigma_f}\right)^2\right) \right). \quad (8.248)$$

Here,  $2\sigma_f$  is a measure of the bandwidth of the wave, see Fig. 8.38(b).

Multiplying the width in the time domain by the width in the frequency domain yields

$$2\sigma_t \cdot 2\sigma_f = \frac{2}{\pi} \approx 0.64. \quad (8.249)$$

Hence, there is a reciprocity between the temporal duration and the bandwidth, as  $\sigma_t \propto \sigma_f^{-1}$ .

This can now be used to elegantly show the relation between the coherence length  $d_K$  and the spectral bandwidth  $\Delta\nu$  of the light (cf. Sec. 2.2.4). Consider a wave packet as in Fig. 8.38(a) that is split into two halves by a beam splitter. After taking two different paths, the two halves are joined again (for example, in an interferometrical setup as in Sec. 7.3.16.1). Only if the optical path difference is smaller than the length  $d_K$  of the wave packet interference effects can occur. The maximum optical path difference which still results in observable interference defines the coherence length,  $d_K$ .

There are different possibilities for defining the length of a gradually decaying signal. If  $2\sigma_t$  is identified with the temporal duration of the wave, the length of the wave packet is given by

$$d_K \approx 2\sigma_t c. \quad (8.250)$$

If  $2\sigma_f$  is identified with the bandwidth  $\Delta\nu$  of the wave,

$$\Delta\nu \cdot d_K \approx c 2\sigma_t 2\sigma_f = \frac{2c}{\pi} \quad (8.251)$$

and thus

$$d_K \approx \frac{c}{\Delta\nu}, \quad (8.252)$$

which corresponds to the result of Sec. 2.2.4. ■

## 8.5 Image signals as stochastic processes

Many problems in the field of signal processing (and especially image processing) require solutions which can be applied to whole classes of signals with certain properties and not only to special single signals. The mathematical model for such a signal class is a so-called **stochastic process**, also called a **random process** [9, 17, 19, 26].

### Definition 8.12: Stochastic process

A stochastic process<sup>7</sup>  $g(x, e)$  consists of a random experiment and an assignment of deterministic functions  $g(x, e_\nu)$ , the so-called sample functions (or realizations) to the elementary events  $e_\nu$  of the random experiment (see Fig. 8.39). For each fixed position  $x_i = \text{const.}$ , the stochastic process  $g(x, e)$  turns into a random variable  $g(x_i, e)$ , which can be described using a probability distribution [17, 19].  $\diamond$

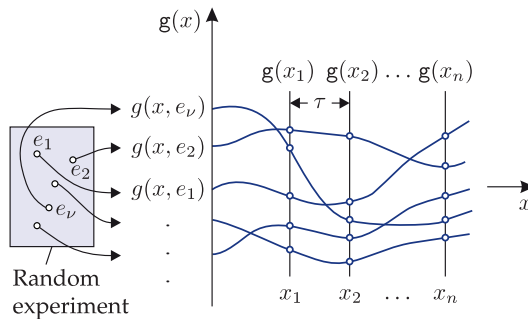


Figure 8.39. Random process.

### Remarks:

- In the case of a stochastic process, the functions  $g(x, e_\nu)$  which are assigned to the random experiment are deterministic. Only the random experiment is affected by chance.
- The quantities  $g$ ,  $x$  and  $e$  can be continuous or discrete.
- For image signals  $g(\mathbf{x})$ , the position  $\mathbf{x} \in \mathbb{R}^2$  is usually two-dimensional and the image  $g \in \mathbb{R}^Q$  is usually vectorial (here, the number of channels is denoted by  $Q$ ). However, for the remainder of this section, only scalar images  $g(\mathbf{x}) \in \mathbb{R}$  will be considered.

A random process  $g(\mathbf{x}, e)$  has two parameters. Depending on whether these parameters are assumed to be constant or variable, the following cases have to be considered (Table 8.3):

1.  $\mathbf{x}$  is variable,  $e$  is variable:

$g(\mathbf{x}, e)$  is a random process, i.e., a set of sample functions. To simplify matters, the elementary event  $e$  is often omitted and just  $g(\mathbf{x})$  is used.

2.  $\mathbf{x}$  is variable,  $e = e_\nu$  is constant:

In this case,  $g(\mathbf{x}, e_\nu)$  is a single realization of the stochastic process and thus a deterministic sample function.

<sup>7</sup>Usually, random variables and random processes are denoted by capital letters and their realizations by lower-case letters. But in this book capital letters are used for frequency spectra, and so random variables will be written in typewriter font, to allow a better discrimination.

Table 8.3. Interpretations of a random process.

Elementary event $e$	Position $\mathbf{x}$	
	Constant	Variable
Constant	Value $g(\mathbf{x}_i, e_\nu)$	Sample function $g(\mathbf{x}, e_\nu)$
Variable	Random variable $g(\mathbf{x}_i, e)$	Random process $g(\mathbf{x}, e)$

3.  $\mathbf{x} = \mathbf{x}_i$  is constant,  $e$  is variable:

$g(\mathbf{x}_i, e)$  is a random variable, assigning to each elementary event  $e$  the corresponding value of the sample function. So, often just  $g(\mathbf{x}_i)$  is used and the elementary event  $e$  is omitted.

4.  $\mathbf{x} = \mathbf{x}_i$  is constant,  $e = e_\nu$  is constant:

In this case,  $g(\mathbf{x}_i, e_\nu)$  is a numerical value.

---

**Example 8.31 (Radio station):** A radio station can be considered as an example of a random process. From the perspective of the listener, songs are played randomly from a collection. The titles contained in the collection represent the available elementary events. The chosen song represents the sample function, which is obviously deterministic. ■

### 8.5.1 Moments of stochastic processes

For a constant position  $\mathbf{x} = \mathbf{x}_i$ , a stochastic process  $g(\mathbf{x})$  turns into a random variable  $g(\mathbf{x}_i)$ . For a simultaneous consideration of two positions  $\mathbf{x}_i$  and  $\mathbf{x}_j$ , the description of the corresponding random variables is no longer sufficient, as their joint statistical properties  $f(g(\mathbf{x}_i), g(\mathbf{x}_j))$  also have to be taken into account, e.g., the random variables might be stochastically dependent [9, 17, 19]. In general, a spatially discrete, stochastic process for arbitrary, finite point sets  $\{\mathbf{x}_1, \mathbf{x}_2, \dots, \mathbf{x}_n\}$ ,  $n \in \mathbb{N}$ , can be completely described by the joint probability density function  $f(g(\mathbf{x}_1), g(\mathbf{x}_2), \dots, g(\mathbf{x}_n))$ .

In many practical cases, it is impossible or too costly to obtain the joint probability density function. Instead, often the first-order and second-order probability density functions (i.e.,  $n = 1, 2$ ), as well as their moments, are used for a compact, approximate characterization of a stochastic process.

---

#### Definition 8.13: $n$ th order statistic

If a statistical analysis of a random process  $g(\mathbf{x})$  considers  $n$  different positions  $(\mathbf{x}_1, \mathbf{x}_2, \dots, \mathbf{x}_n)$ , it is called an  **$n$ th order statistic**, which is completely described by the joint probability distribution function

$$f_g(\mathbf{x}_1, \mathbf{x}_2, \dots, \mathbf{x}_n). \tag{8.253}$$

◇

The moments and moment-generating functions, such as the expected value, the autocorrelation function, etc., describe sample functions in terms of statistical averages and can all be defined on the basis of expected values.

**8.14 Definition 8.14: The expected value of a stochastic process**

The expected value of a stochastic process is calculated as follows:

$$E\{g(\mathbf{x})\} = \int_{-\infty}^{\infty} g f_{g(\mathbf{x})}(g) dg =: \mu_g(\mathbf{x}). \quad (8.254)$$

The expectation operator  $E\{\cdot\}$  results in an averaging over all sample functions for each position  $\mathbf{x}$ . Therefore, the result is in general a function of the position  $\mathbf{x}$ .  $\diamond$

**8.15 Definition 8.15: Moments of a stochastic process**

The  $m$ th moment of a stochastic process  $g(\mathbf{x})$  is defined as follows:

$$\mu_{g,m}(\mathbf{x}) := E\{g^m(\mathbf{x})\} = \int_{-\infty}^{\infty} g^m f_{g(\mathbf{x})}(g) dg. \quad (8.255)$$

The first moment is the expected value  $\mu_g(\mathbf{x})$  and describes the mean local intensity of the image.  $\diamond$

Higher moments are usually centered to the expected value [9,17].

**8.16 Definition 8.16: Central moments of a stochastic process**

The  $m$ th central moment of a stochastic process  $g(\mathbf{x})$  is defined as

$$E\{(g(\mathbf{x}) - \mu_g(\mathbf{x}))^m\} = \int_{-\infty}^{\infty} (g - \mu_g(\mathbf{x}))^m f_{g(\mathbf{x})}(g) dg. \quad (8.256)$$

Except for the centering to the expected value (8.254), this corresponds to the definition in (8.255).  $\diamond$

**8.17 Definition 8.17: Variance of a stochastic process**

The variance of a stochastic process  $g(\mathbf{x})$  is defined as

$$\text{Var}\{g(\mathbf{x})\} = E\{(g(\mathbf{x}) - \mu_g(\mathbf{x}))^2\} = \int_{-\infty}^{\infty} (g - \mu_g(\mathbf{x}))^2 f_{g(\mathbf{x})}(g) dg =: \sigma_g^2(\mathbf{x}). \quad (8.257)$$

So, the variance is the second central moment.  $\diamond$

**8.18 Definition 8.18: The autocorrelation function of a stochastic process**

The autocorrelation function (ACF) of a stochastic process  $g(\mathbf{x})$  is defined as

$$r_{gg}(\mathbf{x}_1, \mathbf{x}_2) = E\{g(\mathbf{x}_1)g(\mathbf{x}_2)\} = \int_{-\infty}^{\infty} \int_{-\infty}^{\infty} g_1 g_2 f_{g(\mathbf{x}_1)g(\mathbf{x}_2)}(g_1, g_2) dg_1 dg_2. \quad (8.258)$$

Writing  $\mathbf{x}_1 = \mathbf{x}$  and  $\mathbf{x}_2 = \mathbf{x} + \boldsymbol{\tau}$ , the ACF can be expressed as

$$r_{\mathbf{g}\mathbf{g}}(\mathbf{x}, \boldsymbol{\tau}) = E\{g(\mathbf{x})g(\mathbf{x} + \boldsymbol{\tau})\} = \int_{-\infty}^{\infty} \int_{-\infty}^{\infty} g_1 g_2 f_{g(\mathbf{x})g(\mathbf{x}+\boldsymbol{\tau})}(g_1, g_2) dg_1 dg_2 \quad (8.259)$$

with  $\boldsymbol{\tau} = (\tau_x, \tau_y)^T$ . Therefore, the ACF of a two-dimensional random process is a function of a four-dimensional argument.  $\diamond$

It is very important to use two different terms for the order  $n$  of a statistic and for the order of a moment. The latter denotes the power  $m$  in (8.255). Hence, the ACF is a second-order moment of a second-order statistic.

---

**Definition 8.19: The cross-correlation function of a pair of stochastic processes**

8.19

The cross-correlation function (CCF) of two stochastic processes  $g(\mathbf{x})$  and  $k(\mathbf{x})$  is defined similarly to the ACF:

$$r_{\mathbf{g}\mathbf{k}}(\mathbf{x}, \boldsymbol{\tau}) = E\{g(\mathbf{x})k(\mathbf{x} + \boldsymbol{\tau})\} = \int_{-\infty}^{\infty} \int_{-\infty}^{\infty} g k f_{g(\mathbf{x})k(\mathbf{x}+\boldsymbol{\tau})}(g, k) dg dk \quad (8.260)$$

with  $\boldsymbol{\tau} = (\tau_x, \tau_y)^T$ .  $\diamond$

---

**Definition 8.20: The autocovariance function and the cross-covariance function**

8.20

The autocovariance function of a stochastic process  $g(\mathbf{x})$  is defined as

$$C_{\mathbf{g}\mathbf{g}}(\mathbf{x}, \boldsymbol{\tau}) = E\{(g(\mathbf{x}) - \mu_g(\mathbf{x}))(g(\mathbf{x} + \boldsymbol{\tau}) - \mu_g(\mathbf{x} + \boldsymbol{\tau}))\}. \quad (8.261)$$

Similarly, the cross-covariance function  $C_{\mathbf{g}\mathbf{k}}(\mathbf{x}, \boldsymbol{\tau})$  is defined by

$$C_{\mathbf{g}\mathbf{k}}(\mathbf{x}, \boldsymbol{\tau}) = E\{(g(\mathbf{x}) - \mu_g(\mathbf{x}))(k(\mathbf{x} + \boldsymbol{\tau}) - \mu_k(\mathbf{x} + \boldsymbol{\tau}))\}. \quad (8.262)$$

Except for the centering around the expected value, these definitions correspond to (8.259) and (8.260) respectively.  $\diamond$

The correlation is a measure of the linear stochastic dependency between two random variables, and in the case of an image signal, of the linear stochastic dependency between the image intensities at a distance of  $\boldsymbol{\tau}$ . Correlation functions satisfy the following equations:

$$r_{\mathbf{g}\mathbf{k}}(\mathbf{x}, \boldsymbol{\tau}) = C_{\mathbf{g}\mathbf{k}}(\mathbf{x}, \boldsymbol{\tau}) + \mu_g(\mathbf{x})\mu_k(\mathbf{x} + \boldsymbol{\tau}), \quad (8.263)$$

$$r_{\mathbf{g}\mathbf{g}}(\mathbf{x}, \mathbf{0}) = \mu_g^2(\mathbf{x}) + \sigma_g^2(\mathbf{x}). \quad (8.264)$$

---

**Definition 8.21: Uncorrelatedness**

8.21

Two stochastic processes  $g(\mathbf{x})$  and  $k(\mathbf{x})$  are said to be uncorrelated if

$$E\{g(\mathbf{x})k(\mathbf{x} + \boldsymbol{\tau})\} = E\{g(\mathbf{x})\} \cdot E\{k(\mathbf{x} + \boldsymbol{\tau})\} \quad (8.265)$$

or

$$C_{\mathbf{g}\mathbf{k}}(\mathbf{x}, \boldsymbol{\tau}) = 0 \quad (8.266)$$

hold for arbitrary positions  $\mathbf{x}$  and displacements  $\boldsymbol{\tau} = (\tau_x, \tau_y)^T$ .  $\diamond$

### 8.22 Definition 8.22: Stochastic independence

Two stochastic processes  $\mathbf{g}(\mathbf{x})$  and  $\mathbf{k}(\mathbf{x})$  are said to be stochastically independent if

$$f_{\mathbf{g}(\mathbf{x})\mathbf{k}(\mathbf{x}+\boldsymbol{\tau})}(g, k) = f_{\mathbf{g}(\mathbf{x})}(g) \cdot f_{\mathbf{k}(\mathbf{x}+\boldsymbol{\tau})}(k) \quad (8.267)$$

holds for arbitrary positions  $\mathbf{x}$  and displacements  $\boldsymbol{\tau} = (\tau_x, \tau_y)^T$ .  $\diamond$

The stochastic independence of two processes as in (8.267) immediately implies that they are uncorrelated. The converse of this rule is only valid if these random processes are normally distributed, as their whole statistics are then determined by the first two moments [17, 19]. For all other cases, two random processes might be uncorrelated and yet stochastically dependent.

**Example 8.32 (Stochastically-dependent and uncorrelated processes):** Let  $a \sim \mathcal{N}(0, \sigma_a^2)$  be a normally distributed random variable with an expected value of zero and a variance of  $\sigma_a^2$ . Let  $b := a^2$  be another random variable, which is calculated by squaring  $a$ . Obviously,  $a$  and  $b$  are stochastically dependent, as either one of them is sufficient for calculating the value of the other.

The calculation of the covariance of  $a$  and  $b$  results in

$$E\{(a - E\{a\})(b - E\{b\})\} = E\{ab\} - E\{a^3\} = 0. \quad (8.268)$$

The first equality results from  $E\{a\} = 0$  and the last one from the symmetry of the normal distribution. In summary,  $a$  and  $b$  are uncorrelated but stochastically dependent.  $\blacksquare$

### 8.5.2 Stationarity and ergodicity

In general, the probability distributions as well as the moments of a stochastic process depend on the position. In particular, the moments of the first order statistic (e.g., the expected value and the variance) are two-dimensional functions of the position; the moments of the second order statistics (autocorrelation function and autocovariance function) are even four-dimensional. Besides the high costs coming with such high-dimensional functions, their calculation often fails, as only a single sample function is present, so that no average over several functions can be obtained. However, for two important classes of random processes, stationary processes and ergodic processes, the calculations can be performed in spite of these difficulties.

### 8.23 Definition 8.23: Stationarity

A stochastic process is called (strictly) stationary if its statistical properties are invariant with respect to spatial displacements.  $\diamond$

If only the first moment of the first order statistic and the second moment of the second order statistic meet the stationarity condition, the process is called *weakly stationary*.



**Definition 8.24: Weak stationarity**

A stochastic process  $g(\mathbf{x})$  is called weakly stationary if its expected value  $\mu_g(\mathbf{x})$  and its autocorrelation function (ACF)  $r_{gg}(\mathbf{x}, \boldsymbol{\tau})$  are invariant with respect to spatial displacements, i.e.:

$$\mu_g(\mathbf{x}) = \mu_g = \text{const.} \tag{8.269}$$

and

$$r_{gg}(\mathbf{x}, \boldsymbol{\tau}) = r_{gg}(\boldsymbol{\tau}). \tag{8.270}$$

Then both moments are independent of  $\mathbf{x}$ . Hence, the ACF of a two-dimensional, weakly stationary process is a function of an argument which is only two-dimensional.  $\diamond$

For normally distributed random processes, weak stationarity implies strict stationarity.

For *ergodic* random processes, the moments can be calculated by a spatial averaging instead of an averaging over all sample functions. Practically, this is quite useful, as often only a single sample function is available.

**Definition 8.25: Ergodicity**

A stochastic process  $g(\mathbf{x})$  is called (strictly) ergodic<sup>8</sup> if the spatial average of an arbitrary sample function  $g(\mathbf{x}, e_\nu)$  equals, with a probability of one, the corresponding average over all sample functions.  $\diamond$

A non-stationary random process cannot be ergodic, as its moments are position dependent. Therefore, stationarity is a necessary condition for ergodicity.

**Definition 8.26: Weak ergodicity**

A stochastic process  $g(\mathbf{x})$  is called weakly ergodic if the spatial averages for the first moment and for the autocorrelation function calculated using an arbitrary sample function  $g(\mathbf{x}, e_\nu)$  are, with a probability of one, equal to the corresponding averages over all sample functions, and therefore if the conditions

$$\lim_{\substack{M \rightarrow \infty \\ N \rightarrow \infty}} \frac{1}{MN} \int_{-\frac{M}{2}}^{\frac{M}{2}} \int_{-\frac{N}{2}}^{\frac{N}{2}} g(\mathbf{x}, e_\nu) \, d\mathbf{x} = E\{g(\mathbf{x})\} = \mu_g \tag{8.271}$$

and

$$\lim_{\substack{M \rightarrow \infty \\ N \rightarrow \infty}} \frac{1}{MN} \int_{-\frac{M}{2}}^{\frac{M}{2}} \int_{-\frac{N}{2}}^{\frac{N}{2}} g(\mathbf{x}, e_\nu) g(\mathbf{x} + \boldsymbol{\tau}, e_\nu) \, d\mathbf{x} = E\{g(\mathbf{x}) g(\mathbf{x} + \boldsymbol{\tau})\} = r_{gg}(\boldsymbol{\tau}) \tag{8.272}$$

are met. The left sides of Equations (8.271) and (8.272) represent an integration of *one single* arbitrary sample function  $g(\mathbf{x}, e_\nu)$ , and thus a spatial averaging. The calculation of expected

---

<sup>8</sup>In practice, rigorously proving that a give stochastic process is ergodic is often impossible. Therefore, ergodicity is often assumed and empirically validated. Details can be found in [9], for example.

values on the right sides of the equations represents an averaging over all sample functions for a fixed position  $\mathbf{x}$ . ◇

**Remarks:**

- For weakly ergodic random processes, the whole process can be represented with respect to the first two moments of the first and second order statistics, by *any* single sample function.
- A weakly ergodic process is also weakly stationary.
- For the **mean power** of a weakly ergodic process, or the mean power of a single sample function of the process, it holds

$$r_{gg}(\mathbf{0}) = \mu_g^2 + \sigma_g^2. \tag{8.273}$$

- If a random process cannot be assumed to be weakly ergodic, it might be possible that there are still some sample functions—just not all—which are representative of the process. In this case, an appropriate selection is necessary.

**8.27 Definition 8.27: Power spectral density**

The power spectral density (PSD) of a weakly stationary stochastic process  $g(\mathbf{x})$  is defined as follows:

$$S_{gg}(\mathbf{f}) := \lim_{\substack{M \rightarrow \infty \\ N \rightarrow \infty}} \mathbb{E} \left\{ \underbrace{\left| \frac{\mathcal{F}\{g(\mathbf{x}) \text{rect}(\frac{x}{M}) \text{rect}(\frac{y}{N})\}}{M \cdot N} \right|^2}_{\text{Periodogram}} \right\}. \tag{8.274}$$

The PSD shows to what extent the various frequencies contribute to the composition of a sample function  $g(\mathbf{x}, e_\nu)$  on average. Then we have  $S_{gg}(\mathbf{f}) \geq 0 \quad \forall \mathbf{f}$ . ◇

**8.16 Theorem 8.16: The Wiener–Khinchin theorem**

The power spectral density of a weakly stationary random process  $g(\mathbf{x})$  is the Fourier transform of the autocorrelation function:

$$S_{gg}(\mathbf{f}) = \mathcal{F}_\tau \{r_{gg}(\boldsymbol{\tau})\} = \int_{-\infty}^{\infty} \int_{-\infty}^{\infty} r_{gg}(\boldsymbol{\tau}) e^{-j2\pi \mathbf{f}^T \boldsymbol{\tau}} d\boldsymbol{\tau}. \tag{8.275}$$

I.e., the autocorrelation function and the power spectral density correspond to each other via the Fourier transform:

$$\text{ACF } r_{gg}(\boldsymbol{\tau}) \quad \circ \bullet \quad \text{PSD } S_{gg}(\mathbf{f}). \tag{8.276}$$

The corresponding random process has to be weakly stationary. ◇

**Proof 8.2 (Wiener–Khinchin theorem):** The proof will only be presented for the one-dimensional case. The inverse Fourier transform of the power spectral density

$$S_{\text{gg}}(f) := \lim_{M \rightarrow \infty} \text{E} \left\{ \frac{|\mathcal{F}\{\mathbf{g}(x) \text{rect}(\frac{x}{M})\}|^2}{M} \right\} = \lim_{M \rightarrow \infty} \text{E} \left\{ \frac{\mathbf{G}_M(f) \mathbf{G}_M^*(f)}{M} \right\} \quad (8.277)$$

with

$$\mathbf{g}_M(x) := \mathbf{g}(x) \text{rect}\left(\frac{x}{M}\right) \quad \circ \bullet \quad \mathbf{G}_M(f) \quad (8.278)$$

is calculated as follows:

$$\mathcal{F}^{-1}\{S_{\text{gg}}(f)\} = \lim_{M \rightarrow \infty} \text{E} \left\{ \frac{\mathcal{F}^{-1}\{\mathbf{G}_M(f) \mathbf{G}_M^*(f)\}}{M} \right\} \quad (8.279)$$

$$= \lim_{M \rightarrow \infty} \text{E} \left\{ \frac{\mathbf{g}_M(x) * \mathbf{g}_M(-x)}{M} \right\} \quad (8.280)$$

$$= \lim_{M \rightarrow \infty} \text{E} \left\{ \frac{\int_{-\infty}^{\infty} \mathbf{g}_M(\alpha) \mathbf{g}_M(\alpha + x) \, d\alpha}{M} \right\} \quad (8.281)$$

$$= \lim_{M \rightarrow \infty} \frac{\int_{-\infty}^{\infty} \text{E}\{\mathbf{g}(\alpha) \mathbf{g}(\alpha + x)\} \text{rect}\left(\frac{\alpha}{M}\right) \text{rect}\left(\frac{\alpha+x}{M}\right) \, d\alpha}{M} \quad (8.282)$$

$$= \lim_{M \rightarrow \infty} \frac{r_{\text{gg}}(x) \int_{-\infty}^{\infty} \text{rect}\left(\frac{\alpha}{M}\right) \text{rect}\left(\frac{\alpha+x}{M}\right) \, d\alpha}{M} \quad (8.283)$$

$$= \lim_{M \rightarrow \infty} r_{\text{gg}}(x) \Lambda\left(\frac{x}{M}\right) \quad (8.284)$$

$$= r_{\text{gg}}(x). \quad (8.285)$$

Here,  $\Lambda(\cdot)$  represents the triangle function (9.35). Renaming  $x$  to  $\tau$  immediately results in the Wiener–Khinchin theorem, cf. (8.275). ■

In summary, there are two alternatives for **spectral analysis**, depending on the actual class of the signal on hand [26]:

- The **harmonic analysis** of a deterministic function  $g(x)$  uses the Fourier transform to calculate its complex-valued spectrum  $G(f)$ . This mapping is completely lossless and can therefore be inverted.
- Usually, the Fourier integral is not convergent for sample functions of a stationary process  $\mathbf{g}(x)$  [17, 19]. Alternatively, in such cases, the properties of the process can be captured by the autocorrelation function  $r_{\text{gg}}(\tau)$ , which can be used to calculate the power spectral density  $S_{\text{gg}}(f)$ . This so-called **generalized harmonic analysis** results in a loss of information, as the phase spectrum is omitted. So, the sample functions  $g(x, e_\nu)$  cannot be reconstructed from the power spectral density  $S_{\text{gg}}(f)$  (cf. Example 8.18), and only an average of the spectral composition of their signals can be obtained.

The mean power  $P_{\mathcal{B}}$  of a frequency band  $\mathcal{B}$  is calculated via the corresponding integration:

$$P_{\mathcal{B}} = \int_{f \in \mathcal{B}} S_{\text{gg}}(f) \, df. \quad (8.286)$$

The mean total power is given by an integration over all frequencies:

$$\int_{-\infty}^{\infty} \int_{-\infty}^{\infty} S_{gg}(\mathbf{f}) \, d\mathbf{f} = r_{gg}(\mathbf{0}). \quad (8.287)$$

Again, by using the Wiener–Khinchin theorem and the properties of the Fourier transform,  $r_{gg}(\mathbf{0})$  represents the mean signal power.

### ► 8.5.3 Passing a stochastic process through an LSI system

In the spatial domain, what happens to a deterministic signal passing through an LSI system is completely characterized by the impulse response  $h(\mathbf{x})$  of the system (cf. Sec. 8.2.3). In the frequency domain, the system response is given by multiplying the system's transfer function  $H(\mathbf{f})$  by the Fourier transform  $G(\mathbf{f})$  of the input signal:

$$k(\mathbf{x}) = h(\mathbf{x}) ** g(\mathbf{x}) \quad \Leftrightarrow \quad K(\mathbf{f}) = H(\mathbf{f}) G(\mathbf{f}). \quad (8.288)$$

As with stationary random processes, the Fourier transform of the sample function converges only in exceptional cases; so the effect of passing through an LSI system is described by its moments.

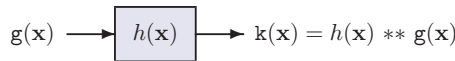


Figure 8.40. Effect of passing a stochastic process  $g(\mathbf{x})$  through an LSI system.

Now consider a stochastic process  $g(\mathbf{x})$  which is the input to an LSI system having the impulse response function  $h(\mathbf{x})$  (see Fig. 8.40):

$$k(\mathbf{x}) = h(\mathbf{x}) ** g(\mathbf{x}). \quad (8.289)$$

The **expected value**  $\mu_k(\mathbf{x})$  of the output process is given by

$$\mu_k(\mathbf{x}) = E\{k(\mathbf{x})\} = E\left\{ \int_{-\infty}^{\infty} \int_{-\infty}^{\infty} g(\boldsymbol{\alpha}) h(\mathbf{x} - \boldsymbol{\alpha}) \, d\boldsymbol{\alpha} \right\} \quad (8.290)$$

$$= \int_{-\infty}^{\infty} \int_{-\infty}^{\infty} E\{g(\boldsymbol{\alpha})\} h(\mathbf{x} - \boldsymbol{\alpha}) \, d\boldsymbol{\alpha} = \mu_g(\mathbf{x}) ** h(\mathbf{x}). \quad (8.291)$$

If the input process  $g(\mathbf{x})$  is weakly stationary,  $\mu_g(\mathbf{x}) = \mu_g$  implies

$$\mu_k(\mathbf{x}) = \mu_g ** h(\mathbf{x}) = \mu_g \int_{-\infty}^{\infty} \int_{-\infty}^{\infty} h(\boldsymbol{\alpha}) \, d\boldsymbol{\alpha} = \mu_g H(\mathbf{0}). \quad (8.292)$$

The constant DC component  $\mu_g$  is transferred by the transfer function at the frequency zero.

The **autocorrelation function**  $r_{kk}(\boldsymbol{\tau})$  of the output process is given by

$$r_{kk}(\boldsymbol{\tau}) = E\{k(\mathbf{x}) k(\mathbf{x} + \boldsymbol{\tau})\} \quad (8.293)$$

$$= E\left\{ \int_{-\infty}^{\infty} \int_{-\infty}^{\infty} h(\boldsymbol{\alpha}) g(\mathbf{x} - \boldsymbol{\alpha}) \, d\boldsymbol{\alpha} \cdot \int_{-\infty}^{\infty} \int_{-\infty}^{\infty} h(\boldsymbol{\beta}) g(\mathbf{x} + \boldsymbol{\tau} - \boldsymbol{\beta}) \, d\boldsymbol{\beta} \right\} \quad (8.294)$$

$$= \iint_{-\infty}^{\infty} \iint_{-\infty}^{\infty} h(\alpha) h(\beta) \underbrace{\mathbb{E}\{g(\mathbf{x} - \alpha) g(\mathbf{x} + \tau - \beta)\}}_{r_{gg}(\tau - \beta + \alpha)} d\alpha d\beta \tag{8.295}$$

$$= \iint_{-\infty}^{\infty} \underbrace{\left( \iint_{-\infty}^{\infty} h(\alpha) h(\alpha + \gamma) d\alpha \right)}_{=: \phi_{hh}(\gamma)} r_{gg}(\tau - \gamma) d\gamma \tag{8.296}$$

$$= \phi_{hh}(\boldsymbol{\tau}) ** r_{gg}(\boldsymbol{\tau}) \tag{8.297}$$

with  $\gamma := \beta - \alpha$ . By (8.296), the function  $\phi_{hh}(\boldsymbol{\tau})$  denotes the autocorrelation function of the impulse response  $h(\mathbf{x})$ , which is formally the result of spatial averaging. As the impulse response is a deterministic function, in this case there is no stochastic correlation and therefore, the term **impulse correlation** is used.

A comparison of (8.288) and (8.297) shows that when considering (weakly stationary) stochastic processes instead of deterministic signals, the signals and the impulse responses, are replaced by the corresponding correlation functions. Finally, the Fourier transform of (8.297) yields a correspondence between the power spectral densities of the input process and the output process<sup>9</sup>:

$$S_{kk}(\mathbf{f}) = |H(\mathbf{f})|^2 \cdot S_{gg}(\mathbf{f}), \tag{8.300}$$

which allows a description in the spatial frequency domain.

**Example 8.33 (White noise):** **White noise** denotes a stationary random process  $n(\mathbf{x})$  having a power spectral density  $S_{nn}(\mathbf{f})$  that is constant for all frequencies  $\mathbf{f}$ :

$$S_{nn}(\mathbf{f}) = c = \text{const.} > 0 \quad \bullet \iff \quad r_{nn}(\boldsymbol{\tau}) = c \delta(\boldsymbol{\tau}). \tag{8.301}$$

This noise is called ‘white,’ as in white light, since all frequencies of the spectrum are present with equal intensity.

The autocorrelation function  $r_{nn}(\boldsymbol{\tau})$  shows that the values at two neighboring points are uncorrelated, no matter how close they are. This signal model is idealized and is not physically realizable, as it has an infinite mean power

$$r_{nn}(\mathbf{0}) \rightarrow \infty. \tag{8.302}$$

However, white noise is still a usable noise model, resulting in realizable signals when passed through real systems, as will be shown in the following Example 8.34.

Figure 8.41(a) shows an example of a white noise process  $n(\mathbf{x})$ . The autocorrelation function  $\hat{r}_{nn}(\boldsymbol{\tau})$  of this random process is estimated by averaging over  $B = 10$  sample functions as well as by a spatial averaging (because of its ergodicity). Figure 8.41(b)

<sup>9</sup>One has

$$\mathcal{F}\{\phi_{hh}(\boldsymbol{\tau})\} = \mathcal{F}\left\{ \int h(\alpha + \boldsymbol{\tau}) h^*(\alpha) d\alpha \right\} = \mathcal{F}\{h(\boldsymbol{\tau}) * h^*(-\boldsymbol{\tau})\} \tag{8.298}$$

$$= H(\mathbf{f}) H^*(\mathbf{f}) = |H(\mathbf{f})|^2. \tag{8.299}$$

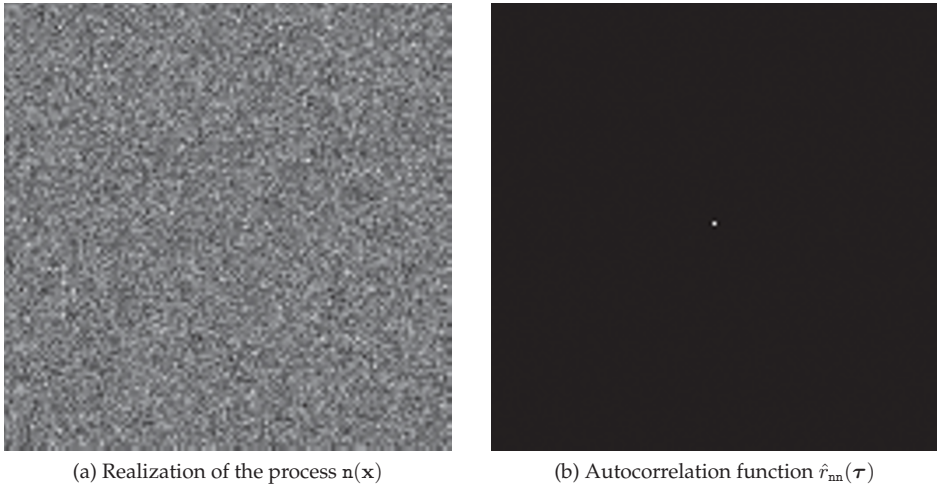


Figure 8.41. A white noise process  $n(\mathbf{x})$ .

shows the estimated function, which is a Dirac delta function. The origin of the coordinate system is located in the center of the image. ■

**Example 8.34 (Colored noise):** So-called **colored noise** can be produced by linearly filtering a white noise process  $n(\mathbf{x})$ :

$$\mathbf{k}(\mathbf{x}) = h(\mathbf{x}) ** n(\mathbf{x}), \quad (8.303)$$

with  $h(\mathbf{x})$  denoting the impulse response of the filter. By (8.297) and (8.301), the autocorrelation function and the power spectral density of the original process  $\mathbf{k}(\mathbf{x})$  are given by

$$r_{\mathbf{k}\mathbf{k}}(\boldsymbol{\tau}) = \phi_{hh}(\boldsymbol{\tau}) ** c\delta(\boldsymbol{\tau}) = c\phi_{hh}(\boldsymbol{\tau}) \quad (8.304)$$

$$\begin{aligned} &\Downarrow \\ S_{\mathbf{k}\mathbf{k}}(\mathbf{f}) &= c|H(\mathbf{f})|^2. \end{aligned} \quad (8.305)$$

The term ‘colored noise’ is also motivated by light spectra but in this case with a non-constant distribution of the spectral components.

The use of a rectangular filter with the impulse response function

$$h(\mathbf{x}) = \frac{1}{L^2} \text{rect}\left(\frac{x}{L}\right) \text{rect}\left(\frac{y}{L}\right) \quad (8.306)$$

results in a low-pass filtering of the white noise:

$$r_{\mathbf{k}\mathbf{k}}(\boldsymbol{\tau}) = c\phi_{hh}(\boldsymbol{\tau}) = c \cdot \Lambda\left(\frac{\tau_x}{L}\right) \Lambda\left(\frac{\tau_y}{L}\right) \quad (8.307)$$

$$\begin{aligned} &\Downarrow \\ S_{\mathbf{k}\mathbf{k}}(\mathbf{f}) &= cL^2 \text{sinc}^2(Lf_x) \text{sinc}^2(Lf_y). \end{aligned} \quad (8.308)$$

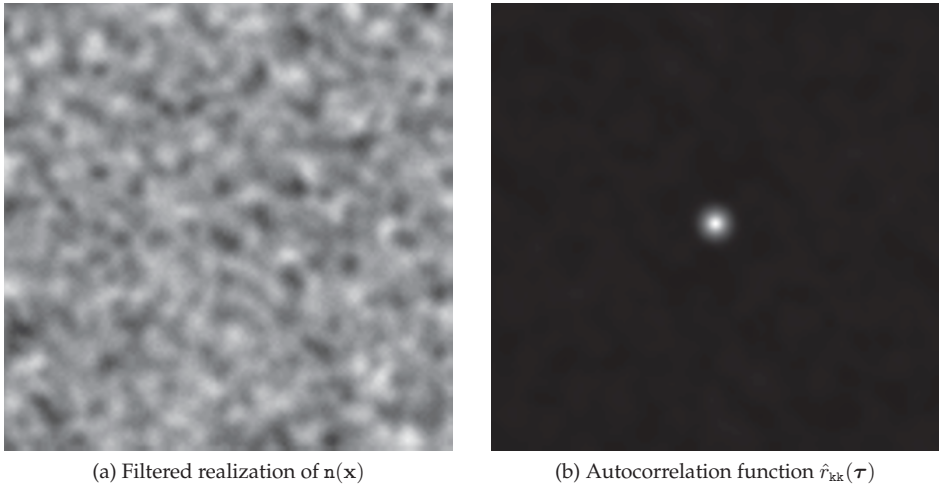


**Figure 8.42.** Generation of a discrete, colored noise process  $k(\mathbf{x})$  by low-pass filtering of a white noise process  $n(\mathbf{x})$ .

After this low-pass filtering, the process  $k(\mathbf{x})$  is correlated for  $\boldsymbol{\tau} \in (-L, L)^2$ . The mean power

$$r_{kk}(\mathbf{0}) = c < \infty \quad (8.309)$$

of the original process is finite. Therefore,  $k(\mathbf{x})$  is a physically meaningful, realizable stochastic process.

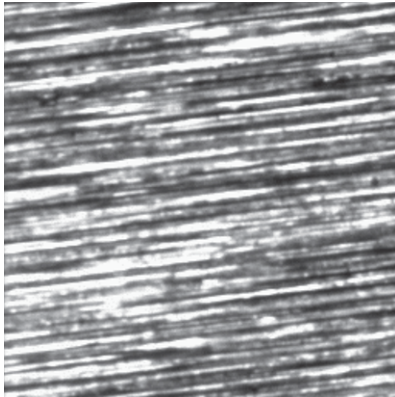
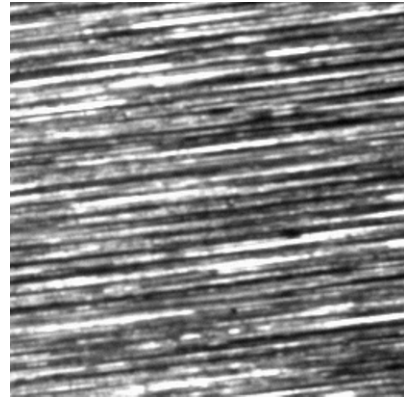
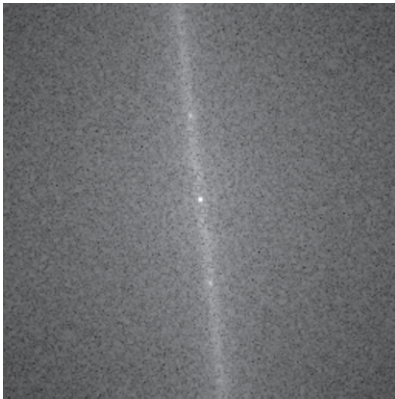
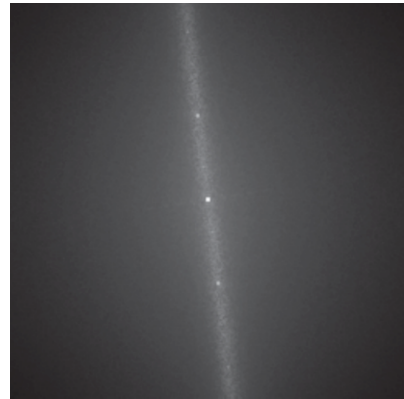
Figure 8.42(a) shows the result of the low-pass filtering of the sample function of Fig. 8.41(a). Here, the image intensities of adjacent discrete positions are highly correlated, which can also be seen by considering the autocorrelation function shown in Fig. 8.42(b), which is widened compared to Fig. 8.41(b). ■

---

**Example 8.35 (Grinding texture as a stochastic process):** After grinding the radial shaft seals of automobiles, their macroscopic texture consists of short, stochastically placed grinding grooves, which might be superposed with periodic scratches (see Fig. 8.43(a)). As these scratches can cause leaks and dry runnings, their period lengths and extents have to be inspected [20].

By rotating the component and by acquiring multiple images, different sections of the surface texture can be captured, which can be considered as sample functions of the same random process  $g(\mathbf{x})$  (see Fig. 8.43(b)). Like in Example 8.33, the autocorrelation function  $\hat{r}_{gg}(\boldsymbol{\tau})$  and the autocovariance function  $\hat{C}_{gg}(\boldsymbol{\tau})$  can be estimated. The autocorrelation function Fig. 8.43(c) shows four different components [2]:

- In the center of the coordinate system, there is a spatially discrete Dirac delta function, which represents the uncorrelated noise of the process.
- In the autocorrelation function, the periodic scratches induce structures with the same orientation, which again are periodic. Periodic signals have periodic autocorrelation functions [19].

(a) Realization of the process  $g(x)$ (b) Realization of the process  $g(x)$ (c) Autocorrelation function  $\hat{r}_{gg}(\tau)$ (d) Autocovariance function  $\hat{C}'_{gg}(\tau)$ (e) Periodogram  $\hat{S}_{gg}(f)$ (f) Averaged periodogram  $\overline{\hat{S}_{gg}(f)}$ **Figure 8.43.** Grinding texture as a stochastic process.



- In the autocorrelation function, the stochastic grinding grooves produce a line through the center of the coordinate system in the direction of the grooves. They have a finite correlation length in the direction of the grooves, because of the finite longitudinal extent of the grinding grooves.
- Finally, the autocorrelation function has a constant offset representing the mean intensity of the process.

Because of the empirical calculation of the autocorrelation function from finitely sized images, it decays towards the image boundaries [13]. Except for the mean intensity, the autocovariance function in Fig. 8.43(d) describes the same components of the process.

By the Wiener–Khinchin theorem (8.275), the Fourier transform of the autocorrelation function is the power spectral density of the random process. Alternatively, the **periodogram**  $\hat{S}_{gg}(f)$  calculated from a sample function can be used as an estimate of the power spectral density (see Fig. 8.43(e)) employing (8.274). But the periodogram is a very noisy estimator for the power spectral density, as the standard deviation of its error of estimation is in the same range as the quantity which is to be estimated [13, 17]. However, if there are multiple sample functions of the random process as in the present case, the mean  $\overline{\hat{S}_{gg}(f)}$  of the corresponding periodograms can be calculated [17, 19]. If an uncorrelated noise is assumed, the variance of the error of estimation can be reduced by a factor of  $\frac{1}{B}$  if  $B$  images are used. The resulting estimate of the power spectral density Fig. 8.43(f) can be interpreted like a DFT magnitude spectrum, but with notably less distortion, as in the present case the calculation is based on  $B = 120$  images. As the grinding texture consists of straight, parallel grooves, the corresponding power components in the spatial frequency domain are concentrated on a line which is perpendicular to the grooves and runs through the center of the coordinate system. Because of the periodicity of the scratches, the corresponding spectral components are represented by an additional comb of Dirac delta functions. The distance between the Dirac delta functions is reciprocal to the period length; the height of the Dirac delta functions describes the extent of the scratches and can therefore be considered as a quality measure for the inspected item. ■

## 8.6 Quantization

For representing images  $g(\mathbf{x})$  in a computer, the positions  $\mathbf{x}$  and the image values  $g$  have to be discretized. To simplify matters, for the rest of this section, any image  $g(\mathbf{x})$  will be assumed to be scalar. The discretization of the image values (also called quantization) assigns a quantized value  $g$ , chosen from a set of  $K$  discrete values<sup>10</sup>, to each image value  $\tilde{g}$ . It is common to denote the resolution of the quantization by the number  $\text{ld } K$  of bits which are needed to encode the values in binary numbers.

The characteristic curve of the quantization can be represented by a step function (Fig. 8.44), mapping the continuous input image values from the interval

$$\tilde{g} \in [g_0, g_K] \tag{8.310}$$

<sup>10</sup>Unlike the usual convention in this book, in this section, continuous image values will be denoted by  $\tilde{g}$  instead of  $g$ . By this means, the notation will remain consistent even if images with discrete image values are used.

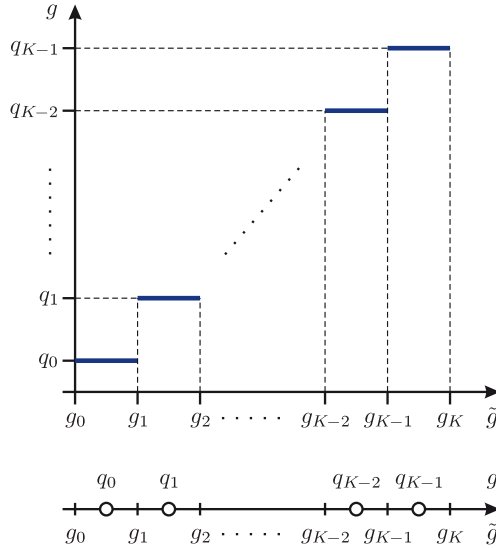


Figure 8.44. Characteristic curve of quantization.

to  $K$  quantization steps

$$g \in \{q_0, q_1, \dots, q_{K-1}\}. \tag{8.311}$$

By means of the quantization thresholds  $g_i, i \in \{0, \dots, K\}$  and the operator  $Q\{\cdot\}$ , the quantization can be described as follows:

$$Q\{\tilde{g}\} = q_i \quad \text{if} \quad \tilde{g} \in [g_i, g_{i+1}). \tag{8.312}$$

Here,  $Q\{\cdot\}$  is a non-linear, memoryless, shift invariant and irreversible operator (Fig. 8.45). Despite the nonlinearity of this operation, it will be shown in Sec. 8.6.2 that the effect of quantization on the statistics of the signal can be described and analyzed with linear system theory.

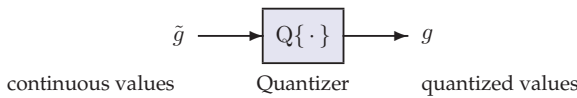


Figure 8.45. Quantizer as a system.

### 8.6.1 Optimal quantization

In order to derive the characteristics of an optimal quantization, the continuous image values are modeled as random variables  $\tilde{g}$  with a probability density function  $f_{\tilde{g}}(\tilde{g})$ , which is assumed to be known. The quantization thresholds  $g_i$  and the quantization steps  $q_i$  are obtained by minimizing a quality criterion, which is usually the mean squared quantization

error:

$$\overline{\varepsilon^2} := \sum_{l=0}^{K-1} \int_{g_l}^{g_{l+1}} (\tilde{g} - q_l)^2 f_{\tilde{g}}(\tilde{g}) d\tilde{g} = E \left\{ \sum_{l=0}^{K-1} (\tilde{g} - q_l)^2 \right\} \xrightarrow{!} \text{Min.} \quad (8.313)$$

The number of quantization steps  $K$ , as well as the lower and upper quantization thresholds  $g_0$  and  $g_K$ , are assumed to be fixed.

First, the derivative of (8.313) with respect to the quantization thresholds  $g_i$  is calculated:

$$\frac{\partial \overline{\varepsilon^2}}{\partial g_i} = (g_i - q_{i-1})^2 f_{\tilde{g}}(g_i) - (g_i - q_i)^2 f_{\tilde{g}}(g_i) \stackrel{!}{=} 0. \quad (8.314)$$

This results in the following condition for the thresholds  $g_i$ :

$$g_i = \frac{q_{i-1} + q_i}{2}. \quad (8.315)$$

So the optimal quantization thresholds  $g_i$  are located in the center between the adjacent quantization steps  $q_{i-1}$  and  $q_i$ .

Differentiating (8.313) with respect to  $q_i$  yields the following condition:

$$\frac{\partial \overline{\varepsilon^2}}{\partial q_i} = -2 \int_{g_i}^{g_{i+1}} (\tilde{g} - q_i) f_{\tilde{g}}(\tilde{g}) d\tilde{g} \stackrel{!}{=} 0 \quad (8.316)$$

and solving for  $q_i$  results in

$$q_i = \frac{\int_{g_i}^{g_{i+1}} \tilde{g} f_{\tilde{g}}(\tilde{g}) d\tilde{g}}{\int_{g_i}^{g_{i+1}} f_{\tilde{g}}(\tilde{g}) d\tilde{g}}. \quad (8.317)$$

Accordingly, the quantization steps have to be placed at the centroid of the probability density function  $f_{\tilde{g}}(\tilde{g})$  inside the interval  $[g_i, g_{i+1}]$ .

To define the characteristic curve of the optimal quantization, the condition (8.315) has to be met for  $i \in \{1, \dots, K-1\}$  and (8.317) for  $i \in \{0, \dots, K-1\}$ . In summary, a system of  $K-1$  linear and  $K$  nonlinear equations has to be solved (usually numerically) in order to obtain the unknown parameters  $g_1, \dots, g_{K-1}$  and  $q_0, \dots, q_{K-1}$ .

---

**Example 8.36 (Optimal quantization for uniformly distributed image values):** If the image values can be assumed to be uniformly distributed

$$f_{\tilde{g}}(\tilde{g}) = \frac{1}{g_K - g_0} = \text{const.} \quad (8.318)$$

inside an interval  $g_0 \leq \tilde{g} \leq g_K$ , the quantization steps can be calculated by using the following linear formula (employing (8.317)):

$$q_i = \frac{\int_{g_i}^{g_{i+1}} \tilde{g} d\tilde{g}}{\int_{g_i}^{g_{i+1}} d\tilde{g}} = \frac{1}{2} \cdot \frac{g_{i+1}^2 - g_i^2}{g_{i+1} - g_i} = \frac{g_{i+1} + g_i}{2}. \quad (8.319)$$

Inserting (8.319) into (8.315) yields

$$g_i - g_{i-1} = g_{i+1} - g_i, \quad (8.320)$$

$$q_i - q_{i-1} = q_{i+1} - q_i. \quad (8.321)$$

In this case, the quantization is called an **equidistant quantization**, as the optimal quantization steps  $q_i$ , as well as the optimal quantization thresholds  $g_i$ , are equidistant. If the distance between two adjacent quantization thresholds is denoted by

$$\Delta g = \frac{g_K - g_0}{K}, \quad (8.322)$$

the mean squared quantization error (8.313) is given by

$$\bar{\varepsilon}^2 = \frac{K}{g_K - g_0} \int_0^{\Delta g} \left( \tilde{g} - \frac{\Delta g}{2} \right)^2 d\tilde{g} \quad (8.323)$$

$$= \frac{1}{\Delta g} \left[ \frac{1}{3} \left( \tilde{g} - \frac{\Delta g}{2} \right)^3 \right]_0^{\Delta g} \quad (8.324)$$

$$= \frac{(\Delta g)^2}{12}. \quad (8.325)$$

This value corresponds to the variance of the so-called quantization noise, see Sec. 8.6.3. ■

---

**Example 8.37 (Optimal equidistant quantization):** Common analog-to-digital converters usually approximate an equidistant quantization of the input signal [22]. If, unlike Example 8.36, the continuous image values  $\tilde{g}$  show no uniform distribution, the quantization results of the mean squared quantization error (8.313) are generally suboptimal.

In order to still achieve an optimal quantization, a nonlinear transformation  $T\{\cdot\}$  can be applied to the signal values  $\tilde{g}$ , yielding values  $k$  which are uniformly distributed within the interval  $[g_0, g_K]$  (Fig. 8.46). Subsequent to the equidistant quantization  $Q\{\cdot\}$  of the values  $k$ , the nonlinear transformation is reversed by  $T^{-1}\{\cdot\}$ . The quantization steps of the resulting quantization are closely spaced for those regions where the probability density function  $f_{\tilde{g}}(\tilde{g})$  has high values. ■

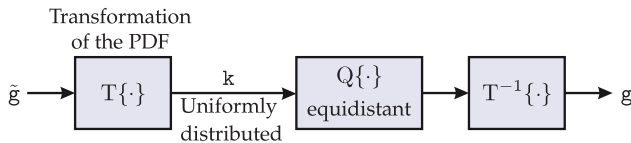


Figure 8.46. Optimal quantization by using an equidistant quantizer.

### ➤ 8.6.2 The quantization theorem

Similar to the sampling of signals, which performs a discretization of the domain of the signal, quantization corresponds to a discretization of the codomain of the function. The

effects of sampling have been discussed in Sec. 8.3.2. By means of linear system theory, the sampling theorem was derived, which provides a necessary condition for an error-free reconstruction of continuous signals by their samples. So one might wonder whether there exists a similar theorem for the ‘sampling’ of the signal values, i.e., if a condition can be formulated, under which the continuous values  $\tilde{g}$  can be reconstructed from their discrete representatives  $g$ .

In the remaining part of this section, an answer to this question will be given for the case of equidistant quantization. As quantization is a nonlinear operation, the methods of linear system theory cannot be directly applied to the signals. However, linear system theory can be used to analyze the probability density functions (PDF) of the quantized signals (Fig. 8.47). Under certain assumptions, the probability density function of the continuous signal can even be reconstructed from the probability density function of the quantized signal. This will be the main point of the following **quantization theorem**, which however is not as powerful as the sampling theorem, inasmuch as it will not be possible to reconstruct the original continuous values  $\tilde{g}$  from the quantized values  $g$  without errors [25].

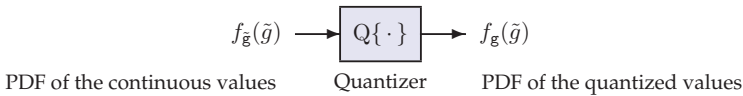


Figure 8.47. Description of quantization by means of linear system theory.

As the quantization must have a finite resolution, the support of the probability density function  $f_g(g)$  of the quantized signal  $g$  is discrete. Hence, each input value is mapped to the nearest quantization value  $q_i$  in accordance with (8.312). Therefore, the resulting probability density function  $f_g(g)$  is an impulse train, weighted by the discrete probabilities of the corresponding quantization intervals of the input probability density functions. The weights are obtained by integrating  $f_{\tilde{g}}(\tilde{g})$  over the appropriate interval (cf. Fig. 8.48). So, quantization represents an ‘area sampling’ of the probability density function.

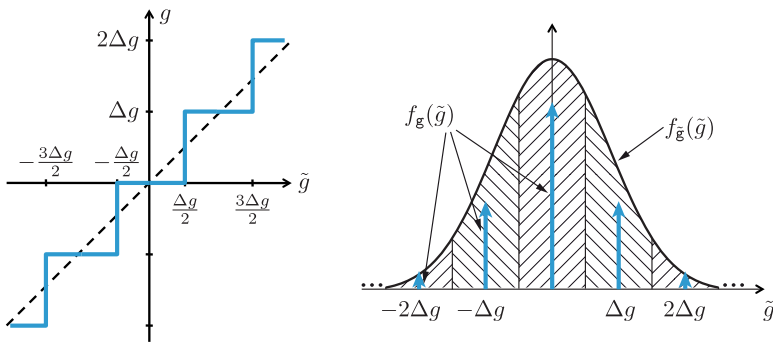
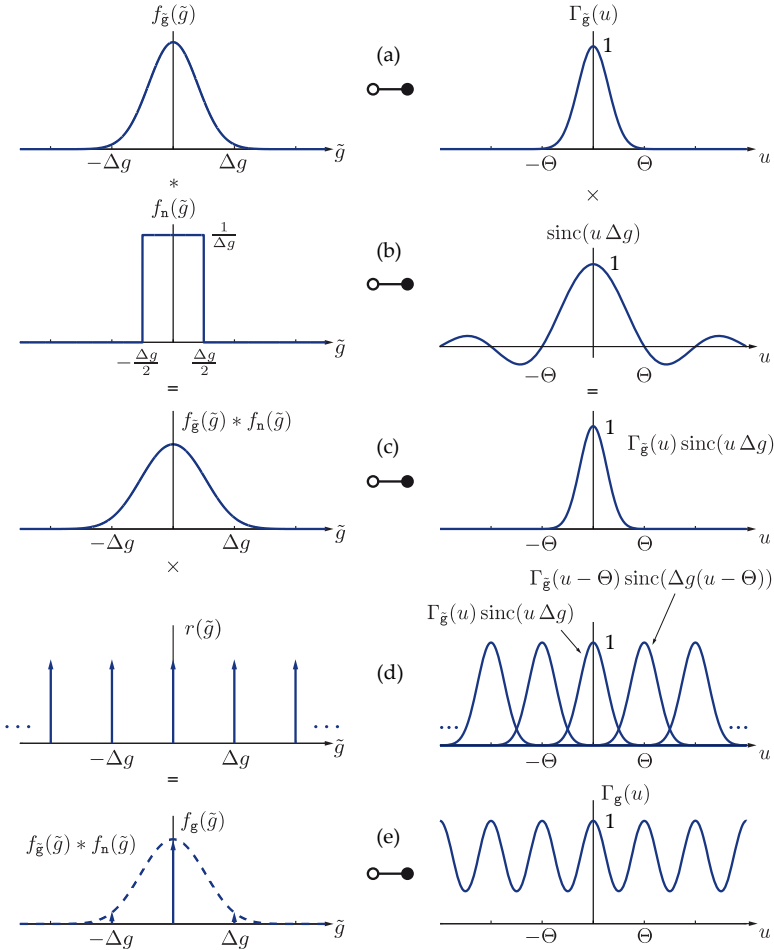


Figure 8.48. Area sampling of the probability density function: (left) Quantization characteristics; (right) Probability density functions  $f_{\tilde{g}}(\tilde{g})$  of the continuous values and  $f_g(g)$  of the quantized values [25].

The ‘area sampling’ of the probability density function  $f_{\tilde{g}}(\tilde{g})$  can be equivalently expressed by a calculation of a moving average and a subsequent sampling. The whole procedure is illustrated in Fig. 8.49 (left). The moving average corresponds to a convolution of



**Figure 8.49.** Area sampling of the probability density function  $f_{\tilde{g}}(\tilde{g})$  of the value range and the corresponding frequency range (adapted from [25]).

$f_{\tilde{g}}(\tilde{g})$  with the rectangular function

$$f_n(\tilde{g}) = \frac{1}{\Delta g} \text{rect}\left(\frac{\tilde{g}}{\Delta g}\right). \tag{8.326}$$

The probability density function  $f_{\tilde{g}}(\tilde{g})$  of the quantized values is the result of a subsequent multiplication by the impulse train  $r(\tilde{g})$ , yielding a series of Dirac delta functions, which are weighted with the corresponding area component of the input probability density function  $f_{\tilde{g}}(\tilde{g})$ :

$$f_{\tilde{g}}(\tilde{g}) = (f_{\tilde{g}}(\tilde{g}) * f_n(\tilde{g})) \cdot r(\tilde{g}) \tag{8.327}$$

$$= \left( f_{\tilde{g}}(\tilde{g}) * \frac{1}{\Delta g} \text{rect}\left(\frac{\tilde{g}}{\Delta g}\right) \right) \cdot \sum_{n=-\infty}^{\infty} \delta(\tilde{g} - n\Delta g) \tag{8.328}$$

$$= \frac{1}{\Delta g} \sum_{n=-\infty}^{\infty} \int_{-\infty}^{\infty} f_{\tilde{g}}(\alpha) \operatorname{rect}\left(\frac{\tilde{g} - \alpha}{\Delta g}\right) d\alpha \cdot \delta(\tilde{g} - n\Delta g) \tag{8.329}$$

$$= \frac{1}{\Delta g} \sum_{n=-\infty}^{\infty} \int_{(n-\frac{1}{2})\Delta g}^{(n+\frac{1}{2})\Delta g} f_{\tilde{g}}(\alpha) \delta(\tilde{g} - n\Delta g) d\alpha \tag{8.330}$$

$$= \sum_{n=-\infty}^{\infty} \delta(\tilde{g} - n\Delta g) \cdot \frac{1}{\Delta g} \int_{(n-\frac{1}{2})\Delta g}^{(n+\frac{1}{2})\Delta g} f_{\tilde{g}}(\alpha) d\alpha. \tag{8.331}$$

In order to derive the quantization theorem, the formulation of the area sampling has to be transformed into the frequency domain. For this purpose, the so-called **characteristic function** of a random variable will now be introduced. This function can be used to determine the moments of the random variable in an elegant way, see Theorem 8.17.

**Definition 8.28: The characteristic function**

8.28

The characteristic function of a random variable  $g$  is defined by an expected value:

$$\Gamma_g(u) = E\{e^{j2\pi u g}\} \tag{8.332}$$

$$= \int_{-\infty}^{\infty} f_g(g) e^{j2\pi u g} dg = \mathcal{F}^{-1}\{f_g(g)\} = \mathcal{F}^*\{f_g(g)\}. \tag{8.333}$$

Obviously, the characteristic function (8.333) corresponds to the inverse Fourier transform (8.32) of the probability density function  $f_g(g)$ . As  $f_g(g)$  is real-valued,  $\Gamma_g(u)$  can also be considered as the complex conjugate of the Fourier transform of  $f_g(g)$ . Therefore, in this case,  $u$  can be interpreted as the frequency corresponding to  $g$ . In particular, the magnitude of  $\Gamma_g(u)$  and the magnitude spectrum  $|\mathcal{F}\{f_g(g)\}|$  are equal.  $\diamond$

**Definition 8.29: Moments of a random variable**

8.29

The  $n$ th moment of a random variable  $g$  is defined similar to (8.255):

$$\mu_{g,n} := E\{g^n\} = \int_{-\infty}^{\infty} g^n f_g(g) dg. \tag{8.334}$$

The first moment is the expected value  $\mu_g$  of the random variable  $g$ .  $\diamond$

**Theorem 8.17: Moments of a random variable**

8.17

The moments of a random variable  $g$  can be calculated by means of the characteristic function  $\Gamma_g(u)$  as follows:

$$\mu_{g,n} = E\{g^n\} = \frac{1}{(j2\pi)^n} \left. \frac{d^n \Gamma_g(u)}{du^n} \right|_{u=0}. \tag{8.335}$$

So, in order to calculate the moments, the characteristic function  $\Gamma_g(u)$  is only needed inside a neighborhood of the point  $u = 0$ .  $\diamond$

**Proof 8.3 (Moments of a random variable):** Equation (8.335) can be proved by means of the derivative property (8.54) of the Fourier transform:

$$\frac{d^n \Gamma_{\tilde{g}}(u)}{du^n} = \mathcal{F}^{-1}\{(j2\pi g)^n f_{\tilde{g}}(g)\} \quad (8.336)$$

$$= \int_{-\infty}^{\infty} (j2\pi g)^n f_{\tilde{g}}(g) e^{j2\pi u g} dg. \quad (8.337)$$

For  $u = 0$ , dividing (8.337) by  $(j2\pi)^n$  immediately yields the defining equation (8.334) of the  $n$ th moment. ■

The characteristic function (8.332) can now be used to express the process of area sampling in the frequency domain. The convolution of  $f_{\tilde{g}}(\tilde{g})$  with the rectangular function (8.326) corresponds to multiplying the characteristic function  $\Gamma_{\tilde{g}}(u)$  by the inverse Fourier transform of (8.326):

$$\mathcal{F}^{-1}\{f_{\tilde{g}}(\tilde{g}) * f_n(\tilde{g})\} = \Gamma_{\tilde{g}}(u) \Gamma_n(u) = \Gamma_{\tilde{g}}(u) \text{sinc}(u \Delta g), \quad (8.338)$$

see Fig. 8.49(a)–(c). The reciprocal

$$\Theta = \frac{1}{\Delta g} \quad (8.339)$$

of the interval width of  $\Delta g$  is called the **quantization frequency**.

Similar to the sampling of signals (Fig. 8.10), the multiplication of the filtered density  $f_{\tilde{g}}(\tilde{g}) * f_n(\tilde{g})$  by the impulse train  $r(\tilde{g})$  in the original domain, results in a periodic repetition of the product  $\Gamma_{\tilde{g}}(u) \text{sinc}(u \Delta g)$  in the frequency domain (see Fig. 8.49(c) right):

$$\Gamma_{\tilde{g}}(u) = \sum_{l=-\infty}^{\infty} \Gamma_{\tilde{g}}(u + l\Theta) \text{sinc}(\Delta g(u + l\Theta)). \quad (8.340)$$

Here, the frequency of the repetition equals the quantization frequency  $\Theta$ , cf. Fig. 8.49(d)–(e).

This result immediately leads to the quantization theorem [25]. If the periodic repetition (8.340) causes no overlap of the characteristic functions,

$$\Gamma_{\tilde{g}}(u) = \mathcal{F}^{-1}\{f_{\tilde{g}}(\tilde{g})\} = 0 \quad \text{if} \quad |u| \geq \frac{\Theta}{2} = \frac{1}{2\Delta g}, \quad (8.341)$$

the characteristic function of the continuous values  $\tilde{g}$ , as well as the corresponding probability density function  $f_{\tilde{g}}(\tilde{g})$ , can be reconstructed from  $\Gamma_{\tilde{g}}(u)$  without errors.

In practice, usually a less strict formulation of the quantization theorem is sufficient. By (8.335), only the neighborhood  $u = 0$  of the characteristic function  $\Gamma_{\tilde{g}}(u)$  is necessary for the calculation of the moments  $\tilde{g}$ . Hence, the moments of the continuous values  $\tilde{g}$  can be calculated from the moments of the quantized values  $g$  if

$$\Gamma_{\tilde{g}}(u) = \Gamma_{\tilde{g}}(u) \text{sinc}(u \Delta g) \quad \text{for} \quad u = 0, \quad (8.342)$$

in other words, if, at the frequency  $u = 0$ , there is no overlap caused by the periodic repetition.



**Theorem 8.18: The quantization theorem**

If the probability density function  $f_{\tilde{g}}(\tilde{g})$  of the continuous signal values  $\tilde{g}$  is band-limited, i.e., if

$$\Gamma_{\tilde{g}}(u) = \mathcal{F}^{-1}\{f_{\tilde{g}}(\tilde{g})\} = 0 \quad \text{if} \quad |u| > \frac{\Xi}{2}, \quad (8.343)$$

then the moments (expected value, variance, and higher moments) of the continuous original values  $\tilde{g}$  can be determined without errors by means of the values  $g$  which have been equidistantly quantized with the quantization step width  $\Delta g$  if the following condition is satisfied:

$$\frac{\Xi}{2} + \varepsilon < \Theta = \frac{1}{\Delta g} \quad \Leftrightarrow \quad \Delta g < \left(\frac{\Xi}{2} + \varepsilon\right)^{-1}, \quad \varepsilon > 0. \quad (8.344)$$

So the quantization theorem states how finely a signal has to be quantized in order to preserve all relevant signal components.  $\diamond$

If the conditions of the quantization theorem are satisfied, the moments of the continuous image values  $\tilde{g}$  can be extracted from the moments of the quantized image values  $g$  as follows:

$$E\{\tilde{g}\} = E\{g\}, \quad (8.345)$$

$$E\{\tilde{g}^2\} = E\{g^2\} - \frac{1}{12}(\Delta g)^2, \quad (8.346)$$

$$E\{\tilde{g}^3\} = E\{g^3\} - \frac{1}{4}E\{g\}(\Delta g)^2, \quad (8.347)$$

$$E\{\tilde{g}^4\} = E\{g^4\} - \frac{1}{2}E\{g^2\}(\Delta g)^2 + \frac{7}{240}(\Delta g)^4. \quad (8.348)$$

The correction needed for the higher-order moments, by means of the right terms in the right-hand sides of (8.346)–(8.348), is, in the field of statistics, called Sheppard's correction [21].

### 8.6.3 Modeling of the quantization

Although quantization is a nonlinear operation, it can be equivalently described by a linear additive model. In order to construct this model, first the addition of two random variables will be studied.

**Theorem 8.19: Addition of stochastically-independent random variables**

If two stochastically-independent random variables  $x$  and  $y$  are added,

$$z = x + y, \quad (8.349)$$

the probability density function  $f_z(z)$  of the resulting random variable  $z$  is given by the convolution

$$f_z(z) = f_x(z) * f_y(z) \quad (8.350)$$

of the probability density functions of the random variables  $x$  and  $y$ .  $\diamond$

**Proof 8.4 (Addition of stochastically-independent random variables):** As  $x$  and  $y$  are stochastically-independent, one has

$$f_{xy}(x, y) = f_x(x) f_y(y). \tag{8.351}$$

By (8.351) and (8.349), the conditional probability density function of the sum  $z$  given  $y$  is

$$f_{z|y}(z|y) = f_x(z - y). \tag{8.352}$$

If  $y$  is given, the difference of the random variables  $x$  and  $z$  is the additive constant  $y$ , which yields the probability density function of  $z$  by shifting the probability density function of  $x$  by  $y$ . Hence, the joint density  $f_{zy}(z, y)$  can be expressed by

$$f_{zy}(z, y) = f_{z|y}(z|y) f_y(y) = f_x(z - y) f_y(y). \tag{8.353}$$

Marginalizing out (integrating out)  $y$  yields the marginal density  $f_z(z)$ :

$$f_z(z) = \int_{-\infty}^{\infty} f_{zy}(z, y) dy = \int_{-\infty}^{\infty} f_x(z - y) f_y(y) dy = f_x(z) * f_y(z), \tag{8.354}$$

corresponding to the convolution (8.350). ■

The ‘area sampling’ of the probability density function  $f_{\tilde{g}}(\tilde{g})$  of the continuous image values has been expressed as a convolution of two density functions in (8.327). By Theorem 8.19, this convolution corresponds to the sum of two independent random variables  $\tilde{g}$  and  $n$ , of which the latter is uniformly distributed by (8.326). In this respect, the ‘area sampling’ and therefore also the quantization procedure can be considered as an additive superposition of an independent, uniformly distributed, zero-mean quantization noise  $n$ . This results in the linear model for the quantization shown in Fig. 8.50.

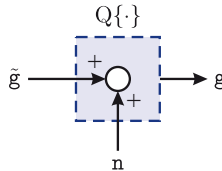


Figure 8.50. Linear model of quantization.

In the case of equidistant quantization  $Q\{\cdot\}$ , the quantization noise  $n$  is characterized by the uniform distribution (8.326), resulting in the expected value

$$\mu_n = E\{n\} = \int_{-\infty}^{\infty} \tilde{g} f_n(\tilde{g}) d\tilde{g} = \frac{1}{\Delta g} \int_{-\Delta g/2}^{\Delta g/2} \tilde{g} d\tilde{g} = 0 \tag{8.355}$$

and the variance

$$\sigma_n^2 = E\{n^2\} = \int_{-\infty}^{\infty} \tilde{g}^2 f_n(\tilde{g}) d\tilde{g} = \frac{1}{\Delta g} \int_{-\Delta g/2}^{\Delta g/2} \tilde{g}^2 d\tilde{g} = \frac{(\Delta g)^2}{12}. \tag{8.356}$$

In addition, it can be shown that if the conditions of the quantization theorem are met, the quantization noise can be described as a white noise process  $\mathbf{n}(\mathbf{x})$ , which is approximately uncorrelated with the input  $\tilde{\mathbf{g}}(\mathbf{x})$  of the quantizer [25]:

$$C_{\tilde{\mathbf{g}}\mathbf{n}}(\boldsymbol{\tau}) = E\{(\tilde{\mathbf{g}}(\mathbf{x}) - \mu_{\tilde{\mathbf{g}}}(\mathbf{x}))(\mathbf{n}(\mathbf{x} + \boldsymbol{\tau}) - \mu_{\mathbf{n}}(\mathbf{x} + \boldsymbol{\tau}))\} \quad (8.357)$$

$$= E\{\tilde{\mathbf{g}}(\mathbf{x})\mathbf{n}(\mathbf{x} + \boldsymbol{\tau})\} - \mu_{\tilde{\mathbf{g}}}(\mathbf{x})E\{\mathbf{n}(\mathbf{x} + \boldsymbol{\tau})\} \quad (8.358)$$

$$= r_{\tilde{\mathbf{g}}\mathbf{n}}(\boldsymbol{\tau}) \approx 0. \quad (8.359)$$

As the quantization noise  $\mathbf{n}(\mathbf{x})$  is broadband, in contrast to the typically band-limited input  $\tilde{\mathbf{g}}(\mathbf{x})$  of the quantizer, quantization errors can be reduced by performing a low-pass filtering [19].

## 8.7 The Karhunen–Loève transform

For solving visual inspection tasks, often vectorial image signals  $\mathbf{g}(\mathbf{x})$  and  $\mathbf{g}_{mn}$  are considered. These include RGB images, which represent the simplest case, but also multispectral images or image series are used (e.g., see Figures 5.21(a) and 8.32(a)). Here, the different channels or components of a vectorial image typically are highly correlated, and are thus redundant to a certain extent.

**Example 8.38 (Correlation between color channels):** As an example, Fig. 8.51 shows the three channels of the RGB image of Fig. 8.32(a), between which a correlation can even be visually suspected. In fact, the correlation coefficient of the red channel and the blue channel is  $\rho_{RB} = 0.955$ , the correlation coefficient of the green channel and the blue channel is  $\rho_{GB} = 0.931$ , and the correlation coefficient of the red channel and the green channel is even  $\rho_{RG} = 0.985$ . ■

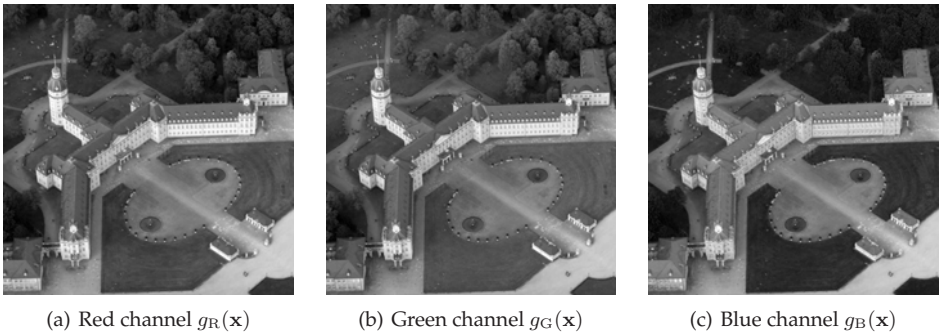


**Figure 8.51.** Color channels of the RGB image in Fig. 8.32(a) of the Karlsruhe Palace, encoded as gray values: (a) red channel  $g_R(\mathbf{x})$ ; (b) green channel  $g_G(\mathbf{x})$ ; (c) blue channel  $g_B(\mathbf{x})$  (source: ONUK).

Hence, it is quite obvious that a transformation of the image which decorrelates the single components might be sensible. This can be done by using the **Karhunen–Loève transform**, which is also known as **principal component analysis (PCA)** or the **Hotelling transform**. Because of its decorrelating properties, the Karhunen–Loève transform is often used for im-

age fusion and for image compression. For the latter purpose, after performing the transformation, the components that contribute least to the signal energy are omitted or are encoded lossily.

### ► 8.7.1 Definition of the Karhunen–Loève transform

In the context of the Karhunen–Loève transform, the vectorial image intensities are stochastically described by the random vector  $\mathbf{g}$ . The mean of the vector is given by the expected value:

$$\boldsymbol{\mu}_{\mathbf{g}} = \mathbb{E}\{\mathbf{g}\}. \quad (8.360)$$

The **covariance matrix** of  $\mathbf{g}$  is defined as follows:

$$\mathbf{C}_{\mathbf{g}\mathbf{g}} = \mathbb{E}\{(\mathbf{g} - \boldsymbol{\mu}_{\mathbf{g}})(\mathbf{g} - \boldsymbol{\mu}_{\mathbf{g}})^{\text{T}}\}. \quad (8.361)$$

#### 8.30

#### Definition 8.30: The Karhunen–Loève transform

The Karhunen–Loève transform is the linear transformation

$$\mathbf{k} = \mathcal{K}\{\mathbf{g}\} = \mathbf{A}(\mathbf{g} - \boldsymbol{\mu}_{\mathbf{g}}) \quad (8.362)$$

of the vector  $\mathbf{g}$  which is centered to the mean  $\boldsymbol{\mu}_{\mathbf{g}}$ , and will from now on be denoted by the operator  $\mathcal{K}\{\cdot\}$ . Here,  $\mathbf{A}$  is a matrix which contains the eigenvectors  $\mathbf{e}_i$ ,  $i = 1, \dots, Q$  of the covariance matrix  $\mathbf{C}_{\mathbf{g}\mathbf{g}}$  as row vectors. The eigenvectors are aligned in decreasing order of their corresponding eigenvalues  $\lambda_i \geq \lambda_{i+1}$  of the covariance matrix  $\mathbf{C}_{\mathbf{g}\mathbf{g}}$ :

$$\mathbf{A} = (\mathbf{e}_1, \dots, \mathbf{e}_i, \dots, \mathbf{e}_Q)^{\text{T}}. \quad (8.363)$$

◇

As the covariance matrix of a real-valued random vector  $\mathbf{g} \in \mathbb{R}^Q$  has to be real-valued, symmetric, and positive semidefinite by definition, all of its eigenvalues are nonnegative  $\lambda_i \geq 0$ . For the image signals that occur in practice,  $\lambda_i > 0$ , especially because of the noise which is always present. Usually, the eigenvalues are distinct.

The following procedure is used for a practical implementation of the Karhunen–Loève transform:

1. Estimate the mean vector  $\boldsymbol{\mu}_{\mathbf{g}}$  and the covariance matrix  $\mathbf{C}_{\mathbf{g}\mathbf{g}}$ , if applicable by spatial averaging and by assuming an ergodic process  $\mathbf{g}_{mn}$ :

$$\hat{\boldsymbol{\mu}}_{\mathbf{g}} = \frac{1}{MN} \sum_{m=0}^{M-1} \sum_{n=0}^{N-1} \mathbf{g}_{mn}, \quad (8.364)$$

$$\hat{\mathbf{C}}_{\mathbf{g}\mathbf{g}} = \frac{1}{MN-1} \sum_{m=0}^{M-1} \sum_{n=0}^{N-1} (\mathbf{g}_{mn} - \hat{\boldsymbol{\mu}}_{\mathbf{g}})(\mathbf{g}_{mn} - \hat{\boldsymbol{\mu}}_{\mathbf{g}})^{\text{T}}; \quad (8.365)$$

2. Solve the eigenvalue problem and sort the eigenvectors  $\mathbf{e}_i$  of  $\hat{\mathbf{C}}_{\mathbf{g}\mathbf{g}}$  in descending order of their eigenvalues  $\lambda_i$ , in order to obtain the transformation matrix  $\mathbf{A}$  as in (8.363);
3. Perform the transformation employing (8.362).

In contrast to the DFT (Sec. 8.3.3) or the wavelet transform (Sec. 15.2), for example, there is no fast algorithm for calculating the Karhunen–Loève transform, which is a drawback. Furthermore, the Karhunen–Loève transform is not separable. However, it is a transformation that is adapted to the signal, as the transformation matrix  $\mathbf{A}$  and therefore also the basis vectors  $\mathbf{e}_i$  used for representing the signal are calculated from the signal itself.

### 8.7.2 Properties of the Karhunen–Loève transform

---

#### Theorem 8.20: Linearity

8.20

The Karhunen–Loève transform (8.362) is a linear signal transformation. As in (8.2),

$$\mathcal{K}\{a \mathbf{g}_1 + b \mathbf{g}_2\} = a \cdot \mathcal{K}\{\mathbf{g}_1\} + b \cdot \mathcal{K}\{\mathbf{g}_2\} \quad (8.366)$$

for arbitrary constants  $a$  and  $b$ . ◇

---

#### Theorem 8.21: Orthogonality

8.21

The Karhunen–Loève transform (8.362) is an orthogonal signal transformation. Hence,

$$\mathbf{A}^{-1} = \mathbf{A}^T. \quad (8.367)$$

This is because the transformation matrix  $\mathbf{A}$  is constructed from the eigenvectors  $\mathbf{e}_i$  of the covariance matrix  $\mathbf{C}_{\mathbf{g}\mathbf{g}}$ , and because the eigenvectors of a symmetric, real-valued matrix  $\mathbf{C}_{\mathbf{g}\mathbf{g}}$  are always an orthogonal basis [7]. ◇

---

#### Theorem 8.22: Invertibility

8.22

The invertibility of the Karhunen–Loève transform

$$\mathbf{g} = \mathcal{K}^{-1}\{\mathbf{k}\} = \mathbf{A}^T \mathbf{k} + \boldsymbol{\mu}_{\mathbf{g}} \quad (8.368)$$

is an immediate result of the defining equation (8.362) in combination with (8.367). ◇

---

#### Theorem 8.23: Zero-mean

8.23

The result  $\mathbf{k}$  of the Karhunen–Loève transform (8.362) is zero-mean:

$$\mathbb{E}\{\mathbf{k}\} = \mathbb{E}\{\mathbf{A}(\mathbf{g} - \boldsymbol{\mu}_{\mathbf{g}})\} = \mathbf{A}(\mathbb{E}\{\mathbf{g}\} - \boldsymbol{\mu}_{\mathbf{g}}) = \mathbf{0}, \quad (8.369)$$

with  $\mathbf{0}$  denoting the null vector. ◇

---

#### Theorem 8.24: Uncorrelated components

8.24

The components of the vector  $\mathbf{k}$  resulting from the Karhunen–Loève transform (8.362) are

uncorrelated. Hence, the corresponding covariance matrix  $\mathbf{C}_{\mathbf{k}\mathbf{k}}$  is a diagonal matrix:

$$\mathbf{C}_{\mathbf{k}\mathbf{k}} = \mathbf{A} \mathbf{C}_{\mathbf{g}\mathbf{g}} \mathbf{A}^T \quad (8.370)$$

$$= \begin{pmatrix} \lambda_1 & & & 0 \\ & \lambda_2 & & \\ & & \ddots & \\ 0 & & & \lambda_Q \end{pmatrix}. \quad (8.371)$$

As the transformation matrix  $\mathbf{A}$  is orthogonal, by (8.367), it performs a unitary and thus energy preserving transformation of the covariance matrix  $\mathbf{C}_{\mathbf{g}\mathbf{g}}$  into the diagonal matrix  $\mathbf{C}_{\mathbf{k}\mathbf{k}}$  of its eigenvalues. Therefore, the components  $\lambda_i = \text{Var}\{\mathbf{k}_i\}$  of the covariance matrix  $\mathbf{C}_{\mathbf{k}\mathbf{k}}$  represent the signal energy, which is the contribution of the  $i$ th component of  $\mathbf{k}$  to the contrast of the vectorial image. As of

$$\mathbb{E}\{(\mathbf{k}_i - \mathbb{E}\{\mathbf{k}_i\})(\mathbf{k}_j - \mathbb{E}\{\mathbf{k}_j\})\} = \mathbb{E}\{\mathbf{k}_i \mathbf{k}_j\} = \lambda_i \delta_i^j, \quad (8.372)$$

the components of  $\mathbf{k}$  are pairwise uncorrelated.

For Gaussian processes, uncorrelated components are necessarily stochastically independent.  $\diamond$

---

**Proof 8.5 (Uncorrelated components):** By (8.369), the covariance matrix  $\mathbf{C}_{\mathbf{k}\mathbf{k}}$  of the transformed vector  $\mathbf{k}$  is

$$\mathbf{C}_{\mathbf{k}\mathbf{k}} = \mathbb{E}\{\mathbf{k} \mathbf{k}^T\} = \mathbb{E}\{\mathbf{A}(\mathbf{g} - \boldsymbol{\mu}_{\mathbf{g}})(\mathbf{g} - \boldsymbol{\mu}_{\mathbf{g}})^T \mathbf{A}^T\} \quad (8.373)$$

$$= \mathbf{A} \mathbb{E}\{(\mathbf{g} - \boldsymbol{\mu}_{\mathbf{g}})(\mathbf{g} - \boldsymbol{\mu}_{\mathbf{g}})^T\} \mathbf{A}^T = \mathbf{A} \mathbf{C}_{\mathbf{g}\mathbf{g}} \mathbf{A}^T \quad (8.374)$$

$$= \begin{pmatrix} \mathbf{e}_1^T \\ \vdots \\ \mathbf{e}_Q^T \end{pmatrix} \mathbf{C}_{\mathbf{g}\mathbf{g}} (\mathbf{e}_1, \dots, \mathbf{e}_Q) \quad (8.375)$$

$$= \begin{pmatrix} \mathbf{e}_1^T \\ \vdots \\ \mathbf{e}_Q^T \end{pmatrix} (\mathbf{C}_{\mathbf{g}\mathbf{g}} \mathbf{e}_1, \dots, \mathbf{C}_{\mathbf{g}\mathbf{g}} \mathbf{e}_Q) \quad (8.376)$$

$$= \begin{pmatrix} \mathbf{e}_1^T \\ \vdots \\ \mathbf{e}_Q^T \end{pmatrix} (\lambda_1 \mathbf{e}_1, \dots, \lambda_Q \mathbf{e}_Q) \quad (8.377)$$

$$= \begin{pmatrix} \lambda_1 \mathbf{e}_1^T \mathbf{e}_1 & \lambda_2 \mathbf{e}_1^T \mathbf{e}_2 & & \\ \lambda_1 \mathbf{e}_2^T \mathbf{e}_1 & \ddots & & \\ & & \ddots & \\ & & & \lambda_Q \mathbf{e}_Q^T \mathbf{e}_Q \end{pmatrix} = \begin{pmatrix} \lambda_1 & & & 0 \\ & \ddots & & \\ 0 & & & \lambda_Q \end{pmatrix}. \quad (8.378)$$

Hence, the eigenvector matrix  $\mathbf{A}$  results in a diagonalization of the covariance matrix  $\mathbf{C}_{\mathbf{g}\mathbf{g}}$ .  $\blacksquare$

**Theorem 8.25: Best linear approximation**

By using the Karhunen–Loève transform, a given random vector  $\mathbf{g}$  of dimension  $Q$  can be optimally approximated by a vector  $\hat{\mathbf{g}}$  of dimension  $\nu < Q$ , in the sense of the mean squared error. In accordance with (8.368), the vector  $\mathbf{g}$  is therefore represented by a series:

$$\mathbf{g} = \mathbf{A}^T \mathbf{k} + \boldsymbol{\mu}_{\mathbf{g}} = \sum_{i=1}^Q \mathbf{e}_i k_i + \boldsymbol{\mu}_{\mathbf{g}}. \quad (8.379)$$

Using the first  $\nu < Q$  terms of the series results in the following estimate of the vector  $\mathbf{g}$ :

$$\hat{\mathbf{g}} = \sum_{i=1}^{\nu} \mathbf{e}_i k_i + \boldsymbol{\mu}_{\mathbf{g}}. \quad (8.380)$$

In this case, the mean energy

$$\mathbb{E}\{\Delta \mathbf{g}^T \Delta \mathbf{g}\} = \sum_{i=\nu+1}^Q \lambda_i \quad (8.381)$$

of the approximation error

$$\Delta \mathbf{g} := \mathbf{g} - \hat{\mathbf{g}} \quad (8.382)$$

is minimal.  $\diamond$

Because of its property of minimizing the energy (8.381) of the representation error, the Karhunen–Loève transform performs an optimal signal compression. By scaling the eigenvalues  $\lambda_i$ , they can be formally interpreted as probabilities

$$\xi_i := \frac{\mathbb{E}\{k_i^2\}}{\sum_{i=1}^Q \mathbb{E}\{k_i^2\}} = \frac{\lambda_i}{\sum_{i=1}^Q \lambda_i} \quad (8.383)$$

resulting in a minimal **entropy**

$$H = - \sum_{i=1}^Q \xi_i \text{ld } \xi_i. \quad (8.384)$$

As the entropy of the variances  $\lambda_i$  is minimal, the Karhunen–Loève transform concentrates the signal energy and, to a certain extent, also the information, into only a few components.

**Proof 8.6 (Best linear approximation):** Let  $\mathbf{e}$  be an arbitrary vector with  $\|\mathbf{e}\| = 1$  and let  $\mathbf{k} = \mathbf{g}^T \mathbf{e}$  be the projection of  $\mathbf{g}$  to  $\mathbf{e}$ . As it is part of the Karhunen–Loève transform, to subtract the mean vector  $\boldsymbol{\mu}_{\mathbf{g}}$  before the projection, the vector  $\mathbf{g}$  is assumed to be zero-mean for this proof. Therefore, the expected value of  $\mathbf{k}$  is

$$\mathbb{E}\{\mathbf{k}\} = \mathbb{E}\{\mathbf{g}^T \mathbf{e}\} = \mathbb{E}\{\mathbf{g}^T\} \mathbf{e} = 0. \quad (8.385)$$

The variance of  $\mathbf{k}$  is

$$\text{Var}\{\mathbf{k}\} = E\{(\mathbf{k} - E\{\mathbf{k}\})^2\} = E\{\mathbf{k}^2\} \quad (8.386)$$

$$= E\{\mathbf{g}^T \mathbf{e} \cdot \mathbf{g}^T \mathbf{e}\} = E\{\mathbf{e}^T \mathbf{g} \mathbf{g}^T \mathbf{e}\} \quad (8.387)$$

$$= \mathbf{e}^T E\{\mathbf{g} \mathbf{g}^T\} \mathbf{e} = \mathbf{e}^T \mathbf{C}_{\mathbf{g}\mathbf{g}} \mathbf{e}. \quad (8.388)$$

Now, the vector  $\mathbf{e}$  that maximizes the variance of  $\mathbf{k}$  has to be determined. Obviously, the term (8.388) is maximal if the vectors  $\mathbf{e}$  and  $\mathbf{C}_{\mathbf{g}\mathbf{g}} \mathbf{e}$  are linearly dependent (i.e., parallel), hence if

$$\lambda \mathbf{e} = \mathbf{C}_{\mathbf{g}\mathbf{g}} \mathbf{e}. \quad (8.389)$$

This equation holds if and only if  $\mathbf{e}$  is an eigenvector of the covariance matrix  $\mathbf{C}_{\mathbf{g}\mathbf{g}}$ , which maps the vector  $\mathbf{e}$  to a multiple  $\lambda \mathbf{e}$  of itself [10]. The maximum possible variance of  $\mathbf{k}$  results from the greatest eigenvalue  $\lambda$ :

$$\lambda = \mathbf{e}^T \mathbf{C}_{\mathbf{g}\mathbf{g}} \mathbf{e}. \quad (8.390)$$

After one has found the projection vector  $\mathbf{e}$  that corresponds to a transformed component  $\mathbf{k}$  with maximum variance, the dimension spanned by  $\mathbf{e}$  is separated,

$$\mathbf{g}' = \mathbf{g} - \mathbf{e} \mathbf{e}^T \mathbf{g}, \quad (8.391)$$

and the procedure is iteratively applied to  $\mathbf{g}'$ . The result after  $Q$  iterations is a set of variances

$$\lambda_1 \geq \lambda_2 \geq \dots \geq \lambda_Q. \quad (8.392)$$

Here, of all the projections in the  $i$ th iteration,  $\lambda_i$  yielded the maximum value. In total, the mean energy (8.381) of the representation error is therefore minimal. ■

### ► 8.7.3 Examples of application of the Karhunen–Loève transform

**Example 8.39 (Decorrelation of color channels):** This example shows how the channels of the RGB image of Fig. 8.32(a) can be decorrelated by the Karhunen–Loève transform. The three components of the Karhunen–Loève transform are shown in Fig. 8.52. The distribution of the eigenvalues  $\lambda_i$  shows that the first component conveys about 97.1 % of the signal energy; in contrast, the contribution of the last component is only about 0.4 % of the signal energy. Hence in this case, in order to compress the image, the last component can be omitted, as no quality drawbacks have to be expected, which will be shown in the following example. ■

**Example 8.40 (Color compression):** For seeing the quality of the color compression, the first  $\nu$  ( $\nu \in \{1, 2, 3\}$ ) components of the Karhunen–Loève transform have been used to reconstruct RGB images (Fig. 8.53). For  $\nu = 1$ , the color space of the resulting image is one-dimensional, which is why the reconstruction Fig. 8.53(a) corresponds to the first



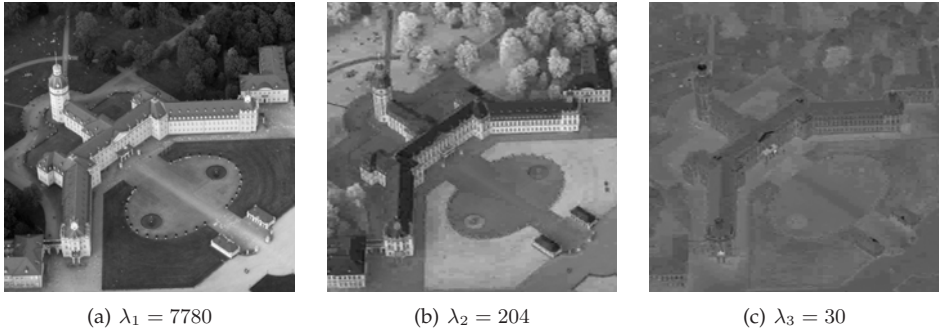


Figure 8.52. Components of the Karhunen–Loève transform of the RGB image Fig. 8.32(a) with the eigenvalues  $\lambda_i$  (original image: ONUK).

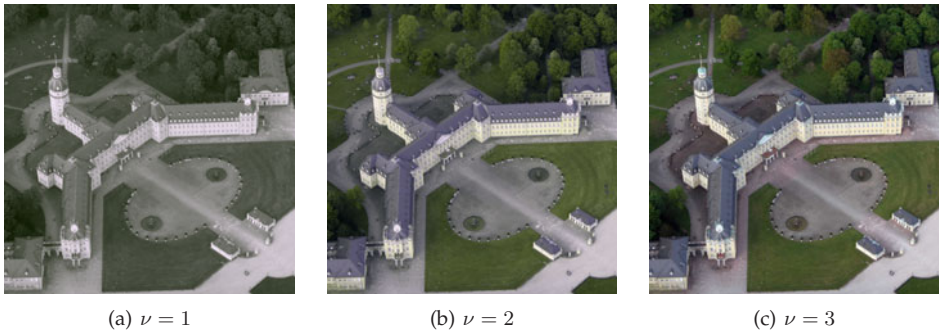


Figure 8.53. Reconstruction of the RGB color image Fig. 8.32(a) by using only the first  $\nu$  components of the Karhunen–Loève transform (original image: ONUK).

component Fig. 8.52(a) of the Karhunen–Loève transform, except for the dominant hue of the original image. The use of two components ( $\nu = 2$ ) already yields a high-quality reconstruction of the original, see Fig. 8.53(b). Only reddish regions of the original (red-brown leaves of single trees, the porch roof, and the terrace of the palace), as well as the cyan colored dome of the tower are not rendered in their true colors by this reconstruction. In the case of a reconstruction based on all  $\nu = 3$  components (Fig. 8.53(c)), there is no difference from the original because of the invertibility of the Karhunen–Loève transform. ■

**Example 8.41 (Color compression for weakly correlated channels):** Now, the color compression resulting from the Karhunen–Loève transform will be discussed for an example with weakly correlated color channels, see Fig. 8.54. Here, the correlation coefficient of the red channel and the green channel is  $\rho_{RG} = 0.585$ , the correlation coefficient of the green channel and the blue channel is  $\rho_{GB} = 0.700$ , and the correlation coefficient of the red channel and the blue channel is  $\rho_{RB} = 0.318$ . In this case, the reconstruction of the color image by using fewer than  $\nu = 3$  components obviously involves notable drawbacks concerning color rendering. ■



Figure 8.54. Reconstruction of an RGB color image by using  $\nu$  components of the Karhunen–Loève transform.

**Example 8.42 (Decorrelation of multispectral images):** For this example, the multispectral image series of Fig. 5.21 is used. Multispectral images typically have high correlation coefficients for spectrally adjacent channels. For the present case, the correlation coefficients of the spectral channels are all inside the interval of  $0.548 \leq \rho \leq 0.997$ . Hence, after performing a Karhunen–Loève transform, 99.5% of the signal energy can be represented by the first three components Fig. 8.55(a)–(c). This circumstance can be used for compression or for image fusion: from nine to three channels, as is shown in the following example. ■

**Example 8.43 (Fusion of multispectral images):** In order to perform an image fusion of multispectral images, the components of the Karhunen–Loève transform of Example 8.42 will be used, see Fig. 8.55. As already the first three components Fig. 8.55(a)–(c) represent 99.5% of the signal energy, it is natural to fuse these three components by interpreting them as a color image with three channels. For color rendering, different color spaces can be used (Sec. 5.2): the images resulting from the fusion are so-called **pseudo-color images** (cf. Sec. 9.1.3). Especially in the pseudo-color image Fig. 8.56(b), for which the first three KLT components were interpreted as an HSV color image, the material of the robot can be distinguished from the wooden block and from the background, which was not possible in the original color image Fig. 5.21(a). ■

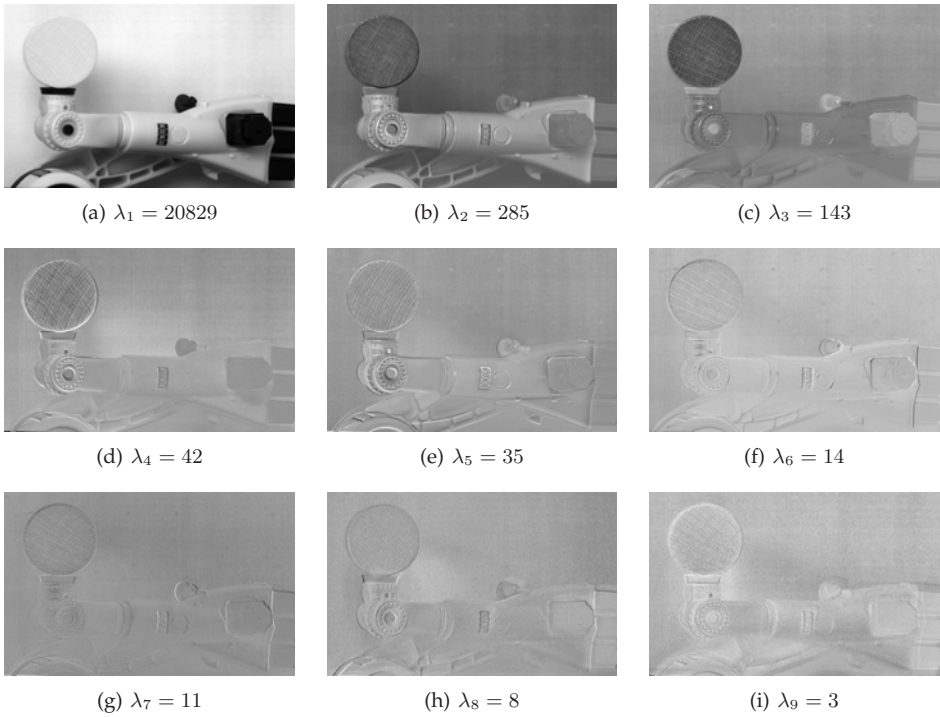


Figure 8.55. Components of the Karhunen–Loève transform with eigenvalues  $\lambda_i$ .

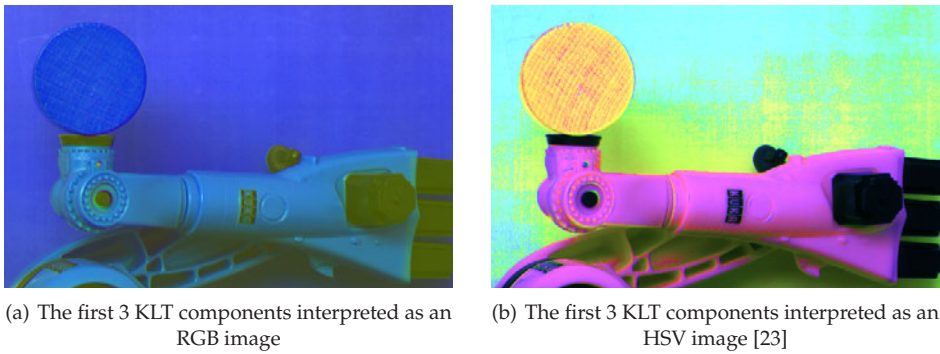


Figure 8.56. Encoding of the three components with the greatest eigenvalues of the Karhunen–Loève transform (KLT) as channels of a color image.

## 8.8 Bibliography

- [1] Richard Bamler. *Mehrdimensionale lineare Systeme*. Springer, 1989.
- [2] Jürgen Beyerer. *Analyse von Riefentexturen*. PhD thesis, Universität Karlsruhe (TH), 1994.
- [3] Ronald Bracewell. *The Fourier transform and its applications*. McGraw-Hill, 3rd edition, 2000.
- [4] Elbert Oran Brigham. *The fast Fourier transform and its applications*. Prentice Hall, 1988.
- [5] Ilja Bronshtein, Konstantin Semendyayev, Gerhard Musiol, and Heiner Mühlig. *Handbook of Mathematics*. Springer, 6th edition, 2015.
- [6] Ward Cheney. *Analysis for applied mathematics*. Springer, 2001.
- [7] Ole Christensen. *Frames and Bases – An Introductory Course*. Birkhäuser, 2008.
- [8] James Cooley and John Tukey. An algorithm for the machine calculation of complex Fourier series. *Mathematics of Computation*, 19(90):297–301, 1965.
- [9] Eberhard Hänsler. *Statistische Signale: Grundlagen und Anwendungen*. Springer, 3rd edition, 2001.
- [10] Harro Heuser. *Funktionalanalysis – Theorie und Anwendung*. Teubner, 4th edition, 2006.
- [11] Harro Heuser. *Lehrbuch der Analysis*, volume 2. Vieweg+Teubner, 14th edition, 2008.
- [12] Bernd Jähne. *Digital image processing*. Springer, 6th edition, 2005.
- [13] Karl-Dirk Kammeyer and Kristian Kroschel. *Digitale Signalverarbeitung – Filterung und Spektralanalyse*. Vieweg+Teubner, 7th edition, 2009.
- [14] Uwe Kiencke, Michael Schwarz, and Thomas Weickert. *Signalverarbeitung – Zeit-Frequenz-Analyse und Schätzverfahren*. Oldenbourg, 2008.
- [15] Robert Lalla. *Verfahren zur Auswertung von Moiréaufnahmen technischer Oberflächen*. PhD thesis, Universität Karlsruhe (TH), 1993.
- [16] Alan Oppenheim and Ronald Schaffer. *Discrete-time signal processing*. Pearson, 3rd edition, 2010.
- [17] Athanasios Papoulis and Unnikrishna Pillai. *Probability, random variables and stochastic processes*. McGraw-Hill, 4th edition, 2002.
- [18] Fernando Puente León and Holger Jäkel. *Signale und Systeme*. De Gruyter Oldenbourg, Berlin, 6th edition, 2015.
- [19] Fernando Puente León and Uwe Kiencke. *Messtechnik – Systemtheorie für Ingenieure und Informatiker*. Springer, 9th edition, 2012.
- [20] Fernando Puente León and Norbert Rau. Detection of machine lead in ground sealing surfaces. *Annals of the CIRP*, 52(1):459–462, 2003.
- [21] Alan Stuart and J. Keith Ord. *Kendall's advanced theory of statistics*, volume 1, Distribution theory. Arnold, 6th edition, 2004.
- [22] Ulrich Tietze, Christoph Schenk, and Eberhard Gamm. *Halbleiter-Schaltungstechnik*. Springer, 13th edition, 2010.
- [23] Scott Tyo and Richard Olsen. PC-based display strategy for spectral imagery. In *IEEE Workshop on Advances in Techniques for Analysis of Remotely Sensed Data*, pages 276–281, 2003.
- [24] Wolfgang Walter. *Einführung in die Theorie der Distributionen*. Bibliographisches Institut, 3rd edition, 1994.
- [25] Bernard Widrow, István Kollár, and Ming-Chang Liu. Statistical theory of quantization. *IEEE Transactions on Instrumentation and Measurement*, 45(2):353–361, April 1996.
- [26] Hellmuth Wolf. *Nachrichtenübertragung: eine Einführung in die Theorie*. Springer, 2nd edition, 1987.



Chapter 9

**Preprocessing and Image Enhancement**

**9**

---

## 9 Preprocessing and Image Enhancement

9.1	Simple image enhancement methods . . . . .	467
9.1.1	Contrast adjustment by histogram stretching . . . . .	467
9.1.2	Histogram manipulation . . . . .	469
9.1.3	Pseudo-color and false-color images . . . . .	472
9.1.3.1	Pseudo-color images . . . . .	472
9.1.3.2	False-color images . . . . .	473
9.1.4	Image sharpening . . . . .	474
9.2	Reduction of systematic errors . . . . .	476
9.2.1	Geometric rectification . . . . .	476
9.2.1.1	Bilinear interpolation . . . . .	478
9.2.1.2	Interpolation in the context of system theory . . . . .	479
9.2.2	Suppression of inhomogeneities . . . . .	480
9.2.2.1	Signal model . . . . .	480
9.2.2.2	Homogeneity . . . . .	481
9.2.2.3	Homomorphic filtering . . . . .	483
9.2.2.4	Homogenization . . . . .	485
9.3	Attenuation of random disturbances . . . . .	491
9.3.1	Linear filters . . . . .	491
9.3.1.1	Low-pass filters for noise reduction . . . . .	496
9.3.1.2	Moving average filter . . . . .	497
9.3.1.3	Cone low-pass filter . . . . .	500
9.3.1.4	Gaussian low-pass filter . . . . .	500
9.3.1.5	Ideal low-pass filters . . . . .	505
9.3.1.6	Constructing high-pass filters, band-stop filters, and band-pass filters from a given low-pass filter . . . . .	506
9.3.1.7	Excursus: The Z-transform . . . . .	506
9.3.2	Noise reduction using nonlinear filters . . . . .	509
9.3.2.1	The median filter . . . . .	509
9.3.2.2	Filters based on order statistics . . . . .	513
9.3.2.3	Bilateral filters . . . . .	514
9.4	Image registration . . . . .	515
9.5	Bibliography . . . . .	518

## 9 Preprocessing and Image Enhancement

The main aims of preprocessing and image enhancement are

- to obtain visually informative images, as well as
- to ease the subsequent signal processing and automated image evaluation steps.

The rather simple image enhancement techniques, which are covered in the following section, are mainly used for improving the visual impression of an image. Section 9.2 introduces methods which can reduce the influence of systematic perturbations caused by inhomogeneous illumination or by poor image acquisition, for example. Section 9.3 is devoted to the suppression of random noise by using linear and nonlinear filters and finally, Sec. 9.4 discusses the topic of image registration.

### 9.1 Simple image enhancement methods

9.1

#### 9.1.1 Contrast adjustment by histogram stretching

Contrast adjustment by **histogram stretching** manipulates the image values in order to exploit the whole range of the available values  $[q_0, q_{K-1}]$ . This is done by a linear stretch of the probability density function (PDF)

$$f_{\mathbf{g}}(g) = \sum_{i=0}^{K-1} P_i \delta(g - q_i) \quad (9.1)$$

of the quantized image values. Here,  $P_i$  denotes the probabilities of the quantized image values  $q_i$  (cf. Fig. 8.44). In practice, the probability density function of the image values is estimated by the so-called **histogram**.

#### Definition 9.1: Histogram

9.1

The histogram of a scalar image  $g_{mn}$  is defined as follows:

$$\hat{P}_i = \frac{1}{MN} \sum_{m=0}^{M-1} \sum_{n=0}^{N-1} \delta_{g_{mn}}^{q_i}, \quad i = 0, \dots, K-1, \quad (9.2)$$

with

$$\delta_a^b := \begin{cases} 1 & \text{if } a = b \\ 0 & \text{if } a \neq b \end{cases} \quad (9.3)$$

denoting the **Kronecker delta**. ◇

Hence, the single values  $\hat{P}_i$  represent the estimated values of the discrete probabilities  $P_i$  of the image values.

Histogram stretching is done by performing the following spatially-invariant transformation of the image values:

$$\gamma(g) = (g - g_{\min}) \frac{q_{K-1} - q_0}{g_{\max} - g_{\min}} + q_0, \quad g_{\min} := \min_{m,n} g_{mn}, \quad g_{\max} := \max_{m,n} g_{mn} \quad (9.4)$$

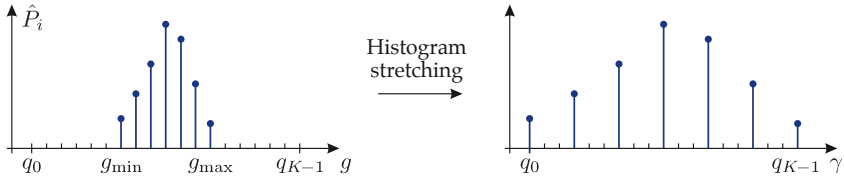


Figure 9.1. Histogram stretching.

with  $g, g_{\min}, g_{\max} \in \{q_0, \dots, q_{K-1}\}$ . The range of the transformed image values is given by  $\gamma(g_{\min}) = q_0$  and  $\gamma(g_{\max}) = q_{K-1}$  (cf. Fig. 9.1). In the context of the transformation (9.4), it has to be noted that in general

$$\gamma(g_i) \notin \{q_0, \dots, q_{K-1}\}, \tag{9.5}$$

which is why the result  $\gamma(g_i)$  of the transformation is usually rounded to the nearest  $q_j$ .

Since the mean value as well as the scatter of the distribution of the image values is changed by this transformation, the histogram stretching manipulates the first two moments of the probability density function. The shape of the probability density function and hence of the histogram remain unchanged.

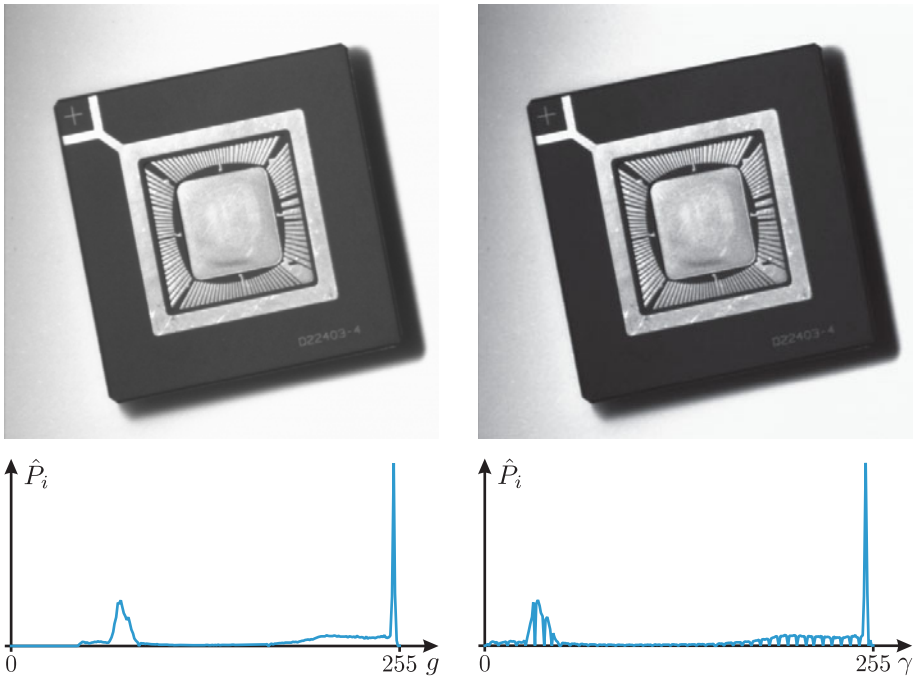


Figure 9.2. Examples of histogram stretching: (left) Original; (right) Result of the histogram stretching. The corresponding histograms are shown below.



**Example 9.1 (Histogram stretching):** As an example of histogram stretching, Fig. 9.2 shows the image of a microchip together with the result of the transformation and the corresponding histograms. Although the same number of gray values are used before and after the transformation, the resulting image appears to be much more detailed because of the higher contrast. ■

► **9.1.2 Histogram manipulation**

Usually, **histogram manipulation** is also used to achieve a contrast improvement, but in contrast to the histogram stretching, the shape of the resulting histogram has to be provided in the sense of a ‘desired histogram.’ The resulting transformation  $\mathcal{T}\{\cdot\}$  is memoryless, spatially invariant, and in general nonlinear (Fig. 9.3).

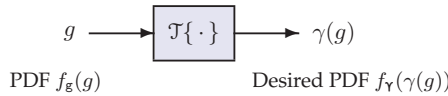


Figure 9.3. Histogram manipulation.

The probability distribution (cumulative probability) of the image values  $g$  which have to be transformed are given by

$$F_g(g) = \int_{-\infty}^g f_g(\alpha) d\alpha. \tag{9.6}$$

This represents the probability of an image value of the input quantity being  $\leq g$  (Fig. 9.4 top).

After the manipulation of the histogram, the transformed image values  $\gamma(g)$  are distributed according to the distribution function

$$F_\gamma(\gamma(g)) = \int_{-\infty}^{\gamma(g)} f_\gamma(\beta) d\beta, \tag{9.7}$$

which represents the probability of an image value of the output quantity being  $\leq \gamma(g)$  (Fig. 9.4 bottom).

Now, at first the image values  $g$  are assumed to be continuously and the cumulative distribution function  $F_\gamma(\gamma)$  is assumed to be strictly monotonically increasing. Accordingly, the following approach is chosen for determining the histogram transformation:

$$F_g(g) \stackrel{!}{=} F_\gamma(\gamma(g)) \quad \Leftrightarrow \quad \gamma(g) = F_\gamma^{-1}(F_g(g)). \tag{9.8}$$

Here, the strict monotonicity of  $F_\gamma(\gamma)$  preserves the ordering of the image values.

By (9.8), the probabilities of intervals remain unchanged by the transformation  $\mathcal{T}\{\cdot\}$ :

$$P([g_1, g_2]) = P([\gamma(g_1), \gamma(g_2)]). \tag{9.9}$$

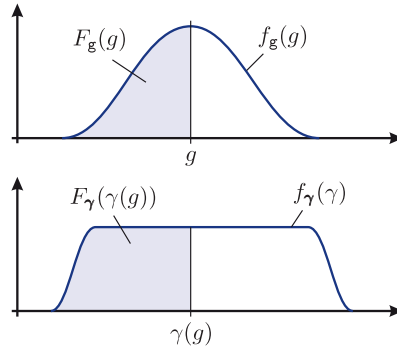


Figure 9.4. Probability density distributions before and after the histogram manipulation.

**Example 9.2 (Histogram equalization):** Histogram equalization is used to obtain an image with uniformly distributed image values. The input image values are to be transformed so that their probability density function  $f_g(g)$  matches the desired probability density function

$$f_\gamma(\gamma) = c \cdot (H(\gamma - \gamma_{\min}) - H(\gamma - \gamma_{\max})), \tag{9.10}$$

with  $H(\gamma)$  denoting the Heaviside function (8.18). By (9.8), the corresponding cumulative distribution functions are related as follows:

$$F_\gamma(\gamma(g)) = \int_{-\infty}^{\gamma(g)} f_\gamma(\beta) d\beta = c \cdot (\gamma(g) - \gamma_{\min}) \tag{9.11}$$

$$\stackrel{!}{=} F_g(g) \quad \text{if} \quad \gamma \in [\gamma_{\min}, \gamma_{\max}] \tag{9.12}$$

$$\Rightarrow \gamma(g) = c^{-1} \cdot F_g(g) + \gamma_{\min}. \tag{9.13}$$

Figure 9.5 illustrates the process of histogram equalization.

Figure 9.6 shows two examples of histogram equalization. The histogram of the orig-

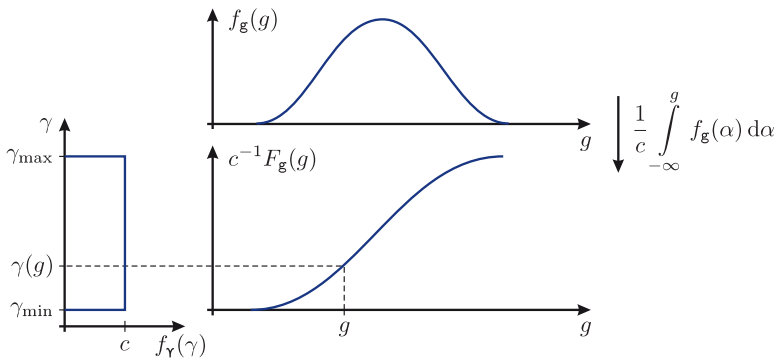


Figure 9.5. Histogram equalization.

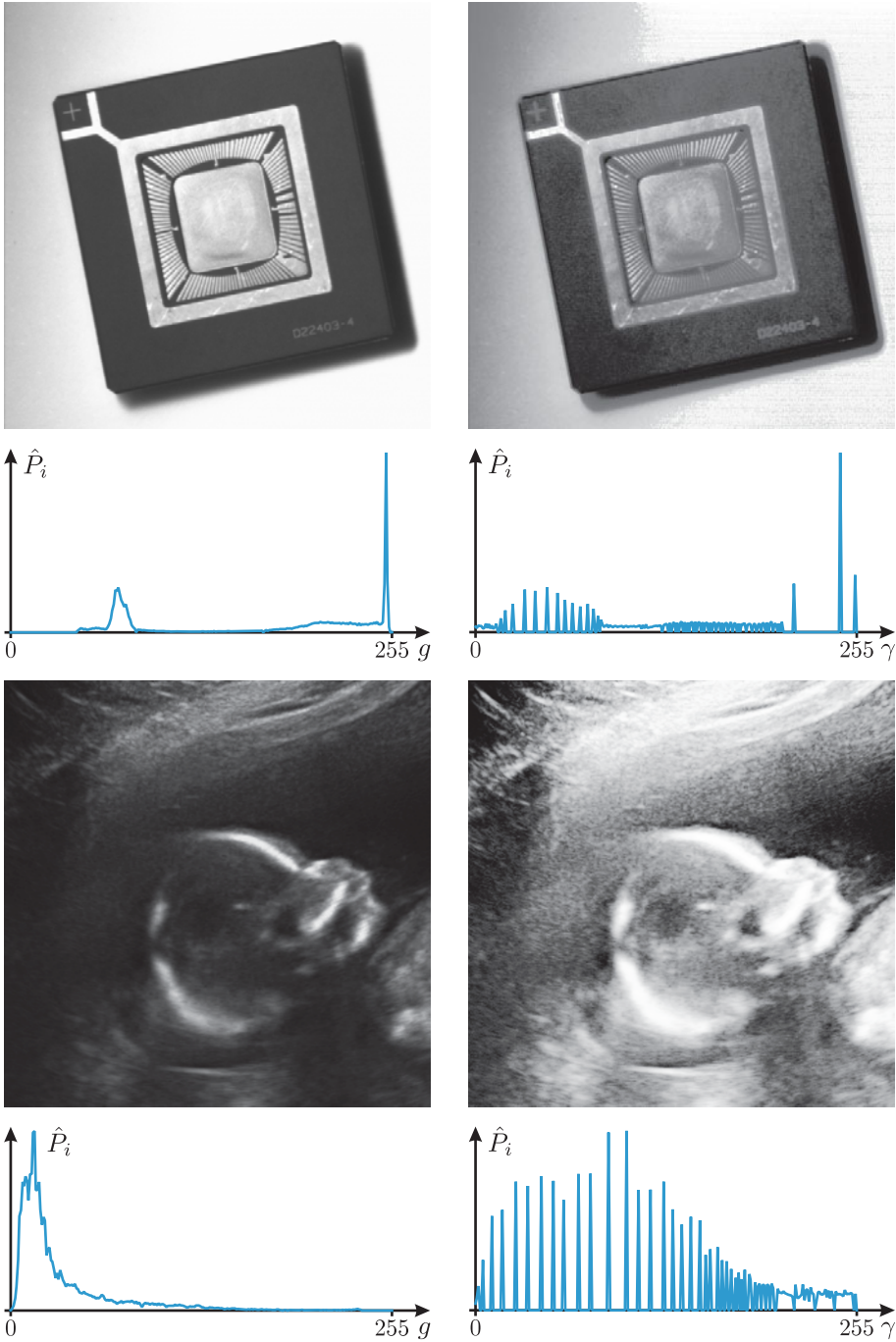


Figure 9.6. An application of histogram equalization: (left) Originals; (right) Results of the histogram equalization. The corresponding histograms are shown below.

inal image of a chip, which is shown in the top left corner, has two distinctive modes, which are 'merged' by the histogram equalization. The resulting image is not visually satisfying.

The histogram of the sonogram, which is shown in Fig. 9.6 (bottom), has a unimodal distribution concentrated on dark gray values. In contrast to the previous example, the histogram equalization of this image reveals new details, especially in the dark image regions.

Because the image values are discrete, the resulting histograms do not appear to be uniformly distributed. In fact, not the probability densities (and the corresponding histograms) are present in (9.8), but their corresponding cumulative distribution functions. ■

By using an arbitrary target histogram for a histogram manipulation, the transformation  $F_{\gamma}^{-1}(\cdot)$  in accordance with (9.8) cannot generally be calculated explicitly. An approach for computationally solving this problem is to choose an assignment of discrete image values  $\gamma(g) = q_i$  which minimizes  $|F_{\gamma}(q_i) - \hat{F}_{\mathbf{g}}(g)|$ .

### ➤ 9.1.3 Pseudo-color and false-color images

In order to obtain visually revealing images, pseudo-color and false-color representations can be used. This is particularly advantageous, as the human eye can distinguish considerably more color values than gray values.

#### ⊙ 9.1.3.1 Pseudo-color images

Pseudo-color images are produced from scalar-valued images  $g(\mathbf{x})$  (typically gray-scale images) by performing a transformation such as

$$g \mapsto \begin{pmatrix} \text{Red}(g) \\ \text{Green}(g) \\ \text{Blue}(g) \end{pmatrix} \quad (9.14)$$

of the image values. In general, the transformation characteristics for the single color channels are nonlinear. As the transformation is independent of the position  $\mathbf{x}$ , it is memoryless and spatially invariant.

---

**Example 9.3 (Pseudo-color image):** This is an example of the image value transformation for producing a pseudo-color image that uses an additive mixture (employing (9.14)) of the three color components  $\text{Red}(g)$ ,  $\text{Green}(g)$  and  $\text{Blue}(g)$  shown in Fig. 9.7. In particular, this representation solves the problem of the relative perception of intensities (cf. Fig. 1.1), as they are transformed into absolutely distinguishable hues.

Figure 9.8 shows an example of a pseudo-color representation according to Fig. 9.7. Although some details are visible less clearly in the resulting color image than in the original image, this representation allows a much better interpretation of the absolute intensities. ■

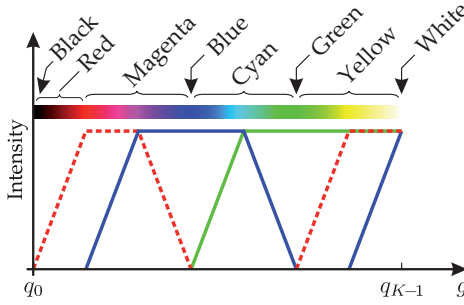


Figure 9.7. Image value transformation for creating pseudo-color images.

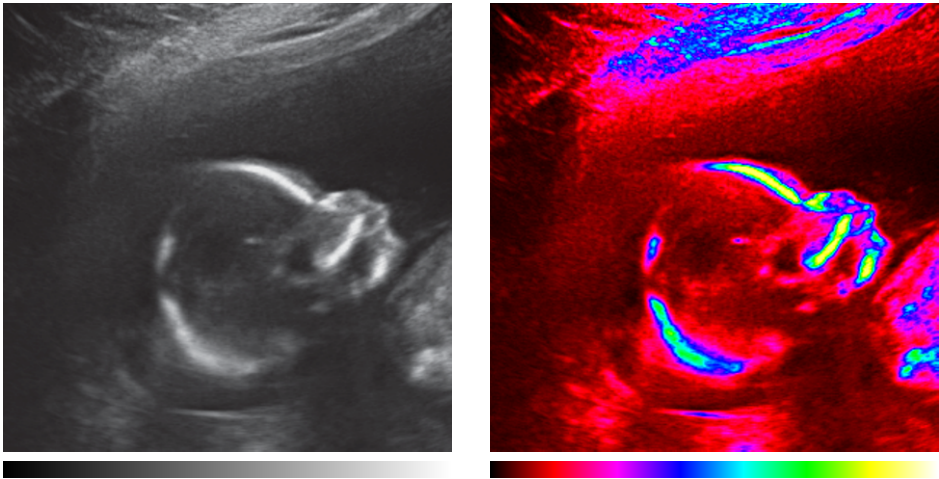


Figure 9.8. A pseudo-color representation: (left) Gray-scale image; (right) Pseudo-color image according to Fig. 9.7.

9.1.3.2 False-color images

In contrast to the creation of pseudo-color images, false-color images result from multi-channel (i.e., vectorial) images  $g(x)$ . The multi-spectral image series shown in Fig. 5.21 is considered as an example. For producing false-color images, the vectorial image values are transformed according to

$$g \in \mathbb{R}^Q \mapsto \begin{pmatrix} \text{Red}(g) \\ \text{Green}(g) \\ \text{Blue}(g) \end{pmatrix}. \tag{9.15}$$

So in general, this is as well a nonlinear, memoryless and spatially-invariant transformation.

False-color images were already presented by the Examples 7.4 and 8.43 on pages 252, respectively, 463, in the context of the fusion of multispectral images.

**Example 9.4 (Change detection):** Figure 9.9 shows another application of false-color images.

Changes affecting two subsequent observations of a scene, which were obtained at the

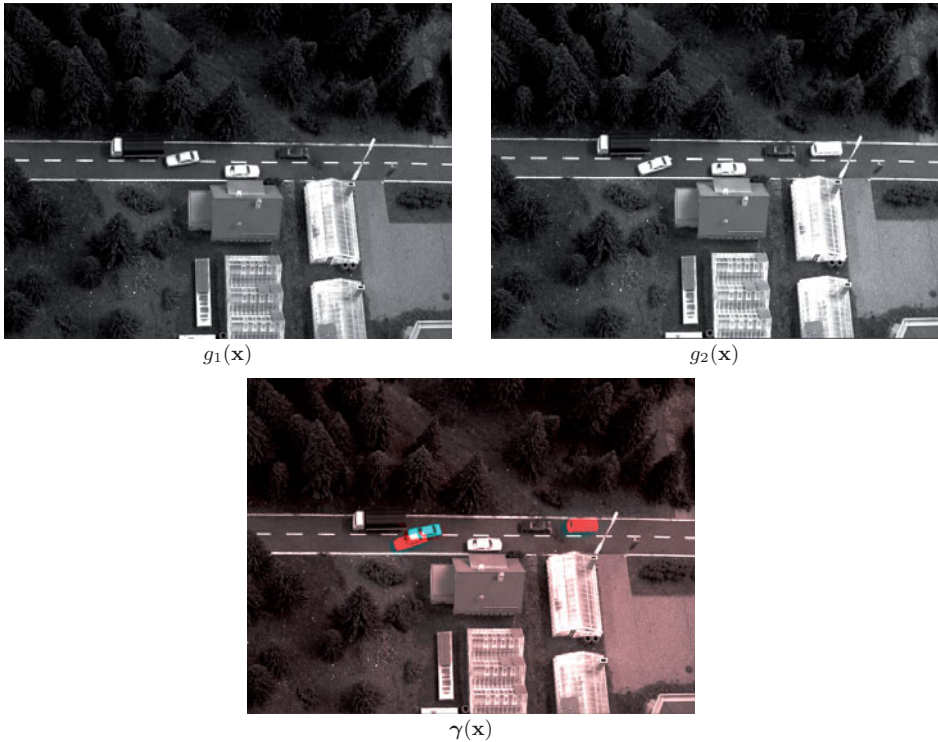


**Figure 9.9.** False-color representation for change detection: (top) Gray-scale images  $g_1(\mathbf{x})$  and  $g_2(\mathbf{x})$  corresponding to two different points in time; (bottom) False-color image  $\gamma(\mathbf{x})$  (the blue channel and the green channel correspond to  $g_1(\mathbf{x})$ ; the red channel corresponds to  $g_2(\mathbf{x})$ ).

times  $t_1$  and  $t_2$  ( $t_2 > t_1$ ), are to be detected. The corresponding gray-scale images are denoted by  $g_1(\mathbf{x})$  and  $g_2(\mathbf{x})$ . In order to highlight these changes in a false-color image, the RGB color channels can be defined as follows:

$$\gamma(\mathbf{x}) = \begin{pmatrix} g_2(\mathbf{x}) \\ g_1(\mathbf{x}) \\ g_1(\mathbf{x}) \end{pmatrix} =: \begin{pmatrix} r \\ g \\ b \end{pmatrix}. \quad (9.16)$$

Changes of  $g_2(\mathbf{x})$  with respect to  $g_1(\mathbf{x})$  will now be highlighted in color in the false-color image (cf. Fig. 9.9 bottom). ■

#### ➤ 9.1.4 Image sharpening

Fine image details correspond to high spatial frequencies. Thus, by amplifying high spatial frequencies, an image can be enhanced to visually appear more sharply. However, this amplifies high-frequency noise as well. It is furthermore required that the mean image value remains unchanged by the image sharpening.

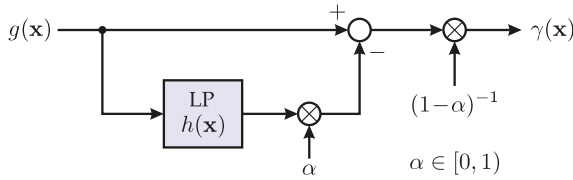


Figure 9.10. Block diagram of the image sharpening.

**Example 9.5 (Image sharpening):** Figure 9.10 shows the block diagram of a system that performs an image sharpening. First, the input image  $g(x)$  is filtered with a low-pass filter

$$h(x) \iff H(f), \quad H(0) = 1, \quad H(f) \xrightarrow{\|f\| \rightarrow \infty} 0 \tag{9.17}$$

and damped by the factor  $\alpha \in [0, 1)$ ; the result is then subtracted from the signal  $g(x)$ . Low-frequency signal components are thereby damped; high-frequency components remain unaffected. A subsequent multiplication by  $(1 - \alpha)^{-1} > 1$  ensures that the mean image value remains unchanged by the process.

Thus, the transfer function of the image sharpening procedure is

$$V(f) := \frac{\Gamma(f)}{G(f)} = \frac{1 - \alpha H(f)}{1 - \alpha} \tag{9.18}$$

with  $\Gamma(f) := \mathcal{F}\{\gamma(x)\}$  and  $G(f) := \mathcal{F}\{g(x)\}$ . For the limiting cases of  $\|f\| \rightarrow 0$  and  $\|f\| \rightarrow \infty$ , one has

$$V(0) = 1, \quad V(f) \xrightarrow{\|f\| \rightarrow \infty} \frac{1}{1 - \alpha} > 1. \tag{9.19}$$

Figure 9.11 shows an example of image sharpening. A binomial filter of size  $11 \times 11$  was used as the low-pass filter (cf. Sec. 9.3.1.1); the factor  $\alpha = 0.75$  causes an amplification of high-frequency components by a factor of 4. In the resulting image, fine details ap-

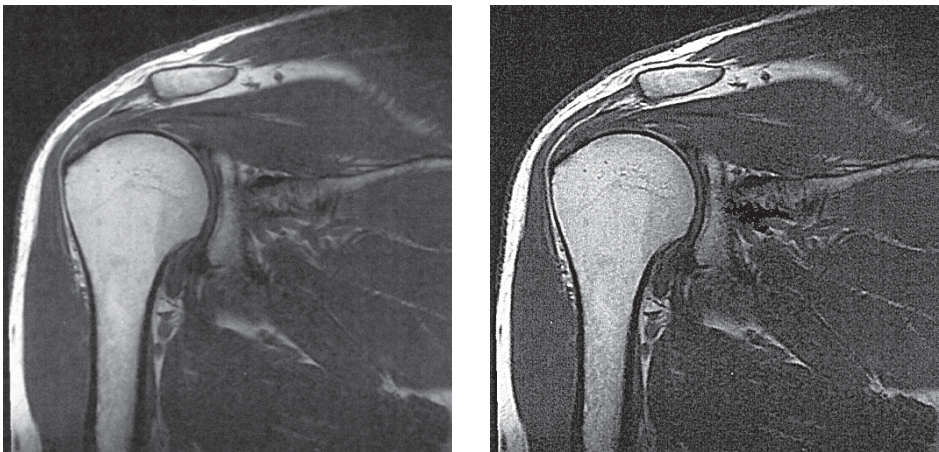


Figure 9.11. Example of image sharpening: (left) MRT image of a human shoulder; (right) result after image sharpening.

pear much more clearly than in the original images, although the information content remained the same. Additionally, any noise present in the image is amplified by the image sharpening. ■

## 9.2 Reduction of systematic errors

Often, the acquisition of images is affected by unwanted systematic errors, e.g., errors caused by the imaging optics, by inhomogeneities in the illumination, or by a spatially-dependent sensitivity of the sensor used. This section covers methods for suppressing such perturbations. These include methods for correcting geometric distortions which are discussed in Sec. 9.2.1 and methods for reducing inhomogeneities of image intensities, which are presented in Sec. 9.2.2.

### 9.2.1 Geometric rectification

In the following, a geometric distortion, which might be caused by optical aberrations (Sec. 3.4.8) or by perspective distortions (Sec. 3.4.6), will be denoted by the operator  $\mathcal{V}$ . As shown in Fig. 9.12, this operator assigns the image coordinates  $(x, y)^T$  to the lateral object coordinates  $(\tilde{x}, \tilde{y})^T$  in accordance with a generally nonlinear mapping:

$$\begin{pmatrix} x \\ y \end{pmatrix} = \mathcal{V} \left\{ \begin{pmatrix} \tilde{x} \\ \tilde{y} \end{pmatrix} \right\}. \quad (9.20)$$

If the mapping  $\mathcal{V}$  is known, a **geometric rectification** of the image  $g(x, y)$  can be performed. Suppose that  $(\xi, \eta)^T$  denotes the discrete image coordinates of the rectified image  $\gamma(\xi, \eta)$ , which are aligned in a regular pattern. Then, the image values  $g(x, y)$  of the distorted image, which are indexed by (9.20), have to be assigned to the correct position of the rectified image:  $\gamma(\xi, \eta) := g(\mathcal{V}\{(\xi, \eta)^T\})$ . Generally, however, the coordinates  $(x, y)^T = \mathcal{V}\{(\xi, \eta)^T\}$  calculated by using (9.20) are located between the grid points of the  $x, y$ -plane, which is why the image values  $g(x, y)$  located between the  $g_{mn}$  have to be interpolated.

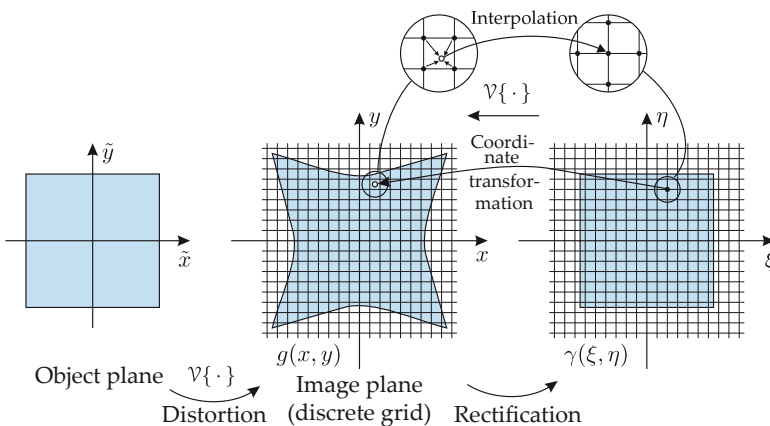


Figure 9.12. Geometric rectification.



For a perfect reconstruction of the continuous image signal  $g(x, y)$ , employing (8.194) and fulfilling the sampling condition (8.193), an ideal interpolation filter with the impulse response

$$i_{\Omega_c}(\mathbf{x}) = \text{sinc}\left(\frac{x}{\Delta x}\right) \text{sinc}\left(\frac{y}{\Delta y}\right) \tag{9.21}$$

should be used. Unfortunately, the impulse response of this filter is infinitely spread and even the implementation of an approximation would be very costly. Therefore, practically usable alternatives are needed:

- Using **nearest neighbor interpolation** (zero-order interpolation), the sampling point  $(x, y)^T$  is assigned the nearest function value of the discrete signal  $g_{mn}$ . For many cases of image interpolation, the results of this method are not satisfying.
- The **bilinear interpolation** (1st order interpolation) introduced in Sec. 9.2.1.1 is often sufficient, especially if the input signal is oversampled.
- Alternatively, higher order interpolations can be performed. In this case, often the **bicubic interpolation** is used (a third-order interpolation), which is based on cubic splines.

**Example 9.6 (Intended distortion):** In some applications, geometric transformations can be performed on purpose. An example for a practically relevant geometric distortion  $\mathcal{V}$  is the transformation from polar coordinates according to

$$\begin{pmatrix} x \\ y \end{pmatrix} = \mathcal{V} \left\{ \begin{pmatrix} r \\ \varphi \end{pmatrix} \right\} = \begin{pmatrix} r \cos \varphi \\ r \sin \varphi \end{pmatrix}; \tag{9.22}$$

see Fig. 9.13. By means of this transformation, radially arranged structures will be arranged in parallel. Information contained in concentric circles will be contained in horizontal lines after the transformation.

An example of the use of a transformation into polar coordinates is presented in the scope of the efficient calculation of the Radon transform (Sec. 14.3.1.3). Another application of this transformation is shown in the following example. ■

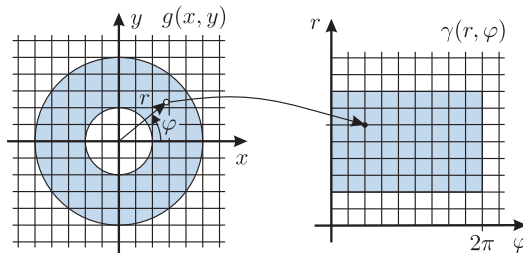


Figure 9.13. Transformation to polar coordinates as a purposive distortion  $\mathcal{V}$ .

**Example 9.7 (Detection of defects affecting brake disks):** Another example of using a purposive distortion is the inspection of the ventilation channels of brake disks of Example 1.4. The useful information in the result of the image acquisition Fig. 1.9(b) is contained in a narrow circular ring. After a transformation to polar coordinates, the information is con-

tained in lines, which allow a spatially-invariant inspection of the ventilation channels, see Fig. 1.9(c). Further details concerning the method can be found in Examples 1.4 and 7.9. ■

### 9.2.1.1 Bilinear interpolation

Bilinear interpolation approximates the function value  $\hat{g}(x, y)$  at the position  $\mathbf{x} = (x, y)^T \in \mathbb{R}^2$  by performing a linear interpolation along two dimensions. Generally,  $\mathbf{x} \notin \mathbb{Z}^2$ , see Fig. 9.14. To simplify matters, the image signal is assumed to be available for all integer (whole-number) sampling points and that the sampling width is given by

$$\Delta x = \Delta y := 1.$$

In the following, the discrete signal values of the sampling points adjacent to  $\mathbf{x}$  will be denoted by

$$g_{00} = g(\lfloor x \rfloor, \lfloor y \rfloor), \quad (9.23)$$

$$g_{01} = g(\lfloor x \rfloor, \lceil y \rceil), \quad (9.24)$$

$$g_{10} = g(\lceil x \rceil, \lfloor y \rfloor), \quad (9.25)$$

$$g_{11} = g(\lceil x \rceil, \lceil y \rceil), \quad (9.26)$$

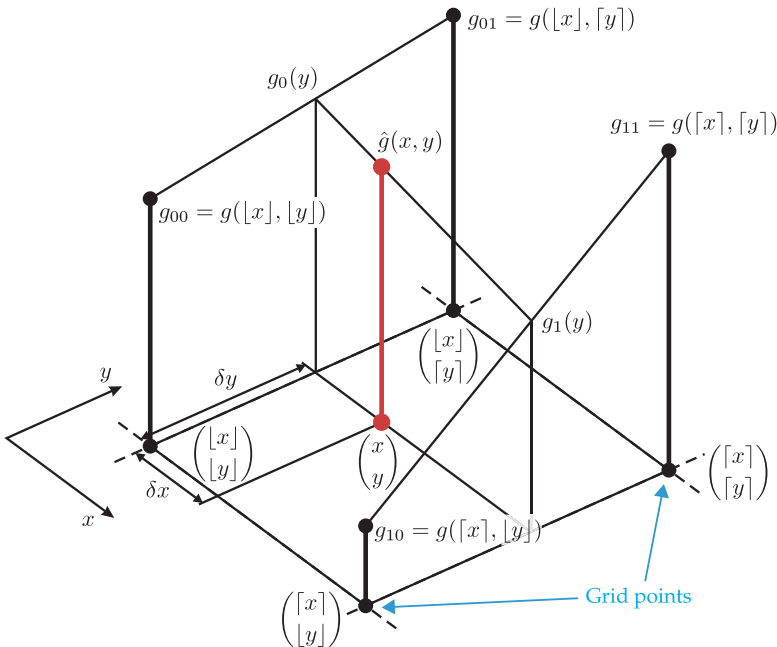


Figure 9.14. Bilinear interpolation.

with  $\lfloor x \rfloor \in \mathbb{Z}$  denoting the greatest integer which is less than or equal to  $x$  and

$$\lceil x \rceil := \lfloor x \rfloor + 1 \in \mathbb{Z} \tag{9.27}$$

denoting the smallest integer which is greater than  $x$ . Finally,

$$x = \lfloor x \rfloor + \delta x, \tag{9.28}$$

$$y = \lfloor y \rfloor + \delta y \tag{9.29}$$

provide the distances  $\delta x$  and  $\delta y$  from  $\lfloor x \rfloor$  and  $\lfloor y \rfloor$  respectively. Now, the intermediate values

$$g_0(y) = (g_{01} - g_{00}) \delta y + g_{00}, \tag{9.30}$$

$$g_1(y) = (g_{11} - g_{10}) \delta y + g_{10} \tag{9.31}$$

can be linearly interpolated in the  $y$ -direction and by a subsequent linear interpolation in the  $x$ -direction

$$\hat{g}(\mathbf{x}) = \text{Bilin}\{g(\mathbf{x})\} = (g_1(y) - g_0(y)) \delta x + g_0(y), \tag{9.32}$$

the value of the function at the position  $\mathbf{x}$  can be estimated. Here, the operator  $\text{Bilin}\{\cdot\}$  represents the bilinear interpolation. The interpolation error is given by the difference  $\hat{g}(\mathbf{x}) - g(\mathbf{x})$  between the interpolated value  $\hat{g}(\mathbf{x})$  and the actual value  $g(\mathbf{x})$ .

⊗ **9.2.1.2 Interpolation in the context of system theory**

In the case of equidistant sampling points, the function  $g_*(\mathbf{x})$  which is to be interpolated can be expressed by multiplying a continuous function  $g(\mathbf{x})$  by a two-dimensional sampling grid, in accordance with (8.190):

$$g_*(\mathbf{x}) = \sum_{m=-\infty}^{\infty} \sum_{n=-\infty}^{\infty} g(m\Delta x, n\Delta y) \delta(\mathbf{x} - m\Delta x \mathbf{e}_x - n\Delta y \mathbf{e}_y). \tag{9.33}$$

Certain interpolation methods can be expressed as a convolution of the discrete signal  $g_*(\mathbf{x})$  with a linear, shift-invariant interpolation filter with the impulse response function  $i(\mathbf{x})$ :

$$\hat{g}(\mathbf{x}) = \left[ \sum_{m=-\infty}^{\infty} \sum_{n=-\infty}^{\infty} g(m\Delta x, n\Delta y) \delta(\mathbf{x} - m\Delta x \mathbf{e}_x - n\Delta y \mathbf{e}_y) \right] ** i(\mathbf{x})$$

Ⓢ

$$\hat{G}(\mathbf{f}) = \left[ \frac{1}{\Delta x \Delta y} \sum_{k,l} G \left( \mathbf{f} - \frac{l}{\Delta x} \mathbf{e}_x - \frac{k}{\Delta y} \mathbf{e}_y \right) \right] \cdot I(\mathbf{f}). \tag{9.34}$$

The two-dimensional convolution of the sampled signal  $g_*(\mathbf{x})$  with the interpolation function  $i(\mathbf{x})$  corresponds to a multiplication in the frequency domain of the periodically repeated spectrum  $G_*(\mathbf{f})$  with the transfer function of the interpolation filter  $I(\mathbf{f})$ . If the interpolation filter  $I(\mathbf{f})$  represents a suitable low-pass filter and if the sampling condition (8.193) is met, the continuous signal can be reconstructed by the multiplication.

Table 9.1. Comparison of interpolation methods.

Interpolation	$i(\mathbf{x})$	$I(\mathbf{f})$
Nearest-neighbor	$\text{rect}\left(\frac{x}{\Delta x}\right) \text{rect}\left(\frac{y}{\Delta y}\right)$	$\Delta x \Delta y \text{sinc}(f_x \Delta x) \text{sinc}(f_y \Delta y)$
Bilinear	$\Lambda\left(\frac{x}{\Delta x}\right) \Lambda\left(\frac{y}{\Delta y}\right)$	$\Delta x \Delta y \text{sinc}^2(f_x \Delta x) \text{sinc}^2(f_y \Delta y)$
Ideal	$\text{sinc}\left(\frac{x}{\Delta x}\right) \text{sinc}\left(\frac{y}{\Delta y}\right)$	$\Delta x \Delta y \text{rect}(f_x \Delta x) \text{rect}(f_y \Delta y)$

Table 9.1 shows an overview of simple interpolation methods and their impulse response functions  $i(\mathbf{x})$  and transfer functions  $I(\mathbf{f})$ . The employed **triangular function** is defined by

$$\Lambda\left(\frac{x}{B}\right) := \text{rect}\left(\frac{x}{B}\right) * \text{rect}\left(\frac{x}{B}\right) = \begin{cases} 1 - \left|\frac{x}{B}\right| & \text{if } |x| < B \\ 0 & \text{otherwise} \end{cases}. \quad (9.35)$$

## 9.2.2 Suppression of inhomogeneities

Many common stochastic models of image signals—e.g., ‘autoregressive’ (AR), ‘moving average’ (MA), ‘autoregressive moving average’ (ARMA), and ‘Markov random field’ models (MRF) [6]—as well as methods used for analyzing textures, like ‘co-occurrence’ methods [4] or an eigenfilter [10], require homogeneous or stationary<sup>1</sup> images. In some cases, these methods can be adjusted to work for inhomogeneous or non-stationary images. However, this is accompanied by a notable increase in the computational complexity.

This section begins with an introduction of the term ‘**homogeneity** of  $m$ th degree’ [2]. Besides, methods will be introduced that allow a **homogenization** of first, second, and infinite degree. Prior to that, the common approach of **homomorphic filtering** will be discussed. And finally, the different methods will be compared by applying them to images of real surfaces and their suitability for correcting image intensities will be judged.

### 9.2.2.1 Signal model

For this section, the image  $g(\mathbf{x})$ —i.e., the measured signal—is assumed to be the result of an operation that combines the signal  $s(\mathbf{x})$  with an unwanted inhomogeneity  $b(\mathbf{x})$ . The undesired component is to be suppressed, in order to improve the signal  $s(\mathbf{x})$ , which conveys the information about a scene or a test object. The inhomogeneity  $b(\mathbf{x})$  is typically caused by, e.g., an inhomogeneous illumination or a spatially-varying sensitivity of the image acquisition system.

For the following considerations, a simple signal model is most suitable:

$$g(\mathbf{x}) = b(\mathbf{x}) \diamond s(\mathbf{x}), \quad (9.36)$$

<sup>1</sup>In this case, the term ‘homogeneity’ only refers to the 1st order statistics. In contrast, stationarity implies that the 2nd and higher order statistics are invariant with respect to the position  $\mathbf{x}$ .

with  $\diamond$  denoting an arbitrary operator. In order to achieve a **homogenization** of the image  $g(\mathbf{x})$ , the inhomogeneity  $b(\mathbf{x})$  has to be suppressed. This is only possible if there is some information about the differences between  $b(\mathbf{x})$  and  $s(\mathbf{x})$ .

As commonly the inhomogeneity  $b(\mathbf{x})$  is given by the setup of image acquisition,  $b(\mathbf{x})$  can sometimes be empirically determined: for example, see Example 9.8. Alternatively,  $b(\mathbf{x})$  is often assumed to be a signal that varies slowly with respect to the position (low-pass signal), whereas the signal  $s(\mathbf{x})$  is assumed to be a bandpass signal [3]. Then, ideally, the Fourier transforms of both components  $B(\mathbf{f}) = \mathcal{F}\{b(\mathbf{x})\}$  and  $S(\mathbf{f}) = \mathcal{F}\{s(\mathbf{x})\}$  should have disjoint supports:

$$\text{supp}\{B(\mathbf{f})\} \cap \text{supp}\{S(\mathbf{f})\} = \emptyset, \quad (9.37)$$

$$\text{supp}\{B(\mathbf{f})\} := \{\mathbf{f} \mid |B(\mathbf{f})| > 0\}. \quad (9.38)$$

Besides, for a successful suppression of  $b(\mathbf{x})$ , suitable information or a plausible assumption about the operator  $\diamond$ , which links the two components, has to be available. For the following sections, the operator  $\diamond$  is considered to be compatible with the introduced term of homogeneity on the one hand, as well as to be suitable for developing powerful homogenization methods on the other hand.

If the signal  $s(\mathbf{x})$  can be assumed to be homogeneous, it can be advantageous to homogenize the image  $g(\mathbf{x})$  in order to ease the subsequent image processing. Besides, such a homogenization usually yields an enhanced image, which might facilitate the visual interpretation of the image.

### ⊙ 9.2.2.2 Homogeneity

For the definition of the term homogeneity of  $m$ th degree, the signal  $g(\mathbf{x})$  is assumed to be the realization of a stochastic process [2].

---

#### Definition 9.2: Homogeneity of $m$ th degree

An image-generating stochastic process is called homogeneous of  $m$ th degree (or  $m$ -homogeneous, for short) if

$$\text{grad}_{\mathbf{x}} E\{g^{\nu}(\mathbf{x})\} \equiv 0 \quad \forall \nu : 1 \leq \nu \leq m, \quad \nu \in \mathbb{N}. \quad (9.39)$$

In other words, a process is called  $m$ -homogeneous if its first  $m$  moments are independent of the position  $\mathbf{x}$ .  $\diamond$

Note that this kind of homogeneity only affects the 1st order statistics. Since the 2nd and higher order statistics describe the relations between neighboring image points, they mainly characterize the geometric composition of the image and should therefore not be subject to a spatial homogenization. Homogeneity is a necessary condition for stationarity [11].

Before the homogenization of an image  $g(\mathbf{x})$  is covered, first some possible reasons for the inhomogeneities of  $g(\mathbf{x})$  resulting from the image acquisition of the test object, which is assumed to be homogeneous, will be thoroughly discussed. Possible reasons are:

1. a spatially-varying illumination of the surface,
2. the sensitivity of the image acquisition system being dependent on the  $\cos^4 \alpha$  term (cf. Sec. 4.4.1),
3. vignetting (cf. Sec. 3.4.3),

4. a spatially-varying sensitivity of the camera sensor, as well as
5. a spatially-varying geometric constellation of surface relief, illumination and imaging optics.

The inhomogeneities considered in points 1 to 4 can be described by a multiplicative signal model:

$$g(\mathbf{x}) = b(\mathbf{x}) \cdot s(\mathbf{x}). \quad (9.40)$$

In this case, the inhomogeneity  $b(\mathbf{x})$  can be suppressed by a homomorphic filtering [3] or by a division by a reference image, which is proportional to  $b(\mathbf{x})$  [16].

However, this approach is not applicable in the case no. 5. Here, the inhomogeneity cannot be described by a simple multiplicative model. Although the relief of the end-milling texture shown in Fig. 9.21(a) (page 488) is homogeneous and the illumination used for the image acquisition is spatially constant, the captured image is obviously inhomogeneous because of the surface structure, even without the influence of factors 1 to 4. This is why homogenization methods using just a multiplicative model, e.g., homomorphic filtering, yield unsatisfying results, see Fig. 9.21(b) on page 488 [2].

---

**Example 9.8 (Multiplicative model):** A multiplicative model as in (9.40) is assumed for the operator in (9.36), so that the observed signal is a multiplication of the inhomogeneity  $b(\mathbf{x})$  by the signal  $s(\mathbf{x})$ . If  $b(\mathbf{x})$  is known, the inhomogeneity can be eliminated by division:

$$s(\mathbf{x}) = \frac{g(\mathbf{x})}{b(\mathbf{x})}. \quad (9.41)$$

Therefore, the inhomogeneity  $b(\mathbf{x})$  can be determined by, e.g., acquiring a reference image of a structureless, diffusely scattering object, for which the signal  $s(\mathbf{x})$  is constant [5, 16].

However, if the inhomogeneity  $b(\mathbf{x})$  cannot be further specified, a homomorphic filtering is a possible approach for its suppression (Sec. 9.2.2.3). ■

---

**Example 9.9 (Division by a reference image):** Figure 9.15(a) shows an image of legumes, which was obtained using an inhomogeneous illumination. After removing the test objects, the

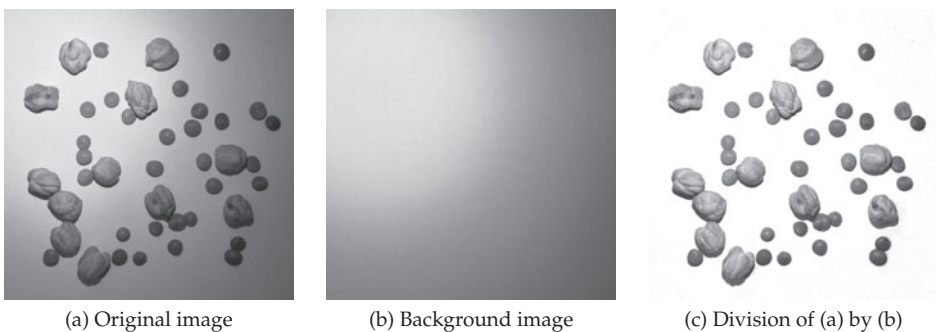


Figure 9.15. Division by a reference image.

reference image Fig. 9.15(b) was acquired, which primarily describes the spatial variation of the illumination. Dividing image (a) by image (b) yields the result shown in Fig. 9.15(c), where all objects are nearly identically illuminated. ■

9.2.2.3 Homomorphic filtering

For homomorphic filtering, a multiplicative model (9.40) is assumed for the inhomogeneity  $b(x)$  and the signal  $s(x)$ . In many practical scenarios, this assumption is physically reasonable, especially if  $b(x)$  represents an inhomogeneous illumination and  $s(x)$  is the ‘reflectance’ of the surface [16].

In order to achieve a suppression of  $b(x)$  without having further information about it,  $b(x)$  is assumed to vary slowly with respect to the position compared to  $s(x)$ . Ideally, the corresponding Fourier spectra  $B(f)$  and  $S(f)$  should have disjoint supports, as in (9.37). Finally,  $g(x)$  is required to have positive values for all  $x$ .

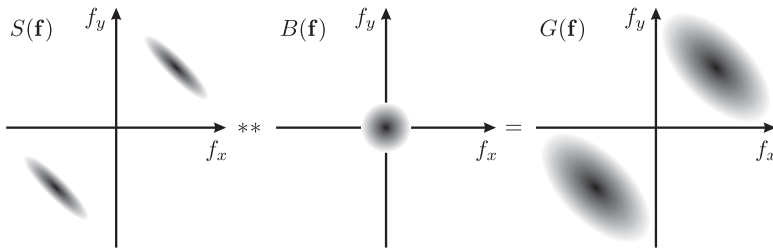


Figure 9.16. A multiplication of the signal  $s(x)$  by the inhomogeneity  $b(x)$  corresponds to a two-dimensional convolution of the respective Fourier spectra  $S(f)$  and  $B(f)$  in the spatial frequency domain.

Figure 9.16 shows an example of two spectra  $S(f)$  and  $B(f)$  of a signal and an inhomogeneity respectively, for which the assumption of disjoint supports is correct. According to the convolution property (8.49), the multiplication of  $s(x)$  and  $b(x)$  corresponds to a two-dimensional convolution of the respective spectra in the spatial frequency domain; cf. Fig. 9.16 (right). Because of the spectral convolution, the components  $S(f)$  and  $B(f)$  cannot be separated by a linear filter, as linear filters require an additive superposition of the corresponding signal components.

Therefore, first the logarithm of the input signal  $g(x)$  is taken, so that the multiplication of  $b(x)$  by  $s(x)$  is transformed into an additive superposition of their logarithms (cf. Fig. 9.17):

$$\ln g(x) = \underbrace{\ln b(x)}_{\substack{\text{spatially} \\ \text{slowly-varying}}} + \underbrace{\ln s(x)}_{\substack{\text{spatially} \\ \text{rapidly-varying}}} \quad (9.42)$$

Since the logarithm function is monotonic and smooth,  $\ln b(x)$  remains a spatially slowly-varying signal and  $\ln s(x)$  remains a spatially rapidly-varying signal, so that  $\ln b(x)$  can now

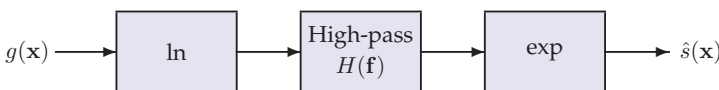


Figure 9.17. Homomorphic filtering.

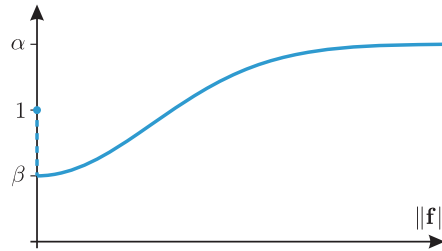


Figure 9.18. Transfer function  $H(\mathbf{f})$  of the high-pass filter (9.43) used for homomorphic filtering.

be suppressed using a linear high-pass filter  $H(\mathbf{f})$ . A transfer function which is often used for this purpose is

$$H(\mathbf{f}) = \begin{cases} 1 & \text{if } \mathbf{f} = \mathbf{0} \\ \alpha - (\alpha - \beta) \exp\left(-\frac{\|\mathbf{f}\|^2}{\rho^2}\right) & \text{otherwise} \end{cases} \quad (9.43)$$

with  $\alpha > \beta$ ; a section through the rotationally symmetric function  $H(\mathbf{f})$  is shown in Fig. 9.18. After the high-pass filtering, the effects of taking logarithms are reversed by applying the exponential function (Fig. 9.17).

**Example 9.10 (Suppression of illumination inhomogeneities by homomorphic filtering):** Figure 9.19 shows an example of homomorphic filtering. As a part of the scene visible in the left image is covered by shadows, only very few details are present. By performing a homomorphic filtering, these regions can be brightened and the visibility of image structures can be increased. However, simultaneously, the brightness of the snow mountain in the background is notably dampened, so that it appears gray in the result. Also the colors



(a) Original image



(b) Homomorphic filtering

Figure 9.19. Homomorphic filtering; (a) Original RGB image; (b) Result of the homomorphic filtering ( $\alpha = 1$ ;  $\beta = 0$ ;  $\rho = 4$ ), which has been separately applied to each channel.



of the resulting image are rather weak. The homomorphic filtering has been separately applied to each color channel. ■

#### ⊙ 9.2.2.4 Homogenization

This section covers methods that allow a homogenization of an image  $g(\mathbf{x})$ . First, a set  $\mathcal{U}$  will be defined that describes a neighborhood of the  $x, y$ -origin of the image coordinate system. This neighborhood is to be chosen sufficiently small, so that the inhomogeneity  $b(\mathbf{x})$  inside the neighborhood  $\mathcal{U}(\mathbf{x})$  of the position  $\mathbf{x}$

$$\mathcal{U}(\mathbf{x}) := \{\chi \mid \chi = \mathbf{x} + \epsilon, \epsilon \in \mathcal{U}\} \quad (9.44)$$

can be assumed to be approximately constant. On the other hand,  $\mathcal{U}$  should be notably larger than the greatest details of  $s(\mathbf{x})$ . This can be at least partially achieved for an appropriate choice of  $\mathcal{U}$ , as (9.37) implies that  $b(\mathbf{x})$  changes only slowly with respect to  $s(\mathbf{x})$ .

Furthermore, the stochastic process of the signal is assumed to be approximately ergodic:

$$E\{s^\nu(\mathbf{x})\} \approx \frac{1}{|\mathcal{U}|} \int_{\mathcal{U}} s^\nu(\mathbf{x} + \epsilon) d\epsilon \quad \forall \nu \in \mathbb{N}, \quad (9.45)$$

with  $|\mathcal{U}|$  denoting the area of  $\mathcal{U}$ . For such a stochastic process, homogeneity of  $m$ th degree means also that the first  $m$  empirical moments on the right-hand side of (9.45) are spatially constant.

In practice, often only a single image, i.e., a single realization of the stochastic process, is available. In this case, (9.45) justifies checking for homogeneity and homogenizing the image by using local neighborhood operators. In the following,  $\mathcal{H}_m\{\cdot\}$  denotes a local neighborhood operator making an image  $m$ -homogeneous.

#### ⊙ Homogenization of first degree

Since (9.39) implies that homogeneity of first degree requires the expected value of  $g(\mathbf{x})$  to be independent of the position  $\mathbf{x}$ , an adequate homogenization should only affect the first moment. Such a homogenization is appropriate if the following additive model applies to the image values:

$$g(\mathbf{x}) = b(\mathbf{x}) + s(\mathbf{x}). \quad (9.46)$$

The homogenization of first degree can be realized using a high-pass filter:

$$\hat{s}(\mathbf{x}) = \mathcal{H}_1\{g(\mathbf{x})\} = g(\mathbf{x}) - \hat{b}(\mathbf{x}) \quad (9.47)$$

with

$$\hat{b}(\mathbf{x}) = \text{LP}\{g(\mathbf{x})\}. \quad (9.48)$$

The low-pass filter  $\text{LP}\{\cdot\}$  can be realized by applying a weighted average to the neighborhood  $\mathcal{U}(\mathbf{x})$ . Here,  $b(\mathbf{x})$  represents the local mean image value of  $g(\mathbf{x})$ . Hence, (9.47) results in a homogenization of the local mean image value.

### ⊗ Homogenization of second degree

For some situations, e.g., for anisotropic textures, neither a pure multiplicative model nor a pure additive model is sufficient to explain and describe the occurring inhomogeneities. In this case, a homogenization of second degree can be useful, which equalizes the local mean image value as well as the local contrast.

Since homogeneity of second degree requires the first two moments of  $g(\mathbf{x})$  to be independent of the position  $\mathbf{x}$ , the following signal model is assumed for the homogenization:

$$g(\mathbf{x}) = \sigma(\mathbf{x}) \cdot s(\mathbf{x}) + \mu(\mathbf{x}). \quad (9.49)$$

Here, the inhomogeneity  $b(\mathbf{x})$  has been separated into two spatially slowly-varying components  $\sigma(\mathbf{x})$  and  $\mu(\mathbf{x})$ . The local mean image value is denoted by  $\mu(\mathbf{x})$  and  $\sigma(\mathbf{x}) > 0 \forall \mathbf{x}$  refers to the local contrast. The rapidly-varying signal  $s(\mathbf{x})$  is assumed to be zero-mean in a sufficiently large region  $\mathcal{U}(\mathbf{x})$ ,

$$\frac{1}{|\mathcal{U}|} \iint_{\mathcal{U}(\mathbf{x})} s(\boldsymbol{\xi}) \, d\boldsymbol{\xi} \approx 0, \quad (9.50)$$

and to have a spatially constant contrast:

$$\frac{1}{|\mathcal{U}|} \iint_{\mathcal{U}(\mathbf{x})} s^2(\boldsymbol{\xi}) \, d\boldsymbol{\xi} \approx \text{const}_{\mathbf{x}}. \quad (9.51)$$

According to these assumptions, a homogenization of second degree can be performed by

$$\hat{s}(\mathbf{x}) = \mathcal{H}_2\{g(\mathbf{x})\} = \frac{g(\mathbf{x}) - \hat{\mu}(\mathbf{x})}{\hat{\sigma}(\mathbf{x})} \cdot \text{const}_{\mathbf{x}}, \quad (9.52)$$

where

$$\hat{\mu}(\mathbf{x}) = \text{LP}\{g(\mathbf{x})\} \quad (9.53)$$

and

$$\hat{\sigma}(\mathbf{x}) = \sqrt{\text{LP}\{(g(\mathbf{x}) - \hat{\mu}(\mathbf{x}))^2\}} \quad (9.54)$$

are estimated by calculating the local spatial average. In (9.52), the subtraction of  $\hat{\mu}(\mathbf{x})$  corresponds to a homogenization of first degree and the division by  $\hat{\sigma}(\mathbf{x})$  represents a homogenization of second degree. Afterwards, the mean image value of the homogenized image  $\hat{s}(\mathbf{x})$  can be set to a spatially constant value  $\mu_0$  and its contrast can be set to a spatially constant value  $\sigma_0 > 0$ :

$$\gamma(\mathbf{x}) = \sigma_0 \cdot \hat{s}(\mathbf{x}) + \mu_0. \quad (9.55)$$

Figure 9.20 is a flow chart illustrating the efficient implementation of the homogenization of second degree in the spatial frequency domain.

#### Remarks:

- Equation (9.52) represents a special case of the so-called Wallis operator [4, 17],

$$\text{Wallis}\{g(\mathbf{x})\} = \frac{b s}{b \hat{\sigma}(\mathbf{x}) + s} [g(\mathbf{x}) - \hat{\mu}(\mathbf{x})] + \beta m + (1 - \beta) \hat{\mu}(\mathbf{x}), \quad (9.56)$$

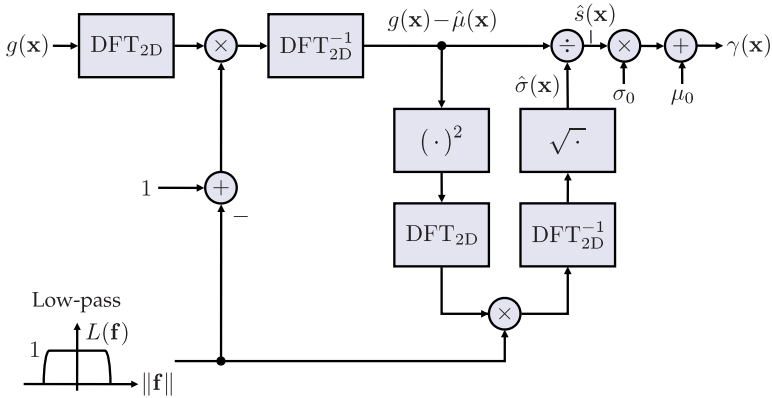


Figure 9.20. Realization of a homogenization of second degree in the spatial frequency domain.

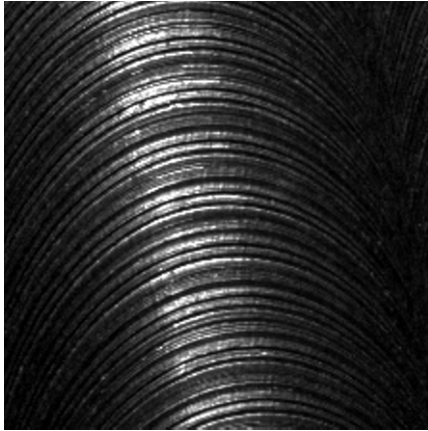
where  $m$  and  $s$  are constants, and  $b \in [3; 25]$  and  $\beta \in [0; \frac{2}{5}]$  are tuning parameters. This operator is used as a tool for the image enhancement of scenic images. Except for an additive constant, (9.56) is (9.52) for  $\beta = 1$  and  $b \rightarrow \infty$ . In fact, these parameter values, which are untypical for the Wallis operator, result in an unwanted amplification of the fine details at the cost of the main features of the scenic data [8], but they are an appropriate choice for enhancing images with textured surfaces.

- The most eye-catching visual inhomogeneities are caused by spatial fluctuations of the local mean image value and the local contrast. Therefore, in most cases, a homogenization of second degree is sufficient to achieve a homogeneous appearance of an image. If a homogenization of an even higher degree is desired, a homogenization of infinite degree is proposed in [2], see page 490.
- A homomorphic filtering of  $\mathcal{H}_1\{\cdot\}$  in accordance with

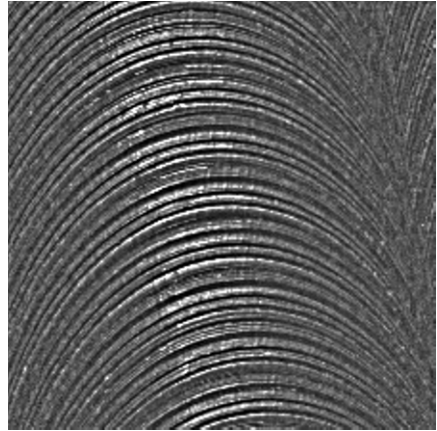
$$\exp(\mathcal{F}^{-1}\{H(\mathbf{f}) \cdot \mathcal{F}\{\log \mathcal{H}_1\{g(\mathbf{x})\}\}\}) \tag{9.57}$$

is not suitable for generating  $\mathcal{H}_2\{\cdot\}$ , as the spatial average of  $g(\mathbf{x}) - \hat{\mu}(\mathbf{x})$  is equal to zero. Here,  $H(\mathbf{f})$  denotes the transfer function of the homomorphic high-pass filter. In order to avoid negative arguments being passed to the logarithm function,  $g(\mathbf{x}) - \hat{\mu}(\mathbf{x})$  could be increased by a positive constant. However, in this case, there would no longer be a multiplicative superposition of  $\sigma(\mathbf{x})$  and  $s(\mathbf{x})$  in the resulting image.

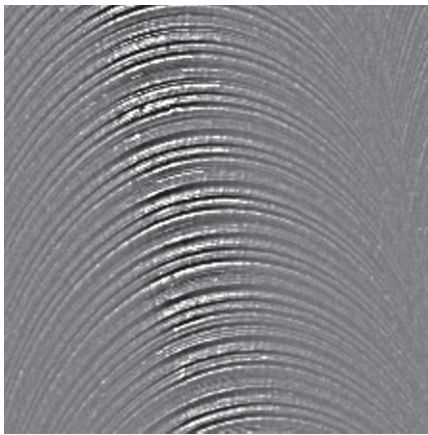
**Example 9.11 (Homogenization of a milling texture):** Figure 9.21(a) shows a homogeneously illuminated end-milling texture. Because of the interaction of the illumination, the surface structure, and the direction of observation, a bright stripe appears in the image. After performing a homomorphic filtering, the inhomogeneities are far less present but still clearly visible, see Fig. 9.21(b). By applying a homogenization of first degree, only the local mean gray value is equalized: the local contrast is still notably increased along the stripe, compared to the image borders, see Fig. 9.21(c). In contrast, a homogenization of the mean local gray value and of the local contrast yields a significantly enhanced image, see Fig. 9.21(d), where details which were hidden before are now visible and without any inhomogeneities. ■



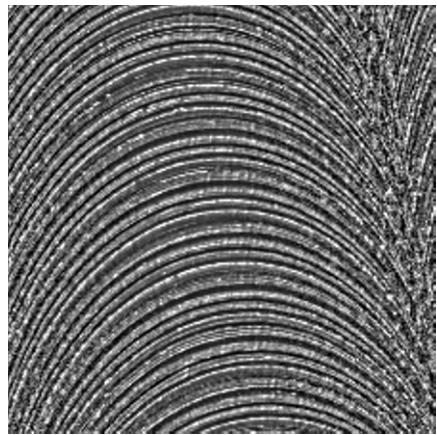
(a) Original image of an end-milling texture



(b) Homomorphic filtering of (a)



(c) Homogenization of 1st degree of (a)

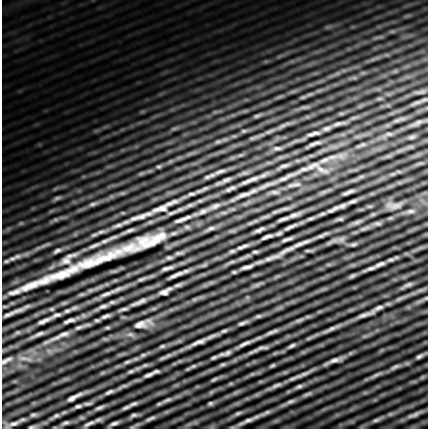


(d) Homogenization of 2nd degree of (a)

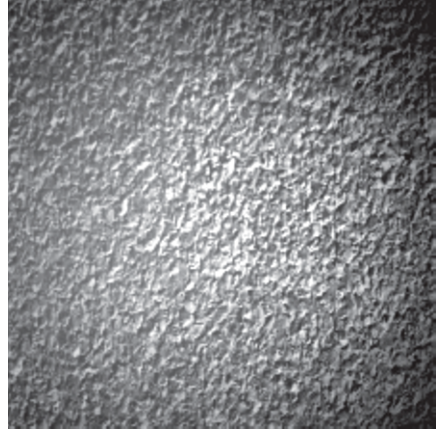
Figure 9.21. Homogenization of an end-milling texture.

**Example 9.12 (Homogenization of a planing texture):** Figure 9.22(a) shows the image of a planing texture with a shadow in the upper left corner, which is caused by inhomogeneous illumination. Again, the homomorphic filtering cannot completely suppress the inhomogeneity, see Fig. 9.22(c). By performing a homogenization of second degree, not only is the shadow gone from the resulting image, but also the planing texture appears more clearly than in the original, cf. Fig. 9.22(e). ■

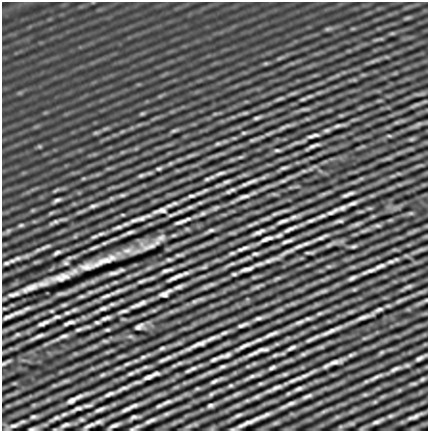
**Example 9.13 (Homogenization of a cork texture):** As a last example of homogenization, Fig. 9.22(b) shows a cork texture with an artificially applied inhomogeneity. The inhomogeneity consists of a smooth transition from a pure additive superposition on the left image border to a pure multiplicative superposition on the right image border [2]. As



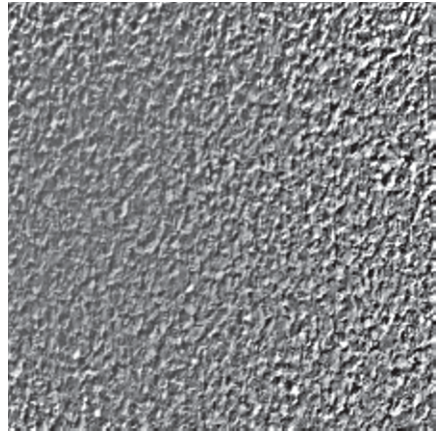
(a) Original image of a planing texture



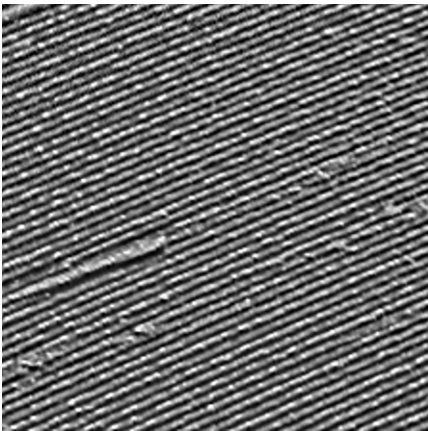
(b) Original image of a cork texture



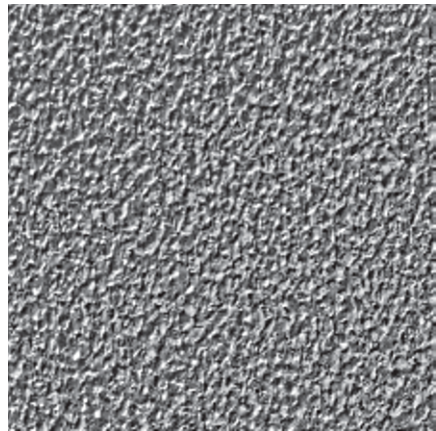
(c) Homomorphic filtering of (a)



(d) Homomorphic filtering of (b)



(e) Homogenization of 2nd degree of (a)



(f) Homogenization of 2nd degree of (b)

Figure 9.22. Suppression of inhomogeneities caused by the image acquisition.

expected, the homomorphic filtering yields better results in the right half of the image, where the multiplicative superposition dominates, cf. Fig. 9.22(d). On the other hand, the left half of the image appears to have low contrast. On the contrary, the result of the homogenization of second degree in Fig. 9.22(f) shows a consistently high contrast in the whole image. ■

⊗ **Homogenization of infinite degree**

A homogeneity of infinite degree requires every moment of the first order statistics to be independent of the position  $\mathbf{x}$ . In other words, every local probability density function  $f_g(g; \mathbf{x})$  is required to be equal to the global, spatially-independent probability density function  $f_g(g)$ . Thus, a homogenization of infinite degree can be performed by equating all local probability density functions.

The image values  $g$  have to be mapped to values  $\gamma(g; \mathbf{x})$  such that  $\gamma(g; \mathbf{x})$  is distributed according to  $f_\gamma(\gamma)$ . Since the cumulative distribution functions  $F_\gamma(\gamma)$  and  $F_g(g; \mathbf{x})$  have to be equal at  $\gamma(g; \mathbf{x})$  [3], in accordance with (9.8), the mapping sought is given by

$$F_\gamma(\gamma(g; \mathbf{x})) = \int_{-\infty}^{\gamma(g; \mathbf{x})} f_\gamma(\beta) d\beta \stackrel{!}{=} \int_{-\infty}^g f_g(\beta; \mathbf{x}) d\beta = F_g(g; \mathbf{x}) \tag{9.58}$$

$$\Rightarrow \gamma(g; \mathbf{x}) = F_\gamma^{-1}(F_g(g; \mathbf{x})). \tag{9.59}$$

Here,  $F_g(g; \mathbf{x})$  performs a spatially-varying transformation of  $g$  to a random variable that is uniformly distributed inside the interval  $[0; 1]$  and which is then mapped to another random variable by  $F_\gamma^{-1}(\cdot)$ , which is distributed according to  $f_\gamma(\gamma)$ , see Fig. 9.23.

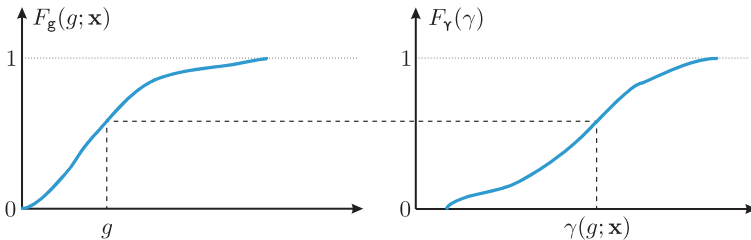


Figure 9.23. Spatially-varying mapping of the image values  $g$  to  $\gamma(g; \mathbf{x})$ .

In order to apply (9.59) to digital images, it has to be considered that the image values (8.311) as well as the positions  $\mathbf{x}$  are discrete. As local ergodicity is assumed as in (9.45), the local probability density functions and distributions can be estimated by local histograms

$$h(g; \mathbf{x}, \mathcal{U}) = \frac{1}{|\mathcal{U}|} \sum_{\epsilon \in \mathcal{U}} \delta_{g(\mathbf{x}+\epsilon)}^g \tag{9.60}$$

and by local, cumulative histograms

$$H(g; \mathbf{x}, \mathcal{U}) = \sum_{\gamma=g_1}^g h(\gamma; \mathbf{x}, \mathcal{U}). \tag{9.61}$$

Now, the neighborhood set  $\mathcal{U}$  is discrete and consists of  $|\mathcal{U}|$  elements. An approximation of the transformation (9.59) is given by

$$\mathcal{H}_\infty\{g(\mathbf{x}); H(g)\} = \arg \min_{\gamma \in \{\gamma_0, \dots, \gamma_{K-1}\}} \{|H(\gamma) - H(g; \mathbf{x}, \mathcal{U})|\}, \quad (9.62)$$

where  $H(g)$  denotes a global, cumulative histogram, which can be arbitrarily set and to which all local distributions of image values should be equal [1].

In some cases a result can be sought that is not only homogeneous but whose higher moments also have certain values. As an example, a homogeneous image could be considered that should additionally have a histogram without skew. Therefore, [2] proposes applying a homogenization of infinite degree and performing an Edgeworth approximation of the desired global histogram. This approximation explicitly depends on the expected value, the standard deviation, the skewness, and the kurtosis of the image values. By means of an Edgeworth series, a fitting to the given data can be achieved (in order to reduce nonlinear distortions [2]), as well as a specific manipulation of the mentioned specific statistic values.

### 9.3 Attenuation of random disturbances

Up to now, only methods for reducing systematic disturbances have been covered. Now, this section will mainly focus on random disturbances. Random disturbances are modeled as a stochastic process  $\mathbf{n}(\mathbf{x})$ , which is usually assumed to be weakly stationary and zero-mean:

$$E\{\mathbf{n}(\mathbf{x})\} = 0. \quad (9.63)$$

Usually, the signal  $\mathbf{s}(\mathbf{x})$  is assumed to be additively combined to the disturbance  $\mathbf{n}(\mathbf{x})$ :

$$\mathbf{g}(\mathbf{x}) = \mathbf{s}(\mathbf{x}) + \mathbf{n}(\mathbf{x}), \quad (9.64)$$

although other relations are possible in practice. It is often further assumed that the signal  $\mathbf{s}(\mathbf{x})$  and the noise  $\mathbf{n}(\mathbf{x})$  are uncorrelated:

$$C_{\mathbf{ns}}(\boldsymbol{\tau}) \equiv 0. \quad (9.65)$$

#### 9.3.1 Linear filters

In image processing, often a linear filter is used, for which (8.2) always holds. In particular, linear filter can mitigate noise if an additive disturbance  $\mathbf{n}(\mathbf{x})$  is assumed as in (9.64) and the spectral supports of the signal and the noise are disjoint:

$$\text{supp}\{\mathcal{F}\{\mathbf{s}(\mathbf{x})\}\} \cap \text{supp}\{\mathcal{F}\{\mathbf{n}(\mathbf{x})\}\} = \emptyset. \quad (9.66)$$

Furthermore, a linear filter can often produce an enhanced image, as is shown in the following example, even when the spectra of the signal and the noise overlap.

**Example 9.14 (Broadband noise):** Consider a process  $\mathbf{g}(\mathbf{x})$  as in (9.64) that consists of an additive superposition of a low-pass signal  $\mathbf{s}(\mathbf{x})$  and a zero-mean, broadband noise  $\mathbf{n}(\mathbf{x})$ . If the two processes are weakly stationary, their essential properties can be described by their autocorrelation functions, as described in Sec. 8.5.3. If  $\mathbf{s}(\mathbf{x})$  and  $\mathbf{n}(\mathbf{x})$  are uncorre-

lated, then

$$r_{gg}(\tau) = r_{ss}(\tau) + r_{nn}(\tau) \tag{9.67}$$



$$S_{gg}(\mathbf{f}) = S_{ss}(\mathbf{f}) + S_{nn}(\mathbf{f}). \tag{9.68}$$

Figure 9.24 illustrates the power spectral density of a possible signal and of some broadband noise. In fact, the noise cannot be completely suppressed by a linear filter, but the shown (linear) low-pass filter with the transfer function  $H(\mathbf{f})$  at least eliminates those components of the noise having frequencies greater than the highest frequency contained in the signal. ■

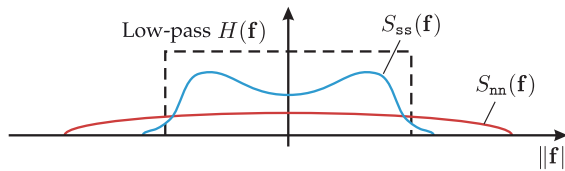


Figure 9.24. Broadband noise.

The result of linear filtering is given by the convolution

$$\mathbf{k}(\mathbf{x}) = \mathbf{g}(\mathbf{x}) ** \mathbf{h}(\mathbf{x}) \tag{9.69}$$

with the impulse response function  $\mathbf{h}(\mathbf{x})$  of the filter; it follows from (8.300) that the result in the spatial frequency domain is given by

$$S_{kk}(\mathbf{f}) = |H(\mathbf{f})|^2 S_{gg}(\mathbf{f}). \tag{9.70}$$

If the spectra of the signal and the noise overlap, the transfer function  $H(\mathbf{f})$  has to be chosen to more intensely damp those frequency bands where the noise is dominant, and to be transparent for the frequency bands dominated by the signal.

In order to obtain a quantitative formula for the design of such a filter, the quotient of the signal-to-noise ratio after and before the filtering is used as a measure of the noise reduction:

$$\frac{SNR\{\mathbf{k}(\mathbf{x})\}}{SNR\{\mathbf{g}(\mathbf{x})\}}. \tag{9.71}$$

Here, the signal-to-noise ratio<sup>2</sup> is defined as the quotient of the power of the signal by the power of the noise:

$$SNR := \frac{\text{Signal power}}{\text{Noise power}}. \tag{9.73}$$

---

<sup>2</sup>Often, signal-to-noise ratios are given in the dimensionless pseudo-unit decibel (dB):

$$SNR/\text{dB} = 10 \log_{10}(SNR). \tag{9.72}$$



Therefore, the signal-to-noise ratio for the signal  $g(\mathbf{x})$  before the filtering is given by

$$SNR\{g(\mathbf{x})\} = \frac{\iint S_{ss}(\mathbf{f}) d\mathbf{f}}{\iint S_{nn}(\mathbf{f}) d\mathbf{f}}. \quad (9.74)$$

Similarly, the result  $k(\mathbf{x})$  of the filtering is given by

$$SNR\{k(\mathbf{x})\} = \frac{\iint S_{ss}(\mathbf{f}) |H(\mathbf{f})|^2 d\mathbf{f}}{\iint S_{nn}(\mathbf{f}) |H(\mathbf{f})|^2 d\mathbf{f}}. \quad (9.75)$$

As (9.74) implies that  $SNR\{g(\mathbf{x})\}$  is independent of the transfer function  $H(\mathbf{f})$  of the filter, an optimization of (9.75) is sufficient for a maximization of (9.71). The optimization has to be performed by varying  $H(\mathbf{f})$  under suitable constraints, which avoid trivial results.

Before we describe linear and nonlinear filters systematically, first their potential will be demonstrated by means of the following two examples.

---

**Example 9.15 (Noise reduction using smoothing filters):** To illustrate the effects of linear and nonlinear smoothing filters, the reference image  $s(\mathbf{x})$  of the portrait (size  $250 \times 250$ ) shown in Fig. 9.25(a) will be used. Figure 9.25(b) shows the test image  $g(\mathbf{x})$ , which has been perturbed by an additive superposition of an artificial, normally distributed white noise  $n(\mathbf{x})$  of variance  $\sigma^2 = 900$ . Hence, the conditions of Example 9.14 are met.

A moving average filter, a cone low-pass filter, and a binomial low-pass filter of size  $7 \times 7$  are used as linear smoothing filters, see Fig. 9.25(c)–(e). All filters will be thoroughly introduced in Sec. 9.3.1.1. Clearly, filtering using a moving average results in the most intense effect: abrupt differences in brightness are smoothed. The weakest smoothing is performed by the binomial low-pass filter.

Figure 9.25(f) shows the result of using a median filter of size  $7 \times 7$ . The median filter is a nonlinear method, which will be covered in Sec. 9.3.2.1. In spite of the extensive effect of the filtering, this result still shows sharp transitions between bright and dark image regions. ■

---

**Example 9.16 (Quasiperiodic disturbances):** Now, the signal

$$g(\mathbf{x}) = s(\mathbf{x}) + n(\mathbf{x}) \quad (9.76)$$

is assumed to be affected by an approximatively periodic disturbance

$$n(\mathbf{x}) = a(\mathbf{x}) \cos(2\pi \mathbf{f}_0^T \mathbf{x} + \varphi). \quad (9.77)$$

The amplitude  $a(\mathbf{x})$  of the disturbance is assumed to be a narrow-band, weakly stationary random process. The phase  $\varphi$  of the periodic disturbance is assumed to be a uniformly distributed random variable, so that the PDF is given by

$$f_\varphi(\varphi) = \frac{1}{2\pi} \text{rect}\left(\frac{\varphi}{2\pi}\right). \quad (9.78)$$

(a) Original image  $s(x)$ (b) Noisy image  $g(x)$ 

(c) Moving average



(d) Cone low-pass



(e) Binomial low-pass



(f) Median filter (nonlinear)

**Figure 9.25.** Noise reduction using smoothing filters of size  $7 \times 7$ .

Furthermore, the amplitude  $a(\mathbf{x})$  and the phase  $\varphi$  are assumed to be stochastically independent. This immediately results in the disturbance  $n(\mathbf{x})$  being zero-mean:

$$\begin{aligned} E\{n(\mathbf{x})\} &= E\{a(\mathbf{x})\} \cdot E\{\cos(2\pi\mathbf{f}_0^T \mathbf{x} + \varphi)\} \\ &= E\{a(\mathbf{x})\} \cdot \underbrace{\frac{1}{2\pi} \int_{-\pi}^{\pi} \cos(2\pi\mathbf{f}_0^T \mathbf{x} + \varphi) d\varphi}_{=0} = 0. \end{aligned} \tag{9.79}$$

The autocorrelation function of the disturbance  $n(\mathbf{x})$  is given by

$$r_{nn}(\mathbf{x}, \boldsymbol{\tau}) = E\{a(\mathbf{x}) a(\mathbf{x} + \boldsymbol{\tau}) \cos(2\pi\mathbf{f}_0^T \mathbf{x} + \varphi) \cos(2\pi\mathbf{f}_0^T (\mathbf{x} + \boldsymbol{\tau}) + \varphi)\} \tag{9.80}$$

$$= r_{aa}(\boldsymbol{\tau}) \cdot \frac{1}{2\pi} \int_{-\pi}^{\pi} \frac{1}{2} [\cos(2\pi\mathbf{f}_0^T \boldsymbol{\tau}) + \underbrace{\cos(4\pi\mathbf{f}_0^T \mathbf{x} + 2\pi\mathbf{f}_0^T \boldsymbol{\tau} + 2\varphi)}_{\int d\varphi = 0}] d\varphi \tag{9.81}$$

$$= r_{aa}(\boldsymbol{\tau}) \cdot \frac{1}{2} \cos(2\pi\mathbf{f}_0^T \boldsymbol{\tau}) \tag{9.82}$$

$$= r_{nn}(\boldsymbol{\tau}). \tag{9.83}$$

Hence, the disturbance process  $n(\mathbf{x})$  is weakly stationary, which is why it can be described using its power spectral density in the spatial frequency domain. A two-dimensional Fourier transform of  $r_{nn}(\boldsymbol{\tau})$  results in:

$$S_{nn}(\mathbf{f}) = \frac{1}{4} (S_{aa}(\mathbf{f} + \mathbf{f}_0) + S_{aa}(\mathbf{f} - \mathbf{f}_0)). \tag{9.84}$$

Figure 9.26 illustrates the power spectral density  $S_{ss}(\mathbf{f})$  of a signal as well as the power spectral density  $S_{nn}(\mathbf{f})$  of an approximately periodic disturbance as in (9.84). Since the disturbance is a band-pass signal, it can successfully be suppressed using a band-stop filter (dashed curve in Fig. 9.26). The effect of the band-stop filter on the signal is insignificant.

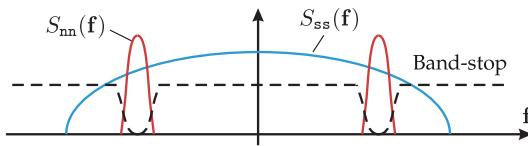
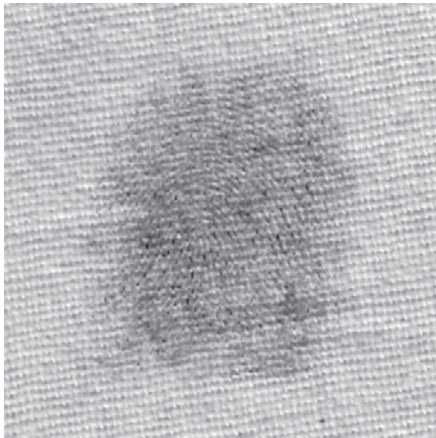


Figure 9.26. Attenuation of disturbances using a band-stop filter.

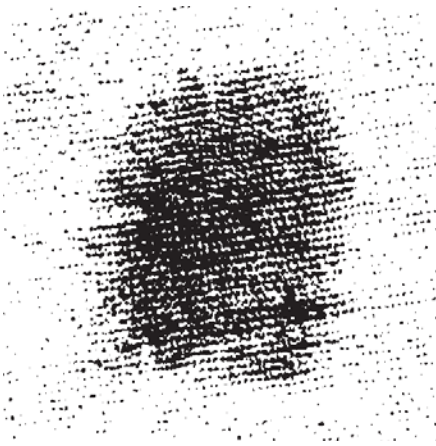
As a practical example of reduction of approximately periodic disturbances, Fig. 9.27(a) shows the original image of a fingerprint on a regularly textured cotton cloth. By suppressing the frequency components which mainly contribute to the formation of the cloth texture (cf. Sec. 13.3.1), the result shown in Fig. 9.27(b) is obtained. In fact, this method cannot completely suppress the disturbing texture, but the fingerprint can be much better extracted after this filtering than before (see Fig. 9.27(a)). In order to make this point clear, Figures 9.27(c) and (d) show the binary conversions of the upper images when using a spatially constant threshold. ■



(a) Original



(b) Noise reduction



(c) Binary conversion of (a)



(d) Binary conversion of (b)

Figure 9.27. Suppression of approximately periodic disturbances.

### ⊗ 9.3.1.1 Low-pass filters for noise reduction

As high-pass, band-pass, and also band-stop filters can be easily constructed from low-pass filters (see Sec. 9.3.1.6), some important linear **low-pass filters** will now be discussed. Suitable low-pass filters should meet the following requirements:

- In order to leave the mean value of  $g(\mathbf{x})$  unaffected, the impulse response function  $h(\mathbf{x})$  of spatially continuous filters has to meet the following condition:

$$\int_{-\infty}^{\infty} \int_{-\infty}^{\infty} h(\mathbf{x}) \, d\mathbf{x} = 1 = H(\mathbf{0}). \quad (9.85)$$

The equivalent condition for the discrete case  $h_{mn}$  is

$$\sum_{m=-\infty}^{\infty} \sum_{n=-\infty}^{\infty} h_{mn} = 1 = H_{00}. \quad (9.86)$$

- Furthermore, the impulse response function of the filter is required to be even, so that the values on both sides of the origin have equal effects on the result of the filtering:

$$h(\mathbf{x}) = h(-\mathbf{x}) \quad (9.87)$$

and for a spatially discrete filter,

$$h_{mn} = h_{-m, -n}. \quad (9.88)$$

There are infinitely many filters meeting both requirements. The most important ones will now be discussed.

### ⊙ 9.3.1.2 Moving average filter

The **moving average** filter is defined by the following impulse response function:

$$h(\mathbf{x}) = \frac{1}{D^2} \operatorname{rect}\left(\frac{x}{D}\right) \operatorname{rect}\left(\frac{y}{D}\right), \quad (9.89)$$

where  $D$  denotes the lateral width of the window.

#### Properties:

- ⊕ **Finite spatial extent:** An outstanding property of the moving average is the finite extent of its impulse response  $h(\mathbf{x})$ , which is beneficial for the computational complexity in the case of a spatially discrete implementation.
- ⊕ **Separability:** In many practical cases, the computational complexity of the filtering of an image can be notably reduced if the corresponding impulse response function is separable—i.e., if it can be decomposed into a horizontal and a vertical one-dimensional impulse response. Especially in the case of the moving average filter, the two-dimensional convolution of an image  $g(\mathbf{x})$  with the impulse response function (9.89) can be separated:

$$g(\mathbf{x}) ** h(\mathbf{x}) = \left( g(\mathbf{x}) \overset{x}{*} \frac{1}{D} \operatorname{rect}\left(\frac{x}{D}\right) \right) \overset{y}{*} \frac{1}{D} \operatorname{rect}\left(\frac{y}{D}\right), \quad (9.90)$$

where  $\overset{x}{*}$  and  $\overset{y}{*}$  denote one-dimensional convolutions in the  $x$ -direction and the  $y$ -direction, respectively.

- ⊖ **Secondary peaks of the transfer function  $H(\mathbf{f})$ :** ‘Good’ low-pass filters should have the important property of more intensely suppressing high-frequency signal components (corresponding to detailed structures in the spatial domain) than low-frequency signal components (i.e., coarser spatial structures). This requirement is not met by the moving average filter. According to (8.77), the transfer function of the one-dimensional moving average filter is a sinc function. Similarly, the two-dimensional Fourier transform of (9.89) is

$$H(\mathbf{f}) = \operatorname{sinc}(f_x D) \cdot \operatorname{sinc}(f_y D). \quad (9.91)$$

As can be seen in Fig. 8.9, this function not only has secondary peaks, but also has negative values for certain spatial frequencies, resulting in an inversion of the contrast for those spatial frequencies, similar to defocused optical imaging (cf. Fig. 8.35).

- ⊖ **Anisotropy:** Furthermore, because of the unwanted anisotropy<sup>3</sup> of the moving average, neither its impulse response function nor its transfer function are rotationally symmetric. This is why diagonal structures of the image are smoothed more strongly than axis-parallel structures.

⊗ **Discrete approximation of the moving average**

The impulse response function (9.89) of the moving average filter can be approximated by the following spatially discrete function, with  $D = L\Delta x = L\Delta y$ :

$$h_{mn,L} = \frac{1}{L^2} \cdot \begin{cases} 1 & \text{if } |m|, |n| \leq \frac{L-1}{2} \\ 0 & \text{otherwise} \end{cases} \quad (9.92)$$

Here, the filter length  $L = 2K + 1$ ,  $K \in \mathbb{N}$ , is chosen to be odd, so that the center of the impulse response is located on a point of the discrete spatial grid—this avoids displacing the image. This filter carries out a homogeneous averaging of every image point inside a square neighborhood of size  $L \times L$  surrounding the point  $(m, n)^T$ : the result of this filtering is assigned to the center pixel  $(m, n)^T$ .

The impulse response function (9.92) can be expressed in matrix notation by

$$h_{mn,L} : \underbrace{\frac{1}{L^2} \begin{pmatrix} 1 & \cdots & 1 \\ \vdots & & \vdots \\ 1 & \cdots & 1 \end{pmatrix}}_L = \underbrace{\frac{1}{L} \begin{pmatrix} 1 \\ \vdots \\ 1 \end{pmatrix}}_{h_{n,L}} \cdot \underbrace{\frac{1}{L} (1 \cdots 1)}_{h_{m,L}} \quad (9.93)$$

This filter is separable, as  $h_{mn,L}$  can be expressed as the matrix multiplication of the column vector  $h_{n,L}$  by the row vector  $h_{m,L}$ .

The discrete Fourier transform of the impulse response function is the DFT transfer function. In the case of a one-dimensional impulse response function  $h_{m,3}$  of length  $L = 3$ , this results in

$$H_k = \frac{1}{3} \left( 1 + e^{-j2\pi \frac{k}{N}} + e^{-j2\pi \frac{k(N-1)}{N}} \right) \quad (9.94)$$

$$= \frac{1}{3} \left( 1 + e^{-j2\pi \frac{k}{N}} + e^{j2\pi \frac{k}{N}} \cdot \underbrace{e^{-j2\pi k}}_1 \right) = \frac{1}{3} + \frac{2}{3} \cos \left( 2\pi \frac{k}{N} \right) \quad (9.95)$$

$\underbrace{\hspace{10em}}_{2 \cos(2\pi \frac{k}{N})}$

The left side of Fig. 9.28 shows the DFT transfer function of the one-dimensional spatially discrete moving average filter with length  $L \in \{3, 5, 7\}$ . The secondary peaks as well as the negative values of the transfer function are clearly visible. For certain applications, the zeros of the transfer function can be used to suppress strictly periodic noise, like power-line hum, for example.

---

<sup>3</sup>Anisotropy means a dependence on the direction.

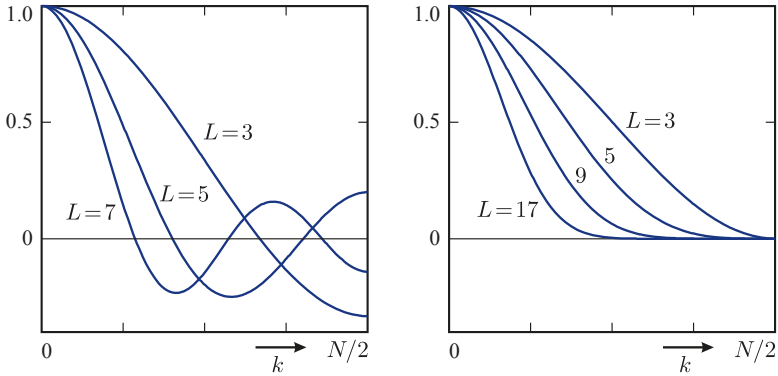


Figure 9.28. DFT transfer function  $H_k$  of the one-dimensional spatially discrete moving average filter (left) and the one-dimensional binomial low-pass filter (right). The frequency index  $N/2$  corresponds to one-half of the sampling frequency and therefore to the highest signal frequency which can be represented.

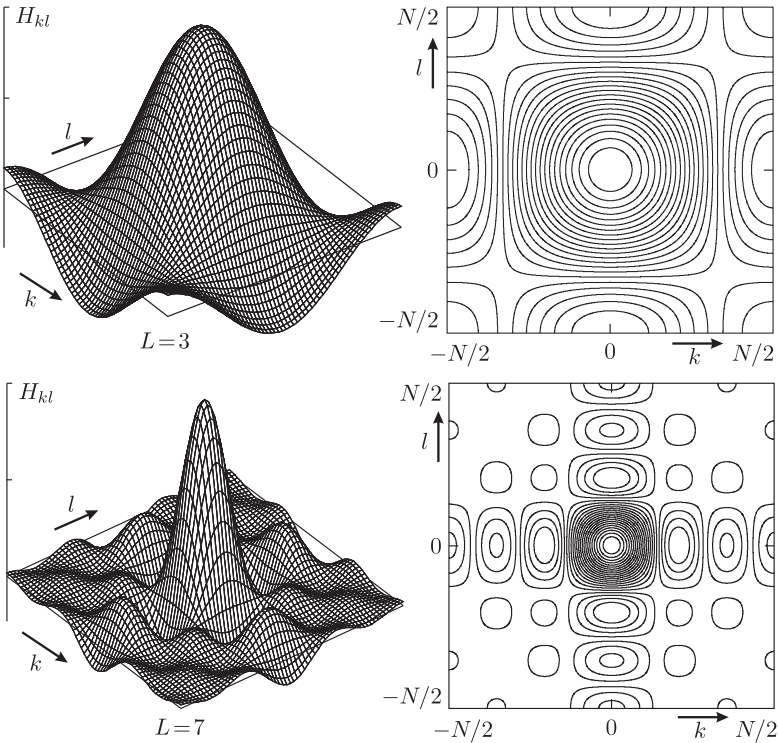


Figure 9.29. DFT transfer function  $H_{kl}$  of the moving average filter for impulse responses of sizes  $L \times L = 3 \times 3$  (top) and  $L \times L = 7 \times 7$  (bottom).

Because of the separability of the moving average filter, (9.95) immediately supplies the two-dimensional DFT transfer function of the filter of size  $3 \times 3$  (cf. Fig. 9.29 top):

$$H_{kl} = \frac{1}{9} \left( 1 + 2 \cos \left( 2\pi \frac{k}{N} \right) \right) \left( 1 + 2 \cos \left( 2\pi \frac{l}{N} \right) \right). \tag{9.96}$$

Figure 9.29 shows the DFT transfer function  $H_{kl}$  of the moving average filter for impulse responses of sizes  $3 \times 3$  (top) and  $7 \times 7$  (bottom). Especially the latter shows a notable anisotropy of the filter.

### ⊙ 9.3.1.3 Cone low-pass filter

The **cone low-pass** filter is characterized by a cone-shaped impulse response function:

$$h(\mathbf{x}) = \frac{3}{\pi D^2} \cdot \Lambda\left(\frac{2\|\mathbf{x}\|}{D}\right) = \frac{3}{\pi D^2} \cdot \begin{cases} 1 - \frac{\|\mathbf{x}\|}{D} & \text{if } \|\mathbf{x}\| \leq D \\ 0 & \text{otherwise} \end{cases}, \quad (9.97)$$

with  $\Lambda(\cdot)$  as defined in (9.35). In fact, it is rotationally symmetric and its transfer characteristics are more beneficial than those of the moving average filter, but it is less practical, as it is not separable and as the Gaussian low-pass filter is superior in almost every aspect. Therefore, this filter will not be further discussed.

### ⊙ 9.3.1.4 Gaussian low-pass filter

The impulse response function of the **Gaussian low-pass** filter is

$$h(\mathbf{x}) = \frac{1}{2\pi D^2} e^{-\frac{1}{2} \frac{\|\mathbf{x}\|^2}{D^2}} \quad (9.98)$$

and is shaped like a two-dimensional Gaussian ‘bell curve.’ Therefore, adjacent points are taken more into account in the result of the averaging than distant points.

#### Properties:

- ⊕ **Monotonicity of the transfer function:** In contrast to the moving average filter, the Gaussian low-pass filter has the beneficial property of more intensely suppressing finer structures. Hence, its transfer function

$$H(\mathbf{f}) = e^{-\frac{1}{2} D^2 \|\mathbf{f}\|^2} \quad (9.99)$$

which is also Gaussian, has no secondary peaks.

- ⊕ **Isotropy:** Furthermore, the filter is rotationally symmetric and therefore isotropic, i.e., independent of the direction.
- ⊕ **Separability:** Like moving average filtering, Gaussian low-pass filtering can be efficiently implemented in several dimensions because of its separability.
- ⊕ **Beneficial smoothing characteristics:** The Gaussian low-pass filter has beneficial smoothing characteristics, as no additional peaks are produced by the filtering but already existent extrema are damped [9]. However, in the strict sense, this only applies for one dimension. Interestingly, the smoothing by a Gaussian low-pass filter is similar to the process of cooling, which reduces local temperature differences, see Sec. 11.3.
- ⊕ **Minimal product of width and bandwidth:** Of all the low-pass filters, the Gaussian low-pass filter has the lowest possible product of the spatial extent of its impulse response function and its bandwidth in the spatial frequency domain<sup>4</sup>. Therefore it allows an optimal localization of the image contents in the spatial domain and simultaneously in the spatial frequency domain.

---

<sup>4</sup>This requires the spatial extent and the bandwidth of a signal to be appropriately defined, see, e.g., [14].



⊖ **Infinite extent:** A particular disadvantage of the Gaussian low-pass filter is its infinite extent in both the spatial domain and the spatial frequency domain, which is why the filter can only be implemented approximately. Therefore, abrupt borders are necessary, which result in secondary peaks, that slightly impair the optimal characteristics of the filter.

⊗ **Discrete approximation: Binomial low-pass filter**

In image processing, the **binomial low-pass** filter has evolved to be an efficient, spatially discrete approximation of the Gaussian low-pass filter. The impulse response function of the one-dimensional binomial filter is defined by

$$h_{m,L} = \frac{1}{2^{L-1}} \binom{L-1}{\frac{L-1}{2} + m}, \quad m \in \{-\frac{L-1}{2}, \dots, \frac{L-1}{2}\}, \tag{9.100}$$

with  $L$  denoting the length of the impulse response function. The formula

$$D = \frac{\sqrt{L-1}}{2} \Delta x \tag{9.101}$$

presents the relation between  $L$  and the standard deviation  $D$  of the Gaussian low-pass filter (9.98).

**Table 9.2.** Pascal’s triangle used for the calculation of the binomial coefficients.

$L$	Scaling factor	Binomial coefficient	Effective filter size
1	1	1	0
	1/2	1 1	1
3	1/4	1 2 1	$\sqrt{2}$
	1/8	1 3 3 1	$\sqrt{3}$
5	1/16	1 4 6 4 1	2
	1/32	1 5 10 10 5 1	$\sqrt{5}$
7	1/64	1 6 15 20 15 6 1	$\sqrt{6}$

In accordance with Table 9.2, the binomial coefficients

$$\binom{L-1}{\frac{L-1}{2} + m} = \frac{(L-1)!}{(\frac{L-1}{2} + m)! (\frac{L-1}{2} - m)!} \tag{9.102}$$

can be calculated recursively using Pascal’s triangle. Hence, the binomial filter can be recursively implemented. In particular,

$$h_{m,3} * h_{m,L} = h_{m,L+2}. \tag{9.103}$$

So, for example, a filtering using the one-dimensional filter

$$h_{m,5} : \frac{1}{16} (1 \ 4 \ 6 \ 4 \ 1) \tag{9.104}$$

can be equivalently performed by two successive applications of binomial filters of the form

$$h_{m,3} : \frac{1}{4} \begin{pmatrix} 1 & 2 & 1 \end{pmatrix}. \quad (9.105)$$

Larger filters  $h_{m,L}$  with  $L > 3$  can be realized by repeated convolutions with  $h_{m,3}$ .

Furthermore, the binomial low-pass filter can be separated, which results in

$$h_{mn,L} = h_{m,L} \cdot h_{n,L} \quad (9.106)$$

for the two-dimensional binomial filter. By this means, the computational complexity is reduced. As an example, the separation of the two-dimensional binomial filter of size  $L \times L = 3 \times 3$  is

$$h_{mn,3} : \frac{1}{16} \begin{pmatrix} 1 & 2 & 1 \\ 2 & 4 & 2 \\ 1 & 2 & 1 \end{pmatrix} = \underbrace{\frac{1}{4} \begin{pmatrix} 1 \\ 2 \\ 1 \end{pmatrix}}_{h_{n,3}} \cdot \underbrace{\frac{1}{4} \begin{pmatrix} 1 & 2 & 1 \end{pmatrix}}_{h_{m,3}}. \quad (9.107)$$

The DFT transfer function of the one-dimensional binomial filter  $h_{m,3}$  of length  $L = 3$  is

$$H_k = \frac{1}{2} + \underbrace{\frac{1}{4} e^{-j2\pi \frac{k}{N}} + \frac{1}{4} e^{-j2\pi \frac{k(N-1)}{N}}}_{\frac{1}{2} \cos(2\pi \frac{k}{N})} = \frac{1}{2} + \frac{1}{2} \cos\left(2\pi \frac{k}{N}\right). \quad (9.108)$$

The right diagram of Fig. 9.28 shows the transfer function  $H_k$  of the binomial low-pass filter for sizes  $L \in \{3, 5, 9, 17\}$ . In every case, the frequency response is monotonically reduced for increasing frequencies. In addition, because of the zero  $H_{\frac{N}{2}} = 0$ , the highest frequency components of the signal are perfectly suppressed by the binomial low-pass filter.

Obviously, in contrast to the moving average filter, the Gaussian low-pass filter requires a notably wider impulse response function in order to realize the same width of the passband. This is caused by the square relating  $D$  and  $L$  in (9.101). In this regard, the comparison of the moving average filter and the binomial filter with equally sized impulse responses in Fig. 9.25(c) and (e) was not completely 'fair.'

The DFT transfer function of the two-dimensional binomial filter of size  $L \times L = 3 \times 3$  can be obtained using (9.108):

$$H_{kl} = \frac{1}{4} \left( 1 + \cos\left(2\pi \frac{k}{N}\right) \right) \left( 1 + \cos\left(2\pi \frac{l}{N}\right) \right). \quad (9.109)$$

Figure 9.30 shows the DFT transfer function  $H_{kl}$  for impulse responses of sizes  $L \times L = 3 \times 3$  (top) and  $L \times L = 5 \times 5$  (bottom). Although there is still a slight anisotropy for  $L = 3$ , the transfer functions seem to be nearly isotropic for  $L \geq 5$ .

As a final remark, it should be mentioned that it follows from the de Moivre–Laplace theorem (which is a special case of the central limit theorem) that the binomial distribution turns into a normal distribution for  $L \rightarrow \infty$  [11]. Hence, the binomial low-pass filter converges asymptotically to the Gaussian low-pass filter as  $L \rightarrow \infty$ .

---

**Example 9.17 (Noise reduction using low-pass filters):** In order to demonstrate the effects of the low-pass filters that have been presented, two test images were synthesized from the image of the chip of Fig. 9.2(a), by adding artificial noise. Figure 9.31(a) shows the additive

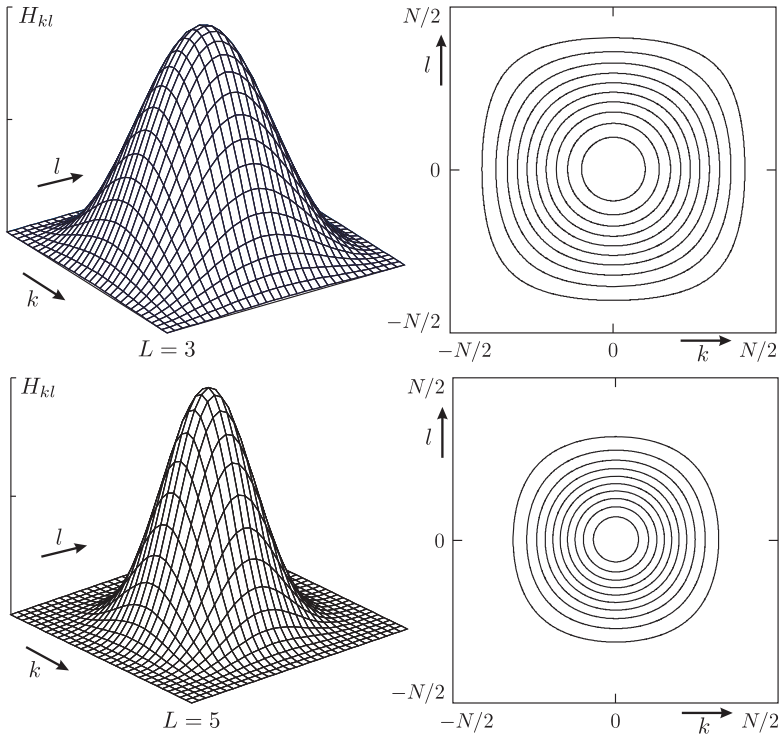


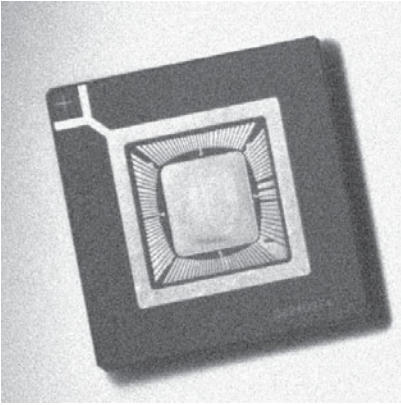
Figure 9.30. DFT transfer function  $H_{kl}$  of the binomial low-pass filter for impulse responses of sizes  $L \times L = 3 \times 3$  (top) and  $L \times L = 5 \times 5$  (bottom).

superposition of normally distributed white noise of variance  $\sigma^2 = 400$ . For Fig. 9.31(b), 15% of the pixels were selected randomly and were disturbed with impulse noise, the so-called **salt-and-pepper noise**, i.e., the selected image points were set either to the value 255 (white) or to zero (black).

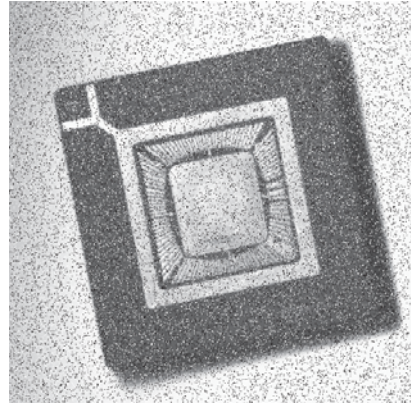
For the analysis of the moving average filter, an impulse response function of size  $L \times L = 5 \times 5$  has been selected. The result visible in Fig. 9.31(c) shows that this filter is especially suitable for suppressing additive, normally distributed noise. However, applying this filter for reducing impulse noise results in an unsatisfying image, as can be seen in Fig. 9.31(d).

Similar to the moving average filter, the binomial filter yields good results when used to mitigate additive, normally distributed noise, see Fig. 9.31(e). In order to compare both filters, the same effective filter width<sup>5</sup> ( $L \times L = 9 \times 9$ ) is used for the binomial filter, cf. Table 9.2 and Fig. 9.28. On the contrary, it is confirmed by Fig. 9.31(f) that linear filters are not suitable for reducing impulse noise. ■

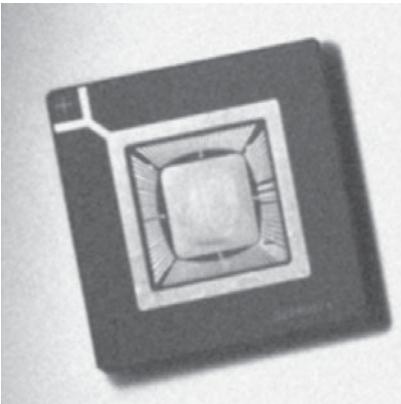
<sup>5</sup>For the definition of the *effective filter width*, the coefficients of the impulse response function are considered as discrete probability values. The effective filter width is given by  $2\sigma$ , where  $\sigma$  denotes the standard deviation of the probability values.



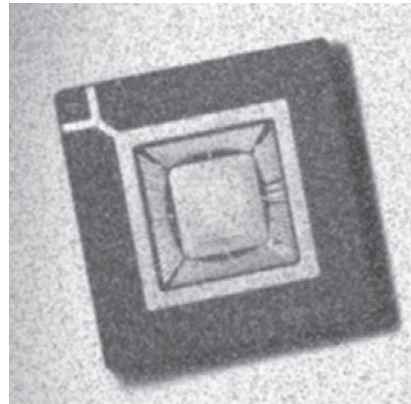
(a) Image with Gaussian noise



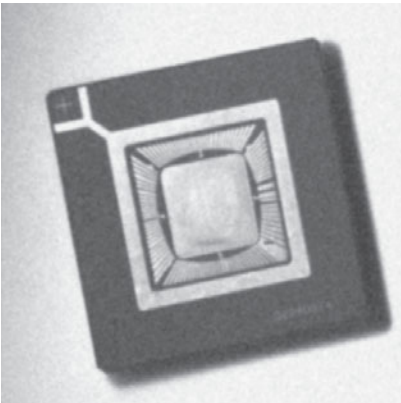
(b) Image with impulse noise



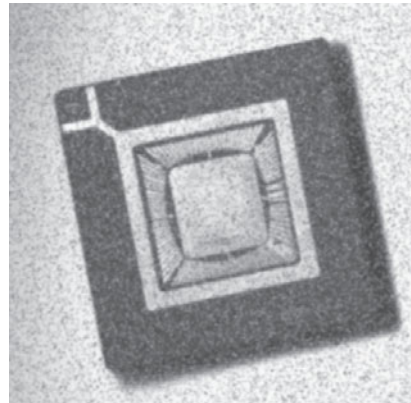
(c) Moving average applied to (a)



(d) Moving average applied to (b)



(e) Binomial filtering applied to (a)



(f) Binomial filtering applied to (b)

Figure 9.31. Noise reduction using local low-pass filters.

### ⊗ 9.3.1.5 Ideal low-pass filters

The transfer function of the ideal low-pass filter is characterized by an abrupt transition from the pass-band to the stop-band:

$$H(\mathbf{f}) = \text{rect}\left(\frac{\|\mathbf{f}\|}{F}\right). \quad (9.110)$$

Here, the bandwidth is denoted by  $F$ , and  $F/2$  represents the cutoff frequency of the filter. The corresponding impulse response is obtained by an inverse Fourier transformation:

$$h(\mathbf{x}) = \frac{F}{2} \cdot \frac{J_1(\pi F \|\mathbf{x}\|)}{\|\mathbf{x}\|}. \quad (9.111)$$

In this equation,  $J_1$  denotes the Bessel function of the first kind (cf. Sec. 2.2.6).

#### Properties:

- ⊕ **Ideal suppression of high frequencies:** As the transition from the pass-band to the stop-band is infinitely steep, the ideal low-pass filter is able to perfectly suppress frequencies greater than the cutoff frequency  $F/2$ .
  - ⊕ **Isotropy:** Furthermore, this filter is independent of the direction, as its impulse response function and its transfer function are rotationally symmetric.
  - ⊖ **Impulse response of infinite length:** As the impulse response function  $h(\mathbf{x})$  of the ideal low-pass is infinitely long, its implementation costs are infinite. Spatially limiting the impulse response function would impair the optimality of the filter's frequency characteristics.
  - ⊖ **Overshoots at jump discontinuities:** The application of the ideal low-pass filter to signals with jump discontinuities results in overshoots, so that such filters can hardly be used in the context of many image processing tasks. This effect is also known as the **Gibbs phenomenon** [14].
- ⊗ **Discrete approximation of the ideal low-pass filter**

As the impulse response function of the ideal low-pass filter is spatially infinite, an implementation in the spatial frequency domain using the DFT seems to be sensible. The DFT transfer function of the ideal low-pass filter is given by

$$H_{kl} = \begin{cases} 1 & \text{in the pass-band (low frequencies)} \\ 0 & \text{in the stop-band (high frequencies)} \end{cases}. \quad (9.112)$$

Still, the intense end effect in the spatial domain caused by the weakly ( $\propto \|\mathbf{x}\|^{-\frac{3}{2}}$ ) decaying impulse response function (9.111) poses a problem. An improvement can be achieved by smoothing the transfer function in the spatial frequency domain.

---

**Example 9.18 (Ideal low-pass filtering using the DFT):** The image of Fig. 9.32(a) shows distinct lines and edges. After a strict band-limitation of the original image using an ideal low-pass filter in the spatial frequency domain, the resulting image Fig. 9.32(b) shows notable overshoots near every edge. These ringing artifacts are caused by the so-called Gibbs phenomenon. ■

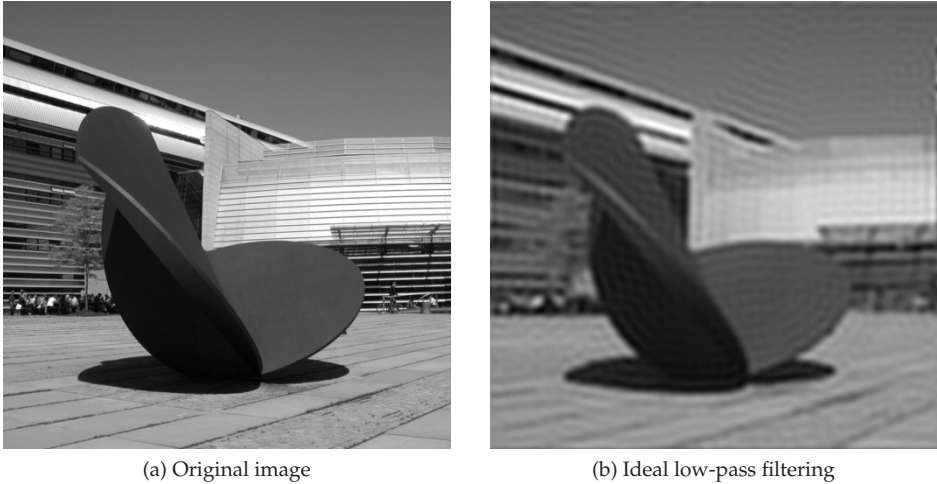


Figure 9.32. Ideal low-pass filtering: (a) Original image; (b) Result obtained by ideal low-pass filtering.

⊗ **9.3.1.6 Constructing high-pass filters, band-stop filters, and band-pass filters from a given low-pass filter**

Up to now, only low-pass filters have been considered for noise reduction. By using so-called **filter transformations**, **high-pass** filters, **band-stop** filters, and **band-pass** filters can be constructed from a given low-pass filter. By this means, the design of all of these types of filters can be reduced to the design of low-pass filters. According to the procedure illustrated in Fig. 9.33, simple linear high-pass filters  $h_{HP}(\mathbf{x})$ , band-stop filters  $h_{BS}(\mathbf{x})$ , and band-pass filters  $h_{BP}(\mathbf{x})$  can be constructed from a given low-pass filter  $h_{LP}(\mathbf{x})$ .

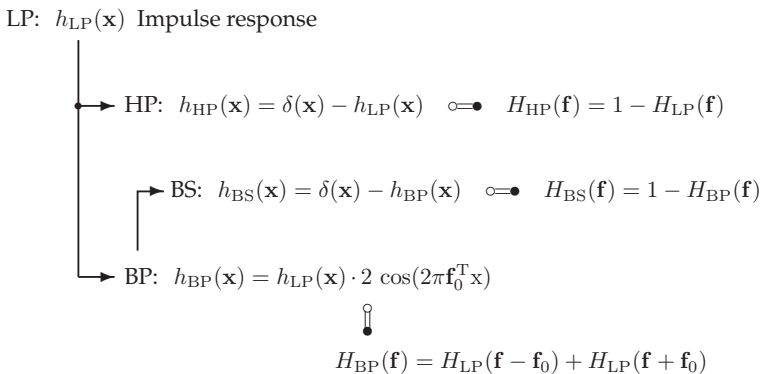


Figure 9.33. Creating simple linear high-pass filters, band-stop filters, and band-pass filters from a given low-pass filter.

⊗ **9.3.1.7 Excursus: The Z-transform**

By applying the Z-transform, a series of values (a discrete signal) is turned into a complex polynomial.

**Definition 9.3: The Z-transform**

The Z-transform  $\mathcal{Z}\{\cdot\}$  maps the discrete signal  $g_n \in \mathbb{R}, n \in \mathbb{Z}$  to a complex-valued polynomial  $p(z) : \mathbb{C} \rightarrow \mathbb{C}$  according to the following formula:

$$\mathcal{Z}\{g_n\} := p(z) = \sum_{l=-\infty}^{\infty} g_l z^{-l}, \quad z \in \mathbb{C}. \tag{9.113}$$

◇

The Z-transform is commonly used for analyzing discrete-time signals. It is rarely used for analyzing images, which are spatially-dependent signals. On the one hand, the two-dimensional generalization

$$\mathcal{Z}\{g_{mn}\} := p(z_1, z_2) = \sum_{m=-\infty}^{\infty} \sum_{n=-\infty}^{\infty} g_{mn} z_1^{-m} z_2^{-n}, \quad p(z_1, z_2) : \mathbb{C}^2 \rightarrow \mathbb{C}, \tag{9.114}$$

of the Z-transform is defined for the four-dimensional domain  $\mathbb{C}^2$ , which is not intuitive and requires a great deal of space. On the other hand, there is no fundamental theorem of algebra for two dimensions, that would ensure a factorization in terms of roots.

Nevertheless, the Z-transform will be covered briefly, since for separable signals  $g_{mn} = p_m q_n$  both factors can be analyzed with the one-dimensional Z-transform.

The examples used in this excursus will show that the discrete convolution of signals can be expressed in the Z-domain by the multiplication of polynomials. Furthermore, longer signals can be decomposed into a convolution of shorter signals in the Z-domain.

**Example 9.19 (Z-transform of discrete signals):** Suppose two discrete signals,  $c_n$  and  $d_n$ :

$$c_n := \begin{cases} -1 & \text{if } n = 0 \\ 1 & \text{if } n = 1 \\ 0 & \text{otherwise} \end{cases}, \quad d_n := \begin{cases} 1 & \text{if } n = -1, n = 1 \\ 2 & \text{if } n = 0 \\ 0 & \text{otherwise} \end{cases}. \tag{9.115}$$

Now, applying the Z-transform to  $c_n$  and  $d_n$  yields

$$\mathcal{Z}\{c_n\} = p_c(z) = -z^0 + z^{-1} \tag{9.116}$$

$$\mathcal{Z}\{d_n\} = p_d(z) = z^1 + 2z^0 + z^{-1}. \tag{9.117}$$

■

Informally, the inverse Z-transform can be performed by collecting the coefficients of the corresponding polynomials—for example, consider the transitions from (9.116), respectively, (9.117) to (9.115).

**Theorem 9.1: Convolution theorem of the Z-transform**

The Z-transform of the convolution of two discrete signals  $g_n, h_n$  is equal to the product of their Z-transforms:

$$\mathcal{Z}\{g_n * h_n\} = \mathcal{Z}\{g_n\} \cdot \mathcal{Z}\{h_n\}. \tag{9.118}$$

The proof is given in [7], for example.

◇

**Example 9.20 (Convolution of two discrete signals):** If the result of the convolution  $g_n = c_n * d_n$  of the two signals  $c_n$  and  $d_n$  of Example 9.19 is sought, it can be obtained using their Z-transforms  $p_c(z), p_d(z)$  and the convolution property (9.118):

$$\mathcal{Z}\{c_n * d_n\} = \mathcal{Z}\{c_n\} \cdot \mathcal{Z}\{d_n\} = p_c(z) \cdot p_d(z) \quad (9.119)$$

$$= (-1 + z^{-1})(z + 2 + z^{-1}) = -z - 1 + z^{-1} + z^{-2}. \quad (9.120)$$

The coefficients immediately yield the result of the convolution:

$$g_n = c_n * d_n = \begin{cases} -1 & \text{if } n = -1, n = 0 \\ 1 & \text{if } n = 1, n = 2 \\ 0 & \text{otherwise} \end{cases}. \quad (9.121)$$

**Example 9.21 (Decomposition of a signal using the Z-transform):** Assume that a signal  $g_n$  is given by its Z-transform:

$$\mathcal{Z}\{g_n\} = p_g(z) = -z - 1 + z^{-1} + z^{-2}. \quad (9.122)$$

Suppose that  $g_n$  is to be decomposed into a convolution of shorter signals. To this end,  $p_g(z)$  can be factored into a product of shorter polynomials:

$$p_g(z) = -z - 1 + z^{-1} + z^{-2} = \frac{-z^3 - z^2 + z + 1}{z^2} \quad (9.123)$$

$$= \frac{(z^2 + 2z + 1)(1 - z)}{z^2} = \frac{(z + 1)^2(1 - z)}{z^2} \quad (9.124)$$

$$= \underbrace{(z + 1)}_{=: \mathcal{Z}\{a_n\}} \underbrace{(1 + z^{-1})}_{=: \mathcal{Z}\{b_n\}} \underbrace{(-1 + z^{-1})}_{=: \mathcal{Z}\{c_n\}}. \quad (9.125)$$

Hence, a decomposition of  $g_n$  into the signals

$$a_n = \begin{cases} 1 & \text{if } n = -1 \\ 1 & \text{if } n = 0 \\ 0 & \text{otherwise} \end{cases}, \quad b_n = \begin{cases} 1 & \text{if } n = 0 \\ 1 & \text{if } n = 1 \\ 0 & \text{otherwise} \end{cases} \quad (9.126)$$

and

$$c_n = \begin{cases} -1 & \text{if } n = 0 \\ 1 & \text{if } n = 1 \\ 0 & \text{otherwise} \end{cases} \quad (9.127)$$

is possible:

$$g_n = a_n * b_n * c_n. \quad (9.128)$$

Accordingly, the Z-transform can be used to decompose a linear shift-invariant system into a series of simpler systems of the same kind with shorter impulse responses.



9.3.2 Noise reduction using nonlinear filters

Most of the linear filters covered until now have a negative effect on the smoothing of images that contain edges or impulse noise: because of their use of weighted averaging, low-pass filters cause a ‘blurring’ of the spatial image information. In the case of abrupt transitions of image values, even the whole neighborhood  $\mathcal{U}(x)$  of the point  $x$  can be blurred.

**Example 9.22 (Moving average filter):** Consider the moving average filter

$$k_m = \frac{1}{5} \sum_{\nu=-2}^2 g_{m-\nu} \tag{9.129}$$

of the discrete one-dimensional signal shown in Fig. 9.34. In this example, the neighborhood has a width of  $|\mathcal{U}| = 5$ . If there is an impulse distortion  $g_m \rightarrow \infty$  at the position  $m$ , it will affect the whole neighborhood  $k_{m-i} \rightarrow \infty, i \in \{-2, -1, 0, 1, 2\}$  after the averaging. ■

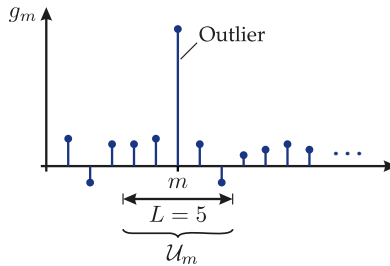


Figure 9.34. Susceptibility of the moving average filter.

A completely different approach to smoothing images is based on sorting the values inside the neighborhood  $\mathcal{U}$ . This method allows the construction of edge-preserving smoothing filters, which, however, have nonlinear transfer characteristics. An important class of nonlinear smoothing filters are the **rank filters**. These include the median filter, which represents the most important filter of this class and will therefore be covered in the following.

9.3.2.1 The median filter

The **median filter** is based on sorting the image values inside a neighborhood  $\mathcal{U}_m$  of the processed image point:

$$\{g_{m-\mu} | \mu \in \mathcal{U}\} \xrightarrow{\text{Sorting}} {}^m g_{(-K)} \leq \dots \leq \underbrace{{}^m g_{(0)}}_{\text{Median}} \leq \dots \leq {}^m g_{(K)} \tag{9.130}$$

with

$$\mathcal{U} := \{-K, -K + 1, \dots, 0, \dots, K\}, \quad K \in \mathbb{N}. \tag{9.131}$$

After the sorting, the **median**, i.e., the value in the middle of the resulting list, is selected:

$$k_m = \text{med}_{\mathcal{U}}\{g_m\} = {}^m g_{(0)}. \tag{9.132}$$

Due to the sorting, potential outliers are moved to the borders of the list. If there are fewer than  $K + 1$  positive outliers  $g_{m-\mu} \rightarrow \infty$  and fewer than  $K + 1$  negative outliers  $g_{m-\mu} \rightarrow -\infty$  inside the neighborhood  $\mathcal{U}_m$ , the resulting median  $k_m$  remains finite. In this case, the outliers do not directly affect the  $k_m$ . In fact, the existent outliers affect the sorting process, but this effect is practically rather insignificant compared to their impact on linear smoothing filters.

In order to realize a two-dimensional median filter, it is sufficient to define the neighborhood  $\mathcal{U}$  as a two-dimensional set of points. An example with the size  $L \times L = 3 \times 3$  is illustrated in Fig. 9.35.

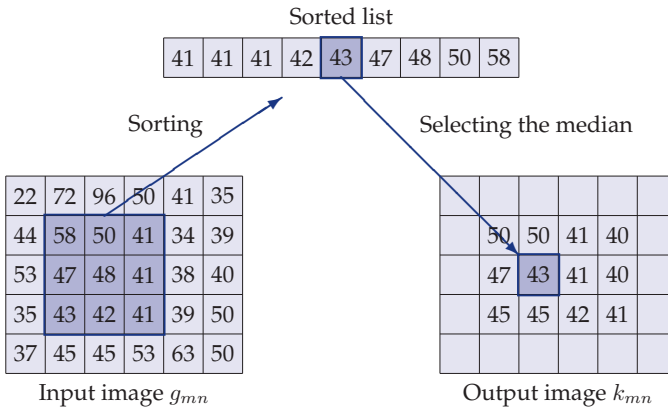


Figure 9.35. Median filter of size  $L \times L = 3 \times 3$  (adapted from [5]).

### Properties:

- ⊕ **Edge-preserving:** the median filter preserves image structures which are wider than  $K$  pixels and especially step edges—i.e., jump discontinuities between two levels of image values (cf. Sec. 11.2).
- ⊕ **Optimal reduction of impulse noise:** furthermore, the median filter allows an optimal reduction for impulse noise (salt-and-pepper noise).
- ⊖ **Unsuitable for additive Gaussian noise:** in the case of additive noise that is normally distributed, linear filters should be chosen to achieve optimal noise reduction.

In order to point out the beneficial characteristics of the median filter with respect to the reduction for impulse noise while preserving edges, Fig. 9.36 shows a comparison of the moving average filtering with the median filtering.

**Example 9.23 (Noise reduction using the median filter):** Figure 9.37 shows the result of the median filtering of the noisy test images of Fig. 9.31(a) and (b). In the case of additive noise that is normally distributed, the median filter only yields moderate results compared to the linear smoothing filters, see Fig. 9.37(a). On the other hand, impulse noise is effectively reduced by the median filter and the edge information is preserved, as can be seen in Fig. 9.37(b). However, if there are many outliers, the median filter fails. ■

**In-depth study of the median filter:** As a nonlinear filter, the median filter cannot be analyzed by means of linear system theory. Nevertheless, in order to gain a deeper understand-

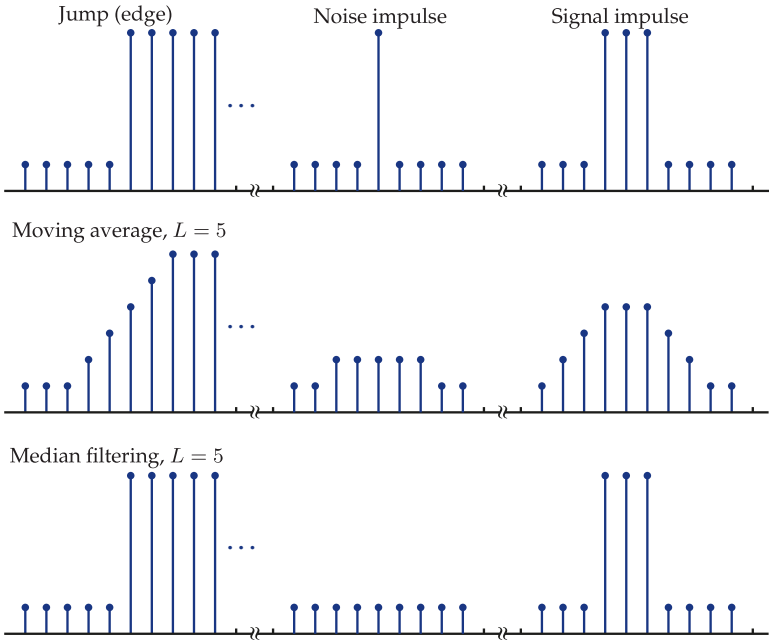
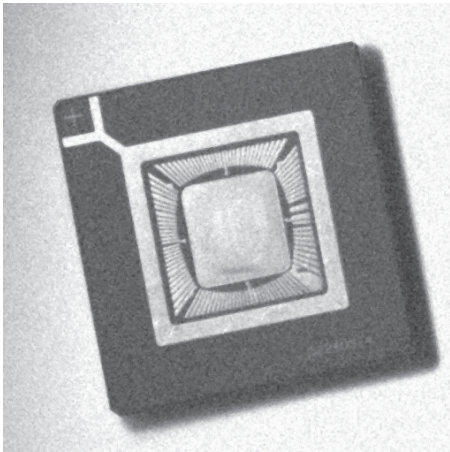
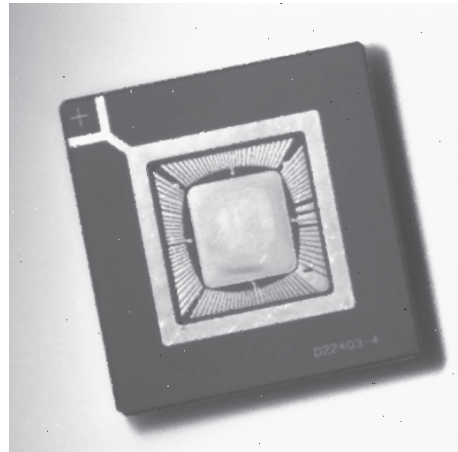


Figure 9.36. Comparison of the moving average and the median filtering.



(a) Median filtering of 9.31(a)



(b) Median filtering of 9.31(b)

Figure 9.37. Noise reduction using a median filter of size  $L \times L = 3 \times 3$ .

ing of this important filter, its optimality will be shown, in the sense of the minimum, mean absolute difference from the filtered values, in other words, in the sense of minimizing an  $l^1$ -metric.

In contrast, it will be shown that the moving average filter introduced in Sec. 9.3.1.2 is

optimal in terms of having the minimal mean squared distance, and is therefore optimal in the sense of an  $l^2$ -metric (Euclidean metric).

## 9.2 Theorem 9.2: Optimality of the median filter

Suppose  $a, b, g_{mn} \in \mathbb{R}$ , then one has

$$\text{med}_{\mathcal{U}}\{g_{mn}\} = \arg \min_{a \in \mathcal{V}_{mn}} \left\{ \sum_{i=1}^L |a - a_i| \right\} \quad (9.133)$$

with

$$\mathcal{V}_{mn} := \{g_{m-\mu, n-\nu} | (\mu, \nu) \in \mathcal{U}\}, \quad L := |\mathcal{V}_{mn}|. \quad (9.134)$$

◇

**Proof 9.1 (Optimality of the median filter):** W.l.o.g., a fixed  $(m, n)$ , i.e., a result of the median filtering of the position  $(m, n)$ , is assumed. Therefore, the subscripts  $(m, n)$  of  $\mathcal{V}$  are omitted, to simplify matters.

In this sketch of a proof, we assume  $a_i \neq a_j$  for  $i \neq j$  and  $L$  to be odd. The function  $J(a)$  is defined as

$$J(a) := \sum_{i=1}^L |a - a_i|, \quad a \in \mathcal{V} = \{a_1, a_2, \dots, a_L\}. \quad (9.135)$$

Now, the following has to be shown:

$$\arg \min_{a \in \mathcal{V}} J(a) = \text{med}_{\mathcal{U}}\{g_{mn}\}. \quad (9.136)$$

Therefore, the derivative of  $J(a)$  will be calculated and set equal to zero. The required derivative of the absolute value  $|\cdot|$  can be expressed using the sign function  $\text{sgn}(\cdot)$  defined in (8.81):

$$\frac{dJ(a)}{da} = \sum_{i=1}^L \text{sgn}(a - a_i) = \sum_{\{i|a_i > a\}} (-1) + \sum_{\{i|a_i = a\}} (0) + \sum_{\{i|a_i < a\}} (1). \quad (9.137)$$

Setting this expression equal to zero results in

$$\frac{dJ(a)}{da} \stackrel{!}{=} 0 \Leftrightarrow |\{i|a_i > a\}| = |\{i|a_i < a\}| = \frac{L-1}{2} \quad (9.138)$$

$$\Leftrightarrow a = \text{med}_{\mathcal{U}}\{g_{mn}\}. \quad (9.139)$$

Hence, the size of the set of elements that are greater than the element sought has to be equal to the size of the set of elements that are less than the element sought. This is why the element sought has to be the median. ■

A possible generalization for vectorial values is given by

$$\text{med}_{\mathcal{U}}\{\mathbf{g}_{mn}\} = \arg \min_{\mathbf{a} \in \mathbb{R}^Q} \left\{ \sum_{i=1}^L \|\mathbf{a} - \mathbf{a}_i\|_1 \right\}, \quad (9.140)$$

with

$$\mathbf{a}_i \in \mathcal{V}_{mn} := \{g_{m-\mu, n-\nu} | (\mu, \nu) \in \mathcal{U}\}, \quad L := |\mathcal{V}_{mn}|. \quad (9.141)$$

For the sake of comparison, we will now consider the moving average that is the arithmetic mean of the points of the set  $\mathcal{V}_{mn}$  corresponding to the position  $(m, n)$ .

---

**Theorem 9.3: Optimality of the moving average**

9.3

One has

$$\bar{a}_{\mathcal{U}} = \arg \min_{a \in \mathbb{R}} \left\{ \sum_{i=1}^L (a - a_i)^2 \right\} \quad (9.142)$$

with

$$\bar{a}_{\mathcal{U}} := \frac{1}{L} \sum_{i=1}^L a_i, \quad a_i \in \mathcal{V}_{mn} := \{g_{m-\mu, n-\nu} | (\mu, \nu) \in \mathcal{U}\}, \quad L := |\mathcal{V}_{mn}|. \quad (9.143)$$

◇

---

**Proof 9.2 (Optimality of the moving average):** The function  $J(a)$  is defined by

$$J(a) := \sum_{i=1}^L (a - a_i)^2, \quad a_i \in \mathcal{V} = \{a_1, a_2, \dots, a_L\}. \quad (9.144)$$

Now, it has to be shown that

$$\bar{a}_{\mathcal{U}} = \arg \min_{a \in \mathbb{R}} J(a). \quad (9.145)$$

The proof is completed by finding the derivative of  $J(a)$  with respect to  $a$  and by calculating its zeros:

$$\frac{dJ(a)}{da} \stackrel{!}{=} 0 \quad \Leftrightarrow \quad 2 \sum_{i=1}^L (a - a_i) = 0 \quad (9.146)$$

$$\Leftrightarrow \quad a = \bar{a}_{\mathcal{U}} = \frac{1}{L} \sum_{i=1}^L a_i. \quad (9.147)$$

■

As the result of the moving average filter is quadratically affected by differences, single outliers can have a notable impact on the filtering. In contrast, the median filter is only linearly affected by differences, so that single outliers have less influence on the result of the filtering. This is another explanation why the median filter is more robust to outliers than the moving average.

⊙ **9.3.2.2 Filters based on order statistics**

Order statistics can be used as a basis for constructing filters that are not susceptible to outliers. Now we will introduce the **trimmed mean filter**, which—besides the median filter—is another filter of this kind.

⊗ **The trimmed mean filter**

Similar to the median filter, the first step of the trimmed mean filter is to sort the image values of a neighborhood  $\mathcal{U}$ . Here, the  $2(K - J)$  most extreme values are considered as outliers. All other image values are subject to a linear averaging:

$${}^m g_{(-K)} \leq \dots \leq {}^m g_{(-J)} \leq \dots \leq \underbrace{{}^m g_{(0)}}_{\text{Median}} \leq \dots \leq {}^m g_{(J)} \leq \dots \leq {}^m g_{(K)}. \quad (9.148)$$

Averaging

Therefore, the result of the trimmed mean filtering is given by

$$k_m = \frac{1}{2J + 1} \sum_{-J}^J {}^m g_{(i)}. \quad (9.149)$$

Trimmed mean filtering can be considered as a generalization of moving average filtering on the one hand, and of median filtering on the other hand, as both represent special cases:

- Choosing  $J = 0$  results in the median filter.
- Choosing  $J = K$  results in the arithmetic mean.

⊗ **9.3.2.3 Bilateral filters**

The **bilateral filtering** constitutes a powerful approach to edge-preserving smoothing [15]. Similar to linear low-pass filters, the bilateral filter is based on a weighted averaging of the spatially adjacent image values. According to Sec. 9.3.1, this process can be represented by convolving the input image with the filter  $h(\mathbf{x})$ :

$$k(\mathbf{x}) = \frac{\int_{-\infty}^{\infty} \int_{-\infty}^{\infty} g(\xi) h(\mathbf{x} - \xi) d\xi}{\int_{-\infty}^{\infty} \int_{-\infty}^{\infty} h(\xi) d\xi}. \quad (9.150)$$

Here, the factor in the denominator results in an unchanged mean value after the filtering, cf. (9.85). In order to avoid the smoothing of edges by the filter, only image points having similar image values are considered by the bilateral filter. This can be achieved by using an additional filter kernel  $f(g)$ :

$$k(\mathbf{x}) = \frac{\int_{-\infty}^{\infty} \int_{-\infty}^{\infty} g(\xi) h(\mathbf{x} - \xi) f(g(\mathbf{x}) - g(\xi)) d\xi}{\int_{-\infty}^{\infty} \int_{-\infty}^{\infty} h(\mathbf{x} - \xi) f(g(\mathbf{x}) - g(\xi)) d\xi}. \quad (9.151)$$

Again, the scaling caused by the denominator ensures that the resulting mean image value remains unchanged. Often, Gaussian functions are used for the filter kernels  $h(\mathbf{x})$  and  $f(g)$ .

As only similar image values are filtered, the bilateral filter is not suitable for reducing impulse noise. However, very good results can be achieved in the case of Gaussian noise.

By extending (9.151) to vectorial image signals  $\mathbf{g}(\mathbf{x})$ , even color images or multispectral images can be processed by the bilateral filter:

$$\mathbf{k}(\mathbf{x}) = \frac{\int_{-\infty}^{\infty} \int_{-\infty}^{\infty} \mathbf{g}(\boldsymbol{\xi}) h(\mathbf{x} - \boldsymbol{\xi}) f(\mathbf{g}(\mathbf{x}) - \mathbf{g}(\boldsymbol{\xi})) d\boldsymbol{\xi}}{\int_{-\infty}^{\infty} \int_{-\infty}^{\infty} h(\mathbf{x} - \boldsymbol{\xi}) f(\mathbf{g}(\mathbf{x}) - \mathbf{g}(\boldsymbol{\xi})) d\boldsymbol{\xi}}. \quad (9.152)$$

By performing the filtering of color images in the CIELAB color space, color deviations in the transitions between different colors can be avoided [15]. In this case, the function  $f$  measures the similarity between the image values by calculating the Euclidean distance in the CIELAB color space.

However, directly evaluating the double integral in (9.151) and (9.152) is computationally suboptimal. An efficient implementation of the bilateral filter is presented in [13]. One should note that the filtering of a scalar spatial signal  $g(\mathbf{x})$  with a (nonlinear) bilateral filter can be expressed via a linear filtering of a binary signal

$$b(\mathbf{x}, g) = \delta_{g(\mathbf{x})}^g \quad (9.153)$$

in a combined space of position  $\mathbf{x}$  and value  $g$  [12].

---

**Example 9.24 (Noise reduction using the bilateral filter):** Figure 9.38 shows the results of the bilateral filtering of the test image of Fig. 9.31(a), which is affected by additive noise. For the four filtering results, different parameters were used for the filter kernels. Prior to the filtering, the image values were scaled to the interval  $[0, 1]$ . Compared to the linear filters of Fig. 9.31(c) and (e), the bilateral filter results in an effective reduction for the noise while preserving the edge information. ■

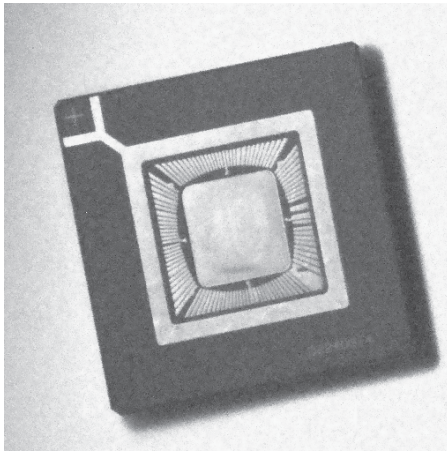
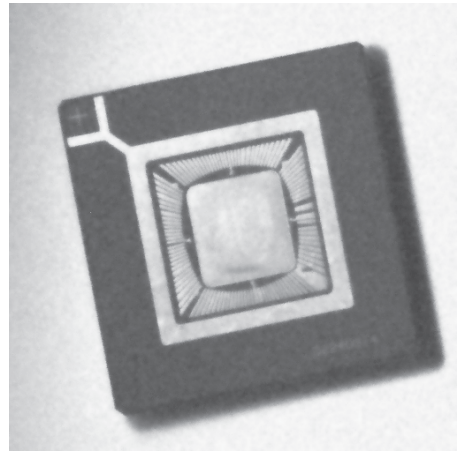
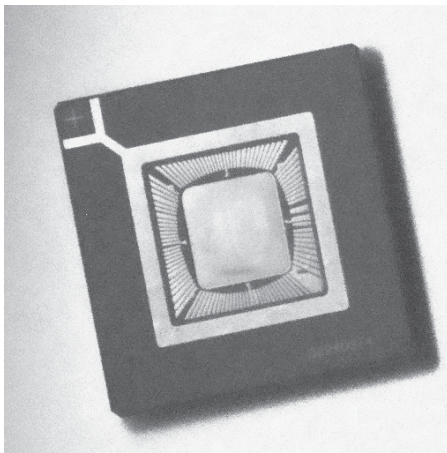
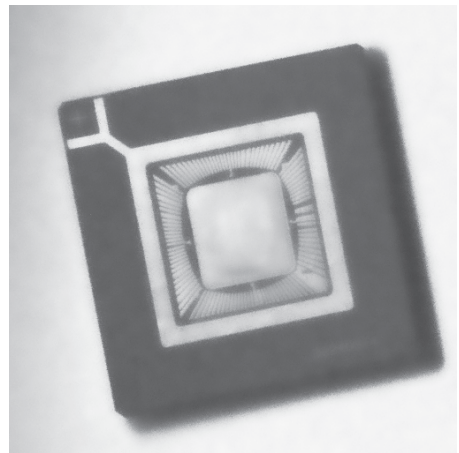
---

**Example 9.25 (Bilateral filtering of color images):** Figure 9.39 shows the results of the bilateral filtering of the RGB color images of Figs. 8.32(a) and 9.19(a). In order to avoid color deviations along the edges, the filtering was performed in the CIELAB color space. Especially areas of weak intensity textures (grass, snow, river, facades) appear notably more homogeneous in the result: distinct edges are still clearly visible. ■

## 9.4 Image registration

The registration of two images means the matching of two different images with respect to spatial position and image values. Image registration is particularly important for the fusion of multiple images into a single image of high quality and/or a larger field of view.

W.l.o.g. two images  $g_1$  and  $g_2$  are assumed to at least partially show the same object or the same scene. By determining corresponding pairs of image points, i.e., image points in  $g_1$  and  $g_2$  that show the same object point, a mapping can be constructed, which geometrically and radiometrically maps the two images to each other. This procedure is called image registration. Formally, two images can be registered by applying two transformations  $T_1$  and  $T_G$ , which perform the mapping of the values and of the positions.

(a)  $\sigma_h = 2, \sigma_f = 0.1$ (b)  $\sigma_h = 2, \sigma_f = 0.3$ (c)  $\sigma_h = 5, \sigma_f = 0.1$ (d)  $\sigma_h = 5, \sigma_f = 0.3$ 

**Figure 9.38.** Results of the filtering of the test image of Fig. 9.31(a) using bilateral filters with different filter widths. For this example, Gaussian kernels  $h(\mathbf{x})$  and  $f(g)$  with standard deviations  $\sigma_h$  and  $\sigma_f$  were used.

The transformation formulas can be estimated by transforming one of the two images in such a way that a certain distance  $D$  between the images is minimized.

$$\left( \hat{T}_1, \hat{T}_G \right) = \arg \min_{T_1, T_G} \{ D(g_1(\mathbf{x}), T_1[g_2(T_G[\mathbf{x}]))] \} \quad (9.154)$$

**Example 9.26 (Registration of two images):** Figure 9.40 shows two images of a cylinder head, which have been registered to each other. ■

By means of the estimated transformations, the two images can then be exactly superposed with respect to their values and to the positions, so that, for example, they can be subjected





(a)  $\sigma_h = 5, \sigma_f = 0.1$



(b)  $\sigma_h = 5, \sigma_f = 0.15$

**Figure 9.39.** Results of the bilateral filtering of the color images of Fig. 8.32(a) and 9.19(a). The Gaussian kernels  $h(\mathbf{x})$  and  $f(g)$  were used with the standard deviations  $\sigma_h$  and  $\sigma_f$ . The filtering was performed in the CIELAB color space.

to a pointwise image fusion:

$$r(\mathbf{x}) = \Phi(g_1(\mathbf{x}), \tilde{g}_2(\mathbf{x})) = \Phi\left(g_1(\mathbf{x}), \underbrace{\hat{T}_1\left[g_2\left(\hat{T}_G[\mathbf{x}]\right)\right]}_{\tilde{g}_2(\mathbf{x})}\right). \tag{9.155}$$

Here,  $\Phi(\cdot)$  denotes a pointwise image fusion operator and  $r(\mathbf{x})$  denotes the result of the image fusion.

**Example 9.27 (Fusion of registered images):** Figure 9.41 shows how a panoramic image can be created by fusing two registered images of one and the same object. ■

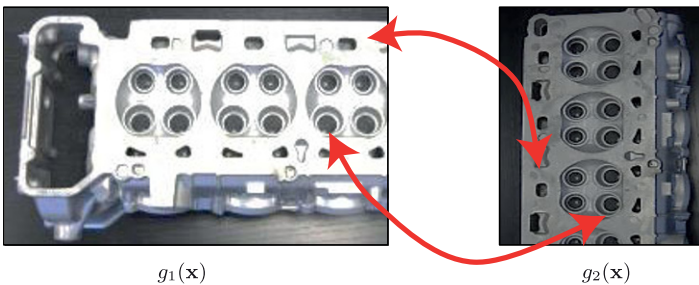


**Figure 9.40.** Two images of one and the same object. By determining a set of pairs of image points that correspond to the same object point, the two images can be registered, i.e., the required geometrical and radiometric mapping can be constructed.

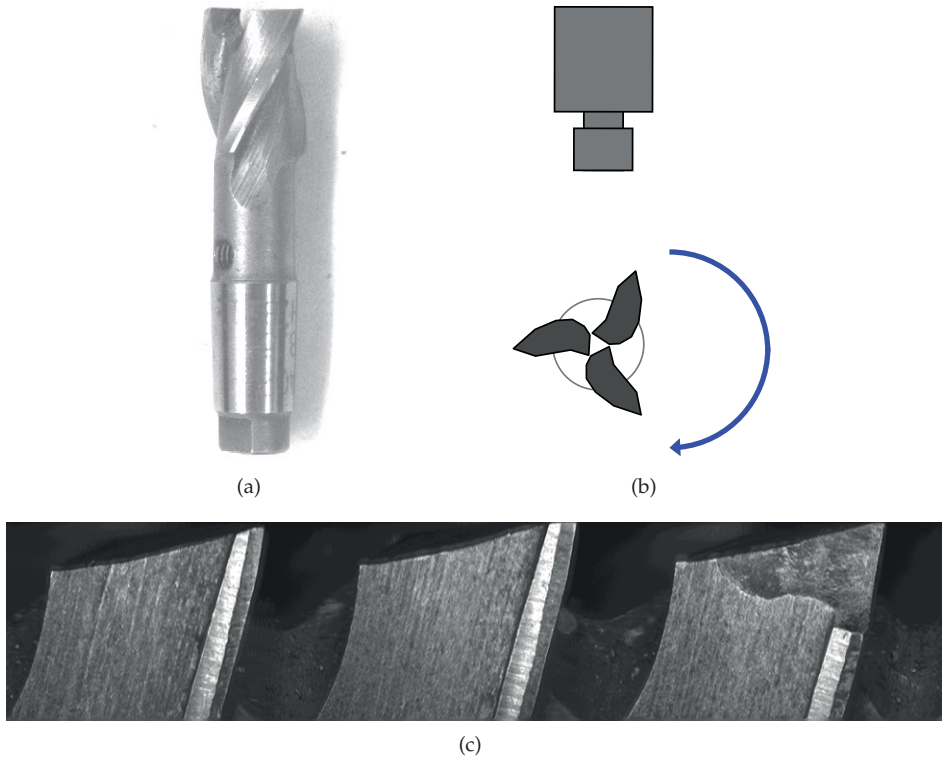


**Figure 9.41.** Fusion of a series of images of a milling cutter (a) in the radial direction (b), acquired for different angles of rotation. The result of the fusion (c) is a panoramic image of the whole circumference of the milling cutter.

## 9.5

## 9.5 Bibliography

- [1] Jürgen Beyerer. *Analyse von Riefentexturen*. PhD thesis, Universität Karlsruhe (TH), 1994.
- [2] Jürgen Beyerer and Fernando Puente León. Suppression of inhomogeneities in images of textured surfaces. *Optical Engineering*, 36(1):85–93, 1997.
- [3] Rafael Gonzalez and Richard Woods. *Digital image processing*. Pearson Prentice Hall, 3rd edition, 2008.
- [4] Robert Haralick and Linda Shapiro. *Computer and robot vision*. Addison-Wesley, 1992.
- [5] Bernd Jähne. *Digital image processing*. Springer, 6th edition, 2005.
- [6] Anil Jain. *Fundamentals of digital image processing*. Prentice Hall, 1989.
- [7] Karl-Dirk Kammeyer and Kristian Kroschel. *Digitale Signalverarbeitung – Filterung und Spektralanalyse*. Vieweg+Teubner, 7th edition, 2009.
- [8] Jong-Sen Lee. Digital image enhancement and noise filtering by use of local statistics. *IEEE Transactions on Pattern Analysis and Machine Intelligence*, 2(2):165–168, 1980.
- [9] Tony Lindeberg. *Scale space theory in computer vision*. Kluwer, 1994.
- [10] Norbert Lins. *Beschreibung von Texturen mithilfe statistischer Methoden für die Anwendung bei der Segmentierung und Qualitätskontrolle*. PhD thesis, ETH Zürich, 1987.

- [11] Athanasios Papoulis and Unnikrishna Pillai. *Probability, random variables and stochastic processes*. McGraw-Hill, 4th edition, 2002.
- [12] Sylvain Paris and Frédo Durand. A fast approximation of the bilateral filter using a signal processing approach. In *Computer Vision—ECCV 2006*, pages 568–580. Springer, 2006.
- [13] Sylvain Paris, Pierre Kornprobst, Jack Tumblin, and Frédo Durand. Bilateral Filtering: Theory and Applications. *Foundations and Trends in Computer Graphics and Vision*, 4(1):1–73, 2009.
- [14] Fernando Puente León and Holger Jäkel. *Signale und Systeme*. De Gruyter Oldenbourg, Berlin, 6th edition, 2015.
- [15] Carlo Tomasi and Roberto Manduchi. Bilateral filtering for gray and color images. In *Proc. Sixth International Conference on Computer Vision (ICCV '98)*, pages 839–846, 1998.
- [16] Friedrich Wahl. *Digitale Bildsignalverarbeitung*. Springer, 1989.
- [17] R. Wallis. An approach to the space variant restoration and enhancement of images. In *Proc. Symp. on Current Mathematical Problems in Image Scenes*, pages 329–340, 1976.

Chapter 10  
**Image Restoration**

**10**

---

**10 Image Restoration**

10.1 Signal model . . . . .	523
10.2 Inverse filter . . . . .	527
10.3 The Wiener filter . . . . .	533
10.4 The geometric mean filter . . . . .	538
10.5 Optimal constraint filter . . . . .	540
10.6 Restoration problems in matrix notation . . . . .	543
10.7 Restoration for participating media . . . . .	546
10.8 Spatially-varying image restoration . . . . .	548
10.9 Bibliography . . . . .	549

## 10 Image Restoration

The image enhancement methods covered in Chap. 9 mainly considered subjective or qualitative criteria. In particular, the visual interpretability of the results was of greater importance than the ‘conservation of the original image traits’. This motivation resulted in mostly heuristic methods, which even altered the images to form pseudo-color images or false-color images (Sec. 9.1.3).

In contrast, **image restoration** tries to reconstruct an original image by using a signal model of the image degradation (Sec. 10.1). An obvious approach is to use these signal models in order to design an **inverse filter**, which allows an ‘inversion’ of the image degradation (Sec. 10.2). However, better results can usually be achieved using the **Wiener filter** (Sec. 10.3), the **geometric mean filter** (Sec. 10.4), or **constraint filters** (Sec. 10.5). In all cases, mainly quantitative criteria for preserving the ‘original image traits’ are of importance and are optimized in order to achieve an adequate reconstruction. Section 10.6 introduces matrix notation for restoration problems and Sections 10.7 and 10.8 cover two special cases of image restoration, the restoration for participating media and spatially varying image restoration, respectively.

### 10.1 Signal model

Figure 10.1 shows the linear signal model on which the image restoration methods of this chapter are based. The input is given by the original signal  $s(\mathbf{x})$ , which might be an idealization—i.e., a ‘perfect’ signal—which cannot be measured directly. By using an ideal acquisition system, it would be possible to directly and faultlessly capture the original signal  $s(\mathbf{x})$ . Instead, in practice the signal  $s(\mathbf{x})$  is distorted by a non-ideal acquisition system, which in most cases can be described by an LSI system having the impulse response function  $h(\mathbf{x})$ . For example, defocused optical systems (Example 10.1) as well as systems that produce a blurred image because of a motion of the camera or of the object (Examples 10.2 and 10.3), are non-ideal acquisition systems. Furthermore, the distorted signal is affected by additive noise  $n(\mathbf{x})$ , so that the signal  $g(\mathbf{x})$  that is actually observed by the acquisition system is given by

$$g(\mathbf{x}) = s(\mathbf{x}) ** h(\mathbf{x}) + n(\mathbf{x}). \quad (10.1)$$

Now, the restoration problem posed is to use an adequate restoration filter with an impulse response function of  $v(\mathbf{x})$  in order to extract an estimation  $\hat{s}(\mathbf{x})$  of the original signal out of

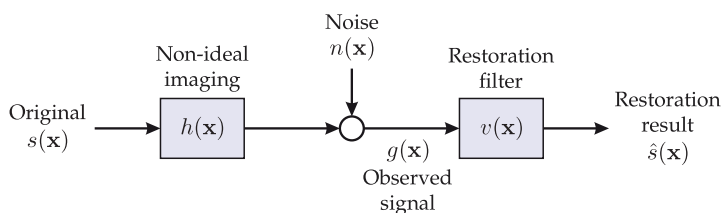


Figure 10.1. Signal model for image restoration.

the observed signal  $g(\mathbf{x})$ . The estimation should approximate the original  $s(\mathbf{x})$  as good as possible.

Figure 10.1 and (10.1) immediately result in

$$\hat{s}(\mathbf{x}) = v(\mathbf{x}) ** g(\mathbf{x}) = v(\mathbf{x}) ** (s(\mathbf{x}) ** h(\mathbf{x}) + n(\mathbf{x})) \tag{10.2}$$

and by applying a two-dimensional Fourier transform,

$$\hat{S}(\mathbf{f}) = V(\mathbf{f}) S(\mathbf{f}) H(\mathbf{f}) + V(\mathbf{f}) N(\mathbf{f}). \tag{10.3}$$

Typically, the transfer function  $H(\mathbf{f})$  of the non-ideal imaging system has zeros in the support  $\text{supp}\{S(\mathbf{f})\}$  of the spectrum  $S(\mathbf{f})$ . In general, it is therefore impossible to achieve an exact restoration of  $s(\mathbf{x})$ , even if  $n(\mathbf{x}) \equiv 0$ .

The following examples will show different formations of non-ideal imaging.

**Example 10.1 (Defocusing):** Defocused optical imaging has already been covered in Sections 3.4, 8.3.4 and 8.4. In this case, a circularly shaped aperture is considered, see Fig. 10.2. Additionally, diffraction effects are neglected. By assuming a lossless imaging, Equation (8.227) results in the transfer function

$$H(\mathbf{f}) = \frac{2}{\pi\varepsilon} \cdot \frac{J_1(\pi\varepsilon\|\mathbf{f}\|)}{\|\mathbf{f}\|}, \tag{10.4}$$

with  $\varepsilon$  denoting the diameter of the blur disk in the image plane and  $J_1$  denoting the Bessel function of the first kind, cf. (2.169). The transfer function  $H(\mathbf{f})$  of a defocused optical imaging has its zeros on concentric circles, see Fig. 10.3. ■

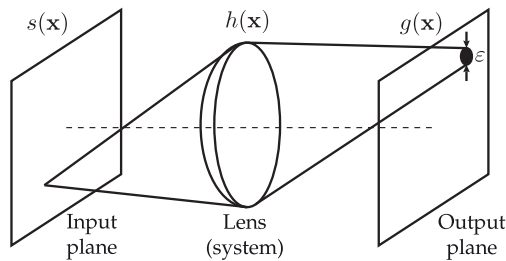


Figure 10.2. Defocused optical imaging.

**Example 10.2 (Motion blur):** For the present example, the image sensor is assumed to be linearly, uniformly moved in the image plane, as is the case if the camera is moved perpendicularly to the optical axis during image acquisition. These assumptions approximately hold for the setup shown in Fig. 10.4, where a two-dimensional measurement of the velocity is to be obtained [6]. The distance  $l$  covered in the image plane is given by

$$l := \mathbf{v} \cdot T = \|\mathbf{l}\| \cdot e \tag{10.5}$$

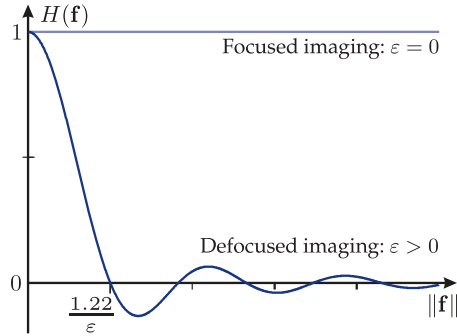


Figure 10.3. Transfer function of defocused optical imaging. As it is rotationally symmetric, it is sufficient to consider a radial section of  $H(\mathbf{f})$ .

with

$$\mathbf{e} = \frac{\mathbf{1}}{\|\mathbf{1}\|} \quad \text{and} \quad \mathbf{e}_\perp : \begin{cases} \|\mathbf{e}_\perp\| = 1 \\ \mathbf{e}^\top \mathbf{e}_\perp = 0 \end{cases}, \tag{10.6}$$

with  $\mathbf{v}$  denoting the velocity in the image plane and  $T$  denoting the exposure time. For a perfectly homogeneous motion, the corresponding non-ideal imaging is represented by the following impulse response  $h(\mathbf{x})$  and transfer function  $H(\mathbf{f})$ :

$$h(\mathbf{x}) = \frac{1}{\|\mathbf{1}\|} \text{rect}\left(\frac{\mathbf{x}^\top \mathbf{e}}{\|\mathbf{1}\|}\right) \cdot \delta(\mathbf{x}^\top \mathbf{e}_\perp) \tag{10.7}$$



$$H(\mathbf{f}) = \text{sinc}(\mathbf{f}^\top \mathbf{1}). \tag{10.8}$$

Hence, the motion blur results in zeros located on parallel lines, see Fig. 10.5(d). By evaluating the distances of the lines, the velocity  $\mathbf{v}$  can be measured in two dimensions (cf. Sec. 13.3) if the exposure time  $T$  is known. ■

**Example 10.3 (Motion blur):** By considering arbitrary, planar, translational motions, this example presents a generalization of Example 10.2. During the exposure process  $t \in [0, T]$ , the sensor is moved on the path  $\mathbf{x}_0(t)$  in the image plane. The observed image is given by

$$g(\mathbf{x}) = s(\mathbf{x}) ** h(\mathbf{x}) + n(\mathbf{x}) = \int_0^T s(\mathbf{x} - \mathbf{x}_0(t)) dt + n(\mathbf{x}). \tag{10.9}$$

The transfer function of the imaging affected by motion blur can be expressed as follows:

$$H(\mathbf{f}) = \mathcal{F} \left\{ \int_0^T s(\mathbf{x} - \mathbf{x}_0(t)) dt \right\} S(\mathbf{f})^{-1}. \tag{10.10}$$



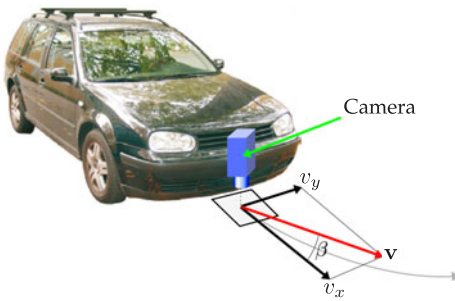
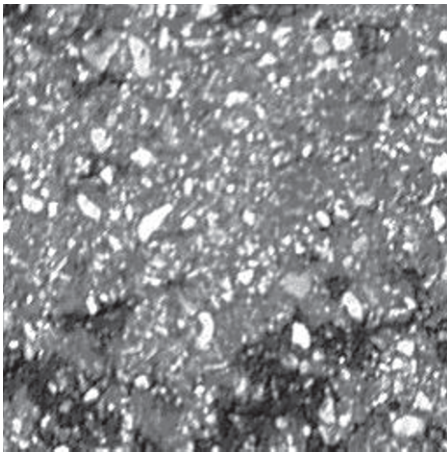
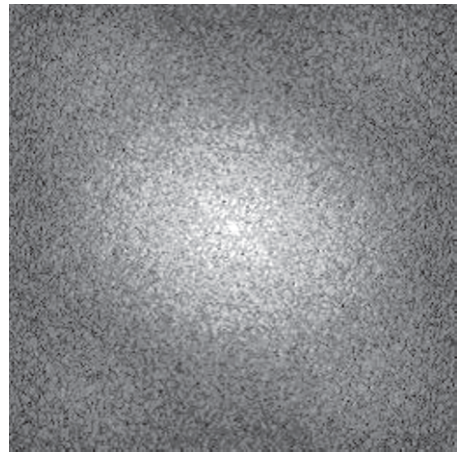


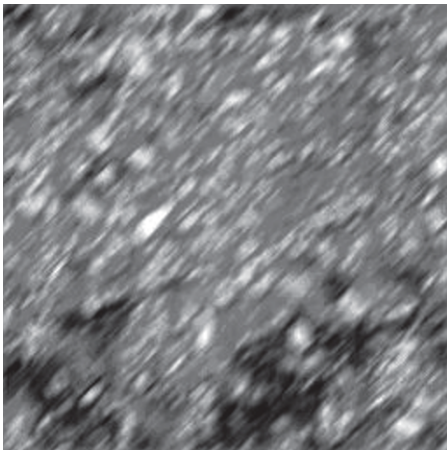
**Figure 10.4.** Two-dimensional measurement of velocity by capturing the motion of the vehicle relative to the street (source: J. Horn [6]).



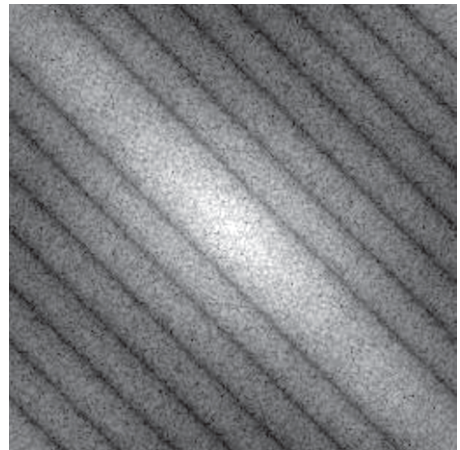
(a) No motion (ideal imaging)



(b) Magnitude spectrum of (a)



(c) Moving street (distorted imaging)



(d) Magnitude spectrum of (c)

**Figure 10.5.** Motion blur. In order to reduce the dynamics, logarithms have been applied to the magnitude spectra (b) and (d) (source: D. vom Stein).

Swapping the order of integration and Fourier transform and using the shift property (8.57) of the Fourier transform results in

$$\mathcal{F} \left\{ \int_0^T s(\mathbf{x} - \mathbf{x}_0(t)) dt \right\} = \int_0^T \mathcal{F}\{s(\mathbf{x} - \mathbf{x}_0(t))\} dt \tag{10.11}$$

$$= \int_0^T S(\mathbf{f}) e^{-j2\pi\mathbf{f}^T \mathbf{x}_0(t)} dt. \tag{10.12}$$

Finally, by inserting (10.12) into (10.10), the following result can be obtained for the transfer function  $H(\mathbf{f})$  and the impulse response function  $h(\mathbf{x})$  of optical imaging affected by motion blur:

$$H(\mathbf{f}) = \int_0^T e^{-j2\pi\mathbf{f}^T \mathbf{x}_0(t)} dt \tag{10.13}$$



$$h(\mathbf{x}) = \int_0^T \delta(\mathbf{x} - \mathbf{x}_0(t)) dt. \tag{10.14}$$

Example 10.7 demonstrates the restoration of an image affected by motion blur. ■

**Example 10.4 (Atmospheric turbulence):** If there is atmospheric turbulence between the imaging optics and the scene which is to be imaged, high spatial frequencies are damped. For a long exposure time, this damping can be described by an optical transfer function of the following kind [7]:

$$H(\mathbf{f}) = \exp\left(-k \|\mathbf{f}\|^{\frac{5}{3}}\right). \tag{10.15}$$

As, in this case, the transfer function  $H(\mathbf{f})$  has no zeros, a restoration is much easier than for a defocused imaging. The factor  $k$  is increased for increasing turbulence. In addition to depending on the strength of the turbulence,  $k$  depends on the focal length and the wavelength. ■

## 10.2 Inverse filter

The inverse filter is the result of minimizing the quadratic difference between the restoration result  $\hat{s}(\mathbf{x})$  filtered with  $h(\mathbf{x})$  and the observation  $g(\mathbf{x})$ :

$$\begin{aligned} & \int_{-\infty}^{\infty} \int_{-\infty}^{\infty} (\hat{s}(\mathbf{x}) ** h(\mathbf{x}) - g(\mathbf{x}))^2 d\mathbf{x} \\ &= \int_{-\infty}^{\infty} \int_{-\infty}^{\infty} (g(\mathbf{x}) ** v(\mathbf{x}) ** h(\mathbf{x}) - g(\mathbf{x}))^2 d\mathbf{x} \xrightarrow{!} \text{Min}. \end{aligned} \tag{10.16}$$

By applying the Plancherel theorem, this equation can be transformed into the spatial frequency domain:

$$\iint_{-\infty}^{\infty} |G(\mathbf{f})V(\mathbf{f})H(\mathbf{f}) - G(\mathbf{f})|^2 d\mathbf{f} \xrightarrow{!} \text{Min}. \quad (10.17)$$

In order to minimize this integral, the integrand has to be as small as possible for every spatial frequency  $\mathbf{f}$ . This is the case if and only if the transfer function of the restoration filter  $V(\mathbf{f})$  is chosen as

$$V(\mathbf{f}) = H^{-1}(\mathbf{f}). \quad (10.18)$$

This transfer function immediately explains the term ‘inverse filter.’ This optimization neglects the effect of the noise  $n(\mathbf{x})$  of the signal model shown in Fig. 10.1.

The Fourier transform of the restoration result is given by

$$\hat{S}(\mathbf{f}) = S(\mathbf{f}) + \frac{N(\mathbf{f})}{H(\mathbf{f})}. \quad (10.19)$$

Finally, an inverse Fourier transform yields

$$\hat{s}(\mathbf{x}) = s(\mathbf{x}) + \mathcal{F}^{-1} \left\{ \frac{N(\mathbf{f})}{H(\mathbf{f})} \right\}. \quad (10.20)$$

This equation shows that the zeros of the transfer function  $H(\mathbf{f})$  of the inverse filter greatly amplify the noise affecting the corresponding spatial frequencies. If  $h(\mathbf{x})$  has low-pass characteristics and if  $n(\mathbf{x})$  represents a broadband signal, the inverse filter results in an amplification of the high-frequency noise. This is why, in practice, the following modified transfer function is often used for the inverse filter:

$$V(\mathbf{f}) = \frac{H^*(\mathbf{f})}{\varepsilon + |H(\mathbf{f})|^2}. \quad (10.21)$$

Here, the parameter  $\varepsilon > 0$  is used to limit the amplitude of the transfer function  $V(\mathbf{f})$ . The following cases can be considered.

- If  $|H(\mathbf{f})|^2 \gg \varepsilon$ , the modified filter operates like an inverse filter:

$$V(\mathbf{f}) \approx H^{-1}(\mathbf{f}). \quad (10.22)$$

- If  $|H(\mathbf{f})|^2 = \varepsilon$ , then

$$V(\mathbf{f}) = \frac{1}{2} H^{-1}(\mathbf{f}). \quad (10.23)$$

- If  $H(\mathbf{f}) = 0$ , i.e., at the zeros of the transfer function, the modification (10.21) results in a completely blocking restoration filter  $V(\mathbf{f})$ :

$$V(\mathbf{f}) = 0. \quad (10.24)$$

Section 10.3 shows that the modified inverse filter (10.21) can also be interpreted as a special case of the Wiener filter for a constant signal-to-noise ratio.

The following examples demonstrate the effect of the inverse filter on RGB color images  $\mathbf{g}(\mathbf{x})$ . In order to achieve an image restoration, the inverse filter  $V(\mathbf{f})$  has to be applied to each of the three color channels separately.

**Example 10.5 (Restoration of a distorted image):** Figure 10.6 shows an example of image restoration using the inverse filter. In order to simulate non-ideal imaging, a Gaussian low-pass filter with the spatial cutoff frequency  $f_c = 80$  was applied to a low-noise RGB color image  $s(\mathbf{x})$  of size  $512 \times 512$ . In addition, normally distributed white noise  $\mathbf{n}(\mathbf{x})$  with a very low variance ( $\sigma^2 = 0.01$ ) was additively superposed on the result of that filtering. The resulting image  $\mathbf{g}(\mathbf{x})$  is shown in Fig. 10.6(a); the transfer function  $H(\mathbf{f})$  of the Gaussian low-pass filter is illustrated in Fig. 10.6(b). In order to allow a better interpretation of the filter, a horizontal section of  $H(\mathbf{f})$  through the origin of the spatial frequency domain is drawn as a dotted line in Fig. 10.6(b).

During the restoration of  $\mathbf{g}(\mathbf{x})$  with the inverse filter (10.18), the high-frequency components of the noise  $\mathbf{n}(\mathbf{x})$  are massively amplified because

$$V(\mathbf{f}) \gg 1 \quad \text{for} \quad \|\mathbf{f}\| \gg f_c \quad (10.25)$$

(cf. Fig. 10.6(d)). Therefore, despite the barely existing noise  $\mathbf{n}(\mathbf{x})$ , the restoration result shown in Fig. 10.6(c) is affected by numerous distortions and is not satisfying at all. Mainly because of its enormous dynamic range, the transfer function  $V(\mathbf{f})$  illustrated in Fig. 10.6(d) seems to be dark except for the border areas: the lowest value  $V(\mathbf{0}) = 1$  is located at the origin ( $\mathbf{f} = \mathbf{0}$ ) of the spatial frequency domain.

The modified inverse filter (10.21) with  $\varepsilon > 0$  blocks for  $H(\mathbf{f}) \rightarrow 0$ —i.e., for high spatial frequencies—and therefore achieves much better results than (10.18). In the present case, the result shown in Fig. 10.6(e) can barely be distinguished from the noise-free original  $s(\mathbf{x})$ . Essentially, the transfer function  $V(\mathbf{f})$  of the modified inverse filter (Fig. 10.6(f)) has band-pass characteristics but the filter can still be passed by low spatial frequencies. ■

**Example 10.6 (Image restoration for defocusing):** Another practically relevant application of inverse filtering is the restoration of defocused images. In order to demonstrate the approach, a low-noise, sharp RGB color image  $s(\mathbf{x})$  of size  $512 \times 512$  (Fig. 10.7(a)) has been convolved with a circular disk having a diameter of 9 pixels, in order to simulate a defocused imaging. The result of the convolution has then been additively superposed with a normally distributed white noise  $\mathbf{n}(\mathbf{x})$  having a variance of  $\sigma^2 = 25$ , see Fig. 10.7(b).

Because of the zeros of the transfer function  $H(\mathbf{f})$  of the defocused optical imaging, a pure inverse filter in accordance with (10.18) is not suitable. Instead, two differently parameterized versions of the modified inverse filter (10.21) have been used. The parameters were chosen to be  $\varepsilon = 0.001$  and  $\varepsilon = 0.01$ , see Fig. 10.7(c) and (d). Obviously, by choosing a greater value of  $\varepsilon$ , the inverse filter blocks for small values of the transfer function  $H(\mathbf{f})$  and achieves an efficient mitigation of the noise of the corresponding spatial frequencies. However, in exchange, the associated components of the desired signal, which in the present case are fine image structures, are also attenuated. This is why Fig. 10.7(c) appears to be sharper than Fig. 10.7(d), despite the distinctive noise.

These considerations are confirmed by an analysis of the corresponding magnitude spectra shown in Fig. 10.7(e) and (f). For better visualization, the amplitudes of the magnitude spectra have been clipped to 1% of the maximum value. ■

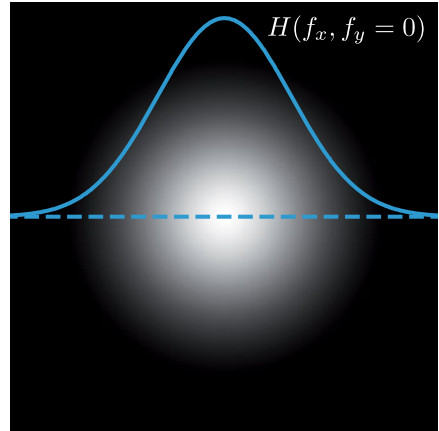
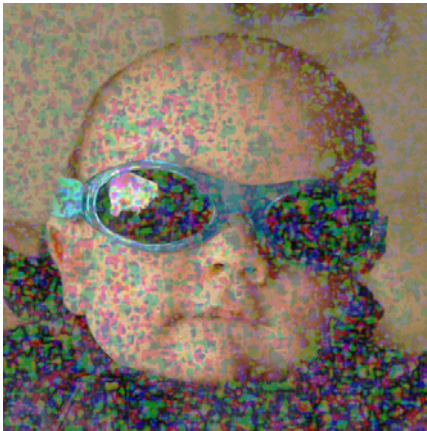
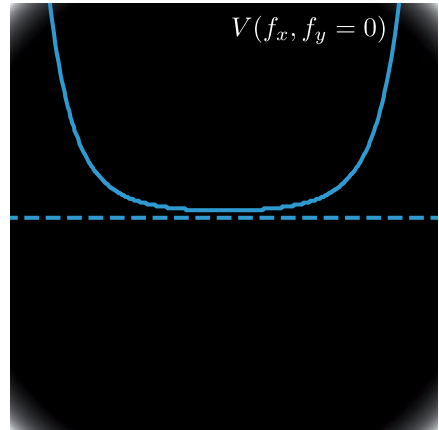
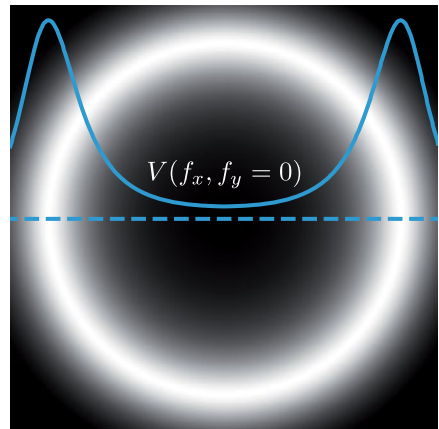
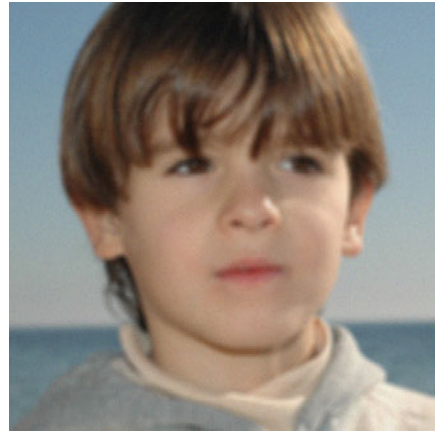
(a) Simulated observation  $g(\mathbf{x})$ (b) Transfer function  $H(\mathbf{f})$  ( $\rho = 80$ )(c) Inverse filtering  $\hat{s}(\mathbf{x})$  ( $\varepsilon = 0$ )(d) Transfer function  $V(\mathbf{f})$  ( $\varepsilon = 0$ )(e) Inverse filtering  $\hat{s}(\mathbf{x})$  ( $\varepsilon = 0.001$ )(f) Transfer function  $V(\mathbf{f})$  ( $\varepsilon = 0.001$ )

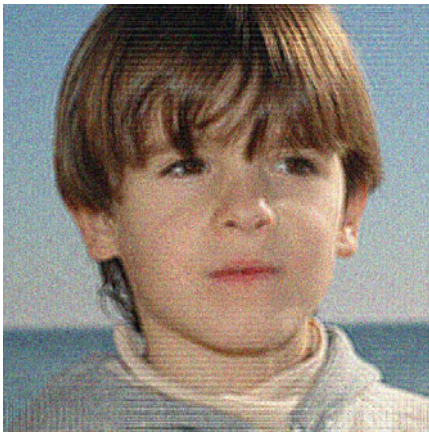
Figure 10.6. Restoration of a distorted image using an inverse filter.



(a) Ideal image  $s(x)$



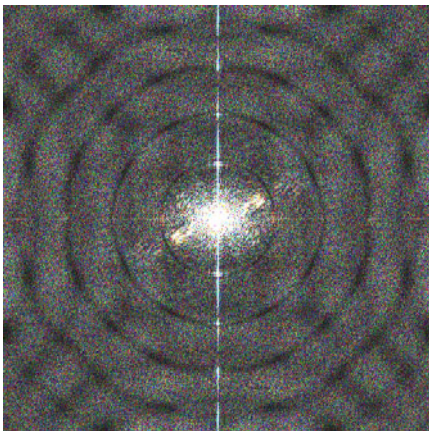
(b) Simulated observation  $g(x)$



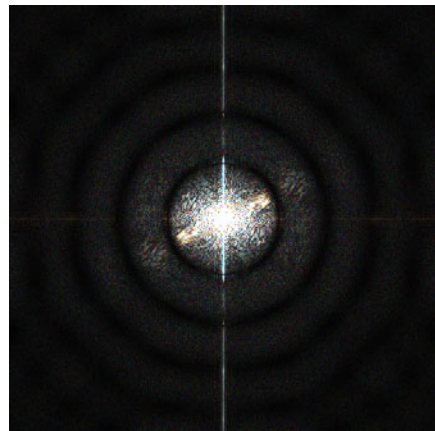
(c) Inverse filtering  $\hat{s}(x)$  ( $\epsilon = 0.001$ )



(d) Inverse filtering  $\hat{s}(x)$  ( $\epsilon = 0.01$ )



(e) Magnitude spectrum  $|\hat{S}(f)|$  of (c)



(f) Magnitude spectrum  $|\hat{S}(f)|$  of (d)

Figure 10.7. Restoration of a defocused image using an inverse filter.

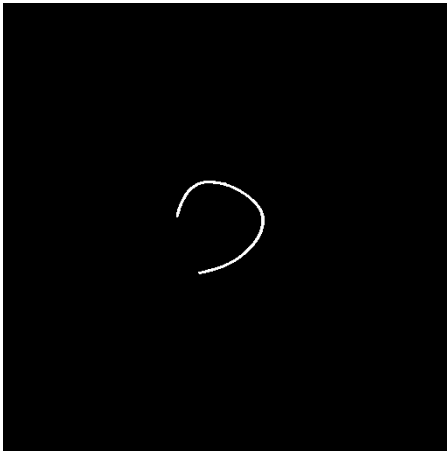
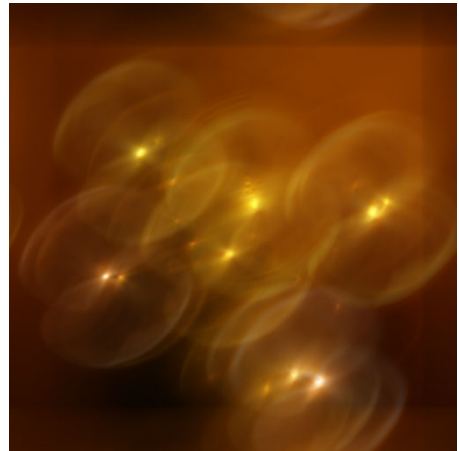
(a) Ideal image without motion blur  $s(x)$ (b) Image affected by motion blur  $g(x)$ (c) Extracted motion pattern  $h(x)$ (d) Result  $\hat{s}(x)$  of the inverse filtering

Figure 10.8. Restoration of an image of fairy lights affected by motion blur.

**Example 10.7 (Image restoration to ameliorate motion blur):** Finally, Fig. 10.8 shows an example of a restoration of an RGB color image affected by motion blur. The ideal signal  $s(x)$  of the steady image of a fairy light is shown in Fig. 10.8(a). The observation  $g(x)$  has been acquired by moving the camera during the exposure of the sensor, see Fig. 10.8(b). By using simple binary morphologic operations (see Chap. 12) after applying a thresholding, the motion pattern shown in Fig. 10.8(c) can be extracted and can be used as an estimate of the impulse response function  $h(x)$  of the non-ideal imaging. By this means, the transfer function  $V(f)$  of a modified inverse filter can be calculated according to (10.21) and the observed image  $g(x)$  can be reconstructed.

However, the limitations of the method are clearly visible in the restoration result  $\hat{s}(x)$  (cf. Fig. 10.8(d)). The zeros of the transfer function  $H(f)$  of the non-ideal imaging result in a loss of information, which is why the resulting image  $\hat{s}(x)$  shows nearly none of the

details of the original scene. Nevertheless, the number and the positions of the individual lights are clearly shown in this image. ■

## 10.3 The Wiener filter

The Wiener filter<sup>1</sup> is an optimal linear filter used for signal estimation, which minimizes the mean squared error between the original signal  $s(\mathbf{x})$  and the estimation result  $\hat{s}(\mathbf{x})$  (cf. Fig. 10.1). In the field of image processing, the Wiener filter is one of the standard tools of image restoration [5].

Unlike the signal model shown in Fig. 10.1, the Wiener filter requires the signals  $s(\mathbf{x})$  and  $n(\mathbf{x})$ —and therefore also the derived signals  $g(\mathbf{x})$  and  $\hat{s}(\mathbf{x})$ —to be weakly stationary random processes, so that they can be described by their power spectral densities in the spatial frequency domain using the Wiener–Khinchine theorem (Theorem 8.16). Furthermore, the noise signal  $n(\mathbf{x})$  is assumed to be zero-mean:

$$\mu_n = E\{n(\mathbf{x})\} = 0. \quad (10.26)$$

To simplify matters, the original signal  $s(\mathbf{x})$  and the zero-mean noise  $n(\mathbf{x})$  are assumed to be uncorrelated:

$$r_{sn}(\boldsymbol{\tau}) = \mu_s \mu_n = 0; \quad (10.27)$$

in fact, the Wiener filter can also be formulated for noise signals which are correlated with  $s(\mathbf{x})$ .

In order to achieve the highest similarity of the restoration result  $\hat{s}(\mathbf{x})$  to the original  $s(\mathbf{x})$  as possible, the optimization minimizes the mean squared error:

$$E\{(s(\mathbf{x}) - \hat{s}(\mathbf{x}))^2\} \xrightarrow{!} \text{Min}. \quad (10.28)$$

Expanding (10.28) in combination with (8.260) and (8.287) yields

$$E\{(s(\mathbf{x}) - \hat{s}(\mathbf{x}))^2\} = E\{s^2(\mathbf{x}) - 2s(\mathbf{x})\hat{s}(\mathbf{x}) + \hat{s}^2(\mathbf{x})\} \quad (10.29)$$

$$= r_{ss}(\mathbf{0}) - 2r_{s\hat{s}}(\mathbf{0}) + r_{\hat{s}\hat{s}}(\mathbf{0}) \quad (10.30)$$

$$= \iint_{-\infty}^{\infty} (S_{ss}(\mathbf{f}) - 2S_{s\hat{s}}(\mathbf{f}) + S_{\hat{s}\hat{s}}(\mathbf{f})) d\mathbf{f}. \quad (10.31)$$

A one-dimensional auxiliary calculation is used to obtain the cross power spectral density  $S_{s\hat{s}}(\mathbf{f})$  depending on  $S_{ss}(\mathbf{f})$ .

---

**Auxiliary Calculation 10.1 (The effect of an LSI system on a random process):** Applying an LSI system to a random process  $g(x)$  results in the process

$$k(x) = g(x) * h(x) = \int g(x - \alpha) h(\alpha) d\alpha, \quad (10.32)$$

---

<sup>1</sup>The Wiener filter (also called the Wiener–Kolmogorov filter) is named after the American mathematician Norbert Wiener (1894–1964).





Figure 10.9. Effect on a stochastic process  $g(x)$  of an LSI system.

where  $h(x)$  denotes the impulse response function of the LSI system (cf. Fig. 10.9). In the case of weak stationarity, (8.260) implies the following for the cross correlation function  $r_{gk}(\tau)$  of the processes  $g(x)$  and  $k(x)$ :

$$r_{gk}(\tau) = E\{g(x) k(x + \tau)\} \quad (10.33)$$

$$= E\left\{g(x) \int g(x + \tau - \alpha) h(\alpha) d\alpha\right\} \quad (10.34)$$

$$= \int E\{g(x) g(x + \tau - \alpha)\} h(\alpha) d\alpha \quad (10.35)$$

$$= \int r_{gg}(\tau - \alpha) h(\alpha) d\alpha. \quad (10.36)$$

Because of the symmetry of the autocorrelation function  $r_{gg}(\tau)$ , this is equivalent to

$$r_{gk}(\tau) = \int r_{gg}(\alpha - \tau) h(\alpha) d\alpha = r_{gg}(\tau) * h(-\tau), \quad (10.37)$$

which results in the following after applying the Fourier transform:

$$S_{gk}(f) = S_{gg}(f) H^*(f). \quad (10.38)$$

■

Because of (10.38) and since  $s(x)$  and  $n(x)$  are uncorrelated as in (10.27), the cross power spectral density  $S_{s\hat{s}}(\mathbf{f})$  can be expressed as

$$S_{s\hat{s}}(\mathbf{f}) = V^*(\mathbf{f}) H^*(\mathbf{f}) S_{ss}(\mathbf{f}) + V^*(\mathbf{f}) \underbrace{S_{sn}(\mathbf{f})}_{=0}. \quad (10.39)$$

Similarly, the following results for the power spectral density  $S_{\hat{s}\hat{s}}(\mathbf{f})$  by employing (8.300):

$$S_{\hat{s}\hat{s}}(\mathbf{f}) = |V(\mathbf{f})|^2 \underbrace{(|H(\mathbf{f})|^2 S_{ss}(\mathbf{f}) + S_{nn}(\mathbf{f}))}_{=: \Gamma(\mathbf{f})} = |V(\mathbf{f})|^2 \Gamma(\mathbf{f}) \quad (10.40)$$

with

$$\Gamma(\mathbf{f}) := |H(\mathbf{f})|^2 S_{ss}(\mathbf{f}) + S_{nn}(\mathbf{f}). \quad (10.41)$$

To simplify matters, the dependency on  $\mathbf{x}$  and  $\mathbf{f}$  will now be omitted. With (10.39) and (10.40), the mean squared error (10.31) is given by:

$$E\{(s - \hat{s})^2\} = \iint (S_{ss} (1 - 2V^*H^*) + |V|^2 \Gamma) d\mathbf{f}. \quad (10.42)$$

The integrand is real-valued if

$$V(\mathbf{f}) = \alpha(\mathbf{f}) H^*(\mathbf{f}), \quad \alpha(\mathbf{f}) \in \mathbb{R}, \quad (10.43)$$

for all  $\mathbf{f}$ . Insertion of (10.43) into (10.42) yields

$$E\{(s - \hat{s})^2\} = \iint (S_{ss}(1 - 2\alpha|H|^2) + \alpha^2|H|^2\Gamma) d\mathbf{f} \xrightarrow{!} \text{Min.} \quad (10.44)$$

In order to minimize the integral (10.44), the integrand has to be minimal for all  $\mathbf{f}$ . Hence, the following necessary condition has to be met:

$$\frac{\partial}{\partial \alpha} = 0 : \quad -2|H|^2 S_{ss} + 2\alpha|H|^2 \Gamma = 0 \quad (10.45)$$

$$\Leftrightarrow \quad \alpha = \frac{S_{ss}}{\Gamma}. \quad (10.46)$$

The sufficient condition for a minimum is always met:

$$\frac{\partial^2}{\partial \alpha^2} > 0 : \quad 2|H|^2 \Gamma > 0. \quad (10.47)$$

Finally, the approach (10.43), (10.46) and (10.41) yields the optimal filter according to Wiener:

$$V(\mathbf{f}) = \frac{H^*(\mathbf{f}) S_{ss}(\mathbf{f})}{|H(\mathbf{f})|^2 S_{ss}(\mathbf{f}) + S_{nn}(\mathbf{f})} = \frac{1}{H(\mathbf{f})} \cdot \frac{|H(\mathbf{f})|^2}{|H(\mathbf{f})|^2 + \underbrace{\frac{S_{nn}(\mathbf{f})}{S_{ss}(\mathbf{f})}}_{SNR^{-1}(\mathbf{f})}}. \quad (10.48)$$

According to the right-hand side of these equations, the Wiener filter is a series of an inverse filter and a modified noise mitigation filter, which often shows a low-pass characteristic. If there is no noise, i.e., if  $\mathbf{n}(\mathbf{x}) \equiv 0$ , then  $V(\mathbf{f})$  turns out to be the transfer function of the inverse filter. Otherwise, the filter is ‘open’ for spatial frequencies where the desired signal dominates the noise, and on the other hand, the filter is ‘blocking’ for spatial frequencies where the noise dominates the signal sought.

As the minimal squared error does not correspond to the human visual perception of quality, the results of this optimal filter are usually not perceived to be optimal in terms of visual quality, which represents a drawback of the Wiener filter. Nevertheless, the following example shows that it is absolutely possible to achieve visually convincing restoration results using the Wiener filter.

---

**Example 10.8 (Restoration of defocused images):** In this example, a color image  $\mathbf{g}(\mathbf{x})$  (Fig. 10.10(a)) is considered, in which some spectral components are attenuated or suppressed by a simulated defocused optical imaging  $H(\mathbf{f})$ . The amplitude  $|H(\mathbf{f})|$  of the defocused optical imaging is rotationally symmetric and has zeros on concentric circles as in Example 10.1; the amplitude is illustrated in Figures 10.10(c) and 10.10(e). Furthermore, the observed signal  $\mathbf{g}(\mathbf{x})$  is affected by an additive normally distributed white noise  $\mathbf{n}(\mathbf{x})$  of variance  $\sigma^2 = 25$ .

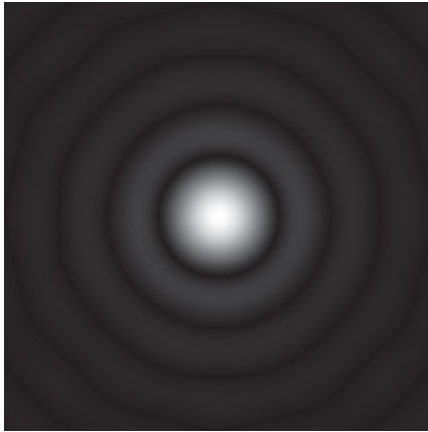
Besides the power spectral density  $S_{nn}(\mathbf{f})$  of the noise  $\mathbf{n}(\mathbf{x})$ , which, by (8.301), is constant for a white noise process and is assumed to be known for this example, the power spectral density  $S_{ss}(\mathbf{f})$  of the undistorted original image  $\mathbf{s}(\mathbf{x})$  is needed for the calculation of the transfer function  $V(\mathbf{f})$  of the Wiener filter. Since usually this quantity is not available, it has been estimated from the observation  $\mathbf{g}(\mathbf{x})$  for the present case. Hence, the periodogram  $\hat{S}_{gg}(f)$  has been calculated and smoothed; subsequently, the known power spectral density  $S_{nn}(\mathbf{f})$  of the noise process was subtracted. Figure 10.10(d) shows



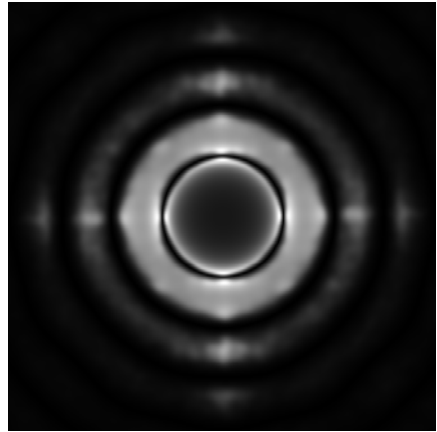
(a) Simulated observation  $g(x)$



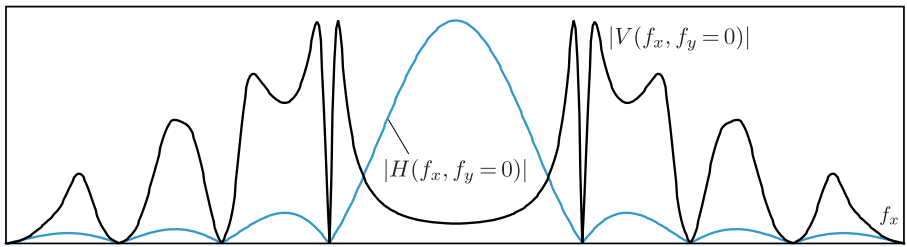
(b) Result  $\hat{s}(x)$  of the Wiener filtering



(c) Amplitude  $|H(f)|$



(d) Amplitude  $|V(f)|$



(e) Amplitudes of defocused imaging  $|H(f)|$  and Wiener filter  $|V(f)|$

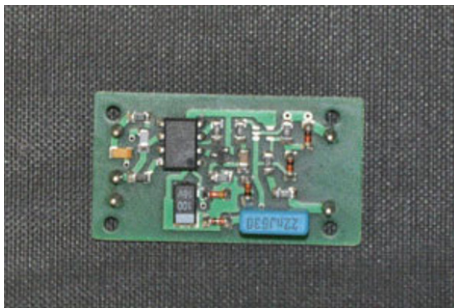
**Figure 10.10.** Wiener filter for image restoration: (a) Observed signal  $g(x)$  ( $h(x) = k \cdot \text{rect}(\|x\|/9)$ ;  $n(x)$ : Normally distributed white noise with  $\sigma^2 = 25$ ); (b) Result  $\hat{s}(x)$  of the restoration with the Wiener filter; (c) Amplitude  $|H(f)|$  of the defocused optical imaging; (d) Amplitude  $|V(f)|$  of the Wiener optimal filter; (e) Comparison of the amplitudes of the defocused optical imaging  $|H(f)|$  with the Wiener filter  $|V(f)|$ .

the transfer function  $V(f)$  of the Wiener filter which was calculated in accordance with (10.48). The result of the Wiener filtering is shown in Fig. 10.10(b). Compared to the results of the inverse filtering shown in Fig. 10.7(c) and (d), the result of the Wiener filter stands out because of its effective noise reduction.

Figure 10.10(e) shows horizontal sections of the amplitudes of  $H(f)$  and  $V(f)$  through the origin of the spatial frequency domain in order to allow a better interpretation of the Wiener filter. Although both amplitudes share the same zeros, the Wiener filter achieves a higher amplification of those spatial frequencies for which the signal dominates the noise, which is constant in the present case. Similarly, the filter 'blocks' those spatial frequencies for which the noise dominates the signal sought. ■

**Example 10.9 (Image restoration for uniform linear motion blur):** Figure 10.11(a) shows an image of a PCB placed on a still conveyor belt. When the conveyor belt is running, the uniform linear motion results in a convolution of the image with an impulse response function according to (10.7). Additionally, every individual pixel is affected by a sensor noise, that is assumed to be independent from that of the other pixels. Based on these assumptions, an artificial image  $g(x)$  affected by noise and motion blur has been simulated (see Fig. 10.11(b)).

The ideal, noise-free image  $s(x)$  can be estimated by acquiring multiple images of the



(a) Motionless image

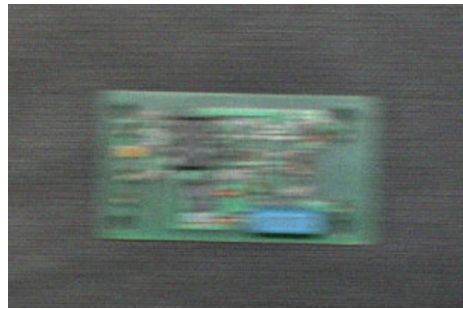
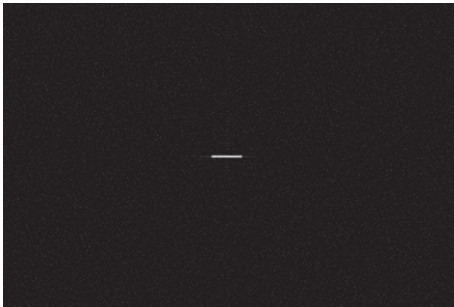
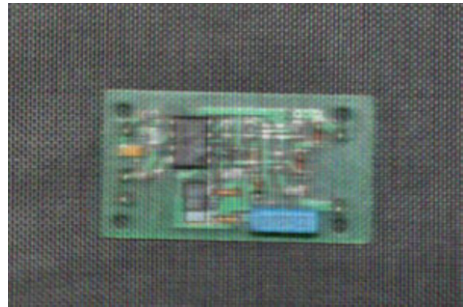
(b) Image  $g(x)$  affected by motion blur(c) Estimated impulse response  $\hat{h}(x)$ (d) Restoration result  $\hat{s}(x)$ 

Figure 10.11. Image restoration for blur caused by a uniform linear motion.

PCB on the still conveyor belt and by averaging these images. The transfer function  $H(\mathbf{f})$  of the non-ideal imaging is described by (10.8); it can be estimated by a system identification, e.g., by computing the following quotient of mean power spectral densities [10]:

$$\hat{H}(\mathbf{f}) = \frac{\overline{\hat{S}_{gs}(f)}}{\overline{\hat{S}_{ss}(f)}} \approx \frac{G(f) \overline{\hat{S}_{ss}(f)}}{\overline{\hat{S}_{ss}(f)}}. \quad (10.49)$$

Figure 10.11(c) shows the corresponding estimated impulse response  $\hat{h}(\mathbf{x})$ . By means of periodograms, the power spectral densities of the noise-free image and of the noise can be estimated. Using the impulse response and the estimated power spectral densities, the optimal restoration filter  $V(\mathbf{f})$  according to Wiener can be designed. By employing this filter, a noise-free and sharp image  $\hat{s}(\mathbf{x})$  can be estimated out of camera images affected by noise and motion blur, which are acquired when the conveyor belt is running (Fig. 10.11(d)). ■

## 10.4 The geometric mean filter

The **geometric mean filter** can be considered as a generalization of the Wiener filter, which is supposed to be superior especially for weak distortions  $n(\mathbf{x})$  or for random variations of a non-ideal imaging  $H(\mathbf{f})$ , (see [1]). It is defined by the transfer function

$$V(\mathbf{f}) = \left( \frac{H^*(\mathbf{f})}{|H(\mathbf{f})|^2} \right)^a \cdot \left( \frac{H^*(\mathbf{f})}{|H(\mathbf{f})|^2 + b \frac{S_{nn}(\mathbf{f})}{S_{ss}(\mathbf{f})}} \right)^{1-a} \quad (10.50)$$

with the real-valued parameters  $a \in [0, 1]$  and  $b \geq 0$ . Different choices of  $a$  and  $b$  result in a parametric family of restoration filters, which contains both the inverse filter and the Wiener filter as special cases:

- Choosing  $a = 1$  results in the inverse filter.
- Choosing  $a = 0$  and  $b = 1$  results in the Wiener filter.
- Choosing  $a = 0$  results in the **parameterized Wiener filter**:

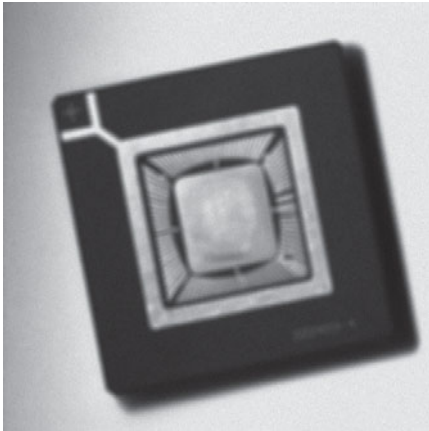
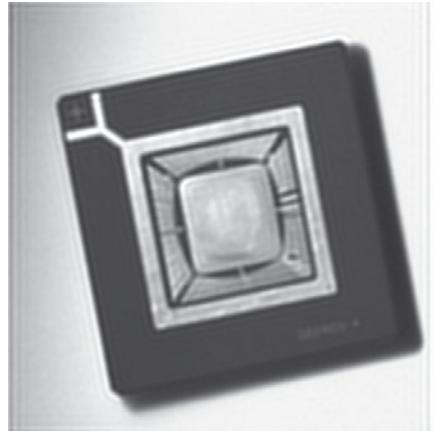
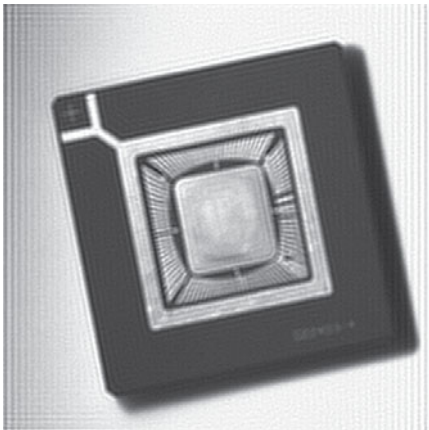
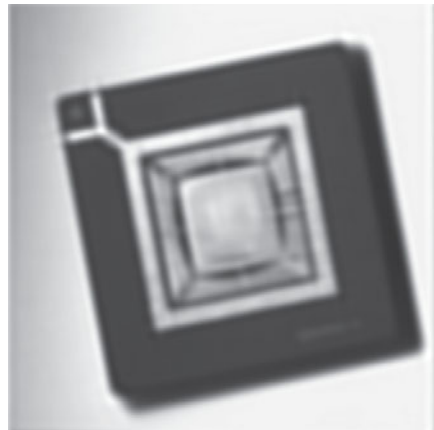
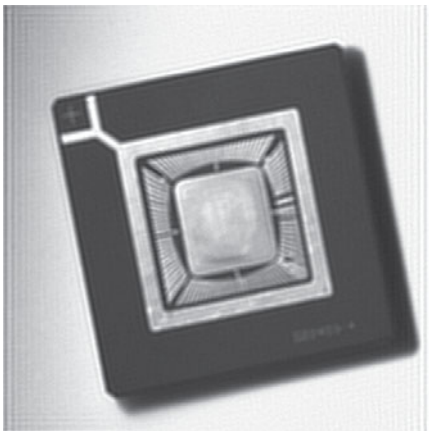
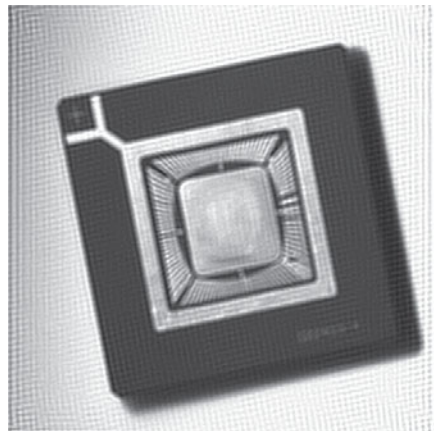
$$V(\mathbf{f}) = \frac{H^*(\mathbf{f})}{|H(\mathbf{f})|^2 + b \frac{S_{nn}(\mathbf{f})}{S_{ss}(\mathbf{f})}}. \quad (10.51)$$

- Choosing  $a = 0.5$  and  $b = 1$  results in the geometric mean filter.

The parameter  $b$  adjusts the amount of noise mitigation and ‘undistortion’. If  $b$  is chosen inside the interval  $0 < b < 1$ , (10.50) and (10.51) are supposed to yield results that are more visually pleasing than the results of the Wiener filter [2].

**Example 10.10 (Image restoration using the geometric mean filter):** In order to illustrate the influence of the two parameters  $a$  and  $b$  of the geometric mean filter, the defocused image of a chip  $g(\mathbf{x})$  shown in Fig. 10.12(a) is considered, which is affected by an additive, normally distributed white noise  $n(\mathbf{x})$  of variance  $\sigma^2 = 25$ . For the simulation of the defocused optical imaging, the transfer function  $H(\mathbf{f})$  has been parameterized as in Example 10.8, cf. Fig. 10.10(c).

Beginning with the parameters of the Wiener filter ( $a = 0$  and  $b = 1$ , cf. Fig. 10.12(b)),

(a) Simulated observation  $g(x)$ (b) Filtering with  $a = 0$  and  $b = 1$ (c) Filtering with  $a = 0$  and  $b = 10^{-3}$ (d) Filtering with  $a = 0$  and  $b = 10^3$ (e) Filtering with  $a = 0.8$  and  $b = 1$ (f) Filtering with  $a = 0.95$  and  $b = 1$ **Figure 10.12.** Restoration of a defocused, noisy image using the geometric mean filter.

the SNR can be weighted in (10.50) by varying  $b$ , so that either inverse filtering or the mitigation of the noise is dominant, see Figs. 10.12(c) and (d), respectively. This corresponds to the parameterized Wiener filter (10.51).

For a constant  $b = 1$ , choosing  $a > 0$  allows a higher influence of the inverse filtering, resulting in a 'sharper' impression of the image. Particularly for  $a = 0.8$ , the fine structures of the chip show much more contrast in the resulting image than in Fig. 10.12(b), without intensely amplifying the noise, cf. Fig. 10.12(e). In contrast, for  $a = 0.95$ , artifacts and distortions are clearly visible, cf. Fig. 10.12(f). ■

## 10.5

## 10.5 Optimal constraint filter

A drawback of the Wiener filter (Sec. 10.3) and the related geometric mean filter (Sec. 10.4) is the need to know the power spectral densities  $S_{ss}(\mathbf{f})$  and  $S_{nn}(\mathbf{f})$  of, respectively, the desired signal and the noise. In contrast, the requirements of the optimal constraint filter can be met rather easily. Besides the observation  $g(\mathbf{x})$  and the impulse response function  $h(\mathbf{x})$  of the non-ideal imaging, only the energy of the noise

$$\rho = \iint_{\Omega_g} n^2(\mathbf{x}) \, d\mathbf{x} \quad (10.52)$$

is required, where  $\Omega_g$  denotes the spatial area of the image  $g(\mathbf{x})$  [4, 8, 14].

As the energy  $\rho$  of the noise is known, it is quite easy to adapt the approach (10.16) of the inverse filter, which minimizes the squared difference of the observation  $g(\mathbf{x})$  and the restoration result  $\hat{s}(\mathbf{x})$  of the filtering with  $h(\mathbf{x})$ , to the following condition:

$$\iint_{\Omega_g} (g(\mathbf{x}) - \hat{s}(\mathbf{x}) ** h(\mathbf{x}))^2 \, d\mathbf{x} \stackrel{!}{=} \rho. \quad (10.53)$$

As there is no unique solution to this equation, it is used as a *constraint* and another optimization target is formulated for the regularization of the restoration problem:

$$\iint_{\Omega_g} (\hat{s}(\mathbf{x}) ** c(\mathbf{x}))^2 \, d\mathbf{x} \xrightarrow{!} \text{Min}. \quad (10.54)$$

The term  $c(\mathbf{x})$  represents an arbitrary design parameter and is the impulse response function of an LSI filter, which usually has high-pass characteristics. Hence, the condition (10.54) requires  $\hat{s}(\mathbf{x})$  to be smooth. By using Parseval's theorem, the conditions (10.53) and (10.54) can be transformed into the spatial frequency domain:

$$\iint_{-\infty}^{\infty} |G(\mathbf{f}) - \hat{S}(\mathbf{f}) H(\mathbf{f})|^2 \, d\mathbf{f} \stackrel{!}{=} \rho, \quad (10.55)$$

$$\iint_{-\infty}^{\infty} |\hat{S}(\mathbf{f}) C(\mathbf{f})|^2 \, d\mathbf{f} \xrightarrow{!} \text{Min}. \quad (10.56)$$

In order to minimize the expression (10.56) with respect to the constraint (10.55), a Lagrange multiplier  $\lambda$  is introduced:

$$\iint_{-\infty}^{\infty} |\hat{S}(\mathbf{f}) C(\mathbf{f})|^2 d\mathbf{f} + \lambda \cdot \left( \iint_{-\infty}^{\infty} |G(\mathbf{f}) - \hat{S}(\mathbf{f}) H(\mathbf{f})|^2 d\mathbf{f} - \rho \right) \xrightarrow{!} \text{Min.} \quad (10.57)$$

With  $\hat{S}(\mathbf{f}) = V(\mathbf{f}) G(\mathbf{f})$ , an auxiliary calculation (for details see [14, pp. 99]) results in

$$V(\mathbf{f}) = \frac{1}{H(\mathbf{f})} \cdot \frac{\lambda |H(\mathbf{f})|^2}{|C(\mathbf{f})|^2 + \lambda |H(\mathbf{f})|^2}. \quad (10.58)$$

Finally, inserting this result into (10.55) yields

$$\iint_{-\infty}^{\infty} \frac{|C(\mathbf{f})|^4 |G(\mathbf{f})|^2}{(|C(\mathbf{f})|^2 + \lambda |H(\mathbf{f})|^2)^2} d\mathbf{f} = \rho. \quad (10.59)$$

This equation has to be solved numerically, in order to determine the Lagrange multiplier  $\lambda$  needed in (10.58).

**Remarks:**

- In the case of the constraint filter, the solution only applies to a single image  $g(\mathbf{x})$ , i.e., for a single sample function, as the Lagrange multiplier  $\lambda$  depends on both the image  $g(\mathbf{x})$  and the energy  $\rho$  of the noise and has to be recalculated if any of these conditions change. In contrast, the Wiener filter fits all sample functions of a stochastic process  $g(\mathbf{x})$ .
- Increasing the energy  $\rho$  of the noise leads to smaller values of the Lagrange multiplier  $\lambda$ . If on the other hand, the energy  $\rho$  reaches zero, the constraint filter turns into the inverse filter:

$$(\rho \rightarrow 0) \Rightarrow V(\mathbf{f}) \rightarrow H^{-1}(\mathbf{f}). \quad (10.60)$$

- Typically, the transfer function  $H(\mathbf{f})$  of a non-ideal imaging shows low-pass characteristics. If  $C(\mathbf{f})$  is chosen as a high-pass, the restoration filter  $V(\mathbf{f})$  corresponds to an inverse filter with a subsequent low-pass.

**Example 10.11 (Restoration of a motion blurred test image):** As an example of image restoration using the optimal constraint filter, consider the video test image shown in Fig. 10.13(a). In this case, non-ideal imaging is simulated as a linear motion blur as in Example 10.2 under an angle of  $21^\circ$  (mathematically positive), see Fig. 10.13(b).

The restoration results shown in Fig. 10.13(c) and (d) were obtained by a modified inverse filtering according to (10.21) and by an optimal constraint filtering. For the constraint filtering, the filter function  $c(\mathbf{x})$  was chosen as a spatially discrete Laplace filter as in (11.59) that is proportional to the squared magnitude of the spatial frequency, penalizing high-frequency components in the restoration result  $\hat{s}(\mathbf{x})$ . Because of the required smoothness (10.54), Fig. 10.13(d) is less affected by high-frequency noise than Fig. 10.13(c). ■



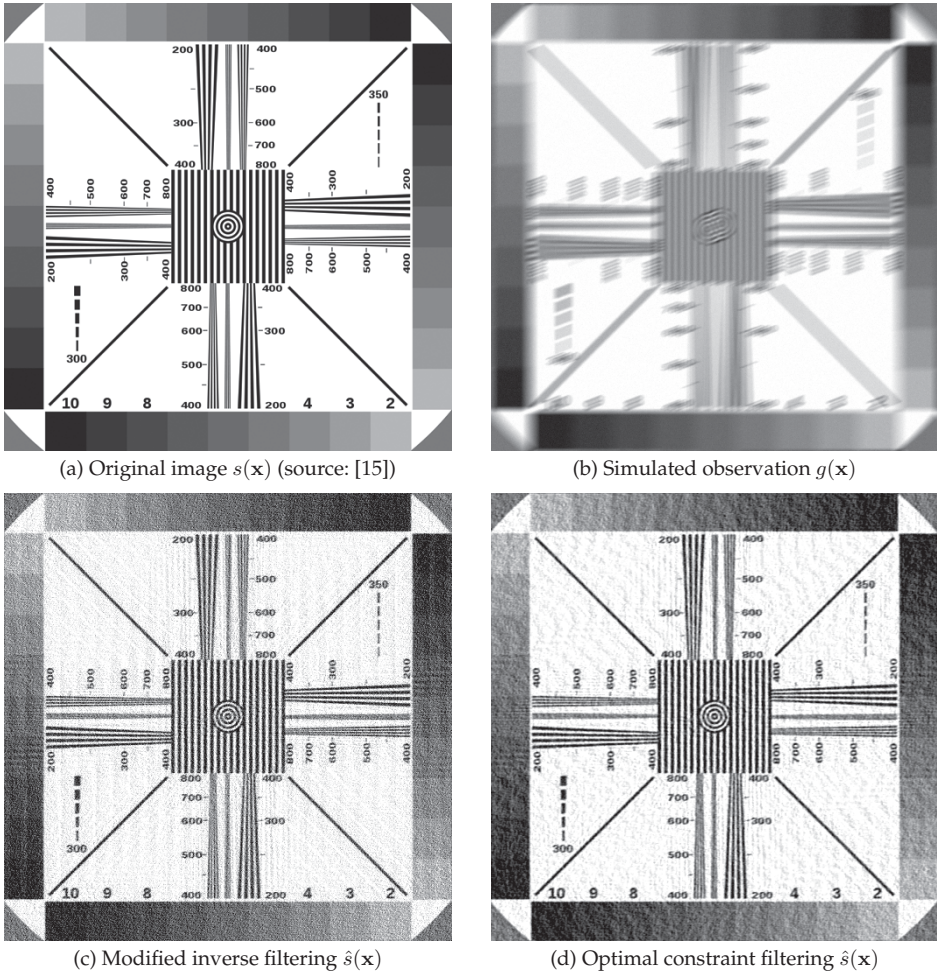
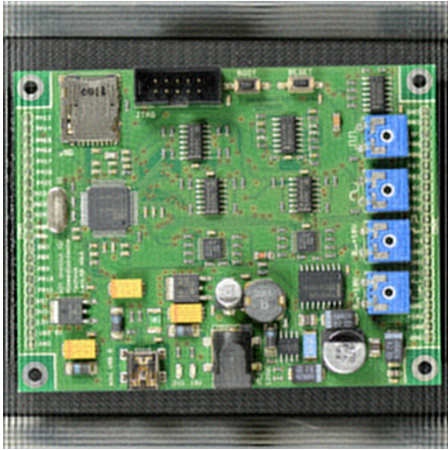


Figure 10.13. Restoration of a motion blurred image.

**Example 10.12 (Optimal constraint filtering of a blurred image):** In order to allow a comparison of the optimal constraint filter with the Wiener filter, Fig. 10.14 shows four different results of restoring the defocused RGB color image of Fig. 10.10(a). The filter function was always chosen as a spatially discrete Laplace filter according to (11.59). As, in practice, the energy  $\rho$  of the noise is usually not exactly known, slightly altered estimates  $\hat{\rho}$  have been used for numerically solving (10.59), in order to evaluate the robustness of the method.

The quality of the results is clearly dependent on the choice of these parameters. Although the best restoration result shown in Fig. 10.14(b) is quite similar to the result of the Wiener filter 10.10(b), here, a noise energy that was 10% higher than the actual value had to be employed. By further increasing this parameter, too many high-frequency details were suppressed (cf. Fig. 10.14(c) and (d)); for smaller choices of the noise energy,



(a) Restoration result  $\hat{s}(\mathbf{x})$  ( $\hat{\rho} = \rho$ )



(b) Restoration result  $\hat{s}(\mathbf{x})$  ( $\hat{\rho} = 1.1 \rho$ )



(c) Restoration result  $\hat{s}(\mathbf{x})$  ( $\hat{\rho} = 1.2 \rho$ )



(d) Restoration result  $\hat{s}(\mathbf{x})$  ( $\hat{\rho} = 1.4 \rho$ )

Figure 10.14. Restoration of the defocused image shown in Fig. 10.10(a) using an optimal constraint filter.

distortions and several overshoots arose (cf. Fig. 10.14(a)).

If the parameter  $\rho$  is chosen to be constant, a similar variation of the constraint filter can be achieved by adjusting the Lagrange multiplier  $\lambda$  with respect to the optimal value. ■

## 10.6 Restoration problems in matrix notation

For the restoration approaches covered up to now, the images were considered to be continuous signals. If they are discretized,

$$g(\mathbf{x}), s(\mathbf{x}), n(\mathbf{x}), h(\mathbf{x}) \xrightarrow{\text{Discretization}} g_{mn}, s_{mn}, n_{mn}, h_{mn}, \quad (10.61)$$

and aligned as column vectors, restoration problems can be formulated in matrix notation.

A discrete original image  $s_{mn}$  of size  $P \times Q$  results in a column vector  $\mathbf{s} \in \mathbb{R}^{PQ}$ . If the observed image  $g_{mn}$  and the noise  $n_{mn}$  consist of  $M \times N$  pixels, the corresponding column vectors are given by  $\mathbf{g}, \mathbf{r} \in \mathbb{R}^{MN}$ . By this means, the restoration problem can be written as

$$\mathbf{g} = \mathbf{H}\mathbf{s} + \mathbf{n}, \quad (10.62)$$

where  $\mathbf{H}$  represents an  $MN \times PQ$  matrix corresponding to  $h_{mn}$ .

This representation is beneficial, as it enables the use of matrix operations. Furthermore,  $\mathbf{H}$  can even describe non-LSI systems. Unfortunately, the matrix  $\mathbf{H}$  is very large and usually ill-conditioned. Therefore, special characteristics of  $\mathbf{H}$  have to be exploited in order to obtain a solution.

---

**Example 10.13 (The Wiener filter in matrix notation):** If the signals shown in Fig. 10.1 are represented as column vectors, according to (10.62), the observed signal is given by

$$\mathbf{g} = \mathbf{H}\mathbf{s} + \mathbf{n}. \quad (10.63)$$

By (10.2), the restoration result is

$$\hat{\mathbf{s}} = \mathbf{V}\mathbf{g} = \mathbf{V}\mathbf{H}\mathbf{s} + \mathbf{V}\mathbf{n}. \quad (10.64)$$

The Wiener filter aims at minimizing the mean squared error (MSE):

$$\text{MSE} = \text{E}\{(\mathbf{s} - \hat{\mathbf{s}})^T(\mathbf{s} - \hat{\mathbf{s}})\} \xrightarrow{!} \text{Min}; \quad (10.65)$$

the statistical properties of the noise  $\mathbf{n}$  and of the desired signal  $\mathbf{s}$  are given by the corresponding correlation matrices:

$$\text{E}\{\mathbf{nn}^T\} = \mathbf{R}_{\mathbf{nn}}, \quad \text{E}\{\mathbf{n}\} = \mathbf{0}, \quad (10.66)$$

$$\text{E}\{\mathbf{ss}^T\} = \mathbf{R}_{\mathbf{ss}}, \quad (10.67)$$

$$\text{E}\{\mathbf{ns}^T\} = \mathbf{0}. \quad (10.68)$$

Finally, the filter matrix  $\mathbf{V}$  that minimizes (10.65) has to be found.

The optimization approach (10.65) can be expressed as follows:

$$\text{MSE} = \text{E}\{(\mathbf{s} - \hat{\mathbf{s}})^T(\mathbf{s} - \hat{\mathbf{s}})\} \quad (10.69)$$

$$= \text{E}\{\text{Trace}((\mathbf{s} - \hat{\mathbf{s}})(\mathbf{s} - \hat{\mathbf{s}})^T)\} \quad (10.70)$$

$$= \text{Trace}(\text{E}\{\hat{\mathbf{s}}\hat{\mathbf{s}}^T - \hat{\mathbf{s}}\mathbf{s}^T - \mathbf{s}\hat{\mathbf{s}}^T + \mathbf{ss}^T\}). \quad (10.71)$$

For the first term of the expected value, one has

$$\text{E}\{\hat{\mathbf{s}}\hat{\mathbf{s}}^T\} = \text{E}\{\mathbf{V}\mathbf{g}\mathbf{g}^T\mathbf{V}^T\} = \mathbf{V}\text{E}\{\mathbf{g}\mathbf{g}^T\}\mathbf{V}^T = \dots \quad (10.72)$$

$$= \mathbf{V}(\mathbf{H}\mathbf{R}_{\mathbf{ss}}\mathbf{H}^T + \mathbf{R}_{\mathbf{nn}})\mathbf{V}^T. \quad (10.73)$$

The remaining terms can be rewritten similarly. Using the positive-definite matrix

$$\mathbf{Q} := \mathbf{H}\mathbf{R}_{\mathbf{ss}}\mathbf{H}^T + \mathbf{R}_{\mathbf{nn}}, \quad (10.74)$$

Equation (10.71) can be expressed as follows:

$$\text{MSE} = \text{Trace}(\mathbf{V} \mathbf{Q} \mathbf{V}^T - \mathbf{V} \mathbf{H} \mathbf{R}_{ss} - \mathbf{R}_{ss} \mathbf{H}^T \mathbf{V}^T + \mathbf{R}_{ss}) \quad (10.75)$$

$$\begin{aligned} & + \mathbf{R}_{ss} \mathbf{H}^T \mathbf{Q}^{-1} \mathbf{Q} \mathbf{Q}^{-1} \mathbf{H} \mathbf{R}_{ss} - \mathbf{R}_{ss} \mathbf{H}^T \mathbf{Q}^{-1} \mathbf{Q} \mathbf{Q}^{-1} \mathbf{H} \mathbf{R}_{ss}) \\ & = \text{Trace}(\underbrace{(\mathbf{V} - \mathbf{R}_{ss} \mathbf{H}^T \mathbf{Q}^{-1}) \mathbf{Q} (\mathbf{V} - \mathbf{R}_{ss} \mathbf{H}^T \mathbf{Q}^{-1})^T}_{\mathbf{A}} \\ & \quad + \underbrace{(\mathbf{R}_{ss} - \mathbf{R}_{ss} \mathbf{H}^T \mathbf{Q}^{-1} \mathbf{H} \mathbf{R}_{ss})}_{\mathbf{B}}). \end{aligned} \quad (10.76)$$

As the second term  $\mathbf{B}$  of (10.76) is independent of  $\mathbf{V}$ , it can be neglected when minimizing the mean squared error with respect to  $\mathbf{V}$ . Because the covariance matrix  $\mathbf{A}$  is positive-semidefinite, Equation (10.76) is minimal if  $\mathbf{A} = \mathbf{0}$ . Then, the following holds for the minimal mean squared error:

$$\text{MSE}_{\min} = \text{Trace}(\mathbf{R}_{ss} - \mathbf{R}_{ss} \mathbf{H}^T \mathbf{Q}^{-1} \mathbf{H} \mathbf{R}_{ss}) \quad (10.77)$$

$$= \text{Trace}(\mathbf{R}_{ss} \mathbf{R}_{nn} (\mathbf{H} \mathbf{R}_{ss} \mathbf{H}^T + \mathbf{R}_{nn})^{-1}). \quad (10.78)$$

The constraint  $\mathbf{A} = \mathbf{0}$  results in the following optimal filter matrix  $\mathbf{V}$ :

$$\mathbf{V} = \mathbf{R}_{ss} \mathbf{H}^T \mathbf{Q}^{-1} \quad (10.79)$$

$$= \mathbf{R}_{ss} \mathbf{H}^T (\mathbf{H} \mathbf{R}_{ss} \mathbf{H}^T + \mathbf{R}_{nn})^{-1} \quad (10.80)$$

$$= (\mathbf{H}^T \mathbf{R}_{nn}^{-1} \mathbf{H} + \mathbf{R}_{ss}^{-1})^{-1} \mathbf{H}^T \mathbf{R}_{nn}^{-1}. \quad (10.81)$$

If the matrices  $\mathbf{H}^T$  and  $\mathbf{R}_{nn}^{-1}$  commute, the filter matrix  $\mathbf{V}$  can be written as

$$\mathbf{V} = (\mathbf{H}^T \mathbf{H} + \mathbf{R}_{ss}^{-1} \mathbf{R}_{nn})^{-1} \mathbf{H}^T. \quad (10.82)$$

As a final remark, the expected value of the cross product of the vector of the estimation error  $(\hat{\mathbf{s}} - \mathbf{s})$  and the observation vector  $\mathbf{g}^T$  can be calculated:

$$\mathbb{E}\{(\hat{\mathbf{s}} - \mathbf{s}) \mathbf{g}^T\} = \mathbb{E}\{(\mathbf{V} \mathbf{g} - \mathbf{s})(\mathbf{H} \mathbf{s} + \mathbf{n})^T\} \quad (10.83)$$

$$= \mathbb{E}\{(\mathbf{V} \mathbf{H} \mathbf{s} + \mathbf{V} \mathbf{n} - \mathbf{s})(\mathbf{s}^T \mathbf{H}^T + \mathbf{n}^T)\} \quad (10.84)$$

$$\begin{aligned} & = \mathbb{E}\{\mathbf{V} \mathbf{H} \mathbf{s} \mathbf{s}^T \mathbf{H}^T + \mathbf{V} \mathbf{n} \mathbf{s}^T \mathbf{H}^T - \mathbf{s} \mathbf{s}^T \mathbf{H}^T \\ & \quad - \mathbf{V} \mathbf{H} \mathbf{s} \mathbf{n}^T + \mathbf{V} \mathbf{n} \mathbf{n}^T - \mathbf{s} \mathbf{n}^T\} \end{aligned} \quad (10.85)$$

$$= \mathbf{V} \mathbf{H} \mathbf{R}_{ss} \mathbf{H}^T + \mathbf{V} \mathbf{R}_{nn} - \mathbf{R}_{ss} \mathbf{H}^T \quad (10.86)$$

$$= \mathbf{V} (\mathbf{H} \mathbf{R}_{ss} \mathbf{H}^T + \mathbf{R}_{nn}) - \mathbf{R}_{ss} \mathbf{H}^T. \quad (10.87)$$

Applying equation (10.80) yields the principle of orthogonality

$$\mathbb{E}\{(\hat{\mathbf{s}} - \mathbf{s}) \mathbf{g}^T\} = \mathbf{0} \quad (10.88)$$

of the vector of the estimation error  $(\hat{\mathbf{s}} - \mathbf{s})$  and the observation vector  $\mathbf{g}$ . ■

## 10.7 Restoration for participating media

If the medium between the illumination, the object, and the camera interacts considerably with the light, the medium is called participating.

Since the distances to the investigated object are typically rather short in automated visual inspection applications, the properties of the medium of air can mostly be neglected. Exceptions are smoke, steam, and the shimmer above heated objects. However, for the medium of water, the transport of the light is affected to such an extent by the absorption and scattering caused by turbidity, that these effects usually have to be taken into account.

There are important applications of automated visual inspection underwater, e.g., the inspection of a ship's hull, submarine cables, underwater pipelines, the foundations of offshore wind farms, etc. Diving missions for underwater inspections are expensive or even impossible for humans, depending on the depth. This is why remotely controlled or autonomous underwater vehicles equipped with artificial illumination and a camera are increasingly used for such tasks. However, this requires restoration methods capable of canceling or at least significantly mitigating the effects of the medium on the image acquisition.

In vacuum, light can propagate freely, so that the radiance  $L(\mathbf{r}, \mathbf{x})$  does not change with respect to the direction of propagation  $\mathbf{r}$ ,

$$\mathbf{r}^T \text{grad}_{\mathbf{x}} L(\mathbf{r}, \mathbf{x}) = 0, \quad (10.89)$$

i.e., the radiance remains constant along the direction of propagation:

$$L(\mathbf{r}, \mathbf{x} + \rho \mathbf{r}) = L(\mathbf{r}, \mathbf{x}), \quad \text{with } \rho \in \mathbb{R}. \quad (10.90)$$

In participating media, such as haze, fog, smoke, or water, there is an interaction between the radiation and the medium. This leads to image degradations, such as color shifts, reductions in contrast, and blurring. Figure 10.15 is an example of an underwater image with these image degradations, which are mainly caused by absorption and scattering.



**Figure 10.15.** (a) Camera image of a pillar illuminated by daylight through the water surface. At this depth, the green and blue components of the spectrum of daylight are obviously already emphasized. The image degradations typical of participating media are clearly visible: color shifts, blurring, and a reduced contrast. (b) Result of image enhancement. By estimating a transmission map [13], the contrast, which had been lost due to the scattering caused by the turbidity, could be increased by means of a local histogram equalization.

Absorption is caused, e.g., if some of the radiation energy is transformed into heat energy by the medium. The change in the radiance induced by this absorption is linearly dependent

on the strength of the radiance

$$\mathbf{r}^T \text{grad}_{\mathbf{x}} L(\mathbf{r}, \mathbf{x}) = -\mu L(\mathbf{r}, \mathbf{x}). \quad (10.91)$$

From this differential equation, the Lambert–Beer law can be derived:

$$L(\mathbf{r}, \mathbf{x} + \rho \mathbf{r}) = L(\mathbf{r}, \mathbf{x}) e^{-\mu \rho}. \quad (10.92)$$

In water, the absorption coefficient  $\mu = \mu(\lambda)$  is heavily dependent on the wavelength  $\lambda$  of light. Since the long-wave components of the visible spectral range are more intensely attenuated than the short-wave components, underwater images usually have a blue or green tint.

Scattering denotes the effect of particles inside the medium stochastically altering the direction of propagation. On the one hand, the radiance at a certain point is reduced by scattering, but on the other hand, it is increased by light scattered to this point from other directions. Together, absorption and scattering lead to the radiative transfer equation (RTE) [3,9]:

$$\mathbf{r}^T \text{grad}_{\mathbf{x}} L(\mathbf{r}, \mathbf{x}) = -(\mu + b) L(\mathbf{r}, \mathbf{x}) + C(\mathbf{r}, \mathbf{x}). \quad (10.93)$$

The scatter-induced increase of the radiance can be determined by integrating the radiance over the unit sphere  $S^2$  at the point  $\mathbf{x}$ :

$$C(\mathbf{r}, \mathbf{x}) := \int_{S^2} L(\mathbf{r}', \mathbf{x}) \beta(\mathbf{r}' \rightarrow \mathbf{r}, \mathbf{x}) \, d\mathbf{r}'. \quad (10.94)$$

Here, the volume scattering function  $\beta(\mathbf{r}' \rightarrow \mathbf{r}, \mathbf{x})$  describes the distribution of the scattering as a function of the angle  $\angle(\mathbf{r}', \mathbf{r})$  between  $\mathbf{r}'$  and  $\mathbf{r}$  at the position  $\mathbf{x}$ . Integrating over the unit sphere results in the scattering coefficient

$$b := \int_{S^2} \beta(\mathbf{0} \rightarrow \mathbf{r}, \mathbf{x}) \, d\mathbf{r}, \quad (10.95)$$

which, in homogeneous media, is independent of the position  $\mathbf{x}$ .

For image restoration, a sufficiently exact model of the image formation process is needed. In [12], the three paths of light propagation are considered, which are the most important for the formation of the image (see Fig. 10.16). Propagation paths with two or more scattering events are neglected here, since they contribute less to the light field.

The direct component includes all paths which originate at the light source, are reflected at the surface, and are captured by the camera sensor. The indirect component contains all light rays which are scattered into the direction of the camera without being reflected at the object surface. The blurring component comprises the light rays which come from the light source, are reflected at the object surface, and are scattered into an adjacent line of sight. Together, all three components can be expressed as an affine transformation in matrix notation:

$$\mathbf{g} = \mathbf{H}\mathbf{s} + \mathbf{b} = (\mathbf{H}_{\text{direct}} + \mathbf{H}_{\text{indirect}}) \mathbf{s} + \mathbf{b}. \quad (10.96)$$

The matrix  $\mathbf{H}$  is the sum of the direct component  $\mathbf{H}_{\text{direct}}$  and the indirect component  $\mathbf{H}_{\text{indirect}}$ . The vector  $\mathbf{b}$  contains the blur component. The elements of the matrix  $\mathbf{H}$  and

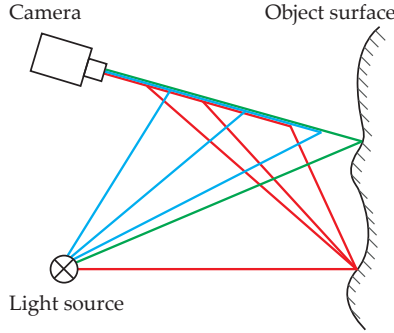


**Figure 10.16.** Separation of the most relevant paths of light propagation into three components. The direct component (green) is the light from the light source that is reflected at the surface. The indirect component (blue) is the light of the light source that is scattered into the line of sight. The blurring component (red) are the light rays that are reflected at the surface and scattered into the line of sight.

of the vector  $\mathbf{b}$  can be determined by means of the radiative transfer equation [12]. If the observed object can be described by a plane perpendicular to the optical axis,  $\mathbf{H}$  describes a linear shift-invariant system.

A difficulty involved in the restoration of images taken in participating media is the estimation of the necessary parameters. Mostly, the coefficient of absorption and the volume scatter function are not known sufficiently exactly. This is why a so-called blind image restoration method is used, which concurrently estimates the model  $\mathbf{H}$  but penalizes differences from an initial model  $\tilde{\mathbf{H}}$ :

$$(\hat{\mathbf{H}}, \hat{\mathbf{s}}) := \arg \min_{\mathbf{H}, \mathbf{s}} \{ \|\mathbf{H}\mathbf{s} + \mathbf{b} - \mathbf{g}\|^2 + \eta_1 Q(\mathbf{s}) + \eta_2 R(\mathbf{H}) \}. \tag{10.97}$$

The regularization term

$$Q(\mathbf{s}) := \sum_i \sqrt{[D_x \mathbf{s}]_i^2 + [D_y \mathbf{s}]_i^2} \tag{10.98}$$

corresponds to the isotropic total variation, with  $D_x$  and  $D_y$  denoting discrete approximations of the partial differentiation operators  $\frac{\partial}{\partial x}$  and  $\frac{\partial}{\partial y}$ . The scalars  $[D_x \mathbf{s}]_i$  and  $[D_y \mathbf{s}]_i$  denote the  $i$ th element of the vectors  $D_x \mathbf{s}$  and  $D_y \mathbf{s}$ . The regularization term

$$R(\mathbf{H}) := \sum_{i,j} \|H_{i,j} - \tilde{H}_{i,j}\|^2 \tag{10.99}$$

quadratically penalizes the difference between the model  $\mathbf{H}$  and the initial estimation  $\tilde{\mathbf{H}}$ .

In order to process color images, the restoration approach can be separately applied to every color channel with individually adjusted parameters: see the example in Fig. 10.17.

## 10.8 Spatially-varying image restoration

Up to now, a spatially-invariant image degradation has been assumed, i.e., every pixel  $\mathbf{x}$  has been affected by the same image degradation. Accordingly, spatially-invariant restoration filters have been used.

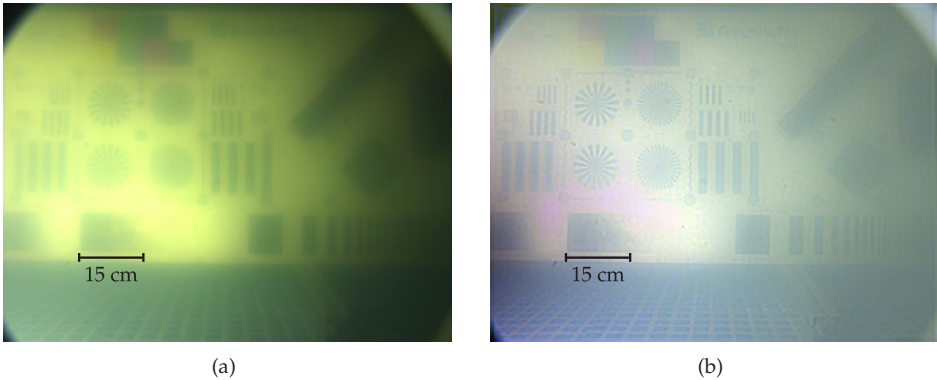


**Figure 10.17.** (a) Image in turbid water of a planar test pattern aligned perpendicularly to the optical axis of the camera at a distance of 1.5 m. (b) Restoration result—both the color shift and the blurring have been significantly reduced [12].

However, spatial invariance does not hold for every application [14]. In general, a spatially-varying image restoration requires much more effort. In some cases it is in fact possible to make a spatially-varying restoration problem spatially-invariant, e.g., by performing a coordinate transformation, cf. Sec. 9.2.1. The spatially-invariant restoration methods covered in this chapter can be applied to the transformed image and the result can be transformed back into the original coordinate system.

**Example 10.14 (Rotational motion blur):** As an example, images affected by a rotational motion blur will be considered. In this case, the function of the image degradation is spatially-varying: the blur is increased for higher distances from the axis of rotation. Points located on a section of an arc around the center of the rotation are superposed during the exposure time and form a blurred image. As the radian measure  $\Delta\varphi$  of the section of the arc is constant, its size increases for greater radii. However, if the image is transformed into polar coordinates  $(r, \varphi)$ , the image degradation is spatially-invariant and corresponds to a convolution with a rectangle

$$h(r, \varphi) = \frac{1}{|\Delta\varphi|} \text{rect}\left(\frac{\varphi}{|\Delta\varphi|}\right) \delta(r) \quad (10.100)$$

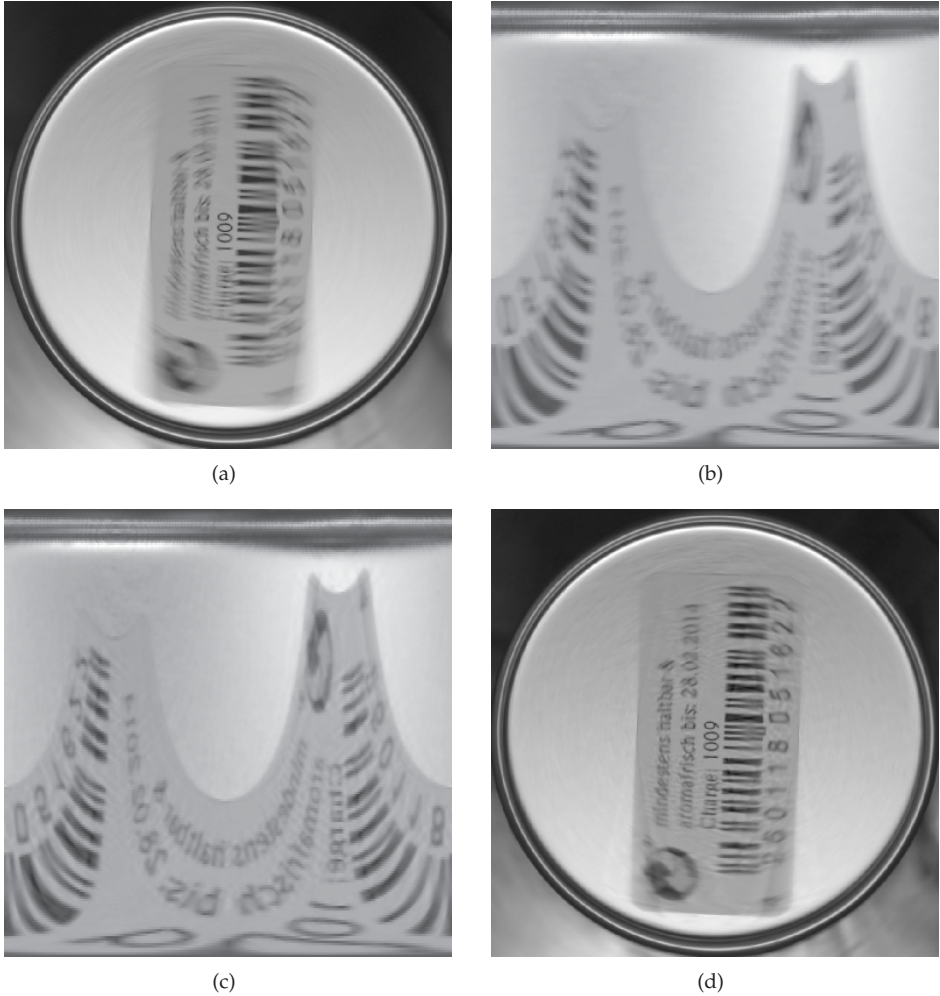
in the direction of the angle coordinate  $\varphi$ . Now the transformed image  $\gamma(r, \varphi)$  can be restored using, for example, a Wiener filter [11]. Finally, the conversion into polar coordinates is undone, so that the restoration result is given in the original coordinate system.

Figure 10.18 shows the results of this method for an image of a rotating can. After the restoration, the writing on the label of the can appears more clearly. ■

## 10.9 Bibliography

- [1] Harry Andrews and Bobby Hunt. *Digital Image Restoration*. Prentice Hall, 1977.
- [2] Kenneth Castleman. *Digital Image Processing*. Prentice Hall, 1996.





**Figure 10.18.** Spatially-varying image restoration using a transformation to polar coordinates: (a) Original image of a can affected by a rotational motion blur; (b) Representation of (a) in polar coordinates—the blur is clearly visible in the horizontal direction ( $\varphi$  direction); (c) Result of the Wiener filter; (d) Restored image in the original Cartesian coordinates.

- [3] Subrahmanyan Chandrasekhar. *Radiative Transfer*. Courier Corporation, 1960.
- [4] Kris Dines and Avinash Kak. Constrained least squares filtering. *IEEE Transactions on Acoustics, Speech and Signal Processing*, 25(4):346–350, 1977.
- [5] Rafael Gonzalez and Richard Woods. *Digital image processing*. Pearson Prentice Hall, 3rd edition, 2008.
- [6] Jan Horn. *Zweidimensionale Geschwindigkeitsmessung texturierter Oberflächen mit flächenhaften bildgebenden Sensoren*. PhD thesis, Universität Karlsruhe (TH), 2007.
- [7] R. Hufnagel and N. Stanley. An algorithm for the machine calculation of complex Fourier series. *Journal of the Optical Society of America*, 54(1):52–61, 1964.

- [8] B. Hunt. The Application of Constrained Least Squares Estimation to Image Restoration by Digital Computer. *IEEE Transactions on Computers*, C-22(9):805–812, 1973.
- [9] Curtis Mobley. *Light and water: Radiative transfer in natural waters*. Academic press, 1994.
- [10] Fernando Puente León and Uwe Kiencke. *Messtechnik – Systemtheorie für Ingenieure und Informatiker*. Springer, 9th edition, 2012.
- [11] Alexander Sawchuk. Space-variant image restoration by coordinate transformations. *Journal of the Optical Society of America*, 64(2):138–144, 1974.
- [12] Thomas Stephan and Jürgen Beyerer. Computergraphical Model for Underwater Image Simulation and Restoration. In *ICPR Workshop on Computer Vision for Analysis of Underwater Imagery (CVAUI)*, pages 73–79, 2014.
- [13] Thomas Stephan, Peter Frühberger, Stefan Werling, and Michael Heizmann. Model based image restoration for underwater images. In *SPIE Optical Metrology 2013*, page 87911F. International Society for Optics and Photonics, 2013.
- [14] Friedrich Wahl. *Digitale Bildsignalverarbeitung*. Springer, 1989.
- [15] Wikipedia. Optical resolution, [http://en.wikipedia.org/wiki/Optical\\_resolution](http://en.wikipedia.org/wiki/Optical_resolution).

Chapter 11  
**Segmentation**

## 11 Segmentation

11.1 Region-based segmentation . . . . .	556
11.1.1 Segmentation by feature-based classification . . . . .	556
11.1.2 Region growing methods . . . . .	562
11.2 Edge-oriented methods . . . . .	562
11.2.1 Gradient filters . . . . .	564
11.2.1.1 Construction of symmetric linear gradient filters . . . . .	566
11.2.1.2 Differentiation using the DFT . . . . .	568
11.2.1.3 Gradient-of-Gaussian filter . . . . .	570
11.2.1.4 Simple edge operators . . . . .	572
11.2.2 Edge detection using the second derivative . . . . .	572
11.2.3 The watershed transformation . . . . .	576
11.3 Diffusion filters . . . . .	578
11.3.1 Linear, homogeneous, isotropic image diffusion . . . . .	579
11.3.2 Linear, inhomogeneous, isotropic image diffusion . . . . .	580
11.3.3 Nonlinear, inhomogeneous, isotropic image diffusion . . . . .	581
11.3.4 Nonlinear, inhomogeneous, anisotropic image diffusion . . . . .	581
11.4 Active contours . . . . .	586
11.4.1 Gradient vector flow . . . . .	591
11.4.2 Vector field convolution . . . . .	593
11.5 Segmentation according to Mumford and Shah . . . . .	594
11.6 Segmentation using graph cut methods . . . . .	596
11.7 Bibliography . . . . .	604

# 11 Segmentation

Segmentation tries to decompose an image  $g(\mathbf{x})$  into separate, meaningful areas. For example, the test object is isolated from the background, or the borders between different objects are detected. An automated analysis of a segmented image is often easier than that of an unprocessed image. The result of the segmentation could be used to determine the position and orientation of the segmented objects in a subsequent processing step.

In medical image processing, segmentation methods are of great importance. Here, the borders between the different organs or tissues have to be found in images acquired using X-rays, ultrasound, or magnetic resonance imaging.

In order to formally describe the segmentation problem, a so-called uniformity criterion is introduced. The interior of the segments of the image is supposed to be uniform to a certain extent, and to simultaneously differ from the adjacent segments. The choice of the uniformity criterion depends on the application on hand.

---

## Definition 11.1: Complete segmentation

11.1

Complete segmentation denotes a division of the set  $\Omega_g$  of all image points of  $g(\mathbf{x})$ ,  $\mathbf{x} \in \Omega_g$  into  $I$  disjoint, non-empty subsets  $\omega_1, \dots, \omega_I$  in such a way that the following holds for a certain uniformity criterion  $\mathcal{E}$  [36, 42]:

1.  $\bigcup_{i=1}^I \omega_i = \Omega_g$ ; the subsets partition the domain.
2.  $\forall i: \omega_i$  is connected.
3.  $\forall i: \mathcal{E}(\omega_i)$  is met.
4. For every union of two adjacent  $\omega_i, \omega_j$ ,  $\mathcal{E}(\omega_i \cup \omega_j)$  is not met.

A uniformity criterion is a function that assigns a truth value to every subset of  $\Omega_g$ :

$$\mathcal{E} : \begin{cases} \mathcal{P}(\Omega_g) & \rightarrow \{\text{true}, \text{false}\} \\ \omega & \mapsto e, \end{cases} \quad (11.1)$$

where  $\mathcal{P}(\Omega_g)$  denotes the power set, i.e., the set of all subsets of  $\Omega_g$ . The uniformity criterion  $\mathcal{E}(\omega)$  depends only on the image values  $g(\mathbf{x})$  of the pixels  $\mathbf{x} \in \omega$ . Besides, it is true for each non-empty subset of a set  $\omega$  if it is true for  $\omega$ :

$$\mathcal{E}(\omega) = \text{true} \quad \Rightarrow \quad \forall \iota \subseteq \omega, \iota \neq \emptyset : \mathcal{E}(\iota) = \text{true}. \quad (11.2)$$

◇

For example, a simple uniformity criterion is one that requires the differences between the image values of the pixels of  $\omega$  to stay below a certain threshold  $\varepsilon$ :

$$\mathcal{E}(\omega) = \text{true} \quad :\Leftrightarrow \quad \forall \mathbf{x}, \mathbf{y} \in \omega : |g(\mathbf{x}) - g(\mathbf{y})| < \varepsilon. \quad (11.3)$$

In general, image segmentation is a hard problem. Often, the observed intensities vary more intensely inside the desired segments than at their borders. Other factors, such as noise and inhomogeneous illumination conditions, further complicate the task. Fig. 11.1 shows an example of a segmentation task, which is hard even for humans.

In the following, two different approaches for solving the segmentation task will be covered: region-based methods and edge-based methods [42].



Figure 11.1. Example of a hard segmentation task: A Dalmatian in snow-covered scenery (source: E. Schneider).

## 11.1 Region-based segmentation

### 11.1.1 Segmentation by feature-based classification

Region-based segmentation methods assign a feature vector  $\mathbf{m}(\mathbf{x}) \in \mathcal{M} \subseteq \mathbb{R}^K$  to every pixel  $\mathbf{x} \in \Omega_g$ .

For example, clustering is used to partition the feature space  $\mathcal{M}$  into  $I$  disjoint decision regions  $\mathcal{R}_i$ :

$$\bigcup_{i=1}^I \mathcal{R}_i = \mathcal{M}, \quad \mathcal{R}_i \cap \mathcal{R}_j = \emptyset \text{ if } i \neq j. \tag{11.4}$$

By means of the assignment

$$\mathbf{m}(\mathbf{x}) \in \mathcal{R}_i \Rightarrow \hat{\omega}(\mathbf{x}) := \omega_i \tag{11.5}$$

a segmentation of the image points can be obtained.

However, the obtained segments  $\omega_i$  are not necessarily connected, in which case the conditions of Def. 11.1 are not met.

In a  $K$ -dimensional feature space, the borders between the decision regions  $\mathcal{R}_i$  are described by  $(K-1)$ -dimensional hyperplanes (Fig. 11.2). These borders constitute the classifier

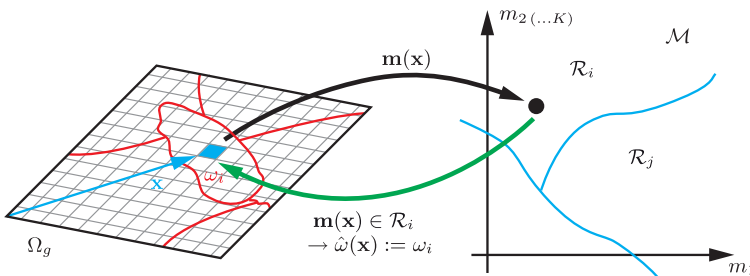


Figure 11.2. Segmentation of an image into regions  $\omega_i$  using a classification in the feature space. The right side illustrates a two-dimensional section through the  $K$ -dimensional feature space  $\mathcal{M}$ .

and have to be learned from examples. The quality of the result depends on the classification performance and hence on the suitability of the chosen features and on the set of training samples.

In this approach, the region-based segmentation is equivalent to the standard classification problem in pattern recognition [4, 18]. The decomposition of  $\mathcal{M}$  into the decision regions  $\mathcal{R}_i$  and the decision rule  $\mathbf{m} \mapsto \hat{\omega} \in \{\omega_1, \dots, \omega_I\}$  represents a **classification** of the image points  $\mathbf{x}$  based on their features  $\mathbf{m}(\mathbf{x})$ . Therefore, common classifiers used in pattern recognition are applicable.

---

**Example 11.1 (Image values as a feature vector):** The easiest way of choosing a feature space is to directly use the image value (the gray value in the case of a gray-scale image) of the pixel as its feature:  $\mathbf{m}(\mathbf{x}) = g(\mathbf{x})$ ,  $K = 1$ .

The segmentation is performed by defining decision regions (in this case gray value intervals) and their boundaries (thresholds).

Similarly, the vector  $\mathbf{g}(\mathbf{x})$  of the color values or spectral values of a pixel  $\mathbf{x}$  can be used as a feature vector for multichannel images or multispectral images [28, 33]. ■

---

**Example 11.2 (Illumination series):** A circuit board is to be segmented into its three regions: ground substrates, gold, and silver (Fig. 11.3). For this purpose, the setup described in Sec. 7.5.1 is used in order to acquire an image series with varying illumination conditions. The image values  $g_i(\mathbf{x})$  of the pixel  $\mathbf{x}$  of the different illumination setups  $i = 1, \dots, K$  describe a possible feature vector for the segmentation:  $\mathbf{m}(\mathbf{x}) = (g_1(\mathbf{x}), \dots, g_K(\mathbf{x}))^T$ . Based on this feature vector, different classifiers, such as linear discriminant analysis or clustering, can be applied [24]. ■

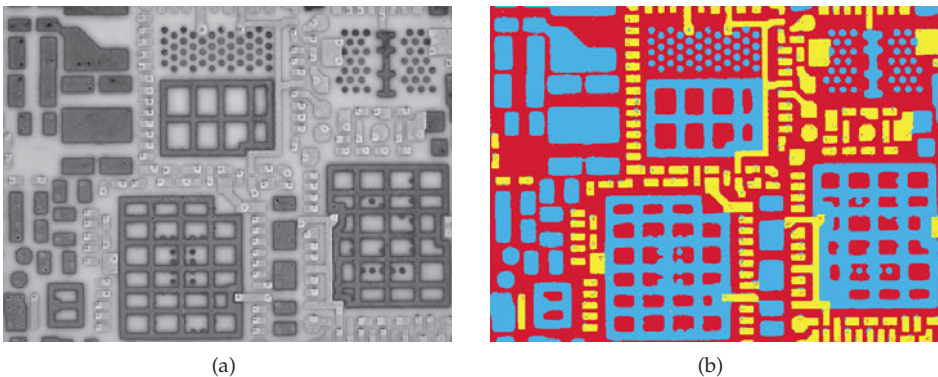


**Figure 11.3.** Segmentation of the different materials of a circuit board: (a) Gray-scale image of the test object acquired under diffuse illumination; (b) Segmentation result in false colors (red  $\hat{=}$  ground substrate, yellow  $\hat{=}$  gold, blue  $\hat{=}$  silver).

**Example 11.3 (Mean and standard deviation):** For some applications, also the statistics of the local distribution of the image values can be used as features. For example,

$$\mathbf{m}(\mathbf{x}) = \begin{pmatrix} \hat{\mu}(\mathbf{x}) \\ \hat{\sigma}(\mathbf{x}) \end{pmatrix} \quad (11.6)$$

is considered with the mean local gray value  $\hat{\mu}(\mathbf{x}) =: m_1(\mathbf{x}) \geq 0$  and the local standard deviation  $\hat{\sigma}(\mathbf{x}) =: m_2(\mathbf{x}) \geq 0$ , see Sec. 9.2.2.

Figure 11.4 shows an example of a feature space with  $I = 2$  regions. The decision boundary shows that both features  $m_1$  and  $m_2$  are necessary for separating the two classes. ■

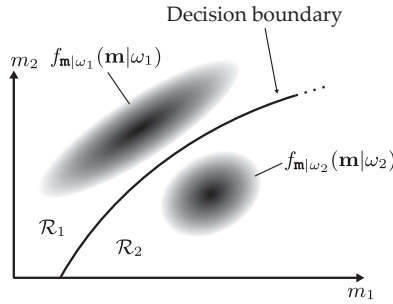


Figure 11.4. Segmentation by classification of a two-dimensional feature space into two regions.

Often, parametric models of the decision regions and their boundaries are used for classification in the feature space. The following considerations assume the most simple case of  $K = 1$  and  $I = 2$ . The features of each class  $\omega_i$  are assumed to be distributed according to a Gaussian density with an expected value  $\mu_i$  and standard deviation  $\sigma_i$ :

$\mathbf{x} \in \omega_i \Rightarrow m(\mathbf{x}) = m$  with probability density function (PDF):

$$f_{m|\omega_i}(m|\omega_i) = \frac{1}{\sqrt{2\pi}\sigma_i} e^{-\frac{1}{2}\left(\frac{m-\mu_i}{\sigma_i}\right)^2}, \quad i = 1, 2. \quad (11.7)$$

The term  $f_{m|\omega_i}(m|\omega_i)$  denotes the conditional probability density of the feature  $m$  if  $\mathbf{x}$  is a member of the class  $\omega_i$ .

Let  $P_i := \Pr\{\mathbf{x} \in \omega_i\}$  denote the a priori probability of  $\mathbf{x}$  being a member of the class  $\omega_i$ . The segmentation can, for example, be based on the maximization of the a posteriori probability  $P(\omega|\mathbf{m})$ :

$$P(\omega_1|m(\mathbf{x})) > P(\omega_2|m(\mathbf{x})) \quad (11.8)$$

$$\Leftrightarrow P_1 f_{m|\omega_1}(m(\mathbf{x})|\omega_1) > P_2 f_{m|\omega_2}(m(\mathbf{x})|\omega_2) \quad (11.9)$$

$$\Leftrightarrow m(\mathbf{x}) \in \mathcal{R}_1 \quad (11.10)$$

$$\Rightarrow \hat{\omega}(\mathbf{x}) := \omega_1. \quad (11.11)$$

In this simple case, the separation in the feature space is determined by one or two thresholds, see Figures 11.5 and 11.6. In the case of Fig. 11.5, a single threshold  $\gamma$  is sufficient to



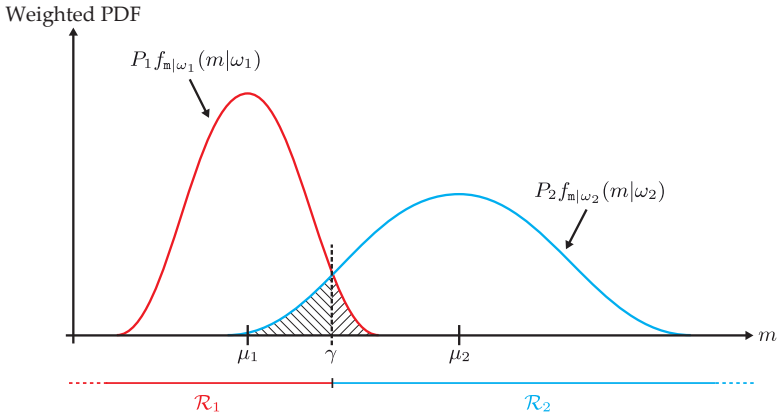


Figure 11.5. Optimal decision boundaries for  $K = 1$  features and  $I = 2$  regions.

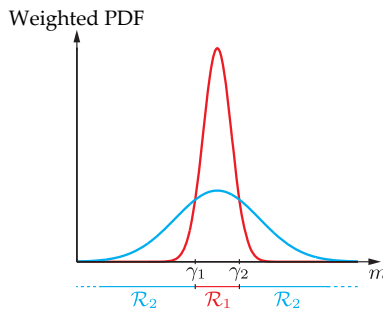


Figure 11.6. Even in a one-dimensional feature space, multiple thresholds  $\gamma$  might be necessary.

separate the decision regions  $\mathcal{R}_1$  and  $\mathcal{R}_2$ . This results in

$$\hat{\omega}(\mathbf{x}) := \omega_1 \iff m(\mathbf{x}) < \gamma. \tag{11.12}$$

The error probability  $\varepsilon$  of the segmentation can be expressed as a function of  $\gamma$ :

$$\varepsilon(\gamma) = P_1 \int_{\gamma}^{\infty} f_{m|\omega_1}(m|\omega_1) dm + P_2 \int_{-\infty}^{\gamma} f_{m|\omega_2}(m|\omega_2) dm. \tag{11.13}$$

Minimizing this expression yields the optimal choice of the threshold  $\gamma$  with respect to the parameters  $\mu_i$ ,  $\sigma_i$  and  $P_i$ . For example, the case  $\sigma_1 = \sigma_2 = \sigma$  results in [42]

$$\gamma_{\text{opt}} = \frac{\mu_1 + \mu_2}{2} - \frac{\sigma^2}{\mu_2 - \mu_1} \ln \frac{P_2}{P_1}. \tag{11.14}$$

For  $K > 1$ , vectors of expected values  $\mu_i$  and covariance matrices  $\Sigma_i$ ,  $i = 1, \dots, I$  are obtained. The histogram  $\hat{h}(m)$  calculated from the training examples can be used to estimate

the parameters  $\mu_i$ ,  $\Sigma_i$  and  $P_i$ . For this purpose, the model

$$f(\mathbf{m}) = f_{\mathbf{m}}(\mathbf{m}|\mu_1, \Sigma_1, P_1, \dots, \mu_I, \Sigma_I, P_I) = \sum_{i=1}^I P_i f_{\mathbf{m}|\omega_i}(\mathbf{m}|\omega_i, \mu_i, \Sigma_i) \quad (11.15)$$

is fitted to the empirically observed histogram using a least squares method, so the following optimization problem is solved:

$$\sum_{\mathbf{m}} (f(\mathbf{m}) - \hat{h}(\mathbf{m}))^2 \rightarrow \text{Min.} \quad (11.16)$$

As (11.15) represents a Gaussian mixture model, no closed solution can be obtained. The expectation-maximization algorithm (EM algorithm) can be used for the optimization [17, 40]. In every iteration  $t$ , the likelihood function

$$Q^{(t)}(\mathbf{m}|\omega_i) = \frac{P_i^{(t)} \frac{1}{\sqrt{(2\pi)^K \det \Sigma_i^{(t)}}} e^{-\frac{1}{2}(\mathbf{m}-\mu_i^{(t)})^T (\Sigma_i^{(t)})^{-1} (\mathbf{m}-\mu_i^{(t)})}}{\sum_{j=1}^I P_j^{(t)} \frac{1}{\sqrt{(2\pi)^K \det \Sigma_j^{(t)}}} e^{-\frac{1}{2}(\mathbf{m}-\mu_j^{(t)})^T (\Sigma_j^{(t)})^{-1} (\mathbf{m}-\mu_j^{(t)})}}$$

is evaluated. Subsequently, the parameters of the probability density are estimated:

$$P_i^{(t+1)} = \sum_{\mathbf{m}} \hat{h}(\mathbf{m}) Q^{(t)}(\mathbf{m}|\omega_i), \quad (11.17)$$

$$\mu_i^{(t+1)} = \frac{1}{P_i^{(t+1)}} \sum_{\mathbf{m}} \hat{h}(\mathbf{m}) Q^{(t)}(\mathbf{m}|\omega_i) \mathbf{m}, \quad (11.18)$$

$$\Sigma_i^{(t+1)} = \frac{1}{P_i^{(t+1)}} \sum_{\mathbf{m}} \hat{h}(\mathbf{m}) Q^{(t)}(\mathbf{m}|\omega_i) (\mathbf{m} - \mu_i^{(t+1)}) (\mathbf{m} - \mu_i^{(t+1)})^T.$$

**Example 11.4 (Histogram-based segmentation):** The image shown in Fig. 11.7(a) is to be segmented into  $I = 3$  regions. Artificial noise  $\mathbf{r}(\mathbf{x})$  is additively superposed on the original image  $g_0(\mathbf{x})$ :

$$g(\mathbf{x}) := g_0(\mathbf{x}) + \mathbf{r}(\mathbf{x}). \quad (11.19)$$

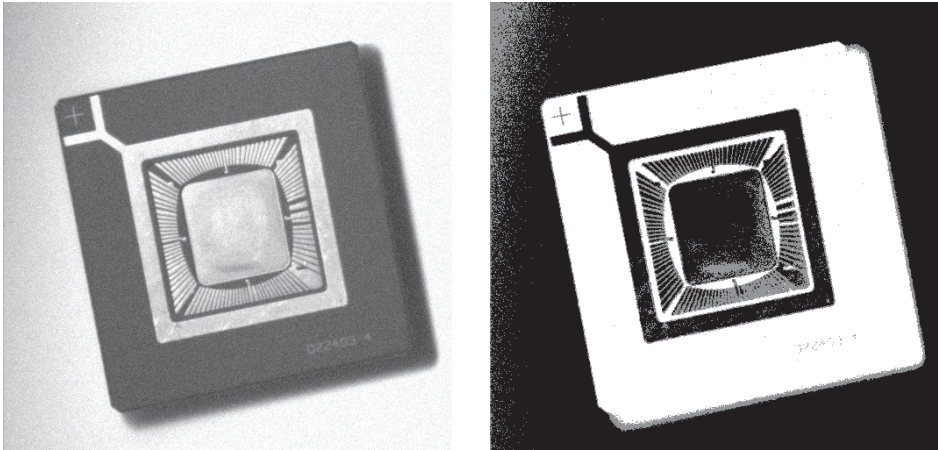
This white, Gaussian noise is zero-mean and has a standard deviation of  $\sigma_{\mathbf{r}} = 10$ :

$$E\{\mathbf{r}(\mathbf{x})\} = 0, \quad E\{\mathbf{r}(\mathbf{x})\mathbf{r}(\mathbf{y})\} = \delta_{\mathbf{x}}^{\mathbf{y}} \sigma_{\mathbf{r}}^2. \quad (11.20)$$

The superposition of an artificially generated noise signal is a common method used for evaluating the robustness of image processing methods.

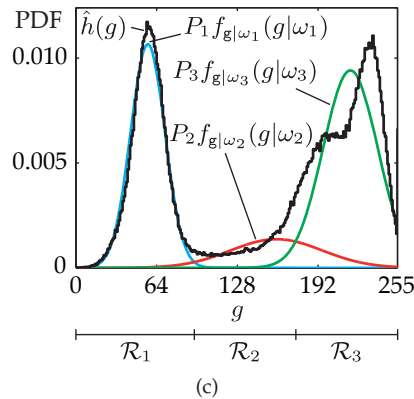
As in Ex. 11.1, the gray value of the image signal is used as a feature:  $m(\mathbf{x}) := g(\mathbf{x})$ . Figure 11.7(c) shows the gray value histogram of the image and the Gaussian densities of the three regions, which have been estimated using the EM algorithm. In the interval  $\mathcal{R}_3$ , there is a clear difference between the histogram and the model, which might be caused by an inadequate model that could be improved by a larger number  $I$  of regions.

The result of the segmentation is shown in Fig. 11.7(b). The segmented regions are disconnected. In addition, there are two further drawbacks: some noisy pixels were assigned to other regions, and objects have not been correctly segmented because of in-



(a)

(b)



(c)

**Figure 11.7.** Region-based segmentation using a probabilistic model of the gray value histogram: (a) Noisy image  $g(\mathbf{x})$ ; (b) Result of the segmentation into  $I = 3$  regions (white  $\hat{=}$   $\omega_1$ , gray  $\hat{=}$   $\omega_2$ , black  $\hat{=}$   $\omega_3$ ); (c) Gaussian densities  $f_{g|\omega_i}(g|\omega_i)$  adjusted to the gray value histogram  $\hat{h}(g)$ .

homogeneous illumination conditions and reflectance properties, e.g., in the background of the top left corner and in the image center. ■

Another possibility for choosing thresholds in the histogram is the maximization of the variance between the two classes. For gray value histograms, this approach is realized by the method of Otsu [23,35].

For some applications it might be reasonable to choose a locally adaptive threshold [42]. This can be achieved by solving the optimization problem (11.16) for local regions of the image. For example, local histograms  $\hat{h}(\mathbf{m})$  can be calculated for partially overlapping rectangular windows. The local thresholds  $\gamma_{ij}(\mathbf{x})$  for discriminating between  $\omega_i$  and  $\omega_j$  at the pixel position  $\mathbf{x}$  can then be determined by an interpolation of the thresholds of the overlapping windows.

### 11.1.2 Region growing methods

In general, the segments resulting from the described classification methods are not connected. This problem is avoided by **region growing methods** [1,25,42]. Here, the segments  $\omega_i$  are iteratively enlarged by appending adjacent points meeting the uniformity criterion. Starting with at least one initial point per segment, the iteration is repeated until all pixels  $x \in \Omega_g$  are assigned to a class  $\omega_i$ . In order to achieve a complete segmentation in which every pixel is assigned to a segment, the uniformity criterion might have to be relaxed during the iterations.

Figure 11.8 shows the result of the region growing method for the test image used in Ex. 11.4. The three marked seed points were set manually. The segmented regions are connected. However, the fine object structures have not been segmented. The method is robust to single noisy pixels.

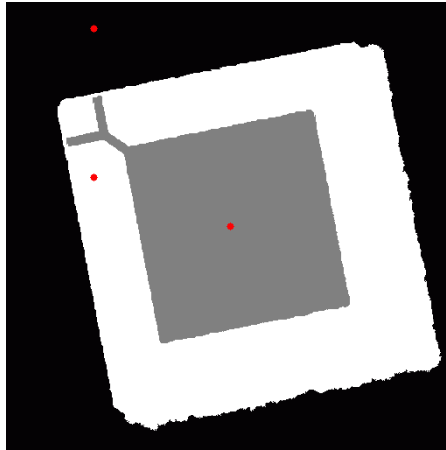


**Figure 11.8.** Result of the region growing method used for segmenting Fig. 11.7(a) into  $I = 3$  regions. The seed points, which were manually set, are marked in red.

Unfortunately, the result of the region growing method is heavily dependent on the choice of the initial seed points. This drawback can be overcome by choosing seed points that can be classified with a high degree of confidence, i.e., which are located far away from the decision boundaries in the feature space.

Another variant of region-based segmentation is given by the pyramid-linking method described in Chap. 15 in the context of image representation using image pyramids.

## 11.2 Edge-oriented methods

In contrast to region-based methods, which use the inner uniformity of the regions as a criterion, edge-oriented segmentation methods try to determine the borders between the regions.

**Definition 11.2: Edge**

An edge is a border between two regions that are homogeneous in terms of a uniformity criterion regarding their interiors. At an edge, the local image properties which are subject to the uniformity criterion show a high spatial variance: ideally, they show a jump discontinuity.  $\diamond$

According to this definition, edges are also called **step edges**, as they represent a ‘step’ between two different regions in terms of the uniformity criterion.

The edges present in an image can be caused by different phenomena of the observed scene (Fig. 11.9(a)):

- Object edges correspond to the actual geometric borders between two objects.
- Reflectance edges are caused by discontinuities of the reflectance of an object’s surface.
- Shadow edges arise at borders between directly illuminated regions and shadowed regions of an object. They can be detected by varying the illumination direction (Fig. 11.9(b)).

The latter two edge types are also referred to as **pseudo-edges**, as they do not correspond to actually existing geometric features of the scene.

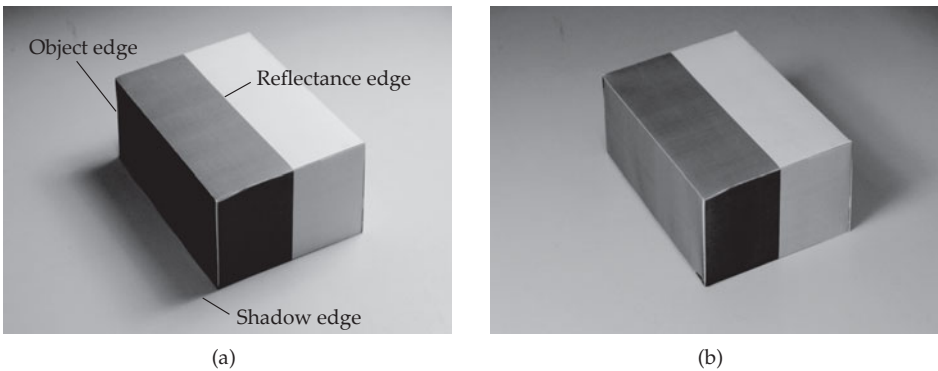


**Figure 11.9.** Edges in the image might be caused by different contents of the scene: (a) Image of a cuboid with object edges, reflectance edges and shadow edges; (b) Image of the same scene under a different illumination.

**Edge detection** is a common problem in image processing. Numerous methods have been proposed for its solution. The most common methods calculate a spatial derivative of the image signal in order to detect edges. An edge is represented

- by an edge in the image signal  $g(x)$  according to the definition of an edge,
- by an extremum of the first derivative (the gradient) of the image signal,
- by a change of sign of the second derivative of the image signal.

Figure 11.10 shows a one-dimensional section through an image signal illustrating the characteristics of an edge in terms of the first and second derivatives. Obviously, the high-frequency noise is amplified by differentiation. This effect is explained by the transfer func-

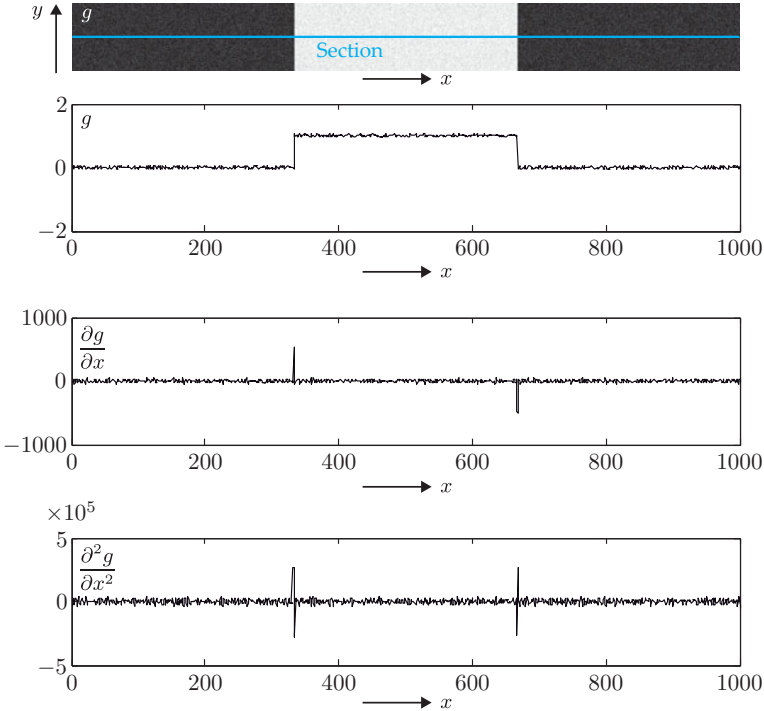


**Figure 11.10.** Effects of edges on the first and second derivatives of the image signal. The diagrams show the image values as well as the first and second derivatives along the section.

tion of the derivative operators, whose magnitudes increase for higher frequencies:

$$\frac{\partial}{\partial x} \iff j2\pi f_x, \tag{11.21}$$

$$\frac{\partial^2}{\partial x^2} \iff -4\pi^2 f_x^2. \tag{11.22}$$

As the image signal is given in a discrete representation, discrete filters for approximating the first or second derivative have to be designed for detecting edges.

► **11.2.1 Gradient filters**

To begin with, the first derivate will be employed for edge detection. The gradient of the image signal is defined as

$$\text{grad } g(\mathbf{x}) := \left( \frac{\partial g(\mathbf{x})}{\partial x}, \frac{\partial g(\mathbf{x})}{\partial y} \right)^T. \tag{11.23}$$

Assume that an edge is located at the position  $\mathbf{x}$ . Then, the absolute value  $\|\text{grad } g(\mathbf{x})\|$  of the gradient is a measure of the intensity of the edge. As the gradient is perpendicular to the

edge, it is a description of the normal to the edge. This normal direction is given by

$$\angle \text{grad } g(\mathbf{x}) = \arctan \left( \frac{\frac{\partial g}{\partial y}}{\frac{\partial g}{\partial x}} \right). \tag{11.24}$$

In what follows, there will be derived some linear discrete filters to be used for approximating the gradient. At first, only one dimension will be considered. A convolution of the discrete signal  $g_m$  with the impulse response function  $d_m$  of the filters sought is supposed to yield an approximation of the signal's gradient:

$$\left. \frac{d}{dx} g(x) \right|_{x=m\Delta x} \approx d_m * g_m, \tag{11.25}$$

where  $m$  denotes the discrete spatial coordinate of the impulse response. Obvious approximations are the asymmetric difference quotient

$$\frac{g(x) - g(x - \Delta x)}{\Delta x} \tag{11.26}$$

and the symmetric difference quotient

$$\frac{g(x + \Delta x) - g(x - \Delta x)}{2\Delta x}, \tag{11.27}$$

each with a discretization step width  $\Delta x$ . A better approximation is Stirling's approximation:

$$\frac{-g(x + 2\Delta x) + 8g(x + \Delta x) - 8g(x - \Delta x) + g(x - 2\Delta x)}{12\Delta x}. \tag{11.28}$$

The corresponding impulse responses are directly given by the coefficients in the quotients, e.g.,

$$\left. \frac{g(x + \Delta x) - g(x - \Delta x)}{2\Delta x} \right|_{x=m\Delta x} = \left( \frac{1}{2} \quad 0 \quad -\frac{1}{2} \right) * g_m. \tag{11.29}$$

Table 11.1 summarizes the impulse responses of the three mentioned gradient filters. The asymmetric difference quotient results in a displacement of the edge position by one-half of a pixel, as the center of its impulse response function is located at  $m = \frac{1}{2}$  and therefore between the points of the pixel grid.

Table 11.1. Impulse response function  $d_m$  of simple linear gradient filters.

Discrete position $m$	-3	-2	-1	0	1	2	3
Asymmetric difference quotient (11.26)	0	0	0	1	-1	0	0
Symmetric difference quotient (11.27)	0	0	$\frac{1}{2}$	0	$-\frac{1}{2}$	0	0
Stirling's approximation (11.28)	0	$-\frac{1}{12}$	$\frac{2}{3}$	0	$-\frac{2}{3}$	$\frac{1}{12}$	0

**Example 11.5 (Symmetric difference quotient):** In the  $x$ -direction and the  $y$ -direction, the symmetric difference quotient of a gray-scale image  $g(x, y)$  is calculated as follows:

$$\frac{\partial g(x, y)}{\partial x} \approx \frac{g(x + \Delta x, y) - g(x - \Delta x, y)}{2\Delta x}, \quad (11.30)$$

$$\frac{\partial g(x, y)}{\partial y} \approx \frac{g(x, y + \Delta y) - g(x, y - \Delta y)}{2\Delta y}. \quad (11.31)$$

The absolute value of the gradient is given by

$$\|\text{grad } g(\mathbf{x})\| = \sqrt{\left(\frac{\partial g(x, y)}{\partial x}\right)^2 + \left(\frac{\partial g(x, y)}{\partial y}\right)^2}. \quad (11.32)$$

Figure 11.11 shows the approximation of the gradient of a sample image using the symmetric difference quotient. Although the derivatives can be negative, the visualized absolute value of the gradient is always positive like the gray values of the original image. ■

### ⊙ 11.2.1.1 Construction of symmetric linear gradient filters

A systematic construction of linear discrete gradient filters can be obtained by considering the transfer function. Employing (8.53), an ideal differentiator has the transfer function  $j2\pi f$ :

$$\frac{d}{dx} g(x) \quad \circ \bullet \quad j2\pi f G(f). \quad (11.33)$$

**Example 11.6 (The transfer function of the symmetric difference quotient):** The symmetric difference quotient has the following DFT transfer function:

$$D_k = \frac{1}{2} \left( -e^{-j2\pi \frac{k}{N}} + e^{-j2\pi \frac{k(N-1)}{N}} \right) = \frac{1}{2} \left( -e^{-j2\pi \frac{k}{N}} + e^{j2\pi \frac{k}{N}} \right) \quad (11.34)$$

$$= j \sin 2\pi \frac{k}{N} \quad (11.35)$$

$$\approx j2\pi \frac{k}{N} \quad \text{if } k \ll N. \quad (11.36)$$

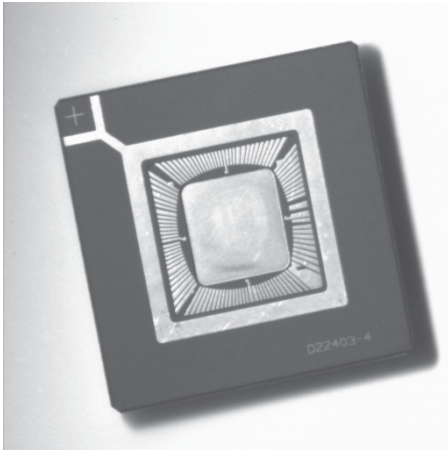
One has  $D_0 = 0$ ,  $D_{\frac{N}{4}} = j < j\frac{\pi}{2}$ ,  $D_{\frac{N}{2}} = 0 \ll j\pi$ . For low discrete frequencies  $\frac{k}{N}$ , the effect of the symmetric difference quotient is similar to an ideal differentiator; however, for higher frequencies, its transfer function decreases. ■

Now, a symmetric linear gradient filter  ${}^r d_m$  of length  $L = 2r + 1$  is to be constructed, i.e.,

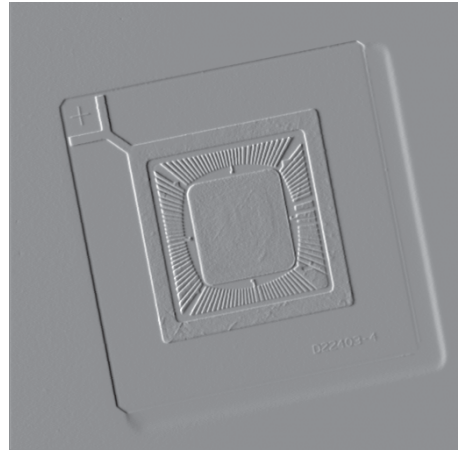
$${}^r d_m = 0 \quad \text{if } m = 0 \vee |m| > r, \quad (11.37)$$

$${}^r d_m = -{}^r d_{-m}. \quad (11.38)$$

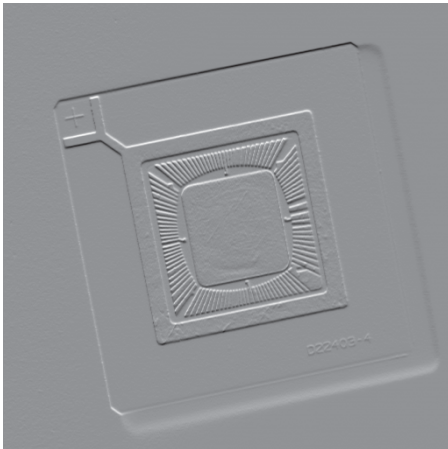




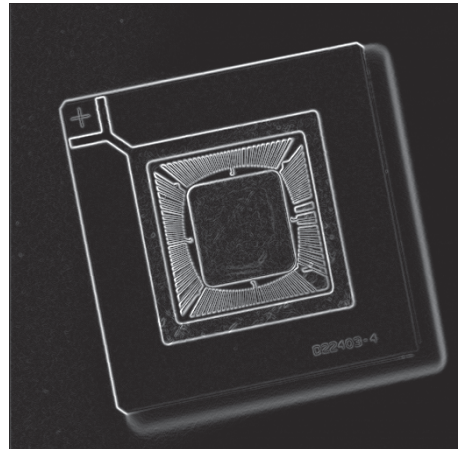
(a)  $g(x, y)$



(b)  $\frac{\partial g(x, y)}{\partial x}$



(c)  $\frac{\partial g(x, y)}{\partial y}$



(d)  $\|\text{grad } g(\mathbf{x})\|$

**Figure 11.11.** Edge detection using the symmetric difference quotient: (a) Original image; (b) Symmetric difference quotient in  $x$ -direction (black  $\hat{=}$  negative values, gray  $\hat{=}$  0, white  $\hat{=}$  positive values); (c) Symmetric difference quotient in  $y$ -direction; (d) Absolute value of the gradient (black  $\hat{=}$  0).

In the spatial frequency domain, the real-valued, odd function  ${}^r d_m$  corresponds to a pure imaginary, odd Fourier transform  ${}^r D_k$ , cf. (11.33):

$${}^r D_k = \sum_{\nu=0}^{N-1} {}^r d_\nu e^{-j2\pi \frac{k\nu}{N}} = \sum_{\nu=1}^r {}^r d_\nu \left( e^{-j2\pi \frac{k\nu}{N}} - e^{j2\pi \frac{k\nu}{N}} \right) \tag{11.39}$$

$$= -2j \sum_{\nu=1}^r {}^r d_\nu \sin \left( 2\pi \frac{k\nu}{N} \right), \quad N > 2r. \tag{11.40}$$

Now expand the sine functions as Taylor series in  $\frac{k}{N}$ . The  $r$  degrees of freedom of the filter are chosen to meet the following requirements:

- The linear term of the Taylor series should be equal to  $j2\pi\frac{k}{N}$ , corresponding to the transfer function of the ideal differentiator.
- The subsequent  $r - 1$  terms should vanish.

**Example 11.7 (Symmetric linear gradient filters of length 5):** A symmetric linear gradient filter of length  $L = 5$  is to be constructed; in this case,  $r = 2$  coefficients have to be determined. From (11.40), it follows that

$${}^2D_k = -2jd_1 \sin\left(2\pi\frac{k}{N}\right) - 2jd_2 \sin\left(4\pi\frac{k}{N}\right). \quad (11.41)$$

Inserting the power series  $x - \frac{x^3}{3!} + \frac{x^5}{5!} \mp \dots$  of the sine results in:

$$\begin{aligned} {}^2D_k &= j2\pi \left( -2d_1\frac{k}{N} + \frac{4}{3}d_1\pi^2\left(\frac{k}{N}\right)^3 \right. \\ &\quad \left. - 4d_2\frac{k}{N} + \frac{32}{3}d_2\pi^2\left(\frac{k}{N}\right)^3 + \mathcal{O}\left(\left(\frac{k}{N}\right)^5\right) \right) \end{aligned} \quad (11.42)$$

$$\begin{aligned} &= j2\pi \left( (-2d_1 - 4d_2)\frac{k}{N} \right. \\ &\quad \left. + \left( \frac{4}{3}\pi^2d_1 + \frac{32}{3}\pi^2d_2 \right) \left(\frac{k}{N}\right)^3 + \mathcal{O}\left(\left(\frac{k}{N}\right)^5\right) \right). \end{aligned} \quad (11.43)$$

Solving the system of equations (from (11.33))

$$-2d_1 - 4d_2 \stackrel{!}{=} 1 \quad \frac{4}{3}d_1 + \frac{32}{3}d_2 \stackrel{!}{=} 0 \quad (11.44)$$

yields

$$d_1 = -\frac{2}{3} \quad d_2 = \frac{1}{12}. \quad (11.45)$$

This corresponds to Stirling's approximation (11.28). ■

A longer gradient filter results in a better approximation of the transfer function of the ideal differentiator (Fig. 11.12). In fact, the decay of the transfer functions of the gradient filters for higher frequencies is preferred in practice, as high-frequency noise is amplified less intensely.

### ⊗ 11.2.1.2 Differentiation using the DFT

Alternatively, the DFT can be used to directly perform the differentiation: first the discrete Fourier transform  $G_k$  of the image is calculated, then this is multiplied by the differential operator  $D_k$  in the spatial frequency domain, and finally the result is transformed back into the spatial domain. For one dimension, this approach results in the following equations:

$$\frac{dg(x)}{dx} \approx \text{DFT}^{-1}\{G_k D_k\}, \quad (11.46)$$

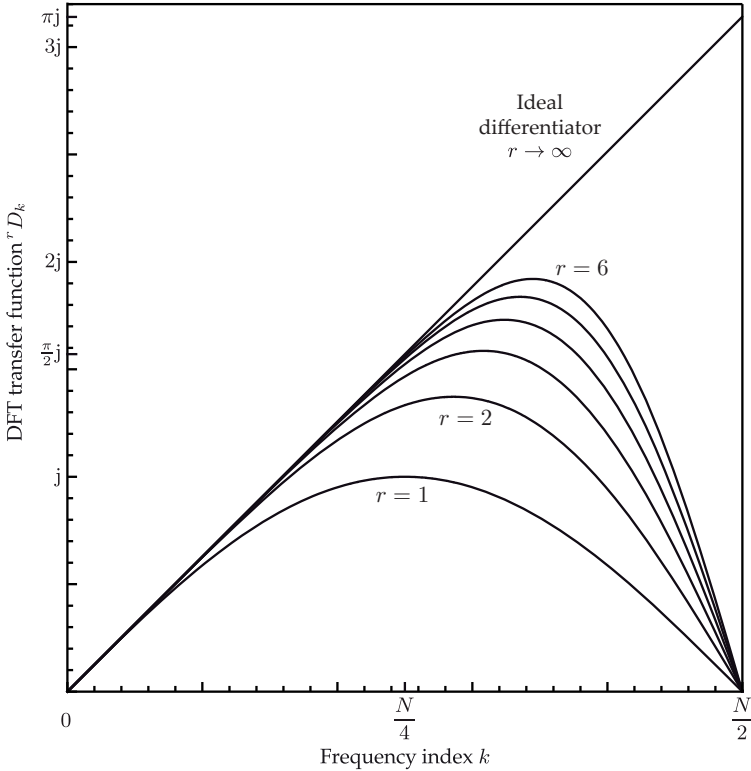


Figure 11.12. Transfer functions of symmetric linear gradient filteres of length  $L = 2r + 1$ .

$$D_k := \begin{cases} j2\pi \frac{k}{N} & \text{if } k < \frac{N}{2} \\ 0 & \text{if } k = \frac{N}{2} \\ j2\pi \frac{k-N}{N} & \text{if } k > \frac{N}{2} \end{cases} \quad k = 0, \dots, N - 1. \tag{11.47}$$

However, this method can be problematic if there is severe spectral leakage (see Chap. 8).

There are a couple of problems that affect all gradient filters. On the one hand, the differentiation amplifies noise, which has to be mitigated by attenuating the high spatial frequencies by means of a low-pass filter. Hence, all in all, suitable linear edge detection filters show band-pass characteristics. Furthermore, widened contours are often visible in the filtered result: the edges cannot be located with pixel accuracy. This issue can be solved by a subsequent edge thinning (see Chap. 12). On the other hand, the contours can also be disconnected. In this case, contour tracing might be a suitable post-processing step [23,38]. Artifacts can even arise, e.g., false contours caused by noise, which have then to be dealt with.

⊗ **11.2.1.3 Gradient-of-Gaussian filter**

The gradient-of-Gaussian filter is a common gradient filter with band-pass characteristics. Because of the simultaneous smoothing of the image  $g(\mathbf{x})$  by the Gaussian  $h(\mathbf{x})$ , this operator is relatively insensitive to noise.

The filtering of a two-dimensional signal  $g(\mathbf{x})$  with the derivative of a Gaussian low-pass filter in the  $x$ -direction can be mathematically described as follows:

$$\frac{\partial g(\mathbf{x})}{\partial x} \approx \frac{\partial}{\partial x}(h(\mathbf{x}) ** g(\mathbf{x})) = \frac{\partial}{\partial x} \int_{-\infty}^{\infty} \int_{-\infty}^{\infty} g(\boldsymbol{\alpha}) h(\mathbf{x} - \boldsymbol{\alpha}) d\boldsymbol{\alpha} \tag{11.48}$$

$$= \int_{-\infty}^{\infty} \int_{-\infty}^{\infty} g(\boldsymbol{\alpha}) \frac{\partial h}{\partial x}(\mathbf{x} - \boldsymbol{\alpha}) d\boldsymbol{\alpha} = \underbrace{\left( \frac{\partial}{\partial x} h(\mathbf{x}) \right) ** g(\mathbf{x})}_{=: d^x(\mathbf{x})}, \tag{11.49}$$

$$h(\mathbf{x}) := \frac{1}{2\pi\sigma^2} e^{-\frac{\|\mathbf{x}\|^2}{2\sigma^2}}, \tag{11.50}$$

$$d^x(\mathbf{x}) = -\frac{x}{2\pi\sigma^4} e^{-\frac{\|\mathbf{x}\|^2}{2\sigma^2}}. \tag{11.51}$$

Differentiation in the  $y$ -direction is performed similarly. The resulting impulse response functions  $d^x$  and  $d^y$  are shown in Fig. 11.13. In all, the gradient is approximated as follows:

$$\text{grad } g(\mathbf{x}) \approx (\text{grad } h(\mathbf{x})) ** g(\mathbf{x}), \tag{11.52}$$

$$\text{grad } h(\mathbf{x}) = -\frac{\mathbf{x}}{\sigma^2} h(\mathbf{x}) =: \begin{pmatrix} d^x(\mathbf{x}) \\ d^y(\mathbf{x}) \end{pmatrix}. \tag{11.53}$$

As is shown by the above calculation, convolution with the derivative of the Gaussian low-pass filter is equivalent to a smoothing and a subsequent differentiation. Analyzing the transfer function leads to the same result: in the spatial frequency domain, the differentiation with respect to  $x$  corresponds to multiplication by  $j2\pi f_x$ , and the convolution with  $h(\mathbf{x})$  corresponds to multiplication by  $H(\mathbf{f})$ , and these two multiplications commute. The transfer function  $D^x(\mathbf{f})$  of the Gaussian low-pass filter  $d^x(\mathbf{x})$  that performs the differentiation in the  $x$ -direction can be obtained using the correspondence  $e^{-\pi\|\mathbf{x}\|} \circ \bullet e^{-\pi\|\mathbf{f}\|}$  and the derivative property of the Fourier transform:

$$D^x(\mathbf{f}) = j2\pi f_x e^{-2\pi^2\sigma^2\|\mathbf{f}\|^2}. \tag{11.54}$$

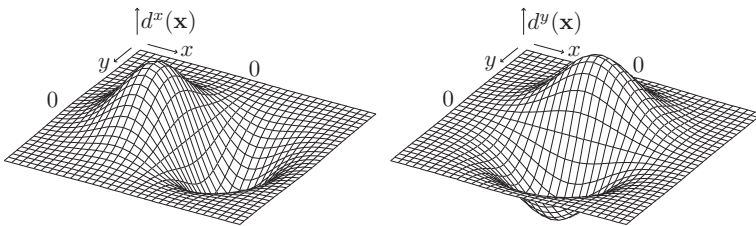
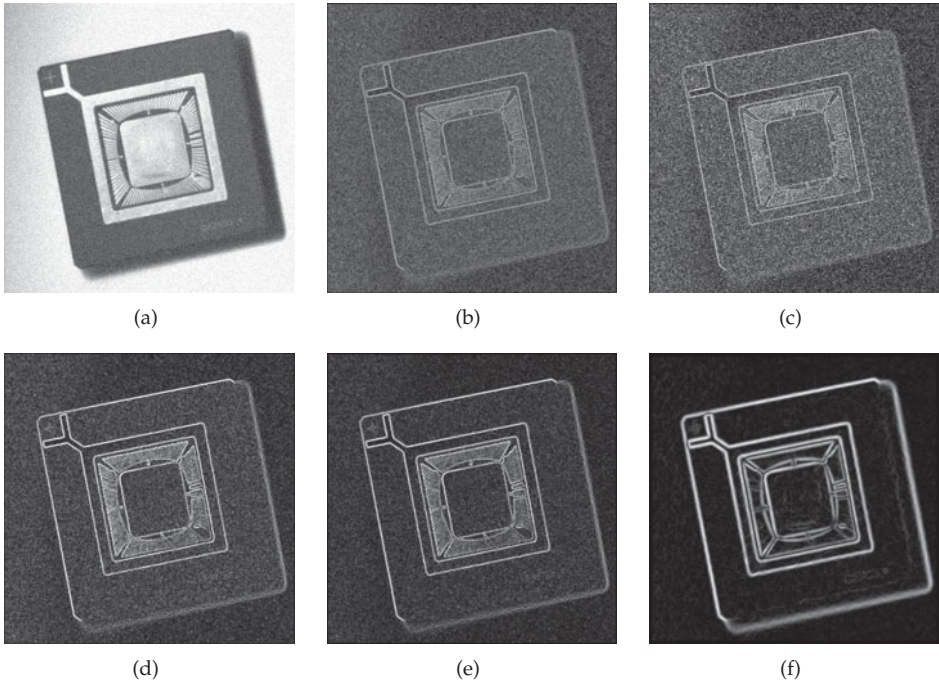


Figure 11.13. Impulse response functions  $d^x(\mathbf{x})$  and  $d^y(\mathbf{x})$  of the differentiated Gaussian low-pass filter.

For small  $\|\mathbf{f}\|$ , this approximates the differential operator  $j2\pi f_x$ ; for large  $\|\mathbf{f}\|$ , one has  $D^x(\mathbf{f}) \rightarrow 0$ , which represents the band-pass characteristics.

Figure 11.14 shows the results of applying the gradient-of-Gaussian filter to an example image. A larger  $\sigma$  results in a better noise reduction. However, the fine edge structures vanish for increasing  $\sigma$ . By adjusting  $\sigma$ , one can set the granularity of the structures which are to be detected, cf. Chap. 15.



**Figure 11.14.** Edge detection using the first derivative: (a) Original image with additive Gaussian noise with standard deviation  $\sigma_r = 20$ , cf. (11.20); (b) Symmetric difference quotient; (c) Roberts operator; (d) Sobel operator; (e) Gradient-of-Gaussian filter with smoothing parameter  $\sigma = 0.8$ ; (f) With  $\sigma = 2.2$ . The images show the absolute value of the gradient for  $q = 2$ .

There are two possibilities for obtaining a discrete formulation of this filter:

- Filtering using a convolution in the spatial domain by sampling  $d^x(\mathbf{x})$  and  $d^y(\mathbf{x})$  to obtain  $d_{mn}^x$  and  $d_{mn}^y$ ;
- Filtering using a multiplication in the spatial frequency domain by sampling  $D^x(\mathbf{f})$  and  $D^y(\mathbf{f})$  to obtain  $D_{kl}^x$  and  $D_{kl}^y$ .

Canny formulated quality criteria, such as the signal-to-noise ratio and localization accuracy, and used them to obtain the optimal edge detector. The differentiated Gaussian low-pass filter is a good approximation to the numerically calculated optimal edge detector [10,23].

⊗ **11.2.1.4 Simple edge operators**

**Sobel filters** can be considered as a rough sampling of the differentiated Gaussian low-pass filters  $d^x$  and  $d^y$  in the spatial domain:

$$s_{mn}^x = \begin{pmatrix} 1 & 0 & -1 \\ 2 & 0 & -2 \\ 1 & 0 & -1 \end{pmatrix}, \quad s_{mn}^y = \begin{pmatrix} -1 & -2 & -1 \\ 0 & 0 & 0 \\ 1 & 2 & 1 \end{pmatrix}. \tag{11.55}$$

Hence, the absolute value of the gradient can be approximated by the **Sobel operator**:


$$(|s_{mn}^x ** g_{mn}|^q + |s_{mn}^y ** g_{mn}|^q)^{\frac{1}{q}}, \quad q \in \{1, 2, \infty\}. \tag{11.56}$$

In the literature, different norms are used for the calculation of the absolute gradient. The choice of  $q = 1$  ( $q = 2$ ) corresponds to the Manhattan norm (Euclidean norm);  $q = \infty$  corresponds to the maximum norm (Chebyshev norm):

$$\max \{|s_{mn}^x ** g_{mn}|, |s_{mn}^y ** g_{mn}|\}. \tag{11.57}$$

The Sobel filter can be represented as a convolution of a binomial low-pass filter (see Sec. 9.3.1.4), which is a discrete approximation of the Gaussian low-pass filter, and the symmetric difference quotient. For example,  $s_{mn}^x$  is obtained by the convolution of the binomial filter  $h_3^y$  with respect to  $y$  and the symmetric difference quotient in the  $x$ -direction:

$$s_{mn}^x = \begin{pmatrix} 1 \\ 2 \\ 1 \end{pmatrix} ** \begin{pmatrix} 1 & 0 & -1 \end{pmatrix}$$



$N \times N$ -DFT

$$s_{kl}^x = \underbrace{2 \left( 1 + \cos \left( 2\pi \frac{l}{N} \right) \right)}_{\text{Low-pass}} \cdot \underbrace{j2 \sin \left( 2\pi \frac{k}{N} \right)}_{\text{Differentiation}}$$

The smallest possible filter mask of size  $2 \times 2$  is used by the so-called **Roberts operator** for the detection of edges:

$$k_{m,n} = (|g_{m,n} - g_{m-1,n-1}|^q + |g_{m-1,n} - g_{m,n-1}|^q)^{\frac{1}{q}} \tag{11.58}$$

with  $q \in \{1, 2, \infty\}$ . In contrast to the Sobel operator, the Roberts operator is much more sensitive to noise, as it does not perform any smoothing, but on the other hand it yields much thinner edges. As the center of symmetry is located in between the pixels, the resulting image is affected by a displacement of the edge positions.

⊗ **11.2.2 Edge detection using the second derivative**

Every additional differentiation amplifies the high-frequency noise. This is why an adequate smoothing is even more important for edge detection using the second derivative. In the second derivative, an edge of the original signal is represented as a zero located between a distinctive maximum and a distinctive minimum.

The simplest approximation of the second derivative is obtained by a convolution of the image with the so-called Laplace filter:

$$g_{mn} ** l_{mn}, \quad l_{mn} = \begin{pmatrix} 0 & 1 & 0 \\ 1 & -4 & 1 \\ 0 & 1 & 0 \end{pmatrix}. \tag{11.59}$$

As no smoothing is performed by this filter, it is very sensitive to noise.

The so-called **Laplacian-of-Gaussian operator**, or **LoG** for short, is a well-known edge filter which was proposed by Marr and Hildreth in 1980 [30]. At first, the image is smoothed with a Gaussian low-pass filter  $h(\mathbf{x})$ , in order to reduce the noise (cf. Chap. 9). Subsequently, the Laplace operator  $\Delta = \frac{\partial^2}{\partial x^2} + \frac{\partial^2}{\partial y^2}$  is applied in order to obtain the second derivative of the smoothed image. As  $\Delta$  and the convolution with  $h(\mathbf{x})$  are linear operators which therefore can be reordered, the same result can be achieved by convolving the original image with the filter  $l(\mathbf{x})$  that is obtained by applying the Laplace operator to the Gaussian low-pass filter:

$$\text{LoG}\{g(\mathbf{x})\} := -\Delta(h(\mathbf{x}) ** g(\mathbf{x})) = \underbrace{(-\Delta h(\mathbf{x}))}_{=: l(\mathbf{x})} ** g(\mathbf{x}), \tag{11.60}$$

$$l(\mathbf{x}) = -\frac{\partial^2 h(\mathbf{x})}{\partial x^2} - \frac{\partial^2 h(\mathbf{x})}{\partial y^2} = \frac{2\sigma^2 - \|\mathbf{x}\|^2}{2\pi\sigma^6} e^{-\frac{\|\mathbf{x}\|^2}{2\sigma^2}} \tag{11.61}$$



$$L(\mathbf{f}) = 4\pi^2 \|\mathbf{f}\|^2 e^{-2\pi^2 \sigma^2 \|\mathbf{f}\|^2}. \tag{11.62}$$

Because  $L(\mathbf{0}) = 0 = L(\infty)$ , the LoG operator has band-pass characteristics and compensates for high-frequency noise. Due to its shape, this operator is also known as the ‘Mexican Hat’ (see Fig. 11.15).

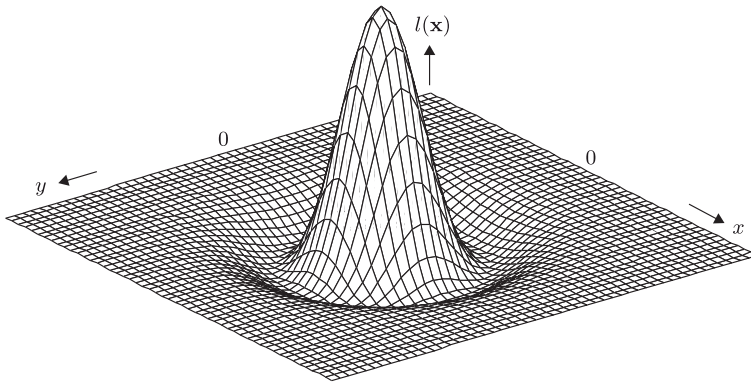


Figure 11.15. Laplacian of Gaussian (‘Mexican Hat’).

The following approaches provide a discrete realization of the LoG operator:

- Sampling of  $l(\mathbf{x})$  to form a discrete impulse response function  $l_{mn}$ . In order to keep the discretization error low, the mask should be large: its length should be at least  $7\sigma$ .

- Sampling of  $L(\mathbf{f})$  to form a DFT transfer function  $L_{kl}$ . Because of the large size of the filter masks in the spatial domain, an implementation using the fast Fourier transform can be beneficial.
- Approximation by the **Difference-of-Gaussians operator**, or **DoG** for short (see Fig. 11.16). The second derivative of the Gaussian function can be approximated by a difference of two Gaussian functions with different standard deviations  $\sigma_1, \sigma_2$ :

$$l(\mathbf{x}) \approx \frac{1}{2\pi\sigma_1^2} e^{-\frac{\|\mathbf{x}\|^2}{2\sigma_1^2}} - \frac{1}{2\pi\sigma_2^2} e^{-\frac{\|\mathbf{x}\|^2}{2\sigma_2^2}} \quad \text{with} \quad \frac{\sigma_2}{\sigma_1} \approx 1.6. \tag{11.63}$$

The corresponding transfer function  $L(\mathbf{f})$  is rotationally symmetric and shows band-pass characteristics:

$$L(\mathbf{0}) = 0, \quad \lim_{\|\mathbf{f}\| \rightarrow \infty} L(\mathbf{f}) = 0. \tag{11.64}$$

The maximum of its absolute value is located at

$$\|\mathbf{f}\|_{\max} = \frac{1}{\pi} \sqrt{\frac{\ln \frac{\sigma_2}{\sigma_1}}{\sigma_2^2 - \sigma_1^2}}. \tag{11.65}$$

The two Gaussian low-pass filters can be approximated by binomial filters (see Chap. 9).

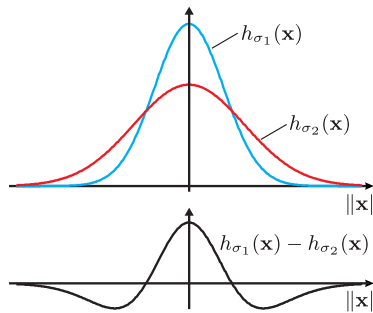
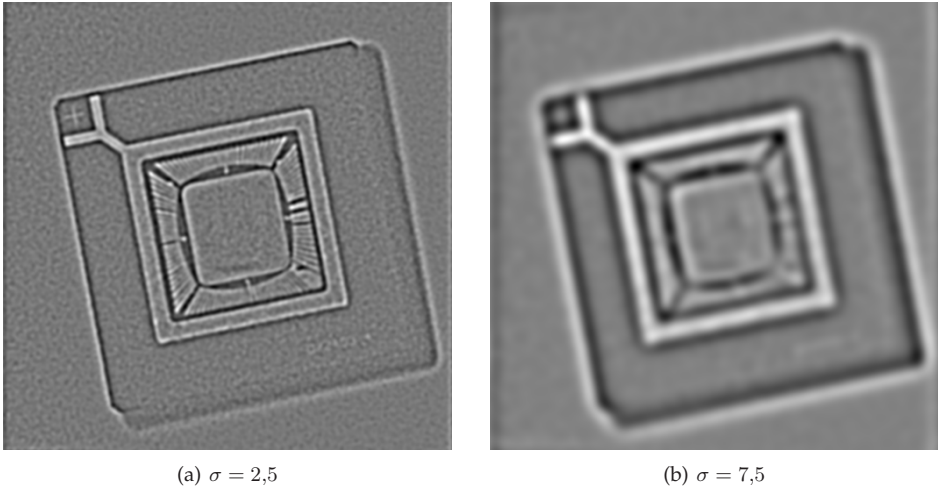


Figure 11.16. Difference of Gaussians.

An important advantage of the second derivative for edge detection is the possibility of precisely locating the zeros which correspond to the inflection points perpendicular to the step edge. As the resulting edges have a width of one pixel, there is no need for a subsequent edge thinning. There is evidence that the human visual system uses a similar principle for edge detection [30].

Besides its sensitivity to noise, the second derivative has another drawback: the requirement  $\Delta g(\mathbf{x}) \stackrel{!}{=} 0$  is only a necessary condition for the presence of an edge. Unfortunately, it is not sufficient, i.e., the zeros of the LoG operator do not necessarily have to correspond to signal edges. Therefore, edge artifacts can often be caused when using the second derivative. Besides, a displacement can be observed, especially at curved edges. A possible solution is given by a combination with a gradient-based method: the absolute value of the gradient can be used to verify the results of the LoG operator.





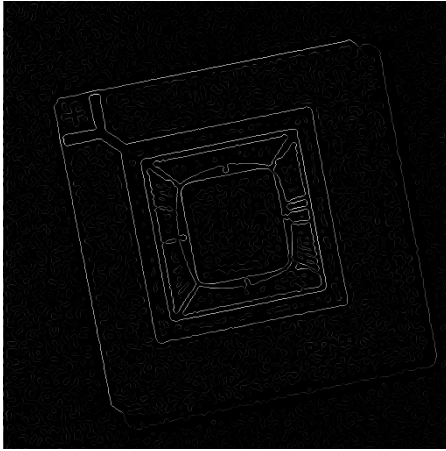
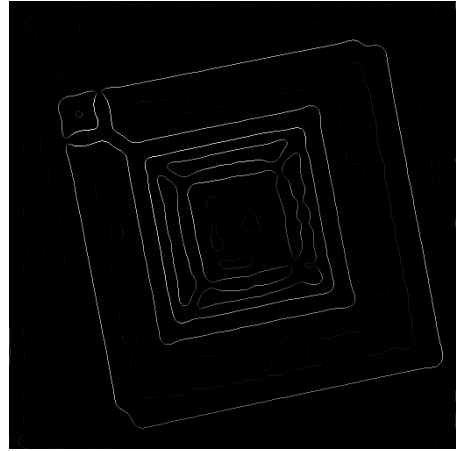
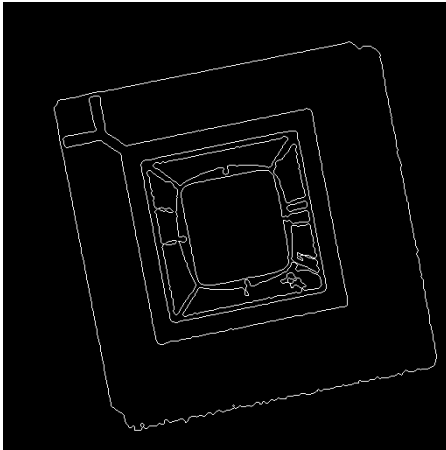
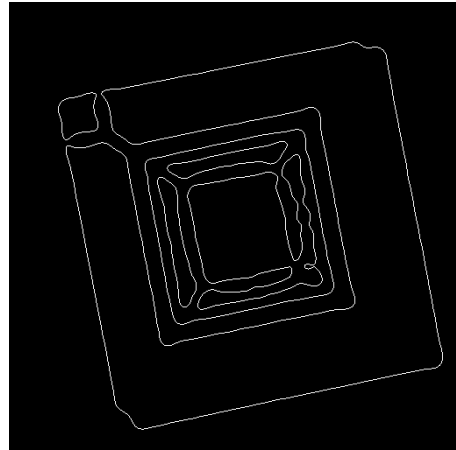
**Figure 11.17.** LoG filtering of the test image Fig. 11.14(a) using different smoothing parameters  $\sigma$ . The edges are located at steep rises or steep falls of the gray-scale levels between the positive (bright) and negative (dark) values.

**Example 11.8 (Edge detection using the LoG operator):** Figure 11.18 demonstrates the detection of edges by means of the LoG operator. The images shown in Fig. 11.17, which were filtered with the LoG operator using different smoothing parameters  $\sigma$ , are used as the input images. The classification of the contours is based on the slope of the zeros, which was approximated by the difference between the maximum value and minimum value inside a local neighborhood; the results of this operation are shown in Figs. 11.18(a) and 11.18(b).

The resulting closed contours are classified separately for every contour by means of the mean gradient of the zeros. The classification results are shown in the images 11.18(c) and 11.18(d). Indeed, the binary result in Fig. 11.18(d) shows smoother contours than Fig. 11.18(c) because of the choice of  $\sigma$ , but previously unconnected image regions located in the center of the image are merged into a common region. ■

**Example 11.9 (Defect detection using the LoG operator):** For the detection of defects in honed surfaces, first an adaptive filtering of the original image Fig. 11.19(a) is performed as explained in Sec. 13.3.4, in order to suppress faultless grooves. Then, a LoG filtering of the resulting background image Fig. 11.19(b) with  $\sigma = 5$  is performed. In order to achieve a sufficiently precise approximation of the impulse response function of the LoG filter, the window size has to be at least  $35 \times 35$  [30], which is why an implementation in the spatial frequency domain is beneficial. Figure 11.19(c) shows the result of such a filtering; the contours of the defects are represented by the zero crossings.

The classification of the contours is based on the gradient at the zeros, which can be easily approximated by the difference between the maximum value and the minimum value within a local neighborhood (Fig. 11.19(d)). In order to detect only closed contour paths, the mean gradient of each closed contour is calculated and assigned to the corre-

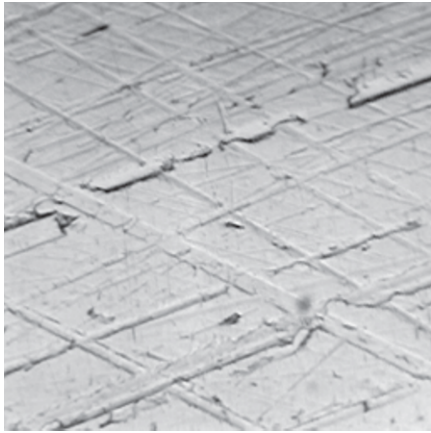
(a) Derivative at the zeros ( $\sigma = 2,5$ )(b) Derivative at the zeros ( $\sigma = 7,5$ )(c) Result of the detection ( $\sigma = 2,5$ )(d) Result of the detection ( $\sigma = 7,5$ )

**Figure 11.18.** Edge detection using the LoG operator: (a)–(b) Derivative at the zeros of the images from Fig. 11.17; (c)–(d) Results of the edge detection.

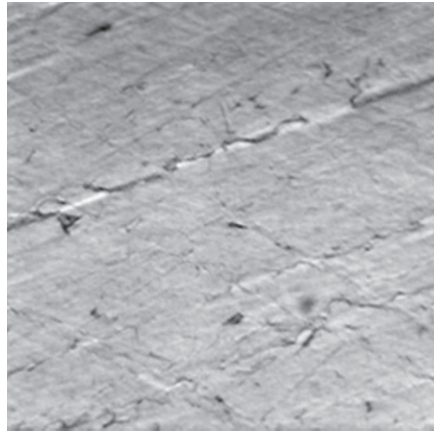
sponding pixels (Fig. 11.19(e)) and a binary detection result is obtained using a spatially constant thresholding (Fig. 11.19(f)). ■

### ➤ 11.2.3 The watershed transformation

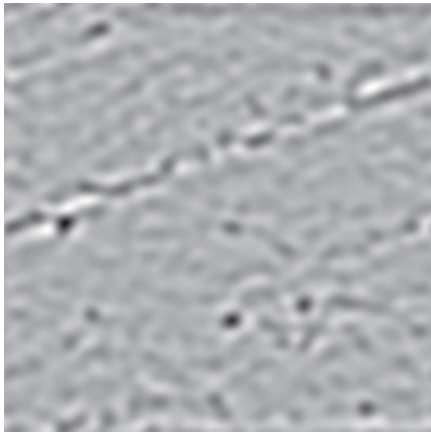
Often, an edge image is sufficient for solving a visual inspection task. For example, the edges can be used to estimate the orientation or the length of the object if two opposing edges are present. If the edge information is insufficient, a segmentation in the sense of Def. 11.1 has to be calculated from the edge image. Later on in this chapter, different edge-based segmentation methods will be presented.



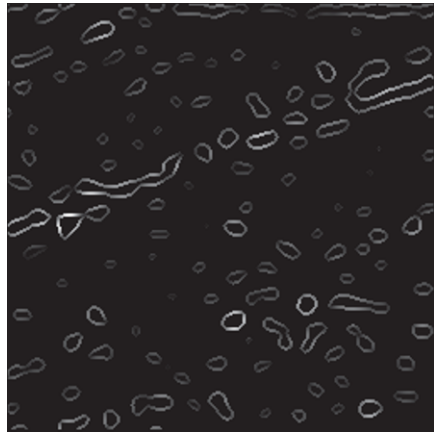
(a) Original image



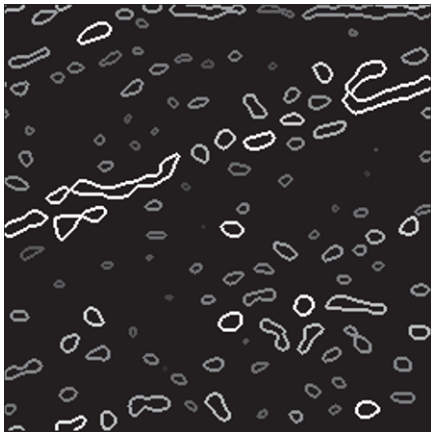
(b) Background image with suppressed grooves



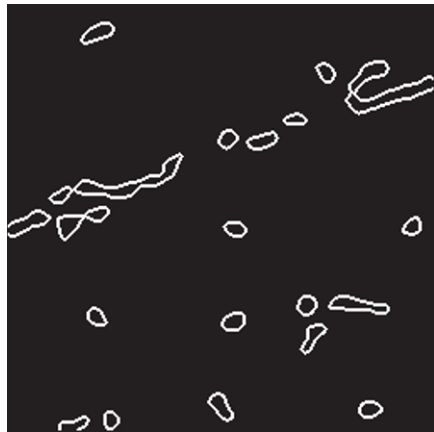
(c) Result of the LoG filtering



(d) Gradient at the zeros



(e) Mean gradient



(f) Detection result

Figure 11.19. Detecting defects using the LoG operator.

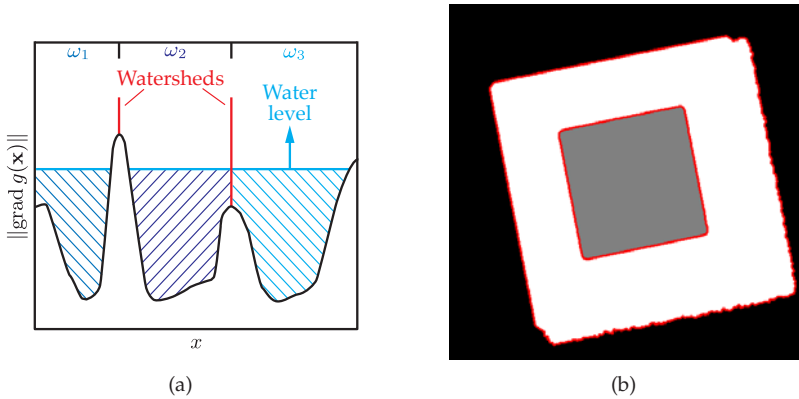


**Figure 11.20.** Image segmentation using the watershed transformation: (a) Illustration of the principle; (b) Result of the watershed transformation applied to the test image shown in Fig. 11.7(a). The watersheds, i.e., the segment borders, are represented by the red lines.

The **watershed transformation** considers the gradient image to be a mountain landscape, whose watersheds represent the borders of the segments. Local minima of the absolute values of the gradient are used as seed points, from which adjacent points are successively analyzed. These points are visited in order of the ascending absolute value of the gradient, simulating a rising water level. The segment of the current pixel is set with respect to its adjacent pixels: if all adjacent pixels are part of the same segment or have not been marked yet, the current pixel is added to the same segment. However, if they correspond to different segments, the current pixel is located on the watershed and represents a border point.

There are different variants and algorithmic realizations of the watershed transformation [23,31,39]. Often, the watershed transformation leads to an over-segmentation, i.e., it results in too many small segments. To resolve this issue, a subsequent clustering of segments or a preprocessing for the extraction of seed points can be performed. Figure 11.20(b) shows the result of the latter variant for an example image.

### 11.3

## 11.3 Diffusion filters

Diffusion filters can be used for smoothing an image. Linear smoothing filters result in a usually unwanted attenuation and widening of edges (cf. Sec. 9.3.1.1). In the ideal case, the smoothing is supposed to yield homogeneous regions that are separated by sharp edges. This can be approximately achieved by anisotropic diffusion filters, which perform an edge-preserving smoothing.

Diffusion filters are part of the image enhancement methods covered in Chap. 9. However, as they perform an edge-preserving smoothing, which represents an important preprocessing step for edge detection, diffusion filters will be discussed here.

The diffusion filter is motivated by the physical process of diffusion, which establishes a concentration or heat equilibrium in gases and liquids or in the heat transfer within solids. The concentration or temperature is assumed to be a function  $u(\mathbf{x}, t)$  of the position  $\mathbf{x}$  and time  $t$ . Concentration or temperature gradients result in diffusion processes. A spatial concentration gradient causes a compensating current  $\mathbf{j}$ , the so-called 'diffusion flux.' The rela-

tion between  $\text{grad } u$  and  $\mathbf{j}$  is described by the diffusion tensor, which is a positive semidefinite, symmetric matrix  $\mathbf{D}$ :

$$\mathbf{j} = -\mathbf{D} \text{grad } u. \quad (11.66)$$

This equation is called Fick's law [43]. In accordance with this law, a current flows in the direction of the negative gradient, so that an equilibrium of the concentrations is established. Additionally, the following continuity equation holds:

$$\frac{\partial u}{\partial t} = -\text{div } \mathbf{j}. \quad (11.67)$$

This equation represents the conservation of mass and energy: the temporal difference of the concentration at a position  $\mathbf{x}$  is exactly equal to the total compensating current originating from that point summed over all spatial directions. Inserting Fick's law (11.66) into the continuity equation (11.67) yields the following **diffusion equation**:

$$\frac{\partial u}{\partial t} = \text{div}(\mathbf{D} \text{grad } u). \quad (11.68)$$

Transferred to image processing, the image values  $g(\mathbf{x})$  are considered to be the initial state of the distribution of concentrations, or of the temperature distribution:

$$u(\mathbf{x}, 0) := g(\mathbf{x}). \quad (11.69)$$

Diffusion is a process running for a simulated time  $t$ . As time goes by, the diffusion processes lead to a smoothing of the resulting image  $u(\mathbf{x}, t)$ , corresponding to a low-pass filtering of the image signal. The mean image value is preserved because of the equation of continuity (11.67). The choice of diffusion tensor  $\mathbf{D}$  determines the characteristics of the diffusion filter [43]:

- Linear diffusion:  $\mathbf{D}$  is independent of the gradient  $\text{grad } u$ ;
- Nonlinear diffusion:  $\mathbf{D}$  is a function of the gradient,  $\mathbf{D} = \mathbf{D}(\text{grad } u)$ ;
- Homogeneous diffusion:  $\mathbf{D}$  is constant with respect to the position  $\mathbf{x}$ ;
- Inhomogeneous diffusion:  $\mathbf{D}$  is a function of the position,  $\mathbf{D} = \mathbf{D}(\mathbf{x})$ ;
- Isotropic diffusion: the relation between the diffusion flux  $\mathbf{j}$  and the gradient is the same for all directions, so that the diffusion flux is parallel to the gradient; hence, the diffusion tensor satisfies  $\mathbf{D} = D \mathbf{I}$  with  $D \in \mathbb{R}$ ,  $D > 0$  (here,  $\mathbf{I}$  denotes the identity matrix);
- Anisotropic diffusion: the relation between the diffusion flux and the gradient depends on the position, and so  $\mathbf{j}$  and  $\text{grad } u$  are not parallel.

By combining the properties of linearity, homogeneity and isotropy, different diffusion filters can be designed, of which some variants will now be presented.

### ➤ 11.3.1 Linear, homogeneous, isotropic image diffusion

In the case of linear, homogeneous, isotropic image diffusion, the diffusion tensor  $\mathbf{D} = D \mathbf{I}$  is constant for the whole image. If  $D = 1$  is used, the diffusion equation (11.68) is given by

$$\frac{\partial u(\mathbf{x}, t)}{\partial t} = \text{div}_{\mathbf{x}}(\mathbf{I} \text{grad}_{\mathbf{x}} u(\mathbf{x}, t)) \quad (11.70)$$

$$= \Delta_{\mathbf{x}} u(\mathbf{x}, t) \quad (11.71)$$

with the Laplace operator<sup>1</sup>  $\Delta_{\mathbf{x}}$ . Together with the initial condition (11.69), this equation is an initial value problem. Its solution is given by

$$u(\mathbf{x}, t) = \begin{cases} g(\mathbf{x}) & \text{if } t = 0 \\ K(\mathbf{x}, t) ** g(\mathbf{x}) & \text{if } t > 0 \end{cases} \quad (11.72)$$

with the convolution kernel

$$K(\mathbf{x}, t) = \frac{1}{2\pi s^2} e^{-\frac{\|\mathbf{x}\|^2}{2s^2}} \Big|_{s=\sqrt{2t}}. \quad (11.73)$$

This convolution kernel corresponds to a Gaussian low-pass filter (see Sec. 9.3.1.1). Hence, the linear, homogeneous, isotropic image diffusion is a low-pass filtering, with the Gaussian function's standard deviation  $s$  increasing in time. In the case of linear, homogeneous, isotropic diffusion, a closed solution of the differential equation can be obtained. This is not possible for more complicated diffusion models, so that an iterative numerical solution will be necessary: the time  $t$  corresponds to the number  $i$  of iterations. In each iteration, the following calculation is performed:

$$u(\mathbf{x}, i + 1) = u(\mathbf{x}, i) + \lambda D \Delta_{\mathbf{x}} u(\mathbf{x}, i), \quad (11.74)$$

where  $0 < \lambda < \frac{1}{4}$  is the step width of the numerical iteration [9,37]. A simple approximation of the Laplace operator  $\Delta$  is given by the convolution with the impulse response function  $l_{mn}$  of (11.59):

$$\Delta u(\mathbf{x}, t) \approx l_{mn} ** u(\mathbf{x}, t), \quad l_{mn} = \begin{pmatrix} 0 & 1 & 0 \\ 1 & -4 & 1 \\ 0 & 1 & 0 \end{pmatrix}, \quad \mathbf{x} = \begin{pmatrix} m \Delta x \\ n \Delta y \end{pmatrix}.$$

### ► 11.3.2 Linear, inhomogeneous, isotropic image diffusion

As mentioned above, a homogeneous low-pass filtering might cause blurred edges. In order to obtain sharp and clear edges between the segment borders, a reduced smoothing should be applied to the image in regions close to edges. Edges present in the image  $g(\mathbf{x})$  are represented by high values of the absolute value of the gradient  $\|\text{grad } g(\mathbf{x})\|$ . For inhomogeneous diffusion, the diffusion tensor can be chosen as a function of the absolute value of the gradient. Still considering a linear and isotropic diffusion results in the following approach for the diffusion tensor:

$$\mathbf{D} = D(\|\text{grad } g(\mathbf{x})\|) \mathbf{I}. \quad (11.75)$$

The scalar weighting function  $D(\cdot)$  should decrease monotonically for increasing absolute values of the gradient  $\|\text{grad } g(\mathbf{x})\|$ , in order to reduce the smoothing near the edges. A pos-

---

<sup>1</sup>In the following, a subscript will be added to the differential operators  $\text{grad}$ ,  $\Delta$  and  $\text{div}$ , telling which variable is subject to differentiation if it is not clear from the context. In the case of image diffusion, the operators just mentioned represent a spatial differentiation with respect to  $\mathbf{x}$ , not to the time  $t$ .

sible choice is

$$D(\|\text{grad } g(\mathbf{x})\|) := \frac{1}{\sqrt{1 + \left(\frac{\|\text{grad } g(\mathbf{x})\|}{\gamma}\right)^p}} \quad (11.76)$$

with parameters  $\gamma > 0$  and  $p$ . Choosing  $p = 1$  results in the model of Charbonnier et al. [5,14,43]. Insertion into (11.68) yields the diffusion equation of the linear, inhomogeneous, isotropic image diffusion:

$$\frac{\partial u(\mathbf{x}, t)}{\partial t} = \text{div}_{\mathbf{x}}(D(\|\text{grad } g(\mathbf{x})\|) \text{grad}_{\mathbf{x}} u(\mathbf{x}, t)). \quad (11.77)$$

Edges in the image are barriers for the diffusion process, so that the smoothing is only applied inside of largely homogeneous regions.

### 11.3.3 Nonlinear, inhomogeneous, isotropic image diffusion

Another variant can be obtained if the diffusion tensor is chosen to be a function of the gradient of the current diffused image  $u(\mathbf{x}, t)$  instead of the gradient of the original image  $g(\mathbf{x})$ :

$$\mathbf{D} = D(\|\text{grad}_{\mathbf{x}} u(\mathbf{x}, t)\|) \mathbf{I}. \quad (11.78)$$

Besides (11.76), the model of Perona and Malik presents a possible choice for the scalar function  $D(\cdot)$ :

$$D(\|\text{grad}_{\mathbf{x}} u(\mathbf{x}, t)\|) := \frac{1}{\sqrt{1 + \left(\frac{\|\text{grad}_{\mathbf{x}} u(\mathbf{x}, t)\|}{\gamma}\right)^p}}. \quad (11.79)$$

Here, the parameter  $\gamma$  corresponds to the standard deviation of the image value differences, which are supposed to be just mitigated by the diffusion. Higher image value differences are considered as edges, which have to be preserved [37].

The diffusion equation (11.68) turns into a nonlinear partial differential equation:

$$\frac{\partial u(\mathbf{x}, t)}{\partial t} = \text{div}_{\mathbf{x}}(D(\|\text{grad}_{\mathbf{x}} u(\mathbf{x}, t)\|) \text{grad}_{\mathbf{x}} u(\mathbf{x}, t)). \quad (11.80)$$

### 11.3.4 Nonlinear, inhomogeneous, anisotropic image diffusion

Inhomogeneous diffusion allows a better preservation of sharp contours in the image. However, there is nearly no smoothing along the edges, so that noise affecting these regions is barely affected. In the ideal case, the smoothing would have to be increased along the edges in order to mitigate the noise, and reduced perpendicular to edges in order to preserve sharp edges. This principle is realized by anisotropic diffusion. Its diffusion tensor depends on the orientation of the edges, which is estimated from the locally predominant direction of the image.

#### Definition 11.3: Direction and orientation

The **direction**  $\alpha \in [0, 2\pi)$  of a vector  $\mathbf{v} = (x, y)^T \in \mathbb{R}^2$ ,  $\mathbf{v} \neq \mathbf{0}$  is its angle with the  $x$ -axis:

$$\alpha = \arctan \frac{y}{x} \in [0, 2\pi). \quad (11.81)$$

The vector  $\mathbf{v}$  can be written as  $\mathbf{v} = \|\mathbf{v}\| (\cos \alpha, \sin \alpha)^T$ .

Its **orientation**  $\beta \in [0, \pi)$  is defined as its direction modulo  $\pi$ :

$$\beta := \begin{cases} \alpha & \text{if } \alpha \in [0, \pi) \\ \alpha - \pi & \text{if } \alpha \in [\pi, 2\pi) \end{cases}. \quad (11.82)$$

According to this definition, two vectors  $\mathbf{v}$  and  $-\mathbf{v}$ , whose directions are opposed by  $180^\circ$ , share the same orientation.  $\diamond$

As the gradient vector  $\text{grad } g(\mathbf{x})$  is the normal vector to an edge, it characterizes the edge's direction  $\alpha \in [0, 2\pi)$ . However, in real images, the direction information of a single pixel is usually too noisy, so that smoothing is required. This is why, for example, a prior smoothing of the image with a Gaussian low-pass filter  $h_\sigma(\mathbf{x})$  could be applied, cf. (11.50):

$$w_\sigma(\mathbf{x}) := h_\sigma(\mathbf{x}) ** g(\mathbf{x}). \quad (11.83)$$

As the calculation of the gradient and the linear filtering can be done in any order,  $\text{grad } w_\sigma(\mathbf{x})$  is equivalent to smoothing the gradient image with a Gaussian low-pass filter:

$$\text{grad } w_\sigma(\mathbf{x}) = \text{grad } (h_\sigma(\mathbf{x}) ** g(\mathbf{x})) = (h_\sigma(\mathbf{x}) ** (\text{grad } g(\mathbf{x}))). \quad (11.84)$$

However, smoothing the gradient vectors does not yield the desired result, as adjacent gradient vectors with the same orientation  $\beta \in [0, \pi)$  but opposed directions  $\alpha_2 = \alpha_1 \pm \pi$  eliminate each other. This is a typical situation for lines with two edges having opposed gradient directions. This is why the information of the orientation can get lost during the spatial averaging of the gradient vectors.

This problem can be avoided by an alternative that describes the information encoded in the orientation by the dyadic product of the gradient vectors:

$$\mathbf{J}_0(\text{grad } w_\sigma(\mathbf{x})) := (\text{grad } w_\sigma(\mathbf{x})) (\text{grad } w_\sigma(\mathbf{x}))^T. \quad (11.85)$$

Here, the parameter  $\sigma$  is chosen small enough so that no considerable elimination of the gradients can occur in regions of the impulse response function  $h_\sigma$  that are notably different from zero, i.e., smaller than the size of the finest structures present in the image, like line widths, for example. The sign is suppressed by calculating the dyadic product. This is why the dyadic product is invariant with respect to a change of sign of the gradient. Hence a spatial averaging is possible without the risk of unwanted extinctions of opposed gradient directions. The smoothing also propagates the orientation information to image points with a low absolute gradient value, where a reliable estimation would not be possible. The smoothed dyadic product is called the **structure tensor**. A Gaussian filter with standard deviation  $\rho$  is used for smoothing:

$$h_\rho(\mathbf{x}) := \frac{1}{2\pi\rho^2} e^{-\frac{\|\mathbf{x}\|^2}{2\rho^2}}, \quad \rho > 0, \quad (11.86)$$

$$\mathbf{J}_\rho(\text{grad } w_\sigma(\mathbf{x})) := h_\rho(\mathbf{x}) ** (\text{grad } w_\sigma(\mathbf{x}) (\text{grad } w_\sigma(\mathbf{x}))^T). \quad (11.87)$$

As opposed directions are merged to one orientation by the structure tensor, the parameter  $\rho$  can be chosen to be greater than  $\sigma$ . The smoothing is performed by separately considering each entry of the dyadic product  $\mathbf{J}_0$  as a function of the position and applying a convolution



with the Gaussian function. Because of the symmetry of the dyadic product, three two-dimensional convolution operations in all have to be performed for the calculation of the structure tensor. The resulting structure tensor represents a description of the orientation of the directed structures at the position  $\mathbf{x}$  of the image  $g(\mathbf{x})$ .

**Example 11.10 (Averaging of orientations using the structure tensor):** The two opposite sides of a line in an image cause gradient vectors with opposed directions. If these gradient vectors are averaged inside an image region, they might be partially or completely eliminated. Inside the considered window of the example shown in Fig. 11.21, there the numbers of gradient vectors of the directions

$$\text{grad } g(\mathbf{x}) = \begin{pmatrix} 1 \\ 1 \end{pmatrix} \quad \text{and} \quad \text{grad } g(\mathbf{x}) = \begin{pmatrix} -1 \\ -1 \end{pmatrix} \quad (11.88)$$

are equal. Hence, the spatial averaging results in

$$\text{grad } (w_\sigma(\mathbf{x})) = h_\sigma(\mathbf{x}) ** \text{grad } g(\mathbf{x}) = \begin{pmatrix} 0 \\ 0 \end{pmatrix}. \quad (11.89)$$

The information about the orientation of the line structure is lost due to the spatial averaging of the gradients.

In contrast, the dyadic product of the gradient vectors is given by

$$\mathbf{J}_0(\text{grad } g(\mathbf{x})) = (\text{grad } g(\mathbf{x})) (\text{grad } g(\mathbf{x}))^T \quad (11.90)$$

$$= \begin{pmatrix} 1 \\ 1 \end{pmatrix} \begin{pmatrix} 1 & 1 \end{pmatrix} = \begin{pmatrix} 1 & 1 \\ 1 & 1 \end{pmatrix} \quad (11.91)$$

and

$$\mathbf{J}_0(\text{grad } g(\mathbf{x})) = (\text{grad } g(\mathbf{x})) (\text{grad } g(\mathbf{x}))^T \quad (11.92)$$

$$= \begin{pmatrix} -1 \\ -1 \end{pmatrix} \begin{pmatrix} -1 & -1 \end{pmatrix} = \begin{pmatrix} 1 & 1 \\ 1 & 1 \end{pmatrix}. \quad (11.93)$$

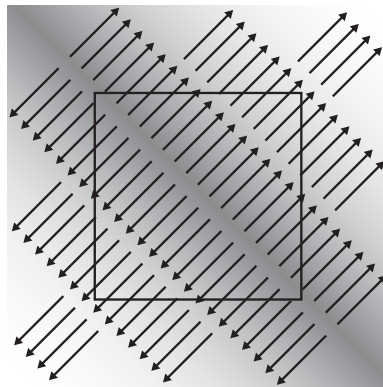


Figure 11.21. Averaging of directions.

The opposed signs are suppressed by the calculation of the dyadic product. A spatial averaging yields the structure tensor

$$\mathbf{J}_\rho(\text{grad } g(\mathbf{x})) = \begin{pmatrix} 1 & 1 \\ 1 & 1 \end{pmatrix}. \quad (11.94)$$

Hence, the calculation of the structure tensor preserves the information about the orientations.

Now consider an arbitrary gradient orientation  $\mathbf{a} \in \mathbb{R}^2$ ,  $\|\mathbf{a}\| = 1$ . The gradient vectors are denoted by

$$\text{grad } g(\mathbf{x}) = r \mathbf{a}, \quad (11.95)$$

and the length  $r \in \mathbb{R}$  of the gradient vectors is assumed to be a zero-mean random variable:

$$E\{r\} = 0. \quad (11.96)$$

If this random process is assumed to be ergodic, the spatially averaged gradient is given by the following expected value:

$$E\{\text{grad } g(\mathbf{x})\} = E\{r\} \mathbf{a} = \mathbf{0}. \quad (11.97)$$

Hence, the orientation information is lost due to the averaging. On the other hand, the structure tensor is given by

$$\mathbf{J}(\text{grad } g(\mathbf{x})) = E\{(\text{grad } g(\mathbf{x})) (\text{grad } g(\mathbf{x}))^T\} \quad (11.98)$$

$$= E\{r \mathbf{a} r \mathbf{a}^T\} = E\{r^2\} \mathbf{a} \mathbf{a}^T. \quad (11.99)$$

The orientation vector  $\mathbf{a}$  is an eigenvector of the structure tensor with eigenvalue  $E\{r^2\}$ , as  $\|\mathbf{a}\| = 1$  implies

$$\mathbf{J}(\text{grad } g(\mathbf{x})) \mathbf{a} = E\{r^2\} \mathbf{a} \mathbf{a}^T \mathbf{a} = E\{r^2\} \mathbf{a}. \quad (11.100)$$

Thus, the orientation information is contained in the eigenvectors of the structure tensor and is preserved despite the spatial averaging. ■

---

**Example 11.11 (Averaging of orientations using complex numbers):** An alternative approach for an orientation preserving averaging is given by the representation of directions as complex numbers. A complex number  $v \in \mathbb{C}$  can be written as

$$v = \mathbf{v}^T \mathbf{e}_x + j \mathbf{v}^T \mathbf{e}_y, \quad (11.101)$$

$$v = |v| e^{j\varphi}, \quad |v| = \|\mathbf{v}\|, \quad \varphi = \angle v = \arctan \frac{\mathbf{v}^T \mathbf{e}_y}{\mathbf{v}^T \mathbf{e}_x}. \quad (11.102)$$

The real part and the imaginary part can be considered to be the components of a vector  $\mathbf{v}$ , whose length is equal to the absolute value of the complex number. The opposed direction is described by the negative complex number  $w$ . A direct averaging of the two

directions  $v$  and  $w$  leads to an elimination of the orientation information:

$$w = -v = |v|e^{j(\varphi+\pi)} \Rightarrow v + w = 0. \quad (11.103)$$

However, an orientation preserving averaging is possible by adding the squares of the complex numbers:

$$v^2 + w^2 = |v|^2 e^{j2\varphi} + |v|^2 e^{j2\varphi} \underbrace{e^{j2\pi}}_{=1} = 2|v|^2 e^{j2\varphi} = 2v^2 \quad (11.104)$$

$$\Rightarrow \sqrt{v^2 + w^2} = v\sqrt{2}. \quad (11.105)$$

Hence, the orientation preserving average of  $N$  complex numbers  $v_i$  can be defined as follows:

$$\sqrt{\frac{1}{N} \sum_{i=1}^N v_i^2}. \quad (11.106)$$

■

The remaining derivation of the anisotropic diffusion will be based on the structure tensor. For each image point  $\mathbf{x}$ , the structure tensor  $\mathbf{J}_\rho(\text{grad } w_\sigma(\mathbf{x})) \in \mathbb{R}^{2 \times 2}$  is represented by a symmetric, positive semidefinite matrix. This is why there exists an orthonormal basis of eigenvectors of the structure tensor,  $\mathbf{v}_1, \mathbf{v}_2 \in \mathbb{R}^2$ , with eigenvalues  $\mu_1, \mu_2 \geq 0$  [2]. W.l.o.g. let  $\mu_1 \geq \mu_2 \geq 0$ . The eigenvectors meet

$$\mathbf{v}_1^T \mathbf{v}_2 = 0, \quad \|\mathbf{v}_1\| = 1, \quad \|\mathbf{v}_2\| = 1. \quad (11.107)$$

Now, the structure tensor can be written as

$$\mathbf{J}_\rho(\text{grad } w_\sigma(\mathbf{x})) = \mu_1 \mathbf{v}_1 \mathbf{v}_1^T + \mu_2 \mathbf{v}_2 \mathbf{v}_2^T. \quad (11.108)$$

The magnitude of the eigenvalue is a measure of the contrast of the image  $w_\sigma(\mathbf{x})$  in the orientation of the corresponding eigenvector. The eigenvector  $\mathbf{v}_1$  of the greatest eigenvalue  $\mu_1$  describes the orientation of the largest change of image values, e.g., an orientation which is perpendicular to an edge of the image. The eigenvector  $\mathbf{v}_2$  denotes the orientation of the least change of image values, e.g., along an edge. The difference between the eigenvalues  $(\mu_1 - \mu_2)^2$  is a measure of the local anisotropy of the image  $w_\sigma$  at the position  $\mathbf{x}$ .

Now, the anisotropic diffusion should reduce the smoothing in the orientation of the greatest difference of image values, in order to preserve edges and lines in the image. In other words, the diffusion is supposed to be low with respect to the orientation  $\mathbf{v}_1$  and high with respect to the orientation  $\mathbf{v}_2$ . These requirements can be met by an appropriate choice of the diffusion tensor  $\mathbf{D}$ . This approach defines a diffusion tensor having the same eigenvectors as the structure tensor but different eigenvalues  $\lambda_1, \lambda_2$ :

$$\mathbf{D}(\mathbf{J}_\rho(\text{grad } w_\sigma(\mathbf{x}))) := \lambda_1 \mathbf{v}_1 \mathbf{v}_1^T + \lambda_2 \mathbf{v}_2 \mathbf{v}_2^T, \quad 0 \leq \lambda_1 \leq \lambda_2. \quad (11.109)$$

As the diffusion is supposed to be minimal in the direction  $\mathbf{v}_1$  of the largest difference of image values,  $\lambda_1 \leq \lambda_2$ . A possible choice for the eigenvalues of the diffusion tensor is given

by

$$\lambda_1 := D(\|\text{grad } w_\sigma(\mathbf{x})\|), \quad (11.110)$$

$$\lambda_2 := \begin{cases} \lambda_1 & \text{if } \mu_1 = \mu_2 \\ \lambda_1 + (1 - \lambda_1) e^{-\frac{C}{(\mu_1 - \mu_2)^{2m}}} & \text{otherwise.} \end{cases} \quad (11.111)$$

As with isotropic diffusion, the first eigenvalue can be chosen according to (11.76) or (11.79), resulting in a stronger smoothing of homogeneous regions than of edges in the direction of the gradient. At positions showing a low first eigenvalue, the second eigenvalue is increased at pixels having a great local anisotropy  $(\mu_1 - \mu_2)^2$ . For example, this results in an intense smoothing along edges perpendicular to the gradient direction. The parameters can be chosen according to  $C > 0$  and  $m \in \mathbb{N}$ ; usually,  $m := 1$ . This diffusion tensor is now inserted into the diffusion equation (11.68):

$$\frac{\partial u(\mathbf{x}, t)}{\partial t} = \text{div}_{\mathbf{x}}(\mathbf{D}(\mathbf{J}_\rho(\text{grad } w_\sigma(\mathbf{x}))) \text{grad}_{\mathbf{x}} u(\mathbf{x}, t)). \quad (11.112)$$

For nonlinear diffusion,  $u(\mathbf{x}, t)$  is used instead of  $g(\mathbf{x})$  for the calculation of  $w_\sigma(\mathbf{x})$  in (11.83). The algorithm of anisotropic diffusion can be summarized as follows:

1. Calculate the current gradient  $\text{grad } w_\sigma(\mathbf{x})$ , for example by convolving with the differentiated Gaussian low-pass filter (11.53) with standard deviation  $\sigma$ .
2. Calculate the structure tensor field  $\mathbf{J}_\rho(\text{grad } w_\sigma(\mathbf{x}))$  in accordance with (11.87), by spatially averaging the dyadic product (11.85) of the gradient using a Gaussian low-pass filter with standard deviation  $\rho > \sigma$ .
3. Determine the eigenvalues and eigenvectors of the structure tensor for every image pixel  $\mathbf{x}$ .
4. Design the diffusion tensor field  $\mathbf{D}(\mathbf{J}_\rho(\text{grad } w_\sigma(\mathbf{x})))$  in accordance with (11.109).
5. Numerically solve the diffusion equation (11.112).

Figure 11.22 shows the results of the described diffusion filter for an example image. Homogeneous diffusion yields similar results to those of a Gaussian low-pass filter: the noise is reduced but fine structures are blurred. This disadvantage is avoided by inhomogeneous diffusion, but the noise along the edges is not reduced. Anisotropic diffusion results in mitigating the noise for the whole image, while simultaneously preserving sharp edges.

## 11.4

### 11.4 Active contours

Active contour models (e.g., ‘snakes’ and ‘balloons’) represent a contour that changes as a function of the local image properties. The contour represents the border between two regions of an image, resulting in a segmentation into  $I = 2$  segments: outside the contour and inside the contour.

The basic idea of active contours can be illustrated as follows: an ‘elastic band’ is placed inside the image, which nestles to the structures of interest and forms a (preferably) short curve. The image is segmented into the two regions inside and outside the closed curve. In fact, there are considerably more degrees of freedom when designing active contours than the physical forces affecting an elastic band.

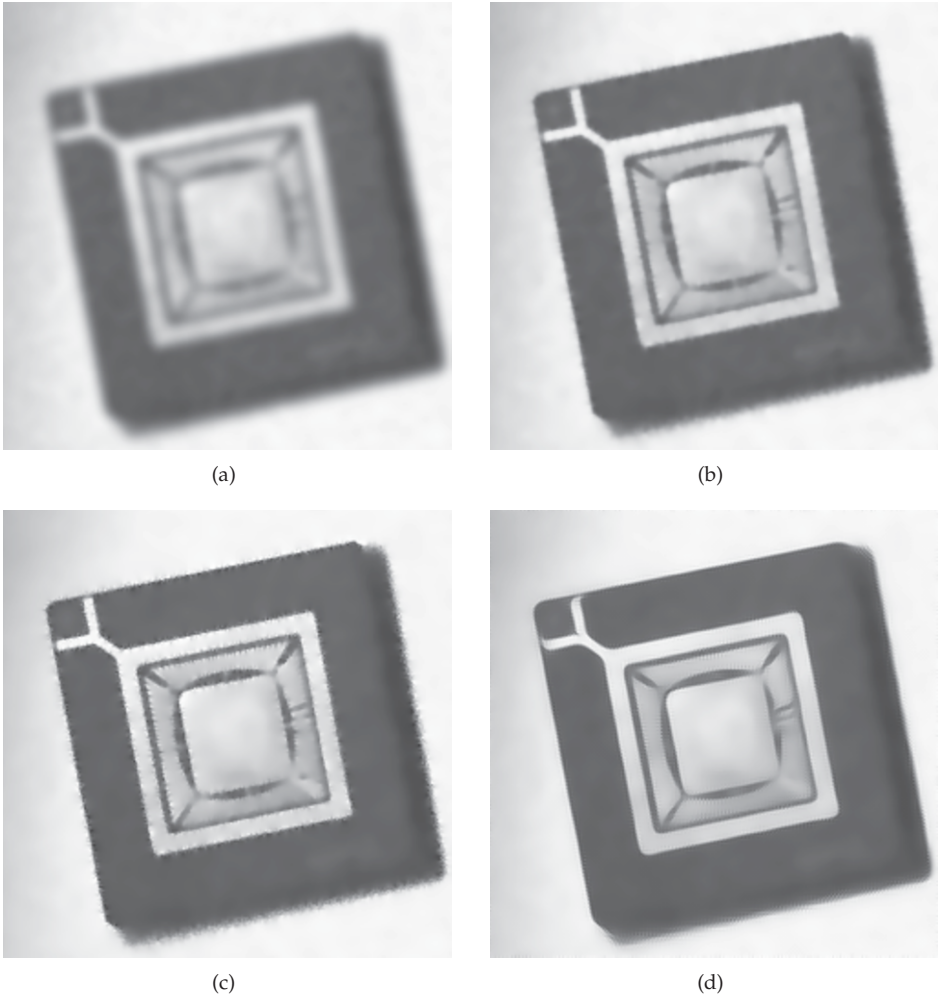


**Figure 11.22.** Different diffusion filters applied to a test image with additive Gaussian noise of standard deviation  $\sigma_r = 20$ , cf. Fig. 11.14(a): (a) Linear, homogeneous, isotropic diffusion in accordance with (11.70); (b) Linear, inhomogeneous, isotropic diffusion in accordance with (11.77); (c) Nonlinear, inhomogeneous, isotropic diffusion (11.80) according to the Perona–Malik model with  $\gamma = \sigma_r = 20$ ; (d) Nonlinear, inhomogeneous, anisotropic image diffusion in accordance with (11.112).

This section focuses on the **snake** model, which is based on Kass, Witkin and Terzopoulos [26]. At first, the original approach will be presented, and then two variants, gradient vector flow and vector field convolution, will be introduced.

Snakes are based on a parametric contour model. For the contour, an energy functional is defined, which corresponds to a potential energy with inner and external forces.<sup>2</sup> The

<sup>2</sup>For force fields  $\mathbf{F}(\mathbf{x})$  with vanishing curl  $\text{rot } \mathbf{F}(\mathbf{x}) = \mathbf{0}$ , a scalar potential  $E(\mathbf{x})$  can be assumed, so that  $\mathbf{F}(\mathbf{x}) = -\text{grad } E(\mathbf{x})$ . Such force fields are called conservative, as the energy necessary to get

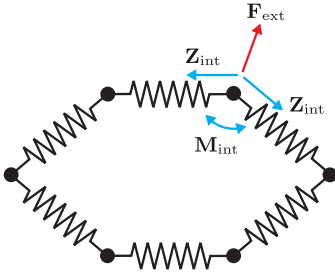


**Figure 11.23.** Active contour pictured as a chain of points connected by springs, which are affected by internal drag forces  $\mathbf{Z}_{\text{int}}$  and internal restoring forces  $\mathbf{M}_{\text{int}}$  on the one hand, and by external forces  $\mathbf{F}_{\text{ext}}$  on the other hand.

contour is adapted to the local image features by minimizing this energy functional. A closed contour is represented as follows:

$$\mathbf{v} : [0, 1] \rightarrow \mathbb{R}^2, \quad \mathbf{v}(s) = \begin{pmatrix} x(s) \\ y(s) \end{pmatrix}, \quad s \in [0, 1], \quad \mathbf{v}(0) = \mathbf{v}(1).$$

The energy functional is composed of the internal and external energy:

$$E_{\text{Snake}}(\mathbf{v}(s)) = \int_0^1 (E_{\text{int}}(\mathbf{v}(s), s) + E_{\text{ext}}(\mathbf{v}(s))) \, ds. \tag{11.113}$$

The internal energy  $E_{\text{int}}$  is responsible for the elasticity and the smoothness characteristics of the contour:

$$E_{\text{int}}(\mathbf{v}(s), s) = \underbrace{\frac{1}{2} w_1(s) \left\| \frac{d}{ds} \mathbf{v}(s) \right\|^2}_{\text{'Elasticity', 'Rigidity'}} + \underbrace{\frac{1}{2} w_2(s) \left\| \frac{d^2}{ds^2} \mathbf{v}(s) \right\|^2}_{\text{'Smoothness'}}. \tag{11.114}$$

The two terms are weighted by the functions  $w_1(s)$  and  $w_2(s)$ , which are often assumed to be constant. An active contour can be visualized as a chain of points that are coupled by drag forces and restoring torques (see Fig. 11.23). The first term of (11.114) corresponds to the drag forces  $\mathbf{Z}_{\text{int}}$  and the second term, which increases for higher curvatures of the contour  $\mathbf{v}(s)$ , corresponds to the restoring torques (bending moments)  $\mathbf{M}_{\text{int}}$ . By decreasing  $w_1$ , the contour will be more stretchable. A smoother contour can be obtained by increasing  $w_2$ .

The external energy is defined as follows:

$$E_{\text{ext}}(\mathbf{v}(s)) = P_{\text{Image}}(\mathbf{v}(s)) + E_{\text{Design}}(\mathbf{v}(s)). \tag{11.115}$$

Here,  $P_{\text{Image}}(\cdot)$  is a scalar potential function associated to the image data, and  $E_{\text{Design}}(\cdot)$  is an energy term for considering problem specific constraints (design term).

The image potential  $P_{\text{Image}}(\mathbf{v})$  causes the contour to be attracted by image features such as lines, edges or corners. The design of the potential function results in local minima of the potential for interesting image features. The image potential in turn can be defined as a weighted sum of multiple terms:

$$P_{\text{Image}} = w_{\text{line}} P_{\text{line}} + w_{\text{edge}} P_{\text{edge}} + w_{\text{term}} P_{\text{term}}. \tag{11.116}$$

---

from point  $\mathbf{x}_1$  to point  $\mathbf{x}_2$  is independent of the choice of the path between  $\mathbf{x}_1$  and  $\mathbf{x}_2$ :  $\int_{\mathbf{x}_1}^{\mathbf{x}_2} \mathbf{F}(\mathbf{x}) \, d\mathbf{x} = E(\mathbf{x}_1) - E(\mathbf{x}_2)$ .

The **line potential**  $P_{\text{line}}$  causes the snake to be attracted by lines in the image. The simplest case is given by

$$P_{\text{line}}(\mathbf{x}) = g(\mathbf{x}). \tag{11.117}$$

The potential coincides with the image value. Depending on the sign of  $w_{\text{line}}$ , the contour is attracted by bright or dark lines.

The **edge potential**  $P_{\text{edge}}$  causes the snake to be attracted by step edges inside the image. In principle, any edge operator can be used, for example,

$$P_{\text{edge}}(\mathbf{x}) = -\|\text{grad } g(\mathbf{x})\|^2. \tag{11.118}$$

An initial smoothing should be performed on images which are severely affected by noise, e.g., by applying a differentiated Gaussian low-pass filter (see Sec. 11.2.1). Because of the **termination potential**  $P_{\text{term}}$ , the snake is attracted by ends of lines:

$$P_{\text{term}} = -\left|(\text{grad } \theta)^T \mathbf{n}_\perp\right|. \tag{11.119}$$

Here,  $\theta$  denotes the gradient angle,

$$\theta = \angle \text{grad } g(\mathbf{x}) = \arctan \frac{\frac{\partial g(\mathbf{x})}{\partial y}}{\frac{\partial g(\mathbf{x})}{\partial x}}, \tag{11.120}$$

and  $\mathbf{n}_\perp$  denotes the normal vector which is perpendicular to the gradient direction:

$$\mathbf{n}_\perp = \begin{pmatrix} -\sin \theta \\ \cos \theta \end{pmatrix} \tag{11.121}$$

Along lines, the gradient of the gradient angle is perpendicular to the edge, which is why the inner product in (11.119) vanishes. At line endings, however, there is a gradient in the direction of the edge, resulting in a negative potential, which attracts the contour. The termination potential (11.119) can be directly calculated as a function of the first and second derivatives of the image signal [26]:

$$P_{\text{term}} = -\left| \frac{\frac{\partial^2 g(\mathbf{x})}{\partial y^2} \left(\frac{\partial g(\mathbf{x})}{\partial x}\right)^2 - 2 \frac{\partial^2 g(\mathbf{x})}{\partial x \partial y} \frac{\partial g(\mathbf{x})}{\partial x} \frac{\partial g(\mathbf{x})}{\partial y} + \frac{\partial^2 g(\mathbf{x})}{\partial x^2} \left(\frac{\partial g(\mathbf{x})}{\partial y}\right)^2}{\left(\left(\frac{\partial g(\mathbf{x})}{\partial x}\right)^2 + \left(\frac{\partial g(\mathbf{x})}{\partial y}\right)^2\right)^{\frac{3}{2}}} \right|.$$

Because of the intensive use of derivatives, extremely noisy images should first be smoothed.

The problem of minimizing the energy is solved using the methods of the **calculus of variations** [11], which will now be briefly presented for the case of a general optimization problem. The energy functional

$$E = \int_{s_1}^{s_2} f(s, \mathbf{v}(s), \mathbf{v}_s(s), \mathbf{v}_{ss}(s)) \, ds \quad \rightarrow \quad \text{Extremum} \tag{11.122}$$

is considered in the following notation

$$\underbrace{\mathbf{v}_{s \dots s}}_n(s) := \frac{d^n \mathbf{v}(s)}{ds^n}. \tag{11.123}$$

The function  $f(\cdot)$  inside the energy functional depends on the parameter  $s$ , the value of the function  $\mathbf{v}(s)$  for  $s$ , and the first two derivatives of  $\mathbf{v}$  at  $s$ .

If a function  $\mathbf{v}(s)$  is an extremum of the energy functional, it will satisfy the **Euler–Lagrange differential equation**:<sup>3</sup>

$$\frac{\partial}{\partial \mathbf{v}} f - \frac{d}{ds} \frac{\partial}{\partial \mathbf{v}_s} f + \frac{d^2}{ds^2} \frac{\partial}{\partial \mathbf{v}_{ss}} f = \mathbf{0}. \quad (11.124)$$

This formalism is now applied to the following energy functional:

$$E_{\text{Snake}}(\mathbf{v}(s)) = \int_0^1 (E_{\text{int}}(\mathbf{v}(s), s) + E_{\text{ext}}(\mathbf{v}(s))) ds \quad (11.125)$$

$$= \int_0^1 \left( \frac{1}{2} w_1(s) \|\mathbf{v}_s(s)\|^2 + \frac{1}{2} w_2(s) \|\mathbf{v}_{ss}(s)\|^2 + P_{\text{Image}}(\mathbf{v}(s)) + E_{\text{Design}}(\mathbf{v}(s)) \right) ds. \quad (11.126)$$

By the Euler–Lagrange equation, one has

$$\frac{\partial}{\partial \mathbf{v}} P_{\text{Image}}(\mathbf{v}(s)) + \frac{\partial}{\partial \mathbf{v}} E_{\text{Design}}(\mathbf{v}(s)) - \frac{d}{ds} (w_1(s) \mathbf{v}_s(s)) + \frac{d^2}{ds^2} (w_2(s) \mathbf{v}_{ss}(s)) = \mathbf{0}. \quad (11.127)$$

For constant  $w_1(s)$  and  $w_2(s)$ , this results in

$$-w_1 \mathbf{v}_{ss}(s) + w_2 \mathbf{v}_{ssss}(s) = -\frac{\partial}{\partial \mathbf{v}} P_{\text{Image}}(\mathbf{v}(s)) - \frac{\partial}{\partial \mathbf{v}} E_{\text{Design}}(\mathbf{v}(s)). \quad (11.128)$$

As on the right-hand side, the forces corresponding to the potentials are calculated by the operation  $-\text{grad}_{\mathbf{v}}$ , the terms on the two sides of the equation can be considered as internal and external forces:

$$\mathbf{F}_{\text{int}}(\mathbf{v}(s)) := -w_1 \mathbf{v}_{ss}(s) + w_2 \mathbf{v}_{ssss}(s), \quad (11.129)$$

$$\mathbf{F}_{\text{ext}}(\mathbf{v}(s)) := -\frac{\partial}{\partial \mathbf{v}} P_{\text{Image}}(\mathbf{v}(s)) - \frac{\partial}{\partial \mathbf{v}} E_{\text{Design}}(\mathbf{v}(s)). \quad (11.130)$$

The energy is minimal in the case of an **equilibrium of forces**:

$$\mathbf{F}_{\text{int}} = \mathbf{F}_{\text{ext}} \quad (11.131)$$

The external forces consist of the actual image force and user-defined, problem-specific forces. In summary, a segmentation using active contours comprises the following steps:

1. Determination of the image structures of interest and design of the appropriate potentials, which correspond to the forces that attract the contour to such structures.
2. Definition of active contours, whose ‘material properties’ are determined by the internal forces or by their potentials.
3. Positioning the initial contour in the image, which is then deformed by the acting forces, until an equilibrium between internal and external forces is reached.
4. In the equilibrium, the contour marks the borders between the two segments.

---

<sup>3</sup>Here, the notation  $\frac{\partial}{\partial \mathbf{v}}$  is short for  $\text{grad}_{\mathbf{v}}$ . Accordingly,  $\frac{\partial}{\partial \mathbf{v}_s}$  and  $\frac{\partial}{\partial \mathbf{v}_{ss}}$  correspond to  $\text{grad}_{\mathbf{v}_s}$  and  $\text{grad}_{\mathbf{v}_{ss}}$ .



The third step does not have to be realized as a quasi-temporal process, but can also be carried out implicitly by directly calculating the position of the equilibrium.

**Remarks:**

- The initial contour has to be placed near the relevant contour of the image, in order to prevent the active contour from collapsing.
- The potential of the image should be defined in such a way as to provide a sufficiently large range for the forces that are caused by the relevant structures. For example, this can be problematic for step edges between regions with constant image values. In this case, the gradient of the image values is zero inside the regions and the contour is not attracted to the edges.

The active contour can be calculated by numerically solving the differential equations, e.g., by means of the

- finite element method (FEM) or the
- finite difference method (FDM).

By these methods, the Euler–Lagrange equation is discretized and solved iteratively [26].

► **11.4.1 Gradient vector flow**

**Gradient vector flow** is an alternative external force for snakes, providing a higher range of attraction to the structures of interest. It has been designed to improve the adaptation of the contour to concave structures and to improve the convergence for more distant initial contours.

The external force field  $\mathbf{F}_{\text{GVF}}(\mathbf{x}) = (\alpha(\mathbf{x}), \beta(\mathbf{x}))^T$  is determined by minimizing a specially developed energy functional  $E_{\text{GVF}}$ , which is defined as follows [44]:

$$E_{\text{GVF}} = \iint_{\Omega_g} \left( \mu (\|\text{grad } \alpha(\mathbf{x})\|^2 + \|\text{grad } \beta(\mathbf{x})\|^2) \right. \quad (11.132)$$

$$\left. + \|\text{grad } g_{\text{edge}}(\mathbf{x})\|^2 \|\mathbf{F}_{\text{GVF}}(\mathbf{x}) - \text{grad } g_{\text{edge}}(\mathbf{x})\|^2 \right) d\mathbf{x}. \quad (11.133)$$

Here,  $g_{\text{edge}}(\mathbf{x})$  is an edge image, e.g.,

$$g_{\text{edge}}(\mathbf{x}) = \|\text{grad } g(\mathbf{x})\|^2, \quad (11.134)$$

The gradient  $\text{grad } g_{\text{edge}}(\mathbf{x})$  of the edge image is oriented towards the edges, so if an adequate external force is present, edges attract active contours, cf. Fig. 11.24(a). Now, Equation (11.133) can be interpreted as follows: because of the summand in the second row, the force field  $\mathbf{F}_{\text{GVF}}$  is equal to the gradient of the edge image, especially at positions of high magnitudes of this gradient. The two summands of the first row of (11.133) smooth  $\mathbf{F}_{\text{GVF}}$  and the relative weight of this smoothing term is determined by  $\mu \geq 0$ . For homogeneous image regions, the smoothing terms are dominant, as the second term is attenuated by the factor  $\|\text{grad } g_{\text{edge}}(\mathbf{x})\|^2$ . Hence, the gradient of the edge image is extended into homogeneous regions, so that the range of the attracting force is increased. This is why the dependency of the initialization of the energy minimization problem is decreased and the adaptation of the active contour to concave structures is improved.

The numerical calculation of the external force can be performed using the Euler–Lagrange equation [44]. In the second step, the right-hand side of Equation (11.128) is re-

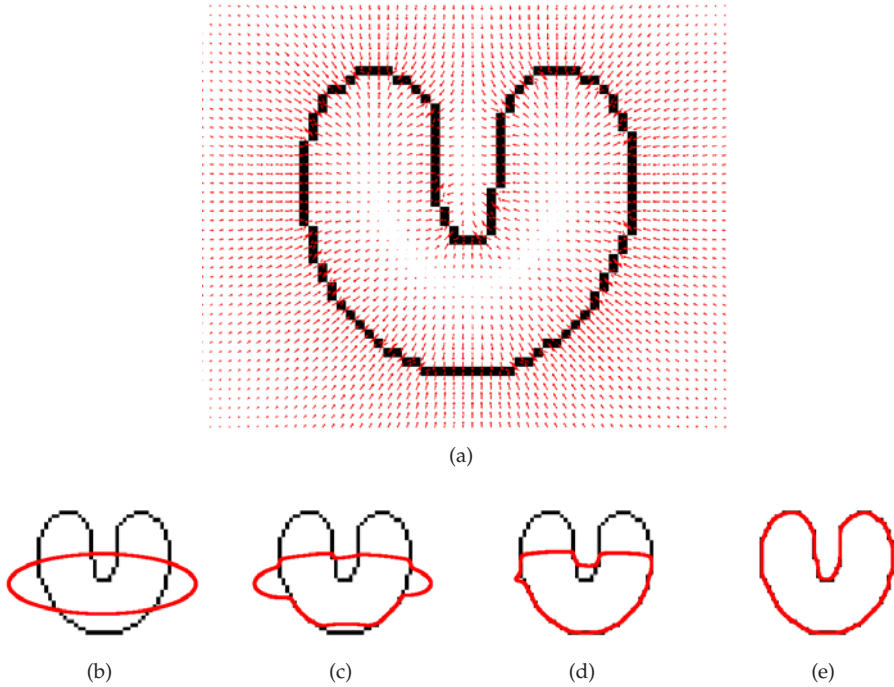


**Figure 11.24.** Adaptation of the contour according to the gradient vector flow method, illustrated using a binary test image: (a) Force field  $\mathbf{F}_{GVF}(\mathbf{x})$ ; (b) Initial contour; (c), (d) Intermediate steps of the numerical contour adaptation; (e) Final result (source: Prof. J. Prince [44]).

placed by the resulting force field  $\mathbf{F}_{GVF}(\mathbf{v}(s))$  and the adaptation of the active contour is again performed numerically.

Figure 11.24 shows the force field for a test image as well as the iterative adaptation of the active contour. The method can also handle images with a high noise level, as is shown by an example from the field of medical imaging (see Fig. 11.25).

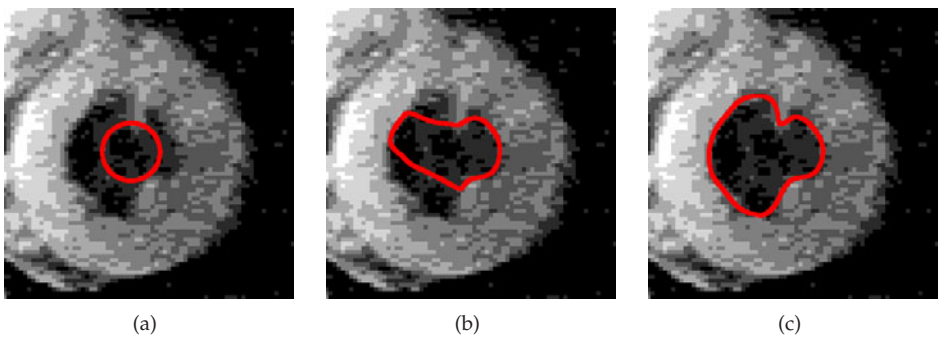


**Figure 11.25.** Segmentation of a magnetic resonance image: (a) Initial contour; (b) Intermediate result; (c) Final result of the contour adaptation (source: Prof. J. Prince [44]).

11.4.2 Vector field convolution

Vector field convolution [29] represents another method for the definition of the external forces for active contours. The aim is an optimal adaptation of the active contour to concave structures and distant initial contours. Simultaneously, the calculation of the external force has to be efficient.

For vector field convolution, the external force is given by a convolution with a suitable kernel  $q(x)$ :

$$F_{VFC}(x) = g_{edge}(x) ** q(x). \tag{11.135}$$

As in the previous section,  $g_{edge}(x)$  denotes the edge image, see Equation (11.134).

The convolution kernel describes an elementary vector field (force field) with a local depression located at the origin. It is defined as the product of a direction field with a scalar decay function (Fig. 11.26):

$$q(x) := m(x) n(x) \tag{11.136}$$

with 
$$n(x) := \begin{cases} -\frac{x}{\|x\|} & \text{if } x \neq 0 \\ 0 & \text{if } x = 0, \end{cases} \tag{11.137}$$

$$m_1(x) := (\|x\| + \varepsilon)^{-\gamma} \quad \text{or, e.g.,} \quad m_2(x) := e^{-\frac{\|x\|^2}{\varepsilon^2}}. \tag{11.138}$$

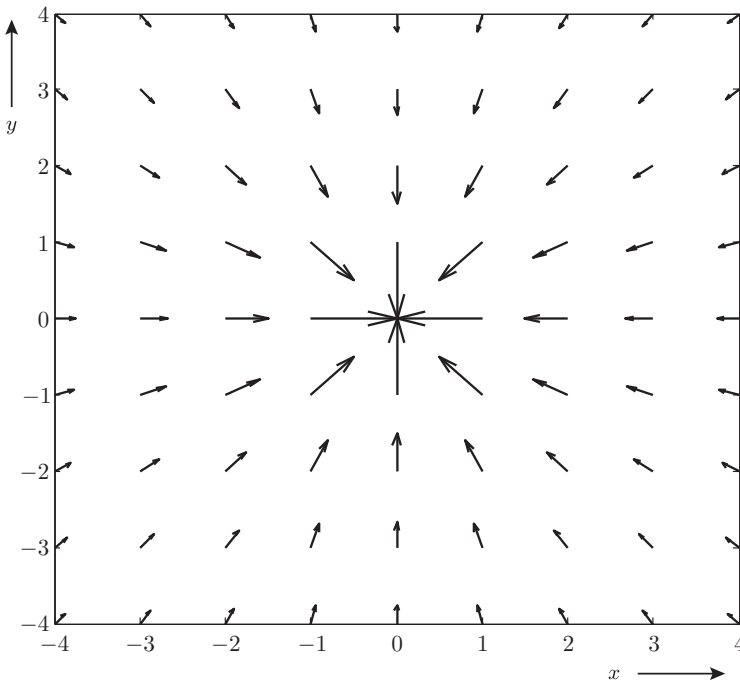


Figure 11.26. Convolution kernel  $q(x) = -\frac{x}{\|x\|^2}$  for vector field convolution ( $m(x) = m_1(x), \varepsilon = 0, \gamma = 1$ ).

The direction field  $\mathbf{n}(\mathbf{x})$  is directed towards the center of the convolution kernel. For the amplitudes  $m(\mathbf{x})$ , the two alternatives  $m_1(\mathbf{x})$  and  $m_2(\mathbf{x})$  have been proposed, where  $\varepsilon > 0$ ,  $\gamma > 0$  and  $\zeta > 0$  are parameters [29]. The range of the external force can be explicitly set by adjusting the size of the convolution kernel and the parameters  $\gamma$  and  $\zeta$ . When using  $m_1(\mathbf{x})$  with  $\gamma = 2$  and  $\varepsilon = 0$ , the resulting convolution kernel corresponds to Newton’s law of gravitation.

The convolution operation required for calculating the external force can be performed using the fast Fourier transform. For this purpose, the vectorial convolution kernel  $\mathbf{q}(\mathbf{x}) = (q_x, q_y)^T$  can be expressed as a complex signal:  $\underline{q}(\mathbf{x}) := q_x + jq_y$ . The real-valued, vectorial convolution with  $\mathbf{q}(\mathbf{x})$  is equivalent to a complex-valued convolution with  $\underline{q}(\mathbf{x})$ :

$$\begin{aligned} \mathbf{F}_{\text{VFC}}(\mathbf{x}) &= g_{\text{edge}}(\mathbf{x}) \ast \ast \mathbf{q}(\mathbf{x}) & \mathbf{F}_{\text{VFC}}, \mathbf{q} \in \mathbb{R}^2 \\ \underline{F}_{\text{VFC}}(\mathbf{x}) &= g_{\text{edge}}(\mathbf{x}) \ast \ast \underline{q}(\mathbf{x}) & \underline{F}_{\text{VFC}}, \underline{q} \in \mathbb{C} \end{aligned} \tag{11.139}$$

$$\mathcal{F}\{\underline{F}_{\text{VFC}}\}(\mathbf{f}) = \mathcal{F}\{g_{\text{edge}}\}(\mathbf{f}) \cdot \mathcal{F}\{\underline{q}\}(\mathbf{f}).$$

In the spatial frequency domain, this convolution corresponds to a multiplication. Before performing the discrete Fourier transform, the domains of the signals need to be suitably increased (by zero padding, cf. Sec. 8.3.9.2). In [29] it is shown that the calculation of  $\mathbf{F}_{\text{VFC}}$  using the fast Fourier transform is more efficient than the calculation of  $\mathbf{F}_{\text{GVF}}$  from the previous section using numerical methods. Besides, the elementary field can be explicitly set or defined, whereas  $\mathbf{F}_{\text{GVF}}$  is the result of a calculation and can only be indirectly adjusted via the parameter  $\mu$ . Furthermore, the VFC method allows a quasi-physical interpretation, as  $g_{\text{edge}}(\mathbf{x})$  can be considered as a distribution of charges and  $q$  as a field of single elementary charges. The superposition of the fields of the elementary charges, which are distributed according to  $g_{\text{edge}}(\mathbf{x})$ , in the surrounding space represents the total force field.

On the one hand, active contours yield good results in edge detection and segmentation even in the presence of severe noise. This is because of the integral character of the calculus of variations.

On the other hand, the need for closed contours is a very strict requirement regarding the topology of the structures of interest. Sensible results are only possible if this model is adequate. The decision of whether or not to apply active contours can be made using background knowledge about the inspection task.

Other generalizations of snakes allow more complicated topologies [3].

11.5

### 11.5 Segmentation according to Mumford and Shah

The energy functionals of Mumford and Shah represent a mathematically well-founded formulation of the segmentation problem [16, 32]. Their approach is based on an empirically motivated assumption about the characteristics of scenic images: the image signal shows discontinuities at object borders and is relatively smooth inside objects. Additionally, the approach of Mumford and Shah assumes that the image signals are piecewise smooth but might have local discontinuities. The borders between segments are modeled by a set  $\Gamma$  of edge points, which are neither described by parametric curves nor have to be connected. The result of the segmentation is an image  $u(\mathbf{x})$ , whose segments are piecewise smooth functions

with a quadratically integrable gradient  $\text{grad } u(\mathbf{x}) \in L^2(\Omega_g \setminus \Gamma)$ . A formulation of the energy functional of Mumford and Shah is

$$E_{\text{MS}}\{u(\mathbf{x}), \Gamma\} := \mu \iint_{\Omega_g} (g(\mathbf{x}) - u(\mathbf{x}))^2 \, d\mathbf{x} + \nu \mathcal{L}\{\Gamma\} + \iint_{\Omega_g \setminus \Gamma} \|\text{grad } u(\mathbf{x})\|^2 \, d\mathbf{x} \quad (11.140)$$

with the weighting factors  $\mu, \nu \geq 0$  and the curve length  $\mathcal{L}\{\Gamma\}$ . The first term of the energy functional hopefully results in a good approximation of the original image  $g(\mathbf{x})$  by the resulting image  $u(\mathbf{x})$  in the sense of the minimal mean squared error. If, for example,  $u(\mathbf{x})$  is modeled as a piecewise constant function, it will have the mean image value of a segment  $\omega_i$  inside the segment:

$$\forall \mathbf{x} \in \omega_i : \quad u_{\min}(\mathbf{x}) = \frac{1}{|\omega_i|} \sum_{\mathbf{x} \in \omega_i} g(\mathbf{x}). \quad (11.141)$$

The second term in (11.140) minimizes the total length  $\mathcal{L}\{\Gamma\}$  of the edges. The third term requires the resulting image  $u(\mathbf{x})$  to be smooth, except for edges. Along the edges, the resulting image may contain discontinuities.

Minimizing the Mumford and Shah functional (11.140) yields the segmentation result  $(u_{\min}(\cdot), \Gamma_{\min})$  with

$$E_{\text{MS}}\{u_{\min}(\mathbf{x}), \Gamma_{\min}\} = \min_{u(\cdot), \Gamma} \{E_{\text{MS}}\{u(\mathbf{x}), \Gamma\}\}. \quad (11.142)$$

Usually, this problem can only be solved numerically. For this purpose, different discrete formulations of the functional have been proposed. For example, the approach of Chan and Vese models the set of the edge points using the level set method:

$$\Gamma = \{\mathbf{x} \in \Omega_g \mid \phi(\mathbf{x}) = 0\} \quad (11.143)$$

with the level set function

$$\phi(\mathbf{x}) : \Omega_g \rightarrow \mathbb{R}, \quad \text{grad } \phi(\mathbf{x})|_{\phi(\mathbf{x})=0} \neq \mathbf{0}. \quad (11.144)$$

This formulation results in a segmentation into  $I = 2$  segments [12, 13]. The two segments  $\omega_1, \omega_2$  are determined by the sign of the level set function [34]:

$$\omega_1 = \{\mathbf{x} \in \Omega_g \mid \phi(\mathbf{x}) > 0\}, \quad (11.145)$$

$$\omega_2 = \{\mathbf{x} \in \Omega_g \mid \phi(\mathbf{x}) < 0\}. \quad (11.146)$$

The zeros of the level set function correspond to the edges between the two segments. The generalization to  $I > 2$  segments is possible using multiple level set functions [41].

The Mumford and Shah functional (11.140) can also be extended to suit multi-channel images  $\mathbf{g}(\mathbf{x}) : \Omega_g \rightarrow \mathbb{R}^Q$ :

$$E_{\text{MS}}\{\mathbf{u}(\mathbf{x}), \Gamma\} := \mu \iint_{\Omega_g} \|\mathbf{g}(\mathbf{x}) - \mathbf{u}(\mathbf{x})\|^2 \, d\mathbf{x} + \nu \mathcal{L}\{\Gamma\} + \iint_{\Omega_g \setminus \Gamma} \sum_{q=1}^Q \|\text{grad } u_q(\mathbf{x})\|^2 \, d\mathbf{x}. \quad (11.147)$$

Figure 11.27 shows the result of this method applied to an example image.

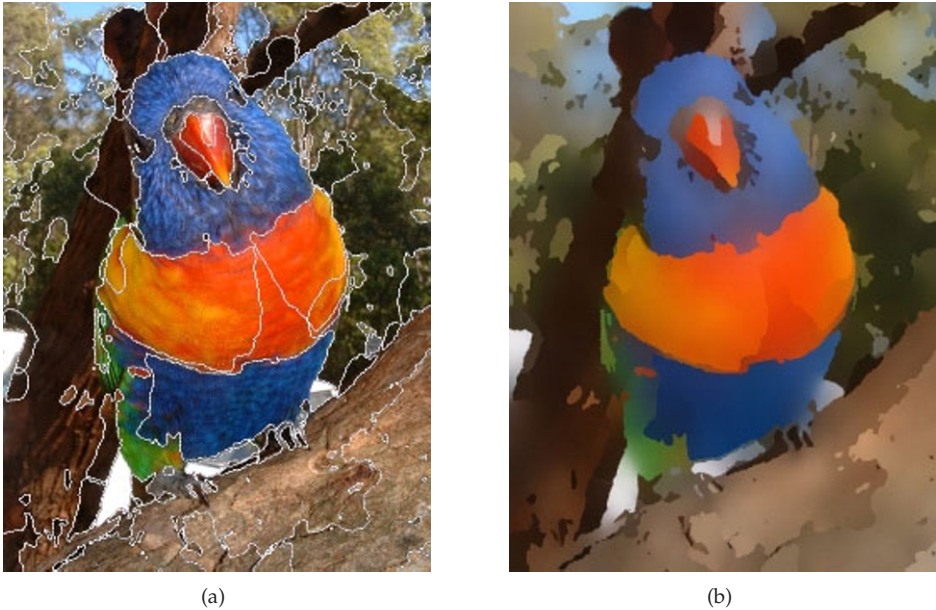


**Figure 11.27.** Segmentation of a color image using the method of Mumford and Shah: (a) Original image  $g(x)$  superposed with the segment borders  $\Gamma$ ; (b) Segmentation result  $u(x)$  (source: Dr. M. Fried, University of Erlangen, Germany [21]).

## 11.6

## 11.6 Segmentation using graph cut methods

Maximum flow and minimal cut algorithms for flow networks provide an efficient way to minimize certain energy functionals. In the following, the basics of the maximization of the network flow will be introduced at first. Then, the application to segmentation problems will be presented.

## 11.4

### Definition 11.4: Flow network

A flow network (or ‘network’, for short)  $\mathcal{N} = (\mathcal{V}, \mathcal{E}, w, \mathcal{T})$  consists of

- a set of vertices (or nodes)  $v \in \mathcal{V}$ ,
- a set of edges (or arcs)  $e \in \mathcal{E} \subseteq \mathcal{V} \times \mathcal{V}$ ,
- a weighting function  $w : \mathcal{E} \rightarrow \mathbb{R}$ , assigning a capacity  $w(e) > 0$  to each edge  $e$ ,
- and a set of terminal vertices  $t \in \mathcal{T} \subseteq \mathcal{V}$ . ◇

Hence, a network is a weighted graph together with a set of terminal vertices (Fig. 11.28(a)). In the case of exactly two terminal vertices,  $\mathcal{T} = \{s, t\}$ , the network is called an  $s$ - $t$ -network with a source  $s$  and a sink  $t$ . Such networks are of particular importance for segmentation. A flow with unlimited capacity is fed into the network at the source  $s$ . At the sink  $t$ , a flow is extracted from the network with unlimited capacity. Now, the maximum flow of the network is to be determined, with respect to the capacity of the edges, which is represented by their weights.

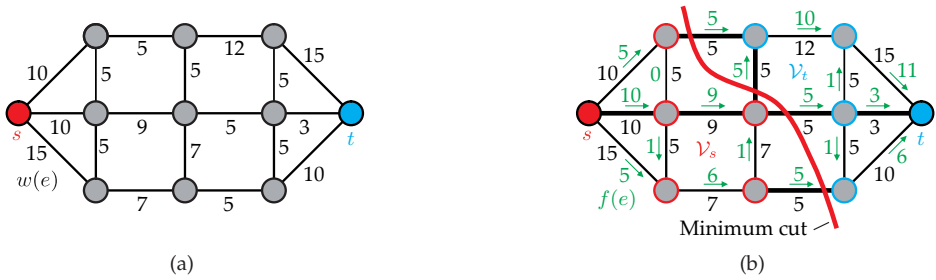


Figure 11.28. Example of a network  $\mathcal{N} = (\mathcal{V}, \mathcal{E}, w, \{s, t\})$ : (a) Capacities  $w(e)$ ; (b) Maximum flow  $f(e)$  and minimum cut  $(\mathcal{V}_s, \mathcal{V}_t)$  with  $c(f) = c(\mathcal{V}_s, \mathcal{V}_t) = 20$ .

**Definition 11.5: Network flow**

11.5

In a network  $\mathcal{N} = (\mathcal{V}, \mathcal{E}, w, \mathcal{T})$ , a flow  $f$  is a mapping  $f : \mathcal{E} \rightarrow \mathbb{R}$  having the following properties:

$$\forall e \in \mathcal{E} : \quad 0 \leq f(e) \leq w(e), \tag{11.148}$$

$$\forall v \in \mathcal{V} \setminus \mathcal{T} : \quad \sum_{e=(u,v) \in \mathcal{E}} f(e) = \sum_{\tilde{e}=(v,\tilde{u}) \in \mathcal{E}} f(\tilde{e}). \tag{11.149}$$

◇

The number  $f(e)$  is called the flow of the edge  $e$ . The first constraint (11.148) ensures that the flow of an edge cannot exceed its capacity. The flow conservation constraint (11.149) states that the sum of incoming flows at a vertex  $v$  has to be equal to the sum of the outgoing flows.

Another important concept strongly connected with the network flow is a so-called cut in a network:

**Definition 11.6: Network cut**

11.6

A partition of the vertices of a network  $\mathcal{N} = (\mathcal{V}, \mathcal{E}, w, \mathcal{T})$  into non-empty, disjoint subsets  $\mathcal{V}_i$ ,  $i = 1, \dots, |\mathcal{T}|$  is called a **cut** if the following requirements are met:

$$\bigcup_{i=1}^{|\mathcal{T}|} \mathcal{V}_i = \mathcal{V}, \tag{11.150}$$

$$\forall i, j \in \{1, \dots, |\mathcal{T}|\} : \quad i \neq j \Rightarrow \mathcal{V}_i \cap \mathcal{V}_j = \emptyset, \tag{11.151}$$

$$\forall i \in \{1, \dots, |\mathcal{T}|\} : \quad |\mathcal{V}_i \cap \mathcal{T}| = 1. \tag{11.152}$$

The set of the edges affected by the cut is

$$\mathcal{E}(\mathcal{V}_1, \dots, \mathcal{V}_{|\mathcal{T}|}) = \{e = (u, v) \in \mathcal{E} \mid u \in \mathcal{V}_i \wedge v \in \mathcal{V}_j \wedge i \neq j\}. \tag{11.153}$$

The capacity  $c$  of the cut is

$$c(\mathcal{V}_1, \dots, \mathcal{V}_{|\mathcal{T}|}) = \sum_{e \in \mathcal{E}(\mathcal{V}_1, \dots, \mathcal{V}_{|\mathcal{T}|})} w(e). \tag{11.154}$$

A cut with minimum capacity in  $\mathcal{N}$  is called a **minimum cut**.

◇

A cut is uniquely identified by either the partition  $(\mathcal{V}_1, \dots, \mathcal{V}_{|\mathcal{T}|})$  or by the cut-set  $\mathcal{E}(\mathcal{V}_1, \dots, \mathcal{V}_{|\mathcal{T}|})$ . In the case of  $\mathcal{T} = \{s, t\}$ , a cut  $(\mathcal{V}_1, \mathcal{V}_2)$  separates the network into two parts, one containing the source  $s$  and the other one containing the sink  $t$ .

Now, the value of the network flow can be defined using the network cut:

---

### 11.7 Definition 11.7: Value of a network flow

The value  $c(f)$  of a flow  $f$  in an  $s$ - $t$ -network  $\mathcal{N} = (\mathcal{V}, \mathcal{E}, w, \{s, t\})$  is given by

$$c(f) = \sum_{e \in \mathcal{E}(\mathcal{V}_s, \mathcal{V}_t)} f(e), \quad (11.155)$$

with  $(\mathcal{V}_s, \mathcal{V}_t)$  denoting an arbitrary cut of the network.

A flow  $f$  with maximum value in  $\mathcal{N}$  is called a **maximum flow**.  $\diamond$

The value  $c(f)$  of a flow  $f$  is the sum of the flow at an arbitrary cut of the network. Because of the flow conservation constraint (11.149), this sum is equal for all possible cuts. As

$$c(f) = \sum_{e=(s,v) \in \mathcal{E}} f(e) = \sum_{e=(v,t) \in \mathcal{E}} f(e), \quad (11.156)$$

the value of the flow is the amount of flow entering the network at the source  $s$  or exiting the network at the sink  $t$ .

The relation between the maximum flow and the minimum cut in an  $s$ - $t$ -network is described by the max-flow min-cut theorem of Ford and Fulkerson (Fig. 11.28(b)).

---

### 11.1 Theorem 11.1: Max-flow min-cut theorem

Let  $f$  denote a maximum flow and  $(\mathcal{V}_s, \mathcal{V}_t)$  denote a minimum cut in a network  $\mathcal{N} = (\mathcal{V}, \mathcal{E}, w, \{s, t\})$ . Then, the value of the flow is equal to the capacity of the cut:

$$c(f) = c(\mathcal{V}_s, \mathcal{V}_t). \quad (11.157)$$

For the proof, see [15].  $\diamond$

If the edge weights  $w(e)$  are interpreted as transport capacities, it is obvious that the maximum flow  $f$  from the source  $s$  to the sink  $t$  must flow through a set of saturated edges with  $f(e) = w(e)$ . The minimum cut of the network runs through saturated edges limiting the network flow the most and therefore showing minimum capacities.

Finding the minimum cut in  $\mathcal{N}$  is equivalent to maximizing the network flow. If a maximum flow  $f$  is known in an  $s$ - $t$ -network, a minimum cut can be obtained as follows: let  $\mathcal{V}_s$  denote the set of all vertices which can be reached from  $s$  via a path of positive residual capacity, i.e., over a connected series of edges  $e$  with  $w(e) - f(e) > 0$ . Then  $(\mathcal{V}_s, \mathcal{V} \setminus \mathcal{V}_s)$  is a minimum cut.

There are two classes of efficient algorithms for finding the maximum network flow in the case of  $\mathcal{T} = \{s, t\}$ : so-called push-relabel algorithms according to Goldberg and Tarjan [22], and so-called augmenting path algorithms according to Ford and Fulkerson [20]. The latter perform a stepwise increase of the flow by finding augmenting paths in the network that still have a positive residual capacity. Based on this principle, an algorithm especially optimized for image processing applications has been proposed by Boykov and Kolmogorov



[7]. The flow maximization problem is of polynomial time complexity in the number of the network's vertices and edges. However for  $|\mathcal{T}| \geq 3$ , finding the minimum cut is NP-hard, i.e., no algorithms are known that can solve the problem in polynomial time. This is why such problems are usually solved only approximately, e.g., by the  $\alpha$ -expansion algorithm [8]. In every iteration, a terminal vertex  $\alpha \in \mathcal{T}$  is selected and a reduced network with only two terminal vertices  $\mathcal{T}_\alpha = (\alpha, t)$  is constructed. The minimum cut of this network can be calculated efficiently and determines the set  $\mathcal{V}_\alpha$  of vertices that should be assigned to the terminal vertex  $\alpha$ . The assignment of the other vertices  $\mathcal{V}_t$  remains unchanged by this iteration. After each terminal vertex  $\alpha \in \mathcal{T}$  has been selected at least once, the resulting partition  $(\mathcal{V}_\alpha)_{\alpha \in \mathcal{T}}$  of the original network constitutes a good approximation of the minimum cut.

Even though the minimum cut and the maximum flow in a given network are not necessarily unique, the value of the maximum flow or the capacity of the minimum cut is unique.

In the field of image processing, the pixels of an image can be considered as the vertices of a network:  $\Omega_g \subseteq \mathcal{V}$ . The edges and capacities of the network can reflect different constraints of the image processing task. Usually, edges are created between adjacent pixels, as well as between pixels and the terminal vertices. Image processing algorithms relying on the maximization of the network flow are known as **graph cut methods**.

For segmentation tasks, the edges between adjacent pixels  $\mathbf{x}_1, \mathbf{x}_2$  represent the similarity of the corresponding feature vectors  $\mathbf{m}$ . To this end, a neighborhood criterion for pixels is necessary. Two definitions of neighborhoods commonly used in image processing are as follows:

---

**Definition 11.8: Neighborhood**

The **4-connected neighborhood**  $N_4(\mathbf{x})$  of a pixel  $\mathbf{x} = (x, y)^T$  includes the horizontally and vertically adjacent pixels:

$$N_4(\mathbf{x}) = \{(x-1, y)^T, (x+1, y)^T, (x, y-1)^T, (x, y+1)^T\}. \quad (11.158)$$

The **8-connected neighborhood**  $N_8(\mathbf{x})$  contains, in addition to the above, the diagonally adjacent pixels as well:

$$N_8(\mathbf{x}) = N_4(\mathbf{x}) \cup \{(x-1, y-1)^T, (x-1, y+1)^T, (x+1, y+1)^T, (x+1, y-1)^T\}. \quad (11.159)$$

◇

For each pixel  $\mathbf{x}_2$  in a neighborhood of  $\mathbf{x}_1$ , such as the 4-connected neighborhood  $N_4(\mathbf{x}_1)$  for example, an edge is created with the capacity  $d(\mathbf{m}(\mathbf{x}_1), \mathbf{m}(\mathbf{x}_2))$ :

$$\mathcal{E}_N := \{(\mathbf{x}_1, \mathbf{x}_2) \in \Omega_g^2 \mid \mathbf{x}_2 \in N_4(\mathbf{x}_1)\}, \quad (11.160)$$

$$w((\mathbf{x}_1, \mathbf{x}_2)) := d(\mathbf{m}(\mathbf{x}_1), \mathbf{m}(\mathbf{x}_2)) \quad \text{if } e = (\mathbf{x}_1, \mathbf{x}_2) \in \mathcal{E}_N. \quad (11.161)$$

An edge  $e$  is assigned a high capacity  $w(e)$  if the features of the connected pixels are similar, so that they should belong to the same segment. As it is assigned a low capacity if the features are markedly different, the minimum cut will preferentially intersect the edges of adjacent pixels with dissimilar features (Fig. 11.29). A possible choice of the weighting

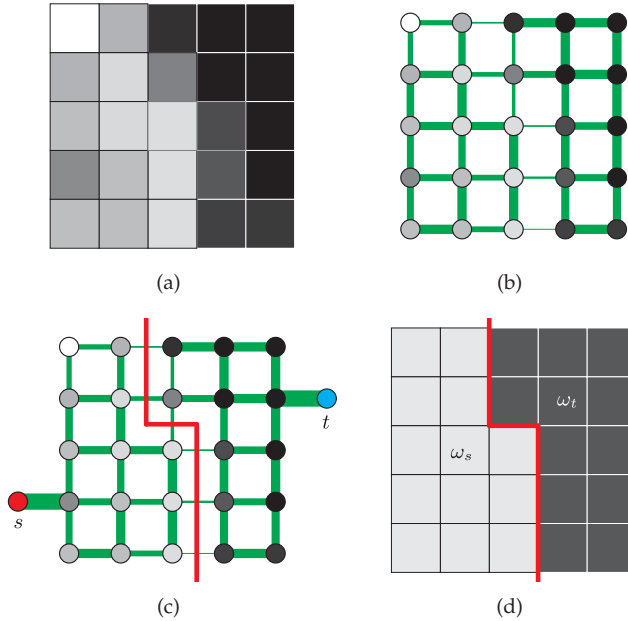


**Figure 11.29.** Principle of segmentation using graph cuts: (a) Gray-scale image  $g(\mathbf{x})$ ; (b) Corresponding pixel graph  $(\Omega_g, \mathcal{E}_N)$ ; if two adjacent pixels have similar gray values, their corresponding vertices are connected by an edge with a high capacity; (c) Introduction of seed points by adding terminal vertices  $s, t$  and calculation of the minimum cut; (d) The minimum cut determines the border between the two segments  $\omega_s, \omega_t$ .

function  $d(\cdot, \cdot)$  is given by

$$d(\mathbf{m}(\mathbf{x}_1), \mathbf{m}(\mathbf{x}_2)) \propto e^{-\frac{\|\mathbf{m}(\mathbf{x}_1) - \mathbf{m}(\mathbf{x}_2)\|}{2\sigma^2}}. \tag{11.162}$$

Here, the parameter  $\sigma$  should approximate the standard deviation of the noise in the image [6].

For the binary segmentation of the image into two segments  $\omega_s, \omega_t$ , two terminal vertices  $s, t$  are added to the network, resulting in the set of vertices

$$\mathcal{V} = \Omega_g \cup \mathcal{T}, \quad \mathcal{T} = \{s, t\}, \tag{11.163}$$

see Fig. 11.29. The terminal vertices correspond to the two image segments sought, e.g., the test object and the background.

In addition, every pixel vertex  $\mathbf{x} \in \Omega_g$  can be connected to each terminal vertex  $i \in \mathcal{T}$  via an edge (Fig. 11.30):

$$\mathcal{E}_{\mathcal{T}} := \Omega_g \times \mathcal{T}. \tag{11.164}$$

In the case of binary segmentation, this corresponds to the set of edges

$$\mathcal{E}_{\mathcal{T}} = \bigcup_{\mathbf{x} \in \Omega_g} \{(s, \mathbf{x}), (\mathbf{x}, t)\}. \tag{11.165}$$

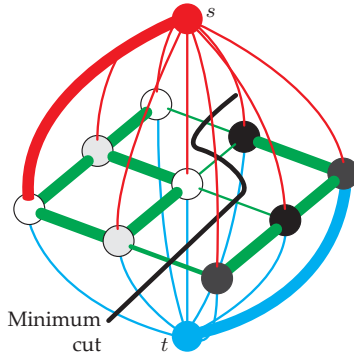


Figure 11.30. Binary segmentation by computing the minimum cut of the network  $\mathcal{N} = (\mathcal{V}, \mathcal{E}, w, \mathcal{T})$ .

The capacity of the terminal vertices can be chosen as a function of the conditional probabilities  $P(\mathbf{m}(\mathbf{x})|\omega_i)$ ,  $i \in \mathcal{T}$  of the occurrence of a feature vector  $\mathbf{m}(\mathbf{x})$  given that the pixel belongs to segment  $\omega_i$ . These probabilities can be estimated from, e.g., the histograms of the respective regions of reference images. By these means, the inner characteristics of the regions that are to be segmented can be introduced into the optimization problem, instead of only considering the edge capacities at the region borders. Additionally, sets of arbitrarily distributed seed points can be used. The seed points of the set  $\mathcal{S}_i$ ,  $i \in \mathcal{T}$  will be part of the segment  $\omega_i$ . Hence, the capacities of the terminal edges can be chosen as follows [6]:

$$w((s, \mathbf{x})) := \begin{cases} \infty & \text{if } \mathbf{x} \in \mathcal{S}_s \\ 0 & \text{if } \mathbf{x} \in \mathcal{S}_t \\ -\lambda \ln P(\mathbf{m}(\mathbf{x})|\omega_t) & \text{otherwise} \end{cases}, \tag{11.166}$$

$$w((\mathbf{x}, t)) := \begin{cases} 0 & \text{if } \mathbf{x} \in \mathcal{S}_s \\ \infty & \text{if } \mathbf{x} \in \mathcal{S}_t \\ -\lambda \ln P(\mathbf{m}(\mathbf{x})|\omega_s) & \text{otherwise} \end{cases}, \tag{11.167}$$

$$\mathcal{S}_s \cap \mathcal{S}_t = \emptyset. \tag{11.168}$$

The capacity of an edge  $e = (\mathbf{x}, i) \in \mathcal{E}_{\mathcal{T}}$  is infinite if  $\mathbf{x} \in \mathcal{S}_i$ , so that a seed point will be certainly assigned to the segment  $\omega_i$ . Accordingly, the capacity of a seed point's edges to the other terminal vertices is zero, so that these edges must be part of the minimum cut. If the probability of a point  $\mathbf{x}$  belonging to segment  $\omega_i$  is high because of its features  $\mathbf{m}(\mathbf{x})$ , the capacity of the corresponding edge  $(\mathbf{x}, i)$  is set to a high value. If, on the contrary, the probability is low, a low value is assigned to the edge, so that chances are high that it will be part of the minimum cut.

The parameter  $\lambda > 0$  determines the relative weighting of the terminal edges and neighbor edges.

Thus, the segmentation problem is mapped to a network  $\mathcal{N} = (\mathcal{V}, \mathcal{E}, w, \mathcal{T})$  with  $\mathcal{V} = \Omega_g \cup \mathcal{T}$ ,  $\mathcal{E} = \mathcal{E}_{\mathcal{N}} \cup \mathcal{E}_{\mathcal{T}}$  and  $\mathcal{T} = \{s, t\}$ . Now, the minimum cut  $(\mathcal{V}_s, \mathcal{V}_t)$  of this network can be calculated efficiently and has the following characteristics:

- For every pixel vertex  $\mathbf{x} \in \Omega_g$ , exactly one terminal edge  $(\mathbf{x}, i) \in \mathcal{E}_{\mathcal{T}}$  is cut.

- If  $\mathbf{x} \in \omega_s$ , the terminal edge  $(\mathbf{x}, t)$  is contained in the minimum cut  $\mathcal{E}(\mathcal{V}_s, \mathcal{V}_t)$ .
- If, on the contrary,  $\mathbf{x} \in \omega_t$ , then  $(s, \mathbf{x}) \in \mathcal{E}(\mathcal{V}_s, \mathcal{V}_t)$ .
- A neighborhood edge  $(\mathbf{x}_1, \mathbf{x}_2) \in \mathcal{E}_N$  is part of the minimum cut  $\mathcal{E}(\mathcal{V}_s, \mathcal{V}_t)$  if and only if  $\mathbf{x}_1$  and  $\mathbf{x}_2$  are assigned to different segments.

The minimum cut separates the two segments. A pixel  $\mathbf{x} \in \Omega_g$  is assigned to the segment  $\omega_s$  if, and only if,  $\mathbf{x} \in \mathcal{V}_s \Leftrightarrow (\mathbf{x}, t) \in \mathcal{E}(\mathcal{V}_s, \mathcal{V}_t)$ .

The steps of binary segmentation using maximum network flow can be summarized as follows:

1. Create a weighted pixel graph  $(\Omega_g, \mathcal{E}_N)$  using the feature vectors  $\mathbf{m}(\mathbf{x})$ , a similarity criterion  $d(\cdot, \cdot)$  for the feature vectors, and a definition of the neighborhoods  $N(\mathbf{x})$ .
2. Determine seed points  $\mathcal{S}_s$  for the object that is to be segmented and  $\mathcal{S}_t$  for the background,  $\mathcal{S}_s, \mathcal{S}_t \subset \Omega_g, \mathcal{S}_s \cap \mathcal{S}_t = \emptyset$ .
3. Add the terminal vertices  $s$  (source) and  $t$  (sink) to the pixel graph.
4. Create the terminal edges  $(s, \mathbf{x})$  and  $(\mathbf{x}, t)$  for all pixels  $\mathbf{x} \in \Omega_g$ .
5. Determine the weights  $w(e)$  for the neighborhood edges and terminal edges, resulting in a network  $\mathcal{N} = (\mathcal{V}, \mathcal{E}, w, \mathcal{T})$  with  $\mathcal{T} = \{s, t\}$ .
6. Calculate the minimum cut  $(\mathcal{V}_s, \mathcal{V}_t)$  separating the terminal vertices  $s$  and  $t$  ( $s \in \mathcal{V}_s, t \in \mathcal{V}_t$ ) using a network flow algorithm.
7. The partition  $(\mathcal{V}_s, \mathcal{V}_t)$  defined by the minimum cut corresponds to a segmentation of the image into the object region  $\omega_s$  and the background region  $\omega_t$ .

The resulting segments do not necessarily have to be connected. The segment borders are not explicitly modeled. Both region-based and edge-based criteria can be used, depending on the features used. As binary segmentation yields the global minimum cut, an optimal result is guaranteed with respect to the chosen model. The generalization to more than two segments is possible using the  $\alpha$ -expansion algorithm, which, however, provides only an approximate solution.

---

**Example 11.12 (Sorting of food):** The setup for sorting bulk goods described in Sec. 7.6.2 uses a hyperspectral line camera, which acquires an image with about 200 channels in the near infrared. The image values  $\mathbf{g}(\mathbf{x})$  of the hyperspectral image are directly used as the feature vectors  $\mathbf{m}(\mathbf{x})$  for determining the edge capacities. As an example from the food industry, Fig. 11.31 shows an image of coffee beans, among which contaminants are to be detected. The conditional probabilities  $P(\mathbf{m}|\omega_i)$  for the three classes coffee beans, contaminants, and background are estimated using manually set seed points, Fig. 11.31(b). The segmentation result of the iterative  $\alpha$ -expansion algorithm is shown in Fig. 11.31(c). ■

The calculation of the minimum cut can be considered as the minimization of an energy functional. The energy is defined to be dependent on the labeling function  $L : \Omega_g \rightarrow \{\omega_1, \dots, \omega_I\}$ , which assigns a segment  $\omega_i$  to every image point  $\mathbf{x} \in \Omega_g$ . The energy functional is composed of two terms, which correspond to the terminal edges and the neighborhood edges of the

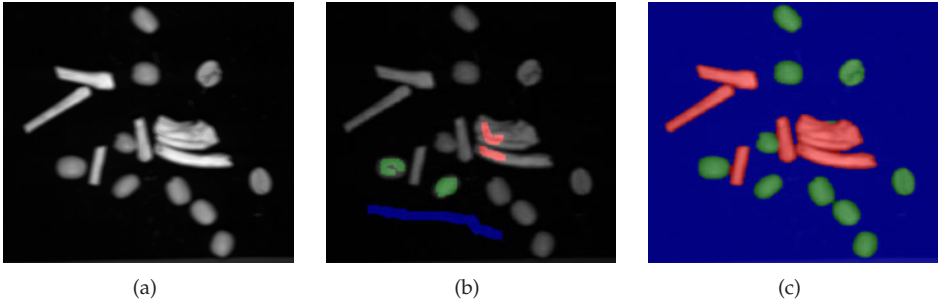


Figure 11.31. Application of segmentation using minimum network cuts to sorting food: (a) One channel of the hyperspectral image; (b) Manually marked sets of seed points; (c) Segmentation into coffee beans, contaminants, and background; superposed on the original image in pseudo colors.

network:

$$E_{GC}\{L\} = \underbrace{\sum_{\mathbf{x} \in \Omega_g} E_D(g(\mathbf{x}), L(\mathbf{x}))}_{\text{Data consistency}} + \underbrace{\sum_{\substack{\mathbf{x}_1 \in \Omega_g \\ \mathbf{x}_2 \in \mathcal{N}(\mathbf{x}_1)}} E_G(g(\mathbf{x}_1), g(\mathbf{x}_2), L(\mathbf{x}_1), L(\mathbf{x}_2))}_{\text{Smoothness}}. \quad (11.169)$$

The first term represents the relation between the assignment  $L(\mathbf{x})$  and the image  $g(\mathbf{x})$  or the extracted features  $\mathbf{m}(\mathbf{x})$  respectively. The second term demands the smoothness of the assignment in a local neighborhood. These two terms are somehow similar to the functional of Mumford and Shah (11.140). However, no explicit attention is paid to the length of the edges between the segments. In fact, it would be possible to consider the edge lengths when constructing the network, so that certain variants of the functional of Mumford and Shah can be minimized using graph cut algorithms [19].

There are even more image processing tasks that can be formulated as an assignment problem [8]. A label, whose meaning depends on the actual application, is assigned to every image point (Table 11.2). An energy functional is constructed that depends on the labeling function  $L$  and is minimized using network flow algorithms. This is possible if the energy functional meets certain conditions [27]. Among others, the single summands may only depend on the labels of a few vertices. In (11.169), for example,  $E_D$  depends only on a single pixel assignment  $L(\mathbf{x})$  and  $E_G$  depends on the assignment of two pixels  $L(\mathbf{x}_1), L(\mathbf{x}_2)$ .

Table 11.2. Application of maximum network flow to image processing.

Application	Meaning of the labels
Segmentation	Segment $\omega_i$
Image restoration	Restored (undisturbed) intensity
Finding stereo correspondences	Object distance
Texture synthesis	Synthesized intensity

## 11.7 Bibliography

- [1] Ludwig Abele. *Statistische und strukturelle Texturanalyse mit Anwendungen in der Bildsegmentierung*. PhD thesis, Technische Universität München, 1982.
- [2] Howard Anton. *Elementary linear algebra*. Wiley, 10th edition, 2010.
- [3] Stephan Bischoff and Leif Kobbelt. Parameterization-free active contour models with topology control. *The Visual Computer*, 20(4):217–228, 2004.
- [4] Christopher Bishop. *Pattern recognition and machine learning*. Springer, 2006.
- [5] Laure Blanc-Féraud, Pierre Charbonnier, Gilles Aubert, and Michel Barlaud. Nonlinear image processing: modeling and fast algorithm for regularization with edge detection. In *Proc. IEEE International Conference on Image Processing*, volume 1, pages 474–477, 1995.
- [6] Yuri Boykov and Gareth Funka-Lea. Graph Cuts and Efficient N-D Image Segmentation. *International Journal of Computer Vision*, 70(2):109–131, 2006.
- [7] Yuri Boykov and Vladimir Kolmogorov. An Experimental Comparison of Min-Cut/Max-Flow Algorithms for Energy Minimization in Vision. *IEEE Transactions on Pattern Analysis and Machine Intelligence*, 26(9):1124–1137, 2004.
- [8] Yuri Boykov, Olga Veksler, and Ramin Zabih. Fast Approximate Energy Minimization via Graph Cuts. *IEEE Transactions on Pattern Analysis and Machine Intelligence*, 23(11):1222–1239, 2001.
- [9] Kristian Bredies and Dirk Lorenz. *Mathematische Bildverarbeitung: Einführung in Grundlagen und moderne Theorie*. Vieweg+Teubner, 2011.
- [10] John Canny. A Computational Approach to Edge Detection. *IEEE Transactions on Pattern Analysis and Machine Intelligence*, 8(6):679–698, 1986.
- [11] Constantin Carathéodory. *Calculus of Variations and Partial Differential Equations of the First Order*. Chelsea, 2nd edition, 1982.
- [12] Tony Chan and Jianhong Shen. *Image processing and analysis: variational, PDE, wavelet, and stochastic methods*. Society for Industrial and Applied Mathematics, 2005.
- [13] Tony Chan and Luminita Vese. Active Contours Without Edges. *IEEE Transactions on Image Processing*, 10(2):266–277, 2001.
- [14] Pierre Charbonnier, Laure Blanc-Féraud, Gilles Aubert, and Michel Barlaud. Two deterministic half-quadratic regularization algorithms for computed imaging. In *Proc. IEEE International Conference on Image Processing*, volume 2, pages 168–172, 1994.
- [15] William Cook, William Cunningham, William Pulleyblank, and Alexander Schrijver. *Combinatorial Optimization*. Wiley, 1998.
- [16] Guy David. *Singular sets of minimizers for the Mumford-Shah functional*. Birkhäuser, 2005.
- [17] Arthur Dempster, Nan Laird, and Donald Rubin. Maximum Likelihood from Incomplete Data via the EM Algorithm. *Journal of the Royal Statistical Society, Series B (Methodological)*, 39(1):1–38, 1977.
- [18] Richard Duda, Peter Hart, and David Stork. *Pattern classification*. Wiley, 2nd edition, 2001.
- [19] Noha El-Zehiry, Prasanna Sahoo, and Adel Elmaghraby. Combinatorial Optimization of the piecewise constant Mumford-Shah functional with application to scalar/vector valued and volumetric image segmentation. *Image and Vision Computing*, 29(6):365–381, 2011.
- [20] Lester R. Ford, Jr. and Delbert Fulkerson. Maximal flow through a network. *Canadian Journal of Mathematics*, 8(3):399–404, 1956.
- [21] J. Michael Fried. Multichannel image segmentation using adaptive finite elements. *Computing and Visualization in Science*, 12(3):125–135, 2009.
- [22] Andrew Goldberg and Robert Tarjan. A new approach to the maximum-flow problem. *Journal of the ACM*, 35(4):921–940, 1988.

- [23] Rafael Gonzalez and Richard Woods. *Digital image processing*. Pearson Prentice Hall, 3rd edition, 2008.
- [24] Robin Gruna and Jürgen Beyerer. Optical feature extraction with illumination-encoded linear functions. In Philip Bingham and Edmund Lam, editors, *Proc. SPIE Image Processing: Machine Vision Applications V*, volume 8300, 2012.
- [25] Robert Haralick and Linda Shapiro. *Computer and robot vision*. Addison-Wesley, 1992.
- [26] Michael Kass, Andrew Witkin, and Demetri Terzopoulos. Snakes: active contour models. *International Journal of Computer Vision*, 1(4):321–331, 1988.
- [27] Vladimir Kolmogorov and Ramin Zabih. What Energy Functions Can Be Minimized via Graph Cuts? *IEEE Transactions on Pattern Analysis and Machine Intelligence*, 26(2):147–159, 2004.
- [28] Hsien-Che Lee. *Introduction to color imaging science*. Cambridge University Press, 2005.
- [29] Bing Li and Scott Acton. Active contour external force using vector field convolution for image segmentation. *IEEE Transactions on Image Processing*, 16(8):2096–2106, 2007.
- [30] David Marr and Ellen Hildreth. Theory of edge detection. *Proc. Royal Society London, Series B – Biological Sciences*, 207:187–217, 1980.
- [31] Fernand Meyer. Topographic distance and watershed lines. *Signal Processing*, 38:113–125, 1994.
- [32] David Mumford and Jayant Shah. Optimal approximations by piecewise smooth functions and associated variational problems. *Communications on Pure and Applied Mathematics*, 42(5):577–685, 1989.
- [33] Burkhard Neumann. *Bildverarbeitung für Einsteiger*. Springer, 2005.
- [34] Stanley Osher and Ronald Fedkiw. *Level set methods and dynamic implicit surfaces*. Springer, 2003.
- [35] Nobuyuki Otsu. A Threshold Selection Method from Gray-Level Histograms. *IEEE Transactions on Systems, Man, and Cybernetics*, 9(1):62–66, 1979.
- [36] Theodosios Pavlidis. *Structural pattern recognition*. Springer, 1977.
- [37] Pietro Perona and Jitendra Malik. Scale-space and edge detection using anisotropic diffusion. *IEEE Transactions on Pattern Analysis and Machine Intelligence*, 12(7):629–639, 1990.
- [38] Andreas Purde. *Speckle-Interferometrie zur Formvermessung unstetiger Oberflächen*. PhD thesis, Technische Universität München, 2006.
- [39] Pierre Soille. *Morphological image analysis: principles and applications*. Springer, 1999.
- [40] Carlo Tomasi. Estimating Gaussian Mixture Densities with EM – A Tutorial. Handout for Course Introduction to Computer Vision, Duke University, <http://www.cs.duke.edu/courses/spring04/cps196.1/>, 2004.
- [41] Luminita Vese and Tony Chan. A Multiphase Level Set Framework for Image Segmentation Using the Mumford and Shah Model. *International Journal of Computer Vision*, 50(3):271–293, 2002.
- [42] Friedrich Wahl. *Digitale Bildsignalverarbeitung*. Springer, 1989.
- [43] Joachim Weickert. A review of nonlinear diffusion filtering. In Bart ter Haar Romeny, Luc Florack, Jan Koenderink, and Max Viergever, editors, *Scale-Space Theory in Computer Vision*, volume 1252 of *Lecture Notes in Computer Science*, pages 1–28. Springer, 1997.
- [44] Chenyang Xu and Jerry Prince. Snakes, shapes, and gradient vector flow. *IEEE Transactions on Image Processing*, 7(3):359–369, 1998.

The background features large, light gray outlines of the numbers '1' and '2' stacked vertically. The top '1' is on the left, and the top '2' is on the right. Below them, a larger '1' and '2' are also visible, partially overlapping. The overall design is minimalist and geometric.

Chapter 12

**Morphological Image Processing**

**12**

---



**12 Morphological Image Processing**

12.1 Binary morphology . . . . .	609
12.1.1 Point sets and structuring elements . . . . .	609
12.1.2 Erosion and dilation . . . . .	611
12.1.2.1 Duality of erosion and dilation . . . . .	618
12.1.3 Opening and closing . . . . .	620
12.1.4 Border extraction . . . . .	623
12.1.5 Region filling . . . . .	624
12.1.6 Component labeling and connected component analysis . . . . .	624
12.1.7 The hit-or-miss operator . . . . .	626
12.1.7.1 Thinning . . . . .	627
12.1.7.2 Thickening . . . . .	629
12.1.8 Skeletonization . . . . .	630
12.1.9 Pruning . . . . .	632
12.2 Gray-scale morphology . . . . .	634
12.2.1 The point set of a gray-scale image . . . . .	634
12.2.2 Erosion and dilation . . . . .	636
12.2.3 Opening and closing . . . . .	641
12.2.4 Edge detection . . . . .	643
12.3 Bibliography . . . . .	645

## 12 Morphological Image Processing

Morphological methods used in the algebra of sets can be used for morphological image processing. They were introduced by Matheron and Serra under the term ‘Mathematical Morphology’ [12, 16, 17]. Here, image signals are considered to be point sets and morphological filters are operations manipulating these sets.

Basically, morphological methods can be applied to binary images (Sec. 12.1) as well as to gray-scale images and color images (Sec. 12.2). As morphological operators are nonlinear, they cannot be described using the methods of linear system theory. Nevertheless, morphological methods are very intuitive, as their local effects are clearly visible and comprehensible. Among other things, this is because of the so-called structuring element, which can to a certain extent be compared to the impulse response function of a linear system.

Morphological methods are suitable for various tasks of image evaluation, e.g., preprocessing, noise mitigation, edge extraction and detection. Because of the variety of possible applications, morphological image processing can hardly be integrated into the chapter structure of this book, which is why it is presented in a distinct chapter.

### 12.1 Binary morphology

12.1

#### 12.1.1 Point sets and structuring elements

As a preparation for applying morphological methods to image signals, first a point set representation of image signals has to be defined. In the usual signal-oriented treatment, continuous binary images are represented by a function

$$g : \begin{cases} \Omega_g \rightarrow \{0, 1\} \\ \mathbf{x} \mapsto g, \end{cases} \quad \mathbf{x} \in \Omega_g \subseteq \mathbb{R}^2, \quad (12.1)$$

which maps the continuous domain  $\Omega_g$  to the discrete values 0 and 1. Discrete binary images are different from this representation, as the image coordinates  $\mathbf{x} \in \Omega_g \subseteq \mathbb{Z}^2$  are sampled on a discrete grid:

$$g : \begin{cases} \Omega_g \rightarrow \{0, 1\} \\ \mathbf{x} \mapsto g, \end{cases} \quad \mathbf{x} \in \Omega_g \subseteq \mathbb{Z}^2. \quad (12.2)$$

---

#### Definition 12.1: The point set of a binary image

12.1

The point set  $\mathcal{G}$  of a binary image  $g(\mathbf{x})$  is the set of all image points with a value of 1:

$$\mathcal{G} = \{\mathbf{x} \mid g(\mathbf{x}) = 1\}. \quad (12.3)$$

◇

In other words,  $\mathcal{G}$  represents the set of image points describing the object of interest. All other image points are assigned to the background. For the visualization of such binary images, ‘black’ corresponds to the value 1 and ‘white’ corresponds to the value 0. As an example, Fig. 12.1 shows a two-dimensional butterfly-shaped point set  $\mathcal{G}$ .

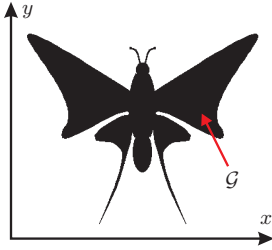
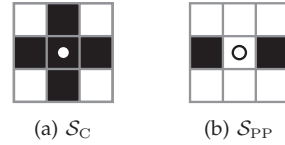
Figure 12.1. Binary image as a point set  $\mathcal{G}$ .

Figure 12.2. Examples of structuring elements.

The assignment between binary images and point sets is bijective, so that a lossless transformation between the two representations is possible. The binary image of a point set  $\mathcal{G}$  is given by the following formula:

$$g(\mathbf{x}) = \begin{cases} 1 & \text{if } \mathbf{x} \in \mathcal{G} \\ 0 & \text{if } \mathbf{x} \notin \mathcal{G}. \end{cases} \quad (12.4)$$

As with linear methods, where the input signal  $g(\mathbf{x})$  is linked to another signal—the impulse response function  $h(\mathbf{x})$  of the system—two point sets are linked by the morphological operators. Here, the nonempty point set used for manipulating the image  $\mathcal{G}$  using morphological operators is the so-called **structuring element**  $\mathcal{S}$ . By changing the size and the shape of  $\mathcal{S}$ , the characteristics of a morphological operation can be adjusted. In practice, suitable structuring elements  $\mathcal{S}$  are usually heuristically determined depending on the application on hand. As an example, Fig. 12.2 shows two simple, discrete structuring elements: the cross

$$\mathcal{S}_C = \{(0, 0)^T, (1, 0)^T, (0, 1)^T, (-1, 0)^T, (0, -1)^T\} \quad (12.5)$$

and the point pair

$$\mathcal{S}_{PP} = \{(-1, 0)^T, (1, 0)^T\}. \quad (12.6)$$

The cross can be considered as an approximation of a circle. The reference point (i.e., the origin) of the structuring element, which is marked by the symbol  $\circ$  in Fig. 12.2, does not necessarily have to be part of  $\mathcal{S}$ .

Before the basic operators of morphological image processing will be covered in the next subsection, some specific operators for point sets are introduced, which allow a more compact and therefore a clearer representation of set operations.

## 12.2

### Definition 12.2: Operations on point sets

The **shift** of the set  $\mathcal{G}$  by the vector  $\mathbf{z}$  refers to the set

$$(\mathcal{G})_{\mathbf{z}} := \{\mathbf{w} \mid \mathbf{w} = \mathbf{x} + \mathbf{z}, \mathbf{x} \in \mathcal{G}\}. \quad (12.7)$$

The **reflection** of the set  $\mathcal{G}$  at its origin is defined as

$$\mathcal{G}^R := \{\mathbf{w} \mid \mathbf{w} = -\mathbf{x}, \mathbf{x} \in \mathcal{G}\}. \quad (12.8)$$

Further, the **complement**  $\overline{\mathcal{G}}$  of a set is the set of elements that are not part of  $\mathcal{G}$ :

$$\overline{\mathcal{G}} := \{\mathbf{w} \in \Omega_g \mid \mathbf{w} \notin \mathcal{G}\}. \quad (12.9)$$

The **difference** of two sets  $\mathcal{G}_1$  and  $\mathcal{G}_2$ ,

$$\mathcal{G}_1 \setminus \mathcal{G}_2 := \{\mathbf{w} \in \Omega_g \mid \mathbf{w} \in \mathcal{G}_1, \mathbf{w} \notin \mathcal{G}_2\} = \mathcal{G}_1 \cap \overline{\mathcal{G}_2}, \quad (12.10)$$

is the set of elements belonging to  $\mathcal{G}_1$  and not to  $\mathcal{G}_2$ .  $\diamond$

### 12.1.2 Erosion and dilation

The basic methods of morphology are erosion and dilation [4, 12].<sup>1</sup>

---

#### Definition 12.3: Erosion

12.3

The erosion  $\mathcal{G} \ominus \mathcal{S}$  of a set  $\mathcal{G}$  by the structuring element  $\mathcal{S}$  is defined as the set of shifts  $\mathbf{w}$  of  $\mathcal{S}$  for which the shifted sets  $(\mathcal{S})_{\mathbf{w}}$  are entirely contained in  $\mathcal{G}$ :

$$\mathcal{G} \ominus \mathcal{S} := \{\mathbf{w} \mid (\mathcal{S})_{\mathbf{w}} \subseteq \mathcal{G}\}. \quad (12.11)$$

 $\diamond$ 

By erosion, the point set  $\mathcal{G}$  is shrunk, depending on the structuring element  $\mathcal{S}$ . The interior of objects larger than the structuring element remains unchanged. However, some points at their margin are removed (Fig. 12.3).

In contrast, dilation enlarges the point set:

---

#### Definition 12.4: Dilation

12.4

The dilation  $\mathcal{G} \oplus \mathcal{S}$  of a set  $\mathcal{G}$  by  $\mathcal{S}$  is defined as the set of shifts  $\mathbf{w}$  of  $\mathcal{S}$  for which the intersections of  $\mathcal{G}$  and the shifted  $\mathcal{S}$  are nonempty:

$$\mathcal{G} \oplus \mathcal{S} := \{\mathbf{w} \mid (\mathcal{S}^R)_{\mathbf{w}} \cap \mathcal{G} \neq \emptyset\}. \quad (12.12)$$

 $\diamond$ 

Figure 12.4 illustrates the results of the erosion and dilation of the two-dimensional butterfly-shaped set  $\mathcal{G}$  using a circular structuring element  $\mathcal{S}$  containing the origin. Obviously, the appendages are removed by the erosion, as at the respective positions, the shifted  $\mathcal{S}$  cannot be a subset of  $\mathcal{G}$ . Furthermore, this erosion results in shrinking  $\mathcal{G}$  by the radius of  $\mathcal{S}$ , as the shifted  $\mathcal{S}$  has to be completely contained in  $\mathcal{G}$  (Fig. 12.3). Thus,

$$\mathcal{G} \ominus \mathcal{S} \subseteq \mathcal{G}. \quad (12.13)$$

In the case of dilation, the set  $\mathcal{G}$  is enlarged by about the size of the radius of  $\mathcal{S}$ , which is why the fine notches disappear; here,

$$\mathcal{G} \subseteq \mathcal{G} \oplus \mathcal{S}. \quad (12.14)$$

---

<sup>1</sup>Erosion and dilation are closely related to the set-theoretic operations Minkowski subtraction and Minkowski addition.

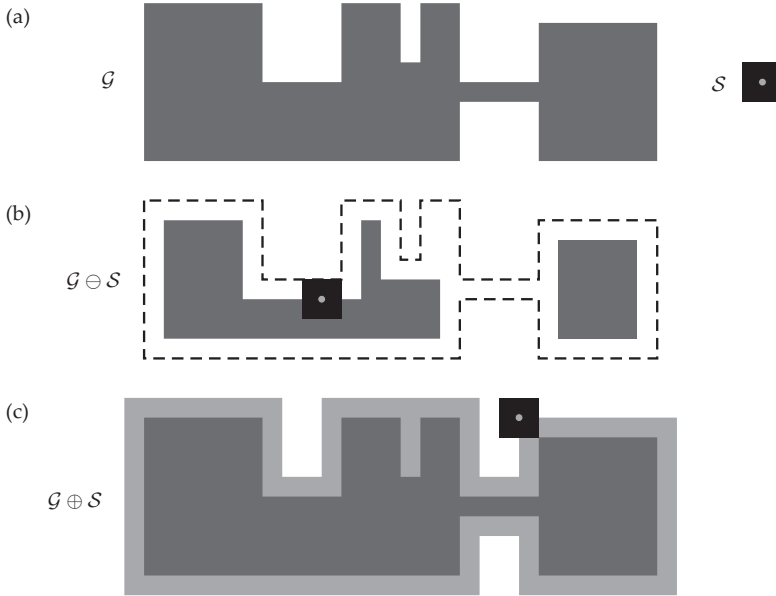


Figure 12.3. Illustration of erosion and dilation: (a) Original set  $\mathcal{G}$  and structuring element  $S$ ; (b) Result of the erosion of  $\mathcal{G}$  by  $S$ ; (c) Result of the dilation of  $\mathcal{G}$  by  $S$ .

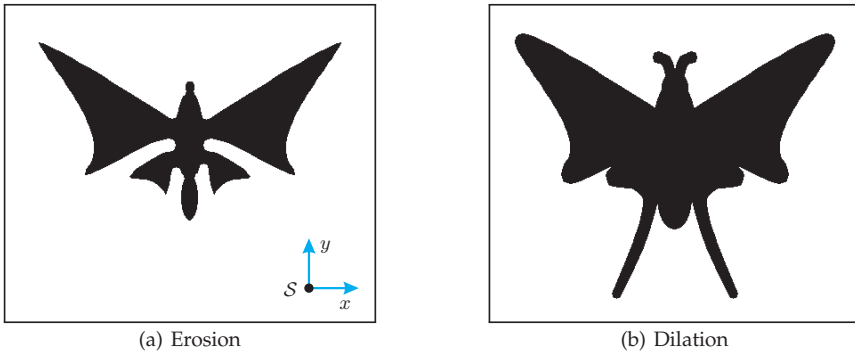


Figure 12.4. Result of erosion and dilation of the binary image of Fig. 12.1 using the structuring element shown,  $S$ .

In the following, further properties of erosion and dilation will be covered, which help in selecting and implementing morphological operators and support the design of the structuring element [7].

**12.1 Theorem 12.1: Properties of erosion**

Let  $\mathcal{G}$ ,  $\mathcal{G}_1$ , and  $\mathcal{G}_2$  denote the point sets of some binary images, and  $S$ ,  $S_1$ , and  $S_2$  denote structuring elements.

1. The erosion of a point set  $\mathcal{G}$  is the intersection of all the point sets resulting from shifts of  $\mathcal{G}$  by  $-\mathbf{z}$  for each  $\mathbf{z} \in \mathcal{S}$ .

$$\mathcal{G} \ominus \mathcal{S} = \bigcap_{\mathbf{z} \in \mathcal{S}} (\mathcal{G})_{-\mathbf{z}}. \tag{12.15}$$

2. The erosion using an ‘impulse,’ i.e., a single-element structuring element  $\{\mathbf{x}_0\}$ , corresponds to the shift of the point set  $\mathcal{G}$  by the vector  $-\mathbf{x}_0$  (Fig. 12.5):

$$\mathcal{G} \ominus \{\mathbf{x}_0\} = (\mathcal{G})_{-\mathbf{x}_0}. \tag{12.16}$$

3. The structuring element  $\{\mathbf{0}\}$  that contains only the origin is the neutral element of the erosion:

$$\mathcal{G} \ominus \{\mathbf{0}\} = \mathcal{G}. \tag{12.17}$$

4. Erosion is not commutative: in general,

$$\mathcal{G} \ominus \mathcal{S} \neq \mathcal{S} \ominus \mathcal{G}. \tag{12.18}$$

However, the ordering of subsequent erosion operations can be arbitrarily chosen:

$$(\mathcal{G} \ominus \mathcal{S}_1) \ominus \mathcal{S}_2 = (\mathcal{G} \ominus \mathcal{S}_2) \ominus \mathcal{S}_1. \tag{12.19}$$

5. Erosion is not associative: in general,

$$\mathcal{G} \ominus (\mathcal{S}_1 \ominus \mathcal{S}_2) \neq (\mathcal{G} \ominus \mathcal{S}_1) \ominus \mathcal{S}_2. \tag{12.20}$$

6. Erosion is shift-invariant: for an arbitrary shift vector  $\mathbf{z}$ ,

$$(\mathcal{G})_{\mathbf{z}} \ominus \mathcal{S} = (\mathcal{G} \ominus \mathcal{S})_{\mathbf{z}}, \tag{12.21}$$

$$\mathcal{G} \ominus (\mathcal{S})_{\mathbf{z}} = (\mathcal{G} \ominus \mathcal{S})_{-\mathbf{z}} = (\mathcal{G})_{-\mathbf{z}} \ominus \mathcal{S}. \tag{12.22}$$

7. The eroded point set is contained in the original point set if the structuring element contains the origin:

$$(0, 0)^T \in \mathcal{S} \Rightarrow \mathcal{G} \ominus \mathcal{S} \subseteq \mathcal{G}. \tag{12.23}$$

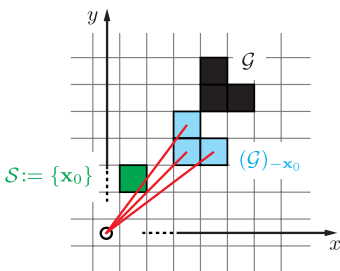


Figure 12.5. The erosion of the point set  $\mathcal{G}$  using the single-element structuring element  $\mathcal{S} := \{\mathbf{x}_0\}$  (‘impulse’) corresponds to the shift of  $\mathcal{G}$  by  $-\mathbf{x}_0$ .

8. Erosion is monotonic with respect to the inclusion relation:

$$\mathcal{G}_1 \subseteq \mathcal{G}_2 \quad \Rightarrow \quad \mathcal{G}_1 \ominus \mathcal{S} \subseteq \mathcal{G}_2 \ominus \mathcal{S}, \quad (12.24)$$

$$\mathcal{S}_1 \subseteq \mathcal{S}_2 \quad \Rightarrow \quad \mathcal{G} \ominus \mathcal{S}_1 \supseteq \mathcal{G} \ominus \mathcal{S}_2. \quad (12.25)$$

9. Erosion can be expressed as

$$\mathcal{G} \ominus \mathcal{S} := \{\mathbf{w} \mid (\mathcal{S})_{\mathbf{w}} \cap \mathcal{G} = (\mathcal{S})_{\mathbf{w}}\}. \quad (12.26)$$

◇

---

**Proof 12.1 (Properties of erosion):**

1. Representation as an intersection: first, suppose that  $\mathbf{w} \in \mathcal{G} \ominus \mathcal{S} = \{\mathbf{w} \mid (\mathcal{S})_{\mathbf{w}} \subseteq \mathcal{G}\}$ . Hence,

$$\forall \mathbf{z} \in \mathcal{S} : \mathbf{y} = \mathbf{z} + \mathbf{w} \in \mathcal{G} \quad (12.27)$$

$$\Rightarrow \forall \mathbf{z} \in \mathcal{S} : \mathbf{w} \in (\mathcal{G})_{-\mathbf{z}} = \{\mathbf{x} \mid \mathbf{x} = \mathbf{y} - \mathbf{z} \wedge \mathbf{y} \in \mathcal{G}\} \quad (12.28)$$

$$\Rightarrow \mathbf{w} \in \bigcap_{\mathbf{z} \in \mathcal{S}} (\mathcal{G})_{-\mathbf{z}}, \quad (12.29)$$

which implies  $\mathcal{G} \ominus \mathcal{S} \subseteq \bigcap_{\mathbf{z} \in \mathcal{S}} (\mathcal{G})_{-\mathbf{z}}$ .

On the other hand, suppose that  $\mathbf{w} \in \bigcap_{\mathbf{z} \in \mathcal{S}} (\mathcal{G})_{-\mathbf{z}}$ . Then,

$$\forall \mathbf{z} \in \mathcal{S} : \mathbf{w} \in (\mathcal{G})_{-\mathbf{z}} \quad (12.30)$$

$$\Rightarrow \forall \mathbf{y} = \mathbf{z} + \mathbf{w} \in (\mathcal{S})_{\mathbf{w}} : \mathbf{w} \in (\mathcal{G})_{-(\mathbf{y}-\mathbf{w})} \quad (12.31)$$

$$\Rightarrow \forall \mathbf{y} \in (\mathcal{S})_{\mathbf{w}} : \mathbf{w} + (\mathbf{y} - \mathbf{w}) \in \mathcal{G} \quad (12.32)$$

$$\Rightarrow (\mathcal{S})_{\mathbf{w}} \subseteq \mathcal{G} \quad (12.33)$$

$$\Rightarrow \mathbf{w} \in \mathcal{G} \ominus \mathcal{S}. \quad (12.34)$$

This yields  $\bigcap_{\mathbf{z} \in \mathcal{S}} (\mathcal{G})_{-\mathbf{z}} \subseteq \mathcal{G} \ominus \mathcal{S}$  and finally implies the identity of the alternative representations and the definition of erosion.

2. Erosion with an impulse:

$$\mathcal{G} \ominus \{\mathbf{x}_0\} = \{\mathbf{w} \mid (\{\mathbf{x}_0\})_{\mathbf{w}} \subseteq \mathcal{G}\} \quad (12.35)$$

$$= \{\mathbf{w} \mid \{\mathbf{x}_0 + \mathbf{w}\} \subseteq \mathcal{G}\} \quad (12.36)$$

$$= \{\mathbf{w} \mid \underbrace{(\mathbf{x}_0 + \mathbf{w})}_{=: \mathbf{z}} \in \mathcal{G}\} \quad (12.37)$$

$$= \{\mathbf{w} \mid \mathbf{w} = \mathbf{z} - \mathbf{x}_0 \wedge \mathbf{z} \in \mathcal{G}\} \quad (12.38)$$

$$= (\mathcal{G})_{-\mathbf{x}_0}. \quad (12.39)$$

3. Neutral element: a consequence of 2, using  $\mathbf{x}_0 = \mathbf{0}$ .

4. Commutativity: from 7, it is obvious that  $\mathcal{G} \ominus \mathcal{S} \subseteq \mathcal{G}$  and  $\mathcal{S} \ominus \mathcal{G} \subseteq \mathcal{S}$ . For disjoint point sets  $\mathcal{G} \cap \mathcal{S} = \emptyset$ , this results in  $\mathcal{G} \ominus \mathcal{S} \neq \mathcal{S} \ominus \mathcal{G}$ . Hence in general, erosion is not commutative. The permutability of (12.19) is shown later in the context of Theorem 12.3.

5. Associativity:  $\mathcal{S}_1 = \mathcal{S}_2 = \mathcal{S} \supset \{\mathbf{0}\}$  and  $\mathcal{G} \ominus \mathcal{S} \subset \mathcal{G}$  is assumed. This results in  $\mathcal{G} \ominus (\mathcal{S} \ominus \mathcal{S}) = \mathcal{G} \ominus \{\mathbf{0}\} = \mathcal{G}$  and  $(\mathcal{G} \ominus \mathcal{S}) \ominus \mathcal{S} \neq \mathcal{G}$ . These counterexamples show that erosion is not associative.

6. Shift-invariance:

$$(\mathcal{G})_{\mathbf{z}} \ominus \mathcal{S} = \bigcap_{\mathbf{x} \in \mathcal{S}} ((\mathcal{G})_{\mathbf{z}})_{-\mathbf{x}} = \bigcap_{\mathbf{x} \in \mathcal{S}} (\mathcal{G})_{\mathbf{z}-\mathbf{x}} = \left( \bigcap_{\mathbf{x} \in \mathcal{S}} (\mathcal{G})_{-\mathbf{x}} \right)_{\mathbf{z}} = (\mathcal{G} \ominus \mathcal{S})_{\mathbf{z}}. \quad (12.40)$$

Furthermore,

$$\mathcal{G} \ominus (\mathcal{S})_{\mathbf{z}} = \bigcap_{\mathbf{y} \in (\mathcal{S})_{\mathbf{z}}} (\mathcal{G})_{-\mathbf{y}} = \bigcap_{\mathbf{x} \in \mathcal{S}} (\mathcal{G})_{-(\mathbf{x}+\mathbf{z})} = \left( \bigcap_{\mathbf{x} \in \mathcal{S}} (\mathcal{G})_{-\mathbf{x}} \right)_{-\mathbf{z}} = (\mathcal{G} \ominus \mathcal{S})_{-\mathbf{z}}. \quad (12.41)$$

The last equation in (12.22) is obtained by applying (12.21).

7. Inclusion relation: assuming  $\mathcal{S} = \{\mathbf{0}\} \cup \mathcal{S}_1$ , we have

$$\mathcal{G} \ominus \mathcal{S} = \{\mathbf{w} \mid (\mathcal{S})_{\mathbf{w}} \subseteq \mathcal{G}\} = \{\mathbf{w} \mid (\{\mathbf{0}\})_{\mathbf{w}} \subseteq \mathcal{G} \wedge (\mathcal{S}_1)_{\mathbf{w}} \subseteq \mathcal{G}\} \quad (12.42)$$

$$\subseteq \{\mathbf{w} \mid (\{\mathbf{0}\})_{\mathbf{w}} \subseteq \mathcal{G}\} = \mathcal{G} \ominus \{\mathbf{0}\} = \mathcal{G}. \quad (12.43)$$

8. Monotonicity:

$$\mathcal{G}_1 \ominus \mathcal{S} = \{\mathbf{w} \mid (\mathcal{S})_{\mathbf{w}} \subseteq \mathcal{G}_1\} \quad (12.44)$$

$$\subseteq \{\mathbf{w} \mid (\mathcal{S})_{\mathbf{w}} \subseteq \mathcal{G}_2\} = \mathcal{G}_2 \ominus \mathcal{S}, \quad (12.45)$$

$$\mathcal{G} \ominus \mathcal{S}_1 = \{\mathbf{w} \mid (\mathcal{S}_1)_{\mathbf{w}} \subseteq \mathcal{G}\} \quad (12.46)$$

$$\supseteq \{\mathbf{w} \mid (\mathcal{S}_1)_{\mathbf{w}} \subseteq \mathcal{G} \wedge (\mathcal{S}_2 \setminus \mathcal{S}_1)_{\mathbf{w}} \subseteq \mathcal{G}\} \quad (12.47)$$

$$= \{\mathbf{w} \mid (\mathcal{S}_2)_{\mathbf{w}} \subseteq \mathcal{G}\} = \mathcal{G} \ominus \mathcal{S}_2. \quad (12.48)$$

9. This is the result of applying elementary set-theoretical operations to the definition of erosion. ■

### Theorem 12.2: Properties of dilation

12.2

Let  $\mathcal{G}$ ,  $\mathcal{G}_1$ , and  $\mathcal{G}_2$  denote point sets of binary images and let  $\mathcal{S}$ ,  $\mathcal{S}_1$ , and  $\mathcal{S}_2$  denote structuring elements.

1. Dilation is the union of all the point sets  $(\mathcal{G})_{\mathbf{z}}$  resulting from shifts of  $\mathcal{G}$  by  $\mathbf{z}$  for each  $\mathbf{z} \in \mathcal{S}$ :

$$\mathcal{G} \oplus \mathcal{S} = \bigcup_{\mathbf{z} \in \mathcal{G}} (\mathcal{S})_{\mathbf{z}} = \bigcup_{\mathbf{z} \in \mathcal{S}} (\mathcal{G})_{\mathbf{z}}. \quad (12.49)$$

2. The dilation of a single-element point set  $\mathcal{G} = \{\mathbf{x}_0\}$  using the structuring element  $\mathcal{S}$  corresponds to the shift of the structuring element by the vector  $\mathbf{x}_0$  (Fig. 12.6):

$$\{\mathbf{x}_0\} \oplus \mathcal{S} = (\mathcal{S})_{\mathbf{x}_0}. \quad (12.50)$$

3. The structuring element  $\{\mathbf{0}\}$  containing only the origin is the neutral element of the dilation:

$$\mathcal{G} \oplus \{\mathbf{0}\} = \mathcal{G}. \quad (12.51)$$

4. Dilation is commutative:

$$\mathcal{G} \oplus \mathcal{S} = \mathcal{S} \oplus \mathcal{G}. \quad (12.52)$$



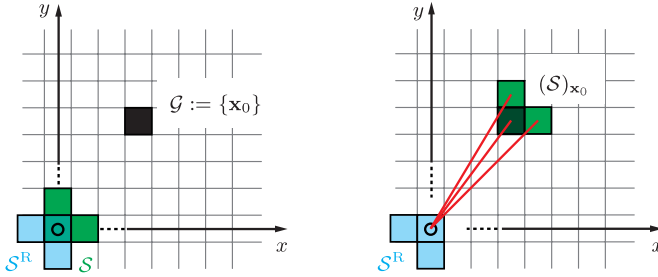


Figure 12.6. The dilation of the single-element point set  $\mathcal{G}$  using a structuring element  $\mathcal{S}$  can be considered as the impulse response of the structuring element.

5. Dilation is associative:

$$\mathcal{G} \oplus (\mathcal{S}_1 \oplus \mathcal{S}_2) = (\mathcal{G} \oplus \mathcal{S}_1) \oplus \mathcal{S}_2. \quad (12.53)$$

6. Dilation is shift-invariant:

$$(\mathcal{G})_{\mathbf{z}} \oplus \mathcal{S} = (\mathcal{G} \oplus \mathcal{S})_{\mathbf{z}}. \quad (12.54)$$

7. The original point set is contained in the dilated point set if the structuring element contains the origin:

$$(0, 0)^T \in \mathcal{S} \Rightarrow \mathcal{G} \subseteq \mathcal{G} \oplus \mathcal{S}. \quad (12.55)$$

8. Dilation is monotonic with respect to the inclusion relation:

$$\mathcal{G}_1 \subseteq \mathcal{G}_2 \Rightarrow \mathcal{G}_1 \oplus \mathcal{S} \subseteq \mathcal{G}_2 \oplus \mathcal{S}. \quad (12.56)$$

◇

### Proof 12.2 (Properties of dilation):

1. Representation as a union of sets: first, assume that  $\mathbf{w} \in \mathcal{G} \oplus \mathcal{S} = \{\mathbf{w} \mid (\mathcal{S}^R)_{\mathbf{w}} \cap \mathcal{G} \neq \emptyset\}$ . Then,

$$\exists \mathbf{x} : \mathbf{x} \in (\mathcal{S}^R)_{\mathbf{w}} \cap \mathcal{G} \quad (12.57)$$

$$\Rightarrow \mathbf{x} \in (\mathcal{S}^R)_{\mathbf{w}} \wedge \mathbf{x} \in \mathcal{G} \quad (12.58)$$

$$\Rightarrow \mathbf{x} \in \{\mathbf{y} \mid \mathbf{y} = \mathbf{r} + \mathbf{w} \wedge \mathbf{r} \in \mathcal{S}^R\} \wedge \mathbf{x} \in \mathcal{G} \quad (12.59)$$

$$\Rightarrow \mathbf{r} = \mathbf{x} - \mathbf{w} \in \mathcal{S}^R \wedge \mathbf{x} \in \mathcal{G} \quad (12.60)$$

$$\Rightarrow \mathbf{s} = -\mathbf{r} = \mathbf{w} - \mathbf{x} \in \mathcal{S} \wedge \mathbf{x} \in \mathcal{G} \quad (12.61)$$

$$\Rightarrow \mathbf{w} = \mathbf{s} + \mathbf{x} \in (\mathcal{S})_{\mathbf{x}} \wedge \mathbf{x} \in \mathcal{G} \quad (12.62)$$

$$\Rightarrow \mathbf{w} \in \bigcup_{\mathbf{x} \in \mathcal{G}} (\mathcal{S})_{\mathbf{x}}. \quad (12.63)$$

This implies  $\{\mathbf{w} \mid (\mathcal{S}^R)_{\mathbf{w}} \cap \mathcal{G} \neq \emptyset\} \subseteq \bigcup_{\mathbf{z} \in \mathcal{G}} (\mathcal{S})_{\mathbf{z}}$ .

Now, assume  $\mathbf{w} \in \bigcup_{\mathbf{z} \in \mathcal{G}} (\mathcal{S})_{\mathbf{z}}$ . Then, there exists a  $\mathbf{z} \in \mathcal{G}$  with

$$\mathbf{w} \in (\mathcal{S})_{\mathbf{z}} \quad (12.64)$$

$$\Rightarrow \mathbf{w} \in \{\mathbf{x} \mid \mathbf{x} = \mathbf{s} + \mathbf{z} \wedge \mathbf{s} \in \mathcal{S}\} \quad (12.65)$$

$$\Rightarrow \exists \mathbf{s} \in \mathcal{S} : \mathbf{w} = \mathbf{s} + \mathbf{z}. \quad (12.66)$$

This results in

$$\mathbf{r} = -\mathbf{s} \in \mathcal{S}^{\mathbf{R}} \quad (12.67)$$

$$\Rightarrow \mathbf{z} = \mathbf{w} - \mathbf{s} = \mathbf{r} + \mathbf{w} \in (\mathcal{S}^{\mathbf{R}})_{\mathbf{w}} \quad (12.68)$$

$$\mathbf{z} \in \mathcal{G} \Rightarrow \mathbf{z} \in ((\mathcal{S}^{\mathbf{R}})_{\mathbf{w}} \cap \mathcal{G}) \quad (12.69)$$

$$\Rightarrow ((\mathcal{S}^{\mathbf{R}})_{\mathbf{w}} \cap \mathcal{G}) \neq \emptyset \quad (12.70)$$

$$\Rightarrow \mathbf{w} \in \{\mathbf{w} \mid (\mathcal{S}^{\mathbf{R}})_{\mathbf{w}} \cap \mathcal{G} \neq \emptyset\}, \quad (12.71)$$

which implies  $\bigcup_{\mathbf{z} \in \mathcal{G}} (\mathcal{S})_{\mathbf{z}} \subseteq \{\mathbf{w} \mid (\mathcal{S}^{\mathbf{R}})_{\mathbf{w}} \cap \mathcal{G} \neq \emptyset\}$  and finally yields the equality of the two representations.

The second representation in (12.49) is proven using the commutativity in 4.

2. Dilation with an impulse: results from 1.

3. Neutral element: results from 2.

4. Commutativity:

$$\mathcal{G} \oplus \mathcal{S} = \bigcup_{\mathbf{z} \in \mathcal{G}} (\mathcal{S})_{\mathbf{z}} = \bigcup_{\mathbf{z} \in \mathcal{G}} \{\mathbf{w} \mid \mathbf{w} = \mathbf{x} + \mathbf{z} \wedge \mathbf{x} \in \mathcal{S}\} \quad (12.72)$$

$$= \{\mathbf{w} \mid \mathbf{w} = \mathbf{x} + \mathbf{z} \wedge \mathbf{x} \in \mathcal{S} \wedge \mathbf{z} \in \mathcal{G}\} \quad (12.73)$$

$$= \bigcup_{\mathbf{x} \in \mathcal{S}} \{\mathbf{w} \mid \mathbf{w} = \mathbf{x} + \mathbf{z} \wedge \mathbf{z} \in \mathcal{G}\} = \bigcup_{\mathbf{x} \in \mathcal{S}} (\mathcal{G})_{\mathbf{x}} = \mathcal{S} \oplus \mathcal{G}. \quad (12.74)$$

5. Associativity:

$$\mathcal{G} \oplus (\mathcal{S}_1 \oplus \mathcal{S}_2) = \bigcup_{\mathbf{z} \in \mathcal{G}} \left( \bigcup_{\mathbf{x} \in \mathcal{S}_1} (\mathcal{S}_2)_{\mathbf{x}} \right)_{\mathbf{z}} \quad (12.75)$$

$$= \bigcup_{\mathbf{z} \in \mathcal{G}} (\{\mathbf{w} \mid \mathbf{w} = \mathbf{x} + \mathbf{y} \wedge \mathbf{x} \in \mathcal{S}_1 \wedge \mathbf{y} \in \mathcal{S}_2\})_{\mathbf{z}} \quad (12.76)$$

$$= \{\mathbf{v} \mid \mathbf{v} = \mathbf{x} + \mathbf{y} + \mathbf{z} \wedge \mathbf{x} \in \mathcal{S}_1 \wedge \mathbf{y} \in \mathcal{S}_2 \wedge \mathbf{z} \in \mathcal{G}\} \quad (12.77)$$

$$= \bigcup_{\mathbf{r} \in \{\mathbf{w} \mid \mathbf{w} = \mathbf{x} + \mathbf{z} \wedge \mathbf{x} \in \mathcal{S}_1 \wedge \mathbf{z} \in \mathcal{G}\}} (\mathcal{S}_2)_{\mathbf{r}} \quad (12.78)$$

$$= \bigcup_{\mathbf{r} \in \bigcup_{\mathbf{z} \in \mathcal{G}} (\mathcal{S}_1)_{\mathbf{z}}} (\mathcal{S}_2)_{\mathbf{r}} = \bigcup_{\mathbf{r} \in (\mathcal{G} \oplus \mathcal{S}_1)} (\mathcal{S}_2)_{\mathbf{r}} = (\mathcal{G} \oplus \mathcal{S}_1) \oplus \mathcal{S}_2. \quad (12.79)$$

6. Shift-invariance:

$$(\mathcal{G})_z \oplus \mathcal{S} = \bigcup_{x \in (\mathcal{G})_z} (\mathcal{S})_x = \bigcup_{x \in \{x \mid x=y+z \wedge y \in \mathcal{G}\}} (\mathcal{S})_x \quad (12.80)$$

$$= \{\mathbf{w} \mid \mathbf{w} = \mathbf{s} + \mathbf{y} + \mathbf{z} \wedge \mathbf{y} \in \mathcal{G} \wedge \mathbf{s} \in \mathcal{S}\} \quad (12.81)$$

$$= (\{\mathbf{v} \mid \mathbf{v} = \mathbf{s} + \mathbf{y} \wedge \mathbf{y} \in \mathcal{G} \wedge \mathbf{s} \in \mathcal{S}\})_z \quad (12.82)$$

$$= \left( \bigcup_{y \in \mathcal{G}} (\mathcal{S})_y \right)_z = (\mathcal{G} \oplus \mathcal{S})_z. \quad (12.83)$$

7. Inclusion relation:

$$\mathcal{G} \oplus \mathcal{S} = \bigcup_{z \in \mathcal{S}} (\mathcal{G})_z = \bigcup_{z \in (\{0\} \cup (\mathcal{S} \setminus \{0\}))} (\mathcal{G})_z = (\mathcal{G})_0 \cup \bigcup_{z \in (\mathcal{S} \setminus \{0\})} (\mathcal{G})_z \supseteq (\mathcal{G})_0 = \mathcal{G}. \quad (12.84)$$

8. Monotonicity:

$$\mathcal{G}_1 \oplus \mathcal{S} = \bigcup_{z \in \mathcal{G}_1} (\mathcal{S})_z \subseteq \bigcup_{z \in \mathcal{G}_2} (\mathcal{S})_z = \mathcal{G}_2 \oplus \mathcal{S}. \quad (12.85)$$

### ⊗ 12.1.2.1 Duality of erosion and dilation

Erosion and dilation, the fundamental operations of morphology, are not inverses. In other words, in general, the composition of the two operations does not yield the original set:

$$(\mathcal{G} \ominus \mathcal{S}) \oplus \mathcal{S} \neq \mathcal{G} \neq (\mathcal{G} \oplus \mathcal{S}) \ominus \mathcal{S}. \quad (12.86)$$

However, the following duality applies to erosion and dilation:

---

#### 12.3 Theorem 12.3: Duality of erosion and dilation

Given point sets  $\mathcal{G}, \mathcal{S}, \mathcal{S}_1, \dots, \mathcal{S}_K$ , it follows that

$$\overline{\mathcal{G}} \oplus \mathcal{S}^R = \overline{\mathcal{G} \ominus \mathcal{S}}. \quad (12.87)$$

Besides,

$$\mathcal{G} \subseteq (\mathcal{G} \oplus \mathcal{S}) \ominus \mathcal{S}, \quad (12.88)$$

$$\mathcal{G} \supseteq (\mathcal{G} \ominus \mathcal{S}) \oplus \mathcal{S}. \quad (12.89)$$

Furthermore, the following relation holds for erosion and dilation:

$$(\mathcal{G} \ominus \mathcal{S}_1) \ominus \mathcal{S}_2 = \mathcal{G} \ominus (\mathcal{S}_1 \oplus \mathcal{S}_2), \quad (12.90)$$

$$(\dots(((\mathcal{G} \ominus \mathcal{S}_1) \ominus \mathcal{S}_2) \ominus \mathcal{S}_3) \dots \ominus \mathcal{S}_K) = \mathcal{G} \ominus (\mathcal{S}_1 \oplus \dots \oplus \mathcal{S}_K). \quad (12.91)$$

◇

**Proof 12.3 (Duality of erosion and dilation):** The proof is carried out by applying De Morgan's laws to the intersection of the point sets:

$$\overline{\mathcal{G} \ominus \mathcal{S}} = \overline{\bigcap_{z \in \mathcal{S}} (\mathcal{G})_{-z}} = \bigcup_{z \in \mathcal{S}} \overline{(\mathcal{G})_{-z}} = \bigcup_{x \in \mathcal{S}^R} (\overline{\mathcal{G}})_x = \overline{\mathcal{G}} \oplus \mathcal{S}^R. \quad (12.92)$$

The inclusion relation is proven as follows:  $\mathbf{w} \in \mathcal{G}$  is assumed to be arbitrary. Thus,

$$\forall \mathbf{z} \in \mathcal{S} : \mathbf{w} + \mathbf{z} \in (\mathcal{G})_{\mathbf{z}} \quad (12.93)$$

$$\Rightarrow \forall \mathbf{z} \in \mathcal{S} : \mathbf{w} + \mathbf{z} \in \bigcup_{x \in \mathcal{S}} (\mathcal{G})_x = \mathcal{G} \oplus \mathcal{S} \quad (12.94)$$

$$\Rightarrow \forall \mathbf{z} \in \mathcal{S} : \mathbf{w} \in (\mathcal{G} \oplus \mathcal{S})_{-\mathbf{z}} \quad (12.95)$$

$$\Rightarrow \mathbf{w} \in \bigcap_{z \in \mathcal{S}} (\mathcal{G} \oplus \mathcal{S})_{-\mathbf{z}} = (\mathcal{G} \oplus \mathcal{S}) \ominus \mathcal{S}. \quad (12.96)$$

Now assume that  $\mathbf{w} \in (\mathcal{G} \ominus \mathcal{S}) \oplus \mathcal{S} = \bigcup_{z \in \mathcal{S}} (\mathcal{G} \ominus \mathcal{S})_{\mathbf{z}} = \{\mathbf{w} \mid \mathbf{w} = \mathbf{y} + \mathbf{z} \wedge \mathbf{y} \in (\mathcal{G} \ominus \mathcal{S}) \wedge \mathbf{z} \in \mathcal{S}\}$ . Because of the last equation, it is obvious that

$$\exists \mathbf{y} \in (\mathcal{G} \ominus \mathcal{S}) \exists \mathbf{z} \in \mathcal{S} : \mathbf{w} = \mathbf{y} + \mathbf{z} \quad (12.97)$$

$$\Rightarrow \mathbf{y} \in \bigcap_{s \in \mathcal{S}} (\mathcal{G})_{-\mathbf{s}} = \bigcap_{s \in \mathcal{S}} \{\mathbf{v} \mid \mathbf{v} = \mathbf{x} - \mathbf{s} \wedge \mathbf{x} \in \mathcal{G}\} \quad (12.98)$$

$$\Rightarrow \forall \mathbf{s} \in \mathcal{S} : \mathbf{y} \in \{\mathbf{v} \mid \mathbf{v} = \mathbf{x} - \mathbf{s} \wedge \mathbf{x} \in \mathcal{G}\} \quad (12.99)$$

$$\Rightarrow \forall \mathbf{s} \in \mathcal{S} : \mathbf{x} = \mathbf{y} + \mathbf{s} \in \mathcal{G} \quad (12.100)$$

$$\mathbf{z} \in \mathcal{S} \Rightarrow \mathbf{y} + \mathbf{z} \in \mathcal{G} \quad (12.101)$$

$$\mathbf{w} = \mathbf{y} + \mathbf{z} \Rightarrow \mathbf{w} \in \mathcal{G}. \quad (12.102)$$

Regarding (12.90):

$$(\mathcal{G} \ominus \mathcal{S}_1) \ominus \mathcal{S}_2 = \bigcap_{z \in \mathcal{S}_2} (\mathcal{G} \ominus \mathcal{S}_1)_{-\mathbf{z}} = \bigcap_{z \in \mathcal{S}_2} \bigcap_{y \in \mathcal{S}_1} (\mathcal{G})_{-\mathbf{z}-\mathbf{y}} \quad (12.103)$$

$$= \bigcap_{\mathbf{x} \in \{\mathbf{x} \mid \mathbf{x} = \mathbf{y} + \mathbf{z} \wedge \mathbf{y} \in \mathcal{S}_1 \wedge \mathbf{z} \in \mathcal{S}_2\}} (\mathcal{G})_{-\mathbf{x}} = \bigcap_{\mathbf{x} \in \bigcup_{y \in \mathcal{S}_1} (\mathcal{S}_2)_y} (\mathcal{G})_{-\mathbf{x}} \quad (12.104)$$

$$= \bigcap_{\mathbf{x} \in (\mathcal{S}_1 \oplus \mathcal{S}_2)} (\mathcal{G})_{-\mathbf{x}} = \mathcal{G} \ominus (\mathcal{S}_1 \oplus \mathcal{S}_2). \quad (12.105)$$

Equation (12.91) results by an induction with respect to  $K$ . Finally, (12.90) and the commutativity of the dilation imply (12.19). ■

The duality of erosion and dilation is illustrated in Fig. 12.7. The dilation of the image background  $\overline{\mathcal{G}}$  with a symmetric structuring element  $\mathcal{S}$  is equivalent to the erosion of the foreground object  $\mathcal{G}$ , and vice versa:

$$\overline{\overline{\mathcal{G}} \oplus \mathcal{S}^R} = \mathcal{G} \ominus \mathcal{S}, \quad \overline{\overline{\mathcal{G}} \ominus \mathcal{S}^R} = \mathcal{G} \oplus \mathcal{S}. \quad (12.106)$$

Although erosion and dilation are only dual methods, they are inverse under certain circumstances, so that the composition of these two methods yields the original point set. For such cases, a perfect reconstruction of the original set  $\mathcal{G}$  is possible using the dual operation. The following section will present examples of such cases, cf. (12.124).

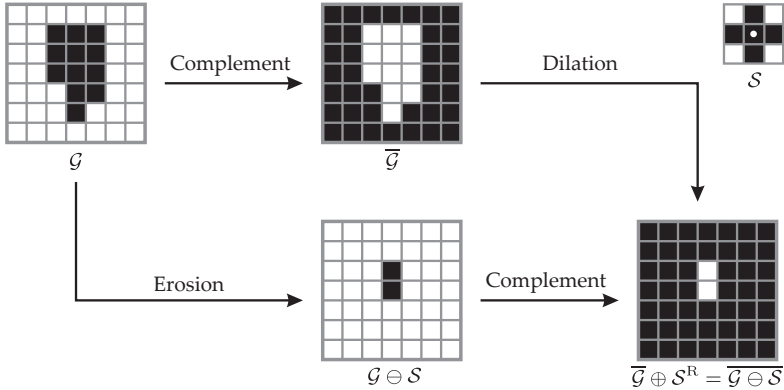


Figure 12.7. Duality of erosion and dilation. For a structuring element with point symmetry as in this example, one has  $S = S^R$ .

The associativity of the dilation as in (12.53) can be exploited to increase computational efficiency: multiple dilation operations with small structuring elements  $S_1, \dots, S_K$  usually need less computation time than a dilation with a composite structuring element  $S_1 \oplus \dots \oplus S_K$ . Furthermore, the intermediate results might be reusable in some applications. Similarly, the following applies to the erosion: a large structuring element can be decomposed according to (12.90) and (12.91) [7].

➤ 12.1.3 Opening and closing

The shrinking caused by erosion can sometimes be mitigated by performing an additional dilation with the same structuring element. Similarly, the growth caused by the dilation can be alleviated by applying a subsequent erosion. The morphological operation of opening, respectively, closing, is defined as the composition of erosion with dilation, respectively, the composition of dilation with erosion.

12.5 Definition 12.5: Opening and closing

Let  $\mathcal{G}$  denote a point set and  $S$  denote a structuring element. The composition of an erosion with a subsequent dilation is called opening:

$$\mathcal{G} \circ S := (\mathcal{G} \ominus S) \oplus S. \tag{12.107}$$

The reverse order of the operations is called closing:

$$\mathcal{G} \bullet S := (\mathcal{G} \oplus S) \ominus S. \tag{12.108}$$

◇

Opening and closing yield sets with borders close to those of the original set  $\mathcal{G}$ . An opening removes fine appendages which are thinner than  $S$  and preserves (i.e., opens) inclusions, whereas closing preserves fine appendages and closes inclusions thinner than  $S$  (Fig. 12.8). An opening removes isolated pixels and objects which are smaller than the structuring element. A closing fills holes in the object that are smaller than the structuring element. Both

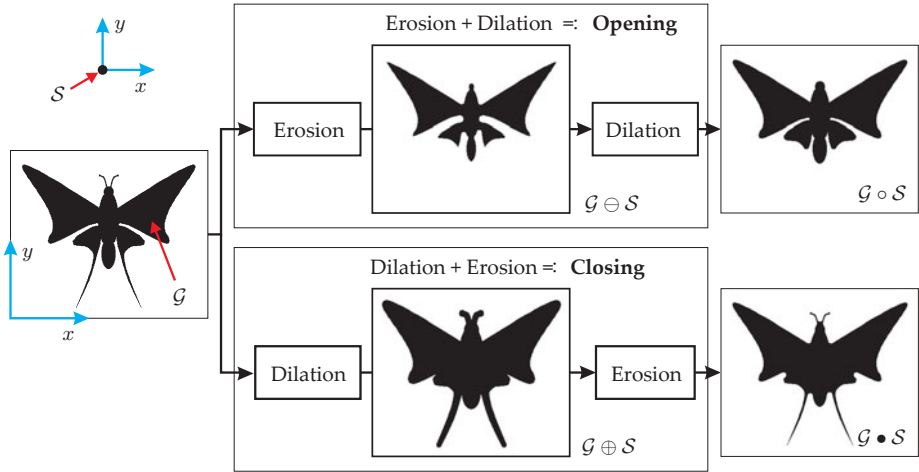


Figure 12.8. Opening and closing applied to the example image shown in Fig. 12.1.

operations can be interpreted as smoothing methods for  $\mathcal{G}$  yielding results that are similar to  $\mathcal{G}$  but differ with respect to details which are smaller than  $\mathcal{S}$ .

**Theorem 12.4: Properties of opening and closing**

1. The opened point set is a subset of the original point set. The closed point set is a superset of the original point set:

$$\mathcal{G} \circ \mathcal{S} \subseteq \mathcal{G} \subseteq \mathcal{G} \bullet \mathcal{S}. \tag{12.109}$$

2. Opening and closing are monotonic with respect to the relation of inclusion:

$$\mathcal{G}_1 \subseteq \mathcal{G}_2 \Rightarrow \begin{cases} \mathcal{G}_1 \circ \mathcal{S} \subseteq \mathcal{G}_2 \circ \mathcal{S} \\ \mathcal{G}_1 \bullet \mathcal{S} \subseteq \mathcal{G}_2 \bullet \mathcal{S}. \end{cases} \tag{12.110}$$

3. Opening using a given structuring element is an idempotent, and so is closing:

$$(\mathcal{G} \circ \mathcal{S}) \circ \mathcal{S} = \mathcal{G} \circ \mathcal{S}, \tag{12.111}$$

$$(\mathcal{G} \bullet \mathcal{S}) \bullet \mathcal{S} = \mathcal{G} \bullet \mathcal{S}. \tag{12.112}$$

4. Opening and closing are dual operations:

$$\overline{\mathcal{G} \bullet \mathcal{S}} = \overline{\mathcal{G}} \circ \mathcal{S}^R, \tag{12.113}$$

$$\overline{\mathcal{G} \circ \mathcal{S}} = \overline{\mathcal{G}} \bullet \mathcal{S}^R. \tag{12.114}$$

5. Opening and closing can be expressed as set operations:

$$\mathcal{G} \circ \mathcal{S} = \bigcup_{\{z \mid (\mathcal{S})_z \subseteq \mathcal{G}\}} (\mathcal{S})_z, \quad (12.115)$$

$$\mathcal{G} \bullet \mathcal{S} = \bigcap_{\{z \mid (\mathcal{S}^R)_z \cap \mathcal{G} = \emptyset\}} \overline{(\mathcal{S}^R)_z}. \quad (12.116)$$

6. The effect of shifts on opening and closing is as follows:

$$(\mathcal{G})_z \circ \mathcal{S} = (\mathcal{G} \circ \mathcal{S})_z, \quad (12.117)$$

$$(\mathcal{G})_z \bullet \mathcal{S} = (\mathcal{G} \bullet \mathcal{S})_z, \quad (12.118)$$

$$\forall \mathbf{w} \in \Omega_g : \mathcal{G} \circ (\mathcal{S})_{\mathbf{w}} = \mathcal{G} \circ \mathcal{S}, \quad (12.119)$$

$$\forall \mathbf{w} \in \Omega_g : \mathcal{G} \bullet (\mathcal{S})_{\mathbf{w}} = \mathcal{G} \bullet \mathcal{S}. \quad (12.120)$$

7. The operations have the following relations to erosion and dilation:

$$\mathcal{G} \ominus \mathcal{S} = (\mathcal{G} \circ \mathcal{S}) \ominus \mathcal{S} = (\mathcal{G} \ominus \mathcal{S}) \bullet \mathcal{S}, \quad (12.121)$$

$$\mathcal{G} \oplus \mathcal{S} = (\mathcal{G} \bullet \mathcal{S}) \oplus \mathcal{S} = (\mathcal{G} \oplus \mathcal{S}) \circ \mathcal{S}. \quad (12.122)$$

◇

---

**Proof 12.4 (Properties of opening and closing):**

1. The inclusion relations immediately result from Theorem 12.3.
2. The monotonicity results from the monotonicity of erosion and dilation.
3. Idempotence of opening: 1 and the monotonicity of erosion results in

$$(\mathcal{G} \circ \mathcal{S}) \subseteq \mathcal{G} \Rightarrow ((\mathcal{G} \ominus \mathcal{S}) \oplus \mathcal{S}) \ominus \mathcal{S} = (\mathcal{G} \circ \mathcal{S}) \ominus \mathcal{S} \subseteq \mathcal{G} \ominus \mathcal{S}.$$

Furthermore, applying 1 to  $\mathcal{G} \ominus \mathcal{S}$  yields

$$\mathcal{G} \ominus \mathcal{S} \subseteq (\mathcal{G} \ominus \mathcal{S}) \bullet \mathcal{S} = ((\mathcal{G} \ominus \mathcal{S}) \oplus \mathcal{S}) \ominus \mathcal{S}. \quad (12.123)$$

So, in all, one has

$$((\mathcal{G} \ominus \mathcal{S}) \oplus \mathcal{S}) \ominus \mathcal{S} = \mathcal{G} \ominus \mathcal{S}. \quad (12.124)$$

Hence, when applied to  $\mathcal{G} \ominus \mathcal{S}$ , dilation and erosion with  $\mathcal{S}$  are inverse to each other. Another dilation performed on both sides of the last equation results in the idempotence of opening:

$$\underbrace{\underbrace{(((\mathcal{G} \ominus \mathcal{S}) \oplus \mathcal{S}) \ominus \mathcal{S}) \oplus \mathcal{S}}_{= \mathcal{G} \circ \mathcal{S}}}_{= (\mathcal{G} \circ \mathcal{S}) \circ \mathcal{S}} = \underbrace{(\mathcal{G} \ominus \mathcal{S}) \oplus \mathcal{S}}_{= \mathcal{G} \circ \mathcal{S}}. \quad (12.125)$$

The idempotence of closing can be proven similarly [7].

4. The duality results from the duality of erosion and dilation (Theorem 12.3):

$$\overline{\mathcal{G} \bullet \mathcal{S}} = \overline{(\mathcal{G} \oplus \mathcal{S}) \ominus \mathcal{S}} = \overline{(\mathcal{G} \oplus \mathcal{S})} \oplus \mathcal{S}^R = (\overline{\mathcal{G}} \ominus \mathcal{S}^R) \oplus \mathcal{S}^R = \overline{\mathcal{G}} \circ \mathcal{S}^R.$$

5. Representation as a set union or intersection: the first step is to write the opening as

$$\mathcal{G} \circ \mathcal{S} = (\mathcal{G} \ominus \mathcal{S}) \oplus \mathcal{S} = \bigcup_{z \in \mathcal{G} \ominus \mathcal{S}} (\mathcal{S})_z = \bigcup_{z \in \{\mathbf{w} \mid (\mathcal{S})_{\mathbf{w}} \subseteq \mathcal{G}\}} (\mathcal{S})_z. \quad (12.126)$$

Using duality, this yields the representation of closing:

$$\mathcal{G} \bullet \mathcal{S} = \overline{\overline{\mathcal{G}} \circ \mathcal{S}^R} = \overline{\bigcup_{z \in \{\mathbf{w} \mid (\mathcal{S}^R)_{\mathbf{w}} \subseteq \overline{\mathcal{G}}\}} (\mathcal{S}^R)_z} = \bigcap_{z \in \{\mathbf{w} \mid (\mathcal{S}^R)_{\mathbf{w}} \cap \mathcal{G} = \emptyset\}} \overline{(\mathcal{S}^R)_z}.$$

6. Shift-invariance: the properties of erosion and dilation with respect to the shift by  $\mathbf{w}$  result in

$$\mathcal{G} \circ (\mathcal{S})_{\mathbf{w}} = (\mathcal{G} \ominus (\mathcal{S})_{\mathbf{w}}) \oplus (\mathcal{S})_{\mathbf{w}} = ((\mathcal{G} \ominus \mathcal{S})_{-\mathbf{w}} \oplus \mathcal{S})_{\mathbf{w}} \quad (12.127)$$

$$= ((\mathcal{G} \ominus \mathcal{S}) \oplus \mathcal{S})_{\mathbf{w} - \mathbf{w}} = \mathcal{G} \circ \mathcal{S}. \quad (12.128)$$

The other equations can be proven similarly.

7. The relations with erosion and dilation, as well as the idempotence, follow from (12.124) and the corresponding proof regarding closing. ■

In contrast to erosion and dilation, the location of the origin of the structuring element is of no importance for opening and closing, as the shifts of successive erosion and dilation operations compensate for each other.

The combination of the introduced basic operations of binary morphology provides a simple and descriptive way to solve numerous image processing tasks. Some examples of composite morphological operators are presented in the following sections.

#### ➤ 12.1.4 Border extraction

In many applications, e.g., for measuring the circumference of an object, its border is of interest. The presented morphological operators binary above allow an easy extraction of the borders of the point set  $\mathcal{G}$  [5]:

$$\text{Border}\{\mathcal{G}\} = \mathcal{G} \setminus (\mathcal{G} \ominus \mathcal{S}). \quad (12.129)$$

Erosion results in shrinking the object and yields the interior of the point set. By calculating the difference from the original binary image, one obtains exactly the border points. A circular set of radius one, whose center is placed in the origin, is used as the structuring element and can be approximated by the cross  $\mathcal{S}_C$  by employing Fig. 12.2(a). The center of the circle is located at the origin of the coordinate system. This results in a contour of the object that has a width of exactly one pixel and which is connected in the sense of 4-connected neighborhoods, i.e., contour points preceding or succeeding a contour point are part of a 4-connected neighborhood  $N_4(\mathbf{x})$  (see Def. 11.8). If a contour according to an 8-connected neighborhood is desired, a  $3 \times 3$  square can be chosen as the structuring element. Larger structuring elements result in wider contours.

Figure 12.9 shows an example of binary morphological border extraction applied to the butterfly-shaped point set  $\mathcal{G}$  from Fig. 12.1.



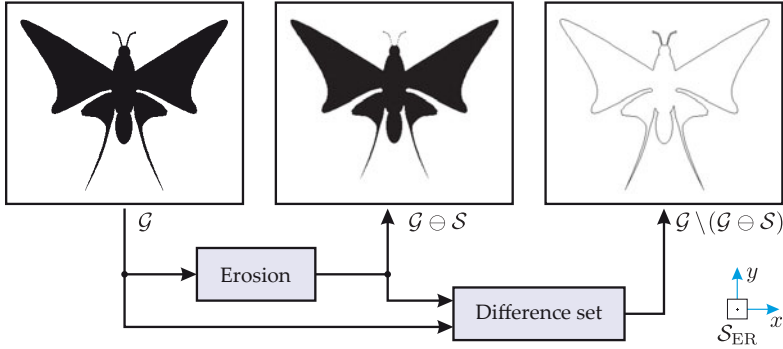


Figure 12.9. Border extraction with  $S_C$ .

➤ **12.1.5 Region filling**

For some applications, a connected component in the image, which is given by its outer contour and which might contain holes, has to be filled, e.g., in order to determine its area. Based on morphological operators, iterative algorithms can be designed that are capable of closing such gaps [5]. Suppose that the point set  $\mathcal{G}$  is connected with respect to 8-connected neighborhoods, and let  $\mathcal{Y}$  denote the region enclosed by  $\mathcal{G}$ , and assume further that  $\mathcal{Y} \cap \mathcal{G} = \emptyset$ . Beginning with a start point  $\mathbf{p} \in \mathcal{Y}$ , the following algorithm finds all other points belonging to  $\mathcal{Y}$ . For this purpose, the set

$$\mathcal{X}_k := (\mathcal{X}_{k-1} \oplus S_C) \cap \overline{\mathcal{G}}, \quad k = 1, 2, 3, \dots \tag{12.130}$$

is calculated iteratively. For the first iteration, set  $\mathcal{X}_0 := \{\mathbf{p}\}$ . The dilation using the cross  $S_C$  as structuring element results in a growth of the regions, and the subsequent calculation of the intersection removes possibly added points that are not part of  $\mathcal{Y}$ . The iteration is finished as soon as

$$\mathcal{X}_k = \mathcal{X}_{k-1}. \tag{12.131}$$

Then, the following holds for the filled gap:  $\mathcal{Y} = \mathcal{X}_k$ .

Figure 12.10 shows a simple example of the determination of an enclosed region  $\mathcal{Y}$ . In this case, the termination condition is met after the fourth iteration. The filled region around the point  $\mathbf{p}$  is the result of the union of the original contour  $\mathcal{G}$  with the enclosed region  $\mathcal{Y}$ .

➤ **12.1.6 Component labeling and connected component analysis**

Binary morphological methods can also be used for extracting connected components (i.e., objects) from an image [5]. Although for a human observer it is clear whether some adjacent points of an image form a connected region, this is not obvious for a computer, as the image is only represented as a matrix of image pixels. A connected component analysis tries to assign a unique label (usually an integer) to each connected component.

In order to label a single component, the approach of Sec. 12.1.5 is used and  $\mathcal{Y} \subseteq \mathcal{G}$  denotes the connected region that is to be extracted. Beginning from a starting point  $\mathbf{p} \in \mathcal{Y}$ , the iterative algorithm finds all other points of  $\mathcal{Y}$ . Similar to the filling of regions, the

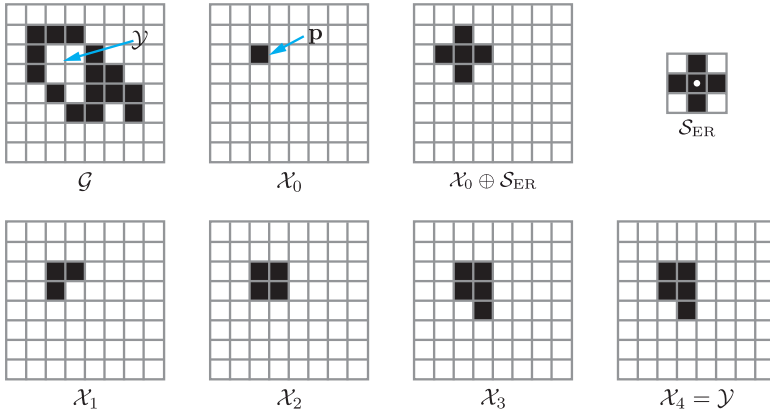


Figure 12.10. Example of region filling.

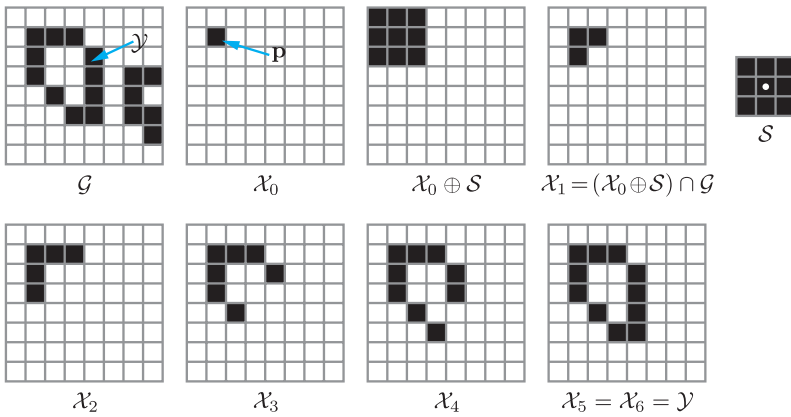


Figure 12.11. Example of component labeling.

algorithm is given by

$$\mathcal{X}_k = (\mathcal{X}_{k-1} \oplus S) \cap \mathcal{G}, \quad k = 1, 2, 3, \dots \tag{12.132}$$

with  $\mathcal{X}_0 = \{p\}$ . As now a component of the object is to be found, the intersection with  $\mathcal{G}$  has to be computed, instead of the complement  $\bar{\mathcal{G}}$  as for the filling of gaps in the background using (12.130). The iteration is finished as soon as the condition  $\mathcal{X}_k = \mathcal{X}_{k-1}$  is met. Then,  $\mathcal{Y} = \mathcal{X}_k$ .

A cross  $S$  as in Fig. 12.2(a) is chosen as the structuring element if the adjacent pixels of an object are required to have a common side (4-connected neighborhood). It is even possible to allow neighborhoods that have at least one common corner (i.e., 8-connected neighborhoods), in which case a square of size  $3 \times 3$  is necessary. For this case, Fig. 12.11 shows an example of component labeling, where the termination condition is met after six iterations.

To perform a complete connected component analysis, all components have to be labeled sequentially. The starting point  $\mathbf{p}$  can be an arbitrary object pixel that is not yet assigned to any component. Then, a unique label is assigned to the component found.

However, there are more efficient algorithms for component analysis, which do not rely on morphological operations [6,8,15].

### ➤ 12.1.7 The hit-or-miss operator

The hit-or-miss operator allows the detection of image pixels having certain relations to adjacent pixels [1,6]. It uses two disjoint structuring elements simultaneously.

#### 12.6 Definition 12.6: The hit-or-miss operator

A composite structuring element  $\mathcal{S}$  consists of two disjoint structuring elements  $\mathcal{V}, \mathcal{W}$ :

$$\mathcal{S} = (\mathcal{V}, \mathcal{W}) \quad \text{with} \quad \mathcal{V} \cap \mathcal{W} = \emptyset. \quad (12.133)$$

The hit-or-miss operator with the composite structuring element  $\mathcal{S} = (\mathcal{V}, \mathcal{W})$  is defined as follows:

$$\mathcal{G} \circledast \mathcal{S} := (\mathcal{G} \ominus \mathcal{V}) \cap (\overline{\mathcal{G}} \ominus \mathcal{W}). \quad (12.134)$$

◇

#### 12.5 Theorem 12.5: The hit-or-miss operator

The hit-or-miss operator can be calculated using one of the following formulas:

$$\mathcal{G} \circledast \mathcal{S} = (\mathcal{G} \ominus \mathcal{V}) \setminus (\mathcal{G} \oplus \mathcal{W}^R) \quad (12.135)$$

$$= \{ \mathbf{z} \mid (\mathcal{V})_{\mathbf{z}} \subseteq \mathcal{G} \wedge (\mathcal{W})_{\mathbf{z}} \subseteq \overline{\mathcal{G}} \}. \quad (12.136)$$

◇

**Proof 12.5 (The hit-or-miss operator):** The duality theorem 12.3 yields

$$\mathcal{G} \circledast \mathcal{S} = (\mathcal{G} \ominus \mathcal{V}) \cap (\overline{\mathcal{G}} \ominus \mathcal{W}) \quad (12.137)$$

$$= (\mathcal{G} \ominus \mathcal{V}) \cap \overline{(\mathcal{G} \oplus \mathcal{W}^R)} \quad (12.138)$$

$$= (\mathcal{G} \ominus \mathcal{V}) \setminus (\mathcal{G} \oplus \mathcal{W}^R). \quad (12.139)$$

The definition of erosion immediately results in the second representation:

$$\mathcal{G} \circledast \mathcal{S} = (\mathcal{G} \ominus \mathcal{V}) \cap (\overline{\mathcal{G}} \ominus \mathcal{W}) \quad (12.140)$$

$$= \{ \mathbf{z} \mid (\mathcal{V})_{\mathbf{z}} \subseteq \mathcal{G} \} \cap \{ \mathbf{z} \mid (\mathcal{W})_{\mathbf{z}} \subseteq \overline{\mathcal{G}} \} \quad (12.141)$$

$$= \{ \mathbf{z} \mid (\mathcal{V})_{\mathbf{z}} \subseteq \mathcal{G} \wedge (\mathcal{W})_{\mathbf{z}} \subseteq \overline{\mathcal{G}} \}. \quad (12.142)$$

■

An image point is detected by the operator if the first structuring element  $\mathcal{V}$  fits in the present object and the second structuring element  $\mathcal{W}$  misses the object. By this means, pixels having

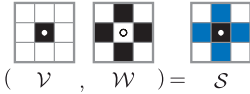


Figure 12.12. Structuring element used to detect isolated points with respect to 4-connected neighborhoods. In order to achieve a compact graphical representation of the pixels of  $S$ , the pixels of  $\mathcal{V}$  are colored black and the pixels of  $\mathcal{W}$  are colored blue.

a specified arrangement of neighbors can be extracted. Possible applications for the hit-and-miss operator are:

- the detection of isolated pixels for which no object pixel belongs to the neighboring pixels (Fig. 12.12),
- the extraction of the endpoints of lines—in this case, at most one object pixel belongs to the neighboring pixels,
- the detection of multiple points and crossings of two or more lines, of which more than two object pixels belong to the neighboring pixels, as well as
- finding contour points for which at least one background pixel has to belong to the neighboring pixels.

Further applications for the hit-or-miss operator will be covered in the following sections.

⊙ 12.1.7.1 Thinning

Thinning the point set  $\mathcal{G}$  using a composite structuring element  $S = (\mathcal{V}, \mathcal{W})$  is defined as follows:

$$\mathcal{G} \circ S := \mathcal{G} \setminus (\mathcal{G} \circledast S) \tag{12.143}$$

Hence, the result of the hit-or-miss operation  $(\mathcal{G} \circledast S)$  is removed from the original point set  $\mathcal{G}$  [5,6].

An algorithm for thinning the point set  $\mathcal{G}$  to a contour of the width of a single pixel with respect to the 8-connected neighborhood performs the following steps: successively, the point set is thinned by  $N$  structuring elements. For thinning with respect to the 8-connected neighborhood,  $N = 8$  structuring elements  $\Sigma = (S_1, \dots, S_8)$  are chosen as follows (Fig. 12.13):

- Thinning of axis-parallel lines: a border point can be removed from the point set  $\mathcal{G}$  if three horizontally adjacent points of  $\mathcal{G}$  are located directly below that point ( $\mathcal{V}_1$ ). In this case ( $\mathcal{W}_1$ ) the border point property is met if the three adjacent points directly above the considered point are not part of the point set  $\mathcal{G}$ . Whether the left or right neighbors are part of  $\mathcal{G}$  or not is irrelevant. These considerations result in the composite structuring element  $S_1 = (\mathcal{V}_1, \mathcal{W}_1)$ . Similarly, successive rotations by  $90^\circ$  yield the structuring elements for detecting border points of horizontal or vertical lines:  $S_3, S_5, S_7$ .
- Thinning at corner points: a point is a corner point of an upper left corner of  $\mathcal{G}$  if the three directly neighboring points on the left, top, and top left of the considered point are not part of  $\mathcal{G}$ . It can be removed during the thinning if the neighboring points on the right, bottom, and bottom right are part of  $\mathcal{G}$ . This results in the composite structuring element  $S_2 = (\mathcal{V}_2, \mathcal{W}_2)$  for thinning with respect to the 8-connected neighborhood. If instead the 4-connected neighborhood is considered, the bottom right pixel of  $\mathcal{W}_2$  can be removed. For the other corner points, the structuring element is successively rotated by  $90^\circ$ :  $S_4, S_6$  and  $S_8$ .

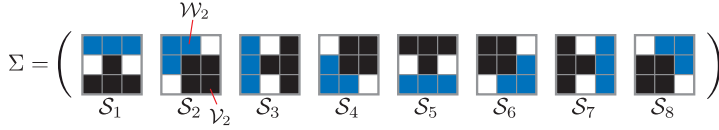


Figure 12.13. A tuple  $\Sigma$  of  $N = 8$  structuring elements  $S_i = (V_i, W_i)$  for thinning. The sets  $V_i$  are shown in black and the sets  $W_i$  are shown in blue.

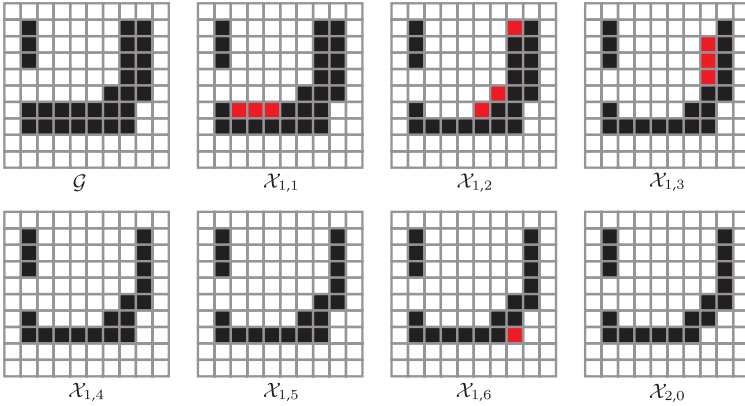


Figure 12.14. Thinning a point set  $\mathcal{G}$  with the structuring elements of Fig. 12.13.

As the discrete pixel grid allows no further possible orientations of directly adjacent pixels of the border contour of a point set, the structuring elements of  $\Sigma$  cover all relevant cases. The algorithm for thinning the point set  $\mathcal{G}$  iteratively applies the structuring elements  $S_1, \dots, S_N \in \Sigma$ . Afterwards, the thinning is applied to the result, again starting with  $S_1$ , and so on:

$$\mathcal{X}_{1,0} := \mathcal{G}, \tag{12.144}$$

$$\mathcal{X}_{k,i} := \mathcal{X}_{k,i-1} \circ S_i = \mathcal{X}_{k,i-1} \setminus (\mathcal{X}_{k,i-1} \circledast S_i), \quad i = 1, \dots, N, \quad k = 1, 2, 3, \dots \tag{12.145}$$

$$\mathcal{X}_{k+1,0} := \mathcal{X}_{k,N}, \quad k = 1, 2, 3, \dots \tag{12.146}$$

A single application of the operation with every structuring element of  $\Sigma$  can also be expressed as

$$\mathcal{G} \circ \Sigma := \mathcal{X}_{2,0} = (\dots((\mathcal{G} \circ S_1) \circ S_2) \dots) \circ S_N. \tag{12.147}$$

The iteration ends as soon as  $\mathcal{X}_{k+1,0} = \mathcal{X}_{k,0}$ . Then,  $\mathcal{X}_{k,0}$  represents the result of the thinning of  $\mathcal{G}$ . If the point set is to be shrunk by a fixed width, the algorithm can also be terminated after the corresponding number of iterations.

As the morphological operators are nonlinear, the order of the structuring elements  $S_i$  in  $\Sigma$  is important. So  $\Sigma$  is an  $N$ -tuple of structuring elements and not a set, whose elements are unordered.

Figure 12.14 shows the intermediate steps of the algorithm applied to an example. The point sets  $\mathcal{X}_{k,i}$  are black; the points  $\mathcal{X}_{k,i-1} \circledast S_i$  that are removed in the corresponding step

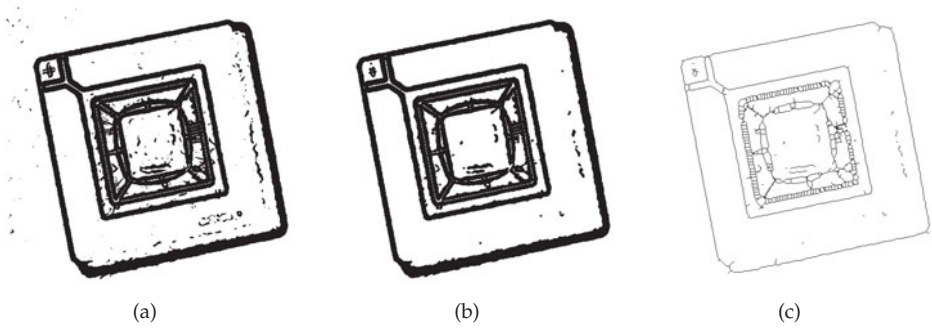


**Figure 12.15.** Binary morphological processing of an edge image: (a) Edge image of Fig. 11.14(f), transformed into a binary image using the gray value histogram shown in Sec. 11.1; (b) Opening in order to mitigate noise; (c) Thinning.

are colored red. The set  $\mathcal{X}_{2,0}$  is the final result of the thinning with respect to the 4-connected neighborhood.

**Example 12.1 (Edge thinning):** A typical application for thinning are edge images. The edge image is obtained by applying an edge operator to a gray-scale image  $g(x)$ . Subsequently, it is transformed into a binary image using a threshold-based segmentation method (Fig. 12.15(a)). Now the morphological thinning is applied to the binary image (Fig. 12.15(c)). The resulting image contains edges having a width of one pixel, representing a sharp border between the image regions.

As the thinning is applied after the transformation into the binary image, it cannot consider the absolute value of the gradient. An alternative method is based on the search for local maxima of the gradient in the edge image and thus yields more precise edge positions. This approach is used by the Canny operator, a commonly used edge detector that usually calculates the gradient using the differentiated Gaussian low-pass filter [3].

⊙ **12.1.7.2 Thickening**

The thickening of a point set  $\mathcal{G}$  is defined as follows:

$$\mathcal{G} \odot S := \mathcal{G} \cup (\mathcal{G} \otimes S). \tag{12.148}$$

Thickening widens the point set  $\mathcal{G}$  by appending points to its border. Similar to thinning, the algorithm performs iterative thickening steps using structuring elements of a tuple  $\Sigma$ . The composite structuring elements for a thickening of one pixel can be obtained by swapping the roles of  $\mathcal{V}$  and  $\mathcal{W}$  of the structuring elements of Fig. 12.13:  $\Sigma = ((\mathcal{W}_1, \mathcal{V}_1) \dots, (\mathcal{W}_8, \mathcal{V}_8))$ .

The iteration of the thickening algorithm ends as soon as the separating lines between the objects have a width of only one pixel.

The thickening operation is dual to the thinning operation: thickening of the object with  $(\mathcal{W}, \mathcal{V})$  is equivalent to thinning the background with  $(\mathcal{V}, \mathcal{W})$ :

$$\mathcal{G} \odot (\mathcal{W}, \mathcal{V}) = \mathcal{G} \cup (\mathcal{G} \otimes (\mathcal{W}, \mathcal{V})) = \mathcal{G} \cup ((\mathcal{G} \ominus \mathcal{W}) \cap (\overline{\mathcal{G}} \ominus \mathcal{V})) \tag{12.149}$$

$$= \overline{\overline{\mathcal{G}} \cap ((\mathcal{G} \ominus \mathcal{W}) \cap (\overline{\mathcal{G}} \ominus \mathcal{V}))} = \overline{\overline{\mathcal{G}} \cap (\overline{\mathcal{G}} \otimes (\mathcal{V}, \mathcal{W}))} \tag{12.150}$$

$$= \overline{\mathcal{G} \setminus (\overline{\mathcal{G}} \otimes (\mathcal{V}, \mathcal{W}))} = \overline{\mathcal{G}} \oslash (\mathcal{V}, \mathcal{W}). \tag{12.151}$$

➤ **12.1.8 Skeletonization**

The skeleton of a point set is a contour starting from the margin of the set and running along the medial axis of the point set (Fig. 12.16). It characterizes the topology of the set independently of its width.

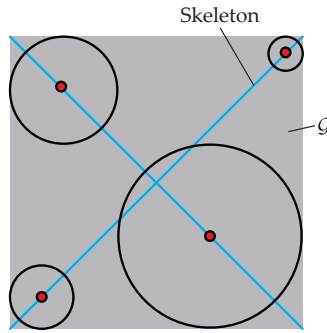


Figure 12.16. The definition of the skeleton.

12.7

**Definition 12.7: Skeleton**

The skeleton of a continuous two-dimensional point set  $\mathcal{G} \subseteq \mathbb{R}^2$  is defined as the set of the center points of all circles that are entirely contained in  $\mathcal{G}$  and touch the border of  $\mathcal{G}$  at at least two points. ◇

Using binary morphological operations, the skeleton of a discrete two-dimensional point set  $\mathcal{G} \subseteq \mathbb{Z}^2$  can be calculated as follows [6]:

$$\text{Skel}(\mathcal{G}) := \bigcup_{k=0}^K \text{Skel}_k(\mathcal{G}), \tag{12.152}$$

$$\text{Skel}_k(\mathcal{G}) := (\mathcal{G} \ominus_k \mathcal{S}) \setminus ((\mathcal{G} \ominus_k \mathcal{S}) \circ \mathcal{S}). \tag{12.153}$$

Here,  $\mathcal{G} \ominus_k \mathcal{S}$  denotes  $k$  iterative erosions of  $\mathcal{G}$  with  $\mathcal{S}$ :

$$\mathcal{G} \ominus_0 \mathcal{S} := \mathcal{G}, \tag{12.154}$$

$$\mathcal{G} \ominus_k \mathcal{S} := (\mathcal{G} \ominus_{k-1} \mathcal{S}) \ominus \mathcal{S}, \quad k = 1, 2, 3, \dots \tag{12.155}$$

In the following, this notation will also be used for multiple applications of other morphological operations.

The set  $\text{Skel}_k(\mathcal{G})$  is called the  $k$ th partial skeleton of  $\mathcal{G}$ . It consists of the points of  $\mathcal{G}$  that have a distance of  $k$  from at least two border points of  $\mathcal{G}$ . The union of all partial skeletons is the sought for approximation of the skeleton of  $\mathcal{G}$ . The iterative calculation of the partial skeletons ends as soon as the erosion results in the empty set and no more partial skeletons can be found:

$$K = \max\{k \mid (\mathcal{G} \ominus_k \mathcal{S}) \neq \emptyset\}. \tag{12.156}$$

The original point set  $\mathcal{G}$  can be exactly reconstructed from the partial skeletons by applying  $k$  dilations to the partial skeletons and calculating the union of the results:

$$\mathcal{G} = \bigcup_{k=0}^K (\text{Skel}_k(\mathcal{G}) \oplus_k \mathcal{S}). \tag{12.157}$$

Figure 12.17 shows an example of the skeletonization and reconstruction with  $K = 2$ . A square of size  $3 \times 3$  is chosen as the structuring element [5]. The result of the method applied to the test image is shown in Fig. 12.18. The slight asymmetry of the original point set clearly affects some regions of the skeleton.

The approximation of the skeleton resulting from the presented approach consists of the points which approximately meet Def. 12.7. In contrast to the thinned point set, the skeleton is not connected in general and is wider than the minimum possible width of a single pixel.

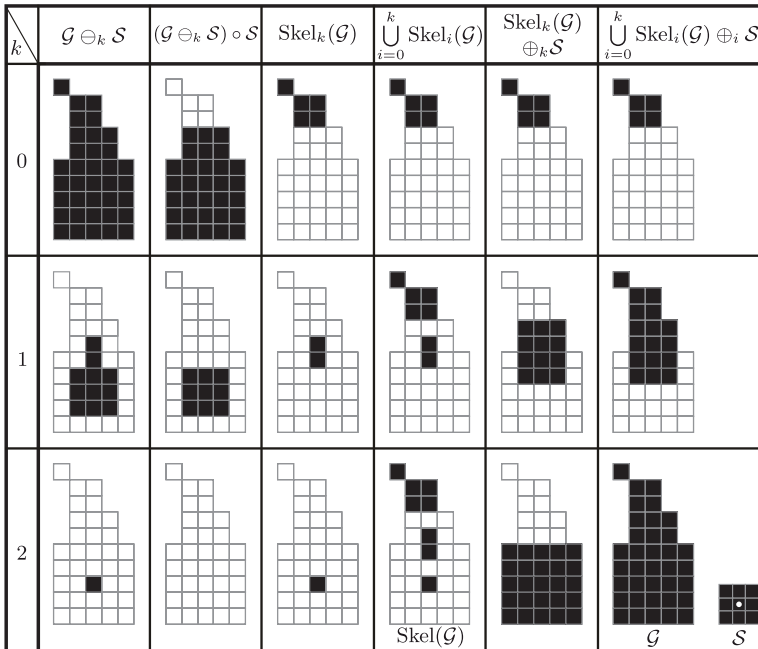


Figure 12.17. Binary morphological skeletonization (adapted from [5]).



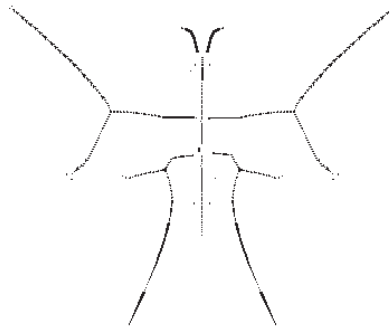


Figure 12.18. Approximated skeleton of the point set of Fig. 12.1 using binary morphology.

➤ 12.1.9 Pruning

Besides the contour of interest, the skeleton of a point set often contains short contour segments reaching from the center axis of the object to its border. These so-called barbs particularly appear at phantom corners of the point set, caused by the bending of its border. Since for the further image processing, usually only the topology of the point set is needed, these barbs represent unwanted noise and should be removed. This processing step is called **pruning**.

Pruning a connected point set can be performed using an algorithm based on binary morphological operations. Let  $K$  denote the maximum length of the barbs which are to be pruned. Depending on the application at hand, the number of partial skeletons (12.156) can be an adequate choice for  $K$ . The following removal of line-ending points is applied  $K$  times to the point set  $\mathcal{G}$ , e.g., the connected skeleton:

$$\mathcal{Y}_0 := \mathcal{G}, \tag{12.158}$$

$$\mathcal{Y}_k := \mathcal{Y}_{k-1} \setminus \left( \bigcup_{i=1}^8 \mathcal{Y}_{k-1} \otimes \mathcal{S}_i \right), \quad k = 1, \dots, K, \tag{12.159}$$

$$\mathcal{X}_1 := \mathcal{Y}_K. \tag{12.160}$$

The tuple  $\Sigma = (\mathcal{S}_1, \dots, \mathcal{S}_8)$  contains eight structuring elements detecting line-endings. Each structuring element corresponds to one of the possible orientations of a line-ending (Fig. 12.19). In the result  $\mathcal{X}_1$ , all lines are shortened by  $K$  points. The barbs are completely removed, as they were assumed to be shorter than  $K$ . However, as any other line is shortened as well, an adequate reconstruction has to be performed.

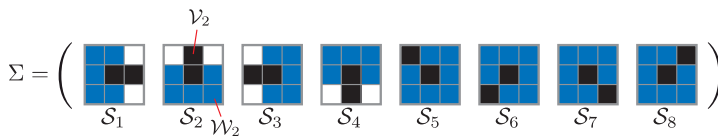


Figure 12.19. Composite structuring elements for detecting line-endings.

For this purpose, all line-ending points of the set  $\mathcal{X}_1$  are detected in the second step of the algorithm:

$$\mathcal{X}_2 := \bigcup_{i=1}^8 (\mathcal{X}_1 \otimes \mathcal{S}_i). \tag{12.161}$$

As the barbs have already been completely removed, the point set  $\mathcal{X}_2$  consists exclusively of the end points of all lines which are to be preserved. In the third step of the pruning,  $K$  dilations are applied to the set of the end points:

$$\mathcal{Z}_0 := \mathcal{X}_2. \tag{12.162}$$

$$\mathcal{Z}_k := (\mathcal{Z}_{k-1} \oplus \mathcal{T}) \cap \mathcal{G}, \quad k = 1, \dots, K, \tag{12.163}$$

A  $3 \times 3$  square is used as the structuring element  $\mathcal{T}$ . By calculating the intersection with the original point set  $\mathcal{G}$ , the dilated point set is restricted to all tails of lines of  $\mathcal{G}$  whose end points were contained in  $\mathcal{X}_2$ .

Finally, the result of the pruning is given by the union of the point set with the shortened lines of step one and the line-endings obtained:

$$\mathcal{X} := \mathcal{X}_1 \cup \mathcal{Z}_K. \tag{12.164}$$

As an example, the method is applied to the binary image of a handwritten character  $a$  (see Fig. 12.20). At the left border of the contour, a barb of length  $K = 3$  is successfully removed.

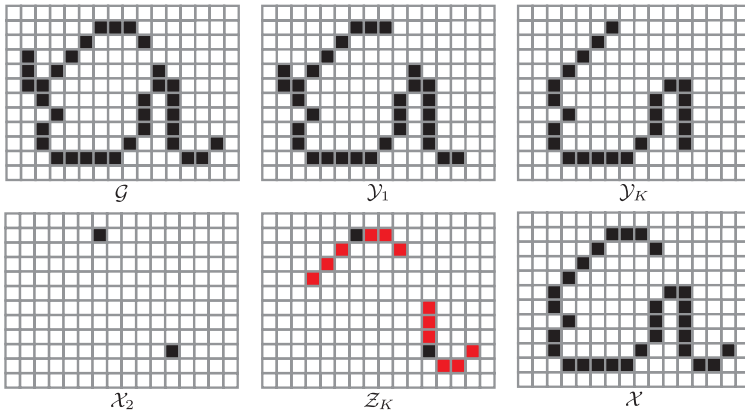


Figure 12.20. Pruning (adapted from [5]).

A drawback of this method is the necessity of knowing the length  $K$  of the barbs that have to be removed, before the algorithm can be applied. If it is chosen too low, longer barbs will be completely preserved. If it is chosen too high, shorter line-endings might get removed. Isolated contour segments shorter than  $2K$  pixels might get completely removed by this approach. On the other hand, barbs near the end points of longer contours might be preserved, as they get reconstructed during the dilation starting from the line-endings.

**Example 12.2 (Optical character recognition):** The section covering binary morphology is concluded by this example showing the interaction of different morphological operations in a complex application: a morphological preprocessing is applied to a scanned text passage with the aim of a subsequent character recognition. First, the gray-scale image shown in Fig. 12.21(a) is binarized using the classification method of Sec. 11.1, see Fig. 12.21(b). The result contains isolated distortions and holes, which can be alleviated by using binary morphological opening and closing. The result of this post-processing is shown in gray in the following images. The skeleton of this intermediate result, approximated using binary morphology, is shown in Fig. 12.21(c). Gaps in the skeleton are closed using a dilation. Subsequently, the point set is thinned, resulting in a contour of a width of one pixel, which is connected with respect to the 4-connected neighborhood, see Fig. 12.21(d). Finally, a pruning is applied, see Fig. 12.21(e).

The variability of the contours is notably reduced in the resulting image, e.g., the differences between normal and boldfaced characters or the differences between the two 'o' characters caused by noise, see Fig. 12.21. These results are beneficial for the further classification of the letters using, e.g., the Fourier descriptors of their contours [2, 14]. ■

As shown in the previous sections, the elementary binary morphological operators can be used to easily construct image processing methods for special applications. The presented methods should be considered as examples showing how to design target-oriented, complex morphological operators. Further specialized morphological methods can be found, e.g., in [5, 18].

## 12.2 Gray-scale morphology

### 12.2.1 The point set of a gray-scale image

The point set of a binary image consists of all pixels having the value 1. Now an adequate definition for the point set corresponding to an image with pixels having more than two values has to be found. A general one-channel image, e.g., a gray-scale image, can be considered to be a scalar function  $g : \Omega_g \rightarrow \mathbb{R}$  corresponding to a surface in the three-dimensional space  $\mathbb{R}^3$ . The image value is the third dimension besides the two spatial dimensions  $x$  and  $y$ . The point set  $\mathcal{U}$  of a scalar image is a subset of this three-dimensional space: the set of all points below the surface  $z = g(x, y)$ :

$$\mathcal{U} = \{(x, y, z)^T \in \mathbb{R}^3 \mid z \leq g(x, y)\}. \quad (12.165)$$

This point set is called the umbra of the image. The image can be reconstructed from the umbra by determining the 'surface' of the point set, i.e., by finding the element of  $\mathcal{U}$  with maximum  $z$ -value for each pixel  $(x, y)^T$ .

The umbra operation can be defined for an arbitrary  $N$ -dimensional space  $R^N$ ,  $N \geq 2$ , for functions  $R^{N-1} \rightarrow R$  [7, 11]. In the following, discrete and quantized one-channel images will be considered, so that  $R = \mathbb{Z}$  and  $N = 3$ . As often gray-scale images are considered, the term gray-scale morphology is used, in accordance with the literature. In fact, also the application of morphological operations to distance images, e.g., to surface reliefs, is particularly descriptive. Furthermore, morphological operations can be separately applied to

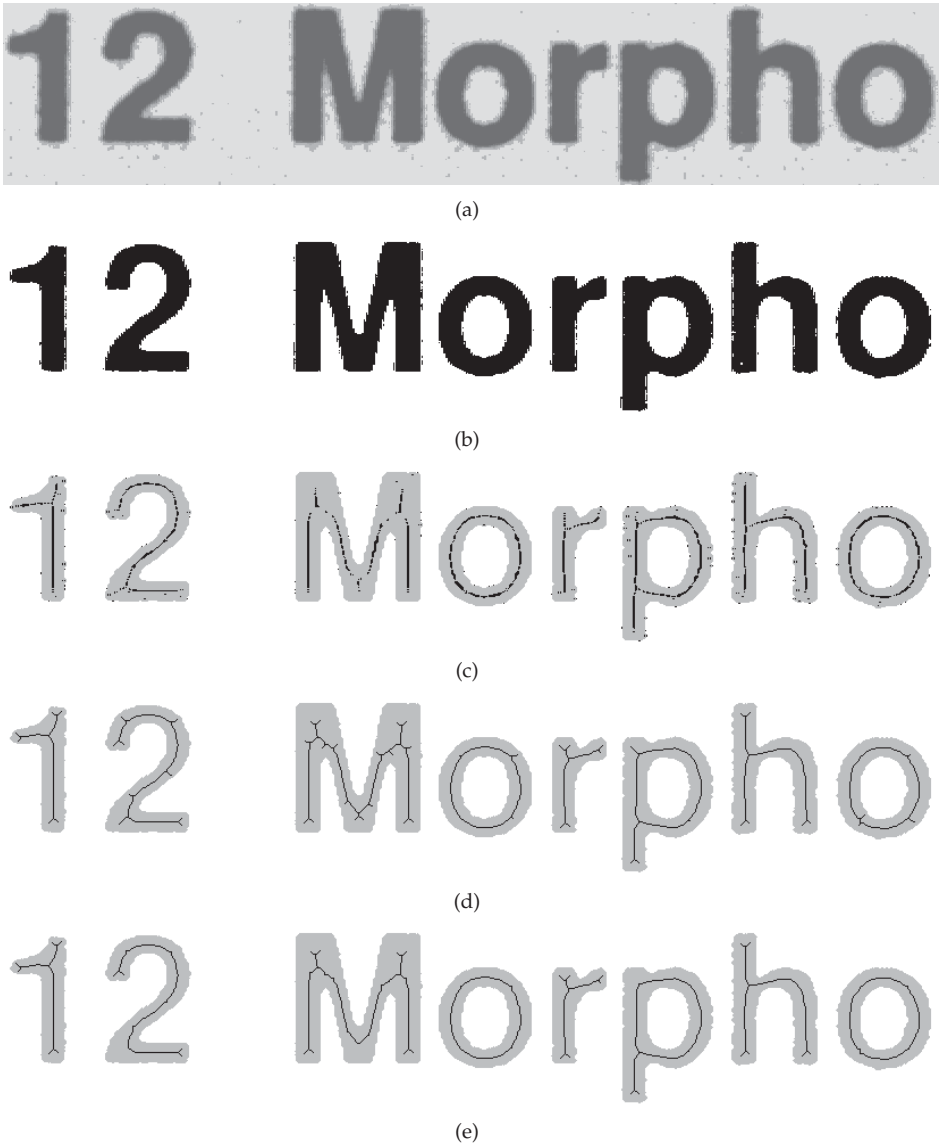


**Figure 12.21.** Morphological processing of scanned text: (a) Scanned text of the table of contents of this book; (b) Binary image; (c) Skeleton  $Skel(G)$ ; (d) Post-processed skeleton; (e) Result of the pruning.

the single channels of a color image. Vector morphology is an alternative approach to using morphological methods on color images, where the operations  $\min$  and  $\max$  are defined using distance metrics or order relations suitable for vectors of image values [9, 10].

## 12.8

**Definition 12.8: Umbra**

A set  $\mathcal{U} \subseteq \mathbb{Z}^N$  is called an umbra if and only if

$$(\mathbf{x}^T, g)^T \in \mathcal{U} \quad \Rightarrow \quad \forall z \leq g : (\mathbf{x}^T, z)^T \in \mathcal{U}, \quad (12.166)$$

with  $\mathbf{x} = (x, y)^T \in \mathbb{Z}^{N-1}$  and  $g, z \in \mathbb{Z}$ . The umbra of a function  $g : \Omega_g \rightarrow \mathbb{Z}$ ,  $\Omega_g \subseteq \mathbb{Z}^{N-1}$ , is given by

$$\mathcal{U}\{g\} := \{(\mathbf{x}^T, z)^T \in \Omega_g \times \mathbb{Z} \mid z \leq g(\mathbf{x})\}. \quad (12.167)$$

The top or top surface of an umbra  $\mathcal{U} \subseteq \mathbb{Z}^N$  is a function

$$\mathcal{T}\{\mathcal{U}\} : \begin{cases} \Omega_g \rightarrow \mathbb{Z} \\ \mathbf{x} \mapsto \max\{g \mid (\mathbf{x}^T, g)^T \in \mathcal{U}\} \end{cases} \quad (12.168)$$

with

$$\Omega_g := \{\mathbf{x} \in \mathbb{Z}^{N-1} \mid \exists g \in \mathbb{Z} : (\mathbf{x}^T, g)^T \in \mathcal{U}\}. \quad (12.169)$$

◇

Consequently,  $\mathcal{U}\{\cdot\}$  is an operator producing a point set, represented by an umbra, from the image  $g(\mathbf{x})$ , and  $\mathcal{T}\{\cdot\}$  is an operator that transforms such a special point set back into an image signal  $g(\mathbf{x})$ . These two operators are inverse to each other:

## 12.6

**Theorem 12.6: Umbra operator**

For an arbitrary  $g(\mathbf{x}) : \Omega_g \rightarrow \mathbb{Z}$ ,  $\Omega_g \subseteq \mathbb{Z}^{N-1}$ ,

$$\mathcal{T}\{\mathcal{U}\{g(\mathbf{x})\}\} = g(\mathbf{x}). \quad (12.170)$$

For every umbra  $\mathcal{U}$ ,

$$\mathcal{U}\{\mathcal{T}\{\mathcal{U}\}\} = \mathcal{U}. \quad (12.171)$$

For a proof, see [7].

◇

A particularly illustrative interpretation of the umbra can be obtained by considering  $z = g(x, y)$  as a surface relief instead of as an intensity image. In this case, the umbra corresponds to a three-dimensional object, whose surface is given by  $g(x, y)$  and which is infinitely large in the negative direction of the  $z$ -axis. Conversely, the surface operator  $\mathcal{T}\{\cdot\}$  yields a function describing the surface relief in positive  $z$ -direction. Morphological operations can be imagined to perform a sampling by mechanically touching the surface relief with a probe head, whose shape is determined by the structuring element (cf. Fig. 12.22). In gray-scale morphology, structuring elements are also represented by functions  $s(\mathbf{x})$ , whose umbras can be calculated.

### ➤ 12.2.2 Erosion and dilation

With the operators umbra  $\mathcal{U}\{\cdot\}$  and surface  $\mathcal{T}\{\cdot\}$ , basic morphological operations can be modified to be applicable to functions: first, the umbras of the functions  $g(\mathbf{x})$  and  $s(\mathbf{x})$  are calculated, then, the known morphological operations are applied to this point set, and fi-

nally the resulting umbra is transformed back into an image [7]. As the binary morphological operators are independent of the dimension of the point set, they can be applied directly to the umbra.

---

**Definition 12.9: Erosion and dilation in gray-scale morphology**

For  $\Omega_g, \Omega_s \subseteq \mathbb{Z}^{N-1}$  and functions  $g : \Omega_g \rightarrow \mathbb{Z}$ ,  $s : \Omega_s \rightarrow \mathbb{Z}$ , erosion  $g \ominus s$  and dilation  $g \oplus s$  are defined by the following scalar functions:

$$g \ominus s := \mathcal{T} \{ \mathcal{U}\{g\} \ominus \mathcal{U}\{s\} \}, \quad (12.172)$$

$$g \oplus s := \mathcal{T} \{ \mathcal{U}\{g\} \oplus \mathcal{U}\{s\} \}. \quad (12.173)$$

Erosion and dilation on umbras is performed according to the corresponding definitions from Sec. 12.1 of these operations for point sets.  $\diamond$

Handling the three-dimensional point sets of gray-scale images comes with considerable computational costs and space requirements. Fortunately, a detailed analysis shows that there are simple signal-oriented operations that are equivalent to the set-based operations [7]. With regard to the signals  $g(\mathbf{x})$  and  $s(\mathbf{x})$ , erosion and dilation can be performed as follows:

---

**Theorem 12.7: Erosion and dilation in gray-scale morphology**

The erosion and dilation of functions according to Def. 12.9 can be calculated as follows:

$$(g \ominus s)(\mathbf{x}) = \min_{\xi \in \Omega_s} \{ g(\mathbf{x} + \xi) - s(\xi) \}, \quad (12.174)$$

$$(g \oplus s)(\mathbf{x}) = \max_{\substack{\xi \in \Omega_s \\ \mathbf{x} - \xi \in \Omega_g}} \{ g(\mathbf{x} - \xi) + s(\xi) \}, \quad (12.175)$$

with  $\Omega_s$  denoting the support of  $s(x)$ .  $\diamond$

---

**Proof 12.6 (Erosion and dilation in gray-scale morphology):**

$$\begin{aligned} (g \ominus s)(\mathbf{x}) &= \mathcal{T} \{ \mathcal{U}\{g\} \ominus \mathcal{U}\{s\} \}(\mathbf{x}) & (12.176) \\ &= \max \{ z \mid (\mathbf{x}^T, z)^T \in (\mathcal{U}\{g\} \ominus \mathcal{U}\{s\}) \} \\ &= \max \{ z \mid (\mathbf{x}^T, z)^T \in \{ (\mathbf{v}^T, w)^T \in \mathbb{Z}^N \mid (\mathcal{U}\{s\})_{(\mathbf{v}^T, w)^T} \subseteq \mathcal{U}\{g\} \} \} \\ &= \max \{ z \mid (\mathbf{x}^T, z)^T \in \\ &\quad \{ (\mathbf{v}^T, w)^T \in \mathbb{Z}^N \mid \forall (\xi, \zeta) \in \mathcal{U}\{s\} : (\xi^T, \zeta)^T + (\mathbf{v}^T, w)^T \in \mathcal{U}\{g\} \} \} \\ &= \max \{ z \mid \forall (\xi, \zeta) \in \mathcal{U}\{s\} : (\xi^T, \zeta)^T + (\mathbf{x}^T, z)^T \in \mathcal{U}\{g\} \} \\ &= \max \{ z \mid \forall \xi \in \Omega_s \forall \zeta \leq s(\xi) : \zeta + z \leq g(\xi + \mathbf{x}) \} \\ &= \max \{ z \mid \forall \xi \in \Omega_s : s(\xi) + z \leq g(\xi + \mathbf{x}) \} \\ &= \max \{ z \mid z \leq \min_{\xi \in \Omega_s} \{ g(\xi + \mathbf{x}) - s(\xi) \} \} \\ &= \min_{\xi \in \Omega_s} \{ g(\xi + \mathbf{x}) - s(\xi) \}. & (12.177) \end{aligned}$$

The proof concerning dilation is similar [7].  $\blacksquare$

With these formulas, the morphological operations can be performed without explicitly calculating the umbras. The computational complexity corresponds to a convolution in the spatial domain with an impulse response function having the domain  $\Omega_s$ . However, as the multiplication is replaced by the calculation of an extremum, the morphological operations are nonlinear.

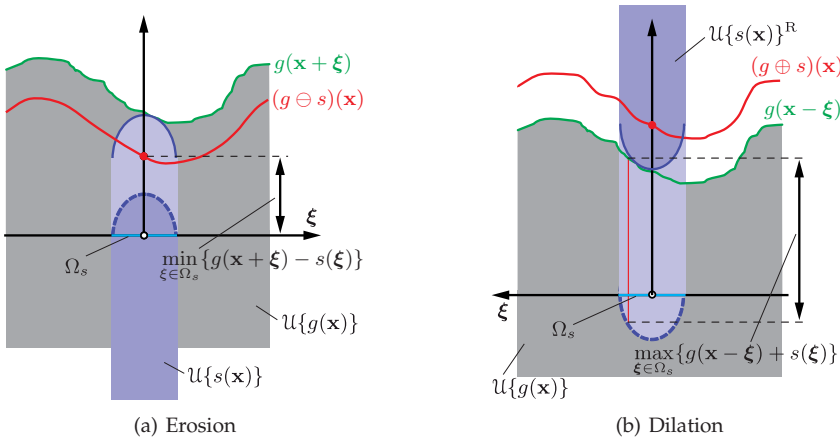


Figure 12.22. Calculation of the basic operations of gray-scale morphology. Shown is a section through the  $x, z$ -plane of the three-dimensional umbras.

The formulas can be visualized by using the comparison to sampling by mechanical touching (Fig. 12.22). The structuring element corresponds to a probe head shaped as  $s(x)$ . The calculation of the minimum needed for the erosion can be described as a sampling of the surface from below, i.e., from the inside of the umbra. At every point  $x$  of the  $x, y$ -plane, the probe head is moved as near to the surface  $z = g(x)$  as possible. Then the origin of the structuring element is part of the surface of the eroded image. The umbra of the image  $\mathcal{U}\{g\}$  is horizontally shifted in two dimensions, the umbra of the structuring element  $\mathcal{U}\{s\}$  is vertically shifted in one dimension. The result of the erosion is given by all those shift constellations where the structuring element touches the signal  $g$  from below.

Because of the calculation of the maximum, the dilation corresponds to a sampling by mechanical touching from above. By definition,

$$g \oplus s = \mathcal{T} \left\{ \left\{ \mathbf{w} \mid ((\mathcal{U}\{s\})^R)_{\mathbf{w}} \cap \mathcal{U}\{g\} \neq \emptyset \right\} \right\}. \tag{12.178}$$

In particular, the structuring element is reflected in the case of the dilation, cf. Def. 12.4. Hence, at every point  $x$ , the turned umbra is moved from above towards the umbra so that it just remains overlapping it. Then, the dilated surface runs through the origin of the structuring element in the  $z$ -position, where it just touches the umbra (Fig. 12.22(b)).

As the umbra operation is a homomorphism, further properties of the gray-scale morphology can be directly obtained from the binary morphology.

**Theorem 12.8: Umbra homomorphism theorem**

1. Let  $\mathcal{U}$  and  $\mathcal{V}$  denote two umbras. Then, the erosion  $\mathcal{U} \ominus \mathcal{V}$  and the dilation  $\mathcal{U} \oplus \mathcal{V}$  also represent umbras.
2. The calculation of the umbra is a homomorphism with respect to the operations erosion and dilation:

$$\mathcal{U}\{g \ominus s\} = \mathcal{U}\{g\} \ominus \mathcal{U}\{s\}, \quad (12.179)$$

$$\mathcal{U}\{g \oplus s\} = \mathcal{U}\{g\} \oplus \mathcal{U}\{s\}. \quad (12.180)$$

3. The relation  $g_1 \leq g_2$  of functions  $g_1, g_2 : \Omega_g \rightarrow \mathbb{Z}$  is equal to the inclusion relation of their umbras:

$$\mathcal{U}\{g_1\} \subseteq \mathcal{U}\{g_2\} \Leftrightarrow \forall \mathbf{x} \in \Omega_g : g_1(\mathbf{x}) \leq g_2(\mathbf{x}). \quad (12.181)$$

◇

**Proof 12.7 (Umbra homomorphism theorem):**

1. See [7].
2. With 1, Theorem 12.6 implies

$$\mathcal{U}\{g \ominus s\} = \mathcal{U}\{\mathcal{T}\{\mathcal{U}\{g\} \ominus \mathcal{U}\{s\}\}\} \quad (12.182)$$

$$= \mathcal{U}\{g\} \ominus \mathcal{U}\{s\} \quad (12.183)$$

and similarly for dilation.

3. First, assume  $\mathcal{U}\{g_1\} \subseteq \mathcal{U}\{g_2\}$ . For an arbitrary  $\mathbf{x} \in \Omega_g$ , we have  $(\mathbf{x}^T, g_1(\mathbf{x}))^T \in \mathcal{U}\{g_1\}$ , and hence also  $(\mathbf{x}^T, g_1(\mathbf{x}))^T \in \mathcal{U}\{g_2\}$ . Then, by the definition of the umbra,  $g_1(\mathbf{x}) \leq g_2(\mathbf{x})$ . Now assume  $g_1(\mathbf{x}) \leq g_2(\mathbf{x})$  for all  $\mathbf{x}$ . For an arbitrary  $(\mathbf{x}^T, z)^T \in \mathcal{U}\{g_1\}$ , we have  $z \leq g_1(\mathbf{x}) \leq g_2(\mathbf{x})$ . This implies  $(\mathbf{x}^T, z)^T \in \mathcal{U}\{g_2\}$ , and hence,  $\mathcal{U}\{g_1\} \subseteq \mathcal{U}\{g_2\}$ . ■

As the gray-scale morphological operators in Def. 12.9 are directly related to the general definition of point sets, all the properties from Sec. 12.1 apply to the operators because of the homomorphism theorem.

**Example 12.3 (Associativity of the gray-scale morphological dilation):** The umbra homomorphism theorem implies that dilation of a gray-scale image  $g$  with the structuring elements  $s_1$  and  $s_2$  is associative:

$$g \oplus (s_1 \oplus s_2) = \mathcal{T}\{\mathcal{U}\{g\} \oplus \mathcal{U}\{s_1 \oplus s_2\}\} \quad (12.184)$$

$$= \mathcal{T}\{\mathcal{U}\{g\} \oplus (\mathcal{U}\{s_1\} \oplus \mathcal{U}\{s_2\})\} \quad (12.185)$$

$$= \mathcal{T}\{(\mathcal{U}\{g\} \oplus \mathcal{U}\{s_1\}) \oplus \mathcal{U}\{s_2\}\} \quad (12.186)$$

$$= \mathcal{T}\{\mathcal{U}\{g \oplus s_1\} \oplus \mathcal{U}\{s_2\}\} \quad (12.187)$$

$$= (g \oplus s_1) \oplus s_2. \quad (12.188)$$

For point sets, the associativity  $\mathcal{U}\{g\} \oplus (\mathcal{U}\{s_1\} \oplus \mathcal{U}\{s_2\}) = (\mathcal{U}\{g\} \oplus \mathcal{U}\{s_1\}) \oplus \mathcal{U}\{s_2\}$  holds by Theorem 12.2. ■



**Example 12.4 (Inclusion relation of the gray-scale morphological erosion):** Let  $(0, 0, 0)^T \in \mathcal{U}\{s\}$ , and thus  $s(\mathbf{0}) \geq 0$ . By Theorem 12.1,

$$\mathcal{U}\{g\} \ominus \mathcal{U}\{s\} \subseteq \mathcal{U}\{g\}. \quad (12.189)$$

Then, the homomorphism theorem implies

$$\mathcal{U}\{g \ominus s\} \subseteq \mathcal{U}\{g\} \quad \Leftrightarrow \quad \forall \mathbf{x} : (g \ominus s)(\mathbf{x}) \leq g(\mathbf{x}). \quad (12.190)$$

Although morphological operations for binary and gray-scale images are based on the same theoretical foundations, there are fundamental differences in their effects on the resulting image: whereas binary morphological operators only affect the margins of the objects in the image, gray-scale operators result in a change in nearly all image values in the image. For example, a dilation increases image values even in spatially homogeneous regions. These differences are caused by the meaning of the dimensions of the point sets: whereas the two-dimensional point set of a binary image only consists of spatial dimensions, the point set of a gray-scale image has the additional dimension of its image values. The morphological operators are identically defined on the point sets, however, their effects differ because of the different semantics of the dimensions.

Like all properties of the binary morphological operations, also the duality of erosion and dilation has a correspondence in gray-scale morphology [6,7]. The complement is replaced by the negation of the function  $g$ . However, the calculation of the negation is not equivalent to the calculation of the complement of the umbras, as can be seen in the example of the structuring element from Fig. 12.22.

12.9

### Theorem 12.9: Duality of erosion and dilation in gray-scale morphology

The following duality applies to the erosion and the dilation of a scalar image  $g$  with a structuring element  $s$ :

$$-(g \oplus s) = (-g) \ominus s^R, \quad (12.191)$$

with  $s^R(\mathbf{x}) := s(-\mathbf{x})$  denoting a function  $s^R : \Omega_s^R \rightarrow \mathbb{Z}$ . ◇

### Proof 12.8 (Duality of erosion and dilation in gray-scale morphology):

$$(-(g \oplus s))(\mathbf{x}) = - \max_{\substack{\xi \in \Omega_s \\ \mathbf{x} - \xi \in \Omega_g}} \{g(\mathbf{x} - \xi) + s(\xi)\} \quad (12.192)$$

$$= \min_{\substack{\xi \in \Omega_s \\ \mathbf{x} - \xi \in \Omega_g}} \{-g(\mathbf{x} - \xi) - s(\xi)\} \quad (12.193)$$

$$= \min_{\substack{\xi \in \Omega_s^R \\ \mathbf{x} + \xi \in \Omega_g}} \{-g(\mathbf{x} + \xi) - s^R(\xi)\} \quad (12.194)$$

$$= ((-g) \ominus s^R)(\mathbf{x}). \quad (12.195)$$

➤ 12.2.3 Opening and closing

As with binary images, opening and closing are defined as a composition of a dilation and an erosion with the same structuring element.

**Definition 12.10: Opening and closing in gray-scale morphology**

12.10

Let  $g : \Omega_g \rightarrow \mathbb{Z}$  denote a scalar image and  $s : \Omega_s \rightarrow \mathbb{Z}$  a structuring element. The opening  $g \circ s$  and the closing  $g \bullet s$  are defined as follows:

$$g \circ s := (g \ominus s) \oplus s, \tag{12.196}$$

$$g \bullet s := (g \oplus s) \ominus s. \tag{12.197}$$

◇

For the commonly used structuring elements, erosion and dilation are inverse to each other for spatially homogeneous regions of the image, so that opening and closing only have an effect on edges and other structures within the images.

Because of the umbra homomorphism theorem 12.8, Theorem 12.4 still applies to gray-scale morphological operations. This is why opening and closing have the following properties:

**Theorem 12.10: Properties of gray-scale morphological opening and closing**

12.10

$$g \circ s \leq g \leq g \bullet s \tag{12.198}$$

$$(g \circ s) \circ s = g \circ s \tag{12.199}$$

$$(g \bullet s) \bullet s = g \bullet s \tag{12.200}$$

$$g \circ s = \mathcal{J} \left\{ \bigcup_{z \in \{z \in \mathbb{Z}^N \mid (\mathcal{U}\{s\})_z \subseteq \mathcal{U}\{g\}\}} (\mathcal{U}\{s\})_z \right\} \tag{12.201}$$

$$-(g \circ s) = (-g) \bullet s^R \tag{12.202}$$

◇

**Proof 12.9 (Properties of gray-scale morphological opening and closing):** The first four relations are the result of Theorem 12.4 using Theorem 12.8. The last equation is obtained using Theorem 12.9 [7]. ■

By means of (12.201), the opening can be visualized as a sampling by mechanically touching: the structuring element  $\mathcal{U}\{s\}$  touches the surface from below, i.e., from the inside of the umbra. The opened umbra is the union of all shifted probe heads that are completely contained within the umbra. This is why the opening removes the narrow maxima of the surface in which the structuring element does not fit (Fig. 12.23(a)).

At every image point  $\mathbf{x}$ , the opened surface corresponds to the maximum value  $s(\xi)$  at a position  $\xi$  of one of the shifted structuring elements. Hence, the maximum is not restricted to the origin or the position of the maximum value of the structuring element, but can be at any position of the whole shifted structuring element [7].

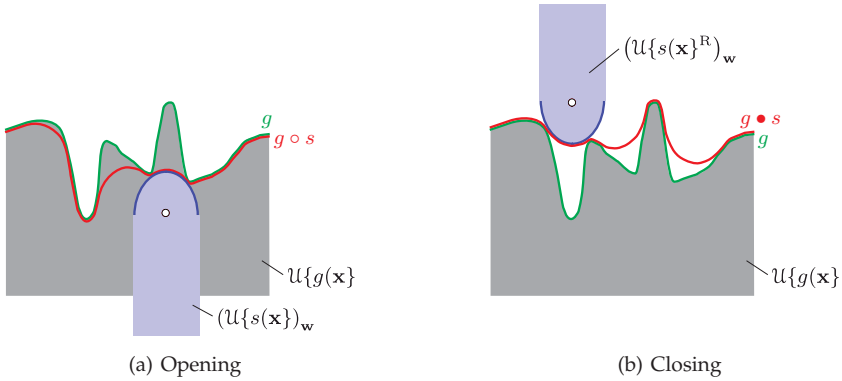


**Figure 12.23.** Visualization of opening and closing of scalar images as a sampling by mechanically touching.

Because of the duality (12.202), closing can be expressed as

$$g \bullet s = -((-g) \circ s^R). \tag{12.203}$$

Therefore, it can be visualized as a sampling by mechanically touching from below of the surface  $-g$ , reflected at the  $x,y$ -plane. This is equivalent to touching the original surface  $g$  from above with the reflected structuring element  $(U\{s\})^R$ . This probe head is moved over the surface  $g$  from above but does not penetrate the object. At the image point  $\mathbf{x}$ , the closed surface runs through the lowest point of one of the shifted probe heads. Narrow valleys of the surface in which the structuring element does not fit are removed (Fig. 12.23(b)).

The gray-scale morphological operations opening and closing are related to the median filtering of Sec. 9.3.2.1 and are therefore suitable for noise reduction [6].

**Example 12.5 (Noise reduction):** Because of the mentioned properties, opening and closing can be used for noise reduction. In contrast to the convention of the illustration of binary images, in gray-scale morphology, high image values  $g$  represent bright image regions, whereas low image values correspond to dark image regions. The opening removes distortions that are smaller than the structuring element and brighter than the surrounding image values. The closing removes distortions that are darker than the surrounding image values. The composition of both operations mitigates both bright and dark distortions.

This is shown in Fig. 12.24 using an example image with artificially added noise. Opening and closing results in a smoothing of structures that are smaller than the structuring element. Larger structures remain nearly unaffected. ■

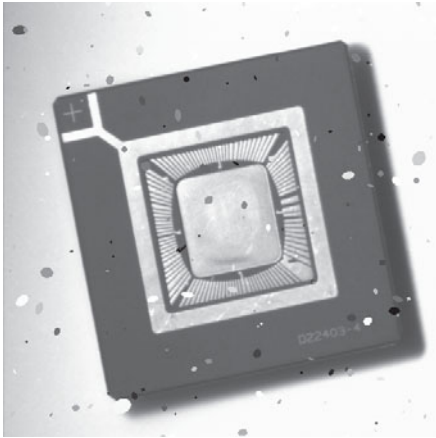
If, on the contrary, only narrow extrema of the image are of interest, e.g., at bright or dark lines, the difference image to the original image can be calculated [5]:

$$g - (g \circ s) \tag{12.204}$$

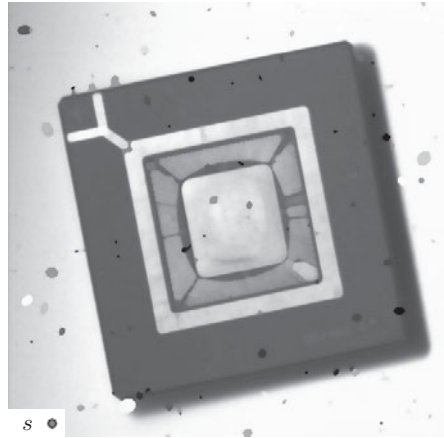
white top-hat

$$(g \bullet s) - g \tag{12.205}$$

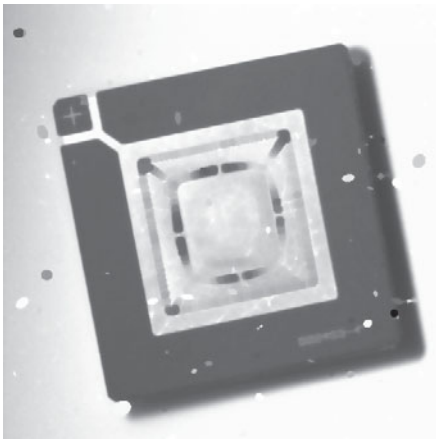
black top-hat



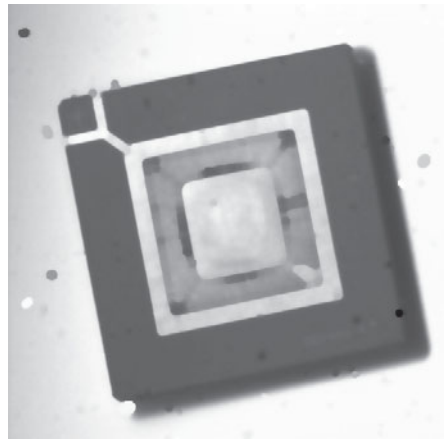
(a)  $g$



(b)  $g \circ s$



(c)  $g \bullet s$



(d)  $(g \circ s) \bullet s$

**Figure 12.24.** Noise compensation using gray-scale morphology: (a) Test image with artificially added bright and dark distortions, (b) Opening with the structuring element  $s$  shown at the bottom left, (c) Closing, (d) Opening and subsequent closing.

Figure 12.25 illustrates the application of these two operations to a test image. The result contains bright and dark structures that are smaller than the structuring element used.

➤ **12.2.4 Edge detection**

Just as binary morphology can be used for the extraction of the borders of binary images, gray-scale morphology allows the detection of the edges in scalar images. As described in Sec. 11.2, the detection of edges can be performed on the basis of the first or second derivative. Both variants can be realized using gray-scale morphology.

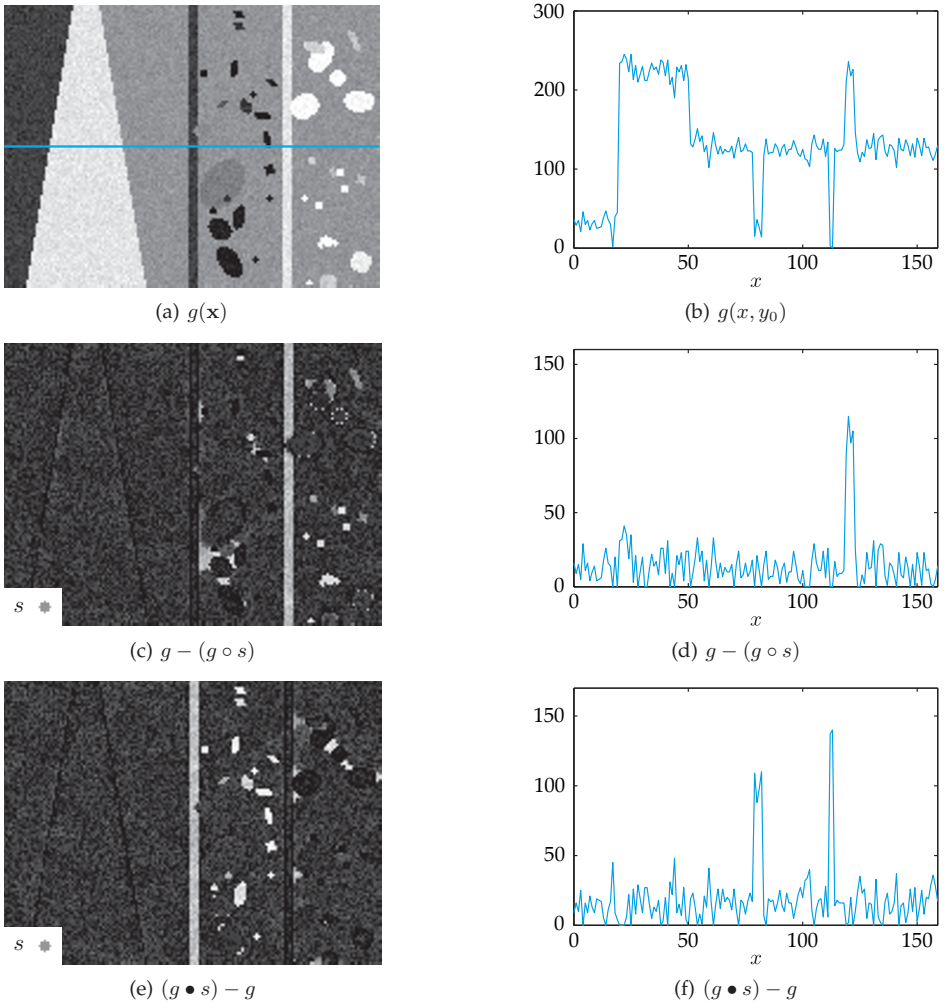


**Figure 12.25.** Extraction of bright and dark points and lines using gray-scale morphology: (a) Test image with artificially superposed white noise; (b) One-dimensional section of gray values along the marked horizontal line; (c), (d) White top hat with the structuring element  $s$ ; (e), (f) Black top hat.

The so-called **Beucher gradient** results in an approximation of the absolute value of the gradient:

$$\|\text{grad } g\| + \text{const.} \approx (g \oplus s) - (g \ominus s). \quad (12.206)$$

The eroded image is subtracted from the dilated image [13].

An approximation for the second derivative can be obtained using the morphological Laplace operator:

$$\Delta g = \text{div}(\text{grad } g) \approx (g \oplus s) + (g \ominus s) - 2g. \quad (12.207)$$

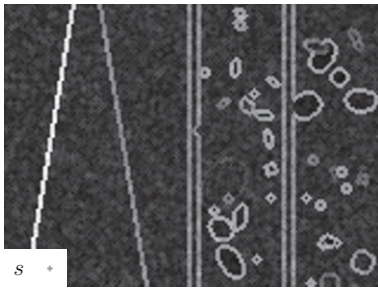
---

**Example 12.6 (Morphological edge detection):** Figure 12.26 shows the result of applying the two edge operators to the test image shown in Fig. 12.25(a). Morphological edge detection also amplifies noise with every differentiation. The use of greater structuring elements results in a certain smoothing but impairs the localization and the detection of fine structures.

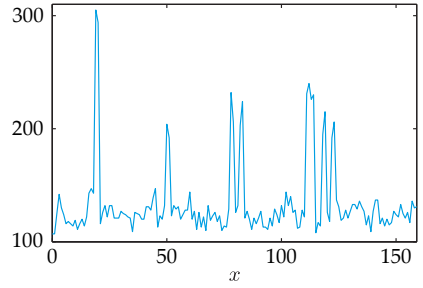
In Fig. 12.27, the results of the application of the two presented morphological edge operators to the example image of Chap. 11 can be compared to other edge operators. ■

## 12.3 Bibliography

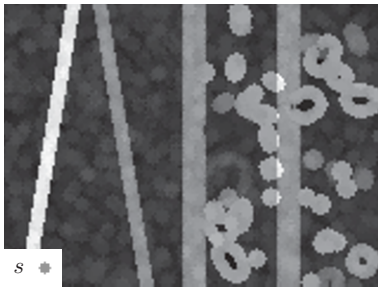
- [1] Wolfgang Abmayr. *Einführung in die digitale Bildverarbeitung*. Teubner, 1994.
- [2] Josef Bigun. *Vision with direction*. Springer, 2006.
- [3] John Canny. A Computational Approach to Edge Detection. *IEEE Transactions on Pattern Analysis and Machine Intelligence*, 8(6):679–698, 1986.
- [4] Charles Giardina and Edward Dougherty. *Morphological methods in image and signal processing*. Prentice Hall, 1988.
- [5] Rafael Gonzalez and Richard Woods. *Digital image processing*. Pearson Prentice Hall, 3rd edition, 2008.
- [6] Robert Haralick and Linda Shapiro. *Computer and robot vision*. Addison-Wesley, 1992.
- [7] Robert Haralick, Stanley Sternberg, and Xinhua Zhuang. Image analysis using mathematical morphology. *IEEE Transactions on Pattern Analysis and Machine Intelligence*, 9(4):532–550, 1987.
- [8] Ramesh Jain, Rangachar Kasturi, and Brian Schunck. *Machine vision*. McGraw-Hill, 1995.
- [9] Patrick Lambert and Jocelyn Chanussot. Extending mathematical morphology to color image processing. In *Proc. International Conference on Color in Graphics and Image Processing*, 2000.
- [10] Gerasimos Louverdis, Maria Vardavoulia, Ioannis Andreadis, and Phillipos Tsalides. A new approach to morphological color image processing. *Pattern Recognition*, 35(8):1733–1741, 2002.
- [11] Petros Maragos and Ronald Schafer. Morphological systems for multidimensional signal processing. *Proceedings of the IEEE*, 78(4):690–710, 1990.
- [12] Georges Matheron. *Random sets and integral geometry*. Wiley, 1975.
- [13] F. Meyer and S. Beucher. Morphological segmentation. *Journal of Visual Communication and Image Representation*, 1(1):21–46, 1990.
- [14] Theodosios Pavlidis. *Structural pattern recognition*. Springer, 1977.
- [15] Azriel Rosenfeld and John Pfaltz. Sequential Operations in Digital Picture Processing. *Journal of the ACM*, 13(4):471–494, 1966.



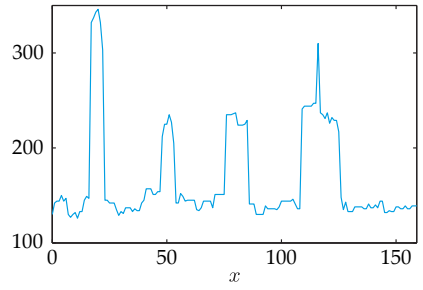
(a)



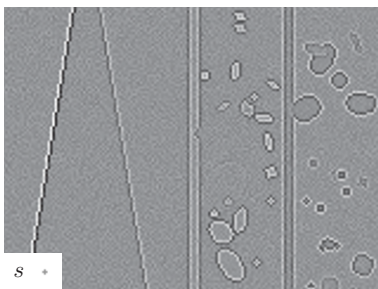
(b)



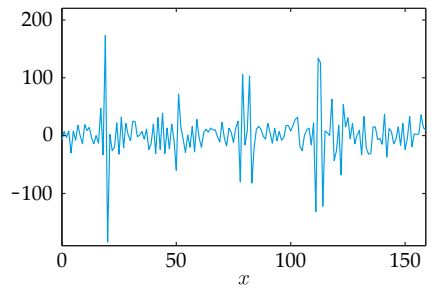
(c)



(d)

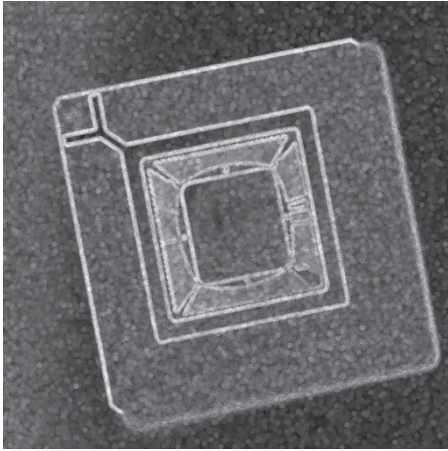


(e)

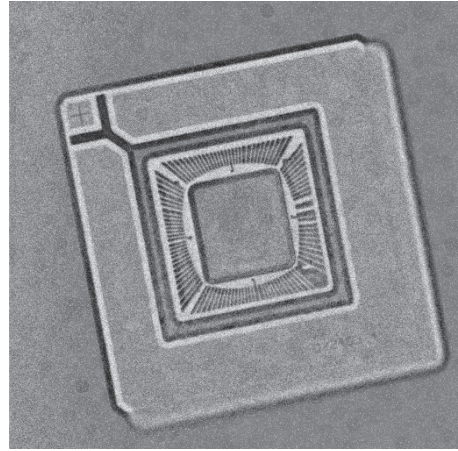


(f)

**Figure 12.26.** Edge extraction using gray-scale morphology: (a) Beucher gradient, calculated for the test image of Fig. 12.25(a) using the structuring element  $s$  with radius 1; (b) One-dimensional section of gray values along the horizontal line marked in Fig. 12.25(a); (c), (d) Beucher gradient calculated with a circular structuring element with radius 3; (e), (f) Result of the morphological Laplace operator.



(a) Beucher gradient



(b) Morphological Laplace operator

Figure 12.27. Morphological edge operators applied to the example image Fig. 11.14(a).

[16] Jean Serra. *Imaging Analysis and Mathematical Morphology – Vol. I*. Academic Press, 1982.

[17] Jean Serra. *Imaging Analysis and Mathematical Morphology – Vol. II: Theoretical Advances*. Academic Press, 1988.

[18] Pierre Soille. *Morphological image analysis: principles and applications*. Springer, 1999.



Chapter 13  
**Texture Analysis**

**13**

---

**13 Texture Analysis**

13.1	Types of textures . . . . .	652
13.1.1	Structural texture type . . . . .	653
13.1.2	Structural-statistical texture type . . . . .	653
13.1.3	Statistical texture type . . . . .	654
13.2	Visual inspection tasks regarding textures . . . . .	655
13.3	Model-based texture analysis . . . . .	656
13.3.1	Analysis of structural textures . . . . .	656
13.3.2	Analysis of structural-statistical textures . . . . .	660
13.3.3	Autoregressive models for analyzing statistical textures . . . . .	663
13.3.4	Separation of line textures . . . . .	666
13.4	Feature-based texture analysis . . . . .	671
13.4.1	Basic statistical texture features . . . . .	672
13.4.2	Co-occurrence matrix . . . . .	673
13.4.3	Histogram of oriented gradients . . . . .	676
13.4.4	Run-length analysis . . . . .	677
13.4.5	Laws' texture energy measures . . . . .	678
13.4.6	Local binary patterns . . . . .	680
13.5	Bibliography . . . . .	681

## 13 Texture Analysis

A **texture** can be defined as a two-dimensional structure with a certain deterministic or statistical regularity. However, there is no standard definition for the term ‘texture’ [13]. Alternatively, a texture can be defined, e.g., by the variations of the image structures, which are smaller than the scales of interest [25].

Textures can be composed, e.g., of lines with regular or stochastic distances and angles, or of two-dimensional primitives which are repeated in a regular pattern (Fig. 13.1). Figure 13.2 shows some images of textures from the Brodatz album [7]. Although these photographs were originally intended to be used by artists and designers, they came to be a reference data set for texture analysis methods. Textures can be generated by production processes, e.g., in textile fabrication or metal machining (Fig. 13.3). Natural processes might also produce textures. The substantial structures of the texture can be of microscopic or macroscopic dimensions.

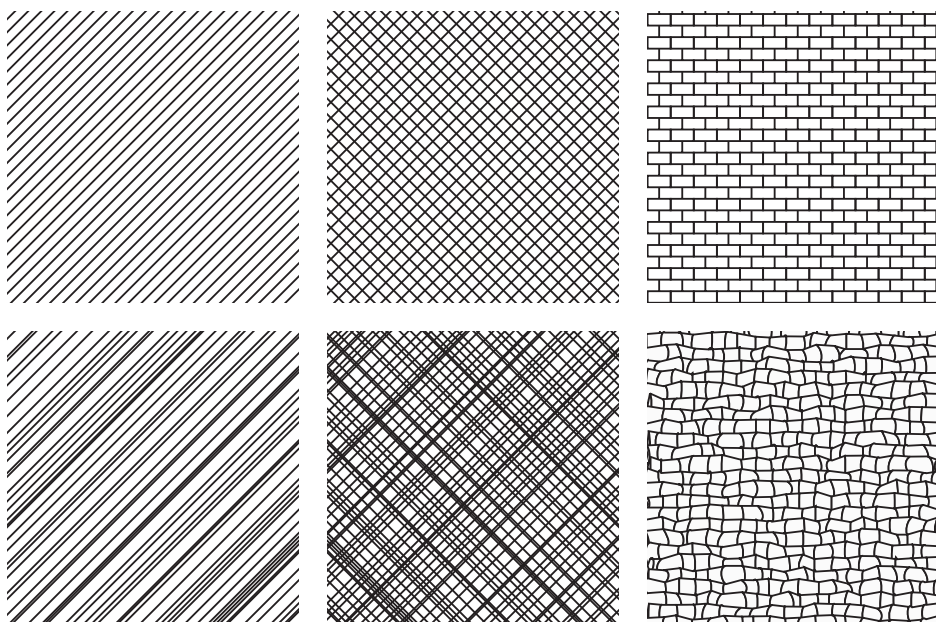


Figure 13.1. Examples of textures.

In the following, first a classification of textures according to their deterministic or statistical regularity will be presented. On this basis, the appearance of textures in image data can be modeled. By means of these models, different tasks of texture analysis can be accomplished (Sec. 13.3). An alternative approach to texture analysis is based on descriptive texture features (Sec. 13.4) instead of on explicit texture models.

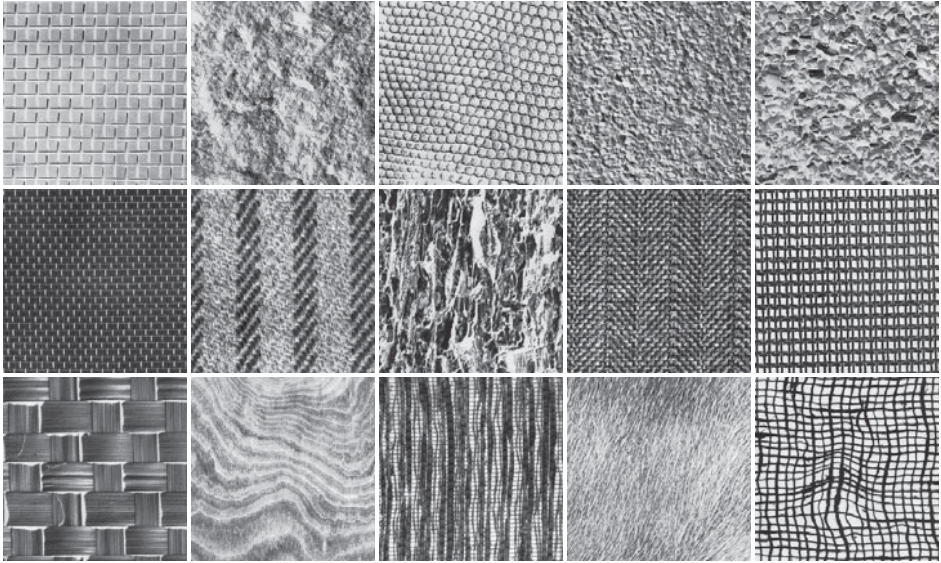
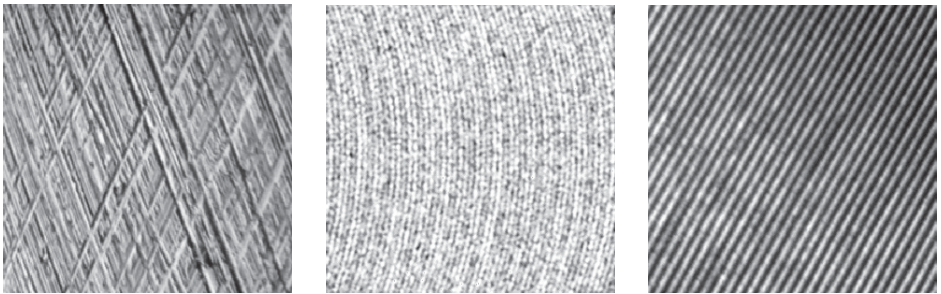


Figure 13.2. Examples of textures [7].



(a) Honing texture

(b) Milling texture

(c) Planing texture

Figure 13.3. Textures of machined surfaces [2, 4].

## 13.1

### 13.1 Types of textures

In the first instance, a texture is a structure in the object space. However, only the image signal  $t(\mathbf{x})$  of the texture produced by an optical imaging is subject to image processing. In the ideal case, the image signal provides a direct description of the real texture. However, in practice, the conditions of the image acquisition are often suboptimal. The most important reasons for differences between the texture and the image signal are given by:

- The structure is affected by a perspective distortion because of the imaging geometry [30]. This cannot be avoided if, e.g., the texture is located on a cylindrical surface instead of a planar surface and if it is observed using a common camera optic.
- The illumination conditions or the reflectance properties of the object's surface can cause an inhomogeneous image signal [4].

Such influences can often be more or less compensated for by using the image enhancement methods presented in Chap. 9. This is why the input image for texture analysis can be assumed to be adequately preprocessed. Hence, real textures and their images are not distinguished in the following sections.

Depending on their deterministic or stochastic nature, texture can be described by different kinds of models [1,24].

### ➤ 13.1.1 Structural texture type

Structural textures consist of elementary patterns that are aligned in a deterministic spatial pattern. An elementary pattern is called a **texel** (or a texture element). The type of structural texture assumes a deterministic texture model. An important special case is that of spatially homogeneous structural textures where both the texels and their alignment are spatially invariant. This corresponds to a two-dimensional periodic signal.

A spatially homogeneous structural texture can be mathematically described as follows: let  $q(\mathbf{x})$  denote the image of the texel and let  $\mathbf{a}_1$  and  $\mathbf{a}_2$  denote linearly independent grid vectors of the alignment. Thus, the grid vectors span a two-dimensional plane:  $\text{span}\{\mathbf{a}_1, \mathbf{a}_2\} = \mathbb{R}^2$ . And hence the structural texture  $t(\mathbf{x})$  is a two-dimensional convolution with a grid of Dirac delta functions:

$$t(\mathbf{x}) = q(\mathbf{x}) ** \sum_{(k,l) \in \mathbb{Z}^2} \delta(\mathbf{x} - k \mathbf{a}_1 - l \mathbf{a}_2) = \sum_{(k,l) \in \mathbb{Z}^2} q(\mathbf{x} - k \mathbf{a}_1 - l \mathbf{a}_2). \quad (13.1)$$

Every grid point is described by a Dirac delta function. The texel is repeated at every grid point. The chosen model is adequate if the texels are non-overlapping, i.e., if they have disjoint supports for different grid points:

$$\text{supp}\{q(\mathbf{x} - k \mathbf{a}_1 - l \mathbf{a}_2)\} \cap \text{supp}\{q(\mathbf{x} - i \mathbf{a}_1 - j \mathbf{a}_2)\} = \emptyset \quad (13.2)$$

for all  $(k, l) \neq (i, j)$ . Because of the periodicity of the texture, the texels are not uniquely determined: a point of the texture can be assigned to the right border of a texel or to the left border of the adjacent texel on the right.

The model (13.1) describes an infinitely expanded texture. In practice, the texture is clipped at the borders of the images or of an image region. The simplest case of an equidistant, rectangular grid with a distance of  $a > 0$  between adjacent grid points is given by  $\mathbf{a}_1 = (a, 0)^T$ ,  $\mathbf{a}_2 = (0, a)^T$ .

Examples of structural textures are crystal lattices and precisely manufactured 2D structures. Structural texture models can also be hierarchically composed, so that every texel of the macro texture has a texture of its own and consists of micro texels.

### ➤ 13.1.2 Structural-statistical texture type

For this texture type, both the texels  $q(\mathbf{x})$  and the alignment  $\{\mathbf{a}_1, \mathbf{a}_2\}$  are not thoroughly deterministic, but are affected by certain stochastic variations (Fig. 13.4). The variations can be caused by, e.g., random effects and perturbations of a natural or technical production process. As their extent is limited, the textures remain clearly distinguishable.

Examples of structural-statistical textures are microscopic images of cell cultures, groove textures on machined metal surfaces, textile structures, etc.

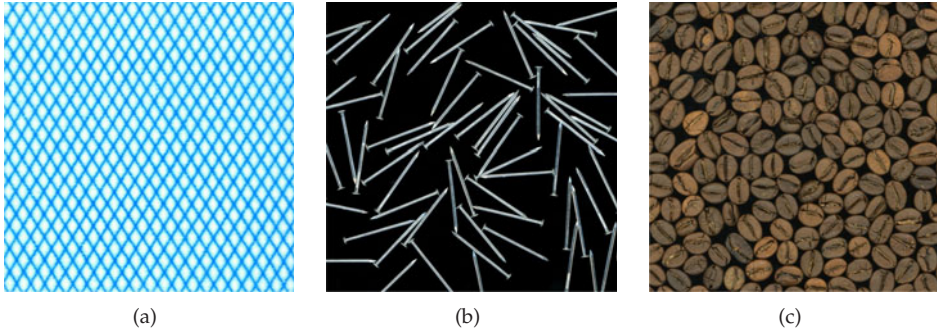


**Figure 13.4.** Images of structural and structural-statistical textures: (a) Printed textiles (texels and their alignment are approximately deterministic); (b) Irregularly aligned nails (stochastic alignment); (c) Coffee beans (stochastic texels and alignment).

### 13.1.3 Statistical texture type

Because of the high stochastic variability of statistical textures, a description of the texture by texels and their alignment is no longer adequate. A statistical texture can be assumed to be a sample function of a random process, which can be described by probability density functions as follows:

$$f_t(t(\mathbf{x}_1), t(\mathbf{x}_2), \dots, t(\mathbf{x}_n)) \quad \text{for all } (\mathbf{x}_1, \mathbf{x}_2, \dots, \mathbf{x}_n) \in \Omega_t^n \text{ and all } n \in \mathbb{N}. \quad (13.3)$$

For a fixed  $n$ , such a probability density function defines a  **$n$ th order statistic** (cf. Def. 8.13). For example,  $f_t(t(\mathbf{x}))$  is the probability of the image point  $\mathbf{x}$  having the value of  $t(\mathbf{x})$ . For  $n = 2$ ,  $f_t(t(\mathbf{x}_1), t(\mathbf{x}_2))$  describes the joint probability density of the image point  $\mathbf{x}_1$  having the value of  $t(\mathbf{x}_1)$  and the image point  $\mathbf{x}_2$  having the value of  $t(\mathbf{x}_2)$  simultaneously.

The visual perception of the human is especially sensitive to differences of the first- and second-order statistics and comparatively insensitive to higher-order statistics [16, 17]. This is why often only the first- and second-order statistics and their corresponding moments, the expected value  $E\{\cdot\}$  (first-order moment), the variance  $\text{Var}\{\cdot\}$ , and the autocorrelation function (both second order), are used for modeling statistical textures.

---

**Example 13.1 (Human perception of differences between textures):** Figure 13.5 shows two images of the same texture, each with a single square, with a different texture. In the left image, the texture differs from the surrounding texture in its second-order statistic, so that the square can be identified by a human observer at first glance. In the second image, the first-order and second-order statistics are identical. Only the third-order statistic is different, which can only be seen by taking a closer look at the image. ■

Natural topographies, fractured surfaces, sand-blasted surfaces, surfaces of sand cast components, and a water surface crinkled by the wind are examples of statistical textures.

The transitions between the three presented texture types are smooth (Fig. 13.6). The more structured is the texture, the more detailed is the way in which it can be described and modeled. In order to achieve an expressive and effective texture model for texture analysis

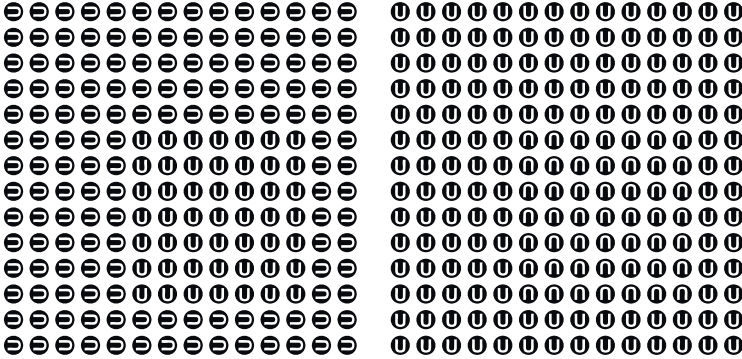


Figure 13.5. Human perception of differences in the statistics of textures (adapted from [17]).

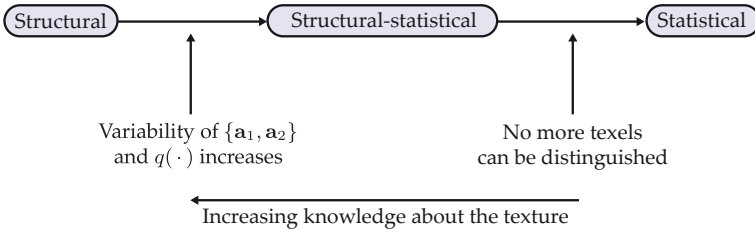


Figure 13.6. Smooth transition between different texture types.

and texture synthesis, preferably all available information about texture should be incorporated into the model.

### 13.2 Visual inspection tasks regarding textures

In terms of automated visual inspection, texture analysis can handle the following tasks:

- **Texture classification:** classification of a texture, discriminating between different textures;
- **Texture segmentation:** segmentation of the image into connected regions of different textures;
- **Texture separation:** separation of texture components and image background (i.e., non-texture image components);
- **Estimation of texture parameters** (e.g., intensities, angles,...);
- **Defect detection:** detection of significant deviations from the texture’s regularity.

An important tool for some of these tasks is the **synthesis of textures**, i.e., the generation of images using texture models. On the one hand, synthesized textures can be used to assess the quality of a texture model by visual comparison to a real texture. On the other hand, texture synthesis can be used to develop methods for suppressing the modeled texture in real images, so that defects not covered by the model are highlighted. By these means, a subsequent defect detection will be easier and more efficient.

### 13.3 Model-based texture analysis

#### 13.3.1 Analysis of structural textures

A possible approach to the analysis of structural textures is based on the Fourier transform of the texture model (13.1):

$$t(\mathbf{x}) = q(\mathbf{x}) ** \sum_{(k,l) \in \mathbb{Z}^2} \delta(\mathbf{x} - k \mathbf{a}_1 - l \mathbf{a}_2) \quad (13.4)$$



$$T(\mathbf{f}) \propto Q(\mathbf{f}) \sum_{(k,l) \in \mathbb{Z}^2} \delta(\mathbf{f} - k \mathbf{f}_1 - l \mathbf{f}_2) \quad \text{with} \quad (\mathbf{a}_1, \mathbf{a}_2) = \begin{pmatrix} \mathbf{f}_1^T \\ \mathbf{f}_2^T \end{pmatrix}^{-1}. \quad (13.5)$$

The correspondence is obtained by means of the convolution theorem (8.148) and the results presented in Sec. 8.3.7.

The first goal is to estimate the grid vectors  $\mathbf{f}_1$  and  $\mathbf{f}_2$  by evaluating the distances between the extrema in the spatial frequency domain, so that the grid vectors  $\mathbf{a}_1$  and  $\mathbf{a}_2$  of the spatial arrangement can be calculated.

Usually, a texture is not a pure harmonic oscillation: the extrema in the spatial frequency domain are not only located at the basis vectors  $\mathbf{f}_1$  and  $\mathbf{f}_2$  but also at integer multiples of their spatial frequencies. These extrema correspond to the harmonics of the periodic signal, similar to the coefficients of a Fourier series. In order to determine the basis vectors of the grid, the four extrema with the smallest distance from the origin are chosen. Because of the symmetry of the Fourier transform of the real-valued image signal  $t(\mathbf{x})$ , these four extrema are located at the grid vectors  $\mathbf{f}_1$  and  $\mathbf{f}_2$  and their reflections  $-\mathbf{f}_1$  and  $-\mathbf{f}_2$ . In the spatial domain, this corresponds to an approximation of the texture  $t(\mathbf{x})$  by two harmonic oscillations, which are the two fundamental frequencies of the texture:

$$\begin{aligned} \tilde{t}(\mathbf{x}) = \mathcal{F}^{-1} \{ & Q(\mathbf{f}_1) \delta(\mathbf{f} - \mathbf{f}_1) + Q(-\mathbf{f}_1) \delta(\mathbf{f} + \mathbf{f}_1) \\ & + Q(\mathbf{f}_2) \delta(\mathbf{f} - \mathbf{f}_2) + Q(-\mathbf{f}_2) \delta(\mathbf{f} + \mathbf{f}_2) \}. \end{aligned} \quad (13.6)$$

A pair  $\delta(\mathbf{f}_i) + \delta(-\mathbf{f}_i)$  represents the Fourier transform of the harmonic oscillation  $2 \cos(2\pi \mathbf{f}_i^T \mathbf{x})$ , see Sec. 8.3.1.3.

**Example 13.2 (Analysis of structural textures using the Fourier transform):** The alignment  $(\mathbf{a}_1, \mathbf{a}_2)$  of the texture of Fig. 13.7(a) is to be determined. For this purpose, the discrete Fourier transform of the texture is calculated and a Hann window (8.127) is used to reduce spectral leakage. The magnitude spectrum shows significant maxima at the positions  $\mathbf{f}_1$ ,  $\mathbf{f}_2$ ,  $-\mathbf{f}_1$ , and  $-\mathbf{f}_2$ , see Fig. 13.7(b). By setting all other spatial frequencies to zero and by transforming the resulting spectrum back into the spatial domain, an approximation of the texture by two harmonic oscillations  $\tilde{t}(\mathbf{x})$  is obtained, cf. Fig. 13.7(c).

Now, the grid vectors  $\mathbf{a}_1$  and  $\mathbf{a}_2$  of the alignment in the spatial domain can be calculated from  $\mathbf{f}_1$  and  $\mathbf{f}_2$  by using (13.5). ■

Now, a real-world application of defect detection in structural textures by means of the Fourier transform will be presented.



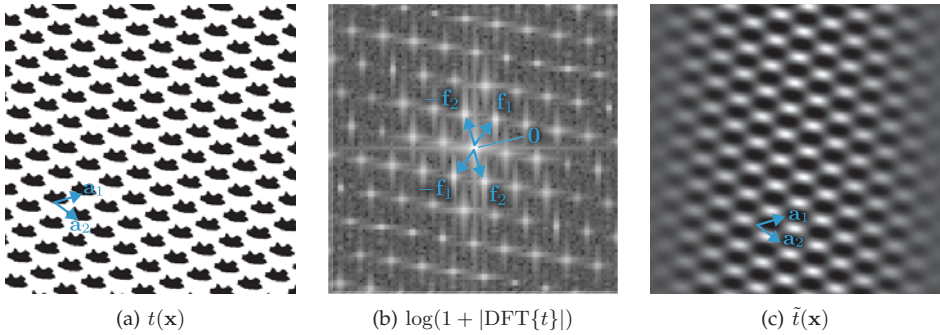


Figure 13.7. Estimation of the alignment ( $\mathbf{a}_1, \mathbf{a}_2$ ) of a structural texture: (a) Example texture  $t(\mathbf{x})$ ; (b) Magnified section of the magnitude of the DFT spectrum of the windowed texture signal shown using logarithmic values; (c) Fundamental oscillation of the texture, transformed back from the grid vectors  $\mathbf{f}_1, \mathbf{f}_2, -\mathbf{f}_1, -\mathbf{f}_2$ .

**Example 13.3 (Analysis of a face milling texture):** In face milling, a rotating milling cutter is moved linearly over the surface of the workpiece. This motion, which is a combination of a linear and a rotational movement, produces a texture on the workpiece consisting of periodically aligned grooves in the shape of cycloidal marks, see Fig. 13.8(a). For example, face milling is used for the sealing surface between the engine block and the cylinder head of combustion engines [4].

In a model of this texture, a texel is represented by a single groove. The alignment is one-dimensional in this case, as it consists of equidistant Dirac delta functions, spaced with the groove distance  $\Delta x$  on the  $x$ -axis:

$$\sum_{m=-\infty}^{\infty} \delta(x - m \Delta x) \delta(y) = \sum_{m=-\infty}^{\infty} \delta(\mathbf{x} - m \Delta x \mathbf{e}_x) \tag{13.7}$$

$$\Downarrow$$

$$\frac{1}{\Delta x} \sum_{k=-\infty}^{\infty} \delta\left(f_x - \frac{k}{\Delta x}\right) 1(f_y). \tag{13.8}$$

In the spatial frequency domain, this alignment corresponds to a series of slice functions with reciprocal distance. The support of the Fourier transform of a cycloid is approximately a subset of a double wedge-shaped area, whose top is located at the origin, see Fig. 13.9(a). This can be explained as follows: when a section of the cycloid is considered, which is small enough to approximate a line, Example 8.21 implies that the corresponding Fourier spectrum has to be approximately a line through the origin of the spatial frequency domain perpendicular to the groove considered. As this applies to every section of the groove, the resulting area is double wedge-shaped with an opening angle depending on the orientations of the grooves present in the texture.

As the convolution of the alignment and the texel corresponds to a multiplication in the spatial frequency domain, the squared magnitude spectrum shows two notable vertical lines, which represent the fundamental oscillation of the groove texture, see Fig. 13.8(b).

The milling cutter considered in this example has three teeth. A typical defect is the

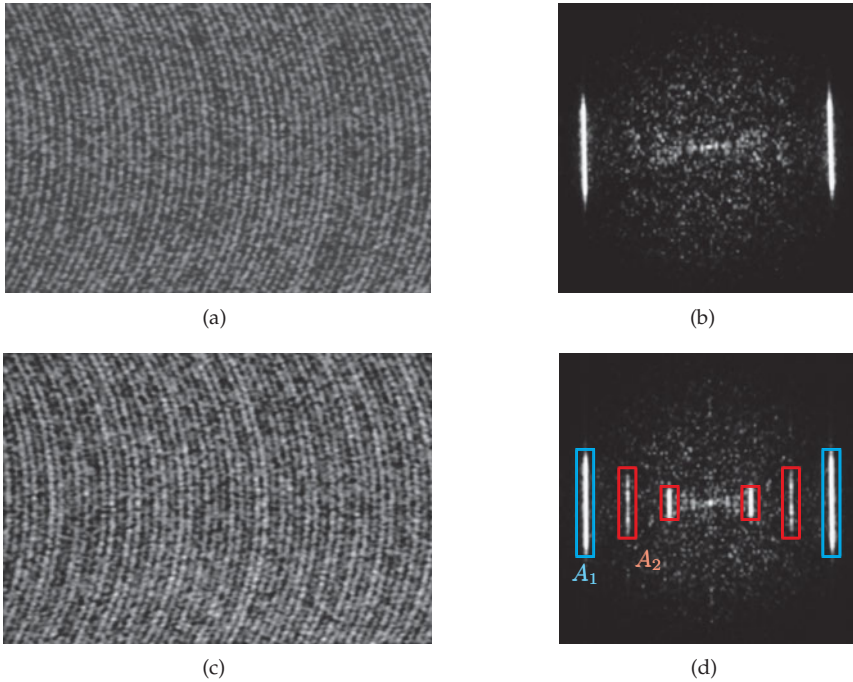


**Figure 13.8.** Analysis of face milling textures: (a) Faultless texture; (b) Magnitude spectrum of the faultless texture (magnification of the section surrounding the origin); (c) Defect texture; (d) Corresponding magnitude spectrum with the regions of integration  $A_1, A_2$  for the calculation of the feature  $\mu$ .

breaking of a cutting edge of one of the teeth. In this case, one of the three parallel grooves is attenuated or is completely lacking, see Fig. 13.8(c). In a model of the resulting texture, the texel consist of three adjacent grooves, of which two are faultless. Only every third Dirac delta function remains present in the alignment (Fig. 13.9(b)):

$$\sum_{m=-\infty}^{\infty} \delta(x - m 3\Delta x) \delta(y) \tag{13.9}$$

$$\Downarrow$$

$$\frac{1}{3\Delta x} \sum_{k=-\infty}^{\infty} \delta\left(f_x - \frac{k}{3\Delta x}\right) 1(f_y). \tag{13.10}$$

In the Fourier domain, this tripled distance corresponds to one-third of the spatial frequency. This is why a defect test object shows significant spectral components at integer multiples of one-third of the original frequency, see Fig. 13.8(d). Now, the frequency of the fundamental oscillation of the texture in Fig. 13.8(c) is only one-third of the frequency of Fig. 13.8(a). The other lines visible in Fig. 13.8(d) represent the first and second harmonics of this fundamental oscillation. With regards to the fundamental oscillation of the texture of the intact cutter (Fig. 13.8(b)), the added lines are subharmonic spectral components. In the spectrum, these subharmonic components allow a reliable detection of

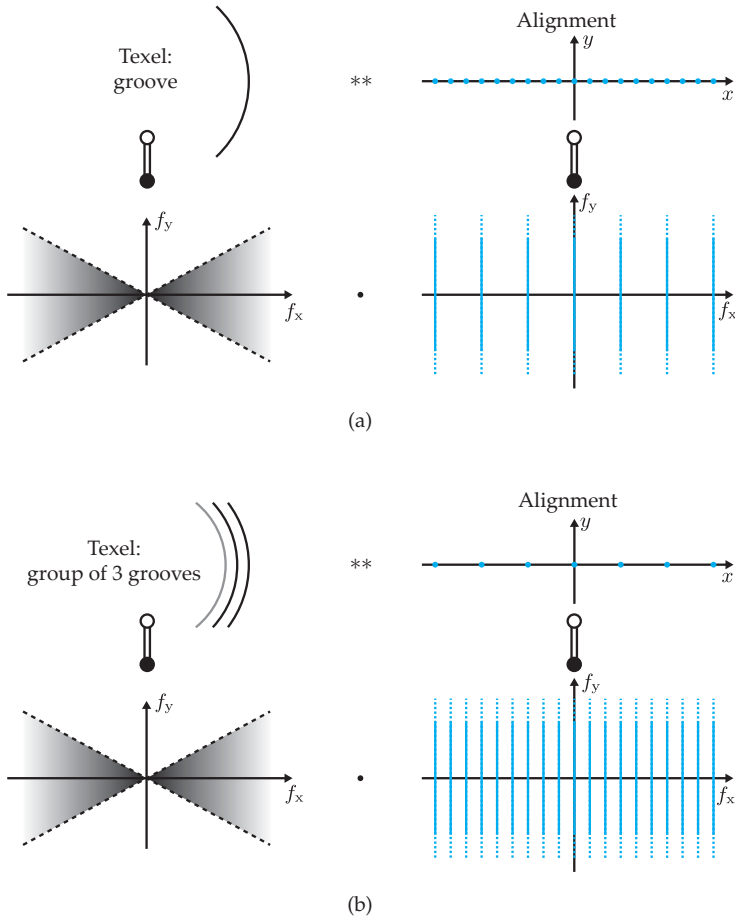


Figure 13.9. Analysis of a face milling texture using the Fourier transform: (a) Faultless cutter; (b) Defect cutter.

any break of a cutting edge using the milling texture. The quotient of the integrals over the corresponding regions of the squared magnitude spectrum can be used as a feature  $\mu$ :

$$\mu := \frac{\int_{A_2} |\mathcal{F}\{t(x, y)\}|^2 df_x df_y}{\int_{A_1} |\mathcal{F}\{t(x, y)\}|^2 df_x df_y}, \tag{13.11}$$

where  $A_1$  denotes the support of the fundamental oscillation and  $A_2$  the support of the two subharmonic components, see Fig. 13.8(d).

Altogether, high values of  $\mu$  signal a defect of the cutter. ■

Methods using the spatial frequency domain for texture analysis can also be used for purposes other than just visual inspection of the texture. For example, the velocity of a vehicle can be estimated using motion blurred or double-exposed images of a textured surface.

**Example 13.4 (Estimation of the direction of motion):** Multiply exposed images of a texture which has been moved relatively to the camera are used for estimating the velocity. For example, a camera mounted on a moving vehicle can observe the texture of the road surface, so that the velocity vector can be measured [14,31].

In the spatial domain, double-exposed images of one and the same texture correspond to a convolution of the texture signal  $t(\mathbf{x})$  with a pair of impulses

$$\delta(\mathbf{x} - \frac{1}{2}\mathbf{l}) + \delta(\mathbf{x} + \frac{1}{2}\mathbf{l}), \quad (13.12)$$

where  $\mathbf{l}$  denotes the translation vector sought. In the spatial frequency domain, this convolution corresponds to a multiplication of the texture's spectrum  $T(\mathbf{f})$  with a cosine function. The frequency of the cosine increases proportionally with the length of the motion vector. Figures 13.10(a) and (d) show two examples of double-exposed images of a single texture with different magnitudes of the motion vector. The respective discrete Fourier transforms in Fig. 13.10(b), (e) correspond to the multiplication of the spectrum of the still texture by a cosine function. In the case of Fig. 13.10(b), the frequency is higher because the translation vector has a greater magnitude.

A simple possibility for estimating the motion vector is given by the so-called **cepstrum**. The cepstrum of a signal  $g(\mathbf{x})$  is defined as

$$\text{Cepstrum}\{g(\mathbf{x})\} := \text{DFT}\{\log(|\text{DFT}\{g(\mathbf{x})\}|)\}. \quad (13.13)$$

Hence, a second Fourier transform is applied to the logarithm of the magnitude spectrum. Thus, the cosine function is again represented by a pair of impulses. Because of the calculation of the magnitude and the logarithm, the resulting oscillation is no longer a pure harmonic oscillation, resulting in the higher corresponding harmonics. The logarithmic scale greatly reduces the dynamic range of the magnitude spectrum, so that the interesting structures are accentuated for higher frequencies and therefore occupy a larger region of the frequency domain. By the reciprocity of the Fourier transform, the maxima that result from these structures after the second Fourier transform, are narrower.

The position of the first maximum in the cepstrum is an estimation of the motion vector  $\mathbf{l}$  sought. Because of the second Fourier transform, lengths in the cepstral domain correspond to lengths in the spatial domain.

If the time between the two exposures is known, the velocity of the motion can be calculated from the motion vector.

A similar approach can also be used for a continuous, longer exposure of the moving texture, Fig. 13.10(g). The motion-blurred image corresponds to the convolution of the texture signal with a one-dimensional rectangular function of the length and orientation of the motion vector (see Ex. 10.2). In the spatial frequency domain, this convolution corresponds to multiplication by a sinc function, see Fig. 13.10(h). The motion vector and hence the velocity can be estimated using the cepstrum, see Fig. 13.10(i) [14]. ■

### ➤ 13.3.2 Analysis of structural-statistical textures

There is no general approach to the analysis of structural-statistical textures, as the choice of adequate features and methods always depends on the properties of the texture at hand.

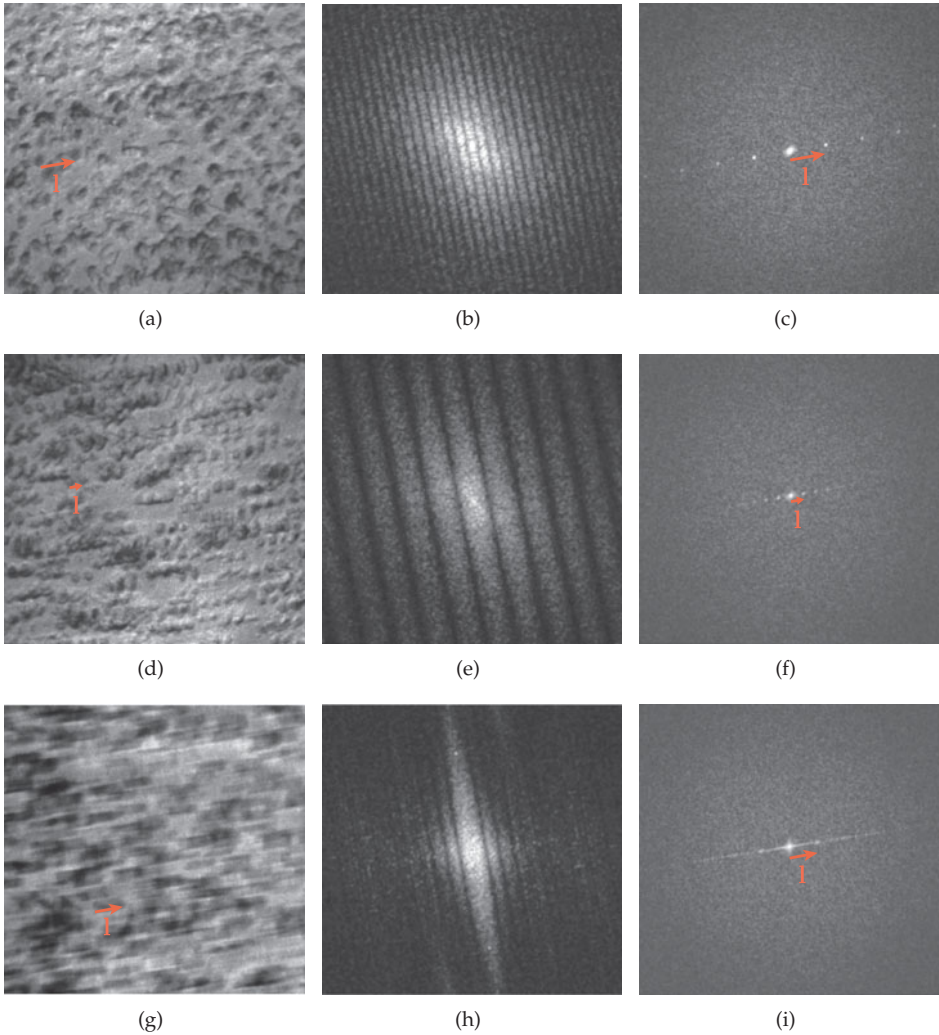


**Figure 13.10.** Estimation of the translation vector between the double-exposed images of a texture (source: D. vom Stein [31]): (a) Double-exposed images of the moved texture at a high velocity, (b) Magnitude of the discrete Fourier transform of (a), (c) Cepstrum of (a), in which the translation vector  $I$  can be determined, (d)–(f) Double-exposed images, DFT and cepstrum for low velocity, (g) Motion-blurred image of the texture, (h) Corresponding DFT, (i) Corresponding cepstrum.

The methods always have to be adapted to meet the requirements of the application. In the following, an example will be used to thoroughly present different methods.

**Example 13.5 (Structural-statistical model of a honing texture):** Honing is an abrasive machining process for surface finishing. Honed surfaces are used inside the cylinders of combustion engines, for example. They contain fine grooves that can hold motor oil for sup-

porting the lubrication of the cylinder's contact surfaces. A surface is honed by moving a hone, which consists of abrasive grains, over the surface in a motion made up from strokes and rotations (Fig. 13.11). The depths and distances of the grooves produced depend on the different dimensions and distances of the irregularly arranged abrasive grains. However, they show two notable predominant directions, of which one corresponds to the upward stroke and the other corresponds to the downward stroke.

A structural-statistical model of the honing texture should consider both the direction structure and the almost random distribution of the distances and shape of the grooves. Here, all random variables are assumed to be stochastically independent and identically distributed. The texels of the structural-statistical texture model are straight grooves. The grooves  $l_\nu(\cdot)$  are assumed to be randomly, identically distributed and stochastically independent. A groove profile models the gray values of a line perpendicular to the direction of the groove (Fig. 13.12). For example, a groove in the  $y$ -direction is given by

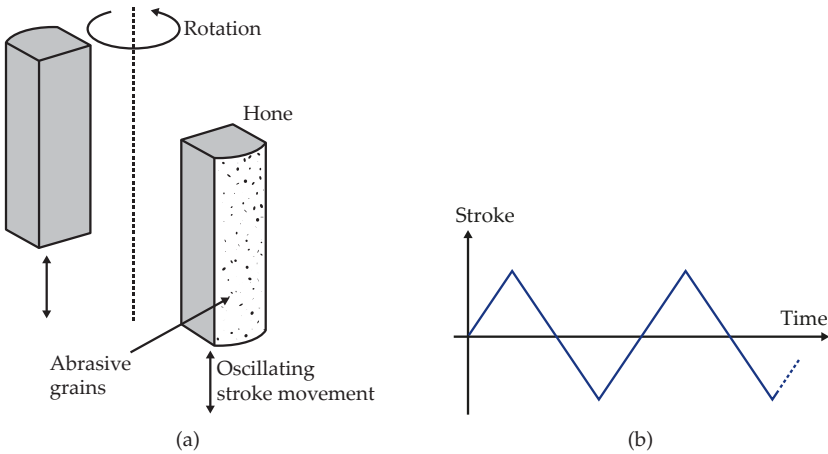


Figure 13.11. Creation of a honing texture [4]: (a) Combination of rotations and strokes, (b) Temporal course of an ideal stroke move.

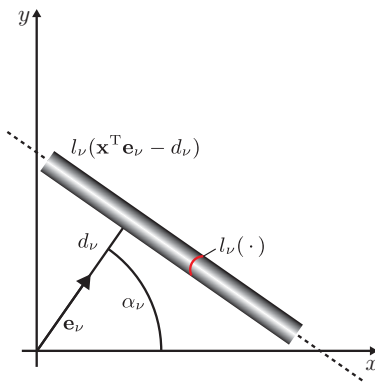


Figure 13.12. Structural-statistical model of the honing texture. The grooves represent the texels.

$q(x, y) = 1_\nu(x)$ , i.e., the gray values along a line are identical for all  $y$ -values. A groove which is rotated by the angle  $\alpha_\nu$  is represented by  $q(\mathbf{x}) = 1_\nu(\mathbf{x}^T \mathbf{e}_\nu)$  with the normal vector  $\mathbf{e}_\nu = (\cos \alpha_\nu, \sin \alpha_\nu)^T$ . The groove angles  $\alpha_\nu \in [0, \pi)$  are also assumed to be identically distributed and stochastically independent random variables. Because of the honing process, the groove angles are not uniformly distributed but show two distinct predominant directions  $\beta_1$  and  $\beta_2$ , which are the only directions present in the ideal case. This results in the following probability distribution  $f_\alpha(\alpha_\nu)$  of the groove angles:

$$f_\alpha(\alpha_\nu) = \frac{1}{2}(\delta(\alpha_\nu - \beta_1) + \delta(\alpha_\nu - \beta_2)). \quad (13.14)$$

Now, the distances between the grooves are modeled. A groove that is shifted by  $d_\nu$  in the direction of the normal from the origin can be described by  $q(\mathbf{x}) = 1_\nu(\mathbf{x}^T \mathbf{e}_\nu - d_\nu)$ . The distances  $d_\nu$  can be assumed to be randomly uniformly distributed, as the abrasive grains are placed independently and homogeneously randomly on the hone. In summary, the structural-statistical model of a honing texture is given by:

$$\mathbf{t}(\mathbf{x}) = \sum_{\nu=-\infty}^{\infty} 1_\nu(\mathbf{x}^T \mathbf{e}_\nu - d_\nu). \quad (13.15)$$

Because of the random placing of the abrasive grains, the number  $n$  of grooves inside an interval of distances to the origin of length  $L$  is assumed to be distributed according to a Poisson distribution:

$$P_n(n) = e^{-\lambda L} \frac{(\lambda L)^n}{n!}, \quad n = 0, 1, \dots, \infty. \quad (13.16)$$

The parameter  $\lambda > 0$  of the Poisson distribution represents the spatial groove density. The randomly distributed parameters  $\alpha_\nu, d_\nu$  define a stochastic alignment. In contrast to the requirement of Sec. 13.1.1, the single texture elements overlap at the intersections of the grooves, which is an anomaly of the honing texture caused by the honing process. The addition of the gray value profiles at the intersections is a model error which however immensely simplifies the usage of the model. This is why the model does not represent the reality at the intersections.

The groove angles  $\beta_1$  and  $\beta_2$ , the spatial groove density  $\lambda$ , and the samples of the expected value  $E\{1_\nu(\cdot)\}$  of the groove profiles are the model parameters. Figure 13.14 shows a texture that has been synthesized with this model, and a real texture. In the synthesized texture, the mentioned model error affecting the intersection has been compensated for.

The model allows the calculation of the power spectral density of a honing texture in terms of the model parameters. The model parameters can be considered to be customized texture features [4]. ■

### 13.3.3 Autoregressive models for analyzing statistical textures

The autoregressive signal model, AR model for short, provides a simple possibility for modeling two-dimensional statistical structures, especially statistical textures [15]. An AR model describes the image value  $g_{mn}$  at a position  $(m, n)$  by a linear combination of the image values in a neighborhood  $\mathcal{U}$  of this position (Fig. 13.13). The weights of this linear combination

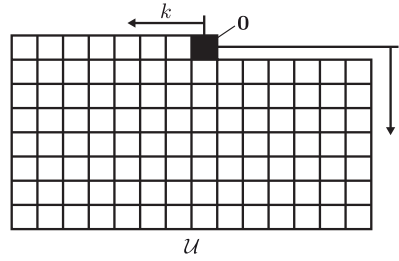


Figure 13.13. Autoregressive model: Causal neighborhood  $\mathcal{U}$  of the origin  $0$ .

are the AR coefficients  $a_{kl}$ . The difference between the actual image value and the image value predicted by the linear combination is modeled as the random variable  $e_{mn}$ .

Hence, the AR model of the signal  $g_{mn}$  is given by

$$g_{mn} = \sum_{(k,l) \in \mathcal{U}} a_{kl} g_{m-k,n-l} + e_{mn}. \tag{13.17}$$

The neighborhood  $\mathcal{U}$  is a so-called causal neighborhood of the origin, so that for a pixel-wise shift in the positive direction to the right, or to the line above if the line-ending has been reached, the neighborhood consists exclusively of already calculated pixels. Originally, AR models were used for the analysis of time series, where only the previous values can be accessed. However, for two-dimensional spatial signals, there is no natural ordering of the points. This is why causality has to be artificially introduced, i.e., defined for images. Then, the image can be sequentially processed in the corresponding order.

The signal  $g_{mn}$  is considered to be a stochastic process, which is weakly stationary and w.l.o.g. zero-mean,  $E\{g_{mn}\} = 0$ . Hence, before the AR model can be applied to an image, the mean value of the image signal has to be subtracted. The last summand  $e_{mn}$  represents a zero-mean, weakly stationary, white noise:  $E\{e_{mn}\} = 0$ ,  $E\{e_{mn} e_{m+i,n+j}\} = \sigma^2 \delta_i^0 \delta_j^0$ .

The causal neighborhood  $\mathcal{U}$  contains only points  $(k, l)$  on one side of the origin  $(0, 0)$ , e.g., those points with  $k > 0$  or  $l > 0$ . The origin itself is not contained in the neighborhood,  $(0, 0) \notin \mathcal{U}$ . By this means, the model can be evaluated recursively: as the points  $(m, n)$  are processed row-by-row and column-by-column, only those values  $g_{mn}$  are needed on the right-hand side of (13.17) which have been already calculated. The number of elements inside the neighborhood, i.e., the number of AR coefficients, is called the order of the AR model, and is denoted by  $|\mathcal{U}|$ .

Equation (13.17) can also be expressed in vector notation by forming vectors from the AR coefficients and the signal inside the neighborhood:

$$g_{mn} = \mathbf{a}^T \boldsymbol{\gamma}_{mn} + e_{mn}, \tag{13.18}$$

$$\boldsymbol{\gamma}_{mn} := (\dots, g_{m-k,n-l}, \dots)^T \in \mathbb{R}^{|\mathcal{U}|}, \tag{13.19}$$

$$\mathbf{a} := (\dots, a_{kl}, \dots)^T \in \mathbb{R}^{|\mathcal{U}|}. \tag{13.20}$$

By the term  $\mathbf{a}^T \boldsymbol{\gamma}_{mn}$ , the current value  $g_{mn}$  of the signal is predicted from the past values  $g_{m-k,n-l}$ ,  $(k, l) \in \mathcal{U}$ . This method is affected by a stochastic error  $e_{mn}$ . The AR model fits a signal optimally if the prediction error  $e_{mn} = g_{mn} - \mathbf{a}^T \boldsymbol{\gamma}_{mn}$  is of minimum variance. This



characteristic can be used for parameter estimation when a signal  $g_{mn}$  is to be approximated by an AR model. The parameters of the AR model are  $\mathbf{a}$  and  $\sigma^2$ .

Hence, for finding the optimal parameters, the following optimization problem has to be solved:

$$\sigma^2 = E\{\mathbf{e}_{mn}^2\} \rightarrow \text{Min.} \quad (13.21)$$

It holds:

$$\sigma^2 = E\{\mathbf{e}_{mn}^2\} = E\{\mathbf{g}_{mn}^2 - 2\mathbf{a}^T \gamma_{mn} \mathbf{g}_{mn} + \mathbf{a}^T \gamma_{mn} \mathbf{a}^T \gamma_{mn}\} \quad (13.22)$$

$$= E\{\mathbf{g}_{mn}^2\} - 2\mathbf{a}^T E\{\gamma_{mn} \mathbf{g}_{mn}\} + \mathbf{a}^T E\{\gamma_{mn} \gamma_{mn}^T\} \mathbf{a}. \quad (13.23)$$

A necessary condition for a minimum of this term is that there is a zero of the gradient with respect to the vector of coefficients  $\mathbf{a}$ :

$$\text{grad}_{\mathbf{a}} E\{\mathbf{e}_{mn}^2\} \stackrel{!}{=} 0 \quad (13.24)$$

$$\Leftrightarrow -2E\{\gamma_{mn} \mathbf{g}_{mn}\} + 2E\{\gamma_{mn} \gamma_{mn}^T\} \mathbf{a} = 0 \quad (13.25)$$

$$\Leftrightarrow \mathbf{a} = \left( \underbrace{E\{\gamma_{mn} \gamma_{mn}^T\}}_{\approx \frac{1}{K} \sum_{m,n} \gamma_{mn} \gamma_{mn}^T} \right)^{-1} \underbrace{E\{\gamma_{mn} \mathbf{g}_{mn}\}}_{\approx \frac{1}{K} \sum_{m,n} \gamma_{mn} g_{mn}}. \quad (13.26)$$

The presented approximations apply to ergodic signals  $\mathbf{g}_{mn}$ : then, the necessary covariance matrices can be estimated by spatial averaging. The number  $K$  of summands subject to the averaging should be chosen to be as high as possible to achieve an adequate estimation. In this case, this results in the following estimation  $\hat{\mathbf{a}}$  of the vector of the AR coefficients:

$$\hat{\mathbf{a}} = \left( \sum_{m,n} \gamma_{mn} \gamma_{mn}^T \right)^{-1} \sum_{m,n} \gamma_{mn} g_{mn}. \quad (13.27)$$

This is a second-order statistic, as all summands are products of two image values of two generally different positions (cf. Sec. 13.1.3). The remaining parameter  $\sigma^2$  can now be estimated using (13.23), this coefficient vector, and the assumed ergodicity:

$$\hat{\sigma}^2 = \frac{1}{K} \sum_{m,n} g_{mn}^2 - \frac{2}{K} \hat{\mathbf{a}}^T \sum_{m,n} \gamma_{mn} g_{mn} + \frac{1}{K} \hat{\mathbf{a}}^T \sum_{m,n} \gamma_{mn} \gamma_{mn}^T \hat{\mathbf{a}}. \quad (13.28)$$

As on the right-hand side of (13.26), both  $E\{\gamma_{mn} \gamma_{mn}^T\}$  and  $E\{\gamma_{mn} \mathbf{g}_{mn}\}$  are matrices which contain only the values of the autocovariance function of  $\mathbf{g}_{mn}$ , the Wiener–Khinchin theorem 8.16 implies that AR models neither contain nor model any phase information. This is why AR models can be used for modeling statistical structures but are inapplicable to scenic images, as for them, the phase information is of particular importance (see Sec. 8.3.9.3).

If AR models are used for texture analysis,  $\mathbf{g}_{mn}$  denotes the image of the texture. After the parameters have been estimated from a sample of images of a texture, the model can be used for texture synthesis.

---

**Example 13.6 (AR model of a honing texture):** For the honing texture of Ex. 13.5, an AR model of order 84 has been estimated using a sample of texture images. Figure 13.14(c) shows an image synthesized using this model. The structural-statistical model (13.15) looks

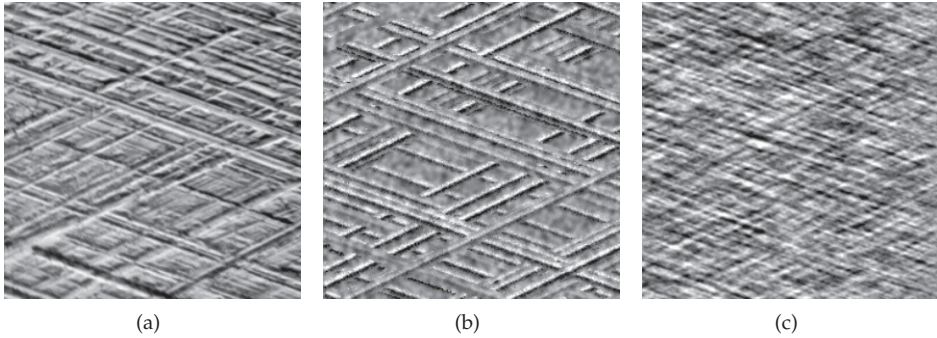


**Figure 13.14.** Synthesis of honing textures: (a) Original image of a honed surface [2]; (b) Synthesized texture using the structural-statistical model (13.15); (c) Synthesized texture using the AR model.

better in terms of a qualitative visual comparison. This is because it contains much more model information about the properties of the honing texture than the generally usable AR model. Therefore, notably fewer parameters have to be estimated from the given sample. However, for some applications, the results of the AR model can be sufficient, as it requires no specialized modeling and can easily be adjusted to suit other textures. ■

The advantage of the AR model is that it is easy to fit it to different textures. For an actual application, the suitability of the model can be evaluated by, e.g., judging the synthesized textures. The use of AR models for defect detection is covered in Sec. 14.2.

### ▶ 13.3.4 Separation of line textures

In this section, the separation of line textures is presented as an example of a complex image processing method [3,6]. This approach illustrates how methods from Chap. 8 can be combined in a smart way.

Let the image  $g(\mathbf{x})$  be additively<sup>1</sup> composed of the line texture  $t(\mathbf{x})$  and the ‘background’  $h(\mathbf{x})$ :

$$g(\mathbf{x}) = t(\mathbf{x}) + h(\mathbf{x}). \quad (13.29)$$

Now, the two additive signals are to be separated, i.e.,  $t(\mathbf{x})$  and  $h(\mathbf{x})$  are to be obtained. If the method is applied to the honing texture from Ex. 13.5, then  $t(\mathbf{x})$  corresponds to the texture model (13.15) and  $h(\mathbf{x})$  represents the image content which is not described by the texture model. The background is only assumed to have no predominant direction. After the separation, the background signal  $h(\mathbf{x})$  contains differences from the honing texture. This is why it can be used for the detection of defects caused by the honing process or which were already present in the material before the actual honing (Fig. 13.15). Conversely, texture parameters, like the groove angle, can be more reliably estimated from the separated texture signal  $t(\mathbf{x})$ .

The first step is to consider the superposition of a single line with the background. A line in an image can be modeled by a function  $l(\mathbf{x}^T \mathbf{e} - d)$  with the normal vector

<sup>1</sup>In the case of a multiplicative superposition  $g(\mathbf{x}) = t(\mathbf{x}) h(\mathbf{x})$ , the method can be applied to the logarithm of the image signal  $\log g(\mathbf{x})$  (cf. Sec. 9.2.2.3).

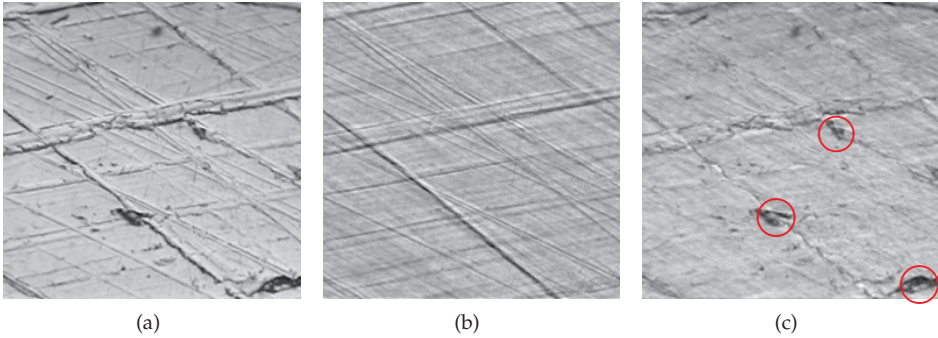


**Figure 13.15.** Separation of grooves and background of a honing texture: (a) Original image  $g(\mathbf{x})$  (from [2]), (b) Line texture  $\hat{l}(\mathbf{x})$ , (c) Background  $\hat{h}(\mathbf{x})$  with marked defects.

$\mathbf{e} = (\cos \alpha, \sin \alpha)^T$  and the distance  $d$  of the line to the origin, as in Ex. 13.5. The separation of the texture can be performed in the spatial frequency domain. The Fourier transform of the image signal is given by

$$g(\mathbf{x}) = l(\mathbf{x}^T \mathbf{e} - d) + h(\mathbf{x}) \quad (13.30)$$

$$\begin{array}{c} \Downarrow \\ G(\mathbf{f}) = L(\mathbf{f}^T \mathbf{e}) \delta(\mathbf{f}^T \mathbf{p}) e^{-j2\pi d \mathbf{f}^T \mathbf{e}} + H(\mathbf{f}) \end{array} \quad (13.31)$$

with the one-dimensional Fourier transform  $L(\eta)$  of the line profile  $l(\xi)$ ,

$$L(\eta) = \int_{-\infty}^{\infty} l(\xi) e^{-j2\pi \eta \xi} d\xi, \quad (13.32)$$

and the unit vector  $\mathbf{p}$  perpendicular to  $\mathbf{e}$ :

$$\mathbf{p} \perp \mathbf{e}, \quad \|\mathbf{p}\| = 1 \quad \Rightarrow \quad \mathbf{p} = \begin{pmatrix} -\sin \alpha \\ \cos \alpha \end{pmatrix}. \quad (13.33)$$

The dependency on the distance  $d$  from the line and the origin is omitted by calculating the magnitude spectrum:

$$|G(\mathbf{f})| \approx |L(\mathbf{f}^T \mathbf{e})| \delta(\mathbf{f}^T \mathbf{p}) + |H(\|\mathbf{f}\|)|. \quad (13.34)$$

In this magnitude spectrum, the line is shaped like a slice function, which is perpendicular to the line in the spatial domain (Fig. 13.16). Calculating the absolute value separately for every single summand represents a good approximation, as always either the first summand dominates the second summand (in the case of  $\mathbf{f}^T \mathbf{p} = 0$ ) or it vanishes (in the case  $\mathbf{f}^T \mathbf{p} \neq 0$ ). The background is assumed to be broadband, so that its magnitude spectrum is approximately rotationally symmetric, i.e., depends only on the distance  $\|\mathbf{f}\|$  to the origin. After a transformation into polar coordinates, the spectrum of the line turns into an axis-parallel structure with the distance  $\alpha$  to the axis of the radius (Fig. 13.16(c)):

$$\begin{pmatrix} f_x \\ f_y \end{pmatrix} \mapsto \rho \begin{pmatrix} \cos \phi \\ \sin \phi \end{pmatrix}, \quad \rho \in \mathbb{R}, \quad \phi \in [0, \pi). \quad (13.35)$$

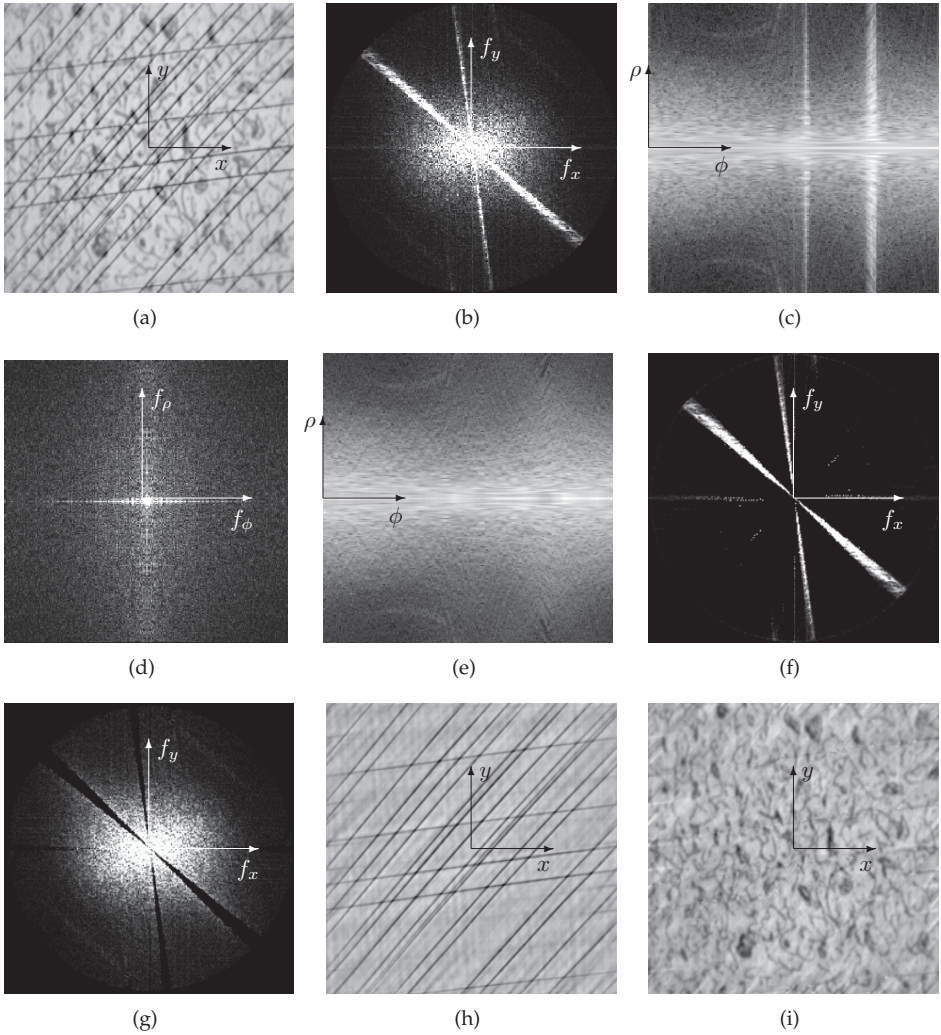


**Figure 13.16.** Separation of line textures: (a) Original image  $g(\mathbf{x})$ ; (b) Magnitude spectrum  $|G(\mathbf{f})|$ ; (c) Magnitude spectrum in polar coordinates, using a logarithmic scale  $\log(1 + |G(\rho \cos \phi, \rho \sin \phi)|)$ ; (d) Absolute value of the Fourier transform  $\mathcal{F}_{\phi, \rho}\{\rho G(\rho \cos \phi, \rho \sin \phi)\}$ ; (e) Estimated magnitude spectrum of the background, represented in polar coordinates  $\log(1 + |\widehat{H}_{\phi, \rho}(\phi, \rho)|)$ ; (f) Estimated magnitude spectrum of the line texture  $|\widehat{T}(\mathbf{f})|$ ; (g) Estimated magnitude spectrum of the background  $|\widehat{H}(\mathbf{f})| = |G(\mathbf{f})| - |\widehat{T}(\mathbf{f})|$ ; (h) Estimated line texture  $\widehat{t}(\mathbf{x})$ ; (i) Estimated background of the image  $\widehat{h}(\mathbf{x})$ .

Because of (13.33), this coordinate transformation results in the following expression for the factor  $\delta(\mathbf{f}^T \mathbf{p})$  in (13.34):

$$\delta(\mathbf{f}^T \mathbf{p}) = \delta(\rho(\sin \phi \cos \alpha - \cos \phi \sin \alpha)) = \underbrace{\delta(\rho \sin(\phi - \alpha))}_{=: a(\phi)}. \quad (13.36)$$

The argument  $a(\phi)$  of the Dirac delta function has a simple root at  $\phi = \alpha$ . The formulas for Dirac delta functions (shown in Table 8.1) result in

$$\delta(a(\phi)) = \frac{1}{\left| \frac{da}{d\phi} \right|} \Big|_{\phi=\alpha} \delta(\phi - \alpha). \quad (13.37)$$

One has

$$\frac{da}{d\phi} = \rho \cos(\phi - \alpha), \quad \left| \frac{da}{d\phi} \right| \Big|_{\phi=\alpha} = |\rho| \quad (13.38)$$

and hence

$$\delta(\mathbf{f}^T \mathbf{p}) = \frac{\delta(\phi - \alpha)}{|\rho|}. \quad (13.39)$$

The factor  $L(\mathbf{f}^T \mathbf{e})$  of (13.34) is given by

$$L(\mathbf{f}^T \mathbf{e}) = L(\rho(\cos \phi \cos \alpha + \sin \phi \sin \alpha)). \quad (13.40)$$

As this factor is multiplied by the Dirac delta function (13.39), only its value for the angle  $\phi = \alpha$  is needed (cf. Table 8.1). In this case, it is  $\mathbf{f}^T \mathbf{e} = \rho$  in (13.40), so that the expression

$$L(\mathbf{f}^T \mathbf{e}) \Big|_{\phi=\alpha} = L(\rho) \quad (13.41)$$

can be used. Therefore, the polar coordinate representation of (13.34) can be written as

$$|G(\rho \cos \phi, \rho \sin \phi)| \approx |L(\rho)| \frac{\delta(\phi - \alpha)}{|\rho|} + |H(\rho)|, \quad \rho \neq 0. \quad (13.42)$$

Because of the polar transformation, the spectral components corresponding to the line are mapped to a line-shaped structure perpendicular to the  $\phi$ -axis and the background is mapped to a broadband structure parallel to the  $\phi$ -axis. In order to achieve a better separability of these signal components, another Fourier transform is applied with respect to the polar coordinates. Prior to this, the magnitude spectrum is multiplied by  $|\rho|$ , in order to reduce the signal's dynamic range. This results in

$$\mathcal{F}_{\phi, \rho}\{\rho G(\rho \cos \phi, \rho \sin \phi)\} \quad (13.43)$$

$$\approx \mathcal{F}_{\rho}\{|L(\rho)|\} \mathcal{F}_{\phi}\left\{\sum_{k=-\infty}^{\infty} \delta(\phi - \alpha - k\pi)\right\} + \mathcal{F}_{\phi, \rho}\{|\rho H(|\rho|)\} \quad (13.44)$$

$$\approx \mathcal{F}_{\rho}\{|L(\rho)|\} \frac{1}{\pi} \sum_{k=-\infty}^{\infty} \delta(f_{\phi} - \frac{k}{\pi}) e^{-j2\pi f_{\phi} \alpha} + \mathcal{F}_{\rho}\{|\rho H(|\rho|)\} \delta(f_{\phi}). \quad (13.45)$$

It has to be mentioned that the magnitude spectrum  $|G(\rho \cos \phi, \rho \sin \phi)|$  is repeated with a period of  $\pi$  (with respect to  $\phi$ ) if it is transformed into polar coordinates. An alternative implementation of this step can be obtained using the logarithm of the signal [6].

Now, the two components of the line and the background approximately belong to two orthogonal subspaces: the background is located on the  $f_\rho$ -axis, while the line is mainly located along the  $f_\phi$ -axis, see Fig. 13.16(d). The supports of these subspaces neither depend on the distance  $d$  to the origin nor on the angle  $\alpha$ , so that the presented relations apply to an arbitrary line of the texture. Hence, the method can not only be used for a single line, but for a texture consisting of many lines with different angles and different distances from the origin.

Now, a separation of the two components is possible in the  $(f_\phi, f_\rho)$ -space. In order to isolate the background component, the components which are inside a rectangle around the  $f_\phi$ -axis are suppressed, and only the components from this rectangle and along the  $f_\rho$ -axis are preserved. This can be realized with a multiplication by a binary mask  $M(f_\phi, f_\rho)$  (cf. Fig. 13.17):

$$\widehat{H}_{\phi,\rho}(f_\phi, f_\rho) = \mathcal{F}_{\phi,\rho}\{|\rho G(\rho \cos \phi, \rho \sin \phi)|\} M(f_\phi, f_\rho). \tag{13.46}$$

As, for this purpose, the parameters of the line do not have to be known, a so-called blind separation can be performed. After an inverse Fourier transform  $\mathcal{F}_{\phi,\rho}^{-1}$  and a transformation back into Cartesian coordinates, this method yields an estimation  $|\widehat{H}(\mathbf{f})|$  of the magnitude spectrum of the background signal.

However, the image signal  $h(\mathbf{x})$  cannot be reconstructed, as the phase information is missing. Instead,  $|\widehat{H}(\mathbf{f})|$  is used for a decision criterion, which performs a spectral decomposition in the spatial frequency domain. This results in the following estimation of the texture components:

$$\widehat{T}(\mathbf{f}) := \begin{cases} G(\mathbf{f}) & \text{if } \frac{|G(\mathbf{f})|}{|\widehat{H}(\mathbf{f})|} > \sqrt{2} \\ 0 & \text{otherwise.} \end{cases} \tag{13.47}$$

For every spatial frequency, it is decided whether the corresponding spectral value contributes to the line texture or rather to the background. The spectral components for which the texture signal exceeds the estimated background signal are preserved and all others are

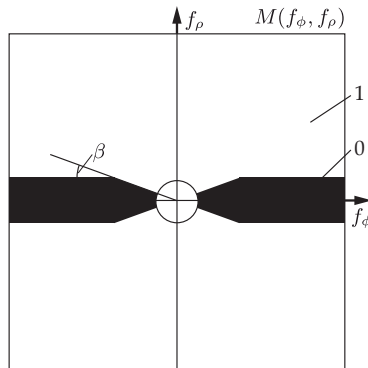
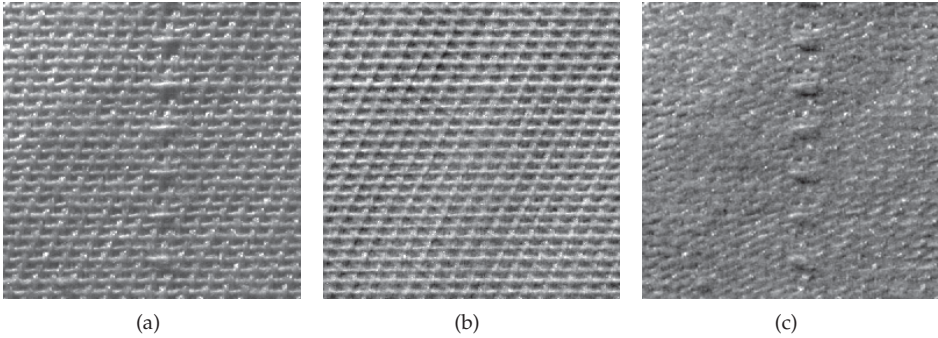


Figure 13.17. Mask for suppressing the line structure in the  $(f_\phi, f_\rho)$ -space.



**Figure 13.18.** Separation of the line texture from the background of a textile: (a) Original image  $g(\mathbf{x})$  (from [7]); (b) Line texture  $\hat{t}(\mathbf{x})$ ; (c) Background  $\hat{h}(\mathbf{x})$  with clearly visible defects.

set to zero, see Fig. 13.16(f). An estimation of the background spectrum  $\hat{H}(\mathbf{f})$  is given by

$$\hat{H}(\mathbf{f}) = G(\mathbf{f}) - \hat{T}(\mathbf{f}). \quad (13.48)$$

This separation rule is similar to a linear filtering of the image using two complementary binary transfer functions. The optimal design of this transfer function leads to the decision rule (13.47) and especially to the threshold  $\sqrt{2}$  [6].

Now, the inverse transformation of (13.47) yields an estimation of the separated texture (Fig. 13.16(h)):

$$\hat{t}(\mathbf{x}) = \mathcal{F}^{-1}\{\hat{T}(\mathbf{f})\}. \quad (13.49)$$

Because of (13.29), the separated image background is estimated by

$$\hat{h}(\mathbf{x}) = g(\mathbf{x}) - \hat{t}(\mathbf{x}). \quad (13.50)$$

The estimated background signal can now be used in a further processing step, e.g., for the detection of defects. Besides the already mentioned honing textures, the analysis of the grooves of firearms and the detection of defects in textiles (Fig. 13.18) are possible applications.

## 13.4 Feature-based texture analysis

For texture analysis, it is not necessary to use an explicit model of the texture. Alternatively, features with a general definition can be used, which are not designed to suit one specific texture. With these features, the texture can be characterized and differences from a reference image can be detected. A texture feature can be applied globally to the whole image of the texture or to a local region of the image. Global features provide information about the mean properties of the texture and can be used, e.g., for the classification of textures. Local features only describe a small region of the image and are therefore suitable for detecting defects with a spatially limited extent. In this section, some of the classic texture features will be discussed [22, 25, 27]. Most of these features can be efficiently calculated.

➤ **13.4.1 Basic statistical texture features**

Basically, any statistical moments can be used as texture features. As mentioned in Sec. 13.1.3, especially first and second order moments are suitable. The mean gray value as an empiric average is a first order moment:

$$m_1 = \frac{1}{|\Omega_t|} \int_{\Omega_t} t(\mathbf{x}) \, d\mathbf{x}. \tag{13.51}$$

As the domain  $\Omega_t$  of the texture is subject to the integration, all pixel positions which are part of the image of the texture will be integrated. The first order second moment is the empirical variance:

$$s^2 = \frac{1}{|\Omega_t|} \int_{\Omega_t} (t(\mathbf{x}) - m_1)^2 \, d\mathbf{x}. \tag{13.52}$$

The empirical variance is a measure of the contrast in the image.

For anisotropic textures, features which characterize orientations, like the angles of the predominant directions, are suitable. Further, there are measures of anisotropy, e.g., the mean difference of the eigenvalue of the structure tensor from Sec. 11.3.4.

Besides, a measure for the granularity of a textures can be defined. An example is the correlation length  $\|\tau\|$ , which is the length of the vector  $\tau$  for which the autocorrelation function  $r_{tt}(\tau)$  of the image of an isotropic texture is less than or equal to  $e^{-1}$ .

In the literature, there are various features which are often obtained from the histogram (a first order statistic) or from an estimation of second order probability densities (i.e., by statistically evaluating pairs of pixels). Some of these features will be covered in the remaining part of this chapter. Furthermore, specific features can be defined for many applications.

**Example 13.7 (Groove angles of a honing texture):** Here, the groove angle  $\varphi$  denotes the direction of the normal vector of the groove, cf. Ex. 13.5. In the Fourier transform  $T(\mathbf{f})$  of the texture image, the predominant directions of a honing texture produce high spectral values along lines through the origin that are perpendicular to the predominant directions, i.e., in the direction  $\varphi$  of the normal, see Figs. 13.19(a) and (b) (cf. Chap. 8). A projection

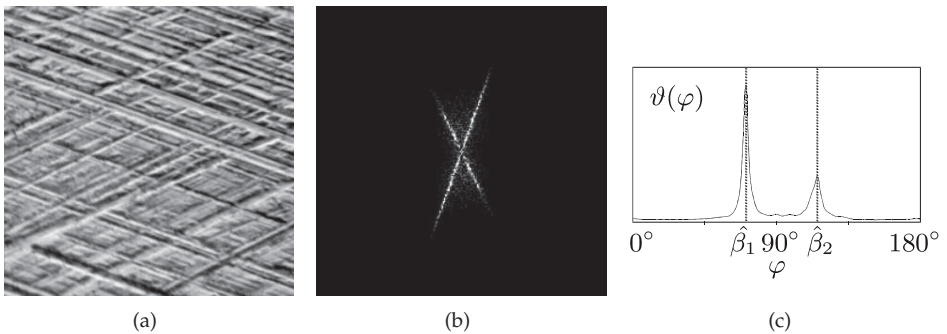


**Figure 13.19.** Groove angle as a feature of a honing texture: (a) Honing texture  $t(\mathbf{x})$  [2]; (b) Magnitude of the discrete Fourier transform  $|T(\mathbf{f})|$ ; (c) Projection function  $v(\varphi)$  [5].



along lines through the origin in direction  $(\cos \varphi, \sin \varphi)^T$  yields a function  $\vartheta(\varphi)$ , which represents the distribution of the signal energy of the texture as a function of the groove angle  $\varphi$ :

$$\vartheta(\varphi) := \int_0^\infty \int_{-\infty}^\infty |T(\mathbf{f})|^2 \delta((-\sin \varphi, \cos \varphi)\mathbf{f}) \, d f_x \, d f_y. \tag{13.53}$$

The positions of the maxima  $\hat{\beta}_1$  and  $\hat{\beta}_2$  of the projection function  $\vartheta(\varphi)$  correspond to the two predominant directions of the honing texture, which are expressed as angles of the normal vectors of the grooves, cf. Fig. 13.19(c) [5]. ■

➤ 13.4.2 Co-occurrence matrix

Co-occurrence matrices describe spatial dependencies in a gray-scale image [10,11,13]. They are special histograms for the values of pairs of pixels and therefore represent second order statistics.

Co-occurrence matrices are defined with regard to the offset vector  $\mathbf{d}$  that describes the relative position of the two pixels under consideration. The elements  $c'_{\mathbf{d},ij}$  of the co-occurrence matrices  $\mathbf{C}'_{\mathbf{d}}$  are calculated as follows:

$$c'_{\mathbf{d},ij} := |\{(x_1, x_2) \in \Omega_g^2 \mid x_2 = x_1 + \mathbf{d}, g(x_1) = i, g(x_2) = j\}| \in \mathbb{N}_0. \tag{13.54}$$

The element  $(i, j)$  of a co-occurrence matrix denotes the number of points  $\mathbf{x}$  in the image for which  $g(\mathbf{x}) = i$  and  $g(\mathbf{x} + \mathbf{d}) = j$  (Fig. 13.20). As the elements of the matrix represent absolute frequencies, they are natural numbers. The row and column indices of a co-occurrence matrix correspond to the gray values, which is why the numbering usually starts with zero. If the gray value is quantized with  $K$  quantization steps, the co-occurrence matrices have a size of  $K \times K$ :  $\mathbf{C}'_{\mathbf{d}} \in \mathbb{N}_0^{K \times K}$ .

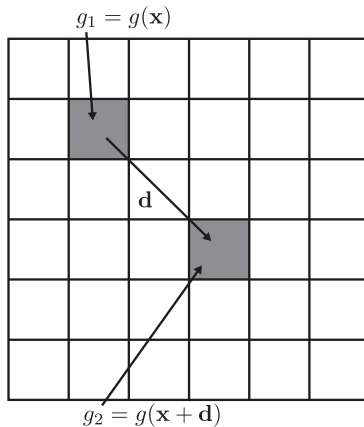


Figure 13.20. Definition of the co-occurrence matrix. The entry  $c'_{\mathbf{d},g_1g_2}$  of a co-occurrence matrix denotes the number of points  $\mathbf{x}$  in the image for which  $g(\mathbf{x}) = g_1$  and  $g(\mathbf{x} + \mathbf{d}) = g_2$ .

**Example 13.8 (Co-occurrence matrices):** In order to exemplify this definition, a simple example of a  $4 \times 4$ -image with  $K = 3$  quantization steps is considered. The image  $g(\mathbf{x})$  is assumed to be

$$\begin{array}{|c|c|c|c|} \hline 1 & 1 & 0 & 0 \\ \hline 1 & 1 & 0 & 0 \\ \hline 0 & 0 & 2 & 2 \\ \hline 0 & 0 & 2 & 2 \\ \hline \end{array}. \quad (13.55)$$

The co-occurrence matrices for the horizontal, vertical, and diagonal offset vectors  $(1, 0)^T$ ,  $(0, 1)^T$ ,  $(1, 1)^T$ , and  $(1, -1)^T$  are given by

$$\mathbf{d} = \begin{pmatrix} 1 \\ 0 \end{pmatrix}, \quad \mathbf{C}'_{\mathbf{d}} = \begin{pmatrix} 4 & 0 & 2 \\ 2 & 2 & 0 \\ 0 & 0 & 2 \end{pmatrix}, \quad (13.56)$$

$$\mathbf{d} = \begin{pmatrix} 0 \\ 1 \end{pmatrix}, \quad \mathbf{C}'_{\mathbf{d}} = \begin{pmatrix} 4 & 0 & 2 \\ 2 & 2 & 0 \\ 0 & 0 & 2 \end{pmatrix}, \quad (13.57)$$

$$\mathbf{d} = \begin{pmatrix} 1 \\ 1 \end{pmatrix}, \quad \mathbf{C}'_{\mathbf{d}} = \begin{pmatrix} 2 & 0 & 2 \\ 2 & 1 & 1 \\ 0 & 0 & 1 \end{pmatrix}, \quad (13.58)$$

$$\mathbf{d} = \begin{pmatrix} 1 \\ -1 \end{pmatrix}, \quad \mathbf{C}'_{\mathbf{d}} = \begin{pmatrix} 3 & 1 & 1 \\ 1 & 1 & 0 \\ 1 & 0 & 1 \end{pmatrix}. \quad (13.59)$$

For example, the first co-occurrence matrix describes the co-occurrences between horizontally adjacent points. The value  $c'_{\mathbf{d},00} = 4$  implies that there are four instances in the image where a pixel with a gray value 0 has an adjacent pixel to its right with a gray value 0. A pixel with a gray value of 0 is the right neighbor of a pixel with a gray value of 1 two times, which is why  $c'_{\mathbf{d},10} = 2$ , and so on.

For this example, the horizontal and the vertical co-occurrence matrix are identical, as the image is symmetric with respect to the main diagonal:  $g(x, y) = g(y, x)$ . ■

A co-occurrence matrix can be normalized by dividing it by the sum of its entries:

$$\mathbf{C}_{\mathbf{d}} = \frac{1}{\mathbf{1}^T \mathbf{C}'_{\mathbf{d}} \mathbf{1}} \mathbf{C}'_{\mathbf{d}}. \quad (13.60)$$

The term in the denominator corresponds to the sum of all the entries of the matrix, which is independent of the gray values in the considered image. Depending on the size of the image and on the offset vector  $\mathbf{d}$ , a certain amount of pixels at the border of the image cannot be considered. After the normalization, the entries of  $\mathbf{C}_{\mathbf{d}}$  sum to 1. The entries of the matrix are all inside of the interval  $[0, 1]$ . They represent relative frequencies and can be interpreted as estimations of the corresponding second order joint probabilities.

The co-occurrence matrices considered until now depend on the sign of the offset vector  $\mathbf{d}$ . In general, the negated offset  $-\mathbf{d}$  yields a different result. If these differences are not relevant for the inspection task, both matrices can be added together to result in a matrix

which is symmetric with respect to the offset direction:

$$\mathbf{C}_{\pm\mathbf{d}} = \mathbf{C}_{\mathbf{d}} + \mathbf{C}_{-\mathbf{d}}. \quad (13.61)$$

Instead of the direction, only the orientation of the structures in the image is taken into consideration, cf. Def. 11.3.

Co-occurrence matrices characterize important texture characteristics. However, they are of relatively high dimensions and are usually not directly used for texture analysis. In fact, features are used that are defined on the basis of the co-occurrence matrices. These include the well-known Haralick features, of which some will now be presented [10, 32]. They are calculated from normalized co-occurrence matrices according to (13.60).

– Energy:

$$\sum_{i=0}^{K-1} \sum_{j=0}^{K-1} c_{\mathbf{d},ij}^2 \quad (13.62)$$

– Entropy:

$$- \sum_{i=0}^{K-1} \sum_{j=0}^{K-1} c_{\mathbf{d},ij} \text{ld}(c_{\mathbf{d},ij}) \quad (13.63)$$

– Contrast:

$$\sum_{i=0}^{K-1} \sum_{j=0}^{K-1} |i-j|^a c_{\mathbf{d},ij}^b \quad (13.64)$$

Typically, the parameters  $a = 2$  and  $b = 1$  are chosen.

– Maximum probability:

$$\max_{i,j} c_{\mathbf{d},ij} \quad (13.65)$$

– Inverse difference moment of order  $\kappa$ :

$$\sum_{i=0}^{K-1} \sum_{j=0}^{K-1} \frac{c_{\mathbf{d},ij}}{1 + |i-j|^\kappa} \quad (13.66)$$

For  $\kappa = 1$ , this feature is also called ‘homogeneity’.

– Correlation:

$$\sum_{i=0}^{K-1} \sum_{j=0}^{K-1} \frac{ij c_{\mathbf{d},ij} - m_i^R m_j^C}{s_i^R s_j^C} \quad (13.67)$$

Here,  $m_i^R$ ,  $m_j^C$  denote the empirical mean values,  $s_i^R$ ,  $s_j^C$  denote the empirical standard deviations (cf. Sec. 13.4.1) of the row sums and column sums

$$\mathbf{c}_{\mathbf{d},i}^R = \sum_{j=0}^{K-1} c_{\mathbf{d},ij} \quad \text{and} \quad \mathbf{c}_{\mathbf{d},j}^C = \sum_{i=0}^{K-1} c_{\mathbf{d},ij}, \quad (13.68)$$

which can be interpreted as the marginal distributions of the co-occurrence probabilities. These features can be used as a basis for texture classification. Alternatively, a feature vector can be constructed as follows [10]: First, the symmetric, normalized co-occurrence matrices

of the whole image region  $\Omega_t$  of the texture are calculated for the four offset directions of Ex. 13.8. Next, some features can be extracted from each of the four co-occurrence matrices. For each feature, the mean value and the variance are calculated with respect to the offset  $\mathbf{d}$ . By this means, a certain rotational invariance can be achieved. The resulting mean values and variances now represent the feature vector which can be used for a subsequent classification.

The best choice of orientations and lengths of the offset vectors for a certain application is not obvious. A possible approach to determining the best offset vectors is to perform some statistical tests. For example, the vector that maximizes the  $\chi^2$  test can be used as an offset vector:

$$\chi^2(\mathbf{d}) = \sum_{i=0}^{K-1} \sum_{j=0}^{K-1} \frac{c_{\mathbf{d},ij}^2}{c_{\mathbf{d},i}^R c_{\mathbf{d},j}^C}. \quad (13.69)$$

Then, the entries of the co-occurrence matrices calculated with  $\mathbf{d}$  as well as their row sums and column sums of (13.68) have to be inserted into this equation. The  $\chi^2$  test yields the offset  $\mathbf{d}$  for which there is a maximum statistical dependency between the respective pairs of pixels. In order to take into account the two dimensions of the texture, at least one further offset direction  $\mathbf{d}_2$  should be considered, which could be chosen, e.g., to be orthogonal to  $\mathbf{d}$ .

### 13.4.3 Histogram of oriented gradients

The histogram of oriented gradients is a possible approach to obtain information about the anisotropy of a texture [29]. This method can be used to determine the predominant directions of a texture and to discriminate between anisotropic textures and isotropic textures.

The histogram of oriented gradients is a histogram of the gradient orientations present in the image  $g(\mathbf{x})$ . Thus, the gradient orientation has to be estimated at every pixel. The gradient  $\text{grad } g(\mathbf{x}) = (g_x(\mathbf{x}), g_y(\mathbf{x}))^T$  can be estimated by different linear filters (see Sec. 11.2). From these derivatives, the orientation  $\theta(\mathbf{x})$  and the norm  $u(\mathbf{x})$  of the gradient at the image pixel  $\mathbf{x}$  can be estimated:

$$\theta(\mathbf{x}) := \arctan \frac{g_y(\mathbf{x})}{g_x(\mathbf{x})} \in [0, \pi), \quad (13.70)$$

$$u(\mathbf{x}) := \|\text{grad } g(\mathbf{x})\| = \sqrt{(g_x(\mathbf{x}))^2 + (g_y(\mathbf{x}))^2}. \quad (13.71)$$

The only pixels which are considered in the calculation of the histogram of oriented gradients are those for which  $u(\mathbf{x})$  exceeds a fixed threshold  $u_{\min}$ , as the direction of low gradients cannot be reliably estimated because of the noise. The gradient direction is quantized into  $K$  equidistant intervals of a width of  $\Delta\theta$ . For each interval, the histogram tells how often the respective gradient direction is present in the image. The absolute frequencies are given by

$$N_\theta(k) := |\{\mathbf{x} \in \Omega_t \mid k \Delta\theta \leq \theta(\mathbf{x}) < (k+1) \Delta\theta \wedge u(\mathbf{x}) > u_{\min}\}|, \quad (13.72)$$

$$\Delta\theta := \frac{\pi}{K}, \quad k = 0, \dots, K-1.$$

Now a normalization is performed in order to obtain the relative frequencies, so that the scaling of the histogram is independent of the size of the image region and of the number of

the pixels considered:

$$H_{\theta}(k) := \frac{N_{\theta}(k)}{\sum_{l=0}^{K-1} N_{\theta}(l)}, \quad k = 0, \dots, K-1. \quad (13.73)$$

Several alternatives are possible when defining these histograms. First of all, the gradient direction  $\in [0, 2\pi)$  can be used instead of the orientation  $\theta \in [0, \pi)$ . In another variant, the magnitudes  $u(\mathbf{x})$  of the gradients of a direction are summed [20], instead of counting the number of the gradients exceeding the threshold  $u_{\min}$ . Then, stronger gradients receive a higher weight.

The histogram of oriented gradients of an anisotropic texture shows a distinctive maximum, which determines the predominant direction of the texture. If there are multiple similarly high maxima, the texture has no predominant direction. Isotropic textures have a flat histogram.

Besides the rather simple evaluation of the maxima, further features, such as the energy, entropy, etc., can be calculated from the histogram of oriented gradients and can be used for the analysis and classification of the texture. Histograms of oriented gradients can also be directly used as a feature vector for a classifier.

For the classification of objects in images, the histograms of oriented gradients of overlapping local windows can be calculated and classified. By an additional normalization, a better invariance with respect to contrast and illumination conditions can be achieved [8].

#### ► 13.4.4 Run-length analysis

The run-length analysis of a texture provides information about the local structure of the texture. A run is a set of pixels that have the same gray values and are directly adjacent with respect to a direction  $\mathbf{d}$  [9]. In general, the gray values do not have to be exactly identical but only within the same interval of an additional quantization scale [33]. These quantization steps are denoted by  $g \in \{0, 1, \dots, g_{\max}\}$ . For a run-length analysis, the histograms  $B_{\mathbf{d}}(g, r)$  are calculated over the number of runs with a certain length  $r$  and within a certain interval  $g$  of gray values. Similar to the co-occurrence matrices from Sec. 13.4.2, the direction  $\mathbf{d}$  can be chosen, however, in this case, the sign of the vector  $\mathbf{d}$  is irrelevant. The histograms characterize the local consistency of the texture. By this means, textures consisting of coarse structures can be discriminated from fine-structured textures. However, the run-length features are said to be susceptible to noisy image signals [33].

Based on run-length histograms, features can be defined that can be used for, e.g., texture classification. Let  $r_{\max}$  denote the maximum length of a run present in the histogram and let  $r_{\text{total}}$  denote the total number of runs,

$$r_{\text{total}} = \sum_{g=0}^{g_{\max}} \sum_{r=1}^{r_{\max}} B_{\mathbf{d}}(g, r). \quad (13.74)$$

At first, it might be interesting to see whether short or long runs are predominant. The feature 'short runs emphasis' emphasizes the short runs independently of their gray values, and normalized with respect to the total number of runs:

$$\frac{1}{r_{\text{total}}} \sum_{g=0}^{g_{\max}} \sum_{r=1}^{r_{\max}} \frac{B_{\mathbf{d}}(g, r)}{r^2}. \quad (13.75)$$

Conversely, longer runs are put into focus by the ‘long runs emphasis’ feature:

$$\frac{1}{r_{\text{total}}} \sum_{g=0}^{g_{\text{max}}} \sum_{r=1}^{r_{\text{max}}} B_{\mathbf{d}}(g, r) r^2. \quad (13.76)$$

The ‘inhomogeneity of the gray values’ can be evaluated as follows:

$$\frac{1}{r_{\text{total}}} \sum_{g=0}^{g_{\text{max}}} \left( \sum_{r=1}^{r_{\text{max}}} B_{\mathbf{d}}(g, r) \right)^2. \quad (13.77)$$

This feature is minimal if the number of runs is uniformly distributed over all gray values.

The ‘inhomogeneity of the run lengths’ provides information about the distribution of the run lengths, independently of their gray value:

$$\frac{1}{r_{\text{total}}} \sum_{r=1}^{r_{\text{max}}} \left( \sum_{g=0}^{g_{\text{max}}} B_{\mathbf{d}}(g, r) \right)^2. \quad (13.78)$$

It is minimal if the number of runs is uniformly distributed over all run lengths.

The ‘run density’ is defined as the quotient of the total number of runs by the number of pixels:

$$\frac{r_{\text{total}}}{\sum_{g=0}^{g_{\text{max}}} \sum_{r=1}^{r_{\text{max}}} B_{\mathbf{d}}(g, r) r} = \frac{r_{\text{total}}}{MN}. \quad (13.79)$$

It is equal to one if the texture contains exclusively runs of length one. The longer the runs, the lower the run density. Thus, it is a measure of the amount of linear structures with an orientation  $\mathbf{d}$ .

### ► 13.4.5 Laws’ texture energy measures

Laws’ texture energy measures represent further classical features for texture classification [13, 18, 19]. They are obtained by a convolution of the gray-scale image  $g(\mathbf{x})$  with the so-called Laws matrices. These matrices are defined as the dyadic products of certain vectors. The matrices and vectors represent the impulse responses of linear, shift-invariant systems, i.e., linear filters expressed in matrix notation. The elementary vectors are given by

$$\mathbf{l}_3 = \begin{pmatrix} 1 \\ 2 \\ 1 \end{pmatrix}, \quad \mathbf{e}_3 = \begin{pmatrix} -1 \\ 0 \\ 1 \end{pmatrix}, \quad \mathbf{s}_3 = \begin{pmatrix} -1 \\ 2 \\ -1 \end{pmatrix}. \quad (13.80)$$

The first filter  $\mathbf{l}_3$  is a binomial low-pass filter, so that the result of the convolution contains only the signal components with low spatial frequencies. The two other filter masks  $\mathbf{e}_3$  and  $\mathbf{s}_3$  have band-pass characteristics and select certain spatial frequencies of the image signal. The filter  $\mathbf{e}_3$  corresponds to the symmetric difference quotient of Sec. 11.2.1 and therefore is an edge operator. The impulse response  $\mathbf{s}_3$  results from the convolution of two asymmetric difference quotients,  $\mathbf{s}_3 = (1, -1)^T * (-1, 1)^T$ , and approximates the second derivative. Further filters of length 5 are the result of convolutions of these elementary impulse responses

of length 3:

$$l_5 = l_3 * l_3 = \begin{pmatrix} 1 \\ 4 \\ 6 \\ 4 \\ 1 \end{pmatrix}, \quad e_5 = l_3 * e_3 = \begin{pmatrix} -1 \\ -2 \\ 0 \\ 2 \\ 1 \end{pmatrix}, \quad (13.81)$$

$$s_5 = l_3 * s_3 = \begin{pmatrix} -1 \\ 0 \\ 2 \\ 0 \\ -1 \end{pmatrix} = -e_3 * e_3, \quad (13.82)$$

$$r_5 = s_3 * s_3 = \begin{pmatrix} 1 \\ -4 \\ 6 \\ -4 \\ 1 \end{pmatrix}, \quad w_5 = s_3 * e_3 = \begin{pmatrix} 1 \\ -2 \\ 0 \\ 2 \\ -1 \end{pmatrix}. \quad (13.83)$$

The Laws matrices represent two-dimensional impulse responses that are the dyadic product of the one-dimensional impulse responses.

**Example 13.9 (Laws matrices):** The dyadic product of the vectors  $e_5$  and  $l_5$  results in the matrix

$$e_5 l_5^T = e_5 ** l_5^T = \begin{pmatrix} -1 \\ -2 \\ 0 \\ 2 \\ 1 \end{pmatrix} \begin{pmatrix} 1 & 4 & 6 & 4 & 1 \end{pmatrix} = \begin{pmatrix} -1 & -4 & -6 & -4 & -1 \\ -2 & -8 & -12 & -8 & -2 \\ 0 & 0 & 0 & 0 & 0 \\ 2 & 8 & 12 & 8 & 2 \\ 1 & 4 & 6 & 4 & 1 \end{pmatrix}. \quad (13.84)$$

The convolution of the gray-scale image of a texture and a Laws matrix results in a feature image, e.g.:

$$\mu_{e_5 l_5^T}(\mathbf{x}) := g(\mathbf{x}) ** (e_5 l_5^T) = \underbrace{(g(\mathbf{x}) ** e_5) ** l_5^T}_{=: \mu_{e_5}(\mathbf{x})}. \quad (13.85)$$

Now, the energy of this feature image is calculated by summing the squared image values, cf. (13.62). It corresponds to the energy of the image signal in different frequency domains, which are selected by the filter masks. In all, the use of multiple Laws matrices provides a set of energy features that can be used for texture classification.

To realize an efficient calculation, the associativity of the convolution can be exploited, so that only convolutions of the image with one-dimensional impulse responses have to be computed, cf. (13.85). Besides, intermediate results, like  $\mu_{e_5}(\mathbf{x})$ , can be reused.

► 13.4.6 Local binary patterns

Local binary patterns (LBPs) represent texture features that are invariant with respect to rotation and monotonic transformations of the gray value [22, 23, 25, 26]. For every point  $\mathbf{x}$ , a certain number of  $P$  image points  $\mathbf{x}_1, \dots, \mathbf{x}_P$  are considered, which are arranged equidistantly on a circle with radius  $R$  around  $\mathbf{x}$  (Fig. 13.21). Now, the differences of the gray values  $g(\mathbf{x}_p)$  of these points from the gray value  $g(\mathbf{x})$  of the reference point are calculated and the signs of these differences are evaluated. The gray values of points which do not exactly lie on the pixel grid are interpolated. The result is a binary vector

$$(H(g(\mathbf{x}_1) - g(\mathbf{x})), \dots, H(g(\mathbf{x}_P) - g(\mathbf{x})))^T \in \{0, 1\}^P, \tag{13.86}$$

where  $H(\cdot)$  denotes the Heaviside function (8.18) and the surrounding points  $\mathbf{x}_p = \mathbf{x}_p(\mathbf{x})$ ,  $p = 1, \dots, P$  are chosen with respect to the reference point  $\mathbf{x}$ . As only the signs of the image value differences are considered, this vector is invariant to monotonic transformations of the image values, which might be caused by, e.g., a homogeneous change of the illumination conditions. This vector can be considered as the binary representation of an integer number of the set  $\{0, 1, \dots, 2^P - 1\}$ .

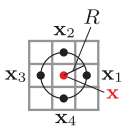
In order to construct a robust, rotation-invariant feature, the number  $U$  of sign changes with respect to a cycle through the binary pattern can be evaluated, for example:

$$U_{P,R}(\mathbf{x}) := \sum_{p=2}^P |H(g(\mathbf{x}_p) - g(\mathbf{x})) - H(g(\mathbf{x}_{p-1}) - g(\mathbf{x}))| + |H(g(\mathbf{x}_P) - g(\mathbf{x})) - H(g(\mathbf{x}_1) - g(\mathbf{x}))|. \tag{13.87}$$

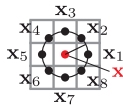
If the binary pattern contains at most one block of positive and at most one block of negative signs, then  $U_{P,R}(\mathbf{x}) \leq 2$ . Such patterns are called uniform. There are  $P + 1$  uniform patterns:

- Two patterns with  $U_{P,R}(\mathbf{x}) = 0$ , which correspond to isolated bright or dark points  $\mathbf{x}$ , as well as to homogeneous areas;
- $P - 1$  patterns with  $U_{P,R}(\mathbf{x}) = 2$ , which represent edges with different curvatures, Fig. 13.22(a).

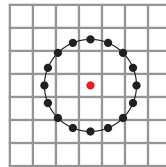
In typical textures, uniform patterns appear much more frequently than non-uniform patterns, so that they can be subject to a robust statistical evaluation [23]. This is why in the following only the uniform patterns will be further investigated and all non-uniform pat-



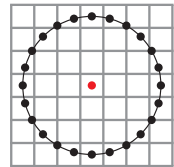
(a)  $P = 4, R = 1$



(b)  $P = 8, R = 1$



(c)  $P = 16, R = 2$



(d)  $P = 24, R = 3$

**Figure 13.21.** Image points for the calculation of the local binary patterns for different values of the number of points  $P$  and the radius  $R$  (adapted from [23]).



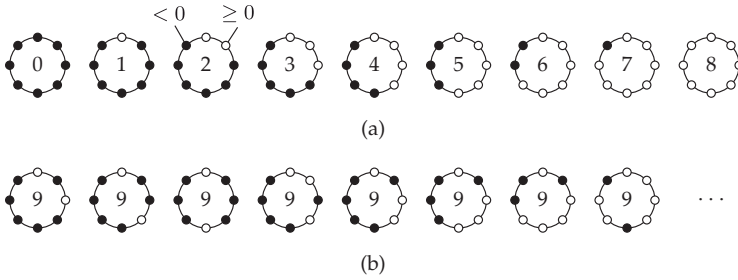


**Figure 13.22.** Local binary patterns for the case  $P = 8$ , normalized with respect to the orientation, and their feature values  $LBP_{8,R}(\mathbf{x})$ : (a) The  $P + 1 = 9$  uniform patterns; (b) Subset of the 27 non-uniform patterns (adapted from [23]).

terns are grouped into one class. This motivates the following definition of the feature:

$$LBP_{P,R}(\mathbf{x}) := \begin{cases} \sum_{p=1}^P H(g(\mathbf{x}_p) - g(\mathbf{x})) & \text{if } U_{P,R}(\mathbf{x}) \leq 2 \\ P + 1 & \text{if } U_{P,R}(\mathbf{x}) > 2. \end{cases} \quad (13.88)$$

For uniform patterns, the number of positive signs is defined to be the value of the feature. As this value does not change when the image is rotated, the feature is rotation-invariant. All non-uniform patterns are assigned the same feature value  $P + 1$ , Fig. 13.22(b).

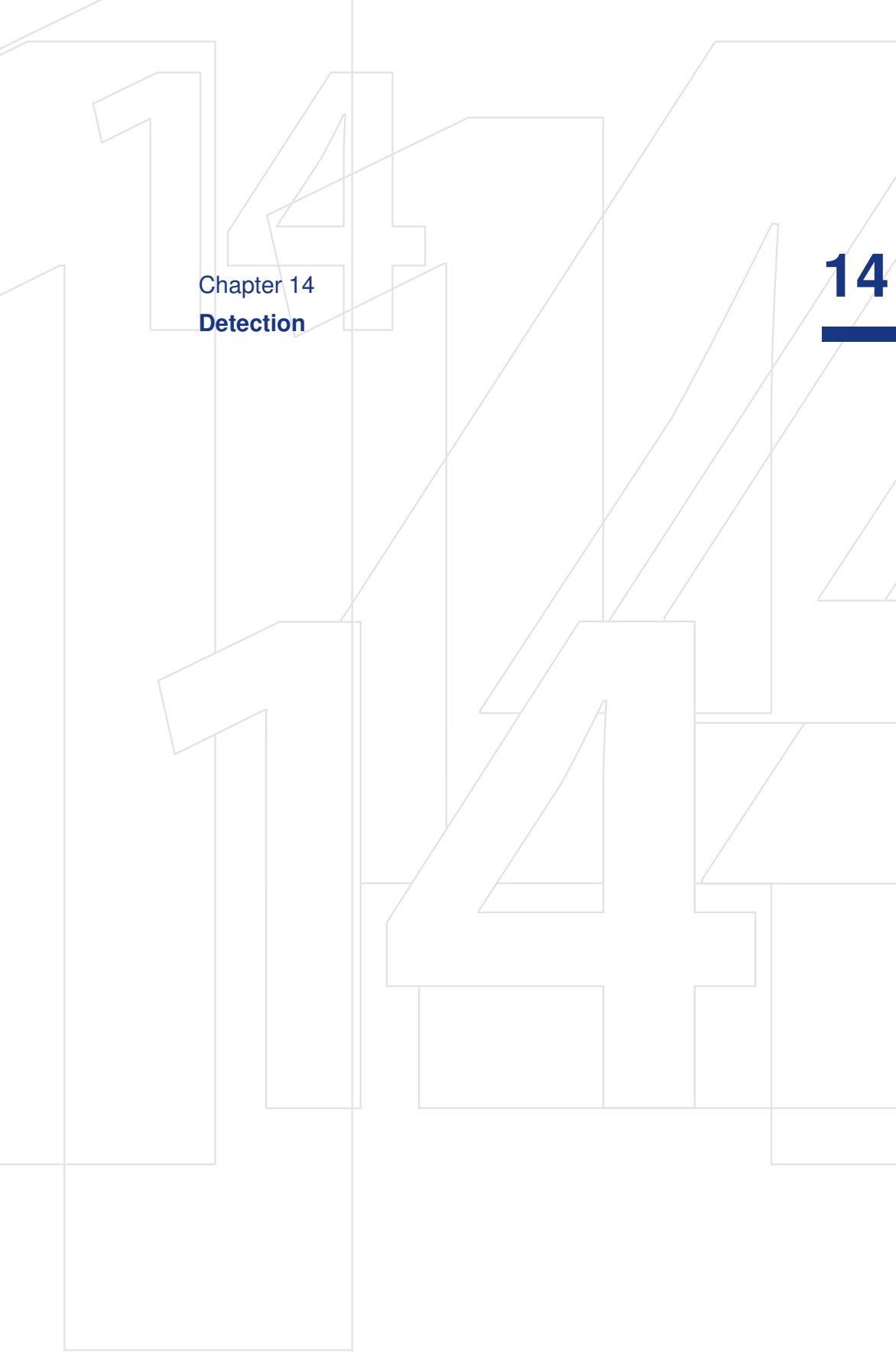
By calculating the feature  $LBP_{P,R}(\mathbf{x})$  for many image points  $\mathbf{x}$  of the texture, a histogram of the feature values can be obtained. This step can be repeated for different numbers  $P$  of points and for different radii  $R$ , e.g., for the values shown in Fig. 13.21(b)–(d). The use of different radii  $R$  corresponds to a multiresolution analysis of the structures in the image, cf. Chap. 15. Based on these histograms, further processing steps, such as texture classification, texture segmentation, or object detection, can be performed [12, 21, 23, 28]. For this purpose, the similarity of the observed histogram to histograms learned from the samples of different texture classes is evaluated.

## 13.5 Bibliography

- [1] Ludwig Abele. *Statistische und strukturelle Texturanalyse mit Anwendungen in der Bildsegmentierung*. PhD thesis, Technische Universität München, 1982.
- [2] AE Goetze GmbH. *Honatlas: Beurteilungskriterien für die Honung von Zylinderlaufflächen*. 1988.
- [3] Jürgen Beyerer. Suppression of stochastically placed, straight toolmarks to enhance objects and defects. *Technisches Messen*, 59(10):389–397, 1992.
- [4] Jürgen Beyerer. *Analyse von Riefentexturen*. PhD thesis, Universität Karlsruhe (TH), 1994.
- [5] Jürgen Beyerer, Doris Krahe, and Fernando Puente León. Progress in the Characterization of Cylinder Bores. In E. Mainsah, J. Greenwood, and D. Chetwynd, editors, *Metrology and Properties of Engineering Surfaces*, pages 243–281. Kluwer, 2001.
- [6] Jürgen Beyerer and Fernando Puente León. Adaptive separation of random lines and background. *Optical Engineering*, 37(10):2733–2741, 1998.
- [7] Phil Brodatz. *Textures: A photographic album for artists and designers*. Dover, 1966.
- [8] Navneet Dalal and Bill Triggs. Histograms of Oriented Gradients for Human Detection. In *Proc. IEEE Conference on Computer Vision and Pattern Recognition*, volume 1, pages 886–893, 2005.

- [9] Mary Galloway. Texture analysis using gray level run lengths. *Computer Graphics and Image Processing*, 4(2):172–179, 1975.
- [10] Robert Haralick, K. Sam Shanmugam, and Its'hak Dinstein. Textural features for image classification. *IEEE Transactions on Systems, Man, and Cybernetics*, 3(6):610–621, 1973.
- [11] Robert Haralick and Linda Shapiro. *Computer and robot vision*. Addison-Wesley, 1992.
- [12] Marko Heikkilä and Matti Pietikäinen. A texture-based method for modeling the background and detecting moving objects. *IEEE Transactions on Pattern Analysis and Machine Intelligence*, 28(4):657–662, 2006.
- [13] Thorsten Hermes. *Digitale Bildverarbeitung: Eine praktische Einführung*. Hanser, 2005.
- [14] Jan Horn. *Zweidimensionale Geschwindigkeitsmessung texturierter Oberflächen mit flächenhaften bildgebenden Sensoren*. PhD thesis, Universität Karlsruhe (TH), 2007.
- [15] Anil Jain. Advances in mathematical models for image processing. *Proceedings of the IEEE*, 69(5):502–528, 1981.
- [16] Bela Julesz. Textons, the elements of texture perception, and their interactions. *Nature*, 290:91–97, 1981.
- [17] Axel Korn. *Bildverarbeitung durch das visuelle System*. Springer, 1982.
- [18] Kenneth Laws. Rapid texture identification. In *Proceedings of the Seminar on Image Processing for Missile Guidance*, pages 376–380. SPIE, 1980.
- [19] Kenneth Laws. Goal-directed textured-image segmentation. In *Proc. SPIE Applications of Artificial Intelligence*, volume 548, pages 19–26, 1985.
- [20] David Lowe. Distinctive Image Features from Scale-Invariant Keypoints. *International Journal of Computer Vision*, 60(2):91–110, 2004.
- [21] Topi Mäenpää, Matti Pietikäinen, and Timo Ojala. Texture classification by multi-predicate local binary pattern operators. In *Proc. 15th International Conference on Pattern Recognition*, volume 3, pages 939 – 942, 2000.
- [22] Majid Mirmehdi, Xianghua Xie, and Jasjit Suri, editors. *Handbook of texture analysis*. Imperial College Press, 2008.
- [23] Timo Ojala, Matti Pietikäinen, and Topi Mäenpää. Multiresolution gray-scale and rotation invariant texture classification with local binary patterns. *IEEE Transactions on Pattern Analysis and Machine Intelligence*, 24(7):971–987, 2002.
- [24] Madhukar Pandit. *Methoden der Digitalen Bildverarbeitung für die Anwendung*. VDI-Verlag, 2001.
- [25] Maria Petrou and Pedro García Sevilla. *Image Processing: Dealing With Texture*. Wiley, 2006.
- [26] Matti Pietikäinen, Abdenour Hadid, Guoying Zhao, and Timo Ahonen. *Computer Vision Using Local Binary Patterns*. Springer, 2011.
- [27] Trygve Randen and John Husøy. Filtering for texture classification: a comparative study. *IEEE Transactions on Pattern Analysis and Machine Intelligence*, 21(4):291–310, 1999.
- [28] Günter Saur and Michael Teutsch. SAR signature analysis for TerraSAR-X-based ship monitoring. In L. Bruzzone, editor, *Proc. SPIE Image and Signal Processing for Remote Sensing XVI*, volume 7830, 2010.
- [29] Hideyuki Tamura, Shunji Mori, and Takashi Yamawaki. Textural Features Corresponding to Visual Perception. *IEEE Transactions on Systems, Man and Cybernetics*, 8(6):460–473, June 1978.
- [30] Emanuele Trucco and Alessandro Verri. *Introductory Techniques for 3-D Computer Vision*. Prentice Hall, 1998.
- [31] Dirk vom Stein. Zweidimensionale Geschwindigkeitsschätzung aus bewegungsunscharfen oder mehrfachbelichteten Einzelbildern. In *Tagungsband X. Meßtechnisches Symposium des Arbeitskreises der Hochschullehrer für Meßtechnik e.V.*, pages 43–49. Technische Universität München, 1996.
- [32] Friedrich Wahl. *Digitale Bildsignalverarbeitung*. Springer, 1989.

- [33] Joan Weszka, Charles Dyer, and Azriel Rosenfeld. A comparative study of texture measures for terrain classification. *IEEE Transactions on Systems, Man, and Cybernetics*, 6(4):269–285, 1976.

The background features a large, light gray outline of the number '14' that spans across the page. The '1' is on the left and the '4' is on the right. The '4' has a distinctive shape with a vertical stem and a horizontal top bar that extends to the right.

Chapter 14  
**Detection**

**14 Detection**

- 14.1 Detection of known objects by linear filters . . . . . 688
  - 14.1.1 Unknown background . . . . . 688
  - 14.1.2 White noise as background . . . . . 690
  - 14.1.3 Correlated, weakly stationary noise as background . . . . . 692
  - 14.1.4 Discrete formulation of the matched filter . . . . . 693
- 14.2 Detection of unknown objects (defects) . . . . . 697
- 14.3 Detection of straight lines . . . . . 699
  - 14.3.1 The Radon transform . . . . . 699
    - 14.3.1.1 Definition . . . . . 699
    - 14.3.1.2 The Fourier slice theorem . . . . . 702
    - 14.3.1.3 Efficient computation of the Radon transform . . . . . 703
  - 14.3.2 Detection of line-shaped structures . . . . . 706
    - 14.3.2.1 Signal-to-noise ratio (SNR) . . . . . 706
    - 14.3.2.2 Detection using correlation filters . . . . . 707
    - 14.3.2.3 Examples of applications . . . . . 707
  - 14.3.3 The Hough transform for the detection of lines . . . . . 710
  - 14.3.4 The Hough transform for the detection of curves . . . . . 711
  - 14.3.5 The generalized Hough transform . . . . . 714
  - 14.3.6 Implicit shape models . . . . . 715
- 14.4 Corner detection . . . . . 715
- 14.5 Bibliography . . . . . 717

## 14 Detection

The term detection refers to the recognition of known or unknown objects in an image and to the determination of their position and orientation. On the one hand, the objects that are to be detected can be test objects, whose presence, orientation or integrity has to be inspected. On the other hand, it might be necessary to detect defects or certain structures such as, e.g., features, in the image.

For describing detection, we assume a linear signal model, in which the objects are additively superposed on a background signal  $h(\mathbf{x})$ . In the image, the objects are represented by signals  $o_i(\mathbf{x})$ , whose amplitudes are weighted with factors  $c_i \in \mathbb{R}$ ,  $c_i > 0$ . In the image  $g(\mathbf{x})$ , these object signals can be shifted, scaled or rotated:

$$g(\mathbf{x}) = \sum_i c_i o_i(s_i \mathbf{A}_i \mathbf{x} - \mathbf{x}_i) + h(\mathbf{x}). \quad (14.1)$$

The vectors  $\mathbf{x}_i \in \mathbb{R}^2$  describe the position of the objects in the image (translation), the  $s_i \in \mathbb{R}$ ,  $s_i > 0$  scale their spatial extent, and the rotation matrices

$$\mathbf{A}_i = \begin{pmatrix} \cos \varphi_i & \sin \varphi_i \\ -\sin \varphi_i & \cos \varphi_i \end{pmatrix}, \quad \varphi_i \in [0, 2\pi), \quad (14.2)$$

rotate the object by the angle  $\varphi_i$ .

The variation of the object signals caused by  $s_i$  and  $\mathbf{A}_i$  can be directly considered during the construction of detection methods, leading to rotation-invariant and scale-invariant detectors. A 'brute force' approach of this kind uses ensembles of detectors for a sufficiently large but finite number of quantized rotation steps and scaling steps. However, this approach involves markedly increased computational costs.

More sophisticated detectors already come with invariance characteristics concerning rotation and scaling, e.g., by integrating features over all possible rotations and scalings. A detailed description of invariant methods can be found in [32]. Actual applications of invariant approaches used in automated visual inspection are given in [27].

Alternatively, the scaling  $s_i$  and the rotation  $\varphi_i$  of the objects in the acquired image can be estimated and compensated for in a normalization step before applying the actual detection method. And, finally, for automated visual inspection, the image acquisition can be constructively adjusted. Very accurate and repeatable geometric relations of the position of the test object with respect to the camera can keep unwanted influences low, like scaling and rotation, or, more generally, changing perspectives.

In contrast, the weightings of the amplitude by the factors  $c_i$  and the displacements  $\mathbf{x}_i$  are of no account for linear detection filters, which are to be covered in the following.

For understanding the presented methods it is sufficient that only one object  $o(\cdot)$  is assumed to be present in the image, without any rotation and scaling:  $\mathbf{A} = \mathbf{I}$ ,  $s = 1$ . Hence, the model (14.1) is simplified to

$$g(\mathbf{x}) = c o(\mathbf{x} - \mathbf{x}_0) + h(\mathbf{x}). \quad (14.3)$$

In the following, detection methods will be distinguished according to the a priori knowledge that they require to be available about the object and the background (Table 14.1). For the various different assumptions, optimal linear detection filters can be designed. Furthermore, the detection of lines and corners will be discussed during the course of this chapter.

**Table 14.1.** Detection filters for different assumptions concerning objects and background.

	Objects known	Objects unknown (e.g., defect detection)
Background is a weakly stationary stochastic process with known autocorrelation function	Matched filter: detection filter with optimum SNR	Search for significant local variations in the background properties, e.g., by prediction error filters
Background is unknown	– correlation filter – phase-only filter – inverse filter – ...	Detection of local texture inhomogeneities using homogeneity tests

**14.1** **14.1 Detection of known objects by linear filters**

The object sought is now assumed to be described by a deterministic signal  $o(\mathbf{x})$ . One must then find the impulse response function  $v(\mathbf{x})$  of a linear detection filter, so as to convolve it with the image signal;

$$k(\mathbf{x}) := g(\mathbf{x}) ** v(\mathbf{x}) . \tag{14.4}$$

The chosen impulse response function  $v(\mathbf{x})$  should lead to  $k(\mathbf{x})$ 's having a maximum at the position  $\mathbf{x}_0$  of the object, greater than all other surrounding signal values. The height of this 'peak' should allow of reliable detection, and the position of this peak should allow of the exact localization of the object.

A particularly important case is when the known objects are represented by lines; this case will be covered in Sec. 14.3.

➤ **14.1.1 Unknown background**

For a single object  $o(\mathbf{x})$  at the position  $\mathbf{x}_0$ , the model (14.3) can be described as follows in the spatial domain and the frequency domain:

$$g(\mathbf{x}) = c o(\mathbf{x} - \mathbf{x}_0) + h(\mathbf{x}) = o(\mathbf{x}) ** c \delta(\mathbf{x} - \mathbf{x}_0) + h(\mathbf{x}) \tag{14.5}$$

$$\Downarrow$$

$$G(\mathbf{f}) = O(\mathbf{f}) c e^{-j2\pi\mathbf{f}^T\mathbf{x}_0} + H(\mathbf{f}) . \tag{14.6}$$

The cross-correlation function

$$r(\boldsymbol{\tau}) = \iint_{-\infty}^{\infty} o(\mathbf{x}) o(\mathbf{x} - \mathbf{x}_0 + \boldsymbol{\tau}) d\mathbf{x} \tag{14.7}$$

of  $o(\mathbf{x})$  and  $o(\mathbf{x} - \mathbf{x}_0)$  is maximal for  $\tau = \mathbf{x}_0$ , as in this case it is equal to the autocorrelation function<sup>1</sup> of  $o(\mathbf{x})$  at the position  $\mathbf{0}$ . The calculation of this cross-correlation function is equivalent to the convolution of  $o(\mathbf{x} - \mathbf{x}_0)$  with the reflected object model  $o(-\mathbf{x})$ . This is why the convolution

$$k(\mathbf{x}) := g(\mathbf{x}) ** o(-\mathbf{x}) \tag{14.8}$$

can be expected to have its maximum at  $\mathbf{x} = \mathbf{x}_0$ . This detection method is called the **correlation filter**. It has the following representation in the spatial domain and the frequency domain:<sup>2</sup>

$$v(\mathbf{x}) = o(-\mathbf{x}) \quad \Leftrightarrow \quad V(\mathbf{f}) = O^*(\mathbf{f}). \tag{14.9}$$

A generalization of the correlation filter is obtained by means of the representation of  $O(\mathbf{f})$  and  $V(\mathbf{f})$  by magnitude and phase:

$$O(\mathbf{f}) = |O(\mathbf{f})| e^{j\angle O(\mathbf{f})}, \tag{14.10}$$

$$V(\mathbf{f}) = |O(\mathbf{f})| e^{-j\angle O(\mathbf{f})}. \tag{14.11}$$

The complex conjugation is equivalent to a negation of the phase. The more general **fractional power filter** (FPF) is obtained by adding the exponent  $q$  to the magnitude [38]

$$V_q(\mathbf{f}) := |O(\mathbf{f})|^q e^{-j\angle O(\mathbf{f})}, \quad q \in [-1; 1]. \tag{14.12}$$

Besides the correlation filter, further important detection filter can be considered as special cases of this parametric family, see Table 14.2.

---

**Example 14.1 (Object detection using correlation filters):** Figure 14.1(a) shows an artificial test image  $g(\mathbf{x})$  with three objects  $o_i(\mathbf{x})$  placed in front of a textured background  $h(\mathbf{x})$ , which can be assumed to be correlated noise. The superposition does not correspond to the additive model (14.3), as the objects occlude the background. For the D-shaped object  $o_1(\mathbf{x})$ , a correlation filter (matched filter)  $v(\mathbf{x}) := o_1(-\mathbf{x})$  is designed according to (14.9), see Fig. 14.1(b). The result  $k(\mathbf{x})$  of the convolution (14.4) is shown in Fig. 14.1(c). There is a distinct maximum at the position of the object  $o_1$ . ■

---

<sup>1</sup>As the Schwarz inequality (14.20) implies:

$$\iint o(\mathbf{x}) o(\mathbf{x} + \tau) \, d\mathbf{x} \leq \iint o^2(\mathbf{x}) \, d\mathbf{x} \cdot \underbrace{\iint o^2(\mathbf{x} + \tau) \, d\mathbf{x}}_{=\iint o^2(\mathbf{x}) \, d\mathbf{x}} = \left( \iint o^2(\mathbf{x}) \, d\mathbf{x} \right)^2.$$

The left-hand side is maximal if equality holds, which is the case for  $o(\mathbf{x}) \propto o(\mathbf{x} + \tau)$ , which does only hold for  $\tau = \mathbf{0}$  in general.

<sup>2</sup>The complex conjugation of the transfer function  $O(\mathbf{f})$  is denoted by  $O^*(\mathbf{f})$ .



**Table 14.2.** Special cases of the fractional power filters.

$q = -1$	$V(\mathbf{f}) = O^{-1}(\mathbf{f})$	<b>Inverse filter</b> for reconstructing $c \delta(\mathbf{x} - \mathbf{x}_0)$ (cf. Sec. 10.2). The inverse filter yields a narrow detection peak but is susceptible to noise: zeros of $O(\mathbf{f})$ lead to an intense amplification of noise. In this regard, the modification known from Sec. 10.2 represents an improvement: $V(\mathbf{f}) = \frac{O^*(\mathbf{f})}{ O(\mathbf{f}) ^2 + \varepsilon}$
$q = 0$	$V(\mathbf{f}) = e^{-j\angle O(\mathbf{f})}$	<b>Phase-only filter</b> (POF): only the phase but not the magnitude of the signal is altered by the filtering. This approach is interesting for an optical realization, as there is no loss of light, i.e., maximum optical efficiency can be achieved [36]. Another advantage over the correlation filter is given by the possibility of discriminating between similar objects [15].
$q = 1$	$V(\mathbf{f}) = O^*(\mathbf{f})$	<b>Correlation filter</b> : the correlation filter is the optimum filter if $h(\mathbf{x})$ is white noise, i.e., under this condition, it provides the maximum signal-to-noise ratio. Just as well, the correlation filter is also optimal with regard to estimating the object's position: it minimizes the so-called 'peak location error' [37]. The correlation filter is also called the <b>matched filter</b> , as it matches the object template $o(\mathbf{x})$ to the image signal $g(\mathbf{x})$ .

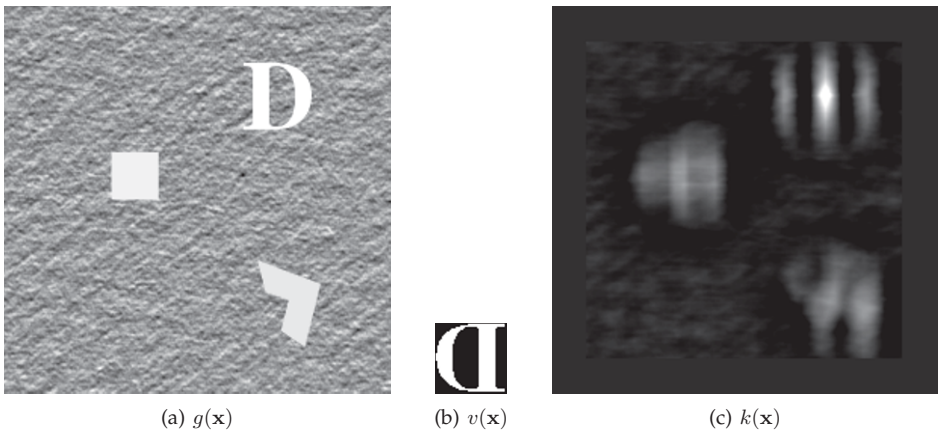


**Figure 14.1.** Object detection using the correlation filter: (a) Test image; (b) Impulse response function of the correlation filter; (c) Result of the filtering.

➤ **14.1.2 White noise as background**

This section considers the special case where the background  $h(\mathbf{x})$  can be described as white noise. Hence, by (8.301), the power spectral density is constant:

$$S_{hh}(\mathbf{f}) \equiv N_h. \tag{14.13}$$

As already mentioned, the matched filter (correlation filter) is the optimum filter in this case, as will now be explained. The filtering of the image signal (14.5) with the impulse response function  $v(\mathbf{x})$  of a linear filter yields

$$k(\mathbf{x}) = g(\mathbf{x}) ** v(\mathbf{x}) = \underbrace{c o(\mathbf{x} - \mathbf{x}_0) ** v(\mathbf{x})}_{\text{signal}} + \underbrace{h(\mathbf{x}) ** v(\mathbf{x})}_{\text{noise}}, \quad (14.14)$$

where the first term represents the signal and the second term represents the noise after filtering. The signal-to-noise ratio of the filtered signal is given by

$$SNR = \frac{P_1}{P_2}, \quad (14.15)$$

with  $P_1$  denoting the power of the signal sought and  $P_2$  denoting the power of the noise signal after the filtering.

Especially at the position  $\mathbf{x} = \mathbf{x}_0$  of the object that is to be detected, the signal's power  $P_1$  is evaluated. For detection and localization it is sufficient that the filtering results in an extremum at that position, which is notably greater than the signal  $k(\mathbf{x})$  surrounding the object. The local power of the signal at the position  $\mathbf{x} = \mathbf{x}_0$  is given by

$$P_1 := |c o(\mathbf{x} - \mathbf{x}_0) ** v(\mathbf{x})|^2 \Big|_{\mathbf{x}=\mathbf{x}_0} = |c o(\mathbf{x}) ** v(\mathbf{x})|^2 \Big|_{\mathbf{x}=\mathbf{0}} \quad (14.16)$$

$$= c^2 |o(\mathbf{x}) ** v(\mathbf{x})|_{\mathbf{x}=\mathbf{0}} = c^2 \left| \iint_{-\infty}^{\infty} O(\mathbf{f}) V(\mathbf{f}) d\mathbf{f} \right|^2. \quad (14.17)$$

To formulate the above equations, the LSI property of the detection filter is exploited and also the central ordinate theorem is applied to the correspondence  $o(\mathbf{x}) ** v(\mathbf{x}) \iff O(\mathbf{f}) V(\mathbf{f})$ .

In contrast to the power  $P_1$  of the desired signal, which denotes the instantaneous power of a deterministic signal  $o(\mathbf{x}) ** v(\mathbf{x})$ , the power  $P_2$  of the noise has to be calculated for a stochastic process  $h(\mathbf{x})$ . This is why  $P_2$  is defined as the mean signal power of  $h(\mathbf{x}) ** v(\mathbf{x})$ . The mean power of the noise signal is given by

$$P_2 = N_h \iint_{-\infty}^{\infty} |V(\mathbf{f})|^2 d\mathbf{f}. \quad (14.18)$$

In order to maximize the signal-to-noise ratio, the Schwarz inequality is applied. For the scalar product

$$\langle f(\mathbf{x}), g(\mathbf{x}) \rangle := \int_{-\infty}^{\infty} f(\mathbf{x}) g^*(\mathbf{x}) d\mathbf{x} \quad (14.19)$$

in the space of quadratically integrable complex-valued functions, it is given by

$$|\langle f(\mathbf{x}), g(\mathbf{x}) \rangle|^2 \leq \langle f(\mathbf{x}), f(\mathbf{x}) \rangle \cdot \langle g(\mathbf{x}), g(\mathbf{x}) \rangle, \quad (14.20)$$

where equality holds if, and only if,  $f(\mathbf{x})$  is a scalar multiple of  $g(\mathbf{x})$  [14,25]. Thus for (14.17), this implies

$$P_1 = c^2 \left| \iint_{-\infty}^{\infty} V(\mathbf{f}) O(\mathbf{f}) \, d\mathbf{f} \right|^2 = c^2 \left| \iint_{-\infty}^{\infty} V(\mathbf{f}) (O^*(\mathbf{f}))^* \, d\mathbf{f} \right|^2 = c^2 |\langle V(\mathbf{f}), O^*(\mathbf{f}) \rangle|^2 \tag{14.21}$$

$$\leq c^2 \langle V(\mathbf{f}), V(\mathbf{f}) \rangle \cdot \langle O^*(\mathbf{f}), O^*(\mathbf{f}) \rangle = c^2 \iint_{-\infty}^{\infty} |V(\mathbf{f})|^2 \, d\mathbf{f} \cdot \iint_{-\infty}^{\infty} |O(\mathbf{f})|^2 \, d\mathbf{f}. \tag{14.22}$$

The left-hand side is maximal, i.e., the inequality turns into an equality, if  $V(\mathbf{f}) \propto O^*(\mathbf{f})$ .

Hence, for a fixed  $P_2$ , the SNR is maximal if the transfer function  $V(\mathbf{f})$  of the detection filter is chosen to be proportional to the complex conjugation of the object’s transfer function:

$$V(\mathbf{f}) = \text{const.} \cdot O^*(\mathbf{f}) \tag{14.23}$$



$$v(\mathbf{x}) = \text{const.} \cdot o(-\mathbf{x}) \tag{14.24}$$

In sum, the matched filter is optimal for white noise in terms of having the maximum SNR at the position  $\mathbf{x} = \mathbf{x}_0$ .

➤ **14.1.3 Correlated, weakly stationary noise as background**

The matched filter can be generalized to suit correlated, weakly stationary noise  $h(\mathbf{x})$  with a known autocorrelation  $r_{hh}(\tau)$ . For the detection filter  $v(\mathbf{x})$ , the following approach is chosen (Fig. 14.2):

$$v(\mathbf{x}) := \tilde{v}(\mathbf{x}) ** w(\mathbf{x}). \tag{14.25}$$

The convolution of the noise term with the impulse response function  $w(\mathbf{x})$  is supposed to decorrelate the noise, i.e., to turn it into white noise, so that subsequently the matched filter  $\tilde{v}(\mathbf{x})$  from the previous section can be used. This is why the filter  $w(\mathbf{x}) \iff W(\mathbf{f})$  is called a **whitening filter**. The convolution of the image  $g(\mathbf{x})$  with the whitening filter results in

$$\gamma(\mathbf{x}) := g(\mathbf{x}) ** w(\mathbf{x}) = c \underbrace{o(\mathbf{x} - \mathbf{x}_0) ** w(\mathbf{x})}_{=: \tilde{o}(\mathbf{x})} + \underbrace{h(\mathbf{x}) ** w(\mathbf{x})}_{=: \rho(\mathbf{x})}. \tag{14.26}$$

The second term  $\rho(\mathbf{x})$  is supposed to be white noise:

$$S_{\rho\rho}(\mathbf{f}) = |W(\mathbf{f})|^2 S_{hh}(\mathbf{f}) \stackrel{!}{=} \text{const.} \tag{14.27}$$

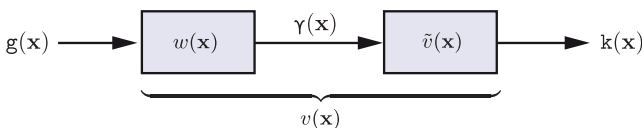


Figure 14.2. Approach for the matched filter  $v(\mathbf{x})$  for correlated, weakly stationary noise (colored noise).

This yields the following condition for the transfer function of the whitening filter:

$$w(\mathbf{x}) \quad \text{with} \quad |W(\mathbf{f})| = \frac{1}{\sqrt{S_{\text{hh}}(\mathbf{f})}}. \quad (14.28)$$

By this means, the problem is turned into the case of white noise and leads to

$$\tilde{v}(\mathbf{x}) = \text{const.} \cdot \tilde{o}(-\mathbf{x}) \quad (14.29)$$

with

$$\tilde{o}(\mathbf{x}) = o(\mathbf{x}) ** w(\mathbf{x}). \quad (14.30)$$

The whitening produces the modified signal  $\tilde{o}(\mathbf{x})$ , which now has to be detected with maximum SNR in white noise. This results in the following matched filter for correlated (colored) noise:

$$v(\mathbf{x}) = \text{const.} \cdot \tilde{o}(-\mathbf{x}) ** w(\mathbf{x}) \quad (14.31)$$

$$= \text{const.} \cdot o(-\mathbf{x}) ** w(-\mathbf{x}) ** w(\mathbf{x}) \quad (14.32)$$



$$V(\mathbf{f}) = \text{const.} \cdot O^*(\mathbf{f}) |W(\mathbf{f})|^2 \quad (14.33)$$

$$= \text{const.} \cdot \frac{O^*(\mathbf{f})}{S_{\text{hh}}(\mathbf{f})}. \quad (14.34)$$

The transfer function of the filter has low values for spatial frequencies for which the power spectral density of the noise is high compared to the sought for signal. Conversely, the filter opens for frequencies for which, in the Fourier domain, the signal sought  $o(\mathbf{x})$  dominates the noise  $h(\mathbf{x})$ .

➤ 14.1.4 Discrete formulation of the matched filter

Until now, the continuous case has been considered for deriving the detection methods. The matched filter can be alternatively expressed in matrix notation, similar to the restoration methods of Sec. 10.6, so that it can be applied to discrete image data.

A region of the image can be written as a column vector  $\mathbf{g}_{mn}$ :

$$\mathbf{g}_{mn} := (\dots, g_{m-i, n-j}, \dots)^T, \quad (i, j) \in \mathcal{U}, \quad \mathbf{g}_{mn} \in \mathbb{R}^{|\mathcal{U}|}, \quad (14.35)$$

with  $\mathcal{U}$  denoting a neighborhood around the origin (Fig. 14.3). Similarly, the vectors  $\mathbf{o}_{mn}, \mathbf{h}_{mn} \in \mathbb{R}^{|\mathcal{U}|}$  are defined for the object and for the background noise. Hence, the discrete formulation of the signal model (14.3) is given by

$$\mathbf{g}_{mn} = \mathbf{o}_{mn} + \mathbf{h}_{mn}. \quad (14.36)$$

The sought for matched filter can also be written as a column vector:

$$\mathbf{v} := (\dots, v_{ij}, \dots)^T \in \mathbb{R}^{|\mathcal{U}|}. \quad (14.37)$$

The result of the filtering at the point  $(m, n)$  is given by the inner product

$$\mathbf{k}_{mn} = \mathbf{v}^T \mathbf{g}_{mn}. \quad (14.38)$$

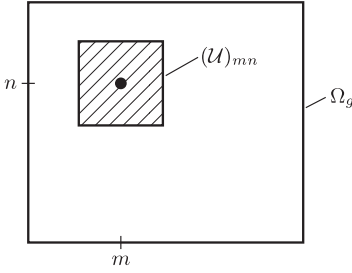


Figure 14.3. The vectors  $\mathbf{g}_{mn}$ ,  $\mathbf{o}_{mn}$  and  $\mathbf{h}_{mn}$  are out of the surrounding  $(U)_{mn}$ , which can be obtained by shifting  $U$  to the position  $(m, n)$ .

This corresponds to a convolution of the image with the impulse response function  $\mathbf{v}$  of a linear, shift-invariant system. To simplify matters, the indices  $mn$  are omitted in the following. So for the image position  $(m_0, n_0)$  of the object, we have

$$\mathbf{k}_{m_0 n_0} = \mathbf{k} = \mathbf{v}^T \mathbf{g} = \mathbf{v}^T \mathbf{o} + \mathbf{v}^T \mathbf{h}. \tag{14.39}$$

Now again, the signal-to-noise ratio has to be maximized:

$$SNR = \frac{P_1}{P_2} \xrightarrow{!} \text{Max}. \tag{14.40}$$

The power of the signal sought at the object position is given by

$$P_1 = (\mathbf{v}^T \mathbf{o})^2. \tag{14.41}$$

And the power of the background signal is

$$P_2 = E\{(\mathbf{v}^T \mathbf{h})^2\} = E\{(\mathbf{v}^T \mathbf{h})(\mathbf{h}^T \mathbf{v})\} = \mathbf{v}^T \underbrace{E\{\mathbf{h}\mathbf{h}^T\}}_{= \mathbf{R}_{hh}} \mathbf{v}. \tag{14.42}$$

The correlation matrix  $\mathbf{R}_{hh}$  of the noise signal is symmetric and positive definite and can therefore be decomposed as follows:<sup>3</sup>

$$\mathbf{R}_{hh} = \mathbf{Q}^T \mathbf{Q}. \tag{14.43}$$

In this representation, the inverse correlation matrix  $\mathbf{R}_{hh}^{-1}$  is given by

$$\mathbf{R}_{hh}^{-1} = \mathbf{Q}^{-1} (\mathbf{Q}^T)^{-1}. \tag{14.44}$$

Setting  $\boldsymbol{\omega} := \mathbf{Q}\mathbf{v}$  results in

$$\mathbf{v} = \mathbf{Q}^{-1} \boldsymbol{\omega}, \tag{14.45}$$

$$\mathbf{v}^T = \boldsymbol{\omega}^T (\mathbf{Q}^{-1})^T. \tag{14.46}$$

Hence, the signal-to-noise ratio is

$$SNR = \frac{(\mathbf{v}^T \mathbf{o})^2}{\mathbf{v}^T \mathbf{R}_{hh} \mathbf{v}} = \frac{(\boldsymbol{\omega}^T (\mathbf{Q}^{-1})^T \mathbf{o})^2}{\boldsymbol{\omega}^T \boldsymbol{\omega}}. \tag{14.47}$$

W.l.o.g. the vector  $\mathbf{v}$  can be scaled so that  $\|\boldsymbol{\omega}\| = 1$ : as the squares of  $\mathbf{v}$  and  $\boldsymbol{\omega}$  are contained in both the numerator and the denominator, the chosen scaling factor can be canceled. This

<sup>3</sup>This is the so-called Cholesky decomposition of the matrix [34].

is why only the numerator has to be considered for the optimization. The inner product in the numerator reaches its maximum if  $\omega$  is parallel to  $(Q^{-1})^T \mathbf{o}$ . Thus, for the discrete formulation of the matched filter, this results in

$$\omega = \text{const.} \cdot (Q^{-1})^T \mathbf{o} \tag{14.48}$$

$$\Rightarrow \mathbf{v} = \text{const.} \cdot Q^{-1} (Q^{-1})^T \mathbf{o} = \text{const.} \cdot R_{hh}^{-1} \mathbf{o}, \tag{14.49}$$

$$k_{mn} = \mathbf{v}^T \mathbf{g}_{mn} \propto \mathbf{o}^T Q^{-1} (Q^{-1})^T \mathbf{g}_{mn}. \tag{14.50}$$

The discrete formulation can be interpreted similarly to the continuous formulation. Here,  $(Q^{-1})^T$  represents the whitening filter and  $\mathbf{o}^T Q^{-1}$  the function which describes the object (template), and which is modified by the whitening.

In general, detection problems are complicated by the fact that the known object models appear affected by additional rotations, scalings or perspective distortions in the image. As the matched filter approaches that have been presented here are not invariant with respect to those transformations, their effectiveness is susceptible to such variations. In order to detect arbitrarily rotated and scaled objects, an ensemble of filters has to be applied to the image, in which every filter detects objects with a certain rotation and scaling [30].

**Example 14.2 (Optical character recognition):** In automated visual inspection, often the labeling of test objects has to be identified, in order to sort the objects or to verify their identity. The characters do not necessarily have to be printed with ink but can also be engraved as a relief, e.g., on cast parts (Fig. 14.4). In this case, a suitable image acquisition has to be performed, e.g., by a stripe projection method, so that the relief data can be turned into a

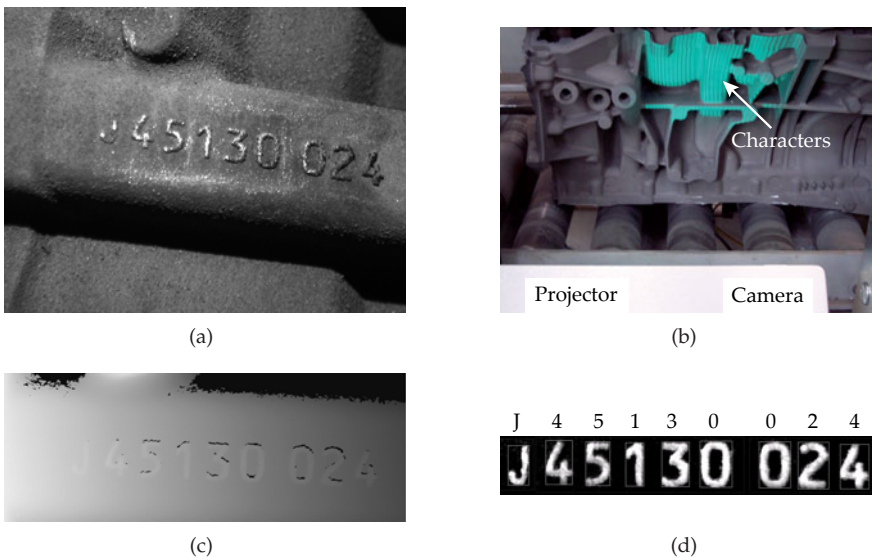


**Figure 14.4.** Optical character recognition on cast parts: (a) Intensity image of the test object; (b) Acquiring the 3D shape of the surface using stripe projection; (c) Surface relief (black  $\hat{=}$  invalid data points); (d) Result of the character recognition.

2D image of the characters after a rectification.

Matched filters can be used for the detection of the single characters: for every relevant character  $i$  (letters, numbers, etc.), an impulse response function  $o_i(\mathbf{x})$  is learned. Next, a convolution of the preprocessed image with each filter  $v_i(\mathbf{x}) := o_i(-\mathbf{x})$  is performed:

$$k_i(\mathbf{x}) := g(\mathbf{x}) ** o_i(-\mathbf{x}). \tag{14.51}$$

The resulting feature image  $k_i(\mathbf{x})$  shows a maximum if the corresponding character is present (Fig. 14.5(b)). A thresholding yields a binary image, which can be used for the detection decision (Fig. 14.5(c)). The three maxima in the upper image clearly represent an occurrence of the number '0', whereas besides the two correct maxima corresponding to the number '1', there are some false detections. However, when considering the known position of the characters within one line, the false detections can be eliminated. The bottom image remains black, as the number '2' is not present in the example sequence. In total, the evaluation of the result of the filtering for all numbers and characters yields the result shown in Fig. 14.5(d). It is remarkable that even the first character has been correctly identified as the capital character 'O', which is a little smaller than the number '0'.

Formally speaking, the decision rule is as follows: the character  $i$  is considered to be detected at position  $\mathbf{x}$  if

$$k_i(\mathbf{x}) > \text{threshold} \tag{14.52}$$

$$\wedge \mathbf{x} \in \text{regions of interest} \subset \Omega_g \tag{14.53}$$

$$\wedge k_i(\mathbf{x}) > k_j(\mathbf{x}) \text{ for all } j \neq i. \tag{14.54}$$



**Figure 14.5.** Optical character recognition using matched filters: (a) Gray-scale image  $g(\mathbf{x})$ ; (b) Filtering results  $k_i(\mathbf{x})$  for the characters '0', '1' and '2'; (c) Binary images, obtained by thresholding (b), superposed with the regions of interest (red rectangles); (d) Detection result.

The first condition requires a minimum height of the peak, i.e., a significant amplitude of the feature  $k_i(\mathbf{x})$  at the position  $\mathbf{x}$ . The second condition prevents false detections outside of the regions of interest (ROIs) in which the characters might occur at all. If multiple filters show a peak for a single position, the third condition selects the most probable character.

For optical character recognition, often much more complex methods are used, which—among other things—consider the probability distributions over the neighborhood of the characters inside of words. For identifying numbers, etc., for which such knowledge is not available, matched filters present a practical solution. Alternative methods for the detection of single characters are artificial neural networks and classifiers, for example [8].

In industry, often 2D bar codes are used for labeling objects, instead of plaintext fonts, as they allow a redundant encoding, which however cannot be directly read by humans. ■

## 14.2 Detection of unknown objects (defects)

For the detection of unknown objects, the object signal  $o(\mathbf{x})$  is considered as a local variation of the embedding background. The background is assumed to be a weakly stationary stochastic process  $h(\mathbf{x})$  with a known autocorrelation function  $r_{hh}(\boldsymbol{\tau})$ . This situation is typical for the detection of defects of all kinds in known textures. The defects appear as significant local variations of the statistical properties of  $g(\mathbf{x})$ . These can be detected by specifically suppressing the background signal  $h(\mathbf{x})$ , so that the defects are highlighted.

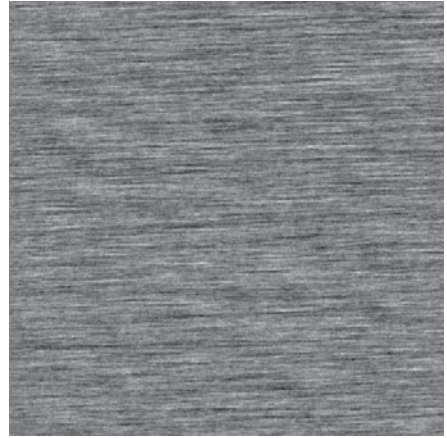
**Example 14.3 (A prediction error filter based on AR models):** The AR model of Sec. 13.3.3 can be used for defect detection in textures. The image value at the position  $(m, n)$  is predicted by the AR model. The prediction error  $e_{mn}$  is a measure for the difference of the texture model

$$e_{mn} = g_{mn} - \underbrace{\mathbf{a}^T \boldsymbol{\gamma}_{mn}}_{\hat{g}_{mn}}. \quad (14.55)$$

The information about the statistical properties of the texture, e.g., the autocorrelation function  $r_{hh}(\boldsymbol{\tau})$  or the correlation matrix  $\mathbf{R}_{hh}$  of the background signal, is represented by the AR coefficients  $\mathbf{a}$ . For local variations of the image signal  $g_{mn}$  and the modeled background signal  $h_{mn}$ , the prediction error  $e_{mn}$  shows a high local power. As  $e_{mn}$  is itself a random variable, a sensible definition for the local power has to be found, e.g., as the local variance  $\sigma_{mn}^2 = \text{Var}\{e_{mn}\}$ . In practice,  $\sigma_{mn}^2$  can be estimated by a local averaging of the sample function  $e_{mn}$ , e.g., elegantly by a low-pass filtering of  $e_{mn}^2$  (cf. the calculation of  $\hat{\sigma}(\mathbf{x})$  in Sec. 9.2.2.3).

As an example, Fig. 14.6 shows the detection of anomalies in a wooden structure. For the textures in Fig. 14.6(a), an AR model has been estimated. Figure 14.6(b) shows a synthesized texture for validating the model. The prediction error  $e_{mn}$  is shown in Fig. 14.6(c). After smoothing the squared error signal with a Gaussian low-pass filter, the



(a) Original image  $g_{mn}$ 

(b) Synthesized texture

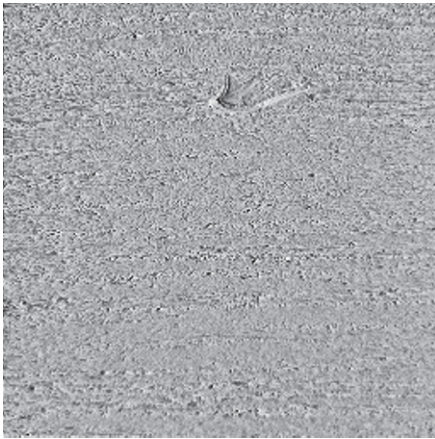
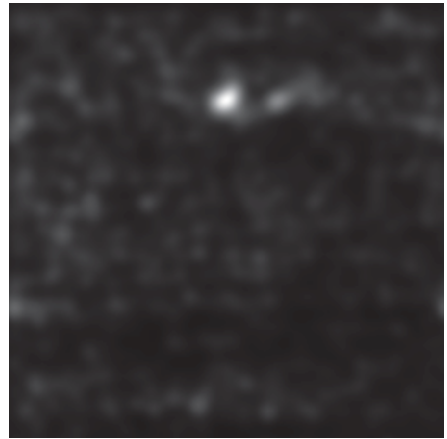
(c) Prediction error  $e_{mn}$ (d) Estimation of the local variance  $\sigma_{mn}^2$ 

Figure 14.6. Defect detection in a wood texture using an AR model.

anomaly of the wooden structure is represented by a distinctive maximum in Fig. 14.6(d). ■

The example shown models the object-free background with an AR model, which is a signal adapted method, in order to accentuate the objects by suppressing the background.

Often even simpler methods, e.g., thresholding, are sufficient, if the objects appear as bright or dark regions compared to the background, cf. Sec. 11.1.

In another important case, the objects (especially the defects) have high-frequency structures in contrast to the background, which can be detected by applying a high-pass filtering, calculating the magnitude, and finally performing a thresholding.

## 14.3 Detection of straight lines

Lines are important components of ‘technical scenes’: many technically built objects have piecewise straight structures or borders. This is why the detection of lines and the determination of their orientation plays an important role for automated visual inspection.

### 14.3.1 The Radon transform

The Radon transform<sup>4</sup> represents an important tool for the detection and localization of lines in images [3, 7]. In contrast to the differentiating edge detection methods of Chap. 11, the Radon transform is an integral transform and is therefore much more robust against noise in the image.

#### 14.3.1.1 Definition

##### Definition 14.1: Radon transform

The Radon transform of a signal  $g(\mathbf{x})$  is defined as

$$\check{g}(u, \varphi) = \mathcal{R}\{g(\mathbf{x})\} := \int_{-\infty}^{\infty} \int_{-\infty}^{\infty} g(\mathbf{x}) \delta(\mathbf{x}^T \mathbf{e}_\varphi - u) \, d\mathbf{x} \quad (14.56)$$

with

$$\varphi \in [0, \pi), \quad u \in \mathbb{R}, \quad \mathbf{e}_\varphi = \begin{pmatrix} \cos \varphi \\ \sin \varphi \end{pmatrix}. \quad (14.57)$$

◇

The  $\delta$ -line

$$\delta(\mathbf{x}^T \mathbf{e}_\varphi - u)' = \begin{cases} 0 & \text{if } \mathbf{x}^T \mathbf{e}_\varphi - u \neq 0 \\ \infty & \text{if } \mathbf{x}^T \mathbf{e}_\varphi - u = 0 \end{cases} \quad (14.58)$$

representing the transformation kernel results in the summation of the values of the signal  $g(\mathbf{x})$  along lines that have the parameters  $u$  (distance to the origin) and  $\varphi$  (line angle), see Fig. 14.7.

Thus for a fixed angle  $\varphi_0$ ,  $\check{g}(u, \varphi_0)$  is equal to the parallel projection of the signal in the  $\varphi_0$ -direction. If every value of the whole domain is considered for  $\varphi$ , it becomes obvious that the Radon transform contains all parallel projections of the signal  $g(\mathbf{x})$  in an ordered manner. The Radon transform expands the signal  $g(\mathbf{x})$  in  $\delta$ -lines. Because of the geometric structure of the transformation kernel, line-shaped signal components are constructively integrated and appear as distinct extrema in the  $u, \varphi$ -domain.

Line-shaped structures will produce a distinct maximum, if the image background is zero-mean. Depending on the homogeneity of the image, it is either sufficient to subtract the global average or a first-order homogenization should be applied that eliminates the local average (see Sec. 9.2.2). Spatially slowly changing components of the image result in wide and strong signal components in the Radon transform, which are irrelevant for the detection of lines and can be compensated for by means of eliminating the local average.

<sup>4</sup>Named after Johann Radon, 1917 [28]

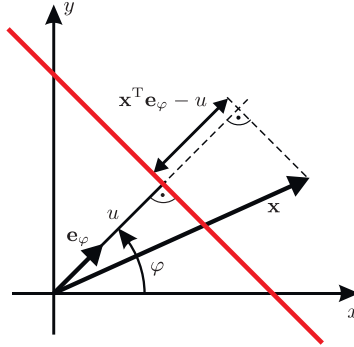


Figure 14.7. Notation used with regard to the Radon transform.

For all examples shown in this chapter, the Radon transform has been applied to zero-mean images.

**Example 14.4 (The Radon transform of textures):** The effect of the Radon transform can be illustrated using images of textures with straight grooves (cf. Chap. 13). The sawing texture in Fig. 14.8(a) consists exclusively of parallel grooves. This is why the corresponding Radon transform shows significant extrema only for one angle  $\varphi_0$  (Fig. 14.8(b)). The minima and maxima correspond to the distances from the origin of the dark and bright straight lines in the texture image.

The honing texture in Fig. 14.8(c) has grooves with two different predominant directions. The corresponding angles  $\varphi_1, \varphi_2$  result in extrema in the Radon transform (Fig. 14.8(d)). As the grooves in the honing texture have random distances and widths, the extrema have different heights and different distances. ■

The inverse Radon transform is given by

$$g(\mathbf{x}) = \mathcal{R}^{-1}\{\check{g}(u, \varphi)\} = \frac{1}{2\pi^2} \int_0^\pi \int_{-\infty}^\infty \frac{1}{\mathbf{x}^T \mathbf{e}_\varphi - u} \frac{\partial \check{g}(u, \varphi)}{\partial u} du d\varphi. \tag{14.59}$$

It yields the signal  $g(\mathbf{x})$  for given projection data  $\check{g}(u, \varphi)$ . Suitable approaches to practically computing Equations (14.56) and (14.59) will be discussed in Sec. 14.3.1.3.

**Example 14.5 (Computed tomography):** The principle of computed tomography (CT) is a practical application of the Radon transform, see Fig. 14.9. Here, parallel X-rays are assumed. For more general ray geometries, such as point-shaped X-ray sources, the reader is referred to standard tomographic literature [18, 19].

The parallel X-radiation emitted by a sender array has the initial intensity  $I_0$  and passes through an object with spatially varying absorption coefficients  $\mu(\mathbf{x})$ , so that the radiation  $I(\mu, \varphi)$  measured by the receiver array is attenuated in obedience to the follow-

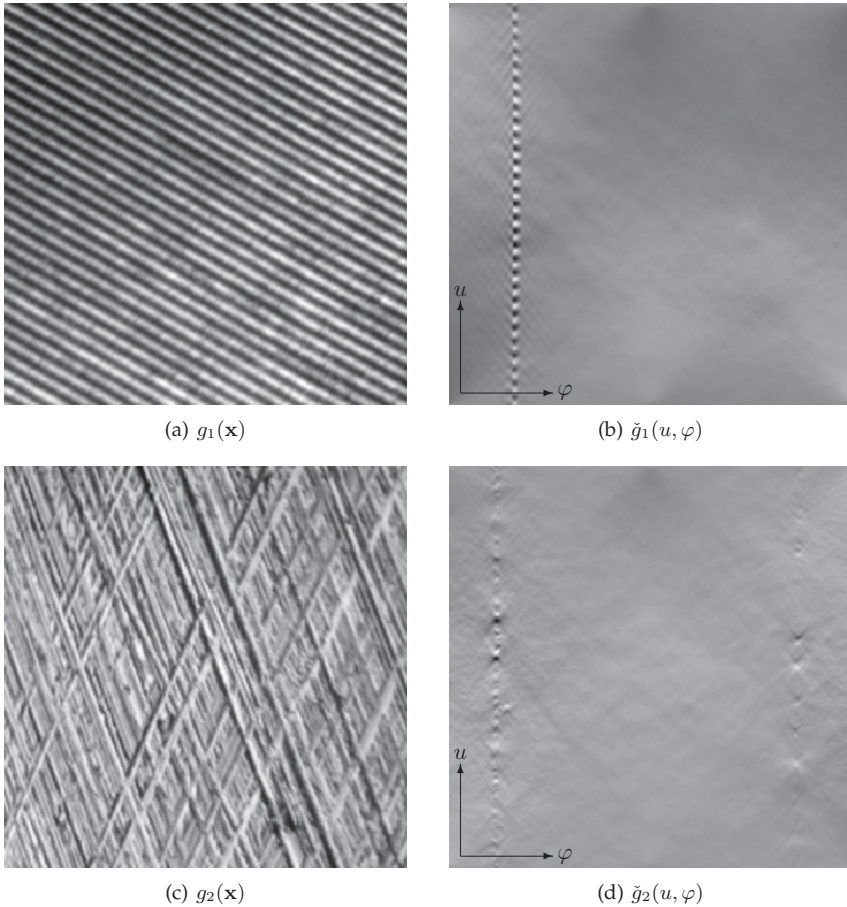


Figure 14.8. Radon transform applied to examples images.

ing equation (see Sec. 7.4.2):

$$I(u, \varphi) = I_0 \exp \left( - \iint \mu(\mathbf{x}) \delta(\mathbf{x}^T \mathbf{e}_\varphi - u) \, d\mathbf{x} \right). \tag{14.60}$$

By dividing by  $I_0$  and taking the logarithm, the measured data corresponds to the line integral of the absorption coefficients  $\mu(\mathbf{x})$  along the rays, i.e., to the Radon transform  $\mathcal{R}\{\mu(\mathbf{x})\}$  of the function  $\mu(\mathbf{x})$ :

$$\ln \left( \frac{I_0}{I(u, \varphi)} \right) = \iint \mu(\mathbf{x}) \delta(\mathbf{x}^T \mathbf{e}_\varphi - u) \, d\mathbf{x} = \mathcal{R}\{\mu(\mathbf{x})\}. \tag{14.61}$$

In order to reconstruct the function  $\mu(\mathbf{x})$  sufficiently precisely, the absorption along many lines with different directions has to be measured by rotating the test object with respect to the tomograph. Then, the inverse Radon transform is applied to the measured data [35].

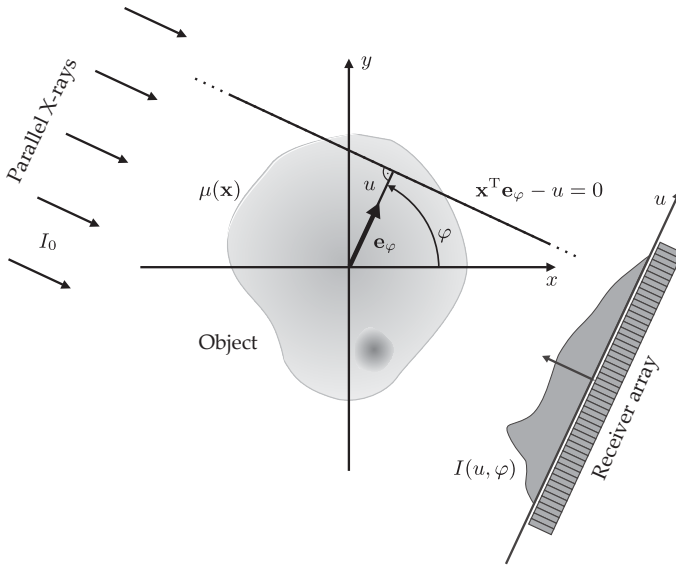


Figure 14.9. Principle of computed tomography.

Also in computed tomography, there is a sampling theorem related to the Radon transform, specifying the roughest quantization of  $u$  and  $\varphi$  with in terms of the bandwidth of  $\mu(\mathbf{x})$  and to the size of the object [29]. ■

### ⊙ 14.3.1.2 The Fourier slice theorem

The Fourier slice theorem (also called projection-slice theorem or central slice theorem) is very important for the practical use of the Radon transform [7]. It gives a relation between the Fourier transform (8.130) and the Radon transform and is illustrated in Fig. 14.10.

14.1

#### Theorem 14.1: The Fourier slice theorem

Via a one-dimensional Fourier transform, a parallel projection of the signal  $g(\mathbf{x})$  is related to a central slice perpendicular to the projection direction of the two-dimensional Fourier transform  $G(\mathbf{f}) = \mathcal{F}_{\mathbf{x}}\{g(\mathbf{x})\}$ :

$$\mathcal{F}_u\{\tilde{g}(u, \varphi)\} = G(f_u \mathbf{e}_\varphi), \quad (14.62)$$

where  $f_u$  denotes the spatial frequency corresponding to  $u$ . ◇

By means of this theorem, the fast Fourier transform (FFT) and an interpolation from rectangular to polar coordinates can be used to efficiently compute the Radon transform, see Sec. 14.3.1.3.

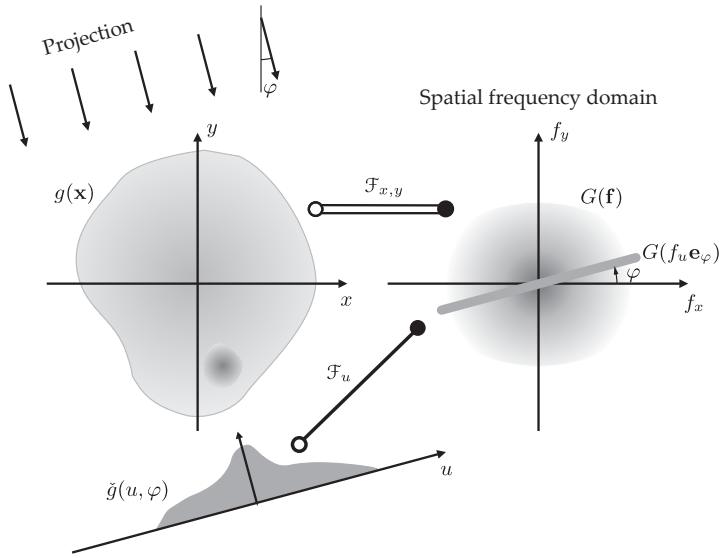


Figure 14.10. Visualization of the Fourier slice theorem.

**Proof 14.1 (Fourier slice theorem):** In order to derive (14.62), the Radon transform of the image  $g(\mathbf{x})$  for  $\varphi = 0^\circ$  is calculated according to Fig. 14.11:

$$\check{g}(u, \varphi = 0) = \iint g(\mathbf{x}) \delta(x - u) \, dx = \int g(u, y) \, dy. \tag{14.63}$$

A Fourier transform with respect to  $u$  yields

$$\begin{aligned} \mathcal{F}_u\{\check{g}(u, 0)\} &= \iint g(u, y) e^{-j2\pi f_u u} \, du \, dy \\ &= \iint g(x, y) e^{-j2\pi f_x x} \, dx \, dy \\ &= \iint g(x, y) e^{-j2\pi(f_x x + f_y y)} \, dx \, dy \Big|_{f_y=0} \\ &= G(f_x, 0) = G(f_x \mathbf{e}_x) = G(f_u \mathbf{e}_\varphi) \Big|_{\varphi=0}. \end{aligned} \tag{14.64}$$

A rotation of the function  $g(\mathbf{x})$  in the spatial domain corresponds to a rotation of the Fourier transform  $G(\mathbf{f})$  (see Theorem 8.13):

$$\mathcal{F}\{g(\mathbf{D}\mathbf{x})\} = G(\mathbf{D}\mathbf{f}) \quad \text{with} \quad \mathbf{D} = \begin{pmatrix} \cos \varphi & \sin \varphi \\ -\sin \varphi & \cos \varphi \end{pmatrix}. \tag{14.65}$$

Together with (14.64), this immediately implies (14.62). ■

⊗ **14.3.1.3 Efficient computation of the Radon transform**

Figure 14.12 shows a practical strategy for computing the Radon transform using the Fourier slice theorem. After a 2D Fourier transform of the original image  $g(\mathbf{x})$ , the complex spectrum

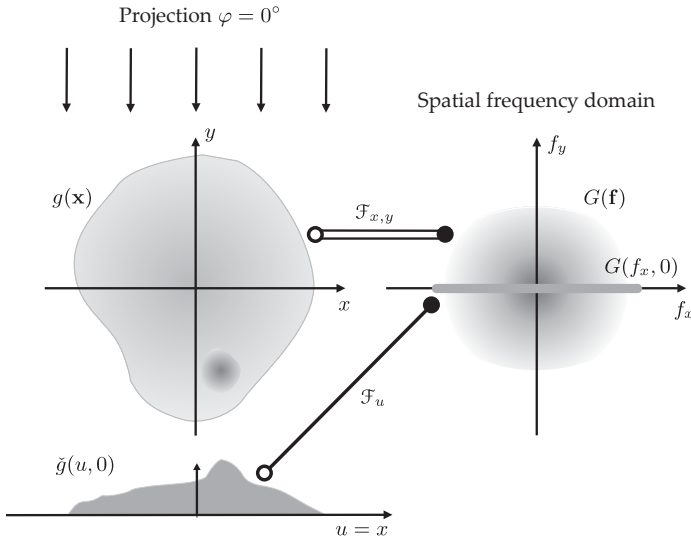


Figure 14.11. Proof of the Fourier slice theorem.

$G(\mathbf{f})$  is interpolated on a polar grid. Then, an inverse one-dimensional Fourier transform is applied to the result of the interpolation ‘column by column’ with respect to the coordinate  $u$ . The result is the Radon transform sought.

The inverse Radon transform is of particular importance to use the Radon transform for image enhancement. Here, the procedure of Fig. 14.12 can simply be inverted: after a 1D-FFT with respect to the parameter  $u$ , an interpolation on a Cartesian grid is performed. Finally, an inverse 2D-FFT is applied to the result.

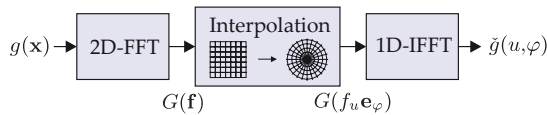


Figure 14.12. Efficient calculation of the Radon transform using the Fourier slice theorem and the FFT.

Generally, this approach is affected by an interpolation error, and so only an approximation of the Radon transform can be achieved. In practice, it is usually sufficient to use a bilinear interpolation, which has also been used to calculate the examples of this section (cf. Sec. 9.2.1).

In the following, the savings in computation time obtained by using the Fourier slice theorem for the calculation of the Radon transform will be estimated. The image size is assumed to be  $N \times N$ , so that  $N = N_\varphi = N_u$ , with  $N_\varphi$  and  $N_u$  denoting the number of quantization steps of  $\varphi$  and  $u$ . The computational costs of the direct evaluation of the Radon integral are  $O(N^3)$ ; in contrast, by using the Fourier slice theorem, the computational costs are only  $O(N^2 \text{ld } N)$ . Especially for high  $N$ , the method illustrated in Fig. 14.12 requires a markedly reduced number of computation steps, as is shown in Table 14.3 for typical values.

**Table 14.3.** Speedup achieved when using the Fourier slice theorem for the calculation of the (inverse) Radon transform.

Image size $N \times N$	$256 \times 256$	$512 \times 512$	$1024 \times 1024$
$\frac{\text{Complexity}_{\text{Radon}} = O(N^3)}{\text{Complexity}_{\text{FST}} = O(N^2 \text{ld } N)}$	$\approx 10$	$\approx 18$	$\approx 32$

**Example 14.6 (Amplifying lines for image enhancement):** As an example of an application of the Radon transform to image processing, the amplification of line-shaped signal components for enhancing images with low SNR will be given [9, 26]. Figure 14.13(b) shows an SAR image (synthetic aperture radar) of the ocean surface captured by a satellite [31]. The image contains traces of the bow wave of a ship. For image enhancement, the Radon transform of the zero-mean image is calculated and then the point operation  $\text{sgn}(k)|k|^p$  is applied. Line-shaped structures which are mapped to local extrema in the  $u, \varphi$ -plane are enhanced for  $p > 1$  with respect to the noise components. Figure 14.13(c) shows the result for  $p = 2$  after an additional inverse Radon transform. Now, the traces of the wave show a notably increased signal-to-noise ratio.

In contrast to the Radon transform, the usual operators for the detection of edges and lines would have amplified the severe noise in the example image because of their differentiating characteristics. Being an integral transform, the Radon transform is beneficial for images with a low SNR. ■

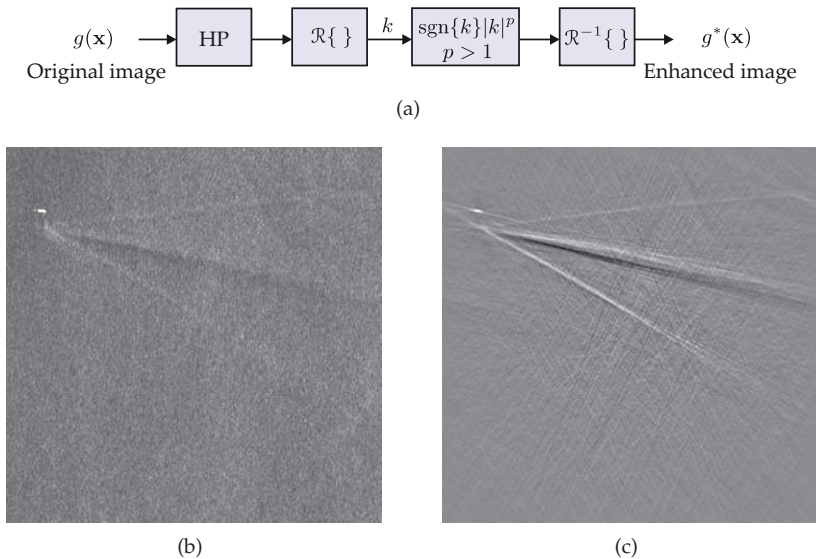


**Figure 14.13.** Image enhancement (accentuation of lines) by means of the Radon transform: (a) Processing steps of the image enhancement; (b) SAR image of a ship with bow wave (source: DLR TerraSAR-X); (c) Result of the image enhancement for  $p = 2$ .



➤ **14.3.2 Detection of line-shaped structures**

The Radon transform has been defined for  $\delta$ -lines, i.e., for infinitely extended and infinitesimally narrow lines. In fact, it can also be used for the detection of finite lines and other line-shaped structures, e.g., for a non-continuous chain of collinear points or line segments. Before discussing such examples, first the signal-to-noise ratio of the Radon transform will be investigated.

➤ **14.3.2.1 Signal-to-noise ratio (SNR)**

By using the Radon transform, a line-shaped structure is somehow concentrated in a small region in the Radon domain. The coordinates  $u$  and  $\varphi$  of an extremum corresponding to a line in the spatial domain are good estimates for the line's distance from the origin and for its angle.

In order to quantify the statistical advantages of the Radon transform, an additive superposition

$$g(\mathbf{x}) = s(\mathbf{x}) + h(\mathbf{x}) \tag{14.66}$$

of a line-shaped signal  $s(\mathbf{x}) = l(\mathbf{x}^T \mathbf{e}_\alpha - d)$  and an unwanted background image  $h(\mathbf{x})$  will be considered, where the profile  $l(\cdot)$  of the line  $s(\mathbf{x})$  is perpendicular to the line  $\mathbf{x}^T \mathbf{e}_\alpha - d$ , see Fig. 14.14(a).

In the following, the signal-to-noise ratio (SNR) of the image is shown before and after the Radon transform [2]:

– Before:  $SNR\{g(\mathbf{x})\} = \frac{s^2}{\sigma^2}$ ; (14.67)

– After:  $SNR\{\check{g}(u, \varphi)\} \approx \frac{(sL)^2}{L^2 \sigma^2 \frac{\xi}{L}} = \frac{s^2 L}{\sigma^2 \kappa}$ . (14.68)

Here,  $\sigma^2 = \text{Var}\{h(\mathbf{x})\}$  denotes the variance of the noise signal,  $\kappa$  denotes the correlation length of  $h(\mathbf{x})$  (cf. Sec. 13.4.1),  $s = \max_{\mathbf{x}}\{|s(\mathbf{x})|\} = \max_{\xi}\{|l(\xi)|\}$  the amplitude of  $s(\mathbf{x})$ , and  $L(u, \varphi) = \mathcal{R}\{I_{\Omega_g}(\mathbf{x})\}$  with the aperture function  $I_{\Omega_g}(\mathbf{x})$  of the image  $g(\mathbf{x})$ , see Fig. 14.14(b).

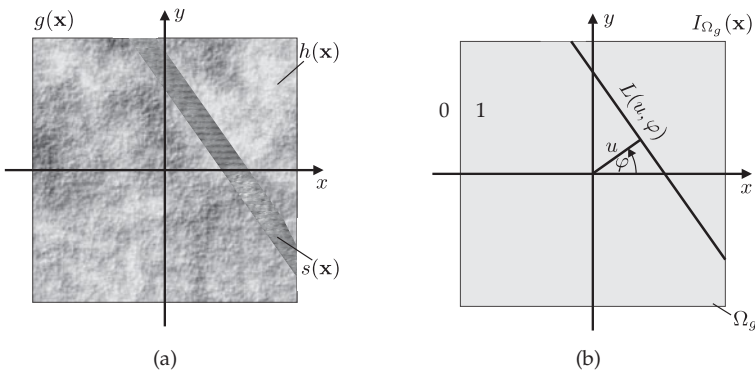


**Figure 14.14.** Calculation of the signal-to-noise ratio of the Radon transform: (a) Line-shaped structures embedded in an unwanted background texture, (b) Definition of aperture function  $I_{\Omega_g}(\mathbf{x})$  and projection length  $L$ .

The  $L(u, \varphi)$  are the lengths of the integration paths of the Radon integral inside the image  $g(\mathbf{x})$ . The aperture function of the image corresponds to the indicator function of the domain  $\Omega_g$ :

$$I_{\Omega_g}(\mathbf{x}) = \begin{cases} 1 & \text{if } \mathbf{x} \in \Omega_g \\ 0 & \text{otherwise.} \end{cases} \quad (14.69)$$

By means of the Radon transform, the SNR is improved by the factor

$$\frac{SNR\{\check{g}(u, \varphi)\}}{SNR\{g(\mathbf{x})\}} \approx \frac{L(u, \varphi)}{\kappa}, \quad (14.70)$$

which is a huge benefit for signal processing, especially for line segments that are significantly longer than the correlation length of the background.

⊗ **14.3.2.2 Detection using correlation filters**

The Radon transform allows an efficient realization of the correlation filter for the detection of line-shaped structures. By this means, the correlation of two signals, which usually requires an  $N$ -dimensional relative shift, is generalized to a shift parameter  $u$  and a rotation parameter  $\varphi$ :

$$\psi_{gl}(u, \varphi) := \int_{-\infty}^{\infty} \int_{-\infty}^{\infty} g(\mathbf{x}) l(\mathbf{x}^T \mathbf{e}_\varphi - u) \, d\mathbf{x}. \quad (14.71)$$

In the sense of a correlation filter,  $\psi_{gl}$ , to which an integral transform has been applied, has extrema at  $u = d$  and  $\varphi = \alpha$  in the  $u, \varphi$ -plane for signal components proportional to  $l(\mathbf{x}^T \mathbf{e}_\alpha - d)$ . These allow an exact and reliable detection and localization of lines with a profile  $l(\cdot)$ .

Expressing the lines  $l(\mathbf{x}^T \mathbf{e}_\varphi - u)$  as a convolution of a slice function and the line profile yields

$$\psi_{gl}(u, \varphi) = \int_{\rho=-\infty}^{\infty} \underbrace{\int_{-\infty}^{\infty} \int_{-\infty}^{\infty} g(\mathbf{x}) \delta(\mathbf{x}^T \mathbf{e}_\varphi - \rho) \, d\mathbf{x}}_{\check{g}(\rho, \varphi)} l(\rho - u) \, d\rho \quad (14.72)$$

$$= \int_{\rho=-\infty}^{\infty} \check{g}(\rho, \varphi) l(\rho - u) \, d\rho = \check{g}(u, \varphi) \overset{u}{*} l(-u). \quad (14.73)$$

This corresponds to a one-dimensional correlation filtering (or convolution) of the Radon transform of  $g(\mathbf{x})$  with the line profile  $l(\cdot)$ . The Radon transform and the Fourier slice theorem allow an efficient implementation of the correlation filter in the  $u, \varphi$ -plane.

⊗ **14.3.2.3 Examples of applications**

As an example of an application, the honing textures of Chap. 13 will be considered. First, the Radon transform can be used for the detection and localization of the grooves in the texture. In combination with the methods of texture analysis, an additional detection of defect grooves is possible [3].

**Example 14.7 (Detecting grooves in honing textures):** The straight grooves of honing textures cause extrema in the corresponding Radon transform. Figure 14.15 shows an example. The extrema in the Radon transform of Fig. 14.15(b) correspond to the line parameters  $(u, \varphi)$  of the grooves of Fig. 14.15(a). By means of the extrema, the positions of distinctive grooves can be reconstructed, see Fig. 14.15(c). ■

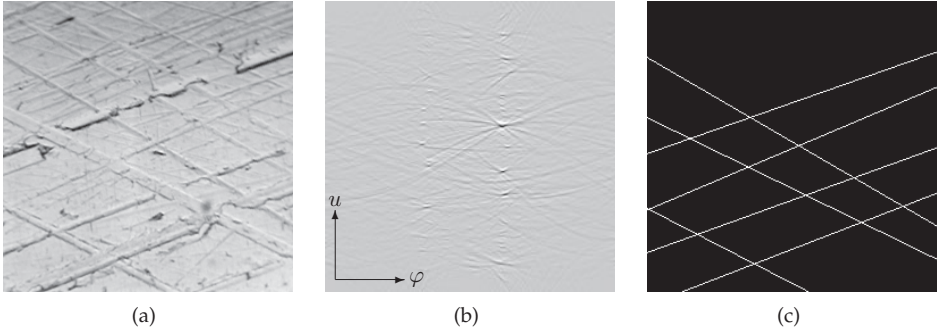


**Figure 14.15.** The detection of grooves in honing textures: (a) Honing texture  $g(\mathbf{x})$ , (b) Radon transform  $\tilde{y}(u, \varphi)$ , (c) Detection result.

**Example 14.8 (Detecting defective grooves in honing textures):** An important type of defect in honed surfaces is folded metal: after the honing process, the grooves might be partially interrupted (Fig. 14.16(a)). This defect is crucial regarding the quality of the cylinder surface in a combustion engine, as peeled-off iron particles might damage the surface during the operation of the engine.

For defect detection, the image  $g(\mathbf{x})$  of the honing texture is first split into a groove texture  $t(\mathbf{x})$  and the background image  $h(\mathbf{x})$  by the method of Sec. 13.3.4 (Fig. 14.16(b), (d)). Intact grooves appear almost exclusively in the texture image  $t(\mathbf{x})$ , whereas folded metal defects are represented in the background image  $h(\mathbf{x})$  by irregular variations along the groove. Hence, a defective groove is present if there are line-shaped structures in the texture image and intensity variations in the background image at the same position. For the detection of the line-shaped structures, the Radon transform is used and the background signal is squared before the transformation, in order to prevent the mutual extinction of bright and dark variations (Fig. 14.16(c), (e), (f)). Finally, the two Radon transforms are multiplied together (Fig. 14.16(g)):

$$\mathcal{R}\{t(\mathbf{x})\} \cdot \mathcal{R}\{(h(\mathbf{x}))^2\}. \quad (14.74)$$

Extrema in this product correspond to the line parameters  $(u, \varphi)$  of the defective grooves, which appear as line-shaped structures in the two separate images. By means of the most pronounced extrema, the position of the defective grooves can be reconstructed, see Fig. 14.16(h). ■

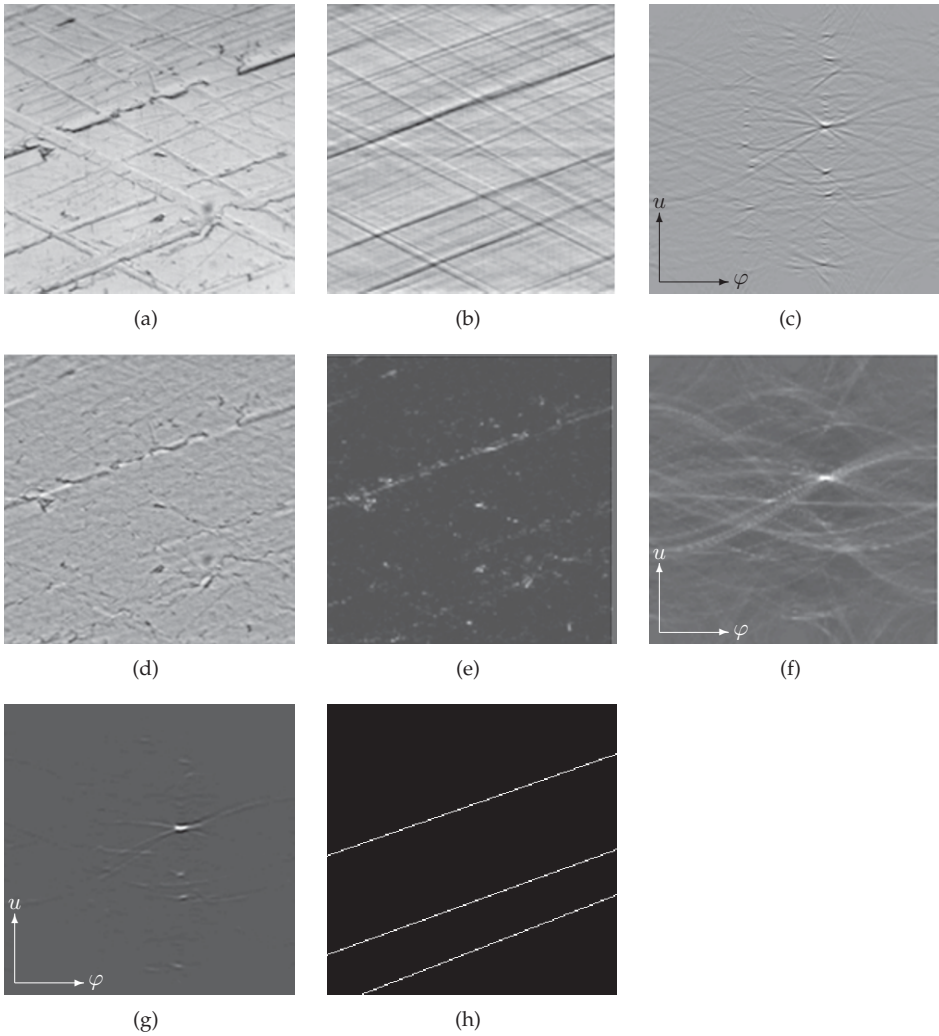


**Figure 14.16.** The detection of defect grooves in honing textures: (a) Honing texture  $g(\mathbf{x})$  with sheet jacket grooves, (b) Separated groove texture  $t(\mathbf{x})$ , (c) Radon transform  $\tilde{t}(u, \varphi)$  of the groove textures, (d) Separated image background  $h(\mathbf{x})$ , (e) Squared background signal  $(h(\mathbf{x}))^2$ , (f) Radon transform of (e), (g) Product of the Radon transforms (c) and (f), (h) Detection result.

### ► 14.3.3 The Hough transform for the detection of lines

To a certain degree, the well-known Hough transform for lines is a discrete special case of the Radon transform suitable for binary images [6, 10, 12, 16, 21]. For counting the image points belonging to a line, the Hough algorithm uses a special technique, which finally corresponds to the integration step of the Radon transform. Initially, the so-called accumulator  $A(u, \varphi)$  is initialized to zero for all discrete samples of the parameters  $u$  and  $\varphi$ . Then, for each pixel  $\mathbf{x}$  and for each discrete value of  $\varphi$ , the distance  $u$  of the line  $\mathbf{x}^T \mathbf{e}_\varphi - u = 0$  from the origin, which has the normal direction  $\varphi$  and which runs through  $\mathbf{x}$ , is calculated. The accumulator bin  $A(u, \varphi)$  is increased if  $g(\mathbf{x}) = 1$  in the binary image. In the case of a gray-scale image, the image value  $g(\mathbf{x})$  is added to the accumulator. Figure 14.17 shows the generalization of the Hough algorithm to gray-scale images. For binary images with  $g \in \{0, 1\}$ , the outer loops, which are evaluated for all image points, can be replaced by a loop that only processes those points  $\mathbf{x}$  that have  $g(\mathbf{x}) = 1$ .

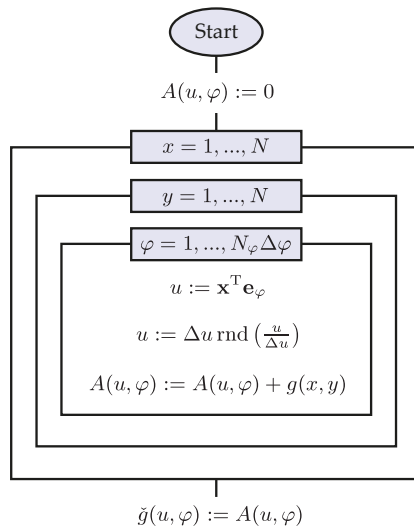


Figure 14.17. Algorithm of the Hough transform.

The Hough transform of a point is a sine-shaped curve running through the distances from the origin and through the angles of all lines containing this point. If in the image, there is a line with the parameters  $(\varphi, u)$ , the sine-shaped curves of its points intersect at the position  $(\varphi, u)$  in the Hough transform, resulting in an extremum. The magnitude of the extremum increases for longer lines. As usually the domain of an image is an axis-parallel rectangle, the number of summed image points varies with respect to the line parameters angle and distance from the origin. This causes a characteristic background pattern in the Hough transform. In most cases, this pattern can be mitigated by applying the transformation to zero-mean images.

---

**Example 14.9 (The Hough transform):** For the binary test image Fig. 14.18(a) with a rectangle and a trapezoid, Fig. 14.18(b) shows the Hough transform of the zero-mean image. As the lines are darker than the image background, they appear as minima in the Hough

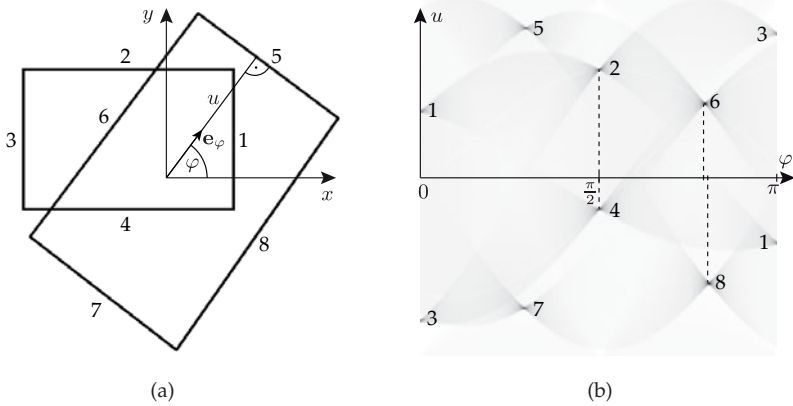


Figure 14.18. Line detection using the Hough transform: (a) Binary test image, (b) Corresponding Hough transform. The numbers represent the assignment of the lines in the image to the extrema of the Hough transform.

transform. The eight most intense minima can clearly be assigned to the lines in the test image. Because of the periodicity of the angles, the minima with  $\varphi = 0$  appear again at  $\varphi = \pi$ , but reflected at the  $\varphi$ -axis, i.e., with a negative  $u$ -value. The second, axially non-parallel quadrilateral is not a rectangle, but a trapezoid. This is quite obvious in the Hough transform, as the normal angles  $\varphi$  of the corresponding sides 6 and 8 of the rectangle are different. ■

In contrast to the Hough transform, the Radon transform can be applied to gray-scale images without any modifications. Besides, linear filter operations can be efficiently and simultaneously performed in the Fourier domain. For this purpose, only the 2D-FFT has to be multiplied by the complex-valued transfer function, before the sampling on the polar grid is carried out.

14.3.4 The Hough transform for the detection of curves

The Hough transform can also be formulated so as to allow the detection of arbitrary curves. Although this section covers the detection of lines and not of curves, the discussion of the generalization of the Hough transform is presented here, as it is quite similar in method. A family  $C$  of curves is assumed to be implicitly given by the equation

$$C(\mathbf{x}, \mathbf{p}) = 0, \quad \mathbf{p} = (p_1, \dots, p_K)^T \in \Pi, \tag{14.75}$$

with  $\mathbf{p}$  denoting the vector of the  $K$  parameters of the function family. The Hough transform for the detection of these curves uses a  $K$ -dimensional accumulator  $A(\mathbf{p})$ .

As long as the conditions of the implicit function theorem (cf. [5, 39]) are satisfied, Equation (14.75) can be solved for  $p_K$  w.l.o.g., resulting in an equation of the form

$$p_K = c(x, y, p_1, \dots, p_{K-1}). \tag{14.76}$$

Now, the Hough algorithm iterated over the pixels  $\mathbf{x}$  as well as over the first  $K - 1$  parameters  $p_1, \dots, p_{K-1}$  and the remaining parameters  $p_K$  is calculated according to this equation. After

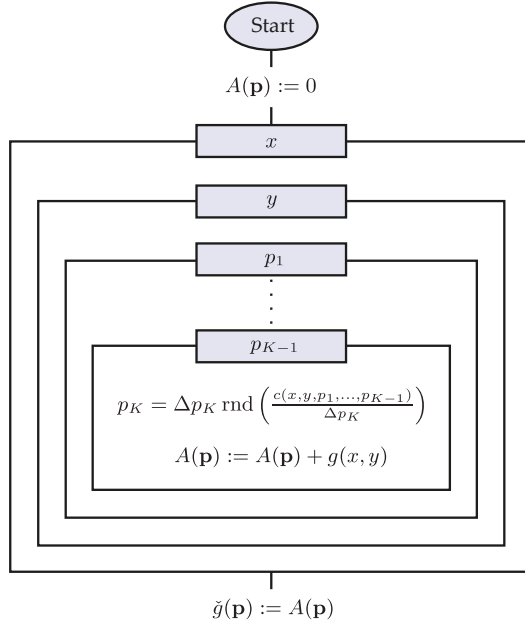


Figure 14.19. Algorithm of the Hough transform for the detection of curves  $C(\mathbf{x}, \mathbf{p}) = 0$ .

rounding to a discrete set of values of  $p_K$ , the accumulator bin  $A(p_1, \dots, p_K)$  is incremented by the image value  $g(\mathbf{x})$  (Fig. 14.19).

**Example 14.10 (Detection of lines):** The special case  $C(\mathbf{x}, \varphi, u) = \mathbf{x}^T \mathbf{e}_\varphi - u$ ,  $K = 2$ ,  $p_1 = \varphi$ ,  $p_2 = u$  results in the Hough transform for the detection of lines (Fig. 14.17). ■

**Example 14.11 (Detection of circles):** Circles can be implicitly defined as a set of curves:

$$0 = C(\mathbf{x}, \mathbf{p}) = (x - a)^2 + (y - b)^2 - \rho^2, \quad \mathbf{p} = (a, b, \rho)^T, \quad (14.77)$$

with  $(a, b)^T$  denoting the coordinates of the center and  $\rho$  denoting the radius. The three-dimensional accumulator  $A(a, b, \rho)$  of the Hough transform has a maximum at the position  $(a, b, \rho)$  if the image  $g(\mathbf{x})$  contains a circle with center  $(a, b)^T$  and radius  $\rho$  [33]. ■

**Example 14.12 (Detection of ellipses):** An ellipse with center  $(a, b)^T$ , semi-axes  $c$  and  $d$ , and rotation angle  $\beta$  (Fig. 14.20) can be described by

$$0 = C(\mathbf{x}, \mathbf{p}) = \frac{((x - a) \cos \beta + (y - b) \sin \beta)^2}{1 - \left(\frac{(y - b) \cos \beta - (x - a) \sin \beta}{d}\right)^2} - c^2, \quad \mathbf{p} = (a, b, c, d, \beta)^T, \quad (14.78)$$

resulting in a five-dimensional accumulator. Figure 14.21 shows the result of the method applied to a test image. The image shows a two-dimensional section through the Hough

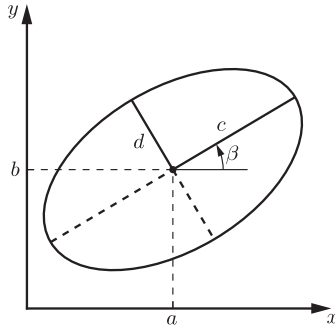


Figure 14.20. Parameters of the equation of an ellipse.

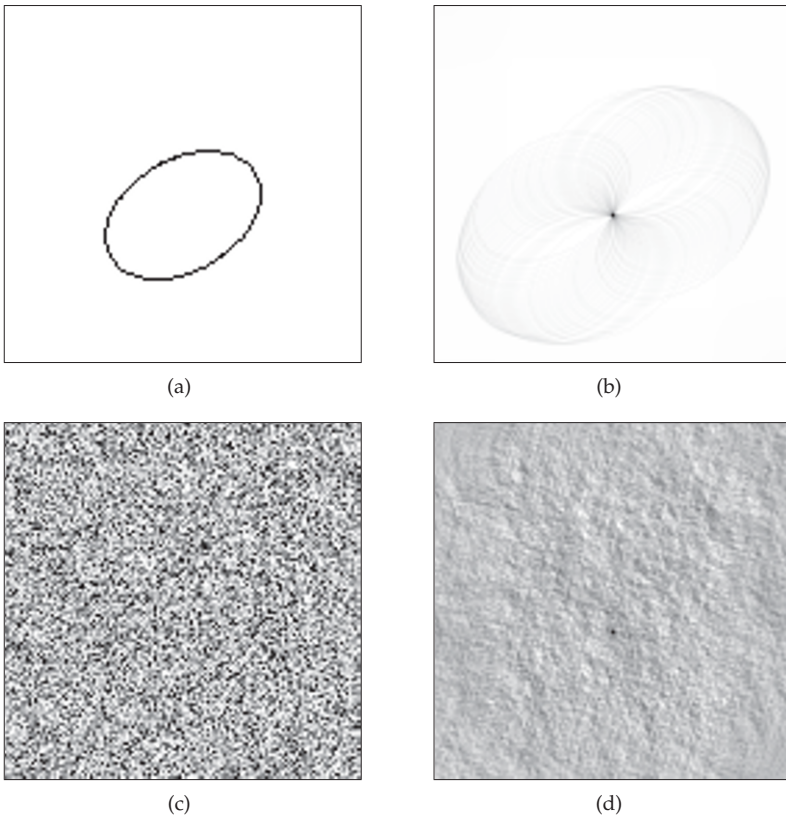


Figure 14.21. Detection of ellipses using the Hough transform: (a) Noise-free image with an ellipse, (b) Two-dimensional section through the Hough transform in the  $a,b$ -plane for  $c = 30, d = 20, \beta = \frac{\pi}{9}$ , (c) Image with artificial noise, (d) Two-dimensional section through the corresponding Hough transform.

transform for the correct parameters  $c = 30, d = 20, \beta = \frac{\pi}{9}$ . The global minimum is located at the center  $(a, b)^T$  of the ellipse and is even detectable in the case of intense



noise. Besides, Fig. 14.21(b) shows secondary peaks on a curve with twice the distance to the semi-axes around the center. Ellipses with these centers are tangent to the ellipse contained in the image. ■

The computational complexity of the Hough transform is  $O(N^{K+1})$  and the space requirement is  $O(N^K)$ , where  $N$  denotes the number of sampling points for each of the coordinate axes  $x, y, p_1, \dots, p_K$ . Thus, line detection has a computational complexity of  $O(N^3)$ , which is already greater than the complexity of the Radon transform (if the latter is implemented using the Fourier slice theorem). For a higher number of parameters  $K$ , the Hough transform for curves has a high computational complexity and high space requirements, so that in most cases, only a rough discretization of the parameter space  $\Pi$  is practically possible.

► **14.3.5 The generalized Hough transform**

There are further generalizations of the Hough transform, which try to detect and localize even more sophisticated structures than parametrized curves [1]. For example, the structures sought might be given as a binary image  $S$ , which can be an arbitrary structure or contour, for which no analytic model (like a set of curves) is needed. Now, a reference point  $\mathbf{a}$  is chosen, e.g., the center of the structure. The structure is represented by the vectors  $\mathbf{r}$  that run from the points of the structure to the reference points (cf. Fig. 14.22):

$$\mathcal{R}_S := \{\mathbf{r} \mid \mathbf{x} + \mathbf{r} = \mathbf{a}, \mathbf{x} \in S\}. \tag{14.79}$$

For the detection of the structure  $S$  in an image  $g(\mathbf{x})$ , the bins  $A(\mathbf{x} + \mathbf{r})$  of the accumulator are incremented for every vector  $\mathbf{r}$  of  $\mathcal{R}_S$ :

$$\forall \mathbf{r} \in \mathcal{R}_S \quad A(\mathbf{x} + \mathbf{r}) := A(\mathbf{x} + \mathbf{r}) + g(\mathbf{x}). \tag{14.80}$$

A structure  $S$  in the image  $g$  with the reference point at the image position  $\mathbf{x}$  causes an extremum at the bin  $\mathbf{x}$  of the accumulator.

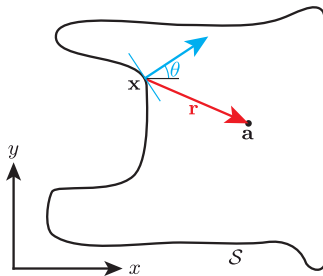


Figure 14.22. Notation for the generalized Hough transform.

If all  $|\mathcal{R}_S|$  accumulator bins are incremented for all structure points, the extrema in the accumulator often do not show an appreciable magnitude. A better signal-to-noise ratio can be achieved using additional information. A common approach is the consideration of the local gradient direction  $\theta(\mathbf{x})$  in the image. In this case, the following representation of the structure  $S$  is obtained, with respect to the gradient direction  $\theta$ :

$$\mathcal{R}_S(\theta) := \{\mathbf{r} \mid \mathbf{x} + \mathbf{r} = \mathbf{a}, \mathbf{x} \in S \wedge \theta_S(\mathbf{x}) = \theta\}, \tag{14.81}$$

with  $\theta_S(\mathbf{x})$  denoting the gradient direction at the position  $\mathbf{x}$  of the structure  $S$ . An adequate discretization has to be applied to the gradient direction  $\theta$ .

The application of the generalized Hough transform considers only those accumulator bins for every point  $\mathbf{x}$  of the image  $g$  for which the local gradient directions  $\theta_g$  of the image and  $\theta_S$  of the sought for structure are equal:

$$\forall \mathbf{r} \in \mathcal{R}_S(\theta_g(\mathbf{x})) \quad A(\mathbf{x} + \mathbf{r}) := A(\mathbf{x} + \mathbf{r}) + g(\mathbf{x}). \quad (14.82)$$

By this means, the set of the corresponding accumulator bins is markedly decreased, resulting in more distinct extrema at the reference points of the structure and in a reduced computational complexity. In the literature, there are further approaches to increasing the efficiency of the generalized Hough transform [20].

To achieve a rotation-invariant and scale-invariant detection, the accumulator can be extended by the dimensions of the rotation angle  $\varphi$  and the scaling factor  $\alpha$ . The accumulator bins  $A(\mathbf{x}, \varphi, \alpha)$  corresponding to an image point  $\mathbf{x}$  can be determined by a simple transformation of the representation  $\mathcal{R}_S(\theta)$  [1]. However, such additional dimensions notably increase the computational costs of the method.

### ► 14.3.6 Implicit shape models

**Implicit shape models** can be considered as a further generalization of the Hough transform [22–24]. These models not only use contours or point sets to describe the object of interest, but annotate the object components with feature descriptors (cf. Sec. 13.4). Typically, corners or other interest points are used for this purpose. For these points, suitable features are calculated, e.g., scale-invariant and rotation-invariant SIFT features or SURF features (see Sec. 15.6). In fact, it is also possible to directly use the image values of a certain region as a feature vector. Both the codebook of the feature descriptors and the spatial distribution of the object components with respect to the object's reference point can be learned from training samples.

For object detection, first the feature descriptors of the interest points of the image are calculated and compared to the learned codebook entries. If there is a sufficient similarity, the accumulator bin of the corresponding reference point of the object is incremented. Again, extrema of the accumulator represent candidates for the object contained in the image.

Besides the detection of objects, the method allows the determination of the position and orientation of the individual components of an object [4, 17].

## 14.4 Corner detection

For various applications, the detection and localization of corners contained in the image is of great interest. In automated visual inspection, a test object can be localized and dimensioned by means of its corners. Furthermore, corners are typical features of the patterns that are used for camera calibration (see Sec. 3.3). Finally, corners or other interest points can be found in multiple images of the same object and can therefore be used for correspondence methods, which are required for evaluating stereo images or image series (see Sec. 7.3.8).

Inside a homogeneous image region, the image value is approximately constant in all directions. Edges show a high change of the image value in the gradient direction, i.e., perpendicular to the edge, whereas the image value barely changes along the edge. A **corner**

is considered to represent an image point for which the image values significantly change in all directions. This is the case for, e.g., the intersection of two edges or also for isolated points which are brighter or darker than their surroundings. In the sense of image processing, a corner does not necessarily have to be a corner of the observed object as in the colloquial sense.

In the following, the **Harris operator** will be presented, which is a famous method for the detection of corners. In order to derive the Harris operator, a local window in the image is considered [11]. By comparing the image signal inside the window with a slightly shifted window, information about edges and corners can be gained: an edge causes a notable change of the image values for a shift in the direction of the gradient and no change for a shift parallel to the edge. Conversely, corners cause changes of the image values for shifts of the window in every direction.

The change of the image values can be quantified by the sum of the squared differences. Here, the window function is a Gaussian function with parameter  $\sigma$ . So for a shift by the vector  $(\Delta x, \Delta y)^T$ , this results in

$$c(x, y) \propto \sum_{u,v} e^{-\frac{(u-x)^2+(v-y)^2}{2\sigma^2}} (g(u, v) - g(u + \Delta x, v + \Delta y))^2. \quad (14.83)$$

By expanding a Taylor series around  $(u, v)^T$ , the shifted image can be written as

$$g(u + \Delta x, v + \Delta y) \approx g(u, v) + \left( \frac{\partial g}{\partial u}(u, v), \frac{\partial g}{\partial v}(u, v) \right) \begin{pmatrix} \Delta x \\ \Delta y \end{pmatrix}. \quad (14.84)$$

Inserting this approximation into (14.83) yields

$$c(x, y) \propto \sum_{u,v} e^{-\frac{(u-x)^2+(v-y)^2}{2\sigma^2}} (g(u, v) - g(u + \Delta x, v + \Delta y))^2 \quad (14.85)$$

$$\approx \sum_{u,v} e^{-\frac{(u-x)^2+(v-y)^2}{2\sigma^2}} \left( g(u, v) - g(u, v) - \left( \frac{\partial g}{\partial u}(u, v), \frac{\partial g}{\partial v}(u, v) \right) \begin{pmatrix} \Delta x \\ \Delta y \end{pmatrix} \right)^2 \quad (14.86)$$

$$= \sum_{u,v} e^{-\frac{(u-x)^2+(v-y)^2}{2\sigma^2}} \left( \left( \frac{\partial g}{\partial u}(u, v), \frac{\partial g}{\partial v}(u, v) \right) \begin{pmatrix} \Delta x \\ \Delta y \end{pmatrix} \right)^2. \quad (14.87)$$

With  $(\mathbf{a}^T \mathbf{b})^2 = \mathbf{a}^T \mathbf{b} \mathbf{a}^T \mathbf{b} = \mathbf{b}^T \mathbf{a} \mathbf{a}^T \mathbf{b}$ , this results in

$$c(x, y) \approx (\Delta x, \Delta y) \sum_{u,v} e^{-\frac{(u-x)^2+(v-y)^2}{2\sigma^2}} \begin{pmatrix} \left( \frac{\partial g}{\partial u}(u, v) \right)^2 & \left( \frac{\partial g}{\partial u}(u, v) \right) \left( \frac{\partial g}{\partial v}(u, v) \right) \\ \left( \frac{\partial g}{\partial u}(u, v) \right) \left( \frac{\partial g}{\partial v}(u, v) \right) & \left( \frac{\partial g}{\partial v}(u, v) \right)^2 \end{pmatrix} \begin{pmatrix} \Delta x \\ \Delta y \end{pmatrix} \quad (14.88)$$

$$= (\Delta x, \Delta y) \mathbf{C}(x, y) \begin{pmatrix} \Delta x \\ \Delta y \end{pmatrix} \quad (14.89)$$

$$\text{with } \mathbf{C}(x, y) := \sum_{u,v} e^{-\frac{(u-x)^2+(v-y)^2}{2\sigma^2}} (\text{grad } g(u, v) (\text{grad } g(u, v))^T). \quad (14.90)$$

The resulting matrix  $\mathbf{C}(x, y)$  corresponds to the structure tensor  $\mathbf{J}_\sigma(\text{grad } g(\mathbf{x}))$  at the image point  $\mathbf{x}$  as in (11.87). The eigenvalues  $\mu_1 \geq \mu_2 \geq 0$  and the corresponding orthogonal eigen-

vectors  $\mathbf{v}_1, \mathbf{v}_2$  of the structure tensor characterize the local changes of the image value at the position  $\mathbf{x}$ :

- 1st case: both eigenvalues  $\mu_1, \mu_2$  are small.  
The change of the image values  $c(\mathbf{x})$  is low for every shift direction. This is, then, a homogeneous image region with an approximately constant image value  $g(\mathbf{x})$ .
- 2nd case: the first eigenvalue  $\mu_1$  is large, the second eigenvalue  $\mu_2$  is small.  
The change  $c(\mathbf{x})$  of image values is large in the shift direction  $\mathbf{v}_1$  and small in the orthogonal direction  $\mathbf{v}_2$ . This corresponds to an edge with normal vector  $\mathbf{v}_1$ .
- 3rd case: both eigenvalues  $\mu_1, \mu_2$  are large.  
For an arbitrary shift vector, the change  $c(\mathbf{x})$  of the image values is high. The window contains a corner.

By means of the eigenvalues of the structure tensor, corners can be detected in the image. However, the Harris operator uses no explicit calculation of the eigenvalues for reasons of complexity. In fact, the determinant and the trace of the matrix are used, which are related to the eigenvalues  $\mu_1$  and  $\mu_2$  as follows

$$\det \mathbf{C} = \mu_1 \mu_2 = ab - d^2, \quad (14.91)$$

$$\text{trace}(\mathbf{C}) = \mu_1 + \mu_2 = a + b, \quad (14.92)$$

with the symmetric structure tensor being written as

$$\mathbf{C} = \begin{pmatrix} a & d \\ d & b \end{pmatrix} \quad (14.93)$$

In contrast to the trace, which has large values for both corners and edges, the determinant is especially large for corners. This motivates the following definition of the Harris operator:

$$\text{corner}(\mathbf{x}) := \det \mathbf{C}(\mathbf{x}) - k (\text{trace}(\mathbf{C}(\mathbf{x})))^2, \quad k > 0. \quad (14.94)$$

This expression shows maxima for corners, negative values for edges, and tends to zero for homogeneous regions.

---

**Example 14.13 (Corner detection using the Harris operator):** The results of the application of the Harris operator with the parameter  $k = 0.04$  to two test images are shown in Fig. 14.23. The binary image clearly shows that corners lead to positive (bright) values and edges lead to negative (dark) values of  $\text{corner}(\mathbf{x})$ , whereas in homogeneous regions,  $\text{corner}(\mathbf{x}) = 0$  (gray areas in Fig. 14.23(b)). For the buildings in Fig. 14.23(c), the corners are mainly detected at windows and doors, but also at isolated plants in the forecourt. ■

Also the local binary patterns mentioned in Sec. 13.4.6 can be used for the detection of interest points [13]. The scale-invariant detection of interest points is discussed in Sec. 15.6.

## 14.5 Bibliography

- [1] Dana Ballard. Generalizing the Hough Transform to Detect Arbitrary Shapes. *Pattern Recognition*, 13(2):111–122, 1981.

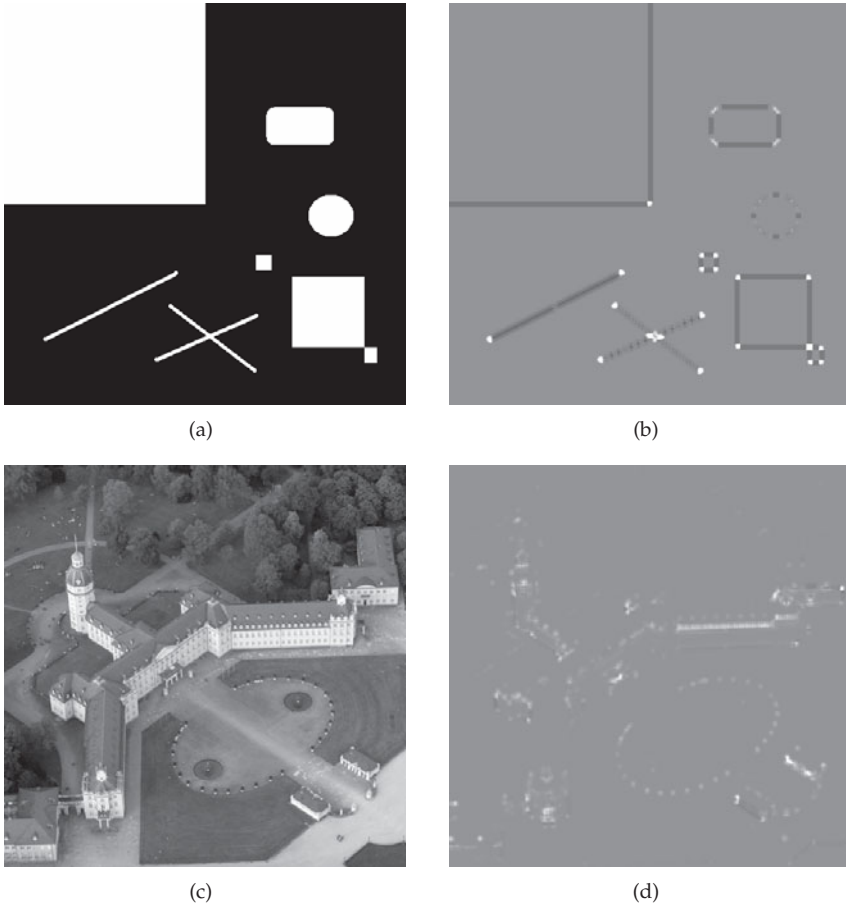


**Figure 14.23.** Edge detection using the Harris operator: (a) Binary test image, (b) Result of the Harris operator applied to (a), (c) Aerial photograph of the Karlsruhe Palace (source: ONUK), (d) Result of the Harris operator applied to (c).

- [2] Jürgen Beyerer. *Analyse von Riefentexturen*. PhD thesis, Universität Karlsruhe (TH), 1994.
- [3] Jürgen Beyerer and Fernando Puente León. Die Radontransformation in der digitalen Bildverarbeitung. *Automatisierungstechnik*, 50(10):472–480, 2002.
- [4] Jürgen Brauer. *Human Pose Estimation with Implicit Shape Models*. PhD thesis, Karlsruhe Institute of Technology, 2014.
- [5] Ward Cheney. *Analysis for applied mathematics*. Springer, 2001.
- [6] Richard Duda and Peter Hart. Use of the Hough transformation to detect lines and curves in pictures. *Communications of the ACM*, 15(1):11–15, 1972.
- [7] Rafael Gonzalez and Richard Woods. *Digital image processing*. Pearson Prentice Hall, 3rd edition, 2008.

- [8] Martin Grafmüller, Jürgen Beyerer, and Kristian Kroschel. Decision Tree Classifier for Character Recognition Combining Support Vector Machines and Artificial Neural Networks. In *Mathematics of Data/Image Coding, Compression, and Encryption with Applications, Proc. SPIE*, volume 7799, San Diego, USA, August 2010.
- [9] Graham Hall, Trevor Terrel, John Senior, and Lesley Murphy. New fast discrete Radon transform for enhancing linear features in noisy images. *Electronics Letters*, 24(14):876–877, 1988.
- [10] Robert Haralick and Linda Shapiro. *Computer and robot vision*. Addison-Wesley, 1992.
- [11] Chris Harris and Mike Stephens. A combined corner and edge detector. In *Proceedings of the 4th Alvey Vision Conference*, pages 147–151, 1988.
- [12] Peter Hart. How the Hough Transform Was Invented. *IEEE Signal Processing Magazine*, pages 18–22, 2009.
- [13] Marko Heikkilä, Matti Pietikäinen, and Cordelia Schmid. Description of interest regions with local binary patterns. *Pattern Recognition*, 42(3):425–436, 2009.
- [14] Harro Heuser. *Funktionalanalysis – Theorie und Anwendung*. Teubner, 4th edition, 2006.
- [15] Joseph Horner and Peter Gianino. Phase-only matched filtering. *Applied Optics*, 23(6):812–816, March 1984.
- [16] Paul Hough. Method and means for recognizing complex patterns. Patent US 3069654, 1962.
- [17] Kai Jüngling. *Ein generisches System zur automatischen Detektion, Verfolgung und Wiedererkennung von Personen in Videodaten*. PhD thesis, Karlsruhe Institute of Technology, 2011.
- [18] Avinash Kak and Malcolm Slaney. *Principles of computerized tomographic imaging*. Society for Industrial and Applied Mathematics, 2001.
- [19] Willi Kalender. *Computed tomography: fundamentals, system technology, image quality, applications*. Publicis, 3rd edition, 2011.
- [20] A. Kassim, T. Tan, and K. Tan. A comparative study of efficient generalised Hough transform techniques. *Image and Vision Computing*, 17(10):737–748, 1999.
- [21] Violet Leavers. *Shape detection in computer vision using the Hough transform*. Springer, 1992.
- [22] Alain Lehmann, Bastian Leibe, and Luc Van Gool. Fast PRISM: Branch and Bound Hough Transform for Object Class Detection. *International Journal of Computer Vision*, 94(2):175–197, 2011.
- [23] Bastian Leibe, Aleš Leonardis, and Bernt Schiele. Combined Object Categorization and Segmentation with an Implicit Shape Model. In *ECCV Workshop on Statistical Learning in Computer Vision*, pages 17–32, 2004.
- [24] Bastian Leibe, Aleš Leonardis, and Bernt Schiele. Robust object detection with interleaved categorization and segmentation. *International Journal of Computer Vision*, 77:259–289, 2008.
- [25] Elliott H. Lieb and Michael Loss. *Analysis*, volume 14 of *Graduate Studies in Mathematics*. American Mathematical Society, 1997.
- [26] Lesley Murphy. Linear feature detection and enhancement in noisy images via the Radon transform. *Pattern Recognition Letters*, 4(4):279–284, 1986.
- [27] Ana Pérez Grassi. *Variable illumination and invariant features for detecting and classifying varnish defects*. PhD thesis, Karlsruhe Institute of Technology, 2010.
- [28] Johann Radon. Über die Bestimmung von Funktionen durch ihre Integralwerte längs gewisser Mannigfaltigkeiten. *Berichte über die Verhandlungen der Königlich Sächsischen Gesellschaft der Wissenschaften, Mathematisch-Physikalische Klasse*, 69:262–277, 1917.
- [29] Paul Rattay and Allen Lindgren. Sampling the 2-D Radon transform. *IEEE Transactions on Acoustics, Speech and Signal Processing*, 29(5):994–1002, October 1981.
- [30] Jennifer Sander, Michael Heizmann, Igor Goussev, and Jürgen Beyerer. Global evaluation of focussed Bayesian fusion. In Jerome Braun, editor, *Multisensor, Multisource Information Fusion: Architectures, Algorithms, and Applications, Proc. SPIE*, volume 7710, 2010.

- [31] Günter Saur, Stéphane Estable, Karin Zielinski, Stefan Knabe, Michael Teutsch, and Matthias Gabel. Detection and classification of man-made offshore objects in TerraSAR-X and RapidEye imagery: Selected results of the DeMarine-DEKO project. In *IEEE OCEANS*, 2011.
- [32] Hanns Schulz-Mirbach. *Anwendung von Invarianzprinzipien zur Merkmalgewinnung in der Mustererkennung*. VDI-Verlag, 1995.
- [33] Wesley Snyder and Hairong Qi. *Machine vision*. Cambridge University Press, 2004.
- [34] Josef Stoer and Roland Bulirsch. *Introduction to numerical analysis*. Springer, 3rd edition, 2002.
- [35] Ansgar Trächtler. *Tomographische Methoden in der Messtechnik*, volume 897 of *Fortschritt-Berichte VDI*, 8. VDI-Verlag, 2001.
- [36] A. vander Lugt. Signal detection by complex spatial filtering. *IEEE Transactions on Information Theory*, 10(2):139–145, 1964.
- [37] Vijaya Kumar, Fred Dickey, and John DeLaurentis. Correlation filters minimizing peak location errors. *Journal of the Optical Society of America A*, 9(5):678–682, 1992.
- [38] Vijaya Kumar and L. Hasebrook. Performance measures for correlation filters. *Applied Optics*, 29(20):2997–3006, 1990.
- [39] Wolfgang Walter. *Analysis 2*. Springer, 4th edition, 1995.

Chapter 15

**Image Pyramids, the Wavelet Transform and  
Multiresolution Analysis**

**15**

---



**15 Image Pyramids, the Wavelet Transform and Multiresolution Analysis**

15.1 Image pyramids . . . . .	723
15.1.1 Gaussian pyramid . . . . .	725
15.1.2 Laplacian pyramid . . . . .	726
15.1.3 Pyramid linking . . . . .	727
15.2 Wavelets . . . . .	728
15.2.1 Continuous wavelet transform . . . . .	728
15.2.2 Discretization of the wavelet transform . . . . .	731
15.3 Multiresolution analysis . . . . .	733
15.4 The fast wavelet transform . . . . .	738
15.5 The two-dimensional wavelet transform . . . . .	742
15.6 Scale-invariant features . . . . .	744
15.7 Bibliography . . . . .	749

## 15 Image Pyramids, the Wavelet Transform and Multiresolution Analysis

Multiresolution analysis is a mathematical concept describing signal analysis on different resolution levels. In contrast to the analysis of the fine details contained in the image, which requires the maximum possible resolution, coarse structures can be analyzed with little effort using a reduced resolution. Two methods for multiresolution analysis, which are covered in this chapter, are image pyramids and the wavelet transform.

### 15.1 Image pyramids

Images contain structures like edges, corners, texels, objects, and defects on different scales, i.e., with different spatial extents. On the one hand, this is because of the size, shape and texture of the observed objects and on the other hand this is caused by the constraints of the image acquisition: depending on the focal length of the camera lens and on the distance of the objects, the structures of interest are imaged with varying magnifications. For many applications of image processing, it is preferable to efficiently analyze structures on different scales, in order to investigate different object properties and to achieve a certain invariance with respect to the magnification.

However, naively applying the image processing methods on multiple scales might cause a huge computational complexity.

For example, the convolution necessary for a correlation filter (see Sec. 14.1) used to detect an object of size  $L \times L$  in an image of size  $N \times N$  requires about  $\mathcal{O}(N^2 L^2)$  operations in the spatial domain. Hence, an analysis on multiple resolutions quadratically increases the computing time with respect to the object width  $L$ . The resulting computing time can easily impair the practicality of a visual inspection system for real-time applications.

In order to reduce the costs of inspecting large image structures, the concept of image pyramids has been introduced by Burt [7, 11, 13]. It uses an iterative filtering and subsampling of the image  $g_{mn}$ . This results in a pyramid of images  $g_{mn}^\nu$ , of which every image represents a certain scale.

The construction of an image pyramid for an w.l.o.g. square image  $g_{mn}$  of size  $N \times N$  requires the following steps:

1. Initialization of the iterative method with the original image:

$$g_{mn}^0 := g_{mn}. \quad (15.1)$$

2. For  $\nu = 1, 2, \dots, K$ , low-pass filtering of  $g_{mn}^{\nu-1}$  to one-half of the original bandwidth.
3. Subsampling by a factor of 2. Because of the previous low-pass filtering, the sampling theorem still applies. The result is the filtered and subsampled image

$$g_{mn}^\nu \quad \text{of size} \quad \frac{N}{2^\nu} \times \frac{N}{2^\nu}. \quad (15.2)$$

4. Continuing the iterative pyramid construction with step 2.

Figure 15.1 shows the resulting image pyramid.

The pyramid contains the image in logarithmic resolution levels (the so-called multiresolution or multigrid principle).

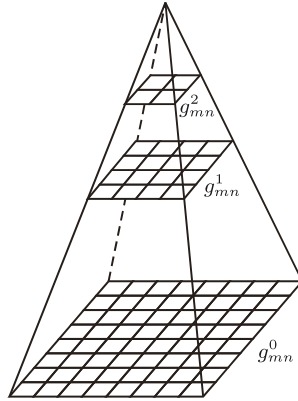


Figure 15.1. Construction of a pyramid from the image  $g_{mn}^0 := g_{mn}$ .

By this means, coarse image structures as well as fine image structures can be evaluated using small local operators. The application of the operator on one of the upper levels of the pyramid ( $\nu > 0$ ) approximately corresponds to the application of the virtually, proportionally enlarged operator to the original image ( $\nu = 0$ ). Because of the pyramid concept, coarse structures get within the reach of local operators.

Considering the example of the detection task again, the costs of level  $\nu > 0$  of the pyramid are reduced to about  $\mathcal{O}(2^{-4\nu} N^2 L^2)$ , as the dimensions of the image and the object are both reduced by the factor  $2^{-\nu}$  to  $2^{-\nu}N \times 2^{-\nu}N$ , respectively,  $2^{-\nu}L \times 2^{-\nu}L$ . Hence, the computational costs are notably reduced for increasing  $\nu$ . This is why also the detection of large objects is efficient but involves the loss of fine details because of the low-pass filtering between the pyramid levels.

Despite the need for storing the image information at multiple resolutions, the costs of a single image pyramid remains manageable. The first subsampled image  $g_{mn}^1$  has the size  $\frac{N}{2} \times \frac{N}{2}$ , the second  $g_{mn}^2$  has the size  $\frac{N}{4} \times \frac{N}{4}$ , and so on. The total amount of image pixels can be estimated using the geometric series [6, 24, 26]:

$$N^2 + \frac{N^2}{4} + \frac{N^2}{16} + \dots \leq N^2 \sum_{\nu=0}^{\infty} \frac{1}{4^\nu} = \frac{4}{3} N^2. \tag{15.3}$$

From now on, the reduction of the resolution inside the pyramid is denoted by the following notation:

$$g_{mn}^\nu = \downarrow g_{mn}^{\nu-1} := \text{Subsampling by the factor 2 of } g_{mn}^{\nu-1} ** h_{mn}. \tag{15.4}$$

First, a convolution with the impulse response  $h_{mn}$  of a suitable low-pass filter is applied to the image  $g_{mn}^{\nu-1}$ , which is then subsampled. The other way around, the image is interpolated, which is called expansion:

$$h_{mn} ** g_{mn}^\nu = \uparrow g_{mn}^{\nu+1} := 4 \sum_{(k,l) \in \mathcal{L}_{mn}} i_{kl} g_{\frac{m-k}{2}, \frac{n-l}{2}}^{\nu+1} \tag{15.5}$$

with

$$\mathcal{I}_{mn} := \{(k, l) \in \mathbb{Z}^2 \mid m - k \text{ and } n - l \text{ are even numbers}\}. \tag{15.6}$$

With  $m - k =: 2p, n - l =: 2q$  and integers  $p, q$  it is  $k = m - 2p, l = n - 2q$  and therefore

$$\uparrow g_{mn}^{\nu+1} = 4 \sum_{(p,q) \in \Omega_{g^{\nu+1}}} i_{m-2p, n-2q} g_{pq}^{\nu+1}, \tag{15.7}$$

with  $\Omega_{g^{\nu+1}}$  denoting the image's domain as usual; in this case  $g_{mn}^{\nu+1}$ . In every coordinate direction, the extent of the expanded image is increased by the factor 2 with respect to  $g_{mn}^{\nu+1}$ . The factor 4 is needed, as for the interpolation only values of the even pixel positions in both coordinate directions are available. In the ideal case, the interpolation filter  $i_{mn}$  corresponds to the sinc function (see Sec. 9.2.1). Often, however  $i_{mn} := h_{mn}$  is set [7]. The low-pass filter  $h_{mn}$  should meet the following requirements:

- Positivity:  $h_{mn} > 0 \quad \forall m, n$ .
- $h_{mn}$  is unimodal, i.e., the impulse response only has a single maximum.
- Point symmetry with respect to the origin:  $h_{mn} = h_{-m, -n} \quad \forall m, n$ .
- Preserving the mean image value:  $\sum_{m,n} h_{mn} = 1$ .
- Every pixel is supposed to make the same contribution to the following level. As only the pixels with even indices are preserved by the subsampling, the sums of the even and odd filter coefficients have to be equal:  $\sum_{i,j} h_{2i,2j} = \sum_{i,j} h_{2i+1,2j} = \sum_{i,j} h_{2i,2j+1} = \sum_{i,j} h_{2i+1,2j+1}$ .
- Separability:  $h_{mn} = h_m h_n$  with a one-dimensional impulse response  $h_n$  [7]. Separability allows an efficient implementation, see Sec. 9.3.1.1.

All these requirements are met by the binomial low-pass filter (cf. Sec. 9.3.1.4).

15.1.1 Gaussian pyramid

An image pyramid constructed with the binomial low-pass  $h_{mn,L}$  is called a Gaussian pyramid. Figure 15.2 visualizes the application of the processing chain of low-pass filtering and subsampling by the factor 2 to a one-dimensional image  $g_m$ .

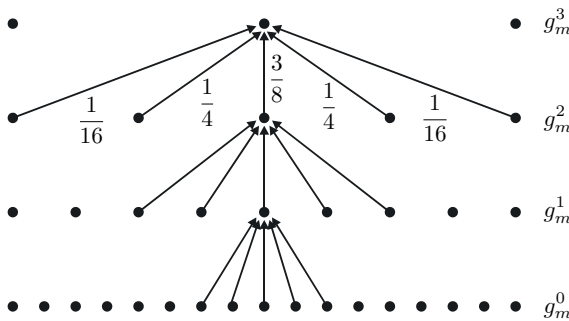


Figure 15.2. Construction of a one-dimensional Gaussian pyramid using a binomial filter of size  $L = 5$ .

### ► 15.1.2 Laplacian pyramid

Until now, image pyramids were constructed using a low-pass filtering. In every step, signal components with a high spatial frequency are filtered out, so that only low spatial frequencies remain at the upper levels of the pyramid.

Alternatively, the pyramids can be constructed to contain a band-pass filtering of the original image. A simple possibility of realizing such a band-pass filtering is the subtraction of two subsequent images of a low-pass pyramid. In the case of the Gaussian pyramid  $g_{mn}^\nu$ , this approach results in the Laplacian pyramid  $\lambda_{mn}^\nu$ :

$$\lambda_{mn}^\nu := g_{mn}^\nu - \uparrow g_{mn}^{\nu+1}. \quad (15.8)$$

The subtraction of the images filtered with the binomial low-pass corresponds to the difference of Gaussian filtering of Sec. 11.2.2. By this means, the  $\lambda_{mn}^\nu$  represent approximations of the second derivative of the original image with different smoothing parameters. On the first level of the Laplacian pyramid, fine edge structures are amplified, whereas on higher levels, coarser edge structures of the original image are visible.

**Example 15.1 (Image pyramids):** Figure 15.3 shows the first levels of the Gaussian and of the Laplacian pyramid of an image  $g_{mn}$ . As each level halves the number of rows and columns, the images shown here are slightly enlarged for  $\nu \geq 1$ . In the Laplacian pyramid, the image value 0 is rendered gray, positive image values appear bright and negative values appear dark. ■

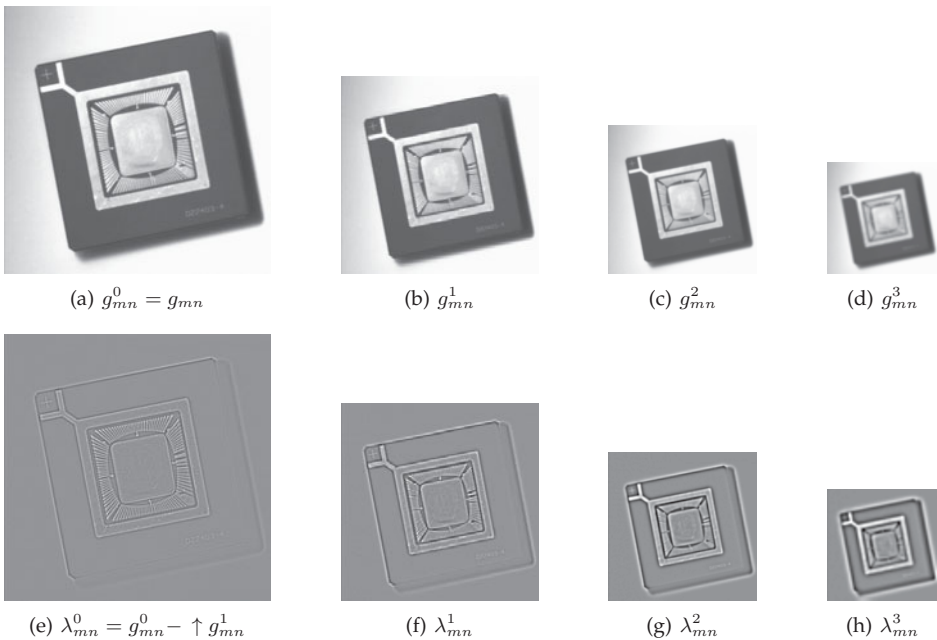


**Figure 15.3.** Image pyramids: (a)–(d) Gaussian pyramid  $g_{mn}^\nu$  according to (15.4), (e)–(h) Laplacian pyramid  $\lambda_{mn}^\nu = g_{mn}^\nu - \uparrow g_{mn}^{\nu+1}$  according to (15.8).

The Laplacian pyramid is a decomposition of the image signal in band-pass regions with a logarithmic frequency scale. The original image can be exactly reconstructed from the Laplacian pyramid and the top image of the Gaussian pyramid:

$$g_{mn}^0 = \sum_{\nu=0}^{K-1} \uparrow^{\nu} \lambda_{mn}^{\nu} + \uparrow^K g_{mn}^K \quad (15.9)$$

$$= \lambda_{mn}^0 + \uparrow \lambda_{mn}^1 + \uparrow\uparrow \lambda_{mn}^2 + \cdots + \underbrace{\uparrow \cdots \uparrow}_{K-1} \lambda_{mn}^{K-1} + \underbrace{\uparrow \cdots \uparrow}_K g_{mn}^K. \quad (15.10)$$

For the construction of the pyramid by subsampling by the factor 2, the following generalizations are possible:

- Reduction by  $p \times q$  per pyramid level by adequately filtering and considering signal anisotropies if necessary.
- Application of optimal (signal-adapted) sampling schemes, cf. Sec. 8.3.7.

### 15.1.3 Pyramid linking

An application of image pyramids is image segmentation (see Chap. 11). The method is known as **pyramid linking** [8,13,20]. It involves the following processing steps:

1. Calculation of the Gaussian pyramid, usually using a mean filter of size  $4 \times 4$  as a low-pass filter.
2. Linking: The image pyramid is considered as a tree structure with the image points representing the nodes of the tree and the edges connecting nodes, i.e., image points of subsequent levels of the pyramid. The possible children of an image point  $g_{mn}^{\nu}$  on level  $\nu$  of the pyramid are given by the 16 image points

$$\left\{ g_{k,l}^{\nu-1} \mid (k,l) \in \mathbb{Z}^2, 2m-1 \leq k \leq 2m+2, 2n-1 \leq l \leq 2n+2 \right\} \quad (15.11)$$

of the next lower level  $\nu-1$ . Conversely, every node  $g_{kl}^{\nu-1}$  of level  $\nu-1$  might have one of four possible parent nodes. Out of these candidates  $g_{mn}^{\nu}$ , that node is chosen which minimizes a distance measure, e.g., the difference of the image values  $|g_{kl}^{\nu-1} - g_{mn}^{\nu}|$ . The edge  $(g_{mn}^{\nu}, g_{kl}^{\nu-1})$  is added to the tree structure.

3. Averaging connected image points: the image values on the levels  $\nu = 1, 2, \dots, K$  are recalculated in this ascending order. For a node  $g_{mn}^{\nu}$  on level  $\nu$ , only its children are considered for the reduction step, i.e., the image value  $g_{mn}^{\nu}$  is obtained by calculating the average of the image values  $g_{kl}^{\nu-1}$  of those nodes that are reachable via the edges  $(g_{mn}^{\nu}, g_{kl}^{\nu-1})$ .
4. Iteratively repeating steps 2 and 3 until a stable result is reached.
5. Assigning the segments: from a certain level or as soon as the differences of the image values of the child nodes are below a certain threshold, all child nodes are recursively assigned the value of the parent node and are grouped into one segment.

By considering the coarse structure at higher levels of the pyramid, the method's robustness is improved, as local distortions can be compensated for. Additionally, the number of segments does not have to be known a priori, which represents another advantage of the presented method. Figure 15.4 shows an example of a segmentation obtained using pyramid linking.

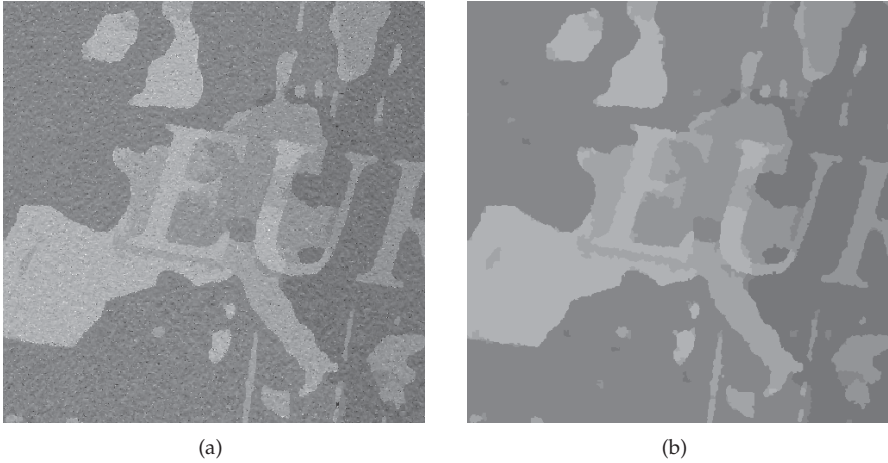


**Figure 15.4.** Example of segmentation using pyramid linking: (a) Surface relief of a coin; (b) Segmentation result (source: A. Purde [20]).

## 15.2

### 15.2 Wavelets

The wavelet transform is an integral transform that can be formulated for one-dimensional or for multi-dimensional signals and is therefore also suitable for image signals [12]. In contrast to the Fourier transform, which uses infinitely spread harmonic oscillations as basis functions, the basis functions of the wavelet transform have compact support. This is also the reason for the name of the transform: the term ‘wavelet’ corresponds to the French term “*ondelette*,” which means “small wave.” The basis functions are not only scaled, corresponding to an expansion of spatial frequencies as with the Fourier transform, but are also shifted in the spatial domain. By this means, the spatial information is preserved by the wavelet transform. The result is a spatially resolved representation of the coarse and fine structures of the signal.

In the following, the wavelet transform will be described for one-dimensional signals first. Then, the relation with multiresolution analysis and the theory of orthogonal filter banks will be discussed. Finally, the transformation of two-dimensional signals will be covered.

#### ➤ 15.2.1 Continuous wavelet transform

First, the continuous formulation of the wavelet transform will be presented, as it is especially beneficial for a theoretical understanding and analytical considerations. For practical use in image and signal processing, an adequate discretization is needed, similar to the Fourier transform. This finally results in the fast wavelet transform.

The continuous transform is defined via an integral [4]:

15.1 **Definition 15.1: The wavelet transform**

The wavelet transform of the signal  $g(x)$  is defined as follows:

$$\Gamma_\psi(s, \tau) := \int_{-\infty}^{\infty} g(x) \psi_{s,\tau}^*(x) dx \tag{15.12}$$

with

$$\psi_{s,\tau}(x) := \frac{1}{\sqrt{s}} \psi\left(\frac{x - \tau}{s}\right), \quad s, \tau \in \mathbb{R}, \quad s > 0. \tag{15.13}$$

The function  $\psi(\cdot)$  is the so-called mother wavelet. The argument  $s$  is the so-called scaling parameter,  $\tau$  is the shift parameter, and  $\psi^*$  denotes the complex conjugation of the wavelet function.  $\diamond$

As the wavelet transform of a one-dimensional signal is two-dimensional, it is highly redundant.

The inverse wavelet transform is given by [1]

$$g(x) = \frac{1}{C_\psi} \int_0^\infty \int_{-\infty}^\infty \Gamma_\psi(s, \tau) \frac{\psi_{s,\tau}(x)}{s^2} d\tau ds \tag{15.14}$$

with

$$C_\psi = \int_{-\infty}^\infty \frac{|\Psi(f)|^2}{|f|} df. \tag{15.15}$$

Here,  $\Psi(f) = \mathcal{F}\{\psi(x)\}$  denotes the Fourier transform of the mother wavelet  $\psi(x)$ . The mother wavelet must satisfy the admissibility condition  $C_\psi < \infty$ . This implies that the DC component of the wavelet is zero:

$$C_\psi < \infty \quad \Rightarrow \quad 0 = \Psi(0) = \int_{-\infty}^\infty \psi(x) dx. \tag{15.16}$$

**Example 15.2 (The one-dimensional continuous wavelet transform):** As an example of the wavelet transform, the mother wavelet

$$\psi(x) = e^{-\frac{x^2}{2}} \sin(2\pi x) \tag{15.17}$$

is considered. By means of the shift property and the scaling property, the Fourier transform of the scaled and shifted wavelet  $\psi_{s,\tau}(x)$  can be calculated:

$$\Psi_{s,\tau}(f) = j \sqrt{\frac{\pi s}{2}} \left( e^{-2\pi^2 (sf+1)^2} - e^{-2\pi^2 (sf-1)^2} \right) e^{-j2\pi\tau f}. \tag{15.18}$$

Figure 15.5 shows the wavelet function  $\psi_{s,\tau}(x)$  and the magnitude of its Fourier spectrum  $|\Psi_{s,\tau}(f)|$  for different scaling and shift parameters  $s$  and  $\tau$ . If the wavelets  $\psi_{s,\tau}(x)$  are considered to be the impulse response functions of LSI systems, the spectra clearly show that they represent band-pass filters, whose frequency decreases for increasing scale parame-



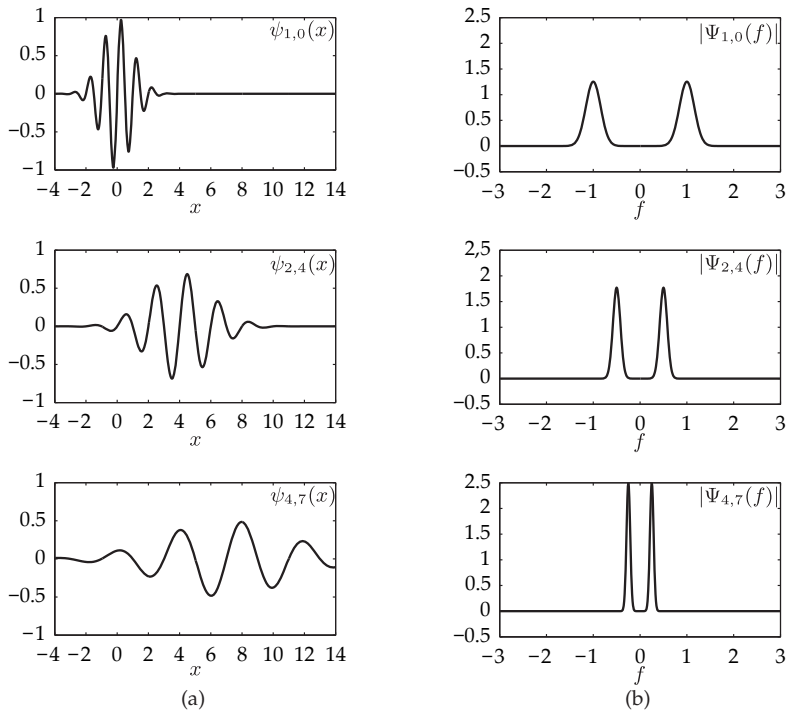


**Figure 15.5.** One-dimensional continuous wavelet: (a) Different scalings and shifts of the mother wavelet (15.17); (b) Magnitude of the corresponding Fourier transforms.

ters  $s$ . Hence, the wavelet transform  $\Gamma_\psi(s, \tau)$  of a signal contains the fine structure of the signal for small  $s$  and the coarse structure for large  $s$ . ■

The wavelet transform has some beneficial properties:

- In contrast to the Fourier transform, it is a local transform. Therefore it allows the simultaneous localization of signal components in space and frequency.
- A fast algorithm for efficiently calculating the transform is available (see Sec. 15.4).
- The choice of the mother wavelet offers great design opportunities.

This is why the wavelet transform is used for analyzing non-stationary processes and to perform a local, spatially resolved spectral analysis. Furthermore, it is of great importance for image compression [23].

**Example 15.3 (Reconstruction of a non-stationary signal):** In order to compare the properties of the Fourier transform and the wavelet transform, the analysis and reconstruction of a one-dimensional non-stationary signal is considered. The signal  $g(x)$  of Fig. 15.6(a) shows jump discontinuities and oscillations but is piecewise constant in-between. By expanding this signal as a Fourier series and by reconstructing it from the 100 Fourier coefficients with the largest magnitudes, the constant parts are affected by harmonic oscillations, see Fig. 15.6(b). As the basis functions of the Fourier transform have a global

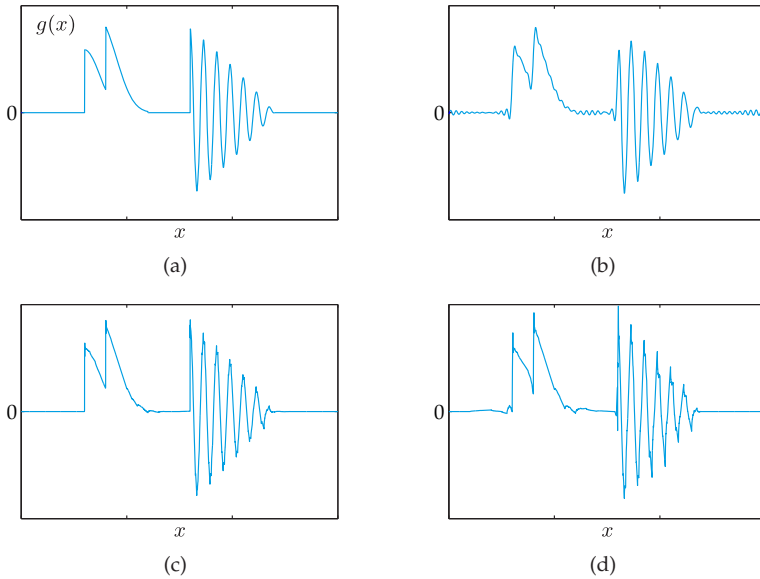


**Figure 15.6.** Example of the reconstruction of a non-stationary signal (adapted from [1]): (a) Original signal  $g(x)$ ; (b) Reconstruction of  $g(x)$  from the first 100 Fourier coefficients with largest magnitudes; (c) Reconstruction from the 100 wavelet coefficients with largest magnitudes; (d) Reconstruction from the 50 wavelet coefficients with largest magnitudes.

reach over the whole domain, it is hard to approximate non-stationary components.

If the fast wavelet transform with the Daubechies filter bank D4 (see Ex. 15.5) is used instead, and if the signal is reconstructed from the 100 wavelet coefficients with the largest magnitudes, the result is a much better approximation, especially of the piecewise constant regions. Basis functions with spatially limited support better suit the transitions between the constant and high-frequency signal components. Also the quantitative approximation error in the sense of the squared error is lower, by many times, than for the Fourier transform. Only 50 wavelet coefficients are sufficient to achieve the same quantitative approximation error, cf. Fig. 15.6(d). ■

► **15.2.2 Discretization of the wavelet transform**

For the discretization of the continuous wavelet transform

$$\Gamma_\psi(s, \tau) = \frac{1}{\sqrt{s}} \int_{-\infty}^{\infty} g(x) \psi^* \left( \frac{x - \tau}{s} \right) dx \tag{15.19}$$

first the continuous signal  $g(x)$  is replaced by the series

$$\sum_n g(n \Delta x) \delta(x - n \Delta x) = \sum_n g_n \delta(x - n \Delta x) \tag{15.20}$$

of samples. Simultaneously, the shift parameter  $\tau = l \Delta x, l \in \mathbb{Z}$  is spatially discretized. By this means, Equation (15.19) turns into

$$\Gamma_\psi(s, l) = \frac{1}{\sqrt{s}} \sum_n g_n \psi^* \left( \frac{(n-l)\Delta x}{s} \right). \tag{15.21}$$

Additionally, a logarithmic discretization is applied to the scale parameter:  $s = 2^p, p \in \mathbb{Z}$ . The shift parameter and the scale parameter are linked as follows:

$$l := s \nu = 2^p \nu \iff \tau = 2^p \nu \Delta x \tag{15.22}$$

This corresponds to a scale-dependent spatial thinning of the wavelet transform, which removes the redundancy of the wavelet transform mentioned above. In other words, short (fine) wavelets are placed so as to be more spatially compact, and long wavelets (for capturing the coarse structure) are placed so as to be less spatially compact. In all, the discretization of the scale by Equation (15.21) results in

$$2^{-\frac{p}{2}} \sum_n g_n \psi^* ((2^{-p} n - \nu)\Delta x). \tag{15.23}$$

Figure 15.7 illustrates the grid which is induced on the plane of the position and the spatial frequency by the discretization of the wavelet transform with respect to the position and the scale. For low spatial frequencies  $f$  (and thus for large scales<sup>1</sup>  $s$ ) a coarse spatial sampling is sufficient, for higher frequencies (low scales), a finer sampling is applied to the position  $x$ . For every octave, i.e., for every doubling of the spatial frequency, the number of the spatial sampling points is doubled. The sampling points of the spatial frequency are located at the scale parameters  $s = 2^p$ , so that  $\Delta p = 1$  corresponds to exactly one octave. For a doubling of the spatial frequency (halving the scale) the number of sampling points is halved with respect to the coordinate of the spatial frequency.

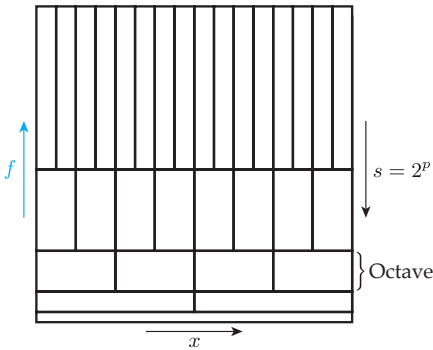


**Figure 15.7.** Discretization of position  $x$ , scale  $s$  and therefore of the spatial frequency  $f$  used for the wavelet transform.

<sup>1</sup>Although the scale parameter  $s$  and the spatial frequency  $f$  have a reciprocal relation, this is only obvious in the strict sense of the inverse proportionality  $f \propto s^{-1}$  for certain wavelets, like (15.17), where a harmonic factor is present, whose frequency is multiplied with  $s^{-1}$ . If, in contrast, the Daubechies wavelets in Fig. 15.10 on page 741 are considered, the relation of frequency and scale is less obvious. Generally, a scaling of  $\psi(x)$  causes a shift of the spectrum  $\Psi(f)$  proportional to  $s^{-1}$  in the spatial frequency domain besides a reciprocal scaling.

Similar to (15.13), the shift and scaling of the mother wavelet in the discrete case can be written as

$$\psi_{p,\nu}(n) := 2^{-\frac{p}{2}} \psi((2^{-p}n - \nu)\Delta x) = 2^{-\frac{p}{2}} \psi\left(\frac{n - 2^p \nu}{2^p} \Delta x\right). \tag{15.24}$$

The forward transform of such a discretized wavelet transform is given by

$$\Gamma_{p,\nu} = \sum_{n=-\infty}^{\infty} g_n \psi_{p,\nu}^*(n). \tag{15.25}$$

And the corresponding inverse transform is given by

$$g_n = \sum_{p=-\infty}^{\infty} \sum_{\nu=-\infty}^{\infty} \Gamma_{p,\nu} \psi_{p,\nu}(n). \tag{15.26}$$

### 15.3 Multiresolution analysis

Multiresolution analysis is a mathematical concept providing a consistent description of image pyramids, wavelets, and filter banks [3, 15]. With each of these methods, image signals can be analyzed at different resolution levels. Filter banks are ensembles of band-pass filters with different center frequencies, which are all applied to the image signal in parallel.

For multiresolution analysis, a function  $g(x)$  is approximated by a linear combination of orthonormal basis functions that span a function space on a certain scale. The finer the scale chosen, the more accurate is the corresponding approximation. The basis functions are constructed using a scaling function  $\varphi(x)$ .

---

#### Definition 15.2: Scaling functions

A scaling function is a function  $\varphi(x) \in L^2(\mathbb{R})$  that satisfies the following conditions:

- Orthonormality: the functions obtained via shifting  $\varphi(x)$  by  $\nu\Delta x$ ,  $\nu \in \mathbb{Z}$ , form an orthonormal system,

$$\langle \varphi(x - \nu), \varphi(x) \rangle = \delta_{\nu}^0, \quad \nu \in \mathbb{Z}, \tag{15.27}$$

with respect to the inner product

$$\langle a(x), b(x) \rangle := \int_{-\infty}^{\infty} a(x) b^*(x) dx \quad \text{in } L^2(\mathbb{R}). \tag{15.28}$$

W.l.o.g. the spatial discretization  $\Delta x := 1$  has been chosen.

- Two-scale relation: the scaling function can be expressed as a linear combination of the shifted scaling functions of the next, finer scale:

$$\varphi(x) = \sqrt{2} \sum_{\nu \in \mathbb{Z}} h_{\nu} \varphi(2x - \nu) \tag{15.29}$$

with suitable coefficients  $h_{\nu} \in \mathbb{R}$ .

– Mean property:

$$\int_{-\infty}^{\infty} \varphi(x) \, dx = 1, \tag{15.30}$$

Hence, by the mean value theorem for integration, there exists a  $\xi \in \mathbb{R}$ , so that  $g(\xi)$  results from the calculation of the inner product with a function  $g(x)$  [6, 26]:

$$\langle g(x), \varphi(x) \rangle = \int_{-\infty}^{\infty} g(x) \varphi^*(x) \, dx = g(\xi) \int_{-\infty}^{\infty} \varphi(x) \, dx = g(\xi). \tag{15.31}$$

– Asymptotic characteristics: outside of a compact interval, the scaling function approaches zero:

$$\lim_{x \rightarrow \pm\infty} \varphi(x) = 0. \tag{15.32}$$

As for the wavelet functions, shifted and scaled variants of  $\varphi(x)$  are defined:

$$\varphi_{p,\nu}(x) := 2^{-\frac{p}{2}} \varphi(2^{-p} x - \nu). \tag{15.33}$$

Hence, the two-scale relation (15.29) can be written as follows:

$$\varphi(x) = \sqrt{2} \sum_{\nu \in \mathbb{Z}} h_{\nu} \varphi(2x - \nu) = \sum_{\nu \in \mathbb{Z}} h_{\nu} \varphi_{-1,\nu}(x). \tag{15.34}$$

◇

For a fixed  $p$ , the shifted scaling functions  $\varphi_{p,\nu}, \nu \in \mathbb{Z}$  form the basis functions of the function space  $V_p$ :

$$V_p := \text{span} \{ \varphi_{p,\nu}(x) \mid \nu \in \mathbb{Z} \}. \tag{15.35}$$

The approximation of a function  $g(x)$  in  $V_p$  can be expressed as:

$$g(x; p) = \sum_{\nu=-\infty}^{\infty} C_{p,\nu} \varphi_{p,\nu}(x) \tag{15.36}$$

with suitable coefficients  $C_{p,\nu} \in \mathbb{R}$ . The approximation step can be considered as an orthogonal projection of the function  $g(x)$  to the space  $V_p$  [1]. The quality of the approximation  $g(x; p)$  of the signal  $g(x)$  increases for lower scale parameters  $p$ . So varying  $p$  yields different representations of the signal on different scales.

**15.1 Theorem 15.1: Multiresolution analysis**

The two-scale relation (15.34) can be generalized to arbitrary scales  $p$  and shifts  $\nu$ :

$$\varphi_{p,\nu}(x) = \sum_{n \in \mathbb{Z}} h_n \varphi_{p-1, n+2\nu}(x) = \sum_{n \in \mathbb{Z}} h_{n-2\nu} \varphi_{p-1, n}(x). \tag{15.37}$$

By (15.27), the shifted scaling functions form an orthonormal basis of the function space  $V_p$ . Besides, the two-scale relation implies  $V_p \subseteq V_{p-1}$ , as the basis functions  $\varphi_{p,\nu}$  of  $V_p$  can be represented as linear combinations from  $V_{p-1}$ . This results in a nested series of function

spaces  $V_p$ :

$$\{0\} \subset \dots V_2 \subset V_1 \subset V_0 \subset V_{-1} \subset V_{-2} \dots \subset L^2(\mathbb{R}) \tag{15.38}$$

◇

During the transition from the scale  $V_{p-1}$  to the next coarser scale  $V_p$ , information concerning the details of the signal are lost.

In order to achieve a signal approximation which is as good as in  $V_{p-1}$ , the basis of  $V_p$  has to be extended by additional functions, which allow a representation of the information lost during the transition from  $V_{p-1}$  to  $V_p$ . Now, the wavelet function  $\psi(x)$  is chosen, so that the shifted wavelets  $\psi_{p,\nu}(x)$  on the scale  $p$  achieve exactly the sought for extension of the basis  $\{\varphi_{p,\nu}(x) \mid \nu \in \mathbb{Z}\}$ . Then, the approximation of the signal  $g(x)$  by the wavelet functions  $\psi_{p,\nu}$ ,  $\nu \in \mathbb{Z}$  yields exactly the missing information concerning the details, so that the representation by the shifted scaling function  $\varphi_{p,\nu}$  can be completed to represent all of the information of the scale  $p - 1$  [17].

---

**Theorem 15.2: Wavelets for multiresolution analysis**

15.2

The function space  $V_{-1}$  can be orthogonally decomposed into the space  $V_0$  and another space  $W_0$ , the so-called wavelet space:<sup>2</sup>

$$V_0 \oplus W_0 = V_{-1}, \quad W_0 = V_0^\perp \text{ in } V_{-1}. \tag{15.39}$$

The basis  $\{\varphi_{0,\nu} \mid \nu \in \mathbb{Z}\}$  of  $V_0$  can be extended by a basis of  $W_0$  to an orthonormal basis of  $V_{-1}$ . The following is chosen for the basis of  $W_0$ :

$$\{\psi(x - \nu) \mid \nu \in \mathbb{Z}\}, \tag{15.40}$$

with  $\psi(x)$  denoting the mother wavelet. As a result of the assumptions made,  $\psi(x) \in V_{-1}$ , so that a representation in terms of the orthonormal basis of  $V_{-1}$  can be obtained for suitable coefficients  $k_\nu$ :

$$\psi(x) = \sum_{\nu \in \mathbb{Z}} k_\nu \varphi_{-1,\nu}(x) = \sqrt{2} \sum_{\nu \in \mathbb{Z}} k_\nu \varphi(2x - \nu). \tag{15.41}$$

This equation is called the two-scale relation for the wavelet function, or, the wavelet equation [21].

With

$$W_p := \text{span}\{\psi_{p,\nu} \mid \nu \in \mathbb{Z}\}, \tag{15.42}$$

the following holds for the scaled and shifted wavelets  $\psi_{p,\nu}$ :

$$V_p \oplus W_p = V_{p-1}, \quad W_p = V_p^\perp \text{ in } V_{p-1}, \tag{15.43}$$

---

<sup>2</sup>As is common in linear algebra, the symbol  $\oplus$  denotes the direct sum of vector spaces [5]. This operation has to be distinguished from the morphological dilation, which is denoted by the same symbol in Chap. 12.

$$\begin{aligned} \dots (V_3 \oplus W_3) = V_2 \subset (V_2 \oplus W_2) = V_1 \\ \subset (V_1 \oplus W_1) = V_0 \subset (V_0 \oplus W_0) = V_{-1} \dots \end{aligned} \tag{15.44}$$

Furthermore, if  $\langle \varphi(x - \nu), \varphi(x - \mu) \rangle = 0$  for all  $\nu, \mu \in \mathbb{Z}, \mu \neq \nu$  and additionally

$$k_\nu = (-1)^\nu h_{M-\nu} \quad \text{for an uneven } M \in \mathbb{Z}, \tag{15.45}$$

then  $\{\psi_{p,\nu} \mid p, \nu \in \mathbb{Z}\}$  is an orthogonal basis of the space  $L^2$  of the quadratically integrable functions [1]. ◊

At the scale  $p$ , a signal  $g(x)$  can now be approximated as follows:

$$g(x; p) = \sum_{\nu=-\infty}^{\infty} C_{p,\nu} \varphi_{p,\nu}(x) \quad \text{with } C_{p,\nu} = \langle g, \varphi_{p,\nu} \rangle, \tag{15.46}$$

$$g(x; p) = \sum_{\mu=p+1}^{\infty} \sum_{\nu=-\infty}^{\infty} \Gamma_{\mu,\nu} \psi_{\mu,\nu}(x) \quad \Gamma_{\mu,\nu} = \langle g, \psi_{\mu,\nu} \rangle. \tag{15.47}$$

The coefficients  $C_{p,\nu}$  and  $\Gamma_{\mu,\nu}$  in these linear combinations are determined by the mentioned inner products, as  $\{\varphi_{p,\nu} \mid \nu \in \mathbb{Z}\}$  and  $\{\psi_{\mu,\nu} \mid \nu \in \mathbb{Z}\}$  are orthonormal bases.

The representation  $g(x; p - 1)$  on the finer scale  $p - 1$  can now be expressed as the sum of the coarser approximation  $g(x; p)$  on the scale  $p$  and the detailed information  $d_p(x)$ , see Fig. 15.8:

$$g(x; p - 1) = g(x; p) + d_p(x), \tag{15.48}$$

$$d_p(x) = \sum_{\nu \in \mathbb{Z}} \Gamma_{p,\nu} \psi_{p,\nu}(x). \tag{15.49}$$

The detailed information  $d_p(x)$  is in the wavelet space  $W_p$ . The coarse representation  $g(x; p)$  (15.46) is based on the scaling functions  $\varphi_{p,\nu}$  in the space  $V_p$ . Recursively applying (15.48) to the right-hand side yields the representation (15.47).

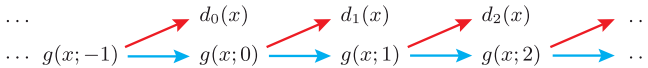


Figure 15.8. Recursive decomposition of the signal  $g(x)$  in a coarse and detailed signal.

The detailed signal  $d_p(x)$  represents a high-pass filtering of the finer signal  $g(x; p - 1)$ . The coarser approximation  $g(x; p)$  corresponds to a low-pass filtering of  $g(x; p - 1)$ . These two filtering operations of multiresolution analysis are similar to the transition from the image signal  $g_{mn}^{\nu-1}$  to the next higher levels  $\lambda_{mn}^\nu$  and  $g_{mn}^\nu$  of the Laplacian or Gaussian pyramid.

**Example 15.4 (The Haar wavelet):** The Haar wavelet is the result of a scaling function which has the shape of a rectangular pulse, see Fig. 15.9(a):

$$\varphi(x) := \text{rect}\left(x - \frac{1}{2}\right) = \begin{cases} 1 & \text{if } 0 \leq x < 1 \\ 0 & \text{otherwise.} \end{cases} \tag{15.50}$$

This function satisfies the requirements of Def. 15.2:

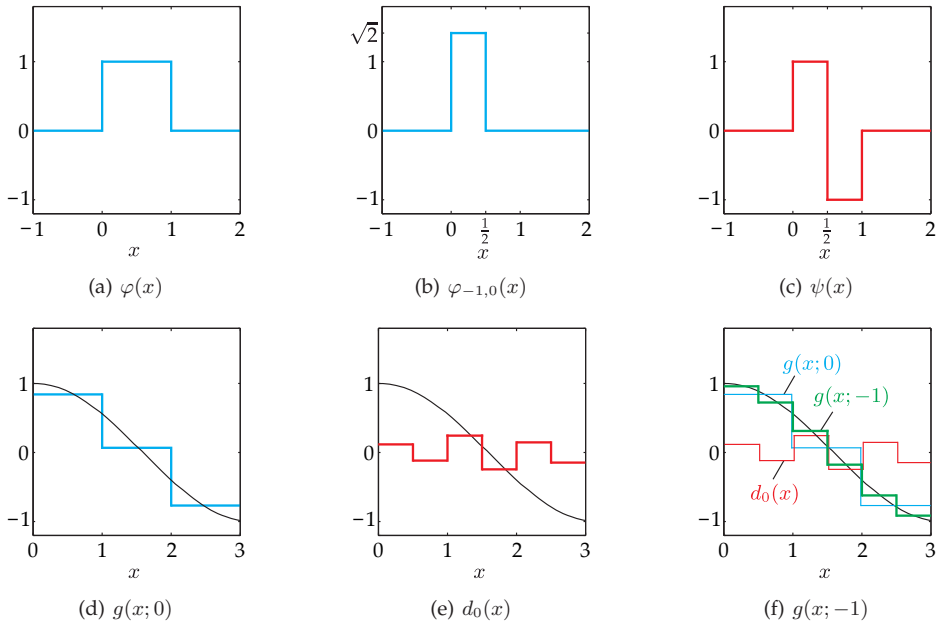


**Figure 15.9.** Approximation of the function  $g(x) = \cos x$  using the Haar wavelet: (a) Scaling function  $\varphi(x) = \varphi_{0,0}(x)$ ; (b) Scaling function  $\varphi_{-1,0}(x) = \sqrt{2}\varphi(2x)$  for the next finer level  $p = -1$ ; (c) Mother wavelet  $\psi_{0,0}(x) = \psi(x) = \varphi(2x) - \varphi(2x - 1)$ ; (d) Coarse approximation  $g(x;0)$  of the function  $g(x) = \cos x$  at the level  $p = 0$ ; (e) Detailed signal  $d_0(x)$ ; (f) Approximation at the next finer level  $p = -1$  as a sum of the coarse signal and the detailed signal at level  $p = 0$ :  $g(x; -1) = g(x;0) + d_0(x)$ .

- As the carriers of the functions, which have been shifted by integer values, are disjoint,  $\langle \varphi(x - \nu), \varphi(x) \rangle = \delta_0^\nu$  for all  $\nu \in \mathbb{Z}$ .
- For the scaling function, the two-scale relation is given by

$$\varphi(x) = \varphi(2x) + \varphi(2x - 1) = \sqrt{2} \left( \frac{1}{\sqrt{2}} \varphi(2x) + \frac{1}{\sqrt{2}} \varphi(2x - 1) \right),$$

i.e.,  $h_0 = h_1 = \frac{1}{\sqrt{2}}$  and  $h_\nu = 0$  for all  $\nu \notin \{0, 1\}$ .

- The mean property and the asymptotic characteristics are obviously satisfied.

With (15.45), (15.41) and  $M := 1$ , the mother wavelet is given by

$$k_0 = h_1 = \frac{1}{\sqrt{2}}, \quad k_1 = -h_0 = -\frac{1}{\sqrt{2}}, \tag{15.51}$$

$$k_\nu = 0 \quad \text{if} \quad k_\nu \notin \{0, 1\}, \tag{15.52}$$

$$\psi(x) = \sqrt{2} \sum_{\nu \in \mathbb{Z}} k_\nu \varphi(2x - \nu) \tag{15.53}$$

$$= \varphi(2x) - \varphi(2x - 1) = \begin{cases} 1 & \text{if } 0 \leq x < \frac{1}{2} \\ -1 & \text{if } \frac{1}{2} \leq x < 1 \\ 0 & \text{otherwise.} \end{cases} \tag{15.54}$$



This function is called the Haar wavelet (Fig. 15.9(c)). It is associated to a high-pass filter with the impulse response function  $(k_0, k_1)$ , whereas  $\varphi(x)$  corresponds to a low-pass filter with the impulse response function  $(h_0, h_1)$ .

The results of Theorem 15.2 can easily be understood by means of this example: because of the disjoint carriers,  $\langle \psi_{p,\nu}, \psi_{p,0} \rangle = \delta_0^\nu$  and obviously  $\langle \psi_{p,\nu}, \varphi_{p,n} \rangle = 0$  for all  $\nu, n \in \mathbb{Z}$ . Hence,

$$\{\varphi_{p,\nu} \mid \nu \in \mathbb{Z}\} \cup \{\psi_{p,\nu} \mid \nu \in \mathbb{Z}\} \quad (15.55)$$

is an orthonormal basis of  $V_{p-1}$ .

The approximation  $g(x; 0)$  of a signal  $g(x)$  with the scaling function of the Haar wavelet corresponds to a representation as a step function. In the example of Fig. 15.9(d), the function  $g(x) = \cos x$  in the interval  $[0, 3)$  is described by three coefficients  $C_{0,\nu}$ . With regard to the Haar wavelet function  $\psi(x)$ , the detailed signal  $d_0(x)$  approximates the difference between the signal and the step function  $g(x; 0)$  and also consists of three coefficients  $\Gamma_{0,\nu}$  (Fig. 15.9(e)). The sum of the coarse signal and the detailed signal results in the function  $g(x; p-1)$  at the next finer level  $p = -1$  (Fig. 15.9(f)). This is equivalent to the approximation of the signal by six coefficients  $C_{-1,\nu}$  in terms of the refined scaling function  $\varphi_{-1,\nu}(x)$  of Fig. 15.9(b). ■

The choice of a suitable mother wavelet depends on different criteria, such as the limited support of the filter, vanishing moments, regularity, symmetry and orthogonality or biorthogonality [17].

## 15.4

### 15.4 The fast wavelet transform

Based on the theory of multiresolution analysis, a fast transform for discrete signals can be derived. It relies on a recursive decomposition into a coarse signal and a detailed signal according to (15.48). The calculation can be realized using filter banks, i.e., by a discrete convolution of the signal with the impulse response functions of the filters that correspond to the scaling function and the wavelet function.

## 15.3

### Theorem 15.3: Fast wavelet transform

Putting together the two-scale relations (15.37) and (15.41) results in the following recursive formulas for calculating the coefficients  $C_{p,n}$  and  $\Gamma_{p,n}$  in the function representation (15.46), (15.47):

$$C_{p,n} = \sum_{l \in \mathbb{Z}} h_{l-2n} C_{p-1,l}, \quad (15.56)$$

$$\Gamma_{p,n} = \sum_{l \in \mathbb{Z}} k_{l-2n} C_{p-1,l}. \quad (15.57)$$

The recursive inverse transformation of the coefficients from level  $p$  to level  $p-1$  is given by

$$C_{p-1,n} = \sum_{\substack{l \in \mathbb{Z} \\ (n-l) \text{ even}}} \left( h_l C_{p, \frac{n-l}{2}} + k_l \Gamma_{p, \frac{n-l}{2}} \right). \quad (15.58)$$

The filter coefficients  $h_n$  and  $k_n$  of (15.37) and (15.41) can be calculated by the following inner products:

$$h_n = \langle \varphi_{0,0}(x), \varphi_{-1,n}(x) \rangle = \sqrt{2} \langle \varphi(x), \varphi(2x - n) \rangle, \tag{15.59}$$

$$k_n = \langle \psi_{0,0}(x), \varphi_{-1,n}(x) \rangle = \sqrt{2} \langle \psi(x), \varphi(2x - n) \rangle. \tag{15.60}$$

Furthermore, the following relations hold for the filter coefficients:<sup>3</sup>

$$\sum_{n \in \mathbb{Z}} h_n = \sqrt{2}, \tag{15.61}$$

$$\sum_{n \in \mathbb{Z}} h_n h_{n-2l} = \delta_0^l, \quad l \in \mathbb{Z}, \tag{15.62}$$

$$k_n = (-1)^n h_{M-n} \tag{15.63}$$

with  $M \in \mathbb{Z}$  odd. ◇

Additionally, an initial condition is required for the recurrence relations (15.56), (15.57) of the fast wavelet transform. In practice, one often sets

$$C_{0,n} := g_n = g(n \Delta x), \tag{15.64}$$

i.e., the coefficients of the finest scale  $p_{\min} := 0$  are set to the values of the discrete or the samples of the continuous signal. As this approach has no theoretical justification, it is called the ‘wavelet crime’.

As with the Gaussian and Laplacian pyramid, the signal  $g(x)$  can be completely reconstructed from the detailed signals  $d_p(x)$ ,  $p = p_{\min} + 1, \dots, p_{\max}$  and the last level  $g(x; p_{\max})$  of the coarse signal:

$$g(x) = g(x; p_{\max}) + \sum_{p=p_{\min}+1}^{p_{\max}} d_p(x). \tag{15.65}$$

In the discrete case, the number of coefficients  $C_{p,n}$  and  $\Gamma_{p,n}$  is reduced by a factor of 2 during the transition to the next scale  $p$ , as in (15.56), for  $M$  coefficients  $C_{p-1,n}$  and an impulse response function  $h_n$  of length  $N$ , only  $\frac{M}{2} + N - 1$  coefficients  $C_{p,n}$  are non-zero. This is why the computational complexity and the space requirements of the fast wavelet transform are linearly proportional to the length  $M$  of the transformed signal [17].

**Example 15.5 (Daubechies wavelet D4 and the corresponding filter banks):** For an impulse response function  $h_n$  of length  $N = 4$ , (15.61) and (15.62) result in the following conditions:

$$h_0 + h_1 + h_2 + h_3 = \sqrt{2}, \tag{15.66}$$

$$h_0^2 + h_1^2 + h_2^2 + h_3^2 = 1, \tag{15.67}$$

$$h_2 h_0 + h_3 h_1 = 0. \tag{15.68}$$

<sup>3</sup>Equation (15.61) is obtained by integrating (15.37) with respect to  $x$  and applying (15.30). The second equation (15.62) results from the orthonormality condition (15.27) of the scaling function [1].

Table 15.1. Summary of formulas concerning the scaling functions and the wavelet functions.

	Scaling function $\varphi(x)$	Wavelet function $\psi(x)$
Scaling and shift	$\varphi_{p,\nu}(x) := 2^{-\frac{x}{2}} \varphi(2^{-p} x - \nu)$	$\psi_{p,\nu}(x) := 2^{-\frac{x}{2}} \psi(2^{-p} x - \nu)$
Orthonormality	$\langle \varphi_{p,\mu}, \varphi_{p,\nu} \rangle = \delta_{\mu\nu}^p$	$\langle \psi_{p,\mu}, \psi_{p,\nu} \rangle = \delta_{\mu\nu}^p$
	$\langle \varphi_{p,\mu}, \psi_{p,\nu} \rangle = 0$	
Two-scale relation	$\varphi_{p,\nu}(x) = \sum_{n \in \mathbb{Z}} h_n \varphi_{p-1, n+2\nu}(x)$	$\psi_{p,\nu}(x) = \sum_{n \in \mathbb{Z}} k_n \varphi_{p-1, n+2\nu}(x)$
Mean property	$\int_{-\infty}^{\infty} \varphi_{p,\nu}(x) dx = (\sqrt{2})^p$	$\int_{-\infty}^{\infty} \psi_{p,\nu}(x) dx = 0$
Filter banks	$\sum_{n \in \mathbb{Z}} h_n = \sqrt{2}$	$k_n = (-1)^n h_{M-n}$
	$\sum_{n \in \mathbb{Z}} h_n h_{n-2l} = \delta_0^l, \quad l \in \mathbb{Z}$	with $M \in \mathbb{Z}$ being odd
Function approximation	coarse structure (low-pass filtering)	detail structure (high-pass filtering)
	$g(x; p) = \sum_{\nu=-\infty}^{\infty} C_{p,\nu} \varphi_{p,\nu}(x)$	$d_p(x) = \sum_{\nu \in \mathbb{Z}} \Gamma_{p,\nu} \psi_{p,\nu}(x)$
	$g(x; p) = \sum_{\mu=p+1}^{\infty} \sum_{\nu=-\infty}^{\infty} \Gamma_{\mu,\nu} \psi_{\mu,\nu}(x)$	
	$g(x; p) = g(x; p+1) + d_{p+1}(x)$	
Calculation of the coefficients	$C_{p,\nu} = \langle g, \varphi_{p,\nu} \rangle$	$\Gamma_{p,\nu} = \langle g, \psi_{p,\nu} \rangle$
	$= \sum_{l \in \mathbb{Z}} h_{l-2\nu} C_{p-1,l}$	$= \sum_{l \in \mathbb{Z}} k_{l-2\nu} C_{p-1,l}$

the filter coefficients are not uniquely determined by these formulas. Rather, there are various degrees of freedom concerning the choice of wavelets and scaling functions. A possible constraint on these degrees of freedom is the requirement proposed by Ingrid Daubechies: the wavelet function  $\psi(x)$  should be differentiable as often as possible [10, 21]. This results in the following coefficients  $h_n$  of the low-pass filter [17]:

$$h_0 = \frac{1 + \sqrt{3}}{4\sqrt{2}}, \quad h_1 = \frac{3 + \sqrt{3}}{4\sqrt{2}}, \tag{15.69}$$

$$h_2 = \frac{3 - \sqrt{3}}{4\sqrt{2}}, \quad h_3 = \frac{1 - \sqrt{3}}{4\sqrt{2}}. \tag{15.70}$$

The coefficients  $k_n$  of the high-pass filter can then be obtained using (15.45) and  $M := N - 1 = 3$ :

$$k_3 = -\frac{1 + \sqrt{3}}{4\sqrt{2}}, \quad k_2 = \frac{3 + \sqrt{3}}{4\sqrt{2}}, \tag{15.71}$$

$$k_1 = -\frac{3 - \sqrt{3}}{4\sqrt{2}}, \quad k_0 = \frac{1 - \sqrt{3}}{4\sqrt{2}}. \tag{15.72}$$

This wavelet filter is called the Daubechies filter D4.

Daubechies filters can be constructed for arbitrary, even-numbered lengths  $N$ . The corresponding scaling functions and wavelet functions have the compact support  $[0, N - 1]$ . However, they can not be represented by closed formulas in general. Instead, the function values have to be recursively calculated by means of the two-scale relations (15.37) and (15.41). Figure 15.10 shows the scaling functions and wavelet functions of the Daubechies wavelets D4 and D12. The additional degrees of freedom of the longer impulse response D12 are used in order to construct smoother functions. The filter D2 equals the Haar wavelet of Ex. 15.4. ■

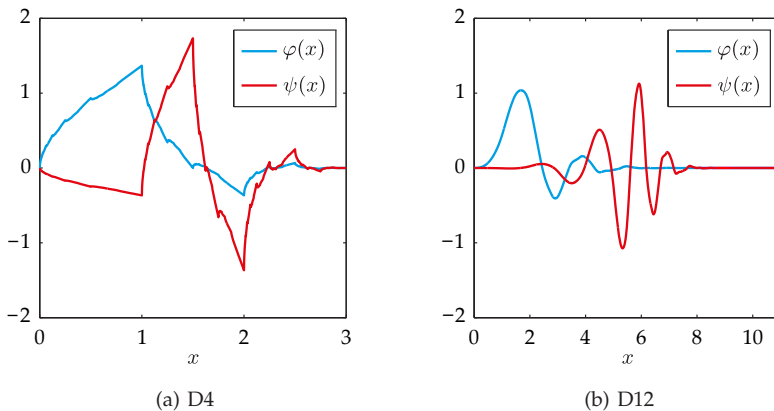


Figure 15.10. Scaling functions  $\varphi(x)$  and wavelet functions (mother wavelets)  $\psi(x)$  of two Daubechies wavelets.

## 15.5 The two-dimensional wavelet transform

In order to transform two-dimensional image signals, the one-dimensional wavelet transform can be applied first to the rows and then to the columns of the image  $g(\mathbf{x})$ . This corresponds to the transformation of the image by means of the following four scaling functions and wavelet functions [11,21]:

$$\varphi(\mathbf{x}) = \varphi(x) \varphi(y), \quad (15.73)$$

$$\psi^H(\mathbf{x}) = \psi(x) \varphi(y), \quad (15.74)$$

$$\psi^V(\mathbf{x}) = \varphi(x) \psi(y), \quad (15.75)$$

$$\psi^D(\mathbf{x}) = \psi(x) \psi(y). \quad (15.76)$$

By definition, these functions are separable. The combination of the coarse signals and detailed signals in the two coordinate directions results in four signal components  $g(\mathbf{x};p)$ ,  $d_p^H(\mathbf{x})$ ,  $d_p^V(\mathbf{x})$ , and  $d_p^D(\mathbf{x})$ . The coarse structure is contained in  $g(\mathbf{x};p)$ ; while  $d_p^H(\mathbf{x})$  corresponds to the horizontal,  $d_p^V(\mathbf{x})$  to the vertical, and  $d_p^D(\mathbf{x})$  to the diagonal fine structures. Here, for example, the horizontal details represent image structures that contain a gradient in the  $x$ -direction, such as vertical edges. Usually, the four signal components are arranged in the quadrants of an image (Fig. 15.11).

The application of the fast wavelet transform to a discrete image signal  $g_{mn}$  is performed as follows: first, the initial condition

$$C_{0,m,n} := g_{mn} \quad (15.77)$$

is chosen. Because of separability, every image line can then be individually transformed, i.e., the filters  $h_m$  and  $k_m$  can be applied in the  $m$ -direction, cf. (15.56), (15.57). As an intermediate result, an image of the original size is obtained, of which the first half of each row corresponds to the coarse structure and the second half corresponds to the detailed structure, Fig. 15.12(a). The two coefficient vectors each consist of half as many entries as the original image row. Next, the wavelet transform is applied column-wise to this image, i.e., the filters  $h_n$  and  $k_n$ . The result of the wavelet transform at scale  $p = 1$  is an image of the original size, which contains the coefficients  $C_{1,m,n}$ ,  $\Gamma_{1,m,n}^H$ ,  $\Gamma_{1,m,n}^V$  and  $\Gamma_{1,m,n}^D$  in its four quadrants, Fig. 15.12(b). To continue the transform to the next scale, the principle just has to be applied to the quadrants containing the  $C_{p,m,n}$ , Fig. 15.12(c), (d). This is why the computational complexity is reduced to one-fourth for every level during the forward transform as well as during the inverse transform. In total, the computational complexity for an image of size

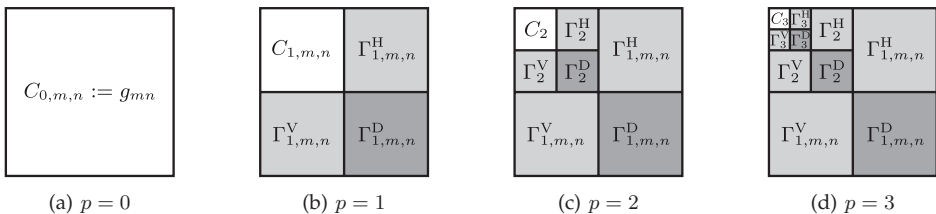
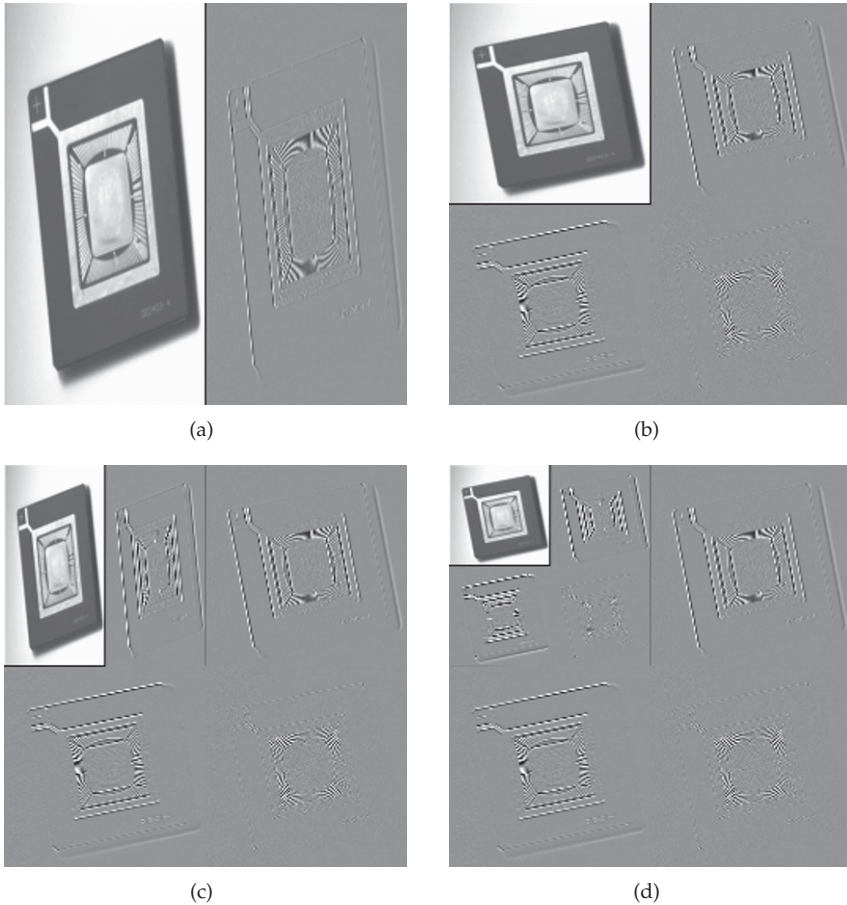


Figure 15.11. Alignment of the coefficients for the two-dimensional wavelet transform (adapted from [11]).



**Figure 15.12.** Wavelet transform of the test image Fig. 15.3(a) with the Daubechies wavelet D4 of Ex. 15.5: (a) Transform of the rows; (b) Transform of the columns (cf. Fig. 15.11(b)); (c), (d) Another transform of the quadrant  $C_{1,m,n}$ , cf. Fig. 15.11(c). In the quadrant of the detailed signal, gray pixels correspond to zero coefficients.

$M \times M$  and for a filter bank of length  $N$  is given by

$$\sum_{p=0}^{p_{\max}} 2 \frac{1}{4^p} N M^2 \leq 2 \frac{1}{1 - \frac{1}{4}} N M^2 = \frac{8}{3} N M^2, \tag{15.78}$$

and is therefore linear with respect to the number  $M^2$  of image pixels for an arbitrary number  $p_{\max}$  of scaling levels [17].

The signal-flow graph of the two-dimensional fast wavelet transform is shown in Fig. 15.13(a). The inverse transform, i.e., the synthesis of the image signal  $g_{mn}$  from the wavelet coefficients  $C_{p_{\max},m,n}$ ,  $\Gamma_{p,m,n}^H$ ,  $\Gamma_{p,m,n}^V$  and  $\Gamma_{p,m,n}^D$ ,  $p = 1, \dots, p_{\max}$ , is obtained by inverting the single steps of the transform: first, the columns of the coefficient matrix are upsampled and convolutions with the impulse response functions  $h_n$  and  $k_n$  are performed. Employing (15.58), a point-wise addition is applied to the two convolution results. Then, the

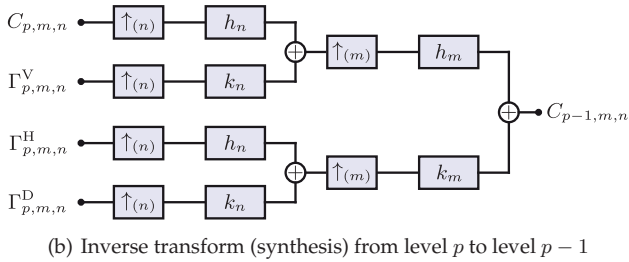
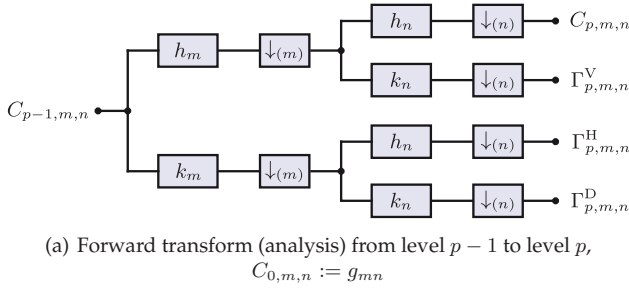


Figure 15.13. Signal-flow graph for the fast two-dimensional wavelet transform (adapted from [11]).

same procedure is repeated for the rows (Fig. 15.13(b)). By this means, an exact reconstruction of the image signal  $g_{mn}$  is achieved.

The wavelet transform of image signals may be used in various applications:

- Multiresolution analysis: similar to an image pyramid, the wavelet transform is a representation of the image at multiple resolutions, in which structures of different extents can be efficiently analyzed.
- Features: the wavelet coefficients can be considered as features, which can be used for different image processing tasks, e.g., texture classification or defect detection.
- Compression: by compressing low-magnitude wavelet coefficients and by means of a coarse quantization especially of the detailed signals, a compression of the image data can be achieved [11,23].

**15.6 Scale-invariant features**

SIFT (scale-invariant feature transform) and SURF (speeded up robust features) represent sophisticated methods for the detection of interest points, which can be easily relocated. For each of the detected image points (keypoints), a set of features, the so-called descriptor, is calculated. The descriptors are invariant with respect to rotations and scalings of the image and are unsusceptible to changes of the perspective and of the illumination. They are used for finding correspondences in image series and for object detection, among other things.

The SIFT method uses a multiresolution representation in order to find interest points [16]. First, a series of images  $\lambda_{mn}^\sigma, \sigma = \alpha^\nu$  is calculated by means of the difference-of-Gaussians method (11.63). The result is similar to the Laplacian pyramid of Sec. 15.1.2 except for the finer sampling  $\alpha$  of the scale parameter  $\sigma$ , resulting in multiple images at

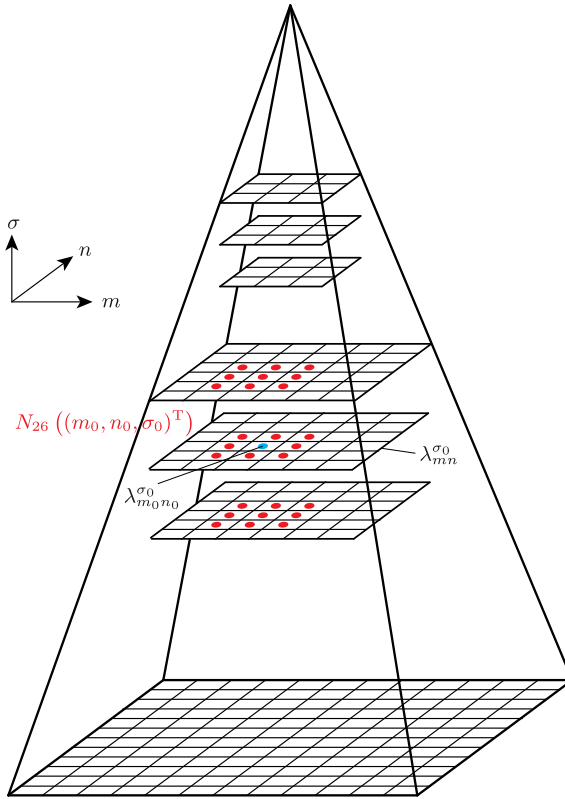


Figure 15.14. Neighborhood definition for the search of SIFT points in the scale space.

a single pyramid level. In this three-dimensional multiresolution representation, extrema with respect to the three coordinate directions  $(m, n, \sigma)^T$  are now found. For this purpose, a generalization of the 8-neighborhood  $N_8(x)$  of Def. 11.8 to a 26-neighborhood is used:

$$N_{26}((m_0, n_0, \sigma_0)^T) := \left\{ (m, n, \sigma)^T \mid |m - m_0| \leq 1 \wedge |n - n_0| \leq 1 \wedge \frac{1}{\alpha} \leq \frac{\sigma}{\sigma_0} \leq \alpha \wedge (m, n, \sigma) \neq (m_0, n_0, \sigma_0) \right\}.$$

Candidates for interest points are points  $(m_0, n_0)$  for which the image value  $\lambda_{m_0 n_0}^{\sigma_0}$  for a  $\sigma_0$  is greater than or less than all other image values in the neighborhood  $N_{26}((m_0, n_0, \sigma_0)^T)$  (cf. Fig. 15.14).

In order to achieve a hopefully stable recognition and localization of the feature points, the set of candidates is reduced by additional tests. For example, extrema along an edge are often not notably intense and allow no exact localization. In this respect, corners in the sense of Sec. 14.4 are more suitable. This is why the SIFT method discards candidates with low contrast and with a curvature of only one direction (e.g., perpendicular to an edge). For this purpose, the Hessian matrix containing the second derivative of  $\lambda_{m_0 n_0}^{\sigma_0}$  is discretely approximated. By means of the trace and the determinant of this Hessian matrix, a criterion



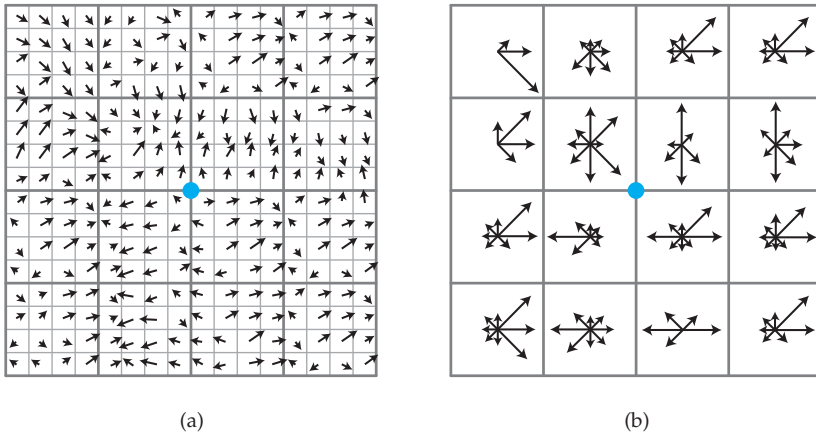


**Figure 15.15.** Calculation of the SIFT feature vector: (a) Gradient vectors in a local neighborhood of the interest point; (b) Resulting histogram of oriented gradients.

similar to Sec. 14.4 can be designed, which discards candidates showing distinct structure changes only in one direction. Besides, a Taylor expansion is performed, in order to achieve a localization of interest points with subpixel accuracy.

In order to achieve rotational invariance, the features are calculated relative to the locally predominant direction of the gradient image. This direction is estimated by means of the histogram of oriented gradients of a local neighborhood of the interest point  $(m_0, n_0, \sigma_0)^T$  in the image  $g_{mn}^{\sigma_0}$  resulting from a Gaussian filtering. If there is no distinct maximum, multiple feature vectors for the same interest point are calculated, in order to achieve greater robustness. An unstable estimation of the direction can impair results of the SIFT method for some applications [14].

The feature vector of an interest point consists of the histogram of oriented gradients of a local neighborhood of the image point  $g_{m_0 n_0}^{\sigma_0}$ . More precisely, the neighborhood is divided into  $4 \times 4$  quadratic subregions and a histogram of oriented gradients is calculated for each subregion (Fig. 15.15). The gradient angles are measured with respect to the predominant direction calculated in the previous step. The histograms use eight quantization steps, corresponding to an angular resolution of  $45^\circ$ . The total dimension of the resulting feature vector is  $4 \cdot 4 \cdot 8 = 128$ . The vector is normalized to unit length in order to compensate for linear changes of illumination.

An alternative method for calculating interest points and feature vectors is the **SURF method** [2]. Here, one performs a convolution of the image with rectangular filter impulse response functions that approximate the second derivative of the Gaussian function. By this means, approximations of the Hessian matrix and its determinant can be calculated. In order to achieve a multiresolution analysis, impulse response functions of different sizes are used. The local maxima of the determinant within the neighborhood  $N_{26}((m_0, n_0, \sigma_0)^T)$  of a point  $(m_0, n_0, \sigma_0)^T$  in the scale space constitute the interest points. They are located with subpixel accuracy by means of an interpolation in all three coordinate directions.

The features of an interest point are based on an analysis by means of the Haar wavelet of Ex. 15.4. In a local neighborhood, whose size and the scaling of the wavelet filter are

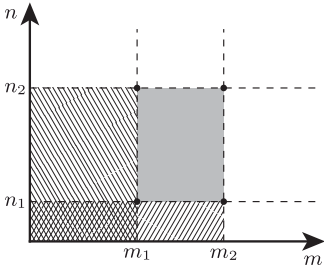


Figure 15.16. Calculation of the sum of the image values of  $g$  in the gray rectangle by means of the integral image  $g_{\Sigma}$  according (15.80).

chosen with respect to  $\sigma_0$ , the wavelet coefficients  $\Gamma_{mn}^H$  and  $\Gamma_{mn}^V$  are calculated for the  $x$ -direction and  $y$ -direction. These are summed two times in  $4 \times 4$  regions: with signs and as absolute values. This results in the following four features for every region:  $\sum \Gamma_{mn}^H$ ,  $\sum \Gamma_{mn}^V$ ,  $\sum |\Gamma_{mn}^H|$ , and  $\sum |\Gamma_{mn}^V|$ . In total, the resulting feature vector has 64 dimensions and is again normalized to unit length to achieve an invariance to illumination changes. Optionally, the locally predominant direction can be estimated by a Haar wavelet analysis and can be used as a reference value.

In order to achieve an efficient implementation, all steps of the SURF method rely on **integral images**, which allow a constant-time calculation of the sum of all image values in an axis-parallel rectangle [9,25]. The integral image  $g_{\Sigma}$  of an image  $g$  is defined by

$$g_{\Sigma,m,n} := \sum_{i=0}^m \sum_{j=0}^n g_{mn} . \tag{15.79}$$

The image value of the integral image at position  $(m, n)$  is equal to the sum of all image values in the axis-parallel rectangle with the corners  $(0, 0)$  and  $(m, n)$  of the original image. The sum of all image values in an arbitrary axis-parallel rectangle with the corners  $(m_1, n_1)$  and  $(m_2, n_2)$  ( $m_1 \leq m_2$ , and  $n_1 \leq n_2$ ) can be now be calculated as follows (cf. Fig. 15.16):

$$\sum_{m=m_1+1}^{m_2} \sum_{n=n_1+1}^{n_2} g_{mn} = g_{\Sigma m_2 n_2} - g_{\Sigma m_1 n_2} - g_{\Sigma m_2 n_1} + g_{\Sigma m_1 n_1} . \tag{15.80}$$

As the impulse response functions of the Haar wavelet and the filters used for approximating the Hessian matrix in the SURF method have larger blocks of constant values, any convolution operation of these filters can be efficiently realized using integral images.

In the literature, various other methods for calculating interest points and features have been proposed and analyzed [18, 19, 22]. Important applications for local image features are correspondence algorithms for image series and the detection of objects. Those feature vectors are sought inside the training data, respectively, in other images of the series, that best fit the feature vectors of the analyzed image. As single false assignments cannot be avoided, robust methods for outlier detection have to be used in order to obtain reliable results. Especially for evaluating stereo images in the fields of machine vision, e.g., for robots or vehicles, these methods play an important role.

Figure 15.17 shows an example of the calculation of interest points using the SIFT and SURF methods.

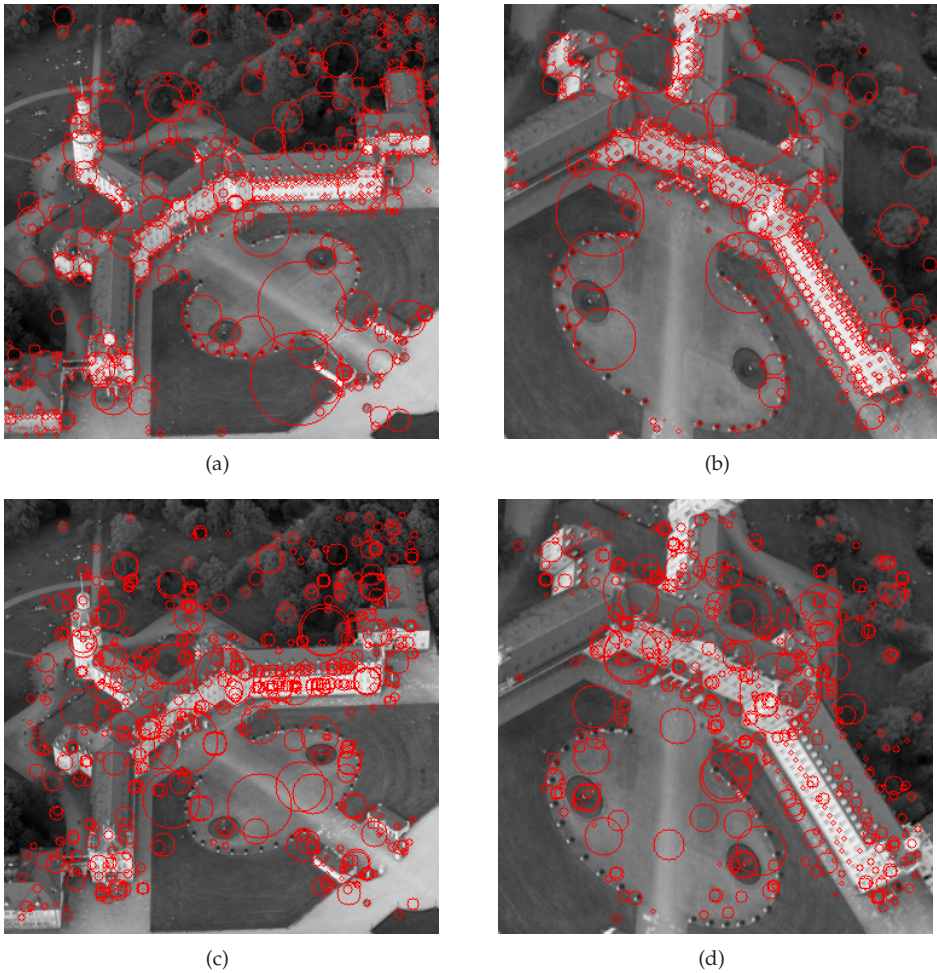


**Figure 15.17.** Example of the SIFT and SURF methods: (a) Result of applying the SIFT method to Fig. 14.23(c); (b) Result of applying the SIFT method to an artificially rotated and scaled section of (a); (c), (d) Result of applying the SURF method to the two test images. The calculated interest points are marked as red circles on the original image. The size of the circles represents the extent of the corresponding feature, i.e., the scale level of the extremum. By means of finding correspondences between the feature vectors, the coordinate transform between the two test images could be reconstructed.

## 15.7 Bibliography

- [1] Werner Bäni. *Wavelets: Eine Einführung für Ingenieure*. Oldenbourg, 2nd edition, 2005.
- [2] Herbert Bay, Tinne Tuytelaars, and Luc Van Gool. SURF: Speeded Up Robust Features. In Aleš Leonardis, Horst Bischof, and Axel Pinz, editors, *9th European Conference on Computer Vision*, pages 404–417. Springer, 2006.
- [3] Josef Bigun. *Vision with direction*. Springer, 2006.
- [4] Kristian Bredies and Dirk Lorenz. *Mathematische Bildverarbeitung: Einführung in Grundlagen und moderne Theorie*. Vieweg+Teubner, 2011.
- [5] Joel G. Broida and S. Gill Williamson. *A comprehensive introduction to linear algebra*. Addison-Wesley, 1989.
- [6] Ilja Bronshtein, Konstantin Semendiyayev, Gerhard Musiol, and Heiner Mühlig. *Handbook of Mathematics*. Springer, 6th edition, 2015.
- [7] Peter Burt and Edward Adelson. The Laplacian pyramid as a compact image code. *IEEE Transactions on Communications*, 31(4):532–540, April 1983.
- [8] Peter Burt, Tsai-Hong Hong, and Azriel Rosenfeld. Segmentation and Estimation of Image Region Properties through Cooperative Hierarchical Computation. *IEEE Transactions on Systems, Man and Cybernetics*, 11(12):802–809, 1981.
- [9] Franklin Crow. Summed-Area Tables for Texture Mapping. *Computer Graphics*, 18(3):207–212, 1984.
- [10] Ingrid Daubechies. *Ten lectures on wavelets*. Society for Industrial and Applied Mathematics, 1992.
- [11] Rafael Gonzalez and Richard Woods. *Digital image processing*. Pearson Prentice Hall, 3rd edition, 2008.
- [12] Barbara Burke Hubbard. *The world according to wavelets: the story of a mathematical technique in the making*. Peters, 2nd edition, 1999.
- [13] Bernd Jähne. *Digital image processing*. Springer, 6th edition, 2005.
- [14] Kai Jüngling. *Ein generisches System zur automatischen Detektion, Verfolgung und Wiedererkennung von Personen in Videodaten*. PhD thesis, Karlsruhe Institute of Technology, 2011.
- [15] Tony Lindeberg. *Scale space theory in computer vision*. Kluwer, 1994.
- [16] David Lowe. Distinctive Image Features from Scale-Invariant Keypoints. *International Journal of Computer Vision*, 60(2):91–110, 2004.
- [17] Stéphane Mallat. *A wavelet tour of signal processing*. Academic Press, 2nd edition, 1999.
- [18] K. Mikolajczyk, T. Tuytelaars, C. Schmid, A. Zisserman, J. Matas, F. Schaffalitzky, T. Kadir, and L. Van Gool. A Comparison of Affine Region Detectors. *International Journal of Computer Vision*, 65:43–72, 2005.
- [19] Krystian Mikolajczyk and Cordelia Schmid. Scale & Affine Invariant Interest Point Detectors. *International Journal of Computer Vision*, 60(1):63–86, 2004.
- [20] Andreas Purde. *Speckle-Interferometrie zur Formvermessung unestetiger Oberflächen*. PhD thesis, Technische Universität München, 2006.
- [21] Desanka Radunović. *Wavelets from math to practice*. Springer, 2009.
- [22] Michael Schweitzer and Hans-Joachim Wuensche. Efficient keypoint matching for robot vision using GPUs. In *IEEE Computer Vision Workshops*, pages 808–815, September 2009.
- [23] Tilo Strutz. *Bilddatenkompression: Grundlagen, Codierung, Wavelets, JPEG, MPEG, H.264*. Vieweg+Teubner, 4th edition, 2009.
- [24] John K. Truss. *Foundations of mathematical analysis*. Clarendon Press, Oxford, 1997.
- [25] Paul Viola and Michael Jones. Rapid Object Detection using Boosted Cascade of Simple Features. In *Proc. IEEE Conference on Computer Vision and Pattern Recognition*, volume 1, pages 511–518, 2001.

[26] Wolfgang Walter. *Analysis I*. Springer, 5th edition, 1999.

Part III  
**Appendix**





Appendix A  
**Mathematical Foundations**

**A**

---

# A

## **A Mathematical Foundations**

A.1	The intercept theorem . . . . .	755
A.2	Inverse problems . . . . .	756
A.3	Bibliography . . . . .	757



# A Mathematical Foundations

## A.1 The intercept theorem

The intercept theorem [1,2] is an important principle for constructing the optical paths in the model of geometric optics (Chap. 3).

### Theorem A.1: The intercept theorem

Two lines  $s$  and  $t$  are assumed to have an intersection at the origin  $O$ . Furthermore,  $p_1$  and  $p_2$  are assumed to denote two parallel lines intersecting  $s$  and  $t$  (Fig. A.1). Then, the lengths<sup>1</sup> of the segments between  $P_1$  and  $Q_1$ , respectively, between  $P_2$  and  $Q_2$ , are in the same relation to each other as the distances from  $O$  to the intersections  $P_1$  and  $P_2$ , respectively,  $Q_1$  and  $Q_2$ :

$$\frac{\overline{P_1Q_1}}{\overline{P_2Q_2}} = \frac{\overline{OP_1}}{\overline{OP_2}} = \frac{\overline{OQ_1}}{\overline{OQ_2}}. \quad (\text{A.1})$$

It is of no relevance whether the parallels are on the same side or on different sides of the origin (Fig. A.1(b)).  $\diamond$

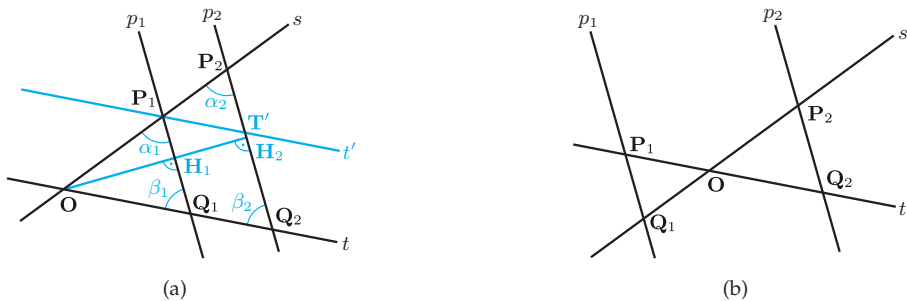


Figure A.1. Intercept Theorem.

**Proof A.1 (The intercept theorem):** For the right triangle  $\text{OH}_1\text{P}_1$ , one has

$$\sin \alpha_1 = \frac{\overline{\text{OH}_1}}{\overline{\text{OP}_1}}. \quad (\text{A.2})$$

Equivalently, the following holds for the triangle  $\text{OH}_2\text{P}_2$

$$\sin \alpha_2 = \frac{\overline{\text{OH}_2}}{\overline{\text{OP}_2}}. \quad (\text{A.3})$$

<sup>1</sup>The length of the segment between the points  $A$  and  $B$  is denoted by  $\overline{AB}$ .

As  $p_1$  and  $p_2$  are parallel,  $\alpha_1 = \alpha_2$  and hence

$$\frac{\overline{OH_1}}{\overline{OP_1}} = \frac{\overline{OH_2}}{\overline{OP_2}} \Leftrightarrow \frac{\overline{OH_1}}{\overline{OH_2}} = \frac{\overline{OP_1}}{\overline{OP_2}}. \quad (\text{A.4})$$

Similarly, the right triangles  $OQ_1H_1$  and  $OQ_2H_2$  imply

$$\beta_1 = \beta_2 \Leftrightarrow \frac{\overline{OH_1}}{\overline{OQ_1}} = \sin \beta_1 = \sin \beta_2 = \frac{\overline{OH_2}}{\overline{OQ_2}} \quad (\text{A.5})$$

$$\Leftrightarrow \frac{\overline{OH_1}}{\overline{OH_2}} = \frac{\overline{OQ_1}}{\overline{OQ_2}}. \quad (\text{A.6})$$

Together, this results in the second equation of (A.1):

$$\frac{\overline{OP_1}}{\overline{OP_2}} = \frac{\overline{OQ_1}}{\overline{OQ_2}}. \quad (\text{A.7})$$

The first equation of the theorem can be derived by means of the line  $t'$  which is parallel to  $t$  in Fig. A.1(a). For this purpose,  $P_2$  is interpreted as the origin, so that (A.7) implies

$$\frac{\overline{P_2P_1}}{\overline{P_2O}} = \frac{\overline{P_2T'}}{\overline{P_2Q_2}} \Leftrightarrow \frac{\overline{P_2O} - \overline{OP_1}}{\overline{P_2O}} = \frac{\overline{P_2Q_2} - \overline{Q_2T'}}{\overline{P_2Q_2}} \quad (\text{A.8})$$

$$\Leftrightarrow \frac{\overline{Q_2T'}}{\overline{P_2Q_2}} = \frac{\overline{OP_1}}{\overline{P_2O}}. \quad (\text{A.9})$$

As  $P_1Q_1Q_2T'$  is a parallelogram,  $\overline{Q_2T'} = \overline{P_1Q_1}$  and the claim is proven,

$$\frac{\overline{P_1Q_1}}{\overline{P_2Q_2}} = \frac{\overline{OP_1}}{\overline{OP_2}}. \quad (\text{A.10})$$

■

## A.2

### A.2 Inverse problems

#### A.1

##### Definition A.1: Well-posed problem

A mathematical problem is called well-posed, according to the definition of Hadamard, if the following three conditions are satisfied [3]:

1. Existence: there exists a solution for the problem.
2. Uniqueness: the solution is unique.
3. Stability: the solution changes continuously with respect to the input data of the problem.

A problem is called ill-posed if one of these conditions is violated.  $\diamond$

Finding the inverse of a mapping  $f : X \rightarrow Y, y = f(x)$  with the domain  $X$  and the codomain  $Y$  represents an inverse problem. The quantity sought is  $x \in X$ . However, only  $y \in Y$  can be observed. An inverse problem is ill-posed if one of the following holds for the inverse mapping  $f^{-1}$ :

1.  $f^{-1}$  is not well-defined, i.e., there exists an  $y \in Y$  for which there is no preimage, so that  $f$  is not surjective.

2.  $x = f^{-1}(y)$  is not uniquely defined, i.e.,  $f$  is not injective.
3.  $f^{-1}$  is not continuous: a limited distance between the images  $y_1 = f(x_1)$  and  $y_2 = f(x_2)$ , i.e.,

$$\|y_1 - y_2\| < \delta \quad \text{with } \delta > 0 \text{ arbitrary,} \quad (\text{A.11})$$

does not imply that the distance between the preimages is limited, i.e., that

$$\|x_1 - x_2\| < \varepsilon \quad \text{with } \varepsilon > 0. \quad (\text{A.12})$$

Regularization methods can be used to solve an ill-posed problem by introducing additional constraints on the solution. These include assumptions, prior knowledge, or desired characteristics, so that a unique solution can be selected out of the manifold of possible solutions. In the field of automated visual and image processing, especially the following two regularization approaches are of greater importance:

- Uniqueness by additional measurements: by means of additional measurement data, a unique solution of an ambiguous inverse problem might be found. An example is the deflectometric reconstruction problem of Sec. 7.3.5, which is made unique by an additional measurement from another angle of view. Also the common intensity-based stereo evaluation can be interpreted in this way: because of the loss of information by the central projection, the reconstruction of the 3D structure from a single camera perspective presents an ill-posed problem. Only by adding an additional camera perspective is the calculation of the depth information possible.
- Continuous solution: demanding a continuous solution results in additional constraints, which contribute to a reduction of the manifold of the solutions. Continuity conditions can be formulated by means of energy functionals. This approach can be applied to different methods for 3D reconstruction, e.g., stereo, shape from shading, structured illumination (see Chap. 7), as well as to image segmentation (see Chap. 11). The additional continuity assumption is not necessarily satisfied by every object.

## A.3 Bibliography

- [1] Ilka Agricola and Thomas Friedrich. *Elementargeometrie: Fachwissen für Studium und Mathematikunterricht*. Vieweg+Teubner, 3rd edition, 2011.
- [2] Euklid. *Die Elemente*, volume 6. Herausgegeben von Clemens Thaer, Deutsch, 2nd edition, 1996.
- [3] Andreas Rieder. *Keine Probleme mit Inversen Problemen: Eine Einführung in ihre stabile Lösung*. Vieweg, 1st edition, 2003.





Appendix B  
**The Fourier Transform**

**B**

---

# B

## **B The Fourier Transform**

B.1	The one-dimensional Fourier transform . . . . .	761
B.1.1	Definition . . . . .	761
B.1.2	Properties and characteristics . . . . .	762
B.1.3	Correspondences . . . . .	763
B.2	The $n$ -dimensional Fourier transform . . . . .	765
B.2.1	Definition . . . . .	765
B.2.2	Correspondences of the two-dimensional Fourier transform . . . . .	765
B.3	The discrete Fourier transform . . . . .	766

## B The Fourier Transform

### B.1 The one-dimensional Fourier transform

#### 🔍 B.1.1 Definition

Definition:	$\mathcal{F}\{g(x)\} := \int_{-\infty}^{\infty} g(x) e^{-j2\pi fx} dx = G(f)$
-------------	---

Inversion:	$g(x) = \int_{-\infty}^{\infty} G(f) e^{j2\pi fx} df = \mathcal{F}^{-1}\{G(f)\}$
------------	--

Angular frequency:	$\omega = 2\pi f$
--------------------	-------------------

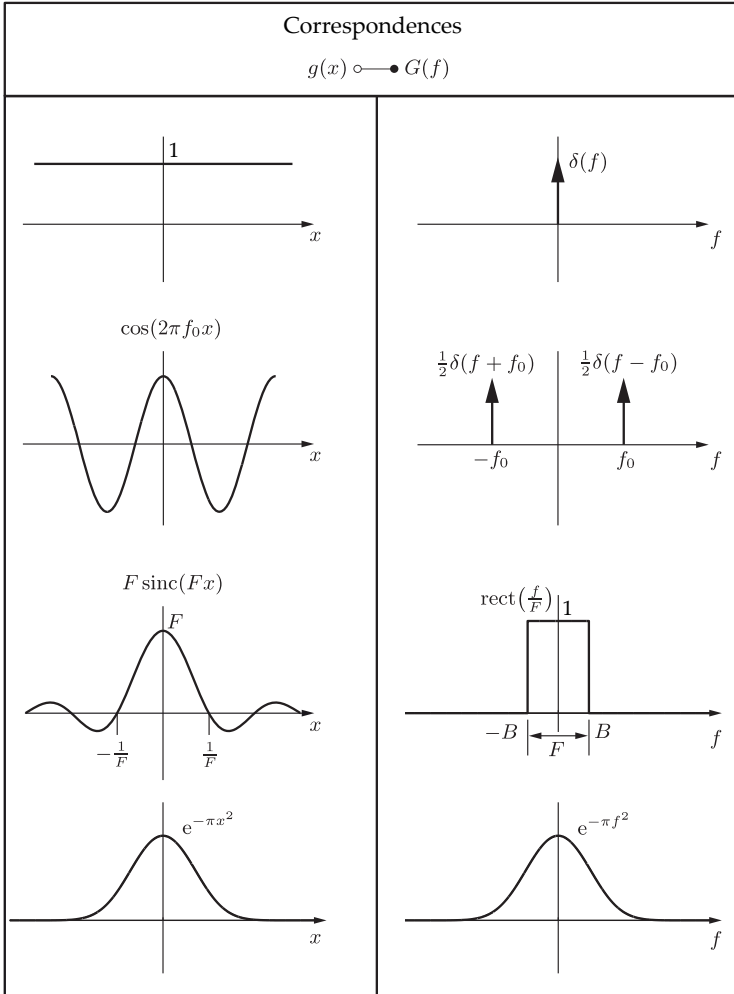
	$[x] = [f]^{-1}, \quad j = \sqrt{-1}$
--	---------------------------------------

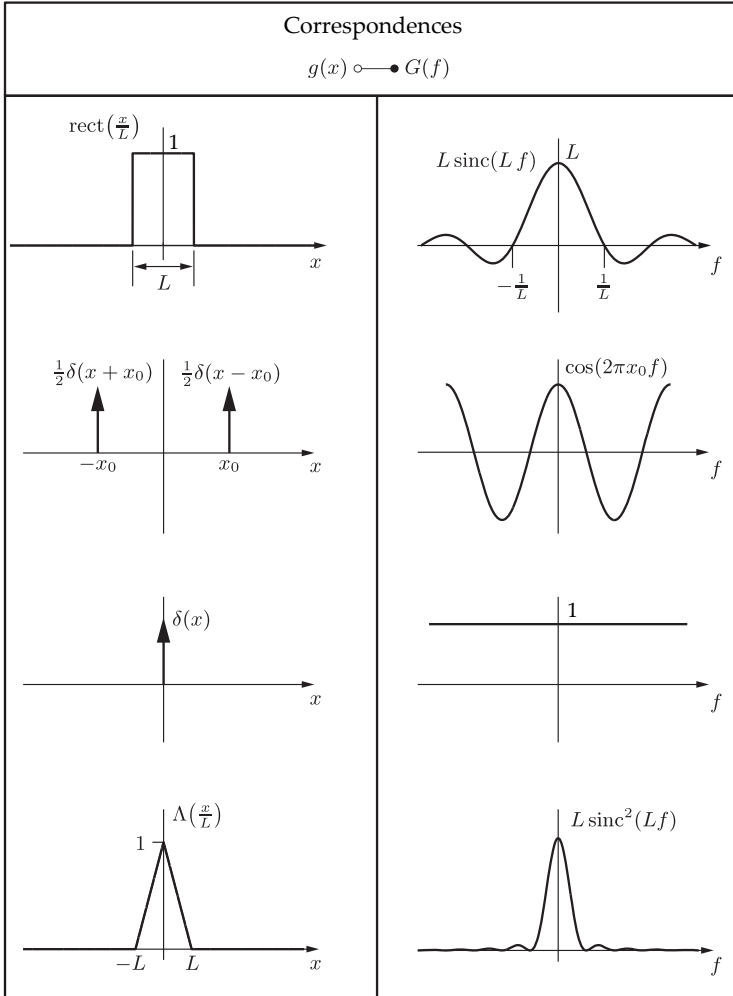
► **B.1.2 Properties and characteristics**

Properties and Characteristics	$g(x)$	○●	$G(f)$
Linearity	$a g_1(x) + b g_2(x)$	○●	$a G_1(f) + b G_2(f)$
Similarity theorem	$g(kx)$ with $k \in \mathbb{R} \setminus \{0\}$	○●	$ k ^{-1} G\left(\frac{f}{k}\right)$
Duality	$G(x)$	○●	$g(-f)$
	$G^*(x)$	○●	$g^*(f)$
Theorem of the conjugated complex-valued functions	$g^*(x)$	○●	$G^*(-f)$
Shift property	$g(x - x_0)$	○●	$G(f) e^{-j2\pi x_0 f}$
	$g(x) e^{j2\pi f_0 x}$	○●	$G(f - f_0)$
Derivative property	$\frac{dg(x)}{dx}$	○●	$j2\pi f G(f)$
	$-j2\pi x g(x)$	○●	$\frac{dG(f)}{df}$
Integration property	$\int_{-\infty}^x u(\tau) d\tau$	○●	$\left[\frac{1}{j2\pi f} + \frac{1}{2} \delta(f)\right] U(f)$
	$\left[\frac{-1}{j2\pi x} + \frac{1}{2} \delta(x)\right] u(x)$	○●	$\int_{-\infty}^f U(\varphi) d\varphi$
Convolution property	$g_1(x) * g_2(x)$	○●	$G_1(f) G_2(f)$
	$g_1(x) g_2(x)$	○●	$G_1(f) * G_2(f)$
Correlation property	$g_1(x) \otimes g_2(x)$	○●	$G_1(f) G_2^*(f)$
	$g_1(x) g_2^*(x)$	○●	$G_1(f) \otimes G_2(f)$
Assignment property	$\Re\{g_g(x)\}$	○●	$\Re\{G_g(f)\}$
	Index: $\Re\{g_u(x)\}$	○●	$j \Im\{G_u(f)\}$
	- g: even component $j \Im\{g_g(x)\}$	○●	$j \Re\{G_g(f)\}$
	- u: odd component $j \Im\{g_u(x)\}$	○●	$\Re\{G_u(f)\}$
Moments	$\int_{-\infty}^{\infty} x^\nu g(x) dx = (-j2\pi)^{-\nu} \frac{d^\nu G(f)}{df^\nu} \Big _{f=0}$		
	$(j2\pi)^{-\nu} \frac{d^\nu g(x)}{dx^\nu} \Big _{x=0} = \int_{-\infty}^{\infty} f^\nu G(f) df$		
Central ordinate theorem	$g(0) = \int_{-\infty}^{\infty} G(f) df$		$G(0) = \int_{-\infty}^{\infty} g(x) dx$
Plancherel's Theorem (Parseval's Theorem)	$\int_{-\infty}^{\infty} g_1(x) g_2^*(x) dx = \int_{-\infty}^{\infty} G_1(f) G_2^*(f) df$		
	$\int_{-\infty}^{\infty}  g(x) ^2 dx = \int_{-\infty}^{\infty}  G(f) ^2 df$		



➤ B.1.3 Correspondences





## B.2 The $n$ -dimensional Fourier transform

### B.2.1 Definition

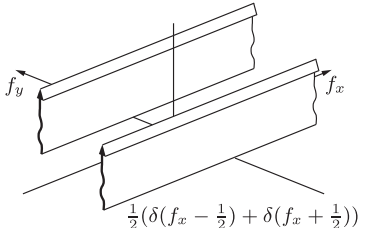
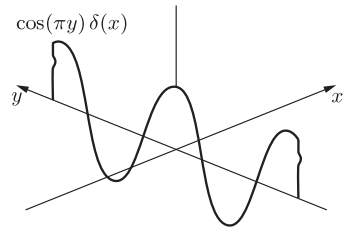
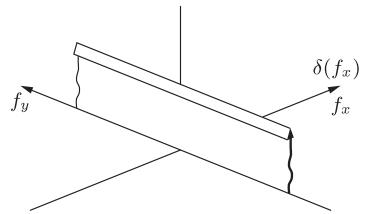
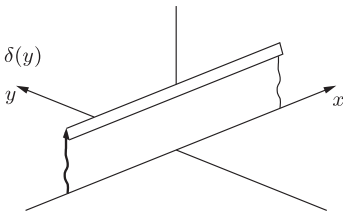
Definition: 
$$\mathcal{F}\{g(\mathbf{x})\} := \int_{-\infty}^{\infty} \dots \int_{-\infty}^{\infty} g(\mathbf{x}) e^{-j2\pi\mathbf{f}^T\mathbf{x}} d\mathbf{x} = G(\mathbf{f})$$

Inversion: 
$$g(\mathbf{x}) = \int_{-\infty}^{\infty} \dots \int_{-\infty}^{\infty} G(\mathbf{f}) e^{j2\pi\mathbf{f}^T\mathbf{x}} d\mathbf{f} = \mathcal{F}^{-1}\{G(\mathbf{f})\}$$

$$\mathbf{x} = (x_1, \dots, x_n)^T \in \mathbb{R}^n, \quad d\mathbf{x} = dx_1 dx_2 \dots dx_n$$

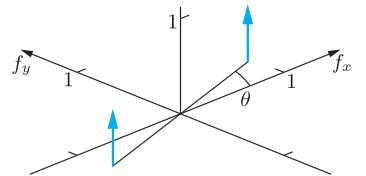
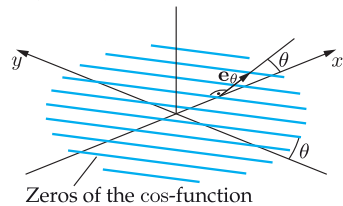
$$\mathbf{f} = (f_1, \dots, f_n)^T \in \mathbb{R}^n, \quad d\mathbf{f} = df_1 df_2 \dots df_n$$

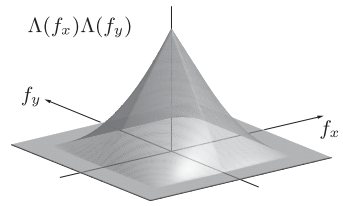
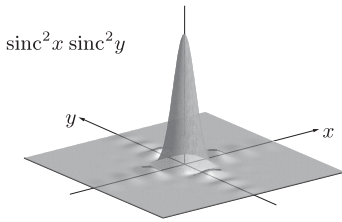
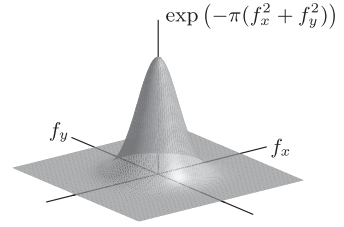
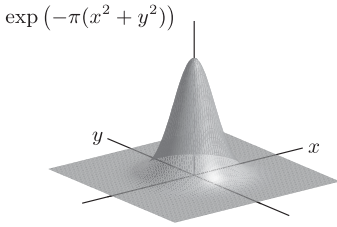
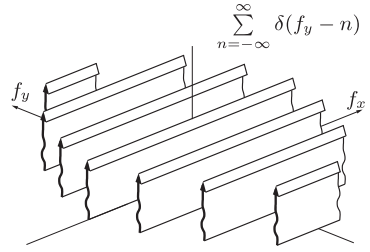
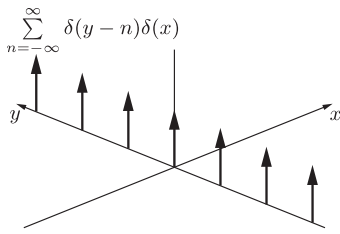
### B.2.2 Correspondences of the two-dimensional Fourier transform



$$\cos(2\pi \mathbf{e}_\theta^T \mathbf{x}) = \cos(2\pi(x \cos \theta + y \sin \theta))$$

$$\frac{1}{2} (\delta(\mathbf{x} + \mathbf{e}_\theta) + \delta(\mathbf{x} - \mathbf{e}_\theta))$$





**B.3 The discrete Fourier transform**

Definition:	$G_l := \sum_{n=0}^{N-1} g_n e^{-j2\pi \frac{ln}{N}}$	with	$g_n := g(n \Delta x) = g\left(\frac{n x_{\max}}{N}\right)$
Inversion:	$g_n = \frac{1}{N} \sum_{l=0}^{N-1} G_l e^{j2\pi \frac{ln}{N}}$		

## Picture Credits

---

Breitmeier Messtechnik GmbH, Ettlingen, Germany: Fig. 6.11

Phil Brodatz: Textures: Fig. 1.4, 13.2, 13.18(a)

German Aerospace Center (Deutsches Zentrum für Luft- und Raumfahrt e.V. - DLR), TerraSAR-X: Fig. 14.13(b)

Dr. Michael Fried, University of Erlangen, Germany: Fig. 11.27

AE Goetze GmbH, Burscheid, Germany: Honatlas: Fig. 13.3(a), 13.14(a), 13.15(a), 14.8(c), 14.15(a), 14.16(a)

Jan Horn, Department of Measurement and Control, Karlsruhe Institute of Technology, Germany: Fig. 10.4

inspectomation GmbH, Mannheim, Germany (former Hottinger Systems GmbH): Fig. 1.9, 3.19, 7.45, 7.73, 7.76, 7.124, 14.4, 14.5

Udo Netzelmann, Günter Walle, Fraunhofer Institute for Nondestructive Testing IZFP, Saarbrücken, Germany: Fig. 7.102

Arne Nowak, Fraunhofer Institute for Integrated Circuits IIS, Erlangen, Germany: Fig. 7.117

Dirk Nüßler, Fraunhofer Institute for High Frequency Physics and Radar Techniques FHR, Wachtberg, Germany: Fig. 7.111

ONUK Photography Bernhard Schmitt, Karlsruhe, Germany: Fig. 8.32(a), 8.51, 14.23(c)

Prof. Dr. Wolfgang Osten, ITO – Institute of Applied Optics, University of Stuttgart, Germany: Fig. 7.93, 7.95, 7.98, 7.99

Prof. Dr. Jerry Prince, Dr. Chenyang Xu: Fig. 11.24, 11.25

Dr. Andreas Purde, Chair in Measurement Systems and Sensor Technology, TU Munich: Fig. 15.4

Dr. Claudio Sedazzari, Opto Engineering srl, Mantova, Italien: Fig. 3.26

Erika Schneider: Fig. 11.1

Norman Uhlmann, Fraunhofer Development Center for X-ray Technology EZRT, Fürth, Germany: Fig. 7.105

Dirk vom Stein: Fig. 10.5, 13.10

Dr. Yaokun Zhang, Department of Intelligent Process Control and Robotics (IPR), Karlsruhe Institute of Technology, Germany: Fig. 7.107

## List of Symbols

### Conventions

$a, b, \dots$ $A, B, \dots$	identifiers
$x, y, \dots$ $A, B, \dots$	scalar variables (italic, lower-case, sometimes capital letters)
$\mathbf{x}, \mathbf{y}, \dots$ $\mathbf{A}, \mathbf{B}, \dots$	vectors (bold, lower-case, sometimes capital letters)
$\mathbf{A}, \mathbf{B}, \dots$	matrices; points (bold, capital letters)
$\mathcal{A}, \mathcal{B}, \dots$	sets
$\mathcal{A}\{\cdot\},$ $\mathcal{B}\{\cdot\}, \dots$	operators
$a, b, \dots$	random variables (typewriter font)

### Operators

$\dot{f}$	derivative of the function $f$ with respect to the time $t$	27
$\downarrow$	reduction step (multiresolution analysis)	724
$\uparrow$	expansion step (multiresolution analysis)	725
$\lfloor x \rfloor$	greatest integer $\leq x$	479
$\lceil x \rceil$	smallest integer $> x$	479
$g^*$	complex conjugation of $g$	388, 689, 729
$\overline{f(t)}$	temporal averaging	33, 47
$\angle \cdot$	argument (phase angle) of a complex-valued quantity or direction of a two-dimensional vector	384, 565
$ \cdot $	absolute value of a real-valued or complex-valued quantity	73, 384
$\ \cdot\ $	norm of a vector	27

$*$	convolution of one-dimensional signals	381, 401
$**$	convolution of two-dimensional signals	406
$\overset{x}{*}$	one-dimensional convolution of multi-dimensional signals with respect to the variable $x$	497
$g(x) \circ \bullet G(f)$	correspondence of the one-dimensional Fourier transform	383
$g(\mathbf{x}) \circ \bullet G(\mathbf{f})$	correspondence of the two-dimensional Fourier transform	402
$\mathbf{x}_1 \leftrightarrow \mathbf{x}_2$	corresponding image points	287
$\mathbf{a} \perp \mathbf{b}$	vector $\mathbf{a}$ is orthogonal to vector $\mathbf{b}$	28
$\propto$	proportionality	60
$\mathbf{a} \sim \mathcal{P}$	random variable $\mathbf{a}$ is distributed according to $\mathcal{P}$	64, 436
$\langle \cdot, \cdot \rangle$	inner product	691, 733
$\stackrel{!}{=}$	is supposed to be equal	392, 447
$a \in \mathcal{A}$	$a$ is element of the set $\mathcal{A}$	10
$\mathcal{A} \cap \mathcal{B}$	intersection of $\mathcal{A}$ and $\mathcal{B}$	130
$\mathcal{A} \cup \mathcal{B}$	union of $\mathcal{A}$ and $\mathcal{B}$	555
$\mathcal{A} \setminus \mathcal{B}$	difference of the sets $\mathcal{A}$ and $\mathcal{B}$	78, 595, 611
$\subset, \subseteq$	subset	10, 611
$\emptyset$	empty set	481
$\bar{\mathcal{G}}$	complement of the point set $\mathcal{G}$	611
$\mathcal{G}^R$	reflection of the point set $\mathcal{G}$	610
$(\mathcal{G})_{\mathbf{z}}$	shift of the point set by the vector $\mathbf{z}$	610
$\oplus$	direct sum of vector spaces	735
$\oplus$	morphological dilation	611, 637
$\ominus$	morphological erosion	611, 637
$\circ$	morphological opening	620, 641
$\bullet$	morphological closing	620, 641
$\otimes$	morphological hit-or-miss operator	626

$\ominus$	morphological thinning	627
$\odot$	morphological thickening	629
$\mathbf{0}$	zero-vector: $\mathbf{0} := (0, 0, \dots, 0)^T$	105
$1(x)$	function equal to 1: $1(x) \equiv 1$	52, 403
$\mathbf{1}$	$\mathbf{1} := (1, 1, \dots, 1)^T$	674
$\Delta \mathbf{F}$	Laplace operator, applied to a vector field $\mathbf{F}$	26, 580, 645
$\forall$	universal quantifier ('for all ...')	177
$\mathcal{A}\{\mathbf{G}\}$	focused optical imaging of the point $\mathbf{G}$ by the optical system $\mathcal{A}$	9, 99
$\arg \min$	argument of the minimum	232
$\frac{df}{dx}$	derivative of the function $f$ with respect to the variable $x$	27
$\frac{\partial f}{\partial x}$	partial derivative of the function $f$ with respect to the variable $x$	25
$\text{DFT}\{g_{mn}\}$	two-dimensional discrete Fourier transform of the discrete image signal $g_{mn}$	401
$\text{div } \mathbf{F}$	divergence of the vector field $\mathbf{F}$	25
$\text{E}\{\cdot\}$	expected value	61, 434, 654, 665
$\exists$	existential quantifier ('there exists a ...')	616
$\mathcal{F}\{g(\mathbf{x})\}$	Fourier transform of the function $g(\mathbf{x})$	51
$\text{grad } g(\mathbf{x})$	gradient of the function $g(\mathbf{x})$	564
$\Im\{\cdot\}$	imaginary part of a complex number	237
$\max$	maximum of a set or of a function	301
$\min$	minimum of a set or of a function	196
$\text{Pr}\{\cdot\}$	probability	61
$\mathcal{R}\{g(\mathbf{x})\}$	Radon transform of the image $g(\mathbf{x})$	699
$\Re\{\cdot\}$	real part of a complex number	29
$\text{rot } \mathbf{F}$	curl of the vector field $\mathbf{F}$	25
$\text{span}\{\cdot\}$	spanned vector space	653, 734



$\text{supp}\{\cdot\}$	support $\text{supp}\{G(\mathbf{f})\} := \{\mathbf{f} \mid  G(\mathbf{f})  > 0\}$	481, 653
$\mathcal{T}\{\cdot\}$	morphological top surface operator	636
$\mathcal{U}\{\cdot\}$	umbra operator	636
$\text{Var}\{\cdot\}$	variance	61, 434, 654

### Greek symbols

$\alpha$	quantum efficiency of an image sensor	63
$\alpha$	half of the lens' angular aperture	114, 121
$\Gamma_{p,\nu}$	wavelet coefficients	733, 738
$\Gamma_{\psi}(s, \tau)$	continuous wavelet transform	729
$\gamma_{mn}$	region of a two-dimensional signal in vector notation	664
$\delta$	penetration depth of electromagnetic waves in a conducting medium	78
$\delta$	optical path difference between the polarization components of an electromagnetic wave	32
$\delta(\cdot)$	Dirac delta function (Dirac distribution)	378
$\delta_i^k$	Kronecker symbol: $\delta_i^k := \begin{cases} 1 & \text{if } i = k \\ 0 & \text{if } i \neq k \end{cases}$	27
$\delta_{mn}$	two-dimensional, spatially discrete Dirac delta function	419
$\delta_n$	one-dimensional spatially discrete Dirac delta function	419
$\varepsilon$	diameter of the blur disk in the image plane	119
$\varepsilon$	permittivity	25
$\varepsilon_0$	permittivity of the vacuum (electric field constant), $\varepsilon_0 \approx 8,854 \cdot 10^{-12} \frac{\text{As}}{\text{Vm}}$	26
$\varepsilon_r$	relative permittivity	26
$\zeta$	length of the reference path of an interferometry setup	310
$H$	entropy	459

$\eta$	light yield	83
$\eta$	attenuation factor of electromagnetic waves in a conducting medium	77
$\theta(\mathbf{x})$	gradient direction at the pixel $\mathbf{x}$	589, 676
$\theta_1$	angle of incidence	67
$\theta$	triangulation angle	259
$\theta_{1B}$	Brewster's angle	74
$\theta_{1C}$	critical angle of incidence	75
$\theta_2$	refraction angle	69
$\theta_e$	angle between the emitted light and the surface normal	152
$\theta_i$	angle of incidence of the illuminating ray	152
$\theta_r$	emergent angle for specular reflection	67
$\Lambda(\frac{x}{B})$	triangle function: $\Lambda(\frac{x}{B}) := \begin{cases} 1 - \left  \frac{x}{B} \right  & \text{if }  x  < B \\ 0 & \text{otherwise} \end{cases}$	480
$\lambda$	wavelength of the light	23, 29
$\lambda_{mn}^\nu$	image signal on the $\nu$ th level of the Laplacian pyramid	726
$\mu$	magnetic permeability	25
$\mu_0$	permeability of the vacuum (magnetic field constant), $\mu_0 = 4\pi \cdot 10^{-7} \frac{\text{Vs}}{\text{Am}}$	26
$\mu_r$	relative permeability	26
$\nu$	frequency of an electromagnetic wave (light wave) in Hz	23, 29
$\nu$	shift parameter in multiresolution analysis	732
$\nu_{21}$	frequency of the light emitted during a transition from energy level $E_2$ to energy level $E_1$	90
$\Delta\nu$	frequency bandwidth	44, 91
$\rho$	reflection factor	152
$\rho$	electric charge density	25

$\Sigma$	set of structuring elements	627
$\sigma$	specific electrical conductance	25, 76
$\sigma^2$	variance	600, 664
$\tau$	shift parameter of the continuous wavelet transform	729
$\Phi$	radiant flux	145
$\Phi_1$	luminous flux	83, 145
$\varphi$	phase of an electromagnetic wave	29
$\varphi$	normal angle of a line	673, 699
$\varphi_{p,\nu}(x)$	scaling function of the multiresolution analysis	734
$\varphi_x, \varphi_y$	phase shift of an electromagnetic wave	31
$\chi$	ellipticity angle of the polarization ellipse	32
$\psi$	angle of the direction of the polarization ellipse	32
$\psi_{p,\nu}(x)$	wavelet function of the multiresolution analysis	733
$\psi_{s,\tau}(x)$	wavelet function of the continuous wavelet transform	729
$\Omega$	solid angle	145
$\Omega_g$	domain of the image $g$	10, 609
$\Omega_t$	domain of the texture $t(\mathbf{x})$	672
$\omega_i$	segment of an image	555
$\omega$	angular frequency of an electromagnetic wave	29

### Latin symbols

$A$	area of a pixel	63
$A(\mathbf{p})$	accumulator of the Hough transform	710, 711
$A_{\text{Col}}(\lambda)$	spectral absorption of a colorant layer	173
$\mathbf{A}$	transformation matrix for a linear color space transformation	176, 194

$a$	absorption coefficient of electromagnetic waves in a conducting medium	77
$a^*$	red-green chromaticity coordinate of the CIELAB color space	185
$a_{\text{Col}}(\lambda)$	constant of absorption of a colorant	173
$a_{kl}$	coefficient of the AR model	664
$\mathbf{a}$	vector of AR coefficients	664
$\mathbf{a}_1, \mathbf{a}_2$	alignment of a structural texture	653
$B$	image size	109
$B_{\text{CIE}}$	color value with respect to the blue CIE primary color	175
$B_{\mathbf{d}}(g, r)$	entry in the run-length histogram with respect to the direction $\mathbf{d}$ , the gray value $g$ and the the run-length $r$	677
$B_s$	blue coordinate of the linear sRGB color space	194
$B'_s$	blue coordinate of the gamma-corrected sRGB color space	195
$\mathbf{B}$	image point	109
$\mathbf{B}$	magnetic flux density	25
$BRDF$	bidirectional reflectance distribution function	152
$b$	image distance	61, 101, 109
$\bar{b}(\lambda)$	color value function of the blue CIE primary color	175
$b^*$	yellow-blue chromaticity coordinate of the CIELAB color space	185
$C$	cyan color value in the CMYK color space	197
$\Delta C$	difference of chroma	189
$C_{\text{ab}}$	chroma, based on the CIELAB color space	185
$C_{\text{B}}$	blue-yellow-chrominance in the $Y C_{\text{B}} C_{\text{R}}$ color space	197
$C_{p,\nu}$	coefficients of the rough structure in multiresolution analysis	734, 738

$C_R$	red-green-chrominance in the $YC_B C_R$ color space	197
$C_d$	co-occurrence matrix	673
$C_{gg}$	covariance matrix	456
$\mathbb{C}$	set of complex-valued numbers	77
$c$	speed of light in a vacuum, $c = 299\,792\,458$ m/s	23, 28
$c_{d,ij}$	entry of the co-occurrence matrix $C_d$	673
$c_{Col}$	concentration of a colorant	173
const.	arbitrary, but fixed constant	27
$D$	aperture diameter (more precisely: diameter of the entrance pupil)	61, 103, 110, 117
$\mathbf{D}$	diffusion tensor	579
$\mathbf{D}$	electric flux density	25
$d$	negative imaginary part of the complex refraction index	77
$d_K$	coherence length	44
$d_{Col}$	thickness of a colorant layer	173
$d_p(x)$	detail signal in multiresolution analysis	736
$\mathbf{d}$	shift vector of the co-occurrence matrix	673
$\det \mathbf{A}$	determinant of the matrix $\mathbf{A}$	288
$E$	amplitude of the electric field strength	27
$E$	energy	63
$E$	irradiance	148
$E_1$	illuminance	148
$\Delta E$	color distance	189
$E\{\cdot\}$	energy functional	588
$E_{0x}, E_{0y}$	amplitude of the polarized electromagnetic wave in $x$ -direction and $y$ -direction	31
$E_i$	$i$ th energy level of an atom	90
$E^s, E^p$	electric field strength perpendicular or parallel to the incidence plane	71

$\mathbf{E}$	electric field strength	25
$\mathbf{E}$	Jones vector	43
$\underline{\mathbf{E}}(\mathbf{x}, t)$	complex wave function of the electric field	29
$\mathcal{E}(\omega)$	uniformity criterion for segments	555
$\mathbf{e}_{mn}$	zero-mean, weakly stationary noise signal in the AR model	664
$\mathbf{e}_\varphi$	two-dimensional unit vector in the direction of $\varphi$ : $\mathbf{e}_\varphi = (\cos \varphi, \sin \varphi)^T$	407, 699
$\mathbf{e}_{\varphi\perp}$	two-dimensional unit vector perpendicular to $\mathbf{e}_\varphi$ : $\mathbf{e}_{\varphi\perp} = (-\sin \varphi, \cos \varphi)^T$	407
$\mathbf{e}_x, \mathbf{e}_y, \mathbf{e}_z$	standard basis vectors	30
$\exp(x)$	exponential function, $\exp(x) = e^x$	80
$\mathbf{F}$	fundamental matrix of a stereo camera setup	287
$\mathbf{F}$	force	588
$f$	focal length	106, 108
$f_\gamma(\cdot)$	gamma correction	193
$f_{\gamma, I_0}(\cdot)$	modified gamma correction	193, 195
$G$	object size	109
$G_{\text{CIE}}$	color value with respect to the green CIE primary color	175
$G_{kl}$	two-dimensional discrete Fourier transform of the discrete image signal $g_{mn}$	416
$G_s$	green coordinate of the linear sRGB color space	194
$G'_s$	green coordinate of the gamma-corrected sRGB color space	195
$\mathcal{G}$	point set of a binary image	609
$\mathbf{G}$	object point	109
$g$	object distance	109
$\Delta g$	depth of field	120

$g(\mathbf{x})$	scalar image, e.g., gray-scale image	10, 63
$g(x; p)$	approximation of the signal $g(x)$ on level $p$ on the multiresolution analysis	734
$\bar{g}(\lambda)$	color value function of the green CIE primary color	175
$\tilde{g}(u, \varphi)$	Radon transform of the image $g(\mathbf{x})$	699
$g_{mn}^\nu$	image signal on the $\nu$ th level of the (Gaussian) pyramid	723
$\mathbf{g}(\mathbf{x})$	multi-channel image, e.g., color image	10
$\mathbf{g}_{mn}$	discrete image signal	10, 373, 664
$H$	radiant exposure	149
$H_1$	luminous exposure	149
$\Delta H$	difference of hue	189
$H(x)$	Heaviside function	380
$H_{\text{HSI}}$	hue in the HSI color space	196
$H_\theta(k)$	histogram of oriented gradients	677
$\mathbf{H}$	magnetic field strength	25
$\underline{\mathbf{H}}(\mathbf{x}, t)$	complex wave function of the magnetic field	29
$h$	height difference, layer thickness	230, 260
$h$	Planck's constant, $h \approx 6,626 \cdot 10^{-34}$ Js	23, 63
$\Delta h$	difference of hue angle	190
$h(\mathbf{x})$	background signal in the image	666, 687
$h_{\text{ab}}$	hue angle in the CIELAB color space	185
$h_\nu$	impulse response of the low-pass filter in the multiresolution analysis	733, 739
$h_\sigma(\mathbf{x})$	Gaussian low-pass	500, 570
$I$	intensity of electromagnetic radiation	31
$I$	number of segments of an image	555
$I$	electric current	83, 210
$I$	radiant intensity	146

$I_l$	luminous intensity	146
$I_A(\lambda)$	spectrum of the CIE standard illuminant A (incandescent lamp)	187
$I_{D65}(\lambda)$	spectrum of the CIE standard illuminant D65 (daylight)	187
$I_E(\lambda)$	spectrum of the CIE standard illuminant E (constant intensity)	175
$I_{HSI}$	intensity in the HSI color space	196
$J_n(z)$	Bessel function of the $n$ th kind	56
<b>J</b>	Jones matrix	43
<b>J</b>	electric current density	25
$j$	imaginary unit	29
$K$	number of quantization steps of the image signal	10, 446
$K$	dimension of the feature space $\mathcal{M}$	556
$K$	black color value in the CMYK color space	197
$K_m$	constant of the photometric base system, $K_m = 683 \frac{\text{lm}}{\text{W}}$	166
$k$	wave number	29
$k$	Boltzmann constant, $k \approx 1,38 \cdot 10^{-23} \text{ J/K}$	80
$k$	scaling factor for the calculation of the normalized color values	178
$k(\mathbf{x})$	result of a (detection) filter	492, 688
$k_\nu$	impulse response of the high-pass filter in multiresolution analysis	735, 739
<b>k</b>	wave vector	29
$L$	radiance	80, 147
$L_l$	luminance	147
$\Delta L^*$	difference of brightness	189
$L^2(\cdot)$	space of the quadratically integrable functions	595, 736
$L_{LQ}^i$	radiance emitted by a light source	151



$L_{OF}^j$	radiance emitted by the object surface (light field, plenoptic function)	151
$L^*$	brightness coordinate of the CIELAB color space	185
$l(\mathbf{x}^T \mathbf{e} - d)$	line as an element of a texture	663, 667
$M$	width of the image (number of columns)	10
$M$	magenta color value in the CMYK color space	197
$\mathbf{M}$	Mueller matrix	36
$\mathcal{M}$	feature space	556
$m_1$	empirical average	672
$\mathbf{m}(\mathbf{x})$	feature vector for the segment classification at the image point $\mathbf{x}$	556
$(m, n)$	discrete image coordinates	10
$N$	height of the image (number of lines or rows)	10
$N_4(\mathbf{x}),$ $N_8(\mathbf{x})$	4-neighborhood, respectively, 8-neighborhood	599
$N_i$	occupation number of the energy level $E_i$	90
$\mathbb{N}$	set of natural numbers (non-negative integers)	386
$NA$	numerical aperture	121
$n$	photon count	63
$n$	refraction index (real-valued)	28, 68
$\underline{n}$	complex refraction index	77
$\mathbf{n}$	normal vector of a surface	67
$\mathcal{N}(\mu, \sigma^2)$	(Gaussian) normal distribution with expected value $\mu$ and variance $\sigma^2$	436
$O$	f-number	61, 117
$O(\mathbf{f})$	Fourier transform of the object signal	689
$\mathcal{O}(f(N))$	function class of asymptotic upper bounds (Big O notation): $\mathcal{O}(f(N)) := \{g(N) \mid \exists c > 0, N_0 > 0 \forall N \geq N_0 \ g(N) \leq c \cdot f(N)\}$	568, 723
$o(\mathbf{x})$	object signal in the image	687

$P$	electric power	83
$\underline{P}(x, y)$	complex aperture function	49
$\hat{P}_i$	entry of the histogram	467, 560
$\mathbf{P}$	projection matrix of the camera model	104
$\mathbf{P}$	Poynting vector of an electromagnetic wave	30
$p$	scale parameter in multiresolution analysis	732
$p$	degree of polarization of an electromagnetic wave	35
$Q$	number of image channels	10
$Q$	radiant energy	149
$Q_1$	luminous energy	149
$q(\mathbf{x})$	texel	653
$R$	surface roughness	61
$R$	ohmic resistance	89, 210
$R_{\text{CIE}}$	color value with respect to the red CIE primary color	175
$R_i$	region in the feature space	556
$R^{ij}$	reflection function of the object surface	151, 186
$R_s$	red coordinate of the linear sRGB color space	194
$R'_s$	red coordinate of the gamma-corrected sRGB color space	195
$R_{12}^s, R_{12}^p$	Fresnel reflectance for light polarized perpendicularly or parallel to the incidence plane	73
$\mathbf{R}_{\text{nn}}$	correlation matrix	544
$\mathbb{R}$	set of real-valued numbers	10
$\bar{r}(\lambda)$	color value function of the red CIE primary color	175
$r_{gg}(\tau)$	autocorrelation function of the stationary stochastic process $g(\mathbf{x})$	437
$r_{gk}(\mathbf{x}, \tau)$	cross-correlation of the stochastic processes $g$ and $k$	435

$r_{12}^s, r_{12}^p$	Fresnel coefficients of reflection for light polarized perpendicularly or parallel to the incidence plane	72
$\text{rect}\left(\frac{x}{\varepsilon}\right)$	rectangular function: $\text{rect}\left(\frac{x}{\varepsilon}\right) := \begin{cases} 1 & \text{if }  x  < \frac{\varepsilon}{2} \\ 0 & \text{otherwise} \end{cases}$	52, 379
$\text{rnd}(\cdot)$	rounding to the next integer	710
$S_{\text{Col}}(\lambda)$	spectral scatter of a colorant layer	173
$S_{gg}(\mathbf{f})$	power spectral density of the stationary stochastic process $g(\mathbf{x})$	438
$S_{\text{HSI}}$	saturation in the HSI color space	196
$S$	point set of a binary structuring element	610
$S_{\text{ER}}$	point set of the binary cross	610
$\mathbf{S}$	Stokes vector, Stokes parameters: $\mathbf{S} = (S_0, S_1, S_2, S_3)^T$	33
$SNR$	signal-to-noise ratio	64, 492, 691
$\text{trace}(\mathbf{A})$	trace of the matrix $\mathbf{A}$ (sum of the diagonal elements)	340
$s$	scale parameter of the continuous wavelet transform	729
$s(\mathbf{x})$	structuring element in gray-scale morphology	636
$s^2$	empirical variance	672
$\text{sinc}(\cdot)$	cardinal sine function: $\text{sinc}(x) := \frac{\sin(\pi x)}{\pi x}$	52, 390
$\text{sgn}(\cdot)$	sign function: $\text{sgn}(x) := \begin{cases} 1 & x > 0 \\ 0 & x = 0 \\ -1 & x < 0 \end{cases}$	705
$T$	exposure time	63
$T$	temperature	80, 83
$T_{12}^s, T_{12}^p$	Fresnel transmittance for light polarized perpendicularly or parallel to the incidence plane	73
$t$	time	25

$t(\mathbf{x})$	image of a texture	653
$t_{12}^s, t_{12}^p$	Fresnel coefficients of transmission for light polarized perpendicularly or parallel to the incidence plane	72
$U$	blue-yellow-chrominance in the YUV color space	197
$U$	electric voltage	83, 210
$U_N$	nominal voltage	83
$\mathcal{U}$	umbra	634
$\mathcal{U}$	neighborhood of the origin	485, 664, 693
$u(\mathbf{x}, t)$	diffused image signal	580
$V$	magnification of an optical imaging	101
$V$	contrast (visibility) of an interference pattern	48
$V$	red-green-chrominance in the YUV color space	197
$V(\lambda)$	luminosity function of the human eye for photopic vision	165, 177
$V'(\lambda)$	luminosity function of the human eye for scotopic vision	165
$V(\mathbf{f})$	transfer function of a detection filter	689
$V_p$	function space in multiresolution analysis	734
$v$	propagation velocity (phase velocity) of an electromagnetic wave	27, 68
$v(\mathbf{x})$	impulse response of a detection filter	688
$\mathbf{v}(s)$	active contour as a parametric curve	588
$W_p$	wavelet space	735
$w(\cdot)$	two times differentiable function in the solution of the wave equation	27, 29
$w(\mathbf{x})$	whitening filter	692
$X$	CIE tristimulus value with respect to the virtual primary color $X$	176
$\mathbf{X}_{\text{prim}}$	basis vector of the virtual primary color $X$	178

$x$	normalized color value $x$ in the CIE chromaticity diagram	179
$\bar{x}(\lambda)$	CIE color matching function of the virtual primary color $X$	176
$\mathbf{x}$	three-dimensional position of an electromagnetic wave	27
$\mathbf{x}$	continuous image coordinates: $\mathbf{x} = (x, y)^T \in \mathbb{R}^2$	10
$\mathbf{x}'$	homogeneous coordinates: $\mathbf{x}' = (x'_1, \dots, x'_N, w)^T$	102
$\mathbf{x}_c$	camera coordinates: $\mathbf{x}_c = (x_c, y_c, z_c)^T$	101
$\mathbf{x}_w$	world coordinates: $\mathbf{x}_w = (x_w, y_w, z_w)^T$	103
$Y$	CIE tristimulus value with respect to the virtual primary color $Y$	176
$Y$	yellow color value in the CMYK color space	197
$Y'$	gamma-corrected brightness in technical color spaces	197
$\mathbf{Y}_{\text{prim}}$	basis vector of the virtual primary color $Y$	178
$y$	normalized color value $y$ in the CIE chromaticity diagram	179
$\bar{y}(\lambda)$	CIE color matching function of the virtual primary color $Y$	176
$Z$	CIE tristimulus value with respect to the virtual primary color $Z$	176
$Z$	durability of a light source	83
$Z$	wave impedance	27
$\mathbf{Z}_{\text{prim}}$	basis vector of the virtual primary color $Z$	178
$\mathbb{Z}$	set of integers	10
$z$	CIE normalized color value $z$	179
$z(\mathbf{x})$	surface relief	263
$\bar{z}(\lambda)$	CIE color matching function of the virtual primary color $Z$	176

## List of Abbreviations

ACF	autocorrelation function	434
A/D	analog/digital	205
AR	autoregressive	480, 663
ARMA	autoregressive moving average	480
AS	aperture stop	110, 114
BP	band-pass	506
BRDF	bidirectional reflectance distribution function	152
BS	band-stop	506
CCD	charge coupled device	211
CCF	cross-correlation function	435
CCT	confocal chromatic triangulation	307
CIE	Commission Internationale de l'Éclairage	173
CMOS	complementary metal oxide semiconductor	213
CT	computed tomography	329, 700
CW	continuous wave	334
DFT	discrete Fourier transform	396
DoG	difference of Gaussians	574
EM	expectation-maximization	560
EnP	entrance pupil	115
EnW	entrance window	115
ExP	exit pupil	115
ExW	exit window	115
FDM	finite difference method	591
FEM	finite element method	591
FFT	fast Fourier transform	400
FIR	far infrared	217
FS	field stop	114

GVF	gradient vector flow	591
HDRC	high dynamic range CMOS	214
HP	high-pass	506
IC	integrated circuit	213
IFFT	inverse fast Fourier transform	400
IR	infrared	24
JPEG	Joint Photographic Experts Group	195
KLT	Karhunen-Loève transform	456
LBP	local binary pattern	680
LED	light emitting diode	86
lidar	light detection and ranging	308
LoG	Laplacian of Gaussian	573
LP	low-pass	425
LSI	linear, shift-invariant	382
LWIR	long-wavelength infrared	217
MA	moving average	480
MLA	micro-lens array	292
MRF	Markov random field	480
MRT	magnetic resonance tomography	329, 555
MSE	mean squared error	544
MWIR	medium-wavelength infrared	217
NA	numerical aperture	121
Nd-YAG	neodymium-doped yttrium aluminum garnet	92
NETD	noise equivalent temperature difference	217
NIR	near infrared	217
OCT	optical coherence tomography	330
OLED	organic light emitting diode	87
OTF	optical transfer function	406
PCA	photoconductive antenna	334

PCA	principal component analysis	456
PCB	printed circuit board	133
PDF	probability density function	449
PSD	position sensitive detector	210
PSF	point spread function	406
QWP	quarterwave plate ( $\frac{\lambda}{4}$ -retardation plate)	39
radar	radiowave detection and ranging	308
SAR	synthetic aperture radar	705
SIFT	scale-invariant feature transform	744
SNR	signal-to-noise ratio	64, 492, 691
SURF	speeded up robust features	744
SWIR	short-wavelength infrared	217
TCS	telecentric stop	280
THz	terahertz	24, 332
UV	ultraviolet	24
VFC	vector field convolution	593
WLI	white light interferometry	313
w.l.o.g.	without loss of generality	31
WP	waveplate / retardation plate	40



## Index

### Symbols

$\delta$ -function ..... *see* Dirac delta function  
 $\frac{\lambda}{4}$ -plate ..... 39  
 4-connected neighborhood ..... 599  
 8-connected neighborhood ..... 599

### A

aberration ..... 133  
   chromatic ..... 136  
   Seidel ..... 133  
   spherical ..... 133  
 absorption ..... 67, 77, 172  
 absorption coefficient ..... 77  
 absorption filters ..... 198  
 absorptivity ..... 321  
 achromat ..... 136  
 active contours ..... 586  
 activity  
   optical ..... 37  
 Airy disk ..... 57, 423  
 albedo ..... 154  
 aliasing ..... 397  
 amplitude ..... 27  
 analog to digital converter ..... 205  
 anamorphic ..... 346  
 angle  
   critical ..... 75  
   of aperture ..... 114  
   of incidence ..... 68, 69  
   of reflection ..... 68  
   of refraction ..... 69  
 angular frequency ..... 29  
 angular wave number ..... 29  
 antenna  
   photoconductive ..... 334  
 anti-aliasing filter ..... 393, 426  
 aperture stop ..... 110, 114  
 apochromat ..... 136  
 AR model ..... 663, 697  
 area sensor ..... 205  
 astigmatism ..... 133  
 autocorrelation function ..... 434, 654, 672  
   of a stochastic process ..... 434  
 autocovariance function  
   of a stochastic process ..... 435  
 autofocus sensor ..... 303  
 autoregressive model ..... 663, 697  
 average ..... 672  
 axis

  optical ..... 107

### B

Babinet's principle ..... 57, 347  
 band-pass ..... 506  
 band-stop ..... 506  
 bandgap ..... 87, 208  
 beam splitter ..... 243  
   dichroic ..... 216  
 Beucher gradient ..... 645  
 bicubic interpolation ..... 477  
 bidirectional reflectance distribution function ..... 152  
 bilateral filter ..... 514  
 bilinear interpolation ..... 477, 478  
 binary image ..... 609  
 binary morphology ..... 609  
 binomial filter ..... 501  
 binomial low-pass ..... 501  
 birefringence ..... 38, 338  
 black top-hat ..... 642  
 blackbody ..... 80  
 bolometer ..... 217, 335  
 Boltzmann statistics ..... 209  
 Boltzmann's constant ..... 80  
 border extraction ..... 623  
 BRDF ..... 152  
 bremsstrahlung ..... 84  
 Brewster's angle ..... 74  
 bundle adjustment ..... 290

### C

calculus of variations ..... 589  
 camera calibration ..... 103, 104, 135  
 camera coordinate system ..... 101  
 camera matrix ..... 104  
 Canny ..... 571  
 Canny operator ..... 629  
 cardinal sine function ..... *see* sinc function  
 CCD camera ..... 211  
 central moment ..... 434  
 central ordinate theorem ..... 387  
 cepstrum ..... 660  
 characteristic function ..... 451  
 charge density ..... 25  
 chroma ..... 185, 196  
 chromaticity coordinates ..... 179  
 chromaticity diagram ..... 181  
 CIE ..... 173  
 CIE chromaticity diagram ..... 181

- CIE primary light source ..... 174  
 CIE XYZ color space ..... 176  
 CIELAB color space ..... 184  
 classification ..... 557  
 closing  
     binary morphology ..... 620  
     gray-scale morphology ..... 641  
 clustering ..... 556  
 CMOS cameras ..... 213  
 CMYK color space ..... 172, 197  
 co-occurrence matrix ..... 673  
 coefficient of reflection ..... 72  
 coefficient of transmission ..... 72  
 coherence ..... 44  
 coherence length ..... 44, 262, 313, 430  
 coherence tomography  
     optical ..... 330  
 coherent ..... 35  
 color ..... 167  
 color balance ..... 171  
 color camera ..... 215  
 color difference ..... 188  
 color filter ..... 198  
 color image ..... 10, 199  
 color matching functions ..... 176  
 color mixing ..... 171  
     additive ..... 171, 181  
     inner ..... 171  
     outer ..... 171  
     subtractive ..... 172  
 color order system ..... 191  
 color profile ..... 198  
 color solid ..... 186  
 color stimulus ..... 170  
 color temperature ..... 81, 186  
 color value ..... 174  
 colorant ..... 172  
 colored noise ..... 442  
 colorimetry ..... 173  
 coma ..... 133  
 complement  
     point set ..... 611  
 complementary colors ..... 182  
 component labeling ..... 624  
 compressed sensing ..... 335  
 Compton scattering ..... 328  
 computed tomography ..... *see* tomography  
 condenser ..... *see* tomography 138  
 conductance ..... 25  
 conduction band ..... 208  
 conductivity ..... 76  
 cone low-pass ..... 500  
 cones ..... 167  
 confocal microscopy ..... 305  
 connected component analysis ..... 624  
 conservation of energy ..... 389  
 constraint filters ..... 523  
 contours  
     active ..... 586  
 contrast ..... 48  
 contrast adjustment ..... 467  
 converging lens ..... 108, 112  
 convolution ..... 381  
     two-dimensional ..... 406  
 convolution theorem ..... 386, 406  
 corner ..... 715  
 corner detection ..... 715  
 correlation filter ..... 689–691, 707  
 correlation length ..... 672  
 correlation matrix ..... 544, 694  
 correspondence problem ..... 286  
 $\cos^4$  law ..... 160  
 covariance matrix ..... 456  
 cross section ..... 86  
 cross-correlation function ..... 435  
     of two stochastic processes ..... 435  
 current density ..... 25  
 cut ..... 597  
     graph  $\sim$  ..... 597  
     minimum  $\sim$  ..... 597
- D**
- dark current ..... 219  
 dark field illumination ..... 352  
 Daubechies filter ..... 741  
 Daubechies wavelets ..... 739  
 daylight ..... 186  
 defect detection ..... 655  
 deflectometry ..... 268  
 demosaicing ..... 216  
 depth of field ..... 117, 295  
 descriptor ..... 744  
 detection ..... 687  
     photon ..... 206, 207  
 detectors  
     balanced ..... 335  
 DFT ..... *see* discrete Fourier transform  
 dielectric ..... 26  
 dielectric constant ..... 25  
 dielectrics ..... 25  
 difference  
     point sets ..... 611  
 Difference-of-Gaussians operator ..... 574  
 differentiation theorem ..... 386

- diffraction ..... 48  
 diffraction limited ..... 60, 137  
 diffusion ..... 578  
   anisotropic ..... 581  
   homogeneous ..... 579  
   inhomogeneous ..... 580  
   isotropic ..... 579  
   linear ..... 579  
   nonlinear ..... 581  
 diffusion equation ..... 322, 579  
 diffusion filters ..... 578  
 diffusion tensor ..... 579  
 digitization ..... 373  
 dilation  
   binary morphology ..... 611  
   gray-scale morphology ..... 637  
 Dirac comb ..... *see* impulse train  
 Dirac delta function ..... 378  
   approximation ..... 378  
   characteristics ..... 379  
   formulas ..... 380  
   similarity transformation ..... 380  
   two-dimensional ..... 408  
 direct component ..... 388  
 direction ..... 581  
 discrete Fourier transform ..... 396  
   two-dimensional ..... 415  
 discretization of function values ..... 373, 374, 376  
 disparity ..... 285  
 dispersion ..... 70, 136  
 displacement law  
   Wien's ..... 81  
 dissipation ..... 67  
 distortion ..... 134  
 distribution ..... 378  
 DoG ..... 574  
 doping ..... 87, 208  
 Doppler broadening ..... 84  
 dye ..... 172
- E**
- edge ..... 563  
 edge detection ..... 563  
 edge potential ..... 589  
 eigenvalue problem ..... 456  
 eight-point algorithm ..... 289  
 electric field constant ..... 26  
 electric field strength ..... 25  
 electric flux density ..... 25  
 electrical ballast ..... 86  
 electroluminescence ..... 83  
 electron-hole pair ..... 208
- elementary charge ..... 325  
 ellipsometry ..... 234  
   imaging ..... 237  
   null ..... 235  
   spectroscopic ..... 239  
 emission  
   stimulated ..... 89  
   thermal ..... 80  
 emissivity ..... 321  
 end effect ..... 401, 417  
 energy ..... 389  
 energy density ..... 389  
 energy flux ..... 30  
 energy functional ..... 587, 594  
 energy signal ..... 389  
 entocentric ..... 126  
 entrance pupil ..... 115, 117  
 entrance window ..... 115  
 entropy ..... 459  
 epipolar geometry ..... 267  
 epipolar line ..... 286  
 epipolar plane ..... 286  
 epipole ..... 287  
 equilibrium of forces ..... 590  
 ergodicity ..... 437  
   strict ..... 437  
   weak ..... 437  
 erosion  
   binary morphology ..... 611  
   gray-scale morphology ..... 637  
 Euler's formula ..... 29, 383  
 Euler-Lagrange differential equation ..... 590  
 exit pupil ..... 115  
 exit window ..... 115  
 expansion ..... 724  
 expected value ..... 434, 451, 654  
   of a random variable ..... 451  
 exponentiation ..... 377  
 eye ..... 167
- F**
- f*-number ..... 61, 117  
 Fabry-Pérot interferometer ..... 91  
 false-color image ..... 472, 473  
 far-field diffraction ..... 48  
 fast Fourier transform ..... *see* FFT  
 FDM ..... 591  
 FEM ..... 338, 591  
 Fermat's principle ..... 100  
 FFT ..... 400  
 Fick's law ..... 579  
 fickle ..... 188

- field stop ..... 114  
fill factor ..... 213, 219  
filter  
    linear ..... 491  
    optical ..... 198  
filter bank ..... 733, 738  
filter transformations ..... 506  
filters based on order statistics ..... 513  
finite difference method ..... 591  
finite element method ..... 338, 591  
flatbed scanner ..... 248  
flow ..... 597  
    maximum ~ ..... 598  
flow network ..... 596  
fluorescence ..... 240  
fluorescence spectroscopy ..... 240  
fluorescent lamp ..... 85  
focal length ..... 108  
focal ratio ..... 117  
focus length ..... 111  
focus series ..... 304  
four color process ..... 198  
Fourier slice theorem ..... 702  
Fourier spectrum ..... 383  
Fourier transform ..... 383  
    central ordinate theorem ..... 387  
    convolution theorem ..... 386, 406  
    differentiation theorem ..... 386  
    discrete ..... 396  
    linear coordinate transformation ..... 404  
    linearity ..... 385  
    modulation property ..... 387  
    real-valued signals ..... 388  
    reciprocity ..... 385  
    reflection ..... 388  
    scaling property ..... 385  
    separation theorem ..... 403  
    shift property ..... 387  
fovea ..... 167  
fractional power filter ..... 689  
Fraunhofer diffraction ..... 48  
freespace electrooptic sampling ..... 335  
frequency ..... 29  
    instantaneous ..... 281  
frequency bandwidth ..... 44  
Fresnel coefficient of reflection ..... 72  
Fresnel coefficient of transmission ..... 72  
Fresnel diffraction ..... 48  
full well capacity ..... 219  
full-frame sensors ..... 213  
fundamental law of photometry ..... 148  
fundamental law of radiometry ..... 148  
fundamental matrix ..... 286, 288
- G**
- gamma correction ..... 193, 194  
gamut ..... 193  
gas-discharge lamp ..... 83  
Gaussian filter ..... 500  
Gaussian function ..... 392  
Gaussian low-pass ..... 500  
Gaussian optics ..... 108  
generalized harmonic analysis ..... 439  
geometric mean filter ..... 523, 538  
geometric rectification ..... 476  
Gibbs phenomenon ..... 505  
gradient filters ..... 564  
gradient vector flow ..... 591  
gradient-of-Gaussian filter ..... 570  
graph cut methods ..... 599  
Grassmann's laws ..... 171  
gray-scale image ..... 10  
gray-scale morphology ..... 634  
groove texture ..... 653, 661
- H**
- Haar wavelet ..... 736  
halogen lamp ..... 81  
Hann window ..... 399  
Haralick features ..... 675  
harmonic analysis ..... 439  
Harris operator ..... 716  
HDRC sensor ..... 214  
heat equation ..... 322  
heat radiation ..... 321  
heat transfer ..... 322, 578  
heat transfer thermography ..... 322  
Heaviside function ..... 380  
Helmholtz reciprocity principle ..... 153  
high dynamic range CMOS ..... 214  
high pressure discharge lamp ..... 83  
high-pass ..... 506  
histogram ..... 467, 672  
histogram equalization ..... 470  
histogram manipulation ..... 469  
histogram of oriented gradients ..... 676  
histogram stretching ..... 467  
hit-or-miss operator ..... 626  
HLS color space ..... 196  
hologram ..... 317  
holography ..... 317  
homocentric ..... 107  
homogeneity ..... 480, 481, 579  
homogeneous coordinates ..... 102

- homogenization ..... 480, 481, 485
  - homomorphic filtering ..... 480, 483
  - honing texture ..... 661, 665, 672
  - Hottelling transform ..... 455
  - Hough transform ..... 710
    - circles ..... 712
    - curves ..... 711
    - ellipses ..... 712
    - generalized ..... 714
    - lines ..... 710, 712
  - HSI color space ..... 195
  - HSL color space ..... 196
  - HSV color space ..... 196
  - hue ..... 181, 195
  - hue angle ..... 185
  - Huygens' principle ..... 67
  - hypercentric ..... 127
  - hyperspectral image ..... 10, 602
- I**
- ideal modulator ..... 377
  - illuminance ..... 148
  - illusion
    - optical ..... 4
  - image ..... 9
    - real ..... 112
    - virtual ..... 112
  - image coordinates ..... 101
  - image distance ..... 100, 108
  - image field curvature ..... 134
  - image fusion ..... 307, 456
  - image intensifier ..... 207
  - image pyramid ..... *see* pyramid
  - image restoration ..... 523
    - for participating media ..... 546
    - spatially-varying ..... 548
  - image sensor ..... 205
  - image sharpening ..... 474
  - image size ..... 108
  - image tube camera ..... 206
  - image value ..... 10
  - imaging
    - optical ..... 99
    - telecentric ..... 123
  - immersion bath ..... 347
  - implicit shape models ..... 715
  - impulse correlation ..... 441
  - impulse response ..... 382
  - impulse train ..... 392, 393, 397, 410, 411
  - incandescent lamp ..... 81
  - index of refraction ..... 68, 331
    - complex ..... 230
  - infrared ..... 24, 216, 250
  - integral image ..... 747
  - intensity
    - electromagnetic radiation ..... 30
    - HSI color space ..... 195
  - intercept theorem ..... 66
  - interference ..... 46, 309
  - interference filters ..... 198
  - interferometry ..... 309
  - interline-transfer sensor ..... 213
  - interpolation
    - bilinear ..... 478
    - pyramid ..... 724
    - system theory ..... 479
  - inverse filter ..... 523, 690
  - irradiance ..... 148
  - isochromate ..... 341
  - isocline ..... 341
  - isolators ..... 25
  - isotropy ..... 579
- J**
- Jones calculus ..... 42
  - Jones matrix ..... 43
  - Jones vector ..... 43
  - JPEG standard ..... 195, 197
- K**
- Karhunen–Loève transform ..... 455
    - best linear approximation ..... 459
    - invertibility ..... 457
    - linearity ..... 457
    - orthogonality ..... 457
    - uncorrelation ..... 457, 458
    - zero-mean ..... 457
  - keypoints ..... 744
  - Kirchhoff's law ..... 321
  - Kronecker delta ..... 467
  - Kubelka–Munk theory ..... 173
- L**
- label ..... 624
  - Lambert–Beer law of absorption ..... 172, 328
  - Laplace filter ..... 573
  - Laplace operator
    - morphological ..... 645
  - Laplacian-of-Gaussian operator ..... 573
  - laser ..... 89, 93, 255
  - laser scanner ..... 246
  - law of reflection ..... 67
  - law of refraction
    - Snell's ..... 69

- Laws matrices ..... 678  
 Laws' texture energy measures ..... 678  
 LBP ..... *see* local binary patterns  
 LED ..... 86  
 lens ..... 106  
   concave ..... 112  
   convex ..... 112  
   spherical ..... 108  
   thick ..... 111  
 level set method ..... 595  
 lidar sensor ..... 308  
 light bundle ..... 114  
 light detection and ranging ..... 308  
 light field ..... 152, 291  
 light quanta ..... 23  
 light ray ..... 28  
 light-emitting diode ..... 86  
 light-field camera ..... 291  
 line of purples ..... 181  
 line potential ..... 589  
 line scan camera ..... 602  
 line textures ..... 666  
 line-scan camera ..... 215, 248  
 line-scan sensor ..... 205  
 linear coordinate transformation ..... 404  
 linear filter ..... 491  
 linearity ..... 374, 579  
 local binary patterns ..... 680, 717  
 local spatial frequency ..... 281  
 lock-in thermography ..... 325  
 LoG ..... 573  
 longshot ..... 121  
 low pressure discharge lamp ..... 85  
 low-pass  
   binomial filter ..... 501  
   Gaussian filter ..... 500  
   ideal ..... 505  
 low-pass filter ..... 496  
 LSI system ..... 381  
 luminance ..... 147  
 luminescent material ..... 85  
 luminescent radiator ..... 80  
 luminosity function ..... 165  
 luminous energy ..... 149  
 luminous exposure ..... 149  
 luminous flux ..... 145  
 luminous intensity ..... 146  
 luminous paint ..... 241
- M**
- macro shot ..... 122  
 magnetic field constant ..... 26  
 magnetic field strength ..... 25  
 magnetic flux density ..... 25  
 magnification ..... 102  
 magnifiers ..... 112  
 magnitude spectrum ..... 384, 387, 388, 451  
 marginal ray ..... 116  
 matched filter ..... 690–692  
 material classification ..... 230, 557  
 material sorting ..... 230, 602  
 maximum norm ..... 572  
 Maxwell vector ..... 43  
 Maxwell's equations ..... 24  
 mean power ..... 438  
 measurement uncertainty ..... 327  
 median ..... 509  
 median filter ..... 509  
 medium  
   active ..... 90  
   metameric ..... 170, 187  
   metamerism ..... 170, 181, 187  
   metamerism index ..... 190  
   micro-channel plate ..... 207  
   microscope ..... 121, 138  
     confocal ..... 305  
     depth of field ..... 122  
   microscope image ..... 122  
 microwaves ..... 24  
 Minkowski addition ..... 611  
 Minkowski subtraction ..... 611  
 mirror ..... 107, 112, 246  
   semi-transparent ..... 243  
 modulation property ..... 387  
 moiré method ..... 276, 278  
 moment ..... 434, 451, 672  
   of a random variable ..... 451  
   of a stochastic process ..... 434  
 monochromatic ..... 174  
 morphology ..... 609  
 moving average ..... 377, 497  
 Mueller matrix ..... 36  
 multiresolution analysis ..... 723, 733  
 multispectral image ..... 10  
 Mumford–Shah functional ..... 594  
 Munsell color order system ..... 191
- N**
- Nd:YAG-lasers ..... 91  
 near-field diffraction ..... 48  
 nearest neighbor interpolation ..... 477  
 negative lenses ..... 112  
 neighborhood ..... 498, 509, 599  
   causal ..... 664

- neodymium-YAG-laser ..... 91  
NETD ..... 217  
Nipkow disk ..... 305  
noise reduction ..... 491, 509  
normal field ..... 273  
normal vector ..... 67  
normalization ..... 467  
normalized color values ..... 179  
 $n$ th order statistic ..... 433, 654  
numerical aperture ..... 121, 138  
Nyquist band ..... 397
- O**
- object distance ..... 108  
objective lens ..... 106, 138  
ocular ..... 138  
OLED ..... 87  
opaque ..... 102  
opening  
    binary morphology ..... 620  
    gray-scale morphology ..... 641  
operator ..... 374  
opponent-process theory ..... 184  
optical coherence tomography ..... 330  
optical rectification ..... 334  
optical transfer function ..... 406  
optimum filter ..... 690, 691  
order of interference ..... 313  
orientation ..... 582
- P**
- PAL television color encoding system ..... 197  
parallax ..... 285  
parameterized Wiener filter ..... 538  
pattern generator ..... 268  
penetration depth ..... 78  
periodogram ..... 445  
permeability ..... 25  
permittivity ..... 25  
perspective ..... 125  
    entocentric ..... 126  
    hypercentric ..... 127  
    telecentric ..... 123, 127  
phase spectrum ..... 384, 388  
phase unwrapping ..... 313  
phase velocity ..... 27  
phase-only filter ..... 690  
phosphorescence ..... 241  
phosphorescent paint ..... 241  
photoconductive antenna ..... 334  
photodiode ..... 207  
photoelasticity ..... 338  
photoelectric effect ..... 206  
    inner ..... 208  
photometric base system ..... 166  
photometric stereo ..... 301  
photometry ..... 145, 165  
photomultiplier ..... 206  
photon ..... 23, 62  
photon energy ..... 333  
photon flux ..... 145  
photopic vision ..... 165  
picket-fence effect ..... 397  
pigment ..... 172  
pinhole camera ..... 100  
pixel ..... 10, 205  
Plancherel theorem ..... 389  
Planck's constant ..... 23, 63  
Planck's law ..... 80  
plane of incidence ..... 71  
plenoptic camera ..... 291  
plenoptic function ..... 152  
Poincaré sphere ..... 35  
point sensor ..... 205, 207  
point spread function ..... 406  
Poisson distribution ..... 64  
polariscope ..... 340  
polarization ..... 31, 234  
polarization ellipse ..... 32  
polarizer ..... 36  
population inversion ..... 90  
position sensitive detector ..... 210  
positive lens ..... 112  
power spectral density ..... 438  
Poynting vector ..... 30  
primary colors ..... 173  
    virtual ..... 176, 177  
principal component analysis ..... 455  
principal plane ..... 108, 111  
principal ray ..... 110, 116  
project execution ..... 15  
projection matrix ..... 104  
projection moiré ..... 284  
projector ..... 137  
pruning ..... 632  
pseudo-color image ..... 462, 472  
pseudo-edge ..... 563  
pulse thermography ..... 324  
push broom ..... 249  
pyramid ..... 723  
    Gaussian ..... 725  
    Laplacian ..... 726  
pyramid linking ..... 727

**Q**

quantization	23, 445
equidistant	448
modeling of the	453
optimal	446
quantization frequency	452
quantization mean	454
quantization noise	455
quantization theorem	448, 449, 453
quantizer	446
quantum efficiency	63, 208, 219
quarter-wave plate	39

**R**

radiance	147
radiant energy	149
radiant exposure	149
radiant flux	145
radiant intensity	146
radiation physics	145
radiative recombination	84
radiator	
blackbody	80, 166
gray-body	81
thermal	321, 334
radiometry	145
Radon transform	699
random process	432
range images	10
rank filters	509
rate of photons	206
Rayleigh criterion	58
reconstruction problem	285
rectangular function	378, 379
rectangular pulse	<i>see</i> rectangular function
reduction	724
reflectance	
Lambertian	153
specular	154
reflected	67
reflection	388
point set	610
reflectometry	230
refraction	68
region filling	624
region growing methods	562
relaxation	91
resolution	58, 335
resonator	
optical	91
retardation plate	38

retroreflector	298, 300
RGB color space	193
ringing	505
Roberts operator	572
rods	167
Roesch color solid	186
rotation	404
roughness	60, 155
run-length analysis	677

**S**

sagittal plane	133
salt-and-pepper noise	503
sample function	432
sampling	393
optimal	413
sampling theorem	393
SAR	705
saturation	181, 195
scale-invariant feature transform	744
scaling function	733
scaling property	385
scattered light	70
scattering	155, 173
scattering angle	251
Scheimpflug condition	130, 255
schlieren imaging	331
schlieren stop	332
schlieren tomography	331
scintillation	329
scotopic vision	165
segmentation	
complete	555
edge-oriented	562
region-based	556
semiconductor	86
semiconductor element	207
sensor	205
separation theorem	403
seven-point algorithm	289
shadow moiré	283
shape from shading	301
shear	404
shearography	315
shift	
point set	610
shift invariance	377
shift property	387
shift registers	211
shrinking	404
shutter	213
Siemens star	426



- SIFT ..... 715, 744
- signal ..... 374, 377
- signal energy ..... 389
- sinc function ..... 390
- single-pixel camera ..... 338
- skeletonization ..... 630
- slice function ..... 407
- spatially discrete ..... 419
- slide projector ..... 138
- snake ..... 587
- Sobel filters ..... 572
- Sobel operator ..... 572
- solid angle ..... 145
- sorting of bulk goods ..... 352, 602
- sorting of materials ..... 352
- space-charge region ..... 211
- Sparrow's resolution limit ..... 60
- spatial discretization ..... 373–375
- spatial scaling ..... 385
- specific electrical conductance ..... 25
- speckle ..... 60
- spectral analysis ..... 439
- spectral color ..... 174, 181
- spectral filters ..... 198
- spectral leakage ..... 397, 398
- spectrometer ..... 185
- spectrophotometry ..... 185
- spectrum
- electromagnetic ..... 23, 167
- Fourier ..... 383
- infrared ..... 217
- speeded up robust features ..... 744
- sRGB color space ..... 194
- stationarity ..... 436
- strict ..... 436
- weak ..... 437
- Stefan–Boltzmann law ..... 81
- step edges ..... 563
- stereo
- photometric ..... 301
- stereo imaging ..... 285
- stochastic process ..... 432
- stress tensor ..... 339
- stretching ..... 404
- structure from motion ..... 291
- structure tensor ..... 582, 672
- structured illumination ..... 263
- structuring element ..... 610
- submillimeter band ..... 333
- SURF ..... 715, 744, 746
- surrounding ..... 694
- synthesis of textures ..... 655
- synthetic aperture radar ..... 705
- system ..... 374, 377
- deterministic ..... 374
- hypercentric ..... 127
- linear ..... 374
- memoryless ..... 377
- non-reactive ..... 374
- shift invariant ..... 377
- telecentric ..... 124
- system characteristics ..... 374
- T**
- tangential plane ..... 133
- telecentric ..... 127
- telecentric stop ..... 123
- telephoto lens ..... 110
- television signals ..... 196
- terahertz gap ..... 333
- terahertz radiation ..... *see* THz radiation
- termination potential ..... 589
- texel ..... 653
- texture ..... 651
- anisotropic ..... 672, 676
- classification ..... 655
- isotropic ..... 672
- parameter estimation ..... 655
- segmentation ..... 655
- separation ..... 655
- statistical ..... 654
- structural ..... 653, 656
- structural-statistical ..... 653, 660
- texture element ..... 653
- texture separation ..... 666
- texture type ..... 653
- the Schwarz inequality ..... 691
- thermal imaging camera ..... 321
- thermal radiator ..... 80
- thermographic camera ..... 216
- thermography ..... 321
- thickening ..... 629
- thin lens equation ..... 109
- thinning ..... 627
- threshold ..... 557, 698
- THz radiation ..... 24, 217, 332
- detection ..... 334
- generating ..... 334
- tilt-shift lens ..... 132
- time of flight ..... 308
- tomography ..... 329, 331, 700
- top operation
- morphology ..... 636
- total internal reflection ..... 75

- total reflection ..... 326  
transmission ..... 66  
transversality ..... 28, 30  
triangular function ..... 480  
triangulation ..... 255  
trifocal tensor ..... 290  
trimmed mean filter ..... 513  
tristimulus ..... 170, 173  
tristimulus values ..... 176, 178  
tube length ..... 139  
two-scale relation ..... 733, 734  
Twyman–Green interferometer ..... 311
- U**
- ultraviolet ..... 24, 241  
umbra ..... 636  
uncertainty principle ..... 422  
unit step function ..... 380
- V**
- valence band ..... 208  
value ..... 196  
variance ..... 434, 654, 672  
vector field convolution ..... 593  
vector morphology ..... 635  
velocity of light ..... 308  
Verdet convention ..... 79  
video projector ..... 138, 263, 348, 353  
vignetting ..... 117  
visibility ..... 48  
visual inspection ..... 3
- W**
- watershed transformation ..... 578  
wave  
    harmonic ..... 29  
    plane ..... 27, 28  
    standing ..... 91  
wave equation ..... 26, 76  
wave number ..... 29  
wave vector ..... 29  
wave–particle duality ..... 23  
wavelength ..... 29  
    complementary ..... 181  
    dominant ..... 181  
wavelet crime ..... 739  
wavelet space ..... 735  
wavelet transform ..... 728  
    continuous ..... 728  
    discretization ..... 731  
    fast ..... 738  
wavenumber ..... 77  
weak ergodicity ..... 437  
weak stationarity ..... 437  
white balance ..... 171  
white light interferometry ..... 313, 330  
white noise ..... 441  
white point ..... 181  
white top-hat ..... 642  
whitening filter ..... 692, 695  
wide-angle lens ..... 110  
Wiener filter ..... 523  
    parameterized ..... 538  
Wiener–Khinchin theorem ..... 438, 439  
window function ..... 399  
Wollaston prism ..... 335
- X**
- X-ray ..... 241, 325  
xenon short-arc lamp ..... 85
- Y**
- YCbCr color space ..... 197  
YIQ color space ..... 197  
YUV color space ..... 197
- Z**
- Z-transform ..... 506  
zero padding ..... 417  
zoom lens ..... 110